

Randall Allemang · James De Clerck  
Christopher Niezrecki · Alfred Wicks *Editors*

# Topics in Modal Analysis, Volume 7

Proceedings of the 31<sup>st</sup> IMAC, A Conference  
on Structural Dynamics, 2013



# Conference Proceedings of the Society for Experimental Mechanics Series

*Series Editor*

Tom Proulx

Society for Experimental Mechanics, Inc.,

Bethel, CT, USA

For further volumes:

<http://www.springer.com/series/8922>



Randall Allemang • James De Clerck • Christopher Niezrecki • Alfred Wicks  
Editors

# Topics in Modal Analysis, Volume 7

Proceedings of the 31st IMAC, A Conference  
on Structural Dynamics, 2013

*Editors*

Randall Allemang  
University of Cincinnati  
Cincinnati, OH, USA

James De Clerck  
The Enterprise Program  
Michigan Technological University  
Houghton, MI, USA

Christopher Niezrecki  
Department of Mechanical Engineering  
University of Massachusetts Lowell  
Lowell, MI, USA

Alfred Wicks  
Department of Mechanical Engineering  
Virginia Polytechnic Institute and State University  
Blacksburg, VA, USA

ISSN 2191-5644                      ISSN 2191-5652 (electronic)  
ISBN 978-1-4614-6584-3            ISBN 978-1-4614-6585-0 (eBook)  
DOI 10.1007/978-1-4614-6585-0  
Springer New York Heidelberg Dordrecht London

Library of Congress Control Number: 2013941353

© The Society for Experimental Mechanics 2014

This work is subject to copyright. All rights are reserved by the Publisher, whether the whole or part of the material is concerned, specifically the rights of translation, reprinting, reuse of illustrations, recitation, broadcasting, reproduction on microfilms or in any other physical way, and transmission or information storage and retrieval, electronic adaptation, computer software, or by similar or dissimilar methodology now known or hereafter developed. Exempted from this legal reservation are brief excerpts in connection with reviews or scholarly analysis or material supplied specifically for the purpose of being entered and executed on a computer system, for exclusive use by the purchaser of the work. Duplication of this publication or parts thereof is permitted only under the provisions of the Copyright Law of the Publisher's location, in its current version, and permission for use must always be obtained from Springer. Permissions for use may be obtained through RightsLink at the Copyright Clearance Center. Violations are liable to prosecution under the respective Copyright Law.

The use of general descriptive names, registered names, trademarks, service marks, etc. in this publication does not imply, even in the absence of a specific statement, that such names are exempt from the relevant protective laws and regulations and therefore free for general use.

While the advice and information in this book are believed to be true and accurate at the date of publication, neither the authors nor the editors nor the publisher can accept any legal responsibility for any errors or omissions that may be made. The publisher makes no warranty, express or implied, with respect to the material contained herein.

Printed on acid-free paper

Springer is part of Springer Science+Business Media ([www.springer.com](http://www.springer.com))

# Preface

*Topics in Modal Analysis, Volume 7*: Proceedings of the 31st IMAC, A Conference on Structural Dynamics, 2013 represents one of seven volumes of technical papers presented at the 31st IMAC, A Conference and Exposition on Structural Dynamics, 2013 organized by the Society for Experimental Mechanics, and held in Garden Grove, California February 11–14, 2013. The full proceedings also include volumes on Nonlinear Dynamics; Experimental Dynamics Substructuring; Dynamics of Bridges; Dynamics of Civil Structures; Model Validation and Uncertainty Quantification; and, Special Topics in Structural Dynamics.

Each collection presents early findings from experimental and computational investigations on an important area within Structural Dynamics. Modal Analysis continues to be the core around which IMAC is built. The topics presented in this volume represent the state of the art in Modal Analysis as well as the latest advances in this area.

The organizers would like to thank the authors, presenters, session organizers, and session chairs for their participation in this track.

Cincinnati, OH, USA  
Houghton, MI, USA  
Lowell, MI, USA  
Blacksburg, VA, USA

Randall Allemang  
James De Clerck  
Christopher Niezrecki  
Alfred Wicks



# Contents

<b>1</b>	<b>Damage Detection Using Flexibility Proportional Coordinate Modal Assurance Criterion</b> .....	<b>1</b>
	Luciana Balsamo, Suparno Mukhopadhyay, Raimondo Betti, and Hilmi Lus	
<b>2</b>	<b>Automated Selection of Damage Detection Features by Genetic Programming</b> .....	<b>9</b>
	Dustin Harvey and Michael Todd	
<b>3</b>	<b>Optimal Selection of Artificial Boundary Conditions for Model Update and Damage Detection – Part 1: Theory</b> .....	<b>17</b>
	Joshua H. Gordis and L.T. Konstantinos Papagiannakis	
<b>4</b>	<b>Optimal Selection of Artificial Boundary Conditions for Model Update and Damage Detection – Part 2: Experiment</b> .....	<b>37</b>
	Joshua H. Gordis	
<b>5</b>	<b>Detection of Mass Change on a Glass Plate</b> .....	<b>61</b>
	Jannick B. Hansen, Rune Brincker, and Manuel L. Aenlle	
<b>6</b>	<b>Vibro-Acoustic Research on a Full-Scale Aircraft Structure</b> .....	<b>67</b>
	Christian Koehne, Delf Sachau, and Mirko Schaedlich	
<b>7</b>	<b>Control of Dynamic Mass as Boundary Condition for Testing Substructures</b> .....	<b>77</b>
	Manuel Baschke, Michael Krepl, and Delf Sachau	
<b>8</b>	<b>Multi-body-Simulation of a Self Adaptive Torsional Vibration Absorber</b> .....	<b>85</b>
	Delf Sachau and Jonas Hanselka	
<b>9</b>	<b>Combined Optimization of Actuator/Sensor Positions and Weighting Matrices for an Active Noise Reduction System</b> .....	<b>93</b>
	Jan Foht and Delf Sachau	
<b>10</b>	<b>SSDI Technique Evolution to Improve Attenuation Performances with Random Disturbances</b> .....	<b>99</b>
	M. Berardengo, S. Manzoni, M. Redaelli, and M. Vanali	
<b>11</b>	<b>Geometrically Nonlinear Dynamic Analysis of Piezoelectric Integrated Thin-Walled Smart Structures</b> .....	<b>107</b>
	S.Q. Zhang and R. Schmidt	
<b>12</b>	<b>Linear/Nonlinear Reduced-Order Substructuring for Uncertainty Quantification and Predictive Accuracy Assessment</b> .....	<b>117</b>
	Timothy Hasselman, George Lloyd, and Ryan Schnalzer	
<b>13</b>	<b>Damage Detection in an Energy Flow Model Including Parameter Uncertainty</b> .....	<b>131</b>
	Marcela Rodrigues Machado and Jose Maria Campos Dos Santos	
<b>14</b>	<b>A Coupled Approach for Structural Damage Detection with Incomplete Measurements</b> .....	<b>141</b>
	George James, Tim Cao, Mo Kaouk, and David Zimmerman	
<b>15</b>	<b>Efficient and Robust Solution of Inverse Structural Dynamic Problems for Vibration Health Monitoring</b> ..	<b>155</b>
	Keng C. Yap	



<b>16</b>	<b>Finite Element-Based Damage Detection Using Expanded Ritz Vector Residuals</b> .....	167
	Stuart G. Taylor, George Khoury, Michael D. Todd, and David C. Zimmerman	
<b>17</b>	<b>Proportional Damping from Experimental Data</b> .....	179
	Brian Schwarz and Mark Richardson	
<b>18</b>	<b>Superior Damping of Hybrid Carbon Fiber Composites Grafted by ZnO Nanorods</b> .....	187
	A. Alipour Skandani, N. Masghouni, and M. Al-Haik	
<b>19</b>	<b>Advanced Identification Techniques for Operational Wind Turbine Data</b> .....	195
	Simone Manzato, Jonathan R. White, Bruce LeBlanc, Bart Peeters, and Karl Janssens	
<b>20</b>	<b>Tracking and Removing Modulated Harmonic Components with Spectral Kurtosis and Kalman Filters</b> ...	211
	Jean-Luc Dion, Cyrille Stephan, Gaël Chevallier, and Hugo Festjens	
<b>21</b>	<b>Vibration Reduction of Brush Cutter</b> .....	225
	Nobuyuki Okubo, Hiroyuki Nakagawa, Kohei Furuya, and Takeshi Toi	
<b>22</b>	<b>Design of a Test Setup for Measuring Dynamic Stiffness of Vibration Isolators</b> .....	235
	Canan Uz, Gokhan O. Ozgen, and Ender Cigeroglu	
<b>23</b>	<b>An Impact Excitation System for Repeatable, High-Bandwidth Modal Testing of Miniature Structures</b> .....	249
	Bekir Bediz, Emrullah Korkmaz, and O. Burak Ozdoganlar	
<b>24</b>	<b>Replicating Aerodynamic Excitation in the Laboratory</b> .....	259
	P.M. Daborn, P.R. Ind, and D.J. Ewins	
<b>25</b>	<b>A Systematic Approach to Modal Testing of Nonlinear Structures</b> .....	273
	A. delli Carri and D.J. Ewins	
<b>26</b>	<b>Fiber Optics Sensing of Stressing and Fracture in Cylindrical Structures</b> .....	287
	Shen-en Chen, Benjamin Smith, and Peng Wang	
<b>27</b>	<b>Real-Time Damage Identification in Nonlinear Smart Structures Using Hyperchaotic Excitation and Stochastic Estimation</b> .....	295
	Shahab Torkamani, Eric A. Butcher, and Michael D. Todd	
<b>28</b>	<b>Damage Detection Based on Electromechanical Impedance Principle and Principal Components</b> .....	307
	Mario Anderson de Oliveira, Jozue Vieira Filho, Vicente Lopes Jr., and Daniel J. Inman	
<b>29</b>	<b>Enhanced Modal Wavelet Analysis for Damage Detection in Beams</b> .....	317
	Mario Algaba, Mario Solís, and Pedro Galvín	
<b>30</b>	<b>Linear Projection Techniques in Damage Detection Under a Changing Environment</b> .....	325
	Salma Mozaffari Kojidi, Michael Döhler, Dionisio Bernal, and Yang Liu	
<b>31</b>	<b>Modal Reduction Based on Accurate Input-Output Relation Preservation</b> .....	333
	M. Khorsand Vakilzadeh, S. Rahrovani, and T. Abrahamsson	
<b>32</b>	<b>Fast Precise Algorithm of Computing FRF by Considering Initial Response</b> .....	343
	J.M. Liu, W.D. Zhu, M. Ying, and S. Shen	
<b>33</b>	<b>Development of Full Space System Model Modes from Expansion of Reduced Order Component Modal Information</b> .....	353
	Christopher Nonis, Louis Thibault, Timothy Marinone, and Peter Avitabile	
<b>34</b>	<b>Damage Localization from the Image of Changes in Flexibility</b> .....	369
	Dionisio Bernal	
<b>35</b>	<b>Spectral Element Method for Cable Harnessed Structure</b> .....	377
	Jiduck Choi and Daniel J. Inman	

<b>36 Analytic Formula Derivation for a Rolling Tire with a Ring Model</b> .....	389
Jongsuh Lee, Peter Kindt, Bert Pluymers, Paul Sas, and Semyung Wang	
<b>37 Nonlinear Identification of the Viscous Damping of the Resistor for Nuclear Plants</b> .....	397
Giancarlo Galli, Francesco Braghin, and Edoardo Sabbioni	
<b>38 Effect of Spin Speed on Stability Lobes in High Speed Machining</b> .....	407
Hasan Yılmaz and Ender Cigeroglu	
<b>39 Chatter Reduction in Turning by Using Piezoelectric Shunt Circuits</b> .....	415
Ufuk Yigit, Ender Cigeroglu, and Erhan Budak	
<b>40 Damage Quantification from the Column Space of Flexibility Changes</b> .....	421
Dionisio Bernal	
<b>41 State Estimate of Wind Turbine Blades Using Geometrically Exact Beam Theory</b> .....	427
Stuart G. Taylor, Darby J. Luscher, and Michael D. Todd	
<b>42 Damage Index Matrix: A Novel Damage Identification Method Using Hilbert-Huang Transformation</b> .....	439
Ali Zarafshan and Farhad Ansari	
<b>43 An Approach to the Moving Load Problem for Multiple Cracked Beam</b> .....	451
N.T. Khiem, T.H. Tran, and N.V. Quang	
<b>44 Detection of Structural Damage Through Nonlinear Identification by Using Modal Testing</b> .....	461
Murat Aykan and H. Nevzat Özgüven	
<b>45 Vibration Fatigue Analysis of a Cantilever Beam Using Different Fatigue Theories</b> .....	471
Yusuf Eldoğan and Ender Cigeroglu	
<b>46 Automated Modal Analysis Based on Statistical Evaluation of Frequency Responses</b> .....	479
Vahid Yaghoubi and Thomas Abrahamsson	
<b>47 The Modal Observability Correlation as a Modal Correlation Metric</b> .....	487
Vahid Yaghoubi and Thomas Abrahamsson	
<b>48 A Modal Test Method Based on Vibro-acoustical Reciprocity</b> .....	495
W.D. Zhu, J.M. Liu, Y.F. Xu, and H.Q. Ying	
<b>49 Reactionless Test to Identify Dynamic Young's Modulus and Damping of Isotropic Plastic Materials</b> .....	511
Peter Blaschke and Torsten Schneider	
<b>50 Real-Time Modal Analysis of Shell-Shaped Objects Using High-Frame-Rate Structured-Light-Based Vision</b> .....	517
Hua Yang, Qingyi Gu, Tadayoshi Aoyama, Takeshi Takaki, and Idaku Ishii	
<b>51 Field and Numerical Testing of the BWE SchRs4600.50 Dynamic Behavior</b> .....	525
Damian Pietrusiak, Przemysław Moczko, and Jerzy Czmochowski	
<b>52 Modal Analysis of Rotating Carbon Nanotube Infused Composite Beams</b> .....	533
C. DeValve, N. Ameri, P. Tarazaga, and R. Pitchumani	
<b>53 Modal Analysis and Dynamic Monitoring of a Concentrating Solar Heliostat</b> .....	543
Adam Moya, Clifford Ho, Jeremy Sment, Todd Griffith, and Joshua Christian	
<b>54 Identification of Stability Cutting Parameters Using Laser Doppler Vibrometry</b> .....	553
D. Olvera, A. Elías-Zúñiga, M. Pineda, E. Macias, O. Martínez, L.N. López de Lacalle, and C. Rodríguez	
<b>55 System Identification Using Kalman Filters</b> .....	561
F. Abid, G. Chevallier, J.L. Blanchard, J.L. Dion, and N. Dauchez	
<b>56 Identification of Time-Varying Nonlinear Systems Using Differential Evolution Algorithm</b> .....	575
Nevena Perisic, Peter L Green, Keith Worden, and Poul Henning Kirkegaard	

<b>57</b>	<b>Experimental Verification and Improvement of Dynamic Characterization Method for Structural Joints...</b>	<b>585</b>
	Şerife Tol and H. Nevzat Özgüven	
<b>58</b>	<b>Transfer Functions to Measure Translational and Rotational Velocities with Continuous-Scan Laser Doppler Vibrometry</b>	<b>597</b>
	Shifei Yang and Matthew S. Allen	
<b>59</b>	<b>Empirical Slow-Flow Identification for Structural Health Monitoring and Damage Detection</b>	<b>617</b>
	Young S. Lee, D. Michael McFarland, Lawrence A. Bergman, and Alexander F. Vakakis	
<b>60</b>	<b>Continuous Scanning for Acoustic Field Characterization</b>	<b>625</b>
	Carlos E. Garcia, Sriram Malladi, and Pablo A. Tarazaga	
<b>61</b>	<b>Operating Deflection Shapes of a Violin String via High Speed/High Resolution Videography</b>	<b>637</b>
	Chuck Van Karsen, Troy Bouman, and Geoff Gwaltney	
<b>62</b>	<b>Automated Measurement Grid Generation for Scanning Laser Doppler Vibrometers</b>	<b>645</b>
	L. Pesaresi and C.W. Schwingshackl	
<b>63</b>	<b>Mode Filtering of Continuous Scanning Laser Doppler Vibration Data</b>	<b>655</b>
	P. Castellini, P. Chiariotti, and M. Martarelli	
<b>64</b>	<b>The Characterization of the Time Delay Problem in Hardware in the Loop System Applications</b>	<b>661</b>
	C.A.G. Carrillo, J.V. Ferreira, and P.S. Meirelles	
<b>65</b>	<b>Optimal Placement of Piezoelectric Patches on a Cylindrical Shell for Active Vibration Control</b>	<b>673</b>
	Caner Gencoglu and H. Nevzat Özgüven	
<b>66</b>	<b>Adaptive Feedback Linearisation and Control of a Flexible Aircraft Wing</b>	<b>683</b>
	S. Jiffri, J.E. Mottershead, and J.E. Cooper	
<b>67</b>	<b>Limit Cycle Assignment in Nonlinear Aeroelastic Systems Using Describing Functions and the Receptance Method</b>	<b>701</b>
	Xiaojun Wei and John E. Mottershead	
<b>68</b>	<b>Investigation of an Active Structural Acoustic Control System on a Complex 3D Structure</b>	<b>715</b>
	S. Kulah, U. Aridogan, and I. Basdogan	
<b>69</b>	<b>Development of a Stabilized Pan/Tilt Platform and the State of the Art</b>	<b>723</b>
	M. Burcak Ozkok and Ali Osman Boyacı	
<b>70</b>	<b>Dynamic Equations for an Anisotropic Cylindrical Shell</b>	<b>731</b>
	Reza Okhovat and Anders Boström	
<b>71</b>	<b>Expansion of Nonlinear System Response Using Linear Transformation Matrices from Reduced Component Model Representations</b>	<b>743</b>
	Tim Marinone, Louis Thibault, and Peter Avitabile	
<b>72</b>	<b>Explicit Construction of Rods and Beams with Given Natural Frequencies</b>	<b>771</b>
	A. Morassi	
<b>73</b>	<b>A Metric for Modal Truncation in Model Reduction Problems Part 1: Performance and Error Analysis</b>	<b>781</b>
	Sadegh Rahrovani, Majid Khorsand Vakilzadeh, and Thomas Abrahamsson	
<b>74</b>	<b>A Metric for Modal Truncation in Model Reduction Problems Part 2: Extension to Systems with High-Dimensional Input Space</b>	<b>789</b>
	Sadegh Rahrovani, Majid Khorsand Vakilzadeh, and Thomas Abrahamsson	
<b>75</b>	<b>On Gramian-Based Techniques for Minimal Realization of Large-Scale Mechanical Systems</b>	<b>797</b>
	Sadegh Rahrovani, Majid Khorsand Vakilzadeh, and Thomas Abrahamsson	

# Chapter 1

## Damage Detection Using Flexibility Proportional Coordinate Modal Assurance Criterion

Luciana Balsamo, Suparno Mukhopadhyay, Raimondo Betti, and Hilmi Lus

**Abstract** In the recent years, vibration-based identification techniques have attracted the attention of the civil engineering community, as these methods can be naturally incorporated into automated continuous structural health monitoring procedures. It is a generally accepted approach to model the damage and deterioration of a structural element through stiffness reduction. For this reason, a feature tailored so as to be well correlated to the expected differences between the undamaged and damaged flexibility matrices, such as the recently proposed Flexibility Proportional Coordinate Modal Assurance Criterion (FPCOMAC), is ideally suited to be exploited as damage sensitive feature. We present a statistical pattern recognition based damage detection method that employs FPCOMAC as damage sensitive feature. The proposed methodology is executed according to the training and testing phases typical of the pattern recognition framework. Particular effort is devoted to test the ability of the method to correctly identify the damage when response time histories used in the training are measured in different environmental conditions. The formulation is derived considering a shear-type structural system. Results obtained by considering a 7 DOFs shear-type system prove the efficiency of the method in detecting and locating the damage, irrespective of damage severity and environmental effects, under the conditions that the damage amount is greater than the structural variations caused by the external factors and the amount of data is reasonably large.

**Keywords** Statistical pattern recognition • Structural damage detection • FPCOMAC

### 1.1 Introduction

The task of ascertaining the health conditions of a structure by analyzing its vibration response is commonly termed as vibration based structural health monitoring. The most common approach to the problem of structural health monitoring is to identify the modal characteristics of the system under known conditions; the assessment of damage occurrence is then pursued by comparing the reference set of modal characteristics against a new set of parameters identified from new instances of the structural vibration response. In the last three decades, these were the methods most dominantly used and, then, the available algorithms are particularly efficient and able not only to detect the damage, but also to locate it as well as to indicate the extent of the detected structural alterations. Nonetheless, to accomplish such a high level of damage detection, the model based methods necessitate of very high quality time histories recorded from a vast number of sensors located at crucial points in the structure. In fact, the performance of the system identification algorithm is intimately correlated to the quality of the available response time histories. Moreover, the system identification algorithm itself may be based on assumptions (e.g. linearity of the system, stationarity of the response) that make it unsuited for certain kind of scenarios.

---

L. Balsamo (✉) • S. Mukhopadhyay

Ph.D. Candidate, Department of Civil Engineering and Engineering Mechanics, Columbia University, New York, NY 10027, USA  
e-mail: [lb2591@columbia.edu](mailto:lb2591@columbia.edu); [sm3315@columbia.edu](mailto:sm3315@columbia.edu)

R. Betti

Professor, Department of Civil Engineering and Engineering Mechanics, Columbia University, New York, NY 10027, USA  
e-mail: [betti@civil.columbia.edu](mailto:betti@civil.columbia.edu)

H. Lus

Associate Professor, Department of Civil Engineering, Bogazici University, 34342 Bebek, Istanbul, Turkey  
e-mail: [hilmilus@boun.edu.tr](mailto:hilmilus@boun.edu.tr)

On the other hand, over the last 10 years, the discipline of statistical pattern recognition has attracted the interest of a vast community within civil engineering. Its most appealing characteristic is that of not requiring a physical model of the system to be identified. Instead, the structure in analysis is represented by the probability distribution model of some damage sensitive features extracted from the vibration measurements, which are not directly correlated to the system structural characteristics: for instance, very popular damage sensitive features for statistical pattern recognition are the Auto-Regressive (AR) or Auto-Regressive with eXogeneous input (ARX) model coefficients (see [1, 2]). The main drawback of this approach is that of requiring a vast number of time histories to be employed while the beneficial effects are results that are not strongly corrupted by noise and input effects, as the large number of data employed filter out noise and external factors effects.

The two approaches, i.e. model and non-model based techniques, are perceived as mutually exclusive; nevertheless, both methods have advantages and disadvantages, and should be then applied in combination. For this reason, in this paper a technique is proposed that makes use of a combination of the two. The deviation from 1 of the recently introduced Flexibility Proportional Coordinate Modal Assurance Criterion (FPCOMAC) is used as damage sensitive feature. FPCOMAC [3] is defined by means of the mode shape matrices of the healthy and possibly damaged systems. Therefore, a system identification algorithm is needed to derive these features from the system time histories. The damage detection method is developed according to the statistical pattern recognition paradigm: during training, a large number of feature vectors are extracted from the time histories of the healthy structure. Small perturbations around the mean value of stiffness and mass properties are considered, in order to represent external factors effects, such as environmental effects. The necessity of approaching the problem within the probabilistic framework is indeed required due to the presence of variations conveyed by environmental or operational effects. During the training operation, a threshold is identified which is able to label as undamaged all the observations of the feature falling within a given confidence level region. During testing, the features extracted from samples recorded on the system under unknown conditions are compared against the trained threshold to assess damage occurrence. The necessary derivations in the formulation of the damage detection algorithm are obtained considering shear-type models of the structural systems. Through numerical simulations, it is shown that the proposed algorithm is capable of locating and estimating damage extent reliably well.

## 1.2 Damage Sensitive Feature

Flexibility Proportional Coordinate Assurance Criterion (FPCOMAC or  $FPCOMAC_k$ ) was recently proposed in an effort to introduce a criterion, whose deviation from 1 gives a measure of the error in the  $(k, k)$ -th element of the flexibility matrix estimated by employing mode shapes identified from the system response time histories, where with error, we refer to the change due to damage in the estimated flexibility matrix.

Let us assume real valued mode shapes are evaluated at *each* degree of freedom (DOF) of a given  $N$ -DOF system: let  $\phi_i \in \mathbb{R}^{N \times 1}$  and  $\psi_i \in \mathbb{R}^{N \times 1}$  be mode shapes for the  $i$ -th mode of vibration of the system in the healthy and damaged states, respectively. Furthermore, let us denote with  $\lambda \in \mathbb{R}^{N \times 1}$  the set of natural frequencies of the healthy structure, and with  $\tau \in \mathbb{R}^{N \times 1}$  the set of natural frequencies of the possibly damaged system. Under the assumptions that damage may be modeled through stiffness reduction, without any mass alteration, and that the mode shapes are mass normalized, the flexibility matrices of the structure under undamaged and damaged conditions may be given as in Eqs. (1.1) and (1.2), respectively

$$\mathbf{F} = \sum_{i=1}^N \frac{\phi_i \phi_i^T}{\lambda_i} \quad (1.1)$$

$$\mathbf{P} = \sum_{i=1}^N \frac{\psi_i \psi_i^T}{\tau_i} \quad (1.2)$$

FPCOMAC is derived in such a way that its deviation from 1 attempts to give a measure of the difference between the values of the  $(k, k)$ -th element of the healthy ( $\mathbf{F}$ ) and damaged ( $\mathbf{P}$ ) system flexibility matrices. The deviation from 1 of the FPCOMAC is denoted as  $eFPCOMAC$ , which is the criterion actually employed as damage sensitive feature in this work, and whose analytical expression is given in Eq. (1.3), for the  $k$ -th DOF:

$$eFPCOMAC_k = 1 - \frac{\sum_{i=0}^N \frac{\|\phi_i\|^2}{\|\psi_i\|^2} \frac{\psi_{i,k}^2}{\tau_i}}{\sum_{i=1}^N \frac{\phi_{i,k}^2}{\lambda_i}} \quad (1.3)$$

A value of eFPCOMAC less than 0 would be indicative of damage, if the representations of the modal characteristics of the reference structure were unique. Nonetheless, when taking into account environmental and operational effects, the modal characteristics of the reference system vary, making it necessary the definition of a new threshold to assess damage occurrence.

### 1.2.1 Mode Shape Normalization

A clarification is necessary regarding the mode shapes employed for the damage detection algorithm. In fact, the mode shapes identified through an output-only system identification algorithm, like Enhanced Canonical Correlation Analysis [4], diagonalize the mass matrix, but are not proportional to mass normalized mode shapes by a single scalar multiplicative constant, whereas the FPCOMAC feature is derived by assuming the mode shapes of the reference system as mass normalized, or at least proportional to the mass normalized ones by a constant. In the present section a normalization procedure valid for systems that can be modeled through a diagonal mass matrix is proposed. Let us then denote with  $\Phi$  the identified  $N \times N$  mode shape matrix, and with  $\mathbf{M}$  the  $N \times N$  diagonal mass matrix so that:

$$\Phi^T \mathbf{M} \Phi = \text{diag}\{d_1, \dots, d_N\} \quad (1.4)$$

while the condition we want to achieve is given in Eq. (1.5):

$$\hat{\Phi}^T \mathbf{M} \hat{\Phi} = \alpha \cdot \mathbf{I} \quad (1.5)$$

where  $\mathbf{I}$  is the  $N \times N$  identity matrix, and  $\alpha$  is a constant multiplicative factor. To pursue the outcome outlined in Eq. (1.5), it is necessary to find a scaling matrix  $\beta$  such that:

$$\hat{\Phi} = \Phi \cdot \beta \quad (1.6)$$

where  $\beta = \text{diag}\{\beta_1, \dots, \beta_N\}$  is a scalar diagonal matrix. By plugging Eq. (1.6) into Eq. (1.5), and setting  $\alpha = \beta_1^2/d_1$ , we obtain the following expression for the inverse of the mass matrix  $\mathbf{M}$ :

$$\mathbf{M}^{-1} = \frac{d_1}{\beta_1^2} \Phi \beta^2 \Phi^T = d_1 \Phi \Gamma \Phi^T \quad (1.7)$$

where the elements of the diagonal matrix  $\Gamma = \text{diag}\{1, \beta_2^2/\beta_1^2, \beta_3^2/\beta_1^2, \dots, \beta_N^2/\beta_1^2\} = \text{diag}\{1, \gamma_2^2, \gamma_3^2, \dots, \gamma_N^2\}$  may be retrieved by solving the system of Eq. (1.8) obtained by taking into account the properties of  $\mathbf{M}$ , i.e. that the matrix is diagonal and then symmetric:

$$\sum_{i=2}^N \gamma_i^2 \phi_{k,i} \phi_{l,i} = -\phi_{k,1} \phi_{l,1} \quad \forall k \neq l, \text{ and } k, l \in [1, \dots, N] \quad (1.8)$$

where  $\phi_{i,j}$  represents the (i,j)-th element of the mode shape matrix  $\Phi$ . The identified mode shape matrix can then be scaled through  $\Gamma$ :

$$\tilde{\Phi} = \Phi \Gamma^{1/2} = \frac{1}{\beta_1} \hat{\Phi} \quad (1.9)$$

This scaling produces a set of normalized mode shapes that differ from the mass normalized ones by one single multiplicative factor  $d_1$ , as shown in Eq. (1.10):

$$\tilde{\Phi}^T \mathbf{M} \tilde{\Phi} = \frac{1}{\beta_1^2} \hat{\Phi}^T \mathbf{M} \hat{\Phi} = \frac{\alpha}{\beta_1^2} \mathbf{I} = \frac{1}{d_1} \mathbf{I} \quad (1.10)$$

### 1.2.2 Damage Location

The flexibility matrix of an  $N$  DOFs shear-type system can be expressed as:

$$F = \begin{bmatrix} f_1 & f_1 & \cdots & f_1 \\ f_1 & f_1 + f_2 & \cdots & f_1 + f_2 \\ \vdots & \vdots & \ddots & \vdots \\ f_1 & f_1 + f_2 & \cdots & \sum_{i=1}^N f_i \end{bmatrix} \quad (1.11)$$

where  $f_i$  is the inter-story flexibility between the  $(i - 1)$ -th and  $i$ -th DOFs. Herein, structural damage is modeled by increasing the inter-story flexibility by a factor  $\sigma_i$  greater than 1. It can be proved that the difference between two consecutive  $eFPCOMAC_k$  coefficients serves as damage locator. In fact,  $eFPCOMAC_k$  is proportional to the ratio between the difference of the  $(k, k)$ -th elements of the undamaged and damaged flexibility matrices, and the  $(k, k)$ -th element of the undamaged flexibility matrix, as clarified by Eq. (1.12):

$$eFPCOMAC_k \propto \frac{F_{k,k} - P_{k,k}}{F_{k,k}} \quad (1.12)$$

Then, Eq. (1.12) may be rewritten in terms of the damage factor  $\sigma_i$ , as shown in Eq. (1.13):

$$eFPCOMAC_k \propto \frac{\sum_{i=1}^k (1 - \sigma_i) f_i}{\sum_{i=1}^k f_i} \quad (1.13)$$

It is worth noting that the parameter  $\sigma_i$  is equal to 1 when no damage occurred between the  $(i - 1)$ -th and  $i$ -th DOFs, while takes on values greater than 1 if the inter-story between  $(i - 1)$ -th and  $i$ -th DOFs is damaged. Then, if the structure is healthy,  $eFPCOMAC_k$  is equal to zero, while if damage has occurred between  $(k - 1)$ -th and  $k$ -th DOFs,  $eFPCOMAC_k$  will show a value lesser than that of  $eFPCOMAC_{k-1}$ . In fact, by using Eq. (1.13), through simple algebraic operations, it is possible to obtain the following relation between the difference of two consecutive  $eFPCOMAC_k$  values:

$$eFPCOMAC_k - eFPCOMAC_{k-1} \propto \sum_{j=1}^{k-1} (\sigma_j - \sigma_k) f_j \quad (1.14)$$

It is then easy to verify that a value of  $eFPCOMAC_k$  smaller than the one of  $eFPCOMAC_{k-1}$  is indicative of damage occurrence between the  $(k - 1)$ -th and  $k$ -th floors:

$$eFPCOMAC_k < eFPCOMAC_{k-1} \Rightarrow \sigma_k > \frac{\sum_{j=1}^{k-1} \sigma_j f_j}{\sum_{j=1}^{k-1} f_j} \quad (1.15)$$

Indeed, by noting that the right-hand-side of the inequality in Eq. (1.15) may take only values greater or equal to 1, it is apparent that  $\sigma_k$  can take only on values strictly greater than 1, i.e. indicative of an increase in flexibility, if  $eFPCOMAC_k$  is lesser than  $eFPCOMAC_{k-1}$ .

### 1.3 Damage Detection Algorithm

Up to this point, it has been shown that eFPCOMAC has a natural threshold at 0, so that if a deterministic model of the reference system was available, the damage detection routine could be performed avoiding any further processing. Nonetheless, external factors such as environmental or operational effects may cause significant changes in the structural characteristics that could be misinterpreted as manifestation of damage. For this reason, it is important to identify a range of values for each of the  $N$  eFPCOMAC<sub>k</sub>'s within which the monitored structure may be considered healthy. In other words, it is necessary to determine a threshold for the damage sensitive feature which is able to distinguish between changes due to external effects and deviations of the vibration response due to damage. As aforementioned, eFPCOMAC is ideally suited as damage detector for shear-type systems. For this reason, the algorithm proposed in the following paragraphs is intended for application on this kind of structures.

#### 1.3.1 Training

Let us assume that  $n$  sets of time histories are recorded on the structure in its reference, usually undamaged, configuration. In this paper, with set of time histories, we refer to the ensemble of time histories measured during a single monitoring session through all the available sensors,  $M$ , placed on the system in analysis. Here, it is important to note that if  $M < N$ , a mode shape expansion approach like the one proposed by Mukhopadhyay in [5] must be applied to get the full mode shape matrix. For each of the  $n$  sets of time histories the following operations take place, where the superscript <sup>(i)</sup> indicates a quantity extracted from the  $i$ -th set of time histories:

1. Identification of the mode shape matrix  $\phi^{(i)} \in \mathbb{R}^{N \times N}$ ;
2. If an output-only system identification procedure is applied, a normalization of  $\phi^{(i)}$  following the procedure described in Sect. 1.2.1 must be performed;
3. Identification of the modal frequencies vector  $\lambda^{(i)} \in \mathbb{R}^{N \times 1}$ ;
4. Evaluation of the threshold for eFPCOMAC<sub>k</sub> executing the following pseudo-code:

**for**  $i = 1$  to  $n$  **do**

- Define  $\mathbf{R} = \phi^{(i)}$ ;
- Define  $\mathbf{r} = \lambda^{(i)}$ ;

**for**  $k = 1$  to  $n$  **do**

- Define  $\mathbf{T} = \phi^{(k)}$ ;
- Define  $\mathbf{t} = \lambda^{(k)}$ ;

**for**  $j = 1$  to  $N$  **do**

Evaluate eFPCOMAC<sub>j</sub> according to equation (17) :

$$\text{eFPCOMAC}_j^{(i-1)n+k} = 1 - \frac{\sum_{i=0}^N \frac{\|\mathbf{R}_i\|^2 T_{i,k}^2}{\|\mathbf{T}_i\|^2 t_i}}{\sum_{i=1}^N \frac{R_{i,k}^2}{r_i}} \quad (1.16)$$

**end for**  $j$

**end for**  $k$

**end for**  $i$

5. Sorting of the  $n^2$  eFPCOMAC<sub>j</sub><sup>(i-1)n+k</sup> in ascending order and pick the element whose value is exceeded by the 95% of the samples as threshold for the  $j$ -th eFPCOMAC.



### 1.3.2 Testing

Herein, it is assumed that the number of data-sets available at testing is  $\tilde{n} < n$ . The testing is performed according to the following operations, where the superscript  $(k)$  refers to the  $k$ -th of the  $\tilde{n}$  vibration response time histories measured on the possibly damaged system:

1. Identification of the modal characteristics of the system in unknown conditions:

- $\psi^{(k)} \in \mathbf{R}^{N \times N}$ , matrix of mode shapes;
- $\tau^{(k)} \in \mathbf{R}^{N \times 1}$ , vector of modal frequencies;

In this case no normalization procedure is required, as the ‘non-proportionality’ of the identified mode shapes to mass normalized mode shapes is taken into account by the norm ratio in the eFPCOMAC definition.

2. Evaluation of  $\tilde{n} \cdot n$  eFPCOMAC<sub>j</sub> executing the following pseudo-code:

**for**  $i = 1$  to  $n$  **do**

- Define  $\mathbf{R} = \phi^{(i)}$ ;
- Define  $\mathbf{r} = \lambda^{(i)}$ ;

**for**  $k = 1$  to  $\tilde{n}$  **do**

- Define  $\mathbf{T} = \psi^{(k)}$ ;
- Define  $\mathbf{t} = \tau^{(k)}$ ;

**for**  $j = 1$  to  $N$  **do**

Evaluate eFPCOMAC\_TEST<sub>j</sub> according to equation (18) :

$$\text{eFPCOMAC\_TEST}_j^{(i-1) \cdot n + k} = 1 - \frac{\sum_{i=0}^N \frac{\|\mathbf{R}_i\|^2 T_{i,k}^2}{\|\mathbf{T}_i\|^2 t_i}}{\sum_{i=1}^N \frac{R_{i,k}^2}{r_i}} \quad (1.17)$$

**end for**  $j$

**end for**  $k$

**end for**  $i$

3. Perform a double check on the retrieved parameters according to the following criteria:

**for**  $s = 1$  to  $n \cdot \tilde{n}$  **do**

**for**  $j = 1$  to  $N$  **do**

**if**  $(\text{eFPCOMAC\_TEST}_j^{(i)} < \text{Threshold}_j) \ \& \ (\text{eFPCOMAC\_TEST}_j^{(i)} < \text{eFPCOMAC\_TEST}_{j-1}^{(i)})$

count<sub>j</sub> = count<sub>j</sub> + 1

**end for**  $j$

**end for**  $k$

**end for**  $i$

4. Damage is located between the  $(j - 1)$ -th and  $j$ -th DOFs if count<sub>j</sub> has a value greater than 60%  $n \cdot \tilde{n}$ . The 60%  $n \cdot \tilde{n}$  threshold value is the result of an optimization problem aimed to minimize the damage location error rate.

**Table 1.1** Results of the algorithm validation

Type I and II error rates of the proposed algorithm							
Damage scenario	First inter-story	Second inter-story	Third inter-story	Fourth inter-story	Fifth inter-story	Sixth inter-story	Seventh inter-story
<i>DS0</i>	0% (Type I)	0% (Type I)	0% (Type I)	0% (Type I)	0% (Type I)	0% (Type I)	0% (Type I)
<i>DS1</i>	1% (Type II)	0% (Type I)	0% (Type I)	0% (Type I)	2% (Type I)	0% (Type I)	1% (Type I)
<i>DS2</i>	0% (Type I)	0% (Type I)	0% (Type II)	0% (Type I)	2% (Type I)	1% (Type I)	1% (Type I)
<i>DS3</i>	0% (Type I)	0% (Type I)	0% (Type I)	0% (Type I)	8% (Type II)	0% (Type I)	1% (Type I)
<i>DS4</i>	0% (Type I)	0% (Type I)	0% (Type I)	0% (Type I)	0% (Type II)	0% (Type I)	1% (Type I)
<i>DS5</i>	0% (Type I)	0% (Type I)	0% (Type II)	0% (Type I)	6% (Type II)	0% (Type I)	1% (Type I)
<i>DS6</i>	0% (Type I)	0% (Type I)	0% (Type II)	0% (Type I)	0% (Type II)	0% (Type I)	0% (Type I)

## 1.4 Results

To test the ability of the proposed algorithm, we consider a 7 DOFs shear-type system whose response is simulated using the MATLAB Control System Toolbox Kit. For the training, 100 data-sets are simulated, i.e.  $n$  is equal to 100. Each data-set, consisting of the ensemble of seven acceleration response time histories recorded at each mass, is obtained by exciting the system at each DOF via white noise 1 min long time histories. Then, for each DOF, the overall training data are 100 min long. At each realization, the values of the  $i$ -th inter-story stiffness  $k_i$  are randomly picked within the range  $[5.7 \times 10^6, 6.3 \times 10^6]$  N/m, the values of the  $i$ -th mass  $m_i$  are randomly picked within the range  $[2.3 \times 10^3, 2.6 \times 10^3]$  kg, while Rayleigh Damping model is employed to account for the damping effects. Testing is performed by using 10 data-sets, i.e.  $\tilde{n}$  is 10, of simulated acceleration response time histories recorded at each DOF of the system, creating a total of 10 min data recording for each DOF. The stochastic subspace identification algorithm ECCA is exploited for the identification of mode shapes and modal frequencies.

Seven damage scenarios are considered:

1. No damage (from here on referred to as *DS0*);
2. Ten percent decrease of the inter-story stiffness between ground and the first floor (*DS1*);
3. Ten percent decrease of the inter-story stiffness between second and third floors (*DS2*);
4. Ten percent decrease of the inter-story stiffness between fourth and fifth floors (*DS3*);
5. Twenty percent decrease of the inter-story stiffness between fourth and fifth floors (*DS4*);
6. Twenty percent decrease of the inter-story stiffness between second and third floors, and between fourth and fifth floors (*DS5*);
7. Twenty percent decrease of the inter-story stiffness between second and third floors, and between fourth and fifth floors (*DS6*);

For each of the 7 damage scenarios, 100 experiments are run and the results of the simulations are presented in Table 1.1 in terms of error rates.

The problem of damage detection may be restated according to the binary decision theory syntax: given the null hypothesis ( $H_0$ ) that the system is in its healthy condition, the task of damage detection is that of assessing whether the null hypothesis can be accepted or rejected. Rejecting the null hypothesis, when instead it should be accepted, is known as Type I error whereas accepting the null hypothesis, when instead it should be rejected, is defined as Type II error. Let us now dwell on the damage location problem, and let us consider the problem of assessing whether the area between the  $(i - 1)$ -th and  $i$ -th DOFs, here onwards referred to as  $i$ -th inter-story, is damaged. If the  $i$ -th inter-story is healthy but it is declared damaged, a Type I error is made, whereas if the  $i$ -th inter-story is damaged but it is declared healthy, a Type II error is made. This is the criterion to consider when reading Table 1.1. For example, Damage scenario 1 represents the condition when damage occurs at the first inter-story; then, a Type II error occurs if the first inter-story is declared healthy, while a Type I error is observed if the other inter-stories are declared damaged. In particular, for damage scenario 1, the Type II error rate is equal to 1%, while Type I error rate is equal to 3%.

The results prove the robustness of the algorithm both in detecting and locating the damage, as both Types I and II error rates are satisfactorily low. Nonetheless, it is worth to make some considerations on the outcomes of damage scenarios *DS3* and *DS5*, both representing the case where damage occurred at the fifth floor, since they are characterized by the poorest, albeit still acceptable, quality. These results are due to the combination of two aspects. Firstly, the characteristics of the FPCOMAC are such that a low damage at higher inter-stories is difficult to detect, as it is evident by analyzing the analytical definition of  $eFPCOMAC_k$  given in Eq. (1.13). In particular, the value of  $eFPCOMAC_5$  depends on the values

of the difference between healthy and damaged flexibilities at the fifth floor as well as at the four preceding floors, which can then mask the presence of damage. Secondly, the threshold employed to take into account the structural characteristic variations caused by external factors can cover the presence of damage, when this is too low. This raises an important issue, not often addressed in the literature, i.e. the question of how to tackle with the problem of model uncertainties caused by diverse factors including environmental and loading conditions, as well as the intrinsic uncertainties introduced by the modeling process itself.

## 1.5 Conclusions

A statistical damage detection algorithm was proposed. The proposed technique attempts to combine the model and non-model based approaches, which are often incorrectly considered as mutually exclusive. The recent advances in the field of system identification permit to extract the modal characteristics from the structural vibration response delivering accurate model of the system at hand, as the case being for ECCA, the stochastic subspace identification algorithm employed in this work. Nonetheless, the trend of using the modal parameters to generate a deterministic model of the system is questionable, as uncertainties associated to the model itself and to the effects of external factors, such as environmental and loading conditions, require the problem to be treated in a probabilistic framework. This is, indeed, the approach that has been proposed in this work, where modal analysis is used to evaluate the damage sensitive feature eFPCOMAC, while the damage detection algorithm is developed according to the training and testing phases typical of a statistical pattern recognition framework. The algorithm is validated by constructing the training model through a database obtained by simulating the response of a system in different operational conditions characterized by a variation in its structural properties during the different simulation sessions. In addition, a methodology apt to normalize the mode shape matrices identified through output only algorithms to be proportional to the mass normalized ones enables the proposed damage detection routine to be used when output-only data are available. The method proved to be effective in detecting and locating the damage for a shear-type system. The results obtained by performing numerous tests employing simulated response of a 7 DOFs system suggest that, even for relatively low damage magnitudes, the algorithm is able to detect the damage location, although some false acceptance error are recorded when low damage occurs at high DOFs. This outcome is due to the way the damage sensitive feature is defined: the eFPCOMAC evaluated at the higher DOF is influenced by the values of all of the preceding flexibilities, i.e. the deviation from the threshold may not be significant for damage scenarios where damage is located in a region far from the ground. On the other hand, the threshold defined during the training phase sometimes could not encompass properly the healthy system behavior, leading to the manifestation of Type II kind of error for relatively small damage. The latter consideration highlights the necessity of making the issue of how to deal with uncertainties correlated to the training model the primary focal point of future research.

## References

1. Sohn H, Farrar CR, Hunter NF, Worden K (2001) Structural health monitoring using statistical pattern recognition techniques. *J Dyn Syst Meas Control* 123:706–711
2. Gul M, Catbas FN (2011) Structural health monitoring and damage assessment using a novel time series analysis methodology with sensor clustering. *J Sound Vib* 330:1196–1210
3. Mukhopadhyay S, Lus H, Hong AL, Betti R (2012) Propagation of mode shape errors in structural identification. *J Sound Vib* 331(17):3961–3975
4. Hong A (2010) Model order determination in stochastic system identification for civil infrastructure systems. Columbia University, New York
5. Mukhopadhyay S, Betti R, Lus H (2013) Output only structural identification with minimal instrumentation. In: *Proceedings of the 31st international modal analysis conference*, Garden, California, USA

# Chapter 2

## Automated Selection of Damage Detection Features by Genetic Programming

Dustin Harvey and Michael Todd

**Abstract** Robust damage detection algorithms are the first requirement for development of practical structural health monitoring systems. Typically, a damage decision is made based on time series measurements of structural responses. Data analysis involves a two-stage process, namely feature extraction and classification. While classification methods are well understood, no general framework exists for extracting optimal, or even good, features from time series measurements. Currently, successful feature design requires application experts and domain-specific knowledge. Genetic programming, a method of evolutionary computing closely related to genetic algorithms, has previously shown promise as an automatic feature selector in speech recognition and image analysis applications. Genetic programming evolves a population of candidate solutions represented as computer programs to perform a well-defined task such as classification of time series measurements. Importantly, genetic programming conducts an efficient search without specification of the size of the desired solution. This preliminary study explores the use of genetic programming as an automated feature extractor for two-class supervised learning problems related to structural health monitoring applications.

**Keywords** Structural health monitoring • Genetic programming • Feature extraction • Damage detection • Supervised learning

### 2.1 Introduction

#### 2.1.1 Structural Health Monitoring

Structural health monitoring (SHM) aims to replace ad-hoc inspection programs and preventative maintenance of civil and aerospace structures with on-line systems providing real-time structural performance and damage state information. One of the biggest roadblocks to implementing these systems is the development of specialized signal processing for each individual application. Robust damage detection algorithms are the first step toward practical structural health monitoring systems. Typically, a damage decision is made based on time series measurements of structural responses. Data analysis involves a two-stage process, namely feature extraction and classification. While classification methods are well understood, no general framework exists for extracting optimal, or even good, features from time series measurements. Currently, successful feature design requires application experts and domain-specific knowledge.

---

D. Harvey (✉)

Graduate Student, University of California, San Diego, 9500 Gilman Dr., La Jolla, CA 92093, USA  
e-mail: [dyharvey@ucsd.edu](mailto:dyharvey@ucsd.edu)

M. Todd

Professor University of California, San Diego, 9500 Gilman Dr., La Jolla, CA 92093, USA  
e-mail: [mdtodd@ucsd.edu](mailto:mdtodd@ucsd.edu)

### 2.1.2 Genetic Programming

Genetic Programming (GP), formally introduced by Koza [1], employs search methods based on the biological processes of natural selection and evolution to solve optimization problems. GP is a unique variant of evolutionary computation methods as candidate solutions are represented as computer programs, hence the name. Importantly, Genetic Programming conducts an efficient search with minimal specification of the size and structure of the desired solution. GP has previously produced human-competitive and patentable solutions in the areas of circuit design, image and signal processing, industrial process control, bioinformatics, financial trading, and others [2]. Genetic Programming is well suited for problems with the following properties [2]:

1. Poorly understood relationships between variables.
2. Solution size and shape unknown.
3. Large datasets.
4. Good solutions are easy to judge but hard to find.
5. No analytic solutions available.
6. Approximate solutions are acceptable.
7. Small performance improvements are beneficial.

### 2.1.3 Paper Overview

This preliminary study explores the use of genetic programming as an automated feature extractor for two-class supervised learning problems related to structural health monitoring applications. This paper is organized into six sections including the current introduction. Section 2.2 briefly covers details of the Genetic Programming system developed for this work. The reader is directed to [1, 2] for deeper understanding of GP concepts and terminology. In Sect. 2.3, GP performance is evaluated on three signal detection problems with known optimal results. Section 2.4 summarizes the findings of this study and proposes future work.

## 2.2 Genetic Programming System

### 2.2.1 Solution Structure

The current problem involves binary classification of vector time series measurements. Classification is a natural task for GP; however, input data to GP typically contains multivariate scalar measurements not structured data such as signals and images. A number of approaches to handling structured data have been proposed such as strongly-typed GP, automatically-defined iterations, and the scanning approach adopted here. As demonstrated in [3], by recursively feeding in samples of the input vector, a type of non-linear digital filter is created that scans along a time series. For input  $X_i$  with  $i = 0, 1, \dots, N - 1$ , each output,  $Y_i$ , is a function of the current input, past output, and sample index with the final output,  $Y_{N-1}$ , saved as the output feature for classification.

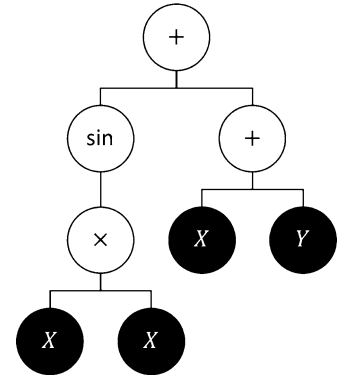
$$Y_i = f(X_i, Y_{i-1}, i) \quad (2.1)$$

Genetic programming is used to search for the function,  $f()$ , that optimizes a fitness measure. The function is represented as a GP tree. A tree is a hierarchical structure where each node has one and only one parent node but an unspecified number of children. In a GP tree, function nodes have as many children as the arity of the function. The end of each branch is a terminal node representing input data or a constant. The tree is evaluated starting at the bottom with outputs from each function passed as inputs to the next level of the tree until the root is reached. For example, the function

$$Y_i = \sin(X_i^2) + X_i + Y_{i-1} \quad (2.2)$$

is produced by the tree in Fig. 2.1. The corresponding program code is `y[i]=sin(x[i]*x[i])+x[i]+y[i-1]`.

**Fig. 2.1** Example GP tree for function in Eq. 2.2. *White nodes* are functions, and *black nodes* are terminals



## 2.2.2 Function and Terminal Sets

The function and terminal sets define the programming language available to build the solution trees. The function set used here consists of the standard addition, subtraction, multiplication, and division operations plus four additional functions. Absolute value, sine, and cosine functions are included as common signal processing operators. Lastly, a three-input sigmoid function defined as  $\text{sigmoid}(a, b, c) = \tanh(c * (a - b))$  provides a degree of switching functionality. The terminal set is composed of the current input, past output, sample index, and ten constants selected to cover four orders of magnitude.

## 2.2.3 Fitness

Fitness of the candidate solutions is measured by area under the receiver operating characteristic's curve (AUC) with the feature  $Y_{N-1}$  used to detect to which of two classes a signal belongs. The receiver operating characteristic's (ROC) curve defines probability of detection (PD) as a function of probability of false alarm (PFA) and fully characterizes the performance of a detector. The AUC provides a scalar indicator of detector performance bounded between 0 and 1 and is therefore a suitable fitness measure. To ease computation requirements, the detector output for each class was assumed to be normally distributed allowing AUC to be calculated analytically from the mean and standard deviation of the two classes. For performance evaluation of the final solution, the normality assumption was removed. Fitness case subsampling was employed to avoid overfitting and further decrease computation requirements with less than 10% of the fitness cases randomly selected for fitness computation during each generation.

## 2.2.4 Breeding

The GP search process operates by preferentially breeding the better solutions from one generation to populate the next generation with offspring through various genetic operators. The crossover operator replaces a subtree in one parent with a randomly selected subtree from another parent. The mutate operator, here implemented as a headless-chicken crossover, replaces a subtree in the parent with a random subtree. Finally, reproduction allows an individual to pass unchanged to the next generation. The three operations of crossover, mutation, and reproduction occur with probabilities of 80, 10, and 10%, respectively. Parents are selected through deterministic four individual tournaments.

## 2.2.5 Genetic Programming Summary

Table 2.1 summarizes the GP system and chosen parameters for this study. For most problems, fifty runs were performed in parallel on six processing cores of a single workstation. A flexible Python implementation of Genetic Programming was developed for this project and future studies. Python was chosen due to its open-source licensing, speed, and parallel processing capabilities.

**Table 2.1** Koza tableau of GP parameter settings

Parameter	Setting
Objective	Find program with best performance for binary class signal detection problem
Structure	Solutions scan along vector time series with final output saved as detector feature
Function set	+, −, ×, ÷, absolute value, sine, cosine, sigmoid
Terminal set	Input, past output, sample index, 0.01, 0.05, 0.1, 0.5, 1, $e$ , $\pi$ , 5, 10, 50
Fitness	Area under receiver operating characteristic's curve assuming classes normally distributed
Fitness case sampling	500 cases randomly selected from each class for each generation
Population initialization	Ramped half-and-half (grow and full) to maximum size of 50 nodes
Population size	1,000
Selection	Tournament (deterministic, size 4)
Genetic operators	Crossover (single child), 80%; Mutate (HCC, up to 20 nodes), 10%; Reproduce, 10%
Individual size limit	1 million nodes
Termination	50 generations

## 2.3 Signal Detection Results

### 2.3.1 Motivation

For SHM, damage detection requires classifying whether a response measurement comes from the undamaged or damaged state of a structure. For most structures, little knowledge is available concerning how the damaged and undamaged signals differ. Furthermore, without accurate models of the undamaged and damaged structure finding an optimal result is not viable. Therefore, to benchmark a detection algorithm, one can either compare results to previously established suboptimal results or find a similar problem where an optimal result exists. Here, the problem of identifying various signal types buried in white, Gaussian noise is studied to determine if Genetic Programming can reproduce the analytical optimal detectors.

### 2.3.2 Problem Description

The problems to be studied are simple in nature which permits optimal analytic solutions. In each problem, a 100-sample signal of interest is obscured by an independent noise process. By choosing an appropriate signal-to-noise ratio (SNR), the difficulty of the classification task can be controlled. The three signals to be detected are a  $-3$  dB SNR independent white, Gaussian noise process, a  $-10$  dB SNR deterministic sinusoid (0.63 cycles/sample frequency and 0 rad phase), and a  $-10$  dB SNR random phase sinusoid (0.63 cycles/sample frequency and uniformly distributed phase from  $-\pi$  to  $\pi$ ). In each problem, class 0 contains 5,000 noise-only signals, and class 1 contains 5,000 cases of noise plus signal. Figure 2.2 shows example realizations of each signal class.

For all three problems, the analytic optimal solution is a well known and logical result. The optimal detector for a white noise signal buried in white noise is simply the energy of the signal as shown in Eq. 2.3. There is no structure to the noise signal for the detector to exploit, so the best solution is simply to measure the energy of the entire signal. For the deterministic sinusoid, the optimal detector is the matched filter output in Eq. 2.4 which is a measure of how correlated the measured signal is with the expected signal. With uniformly distributed phase in the third problem, the optimal detector incoherently adds the in-phase and quadrature matched filters as in Eq. 2.5.

$$D_{noise} = \sum_{i=0}^{N-1} X_i^2 \quad (2.3)$$

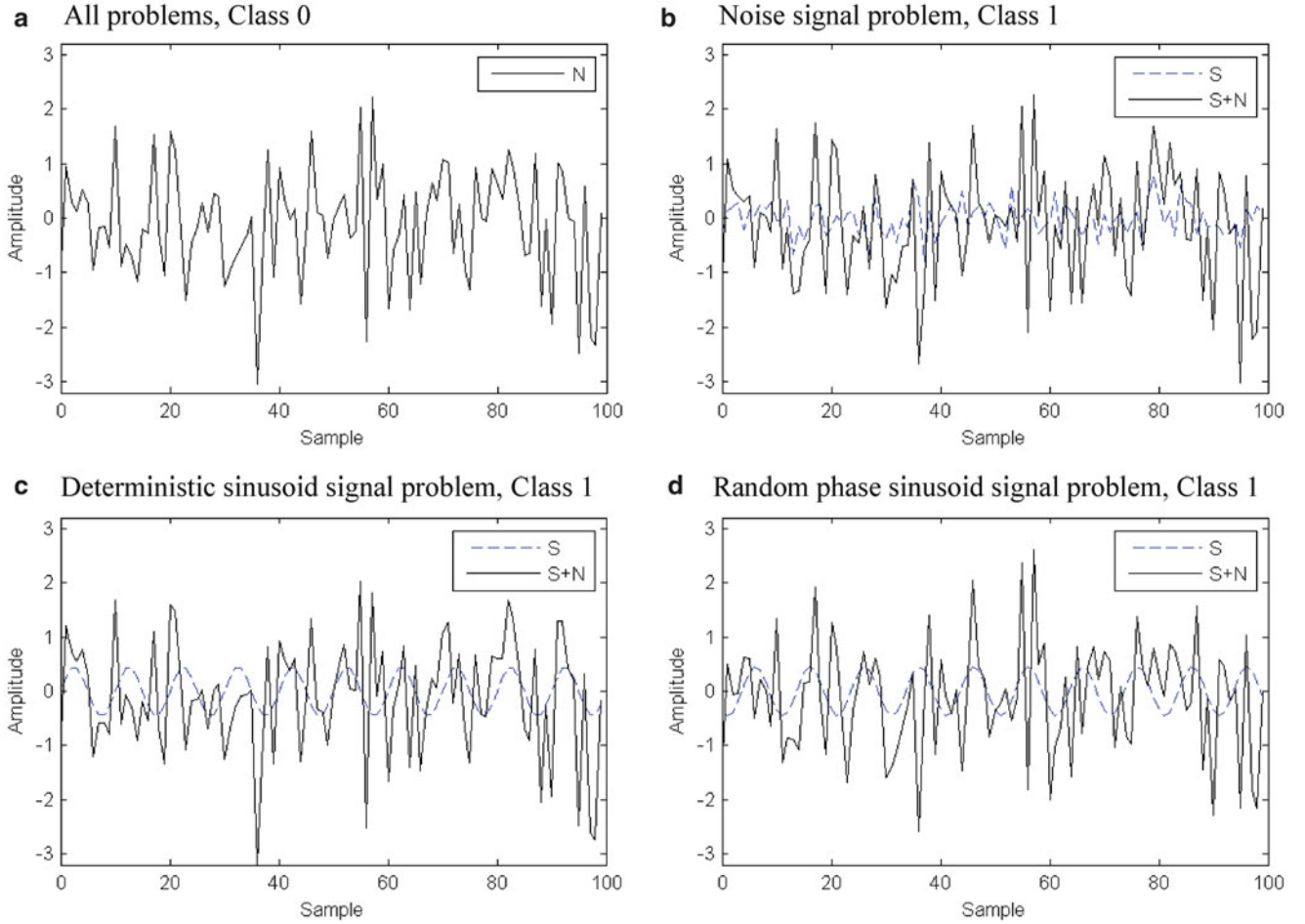


**Fig. 2.2** Example signal realizations for three signal detection problems (noise,  $N$ ; signal,  $S$ ; and corrupted signal,  $S + N$ ). (a) All problems, Class 0. (b) Noise signal problem, Class 1. (c) Deterministic sinusoid signal problem, Class 1. (d) Random phase sinusoid signal problem, Class 1

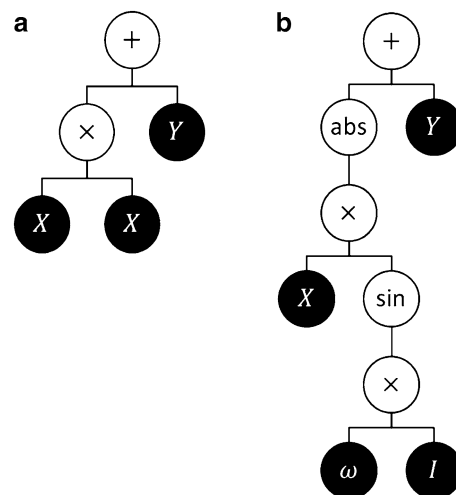
$$D_{deterministic\ sinusoid} = \sum_{i=0}^{N-1} X_i \sin(\omega i) \quad (2.4)$$

$$D_{random\ phase\ sinusoid} = \left( \sum_{i=0}^{N-1} X_i \sin(\omega i) \right)^2 + \left( \sum_{i=0}^{N-1} X_i \cos(\omega i) \right)^2 \quad (2.5)$$

These three problems represent increasingly difficult classification tasks for the GP search. The noise signal problem is almost trivially difficult, and there is no signal knowledge missing that would improve the search. The optimal tree solution for this problem is shown in Fig. 2.3a. In the second problem, the GP system lacks the knowledge of signal structure, phase, and frequency information necessary to generate the matched filter making the problem more difficult. Figure 2.3b gives a possible representation of the optimal detector as a GP tree. Note that the required frequency constant could be generated in a variety of ways within the tree, but the exact value is not provided as a constant terminal. In the final problem, the solution structure available to the GP system is over constrained to admit the optimal solution. There is no possibility of memory allowed in the current framework to store the in-phase and quadrature components of the solution making the last problem difficult if not impossible to achieve an optimal result.



**Fig. 2.3** Optimal detectors for two signal detection problems represented as Genetic Programming tree individuals. “ $\omega$ ” terminal represents a subtree that produces correct frequency constant (rad/s). (a) Noise signal problem. (b) Deterministic sinusoid signal problem



### 2.3.3 Detection Results

For each problem, the best detector from multiple GP runs is compared to the known optimal solution on an independent set of one million signal realizations. Ideally, the distributions of the detector output or feature from each class would be completely separate and distinct. Because the chosen SNR levels are insufficiently high, significant overlap appears in the distributions even with the optimal detectors. Histograms of the features for all three problems are given in Fig. 2.4. Note that the feature values are normalized to class 0 for the GP results since the actual levels are meaningless for these detectors. For the noise signal and deterministic sinusoid signal problems, the GP solution shows similar separation to the optimal result. In fact, the plots in Fig. 2.4c, d are nearly identical other than scaling. However, in the last problem, the GP solution gives an irregular distribution for class 1 with significant overlap between the two classes. Because the distribution for class 1 is clearly not normal, the assumption of normality in calculation of the fitness may degrade performance in this case.

Due to the overlapping classes, there is a tradeoff between false positive and false negative results when selecting a classification threshold. ROC curves show this tradeoff as a threshold is moved over the range of the detector output. Figure 2.5 shows that the GP produced detectors for the noise signal and deterministic sinusoid signal problems perform identically to the analytical optimal results. This result is especially impressive in the case of the sinusoid signal as the GP system had no knowledge of the signal while the optimal result requires full signal knowledge which is never available in SHM. In the case of the random phase sinusoid signal problem, the GP solution shows significantly reduced performance compared to the optimal detector. The suboptimal performance of GP in this case is not a surprise since the optimal detector is unrealizable with the current solution structure.

The AUC for each detector is given in Table 2.2. The AUC for the GP solution to the random phase sinusoid signal problem is 0.77 which is significantly lower than the optimal value of 0.96 but would still be considered “fair” detection. The average run AUC confirms the difficulty level of the three problems. For the noise signal, most runs achieved an optimal result of 0.98. In the deterministic sinusoid problem, the best run achieved the optimal value of 0.99 while the average run AUC is only 0.82. Finally, in the most difficult problem the average GP run reached an AUC of 0.69.

Table 2.2 also gives two measures of the size and complexity of the GP solutions. Tree nodes is the total count of functions and terminals in the best detector’s tree. Tree depth measures the overall “height” of the tree. In each case, it is evident that the GP solutions are significantly more complex than the optimal solution. In fact, they are far too large to meaningfully interpret by hand due to the issue of bloat. Bloat is a known issue with GP that causes exponential growth of the solution size once the search stagnates. There are a number of approaches to dealing with bloat by adding pressure towards selecting parsimonious solutions. However, the solutions in this case are still trivial in computational complexity for modern processors.

## 2.4 Conclusion

This study demonstrates that Genetic Programming can reproduce optimal results when tasked with classifying structured data such as time series measurements. GP successfully found the optimal detector for noise signals and deterministic

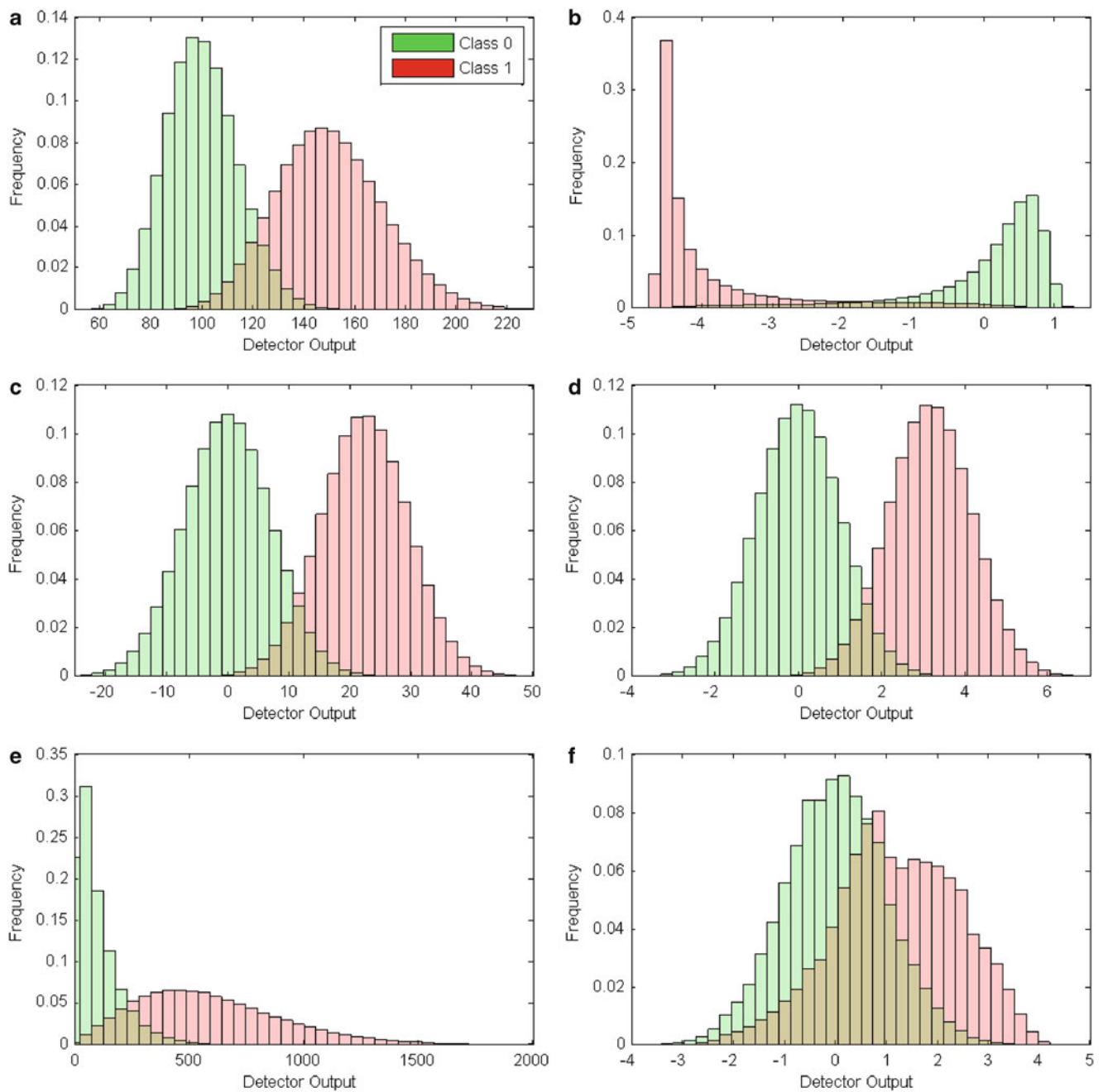


**Fig. 2.4** Feature histograms for signal detection problems. (a) Noise signal, Optimal detector. (b) Noise signal, GP detector. (c) Deterministic sinusoid signal, Optimal detector. (d) Deterministic sinusoid signal, GP detector. (e) Random phase sinusoid signal, Optimal detector. (f) Random phase sinusoid signal, GP detector

sinusoid signals buried in white noise with none of the signal knowledge required to derive the optimal detector. This is a promising result for development of damage detection algorithms in structural health monitoring as knowledge of how damage affects structural response measurements is limited. In the case of a random phase sinusoid signal, the current solution structure was insufficient to reproduce the optimal result. Future work will expand the allowable complexity of the

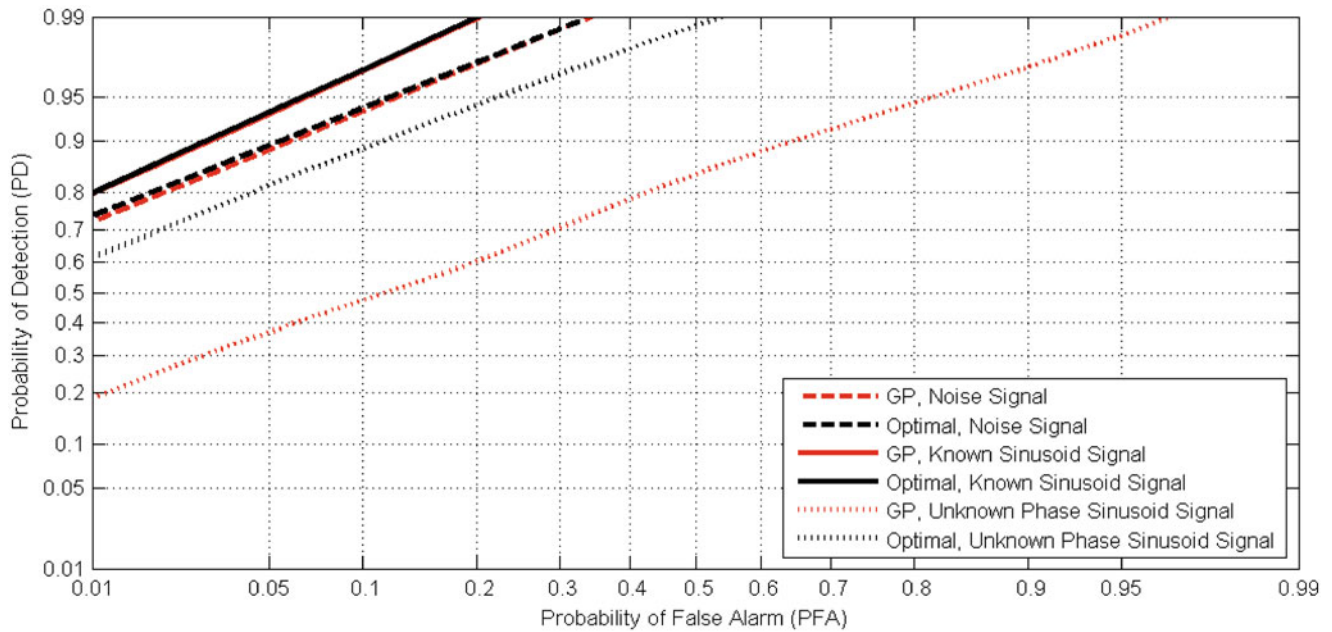


Fig. 2.5 Receiver operating characteristic's curves for signal detection problems

Table 2.2 Detector summaries for signal detection and three-story structure problems

Problem	Detector	AUC	Average run AUC	Tree nodes	Tree depth
Noise signal	Optimal	0.98	–	5	3
Noise signal	GP	0.98	0.98	85	15
Deterministic sinusoid signal	Optimal	0.99	–	8 + constant	6 + constant
Deterministic sinusoid signal	GP	0.99	0.82	457	53
Random phase sinusoid signal	Optimal	0.96	–	–	–
Random phase sinusoid signal	GP	0.77	0.69	503	45

current vector scanning framework as well as comparing other approaches for handling structured input data in GP. Perhaps the largest difficulty with GP is the massive computational effort required, but with modern processing extra computation time is insignificant compared to the modeling effort and expert knowledge currently required to develop SHM algorithms.

**Acknowledgements** This work was supported by the Department of Defense (DoD) through the National Defense Science and Engineering Graduate Fellowship (NDSEG) Program.

## References

1. Koza JR (1992) Genetic programming: on the programming of computers by means of natural selection. MIT, Cambridge
2. Poli R, Langdon WB, McPhee NF (2008) A field guide to genetic programming. Published via <http://lulu.com> and freely available at <http://www.gp-field-guide.org.uk> (with contributions by Koza JR)
3. Conrads M, Nordin P, Banzhaf W (1998) Speech sound discrimination with genetic programming. In: Proceedings of the first European workshop on genetic programming, Paris, pp 113–129. April 1998

## Chapter 3

# Optimal Selection of Artificial Boundary Conditions for Model Update and Damage Detection – Part 1: Theory

Joshua H. Gordis and L.T. Konstantinos Papagiannakis

**Abstract** Sensitivity-based model error localization and damage detection is hindered by the relative differences in modal sensitivity magnitude among updating parameters. The method of artificial boundary conditions is shown to directly address this limitation, resulting in the increase of the number of updating parameters at which errors can be accurately localized. Using a single set of FRF data collected from a modal test, the artificial boundary conditions (ABC) method identifies experimentally the natural frequencies of a structure under test for a variety of different boundary conditions, without having to physically apply the boundary conditions, hence the term “artificial.” The parameter-specific optimal ABC sets applied to the finite element model will produce increased sensitivities in the updating parameter, yielding accurate error localization and damage detection solutions. A method is developed for identifying the parameter-specific optimal ABC sets for updating or damage detection, and is based on the QR decomposition with column pivoting. Updating solution residuals, such as magnitude error and false error location, are shown to be minimized when the updating parameter set is limited to those corresponding to the QR pivot columns. The existence of an optimal ABC set for a given updating parameter is shown to be dependent on the number of modes used, and hence the method developed provides a systematic determination of the minimum number of modes required for localization in a given updating parameter. These various concepts are demonstrated on a simple model with simulated test data.

**Keywords** Updating • Identification • Artificial boundary conditions

### 3.1 Introduction

In sensitivity-based finite element (FE) model updating and damage detection (here, collectively referred to as “updating”), there are typically a large number of physical parameters which need to be identified, either as “corrections” to the FEM in model updating, or as “flags” for potential damage in the test article in damage detection. The number of these updating parameters frequently exceeds the number of measured modes available for use in the updating process. This disparity between the number of available modes and the number of updating parameters has motivated much prior and current research into ways to increase the size of the available measured dataset. An increase in the size of the dataset, however valuable, does not directly address a fundamental limitation in the sensitivity-based approach to model updating. The updating solution for each parameter is dependent on the relative magnitude of its modal sensitivities, calculated from the FE model. Given the limited bandwidth of a modal test, the modal sensitivities calculated for the various updating parameters are of different magnitudes, and hence updating solutions are biased towards those parameters associated with higher sensitivity values. A low relative modal sensitivity of a given updating parameter will prevent the updating solution from localizing an error in this parameter, and prevent the estimation of the true error magnitude. In fact, without an accurate localization, it is in general not possible to accurately estimate the error magnitude. As has been noted previously [1], accurate localization is

---

J.H. Gordis (✉)

Department of Mechanical and Aerospace Engineering – Code ME/Go, Naval Postgraduate School,  
700 Dyer Road Bldg. 245 Room 313, Monterey, CA 93943-5146, USA  
e-mail: [jgordis@nps.edu](mailto:jgordis@nps.edu)

L.T.K. Papagiannakis  
Hellenic Navy, Athens, Greece

critical, as once the parameters in error have been identified, the updating can be carried out and the updating solution residual (however defined) between measured and calculated response minimized, or even driven to zero. This minimization can occur regardless of whether or not a “correct” selection of updating parameters (i.e. localization) has been made. A clear reminder is given in [2] that in sensitivity-based updating, a low sensitivity value does not imply that a parameter is not in error, but can impede both localization and estimation.

The use of artificial boundary conditions (ABC) addresses this fundamental limitation. Through the application of selected sets of ABC to the FRF data normally collected in a modal test, an accurate localization solution for a greater number of, and possibly all, individual updating parameters can be obtained. When the measured FRF are insufficient, either in spatial completeness and/or bandwidth, to localize the error in a given parameter, the method clearly indicates this insufficiency, for each updating parameter. As will be shown, this is accomplished through the application of multiple ABC sets, where a large number of alternative sensitivity matrices are generated, and these alternative sensitivity matrices are queried as to whether or not the localization of each updating parameter is possible. This large number of alternative sensitivity matrices made available by the method substantially increases the possibility of generating an accurate localization solution for each updating parameter. This application of multiple ABC sets also relaxes the demand on test bandwidth required (i.e. number of modes) for accurate localization.

## 3.2 Background

In a modal test of a structure, a single set of boundary conditions are typically used, due to the prohibitive demands in time, cost, and practicality of physically altering the boundary conditions and retesting the structure. The modal test yields spatially incomplete frequency response function (FRF) data at each frequency point in the measurement bandwidth. From this FRF data, the modal parameters of the structure can be identified. These parameters include a single set of natural frequencies and the associated mode shapes and damping ratios, and are specific to the “as-tested” configuration (e.g. boundary conditions) of the test article. Given the typically large number of physical parameters for which errors or damage need to be identified (updating parameters), the use of natural frequencies alone can therefore result in an underdetermined system of updating equations in the unknown parameters. A basic solution to an underdetermined problem is non-unique, while a least-norm solution tends to smear the identified location of errors, in that falsely non-zero values are produced for parameters other than those truly in error. One strategy for increasing the number of equations in the updating system is by the inclusion of mode shape sensitivity data, which can provide a sufficient number of additional equations such that the problem is rendered overdetermined. For an overdetermined problem, the least-squares solution again tends to smear error location. For brevity, we will refer collectively to FEM updating and damage detection as “updating,” and to the solution of either problem as “errors” in the updating parameters.

The advantages of the use of natural frequencies only (excluding mode shape data) as a response metric are well known. These advantages include the higher accuracy with which natural frequencies can be identified as compared to mode shape data, the elimination of both the mode shape estimation process and the identification of real mode shapes from complex shapes. Despite the relative quality of the natural frequencies in the updating process, the limited number of measured natural frequencies can restrict the effectiveness of updating.

Another strategy for enlarging the measured data set is by the direct use of FRF data, due to the large amount of potentially useful data contained therein. This advantage is mitigated by the realization that not all FRF frequency points are of value, and a frequency selection algorithm is therefore needed. The use of antiresonance frequencies in addition to (or in place of) natural frequencies has also been explored; see for example [2–6]. Antiresonances are a potent response quantity for updating due to their being functions both of the (global) natural frequencies and the (local) mode shape elements specific to the excitation and response coordinates of the FRF. However, antiresonances are not without their peculiar limitations; it has been shown that antiresonances of transfer FRF are very sensitive to small changes in a structural model and excitation location, and that the robustness of the updating process is improved if restricted to the use of antiresonances from driving point FRF [4]. However, in a standard single-input modal test, only a single point FRF is measured. Other point FRF can be synthesized using the (incomplete) identified modes, and the resulting error in antiresonance locations (along the frequency axis) compensated for by the inclusion of low and high frequency residuals calculated from the model [6]. Furthermore, antiresonance sensitivities have been shown to be linear combinations of eigenvalue and mode shape sensitivities, and hence antiresonance data can replace, but not augment, mode shape data [3]. The overall performance of updating has been compared when using resonances versus using resonances along with some antiresonances. It was concluded that the improvement of the updating results upon inclusion of the antiresonances is dependent on the updating parameters selected as well as the location of the errors [7].

Yet another strategy for enlarging the data set for updating is by physically modifying the boundary conditions of the structure, and/or the addition or removal of mass and/or stiffness, generally referred to as perturbed boundary conditions. The physical alteration of the boundary conditions yields a distinct dynamic system with a different eigenvalue spectrum. Along with the similarly modified FE model, this provides independent rows for the sensitivity-based updating equation. This has been shown to be an effective strategy [8–12], but of course comes with the various demands of physically altering the boundary conditions.

### 3.3 Artificial Boundary Condition Sets

Both the antiresonance and perturbed boundary approaches to enlarging the data set do have significant benefits for updating. The method of Artificial Boundary Conditions [13], or “pseudo-tests” [14] offers those benefits while avoiding some of their drawbacks. The theory of ABC originates in the concept of the omitted coordinate system (OCS) [15] which plays a central role in the underlying properties of advanced model reduction techniques and frequency domain updating; see for example, [16–22]. With respect to an experimentally derived model, an OCS is the dynamic system which results when some of the measured coordinates are restrained (i.e. “pinned” to ground). In [13], it is shown that the natural frequencies of the structure under test, from a potentially large number of different boundary conditions, are available from a square FRF matrix measured from the structure, without having to physically apply the boundary conditions, i.e. artificial boundary conditions (ABC). If we take “a” as the number of measured coordinates, then the total number of ABC sets available from a single FRF matrix of size  $a \times a$ , and including the as-tested configuration, is given by the sum of the numbers of all k-combinations

$$C = \sum_{k=0}^a \binom{a}{k} \quad (3.1)$$

which is potentially a large number relative to the typical number of sensors used in a modal test. For example, if we use 10 accelerometers to measure the FRF matrix, and limit the number of coordinates at which to apply ABC to two, then the available number of ABC sets (and therefore OCS systems) is 55. If we include the as-tested configuration, the total number of distinct boundary condition sets is  $C = 56$ . If we increase the number of ABC coordinates to four, this total number of distinct boundary condition sets becomes 386. This potentially large number of ABC sets for which OCS natural frequencies can be identified leads to the primary focus of this work, which is how to select those sets which are most effective for model updating. The determination of optimal ABC sets has been previously explored [20] where genetic algorithms were used in the selection process. In that work, it was shown that effective updating is possible using a few low-order natural frequencies, and a few ABC sets. Here, we will also address the selection of optimal ABC sets, but rather than using optimization strategies, our selection will be based on an examination of underlying properties of the solutions to the parametric updating equations associated with a given ABC configuration.

### 3.4 Identification of Natural Frequencies for an Omitted Coordinate System

The full development of the theory can be found in [13, 15]. The experimental identification of the natural frequencies of an OCS involves the elimination of the rows and columns of  $H_{aa}$  corresponding to the a-set coordinates to be artificially “pinned” to ground. The proper subset of the measured (a-set) coordinates which are to be artificially pinned are denoted as the “o-set” and the associated partition of  $H_{aa}$  is denoted  $H_{oo}$ :

$$[H_{aa}] = \begin{bmatrix} H_{a-o, a-o} & H_{a-o, o} \\ H_{o, a-o} & H_{oo} \end{bmatrix} \quad (3.2)$$

where a-o indicates the set complement, i.e. all coordinates in the a-set, but not in the o-set. The mass and stiffness matrices implicitly defined by  $[H_{oo}]$  are obtained by the restraint of the a-set coordinates, and define an omitted coordinate system (OCS). The FRF matrix  $H_{oo}$  is then inverted yielding the impedance matrix  $Z_{oo} = H_{oo}^{-1}$ . If this is done as a function of frequency, peaks in the individual  $Z_{oo}$  will occur at the natural frequencies of the OCS. This has been demonstrated experimentally in [15, 21]. In [14], both the natural frequencies and mode shapes of the OCS are used in updating. The experimental study of the identification of OCS natural frequencies, reported in [21], demonstrated that OCS natural frequencies do indeed appear clearly as peaks in the OCS impedance spectra. It was also pointed out that with a significant noise content in the data can induce spurious spikes in the impedance spectra. It is noted that any measured FRF matrix

represents a reduced-order realization of an infinite-dimensional system with a set of restraints (pins) at its (un-measured) a-set coordinates [22]. Note that the case where the p-set contains a single coordinate corresponds to an ABC set with a single “pin.” In this case, from the eigenvalue separation theorem [23], the natural frequencies of associated OCS will interlace those of the baseline (as-tested) configuration.

This procedure for identifying the natural frequencies of the OCS assumes that a square FRF matrix is available. The direct measurement of a square FRF matrix requires the application of a suitable excitation at each response coordinate. This places an additional demand on the experiment. The synthesis of unmeasured FRF is possible once the measured FRF have been curvefitted. However, as the identification of OCS mode frequencies requires accurate FRF data at all frequencies in the bandwidth of interest, not just at modal peaks, the sensitivity of antiresonance frequencies to both the number and precision of estimated modes becomes a significant issue. This sensitivity was also shown to vary with distance from the driving point FRF. This was explored in some detail in [25], where both simulated and actual test data was used.

Here, we assume a square FRF matrix is available, to allow us to focus on two principle issues. The first issue is the development of a strategy for the selection of an optimal ABC set for the identification of specific updating or damage parameter(s). We will examine several updating metrics and show how they are minimized by the use of optimal ABC sets. The second issue pertains to the number of modes required in order for an ABC solution to identify errors in specific parameters. An ABC set can only be optimal if a sufficient number of modes are included in the identification.

### 3.5 The Updating Problem and Its Solutions

The parametric updating problem can be constructed from the first-order structural eigenvalue sensitivities as

$$\{\delta\Lambda\} = [S] \{u\} \quad (3.3)$$

where  $\{\delta\Lambda\} \in \mathbb{R}^{m \times 1}$  is a vector of the differences between the measured and calculated squared natural frequencies,  $\{u\} \in \mathbb{R}^{n \times 1}$  is a vector of updating parameter changes (e.g. model “errors”) to be identified, and  $[S] \in \mathbb{R}^{m \times n}$  is the matrix of eigenvalue sensitivities, calculated from the FE model. The number of modes used is “m” and the number of updating parameters is “n”.

We again note that the identification problem requires both error localization and error magnitude estimation. With respect to  $\{u\}$ , the localization problem consists of identifying which elements are truly in error. The magnitude estimation problem consists of estimating the individual element magnitudes of  $\{u\}$ . Most commonly, the system Eq. (3.3) is underdetermined, i.e.  $n > m$ , as the number of model parameters which are in question exceeds the number of experimentally identified natural frequencies. We will here focus on this underdetermined case.

With regards to the solution of Eq. (3.3) with  $m < n$ , and  $\text{rank}([S]) = m$ , we will briefly review two possible solutions for  $\{u\}$ . The first of these is the least-norm solution, for which  $\|\{u\}\|_2$  is a minimum, denoted  $\{u_{\text{ln}}\}$ . The least-norm solution minimizes the length of the solution vector, (in contrast to a least-squares solution, which minimizes the length of the residual [26]). The least-norm solution can be found from the pseudo-inverse, i.e.

$$\{u_{\text{ln}}\} = [S]^T \left( [S] [S]^T \right)^{-1} \{\delta\Lambda\} \quad (3.4)$$

Note that if  $[S]$  is full rank and well conditioned, the same solution is found from the SVD.

The second solution of relevance here is a *basic* solution, and can be found as follows. Given that  $[S]$  is  $m \times n$ , we partition  $[S]$  into sets of basic and non-basic columns as follows:

$$[S] = [S_1 \ S_2] \quad (3.5)$$

where a selection of m columns of  $[S]$  is made such that  $\text{rank}([S_1]) = m$ . These columns comprise the basis, and the corresponding elements of the solution vector are the basic parameters. The associated partitioning of  $\{u\}$  is written as

$$\{u\} = \begin{Bmatrix} u_1 \\ u_2 \end{Bmatrix} \quad (3.6)$$

The solution of Eq. (3.3) can be written

$$\{u_1\} = [S_1]^{-1} (\{\Delta\omega^2\} - [S_2] \{u_2\}) \quad (3.7)$$

and Eq. (3.3) is satisfied for any choice of the vector  $\{u_2\}$ , which contains the non-basic parameters. Throughout, we will focus on the choice,

$$\{u_2\} = \{0\} \quad (3.8)$$

and which results in the following solution:

$$\{u_{QR}\} \triangleq [S_1]^{-1} \{\Delta\omega^2\} \quad (3.9)$$

We denote this basic solution with the subscript ‘‘QR’’ as this solution will be calculated from the QR decomposition of  $[S]$  with column pivoting [27]. As we will see, the set of pivot columns selected by the QR algorithm determines the ability of an ABC set to provide a localization solution.

### 3.5.1 Least-Norm Versus Basic Solutions

We first illustrate some distinguishing characteristics of the two important classes of solution to Eq. (3.3) described above. We will illustrate the difference between  $\{u_{in}\}$  and  $\{u_{QR}\}$  with a simple numerical example.

For  $[S]$ , we will assume a random 3 by 4 matrix, corresponding to an updating problem using three modes and four updating parameters:

$$[S] = \begin{bmatrix} 0.6557 & 0.9340 & 0.7431 & 0.1712 \\ 0.0357 & 0.6787 & 0.3922 & 0.7060 \\ 0.8491 & 0.7577 & 0.6555 & 0.0318 \end{bmatrix} \quad (3.10)$$

We assume that a single error exists in the first updating parameter, and hence the ‘‘true’’ updating solution vector is:

$$\{u\} = [1 \ 0 \ 0 \ 0]^T \quad (3.11)$$

We first calculate the associated ‘‘true’’ mode frequency changes (i.e. the right-hand side), which is  $\{\delta\Lambda\} = [S]\{u\} = [0.6557, 0.0357, 0.8491]^T$ . Assuming now that  $\{u\}$  is unknown, the problem to be solved is

$$\begin{Bmatrix} 0.6557 \\ 0.0357 \\ 0.8491 \end{Bmatrix} = \begin{bmatrix} 0.6557 & 0.9340 & 0.7431 & 0.1712 \\ 0.0357 & 0.6787 & 0.3922 & 0.7060 \\ 0.8491 & 0.7577 & 0.6555 & 0.0318 \end{bmatrix} \begin{Bmatrix} u_1 \\ u_2 \\ u_3 \\ u_4 \end{Bmatrix} \quad (3.12)$$

We will compare the results of the two solutions,  $u_{in}$  and  $u_{QR}$ . The two solutions are:

$$\{u_{in}\} = [0.9928 \ -0.0503 \ 0.0669 \ 0.0116]^T \quad \{u_{QR}\} = [1 \ 0 \ 0 \ 0]^T \quad (3.13)$$

and  $\|u_{in}\| = 0.9964$  and  $\|u_{QR}\| = 1$ . Comparing these two solutions to the true solution of Eq. (3.11), it is seen that in this case of a well-conditioned, full rank  $S$ , the least-norm solution  $u_{in}$  fails to provide a localization (or magnitude) solution, while the basic solution  $u_{QR}$  (calculated using the QR decomposition with column pivoting) provides an exact localization (and magnitude) solution.

We will now repeat this calculation, with the only change being the location of the error. If we place the error in the third update parameter, i.e.

$$\{u\} = [0 \ 0 \ 1 \ 0]^T \quad (3.14)$$

We again first calculate the associated mode frequency errors, which are  $\{\delta\Lambda\} = [S]\{u\} = [0.7431 \ 0.3922 \ 0.6555]^T$ . Assuming that  $\{u\}$  is unknown, the system to be solved is,

$$\begin{Bmatrix} 0.7431 \\ 0.3922 \\ 0.6555 \end{Bmatrix} = \begin{bmatrix} 0.6557 & 0.9340 & 0.7431 & 0.1712 \\ 0.0357 & 0.6787 & 0.3922 & 0.7060 \\ 0.8491 & 0.7577 & 0.6555 & 0.0318 \end{bmatrix} \begin{Bmatrix} u_1 \\ u_2 \\ u_3 \\ u_4 \end{Bmatrix} \quad (3.15)$$



and the two solutions are:

$$\{u_{in}\} = [0.0669 \ 0.4680 \ 0.3776 \ -0.1075]^T \quad \{u_{QR}\} = [0.1075 \ 0.7518 \ 0 \ -0.1726]^T \quad (3.16)$$

It is clear that in this case neither solution is able to locate the error; however, the least-norm solution in general cannot provide localization.

### 3.5.2 QR Decomposition with Column Pivoting for Subset Selection

The failure of the QR solution to provide the correct error location in this second example is due to the column of [S], associated with the updating parameter in error, not being included as a pivot column. We will describe the QR decomposition algorithm with pivoting as this, in effect, provides the subset selection strategy which identifies those updating parameters which can be localized by a given ABC set.

The QR decomposition of [S] is,

$$[Q][R] = [S][P] \quad (3.17)$$

where  $[Q] \in \mathbb{R}^{m \times m}$  is an orthogonal matrix,  $[R] \in \mathbb{R}^{m \times n}$  is an upper triangular matrix, and  $[P] \in \mathbb{R}^{n \times n}$  is a permutation matrix. We will refer to the set of pivot column indices as “p”. Several methods are available for calculating the decomposition, such as Gram-Schmidt orthogonalization, Givens rotations, or Householder reflections [26]; the latter is used here. With respect to the use of Householder reflections, the key aspect of the algorithm is that at the *i*th iteration, prior to the *i*th Householder reflection, the norms of the columns of  $[R(i:m, i:n)]$  are calculated, and the *i*th column of  $[R(i:m, i:n)]$  is swapped with that column having the maximum norm. This procedure produces a decomposition with a column permutation identical to that of MATLAB [28]. This criteria for the permutation of the columns in effect selects updating parameters to serve as basic variables (subset selection). The underdetermined solution of Eq. (3.3) can only provide exact localization solutions for those updating parameters in this QR basis. Note that column pivoting in conjunction with the QR method is effective for dealing with near-rank deficiency, and can improve numerical accuracy, so its use as a subset selection strategy does not compromise the numerical aspects of the problem. The use of the QR algorithm in the context of model updating with artificial boundary conditions (“pseudo-tests”) has also been explored in [14].

The reason for this difference in performance in the above examples lies in the set of column pivots (QR basis) which are a property of the matrix [S]. The QR decomposition of [S] above, Eq. (3.10), is:

$$[Q][R] = [S][P] \quad (3.18)$$

$$[Q] = \begin{bmatrix} 0.6763 & -0.2813 & -0.6808 \\ 0.4915 & 0.8607 & 0.1326 \\ 0.5487 & -0.4243 & 0.7204 \end{bmatrix} \quad (3.19)$$

$$[R] = \begin{bmatrix} 1.3810 & 0.4802 & 0.9269 & 1.0550 \\ 0 & 0.5460 & -0.5140 & -0.1495 \\ 0 & 0 & 0.1700 & 0.0183 \end{bmatrix} \quad (3.20)$$

$$[P] = \begin{bmatrix} 0 & 0 & 1 & 0 \\ 1 & 0 & 0 & 0 \\ 0 & 0 & 0 & 1 \\ 0 & 1 & 0 & 0 \end{bmatrix} \quad p = [2, 4, 1] \quad (3.21)$$

The first  $m = 3$  columns of the permutation matrix [P], Eq. (3.21), reveal that the QR basis includes the updating parameters (scalar elements of the solution),  $u_2$ ,  $u_4$ , and  $u_1$ . We will refer to this parameter set as  $p = \{2, 4, 1\}$ . Element #3 is not included, and hence this sensitivity matrix [S] cannot localize a potential error in element #3, as seen in the solution  $\{u_{QR}\}$  above, Eq. (3.16).

The inability of the underdetermined solution of Eq. (3.3) to provide an exact localization solution for all updating parameters limits traditional (single boundary condition set) updating strategies. As seen above, this is due to the fact that a single sensitivity matrix can produce only one QR basis that satisfies the maximum column norm pivot criterion of the QR algorithm (described above). The ABC method directly addresses this problem by the fact that many different ABC

configurations can be applied, using the same set of measured FRF data from the “as-tested” configuration. As the number of ABC configurations increases, the probability increases of generating a sensitivity matrix for which the QR pivot columns include a column associated with a given updating parameter. In other words, it is possible to find an ABC configuration which has sufficiently high modal sensitivities relative to a given updating parameter. This result guides the selection of ABC sets which are able to reveal errors for a given updating parameter. An optimal ABC set for an updating parameter “i” generates QR solutions with permutation set  $p$ , such that  $i \in p$ . Furthermore, the process clearly identifies the minimum number of measured modes required in order to identify a specific parameter, as will be demonstrated.

More generally, we can see that a related and broader requirement of a localization solution is that it be able to provide the necessary sparsity. A solution which maximizes sparsity, minimizes the zero-norm,  $\|\bullet\|_0$ , the number of nonzero components of the solution vector [29]. It has been shown [30] that for most large underdetermined systems, the sparsest solution (also) minimizes the 1-norm,  $\|\bullet\|_1$ . Therefore, the least-norm solution which minimizes the 2-norm is an inappropriate choice for localization. The two solutions shown in Eq. (3.13) demonstrate their relative ability to yield an appropriate sparsity to localize errors. While the basic solution (generated by the QR decomposition) is not a 1-norm minimizer, this solution can provide the necessary sparsity to reveal error locations. We demonstrate this more fully in what follows, with respect to ABC updating solutions.

### 3.6 Simulation Model and OCS Frequencies

Our simulated updating problem will make use of a cantilevered beam of length 3.048 m, cross-section area of  $5.163 \times 10^{-3} \text{ m}^2$ ,  $EI = 2.206 \times 10^3 \text{ MPa}$ , and density of  $7.833 \times 10^3 \text{ kg/m}^3$ . The FE model, shown in Fig. 3.1, is comprised of 10 two-noded elements with two DOF/node (lateral translation and slope). We will assume that a measured frequency response is available from every translational DOF, and that an excitation has been applied to every translational DOF, yielding a square  $10 \times 10$  FRF matrix. The cantilevered boundary conditions constitute the “as-tested,” configuration. All artificial boundary conditions (ABC) are relative to this as-tested (cantilevered) configuration.

The first five elastic mode frequencies are shown in Table 3.1:

In order to examine the ability to localize model errors (or structure damage), EI errors will be placed in one element at a time, as shown in Fig. 3.2. For localization, the updating parameters comprising the vector  $\{u\}$  will include the EI errors at each element. The goal is to select ABC configurations which include  $u_i$  in the QR basis, and thus have the ability to identify an error in element “i,” e.g.  $u_i \equiv \Delta EI_i$ .

We here assume that all OCS frequencies of interest have been already been obtained (from simulated test data) in order to focus on the selection of ABC sets. However, we will demonstrate briefly the process of identifying the OCS frequencies from an FRF matrix. We start with a square,  $10 \times 10$  FRF matrix, assumed measured from the as-tested configuration, or calculated from an FE model. Figure 3.3 shows a point FRF,  $H_{11}(\Omega)$ . The lowest five peaks correspond to the frequencies in Table 3.1.

For a  $10 \times 10$  FRF matrix, there are  $C(10, 9) = 1,024$  possible ABC configurations (including the as-tested configuration). If we limit the number of ABC pins to two, then there are  $C(10, 2) = 56$  possible ABC configurations. For the purpose of illustrating the identification of OCS frequencies, we arbitrarily choose to artificially apply two pins, restraining the translations at nodes 9 and 10. This configuration is shown in Fig. 3.4.

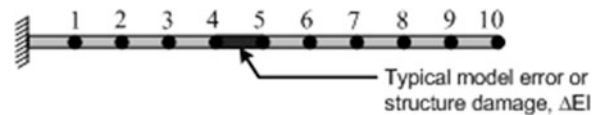
**Fig. 3.1** Simulation model – cantilevered beam



**Table 3.1** Natural frequencies (Hz) of “as-tested” configuration

Mode #1	Mode #2	Mode #3	Mode #4	Mode #5
<b>9.08</b>	56.92	159.40	312.58	517.53

**Fig. 3.2** Typical parameter error, shown here in element #5



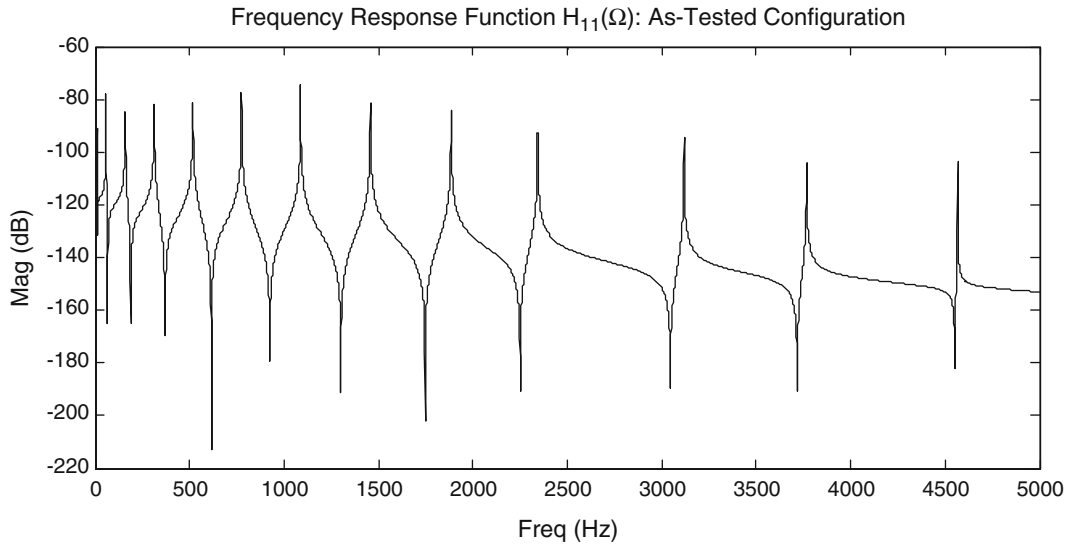


**Fig. 3.3** Point FRF from as-tested configuration

**Fig. 3.4** As-tested structure with ABC set comprised of two pins

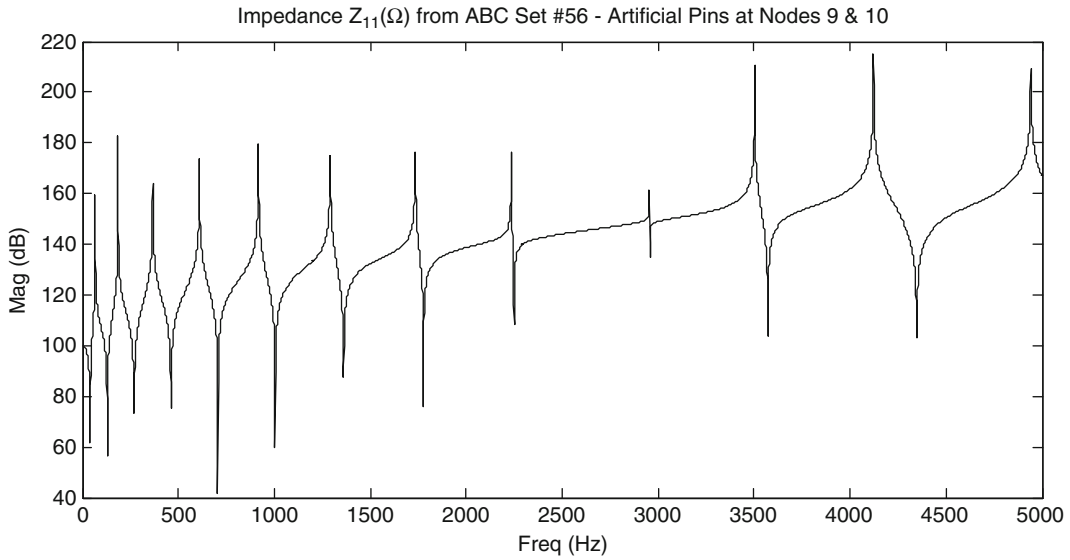
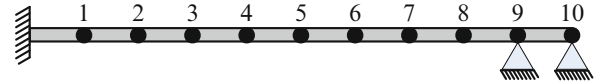


**Fig. 3.5** OCS impedance

The coordinate sets of Eq. (3.2) have the membership  $a = [1 : 10]$ , and  $o = [9:10]$ , all of which are translational DOF at the indicated nodes. The measured FRF can be written as:

$$[H] = \begin{bmatrix} H_{1:8,1:8} & H_{1:8,9:10} \\ H_{9:10,1:8} & H_{9:10,9:10} \end{bmatrix} \quad (3.22)$$

We invert  $[H_{9:10,9:10}]$  at each frequency in the test bandwidth, and then plot one of the elements of the resulting  $2 \times 2$  OCS impedance,  $[Z^{ABC}]$ , as shown in Fig. 3.5.

If we apply these ABC to the FE model, the calculated lowest 12 mode frequencies match exactly the peaks in the impedance of Fig. 3.5, and are shown in Table 3.2.

**Table 3.2** Natural frequencies (Hz/1,000) of 2-pin ABC configuration

#1	#2	#3	#4	#5	#6	#7	#8	#9	#10	#11	#12
<b>0.0671</b>	0.1860	0.3667	0.6098	0.9172	1.2914	1.7344	2.2347	2.9546	3.5029	4.1222	4.9415

**Table 3.3** All ABC sets for 10 nodes, taken one, and then two, at a time

Set #	ABC pin location – node #									
	1	2	3	4	5	6	7	8	9	10
<b>1</b>	0	0	0	0	0	0	0	0	0	0
<b>2</b>	1	0	0	0	0	0	0	0	0	0
<b>3</b>	0	1	0	0	0	0	0	0	0	0
<b>4</b>	0	0	1	0	0	0	0	0	0	0
<b>5</b>	0	0	0	1	0	0	0	0	0	0
<b>6</b>	0	0	0	0	1	0	0	0	0	0
<b>7</b>	0	0	0	0	0	1	0	0	0	0
<b>8</b>	0	0	0	0	0	0	1	0	0	0
<b>9</b>	0	0	0	0	0	0	0	1	0	0
<b>10</b>	0	0	0	0	0	0	0	0	1	0
<b>11</b>	0	0	0	0	0	0	0	0	0	1
<b>12</b>	1	1	0	0	0	0	0	0	0	0
<b>13</b>	1	0	1	0	0	0	0	0	0	0
<b>14</b>	1	0	0	1	0	0	0	0	0	0
⋮										
<b>47</b>	0	0	0	0	0	1	1	0	0	0
<b>48</b>	0	0	0	0	0	1	0	1	0	0
<b>49</b>	0	0	0	0	0	1	0	0	1	0
<b>50</b>	0	0	0	0	0	1	0	0	0	1
<b>51</b>	0	0	0	0	0	0	1	1	0	0
<b>52</b>	0	0	0	0	0	0	1	0	1	0
<b>53</b>	0	0	0	0	0	0	1	0	0	1
<b>54</b>	0	0	0	0	0	0	0	1	1	0
<b>55</b>	0	0	0	0	0	0	0	1	0	1
<b>56</b>	0	0	0	0	0	0	0	0	1	1

This brief numerical example demonstrates how OCS natural frequencies for one of potentially many ABC sets can be identified from the FRF data acquired from a single test.

### 3.6.1 Generation of Artificial Boundary Condition (ABC) Sets

As discussed above, the imposition of a set of artificial boundary conditions (ABC) results in the definition of an omitted coordinate systems (OCS). Given the 10 measurement locations for the system shown in Fig. 3.4, all possible ABC sets comprised of either one or two pins are generated. These sets include all combinations of the 10 measurement locations, taken both one, and then two, at a time (see Eq. (3.1)). These ABC sets are shown in Table 3.3, with Sets #15 through #46 removed to save space. In this table, a “1” indicates a node to be pinned, and a “0” indicates that the node remains free. Note that Set #1 shows no pins, as this set corresponds to the as-tested configuration.

For each of the above sets, the OCS natural frequencies are determined by the FRF matrix partition inversion process demonstrated above. Peak picking or curve-fitting can be used. We can plot the natural frequencies of the various OCS defined by the boundary conditions in Table 3.3. The lowest three mode frequencies of all 56 systems are plotted in Fig. 3.6.

In Fig. 3.6, the horizontal lines, labeled “Mode  $i$  Nat Freq – As Tested,” are the frequencies of the first five modes of the as-tested configuration (ABC set #1). The jagged curves which depart from the lowest three of these horizontal lines are the mode frequencies for the various OCS systems defined by the ABC sets. As can be seen, the as-tested configuration mode frequencies are lower bounds for the frequencies of all OCS systems. Furthermore, for this system, all of the OCS systems have three modes within the bandwidth spanned by the lowest five modes of the as-tested configuration, indicating that the application of ABC do not necessarily move modes out of a reasonable test bandwidth.

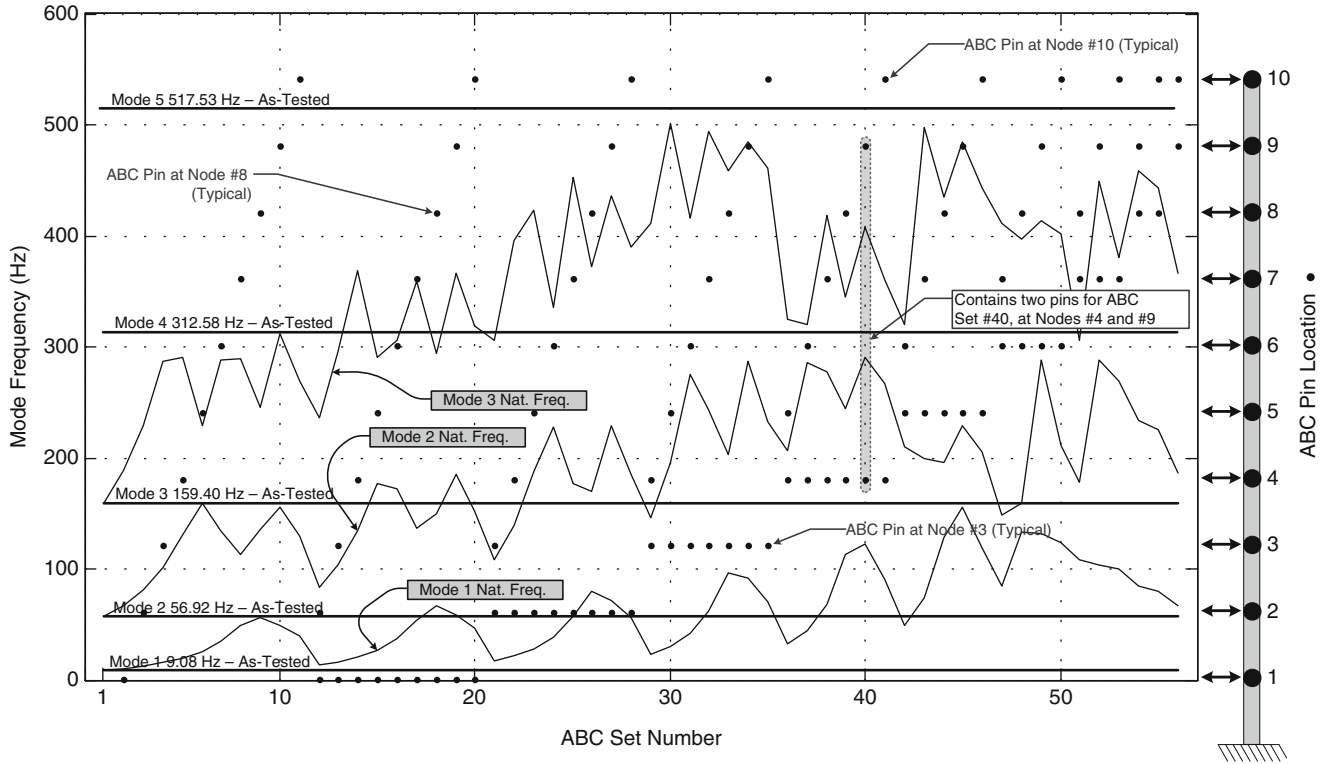


**Fig. 3.6** First three mode frequencies for all OCS systems defined by the 56 ABC configurations. ABC pin locations are indicated by the *dots*, which line up horizontally with the nodes on the beam to the *right*. For example, the *shaded oval* at ABC set #40 contains two *black dots*, which line up with nodes #4 & #9 on the beam, indicating the artificial pin locations for this set. The as-tested beam natural frequencies are ABC set #1, and these frequency values are extended across the graph as the *horizontal lines* (as indicated)

We will now define a boolean flag which is set when an updating parameter index is included in the QR basis calculated from one of the OCS system sensitivity matrices. We will also define several updating solution performance metrics to gauge the effectiveness of an updating solution in both localization and magnitude estimation. We will refer to the quantities calculated for the  $c$ th OCS using a superscript. For example,  $u^{(c)}$  indicates the solution for the updating parameters found from the  $c$ th OCS. Here,  $c \in 1:C$ , and  $c = 1$  corresponds to the as-tested configuration (no ABC). Again, for our example,  $C(10, 2) = 56$ .

### 3.6.2 QR Basis Inclusion Flag

The ability of a solution, found from the application of a specific ABC set, to localize an error in a specific updating parameter is dependent upon whether the associated column of  $[S]$  is included in the QR basis (i.e. pivot column). We will quantify whether this criterion is satisfied for each ABC configuration, in the following manner.

Associated with ABC set “ $c$ ” is the updating problem,

$$\{\delta\Lambda^{(c)}\} = [S^{(c)}] \{u^{(c)}\} \quad (3.23)$$

where  $\{\delta\Lambda^{(c)}\}$  are the differences in natural frequency squared between the experimentally identified OCS and the similarly constrained FE model. The sensitivity matrix  $[S^{(c)}]$  is calculated from this constrained model. The updating parameter vector  $\{u^{(c)}\}$  is calculated from Eq. (3.23) using the QR method with column pivoting. The QR basis for  $[S^{(c)}]$  is the parameter set  $p(c)$ .

A boolean flag is used to signal whether the  $i$ th updating parameter is included in  $p(c)$ , rendering error localization for this parameter possible, for updating problem “ $c$ ”. We define

$$QRB_c = \begin{cases} 0 & \text{if } i \in p(c) \\ 1 & \text{if } i \notin p(c) \end{cases} \quad (3.24)$$

( $QRB_c = 0$  indicates a “positive” result). This QRB flag will be plotted alongside several updating solution performance metrics, described in the following.

### 3.6.3 Updating Solution Performance Metrics

We will employ several metrics for comparing the effectiveness of each of the  $C = 56$  OCS systems (and their solutions) for parametric updating. As we will see, the correlation between these metrics and the QRB flag reveals which ABC set (OCS system) can localize an error in a specific updating parameter.

*Equation Residual e*: From Eq. (3.23), we will calculate, for each solution,

$$e_c = \left\| \left\{ \delta\Lambda^{(c)} \right\} - \left[ S^{(c)} \right] \left\{ u^{(c)} \right\} \right\|_2 \quad (3.25)$$

Note that to allow plotting of  $e_c$  on the same axes with the other metrics, the set of all  $e_c$  values is normalized such that  $\max_c (e_c) = 1$ .

*Relative Magnitude Error (RME)*: For the true error in parameter “i” given as  $u_i^{true}$ , the relative magnitude error is calculated as

$$RME_c = \text{abs} \left( u_i^{(c)} - u_i^{true} \right) / \text{abs} \left( u_i^{true} \right) \quad (3.26)$$

*Maximum False Alarm (MFA)*: This metric is a measure of the ability of a solution to suppress the reporting of false error locations

$$MFA_c = \max_{j, j \neq i} \left( \text{abs} \left( u_j^{(c)} \right) / u_i^{true} \right) \quad (3.27)$$

We briefly mention the sensitivity matrix condition number  $\rho_c$ , and the angle between the subspace spanned by the columns of  $[S]$  and that spanned by  $[\delta\Lambda]$ . Neither the condition number nor this angle, calculated for each OCS, are correlated with the ability to localize the error or estimate its magnitude. The variation in the condition number and subspace angle is not correlated with any of the above metrics, and hence neither the condition number nor this angle are needed, with respect to our purpose of selecting optimal ABC configurations. In practice, only the QRB flag need be calculated. Dependent columns due to model parameters with similar sensitivity values are identified in the QR process, and different ABC sets would be identified for each of these model parameters, thereby eliminating the column dependency. The use of an appropriate ABC set eliminates such dependencies, including those arising due to symmetry.

### 3.6.4 Simulation Results

*One Mode Solution  $m = 1$* : A single mode is assumed to have been identified from the measured FRF data for each ABC set, and is used to generate the sensitivity matrix and  $\delta\Lambda$ , as follows. We place a known EI error of 10 % in element #1 of the system shown in Fig. 3.1. The true solution vector for this case is  $\{u^{true}\} = [0.1 \ 0 \ \dots \ 0]^T$ . For each OCS, the first-order eigenvalue sensitivity matrix is calculated for  $m = 1$  mode and for all  $n = 10$  updating parameters, which are the EI errors for each of the 10 elements. The solution  $\{u^{(c)}\}$  is calculated using the QR decomposition. In Fig. 3.7, the three metrics, (equation residual  $e$ ; relative magnitude error, RME; and maximum false alarm, MFA), along with the QR basis flag, QRB, are plotted versus ABC set number. It is seen that the equation residual,  $e$ , drops to relative minimum values at only selected ABC sets. It is also seen that the RME and MFA also drop to minima at exactly the same ABC sets, indicating that the updating problems defined by these ABC sets produce accurate solutions for the identification.

Finally, it is seen that the QRB flag drops to zero at the identical ABC set numbers, indicating that an exact identification solution (localization and magnitude) is available for parameter “i” only when the  $i$ th column of the sensitivity matrix  $[S^{(c)}]$  is included in the QR basis. From inspection of Fig. 3.7, these optimal ABC sets for element #1 are  $c_1^{QR} =$

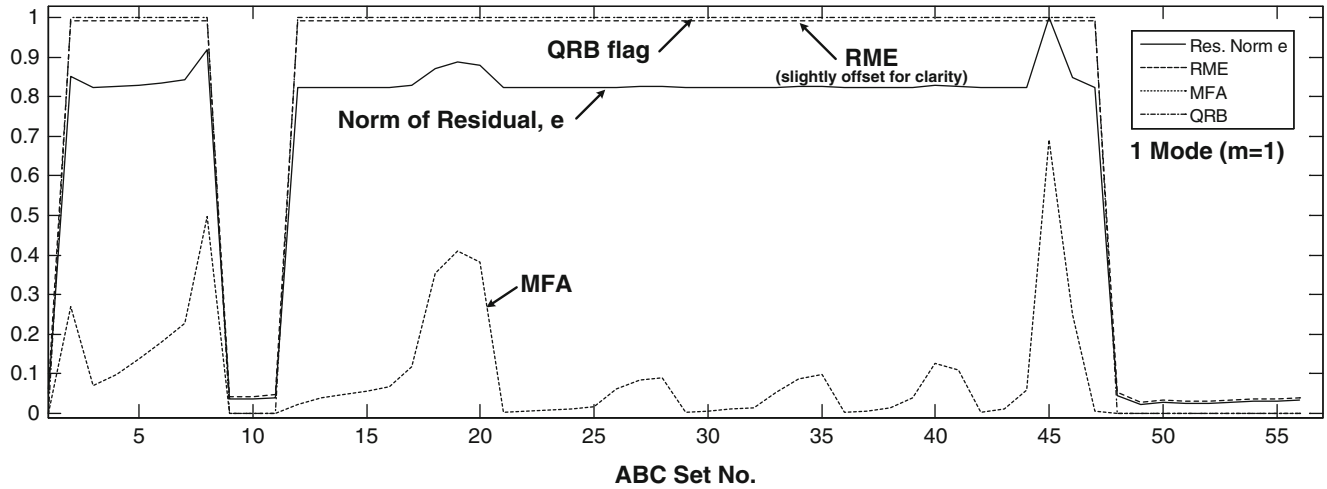


Fig. 3.7 Solution metrics and QRB flag for element #1, versus ABC set number,  $m = 1$  mode used

Fig. 3.8 Localization is exact for as-tested configuration

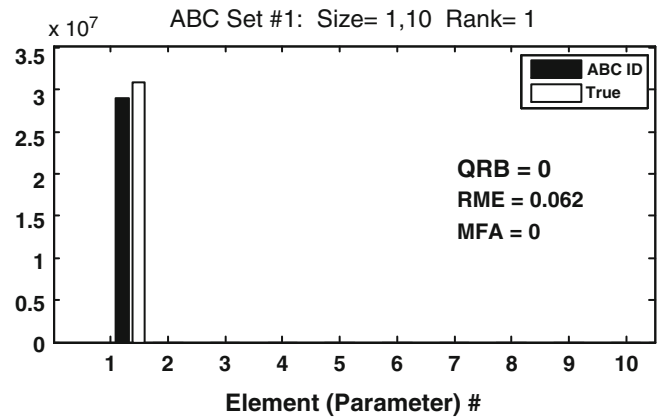
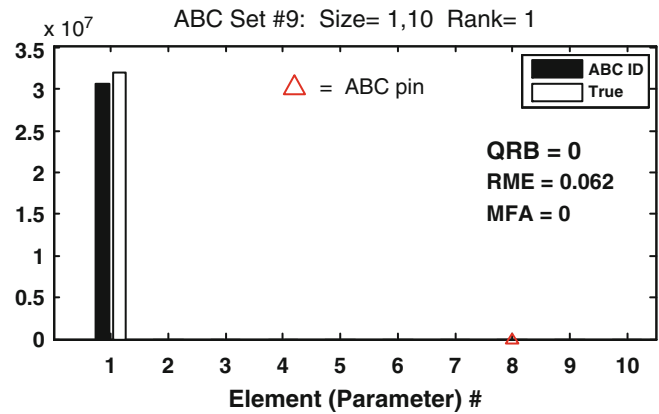


Fig. 3.9 Localization is exact for ABC set #9



{1, 9, 10, 11, 48 : 56}. Hence, the QRB flag being set “zero” is a condition which can be used to select ABC sets. Figure 3.7 makes it clear that only a subset of all the ABC sets can be used to locate error in element #1, specifically, those ABC sets,  $c_1^{QR}$ , at which the QRB flag is zero.

We will plot the solution vector  $u^{(c)}$  for several selected ABC configurations for which the QRB flag is zero (including the as-tested, i.e.  $c = 1$ ), and also for one ABC configuration for which the QRB flag equals one (failed solution). These four solutions are shown in Figs. 3.8 through 3.11. The as-tested configuration produces an accurate localization (Fig. 3.8), as does ABC sets #9 & #48. These three solutions all have  $QRB = 0$ . The artificial pin locations are indicated by the small triangle. ABC set #33 does not produce an accurate solution, as predicted by  $QRB = 1$ .

**Fig. 3.10** Localization is exact for ABC set #48

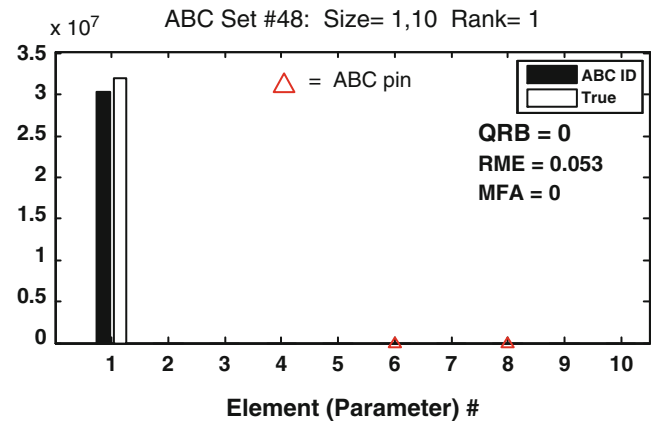


**Fig. 3.11** Localization fails for ABC set #33 (QRB = 1)

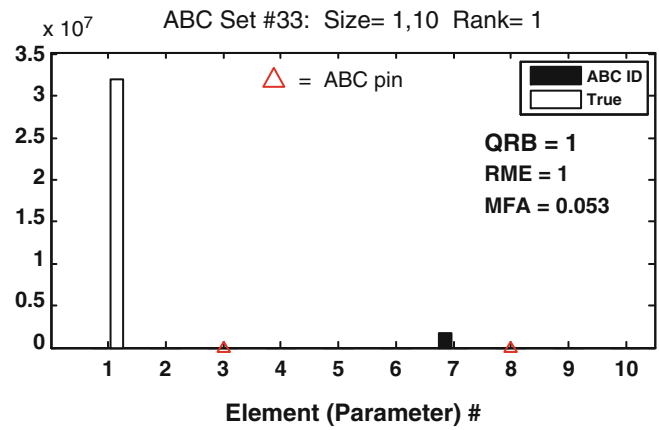
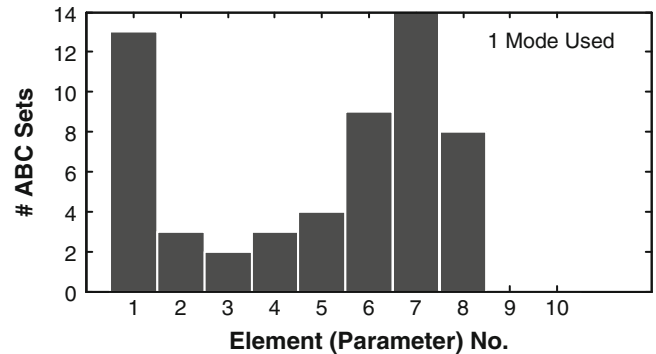


**Fig. 3.12** Histogram of updating parameter inclusion in QR basis sets, m = 1 mode used



We can also ask, for a given updating parameter  $u_i$ , how many ABC configurations can localize a potential error? This is given by the histogram, shown in Fig. 3.12, where again, only  $m = 1$  mode was used. This histogram shows the number of ABC sets for which each updating parameter is included in the QR basis, each basis having been calculated from one of the  $C = 56$  one-mode sensitivity matrices. For example, Fig. 3.12 indicates that element #1 is included in the QR basis for 13 of the 56 OCS systems. These 13 systems are listed above as members of the set  $c_1^{QR}$ .

From Fig. 3.12, it is also seen that none of the 56 OCS produce a QR basis which includes either element #9 or element #10, and hence none of these 56 OCS can be used to identify errors or damage in these two. Recalling that all of these updating problems were generated using a single mode, we will now repeat the identification calculations of Fig. 3.7, with the only difference that we now include two modes in all solutions,  $m = 2$ . This is shown in Fig. 3.13. Comparing Fig. 3.13 with Fig. 3.7, it is seen that there is a greater number of ABC sets at which the QRB flag and solution metrics drop to a minimum. This reveals that the use of two modes (rather than one) increases the number of ABC sets which produce an updating system capable of localizing errors or damage in element #1.



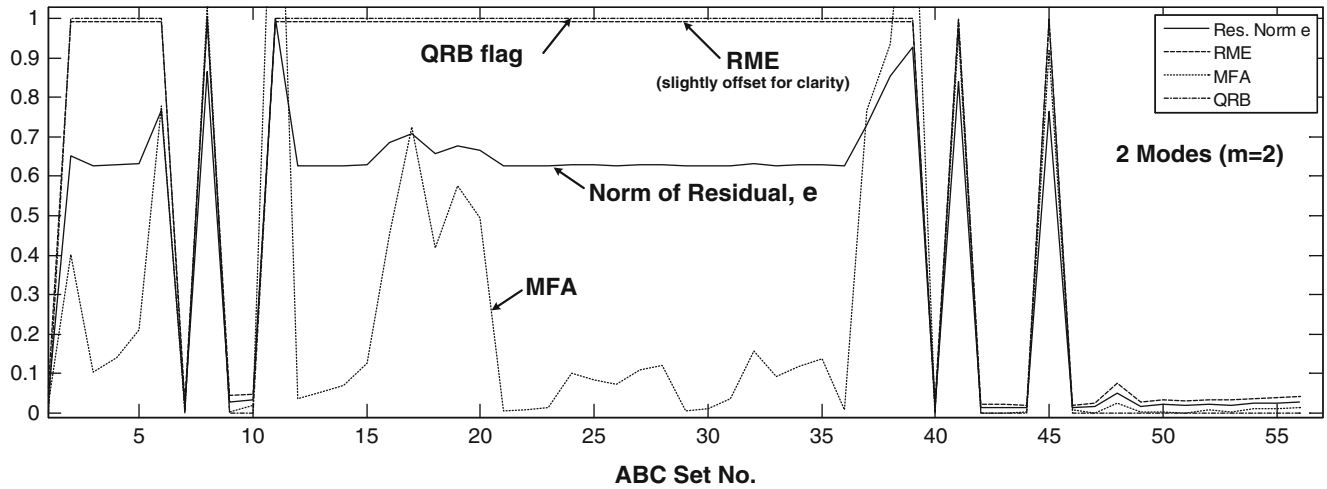
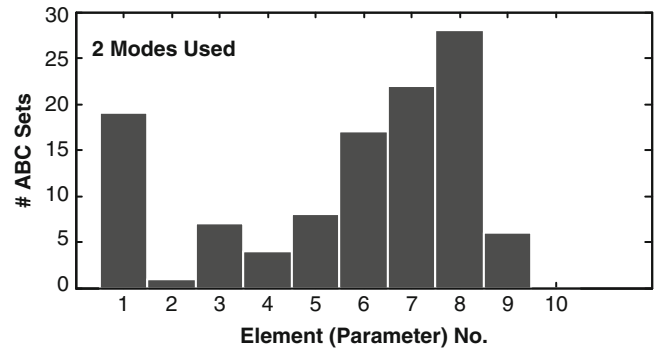


**Fig. 3.13** Solution metrics and QRB flag for element #1, versus ABC set number, two modes ( $m = 2$ ) used

**Fig. 3.14** Histogram of updating parameter inclusion in QR basis sets,  $m = 2$  modes used



Again plotting the histogram for  $m = 2$  modes, shown in Fig. 3.14, we see that there are now more ABC sets which can be used to localize errors in element #1. Using one mode to construct the updating problem yielded 13 optimal ABC sets (see Fig. 3.12) for element #1, while using two modes increased this to 19 sets. Also, the use of two modes now produces six optimal ABC sets which are able to localize errors in element #9; the use of one mode had produced no ABC sets able to do so. The number of optimal ABC sets for element #2 actually decreases. Therefore, this procedure constitutes a means of determining modal sufficiency, for each potential updating parameter.

With an error placed in element #9, we again calculate the solution metrics and QRB flag versus ABC set number, and we see in Fig. 3.15 that there are precisely six ABC sets at which  $QRB = 0$  (and at which the solution metrics drop to their respective minima).

Finally, we address the ability to localize errors in element #10. As this element is at the free end of the beam, it presents some difficulty for a sensitivity-based algorithm due to the greater number of modes required to generate sensitivities of sufficient magnitude. From the histograms shown in Figs. 3.12 and 3.14, it is seen that neither one mode nor two modes is sufficient to localize error in element #10. The use of three modes is still insufficient to identify errors in element #10, as shown in Fig. 3.16. However, using four modes does produce three ABC sets at which  $QRB = 0$ , as shown in Fig. 3.17. In other words, a minimum of four modes is required in order for element #10 to be included in the QR basis. This makes clear the correlation between the QR column pivot selection algorithm and obtaining a sensitivity matrix of sufficient sensitivity to errors in element #10.

The solution metrics for an error in element #10, and the QRB flag, are plotted in Fig. 3.18, where the three optimal ABC sets can be identified.

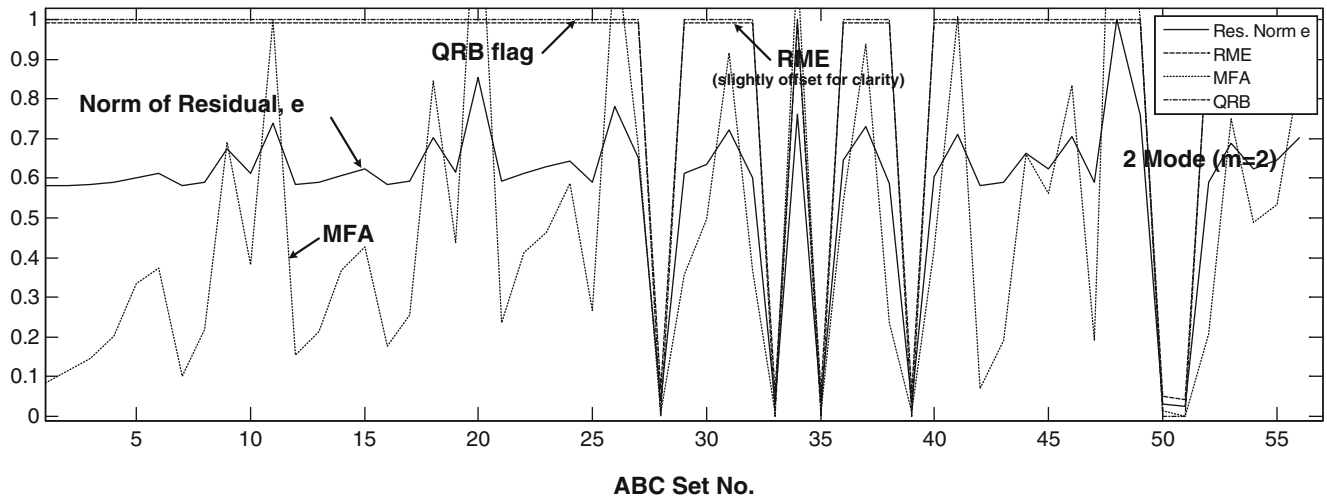


**Fig. 3.15** Solution metrics and QRB flag for element #9, versus ABC set number, two modes ( $m = 2$ ) used

**Fig. 3.16** Histogram of updating parameter inclusion in QR basis sets,  $m = 3$  modes used. No optimal ABC sets for element #10 are produced

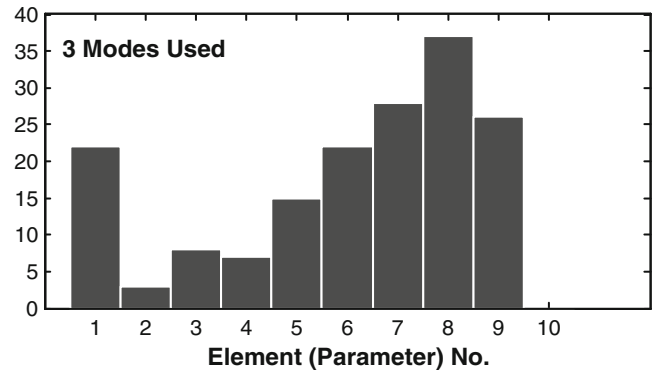
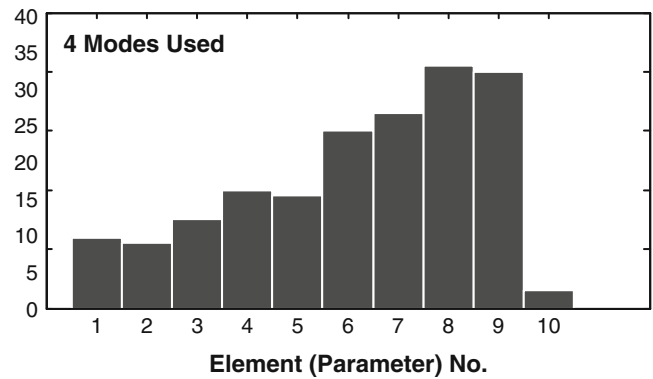


**Fig. 3.17** Histogram of updating parameter inclusion in QR basis sets,  $m = 4$  modes used. Three optimal ABC sets for element #10 are produced



### 3.6.5 Multiple OCS

The use of an updating system, Eq. (3.3), with  $m = 1$  can uniquely identify a single parameter error; for two parameters errors,  $m \geq 2$  is required, and so forth. In order to identify multiple parameter errors, potentially in any, and possibly all, updating parameters,  $m \geq n$  is required. A single updating system is assembled, comprised of rows selected from the  $c_i^{QR}$ , and  $i = 1, 2, 3, \dots, n$ .

We compile a database of optimal ABC sets for each element, based on the use of four modes, which was determined to be required to localize errors in all elements. We can tabulate this information in two useful ways. The first way tabulates, for each element “i” (updating parameter), the optimal ABC set indices,  $c_i^{QR}$ ,  $i = 1, 2, 3, \dots, n$ . We provide an abbreviated

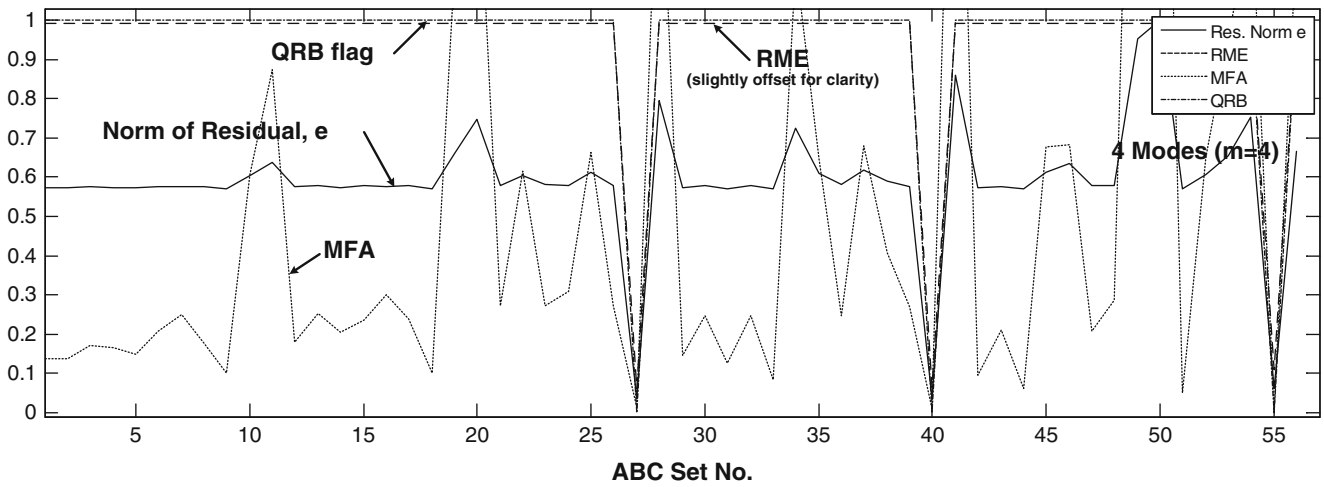


**Fig. 3.18** Solution metrics and QRB flag for element #10, versus ABC set number, four modes ( $m = 4$ ) used

**Table 3.4** Optimal ABC sets by element Index (updating parameter). Only the first 17 configurations for each element are shown, for compactness. Four modes used

	ABC set index, c																	
<b>Elem. no.</b>	<b>1</b>	1	7	36	37	39	41	47	49	50	53	54	55	0	0	0	0	0
<b>2</b>	2	4	20	29	30	31	32	33	34	35	48	0	0	0	0	0	0	0
<b>3</b>	3	5	8	9	12	14	18	38	40	42	43	44	46	51	52	0	0	0
<b>4</b>	4	13	15	16	20	21	23	24	26	28	42	43	44	45	46	48	51	51
<b>5</b>	5	6	7	14	15	16	18	20	22	25	26	29	31	32	47	48	49	49
<b>6</b>	1	2	3	7	8	9	10	11	12	14	16	17	18	19	20	23	24	24
<b>7</b>	1	4	5	6	9	10	11	13	14	17	19	21	22	25	26	28	29	29
<b>8</b>	1	2	3	4	6	7	8	9	10	11	12	13	15	16	17	18	19	19
<b>9</b>	2	3	5	6	8	10	11	12	13	15	17	19	21	22	23	24	25	25
<b>10</b>	27	40	55	0	0	0	0	0	0	0	0	0	0	0	0	0	0	0

list for illustration in Table 3.4, where for compactness of presentation, we limit the number of configurations displayed for each element to a maximum of 17. Table 3.4 shows the ABC set numbers for which an element is in the QR basis. For example, to identify an error in element #2, the OCS natural frequencies for ABC sets numbered 2, 4, 20, 29, etc., may be used. The sensitivity matrices calculated with these ABC applied to the FE model will result in element #2 being included in the QR basis. Alternatively, this information can be tabulated as shown in Table 3.5, where the membership of the QR basis set, for each ABC set, is shown. Again, four modes were used.

The information contained in Table 3.5 identifies a minimum number of ABC sets for which updating systems (i.e. Eq. (3.23)) need to be generated. In fact, only selected rows from each of these selected ABC sets need be included. For our example problem, with 10 elements (10 updating parameters), we search Table 3.5 to find a minimum number ABC set indices such that each updating parameter is included once as a QR basis parameter. This not only down-selects the number of ABC sets, but from within each selected ABC set, down-selects the individual rows of  $[S^{(c)}]$ .

For our 10-element beam, the rows containing the shaded cells in Table 3.5 indicate those ABC sets which are selected, and the corresponding columns indicate the specific QR basic parameters (rows of  $[S^{(c)}]$ ) which will be included. There are six ABC sets for which OCS need to be generated (which includes ten shaded cells). Therefore, it is not necessary to actually construct all of the OCS, beyond that needed to make this selection possible. From each of these six OCS, the selected rows of the sensitivity matrices are used to construct a final “composite” sensitivity matrix. This amounts to a total of 10 rows, which results in a square composite sensitivity matrix. Based on the shaded cells in Table 3.5, we use all four rows of the sensitivity matrix  $[S^{(1)}]$  calculated from the FE model in the as-tested configuration (ABC set #1). These rows provide a basis for elements 8,7,6, and 1. For the remaining elements 2,3,4,5,9, and 10, we use rows 1 and 4 of  $[S^{(2)}]$ , calculated from the application of ABC set #2 to the FE model, and which represent elements 9 and 2. With the additional rows needed, the composite sensitivity matrix is illustrated as follows.

**Table 3.5** Updating parameters in the QR basis for each ABC set. Four modes used,  $m = 4$

Set #	Elem. # in QR basis, $m = 4$			
	Row #1	Row #2	Row #3	Row #4
<b>1</b>	<b>8</b>	<b>7</b>	<b>6</b>	<b>1</b>
<b>2</b>	<b>9</b>	8	6	<b>2</b>
<b>3</b>	9	8	6	<b>3</b>
<b>4</b>	2	8	7	<b>4</b>
<b>5</b>	9	3	7	<b>5</b>
<b>6</b>	9	8	7	5
<b>7</b>	5	8	1	6
<b>8</b>	9	3	8	6
<b>9</b>	7	6	8	3
<b>10</b>	9	8	7	6
<b>11</b>	7	6	8	9
<b>12</b>	9	8	6	3
<b>13</b>	9	8	7	4
<b>14</b>	3	6	7	5
⋮				
<b>47</b>	9	5	1	8
<b>48</b>	2	5	8	4
<b>49</b>	9	5	8	1
<b>50</b>	8	5	9	1
<b>51</b>	4	3	9	6
<b>52</b>	9	4	3	6
<b>53</b>	4	9	6	1
<b>54</b>	9	7	6	1
<b>55</b>	<b>10</b>	7	6	1
<b>56</b>	4	5	7	8

$$\left\{ \begin{array}{l} \delta\Lambda_1^{(1)} \\ \delta\Lambda_2^{(1)} \\ \delta\Lambda_3^{(1)} \\ \delta\Lambda_4^{(1)} \\ \delta\Lambda_1^{(2)} \\ \delta\Lambda_4^{(2)} \\ \delta\Lambda_4^{(3)} \\ \delta\Lambda_4^{(4)} \\ \delta\Lambda_4^{(5)} \\ \delta\Lambda_1^{(55)} \end{array} \right\} = \left[ \begin{array}{l} \dots S_{row1}^{(1)} \dots \\ \dots S_{row2}^{(1)} \dots \\ \dots S_{row3}^{(1)} \dots \\ \dots S_{row4}^{(1)} \dots \\ \dots S_{row1}^{(2)} \dots \\ \dots S_{row4}^{(2)} \dots \\ \dots S_{row4}^{(3)} \dots \\ \dots S_{row4}^{(4)} \dots \\ \dots S_{row4}^{(5)} \dots \\ \dots S_{row1}^{(55)} \dots \end{array} \right] \left\{ \begin{array}{l} u_1 \\ u_2 \\ u_3 \\ u_4 \\ u_5 \\ u_6 \\ u_7 \\ u_8 \\ u_9 \\ u_{10} \end{array} \right\} \quad (3.28)$$

Using this system shown, Eq. (3.28), we perform the identification for a known error installed successively in each element. The results of these 10 identification problems are shown in Fig. 3.19. The composite system is able to precisely locate the error, regardless of its location. This is due to the composite system possessing a QR basis which includes every updating parameter,  $u_i$ . It should be noted that similarly constructed overdetermined systems will also localize the error, regardless of location, as long as the QR basis includes at least one row for each element.

In order to demonstrate the ability distinguish multiple errors, we will install four simultaneous known EI errors of 2 % at element #3, and 1.5, 1, 0.5 %, respectively at the three adjacent elements at the free end of the cantilever, Elements #8,9,10. Using two modes and eight ABC sets (yielding a square composite sensitivity matrix), the solution shown in Fig. 3.20. Simultaneous ID of four errors using eight ABC sets is obtained.

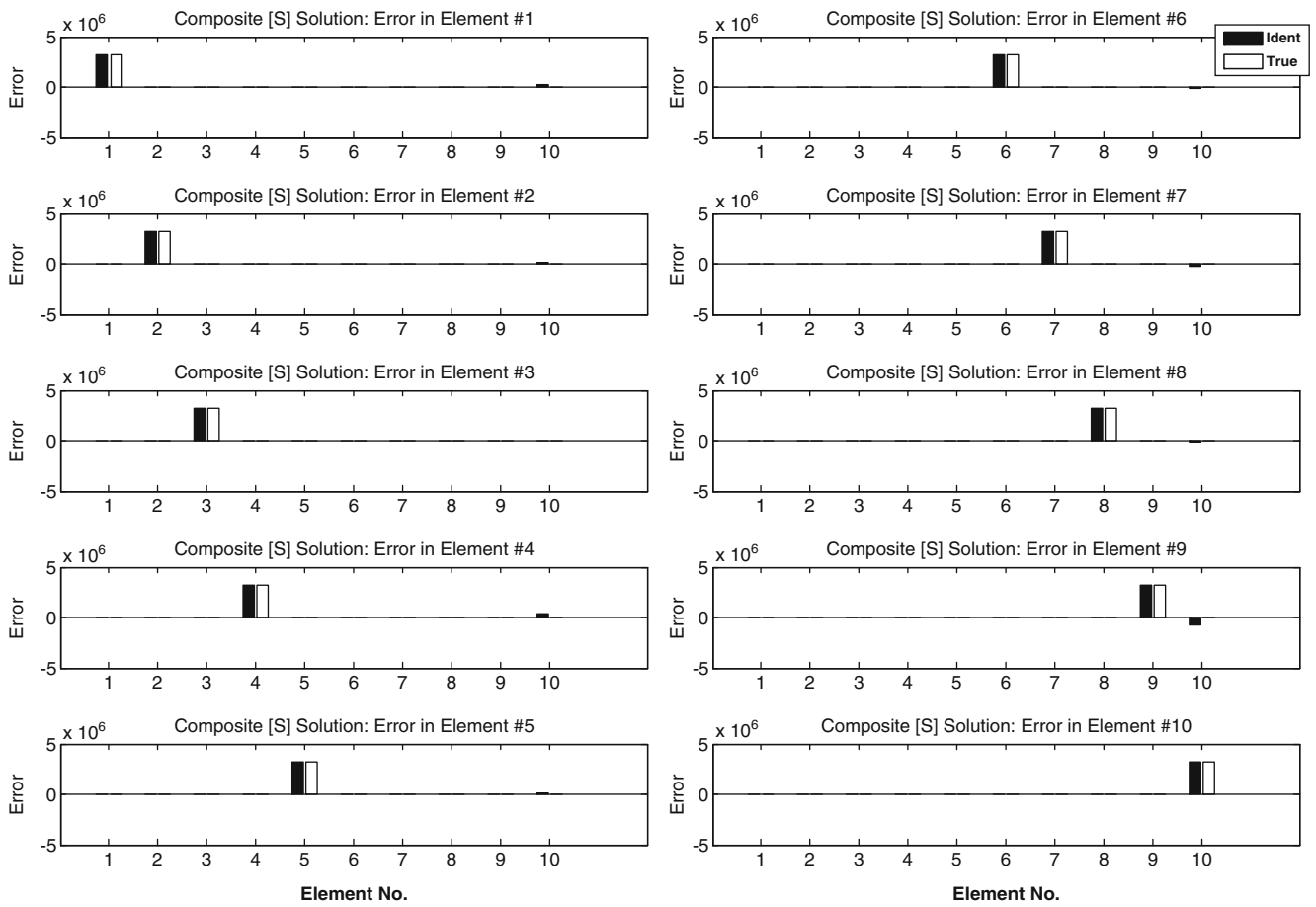
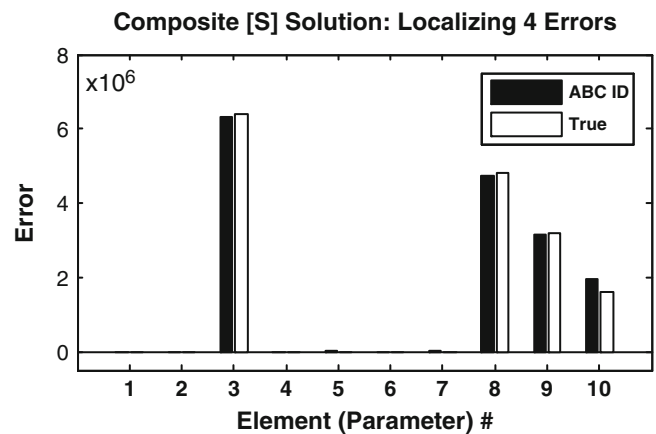


**Fig. 3.19** Solution using composite updating system assembled from multiple OCS. True error is installed in every element sequentially, demonstrating that the composite system is able to uniquely localize the error in every element

**Fig. 3.20** Simultaneous ID of four errors using eight ABC sets



### 3.7 Summary and Conclusions

A square experimentally measured FRF matrix can easily be processed to identify the natural frequencies for a potentially large number of distinct sets of artificial boundary conditions (ABC), the term artificial indicating that these boundary conditions need not be physically applied to the structure. A set of ABC defines an omitted coordinate system (OCS), which corresponds to the structure with additional restraints (“pins”) artificially placed at some combination of a subset of the measurement locations. The number of combinations is given by the binomial coefficient. These same boundary conditions

are easily applied to the FE model of the structure, starting in its “as-tested” configuration. From each OCS, a system of equations for model updating is defined which include a sensitivity matrix and a vector of differences in the square of the experimentally-identified and FE-calculated natural frequencies. Using a simple beam example with 10 simulated measured responses, the parametric updating systems were generated and solved for all combinations of two ABC pins. The solution was performed using the QR decomposition with column pivoting, which in the underdetermined case, provides a basic solution (not least-norm). The accuracy of these identification solutions were quantified using metrics defined for error localization and magnitude, the Relative Magnitude Error (RME) and Maximum False Alarm (MFA). The RME and MFA were plotted versus ABC set number, and when the RME and MFA drop to zero, the updating parameter error location and magnitude are precisely estimated. It is shown that the ability of an OCS updating system (generated by a single ABC set) to successfully localize error in a specific updating parameter requires that the associated column of the sensitivity matrix be included in the QR basis. The permutation matrix of the QR decomposition reveals whether the updating parameter (i.e. its matrix column) is included in the basis. This inclusion in the QR basis is tracked, versus ABC set number, by a boolean flag, QR Basis (QRB), defined for this purpose. The QRB flag is shown to be exactly correlated with the RME and MFA. Therefore, the QR decomposition with column pivoting provides an effective updating parameter subset selection strategy. This strategy identifies those updating parameters for which errors can be localized by the OCS, resulting from a specific ABC set. We refer to these ABC sets as optimal ABC sets, but in fact they are not simply optimal, but for a given updating parameter, their use is required in order to localize errors. Conversely, there are updating parameters which cannot be localized by the updating systems produced by the non-optimal ABC sets. The use of ABC provides numerous updating systems and can significantly increase the likelihood of generating an OCS sensitivity matrix for which the QR basis includes each updating parameter of interest. Also, it is worth noting that this QR basis strategy for identifying optimal ABC sets reveals the minimum number of ABC pins that are required in order to localize all parameters in question.

It is also shown that the minimum number of modes required to successfully perform model update is established by the requirement that, for every updating parameter, at least one ABC set have a QRB flag set to zero. This requirement translates into a requirement on the minimum number of modes needed to produce such an ABC set. The number of ABC sets with a zero QRB flag, for each updating parameter, was plotted as a histogram.

The use of multiple OCS system sensitivity matrices, assembled into a composite updating system, was shown to uniquely localize a parameter error, regardless of its location. Furthermore, multiple simultaneous parameters were also successfully localized. This ability is dependent simply on constructing a basis which includes representation from each updating parameter. The ability to generate many ABC sets greatly increases this practical possibility, with a moderate demand on the number of required modes.

## References

1. Lallement G, Piranda J (1990) Localisation methods for parameter updating of finite element models in elastodynamics. In: 8th international modal analysis conference, Orlando, FL, pp 579–585
2. D’Ambrogio W, Fregolent A (2004) Dynamic model updating using virtual antiresonances. *Shock Vib* 11:351–363
3. Mottershead JE (1998) On the zeros of structural frequency response functions and their sensitivities. *Mech Syst Signal Process* 12(5):591–597
4. D’Ambrogio W, Fregolent A (2000) The use of antiresonances for robust model updating. *J Sound Vib* 236(2):227–243
5. Jones K, Turcotte J (2002) Finite element model updating using antiresonant frequencies. *J Sound Vib* 252(4):717–727
6. D’Ambrogio W, Fregolent A (2003) Results obtained by minimizing natural frequency and antiresonance errors of a beam model. *Mech Syst Signal Process* 17(1):29–37
7. Hanson D, Waters TP, Thompson DJ, Randall RB, Ford RAJ (2007) The role of anti-resonance frequencies from operational modal analysis in finite element model updating. *Mech Syst Signal Process* 21:74–97
8. Li S, Shelley S, Brown D (1995) Perturbed boundary condition testing. In: Proceedings of the 13th international modal analysis conference, vol 1, Nashville, TN, pp 902–907
9. Wada BK, Kui CP, Glaser RJ (1986) Extension of ground-based testing for large space structures. *J Spacecr* 23(2):184–188
10. Wada BK, Kuo CP, Glaser RJ (1986) Multiple boundary condition tests (MBCT) for verification of large space structures. AIAA Paper 86-0905
11. Kuo CP, Wada BK (1987) System identification of a truss type space structure using the multiple boundary condition test (MBCT) method. AIAA Paper 87-0746
12. Kuo CP, Wada BK (1988) Multiple boundary condition test (MBCT): identification with mode shapes. AIAA Paper 88-2353
13. Gordis JH (1999) Artificial boundary conditions for model updating and damage detection. *J Mech Syst Signal Process* 13(3):437–448
14. Lallement G, Cogan S (1999) Parametric identification based on pseudo-tests. In: Silva JMM, Maia NMM (eds) *Modal analysis and testing*. Kluwer Academic, Dordrecht, pp 265–280
15. Gordis JH (1996) Omitted coordinate systems and artificial constraints in spatially incomplete identification. *Int J Anal Exp Modal Anal* 11(1–2):83–95
16. Gordis JH (1992) Spatial, frequency domain updating of linear, structural dynamic models. In: Proceedings of the 34th AIAA/ASME/ASCE/AHS/ACS structures, structural dynamics, and materials conference, La Jolla, CA, pp 3050–3058

17. Gordis JH (1994) An analysis of the improved reduced system model reduction procedure. *Int J Anal Exp Modal Anal* 9(4):269–285
18. Gordis JH (1995) An exact formulation for structural dynamic model error localization. *Int J Anal Exp Modal Anal* 10(1):19–33
19. Berman EJ, Allen MS, Kammer DC, Mayes RL (2010) Probabilistic investigation of sensitivities of advanced test-analysis model correlation methods. *J Sound Vib* 329:2516–2531
20. Tu Z, Lu Y (2008) FE model updating using artificial boundary conditions with genetic algorithms. *Comput Struct* 86:714–727
21. Lu Y, Tu Z (2008) Artificial boundary condition approach for structural identification: a laboratory perspective. In: 26th international modal analysis conference, Orlando, FL
22. Berman A (1984) System identification of structural dynamic models – theoretical and practical bounds. In: Proceedings of the AIAA/ASME/ASCE/AHS 25th structures, structural dynamics, and materials conference, pp 123–128
23. Wilkinson JH (1965) The algebraic eigenvalue problem. Oxford University Press, Oxford
24. Rade DA, Lallement G (1998) A strategy for the enrichment of experimental data as applied to an inverse eigensensitivity-based FE model updating method. *Mech Syst Signal Process* 12(2):293–307
25. Fernandez C (2004) Artificial boundary conditions in sensitivity based finite element model updating and structural damage detection. Master's thesis, Naval Postgraduate School, Monterey, CA
26. Boyd S (2007–2008) Lecture 8 Least-norm solutions of underdetermined equations. EE263 Autumn Stanford University
27. Golub GH, Van Loan CF (1996) Matrix computations, 3rd edn. The Johns Hopkins University Press, Baltimore
28. MATLAB<sup>®</sup>R2010A. The Mathworks Inc., Natick, MA
29. Lai MJ (2009) On sparse solutions of underdetermined linear systems. *J Concr Appl Math*
30. Donoho DL (2006) For most large underdetermined systems of linear equations the minimal  $L_1$ -norm solution is also the sparsest solution. *Commun Pure Appl Math* LIX:0797–0829

# Chapter 4

## Optimal Selection of Artificial Boundary Conditions for Model Update and Damage Detection – Part 2: Experiment

Joshua H. Gordis

**Abstract** Sensitivity-based model error localization and damage detection is hindered by the relative differences in modal sensitivity magnitude among updating parameters. The method of artificial boundary conditions is shown to directly address this limitation, resulting in the increase of the number of updating parameters at which errors can be accurately localized. Using a single set of FRF data collected from a modal test, the artificial boundary conditions (ABC) method identifies experimentally the natural frequencies of a structure under test for a variety of different boundary conditions, without having to physically apply the boundary conditions, hence the term “artificial.” The parameter-specific optimal ABC sets applied to the finite element model will produce increased sensitivities in the updating parameter, yielding accurate error localization and damage detection solutions. A method is developed for identifying the parameter-specific optimal ABC sets for updating or damage detection, and is based on the QR decomposition with column pivoting. Frequency response data collected from a simple laboratory experiment is used, along with the corresponding finite element-generated data, to demonstrate the effectiveness of the ABC-QR method.

**Keywords** Updating • Identification • Artificial boundary conditions

### 4.1 Introduction

Mode sensitivities are an effective means of relating natural frequency errors to physical parameters in a FEM. However, they are limited in their effectiveness in localizing model errors or structure damage due to the following two reasons:

1. The updating solution for each parameter is dependent on the relative magnitude of its modal sensitivities, calculated from the FE model. Given the limited bandwidth of a modal test, the modal sensitivities calculated for the various updating parameters are of different magnitudes, and hence updating solutions are biased towards those parameters associated with higher sensitivity values. A low relative modal sensitivity of a given updating parameter will prevent the updating solution from localizing an error in this parameter, and prevent the estimation of the true error magnitude. In fact, without an accurate localization, it is in general not possible to accurately estimate the error magnitude.
2. The performance of traditional sensitivity-based solutions is limited due to the limited number of modes which can be identified in a modal test, relative to the large number of model parameters which must be included in the solution. Such an underdetermined solution can also contribute to the “smearing” of model error or damage localization solutions.

The method of artificial boundary conditions (ABC) has been shown, theoretically, to be highly effective in the localization of finite element model errors or in localizing damage in a structure (relative to a validated, undamaged FEM) [1]. This effectiveness is due to the fact that the ABC method addressed both of the above-listed limitations. Through the application of selected sets of ABC to the FRF data normally collected in a modal test, an accurate localization solution for a greater number of, and possibly all, individual updating parameters can be obtained. When the measured FRF are insufficient, either in spatial completeness and/or bandwidth, to localize the error in a given parameter, the method clearly indicates

---

J.H. Gordis (✉)

Department of Mechanical & Aerospace Engineering – Code ME/Go, Naval Postgraduate School,  
700 Dyer Road Bldg. 245 Room 313, Monterey, CA 93943-5146, USA  
e-mail: [jgordis@nps.edu](mailto:jgordis@nps.edu)



this insufficiency, for each updating parameter. This is accomplished through the application of multiple ABC sets, where a large number of alternative sensitivity matrices are generated, and these alternative sensitivity matrices are queried as to whether or not the localization of each updating parameter is possible. This large number of alternative sensitivity matrices made available by the method substantially increases the possibility of generating an accurate localization solution for each updating parameter. This application of multiple ABC sets also relaxes the demand on test bandwidth required (i.e. number of modes) for accurate localization.

It should be noted that the following assumptions are in place:

1. A model error or structure damage are “local” in nature – they occupy a bounded sub-domain of the entire structure domain.
2. The selected model parameters for localization will include the (unknown) model error or structure damage.

It is known that error magnitudes can only be accurately estimated if the error location is known [1–3].

In this paper, we will present an experimental study of the use of the ABC-QR method [4–6] for error localization. The term “error localization” will refer to both FEM error localization/identification, and damage detection. The ability of the method to localize errors will be demonstrated, and issues pertaining to the finite element model and the measured FRF data will be discussed. The identification of the ABC frequencies will be demonstrated, for a large number of ABC configurations. The ABC-QR method also provides a quantitative assessment of the number of modes required in order to identify errors in a given parameter. The ABC-QR software developed will be described. The ability of the method to reveal individual and multiple localized errors will be demonstrated.

## 4.2 Description of Experiment

In order to assess the effectiveness of the ABC-QR method, a beam in a free-free-configuration is tested. A free-free configuration was chosen as no physical boundary conditions need be established (although the method works equally well regardless of any physical boundary conditions applied). The ABC method artificially imposes boundary conditions, so we emphasize that throughout the experiment, no physical boundary conditions were ever applied, beyond the fishing-line suspension of the beam in simulated free-free conditions.

The beam is steel, with the following properties (Table 4.1):

Ten accelerometers were attached using studs to the beam. The accelerometers were equally spaced, with 0.5 in. of beam extending out beyond Accels #1 and #10. See Fig. 4.1 for a schematic of this configuration.

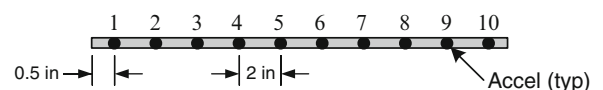
## 4.3 Initial Mass Modeling

Each accelerometer weighed 0.0094 lbf. The beam with all accelerometers mounted was weighed, and the actual beam density was backed out, which accounted for mounting holes, studs, and other incidental mass accounting inaccuracies. Finally, a mass update (adjustment in the density) was made in order to bring the calculated free-free natural frequencies in agreement with the corresponding measured frequencies. Table 4.2 compares the first three mode frequencies, as measured from test, and as calculated prior to the density adjustment, and after. As can be seen, the initial errors were small, but were then all driven below 1 %. Given the small overall size of the beam, it’s possible that this adjustment also accounted for some participating cable mass. The FE model with the density adjustment will be used for the damage localization.

**Table 4.1** Properties of beam

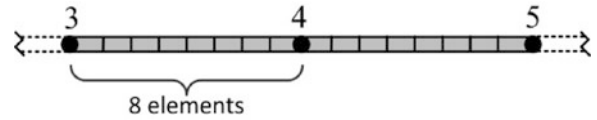
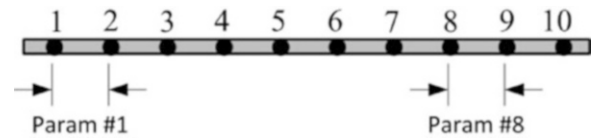
Length	19 in.
Width	1.005 in.
Depth	0.38 in.
Nominal modulus of elasticity	29E6 psi
Density	0.283 lbf/in. <sup>3</sup>

**Fig. 4.1** Test configuration of beam



**Table 4.2** Initial mass updating

	Mode #1		Mode #2		Mode #3	
	Freq (Hz)	% error	Freq (Hz)	% error	Freq (Hz)	% error
Test	197.75	–	544.92	–	1,058.35	–
FE (no density adjustment)	200.94	1.59	553.92	1.63	1,085.97	2.54
FE (with density adjustment)	197.67	–0.041	544.89	–0.006	1,068.25	–0.93

**Fig. 4.2** Element Configuration between Accelerometers #3 and #4**Fig. 4.3** Damage parameters for the beam (two of nine labeled)

#### 4.4 Finite Element Modeling: Localization Parameters

The beam is modeled using 76 4-noded simple beam elements. The element length is 0.25 in. There are eight elements between neighboring accelerometers, spanning two inches. Figure 4.2 shows a partial span of the beam between accelerometers #3 and #4. A single EI sensitivity value is calculated for all eight of these elements. There are two elements extending outboard of both the first and 10th accelerometers. Note that the test beam is undamaged, and the damage is represented in the FE model by an EI reduction in all elements between two accelerometer locations. The localization parameters are the nine EI values for each of the nine element groups, as shown in Fig. 4.3.

#### 4.5 Set Definitions

Model parameter indices selected for error localization:  $u_p, p = 1 : P$

- where  $P = 9$ , corresponding to the nine damage parameters shown in Fig. 4.3.

ABC sets:  $c = 1 : C$

- where  $C = 56$  (10 accelerometers, maximum of two ABC pins)

Optimal (QR) ABC configurations (ABC set indices) for each model parameter,  $p$ :  $s(u_p)$

#### 4.6 ABC-QR Procedure

The following steps are accomplished using the MATLAB software, ABC-QR.

1. Choose the maximum number of ABC,  $k$ , to use.
  - For this experimental study,  $k = 2$  ABC pins are used.
2. Calculate the number of ABC configurations,  $C$ , defined by the number of measured responses,  $a$ , and the maximum number of ABC pins to be applied,  $k$ , Eq. (4.1).
  - 10 responses and two ABC pins results in 55 ABC sets. Along with the baseline free-free configuration, a total of 56 unique boundary condition sets are available.

$$C = \sum_{k=0}^a \binom{a}{k} \quad (4.1)$$

From the FRF data measured from a single baseline test:

1. For each ABC set,  $c$ , extract the rows and columns of the full FRF matrix  $[H]$  corresponding to the desired ABC pin locations, forming  $[H_{ABC}]$ .
2. At each test frequency, invert  $[H_{ABC}]$  to form  $[Z_{ABC}]$ .
3. Average the diagonal terms of  $[Z_{ABC}]$  forming the scalar averaged impedance  $\tilde{Z}_{ABC}^{(i)}$ .
  - As we are interested only in the ABC frequencies, the diagonal terms are sufficient to identify all of the ABC frequencies.
4. Peak-pick the ABC frequencies from each  $\tilde{Z}_{ABC}^{(i)}$ , yielding  $\{\lambda^{(c)}\}_{test}$ , a vector of length  $n_{test}^{(c)}$  which is the number of ABC frequencies found from ABC set  $c$ .

For the finite element model:

1. Select some or all model parameters as potential error/damage locations,  $u_p$ ,  $p = 1, 2, \dots, P$
2. Set the number of measurement points,  $a$ .
3. For each ABC set,  $c$ , apply the boundary conditions to the finite element model, corresponding to the ABC pin DOF. Calculate the eigenvalues,  $\{\lambda^{(c)}\}_{FE}$ , and the sensitivity matrix,  $[S_c]$ ,  $c = 1, 2, \dots, C$ . Retain only those modes within the test bandwidth,  $n_{FE}^{(c)}$ .
4. For each ABC set,  $c$ , calculate the QR decomposition of  $[S_c]$ , specifically determining the pivot columns. The set of pivot column indices are  $u^*(c)$ , and the number of them corresponds to the number of modes in the test bandwidth,  $n_{FE}^{(c)}$ . The pivot column indices correspond to the model parameters whose damage, or error, can be determined by that ABC set. The corresponding rows of  $[S(c(p))]$  can be used for error localization for these model parameters.
5. For each model parameter,  $p$ , find a parameter-optimal ABC set, “ $c(p)$ ”, whose QR pivot column indices  $\{u^*(c)\}$ , include the parameter,  $p$ . The index of the  $u^*(c)$  which refers to the parameter  $p$  is the parameter-optimal mode from the parameter-optimal ABC set, “ $c(p)$ ”. Therefore, for each parameter, we will find both the parameter-optimal ABC set, “ $c(p)$ ”, and the parameter-optimal mode,  $u_p^*(c(p))$ , meaning the  $i$ th mode from ABC set  $c(p)$  should be included in the localization.

Therefore, we extract the corresponding row,  $u_p^*(c(p))$  from the  $[S(c(p))]$  to be used in a composite sensitivity matrix,  $[S]$ . This row will be able to localize damage in parameter  $p$ . The subset of all ABC sets so identified for error localization is  $\{c^*(P)\}$ , a vector containing the indices of the (minimum of) “ $P$ ” selected ABC sets. There will be at most one ABC set for each model parameter. It is possible that one can select multiple rows from a single ABC sensitivity matrix,  $[S(c(p))]$ , set will include optimal sensitivity rows for more than one model parameter.

From the FE and Test Databases...

1. Establish mode correlation between  $\{\lambda^{(c)}\}_{test}$  and  $\{\lambda^{(c)}\}_{FE}$  for each. The number of eigenvalues for which correlation has been established is  $n(c^*(p))$ , where  $p$  refers to the  $p$ th damage parameter,  $c^*(p)$  refers to a single ABC set selected for parameter  $p$ . This defines the upper limit on the number of modes that can be included from ABC set,  $c(p)$ . Note that, in general, there will be more FE frequencies than ABC frequencies, as the impedance  $\tilde{Z}_{ABC}^{(c)}$  may not show a peak corresponding to every  $(\lambda_j^{(c)})_{FE}$  calculated for ABC set “ $c$ ”.
2. Form the eigenvalue error for each ABC frequency found, and the corresponding FE frequency.

$$\Delta\lambda_j^{(c(p))} = (\lambda_j^{(c(p))})_{test} - (\lambda_j^{(c(p))})_{FE}, \quad j = 1, 2, \dots, n(c^*(p)) \quad (4.2)$$

3. Solve the composite error localization system for the errors,

$$\left\{ \begin{array}{c} \Delta\lambda(u_i^*(c(p))) \\ \text{-----} \\ \Delta\lambda u_i^*(c(p)) \\ \text{-----} \\ \vdots \\ \text{-----} \\ \Delta\lambda u_i^*(c(p)) \end{array} \right\} = \left[ \begin{array}{c} [S(u_1^*(c(1)))] \\ [S(u_1^*(c(2)))] \\ \vdots \\ [S(u_1^*(c(P)))] \end{array} \right] \left\{ \begin{array}{c} u_1 \\ u_2 \\ \vdots \\ u_P \end{array} \right\} \quad (4.3)$$

or

$$\{\Delta\lambda\} = [S] \{u\} \quad (4.4)$$

In Eq. (4.4), each row of  $[S]$  is the row extracted from the sensitivity matrix  $[S(u_1^*(c(1)))]$ , which is the sensitivity matrix calculated from the FE model with the parameter-optimal ABC set applied (i.e. the corresponding pins are applied as boundary conditions). This row corresponds to the parameter-optimal mode number,  $u_i^*(c(p))$ .

## 4.7 Measured FRF Data

An impact test was performed with a bandwidth of 0–1,317.6 Hz. The frequency spacing was 0.7324 Hz, with 1,600 lines. A square,  $10 \times 10$  FRF matrix was acquired, using the 10 accelerometers and roving an impact hammer over all 10 response locations. Five averages were taken. The 10 driving point measurements are shown in Fig. 4.4. The measurement bandwidth is  $f_{\max} = 1,317.6$  Hz.

## 4.8 ABC Frequency Identification: Theory

As mentioned in the ABC-QR procedure above, the first step in identifying the ABC frequencies for a particular ABC configuration is to extract the rows and columns of the FRF matrix,  $H$ , corresponding to the response locations where ABC pins are to be “applied.” This extraction yields  $[H_{ABC}]$ . We will now explain why this is so.

For a structure of  $n$  DOF, we select “a” DOF at which we would like to constrain to ground. The remaining “o” DOF will remain free. Such a partitioning results in the following system:

$$\begin{Bmatrix} x_a \\ x_o \end{Bmatrix} = \begin{bmatrix} H_{aa} & H_{ao} \\ H_{oa} & H_{oo} \end{bmatrix} \begin{Bmatrix} f_a \\ f_o \end{Bmatrix} \quad (4.5)$$

If we require that  $\{x_a\} = \{0\}$  then the following results:

$$\{x_o\} = -[H_{oa}][H_{aa}]^{-1}[H_{ao}]\{f_o\} \quad (4.6)$$

where  $[H_{aa}] = [H_{ABC}]$ , and  $[H_{aa}]^{-1} = [Z_{ABC}]$ . It is seen that the responses  $\{x_o\}$  will be “large” at the frequencies of the original system, but also at the natural frequencies of the system defined by the “a” DOF with all “o” DOF fixed to ground. In order to identify the ABC frequencies, we simply make use of  $[H_{aa}] = [H_{ABC}]$ , such that the natural frequencies of the original system are removed.

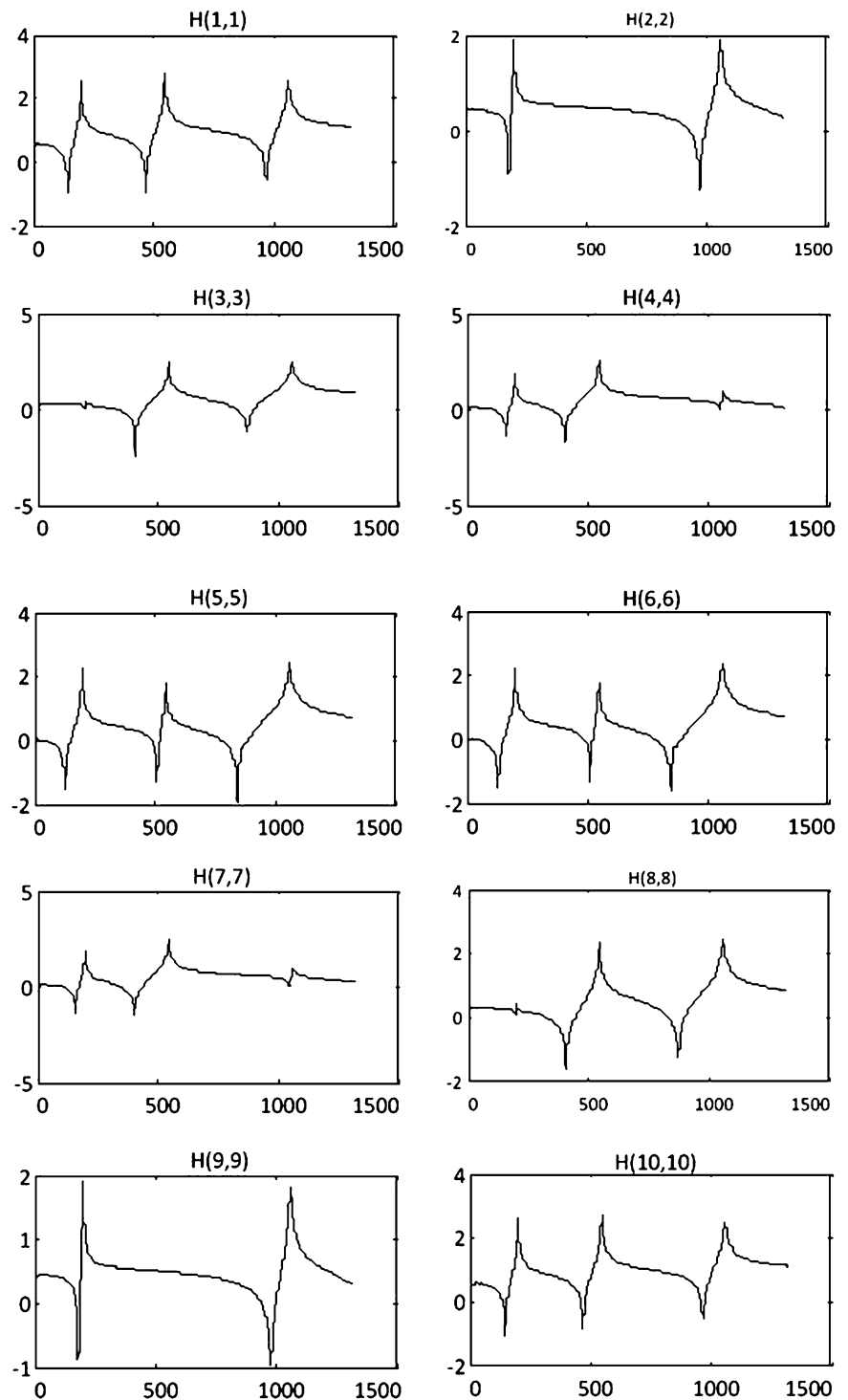
The ABC-QR software provides an interactive means of identifying the ABC frequencies. In this process, we assume that damping is small, and that the peaks of  $[Z_{ABC}]$  can be taken as the  $\{\lambda_{ABC}^{(c)}\}_{test}$ .

The measured FRF data is loaded into the ABC-QR software, and the  $[Z_{ABC}]$  is calculated. The diagonal terms of  $[Z_{ABC}]$  are averaged, such that all ABC mode peaks can be seen. This averaged impedance is  $\tilde{Z}_{ABC}^{(c)}$ . The individual diagonal terms of  $[Z_{ABC}]$  are superimposed on  $\tilde{Z}_{ABC}^{(c)}$  so that the user can verify that a peak found from  $\tilde{Z}_{ABC}^{(c)}$  also exists in most, if not all of the diagonal terms of  $[Z_{ABC}]$ . The software will cycle through all ABC sets defined by the user.

## 4.9 ABC Frequency Calculation

We will now demonstrate the identification of ABC frequencies. All of these frequencies are obtained from a single set of test data, taken from the structure in a single configuration (i.e. boundary condition set). For these calculations, the beam under test is *undamaged*, and the *FE model used is also undamaged*, and the model described above that was mass-updated using a simple density adjustment (See Table 4.1). These calculations will serve to demonstrate that the ABC frequencies for a structure can be accurately predicted by a FE model. In actuality, one would not have the luxury of both the FE model and test structure being in similar conditions (i.e. both undamaged). Here, we are demonstrating the accuracy in ABC frequencies obtainable from a FE model, and hence we use an undamaged model.

Fig. 4.4 Driving point FRF



The first ABC set is the baseline configuration, in this case, the free-free beam with no ABC pins. This impedance  $\tilde{Z}_{ABC}^{(1)}$  is shown in Fig. 4.5. The heavy green curve is  $\tilde{Z}_{ABC}^{(1)}$  while the multiple, fainter curves are the diagonal terms of  $[Z_{ABC}^{(1)}]$ . The three vertical red lines indicate the mode frequencies for the ABC set, as predicted by the FE model. As can be seen (and reflecting the values shown in Table 4.1), the frequency agreement is excellent for modes #1 and #2, with some difference for mode #3. The thin vertical green line close to 0 frequency is the user-defined rigid-body mode cutoff. When ABC peaks are selected using the threshold tool, any peaks with a frequency below this cutoff are automatically discarded. The first four mode shapes calculated from the FE model are shown in Fig. 4.6, and are the standard mode shapes for a free-free beam.

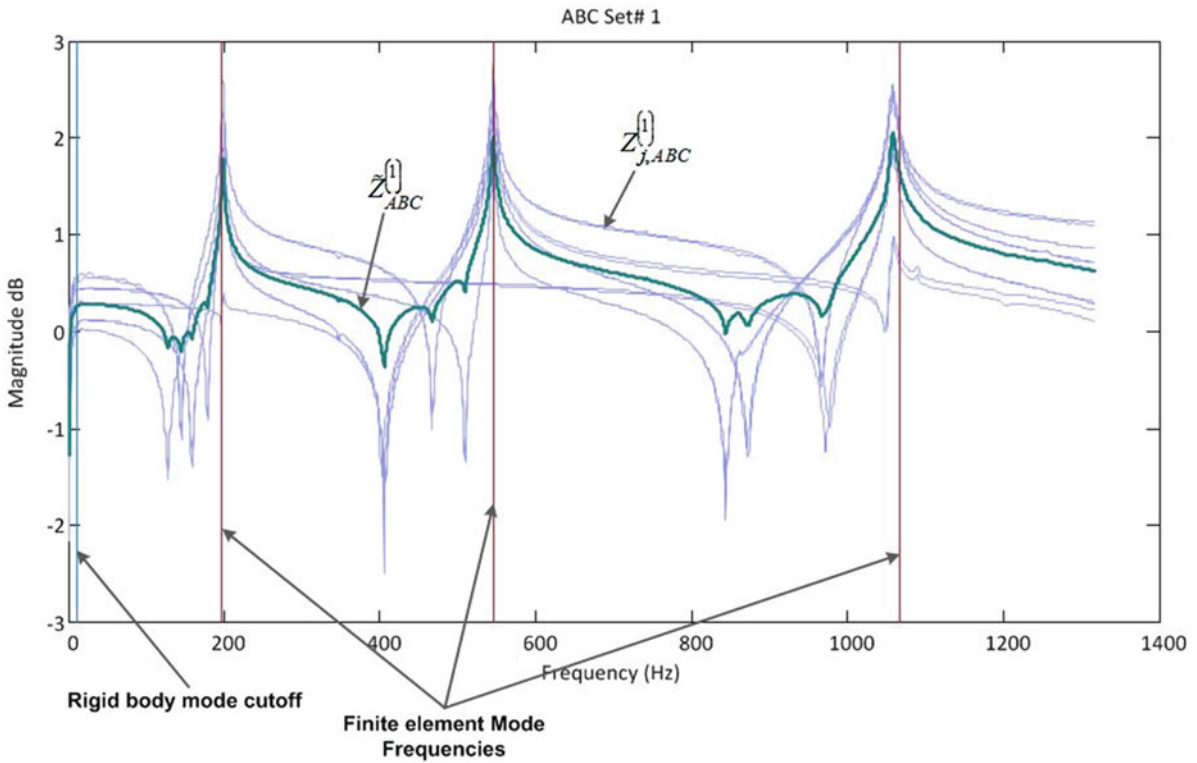


Fig. 4.5 Baseline configuration – ABC set #1 free-free

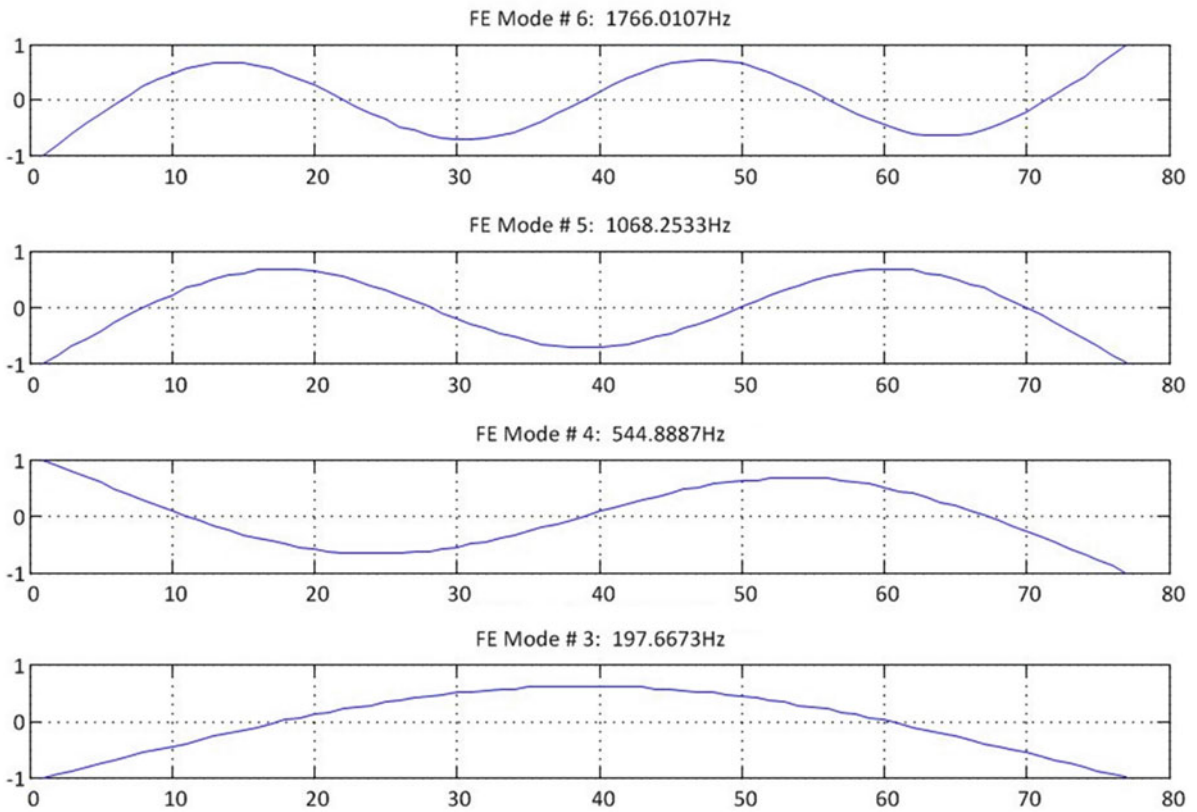


Fig. 4.6 Baseline configuration – FE mode shapes – ABC set #1 free-free

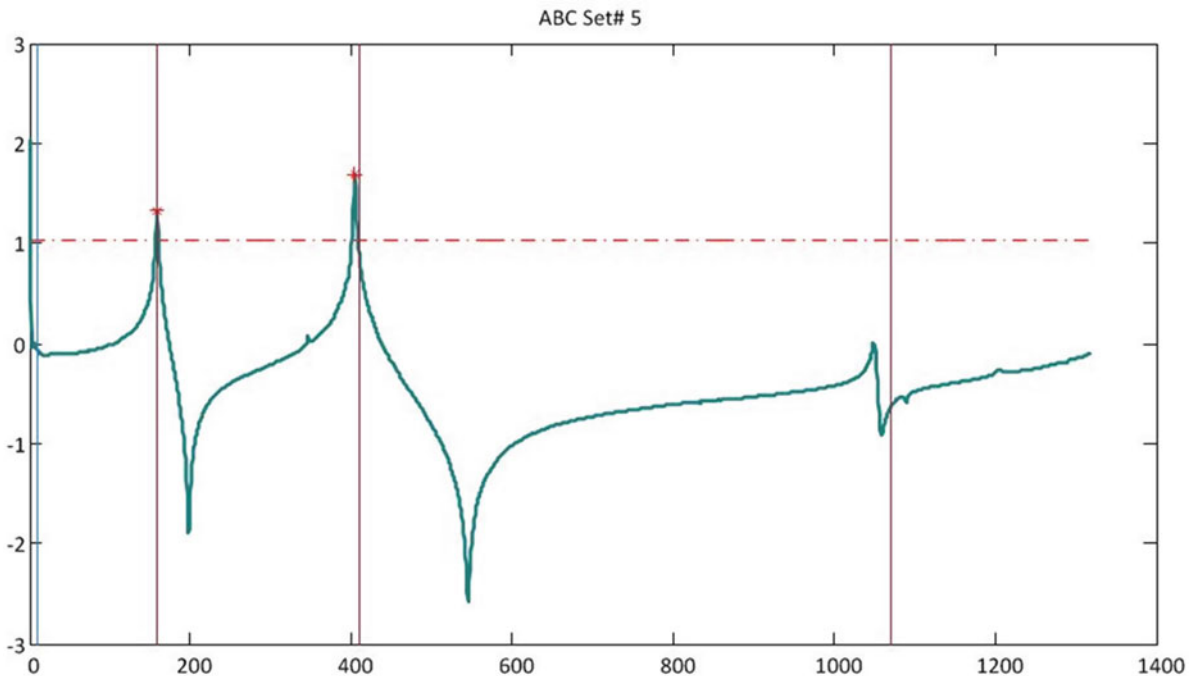


Fig. 4.7 ABC set #5 – one ABC pin

Moving up in ABC set number, the impedance for ABC set #5 is shown in Fig. 4.7. To identify the ABC frequencies, the user clicks on the plot (Fig. 4.7) to specify a peak-picking threshold (as shown, the horizontal dashed line), above which all peaks will be selected. Shown selected are two peaks above this line tagged with red asterisks. The third peak, without a red asterisk, was subsequently picked using the peak-picking box tool, completing the identification of the three ABC modes available in the test bandwidth, for this ABC set #5. The corresponding FE mode shapes are shown in Fig. 4.8. There is a single ABC pin generated in this set, as indicated in Fig. 4.8 by the single red triangle, indicating the position on the beam where this single ABC pin has been generated.

We now move to ABC set #12, which involves two ABC pins. The impedance is shown in Fig. 4.9, and the corresponding FE mode shapes are shown in Fig. 4.10, where the location of the two ABC pins is indicated. From Fig. 4.9, the lack of a clear peak for mode #1 is evident. Note that the two pins are adjoining. This situation of two adjoining pins can create distortion in the impedance peaks. Also note that the FE model does predict these three modes pretty well. As the ABC pins move apart with higher ABC set number, (see Fig. 4.11) the first mode peak sharpens once again. We also see the presence of a fourth ABC mode for this set. The FE model also predicts four modes for this set. We can surmise that ABC sets with adjoining pin locations may not be a good choice for localization (Fig. 4.12).

ABC set #15 is shown in Figs. 4.13 and 4.14. In Fig. 4.13 we see that a double peak was generated by the ABC impedance calculation instead of a single mode #3, while the corresponding FE model predicts a single peak. This situation warrants further algorithmic development such that the choice of either of the two closely-spaced peaks on the damage localization can be assessed. ABC sets #24 and #42 are shown in Figs. 4.15, 4.16, 4.17 and 4.18, in order to provide further examples of the effect of ABC on the mode frequencies of a structure. There are a total of 56 sets (including the free-free baseline set). All of these sets potentially can serve in the localization process. The choice of which sets to be included will be addressed next.

## 4.10 Localization Experiments

In this experiment, we install a known error, or damage, in the FE model. Installing these errors in the model rather than in the actual beam facilitates repeating the localization for different error locations, without having to prepare a multitude of test beams with damage installed. Also, we will compare some of the localization results to those obtained when the actual test data is replaced with the simulated test data. This will not only demonstrate the potential performance of the ABC-QR method, but also point to where some challenges remain in order to improve the performance with actual test data.

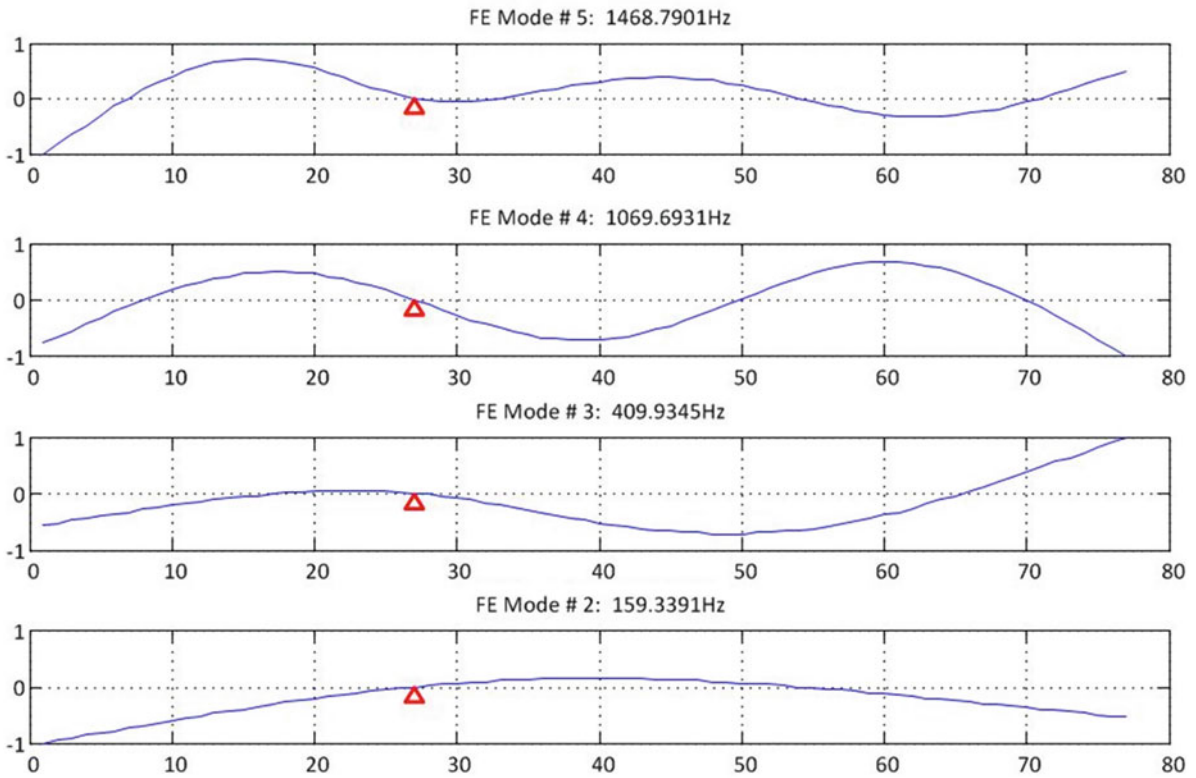


Fig. 4.8 ABC set #5 – FE mode shapes

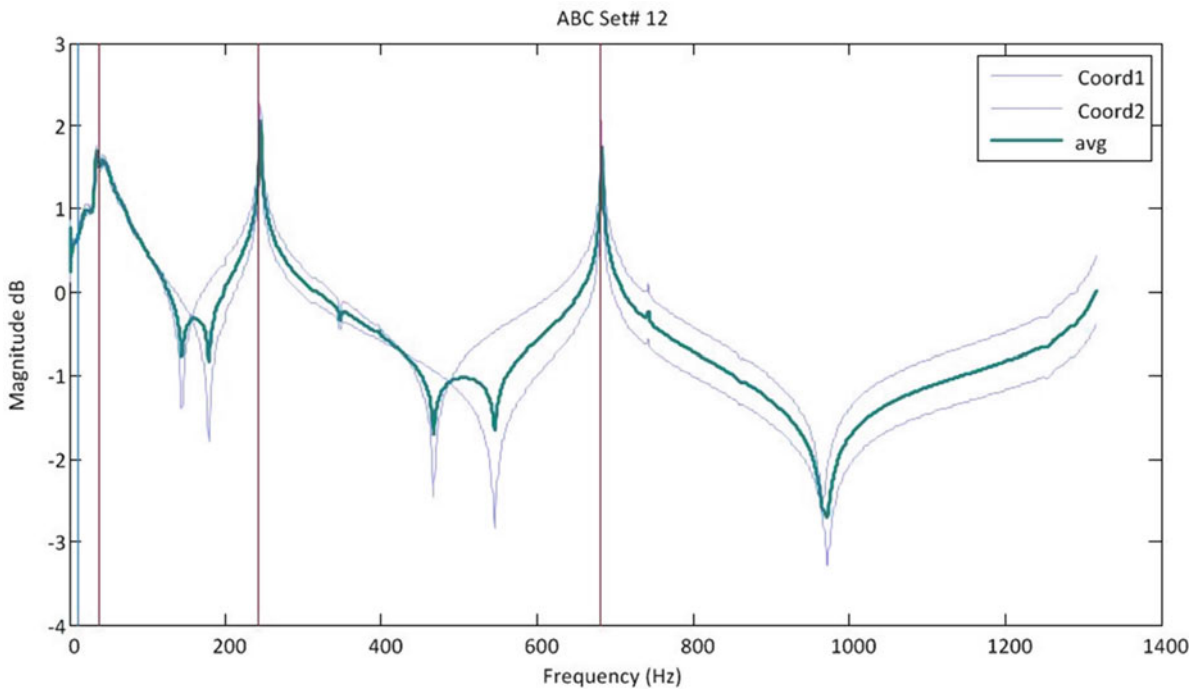


Fig. 4.9 ABC set #12 two ABC pins



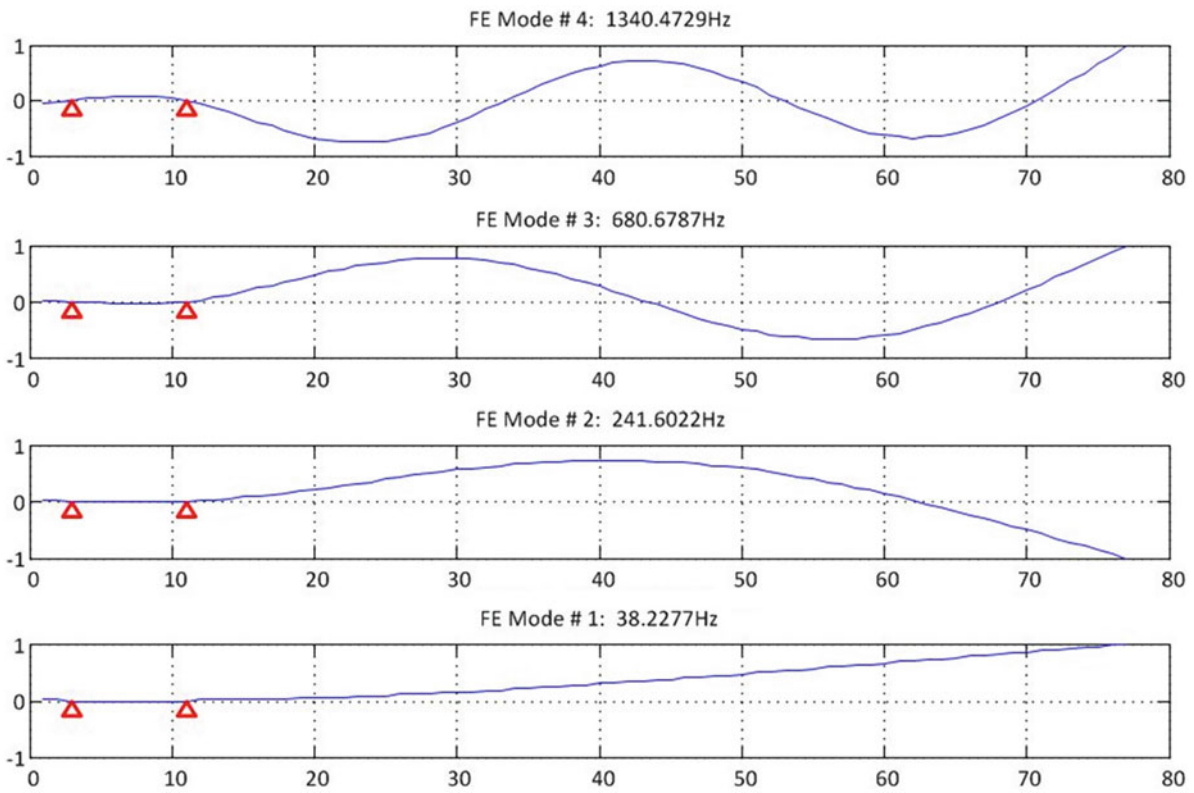


Fig. 4.10 ABC set #12 – FE mode shapes

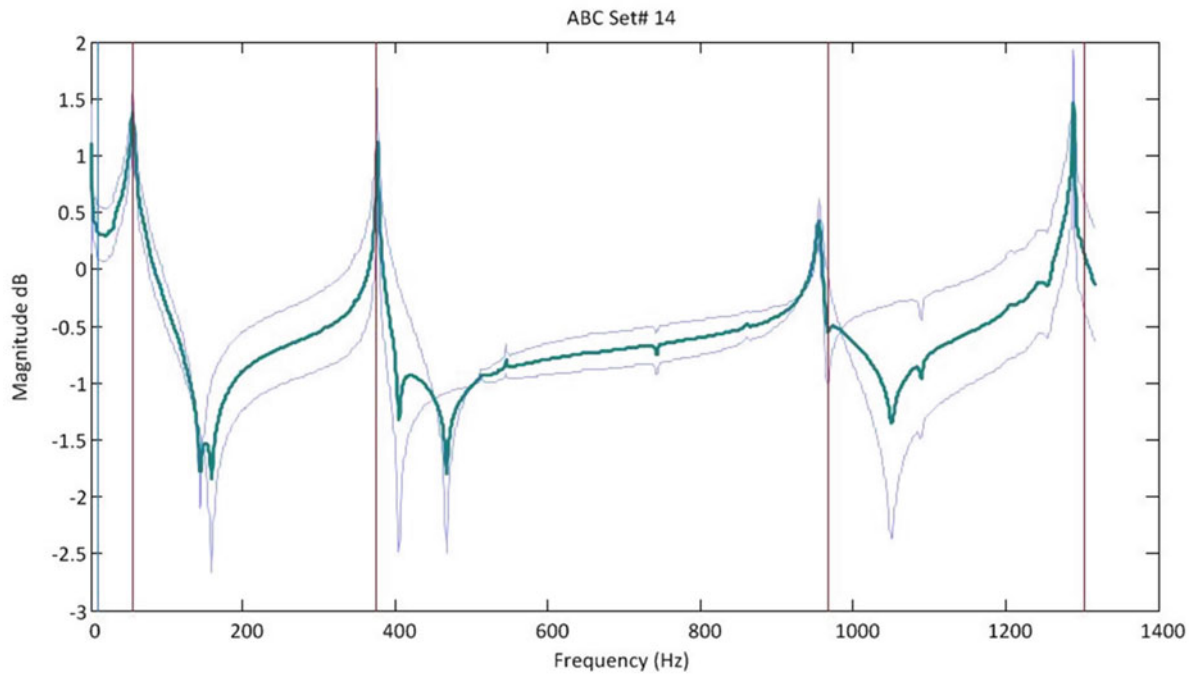


Fig. 4.11 ABC set #14 two ABC pins

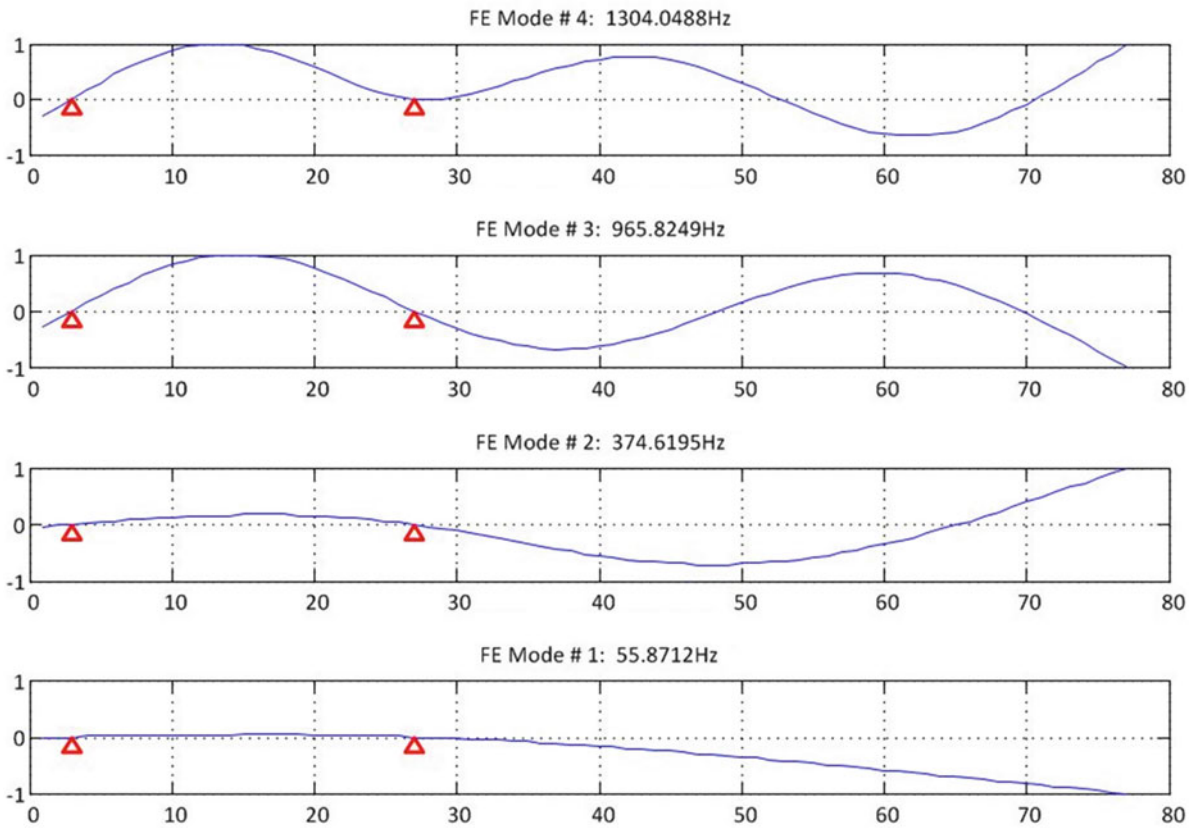


Fig. 4.12 ABC set #14 – FE mode shapes

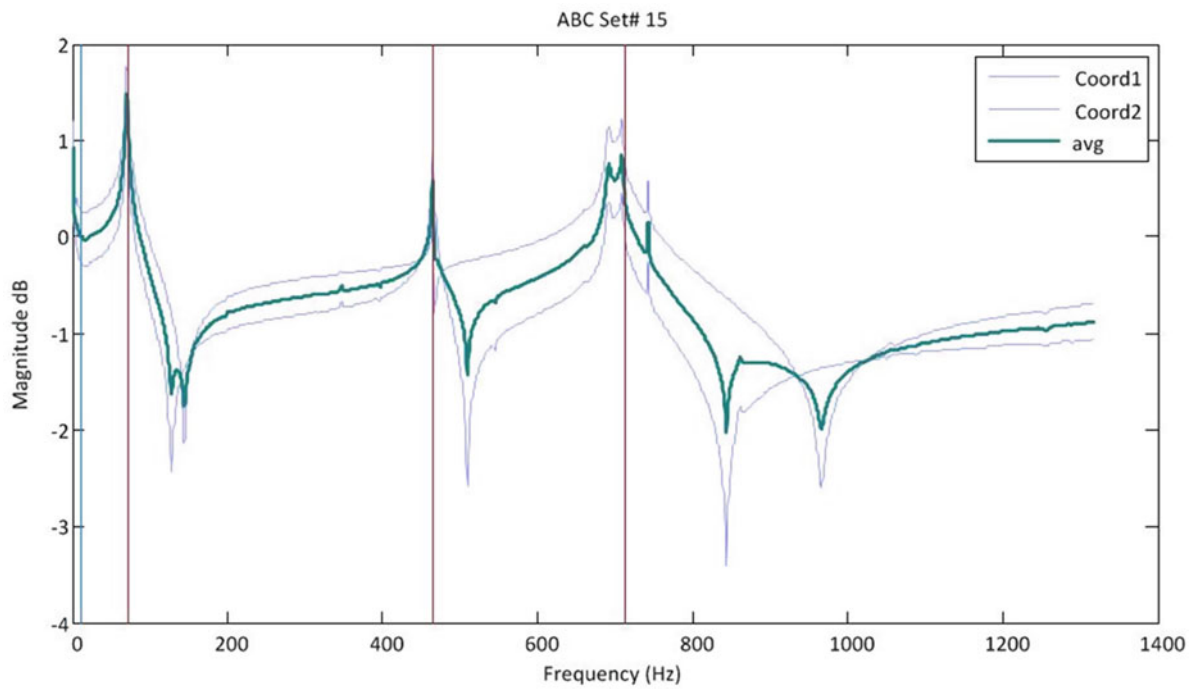


Fig. 4.13 ABC set #15 two ABC pins

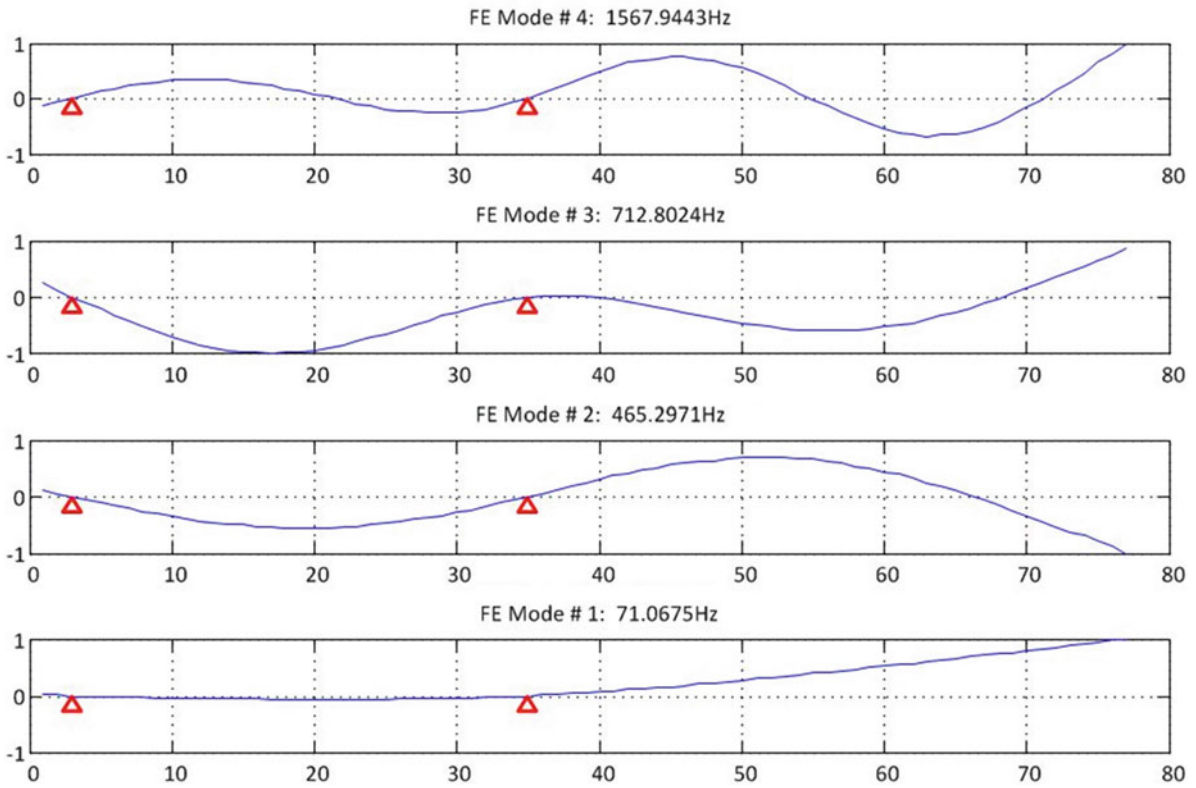


Fig. 4.14 ABC set #15 – FE mode shapes

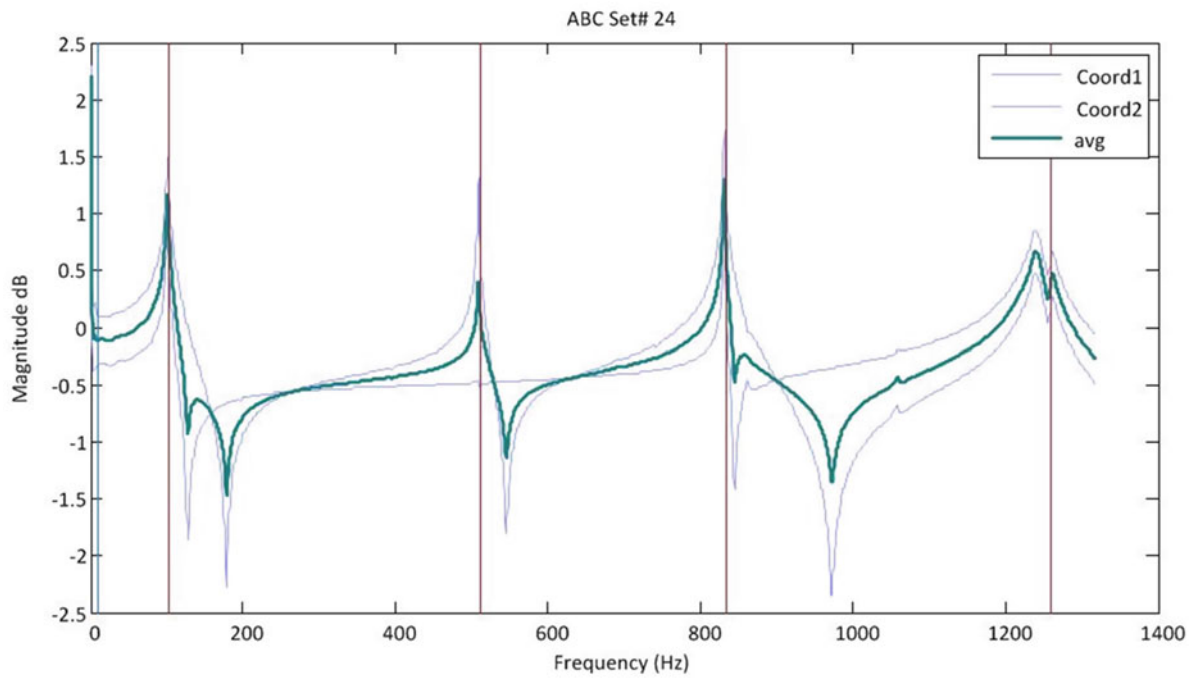


Fig. 4.15 ABC set #24 two ABC pins

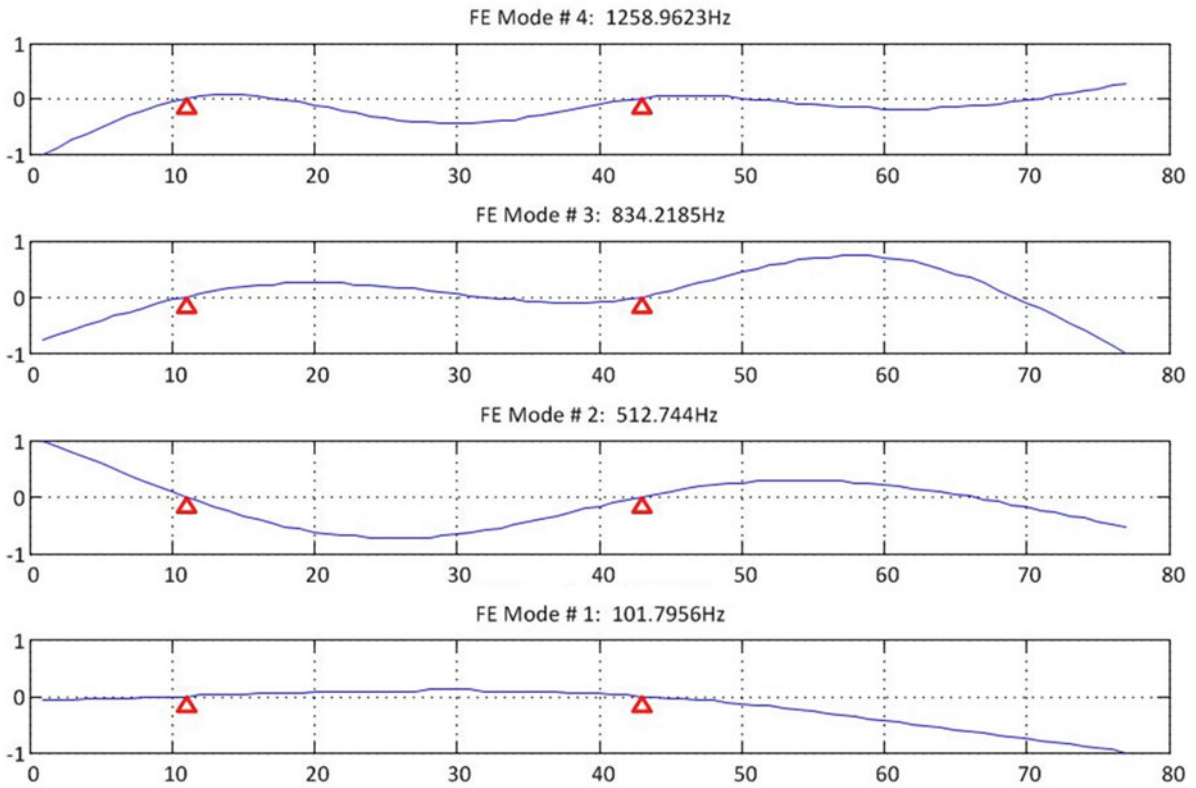


Fig. 4.16 ABC set #24 – FE mode shapes

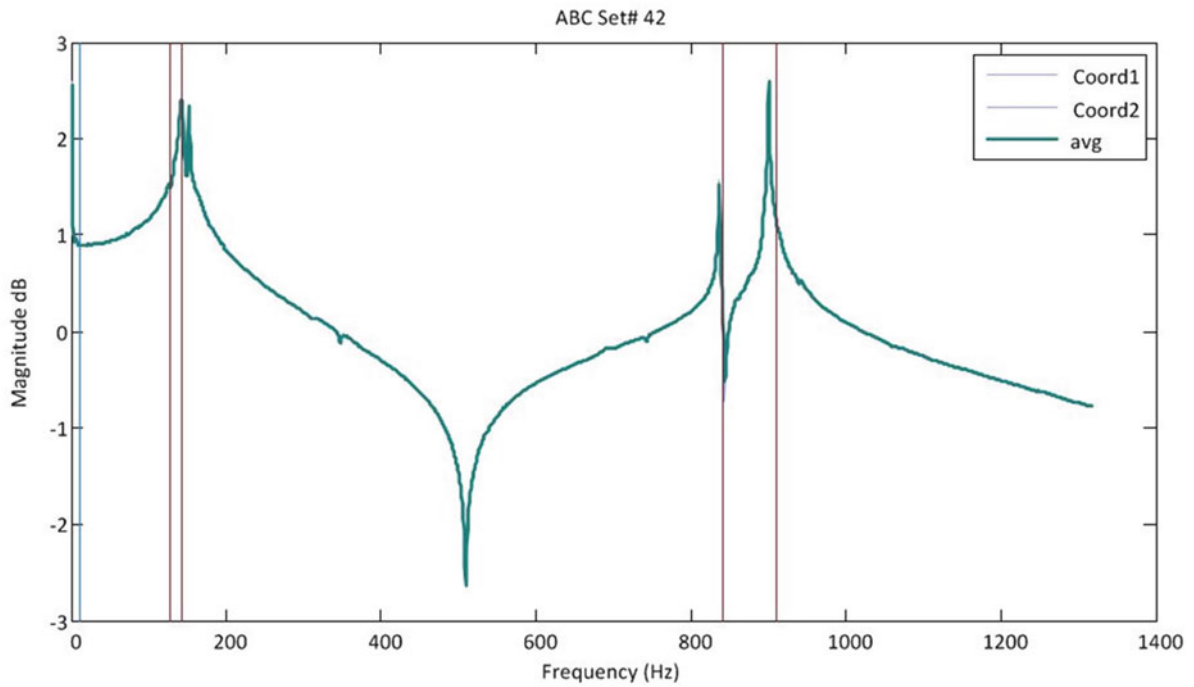


Fig. 4.17 ABC set #42 two ABC pins

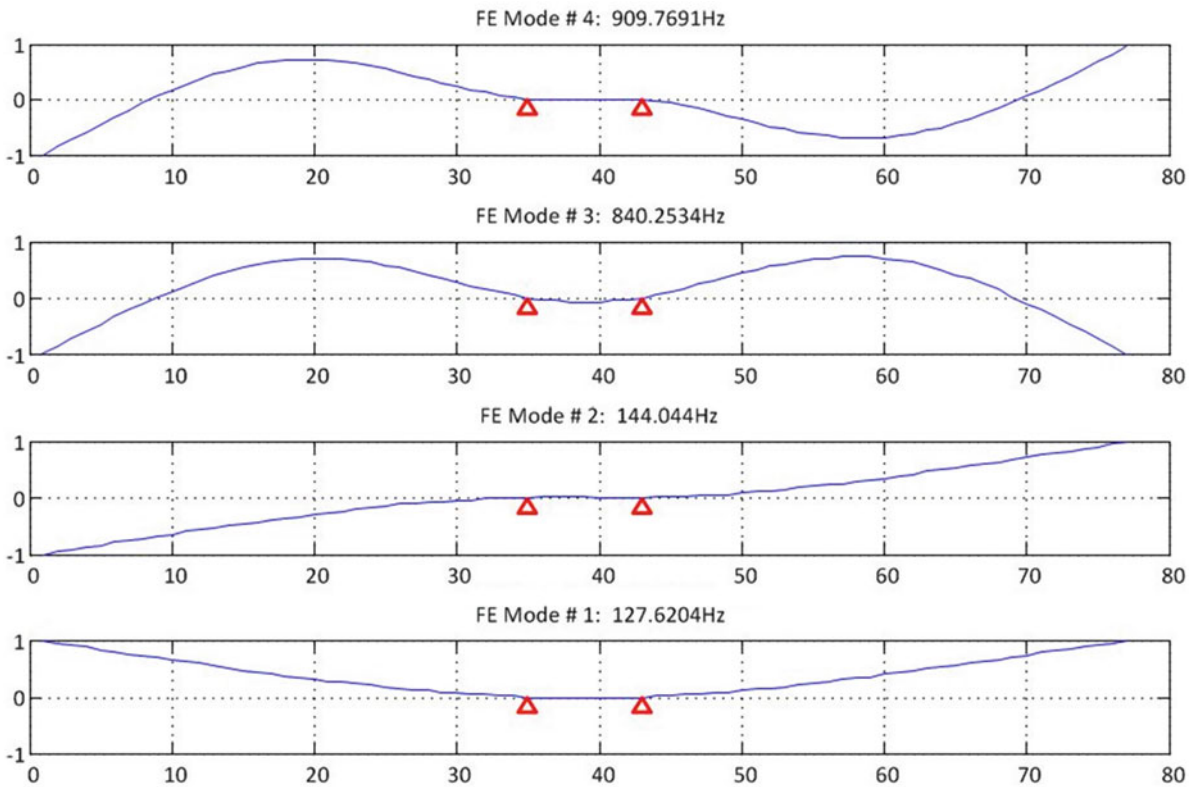


Fig. 4.18 ABC set #42 – FE mode shapes

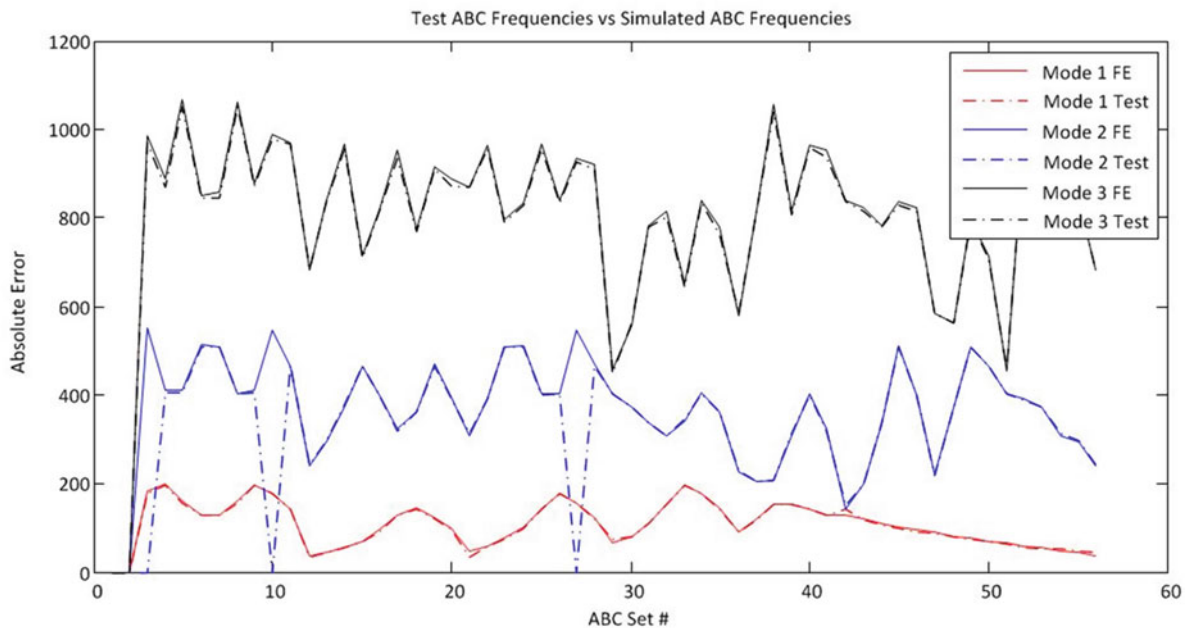
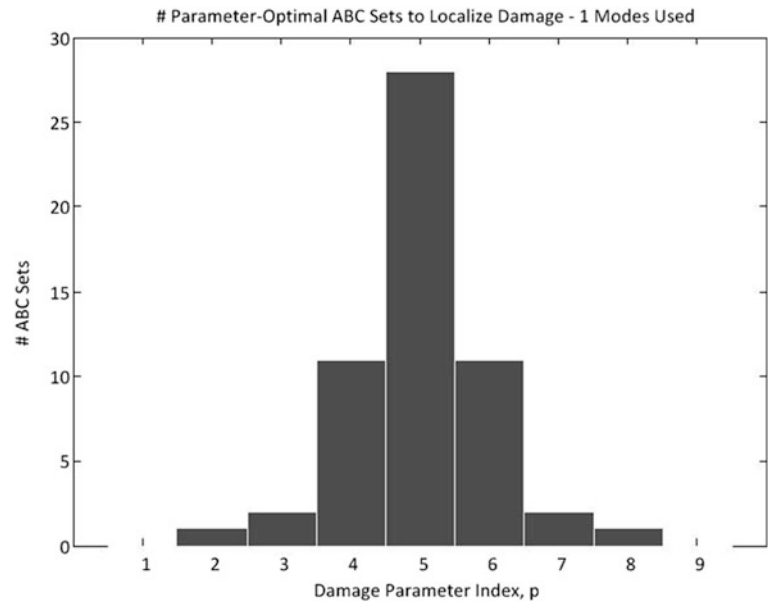


Fig. 4.19 Comparison of measured ABC frequencies with simulated (FE) ABC frequencies

In preparation for this use of the simulated test data, we show a frequency comparison of the measured ABC frequencies with the simulated ABC frequencies. This is shown in Fig. 4.19. Note that this comparison is for an undamaged FE model. To repeat, in these experiments, the measured ABC frequencies are from an undamaged beam, and the damage is simulated in the FE model by an EI reduction for all elements comprising a localization parameter (See Figs. 4.2 and 4.3). Therefore, the accuracy of the actual measured ABC frequencies relative to an undamaged FE simulation is shown (Fig. 4.19).

**Fig. 4.20** Mode sufficiency histogram – one mode used



In Fig. 4.19, the second mode test curve drops to zero at ABC sets #3, #10, and #27. This is because the ABC frequencies are picked off an impedance curve, and for these ABC set impedance curves, the second mode did not appear. Therefore, the second mode for these ABC sets is not available for localization. These second mode frequencies are present in the FE data, as all frequencies are found from the eigensolution.

Referring to Fig. 4.3, localization parameter #1 refers to the eight elements at the left end of the beam. This parameter is the most difficult in which to localize damage, due to the low modal strain energy for the modes in the test bandwidth, and hence this experiment serves as an “acid test” for the method.

The ABC-QR method provides a clear quantification of how many modes are necessary in order to localize damage in any and all parameters. We refer to this as *mode sufficiency* for localization parameter,  $p$ . In other words, in order to localize damage in parameter “ $p$ ”, the mode sufficiency calculation will determine how many ABC modes must be measured and included in the localization. The mode sufficiency is determined by the number of parameter-optimal ABC sets are found for each parameter. If at least one set is found, the parameter-optimal mode of that set determines the minimum number of modes required to localize damage in that parameter.

For this experiment, we will place a 10 % EI reduction in the localization parameter #1 of the FE model (again, the test specimen is undamaged). The ABC-QR algorithm generates a mode sufficiency histogram, calculated for a specified number of modes. Figure 4.20 shows the mode sufficiency histogram calculated using one mode. This histogram shows the number of parameter-optimal ABC sets for each parameter,  $p$ . As can be seen in the figure, there are no ABC sets which are optimal for parameter #1 or #9, therefore one mode is not sufficient to identify damage in parameters #1 or #9.

If we repeat the calculation using two and then three modes, we obtain the histogram shown in Figs. 4.21 and 4.22. While the number of parameter-optimal ABC sets has increased for parameters #2 through #8, there are still no ABC sets which can be used to identify damage in parameters #1 and #9. We will now recalculate the histogram using four modes, as shown in Fig. 4.22. Four modes is sufficient to produce three parameter-optimal ABC sets for parameter #1 and two for parameter #9. This asymmetry is due to the fact that our experiment places the damage in the finite element model (in parameter #1). It is worth emphasizing that these mode sufficiency histograms are calculated solely from the FE model, and hence can be used for test planning (i.e. required test bandwidth) (Fig. 4.23).

Now having the required number of modes in order to perform localization in all the damage parameters, the ABC-QR software generates a list of parameter-optimal ABC sets, and the parameter-optimal mode number in that set, shown in Table 4.3. We show a truncated list due to space limitations. This table lists the ABC set numbers, and mode numbers (sensitivity matrix rows), that can be used for localization for a given parameter. Note also that the table indicates which modes cannot be used as  $\Delta\lambda$  was set to 0 (by the software) to indicate that no associated peak was found from the ABC impedance.

Using Table 4.3, we will compile a system for localization. We will select nine ABC modes, including the sensitivity matrix row,  $S(u_p^*(c(p)), :)$ , and the associated  $\Delta\lambda_i^{(c(p))}$ . This selection is shown in Table 4.4.

**Fig. 4.21** Mode sufficiency histogram – two modes used

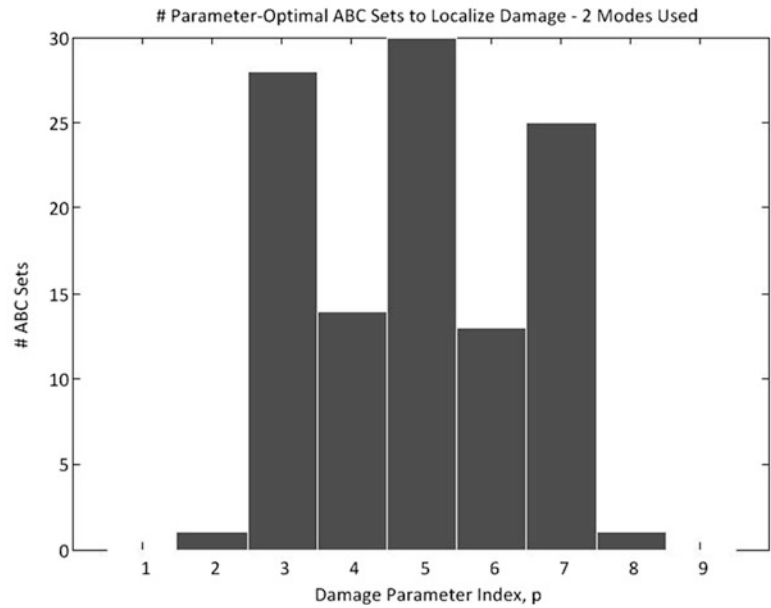
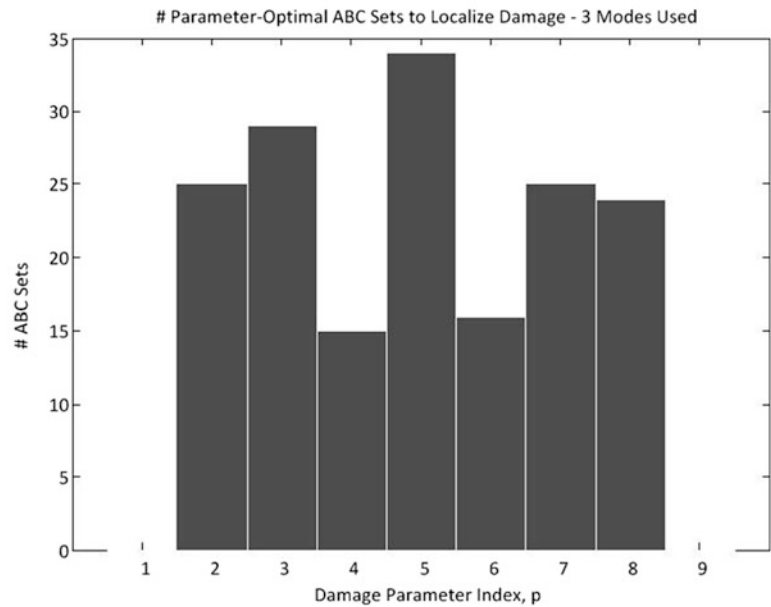


**Fig. 4.22** Mode sufficiency histogram – three modes used



We present the two solutions. In Fig. 4.24 is the localization solution using the actual measured test data. While the true error location (parameter #1) is evident, the solution does not yield a completely unambiguous result. Also, the scaling of this solution is way off. We compare to the same solution, except that the measured ABC frequencies are replaced with those from the simulation (FE model). We can see that an excellent solution is obtained. This not only validates the software, but also points to the source of the inaccuracy in the solution using the test data.

The only difference between the two solutions is in the ABC frequencies for the undamaged beam. In the solution of Fig. 4.24, the actual measured frequencies for the undamaged beam are used, while in the solution of Fig. 4.25, the simulated frequencies for the undamaged beam are used. Therefore, the measured ABC frequencies, or perhaps the choice of optimal ABC sets and modes, are the sources of the inaccuracy in the localization. In order to further examine the effect of choice of ABC sets on the solution, we will now repeat the solution, using all available ABC sets. This comprises a highly overdetermined system. Deleting ABC modes for which no frequency was found, this yields a system that is  $177 \times 9$ . The result of this calculation using measured data is shown in Fig. 4.26. The same calculation using simulated data is shown in

**Fig. 4.23** Mode sufficiency histogram – four modes used

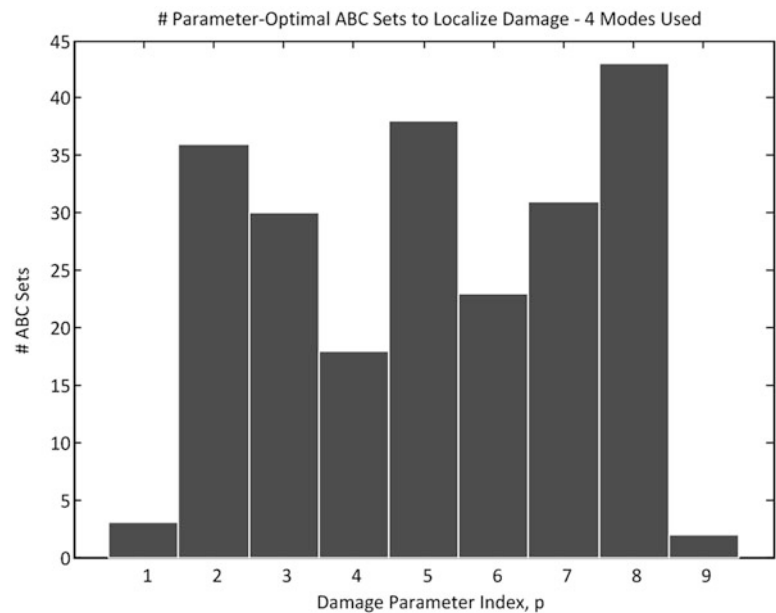


Fig. 4.27. This indicated that even highly overdetermined solutions cannot compensate for measurement inaccuracies, and that the choice of ABC sets also cannot suppress the effect of inaccuracy of the experimentally-identified ABC frequencies.

We will now take a different approach for ABC set/mode selection. This approach makes use of the simulation to find both a subset of ABC sets and the maximum number of modes to use in each ABC set. Various combinations of these settings are tried with the simulation (i.e. noise-free), until a combination is found which successfully finds the error location.

We place a 10 % EI error in parameter #3. By trying a variety of combinations of ABC parameter subsets and maximum number of modes per subset, we find a combination which successfully finds the error in parameter #3. This is shown in Fig. 4.29. Then, the experimentally-identified ABC frequencies are used, and the solution is shown in Fig. 4.28. As can be seen, the error was successfully located using the measured data. Also note that the simulation (Fig. 4.29) shows a small “false-alarm” in parameter #7. This indicates that the same false-alarm will be found using the measured data, as is demonstrated in Fig. 4.28.

Finding another combination using the simulation yields the results in Figs. 4.30 and 4.31, where it is seen that the ABC subset/max mode number combination which successfully located the error in parameter #3 for the simulation, also found the error using the actual test-identified ABC frequency data. Again, the false-alarm locations predicted by simulation (Fig. 4.31) are also found when using the actual test-identified ABC frequencies.

As a final example, we place an error in parameter #6. The results using the simulation are in Fig. 4.33, and using the test data in Fig. 4.32. In Fig. 4.33, we see that this choice of ABC subset and mode number produces a strong localization in parameter #6, it predicts false alarms in parameters #3,4,5,7 and 8. The results using the test data confirm this prediction.

## 4.11 Conclusions and Discussion

The ABC-QR method has been shown to provide an extended theoretical framework for sensitivity-based model update and damage localization. Using data from a simple free-free beam experiment, the ABC frequencies were identified. They were compared with a FE simulation using an updated model. This comparison shows that the experimentally-identified ABC frequencies are indeed close to their simulated counterparts. No spurious modes were found, as reported in [7]. Using a standard square ABC-QR solution or a maximum row-dimension (overdetermined) solution failed to find the error location. While the visual agreement between the test-identified ABC frequencies and the “closest-model” simulation frequencies is excellent, the small experimental in the ABC frequencies rendered these calculations ineffective.

This led to a new approach for the selection of ABC sets and modes. In this approach, the full library of ABC set sensitivity matrices is calculated for all modes in the test bandwidth. This library is calculated once from the simulation model.



**Table 4.3** Parameter-optimal ABC sets and modes

Parameter #	Set #	Mode #	$\Delta\lambda$	$\ S(u_1^*(c(p)), :)\ $
1	21	1	-5.192e + 04	3.569e - 01
1	26	2	-6.192e + 03	2.257e + 01
1	27	2	0.000e + 00	3.632e + 01
2	3	1	1.045e + 06	4.307e + 00
2	5	1	-4.645e + 03	3.463e + 00
2	7	1	-2.413e + 04	2.414e + 00
2	9	1	-2.244e + 04	5.060e + 00
2	11	1	4.371e + 03	2.598e + 00
2	29	2	3.203e + 04	1.968e + 01
⋮	⋮	⋮	⋮	⋮
2	52	2	-4.499e + 04	2.007e + 01
2	54	2	3.448e + 04	1.217e + 01
2	12	4	0.000e + 00	2.040e + 02
3	47	2	-6.157e + 04	9.487e + 00
3	48	2	7.174e + 04	2.502e + 01
⋮	⋮	⋮	⋮	⋮
3	52	3	3.936e + 05	1.452e + 02
3	53	3	-5.896e + 05	1.094e + 02
3	55	3	-5.628e + 02	8.594e + 01
3	13	4	0.000e + 00	3.083e + 02
3	14	4	-7.402e + 05	1.815e + 02
3	21	4	1.358e + 06	3.095e + 02
3	42	4	-4.998e + 05	9.098e + 01
0	0	0	0.000e + 00	0.000e + 00
4	16	1	-4.758e + 03	1.192e + 00
4	18	1	-2.160e + 04	2.653e + 00
4	31	1	-6.978e + 03	1.850e + 00
4	9	2	-1.162e + 05	2.288e + 01
⋮	⋮	⋮	⋮	⋮
4	56	3	9.669e + 04	5.389e + 01
4	15	4	0.000e + 00	3.182e + 02
4	22	4	-5.834e + 05	1.556e + 02
4	29	4	-1.070e + 06	1.779e + 02
4	39	4	0.000e + 00	3.011e + 02
4	40	4	0.000e + 00	2.527e + 02
4	43	4	0.000e + 00	3.088e + 02
5	1	2	2.195e + 04	3.585e + 01
5	20	2	-1.173e + 05	1.841e + 01
5	32	2	2.761e + 03	1.386e + 01
⋮	⋮	⋮	⋮	⋮
5	44	4	0.000e + 00	2.535e + 02
5	45	4	6.673e + 05	2.182e + 02
⋮	⋮	⋮	⋮	⋮
8	51	2	5.518e + 03	1.970e + 01
8	20	4	0.000e + 00	2.716e + 02
8	56	4	0.000e + 00	2.036e + 02
9	54	1	2.091e + 04	3.580e - 01
9	34	2	-4.600e + 04	2.260e + 01

From a variety of trials, we find the following.

1. The simulation model can be used as a “laboratory” in which to find a subset of ABC sets, and the number of modes to retain for each set, which successfully locates an error in a specific parameter. We refer to such a successful combination of ABC subsets and number of modes as an optimal ABC set/mode combination. Note that these calculations are relatively inexpensive as once the full library of ABC sensitivity matrices is calculated, this process is can be done as a brute-force

**Table 4.4** Selected parameter-optimal ABC sets and modes

Parameter #	ABC set #	Mode #
1	21	1
2	56	1
3	56	2
4	16	1
5	42	2
6	20	1
7	12	2
8	12	1
9	54	1

**Fig. 4.24** Using measured test data – true error in param. #1

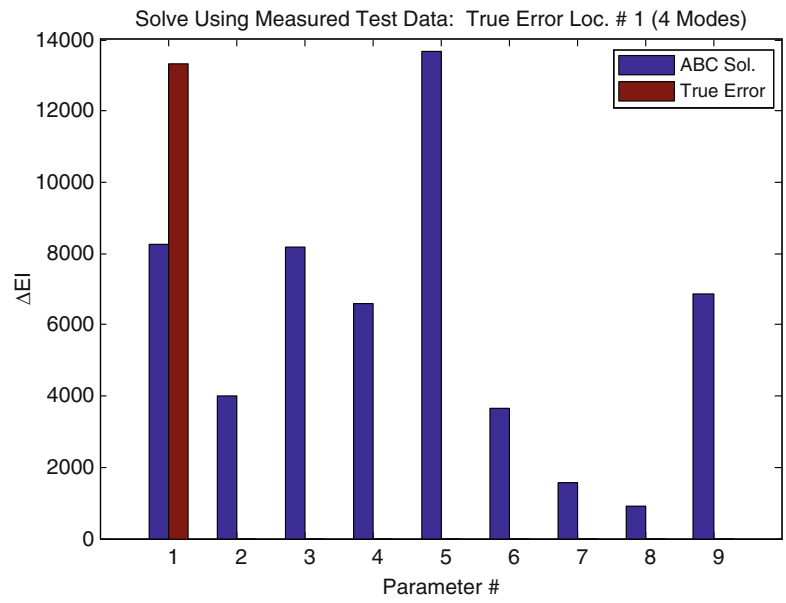


**Fig. 4.25** Using simulated test data – true error in param. #1

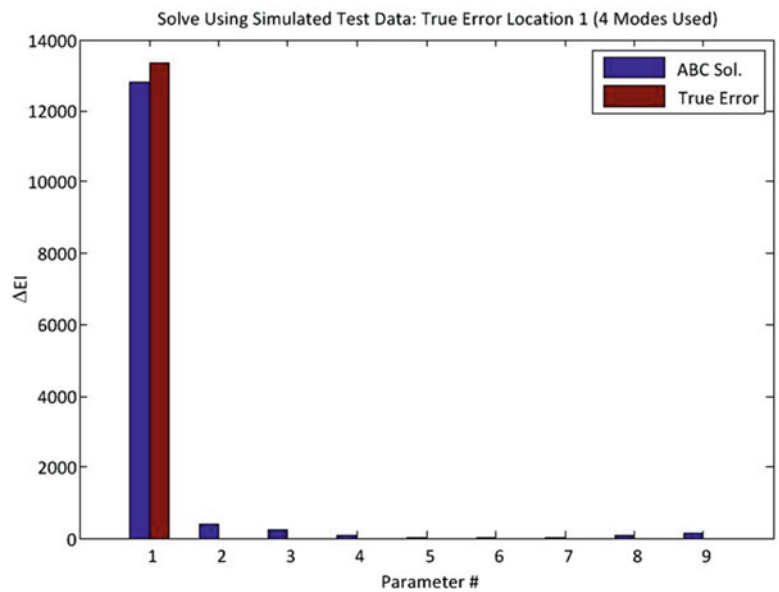


**Fig. 4.26** Measured data –  
177 × 9 solve

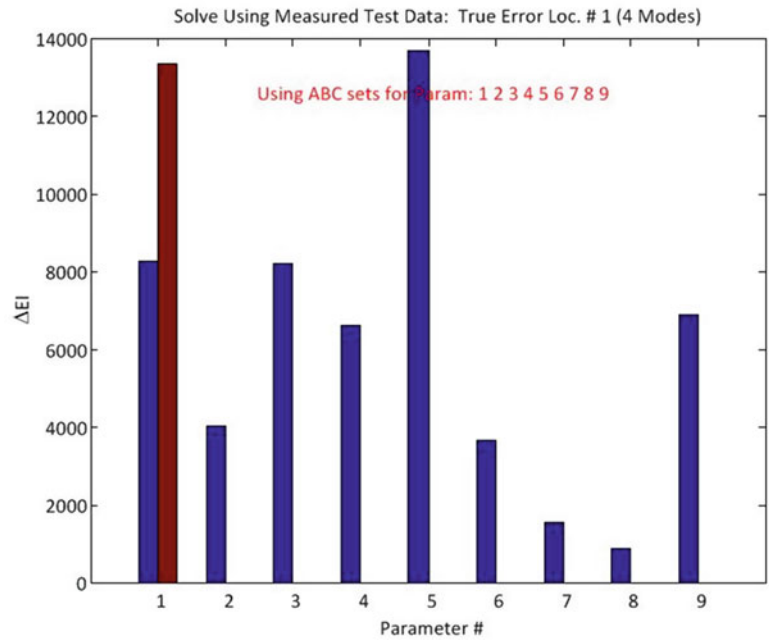
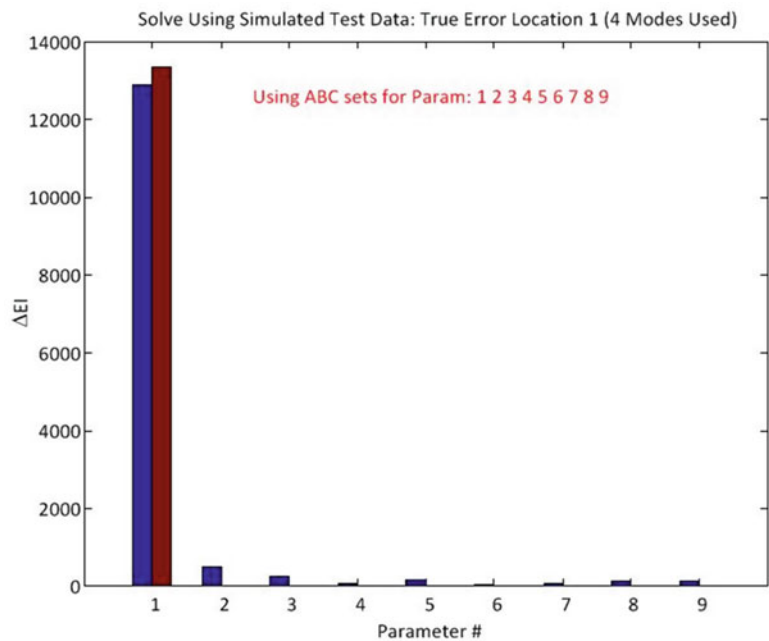


**Fig. 4.27** Simulated data –  
177 × 9 solve



trial-and-error search. However, an error would have to be successively moved from one parameter to the next to calculate the ABC frequencies. This can be efficiently done using frequency domain structural synthesis [8]. More sophisticated ways of determining this optimal ABC set/mode combination is under continuing research.

2. An error in a specified parameter cannot be found if the simulation is not able to find it. In other words, an error in a specified parameter can only be found using an optimal ABC set/mode combination for that parameter.
3. For a given optimal ABC set/mode combination, those parameters which are identified as “false-alarm” parameters will show false alarms using the test data.
4. The optimal ABC set/mode combinations for a given parameter may or may not include the ABC-QR-optimal set number for the parameter.

**Fig. 4.28** Measured data – param. #1 – two modes/param

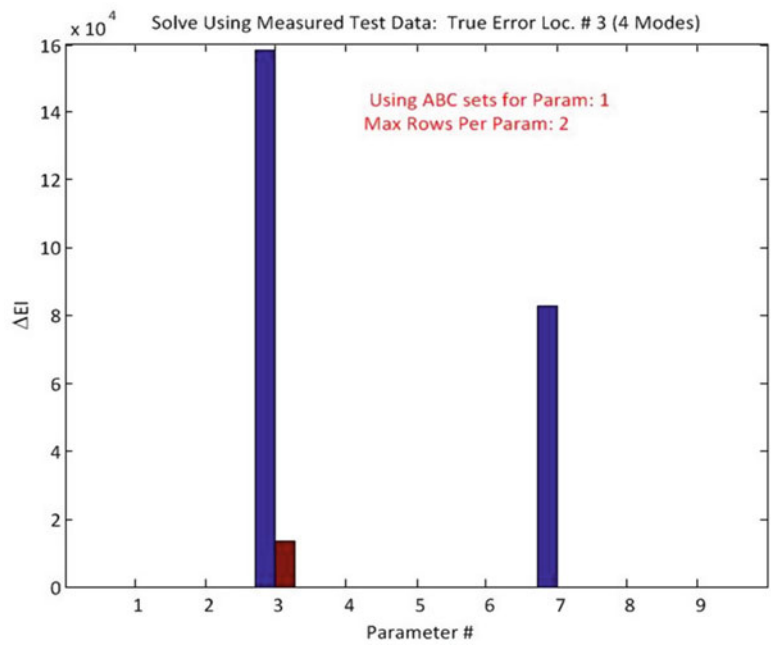
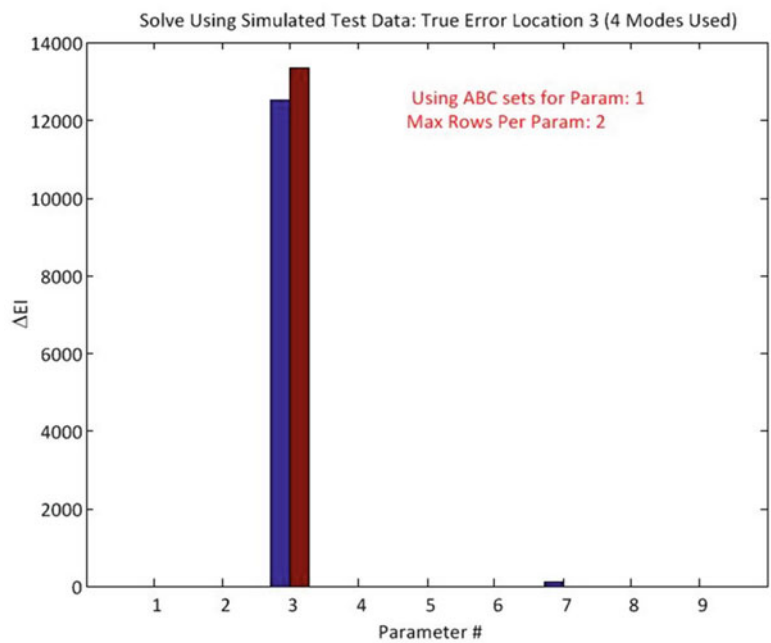


**Fig. 4.29** Simulated data – param. #1 – two modes/param



The optimal optimal ABC set/mode combinations can be seen as identify “channels” through which parameter error or false alarms can be detected. The use of other than optimal ABC set/mode combinations are used for a parameter suppresses both true error localization and false alarms. This is a potentially valuable result which warrants further research.

This work has not focused on the distortion present in the test-identified ABC frequencies. In addition to measurement noise, a particular experimental challenge relevant to the ABC method is the need to accurately measure the full FRF, including anti-resonance locations as well. This has been studied in [9], where an SVD-Hankel matrix approach was used to remove measurement noise from the FRF. Much work remains, but the ABC-QR remains fundamentally sound in its ability to expand a measured dataset, producing additional independent rows of a sensitivity matrix.

**Fig. 4.30** Measured data –  
param. #1,6,7 – one mode/param

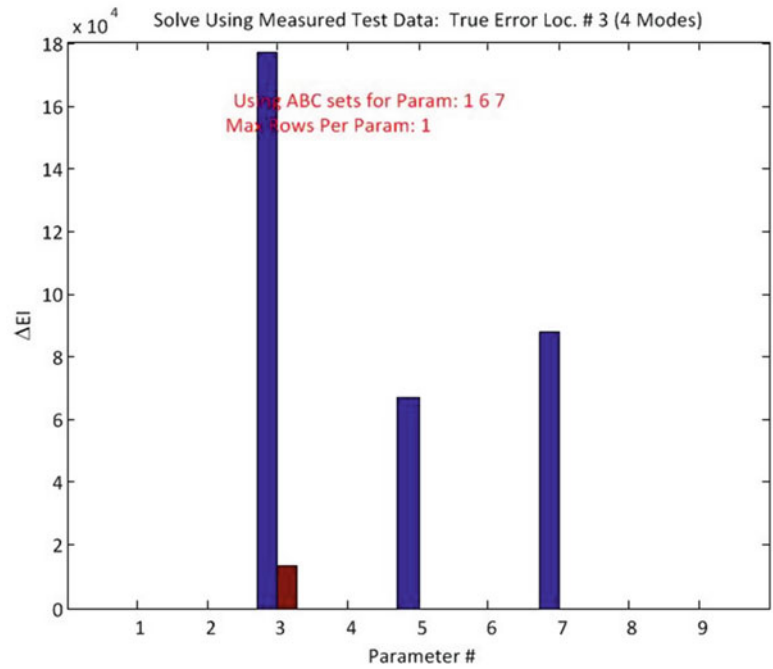


**Fig. 4.31** Simulated data –  
param. #1,6,7 – one mode/param

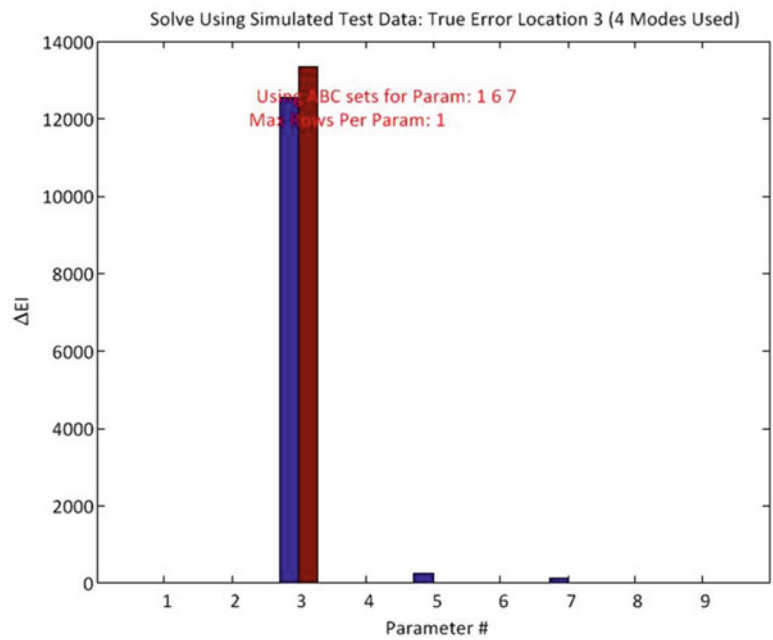


**Fig. 4.32** Measured data – param. #1,6,7 – two modes

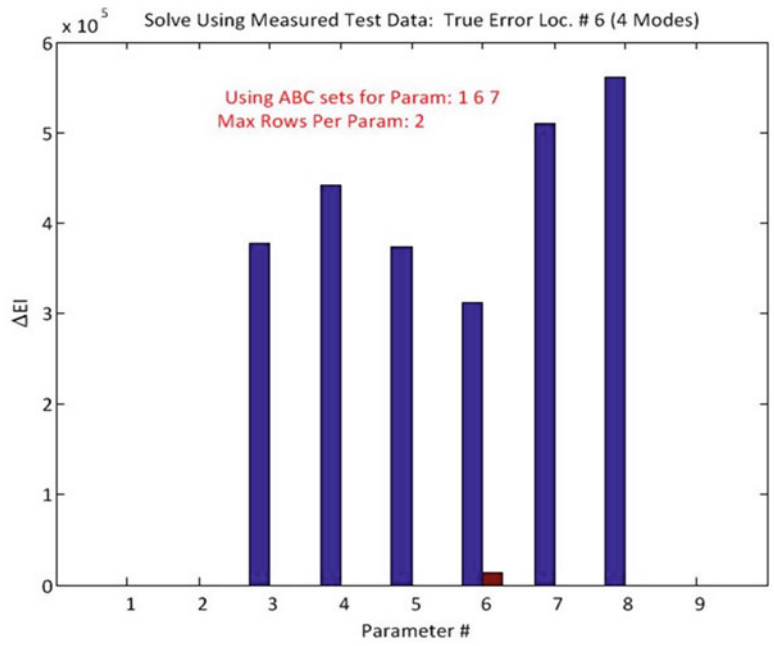
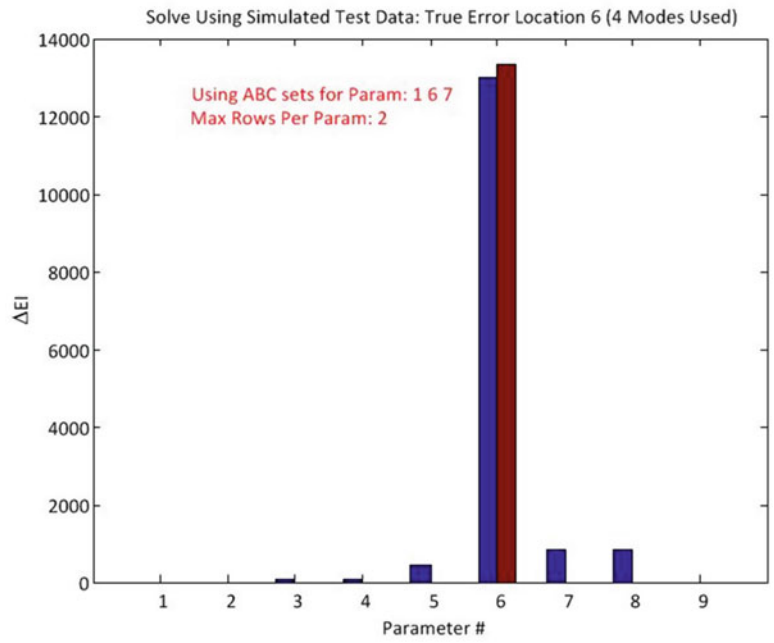


**Fig. 4.33** Simulated data – param. #1,6,7 – two modes



**Acknowledgements** I would like to acknowledge my wife, Kelleyanne Gordis, for the helpful discussions regarding this research.

## References

1. Lallement G, Piranda J (1990) Localisation methods for parameter updating of finite element models in elastodynamics. In: 8th international modal analysis conference, Orlando, FL, USA, pp 579–585
2. Gordis JH (1992) Spatial, frequency domain updating of linear, structural dynamic models. In: Proceedings of the 34th AIAA/ASME/ASCE/AHS/ACS structures, structural dynamics, and materials conference, San Diego, CA, USA, pp 3050–3058
3. Gordis JH (1990) A frequency domain theory for structural identification. *J Am Helicopter Soc* 38(2):25–33, Apr 1993
4. Gordis JH, Papagiannakis K (2011) Optimal selection of artificial boundary conditions for model update and damage detection. *Mech Syst Signal Process* 25:1451–1468
5. Gordis JH (1999) Artificial boundary conditions for model updating and damage detection. *J Mech Syst Signal Process* 13(3):437–448
6. Gordis JH (1996) Omitted coordinate systems and artificial constraints in spatially incomplete identification. *Int J Anal Exp Modal Anal* 11(1–2):83–95
7. Lu Y, Tu Z (2008) Artificial boundary condition approach for structural identification: a laboratory perspective. In: Proceedings of the 26th international modal analysis conference, Orlando, FL, USA
8. Gordis JH (1994) Structural synthesis in the frequency domain: a general formulation. *Shock Vib* 1(5):461–471
9. Mao L, Lu Y (2011) Extraction of artificial boundary frequencies for damage identification. *J Phys: Conf Ser* 305:012051

# Chapter 5

## Detection of Mass Change on a Glass Plate

Jannick B. Hansen, Rune Brincker, and Manuel L. Aenlle

**Abstract** In model updating the aim is to reach the optimal correlation between FE model and test data by modifying model parameters. The traditional solution to an updating problem is obtained by non-linear optimization processes governed by the selected updating parameters and target responses. Due to imprecision and lack of information in measurements, inaccuracy in model and several possible updating parameters a wide range of potential solutions to the same problem is present.

This paper proposes a technique in which the updating problem is solved in one step using modal properties, i.e. natural frequencies and mode shapes, as target responses. The method utilizes mode shape sensitivity equations combined with the Bernal Projection equation to detect mass and stiffness discrepancies between model and experimental data. The proposed one step solution will only work accurately in cases where a reasonable FE model is available. The technique is demonstrated on simulated data of modal properties before and after mass perturbation of a glass plate. The data is polluted with noise in the range of what can be expected from real measured data.

**Keywords** Model updating • Damage detection • Modal parameters

### 5.1 Introduction

Improving an FE model using test data has through many years proven to be a challenging task. There are potentially multiple sources to discrepancies between model and data and even more updating parameters. Ultimately, the solution to a specific model calibration problem is governed by parameter and target response selection and furthermore user intuition and experience. The concepts of model updating and damage detection are closely related in the sense that in both cases the aim is to obtain dissimilarity between two sets of responses. One might argue that damage detection using vibration data is model updating, limited to stiffness- and mass related parameters utilizing only the modal parameters as target responses.

The boundaries of damage detection using modal parameters reduce the amount of possible solutions. By means of mode shape and frequency sensitivity equations it is possible to obtain an estimate of damage without relying non-linear optimization processes. The proposed method detects change in structural mass and stiffness based on observed changes in modal properties, i.e. natural frequencies and corresponding mode shapes. Similar methods have with success identified structural defects by interpreting change in modal parameters [1] and the present method contributes by introducing the Bernal Projection equation [2] to calculate frequency sensitivities. The proposed method can to some extent be utilized as a model calibration tool, however, the main intent lies within the area of damage detection.

---

J.B. Hansen (✉)

Ph.D. student, Department of Engineering, Aarhus University, Finlandsgade 22, 8200 Aarhus N, Denmark  
e-mail: [jbha@iha.dk](mailto:jbha@iha.dk)

R. Brincker

Professor, Department of Engineering, Aarhus University, Finlandsgade 22, 8200 Aarhus N, Denmark  
e-mail: [rub@iha.dk](mailto:rub@iha.dk)

M.L. Aenlle

Lecturer, Department of Construction and Manufacturing Engineering, University of Oviedo,  
Campus de Gijón, Zona Oeste, Edificio 7, 33203 Gijón, Spain  
e-mail: [aenlle@uniovi.es](mailto:aenlle@uniovi.es)



The approach is to compute mode shape and frequency sensitivities towards both mass and stiffness change. Hereafter, the location of a mass or stiffness change can be pinpointed by combining the information on the behavior of the system towards alterations with the actual observed changes in modal properties. In order to calculate mode shape sensitivities a reasonable FE model of the specific structure and the estimated modal parameters of the structure in the unperturbed or virgin state are required. In the process of calculating the frequency sensitivities the modal parameters of the perturbed system are necessary as well.

Naturally, a few aspects of the method are simplified by using simulated data. For instants, a perfect FE model is available for calculating sensitivities and there are no restrictions on the bandwidth of the “measured” data.

## 5.2 Theoretical Aspects

This method utilizes both frequency and mode shape shifts as target responses to detect change in the parameters of the regarded system and is based on two equations. The initial equation is the well-known mode shape sensitivity equation [3]. The second equation is the Bernal Projection equation [2] originally intended for mode shape scaling but in this context used for determining a measure for frequency sensitivity. Both equations are featured in the final system of equations contributing to the estimate of the damage vector, i.e. the measure of change in either mass or stiffness, both location and magnitude. For brevity only the equations for detecting mass change is deduced in the following theoretical review.

### 5.2.1 Mode Shape Sensitivity Equation

The mode shape sensitivity equation is the first order derivative of mode shape  $i$  with respect to a local change parameter  $u$  in the mass and/or stiffness matrix.

$$\frac{\partial \mathbf{b}_i}{\partial u} = -\frac{1}{2m_i} \mathbf{b}_i^T \frac{\partial \mathbf{M}}{\partial u} \mathbf{b}_i \mathbf{b}_i + \sum_{r=1, r \neq i}^M \frac{1}{\omega_i^2 - \omega_r^2} \frac{1}{m_r} \mathbf{b}_r^T \left( -\omega_i^2 \frac{\partial \mathbf{M}}{\partial u} + \frac{\partial \mathbf{K}}{\partial u} \right) \mathbf{b}_i \mathbf{b}_r \quad (5.1)$$

where  $\mathbf{b}$  is a mode shape vector,  $\omega$  is angular frequency,  $m$  is the modal mass,  $\mathbf{M}$  and  $\mathbf{K}$  is the mass and stiffness matrix respectively, subscript  $i$  denotes the regarded mode shape and subscript  $r$  denotes the remaining mode shapes of the system. Equation (5.1) can be reduced by considering a finite change in the mass matrix only. Written in matrix form

$$\Delta \mathbf{b}_i \cong \mathbf{B} \Gamma_{M,i} \mathbf{B}^T \Delta \mathbf{M} \mathbf{b}_i \quad (5.2)$$

where  $\Delta \mathbf{b}$  is the mode change vector,  $\mathbf{B}$  is the mode shape matrix,  $\Gamma$  is a diagonal matrix and subscript  $M$  denotes the case of mass change. For unit mass changes in all degrees of freedom (DOF), the matching mode shape derivatives are calculated one by one. This procedure is repeated for all mode shapes. The mode shape derivatives are collected in a matrix consequently describing how the system will react to a mass change in an arbitrary DOF, this matrix will henceforth be referred to as the sensitivity matrix. The mode shape derivatives are arranged so that a multiplication with the change vector will single out the columns of the sensitivity matrix which contribute to the resulting mode shape change. In math terms

$$\Delta \mathbf{b}_M = \Delta \mathbf{B}_M \Delta \mathbf{u}_M \quad (5.3)$$

where  $\Delta \mathbf{B}$  is the mode shape sensitivity matrix and  $\Delta \mathbf{u}$  is the mass change vector. This vector can be determined by left multiplying Eq. (5.3) with the inverse of the sensitivity matrix. Due to the fact that the mode shape derivatives of all available modes are stacked in the sensitivity matrix it cannot be quadratic. Therefore, the sensitivity matrix is inverted by means of the Moore-Penrose pseudo inverse, thus

$$\Delta \mathbf{u}_M = \Delta \mathbf{B}_M^+ \Delta \mathbf{b}_M \quad (5.4)$$

A similar expression for change in stiffness can be deduced by repeating the considerations above.

### 5.2.2 Bernal Projection Equation

The second equation, the Bernal Projection equation, utilizes the observed change in frequencies to detect change in either mass or stiffness in the DOF's of the system. The equation originates from research concerning scaling of mode shapes determined by operational identification techniques and reads

$$\frac{1}{m_i} = \frac{(\omega_{bi}^2 - \omega_{ai}^2)T_{ii}}{\mathbf{b}_i^T (\omega_{ai}^2 \Delta \mathbf{M} - \Delta \mathbf{K}) \mathbf{a}_i} \quad (5.5)$$

where  $\mathbf{b}$  is a mode shape vector for the initial system,  $\mathbf{a}$  is a mode shape vector for the perturbed system,  $m$  is the modal mass for the initial system,  $T$  is a matrix describing the linear transformation between the two sets of mode shapes, subscript  $i$  denotes the regarded mode and subscript  $a$  and  $b$  denotes the perturbed and initial system respectively. Considering mass change only and rearranging Eq. (5.5) a term for change in modal mass can be defined as

$$\Delta m_i = \frac{(\omega_{bi}^2 - \omega_{ai}^2)T_{ii}}{\omega_{ai}^2} m_i = \mathbf{b}_i^T \Delta \mathbf{M} \mathbf{a}_i \quad (5.6)$$

By repeating the operation of subjecting the system with unit mass changes in all DOF's, the corresponding modal mass change is determined. This procedure is conducted by means of the right-hand side of Eq. (5.6) and is repeated for all mode shapes. Hereby, a row vector for each mode can be constructed. This vector contains information on how the modal mass of a specific mode will vary due to sequential mass change in all the DOF's of the system. Therefore, the observed change  $\Delta m_i$  can be expressed as

$$\Delta m_i = \Delta \mathbf{m}_i^T \Delta \mathbf{u}_M \quad (5.7)$$

where  $\Delta \mathbf{u}$  is the change vector. The observed modal mass change can be calculated by means of the middle term in Eq. (5.6) hence the change vector becomes the only unknown of Eq. (5.7). A similar equation for stiffness changes can be reached by excluding the mass change matrix in Eq. (5.5) and following the same approach.

### 5.2.3 Final System of Equations

By combining the derived expressions based on the mode shape sensitivities and the Bernal Projection equation regarding mass change, i.e. Eqs. (5.4) and (5.7), a system of equations can be obtained. For mode  $i$  we obtain

$$\begin{Bmatrix} \Delta m_i \\ \Delta \mathbf{b}_i \end{Bmatrix} = \begin{Bmatrix} \Delta \mathbf{m}_i^T \\ \Delta \mathbf{B}_{M,i} \end{Bmatrix} \Delta \mathbf{u}_M \quad (5.8)$$

Hence, Eq. (5.8) utilizes the observed changes in both frequencies and mode shapes hereby drawing more information into the process of determining the damage vector and ultimately increasing the robustness of the technique. Equation (5.8) can be extended to cover changes in stiffness by inserting the stiffness versions of Eqs. (5.4) and (5.7). For mode  $i$  the final system of equations will read

$$\begin{Bmatrix} \Delta m_i \\ \Delta k_i \\ \Delta \mathbf{b}_i \end{Bmatrix} = \begin{bmatrix} \Delta \mathbf{m}_i^T & [0] \\ [0] & \Delta \mathbf{k}_i^T \\ \Delta \mathbf{B}_{M,i} & \Delta \mathbf{B}_{K,i} \end{bmatrix} \begin{Bmatrix} \Delta \mathbf{u}_M \\ \Delta \mathbf{u}_K \end{Bmatrix} \quad (5.9)$$

where  $\Delta k$  is the observed change in modal stiffness,  $\Delta \mathbf{k}$  is the sensitivity vector and subscript  $K$  denotes the case of stiffness change. The vector on the left-hand side is defined as the change vector  $\Delta \mathbf{c}_i$  and the vector on the right-hand side is defined as the damage vector  $\Delta \mathbf{u}$ . Finally, the matrix in Eq. (5.9) is defined as the combined sensitivity matrix  $\mathbf{S}_i$ . Thus, Eq. (5.9) can be expressed as

$$\Delta \mathbf{c}_i = \mathbf{S}_i \Delta \mathbf{u} \quad (5.10)$$

So for all modes of the system the damage vector is found as

$$\Delta \mathbf{u} = \mathbf{S}^+ \Delta \mathbf{c} \quad (5.11)$$

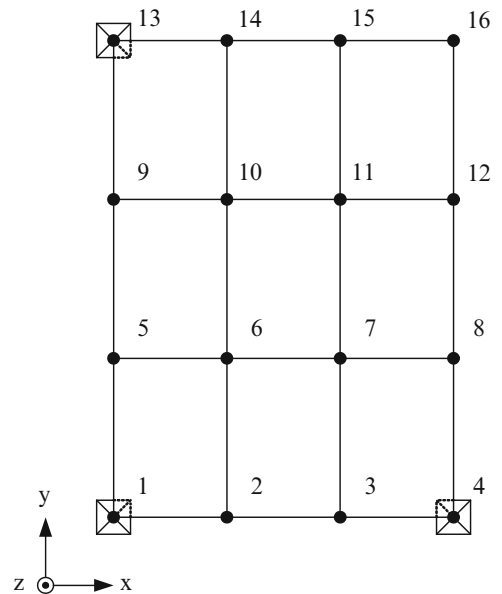
**Fig. 5.1** Glass plate model: nodes and supports

Geometrical properties:

- Length 1,4 m
- Width 1 m
- Thickness 10 mm

Material properties:

- Young's modulus 70 GPa
- Poisson's ratio 0.2
- Density 2548 kg/m<sup>3</sup>
  
- Total weight 35.672 kg



### 5.3 Case Study: Glass Plate

In this section the theory described above is utilized in a case study of an FE model of a rectangular glass plate. The data gathered in the simulation are results of a dynamic analysis routine from FE software executed before and after mass perturbation. The main focus has been centered on mass change detection for several reasons but primarily due to the fact that the computational routines regarding mass detection are less burdensome.

The simulation procedure; Initially, the mode shapes and frequencies of the undisturbed system are used to build up the sensitivity matrix. Secondly, the system is subjected to either mass or stiffness alterations, then the modal properties are extracted from the “damaged” system. Finally, the damage vector is determined by multiplying the calculated change in modal properties with the sensitivity matrix in question.

#### 5.3.1 Finite Element Model

The dynamic characteristics of the glass plate are computed by means of a FE structure modelled in SDTools [4]. The plate is subdivided into a  $3 \times 3$  mesh of QUAD4 shell elements resulting in a total of 16 node points. At all node points the rotational- and in-plane degrees of freedom (DOF) are fixed leaving only the out-of-plane DOF's released. Furthermore, the DOF's in 3 of the 4 corners of the plate are retained towards out plane motion thus constituting a dynamic system with 13 DOF's. The Fig. 5.1 below shows the nodes and supports of the FE model.

Geometrical properties:

- Length 1,4 m
- Width 1 m
- Thickness 10 mm

Material properties:

- Young's modulus 70 GPa
- Poisson's ratio 0.2
- Density 2, 548 kg/m<sup>3</sup>
- Total weight 35.672 kg

Due to the coarse mesh and the small amount of DOF's the FE model has little resemblance to the properties of a similar physical glass plate, however, the purpose of this study is not to mimic reality but merely to validate the theoretical considerations described in the previous section.

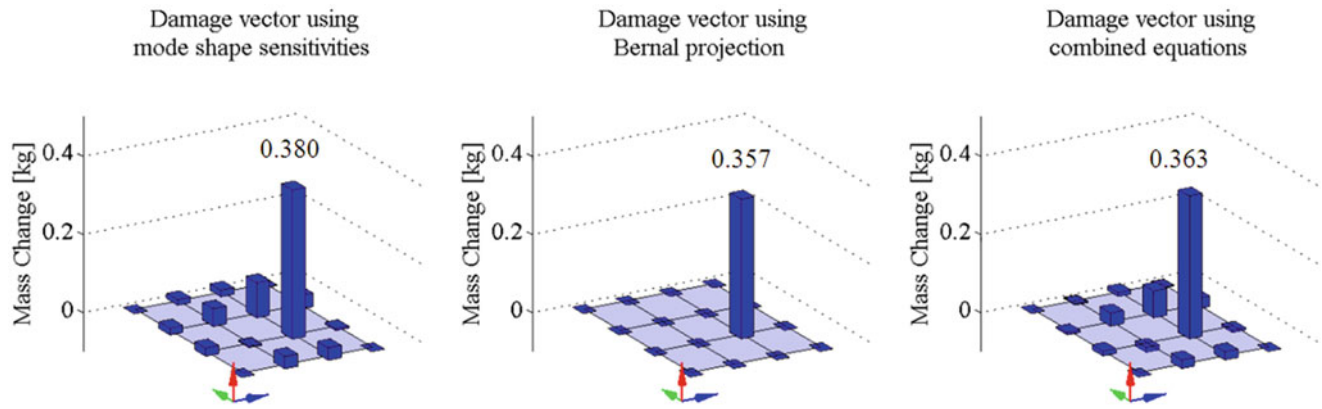


Fig. 5.2 Damage vectors 1 % mass change in node 7 with 13 modes

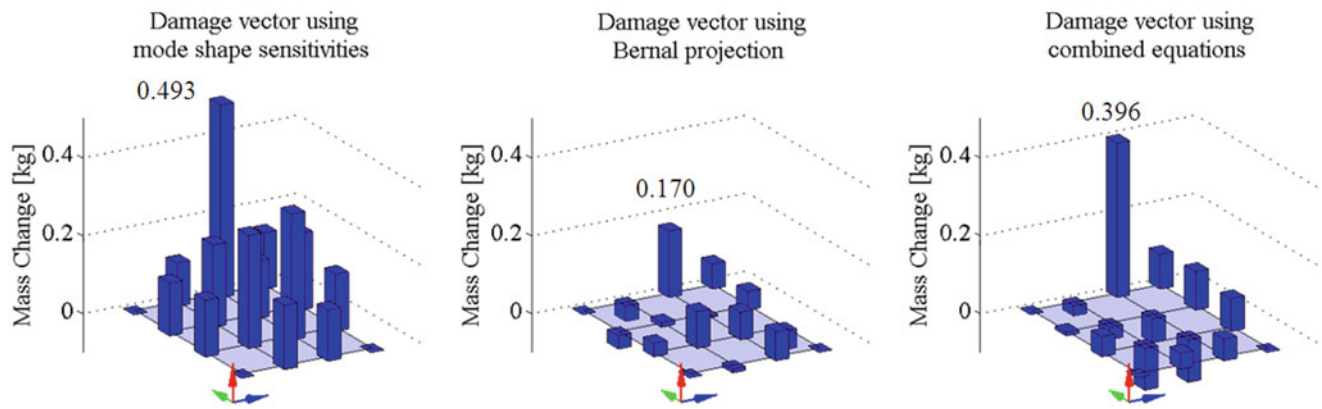


Fig. 5.3 Damage vectors 1 % mass change in node 15 with 7 modes

### 5.3.2 Simulation Results

In this subsection the results of a series of simulation cases are presented. Besides proving the validity of the method, the purpose is to highlight the extent in which the technique has been tested and display the immediate limitations. All results are displayed in bar plots on a surface resembling the geometry of the FE model.

In Fig. 5.2 below a simulation result of a mass change in node 7 is displayed. The size of the mass change is 1 % of the total weight of the glass plate model, 0.357 kg. All 13 modes are used in the calculation of the sensitivity matrix.

The two initial bar plots in Fig. 5.2 are the results of Eqs. (5.4) and (5.7) respectively whereas the outermost right bar plot is the result of the combined equation, i.e. Eq. (5.11). All three damage vectors clearly indicate a mass change in node 7 along with an accurate estimate of mass size. The damage vector estimated by means of mode shape sensitivities display some scatter in the remaining nodes, this is not unexpected due to the fact that the sensitivity equation is not exact for finite mass changes. In fact the equation will become decreasingly accurate proportional to the increase in value of the mass alteration. On the other hand the damage vector calculated by means of Eq. (5.7) is exact, because the Bernal projection equation is exact given all modes of the system are utilized.

In Eq. (5.11) the sensitivity matrix is inverted by means of the Moore-Penrose pseudo inverse. Similar damage detection techniques [1] claims to have issues regarding the amount of mode shapes needed in proportion to the number of DOF's in order to obtain a valid damage vector. Therefore, a study with a decreasing number of modes used in the calculation of the sensitivity matrix has been undertaken. Figure 5.3 displays the results from a simulation where only 7 of the modes are used in the calculation of the sensitivity matrix.

The lack of information from the higher modes clearly affects the resulting damage vectors which is evident from the plots in Fig. 5.3. The damage vectors shown in Fig. 5.3 are not as distinct as the plots in Fig. 5.2 and suggest mass changes in other locations than the position of the actual mass change. The source of this problem lies in the inversion of the sensitivity

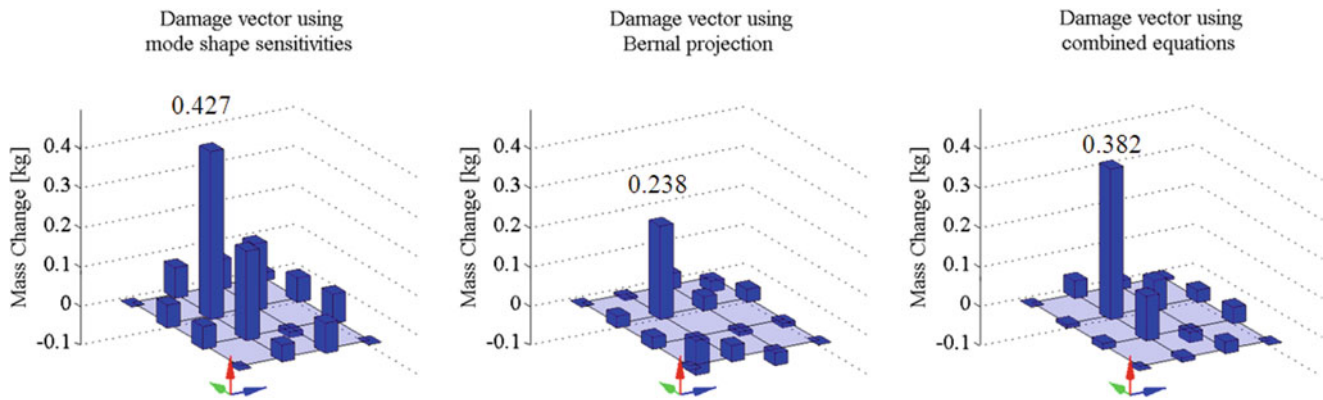


**Fig. 5.4** One percent mass change in node 10, 10 modes, 0.1 % noise on frequencies and 2 % noise on mode shapes

matrix which has been clarified by researchers working with similar methods [5] and a solution using a so-called “weighted” pseudo-inverse has been suggested. Another important note regarding Fig. 5.3 is that the combination of the mode shape sensitivity and Bernal projection equation results in a sensitivity matrix holding more information and therefore leads to an improved damage vector.

In the final simulation presented in this paper the frequencies and mode shape has been polluted with noise in the range of what can be expected from real measured data in order to create a realistic dataset. The solution using the combined equation, shown in the outermost right plot in Fig. 5.4, is proven to be quite robust even if the identified modal parameters contain noise.

## 5.4 Conclusions and Future Work

The result of the simulations presented in this paper clearly states that the proposed method can detect mass change, position and magnitude, by using modal properties. Furthermore the technique exhibits sturdiness towards noise. The inverse issue will become the main subject of interest in the ongoing research.

Due to practical reasons the mass detecting part of the technique, at this point, has been tested more extensively than the stiffness detecting part. The latter part, however, is expected to perform just as well as mass detecting part – at this point there is no immediate circumstance that suggests the opposite.

## References

1. Parloo E, Guillaume P, Van Overmeire M (2003) Damage assessment using mode shape sensitivities. *Mech Syst Signal Process* 17(3):499–518
2. Bernal D (2004) Modal scaling from known mass perturbations. *J Eng Mech* 130(9):1083–1088
3. Heylen RB, Lammens S, Sas P (1997) Modal analysis theory and testing. Faculty of Engineering, Department of Mechanical Engineering, Katholieke Universiteit Leuven, Leuven
4. SDTools – Vibration software and consulting. [www.sdtools.com](http://www.sdtools.com)
5. Parloo E, Vanlanduit S, Guillaume P, Verboven P (2004) Increased reliability of reference-based damage identification techniques by using output-only data. *J Sound Vib* 270:813–832

# Chapter 6

## Vibro-Acoustic Research on a Full-Scale Aircraft Structure

Christian Koehne, Delf Sachau, and Mirko Schaedlich

**Abstract** The new transport aircraft A400M is designed for worldwide military and humanitarian missions. It is a turbo-propeller aircraft able to fly high, fast and over long distances and to take off and land on short rough runways. Regarding interior noise and vibration harshness, the A400M meets the state-of-the-art requirements. A disused A400M pre-series fuselage is currently incorporated into a vibro-acoustic test environment. Airbus has made the 30 m long, 6 m wide and 13 ton heavy fuselage part available for research at Helmut-Schmidt-University of the Federal Armed Forces in Hamburg (HSU). The possibility to analyse the interdependency of acoustics and structure in a controlled laboratory environment on an entire fuselage of the most modern propeller-driven large transport aircraft is a worldwide novelty. The enhancement of passive and active noise reduction technologies for aircraft structures will be one of the potential research key aspects. Transporting the fuselage from the Airbus production site in Bremen to the HSU campus was a logistical master piece – whether by land, air or sea. This paper gives a brief overview of a few selected past and present aircraft interior acoustics research projects, describes the transport of the A400M fuselage to HSU, highlights the first steps in the design of the test rig and introduces a potential scenario for a vibro-acoustic test series taking advantage of this unique test environment.

**Keywords** A400M • Active noise control (ANC) • Tunable vibration absorber system (TVAS)

### 6.1 The A400M

The A400M is a newly developed military transport aircraft, which is aimed at replacing older aircrafts like C-130 Hercules or C-160 Transall within the fleet of the nations (Fig. 6.1). The A400M is powered by four turboprop engines each having an eight-bladed composite propeller capable of delivering more than 11,000 shp each. These engines provide a maximum operating altitude of 12,200 m (40,000 ft) and a maximum cruising speed of Mach 0.72. The range depends on the payload where the aircraft has a maximum range of 8,700 km (4,700 nm). With the maximum payload of 37,000 kg the A400M can cover a distance of 3,300 km (1,780 nm) [2, 5].

The specifically designed TP400 turboprop engines possess a number of advantages. In comparison with turbofans, the fuel consumption is significantly lower while at the same time the necessary capability is provided for operating the aircraft at all required conditions, for example aerial delivery, fighter and helicopter refuelling or maximum cruise. The down-between-engines (DBE) counter-rotation of the propellers leads to a more symmetric airflow so that the size of the vertical stabilizer is reduced [2, 5] but contributes also to a reduction of the noise excitation on the fuselage and thus inside the cabin.

One major challenge when operating turboprop engines are the higher noise levels and the annoyance of their characteristic signature dominated by multiple pure tones. The propeller blades of the A400M have been optimized not only for performance, durability and maintenance but also for acoustics.

---

C. Koehne • D. Sachau (✉)

Mechatronics, Helmut-Schmidt-University, University of the Federal Armed Forces Hamburg, Holstenhofweg 85, 22043, Hamburg, Germany  
e-mail: [christian.koehne@hsu-hh.de](mailto:christian.koehne@hsu-hh.de); [sachau@hsu-hh.de](mailto:sachau@hsu-hh.de)

M. Schaedlich

Airbus Operations GmbH, Kreetzslag 10, 21129 Hamburg, Germany  
e-mail: [mirko.schaedlich@airbus.com](mailto:mirko.schaedlich@airbus.com)

**Fig. 6.1** A400M [2]

The noise in the near field of the aircraft is dominated by high sound pressure levels impinging at the fuselage exterior at the blade passing frequencies (BPF). The aircraft structure together with its passive noise treatment concepts already attenuates significantly the noise levels at the aircraft interior. However, noise transmission through the fuselage can be further reduced by an active noise control system. Two different examples of such a noise reduction system – both have been investigated during the aircraft development phase – are described below: (1) Active Noise Control (ANC) and (2) Tunable Vibration Absorber System (TVAS) [5].

## 6.2 Research and Development of Active Noise and Vibration Suppression

### 6.2.1 Active Noise Control in the Load Master Area

The cargo handling system of the A400M is primarily controlled by a Load Master (LM) as a regular member of the aircraft crew (Fig. 6.2). He is positioned in the Load Master Work Area (LMWA) located at the forward end of the cargo hold. Amongst other duties, the LM's main tasks are cargo on and off loading, including air drop (cargo and paratroopers) and air-to-air refuelling. Additionally, the LM is also responsible for operating the aircraft environmental control systems (ECS) such as air conditioning, lighting etc. The LMWA has stringent requirements for safety and comfort, including noise. Given the fact that it is difficult to introduce additional passive treatments (door, curtain, etc.) due to design restrictions, the applicability and potential performance of an active noise-cancelling system has been investigated in a cooperation between Airbus and the HSU [5, 7].

The main components of such a system are: microphones, loudspeakers and a controller, which adjusts the loudspeaker output such as to minimise the noise at the LM seating positions depending on the signal received from the microphones. First studies were focused on error microphone positions in the head rest of the load master seat. But performance issues and the fact that placing the microphones at these positions would have been too expensive for implementation in a series solution, alternative positions inside the lining of the load master area for both, microphones and loudspeakers were determined. The research studies at HSU faced two main challenges: firstly, the noise had to be reduced within a certain volume of considerable size, in which different anthropological representations of LMs show head movement while on duty. The difficulty clearly was that no microphone installation was permitted within this control volume. The second issue of rather long distances between the control volume and both, the error microphones and loudspeakers, including effects from biased transfer paths between the two, required the development of a robust control algorithm. Despite the challenges and complexity of the problem, the HSU developed ANC system exceeded the required performance while at the same time showing an excellent stability of the control mechanism [7].

### 6.2.2 Tunable Vibration Absorber System

In contrast to the ANC-System, which uses loudspeakers as actuators, the Tunable Vibration Absorber System (TVAS) controls the vibration of the fuselage structure in order to reduce the sound pressure level inside the aircraft. The principle of noise transmission from the propeller blades into the aircraft interior is that the sound pressure at the outside of the fuselage induces vibrations in the aircraft structure. The noise inside the aircraft is caused by these vibrations. Within the A400M

**Fig. 6.2** Load master area mock up



noise control treatment development activities two different types of TVAS were considered: (a) passive mass damper with adjustable natural frequencies having the advantage of a low impact profile with respect to integration cost on aircraft level; (b) TVAS acts as an electrodynamic shaker. The moving mass inside the TVA is used to create a force at the mounting location of the TVA counteracting the vibrations induced by the external sound pressure field. There are a number of significant advantages of such an active system if compared to the purely passive type. Since the mechanical resonant frequency can be constantly tuned, it is possible to exactly control at the excitation frequency despite the fact that resonance frequency of the combined system (TVAS + aircraft structure) strongly depend on the mounting location of the TVA (series law for dynamic stiffness). Furthermore, within a certain frequency band, several excitation frequencies can be controlled with a single mass-spring system. The price to pay for such flexibility is the significant cost for integration and the system's energy consumption rate [5].

### 6.3 State of the Art of Vibro-Acoustic Test Environments

The following chapter briefly describes a number of test rigs and associated experiments used for acoustics and vibro-acoustics research activities. The list is not intended to be exhaustive.

#### 6.3.1 Aircraft Panel Structure (*Helmut-Schmidt-University*)

A 1.55 m wide and 2.75 m high aircraft structure panel is used for ANC development at the Helmut-Schmidt-University in Hamburg. It is integrated in a wall between two laboratory rooms. It only consists of the main aircraft structure components: skin fields, stringer and frames. The volume of the room at the inner side of the panel is somewhat similar to the cargo compartment of the A400M so there are some aspects which could be compared (Figs. 6.3 and 6.4). The excitation of the structure is performed using a shaker [6].

#### 6.3.2 Wooden Mock Up for ANC Development (*Helmut-Schmidt-University*)

In support of research activities for future aircraft concepts, a wooden mock up has been built at Helmut-Schmidt-University to investigate noise control treatments at several frequency ranges (Figs. 6.5 and 6.6). The mock up was primarily designed

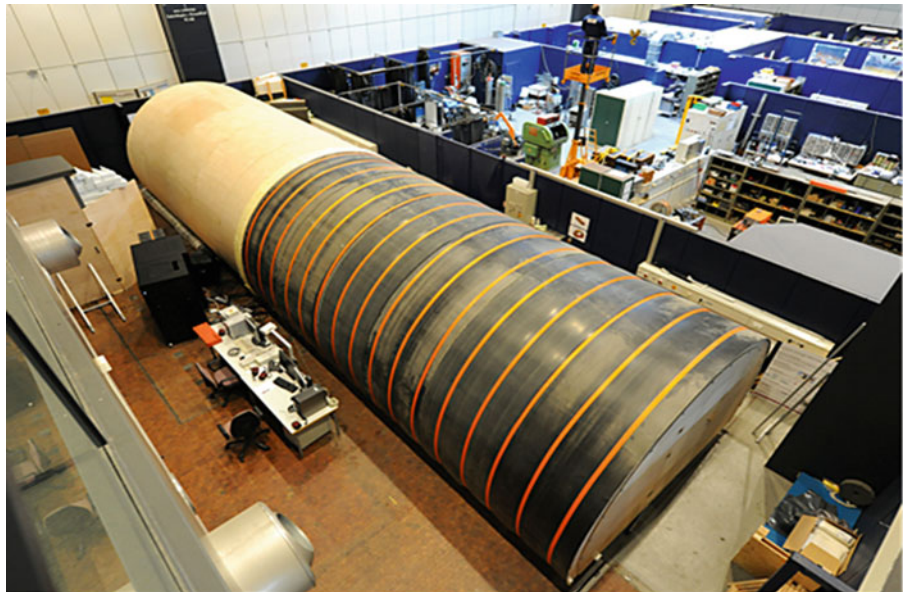


**Fig. 6.3** Panel from the inside [6]



**Fig. 6.4** Panel from the outside [6]



**Fig. 6.5** Wooden mock up**Fig. 6.6** Primary source

for tests with ANC-systems. It consists of a cylindrical structure with the main elements skin, stringer and frames, which are all made of plywood. The structure diameter is comparable to the current short-range aircraft fuselage sections. Only the passenger cabin is modelled. The sound excitation source consists of a subwoofer array with 16 speakers. The ANC system consists of 90 loudspeaker and 60 microphones. Inside the mock up a microphone array is mounted on an automatically moving frame for monitoring the sound field.

### **6.3.3 Beechcraft Starship Fuselage (BSF) and Aluminium Testbed Cylinder (ATC) at NASA Langley Research Center**

There are two rigs for vibro-acoustic tests at NASA Langley Research Center. The main task was to validate numerical models. The first rig is a self-made cylindrical aluminium fuselage with the main structure elements skin, stringer and frames. It has a diameter of 1.20 m and a length of 3.65 m. The fuselage is equipped with a passenger floor and end caps, which allow simulating flight conditions by pressurisation. The second rig is an original aircraft structure from the Beechcraft Starship

**Fig. 6.7** Beechcraft starship fuselage (BSF) [8]



**Fig. 6.8** Aluminium testbed cylinder (ATC) [8]



**Fig. 6.9** Unducted fan engine (UDF) [13]



(Figs. 6.7 and 6.8). It consists of the main fuselage structure which is completely made of composite materials. The structure is 12.20 m long and in the cabin section it has a diameter of 1.80 m. The Beechcraft Starship was the first all-composite plane certified by the FAA [8].

#### **6.3.4 UHB (Ultra High Bypass) Demonstrator MD-80**

The McDonnell Douglas MD-80 is a passenger aircraft with turbofan engines at the rear of the fuselage [9]. The aircraft left-hand side engine was replaced by a single unducted fan (UDF) prototype engine from General Electric with two disks of counter-rotating propeller blades (Figs. 6.9 and 6.10). By testing a  $8 \times 8$  and a  $10 \times 8$  configuration (forward  $\times$  aft rotor) one of the main objective of the study was to analyze the sound field inside the aircraft cabin to subsequently develop efficient noise control treatments in order to reach a desired sound pressure level of 82 dB(A). An important part of the study was the analysis of the noise transmission paths into the cabin.

**Fig. 6.10** MD-80  
UHB-demonstrator [3]



**Fig. 6.11** Dornier 228 [11]



### 6.3.5 Advanced Study for Active Noise Control in Aircraft (ASANCA)

The ASANCA-project was conducted to test active noise reduction systems in propeller-driven aircrafts. There was also some research on helicopters but the main focus was on fixed wing aircrafts. Four different in-service aircrafts were available for flight tests: Dornier 228, Saab 340, ATR 42 and Fokker 100 (Figs. 6.11, 6.12, 6.13, and 6.14). Some characteristic differences did exist between these aircrafts which had been selected to test the ANC-system in varying acoustic environments. The Dornier 228 is a propeller-driven aircraft in a high-wing configuration and an unpressurized fuselage with a rectangular cross section. The other aircrafts have a pressurized fuselage with a cylindrical cross section. The ATR 42 also has a high-wing configuration but the other two come with a standard low wing design. The Fokker 100 is the only model with aft mounted turbofan engines. All aircrafts exhibit noise at low frequency but rather high sound pressure and vibration levels [4].

## 6.4 A400M Test Structure at Helmut-Schmidt-University

The A400M fuselage made available at HSU by Airbus consists of the main aluminium structure covering almost the entire cargo hold but without the nose fuselage section (Fig. 6.15). It is 30 m long with a diameter of almost 6 m and a total weight of more than thirteen metric tonnes. The extraordinary dimensions of the fuselage required special efforts to transport it from the Airbus site in Bremen to the campus of the Helmut-Schmidt-University in Hamburg. For the first part from Bremen to Hamburg-Finkenwerder Airbus Transport provided a Beluga flight. Once in Hamburg-Finkenwerder, the fuselage was loaded into a transport ship thus taking advantage of the harbour at the Airbus site. However, the last leg to the HSU Campus was

**Fig. 6.12** Saab 340 [10]**Fig. 6.13** ATR 42 [1]**Fig. 6.14** Fokker 100 [12]

done on the road. This turned out to be the most difficult part of the venture as the first challenge was to find a suitable place to transfer the fuselage from the ship to a special road trailer. Second, how to find a suitable route avoiding to cross under bridges and which provides enough space for turning manoeuvres of the heavily oversized trailer. A joined effort involving all partners made this possible and the transport crossing large parts of the city was performed at night in order to minimise the impact on regular traffic.



**Fig. 6.15** A400M pre-series fuselage

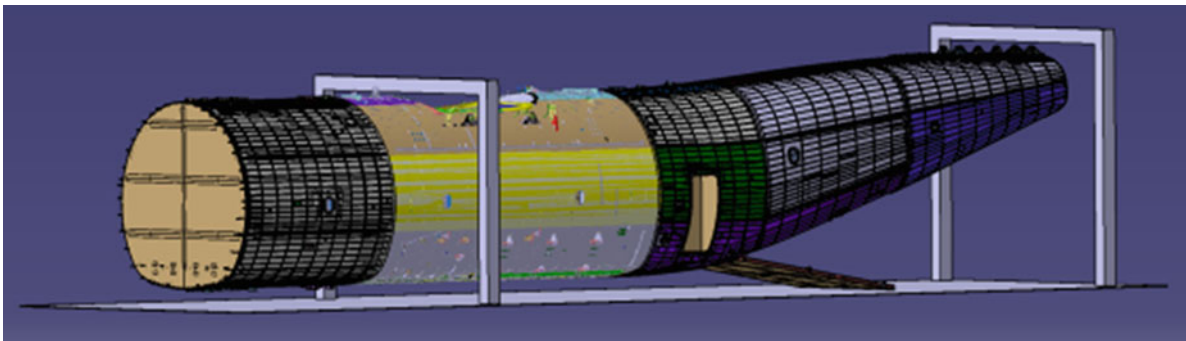


**Fig. 6.16** Design proposal for the VAiTE /FS test rig

Before starting any research activities, the next step is to integrate the fuselage into a full-scale vibro-acoustic integrated test environment VAiTE /FS (*Vibro-Acoustic integrated Test Environment/Full-Scale*) (Fig. 6.16). A portal framework structure will support the fuselage in an almost natural in-flight condition on the wing box attachment points to minimise a structure vibration response bias, and hence an impact on the acoustic behaviour, due to artificially changed boundary conditions on ground. The A400M is an aircraft with a high-wing configuration where the empennage is designed as a T-tail. Naturally, the fuselage is hanging below the wing during flight. Because of the empennage configuration there are also vertical loads at the tail of the fuselage. Two gantries for supporting the structure on ground, one at the position of the wing and the other at the tail will be used. The suspension shall be isostatic, so there is a need of six different braces in order to completely restrict the degrees of freedom. A built-in system will constantly monitor the load distribution at the attachment points, which becomes especially important when comparing test rig structure response measurements with results from numerical models. Assembly of the test environment will be done in two steps: (1) construction of the two gantries and a plane work space area below the fuselage; (2) deployment of a hangar to protect test object, equipment and workers from adverse weather conditions.

## 6.5 Prospective Future Research Activities

Main purpose of VAiTE /FS is to better understand the vibro-acoustic behaviour of a full-scale aircraft structure, especially in the context of discrete frequency excitation. This is the essential requirement for developing noise treatments with excellent performance and minimum impact on aircraft integration, maintenance and operation. A number of different scenarios are currently considered on how to achieve this ambitious goal in the most realistic and efficient manner possible. Some major

points are briefly described in what follows. The main task to accompany the first tests would be the adaption of a suitable numerical model based on a finite element method (FEM) approach. A structure vibration modal analysis of the fuselage would be used to update the FE model. Main research activities focus shall be put on investigating to what degree of accuracy structure and acoustic response as measured during in-flight conditions can be reproduced on ground. It is apparent, that this requires a precise reproduction of the two components: (1) fuselage structure together with equipment furnishing, and (2) the external sound pressure excitation field. A possible methodology to address the first point is to constantly equip the fuselage with aircraft systems major components and cargo hold furnishing (thermal/acoustic insulation, lining, etc.), while monitoring the impact on structural and acoustic behaviour. Point two requires a new way of reproducing the sound pressure excitation at the fuselage exterior on ground in the same manner as measured during flight. A combination of both approaches including correlation of the associated structural and acoustic responses to in-flight measurements obtained from the current fleet of A400M test aircrafts will be a key enabler to conduct “flight testing on ground” using VAiTE /FS as “calibrated” flight test aircraft. This gives the test environment a unique status compared to all previously listed test objects with respect to research flexibility, test rig size and maintenance costs.

A subsequent third step would then focus on the performance evaluation of active and passive noise control treatments to directly estimate their benefits at aircraft level. Due to its origin, VAiTE /FS has the potential to mainly accommodate treatments based on structure vibration response control whereas other mock-ups similar in their geometrical size and design to future aircrafts will form the basis for dedicated noise control treatments or specifically tailored structural solutions based on the modern design philosophy of the future aircraft.

## References

1. Aerospace-Technology (2012) [http://www.aerospace-technology.com/projects/atr\\_42/atr\\_426.html](http://www.aerospace-technology.com/projects/atr_42/atr_426.html), 26 Oct 2012
2. Airbus Military (2012) <http://a400m.com/Aircraft/A400M/A400MAbout.aspx>, 14 Sep 2012
3. AirTeamImages (2012) [http://www.airteamimages.com/mcdonnell-douglas-md-80\\_N980DC\\_mcdonnell-douglas\\_149669.html](http://www.airteamimages.com/mcdonnell-douglas-md-80_N980DC_mcdonnell-douglas_149669.html), 26 Oct 2012
4. Borchers IU et al (1992) Advanced study for active noise control in aircraft (ASANCA). In: DGLR/AIAA 14th aeronautics conference, Aachen, pp 129–133
5. Breitbach H, Sachau D, Böhme S (2006) Acoustic challenges of the A400M for active systems. Proc. of SPIE Vol. 6171, Smart Structures and Materials: Industrial and Commercial Applications of Smart Structures Technologies, San Diego, California, United States
6. Greßkowski J (2012) Aktive Reduktion der Schallabstrahlung von schwingenden Strukturen am Beispiel eines A380 Paneels. Dissertation, Helmut-Schmidt-Universität, Hamburg, p 41
7. Kochan K (2009) Robuste aktive Schallreduktion in Flugzeugen. Dissertation, Helmut-Schmidt-Universität, Hamburg, pp 2, 3, 56
8. Pappa RS, Pritchard JJ, Buehrle RD (1999) Vibro-acoustics modal testing at NASA Langley Research Center, pp 1, 2, 7, 8
9. Simpson MA et al (1989) UHB demonstrator: interior noise control – flight tests and analysis. NASA Contract Report 181897, Douglas Aircraft Company, McDonnell Douglas Corporation, Long Beach, CA, pp 1–6
10. Wikipedia (2012) [http://de.wikipedia.org/wiki/Saab\\_340](http://de.wikipedia.org/wiki/Saab_340), 26 Oct 2012
11. Wikipedia (2012) [http://en.wikipedia.org/wiki/Dornier\\_Do\\_228](http://en.wikipedia.org/wiki/Dornier_Do_228), 26 Oct 2012
12. Wikipedia (2012) [http://en.wikipedia.org/wiki/Fokker\\_100](http://en.wikipedia.org/wiki/Fokker_100), 26 Oct 2012
13. Wikipedia (2012) [http://en.wikipedia.org/wiki/General\\_Electric\\_GE36](http://en.wikipedia.org/wiki/General_Electric_GE36), 26 Oct 2012

# Chapter 7

## Control of Dynamic Mass as Boundary Condition for Testing Substructures

Manuel Baschke, Michael Krepl, and Delf Sachau

**Abstract** The vibro-acoustic behavior of large lightweight structures such as aircraft fuselage has to be tested, especially to improve active and passive means. Acoustic transmission laboratories with reverberant and anechoic rooms supply reliable test conditions for aircraft panels of a size up to several square meters. Shock mounts support these panels to realize free or pinned boundary conditions with minor damping, which is sufficient for high frequencies. For low frequencies the vibration of the whole fuselage has to be considered. Therefore the support of the panel under test should provide the same dynamic mass as the fuselage to which the panel will be connected in the aircraft. This paper describes two examples how to realize such boundary conditions. Therefore the dynamical behavior of adjacent flexible structural elements is simulated. Force and acceleration sensor signals are combined with real time control on a rapid control prototyping system. Electrodynamic shakers are used as actuators. In the first experiment the performance is demonstrated by the simulation of a variedly excited damped two mass-spring system with an adaptive LMS algorithm in time domain; in the second experiment by the test of a flexible beam under harmonic load regarding the second eigenmode with internal model in frequency domain.

**Keywords** Active control • Adaptive control • Internal model control • Dynamic mass as boundary condition • Substructures

### 7.1 Introduction of Damped Two Mass-Spring System

The realization of adaptive boundary conditions should be simulated and tested on elementary physical experiments before it will be tested on more complex experiments like an aircraft panel. The reason is, that the equations are analytical solvable and so the measured results can be compared with the analytical correct solutions. In our case we start with a damped two mass-spring system, which is harmonically excited at the upper mass  $m_1$  with the primary force  $F_p$ . Figure 7.1 left shows the schematic illustration.

This system is cut in the middle of the lower mass  $m_2$ , Fig. 7.1 middle. At this point the boundary condition should be the dynamic mass  $M = F_s/a_2$ , which is defined as the ratio between force and acceleration at one point. To calculate the dynamic mass at the point of interest it is necessary, to solve the ordinary differential equation of second order of the cut system (Fig. 7.1, middle bottom). On the condition that the movement of the system takes place around the static idle position it results in:

$$F_s = (m_2 - m_c)a_2 + b_3v_2 + k_3x_2. \quad (7.1)$$

The secondary force  $F_s$ , which will be controlled later, depends on the position ( $x_2$ ), the velocity ( $v_2 = \dot{x}_2$ ) and the acceleration ( $a_2 = \ddot{x}_2$ ) of the mass  $m_2 - m_c$ . This results in the dynamic mass:

$$M(j\omega) = \frac{F_s(j\omega)}{A_2(j\omega)} = \frac{((j\omega)^2(m_2 - m_c) + j\omega b_3 + k_3)X_2}{(j\omega)^2 X_2} = (m_2 - m_c) + b_3/j\omega + k_3/(j\omega)^2. \quad (7.2)$$

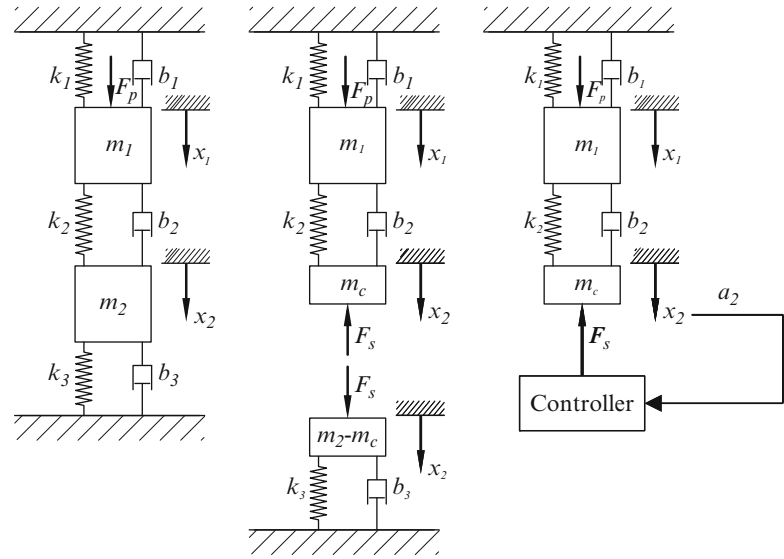
---

M. Baschke • M. Krepl • D. Sachau (✉)

Mechatronics, Helmut-Schmidt-University, University of the Federal Armed Forces Hamburg, Holstenhofweg 85, 22043 Hamburg, Germany  
e-mail: [baschkem@hsu-hh.de](mailto:baschkem@hsu-hh.de); [michael.krepl@hsu-hh.de](mailto:michael.krepl@hsu-hh.de); [sachau@hsu-hh.de](mailto:sachau@hsu-hh.de)



**Fig. 7.1** Damped two mass-spring system uncut (left), cut (middle) and partial replacement (right)



The aim of this work is to realize the same accelerations  $a_2$  in both systems. Alternatively to the used control of the dynamic mass also a control of the mechanical impedance  $Z = F_s/v_2$  would have been possible. The reason for the choice to control the dynamic mass is that later in the experiments acceleration sensors are used, which allows a direct use of these signals.

For the control of the mechanical impedance the equation would be:

$$Z(j\omega) = \frac{F_s(j\omega)}{v_2(j\omega)} = \frac{((j\omega)^2(m_2 - m_c) + j\omega b_3 + k_3)X_2}{j\omega X_2} = j\omega(m_2 - m_c) + b_3 + k_3/j\omega. \quad (7.3)$$

This equation shows the optimal controller, a PID-controller with the shown coefficients.

## 7.2 Simulation of Damped Two Mass-Spring System

The models of the different systems are implemented with a state space block in MATLAB Simulink. The whole simulation in MATLAB Simulink takes place in time domain. In the passage above the optimal controller was already mentioned. It was implemented firstly in the model to assure, that the models were built correctly. After validation of the models the different parameters of the systems like the masses, the stiffness of the springs and the damping values have been varied to align them to the existing equipment for the possible implementation in a real experiment.

The used values for the different variables are:

- Spring constants:  $k_1 = k_2 = k_3 = 200$  N/m
- Damping constants:  $b_1 = b_2 = b_3 = 2$  Nm/s
- Masses:  $m_1 = m_2 = 0.5$  kg;  $m_c = 0.25$  kg
- Force amplitude:  $F_p = 1$  N

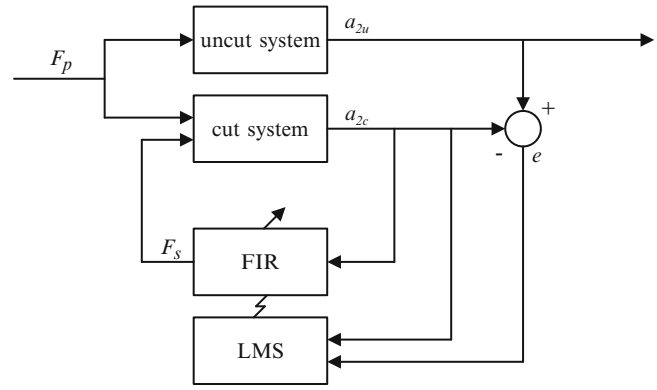
The mass of the cut system  $m_c$  is chosen to the half of the other masses, to avoid a too stiff system, which might cause numerical problems in the simulation. This point will not be highlighted in detail during this work. With these chosen values the first two eigenfrequencies are round about 3.2 and 5.5 Hz. During the simulation the frequencies for the primary force  $F_p$  are in the same order of magnitude as these two frequencies.

Instead of using the above mentioned PID-controller for realizing the boundary condition an adaptive LMS algorithm is used. It is used, because with this algorithm the boundary conditions can be realized automatically. It is not necessary to have an analytic model of the cut system ( $m_c, b_3, k_3$ ). Instead of this it is identified by the comparison with the uncut system.

This algorithm has also been implemented and tested in MATLAB Simulink. Figure 7.2 shows the block diagram for the simulation.

The adaptive algorithm minimizes the error signal, which consists of the difference between the accelerations  $a_{2u}$  and  $a_{2c}$  of both systems. For this adaption the algorithm requires a reference signal, which is the acceleration of the cut system.

**Fig. 7.2** Block diagram of damped two mass-spring system



To minimize this error the algorithm adapts the filter coefficients. For details about the adaptive finite impulse response filter see [1]. With this control concept the error signal can be reduced to a numerical zero for a harmonic load between 0 and 10 Hz. For a white band noise between 0 and 10 Hz the reached reduction is not as high as for a harmonic load, but the amplitudes of the error signal can be reduced at least to 5 %.

### 7.3 Introduction Flexible Beam

The aim of the second experiment, which is presented in this work, is to control the dynamic mass of a flexible beam in its first two eigenmodes. This beam is excited at one quarter of its length. Comparable with the experiment above, we separate this system in the middle of its length and examine the left half and want it to behave like the uncut beam.

Both beams are of the same material and have the same cross section. Furthermore they have an identical bearing on the left side. In the presented case following parameters are used:

- Length:  $l = 1.50$  m
- Height:  $h = 0.005$  m
- Width:  $b = 0.02$  m
- Material: Steel (S235JR)
- Modulus of elasticity:  $E = 206$  kN/mm<sup>2</sup>

These parameters lead to the first two natural frequencies at round about 8 and 23 Hz. For controlling the cut beam in the first two eigenmodes of the uncut beam, it is necessary to know the first two eigenmodes. They are shown in Fig. 7.4.

In the first eigenmode the beam has a maximum displacement  $w$  at the half of its length. In the second eigenmode the displacement at the middle of the uncut beam is zero. For the control of the dynamic mass of a flexible beam it is also necessary to know the torque  $T$  and the shear force  $S$ . According to [2, p. 174] they are:

$$T(x, t) = -EIw''(x, t); S(x, t) = -EIw'''(x, t). \quad (7.4)$$

These equations are valid on the assumption of small displacements and constant modulus of elasticity  $E$  and moment of inertia  $I$ . The shear force depends on three values, on the modulus of elasticity, the third partial derivative of the displacement  $w$  and the moment of inertia  $I = bh^3/12$ , which can be calculated with the above mentioned parameters. Equation (7.4) also shows that the torque in the first eigenmode is unequal zero, but in the second eigenmode it is zero. This is the reason, why the following control concept is only tested for the second eigenmode. Just one actuator is used to control the boundary condition. For the control in the first eigenmode two actuators would be necessary to realize the torque at the end of the cut beam.

With these basic equations it is possible to calculate the dynamic mass of the beam in its second eigenmode. The dynamic mass  $M$  is defined as the ratio between the force and acceleration at the end of the cut beam:

$$M(x = 0.5l, t) = \frac{S(x = 0.5l, t)}{\ddot{w}(x = 0.5l, t)} = \frac{S(x = 0.5l, t)}{a(x = 0.5l, t)}. \quad (7.5)$$

For the second eigenmode the displacement in the middle of the beam is zero at all times (Fig. 7.4), which also results in an acceleration of zero at this point. With Eq. (7.5) the theoretical dynamic mass of the second natural frequency becomes infinite, because the shear force is not zero.

### 7.4 Experiment with Flexible Beam

To realize the above mentioned dynamic mass control a test stand with two beams, one uncut beam shown in Fig. 7.5 (foreground) and one cut beam (Fig. 7.5 background), is built [3].

The primary forces in both beams  $F_p$  according to Fig. 7.3 and the secondary force  $F_s$ , which is controlling the shear force at the end of the cut beam, are realized with electrodynamic shakers (Type 4824 from Brüel&Kjær). The movements of both beams are measured with piezoelectric accelerometers (Type 4507 from Brüel&Kjær), they are equidistant mounted on both beams. At the positions of the forces the dynamic loads are measured with piezoelectric force sensors (Type 8200 from Brüel&Kjær).

The dynamic mass control is realized on a rapid control prototyping system (Type: dSPACE rti 1103) and the controller is implemented in MATLAB Simulink in frequency domain. The signals are filtered and amplified with conventional amplifiers and anti-aliasing filters. Before the implementation of the controller took place, the first two natural frequencies which were determined before, have been validated in the measurements [3, p. 26].

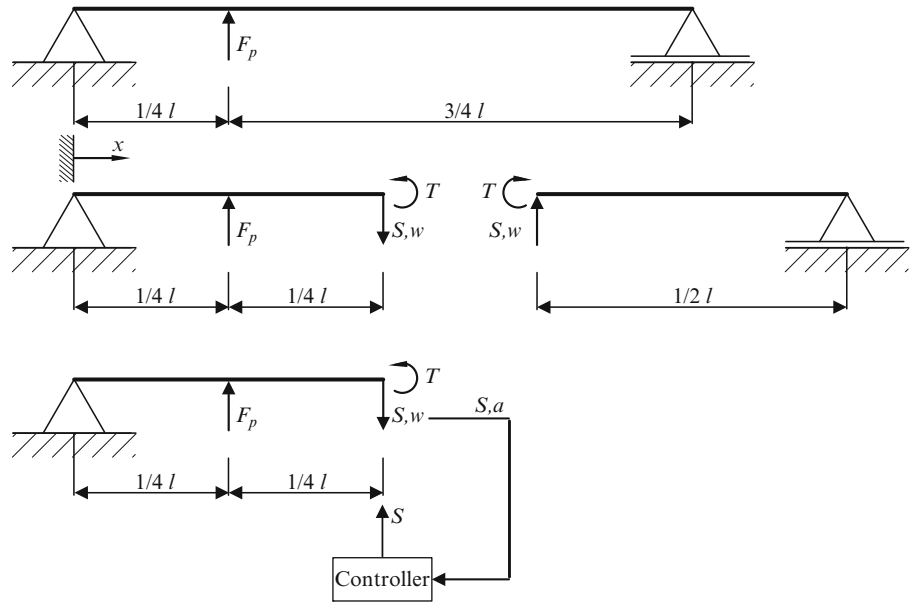


**Fig. 7.3** Flexible beam with primary excitation uncut (top), cut (middle) and partial replacement (bottom)

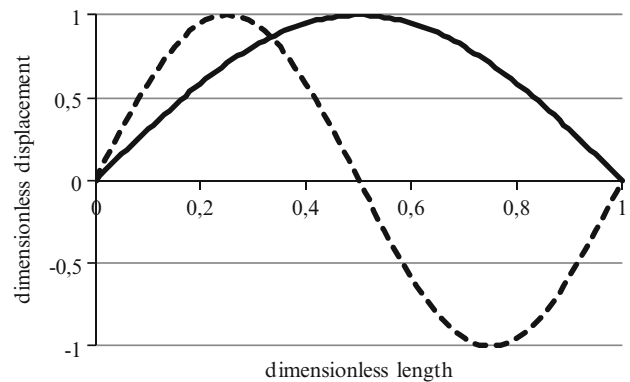


**Fig. 7.4** First two eigenmodes of a flexible beam

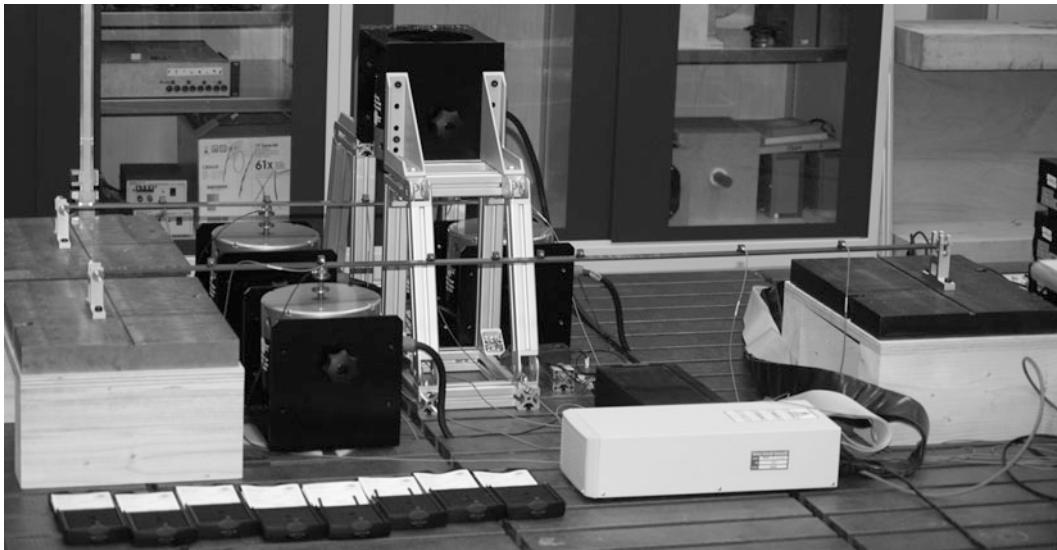


**Fig. 7.5** Test stand flexible beam uncut (*foreground*) and cut (*background*) [3, p. 25]

**Fig. 7.6** Connection shaker to beam

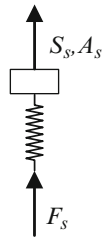
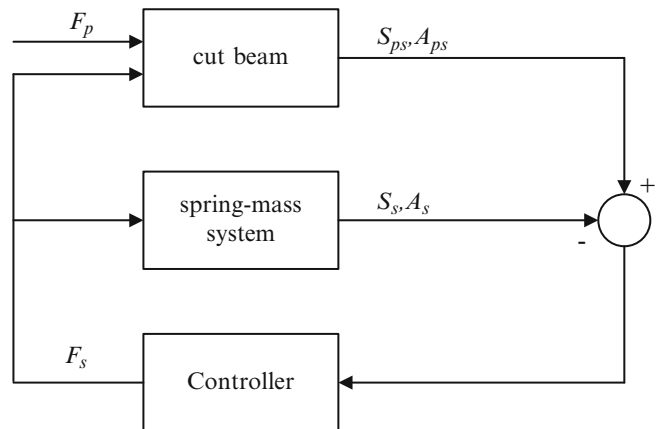


**Fig. 7.7** IMC for cut beam



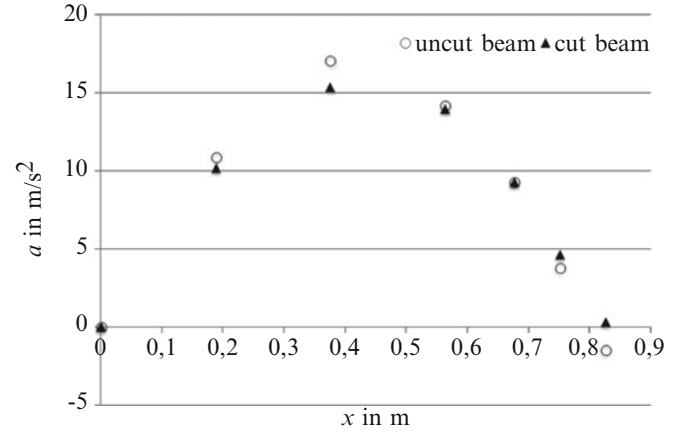
The shaker does not directly excite the beam. It is connected with a spring-mass system to the beam, to increase the amplitudes of the displacement of the cut beam, see Fig. 7.6. This is the reason, why an IMC is used to realize the control concept. Figure 7.7 shows the block diagram of the control concept. Details about IMC can be found in [4].

The transfer characteristics ( $G_F$  and  $G_A$ ) of the spring-mass system are determined by exciting the system with a known signal  $F_s$  and measure the resulting shear force  $S_s$  and acceleration  $A_s$  at the end of the cut beam.

The desired dynamic mass for our case has already been calculated. The following control concept can be found in [5]. The purpose of the controller is to control the dynamic mass, according to Eq. (7.5).

In contrast to the above calculated ideal dynamic mass, it is calculated here by the ratio between the measured shear force  $S_{ps}(j\omega)$  and the measured acceleration  $A_{ps}(j\omega)$  at this point.

**Fig. 7.8** Measured accelerations for second eigenmode [3]



The system is excited with the primary force  $F_p$ . The measured values of force and acceleration consist of the disturbances (Index D), which are caused by the primary force, and the compensation values (product of transfer function ( $G_F$ ,  $G_A$ ) and regulating variable  $F_s$ ):

$$\begin{aligned} S_{ps}(j\omega) &= S_D(j\omega) + G_F(j\omega) \cdot F_s(j\omega) \\ A_{ps}(j\omega) &= A_D(j\omega) + G_A(j\omega) \cdot F_s(j\omega). \end{aligned} \quad (7.6)$$

The controller calculates the regulating variable  $F_s$  out of the differences of the force and acceleration values (cut beam and spring-mass system). On the assumption of correctly established transfer functions the following optimal regulating variable results to:

$$F_{s,opt}(j\omega) = \frac{\bar{M}(j\omega) \cdot A_D(j\omega) - S_D(j\omega)}{G_F(j\omega) - \bar{M}(j\omega) \cdot G_A(j\omega)}. \quad (7.7)$$

In this equation  $\bar{M}$  is the above calculated desired dynamic mass.

With this control concept it is possible to regulate the behavior of the cut beam like the uncut beam. Figure 7.8 presents the results of the above exemplified control concept. For these results the dynamic mass  $\bar{M}$  was set to  $10^6$  kg. In the second eigenmode the dynamic mass forces the desired knot point at the end of the cut beam. So it behaves like an infinite stiff bearing. In contrast to the above mentioned ideal cut in the middle of the beam, the cut is not exactly at the half of the original length. It is cut at 82.5 cm instead of 75 cm, which would be the middle. This difference is necessary to realize a torque at the position  $x = 75$  cm, which is needed to control the dynamic mass not only for the second eigenmode. This is also the reason, why the accelerations of the cut beam can be measured at 82.5 cm, Fig. 7.8.

In addition to the already mentioned disagreements between the theory and the real experiment, the occurred discrepancies are caused by production tolerances especially in the bearings and measuring tolerances.

## 7.5 Conclusion

With both above illustrated experiments it is shown, that it is possible in principle to sever parts of a whole model and to make the severed part to behave like it is connected to the rest of the model. One of the next steps will be to implement an adaptive algorithm like it was shown in the damped two mass-spring system in the beam experiment to reduce discrepancies between the both beams and to extend the control of the beam experiment to other primary loads than the second natural frequency.

## References

1. Moschytz G, Hofbauer M (2000) Adaptive filter – Eine Einführung in die Theorie, pp 85 f. ISBN 3-540-67651-1
2. Brommundt E, Sachs G, Sachau D (2007) Technische Mechanik – Eine Einführung, 4th issue. ISBN 3-486-58111-2
3. Krepl M (2011) Aktive Regelung mechanischer Impedanzen. Bachelor thesis, Helmut-Schmidt-University, University of the Federal Armed Forces Hamburg, Germany
4. Lunze J (2006) Regelungstechnik 1 – Systemtheoretische Grundlagen – Analyse und Entwurf einschleifiger Regelungen, 5th issue, pp 497 f. ISBN 3-540-28326-9
5. Kletschkowski T, Sachau D (2012) Regelung mechanischer Impedanzen mit Hilfe interner Modelle. In: Conference paper DAGA, pp 1–2

# Chapter 8

## Multi-body-Simulation of a Self Adaptive Torsional Vibration Absorber

Delf Sachau and Jonas Hanselka

**Abstract** Automotive manufacturers try to decrease emissions and fuel consumption by downsizing the engine. This means the number of pistons and the swept volume are reduced. Unfortunately, this increases the vibrations which are caused by the oscillating movement of the pistons. The vibrations are transferred through the power train and the car body to the passenger seats. To reduce these vibrations absorbers are installed into the power train. In this paper a vibration absorber is simulated by general purpose multi-body simulation software. Swing arms which are clamped to a disc in radial direction are modelled as flexible bodies. Each swing arm has got a mass at its end which is in form of a rigid body. Because of the centrifugal force which increases the geometric stiffness of the swing arms, the vibration absorber's eigenfrequency continuously adapts to the current engine rotational speed. Thus the adaptive vibration absorber is able to reduce vibrations from idle up to maximum speed. The paper describes the multi-body system with flexible bodies, the linearization of the nonlinear equations of motion and the results of a parameter study.

**Keywords** Vibration reduction • Adaptive vibration absorber • Flexible body • Multibody simulation

### 8.1 Introduction

Automotive manufacturers try to decrease emissions and fuel consumption by downsizing the engine. This means the number of pistons and the swept volume are reduced. Unfortunately, this increases the vibrations which are caused by the oscillating movement of the pistons. The vibrations are transferred through the power train and the car body to the passenger seats. To reduce these vibrations absorbers are installed into the power train.

### 8.2 Design of Vibration Absorber

#### 8.2.1 Multibody Model

The adaptive absorber is modelled as a flexible multibody system using the simulation tool SIMPACK and the pre-processor BEAM. Figure 8.1 shows the tree structure of the flexible MBS which is given by the disc connected to the inertial frame, herewith only rotation is possible. Three swing arms are clamped to the disc in radial direction. They are modelled as flexible bodies. Each swing arm has got a point mass at its end which is a rigid body. The disc is excited by a torque.

Starting point for the recursive computational scheme of the multibody program SIMPACK are the equations of motion for the bodies. To describe the motion of a flexible body, the coordinate systems shown in Fig. 8.2 are used. They are the inertial frame  $\{O^I, \underline{e}^I\}$  and the body reference frame  $\{O^1, \underline{e}^1\}$  located at one end of the body in the reference configuration.

---

D. Sachau (✉) • J. Hanselka  
Helmut-Schmidt-University, University of the Federal Armed Forces Hamburg, Holstenhofweg 85, 22043 Hamburg, Germany  
e-mail: [sachau@hsu-hh.de](mailto:sachau@hsu-hh.de)

**Fig. 8.1** Dynamic vibration absorber, principal sketch (left), SIMPACK model (right)

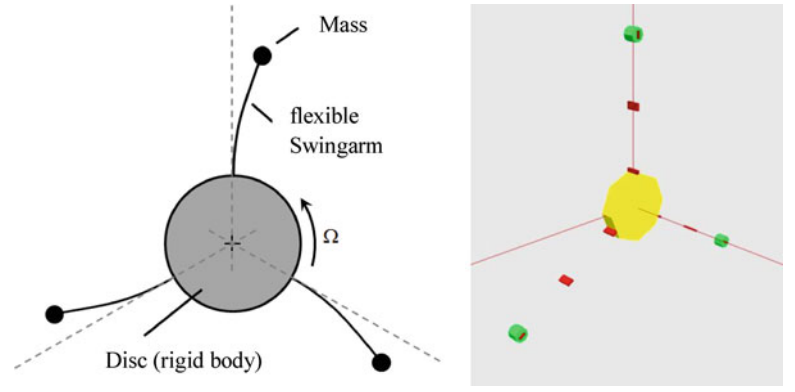
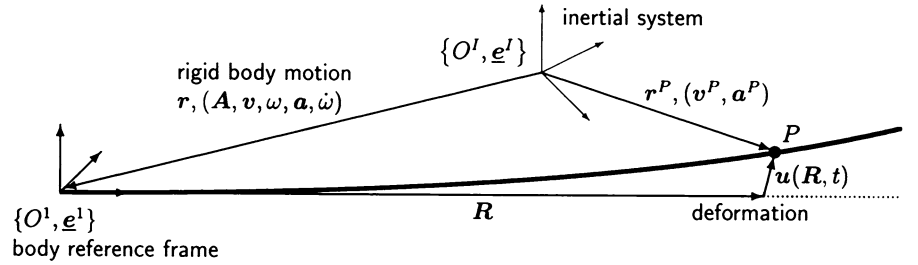


**Fig. 8.2** Kinematics of a flexible body



In general, all vectors will be resolved in the reference frame  $\{O^1, \underline{e}^1\}$ , e.g.  $\underline{r} = r^T \underline{e}^1$  [2]. The motion of a representative material point  $P$  inertial space is described as:

$$\mathbf{r}^P(\mathbf{R}, t) = \mathbf{r}(t) + \mathbf{R} + \mathbf{u}(\mathbf{R}, t). \quad (8.1)$$

In this representation the body motion is given in terms of the reference or rigid body motion as described by  $\mathbf{r}(t)$  and  $\mathbf{A}(t)$  and in terms of small displacements  $\mathbf{u}$ , i.e.

$$\mathbf{u} = \bar{\mathbf{u}}(\mathbf{R}^u, y(\mathbf{R}^y, t)), \quad \mathbf{R} = \begin{bmatrix} \mathbf{R}^u \\ \mathbf{R}^y \end{bmatrix}. \quad (8.2)$$

The displacements are expressed in terms of deformation variables  $\mathbf{y}$  [1], e.g. for beams the deflection of the neutral axis. The representation of the body motion is suitable for incorporating the assumption of small deformations [4]. The coordinates of the absolute velocity and acceleration of mass element  $dm$  at point  $P$  w. r. t. reference frame are derived from (8.1)

$$\mathbf{v}^P = \mathbf{v} + \tilde{\omega}(\mathbf{R} + \mathbf{u}) + \dot{\mathbf{u}}, \quad \mathbf{v} = \dot{\mathbf{r}} + \tilde{\omega} \mathbf{r} \quad (8.3)$$

$$\mathbf{a}^P = \mathbf{a} + \tilde{\omega} \tilde{\omega}(\mathbf{R} + \mathbf{u}) + \dot{\tilde{\omega}}(\mathbf{R} + \mathbf{u}) + 2\tilde{\omega} \dot{\mathbf{u}} + \ddot{\mathbf{u}} \quad (8.4)$$

where  $\mathbf{v}$  and  $\mathbf{a}$  are the reference point velocity and acceleration,  $\omega$  and  $\dot{\omega}$  are the angular velocity and acceleration of the reference frame respectively. The tilde operator represents the cross product of vectors. Differentiation of displacements  $\mathbf{u}$  w. r. t. time yields

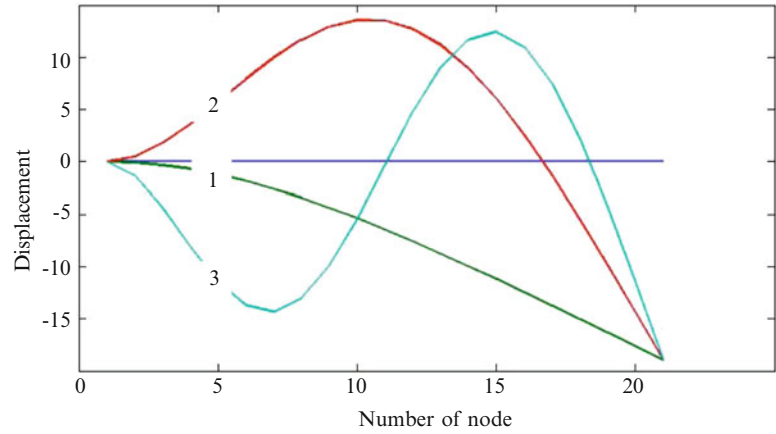
$$\dot{\mathbf{u}} = \mathbf{J}(\mathbf{y}) \dot{\mathbf{y}}, \quad \mathbf{J} = [J_{ai}] = \left[ \frac{\partial u_a}{\partial y_i} \right] \quad (8.5)$$

with the Jacobian  $\mathbf{J}$  containing the derivatives of  $\mathbf{u}$  w. r. t.  $\mathbf{y}$ . Deformations are measured by the symmetric Green-Lagrange strain tensor [8]. A common matrix form is

$$\boldsymbol{\varepsilon} = [\varepsilon_{11}, \varepsilon_{22}, \varepsilon_{33}, 2\varepsilon_{12}, 2\varepsilon_{23}, 2\varepsilon_{31}]^T = \left[ \mathbf{L}^0 + \frac{1}{2} \mathbf{L}^1(\mathbf{u}) \right] \mathbf{u} \quad (8.6)$$

where operator matrix  $\mathbf{L}^0$ , which is well known from the linear theory of elasticity, contains partial derivatives w. r. t. the material coordinates  $\partial_a = \partial(\cdot)/\partial \mathbf{R}_a$ . Products of  $\partial_a$  and  $\mathbf{u}_{a,\beta}$ , so-called bilinear terms, are collected in  $\mathbf{L}^1$ . They result from the



**Fig. 8.3** Beam eigenmodes

nonlinear terms of the strain-displacement relation. Stresses are represented here by the symmetric second Piola-Kirchhoff stress tensor. For a linear material law, the stresses are related to the strains by

$$\boldsymbol{\sigma} = [\sigma_{11}, \sigma_{22}, \sigma_{33}, \sigma_{12}, \sigma_{23}, \sigma_{31}]^T = \mathbf{H}\boldsymbol{\varepsilon} \quad (8.7)$$

with the  $6 \times 6$  Hookean matrix  $\mathbf{H}$ . Its elements are given in terms of two independent elasticity constants Young's modulus  $E$  and Poisson's ratio  $\nu$  of the isotropic material. A Ritz-approximation of the deformation variables  $\mathbf{y}$

$$\mathbf{y}(\mathbf{R}^y, t) = \Psi(\mathbf{R}^y)\mathbf{q}(t) \quad (8.8)$$

is used with the  $n_q$  unknown nodal coordinates  $\mathbf{q}(t)$  and interpolation functions  $\Psi$ . Introducing (8.8) into Hamilton's principle and using the fundamental lemma of variational calculus yields the equations of motion

$$\mathbf{M}(\mathbf{q}) \begin{bmatrix} \mathbf{a} \\ \dot{\boldsymbol{\omega}} \\ \ddot{\mathbf{q}} \end{bmatrix} + \mathbf{k}(\boldsymbol{\omega}, \mathbf{q}, \dot{\mathbf{q}}) + \begin{bmatrix} 0 \\ 0 \\ \mathbf{K}(\mathbf{q})\mathbf{q} \end{bmatrix} = \mathbf{h}(\mathbf{r}, \mathbf{A}, \mathbf{q}, \dots) \quad (8.9)$$

where matrix  $\mathbf{M}$  contains the inertia terms,  $\mathbf{k}$  the gyroscopic terms,  $\mathbf{K}$  the stiffness terms, and  $\mathbf{h}$  the applied forces. The equations of motion (8.9) are linearized w.r.t. the deformation variables [7]. In the MBS simulation the motion of selected is represented by linear terms in the deformation coordinates. Here, coordinate frames, so-called markers, are attached to the flexible body. At markers joints can be attached or forces can act. The coefficients for the equation of motion are calculated using the preprocessor FEMBS. The first three eigenmodes for the clamped-free beam are used to describe the displacement field, see Fig. 8.3. Together with one degree of freedom (DOF) in the revolute joints, the MBS has 10 DOF.

The centrifugal force on the dynamic vibration absorber is proportional to the square of the rotational speed. This force leads to a geometric stiffening of the beam. Therefore the eigenfrequencies of the dynamic absorber depend on the rotational speed. This effect is used to adapt the vibration absorber to the second order of the engine torque. The nonlinear equations of motion are linearized about the nominal rotational speed [6]. It is important that the SIMPACK model includes the geometric stiffness terms. From SIMPACK the linear system matrices in state space form ( $\mathbf{A}$ ,  $\mathbf{B}$ ,  $\mathbf{C}$ ,  $\mathbf{D}$ ) are exported for each rotational speed. Matlab calculates the eigenfrequencies. These are plotted over the rotational speed, see e.g. Fig. 8.4.

### 8.2.2 Dynamic Influence of Absorber Mass

First the influence of the absorber mass is studied. Therefore the disc radius  $R = 25.4\text{e-}3\text{ m}$  and the length of the beam  $L = 94.6\text{e-}3\text{ m}$  are chosen. The absorber mass is varied from 0.01 kg up to 0.5 kg. Figure 8.4 shows the eigenfrequency depending on the rotational speed. Also shown is the second order engine frequency as straight green line. Increase of tip mass leads to lower eigenfrequency but does not influence the gradient.

**Fig. 8.4** Eigenfrequency of an absorber depending on tip mass

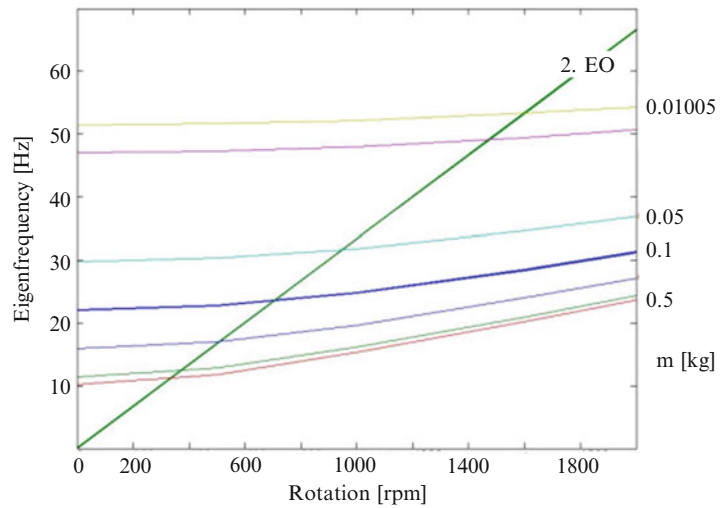
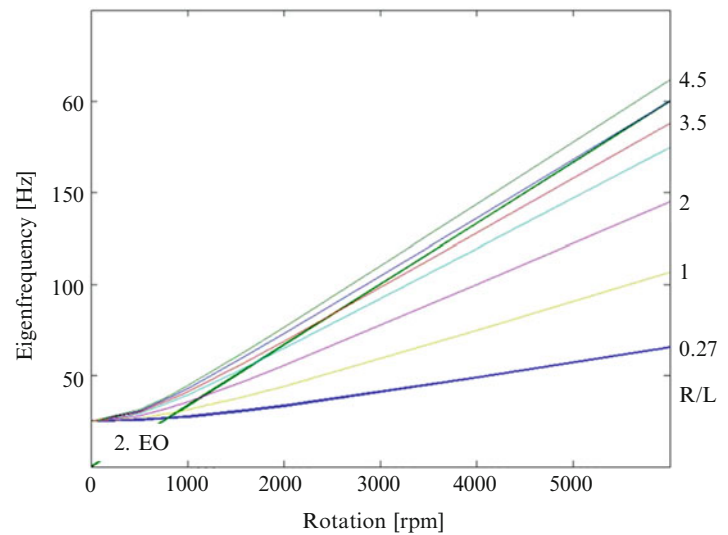


**Fig. 8.5** Influence of the ratio R/L on the eigenfrequency of an absorber



### 8.2.3 Dynamic Influence of Beam Length

The ratio of disc radius to beam length (R/L) has a large influence on the gradient of the eigenfrequency over rotational speed, see Fig. 8.5. In this study the beam length is chosen to  $L = 94.6 \cdot 10^{-3}$  m and the absorber mass to  $m_E = 0.075$  kg. For these parameters and  $R/L = 4.5$  the curve is nearly parallel to the second order engine speed.

### 8.2.4 Design Parameters

The parameter study results in the following system parameters: disc radius  $R = 0.115$  m, disc moment of inertia  $0.02 \text{ kg m}^2$ , absorber mass  $0.3$  kg, beam: material density  $7,860 \text{ kg/m}^3$ , Young's Modulus  $210 \text{ GPa}$ , cross section height  $3.6 \cdot 10^{-4}$  m and width  $2.4 \cdot 10^{-3}$  m, beam length  $22.7 \cdot 10^{-3}$  m.

## 8.3 Power Train with Vibration Absorber

The power train for a four wheel driven car is shown in Fig. 8.6. The dynamics of a rear-wheel drive can be described by a chain of rotational inertia connected by rotational spring-damper. Regarding a typical car leads to the parameters listed in Table 8.1.

**Fig. 8.6** Power train  
(ClearMechanic.com)

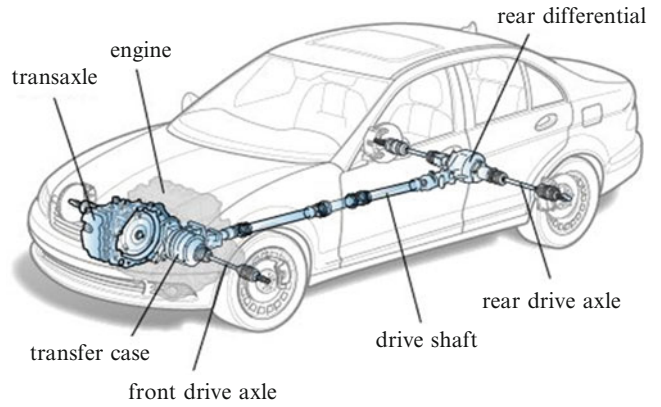
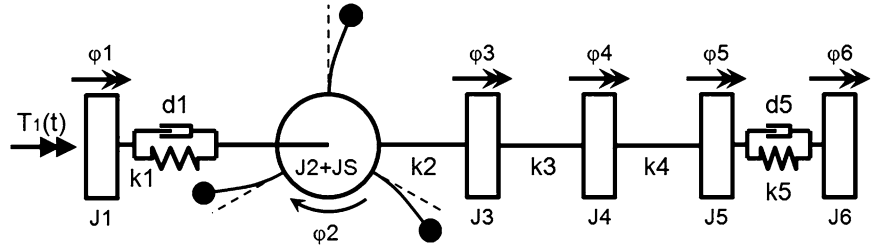


**Table 8.1** Parameters of power train, compare [5]

Inertia	$10^{-3} \text{ kg m}^2$		Stiffness	$10^3 \text{ Nm/rad}$	Damping	$\text{Nms/rad}$
J1	160	IC engine	k1	0.6	d1	$0.001*k1$
J2	115	Coupling	k2	5		
J3	70.4	Transaxle	k3	29		
J4	5.6	Differential	k4	0.7		
J5	124.1	Wheels	k5	2.9	d5	$0.01*k5$
J6	4,748	Vehicle				

**Fig. 8.7** Power train with vibration absorber [3]



### 8.3.1 Multibody Model

The tree structure of the power train is given by the first body of the MBS (IC engine) connected to the inertial frame, herewith only rotation is possible. The body 1 is connected to body 2 (coupling), body 2 to body 3 (transaxle) and so forth by revolute joints. The first body in the power train is excited by the drive torque  $T_1$ . The vibration absorber is connected to the second body by a zero degree of freedom joint, see Fig. 8.7.

### 8.3.2 System Dynamics

The nonlinear multibody system is linearized about the nominal rotational speed [6]. The engine torque is the input to the linear model. The acceleration of the absorber disc angle  $\ddot{\varphi}_2$  is observed. Figure 8.8 (left) shows the absorber effect. High vibration amplitudes are marked in red. The power train eigenfrequencies without vibration absorber can be seen on the left hand side of the plot for zero rotational speed ( $\Omega = 0$ ). The power train is a linear system. Therefore these system eigenfrequencies would be identical over the whole range of rotational speed. The most critical point is at  $\Omega = 1, 500$  where the second engine order hits a power train eigenfrequency. The vibration absorber leads to a significant reduction of the response. This effect can be observed over the whole range of rotational speed from idle up to 6,000 rpm. But the absorber comes with a drawback. There is a response amplification close to the second engine order. The designer can take care of this by introducing damping. Figure 8.8 (right) shows the amplitude of the bending angle at the end of the beam w.r.t to the clamp. For more detailed interpretation the speed range is cut from 500 to 2,000 rpm. Overall it shows the same characteristic as the angular acceleration. The vibration absorber changes the eigenfrequency of the system in a way that there is no excitation of the resonance by the second engine order. The eigenfrequencies increase close to the engine orders. The maxima of the angle amplitude are less than  $1^\circ$ . These small deformations are well covered by the linear equations of motion.

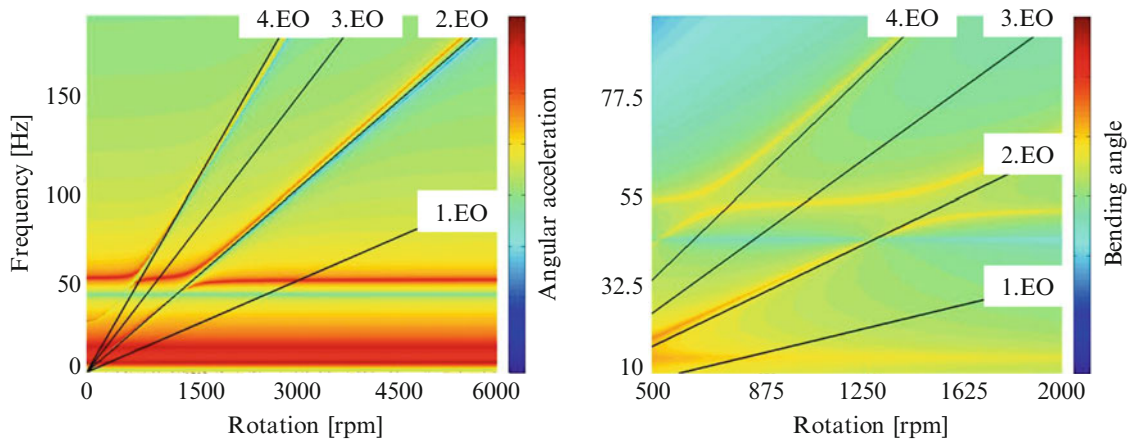


Fig. 8.8 Dynamic response with vibration absorber: J2 (left), bending angle of beam 1 (right)

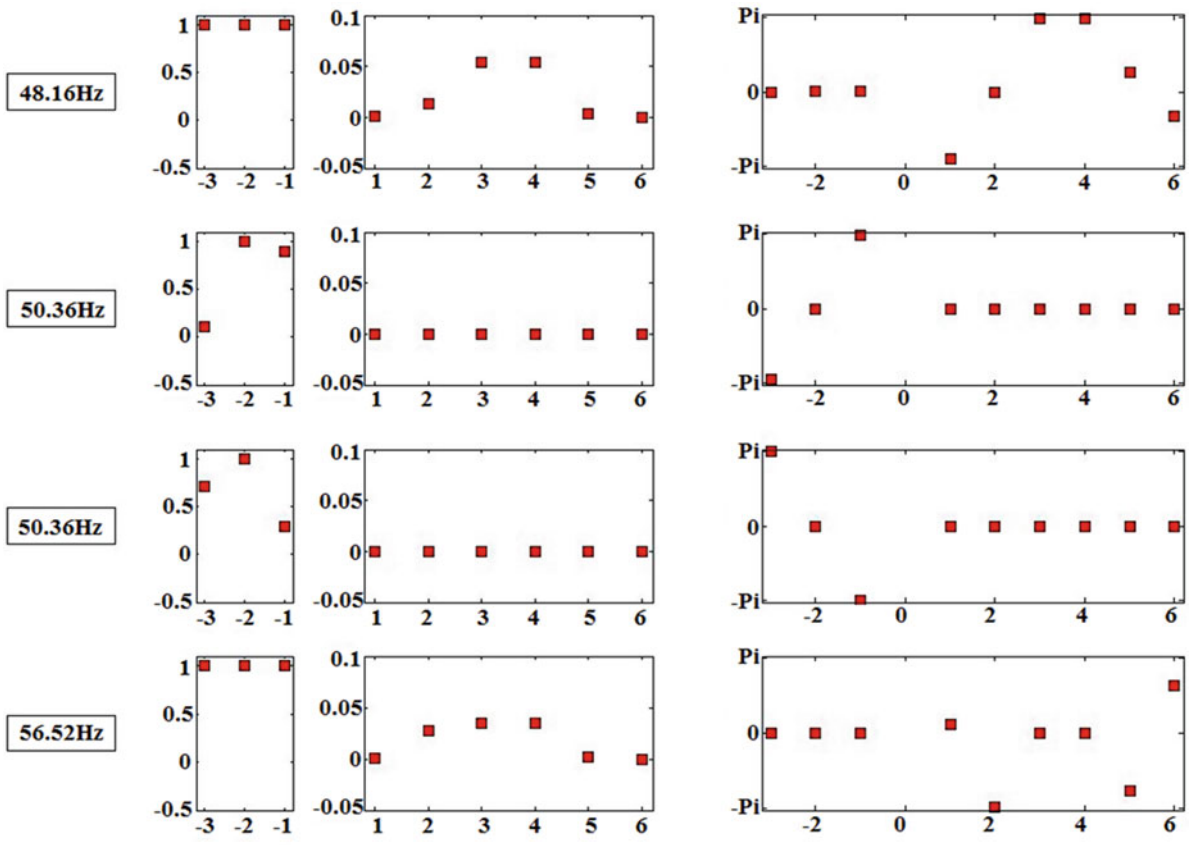


Fig. 8.9 Eigenmodes of power train with vibration absorber at 1,500 rpm

In Fig. 8.9 the eigenmodes of the system are visualized separated in phase and angle. The masses J1–J6 are numbered 1–6 and the beams –1 to –3. The eigenmodes are analyzed for the critical eigenfrequencies at 50 Hz which hit the second engine order at 1,500 rpm. The amplitude is normalized. In the first line the eigenmode of the powertrain is shown. Therefore the amplitudes of the beams are 1 and the phases are 0. This indicates the rigid body movement. In the second and the third line the first two eigenfrequencies of the beams are shown. Beam 1 and beam 3 are in phase, beam 2 is phase shifted by 180°.

Depending on the frequency beam 2 and 3 or beam 1 and 2 have nearly the same amplitude. Because of that the influence on the system by these two beams neutralizes and the absorption of the vibrations is only done by one beam. By synchronizing the beams the effect of the vibration absorber could be improved by a factor of three.

## 8.4 Conclusion

The concept of a rotational vibration absorber with flexible beams is introduced. The adaptation to the second engine order is on account of the geometric stiffening. Optimal parameters are found by a nonlinear MBS parameter study. The proof of concept is achieved by linear system analysis of a power train with realistic vehicle parameters.

## References

1. Brommundt E, Sachau D (2008) Schwingungslehre mit Maschinendynamik. B.G. Teubner/GWV Fachverlage GmbH, Wiesbaden
2. Brommundt E, Sachs G, Sachau D (2007). Technische Mechanik, Eine Einführung. Oldenbourg Wissenschaftsverlag GmbH, München
3. Butter J (2010) Adaptive Schwingungsreduktion in rotierenden Torsionsschwingerketten, Master Thesis Private Fachhochschule Goettingen
4. Dietz S, Sachau D, Gerl J (1997) FEMBS<sup>-1</sup>: Von SIMPACK zurück zum FEM-Programm. SIMPACK News 5
5. Dresig H (2006) Schwingungen mechanischer Antriebssysteme. Springer, Auerswalde
6. Hanselka J (2010) Mehrkörpersimulation eines adaptiven Drehschwingungstilgers für Antriebsstränge, Hamburg
7. Sachau D (1993) Berücksichtigung elastischer Körper in Mehrkörpersimulationen, Oberpfaffenhofen
8. Timoshenko S, Goodier J (1970) Theory of elasticity. McGraw-Hill International Book Company, Tokyo

# Chapter 9

## Combined Optimization of Actuator/Sensor Positions and Weighting Matrices for an Active Noise Reduction System

Jan Foht and Delf Sachau

**Abstract** Optimization of actuator and sensor positions is a crucial part of the design process of an active noise reduction (ANR) system. A common variant is to identify a set of actuator and sensor positions from a superset of possible locations that are specified by construction and design factors. Effective tools for this task are optimization algorithms like for example the genetic algorithm. A proven method to make the active noise control algorithm robust against disturbances and to transfer the zone of noise reduction from the error microphones to a wanted area is the implementation of weighting matrices in conjunction with a frequency domain FxLMS control algorithm. Computation of the weighting matrices is also done with the help of non-linear optimization algorithms. This paper shows a method how to combine both optimizations into one single optimization process. Furthermore, different restrictions like maximum loudspeaker actuation are taken into account. The described method is implemented for an example of an industrial working station. In this context it is compared to both a sole component optimization and a sole weighting optimization.

**Keywords** Noise reduction • Active noise control (ANC) • Position optimization • Weighting matrices • Genetic algorithm

### 9.1 Introduction

Industrial working environments are often exposed to high sound pressure levels. Figure 9.1 shows a semi-enclosed work station which is from one direction affected by noise. Here the sound is caused by a rotating machine and consists of a tone of a certain frequency and its higher harmonics. Due to noise regulations the sound pressure level at the workers ear must remain within certain tolerances. In the low frequency range ( $f < 500$  Hz) passive noise treatments are difficult especially as the workstation is open to one side. For low frequencies active noise control (ANC) is a proven means, which is already successfully applied to airplanes [1] and automobiles [2].

The potential noise reduction of an ANC system depends on the beneficial positioning of error microphones and loudspeakers. Typically positions are chosen from a superset of possible locations that are specified by construction and design factors. Due to the high number of possible combinations testing of all solutions is not possible. This leads to a non linear optimization problem which is often solved by genetic optimizations [3].

A different application of optimization is described in [4]. Based on a fixed set of loudspeaker and microphone positions weighting matrices are optimized and used in the controller to relocate noise reduction from the error microphones to a wanted area in space. If further typical disturbances of the system can be measured beforehand they can be included during optimization and that makes the controller robust against such disturbances afterwards.

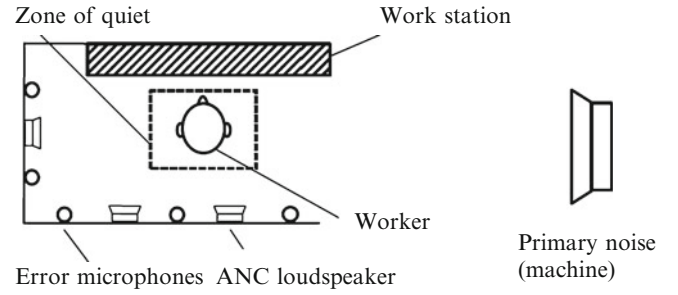
This paper describes an optimization that combines a selection of positions from a superset with the estimation of weighting matrices. The first section describes the objective function, the restrictions, the free optimization parameters and the implementation as a genetic algorithm. The second section describes the application to an industrial working station. The predicted results of the combined optimization are compared to the ones of a position optimization and a weighting optimization. Afterwards the optimization results are validated with ANC experiments at a test bench.

---

J. Foht (✉) • D. Sachau

Helmut-Schmidt-University, University of the Federal Armed Forces Hamburg, Holstenhofweg 85, 22043 Hamburg, Germany  
e-mail: [jfoht@hsu-hh.de](mailto:jfoht@hsu-hh.de); [sachau@su-hh.de](mailto:sachau@su-hh.de)

**Fig. 9.1** Workstation with ANC system



## 9.2 Combined Optimization

### 9.2.1 Basic Equations

The active noise system consists of  $N_E$  error microphones and  $N_L$  loudspeakers. As indicated in Fig. 9.1 these are mounted in walls and ceiling while the wanted zone of noise reduction is a square around the head of the worker. This zone is covered with monitoring microphones for transfer function measurement during set-up phase but not during operation. This leads to the principle scheme in Fig. 9.2.

The primary noise is at the error microphones  $\mathbf{d}$  and at the head of the worker  $\mathbf{d}_M$ . The controller  $\mathbf{C}$  minimizes a cost function of error signals  $\mathbf{e}_i$  and actuation signals  $\mathbf{u}_i$

$$J_i = \mathbf{e}_i^H \mathbf{Q}_i \mathbf{e}_i + \mathbf{u}_i^H \mathbf{R}_i \mathbf{u}_i, \quad (9.1)$$

for each frequency  $i$  separately. The diagonal matrices  $\mathbf{Q}_i = \text{diag}(q_{i,1}, \dots, q_{i,N_E})$  and  $\mathbf{R}_i = \text{diag}(r_{i,1}, \dots, r_{i,N_L})$  weight the microphones and loudspeakers independently. In the following the frequency index  $i$  will be neglected where not necessary for understanding.

The adaptive control algorithm (filtered reference least mean square, FxLMS) converges to the optimum actuation [4]

$$\mathbf{u}_{opt} = -[\mathbf{G}^H \mathbf{Q} \mathbf{G} + \mathbf{R}]^{-1} \mathbf{G}^H \mathbf{Q} \mathbf{d}. \quad (9.2)$$

The actuation  $\mathbf{u}$  affects the error and the monitoring microphones with the transfer function matrix  $\mathbf{G}$  respectively  $\mathbf{G}_M$

$$\mathbf{e} = \mathbf{G} \mathbf{u} + \mathbf{d} \text{ and } \mathbf{e}_M = \mathbf{G}_M \mathbf{u} + \mathbf{d}_M. \quad (9.3)$$

The matrix  $\mathbf{G}$  and the vector  $\mathbf{d}$  depend on the positions that are chosen. They are subsets of the transfer matrix  $\mathbf{G}_{all}$  and primary noise vector  $\mathbf{d}_{all}$  to all possible locations. For  $\mathbf{G}_M$  only the transfer functions of the used loudspeakers are considered but  $\mathbf{d}_M$  is fixed as the number and positions of the monitoring microphones do not change.

### 9.2.2 Objective Function and Optimization Parameters

The optimization process has the goal to reduce the residual noise at the monitoring microphones around the head of the loadmaster. Hence the squared Euclidian norm of all monitoring microphones is chosen as objective function which is minimized:

$$\underset{\mathbf{Q}, \mathbf{R}, \text{Pos}}{\text{minimize}} \quad 10 \log_{10} \|\mathbf{e}_M\|_2^2. \quad (9.4)$$

For optimal control ( $\mathbf{u} = \mathbf{u}_{opt}$ ) and with Eq. (9.3) this can be written as

$$\underset{\mathbf{Q}, \mathbf{R}, \text{Pos}}{\text{minimize}} \quad 10 \log_{10} \|\mathbf{G}_M \mathbf{u}_{opt}(\mathbf{Q}, \mathbf{R}) + \mathbf{d}_M\|_2^2. \quad (9.5)$$

In case that more than one frequency is controlled the objective function is expanded to minimize the total residual noise of all frequencies. The free optimization parameters are the elements of the weighting matrices  $\mathbf{Q}$  and  $\mathbf{R}$  and the selection of the positions from a superset of possible locations.

**Fig. 9.2** Principle schemes of primary system and controller

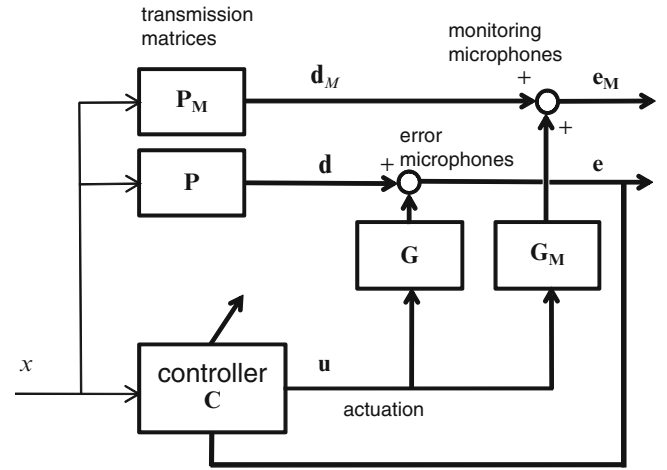
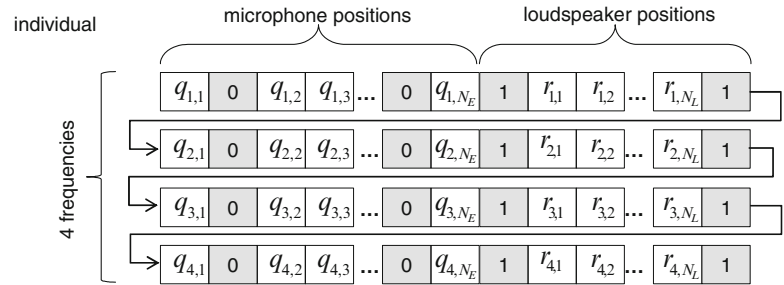


**Fig. 9.3** Encoding of individual



### 9.2.3 Constraints and Restrictions

The optimization has the following constraints. The number of used loudspeakers and microphones are limited. The loudspeakers should be actuated only to a certain value, as otherwise nonlinear effects can occur. To assure that the controller cost function (9.1) has a minimum, the weighting matrices  $\mathbf{Q}$  and  $\mathbf{R}$  have to be positive definite [4]. The stability of the FxLMS controller can be guaranteed if the smallest eigenvalue  $\lambda_{\min}$  of the matrix  $[\mathbf{G}^H \mathbf{Q} \mathbf{G} + \mathbf{R}]$  is positive [5]. This leads to the following constraints:

1. Number of components:

$$N_L \leq N_{L,\max}, \quad N_E \leq N_{E,\max} \quad (9.6)$$

2. Actuation:

$$u_{\text{allowed}}^{\max} - u_{\text{opt}}^{\max}(\mathbf{Q}, \mathbf{R}) > 0 \quad (9.7)$$

3. Definiteness:

$$\mathbf{Q} > 0, \quad \mathbf{R} > 0 \quad (9.8)$$

4. Stability:

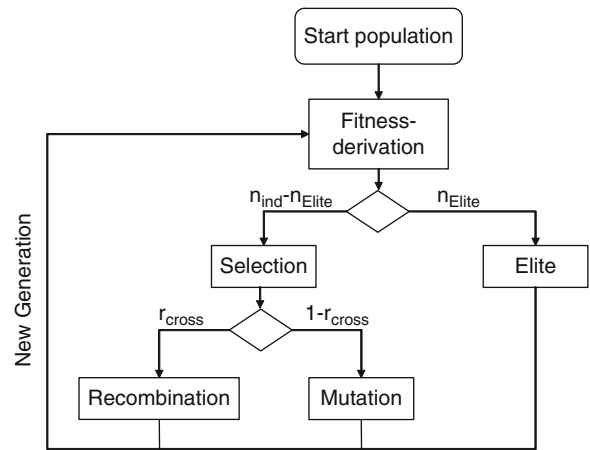
$$\lambda_{\min}(\mathbf{Q}, \mathbf{R}) > 0 \quad (9.9)$$

### 9.2.4 Implementation

The genetic algorithm from the Matlab® *Global Optimization Toolbox* [6] is used for the optimization. The free optimization parameters of an individual are encoded as a vector, see Fig. 9.3. An individual consists of entries for all possible microphone and loudspeaker positions at all frequencies. Unused microphones are marked by zeros and unused loudspeakers by ones



**Fig. 9.4** Flow chart of genetic algorithm



for all frequencies as indicated in Fig. 9.3. The weighting factors of  $\mathbf{Q}$  and  $\mathbf{R}$  range from 0...1. The number of microphone scaling factors  $N_E$  is equal or less the number of allowed microphones  $N_{E,max}$  and the number of loudspeaker scaling factors  $N_L$  is equal or less the number of allowed loudspeakers  $N_{L,max}$ .

The basic principle of the genetic optimization is Darwin's "Survival of the fittest" [7]. That means that out of a population those individuals will prevail that are most suitable and have the highest fitness. The flow chart of the implemented optimization is visualized in Fig. 9.4. At first in the generation function of the start population a random template vector of active components is created for each individual. The number of components is equal or less the allowed maximum so that constraint (9.6) is fulfilled. The active component entries are filled with random values.

In the fitness function the fitness value according to formula (9.5) is computed for each individual. If an individual does not fulfill restrictions (9.7), 9.8 and (9.9) a punishing term is added. Restriction (9.6) is not checked here as all functions are implemented such that only individuals with an allowed number of components can exist. This prevents an excess of punished individuals and increased computational effort due to unnecessary inverse calculations in the cost function.

The  $n_{Elite}$  best individuals are transferred without modifications to the next generation. Further individuals are selected for recombination and mutation with the 'tournament method' [7], which is random based but prefers individuals with a high fitness.

In the recombination function  $r_{cross}$  new individuals are generated as a combination of parent individuals. In a first step the active components are estimated. A component that is active at both parent individuals will be active in the new individual. All other active components are chosen by random from the active components of one of the parents as long as requirement (9.6) is fulfilled. The value is then calculated between the ones of the two parents with a random scaling parameter defining the proportion.

In the mutation function entries of individuals are changed randomly. Level of change depends on the progress of optimization. This leads to high diversity at the beginning and focus on one solution at the end [4].

Then the fitness values of the individuals of the new generation are calculated. After a defined number of generations or lack of improvement for a defined number of generations the optimization is stopped.

The functions for fitness, mutation and recombination are problem specific implemented and provided to the genetic toolbox algorithm.

### 9.3 Application to Work Station

The combined optimization is applied to the noise problem of the work station. Figure 9.5 shows the test bench. It is not an original work station but reused from former project work [4] and sufficient for the analysis of the described problem.

The machine noise is simulated by two loudspeakers that are actuated at a base frequency of 90 Hz and its harmonics at 180, 270 and 360 Hz. The SPL of each frequency is adjusted to about 75 dB at the ears of the worker. As a linear system is assumed the noise reduction should not depend on the primary level as long as no nonlinear effects occur.

The primary noise and transfer function data is measured from eight possible loudspeaker positions to 16 possible error microphone positions and to 14 monitoring microphones in the workers head area. Goal is to find the solution which minimizes the total residual noise level at the monitoring microphones with a maximum of four loudspeakers and eight microphones ( $N_L \times N_E: 4 \times 8$ ).

**Fig. 9.5** Work station test bench [4]



**Table 9.1** Noise reduction [dB] for three different optimizations

Optimization of	90 Hz	180 Hz	270 Hz	360 Hz	Total
Positions	-5.2	-4.6	-3.9	-4.3	-4.5
Weighting	-13.1	-8.6	-6.0	-6.1	-7.6
Combined	-10.4	-9.6	-6.6	-8.1	-8.4

### 9.3.1 Comparison of Optimization Results

The combined optimization is compared with two alternatives. First a position optimization switches components on and off, as described in [3] and implemented in [8]. The controller cost function (9.1) reduces in this case to  $J = \mathbf{e}^H \mathbf{e} + \beta \mathbf{u}^H \mathbf{u}$  and the restrictions (9.8) and (9.9) are not necessary. Second a weighting optimization works on a fixed set of components and optimizes separately for each frequency, [4]. The positions of the fixed set ( $4 \times 8$ ) are estimated previously by the position optimization. The weighting optimization uses the controller cost function (9.1) but not restriction (9.6). The total allowed actuation voltage  $u_{allowed}^{max}$  in restriction (9.7) is split up into allowed actuation voltages for each frequency.

The optimization results are printed in Table 9.1. Shown are the predicted values for the noise reduction at 90, 180, 270 and 360 Hz and the resulting over all noise reduction, which is the important performance indicator to fulfill the legal requirements. The combined optimization leads to the best overall noise reduction and to the best reduction in the single frequencies except at 90 Hz. Here the weighting optimization leads to the highest result.

Although the weighting optimization is based on the locations estimated by the position optimization and although it has the highest reduction at 90 Hz it leads to nearly 1 dB less total reduction. This shows that a successive execution of position and weighting optimization is not as effective as a combined optimization which solves the optimization problem for all four frequencies together and minimizes directly the total reduction. Hence a position set is chosen that might have less reduction at some frequencies but a better total value.

The position optimization leads to the worst results in the total reduction as well as in all single frequencies. This is also understandable as the optimization process can only choose positions but has no possibility to weight the components.

The maximum actuation voltage is estimated as 1.92 [V] for the position optimization, 1.27 [V] for the weighting optimization and 0.98 [V] for the combined optimization. This low actuation is advantageous as it leads to more robust ANC systems [5].

For all three optimizations the number of generations is set to 3,000. The position optimization stops after about 50 generations as the final solution is already found. Computation time is less then 10 min. The weighting optimization needs for every frequency about 30 min so in total about 2 h. The combined optimization needs about 1 h 40 min. As the optimization is normally done only once in the ANC design process the computational effort is negligible.

**Table 9.2** Predicted and measured noise reduction [dB] for combined optimization

	90 Hz	180 Hz	270 Hz	360 Hz
Prediction	-10.4	-9.6	-6.6	-8.1
Measurement	-9.0	-8.7	-6.2	-8.0

### 9.3.2 Validation of Optimization Results

Table 9.2 shows that the measured noise reduction deviates for all four frequencies less than 1.5 dB from the predicted values. So the optimization predicts the reachable noise reduction with sufficient precision.

## 9.4 Conclusion and Outlook

This study presents an optimization that combines the advantages of a weighting optimization regarding shift of noise reduction with the possibility to choose positions from a superset of possible locations. The optimization results leads to better total noise reduction than a weighting optimization and than a position optimization. For the described problem to choose a set of  $4 \times 8$  components out of a superset of  $8 \times 16$  components the computational effort is nearly the same for combined and weighting optimization. As the size of the individual equals the sum of possible positions for microphones and loudspeakers times the number of frequencies, the search space of the combined optimization problem raises drastically for higher number of components or frequencies. This might lead to computational problems and requires more advanced techniques to be implemented. Therefore the application of the combined optimization to a problem with higher component number is the next planned step.

## References

1. Ultra Electronics Controls (2012) <http://www.ultra-controls.com/productdetails.php?productID=15>. 15 Oct 2012
2. Honda (2012) <http://legend.honda.com.au/>. 15 Oct 2012
3. Elliot S (2001) Signal processing for active control. Signal processing and its applications. Academic, San Diego/London
4. Kochan K (2009) Robuste aktive Schallreduktion in Flugzeugen. Bericht aus der Professur für Mechatronik, Helmut-Schmidt-University, Hamburg
5. Elliott SJ, Boucher CC, Nelson PA (1992) The behavior of a multiple channel active control system. IEEE Trans Signal Process 40(5):1041–1052
6. The Mathworks (2012) <http://www.mathworks.com/products/global-optimization/>. 26 Oct 2012
7. Sivanandam SN, Deepa SN (2008) Introduction to genetic algorithms. Springer, Berlin/Heidelberg
8. Mattausch H (2012) Multitonale Positionsoptimierung mit dem genetischen Algorithmus. Helmut-Schmidt-University, Hamburg

# Chapter 10

## SSDI Technique Evolution to Improve Attenuation Performances with Random Disturbances

M. Berardengo, S. Manzoni, M. Redaelli, and M. Vanali

**Abstract** This paper deals with semi-active vibration reduction by means of piezo-actuators shunted to time-variant impedances. Particularly, attention is focused on the Synchronized Switch Damping on Inductance technique applied to single mode control in presence of a random disturbance.

Drawbacks of the mentioned method are evidenced, showing that sometimes it can fail. Therefore, an alternative method (which actually is an evolution of SSDI) is proposed and its effectiveness is proved numerically through a model. Such a model is validated experimentally within the paper.

**Keywords** Vibration control • Semi-active control • Piezo-actuator • Shunt • Damping

### 10.1 Introduction

The control of vibrating structures is an essential tool for improving machine durability, preventing fatigue failures. Furthermore, benefits of vibration control also involve people comfort since unwanted and annoying noise can be avoided through the reduction of vibration levels.

Currently, one of the most attracting approaches in the industrial field is the adoption of piezo-actuators, which are quite cheap and are often able to provide enough force to achieve satisfying vibration reduction. These actuators can be employed with many different control algorithms and systems. Semi-passive and semi-active strategies are currently under deep investigation because they can provide significant vibration reduction at an attainable cost; this makes them very suitable for industries and that is the main reason for such interest gained among researchers.

The mentioned methods are based on linking the piezo-actuator to a time invariant (semi-passive) or time-variant (semi-active) electrical network capable to dissipate energy or to provide mechanical actions in opposition to vibration. The network can have different layouts, depending on the required type of control (e.g. mono-modal [1, 2], multi-modal [3–5], broadband [6–8]).

This paper deals with mono-modal semi-active control in presence of random disturbances. Different techniques are already available in the state of the art for such a problem. The purpose of this paper is to show the limits of the most adopted algorithm in the mentioned situation (i.e. mono-modal control with random disturbance) and to propose an evolution to improve the control performance. The method under investigation is the Synchronized Switch Damping on Inductance (SSDI), which has been presented by Clark and Corr in [9] and Richard et al. in [10, 11]. Section 10.2 will describe this approach, showing its working principle and underling its drawbacks in the case of mono-modal control with random disturbance. Then, Sect. 10.3 will introduce a test-case structure (i.e. vibrating structure + piezo-actuator + SSDI electrical network) and the model used to describe its behaviour. Finally, Sect. 10.4 will introduce the proposed SSDI evolution to overcome the discussed drawbacks.

---

M. Berardengo • S. Manzoni (✉) • M. Redaelli  
Department of Mechanics, Politecnico di Milano, Via La Masa 1 - 20156 Milan, Italy  
e-mail: [marta.berardengo@mail.polimi.it](mailto:marta.berardengo@mail.polimi.it); [stefano.manzoni@polimi.it](mailto:stefano.manzoni@polimi.it); [matteo.redaelli@polimi.it](mailto:matteo.redaelli@polimi.it)

M. Vanali  
Department of Industrial Engineering, Università degli Studi di Parma, Parco Area delle Scienze, 181/A - 43124 Parma, Italy  
e-mail: [marcello.vanali@unipr.it](mailto:marcello.vanali@unipr.it)

## 10.2 The Synchronized Switch Damping on Inductance Method

The piezo-actuator is short-circuited and open-circuited to an electrical impedance by means of a switch. The impedance is composed by the series of a resistance and an inductance (Fig. 10.1). Therefore, the resulting electrical network (i.e. resistance  $R$  + inductance  $L$  + capacitance of the piezo-actuator  $C_p$ ) is a second order system, thus characterized by a single eigenfrequency. Usually the electrical resonance frequency is chosen so that it is about ten times higher than the higher mechanical eigenfrequency to control (i.e. the value of  $L$  is chosen to satisfy such a condition) [9]. The circuit is close-circuited when the bender deflection is in correspondence of a maximum or a minimum so that the charge accumulated by the capacitance of the piezo-bender is dissipated. The voltage step input due to switch closure makes the electrical system vibrating with its resonance frequency  $f_r$ , which is [1]:

$$f_r = \frac{1}{2\pi\sqrt{LC_p}} \quad (10.1)$$

Figure 10.2a shows the typical time-histories of bender deflection and voltage at its electrodes when switch is closed. The oscillation of voltage can be stopped by opening the switch after a half of the electrical semi-period  $t_0$ :

$$t_0 = \pi\sqrt{LC_p} \quad (10.2)$$

Therefore the voltage value  $V_1$  just after switch opening assumes the value  $V_{1a}$  [4]:

$$V_{1a} = -V_{1b}\exp\left(\frac{-\pi}{2Q_i}\right) \quad (10.3)$$

**Fig. 10.1** Piezo-shunt (a) and the equivalent electrical model (b);  $V_1$  is the voltage applied across the conducting electrodes of the shunt bender of the shunt bender and  $V_2$  is the induced piezoelectric voltage

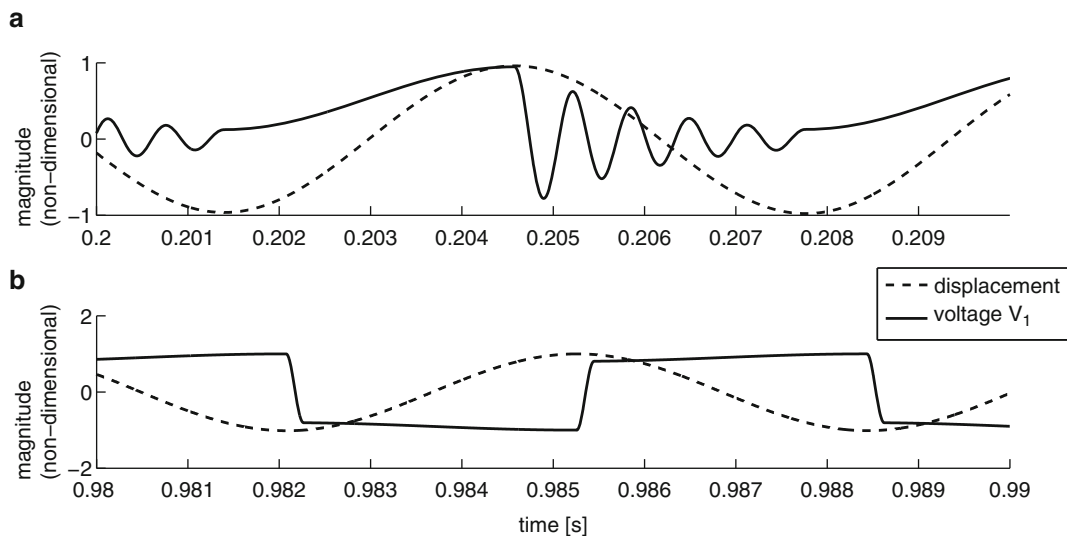
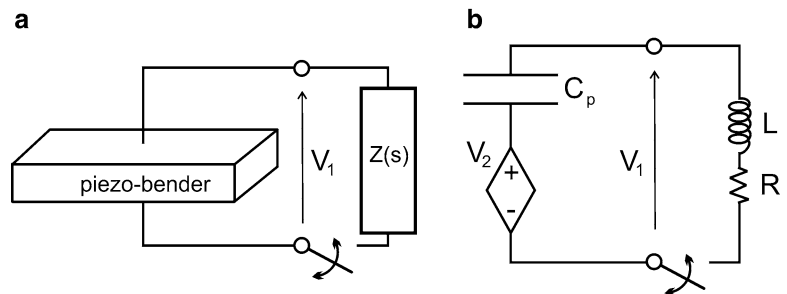


**Fig. 10.2** Trend of voltage  $V_1$  when closing the switch in correspondence of maxima/minima of structure deflection (and thus of structure displacement). Time histories when the switch is not immediately re-opened (a) and when voltage oscillation is stopped by a time equal to an electric semi-period (numerical results)

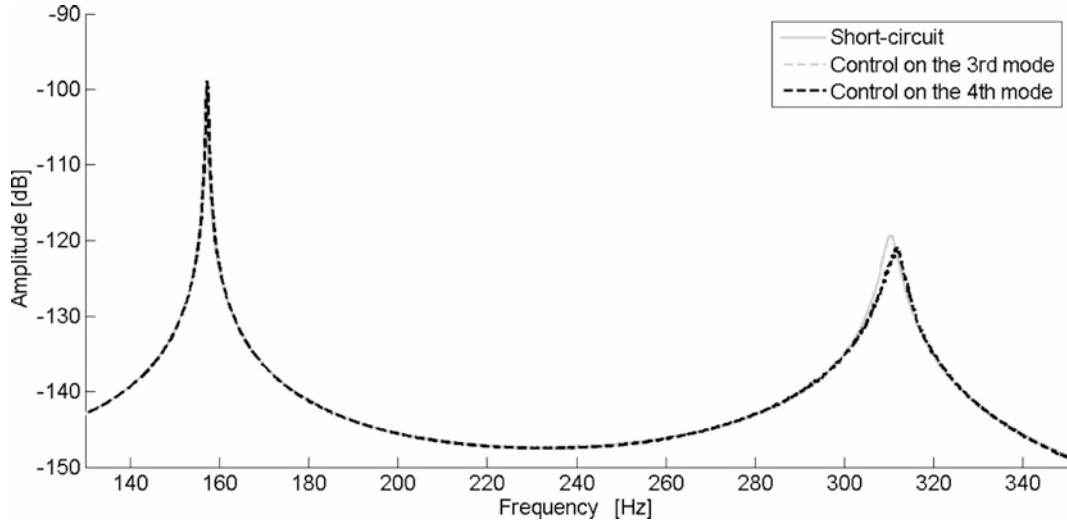


**Fig. 10.3** Amplitude of  $T_{zw}$  in case of short-circuit configuration and when controlling two different modes (i.e. the third and the fourth of the cantilever beam described in Sect. 10.3) with the SSDI method (numerical results)

Where  $V_{1b}$  is the voltage  $V_1$  value just before switch opening and  $Q_i$  is the quality factor of the resonant electrical network [4]:

$$Q_i = \frac{\sqrt{L}}{R\sqrt{C_p}} \quad (10.4)$$

The trend of the voltage at bender electrodes is shown in Fig. 10.2b. The moment exerted by the piezo-bender on the structure is proportional to the voltage at its electrodes. Therefore, the inversion of voltage sign (Eq. 10.3) means the inversion of moment sign and thus the moment exerted by the bender is opposite to the structure deflection rate for the entire cycle of vibration. The higher the voltage jump (when closing and opening the switch) is, the more effective the control technique is.

When a mono-modal control is required in presence of a broadband random disturbance, problems arise due to the following fact. The signal used to control the switch status is the voltage measured at bender electrodes. It is good practice to use two co-located benders, one linked to the electrical network by the switch for the SSDI implementation and the other used to measure structure deflection in order to control the switch status. The signal of this second bender must be band-pass filtered since only one mode is under control in this case. The band-pass filter must have the low cut-off frequency at a frequency a slightly lower than the resonance to control, while the high cut-off frequency must be at a slightly higher frequency than the resonance. The filtered signal is then used to drive the switch. If the switch is opened (and then closed) in correspondence of the maxima and minima of this drive filtered signal, the control performance can be poor. This is proved in Fig. 10.3. The reason for such an unsatisfying vibration attenuation is that the maxima and minima of the filtered signal can mismatch those of the unfiltered signal (maxima/minima of the drive filtered signal can even be in correspondence of the zeros of the unfiltered signal, thus having a null vibration attenuation). Small voltage jumps are achieved in this case when switching, thus with poor vibration attenuation.

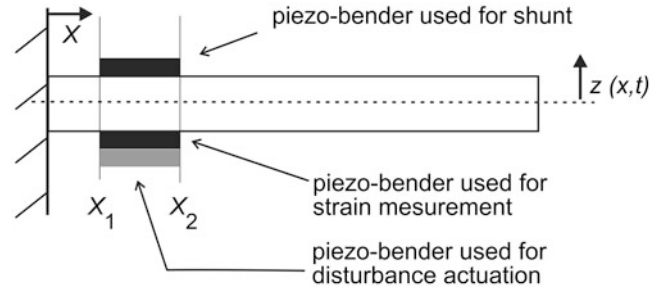
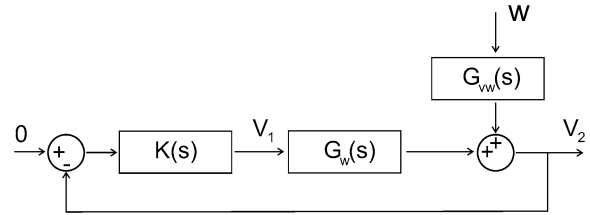
Therefore, the necessity to find a more effective method to apply the SSDI technique is evident. This issue will be discussed in Sect. 10.4.

### 10.3 Test Case Structure and Its Model

A test case structure has been chosen in order to test an evolution of the SSDI technique, able to overcome the mentioned problem. This structure is a steel cantilever beam, whose main technical data are given in Table 10.1. Three co-located piezo-benders have been used to implement the SSDI method (Fig. 10.4).

**Table 10.1** Technical data of the test set-up

Beam Young's modulus	210 GPa
Beam density	7,800 kg/m <sup>3</sup>
Overall length of the piezo-actuator	0.101 m
Overall thickness of the piezo-actuator	0.5 mm
Overall width of the piezo-actuator	0.025 m
Length of a single patch (active element)	0.092 m
Thickness of a single patch (active element)	0.13 mm
Width of a single patch (active element)	0.021 m
Overall Young's modulus of the piezo-actuator	69 GPa
Bender capacitance	0.165 $\mu$ F
Piezoelectric constant $d_{31}$	-179 pm/V
Electromechanical coupling coefficient	0.63

**Fig. 10.4** Test set-up**Fig. 10.5** Feed-back interpretation of piezo-shunt

A model has been developed to simulate the behavior of this system. This model is based on that proposed by Moheimani et al. [12]. Although other models are available in literature [13, 14], this can provide an interpretation of piezo-shunt like a sort of feed-back control. This makes possible to design the shunt relying on traditional feed-back control concepts.

Figure 10.5 shows the conceptual scheme of this feed-back interpretation [12], where  $V_1$  is the voltage applied across the conducting electrodes of the shunt bender,  $V_2$  is the induced piezoelectric voltage,  $w$  is the disturbance (i.e. the input voltage to the disturbance piezo-bender in this case),  $G_{vw}$  is the transfer function between  $V_1$  and  $V_2$  and  $G_{vw}$  is the transfer function between  $w$  and  $V_2$ . Finally  $K$  is the transfer function describing the feed-back effect due to shunt. Its Laplace expression is

$$K(s) = \frac{sC_p Z(s)}{1 + sC_p Z(s)} \quad (10.5)$$

$Z(s)$  is the Laplace expression of the shunt impedance, which is a series of a resistance and an inductance when the switch is close and an open circuit when the switch is open.

Finally the closed loop transfer function  $T_{zw}$  between the disturbance  $w$  and the axial displacement  $z$  of structure is expressed in Eq. 10.6:

$$T_{zw}(x, y, s) = \frac{G(x, y, s)}{1 + K(s)G_{vw}(s)} \quad (10.6)$$

where  $G(x, y, s)$  is the open loop transfer function between disturbance  $w$  and axial displacement  $z$  at point  $(x, y)$ .

A numerical model working in the time domain and based on the abovementioned analytical model has been developed to simulate the dynamical behavior of the cantilever beam. Figure 10.6 shows the numerical and experimental transfer function  $T_{zw}$  (the experimental curves have been calculated on a limited frequency range because step sine tests have been carried out

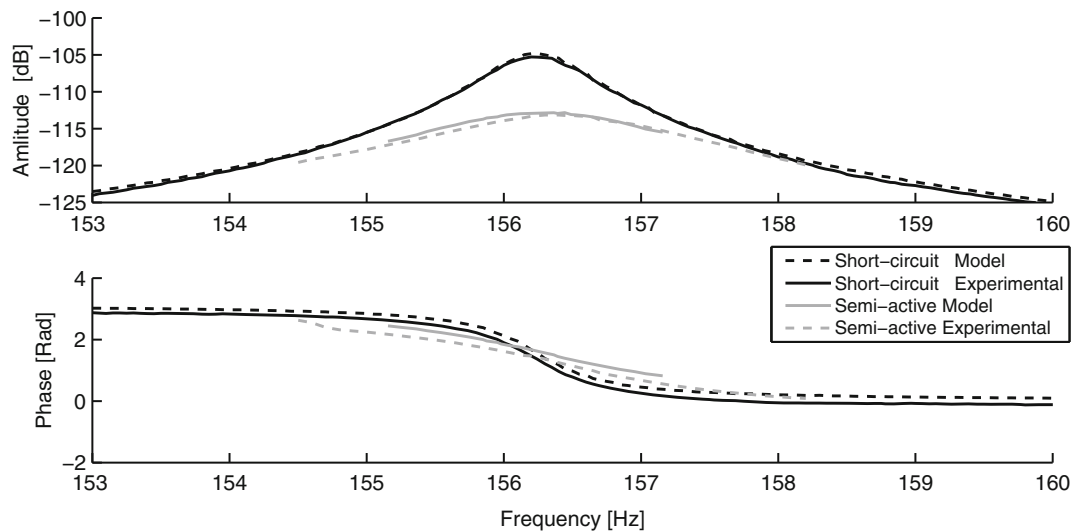


**Fig. 10.6** Experimental validation of the model presented in Sect. 10.3; the shown graphs are the amplitude and the phase of  $T_{zw}$

to achieve them; in fact these tests are quite long to perform). The model is capable to achieve a satisfactory description of experimental evidence. The switch was controlled by means of a very fast FPGA processor during tests.

The next section proposes the SSDI method evolution to control a single mode with random disturbance, allowing to overcome the problems evidenced at the end of Sect. 10.2.

## 10.4 Evolution of the SSDI Technique

The necessity to improve the SSDI technique has been underlined at the end of Sect. 10.2.

Therefore, a different approach has been adopted, trying to improve the control performance. The switch is not closed in correspondence of the maxima/minima of the filtered signal in this case. When a maximum/minimum of this filtered signal is recognized, the following maximum/minimum of the unfiltered signal is waited for acting on the switch. This allows to have a high voltage jump and thus a satisfying control performance. Figure 10.7 shows the signal time-histories with this new approach, while Fig. 10.8 depicts the attenuation achieved when controlling the two different modes. The results shown in Figs. 10.7 and 10.8 are numerical. The next task is the experimental validation of the new proposed technique.

It is obvious that the time lag between the maxima/minima of the filtered and unfiltered signals must be as less as possible in order to obtain the maximum control performance [15].

Figure 10.8 shows that controlling the mode at about 310 Hz allows to achieve vibration attenuation also on the mode at about 155 Hz. The reason is that the latter mode has a frequency which is about half of the former mode, in accordance with literature.

## 10.5 Conclusion

This paper focuses on semi-active vibration reduction by means of piezo-benders and shunt time-variant impedances. Particularly, attention is focused on the SSDI technique applied to single mode control in presence of a random disturbance.

Drawbacks of the mentioned method are underlined within the paper, showing that sometimes it can fail. Therefore, an alternative method (which actually is an evolution of SSDI) is proposed and its effectiveness is proved numerically. The next task is its experimental validation.



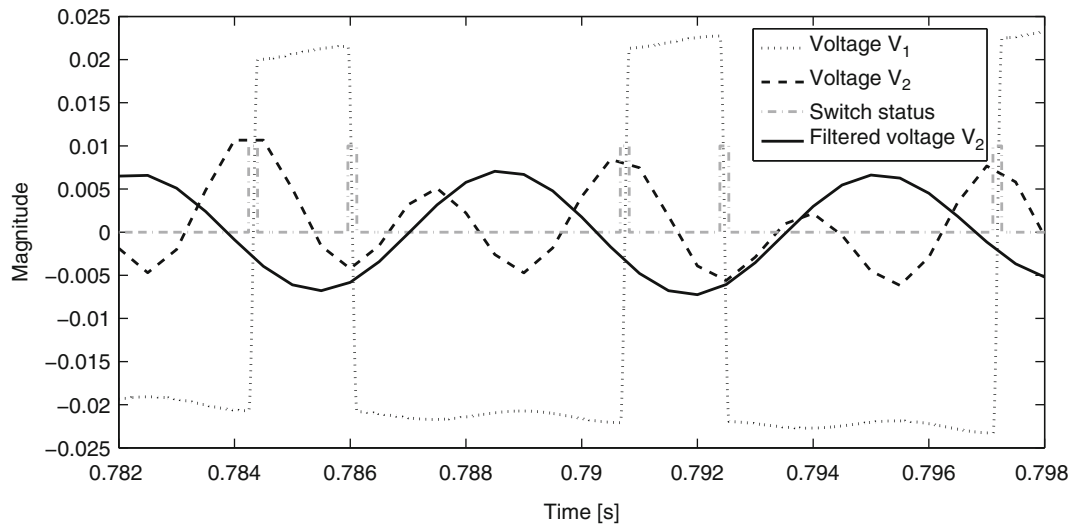


**Fig. 10.7** Time-histories of the electric variables for the improved SSDI technique (numerical results)

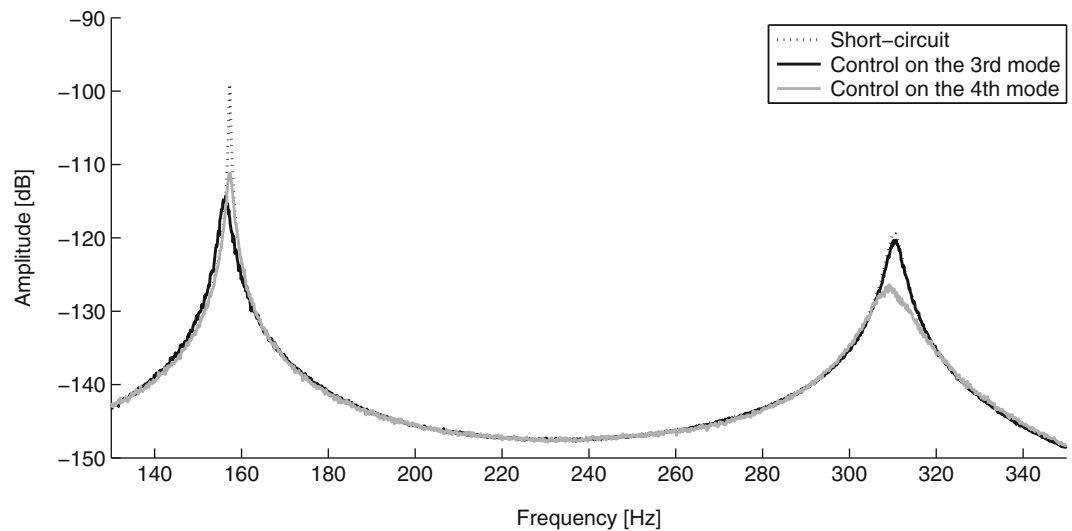


**Fig. 10.8** Amplitude of  $T_{zw}$  in case of short-circuit configuration and when controlling two different modes (i.e. the third and the fourth of the cantilever beam described in Sect. 10.3) with the new proposed evolution of the SSDI method (numerical results)

## References

1. Hagood NW, von Flotow A (1991) Damping of structural vibrations with piezoelectric materials and passive electrical networks. *J Sound Vib* 146:243–268
2. Neubauer M, Han X, Schwarzendahl SM (2011) Enhanced switching law for synchronized switch damping on inductor with bimodal excitation. *J Sound Vib* 330:2707–2720
3. Behrens S, Moheimani SOR, Fleming AJ (2003) Multiple mode current flowing passive piezoelectric shunt controller. *J Sound Vib* 266:929–942
4. Lefeuvre E, Badel A, Petit L, Richard C, Guyomar D (2006) Semi-passive piezoelectric structural damping by synchronized switching on voltage source. *J Intell Mater Syst Struct* 17:653–660
5. Cigada A, Manzoni S, Redaelli M, Vanali M (2012) Optimization of the current flowing technique aimed at semi-passive multi-modal vibration reduction. *J Vib Control* 18:298–312
6. de Marneffe B, Preumont A (2008) Vibration damping with negative capacitance shunts: theory and experiment. *Smart Mater Struct* 17:article number 035015
7. Manzoni S, Moschini S, Redaelli M, Vanali M (2012) Vibration attenuation by means of piezoelectric transducer shunted to synthetic negative capacitance. *J Sound Vib* 331:4644–4657

8. Guyomar D, Badel A (2006) Nonlinear semi-passive multimodal vibration damping: an efficient probabilistic approach. *J Sound Vib* 294:249–268
9. Corr LR, Clark WV (2001) Energy dissipation analysis of a piezoceramic semi-active vibration reduction. *J Intell Mater Syst Struct* 12:729–736
10. Richard C, Guyomar D, Audigier D, Ching G (1999) Semi-passive damping using continuous switching of a piezoelectric device. *Proc SPIE – Int Soc Opt Eng* 3672:104–111
11. Richard C, Guyomar D, Audigier D, Bassaler H (2000) Enhanced semi passive damping using continuous switching of a piezoelectric device on an inductor. *Proc SPIE – Int Soc Opt Eng* 3989:288–299
12. Moheimani SOR, Fleming AJ (2006) Piezoelectric transducers for vibration control and damping. Springer, London
13. Preumont A (2006) Mechatronics: dynamics of electromechanical and piezoelectric systems. Springer, Dordrecht
14. Agneni A, Balis Crema L, Sgubini S (2003) Damping by piezoceramic devices with passive loads. *Mech Syst Signal Process* 17:1097–1114
15. Chérif A, Richard C, Guyomar D, Belkhiat S, Meddad M (2012) Simulation of multimodal vibration damping of a plate structure using a modal SSDI-Max technique. *J Intell Mater Struct* 23:675–689

# Chapter 11

## Geometrically Nonlinear Dynamic Analysis of Piezoelectric Integrated Thin-Walled Smart Structures

S.Q. Zhang and R. Schmidt

**Abstract** In this work, a fully geometrically nonlinear dynamic finite element (FE) model, which considers the kinematics of small strains but large rotations, is developed for transient analysis of piezolaminated thin-walled structures based on first-order shear deformation (FOSD) hypothesis. Linear electro-mechanically coupled constitutive equations and the assumption of linearly distributed electric potential through the thickness of the piezoelectric layers are employed. An eight-node quadrilateral plate/shell element with five mechanical degrees of freedom (DOFs) per node and one electrical DOF per smart layer is adopted in the finite element formulation. The second order differential dynamic equation is solved by the central difference algorithm. The mathematical method is validated by transient analysis of three different examples of a beam, a plate, and a cylindrical shell. The results illustrate that the geometrical nonlinearity affects the structural dynamic responses significantly.

**Keywords** Geometrically nonlinear • Large rotation • Smart structure • Piezoelectric • Dynamic analysis

### 11.1 Introduction

Smart structures are those integrated with smart materials, e.g. piezoelectrics, electrostrictives, magnetostrictives, etc. as sensors and actuators in a feedback architecture. Due to a number of beneficial properties of thin-walled smart structures, the applications are increasingly implemented in many fields of technology, like e.g. automotive and aerospace engineering, for vibration control, shape control, noise and acoustic control, damage detection, health monitoring, etc. Numerous papers in literature presented linear two-dimensional (2D) finite element models using various hypotheses, e.g. Bernoulli beam theory [27, 28], classical Kirchhoff-Love plate/shell theory [12, 15, 19, 29], Timoshenko beam theory [21, 22], and Mindlin-Reissner plate/shell theory known as FOSD hypothesis [1, 2, 18, 20, 24, 31]. In order to deal with thick structures, third-order shear deformation (TOSD) hypothesis or higher-order shear deformation (HOSD) hypothesis have been developed by Reddy [25], Hanna and Leissa [10], Correia et al. [5, 6], and Schmidt [26] among many others. Besides, many other shear deformation hypotheses, like e.g. zigzag [8, 11] and layerwise [30] shear deformation theories have been developed for laminated structures.

Linear theory is only valid in the range of small deformations, since geometrical nonlinearity significantly affects both the static and dynamic responses of largely deformed thin-walled smart structures. Most of the papers in literature concerning geometrical nonlinearity are dealing with isotropic or orthotropic thin-walled structures using various nonlinear theories, e.g. von Kármán type nonlinear theory, moderate rotation theory, and large rotation theory. There are some papers in literature

---

S.Q. Zhang (✉)  
Institute of General Mechanics, RWTH Aachen University, Templergraben 64,  
D-52062 Aachen, Germany

School of Mechanical Engineering, Northwestern Polytechnical University,  
710072 Xi'an, P. R. China  
e-mail: [shunqi@iam.rwth-aachen.de](mailto:shunqi@iam.rwth-aachen.de); [sqzhangnpu@hotmail.com](mailto:sqzhangnpu@hotmail.com)

R. Schmidt  
Institute of General Mechanics, RWTH Aachen University, Templergraben 64,  
D-52062 Aachen, Germany  
e-mail: [schmidt@iam.rwth-aachen.de](mailto:schmidt@iam.rwth-aachen.de)

taking geometrical nonlinearity into account in static and dynamic analysis of smart structures recently, but only a few of them consider large rotations in their theories. Dash [7], Panda [23], Schmidt and Vu [26], etc. developed nonlinear FE models for piezoelectric embedded structures based on refined von Kármán nonlinear theory. Lentzen and Schmidt [16, 17] presented a moderate rotation theory for dynamic analysis of piezoelectric integrated smart structures in FOSD hypothesis. Yi et al. [32] developed a solid nonlinear FE model for transient analysis of smart structures. Furthermore, Chróscielewski, Klosowski and Schmidt [3, 4] developed a model based on fully nonlinear large rotation theory for shape and vibration control of curved beams.

Von Kármán type nonlinear theory and moderate rotation theory can predict structural dynamic behavior only in the range of validity of the underlying kinematical assumptions leading to simplified nonlinear strain-displacement relations. The aim of this paper is to develop a fully geometrically nonlinear dynamic finite shell element model by large rotation theory based on FOSD hypothesis for transient analysis of piezoelectric integrated thin-walled smart structures. Linear electro-mechanically coupled constitutive equations and the assumption of constant electric field intensity through the thickness of a piezoelectric layer are employed. An eight-node quadrilateral plate/shell element with five mechanical DOFs per node and one DOF per smart layer is adopted in the finite element modeling. The present nonlinear finite element model is implemented for the simulation of the dynamic responses of a beam, a plate and a cylindrical shell with piezoelectric integrated patches.

## 11.2 Numerical Methods

### 11.2.1 Nonlinear Strain Terms

The large rotation theory, which contains fully geometrically nonlinear strain-displacement relations with six independent kinematic parameters but expressed by five parameters, is abbreviated as LRT56 theory. This paper is based on the previous development of LRT56 theory by Kreja and Schmidt [13, 14], which was used for static analysis of isotropic or orthotropic laminated structures. The Green-Lagrange strain tensors for LRT56 theory based on FOSD hypothesis with the kinematics of small strains but large rotations are expressed by Habip [9]

$$\varepsilon_{\alpha\beta} = \varepsilon_{\alpha\beta}^0 + \Theta^3 \varepsilon_{\alpha\beta}^1 + (\Theta^3)^2 \varepsilon_{\alpha\beta}^2 \quad (11.1)$$

$$\varepsilon_{\alpha 3} = \varepsilon_{\alpha 3}^0 + \Theta^3 \varepsilon_{\alpha 3}^1 \quad (11.2)$$

$$\varepsilon_{33} = 0 \quad (11.3)$$

The transverse normal strain is neglected, since no thickness change is considered. The components of the Green-Lagrange strain tensor in Eqs. (11.1) and (11.2) are given by

$$2\varepsilon_{\alpha\beta}^0 = \varphi_{\alpha\beta}^0 + \varphi_{\beta\alpha}^0 + a^{\lambda\delta} \varphi_{\lambda\alpha}^0 \varphi_{\delta\beta}^0 + \varphi_{3\alpha}^0 \varphi_{3\beta}^0 \quad (11.4)$$

$$\begin{aligned} 2\varepsilon_{\alpha\beta}^1 &= \varphi_{\alpha\beta}^1 + a^{\lambda\delta} \varphi_{\lambda\alpha}^0 \varphi_{\delta\beta}^1 + \varphi_{3\alpha}^0 \varphi_{3\beta}^1 - b_{\beta}^{\lambda} \varphi_{\lambda\alpha}^0 \\ &+ \varphi_{\beta\alpha}^1 + a^{\lambda\delta} \varphi_{\lambda\alpha}^1 \varphi_{\delta\beta}^0 + \varphi_{3\alpha}^1 \varphi_{3\beta}^0 - b_{\alpha}^{\delta} \varphi_{\delta\beta}^0 \end{aligned} \quad (11.5)$$

$$2\varepsilon_{\alpha\beta}^2 = a^{\lambda\delta} \varphi_{\lambda\alpha}^1 \varphi_{\delta\beta}^1 + \varphi_{3\alpha}^1 \varphi_{3\beta}^1 - b_{\beta}^{\lambda} \varphi_{\lambda\alpha}^1 - b_{\alpha}^{\delta} \varphi_{\delta\beta}^1 \quad (11.6)$$

$$2\varepsilon_{\alpha 3}^0 = v_{\alpha}^1 + a^{\lambda\delta} \varphi_{\lambda\alpha}^0 v_{\delta}^1 + \varphi_{3\alpha}^0 v_{3}^1 + \varphi_{3\alpha}^0 \quad (11.7)$$

$$2\varepsilon_{\alpha 3}^1 = a^{\lambda\delta} \varphi_{\lambda\alpha}^1 v_{\delta}^1 + \varphi_{3\alpha}^1 v_{3}^1 + \varphi_{3\alpha}^1 - b_{\alpha}^{\delta} v_{\delta}^1 \quad (11.8)$$

with

$$\varphi_{\lambda\alpha}^n = v_{\lambda|\alpha}^n - b_{\lambda\alpha}^n v_3^n$$

$$\varphi_{3\alpha}^n = v_{3,\alpha}^n + b_{\alpha}^{\delta} v_{\delta}^n$$

$$v_{\lambda|\alpha}^n = v_{\lambda,\alpha}^n - \Gamma_{\lambda\alpha}^{\delta} v_{\delta}^n$$

in which  $b_{\lambda\alpha}$  and  $b_{\alpha}^{\lambda}$  are the covariant and mixed components of the curvature tensor,  $\Gamma_{\lambda\alpha}^{\delta}$  the Christoffel symbols of the second kind, and  $(\cdot)_{,\alpha}$  represents the spacial derivative with respect to the coordinate axis  $\Theta^{\alpha}$ . In Eqs. (11.4)–(11.8), six independent kinematical parameters, namely, the three mid-surface displacements ( $v_1^0$ ,  $v_2^0$  and  $v_3^0$ ), and three generalized rotational displacements ( $v_1^1$ ,  $v_2^1$  and  $v_3^1$ ), are considered. Following [14], the latter ones are expressed by two Euler angles using the assumption of an inextensible director.

### 11.2.2 Constitutive Equations

Linear electro-mechanically coupled constitutive equations are employed in the present model, which are given by

$$\{\alpha\} = [c]\{\''\} - [e]^T\{E\} \quad (11.9)$$

$$\{D\} = [e]\{\''\} + [\epsilon]\{E\} \quad (11.10)$$

where  $\{\alpha\}$ ,  $\{\''\}$ ,  $\{D\}$ , and  $\{E\}$  denote the stress vector, the strain vector, the electric displacement vector, and the electric field vector, respectively. Furthermore,  $[c]$  represents the elasticity matrix,  $[e] = [d][c]$ ,  $[d]$  is the piezoelectric constant matrix, and  $[\epsilon]$  the dielectric constant matrix. The electric field intensity is calculated as the negative gradient of the electric potential  $\{\mathcal{E}\}$  applied on each piezoelectric layer, which can be expressed as

$$\{E\} = -\text{grad}\{\mathcal{E}\} = [B_{\mathcal{E}}]\{\mathcal{E}\} \quad (11.11)$$

where  $[B_{\mathcal{E}}]$  is the electric field matrix.

### 11.2.3 Dynamic Equations

By using Hamilton's principle and finite element method, the nonlinear dynamic equation and the sensor equation can be derived as

$$[{}^1M_{uu}]\{\Delta\ddot{q}\} + [{}^1\bar{K}_{uu}]\{\Delta q\} + [{}^1K_{u\mathcal{E}}]\{\Delta\mathcal{E}\} = \{F_{ue}\} - \{{}^1F_{ui}\} \quad (11.12)$$

$$[{}^1K_{\mathcal{E}u}]\{\Delta q\} + [{}^1K_{\mathcal{E}\mathcal{E}}]\{\Delta\mathcal{E}\} = \{G_{\mathcal{E}e}\} - \{{}^1G_{\mathcal{E}i}\} \quad (11.13)$$

where  $[{}^1M_{uu}]$  denotes the mass matrix,  $[{}^1\bar{K}_{uu}]$  the total stiffness,  $[{}^1K_{u\mathcal{E}}]$  the coupling stiffness,  $[{}^1K_{\mathcal{E}u}]$  the coupling capacity,  $[{}^1K_{\mathcal{E}\mathcal{E}}]$  the piezoelectric capacity,  $\{F_{ue}\}$ ,  $\{{}^1F_{ui}\}$ ,  $\{G_{\mathcal{E}e}\}$  and  $\{{}^1G_{\mathcal{E}i}\}$  are the external force, the in-balance force, the external charge and the in-balance charge, respectively. Additionally, the total stiffness, the in-balance force and charge are composed of nonlinear terms as

$$[{}^1\bar{K}_{uu}] = [{}^1K_{uu}] + [{}^1K_{ug}] + [{}^1K_{\mathcal{E}g}] \quad (11.14)$$

$$\{{}^1F_{ui}\} = \{{}^1F_{uu}\} + \{{}^1F_{u\mathcal{E}}\} \quad (11.15)$$

$$\{{}^1G_{\mathcal{E}i}\} = \{{}^1F_{\mathcal{E}u}\} + \{{}^1F_{\mathcal{E}\mathcal{E}}\} \quad (11.16)$$

Here,  $[{}^1K_{uu}]$  denotes the linear stiffness,  $[{}^1K_{ug}]$  and  $[{}^1K_{\mathcal{E}g}]$  are the geometrically induced stiffnesses obtained by mechanically and electrically induced stresses respectively. Furthermore,  $\{{}^1F_{uu}\}$  and  $\{{}^1F_{u\mathcal{E}}\}$  represent the mechanically and electrically induced in-balance force,  $\{{}^1F_{\mathcal{E}u}\}$  and  $\{{}^1F_{\mathcal{E}\mathcal{E}}\}$  are the mechanically and electrically induced in-balance charge.

### 11.2.4 Central Difference Method

The dynamic equation without any external electric potential applied on the piezoelectric layer at time  $t$  is expressed as

$$[M_{uu}]_t\{\ddot{q}\}_t + [K_{uu}]_t\{\Delta q\} = \{F_{ue}\}_t - \{F_{ui}\}_t \quad (11.17)$$

The central difference method is designed for solving the second order nonlinear dynamic differential equation. The approximations of acceleration  $\{\ddot{q}\}$  and velocity  $\{\dot{q}\}$  at time  $t$  are defined as

$$\{\ddot{q}\}_t = \frac{1}{(\Delta t)^2} \left( \{q\}_{t+\Delta t} - 2\{q\}_t + \{q\}_{t-\Delta t} \right) \quad (11.18)$$

$$\{\dot{q}\}_t = \frac{1}{2(\Delta t)} \left( \{q\}_{t+\Delta t} - \{q\}_{t-\Delta t} \right) \quad (11.19)$$

Substituting these two assumptions into the equation of motion yields the displacement at time  $t + \Delta t$  as

$$\{q\}_{t+\Delta t} = \frac{1}{(\Delta t)^2} [M_{uu}]_t^{-1} \{F^{\text{Residual}}\}_t \quad (11.20)$$

where

$$\begin{aligned} \{F^{\text{Residual}}\}_t &= \{F_{ue}\}_t - \{F_{ui}\}_t + \frac{1}{(\Delta t)^2} [M_{uu}]_t (2\{q\}_t - \{q\}_{t-\Delta t}) \\ &+ [K_{uu}]_t (\{q\}_{t-\Delta t} - \{q\}_t) \end{aligned} \quad (11.21)$$

For the first step, the displacement at time  $t - \Delta t$  can be derived as

$$\{q\}_{t-\Delta t} = \{q\}_t + (\Delta t)\{\dot{q}\}_t + \frac{(\Delta t)^2}{2}\{\ddot{q}\}_t \quad (11.22)$$

where  $\{q\}_t$  and  $\{\dot{q}\}_t$  are prescribed, and  $\{\ddot{q}\}_t$  is calculated as

$$\{\ddot{q}\}_t = [M_{uu}]_t^{-1} \left( \{F_{ue}\}_t - \{F_{ui}\}_t - [K_{uu}]_t \{\Delta q\}_t \right) \quad (11.23)$$

### 11.3 Example Simulations

In this section, the transient analysis of smart plates and shells, which considers the fully geometrically nonlinear strains with large rotations, are presented. These examples which can be found in [32] are calculated using the present nonlinear dynamic equation and sensor equation. The piezoelectric materials involved are the same in all examples. The material properties are taken as  $E = 67 \text{ GPa}$ ,  $\nu = 0.33$ ,  $\rho = 7,800 \text{ kg/m}^3$ ,  $d_{31} = d_{32} = -1.7119 \times 10^{-10} \text{ C/N}$ , and  $\epsilon_{33} = 2.03 \times 10^{-8} \text{ F/m}$ . An eight-node quadrilateral element with five mechanical DOFs per node and one DOF per smart layer, the element type of which is abbreviated as SH851FI, is employed through the following calculations.

#### 11.3.1 Cantilevered Beam

The first example is a cantilevered beam bonded with a piezoelectric patch, presented in Fig. 11.1. The host structure is made of an isotropic material with the Young's modulus  $E = 197 \text{ GPa}$ , the Poisson's ratio  $\nu = 0.33$ , and the density  $\rho = 7,900 \text{ kg/m}^3$ . The dimensions of the host structure and the PZT patch are  $300 \times 15 \times 1 \text{ mm}$  and  $60 \times 15 \times 1 \text{ mm}$ , respectively. The piezoelectric patch is bonded on the host beam at a distance of 60 mm from the cantilevered end. The structure is meshed with  $10 \times 1$  SH851FI elements along  $\Theta^1$  and  $\Theta^2$  axes, 53 nodes in total. A step force of 10 N is applied on the tip point at the free end. The linear dynamic response is solved by Newmark algorithm with a time step of  $1 \times 10^{-3} \text{ s}$ , and the nonlinear case is calculated by central difference method with a time step of  $1 \times 10^{-7} \text{ s}$ , which are shown in Fig. 11.2. The corresponding voltages output from the piezoelectric patch are presented in Fig. 11.3. It can be seen that there is a big difference between the linear and nonlinear simulations, since the beam undergoes large deformation. The linear theory overpredicts the displacements and consequently the sensor output voltages. The nonlinear theory accounts for the shear stiffening resulting in smaller amplitude and higher frequency.

**Fig. 11.1** Cantilevered beam with a bonded piezoelectric patch

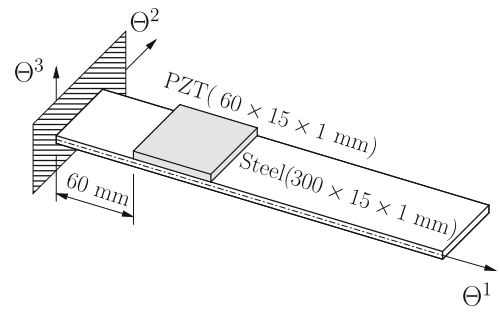


**Fig. 11.2** Tip displacement of the cantilevered beam over time

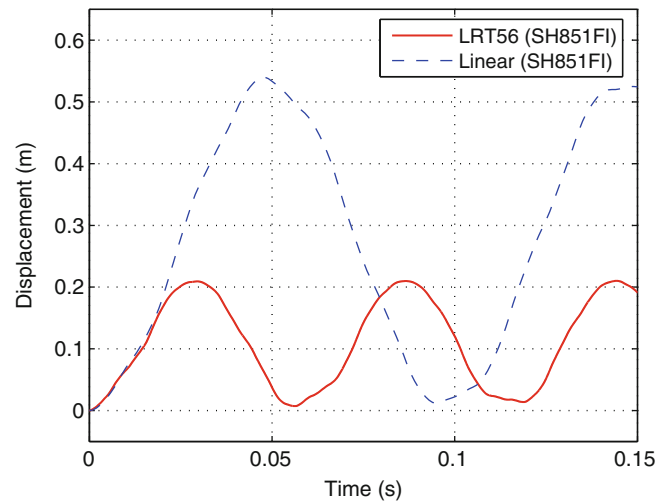
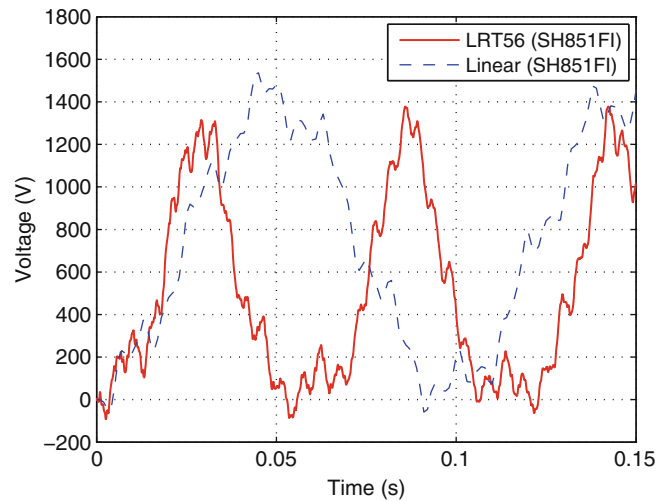


**Fig. 11.3** Sensor voltage output of the cantilevered beam over time



### 11.3.2 Fully Clamped Plate

The second example is a fully clamped plate with a piezoelectric patch centrally bonded on the top surface, illustrated in Fig. 11.4. The material properties of the host structure are the same as for the cantilevered beam in the first example. The dimensions of the host plate are  $100 \times 100 \times 1$  mm, and  $20 \times 20 \times 1$  mm for the piezoelectric patch. A quarter plate with a mesh of  $5 \times 5$  elements, 96 nodes in total, is simulated by using the same element type and integration scheme as the beam in the first application. The plate is subjected to a uniformly distributed step load of  $2 \times 10^4$  N/m<sup>2</sup>. The linear and nonlinear dynamic responses are calculated by the same methods as the beam, but with a time step of  $2 \times 10^{-5}$  s for linear

**Fig. 11.4** Fully clamped plate with a piezoelectric patch centrally bonded

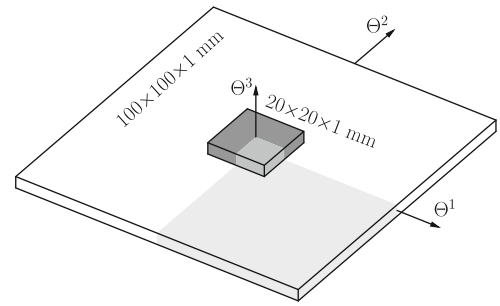


**Fig. 11.5** Central displacement of the clamped plate over time

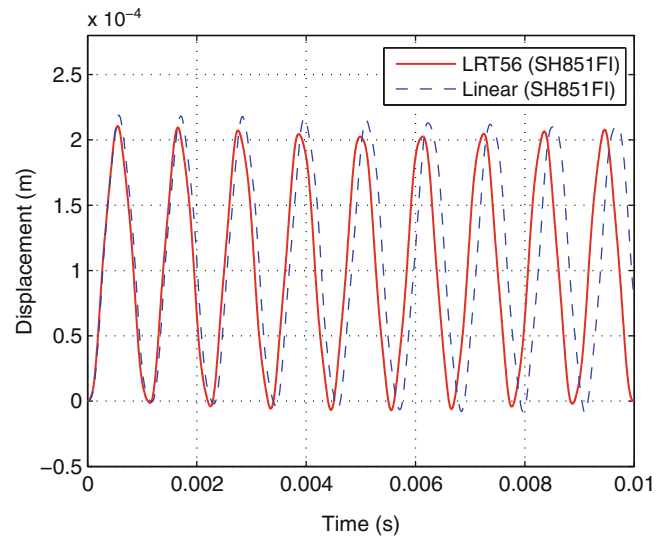
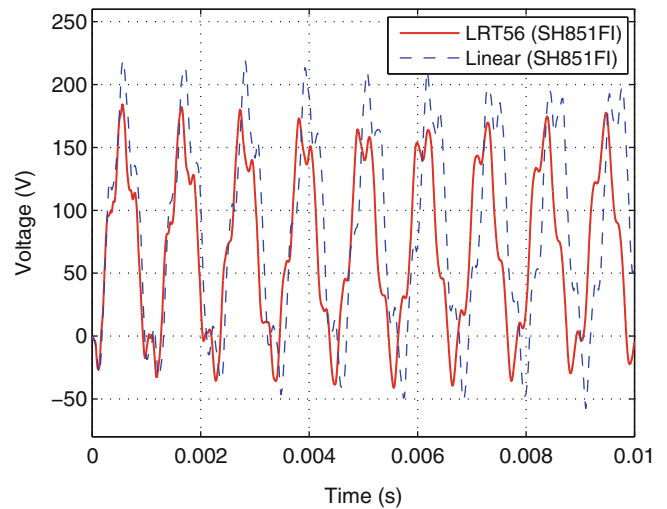


**Fig. 11.6** Sensor voltage output of the clamped plate over time



case, and  $1 \times 10^{-7}$  s for nonlinear case. The displacement of the mid-point and the sensor output voltage for both linear and nonlinear simulations of the dynamic response are presented in Figs. 11.5 and 11.6, respectively. The results illustrate that small deformations lead to small nonlinear effects on structural dynamics. Like in the previous example, the linear simulation overpredicts both the deflections and the sensor voltages.



**Fig. 11.7** Fully clamped cylindrical shell with a piezoelectric patch centrally bonded

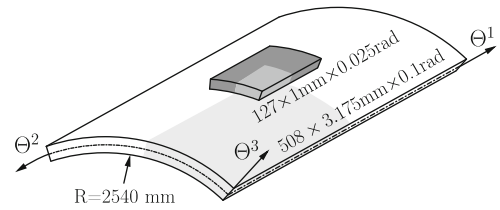


**Fig. 11.8** Central displacement of the clamped cylindrical shell over time

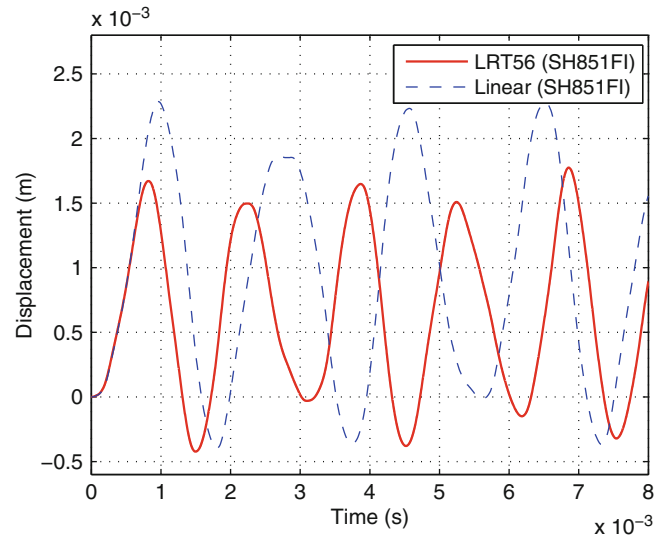
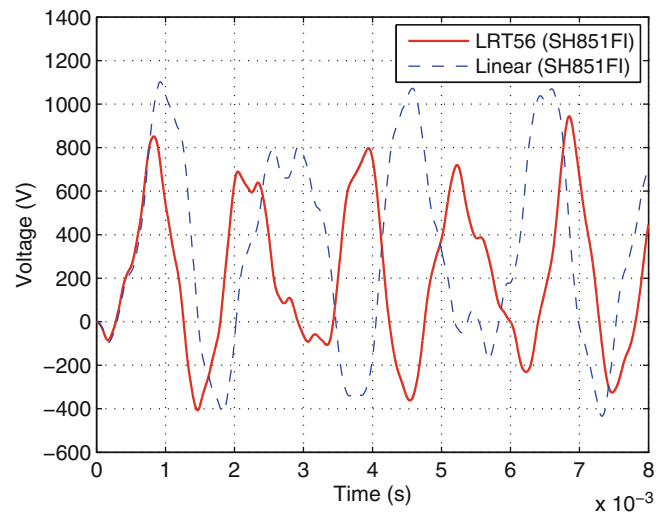


**Fig. 11.9** Sensor voltage output of the clamped cylindrical shell over time



### 11.3.3 Fully Clamped Cylindrical Shell

The last example is a fully clamped cylindrical shell with a piezoelectric patch bonded on the center of the top surface as depicted in Fig. 11.7. The host structure is made up of an orthotropic material with a fiber reinforcement along the  $\Theta^1$  direction. The material parameters of the host cylindrical shell are taken as  $E_1 = 124$  GPa,  $E_2 = 96.53$  GPa,  $\nu_{12} = \nu_{23} = 0.34$ ,  $G_{12} = G_{13} = G_{23} = 6.205$  GPa, and  $\rho = 1,520$  kg/m<sup>3</sup>. A uniform step pressure of  $6 \times 10^4$  N/m<sup>2</sup> is applied in the outward direction. Due to the symmetry of the structure, a quarter of the cylindrical shell with a mesh of  $8 \times 4$  along the  $\Theta^1$  and  $\Theta^2$  axes is considered for computation. The time steps for linear and nonlinear calculations are the same as for the fully clamped plate in the second example. The linear and nonlinear results are displayed in Figs. 11.8 and 11.9, respectively. In

contrast to the previous example, here the nonlinear effects are profound. Again, the linear theory, which does not account for the stress stiffening effects, predicts considerably larger displacements and sensor voltages than the nonlinear theory.

## 11.4 Conclusion

A fully geometrically nonlinear theory with the kinematics of small strains but large rotations has been proposed to perform transient analysis for plate/shell structures. The nonlinear dynamic electro-mechanically coupled equation and the sensor equation have been derived based on FOSD hypothesis and solved by central difference algorithm. Three examples have been analyzed with the present dynamic and sensor equation. The results show that the geometrical nonlinearity has significant influence on the structural dynamic responses.

## References

- Balamurugan V, Narayanan S (2001) Shell finite element for smart piezoelectric composite plate/shell structures and its application to the study of active vibration control. *Finite Elem Anal Des* 37:713–738
- Cen S, Soh AK, Long YQ, Yao ZH (2002) A new 4-node quadrilateral FE model with variable electrical degrees of freedom for the analysis of piezoelectric laminated composite plates. *Compos Struct* 58:583–599
- Chróscielewski J, Klosowski P, Schmidt R (1997) Numerical simulation of geometrically nonlinear flexible beam control via piezoelectric layers. *ZAMM Suppl* 1:S69–S70
- Chróscielewski J, Klosowski P, Schmidt R (1998) Theory and numerical simulation of nonlinear vibration control of arches with piezoelectric distributed actuators. *13. Mach Dyn Probl* 20:73–90
- Correia IFP, Soares CMM, Soares CAM, Herskovits J (2002) Active control of axisymmetric shells with piezoelectric layers: a mixed laminated theory with a high order displacement field. *Comput Struct* 80:2265–2275
- Correia VMF, Gomes MAA, Suleman A, Soares CMM, Soares CAM (2000) Modelling and design of adaptive composite structures. *Comput Methods Appl Mech Eng* 185:325–346
- Dash P, Singh BN (2009) Nonlinear free vibration of piezoelectric laminated composite plate. *Finite Elem Anal Des* 45:686–694
- Fares ME, Elmaghany MKh (2008) A refined zigzag nonlinear first-order shear deformation theory of composite laminated plates. *Compos Struct* 82:71–83
- Habip LM (1965) Theory of elastic shells in the reference state. *Ingenieur-Archiv* 34:228–237
- Hanna NF, Leissa AW (1994) A higher order shear deformation theory for the vibration of thick plates. *J Sound Vib* 170:545–555
- Kapuria S (2001) An efficient coupled theory for multilayered beams with embedded piezoelectric sensory and active layers. *Int J Solids Struct* 38:9179–9199
- Kioua H, Mirza S (2000) Piezoelectric induced bending and twisting of laminated composite shallow shells. *Smart Mater Struct* 9:476–484
- Kreja I (2007) Geometrically non-linear analysis of layered composite plates and shells. Habilitation Thesis, Politechnika Gdańska
- Kreja I, Schmidt R (2006) Large rotations in first-order shear deformation FE analysis of laminated shells. *Int J Nonlinear Mech* 41:101–123
- Lam KY, Peng XQ, Liu GR, Reddy JN (1997) A finite-element model for piezoelectric composite laminates. *Smart Mater Struct* 6:583–591
- Lentzen S, Schmidt R (2005) A geometrically nonlinear finite element for transient analysis of piezolaminated shells. In: *Proceedings fifth EUROMECH nonlinear dynamics conference, Eindhoven, 7–12 August 2005*
- Lentzen S, Klosowski P, Schmidt R (2007) Geometrically nonlinear finite element simulation of smart piezolaminated plates and shells. *Smart Mater Struct* 16:2265–2274
- Lin CC, Hsu CY, Huang HN (1996) Finite element analysis on deflection control of plates with piezoelectric actuators. *Compos Struct* 35:423–433
- Liu GR, Peng XQ, Lam KY, Tani J (1999) Vibration control simulation of laminated composite plates with integrated piezoelectrics. *J Sound Vib* 220:827–846
- Liu GR, Dai KY, Lim KM (2004) Static and vibration control of composite laminates integrated with piezoelectric sensors and actuators using the radial point interpolation method. *Smart Mater Struct* 13:1438–1447
- Manjunath TC, Bandyopadhyay B (2009) Vibration control of Timoshenko smart structures using multirate output feedback based discrete sliding mode control for SISO systems. *J Sound Vib* 326:50–74
- Narayanan S, Balamurugan V (2003) Finite element modeling of piezolaminated smart structures for active vibration control with distributed sensors and actuators. *J Sound Vib* 262:529–562
- Panda S, Ray MC (2008) Nonlinear finite element analysis of functionally graded plates integrated with patches of piezoelectric fiber reinforced composite. *Finite Elem Anal Des* 44:493–504
- Ray MC, Reddy JN (2005) Active control of laminated cylindrical shells using piezoelectric fiber reinforced composites. *Compos Sci Technol* 65:1226–1236
- Reddy JN (1990) A general non-linear third-order theory of plates with moderate thickness. *Int J Nonlinear Mech* 25:677–686
- Schmidt R, Vu TD (2009) Nonlinear dynamic FE simulation of smart piezolaminated structures based on first- and third-order transverse shear deformation theory. *Adv Mater Res* 79–82:1313–1316
- Stavroulakis GE, Foutsitzi G, Hadjigeorgiou E, Marinova D, Baniotopoulos CC (2005) Design and robust optimal control of smart beams with application on vibrations suppression. *Adv Eng Softw* 36:806–813

28. Tzou HS, Chai WK (2007) Design and testing of a hybrid polymeric electrostrictive/piezoelectric beam with bang-bang control. *Mech Syst Signal Process* 21:417–429
29. Tzou HS, Gadre M (1989) Theoretical analysis of a multi-layered thin shell coupled with piezoelectric shell actuators for distributed vibration controls. *J Sound Vib* 132:433–450
30. Vasques CMA, Rodrigues JD (2005) Coupled three-layered analysis of smart piezoelectric beams with different electric boundary conditions. *Int J Numer Methods Eng* 62:1488–1518
31. Wang SY (2004) A finite element model for the static and dynamic analysis of a piezoelectric bimorph. *Int J Solids Struct* 41:4075–4096
32. Yi S, Ling SF, Ying M (2000) Large deformation finite element analyses of composite structures integrated with piezoelectric sensors and actuators. *Finite Elem Anal Des* 35:1–15

# Chapter 12

## Linear/Nonlinear Reduced-Order Substructuring for Uncertainty Quantification and Predictive Accuracy Assessment

Timothy Hasselman, George Lloyd, and Ryan Schnalzer

**Abstract** Modal testing is routinely performed on space craft and launch vehicles to “verify” (calibrate and validate) analytical models. Large multi-component structures such as the Space Transportation System (STS) or “Space Shuttle,” and the newly proposed NASA Space Launch System (SLS), are impractical to test in their assembled configurations. Alternatively, substructure testing of these multi-component structures has been performed and used to calibrate/validate analytical models of the substructures, which are then assembled to analyze system response to applied loads. This paper describes a methodology applicable to uncertainty quantification (UQ) of reduced (modal) models of linear (or linearized) finite element models of substructures, as well as reduced (stochastic neural net (SNN)) models of nonlinear substructures, such as joints. The UQ at reduced substructure levels is propagated to higher levels of assembly by efficient means, enabling predictive accuracy assessment at the coupled system level. UQ is based entirely on comparisons on analysis and test data at the substructure level so that recourse to the specification and quantification of element-level random variables is not necessary. Examples are presented to illustrate the methodology.

**Keywords** Uncertainty quantification • Linear and nonlinear substructuring • Reduced-order models component mode synthesis • Stochastic neural networks • Uncertainty propagation • Predictive accuracy assessment

### 12.1 Introduction

Neither the classical Craig-Bampton CMS method requiring fixed-interface static and dynamic modes nor any of the free-interface dynamic mode CMS methods requiring flexibility-based attachment modes [1] are appropriate for CMS based on experimental modes (a requirement for the test-analysis type of UQ proposed here) because of the implied requirement for special test fixturing. An attractive alternative is based on mass-loaded (or mass-additive) free-free modes described in [2–4]. However, except for Reference [4] which does suggest a simplified “mass-additive” approach (not requiring static structural flexibility information or the transformation of free-free modes back to fixed interface modes suitable for the Craig-Bampton CMS approach), these methods are also awkward for substructure UQ and the propagation of substructures uncertainty to system levels. The following derivation is for direct CMS of substructures with mass-loaded interfaces.

This appendix follows the derivation in [5] with some notational changes to accommodate the data-based method of uncertainty quantification documented in [6] and the substructure-based method of uncertainty propagation documented in [12]. Together, [5, 6, 12] form the basis for the linear substructure uncertainty quantification and propagation proposed for this project.

---

T. Hasselman (✉) • G. Lloyd • R. Schnalzer  
ACTA Incorporated, 2790 Skypark Dr., Suite 310, Torrance, CA, USA  
e-mail: [hasselmann@actainc.com](mailto:hasselmann@actainc.com); [lloyd@actainc.com](mailto:lloyd@actainc.com); [Schnalzer@actainc.com](mailto:Schnalzer@actainc.com)

## 12.2 Reduced-Order Linear/Linearized Substructure Models

### 12.2.1 Substructure Equations of Motion

The derivation begins by writing the linear equations of motion for a major substructure, in this case Substructure A where here for notational simplicity the nodal degrees of freedom are ordered such that the boundary (interface) degrees of freedom follow the internal DOFs:

$$M^A \ddot{u}^A(t) + C^A \dot{u}^A(t) + K^A u^A(t) = F^A(t) \quad (12.1)$$

where  $M^A$ ,  $C^A$  and  $K^A$  represent the mass, damping and stiffness matrices of the substructure in the physical finite element model (FEM) nodal displacement coordinate system,  $u^A$ . The undamped eigenproblem may be stated

$$\left( K^A - \lambda_j^A M^A \right) \phi_j^A = 0 \quad (12.2)$$

where  $\lambda_j^A$  represents the  $j$ th eigenvalue and  $\phi_j^A$ , the corresponding modal eigenvector of the substructure equations of motion. Let us assume that these equations of motion represent the free-free configuration of the substructure, i.e. the substructure is suspended in space with no attachments. In reality, the structure must be supported for laboratory testing in a one-g environment. Bunge cords are typically used in such testing so that the rigid-body modes of the structure are well below the first flexural frequency.

### 12.2.2 Mass-Loaded Substructure Interfaces

Substructure boundaries or interfaces that connect to other substructures can be mass-loaded to exercise those portions of a substructure affected by connection with other substructures. These added masses are typically selected with the aid of finite element analysis (FEA) so as to achieve interface modes with frequencies in the range of the lowest structural system modes. Equation (12.1) can be rewritten to account for this added mass, denoted by  $\Delta M$ , as follows:

$$\left( M^A + \Delta M^A \right) \ddot{u}^A(t) + C^A \dot{u}^A(t) + K^A u^A(t) = F^A(t) \quad (12.3)$$

with the corresponding undamped eigenproblem

$$\left[ K^A - \bar{\lambda}_j^A \left( M^A + \Delta M^A \right) \right] \bar{\phi}_j^A = 0 \quad (12.4)$$

The “bar” notation on  $\bar{\lambda}^A$  and  $\bar{\phi}^A$  is used to denote variables associated with a substructure to which masses has been added to interface boundaries. The modes associated with Eq. (12.4) provide a transformation from the physical  $u^A$  coordinates to a set of reduced modal coordinates,  $p^A$ , associated with the mass-loaded free interface (MLFI) modes.

$$u^A = \bar{\phi}^A p^A \quad (12.5)$$

Transformation of Eq. (12.3) to the mass-loaded modal coordinates,  $\bar{p}^A$ , results in

$$\left( \bar{\phi}^{A^T} \bar{M}^A \bar{\phi}^A \right) \ddot{\bar{p}}^A + \left( \bar{\phi}^{A^T} C^A \bar{\phi}^A \right) \dot{\bar{p}}^A + \left( \bar{\phi}^{A^T} K^A \bar{\phi}^A \right) \bar{p}^A = \left( \bar{\phi}^A \right)^T F^A(t) \quad (12.6)$$

where the substitution  $\bar{M}^A = M^A + \Delta M^A$  has been made, and the argument,  $(t)$ , has been omitted from the LHS of the equation for simplicity.

Normalization of  $\bar{\phi}^A$  to unit modal mass results in

$$I^A \ddot{\bar{p}}^A + \bar{\xi}^A \dot{\bar{p}}^A + \bar{\lambda}^A \bar{p}^A = \left( \bar{\phi}^A \right)^T F^A(t) = F_p^A(t) \quad (12.7)$$

where  $I^A$  is an identity matrix corresponding to the mass-loaded mass matrix of Substructure A and  $\bar{\lambda}^A$  is the diagonal matrix of eigenvalues (modal frequencies squared). In general, the modal damping matrix,  $\bar{\xi}^A$ , will not be diagonal; however, when the modal frequencies are well separated, it may be approximated as a diagonal matrix where

$$\left( \bar{\xi}^A \right)_j = 2 \left( \bar{\xi}^A \right)_j \left( \bar{\omega}^A \right)_j \quad (12.8)$$

### 12.2.3 Substructure Uncertainty Quantification

The reason for using a free-free mode formulation of CMS is that it is not necessary to generate fixed interface modes experimentally for comparison with the analytical modes. The reason for using mass-loaded interface modes is so that the mass and stiffness properties of the substructures near their interface boundaries are represented in the absence of fixed interface modes. Using this approach, modeling uncertainty can be estimated at the substructure level by (1) directly comparing corresponding pairs of mass-loaded analysis and test mode sets, and (2) performing statistical analysis of these data to obtain correlated modal mass and stiffness parameters.

Some additional notational changes are introduced here to accommodate essential concepts in [6, 12]. In preparation for uncertainty quantification (UQ) as described in [6], it will be necessary to distinguish between analysis modes and test modes. However, unlike the notation in [6] where *analytical* eigenvalues and eigenvectors are denoted by  ${}^o\lambda$  and  ${}^o\phi$  respectively, we shall denote the MLFI *analysis* eigenvalues and eigenvectors as  ${}^a\bar{\lambda}^A$  and  ${}^a\bar{\phi}^A$  for substructure  $A$ , and  ${}^a\bar{\lambda}^B$  and  ${}^a\bar{\phi}^B$  for substructure  $B$ . Similarly, the corresponding MLFI *test* eigenvalues and eigenvectors are denoted by  ${}^t\bar{\lambda}^A$ ,  ${}^t\bar{\phi}^A$ ,  ${}^t\bar{\lambda}^B$ ,  ${}^t\bar{\phi}^B$  for substructures  $A$  and  $B$  respectively. Extension of the methodology to more than two substructures is straightforward, where numerals could replace letters, and indexed accordingly.

Equations (12.1) through (12.8) are formally written in terms of analytical quantities. But as indicated above, the analytical modal parameters have experimental (or test) counterparts, and the differences between analytically predicted and experimentally measured modes form the basis for uncertainty quantification.

The equations of motion for both analysis and test must be written in the ‘‘TAM’’ coordinate system. TAM is an abbreviation for ‘‘test-analysis model’’ where the u-coordinates are reduced from the original node coordinates of the finite element model (FEM), to a set of test measurement coordinates by static reduction [7], with correspondingly reduced mass and stiffness matrices. This is the reduced coordinate system in which both analysis and test modes are compared. The reduced analytical mass matrix is then used to normalize both analysis and test modes.

The modal matrix  ${}^a\bar{\phi}^A$  is ortho-normal with respect to the analytical (TAM) mass matrix.

The experimental counterpart of  ${}^a\bar{\phi}^A$ , i.e.  ${}^t\bar{\phi}^A$ , in general is not ortho-normal with respect to  $\bar{M}$ , but nevertheless is normalized so that the individual modes  $({}^t\bar{\phi}^A)_j$  of  ${}^t\bar{\phi}^A$  are normalized to unit modal mass with respect to the analytical TAM mass matrix,  ${}^aM^A$ . The experimental counterpart of

$$({}^a\bar{\phi}^A)^T ({}^aM^A + \Delta M^A) {}^a\bar{\phi}^A = I \quad (12.9)$$

is

$$({}^t\bar{\phi}^A)^T ({}^aM^A + \Delta M^A) ({}^t\bar{\phi}^A) = {}^t\bar{m}^A \quad (12.10)$$

where the modal mass matrix  ${}^t\bar{m}^A$  has unit values on the diagonal but nonzero off-diagonal elements. Thus, while (12.9) results in an identity matrix of dimension  $N_{modes}$  equal to the number of substructure analysis and test modes being compared for UQ purposes, (12.10) is a fully populated matrix of dimension  $N_{modes}$  with unit values on the diagonal. Since the matrix  ${}^t\bar{m}^A$  has ones on the diagonal, it may be written

$${}^t\bar{m}^A = I + \Delta\bar{m}^A \quad (12.11)$$

This equation is consistent with Equation (12.27) of [6]. However, Kammer [8] has pointed out an inconsistency between Equations (12.27) and (12.12) of [6]. In (12.12) of [6], the test modes are normalized *w.r.t.* the (unknown) ‘‘true’’ mass matrix, not the TAM mass matrix implied in (12.27). But, because the ‘‘true’’ mass matrix is not known and the test modes in practice are normalized *w.r.t.* the analytical TAM matrix, an additional term, call it  $\delta m_{jj}^A$ , should be added to (12.13a) of [6]. In the present substructure notation, this would be written as

$$\Delta\bar{m}_{jj}^A = -2\Delta\bar{\psi}_{jj}^A + \delta\bar{m}_{jj}^A \quad (12.12)$$

where  $\bar{\psi}^A$  is the cross-orthogonality matrix between analysis and test nodes, i.e.  $\bar{\psi}^A = ({}^a\bar{\phi}^A)^T {}^a\bar{M}^A {}^t\bar{\phi}^A$

However,  $\delta m_{jj}^A$  can only be determined if the ‘‘true’’ modal mass (in the TAM coordinate system) can be estimated experimentally. There are possible ways to do this, but it is not standard practice to do so. The details will not be discussed here; for the time being, we therefore choose to ignore  $\delta\bar{m}_{jj}^A$ , with the consequence of possibly underestimating modeling uncertainty, to the extent that  $|\delta\bar{m}_{jj}^A|$  is not small compared to  $|2\Delta\bar{\psi}_{jj}^A|$ . The rest of [6] is directly applicable to the UQ problem at hand with the understanding that [6] addresses the structural dynamics UQ problem from a complete system perspective, whereas the present application addresses it from a substructuring perspective.

A brief summary of the relevant portions of [6] is contained in the following paragraphs. The primary goals of [6] in the present context of substructure UQ using MLFI modes, are (1) to first quantify the uncertainty in substructure modal mass and stiffness matrices in terms of the differences between analysis modes and test modes, and (2) to evaluate the first and second-order statistics of these differences where analysis and/or test modes may vary. In substructure-specific cases where there is a single analytical model of test hardware and multiple (replicate) tests, the differences (for the  $i$ th replicate test)

$$\Delta \bar{m}_i^A = {}^t \bar{m}_i^A - {}^a \bar{m}^A = {}^t \bar{m}_i^A - I \quad (12.13a)$$

$$\Delta \bar{k}_i^A = {}^t \bar{k}_i^A - {}^a \bar{k}^A = {}^t \bar{k}_i^A - {}^a \bar{\lambda}^A \quad (12.13b)$$

will produce both a mean vector and a covariance matrix. The mean vector can be used to “calibrate” the analytical modal model, while the resulting covariance matrix is used to quantify the uncertainty of the analytical model based on replicate modal tests.

The primary conclusion of [6] is that  $\Delta \bar{m}_i^A$  and  $\Delta \bar{k}_i^A$  in (12.13a,b) can be derived, to 1st order approximation, from the difference between test and analysis eigenvalues and the cross-orthogonality between analysis and test eigenvectors, both sets of eigenvectors normalized *w.r.t.* the TAM mass matrix. It follows that

$$\Delta \bar{m}_i^A = (I - \bar{\psi}_i^A) + (I - \bar{\psi}_i^A)^T \quad (12.14a)$$

$$\Delta \bar{k}_i^A = \Delta \bar{\lambda}_i^A + {}^a \bar{\lambda}_i^A (I - \bar{\psi}_i^A) + (I - \bar{\psi}_i^A)^T {}^a \bar{\lambda}_i^A \quad (12.14b)$$

where  $\bar{\psi}_i^A$  is the cross-orthogonality between analysis modes,  ${}^a \bar{\phi}_i^A$ , and test modes,  ${}^t \bar{\phi}_i^A$ , representing the  $i$ th replicate test.

$$\bar{\psi}_i^A = ({}^a \bar{\phi}_i^A)^T {}^a \bar{M}^A ({}^t \bar{\phi}_i^A) \quad (12.15)$$

One further normalization is required to scale  $\Delta \bar{k}_i^A$  so as to be compatible with  $\Delta \bar{m}_i^A$  when evaluating the correlated statistics of  $\Delta \bar{m}_i^A$  and  $\Delta \bar{k}_i^A$ . The matrices  $\Delta \bar{k}_i^A$ , must be normalized by their corresponding analytical eigenvalues,  ${}^a \bar{\lambda}_i^A$ .

$$\Delta \tilde{k}_i^A = ({}^a \bar{\lambda}_i^A)^{-1/2} \Delta \bar{k}_i^A ({}^a \bar{\lambda}_i^A)^{-1/2} \quad (12.16)$$

For purposes of substructure uncertainty propagation taken up in the next section, the  $\Delta \tilde{k}_i^A$  substructure matrices can be scaled back to  $\Delta \bar{k}_i^A$ .

The differences in modal mass and stiffness are correlated, so that both the mean vector and covariance matrix must include both modal mass and stiffness. To this end, the upper triangular portions of both (symmetric) matrices are concatenated in the form

$$\Delta \tilde{r}^A = \begin{Bmatrix} \text{vec } \Delta \bar{m}^A \\ \text{vec } \Delta \bar{k}^A \end{Bmatrix} \quad (12.17)$$

where the mean of the vector of random variables  $\Delta \tilde{r}^A$  is

$$\mu_{\Delta \tilde{r}}^A = E[\Delta \tilde{r}^A] = \frac{1}{N} \sum_i \Delta \tilde{r}_i^A \quad (12.18)$$

and the corresponding covariance matrix is

$$S_{\Delta \tilde{r}^A \Delta \tilde{r}^A} = E \left[ \left( \Delta \tilde{r}^A - \mu_{\Delta \tilde{r}}^A \right) \left( \Delta \tilde{r}^A - \mu_{\Delta \tilde{r}}^A \right)^T \right] = \frac{1}{N-1} \sum_i \left( \Delta \tilde{r}_i^A - \mu_{\Delta \tilde{r}}^A \right) \left( \Delta \tilde{r}_i^A - \mu_{\Delta \tilde{r}}^A \right)^T \quad (12.19)$$

### 12.3 Reduced-Order Nonlinear Substructure Models

Neural networks are universal function approximators and are suitable in principle for non-parametric modeling of any mapping [9]. Due to a number of “stochastic” factors (such as the sparsity of data and the estimation process itself), the fit of any specific NN must be regarded as a realization of a random process. Thus the estimated behavior of an underlying non-linear system must be obtained from an ensemble of network models.

The basis for the NN-based non-linear model of the joint is the multi-layer perceptron [10]. As a brief recap, in a multilayer perceptron (MLP) there are  $n$  inputs corresponding to the independent parameters  $x$  (i.e., the relative displacement and velocity across the joint in this paper). The network has one hidden layer with  $s$  nodes and one output node, corresponding to the force through the joint. The connection matrix between the input and the hidden layer is denoted by  $W_{(1)}$ , such that  $W_{(1)ij}$  denotes the weight of the connection between the  $j$ th input node and the  $i$ th hidden layer node. The connection matrix between the hidden layer and output nodes is denoted by  $W_{(2)}$  (with row dimension equal to one, in this instance). The biases of the nodes are denoted in an analogous manner by  $b_{(1)}$  and  $b_{(2)}$ . With this notation, the network model has the general form:

$$\begin{aligned} g(x) &= f_2(W_{(2)} \cdot f_{(1)}(W_{(1)} \cdot x + b_{(1)}) + b_{(2)}) \\ &= N(x)(p|D) \end{aligned} \quad (12.20)$$

The topology, size, and transfer functions in the network specify a generalized functional mapping, denoted by  $N(x)(p|D)$ , read as the mapping  $N$  at  $x$ , given the training data  $D$ . The selection of these attributes is not directly conditioned on the data and apart from the selection of the transfer functions is of little consequence using modern training procedures. The coefficients of the network elements, denoted by  $p$ , are an outcome of the training process. The transfer functions were selected to be variants of the logistic function,

$$\begin{aligned} f_{(1)i} &= \frac{2}{(1 + e^{-2u})} - 1 \\ f_{(2)i} &= (1 + e^{-u})^{-1} \end{aligned} \quad (12.21)$$

so that Eq. (12.20) represents the successive composition of linear and non-linear functions,.

$$f_n \circ f_l \circ f_n \circ f_l(x) \quad (12.22)$$

The network training procedure commenced with initialization using the Nguyen-Widrow method. The fitting of the parameters  $p$ , was then performed through optimization of a regularized merit function using Levenberg-Marquardt back propagation [11]. Use of a regularized merit function eliminates the need for generally ad-hoc procedures such as early-stopping.

It is proper to think of the result of a particular training, denoted by  $N_i(x)(p|D)$ , as a realization of a random process. Note that the evaluation of a specific realization gives the corresponding relative force across the joint, conditioned on that network realization:  $F(x, \dot{x})|N_i$ . The variability involved in the estimation of the network is directly conditioned on the number and distribution of the data. As a result, the interpretation of a network as a realization of a stochastic process is very useful for estimating the expected probability of inter-component resisting force as well as its model and sampling uncertainty.

The procedure that was as follows. The training points were segregated into a reduced training set (size  $n_{t,r}$ ) and cross-validation set (size  $n_{cv}$ ). Specifically, the reduced training set consisted of 90% of the full training set. The choice of 90% was based on judgment. Clearly, the smaller the reduced training set, the greater the variance expected in the ANN realizations. Conversely, as a greater percentage of the full training set that is employed for training, the greater the bias (to the training set) that is to be expected. Because ANNs are non-parametric models and because the number of total training points was rather small given the size of the parameter space, the decision was made to weight the procedure toward narrowing the allowable function space (by using a large percentage of the full training set).

For each reduced set of training data 20 model (ANN) realizations were trained. By construction, each of the ANNs are equally likely, given the reduced training set. The process was repeated a total of 50 times (with 50 different reduced training sets), yielding a total of 1,000 ANNs.

Each ANN was subsequently examined in order to rank the models and to generate ranking statistics. There is *a priori* no unique method to do so that statistically justifiable, since no statistical model is appropriate for the training data. As a simple expedient, the mean total absolute deviation was used, this being simply the sum of the absolute values of the residuals divided by the size of the reduced training set. The value of this metric was used to rank order the models within each reduced training set (this constitutes a relative form of self-validation). The best five models resulting from this ordering procedure were retained for further scrutiny.

This reduced ensemble of models, *all of which were equally likely given their respective reduced training data*, was subjected to a comparison—model by model—against the *cross validation* points (using the same metric, but with using the cross-validation training cases omitted during training). The best model (i.e., the one generalizing best in the sense of the metric above was retained). A total of 50 models ( $n_m = 50$ ) thus constituted the final ensemble of ANNs which comprise the non-linear stochastic joint model, i.e. the joint SNN.



Recall that  $\sigma_m$  represents uncertainty inherent in the response, arising from limited data and stochastic processing that occur during training of the models. This uncertainty can be directly estimated at any design point by direct evaluation of the ensemble, which is necessary in any case when performing a prediction. Recall that there are  $n_m = 50$  models. A general non-parametric method to evaluate statistics from the empirical distribution of this data is by using the bootstrap, which is denoted by  $\pi^k$  in this paper. The meaning of this symbol, which is a stochastic operator on an empirical distribution, is as follows. The bootstrap samples uniformly with replacement from the  $n_m$  models; this results in a vector of  $n_m$  outcomes. The process is repeated  $n_b$  times. The  $k$ th realization from this process is denoted by  $\pi^k (\{N(x) (p|D)\}_{models})$ .

Using the bootstrap it is straightforward to estimate both the mean and the variance according to the following formulas:

$$\begin{aligned}\hat{\mu}_{x(N)} &= \frac{1}{n_b} \sum_{k=1}^{n_b} \pi^k (\{N(x) (p|D)\}_{models}) \\ \hat{\sigma}_{x(N)}^2 &= \frac{1}{n_b-1} \sum_{k=1}^{n_b} [\pi^k (N(x) (p|D)_{models}) - \hat{\mu}_{\pi(N)}]^2\end{aligned}\quad (12.23)$$

Moreover, because multiple realizations of the statistics are available it is also straightforward to calculate non-parametric confidence limits for them.

## 12.4 Substructure Coupling

This section addresses the situation where linear substructures are connected through a nonlinear joint represented by an empirically-based response surface. In general this response surface could be derived from any functional fit of force across the joint as a function of the relative displacements and velocities across the joint. The goal here, however, is to fit this surface with a stochastic neural network (SNN) so as to account for modeling and experimental uncertainty.

### 12.4.1 Nodal Force Coupling

The substructure coupling procedure for a nonlinear joint connecting two linear substructures may begin with

$$\begin{bmatrix} I^A & 0 \\ 0 & I^B \end{bmatrix} \begin{Bmatrix} \ddot{p}^A \\ \ddot{p}^B \end{Bmatrix} + \begin{bmatrix} \bar{\xi}^A & 0 \\ 0 & \bar{\xi}^B \end{bmatrix} \begin{Bmatrix} \dot{p}^A \\ \dot{p}^B \end{Bmatrix} + \begin{bmatrix} \bar{\lambda}^A & 0 \\ 0 & \bar{\lambda}^B \end{bmatrix} \begin{Bmatrix} p^A \\ p^B \end{Bmatrix} = \begin{bmatrix} \bar{\phi}^{A^T} & 0 \\ 0 & \bar{\phi}^{B^T} \end{bmatrix} \begin{Bmatrix} F^A \\ F^B \end{Bmatrix}\quad (12.24)$$

where the force vector on the RHS of the equation represents the interactive forces between Substructures A and B. Instead of direct coupling of Substructures A and B the coupling is indirect through the nonlinear joint which we shall call Substructure C.

We can consider the nonlinear joint in this case to be a massless “blackbox” as illustrated in Fig. 12.1 where both the “input” and “output” are force vectors related to each other by Newton’s third law which states that the sum of external forces acting on the (geometrically simplified) joint must equal zero for the body (joint) to be in equilibrium. We designate

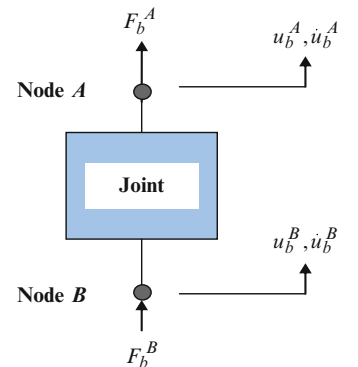


**Fig. 12.1** Schematic of nonlinear joint

the 6-dof force vector at the Substructure A interface as  $F_b^A$  and the opposing 6-dof force vector at Substructure B as  $F_b^B$ . The two force vectors are geometrically related by the  $6 \times 6$  constant matrix,  $C^{BA}$ , so that

$$F_b^B = -C^{BA} F_b^A \quad (12.25)$$

If the nonlinear Substructure C were dimensionless, i.e. if Node A and Node B at the interfaces of Substructures A and B, respectively, were coincident, then,  $C^{BA} = I$ , a  $6 \times 6$  identity matrix.

Now we shall consider  $F_b^A$  to be related to the relative displacements and velocities across the joint, such that

$$F_b^A = f^A [(u_b^A - u_b^B), (\dot{u}_b^A - \dot{u}_b^B)] = f^A (\Delta u_b^{AB}, \Delta \dot{u}_b^{AB}) \quad (12.26)$$

where  $F_b^A$  is a  $6 \times 1$  vector of attachment (boundary) forces at the Substructure A interface,  $f^A$  is a  $6 \times 1$  vector function of forces, each in general dependent on the relative displacement vector,  $\Delta u$ , and relative velocity vector,  $\Delta \dot{u}$ , between the attachment nodes A and B shown in Fig. 12.1. Equation (12.26) can be thought of as symbolically representing the response surface characterizing the nonlinear joint.

Returning to Eq. (12.9), if we assume for now that  $F^A$  and  $F^B$  are non-zero only at the interface boundaries of the two components, then

$$F^A = \begin{Bmatrix} 0 \\ \dots \\ F_b^A \end{Bmatrix} \text{ and } F^B = \begin{Bmatrix} 0 \\ \dots \\ F_b^B \end{Bmatrix} \quad (12.27)$$

Expanding the undamped homogeneous form of (12.24), we find that the uncoupled equations in (12.24) are of the form

$$\begin{bmatrix} I_i^A & 0 & 0 & 0 \\ 0 & I_b^A & 0 & 0 \\ 0 & 0 & I_i^B & 0 \\ 0 & 0 & 0 & I_b^B \end{bmatrix} \begin{Bmatrix} \ddot{p}_i^A \\ \ddot{p}_b^A \\ \ddot{p}_i^B \\ \ddot{p}_b^B \end{Bmatrix} + \begin{bmatrix} \bar{\lambda}_i^A & 0 & 0 & 0 \\ 0 & \bar{\lambda}_b^A & 0 & 0 \\ 0 & 0 & \bar{\lambda}_i^B & 0 \\ 0 & 0 & 0 & \bar{\lambda}_b^B \end{bmatrix} \begin{Bmatrix} p_i^A \\ p_b^A \\ p_i^B \\ p_b^B \end{Bmatrix} = \begin{bmatrix} \bar{\phi}_{ii}^A & \bar{\phi}_{ib}^A & 0 & 0 \\ \bar{\phi}_{bi}^A & \bar{\phi}_{bb}^A & 0 & 0 \\ 0 & 0 & \bar{\phi}_{ii}^B & \bar{\phi}_{ib}^B \\ 0 & 0 & \bar{\phi}_{bi}^B & \bar{\phi}_{bb}^B \end{bmatrix}^T \begin{Bmatrix} 0 \\ F_b^A \\ 0 \\ F_b^B \end{Bmatrix} \quad (12.28)$$

where the  $I$ 's are identity matrices, the  $\bar{\lambda}$ 's are diagonal matrices, and  $F_b^A$  and  $F_b^B$  are given by Eqs. (12.25) and (12.26), for the cases where no external forces are applied to the system.

#### 12.4.2 Removal of Added Mass (and Stiffness)

When linear substructures are coupled implicitly through a nonlinear substructure such as a nonlinear joint, the linear substructure equations of motion on the left hand side will be uncoupled; that is, the substructure equations of motion in substructure modal coordinates will be block-diagonal. However, the added masses and/or stiffnesses applied to generate the component modes must be removed prior to solving the system equations of motion. In this case, Eq. (12.28) becomes

$$\begin{aligned} & \begin{bmatrix} [I_i^A] & 0 & 0 & 0 \\ 0 & I_b^A - (\bar{\phi}_{bb}^A)^T \Delta M^A \bar{\phi}_{bb}^A & 0 & 0 \\ 0 & 0 & [I_i^B] & 0 \\ 0 & 0 & 0 & I_b^B - (\bar{\phi}_{bb}^B)^T \Delta M^B \bar{\phi}_{bb}^B \end{bmatrix} \begin{Bmatrix} \ddot{p}_i^A \\ \ddot{p}_b^A \\ \ddot{p}_i^B \\ \ddot{p}_b^B \end{Bmatrix} \\ & + \begin{bmatrix} [\bar{\lambda}_i^A] & 0 & 0 & 0 \\ 0 & \bar{\lambda}_b^A - (\bar{\phi}_{bb}^A)^T \Delta K^A \bar{\phi}_{bb}^A & 0 & 0 \\ 0 & 0 & [\bar{\lambda}_i^B] & 0 \\ 0 & 0 & 0 & \bar{\lambda}_b^B - (\bar{\phi}_{bb}^B)^T \Delta K^B \bar{\phi}_{bb}^B \end{bmatrix} \begin{Bmatrix} p_i^A \\ p_b^A \\ p_i^B \\ p_b^B \end{Bmatrix} \\ & = \begin{bmatrix} \bar{\phi}_{ii}^A & \bar{\phi}_{ib}^A & 0 & 0 \\ \bar{\phi}_{bi}^A & \bar{\phi}_{bb}^A & 0 & 0 \\ 0 & 0 & \bar{\phi}_{ii}^B & \bar{\phi}_{ib}^B \\ 0 & 0 & \bar{\phi}_{bi}^B & \bar{\phi}_{bb}^B \end{bmatrix}^T \begin{Bmatrix} 0 \\ F_b^A \\ 0 \\ F_b^B \end{Bmatrix} \end{aligned} \quad (12.29)$$

### 12.4.3 External Forces and Damping

In order to calculate forced response, we must add back in the external forces and damping. It is standard practice to use measured modal damping in the diagonalized modal equations of motion. With the present formulation of the problem, measured modal damping will correspond to the mass-loaded (and possibly stiffness-loaded as well) test nodes. Subtracting the added mass and/or stiffness would theoretically alter the measured modal damping. However, we will assume for the time being that the difference is small, and therefore ignore it. Under this assumption, the diagonal modal damping added to the left hand side of Eq. (12.29) will be of the form:

$$\begin{bmatrix} \bar{\xi}_{ii}^A & 0 & 0 & 0 \\ 0 & \bar{\xi}_{bb}^A & 0 & 0 \\ 0 & 0 & \bar{\xi}_{ii}^B & 0 \\ 0 & 0 & 0 & \bar{\xi}_{bb}^B \end{bmatrix} \begin{Bmatrix} \dot{p}_i^A \\ \dot{p}_b^A \\ \dot{p}_i^B \\ \dot{p}_b^B \end{Bmatrix} \quad (12.30)$$

where the modal damping sub-matrices are diagonal and the diagonal elements are given by (12.7) and (12.8).

To avoid confusion, we shall assume that the *external* forces are applied to the “*internal*” nodal degrees of freedom, so as to separate them from the force balance equation of Eq. (12.25). Then the right-hand-side of Eq. (12.29) becomes

$$m^{AB} \ddot{p}^{AB} + \bar{\xi}^{AB} \dot{p}^{AB} + k^{AB} p^{AB} = (\bar{\phi}^{AB})^T \begin{Bmatrix} F_i^A \\ F_b^A \\ F_i^B \\ F_b^B \end{Bmatrix} = (\bar{\phi}^{AB})^T F^{AB}(t) = F_p^{AB}(t) \quad (12.31)$$

where the external nodal forces are contained in  $F_i^A$  and  $F_i^B$ , and all vectors are assumed to be time-dependent. Note that the bars have been removed from  $m^{AB}$  and  $k^{AB}$ , because the added mass and stiffness have been subtracted off in Eq. (12.29). However, we retain the bar over the modal damping matrix to remind ourselves that the measured modal damping is still associated with the measured test modes that reflect the added mass and/or stiffness, but is assumed to approximate the modal damping matrix of the “unloaded modes.” We are also reminded that  $m^{AB}$  and  $k^{AB}$  are no longer diagonal, but block-diagonal as shown in Eq. (12.29).

Although the uncoupled substructure equations of motion, written in the mass (and/or stiffness) loaded component modes, have had the added mass and stiffness removed in Eq. (12.29), there will in general remain some extraneous degrees of freedom that need to be eliminated. One way of doing this is through displacement compatibility equations.

$$\{p^{AB}\} = [\bar{\beta}] \{p\} \quad (12.32)$$

With the addition of modal damping, Eq. (12.29) becomes Eq. (12.31). Then Eq. (12.31) becomes

$$(\bar{\beta}^T M^{AB} \bar{\beta}) \ddot{p} + (\bar{\beta}^T \bar{\xi}^{AB} \bar{\beta}) \dot{p} + (\bar{\beta}^T k^{AB} \beta) p = \bar{\beta}^T (\bar{\phi}^{AB})^T F^{AB}(t) \quad (12.33)$$

or

$$m \ddot{p}(t) + c \dot{p}(t) + kp(t) = F_p(t)$$

where

$$m = \bar{\beta}^T m^{AB} \bar{\beta} \quad (12.34a)$$

$$c = \bar{\beta}^T \bar{\xi}^{AB} \bar{\beta} \quad (12.34b)$$

$$k = \bar{\beta}^T k^{AB} \bar{\beta} \quad (12.34c)$$

$$F_p(t) = \bar{\beta}^T F_p^{AB}(t) \quad (12.34d)$$

This is the form of the equations of motion used to calculate the time-dependent response of the coupled structure to externally applied force time-histories. Clearly, none of the three matrices,  $m$ ,  $c$  or  $k$  will any longer be diagonal or even block diagonal; the  $\bar{\beta}$  transformation couples the block-diagonal  $m^{AB}$ ,  $\bar{\xi}^{AB}$  and  $k^{AB}$  component matrices. Nevertheless, the substructure covariance matrices can still be used to generate random realizations of these matrices; they just have to be coupled using the coupling matrix as shown in (12.33).

## 12.5 Uncertainty Propagation

### 12.5.1 Linear Substructures

By way of review, the reason for using a free-free mode formulation of CMS is that it is not necessary to generate fixed interface modes experimentally for comparison with the analytical modes. The reason for using mass-loaded free-interface modes is so that the mass and stiffness properties of the substructures near their interface boundaries are represented in the absence of fixed interface modes. Using this approach, modeling uncertainty can be estimated at the substructure level by (1) directly comparing corresponding pairs of mass-loaded analysis and test mode sets, (2) performing statistical analysis of these data to obtain correlated modal mass and stiffness parameters, and (3) propagating these statistics to higher levels of structural assembly. For linear structures and linear relationships between substructure parameters and system response, this can be accomplished using linear covariance propagation as presented in [12]. For nonlinear structures or for linear structures where the response quantities of interest, e.g. frequency response functions, are not linear functions of the structure (or substructure) parameters, alternative methods such as interval propagation or Monte-Carlo type simulation methods can be used [13].

Before moving on to discuss uncertainty propagation, we must first consider how to introduce damping uncertainty at the substructure level. In practice, structural damping, and by implication substructure damping, is introduced to the modal equations of motion by assuming uncoupled modal damping based on test measurements.

Returning to Eq. (12.17), the vector  $\Delta \tilde{r}^A$  (and by implication  $\Delta \tilde{r}^B$  as well) can be augmented with elements of the corresponding modal damping matrix so that  $\Delta \tilde{r}^A$  becomes

$$\Delta \tilde{r}^A = \begin{Bmatrix} \text{vec } \Delta \tilde{m}^A \\ \text{vec } \Delta \tilde{k}^A \\ \text{vec } \Delta \tilde{\zeta}^A \end{Bmatrix} \quad (12.35)$$

where again the bars indicate MLFI modes. Then the substructure covariance matrix becomes

$$S_{\Delta \tilde{r}^A \Delta \tilde{r}^A}^A = \begin{bmatrix} S_{\tilde{m}\tilde{m}}^A & S_{\tilde{m}\tilde{k}}^A & 0 \\ S_{\tilde{k}\tilde{m}}^A & S_{\tilde{k}\tilde{k}}^A & 0 \\ 0 & 0 & S_{\tilde{\zeta}\tilde{\zeta}}^A \end{bmatrix} \quad (12.36)$$

where the covariance matrix of damping uncertainty,  $S_{\tilde{\zeta}\tilde{\zeta}}^A$ , is independent of modal mass and stiffness uncertainty and is treated as being diagonal.

The propagation of substructure uncertainty for linear or linearized substructures through the substructure coupling process of Eq. (12.33) begins with the transformation of substructure UQ parameters represented by modal mass, stiffness and damping, and their covariance matrix,  $S_{\Delta \tilde{r}^A \Delta \tilde{r}^A}^A$ , to an equivalent set of uncorrelated parameters. These parameters in general are not independent, but they can be sampled independently for purposes of uncertainty propagation through nonlinear joints or substructures using Markov Chain Monte Carlo (MCMC) simulation procedures. When the uncertainty distributions of these uncorrelated parameters are or can be assumed Gaussian, the uncorrelated parameters are also independent.

The covariance matrix,  $S_{\Delta \tilde{r}^A \Delta \tilde{r}^A}^A$ , is symmetric and non-negative definite. It can be transformed to an equivalent set of singular values (eigenvalues) and associated singular vectors (eigenvectors) by singular value decomposition [14, 15], such that

$$S_{\Delta \tilde{r}^A \Delta \tilde{r}^A}^A = V^A \Sigma^A (V^A)^T \quad (12.37)$$

where the matrix  $\Sigma^A$  is a diagonal matrix of singular values representing the variances (standard deviations squared),  $(\sigma_i^A)^2$ , of the uncorrelated transformed parameters, and  $V^A$  is the associated matrix of singular vectors. The calibrated modal mass, stiffness and damping UQ parameters can be expressed as a Karhunan-Loeve (KL) expansion in the new set of uncorrelated random variates,

$$\Delta \tilde{r}^A = \mu_{\Delta \tilde{r}^A}^A + \sum_l \sigma_l^A v_l^A V_l^A \quad (12.38)$$

where  $\mu_{\Delta \tilde{r}^A}^A$  is the mean vector of *calibrated* modal matrix elements and  $v_l^A$  is a scalar random variable having a Gaussian (Normal) probability distribution  $N(0,1)$  with zero mean and unit variance.

The covariance matrix,  $S_{\Delta \tilde{r}^A \Delta \tilde{r}^A}^A$ , will normally be singular whenever the number of replicate tests used to generate the covariance matrix is less than the number of modal mass and stiffness matrix elements used to characterize substructure

uncertainty, i.e.,  $N(N + 1)$  where  $N$  is the number of modes retained after truncation of the substructure modes. The number of singular values will be equal to the rank of  $S_{\Delta\tilde{r}\Delta\tilde{r}}^A$ , however, further coordinate reduction is usually possible by truncation of those “modes” (generalized eigenvectors of the SVD) associated with relatively small singular values. The trace of  $S_{\Delta\tilde{r}\Delta\tilde{r}}^A$  is equal to the sum of its diagonal elements, which in turn is equal to the sum of the singular values in  $\Sigma^A$ . Thus, neglecting the very small singular values in the summation of singular values can lead to a significant reduction in the number of uncorrelated random variables characterizing substructure uncertainty. Substructure uncertainty in terms of the original modal mass, stiffness and damping matrix elements can be reconstituted in terms of the K-L expansion (12.38). In this way, random perturbations of the linear/linearized substructure mass, stiffness and damping parameters can be generated by sampling the truncated, uncorrelated parameters,  $v$ , and transforming them back to the  $\tilde{r}$  coordinates.

One final step is required before sampled perturbations of modal mass, stiffness and damping matrix elements can be added to the nominal modal matrix elements of the analytical modal as given in (12.31), (12.29) and (12.30). The normalized modal stiffness and damping matrix elements must be scaled back to their frequency-dependent counterparts. So the normalization process represented by (12.16) and the inverse of (12.8) must be reversed, i.e.

$$\Delta\bar{k}^A = (\bar{\lambda}^A)^{1/2} \Delta\tilde{k}^A (\bar{\lambda}^A)^{1/2} \quad (12.39)$$

$$\Delta\bar{\xi}^A = 2\Delta\tilde{\xi}^A (\bar{\lambda}^A)^{1/2} \quad (12.40)$$

where  $\bar{\lambda}^A$ ,  $\Delta\tilde{\xi}^A$  and  $\Delta\tilde{k}^A$  are all diagonal matrices.

Before samples of the modal mass, stiffness and damping matrix elements of a linear substructure as described above can be combined with samples of reduced-order nonlinear substructure and joint models, the sampled sets of perturbed substructure modal mass and stiffness matrices of the linear substructures must be “censored” to remove any samples yielding unrealistic structural characteristics; i.e., negative substructure eigenvalues.

### 12.5.2 Nonlinear Substructures

The propagation of uncertainty in reduced nonlinear joint and substructure models to higher levels of structural assembly is performed in a similar fashion to the propagation of uncertainty in linear/linearized substructures; that is by sampling from the stochastic neural net (SNN) substructure model to obtain the coupling forces,  $F_b^A$  and/or  $F_b^B$ , on the right-hand-side of Eq. (12.31), and evaluating the response of the sampled structural system to the prescribed excitation (forcing function),  $F_i^A$ , and/or  $F_i^B$ . By sampling repeatedly from the randomly generated substructures and compiling the statistics of system response resulting from these randomly sampled and coupled structural systems, an ensemble of response time-histories is generated, from which response statistics can then be calculated.

## 12.6 Numerical Example

To illustrate the foregoing methodology, we have chosen a simple numerical example consisting of two linear substructures (components) connected by a nonlinear joint (see Fig. 12.2). Component 1 is a 20 DOF spring mass chain fixed at its base to ground. When the component is base excited, the input is through base motion denoted by  $x_0$ . In the present example,

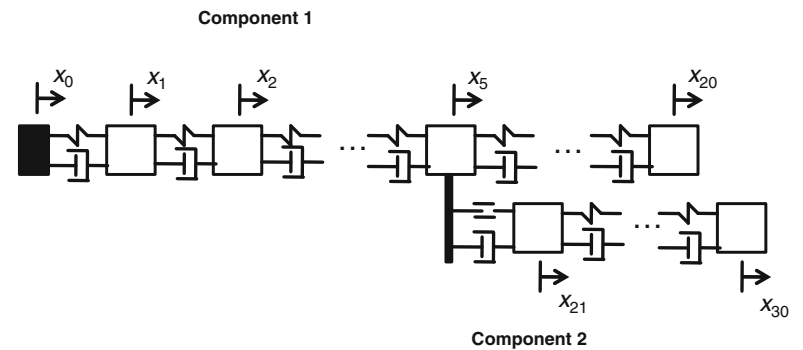


**Fig. 12.2** Schematic of 30 DOF numerical example

**Fig. 12.3** Hysteresis loop produced by Iwan joint element

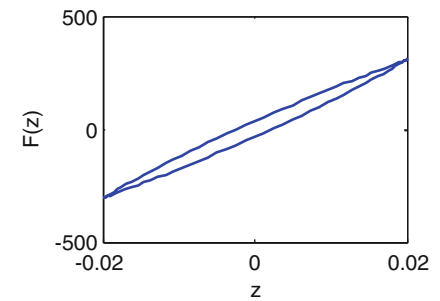
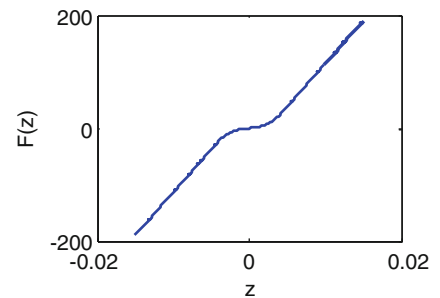


**Fig. 12.4** Gap element restoring force



however, a constant force is suddenly applied at DOF 20 on Component 1, i.e. a step force of either 200 or 20 lb. The total mass (weight) of Component 1 is  $1.37 \text{ lb-sec}^2/\text{in}$  (530 lbs). The total mass (weight) of component 2 is  $0.409 \text{ lb-sec}^2/\text{in}$  (158 lbs). The fundamental mode frequency of the coupled *linearized* system is approximately 13.8 Hz. Component 1 is deterministic. In Component 2, the springs have been “randomized” by assuming that the spring stiffnesses are independent Gaussian random variables with nominal means and coefficients of variation equal to 5%.

A stochastic neural net (SNN) representation of the nonlinear joint was used to couple the two linear components. The nonlinear joint model consists of a nonlinear gap element in parallel with an Iwan hysteresis model [16] having the force-deflection property shown in Fig. 12.3. Twenty realizations of the random Iwan element parameters were used as training data in the formulation of the stochastic neural net (SNN) representation of the nonlinear joint.

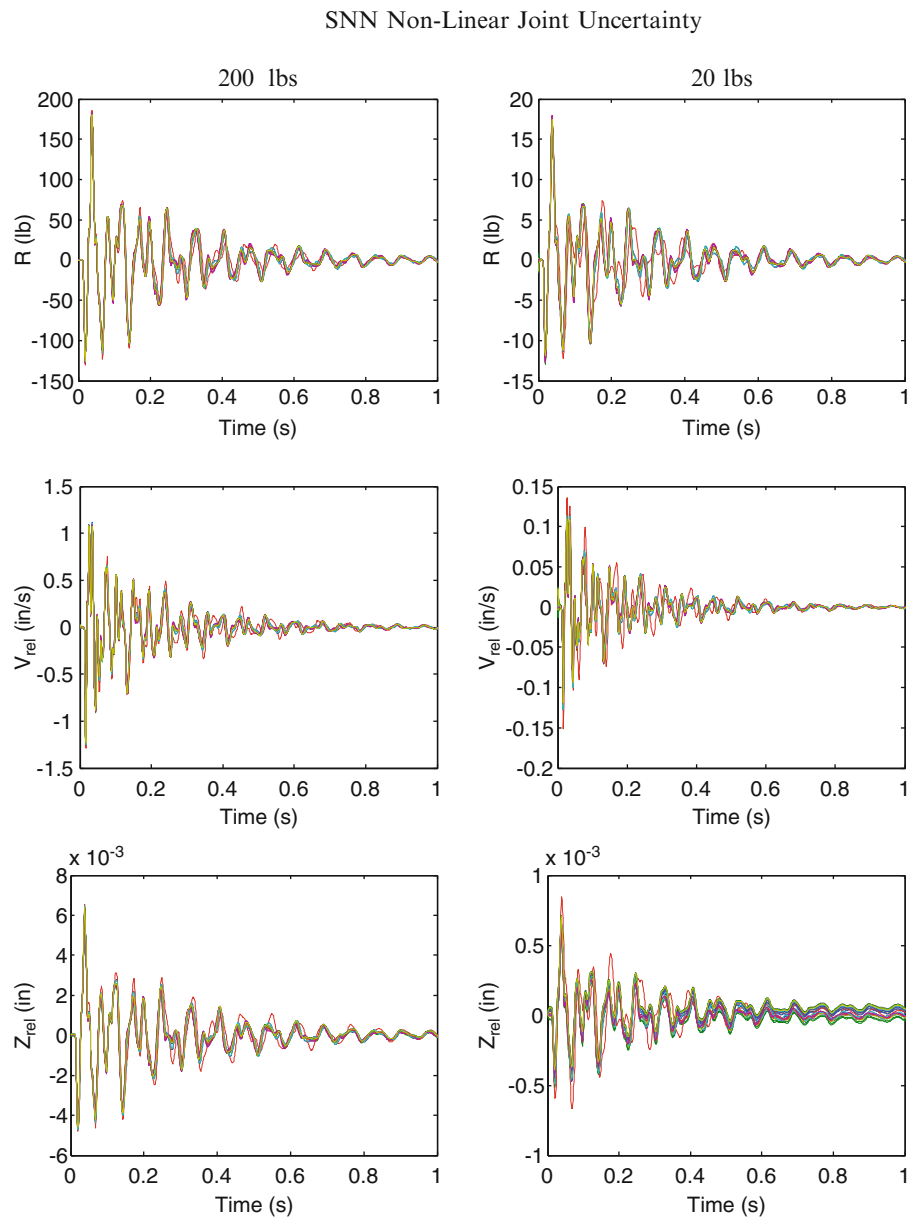
The second nonlinear element in the joint connecting the two substructures is a gap element; it is situated in parallel with a linear spring, a linear damper, and the Iwan element described above. The gap element is one that has linear stiffness at large positive relative displacements across the joint, and the same stiffness at large negative relative displacements. At small relative displacements a cubic function connects the two linear stiffnesses, smoothly. The restoring force curve for the gap element is shown in Fig. 12.4. Twenty realizations from the random source of the gap element parameters were generated to train the SSN.

Response across the nonlinear joint is illustrated in Fig. 12.5 where the left column of plots shows 20 realizations of (1) force across the joint, (2) relative velocity across the joint, and (3) relative displacement across the joint. The left column of plots shows the response across the joint for a 200 lb. constant force suddenly applied to DOF 20 of Component 1, i.e. a 200 lb. step force input. The right column of plots shows the same response across the joint for a 20 lb. step force applied at the same location. The response shown on the right reveals more uncertainty as the response damps out, because that very low level of response represents response within the range of the gap in the nonlinear joint, where the nonlinearity has greatest effect. For service-type loads, this low level of excitation is generally not important; however, low excitation levels are typically used in modal testing, so that noise contributed by “rattling” due to free-play in joints (modeled here by the gap element) can be significant.

## 12.7 Conclusions

This paper has emphasized the formulation of reduced-order substructuring methods, with experimentally-based uncertainty quantification (UQ) at the substructure level and its propagation to higher levels of assembly, including structural systems comprised of linear substructures connected by nonlinear joints. The reduced-order linear models are based on the use of mass-loaded free-interface modes for both analysis and testing, recognizing (1) that fixed interface modes are difficult to

**Fig. 12.5** Multiple realizations of response across the nonlinear joint at different input levels



achieve in testing, especially for large massive structures, and (2) that it is difficult as well as impractical to fully quantify substructure uncertainty based either on fixed-base or free-free modal testing. Reduced-order nonlinear models of nonlinear joints are represented by stochastic neural networks (SNNs) derived from vibration test data on the isolated joints themselves, loaded with masses to simulate the range of operating frequencies that the joint is expected to experience in practice, i.e. during normal operation.

A numerical example has been presented to illustrate these principles as follows:

- Reduced-order modal modeling of both deterministic and non-deterministic linear substructures using mass-loaded free-interface modes,
- Experimentally-based UQ for linear substructures where uncertainty is quantified in terms of correlated modal mass, stiffness and damping matrix elements derived from differences between replicate test modes and their analytical counterparts,
- Experimentally-based UQ for a nonlinear joint based on experimental data used to train a SNN, usually the response of a mass-loaded joint to random vibration input,
- Substructure coupling based on modeling the interaction forces on the right-hand side of the equations of motion through the use of a SSN,

- Random realizations of system response based on sampling the reduced-order stochastic models of both linear substructures and nonlinear joints,
- And finally, statistical analysis of the system response to quantify system-level uncertainty resulting from experimentally-based stochastic models at the substructure/component level.

In the end, Markov Chain Monte Carlo (MCMC) will be used to generate probability distributions of selected system response variables using the sampled realizations of the reduced-order substructure-based models. Computational efficiency is achieved through the use of reduced-order stochastic models and MCMC methods that require many fewer realizations to generate probability distributions of structural response compared with conventional Monte Carlo.

**Acknowledgements** This work has been supported by the Jet Propulsion Laboratory of Pasadena, California under a NASA STTR contract. The authors wish to thank Dr. Lee Peterson as COTR for his support and guidance on the project which addresses the quantification of margins and uncertainties (QMU) for integrated spacecraft systems. The authors also acknowledge the technical support provided by Dr. Thomas Paez who has contributed his expertise in probabilistic shock and vibration analysis, and has been very helpful in providing analytical models and software used in the numerical demonstrations.

## References

1. Craig RR, Kurdila AJ (2006) Fundamentals of structural dynamics. Wiley, Hoboken
2. Admire JR, Tinker ML, Ivey EW (1992) Mass-additive modal test method for verification of constrained structural models. In: Proceedings of the 10th international modal analysis conference, San Diego, CA
3. Gwinn KW, Lauffer JP, Miller AK (1988) Component mode synthesis using experimental modes enhanced by mass loading. In: Proceedings of the 6th international modal analysis conference, Kissimmee, FL, pp 1088–1093
4. Chandler KO, Tinker ML (1997) A general mass-additive method for component mode synthesis. In: Paper AIAA-97-1381, Proceedings of the 38th structures, structural dynamics and materials conference, Kissimmee, FL, pp 93–103
5. Hasselman TK, Lloyd GM, Red-Horse JR, Paez TL (2011) Quantification of margins and uncertainties (QMU) for integrated spacecraft system models, STTR Phase I Final Report, Report No. 11-744-1, ACTA Inc.
6. Hasselman TK (2001) Quantification of uncertainty in structural dynamic models. *ASCE J Aerosp Eng* 14(4):158–165
7. Guyan RJ (1965) Reduction of stiffness and mass matrices. *AIAA J* 3(2):380
8. Kammer D, Nimityongskul S (2011) Propagation of uncertainty in test/analysis correlation of substructured spacecraft. *J Sound Vib* 330: 1211–1224.
9. Lloyd G, Hasselman T, Paez T (2005) A proportional hazards neural network for performing reliability estimates and risk prognostics for mobile systems subject to stochastic covariates. In: Proceedings: ASME IMECE, Safety engineering and risk analysis/methods and tools for complex systems analysis, Orlando, FL
10. Bishop C (2000) Neural networks for pattern recognition. Oxford University Press, Oxford
11. Girosi F, Jones M, Poggio T (1995) Regularization theory and neural networks architectures. *Neural Comput* 7(2):219–269
12. Hasselman TK, Hart GC (1972) Modal analysis of random structural systems. *J Eng Mech Div ASCE* 98(EM3):561–579
13. Hasselman T, Chrostowski J (1994) Propagation of modeling uncertainty through structural dynamic models. Presented at the 35th AIAA/ASME/ASCE/AHS/ASC structures, structural dynamics and materials conference, Hilton Head, SC, 18–20 April 1994
14. Klema VC, Laub AJ (1980) The singular value decomposition; its computation and some applications. *IEEE Trans Autom Control* AC25(2):164–176.
15. Jackson JE (1991) A user's guide to principal components. Wiley, New York
16. Iwan WD (1966) Distributed-element model for hysteresis and its steady state dynamic response. *J Appl Mech* 33(4):893–900. *Trans. ASME, Vol. 88, Series E, Dec*



# Chapter 13

## Damage Detection in an Energy Flow Model Including Parameter Uncertainty

Marcela Rodrigues Machado and Jose Maria Campos Dos Santos

**Abstract** Structural energy dissipation pattern is modified by the presence of discontinuities like a crack. Crack nucleation and growth reduces the structural stiffness which makes this effect useful as a damage indicator. Computational models have become the main tool for understanding the behavior of complex structures when experimental evaluation can be difficult to perform. However, many of this classical numerical analysis assumes a deterministic model and almost nothing is understood about the effect of uncertainty in the parameters, external forces and boundary conditions. This work presents a study about the energy flow patterns caused by localized damage in structures like rod, including uncertainties in a geometric parameter. The problem is solved in two steps. First, the structure is modeled by the Spectral Element Method (SEM). The mean and variance of displacement responses are obtained by using the Polynomial Chaos (PC) expansion. In PC the stochastic solutions are expanded as orthogonal polynomials of the input random parameters. Second, by using the displacements obtained in the step before, the mean and variance of energies are calculated by applying the expectation into the equations of energy density and energy flow. However, this approach produces unusual equations for expected values and covariances. Like, the expected value for a product of three random correlated variables, whose solution includes the covariance between one variable and a product of two others variables. A formulation is developed and proposed to solve this problem. Monte Carlo Simulation (MCS) is used to validate the results obtained by these solutions. Numerical examples are analyzed for some different cases, which present good approximation as compared with MCS results.

**Keywords** Uncertainty quantification • Polynomial chaos • Damage detection • Energy flow • Spectral element method

### 13.1 Introduction

In general, changes in either global or local structural properties can be associated with damage parameters. In the last decades, many works were performed to develop non-destructive evaluation (NDE) methods based on vibration theory, which allows fault identification and evaluation from modal parameters and dynamic response [1,2]. However, these techniques are well suited to detect large defects rather than small defects like a crack, which do not impose appreciable changes in the lower frequencies and the global structure behavior is unaffected. The presence of a crack in a structure introduces a local flexibility that affects its vibration response. Also, generate changes in elastic waves that propagate in the structure. Recently new researches about damage detection are concentrated on methods that use elastic wave propagation in structures at medium and high frequencies [3]. They utilize the evidence that material discontinuities, such as a crack, generate changes in elastic waves propagating in the structure [4]. Elastic wave-based damage detection presents some particular advantages like capability of propagation over a significant distances and high sensitivity to discontinuities near the wave propagation path.

Spectral Element Method (SEM) [5] is a frequency domain exact analytical solution of the wave equation, using displacement formulation, tailored with the matrix ideas of the finite element method (FEM). Built-up structures with geometrically uniform members can be modeled with a single spectral element, by reducing significantly the total number of degrees of freedom as compared with other similar methods. It can be shown that one spectral element is equivalent to

---

M.R. Machado (✉) • J.M.C.D. Santos

Computational Mechanics Department, State University of Campinas - Unicamp, CEP 13.083-970, Campinas-SP, Brazil  
e-mail: [marcelam@fem.unicamp.br](mailto:marcelam@fem.unicamp.br); [zema@fem.unicamp.br](mailto:zema@fem.unicamp.br)

an infinite number of finite elements. In addition, the theoretical wave propagation behavior in the members is accurately expressed because the exact solution of its differential equation in the frequency domain is obtained.

Damage detection methods considers that they can provide a very close dynamic response of a real structures, but all the parameters used in the models are considered deterministic. Uncertainties such as parameters, modeling and measurement errors are inherently involved in the damage detection procedure for building structures. Stochastic approach, in the framework of understanding the magnitude of uncertainty on simulation results is recent. However, during the last few years, this research area has undergone remarkable expansion and fast development. The method most usually used is Monte Carlo simulation (MCS). It is a sampling method that consists in generates independent realizations of random variables based on their probability distributions. By solving the deterministic problem for each realization, and collecting an ensemble of solutions statistical moments can be calculated [6]. Although it is easy to apply a large number of samples are needed to obtain the convergence, which means high computational cost. A nonsampling approach, nominated Perturbation Method, consists in to expand the random fields in a truncated Taylor series around their mean. Its main drawback is the limitation of the magnitude of uncertainties that can not be too large (typically <10%). The Direct Method consists in apply the moment equations directly to obtain the random solutions. The unknowns are the moments and their equations are derived bi taking averages over the original stochastic governing equations. The problem is that a statistical moment almost always requires information about higher moments. Polynomial Chaos was first introduced by Wiener, in 1938. Although, [7] used this method to solve mechanical problems with the spectral approach of stochastic finite element method. PC is a nonsampling method where the stochastic solutions are expanded as orthogonal polynomials of the random variables. The polynomial basis properties are used to create a linear system of equations, whose solution leads to an expansion that can be used to find the mean, the variance, or the probability distribution [8].

This work presents a study about the energy flow patterns caused by localized damage in structures like rod, including uncertainties in a geometric parameter. The problem is solved in two steps. In the first step the structure is modeled by the Spectral Element Method (SEM), and the mean and variance of displacement responses are obtained by using the Polynomial Chaos (PC) expansion. In the second step, by using the displacements obtained in the step before, the mean and variance of energies are calculated by applying the statistical moments (expected value and variance) directly into the energy density and energy flow equations. However, this approach produces unusual equations for expected values and covariances. Like, for example, the expected value for a product of three random correlated variables, whose solution includes the covariance between one variable and a product of two others variables. A new formulation using the direct method is developed and proposed to solve this problem. Monte Carlo Simulation (MCS) is also performed in order to validate the results obtained by the proposed solution. Numerical examples are analyzed for some different cases, which present good approximation as compared with MCS results.

## 13.2 Theoretical Basis

### 13.2.1 Spectral Element Method

The SEM is a matrix methodology similar to the FEM for handling structural wave propagation problems. The frequency domain dynamic stiffness relation for the spectral element is established via dynamic shape functions between element nodes, which are the exact displacement distributions of the theory considered.

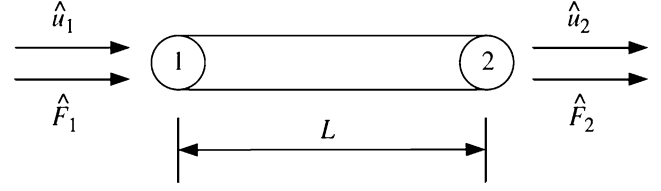
In this paper, the fundamental equation is derived for a longitudinal wave propagation in a rod. Figure 13.1 shows an elastic two-noded rod element with a uniform cross-section subjected to dynamic forces at both ends. Considering that rod deformation depends on the undamped elementary rod theory, an equilibrium equation and boundary conditions at both ends are obtained as [5],

$$EA \frac{d^2 u}{dx^2} - \rho A \frac{d^2 u}{dt^2} = 0 \quad (13.1)$$

where  $E$ ,  $A$ , and  $\rho$  are Young's modulus, cross-section area, and mass density, respectively;  $u$  is the longitudinal displacement, which is a function of the spatial coordinate  $x$  and time  $t$ ;  $F$  is the external axial force; and subscripts 1 and 2 denote values at the element rod node numbers 1 and 2, respectively. By applying the Fourier transform to both sides of Eq. (13.1), its spectral representation can be written as

$$EA \frac{d^2 \hat{a}}{dx^2} + \omega^2 \rho A \hat{a} = 0 \quad (13.2)$$

**Fig. 13.1** Nodal displacements and forces for two-node rod elements under axial loading



where  $\hat{\cdot}$  denotes that the function is Fourier transformed and  $\omega$  is the circular frequency. A damping term is introduced into the rod formulation by using a complex Young's modulus. It is defined as  $E_c = E(1 + i\eta)$ , where  $\eta$  is the hysteretic structural damping loss factor and  $i = \sqrt{-1}$ . The general solution to the Eq. (13.2) can be expressed using arbitrary constants  $\mathbf{A}$  and  $\mathbf{B}$  as

$$\hat{u}(x) = \mathbf{A}e^{-ikx} + \mathbf{B}e^{-ik(L-x)} \quad (13.3)$$

where  $L$  is the rod element length,  $k$  is the complex wavenumber given by  $k = \omega/c$ , and  $c = \sqrt{E_c/\rho}$  is the rod phase velocity, Constants  $\mathbf{A}$  and  $\mathbf{B}$  are determined applying the boundary conditions of the rod. The displacement end conditions for the two-noded element are

$$\hat{u}(0) \equiv \hat{u}_1 = \mathbf{A} + \mathbf{B}e^{-ikL}; \quad \hat{u}(L) \equiv \hat{u}_2 = \mathbf{A}e^{-ikL} + \mathbf{B} \quad (13.4)$$

where  $\hat{u}_1$  and  $\hat{u}_2$  are the nodal displacements at the rod element node numbers 1 and 2, respectively. By rewriting Eq. (13.4) in a matrix form and solving for  $\mathbf{A}$  and  $\mathbf{B}$  in terms of nodal displacements, one has

$$\begin{Bmatrix} \mathbf{A} \\ \mathbf{B} \end{Bmatrix} = \begin{bmatrix} 1 & e^{-ikL} \\ e^{-ikL} & 1 \end{bmatrix}^{-1} \begin{Bmatrix} \hat{u}_1 \\ \hat{u}_2 \end{Bmatrix} \quad (13.5)$$

From Eq. (13.2) the loads at the rod element nodes are

$$\hat{F}_1 = \hat{F}(0) = -E_c A[-ik\mathbf{A} + ik\mathbf{B}e^{-ikL}]; \quad \hat{F}_2 = \hat{F}(L) = -E_c A[-ik\mathbf{A}e^{-ikL} + ik\mathbf{B}] \quad (13.6)$$

which can be rewritten in matrix form as

$$\begin{Bmatrix} \hat{F}_1 \\ \hat{F}_2 \end{Bmatrix} = E_c A \begin{bmatrix} ik & -ike^{-ikL} \\ -ike^{-ikL} & ik \end{bmatrix}^{-1} \begin{Bmatrix} \mathbf{A} \\ \mathbf{B} \end{Bmatrix} \quad (13.7)$$

Substituting Eq. (13.5) in Eq. (13.7), the dynamic stiffness matrix for the two-noded rod element,  $\hat{K}_S$ , can be obtained as

$$\begin{Bmatrix} \hat{F}_1 \\ \hat{F}_2 \end{Bmatrix} = \frac{E_c A ik L}{L(1 - e^{-i2kL})} \begin{bmatrix} 1 + e^{-i2kL} & -2e^{-i2kL} \\ -2e^{-i2kL} & 1 + e^{-i2kL} \end{bmatrix}^{-1} \begin{Bmatrix} \hat{u}_1 \\ \hat{u}_2 \end{Bmatrix} \quad (13.8)$$

For harmonic excitation, the time-averaged energy density for longitudinal waves in a rod can be written as a summation of the potential and kinetic energy densities,

$$e = \frac{1}{4} E_c A \left\{ \frac{\partial \hat{u} \partial \hat{u}^*}{\partial x \partial x} \right\} + \frac{1}{4} \rho A \left\{ \frac{\partial \hat{u} \partial \hat{u}^*}{\partial t \partial t} \right\} \quad (13.9)$$

where  $*$  represent the time-averaged quantity and the complex conjugate, respectively. The time-averaged energy flow for longitudinal waves in a rod is given by

$$q = \frac{1}{2} \Re \left\{ -\hat{F} \frac{\partial \hat{u}^*}{\partial t} \right\} \quad (13.10)$$

where  $\Re$  is the real part of a complex number.

### 13.2.2 Polynomial Chaos Expansion

The Polynomial Chaos basic concept is understood as a stochastic solution projected on a basis of orthogonal polynomials whose variables are orthogonal and gaussian. The polynomial basis properties generate a linear equation system through projections on the polynomial [9]; [10]. The stochastic problem can be formulated as [7]:

$$\Lambda(\mathbf{x}, \theta)u(\mathbf{x}, \theta) = [\mathbf{L}(\mathbf{x}) + \Pi(\mathbf{x}, \theta)]u(\mathbf{x}, \theta) = F(\mathbf{x}, \theta), \quad (13.11)$$

where  $L$  is deterministic part and  $\Pi$  is random part of stochastic operator  $\Lambda$ . It is possible to write a mechanical problem as follows [8]:

$$\left( [L] + \sum_{q=1}^N \xi_q \left[ \Pi_q \right] \right) \{u\} = \{F\} \quad (13.12)$$

where  $\xi_q$  are gaussian orthonormal variables, and the correlation function of  $\Pi$  is knowing.

The vector  $\{u\}$  is expanded in polynomials with  $Q$  orthogonal variables:

$$\{u\} = \sum_{n=0}^N \{u_n\} \Psi_n(\{\xi_i\}_{i=1}^Q) \quad (13.13)$$

By substituting Eq. (13.13) in Eq. (13.12), multiplying by  $\Psi_m$ , calculating the mean and using the orthogonality property of the polynomial, the displacement is obtained as:

$$\{u_m\} \langle \Psi_m^2 \rangle = \sum_{q=1}^Q \sum_{n=0}^N \{u_n\} \langle \xi_q \Psi_n \Psi_m \rangle [\Pi_q] = \{F\} \langle \Psi_m \rangle \quad (13.14)$$

It is important to observe that the values  $\langle \Psi_m^2 \rangle$  and  $\langle \xi_q \Psi_n \Psi_m \rangle$  should be computed only once, and used for all other calculus in this method.

The Eq. (13.14) for all  $m = 0, \dots, N$  produces a system of  $(N + 1)$  linear algebraic equations, whose solution gives the vectors  $\{u_n\}$  [11]. Once all  $\{u_n\}$  are known, is possible to calculate the mean and variance of  $\{u\}$  given by:

$$\mu = \{u_0\} \quad (13.15)$$

and

$$\sigma^2 = \sum_{n=1}^N \{u_n^2\} \langle \Psi_n^2 \rangle \quad (13.16)$$

### 13.2.3 Moment Equations

In this approach the statistical moments of the random solution (expected value and variance) are calculated directly for the energy density and energy flow. In order to make this development easy to manage Eq. (13.9) is rewritten in two parts, potential and kinetic energy density, and Eq. (13.10) is recasted to obtain:

$$e_p = \frac{1}{4} E_c A \{\hat{u} \hat{u}^*\}; \quad e_k = -\frac{1}{4} \rho \omega^2 A \{\hat{u} \hat{u}^*\}; \quad q = \frac{1}{2} \Re \{-i \omega E_c A \{\hat{u} \hat{u}^*\}\} \quad (13.17)$$

where  $\hat{u}' = \partial \hat{u} / \partial x$ . Based on the similarities of Eq. (13.17) in terms of relationship with the random variables ( $A$ ,  $\hat{u}'$ ,  $\hat{u}$ ), and for the sake of conciseness it will be show in more detail only the development for expected value and variance for the potential energy density. Considering that  $A$  and  $\hat{u}'$  are correlated random variables the expected value of potential energy density can be written as,

$$\mathbb{E}[e_p] = \frac{1}{4} E_c \mathbb{E}[A\hat{u}\hat{u}^*] = \frac{1}{4} E_c \mathbb{E}[AD] \quad (13.18)$$

where  $D = \hat{u}\hat{u}^*$ . From the properties of expected value and variance of a product of two correlated random variables [12],

$$\mathbb{E}[AD] = C(A, D) + \mathbb{E}[A]\mathbb{E}[D] \quad \text{or} \quad \mathbb{E}[A\hat{u}\hat{u}^*] = C(A, \hat{u}\hat{u}^*) + \mathbb{E}[A]\mathbb{E}[\hat{u}\hat{u}^*] \quad (13.19)$$

where  $C$  is the covariance. Under multivariate normality [13] shows that  $C(x, yz) = \mathbb{E}[y]C(x, z) + \mathbb{E}[z]C(x, y)$ , and from [14] the variance of a complex random variable is  $V(z) = C(z, z^*) = \mathbb{E}[zz^*] - \mathbb{E}[z]\mathbb{E}[z^*]$ , then

$$\mathbb{E}[A\hat{u}\hat{u}^*] = \mathbb{E}[\hat{u}]C(A, \hat{u}^*) + \mathbb{E}[\hat{u}^*]C(A, \hat{u}) + \mathbb{E}[A](V(\hat{u}) + \mathbb{E}[\hat{u}]\mathbb{E}[\hat{u}^*]) \quad (13.20)$$

where  $V$  is the variance. It can be shown that  $C(x, y) = \gamma_{x,y}[V(x)V(y)]^{1/2}$ , where  $\gamma_{x,y}$  is the linear correlation coefficient. Inserting this into Eq. (13.20) we obtain

$$\mathbb{E}[A\hat{u}\hat{u}^*] = \mathbb{E}[\hat{u}]\gamma_{A,\hat{u}^*}[V(A)V(\hat{u}^*)]^{1/2} + \mathbb{E}[\hat{u}^*]\gamma_{A,\hat{u}}[V(A)V(\hat{u})]^{1/2} + \mathbb{E}[A](V(\hat{u}) + \mathbb{E}[\hat{u}]\mathbb{E}[\hat{u}^*]) \quad (13.21)$$

Considering that  $\mathbb{E}[x] = \mu_x$  and  $V(x) = \sigma_x^2$ , the Eq. (13.21) becomes,

$$\mathbb{E}[A\hat{u}\hat{u}^*] = \gamma_{A,\hat{u}^*}\sigma_A(\mu_{\hat{u}}\sigma_{\hat{u}^*} + \mu_{\hat{u}^*}\sigma_{\hat{u}}) + \mu_A(\sigma_{\hat{u}}^2 + \mu_{\hat{u}}\mu_{\hat{u}^*}) \quad (13.22)$$

Substituting Eq. (13.22) into Eq. (13.18) we obtain the mean of potential energy density as,

$$\mu_{e_p} = \mathbb{E}[e_p] = \frac{1}{4} E_c \{ \gamma_{A,\hat{u}^*}\sigma_A(\mu_{\hat{u}} + \mu_{\hat{u}^*}^*) + \mu_A(\sigma_{\hat{u}}^2 + \mu_{\hat{u}}\mu_{\hat{u}^*}^*) \} \quad (13.23)$$

Using the same development for the kinetic energy density and energy flow equations, we obtain their corresponding means as

$$\mu_{e_k} = \mathbb{E}[e_k] = \frac{1}{4} \rho \omega^2 \{ \gamma_{A,\hat{u}}\sigma_A\sigma_{\hat{u}}(\mu_{\hat{u}} + \mu_{\hat{u}}^*) + \mu_A(\sigma_{\hat{u}}^2 + \mu_{\hat{u}}\mu_{\hat{u}}^*) \} \quad (13.24)$$

$$\mu_q = \mathbb{E}[q] = \frac{1}{2} \Re \{ -i\omega E_c \sigma_A (\gamma_{A,\hat{u}}\mu_{\hat{u}}\sigma_{\hat{u}}^* + \gamma_{A,\hat{u}^*}\mu_{\hat{u}}^*\sigma_{\hat{u}}) + \mu_A(\gamma_{\hat{u},\hat{u}}\sigma_{\hat{u}}\sigma_{\hat{u}}^* + \mu_{\hat{u}}\mu_{\hat{u}}^*) \} \quad (13.25)$$

The mean value of total energy density can be written as  $\mu_e = \mu_{e_p} + \mu_{e_k}$ . The variance of potential energy density can be written as,

$$V(e_p) = \mathbb{E}[e_p^2] - \mathbb{E}^2[e_p] \quad (13.26)$$

where the expected value of squared potential energy density can be written as,

$$\mathbb{E}[e_p^2] = \frac{1}{16} E_c^2 \mathbb{E}[A^2\hat{u}^2\hat{u}^{*2}] = \frac{1}{16} E_c^2 \mathbb{E}[A^2D^2] \quad (13.27)$$

where  $D = \hat{u}\hat{u}^*$ . From the properties of expected value of a product of two squared correlated random variables [13], where  $\mathbb{E}[x^2v^2] = V(xv) + \mathbb{E}^2[xv]$ . Considering that the variance and squared expected value of a product of two correlated random variables, where  $V(xv) = \mathbb{E}^2[x]V(v) + \mathbb{E}^2[v]V(x) + 2\mathbb{E}^2[x]\mathbb{E}^2[v]C(x, v) + V(x)V(v) + C^2(x, v)$ , and  $\mathbb{E}^2[xv] = (C(x, v) + \mathbb{E}[x]\mathbb{E}[v])^2$ , we obtain

$$\mathbb{E}[x^2v^2] = \mathbb{E}^2[x]V(v) + \mathbb{E}^2[v]V(x) + 4\mathbb{E}[x]\mathbb{E}[v]C(x, v) + V(x)V(v) + 2C^2(x, v) + \mathbb{E}^2[x]\mathbb{E}^2[v]. \quad (13.28)$$

By doing  $x = A$ ,  $v = D = \hat{u}\hat{u}^*$ , and simplifying, we obtain

$$\mathbb{E}[A^2\hat{u}^2\hat{u}^{*2}] = \{ \mathbb{E}^2[A] + V(A) \} \{ V(\hat{u}\hat{u}^*) + \mathbb{E}^2[\hat{u}\hat{u}^*] \} + 4\mathbb{E}[A]\mathbb{E}[\hat{u}\hat{u}^*]C(A, \hat{u}\hat{u}^*) + 2C^2(A, \hat{u}\hat{u}^*) \quad (13.29)$$

It will not be shown here all the intermediate steps to obtain the final equations. Then, by using the properties for variance and covariance of a product of two variable multivariate gaussian, substituting into de Eq. (13.29) and simplifying, we get:

$$\begin{aligned} \mathbb{E}[e_p^2] = & \frac{1}{16} E_c^2 \{ (\mu_A^2 + \sigma_A^2) [\sigma_{\hat{u}'}^2 (\mu_{\hat{u}'}^2 + \mu_{\hat{u}'}^{*2} + 4\mu_{\hat{u}'} \mu_{\hat{u}'}^*) + 3\sigma_{\hat{u}'}^4 + \mu_{\hat{u}'}^2 \mu_{\hat{u}'}^{*2}] + 2\gamma_{A,\hat{u}'} \sigma_A^2 \sigma_{\hat{u}'}^2 (\mu_{\hat{u}'} + \mu_{\hat{u}'}^*)^2 \\ & + 4\gamma_{A,\hat{u}'} \mu_A \sigma_A \sigma_{\hat{u}'} (\mu_{\hat{u}'} + \mu_{\hat{u}'}^*) (\sigma_{\hat{u}'}^2 + \mu_{\hat{u}'} \mu_{\hat{u}'}^*) \} \end{aligned} \quad (13.30)$$

Substituting Eqs. (13.23) and Eq. (13.30) into the Eq. (13.26) the variance of potential energy density is obtained. Similar developments will produce the expected values of squared kinetic energy density and energy flow as,

$$\begin{aligned} \mathbb{E}[e_k^2] = & \frac{1}{16} \rho^2 \omega^4 \{ (\mu_A^2 + \sigma_A^2) [\sigma_{\hat{u}}^2 (\mu_{\hat{u}}^2 + \mu_{\hat{u}}^{*2} + 4\mu_{\hat{u}} \mu_{\hat{u}}^*) + 3\sigma_{\hat{u}}^4 + \mu_{\hat{u}}^2 \mu_{\hat{u}}^{*2}] + 2\gamma_{A,\hat{u}} \sigma_A^2 \sigma_{\hat{u}}^2 (\mu_{\hat{u}} + \mu_{\hat{u}}^*)^2 \\ & + 4\gamma_{A,\hat{u}} \mu_A \sigma_A \sigma_{\hat{u}} (\mu_{\hat{u}} + \mu_{\hat{u}}^*) (\sigma_{\hat{u}}^2 + \mu_{\hat{u}} \mu_{\hat{u}}^*) \} \end{aligned} \quad (13.31)$$

$$\begin{aligned} \mathbb{E}[q^2] = & \frac{1}{4} \omega^2 E_c^2 \{ (\mu_A^2 + \sigma_A^2) (\mu_{\hat{u}'}^2 \sigma_{\hat{u}}^{*2} + \mu_{\hat{u}}^{*2} \sigma_{\hat{u}'}^2 + 2\gamma_{\hat{u}',\hat{u}} \mu_{\hat{u}'} \mu_{\hat{u}}^* + (1 + \gamma_{\hat{u}',\hat{u}}) \mu_{\hat{u}'}^2 \sigma_{\hat{u}}^{*2} \sigma_{\hat{u}}^{*2} + \mu_{\hat{u}}^2 \mu_{\hat{u}}^{*2}) \\ & + 4\mu_A \sigma_A (\gamma_{\hat{u}',\hat{u}} \sigma_{\hat{u}} \sigma_{\hat{u}}^* + \mu_{\hat{u}} \mu_{\hat{u}}^*) (\gamma_{A,\hat{u}} \mu_{\hat{u}'} \sigma_{\hat{u}}^* + \gamma_{A,\hat{u}'} \mu_{\hat{u}}^* \sigma_{\hat{u}}) + 2\sigma_A^2 (\gamma_{A,\hat{u}} \mu_{\hat{u}'} \sigma_{\hat{u}}^* + \gamma_{A,\hat{u}'} \mu_{\hat{u}}^* \sigma_{\hat{u}})^2 \} \end{aligned} \quad (13.32)$$

Finally the variances of kinetic energy density and energy flow are obtained by:

$$\sigma_{e_k}^2 = \mathbf{V}(e_k) = \mathbb{E}[e_k^2] - \mathbb{E}^2[e_k] \quad (13.33)$$

$$\sigma_q^2 = \mathbf{V}(q) = \mathbb{E}[q^2] - \mathbb{E}^2[q] \quad (13.34)$$

The variance of total energy density can be obtained using [13]:  $\sigma_e^2 = \sigma_{e_p}^2 + \sigma_{e_k}^2 - 2\gamma_{e_p,e_k} \sigma_{e_p} \sigma_{e_k}$ .

### 13.3 Numerical Simulations

In order to evaluate the method, a numerical example is performed on a free-free rod with the following dimensions and material properties:  $L1 = 0.9$  m,  $L = 3.0$  m,  $h = 0.02$  m,  $b = 0.02$  m,  $E = 71$  GPa,  $\eta = 0.01$ , and  $\rho = 2700$  kg/m<sup>3</sup>. In this numerical test the spectral model is excited with a longitudinal harmonic point force applied at left-hand side of the rod, with magnitude  $F = 1$  N. The crack is imposed at the position  $x = L1$ , with a crack depth of 25% cross section height. The cross section area ( $A$ ) is considered as a gaussian random variable with mean  $\mu_A = 0.004$  m<sup>2</sup>, and coefficient of variation  $COV_A = 0.1$ . The correlation coefficients ( $\gamma$ ) were chosen randomly instead of be statically estimated.

Figure 13.2 shows two results for the mean of energy density calculated by Monte Carlo simulation (MC) and Polynomial Chaos expansion with Moment equation (PC). The results were obtained for healthy and cracked rods calculated by SEM in a 1/3-octave frequency band with center frequency  $f_c = 160$  kHz. The polynomial chaos model was calculated with a Hermite polynomial of order 1 (PC1) with correlation coefficients of  $\gamma = 0.0$  and  $\gamma = 0.75$ . The MC simulation results was obtained with 500 samples.

As can be seen the mean of energy density presents a good agreement between the MC and PC methods, which represents a typical behavior that was observed for all others evaluations using different values of polynomial order and correlation coefficient. Figure 13.3 shows the corresponding results for the standard deviation of energy density. For this cases, it can be seen that PC results does not match very well with the MC results. However, there is a better approximation when  $\gamma = 0.75$  as compared with  $\gamma = 0.0$ , which indicates that the correlation coefficient can improve the results if evaluated at statistical basis. For the PC damage model it was also observed an oscillatory behavior at the regions close to the crack position and at the rod right end. It seems to come from the approximations at the moment equations.

Figures 13.4 and 13.5 show the results for the the mean and standard deviation of energy flow calculated by MC and PC. The PC model was of order 1 (PC1) and the correlation coefficients values were  $\gamma = 0.0$  and  $\gamma = 0.75$ . The MC simulation results was performed using 500 samples.

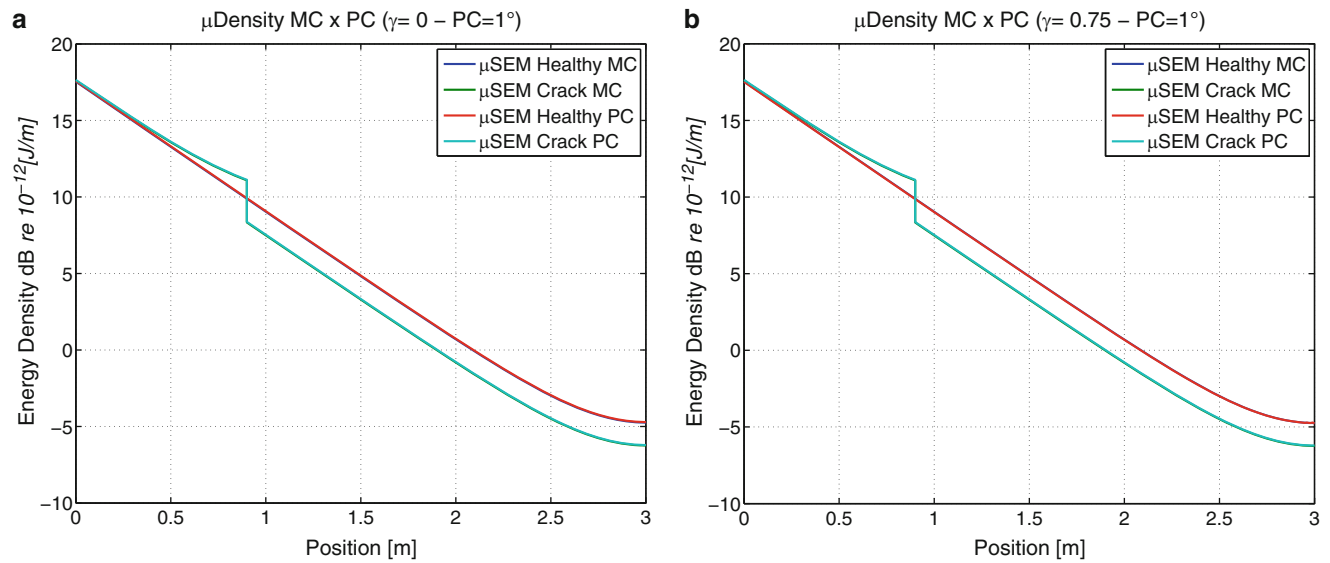


**Fig. 13.2** Mean of energy density for healthy and cracked rod using PC-order 1 with: (a)  $\gamma = 0.0$ ; (b)  $\gamma = 0.75$

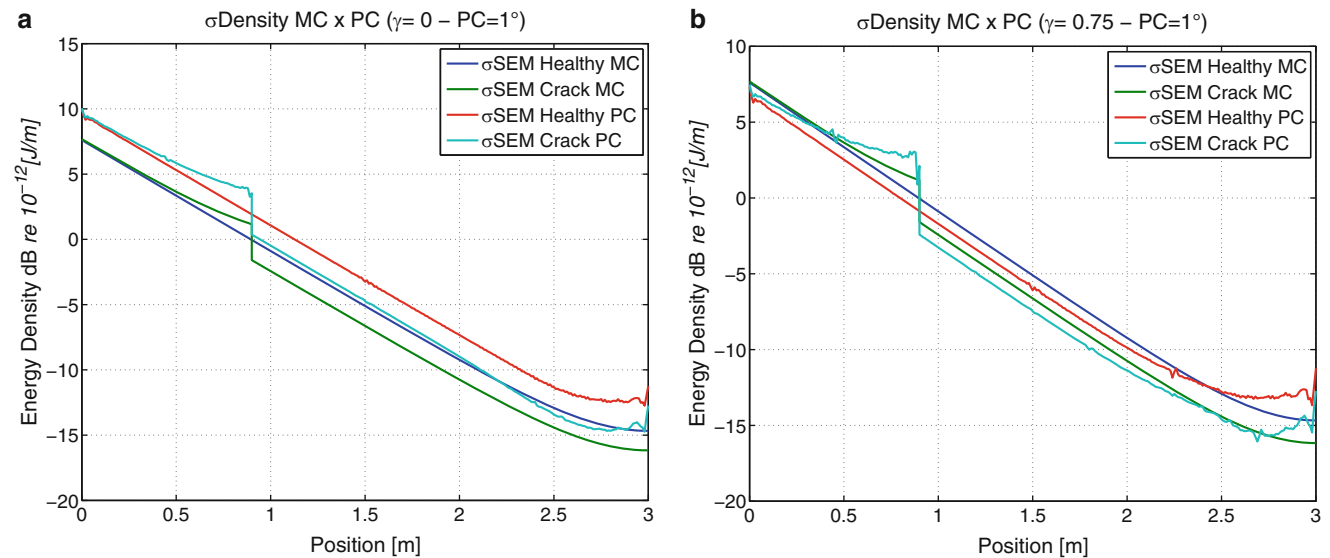


**Fig. 13.3** Standard deviation of energy density for healthy and cracked rod using PC1 with: (a)  $\gamma = 0.0$ ; (b)  $\gamma = 0.75$

As can be seen the results present a similar behavior as observed for the energy density, where there is a good agreement for the means while for the standard deviation the approximation depends on the correlation coefficient. Also, for the PC damage model it was observed an divergent behavior at the regions close to the crack position and at the rod right end.

Figures 13.6–13.9 shows the results for the mean and standard deviation of energy density and energy flow calculated by MC and PC, with the same values of sample size, material properties, rod geometry and correlation coefficients, but with a Hermite polynomial of order 2 (PC2). These results confirms the observations extracted in the analysis of the case PC1.

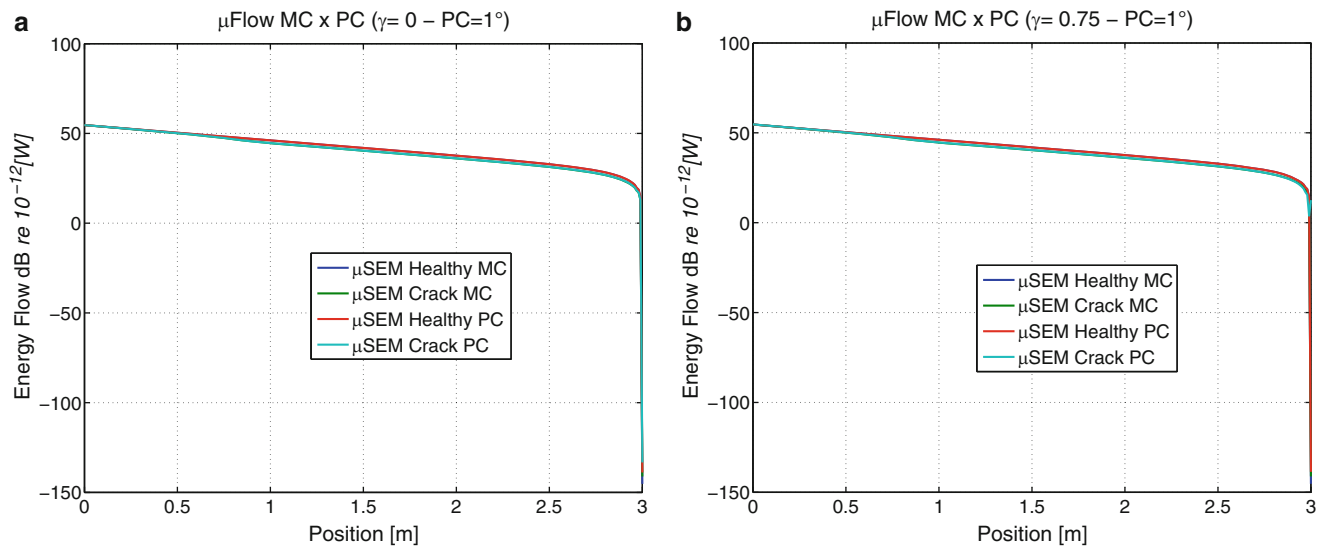


Fig. 13.4 Mean of energy flow for healthy and cracked rod using PC1 with: (a)  $\gamma = 0.0$ ; (b)  $\gamma = 0.75$

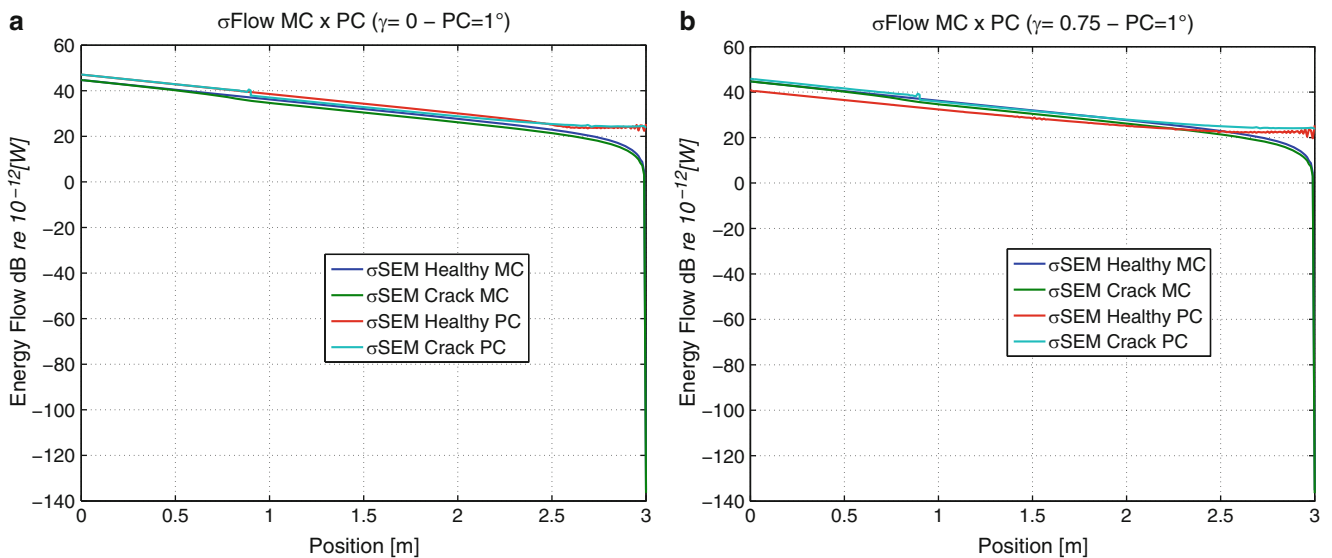


Fig. 13.5 Standard deviation of energy flow for healthy and cracked rod using PC1 with: (a)  $\gamma = 0.0$ ; (b)  $\gamma = 0.75$

## 13.4 Final Remarks

A study about the energy flow patterns caused by localized damage in structures like rod, including uncertainties in a geometric parameter is presented. A new formulation is developed and proposed to solve this problem in two steps: first, the structure is modeled by the SEM and the mean and variance of displacement responses are obtained by using the Polynomial Chaos expansion; second, the mean and variance of energies are calculated applying the expectation into the equations of energy density and energy flow. Monte Carlo Simulation (MCS) is used to validate the results obtained by these solutions. For all simulated cases the mean of energy density and energy flow presents a good agreement between the MC and PC methods independently of the values of polynomial order and correlation coefficients. However, the standard deviation does not converge very well, but its results indicates that it can be improved with a better estimation of the correlation coefficients. Of course, this are preliminaries results using a very simple examples in order do check the ideas of the method. Then, more tests needs to be conducted to verify the extension and robustness of the method.

**Acknowledgements** The authors would like to thank, CNPq, Fapesp, and CAPES for supporting this work.



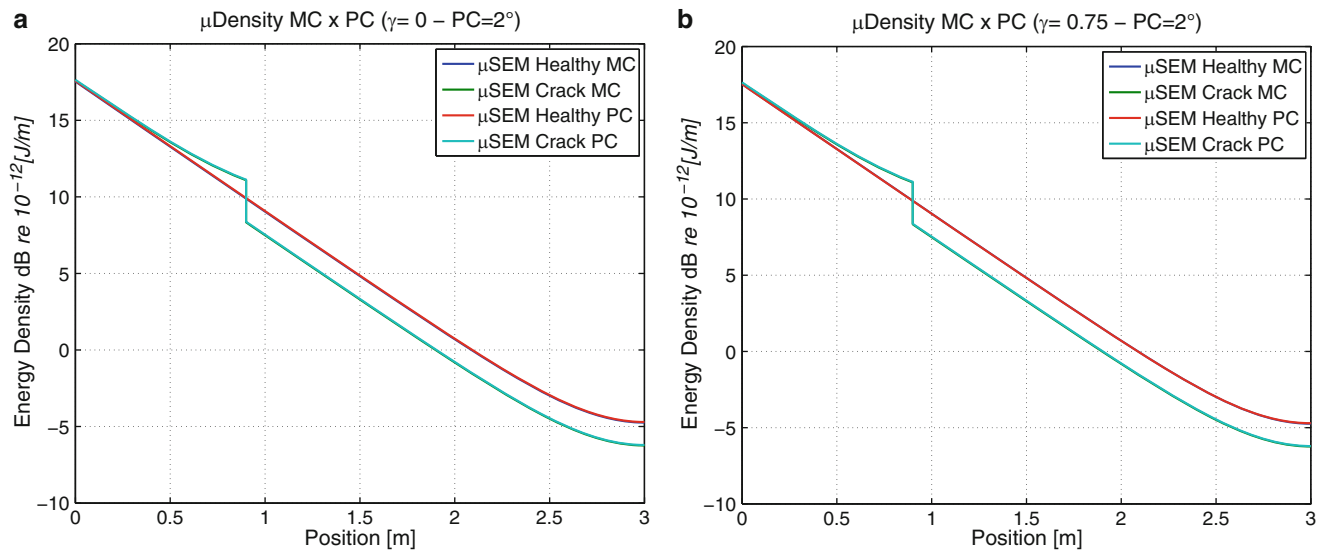


Fig. 13.6 Mean of energy density for healthy and cracked rod using PC2 with: (a)  $\gamma = 0.0$ ; (b)  $\gamma = 0.75$

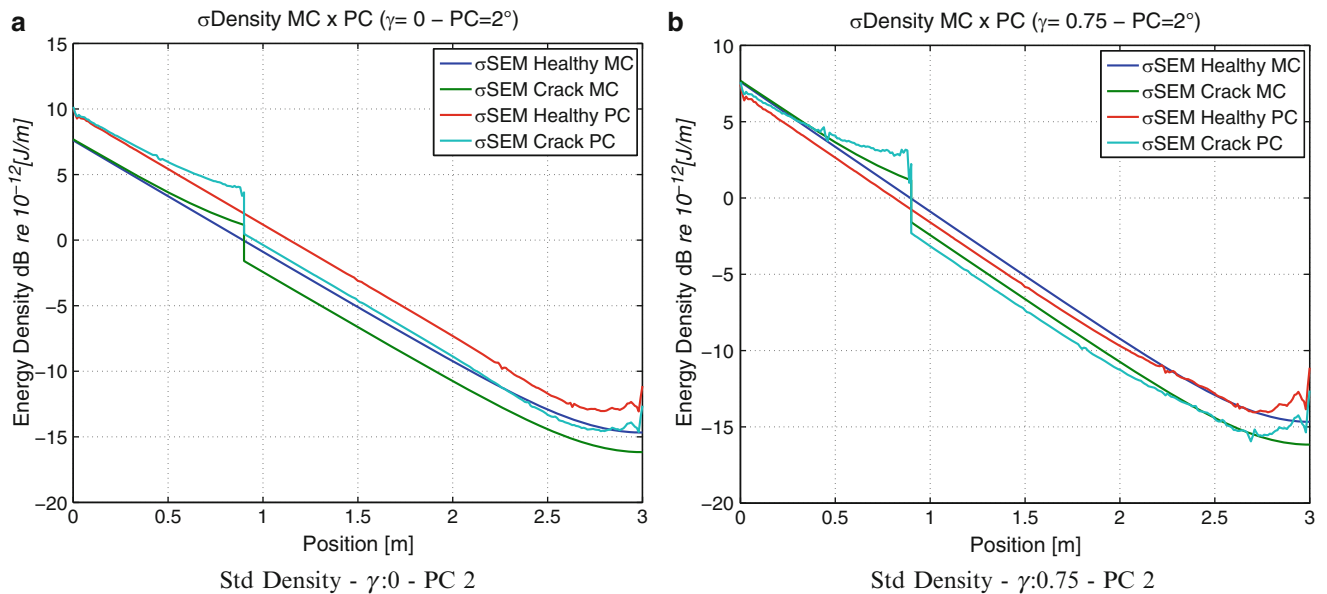
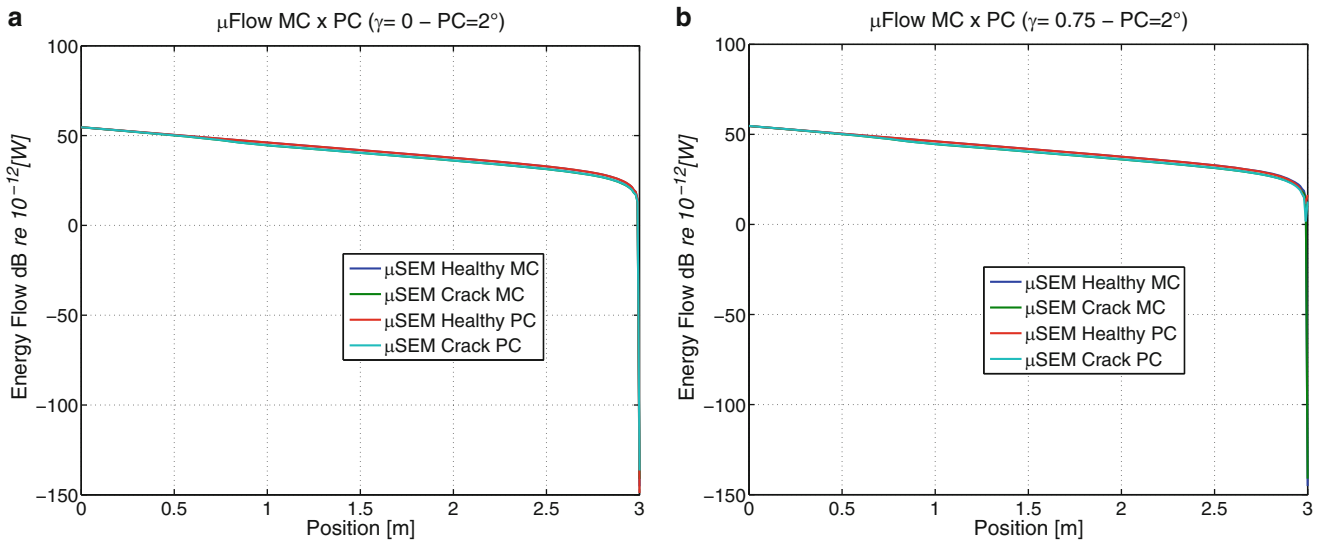


Fig. 13.7 Standard deviation of energy density for healthy and cracked rod using PC2 with: (a)  $\gamma = 0.0$ ; (b)  $\gamma = 0.75$

## References

1. Doebling, S. W., Farrar, C. R., and Prime, M. B. (1998) *The Shock and Vibration Digest* **30**, 91–105.
2. Montalvo, D., Maia, N., and Ribeiro, A. (2006) *The Shock and Vibration Digest* **38**, 0 – 0.
3. Krawczuk, M., Grabowska, J., and Palacz, M. (2006) *Journal of Sound and Vibration* **295**, 461–478.
4. Santos, E., Arruda, J., and Santos, J. D. (2008) *Journal of Sound and Vibration* **36**, 1 – 24.
5. Doyle, J. F. (1997) *Wave propagation in structures : spectral analysis using fast discrete Fourier transforms*, Mechanical engineeringSpringer-Verlag New York, Inc., New York second edition.
6. Sobol, I. M. (1994) *A primer for the Monte Carlo method*, CRC Press, .
7. Ghanem, R. and Spanos, P. (1991) *Stochastic Finite Elements - A Spectral Approach*, Sprin, .
8. Dessombz, O., Thouverez, F., Laine, J.-P., and Jezequel, L. Calcul des valeurs et vecteurs propres d'une structure stochastique par projection sur un chaos polynomial. calcul de fonctions de transfert stochastiques Technical report Ecole Centrale de Lyon - Laboratoire de Tribologie et Dynamique des Systemes (2000).
9. Ghanem, R. and Brzakala, W. (1996) *Journal of Engineering Mechanics* **122**, 361–369.
10. Ghanem, R. and Kruger, R. M. (1996) *Computers Methods Apply Mechanical Engineering* **129**, 289–303.



**Fig. 13.8** Mean of energy flow for healthy and cracked rod using PC-order 2 with: (a)  $\gamma = 0.0$ ; (b)  $\gamma = 0.75$

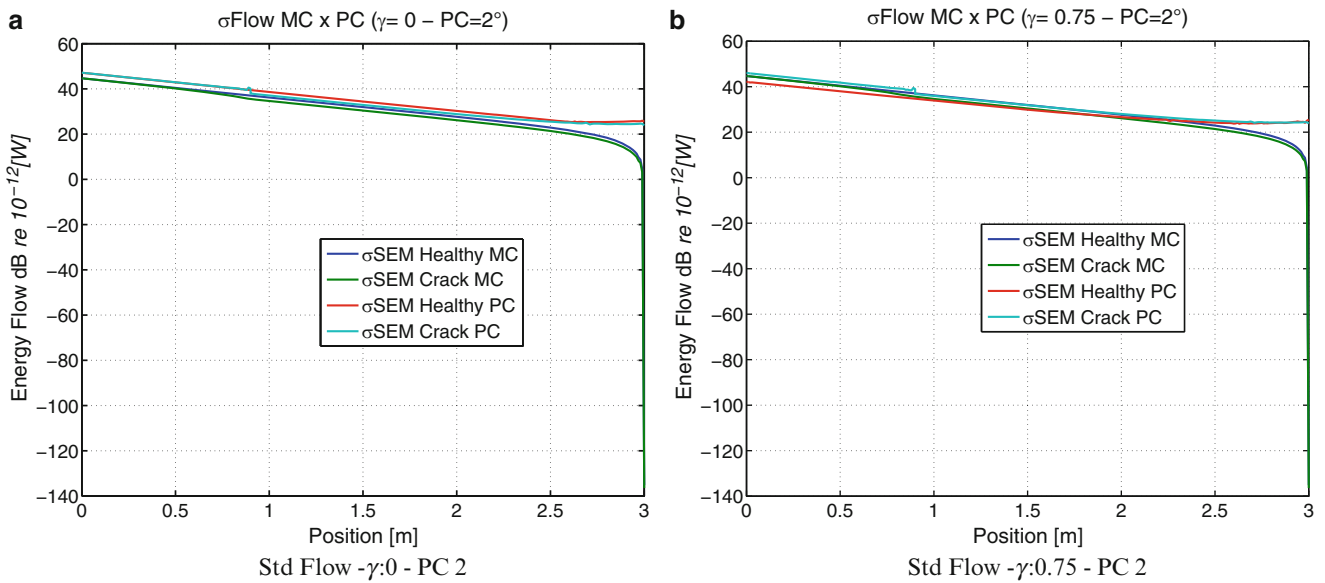


**Fig. 13.9** Standard deviation of energy flow for healthy and cracked rod using PC2 with: (a)  $\gamma = 0.0$ ; (b)  $\gamma = 0.75$

11. Dessombz, O., Thouverez, F., Laine, J.-P., and Jezequel, L. Expansion of stochastic frequency response function on polynomial chaos Technical report Ecole Centrale de Lyon (2001).
12. Goodman, L. A. (1960) *Journal of the American Statistical Association* (55) 292, 708–713.
13. Bohrnstedt, G. W. and Goldberger, A. S. (1969) *Journal of the American Statistical Association* (64) 328, 1439–1442.
14. Miller, S. and Childers, D. (2012) *Probability and Random Processes*, Academic Pres, .

# Chapter 14

## A Coupled Approach for Structural Damage Detection with Incomplete Measurements

George James, Tim Cao, Mo Kaouk, and David Zimmerman

**Abstract** Abstract This historical work couples model order reduction, damage detection, dynamic residual/mode shape expansion, and damage extent estimation to overcome the incomplete measurements problem by using an appropriate undamaged structural model. A contribution of this work is the development of a process to estimate the full dynamic residuals using the columns of a spring connectivity matrix obtained by disassembling the structural stiffness matrix. Another contribution is the extension of an eigenvector filtering procedure to produce full-order mode shapes that more closely match the measured active partition of the mode shapes using a set of modified Ritz vectors. The full dynamic residuals and full mode shapes are used as inputs to the minimum rank perturbation theory to provide an estimate of damage location and extent. The issues associated with this process are also discussed as drivers of near-term development activities to understand and improve this approach.

**Keywords** Damage detection • Structural health monitoring • Model order reduction • Mode shape expansion • Ritz vectors

### 14.1 Introduction

The use of changing structural dynamics parameters as indicators of damage state and structural health has received increasing attention in recent years. The global nature of these parameters provides a unique capability to monitor internal components of aerospace, civil, mechanical, naval, and nuclear structures. The ability to model the structural response analytically enhances this unique capability to locate damage in unmeasured locations as well as to provide tools to determine the extent of the damage. However, much work needs to be done to use experimental and analytical models properly in a coordinated fashion to perform damage identification. One of the most difficult issues to overcome is the incomplete measurement problem, which means that (1) there is an inherent mismatch between the experimental and the analytical degrees of freedom (DOFs) and (2) there is a mismatch between the numbers of measured and analytical modes. Another difficult issue is that neither the experimental measurements (noise) nor the analytical model (modeling errors) is correct. The last statement is especially true in damage identification as the analytical model is typically produced for the undamaged structure.

The incomplete measurement problem means that model order reduction [1–6] and/or test data expansion [4–11] must be performed to utilize both data sets fully. However, it has been found that most reduction expansion techniques are not extremely useful for damage identification [6, 10, 11]. It has been suggested that reduction/damage identification/expansion should be handled as coupled problems [6]. This work describes the development of such an integrated procedure that is initiated by first disassembling the structural stiffness matrix [12–15] into a connected set of springs. The columns of the spring connectivity matrix are then used as a set of candidate basis vectors for estimating the full dynamic residual. This candidate set is down selected using the modal assurance criteria (MAC) between the reduced dynamic residual and a

---

G. James (✉) • T. Cao • M. Kaouk

Loads and Structural Dynamics Branch, NASA Johnson Space Center, Houston, TX 77058, USA  
e-mail: [george.h.james@nasa.gov](mailto:george.h.james@nasa.gov); [timothy.t.cao@nasa.gov](mailto:timothy.t.cao@nasa.gov); [mohamed.kaouk@nasa.gov](mailto:mohamed.kaouk@nasa.gov)

D. Zimmerman

University of Houston, Houston, TX 77204, USA

reduction of each candidate vector averaged over the modes of interest. A least-squares fit is then used to scale the remaining basis vectors to match the dynamically reduced residuals for each mode. The estimated full residuals provide damage location information and are used to initiate a modified Ritz vector [16] calculation process. A set of Ritz-like vectors are calculated and used as a set of basis vectors to expand the mode shapes and to guarantee mass orthogonality. The full dynamic residuals and full mode shapes are then used as inputs to the minimum rank perturbation theory (MRPT) [17–19] to provide an estimate of damage. The process suggested herein was originally published in Refs. [20, 21].

## 14.2 Technical Background of Original Work

This section briefly describes the basic theoretical components used in the coupled damage detection approach.

### 14.2.1 Dynamic Residual Formulation

This study will proceed with a standard math model for a dynamical system (ignoring damping):

$$[M] \{\ddot{U}\} + [K] \{U\} = \{F\}. \quad (14.1)$$

The corresponding eigenvalue problem for the undamaged structure is given as:

$$[M \omega_{ui}^2 - K] \{\phi_{ui}\} = 0; \quad (14.2)$$

where the subscript  $u$  denotes undamaged and  $i$  denotes the  $i$ th mode of vibration. The eigenvalue problem for the damaged structure is:

$$[(M - \Delta M) \omega_i^2 + (K - \Delta K)] \{\phi_i\} = 0; \quad (14.3)$$

where the  $\Delta$  matrices represent the effect of damage on the structural property matrices. Now Eq. (14.3) can be rewritten in dynamic residual form:

$$[M \omega_i^2 + K] \{\phi_i\} = \{b\} = [\Delta M \omega_i^2 + \Delta K] \{\phi_i\}. \quad (14.4)$$

#### 14.2.1.1 Model Reduction

The dynamic residual form can be rearranged into an active or measured set of DOFs and an omitted or unmeasured set of DOFs. It is commonly assumed that the model of the undamaged structure can be used to create a transformation relating the unmeasured and measured DOFs. One approach is to produce a physical-coordinates based transformation [7] that for a single mode shape has the following form:

$$\{\phi_i\} = \begin{Bmatrix} \phi_{ai} \\ \phi_{oi} \end{Bmatrix} = [T] \{\phi_{ai}\} = \begin{bmatrix} T_{aa} \\ T_{oa} \end{bmatrix} \{\phi_{ai}\}. \quad (14.5)$$

The transformation matrix  $[T]$  in Eq. (14.5) can be calculated from the stiffness matrix  $[K]$  using the static or Guyan–Irons [1, 2] reduction/expansion. A scaled sum of the mass  $[M]$  and stiffness matrices can also be used to estimate  $[T]$  as suggested by dynamic reduction/expansion [3]. The transformation matrix  $[T]$  denoted in Eq. (14.5) can be used to reduce the order of the analytical model. Substituting Eq. (14.5) into Eq. (14.4) and premultiplying by  $[T]^T$ , one finds that the reduced equations of motion are:

$$[T]^T [M \omega_i^2 + K] [T] \{\phi_{ai}\} = \{b_{ri}\} = [T]^T \{b_i\}. \quad (14.6)$$

The reduced dynamic residual,  $\{b_{ri}\}$ , given in Eq. (14.6) has been shown to be of importance in damage identification [17–22] to localize and to calculate the extent of damage. However, these capabilities are limited by the application of the transformation  $[T]$ , which tends to redistribute residual forces to undamaged DOFs. A primary contribution of this work is

to provide an approach to retain these capabilities by first estimating the full dynamic residual  $\{b_i\}$ . The procedure suggested to perform this estimation begins by performing a matrix disassembly on the stiffness matrix [12–15]. This will produce a set of basis vectors used to estimate the full dynamic residual.

### 14.2.1.2 Matrix Disassembly

Matrix disassembly is a process that decomposes a structural matrix into a matrix representation of the connectivity between DOFs and a matrix containing the magnitude information [12–15]. This formulation has the following form for the stiffness matrix:

$$[K] = [CPC^T]. \quad (14.7)$$

Advanced applications utilize a disassembly into the same finite elements that were used to create the model [14]. However, this work utilizes a disassembly into a set of equivalent springs. This produces a general technique that can be applied to any model without detailed knowledge about the actual elements used in the assembly. The matrix  $[C]$  is an  $n \times m$  matrix, where  $n$  is the matrix dimension for  $[K]$  and  $m$  is equal to the total number of unique entries in  $[K]$  (for symmetric  $[K]$  this amounts to the nonzero entries in the upper triangular portion of the stiffness matrix). The diagonal matrix  $[P]$  is calculated as:

$$\begin{aligned} P(i, i) &= \sum_{j=1}^n K(i, j), \text{ for } i = 1:n; \text{ and} \\ P(i, i) &= -K(j, k), \text{ for } i = n + 1:m. \end{aligned} \quad (14.8)$$

The first  $n$  columns/rows of  $[C]$  form an  $n \times n$  identity matrix. The remaining  $(m - n)$  columns are defined according to the element locations of the unique entries in the matrix  $[K]$ . For the element  $K(j, k)$ , which is used to define the  $i$ th row/column of  $[P]$  for the index  $i$  running from  $n + 1$  to  $m$ , the  $i$ th column of  $[C]$  is given as:

$$\begin{aligned} C(j, i) &= 1.0; \text{ and} \\ C(k, i) &= -1.0. \end{aligned} \quad (14.9)$$

### 14.2.1.3 Estimating the Expanded Dynamic Residual

For each mode of interest, Eq. (14.6) relates a known quantity ( $\{b_{ri}\}$ , the reduced dynamic residual) to an unknown quantity ( $\{b_i\}$ , the full dynamic residual). This work assumes that the full dynamic residual can be described as a linear combination of the columns of the connectivity matrix. Therefore, each column will initially be considered a candidate for inclusion in the calculation of the full dynamic residual vector for that mode. The first issue is to down select the set of columns of  $[C]$  to the most promising subset for further analysis. Although it was not rigorously necessary, this work constrained the selected subset to have linearly independent columns. (The full  $[C]$  matrix contains a high degree of column linear dependence.) Each candidate vector from  $[C]$ ,  $\{c_j\}$ , will serve as an approximate full dynamic residual vector. The resulting reduced dynamic residual basis vector  $\{\beta_{rij}\}$  is calculated from Eq. (14.6) by replacing  $\{b_i\}$  with  $\{c_j\}$ . In this work, a comparison with the actual reduced dynamic residual for that mode is made using the MAC, which relates the global similarity between two vectors:

$$MAC_{ij} = \frac{\|b_{ri}^T \beta_{rij}\|^2}{\|b_{ri}^T b_{ri}\| \|\beta_{rij}^T \beta_{rij}\|}. \quad (14.10)$$

The MAC values are averaged over the modes of interest. These averaged values then provide a discriminator between the candidate columns of the connectivity matrix. Columns  $\{c_j\}$ , which produce large MAC values over a wide range of modes, are candidates for down selection. The user must select the number of the largest average MAC candidate basis vectors to include in the next analysis. This selection is made based on the relative sizes of the average MAC values, the spatial relationship between the candidate vectors, and the linear dependence of the resulting set of vectors.

The next step is to use the selected vectors as basis vectors for approximating the full dynamic residual. Substituting a linear combination of the basis vectors into Eq. (14.6) yields:

$$\{b_{ri}\} = [T]^T \{b_i\} = [T]^T [C_{\text{selected columns}}] \{\alpha_i\}, \quad (14.11)$$

where the unknown coefficient  $\alpha_i$  is determined by a least-squares approach. (Note that the reduction transformation will change with each mode if dynamic reduction is used.) The critical output of this step is a set of full dynamic residual vectors that match the reduced equations. The next step will be to use these expanded residuals to expand the mode shapes.

#### 14.2.1.4 Mode Shape Expansion

Mode shape expansion estimates the unmeasured DOFs given the undamaged model, the experimental modal frequency, the measured mode shape DOFs, and the full dynamic residual. However, the physical coordinate transformation approach listed earlier typically assumes that the omitted partition of the dynamic residual is zero [1–3]. Because this may not be the case for the damage identification problem, this approach must be modified assuming a nonzero residual vector.

An approach called eigenvalue filtering (EV) utilizes the full residual to expand the mode shape. This approach uses Eq. (14.4) to generate the expansion by inverting the dynamic stiffness matrix  $[D]$  using the associated experimental modal frequency  $\omega_i$  (Ref. [23]):

$$\{\phi_i\} = [M\omega_i^2 + K]^{-1} \{b_i\} = [D_i]^{-1} \{b_i\}. \quad (14.12)$$

The EV approach ensures that the full mode shape produces the estimated dynamic residual when operating on the undamaged model shifted with the experimental modal frequency. However, it should be noted that the active partitions of the mode shapes are not constrained to be the measured values. One contribution of this work is to extend this approach to allow the user to add in these constraints in an incremental process.

The modified approach assumes that the full mode shapes are a linear combination of basis vectors. A modified Ritz vector calculation will be used to generate a set of basis vectors to expand the mode [16]. The Ritz vector calculation procedure provided in Ref. [16] initiates the process by operating on a force vector with the inverse of the stiffness matrix. The resulting deflection vector is mass normalized and used as the input vector to an inverse iteration with the stiffness matrix inverse and mass matrix as the multipliers. The successive Ritz vectors are orthogonalized with a modified Gram–Schmidt process and mass normalized.

The modified process will generate a set of Ritz-like vectors for each mode of interest using the dynamic residual for each mode as the initial force vector. Two additional modifications to the Ritz vector calculation approach referenced earlier are required. First, to be consistent for perfect data and perfect dynamic residuals, the stiffness matrix is replaced with the dynamic stiffness matrix  $[D]$  appropriate for each mode. The next modification is that the mass orthogonalization step includes not just the previously calculated Ritz vectors for that mode but also the previously expanded mode shapes. Hence, a set of basis vectors responding to the forces represented by the dynamic residual and mass orthogonal to themselves and the previously expanded modes of the system will be calculated. Therefore, a linear combination of these basis vectors will be mass orthogonal to the previously expanded modes of the system. These basis vectors will be linearly combined to match the active partition of the mode of interest. Hence for the  $l$ th mode of the system the following equations are used:

$$\{\bar{v}_1\} = [D_l]^{-1} \{b_l\}; \quad (14.13)$$

$$\{v_1\} = \frac{\{\bar{v}_1\}}{(\bar{v}_1^T M \bar{v}_1)^{1/2}}; \quad (14.14)$$

$$\{\bar{v}_i\} = [D_l]^{-1} [M] \{v_{i-1}\}; \quad (14.15)$$

$$\{v_i\} = \{\bar{v}_i\} - \sum_{j=1}^{i-1} (v_j^T M \bar{v}_i) \{v_j\} - \sum_{k=1}^{l-1} (\phi_k^T M \bar{v}_i) \{\phi_k\}; \quad (14.16)$$

$$(v_i^T M v_i) = 1; \quad (14.17)$$

$$\{\phi_l\} = \sum_{i=1}^n \gamma_{li} \{v_i\}. \quad (14.18)$$

This procedure produces a set of expanded mode shapes that are mass orthogonal and consistent with the full dynamic residuals. It is important to note that the first vector is equivalent to the full mode shape calculated with the EV approach given in Eq. (14.12). The coefficients  $\gamma_{li}$  in Eq. (14.18) are determined by partitioning Eq. (14.18) into the active and omitted

sets and then solving a least-squares problem involving only the active set. Hence, by allowing additional terms in the expansion process, the user can trade off confidence in the expanded dynamic residual for confidence in the measured mode shape DOFs.

#### 14.2.1.5 Damage Location and Extent: MRPT

The estimation of damage location and extent is performed via the Minimum Rank Perturbation Theory (MRPT) [17–20]. The underlying philosophy of the MRPT is that reduced rank perturbations to the structural matrices are the manifestation of damage. In this approach, damage results in a zero–nonzero pattern in the dynamic residual as given by Eq. (14.4). Typically, measurement noise and model order reduction or expansion destroys this pattern. Hence, a significant result of this approach is that the zero–nonzero pattern of the dynamic residual will be controlled by the columns of the connectivity matrix that are used to create it.

The estimation of damage extent using a minimum rank formulation utilizes the following calculation (assuming that all damage is manifested only in the stiffness matrix):

$$[\Delta K] = [B] [\Phi^T B]^{-1} [B^T]; \quad (14.19)$$

where  $[B]$  is the matrix formed of all column vectors of the expanded dynamic residuals for the modes of interest and  $[\Phi]$  is the matrix of the expanded modal vectors.

### 14.3 Example Application of Original Work

The example application chosen for this section closely parallels the examples provided in precursory work to provide a context for interpreting the results [6, 11].

#### 14.3.1 NASA Eight-Bay Truss

For the comparisons in this work the NASA eight-bay truss structure [24] is utilized. The eight-bay truss structure is an experimental test article developed to study a variety of damage identification issues. The cantilevered truss includes 32 nodes, each of which was instrumented with triaxial accelerometers. Fifteen unique damage cases were produced by removing individual truss members. The structure and representations of the damage cases (denoted by alphabetic characters) are provided in Fig. 14.1. This work uses 12 modes from a 96-DOF analytical model of the undamaged structure and the damage cases to explore the developments discussed in previous sections. The DOFs that are assumed to be active or measured for the example provided in this section are denoted by circles in Fig. 14.1. At these nodes, full triaxial measurements are utilized, resulting in a total measurement set of 24 DOFs. Case D will be used for the examples provided in this section.

#### 14.3.2 Spring Disassembly

The structural matrices for this model include 9,216 ( $96 \times 96$ ) potential entries. However, there are only 320 unique (excluding symmetric entries) nonzero entries in this matrix. After reordering the matrices into analysis and omitted DOFs, the 224 off-diagonal elements are disassembled into 224 springs between DOFs. The 96 diagonal entries are disassembled as springs to ground. Note that this disassembly process does not disallow negative spring stiffness as these springs are usually a simplified representation of a more complicated structural element. It is also important to note that this connectivity pattern becomes an inherent part of subsequent estimations of full residuals, damage location, expanded mode shapes, and damage extent using the procedure outlined in the preceding section.

**Fig. 14.1** NASA eight-bay truss structure

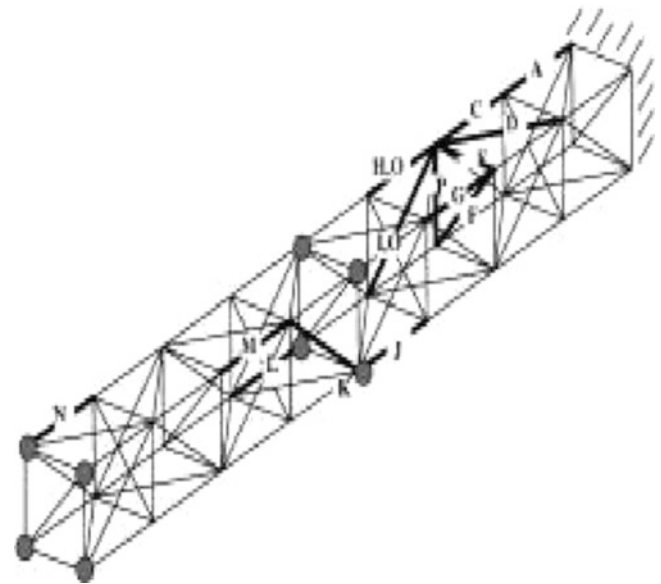
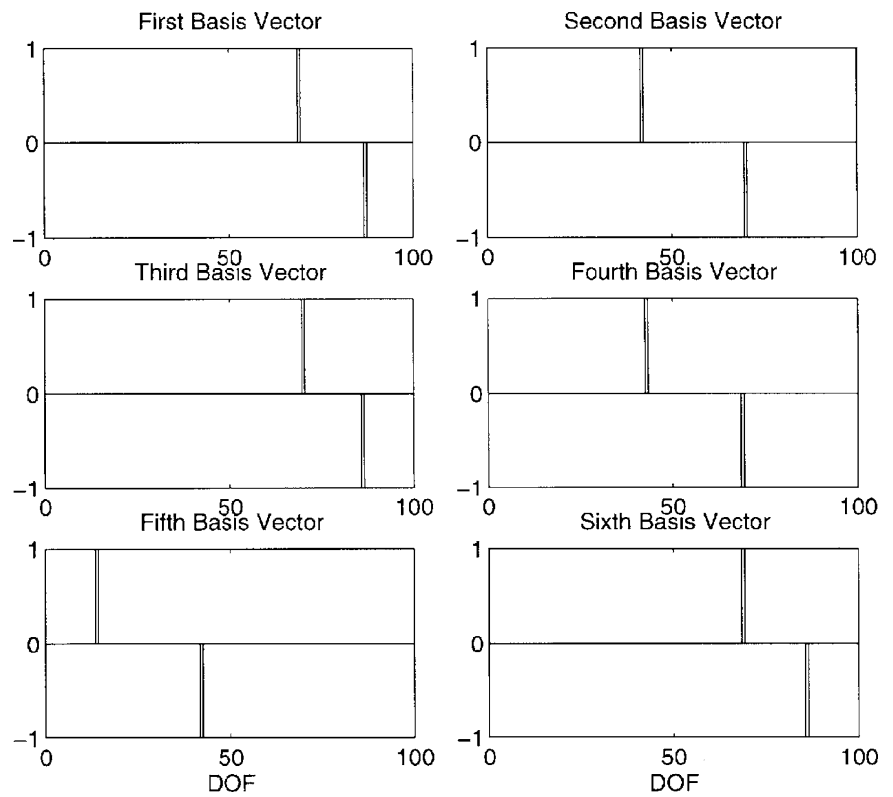


**Fig. 14.2** Six selected basis functions



### 14.3.3 Selection of Residual Basis Functions

The example presented herein ignored the 96 springs to ground representing the diagonal elements. This enhanced the column linear independence of the down-selected subset. Of the remaining 244 possible basis vectors, fewer than 20 had average MAC values over 0.4. Of these, the six with the highest averaged MAC values were selected. The general rule used to date is to select a number equal to half of the number of modes of interest unless a break in the connectivity of the elements or a rank deficiency (column linear dependence) sets in. Figure 14.2 provides plots of the six candidate basis functions chosen.



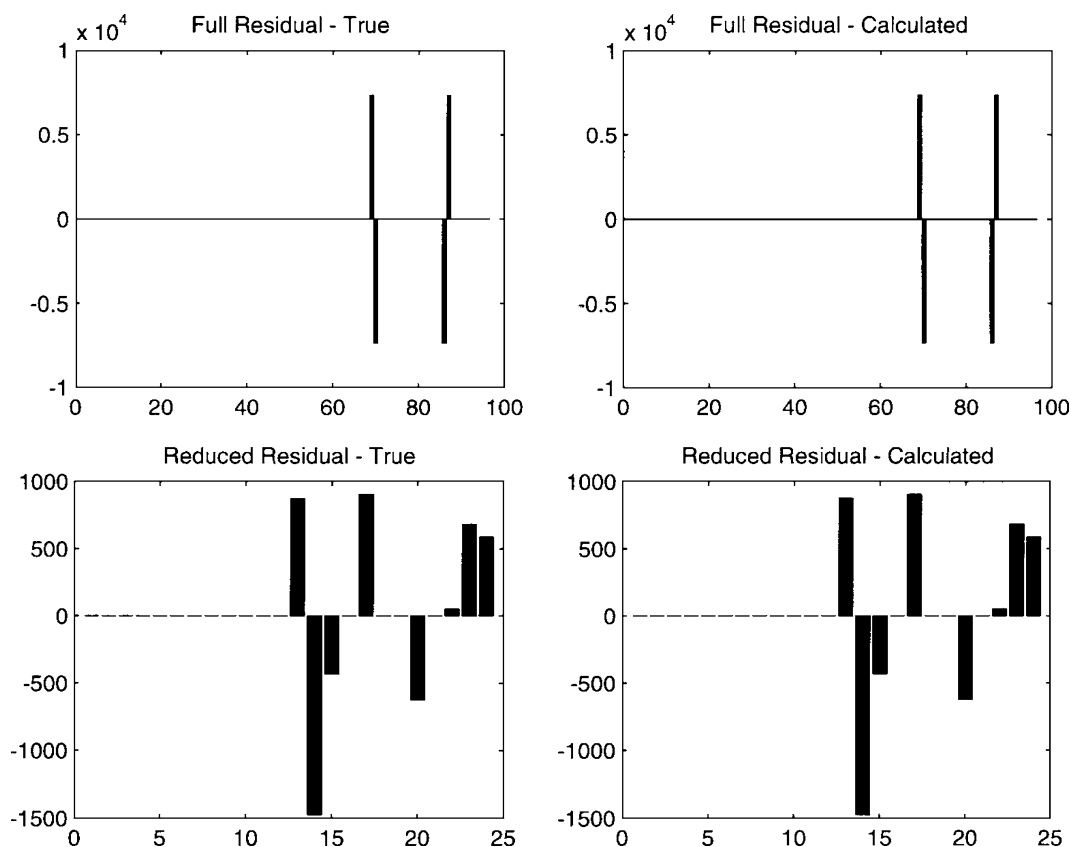


Fig. 14.3 First mode dynamic residuals

These functions do seem to be targeting certain locations on the structure. In fact, the affected DOFs of damage case D (69, 70, 86, and 87) are well represented in these vectors. The first, third, and sixth vectors exclusively relate to these affected DOFs.

#### 14.3.4 Dynamic Residual Reduction/Expansion

The coefficients for the fit of the six basis vectors shown in Fig. 14.2 to the first dynamic residual using Eq. (14.11) are  $-0.7328, 0, -0.7328, 0, 0,$  and  $1.4657$ . Hence, the first, third, and sixth basis vectors are pulled out as the true components of the full dynamic residual, as indicated in Fig. 14.3. The true and calculated full residuals for the first mode are given in the upper plots of Fig. 14.3. The true and calculated reduced residuals for the first mode are provided in the lower plots. It is obvious that the correct residuals have been obtained in both cases. However, a more important observation is that the reduced residuals do not maintain the location information in a form that is easily or visually interpreted. Hence, the primary thrust of this work (the estimation of the full residuals) is strongly suggested as important to advancing the field.

#### 14.3.5 Mode Shape Expansion

For the example provided in this section, 12 Ritz-like basis vectors were calculated using Eqs. (14.13–14.17 and 14.18). The fact that noise-free measurements are being utilized produces a situation where the first basis vector exactly matches the expanded mode shape. Figure 14.4 supports these results for the first mode. The expanded and true mode shapes are provided in the upper plots and are seen to be equivalent. The first and second basis vectors are provided in the lower plots. It is obvious that the first basis vector captures the first expanded mode shape. This important point can be used to monitor the consistency of a data set and/or the selection of dynamic residual basis vectors.

**Fig. 14.4** First expanded mode shape

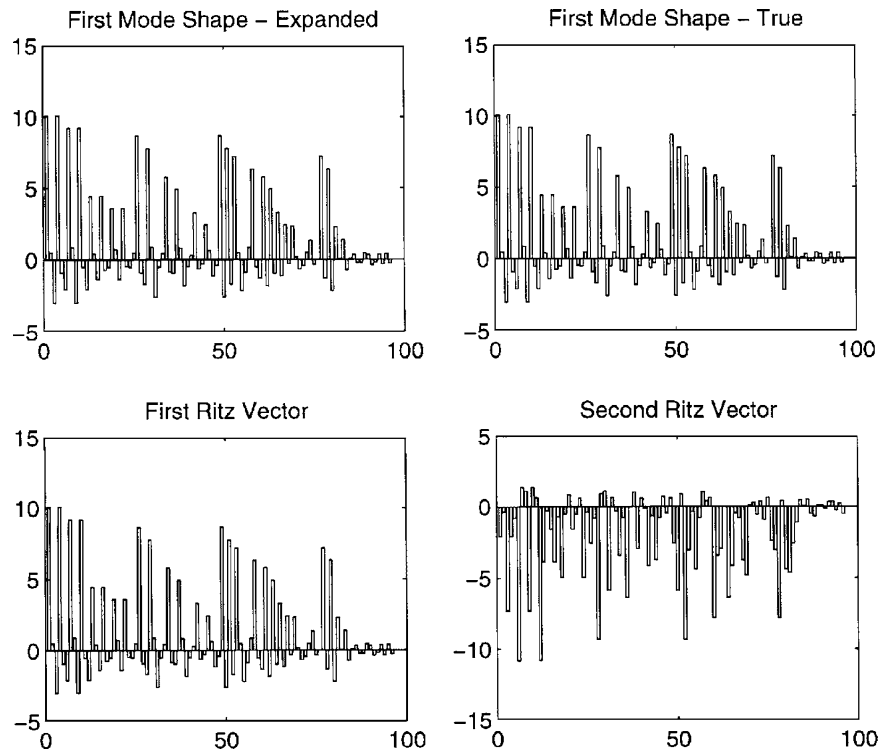
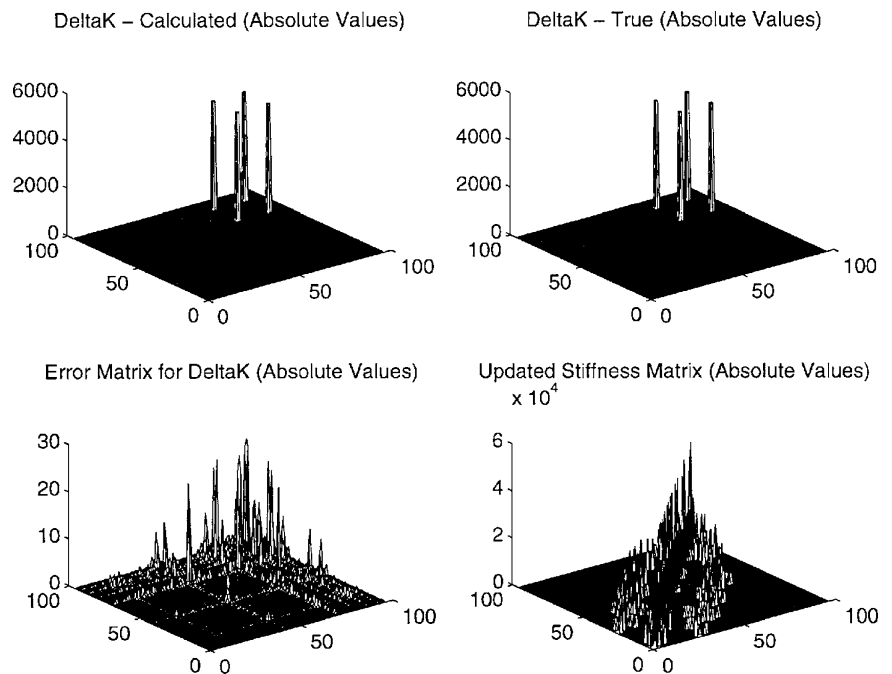


**Fig. 14.5** Damage extent calculation



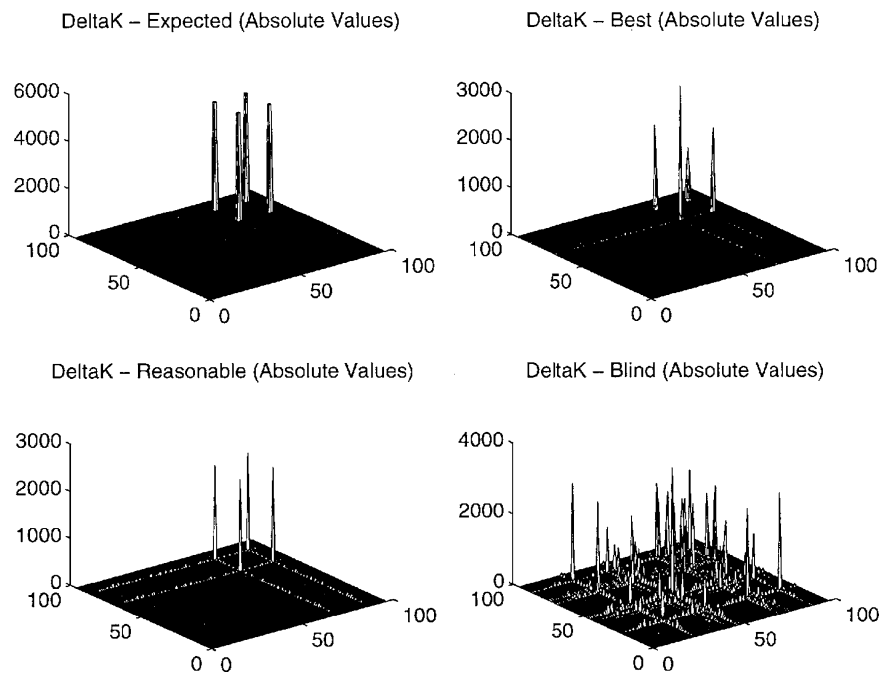
**14.3.6 Damage Extent**

The MRPT update is then calculated using the expanded mode shapes and full dynamic residuals. The upper-left-hand plot of Fig. 14.5 shows the absolute value of this update. The upper-right-hand plot shows the true update, which suggests that the update is very close. In fact, the lower-left-hand plot provides the error or difference between the two  $[\Delta K]$  matrices. The magnitudes of the differences are at least two orders of magnitude less than the true values. The updated stiffness matrix

**Table 14.1** Order of basis vectors vs. number of modes for experimental data

Number of modes	Vector 198	Vector 196	Vector 197
1	1	10	16
2	1	11	16
3	2	18	25
4	2	14	37
5	2	14	38

**Fig. 14.6** Experimental update matrices



is provided in the lower-right-hand plot as a point of reference. Besides providing an example of the process developed earlier, this example shows that the process does provide the correct results for perfectly measured data. However, the selection of dynamic residual basis vectors is critical.

## 14.4 Application of Original Method to Experimental Data

The coupled damage identification procedure developed earlier was applied to the experimental data for damage case D of the NASA eight-bay truss structure. The data contained five modes with 96 measurement locations as listed earlier. However, only the 24 active DOFs shown in Fig. 14.1 were used in this example. This represents one of the most difficult active sensor sets due to the lack of even spatial distribution. It was found that not all modes contributed to the selection of the dynamic residual basis vectors. Modes 4 and 5 had almost no ability to discriminate between the vectors. This may be due in part to the analytical model used in the experimental study. The stiffness matrix was fully populated as a result of the update procedure required to fit the experimental undamaged data. The original sparse stiffness matrix for this system did show these modes as having the ability to discriminate between the vectors. However, the inability of this model to match the undamaged data precluded its use in this study.

Table 14.1 lists the order of appearance of each of the primary vectors, as determined from the analytical study (196, 197, and 198), as a function of the number of experimental modes used. Vector 198 is consistently high (place 1 or 2). Vector 197 is much lower than in the analytical studies but still reasonably high. Vector 196 was outside the range of reasonable orders to consider.

Figure 14.6 provides plots of four different manifestations of the model update matrices. The upper-left-hand plot is the analytical update matrix that provides the best estimate of what the experimental results should produce. The upper-right hand plot provides what could be considered the best estimate of the update matrix if the user knew the results of the previous analytical study and the damage location. For this estimation, the first two modes and basis vectors 198, 197, and 196 were

used. The magnitudes are about half of the expected magnitudes, and the sparsity is reasonable. Note that two Ritz-like basis vectors were used to expand the modes. The lower-left-hand plot contains what might be considered a reasonable update for a user with no knowledge of the damage location but plenty of time to work with the data and to develop the proper insight. For this update, the first two modes were used to select the residual basis vectors, and only one basis vector was used – vector 198. The lower-right-hand plot represents a blind application of the process. All five modes were used, and the first six residual basis vectors were selected. Changes were seen at many other locations in the structure, however the region of the model affected by the damage is dense with large changes. The magnitudes of the changes were roughly equivalent to the other two experimental updates.

## 14.5 Assessment of Issues with Original Work

The original work [20, 21] studied the sensitivity of the original procedure to three implementation issues including: (a) the number of residual basis vectors selected, (b) the number of modes used, and (c) the noise in the measurements. The previous studies suggested that additional work was needed to develop experience and techniques for sorting and choosing residual basis vectors. Additionally, the previous efforts suggested that there existed a minimum number of modes to discriminate between the residual basis vectors. And finally, the original process appears to be fairly robust with respect to noise based on the limited studies performed previously. In actuality, these issues are a subset of technical issues that need to be systematically assessed and mitigated if possible with this coupled damage detection approach. Figure 14.7 suggests a more complete set of technical issues that are associated with each step in the original process.

### 14.5.1 Model of Undamaged Structure

The primary issue with this step is the need for the original undamaged model to correlate with the actual structure of interest. It can be assumed that the technical errors associated with this step may be reduced or eliminated for some measured modes if a model updating step is performed using undamaged data from the structure.

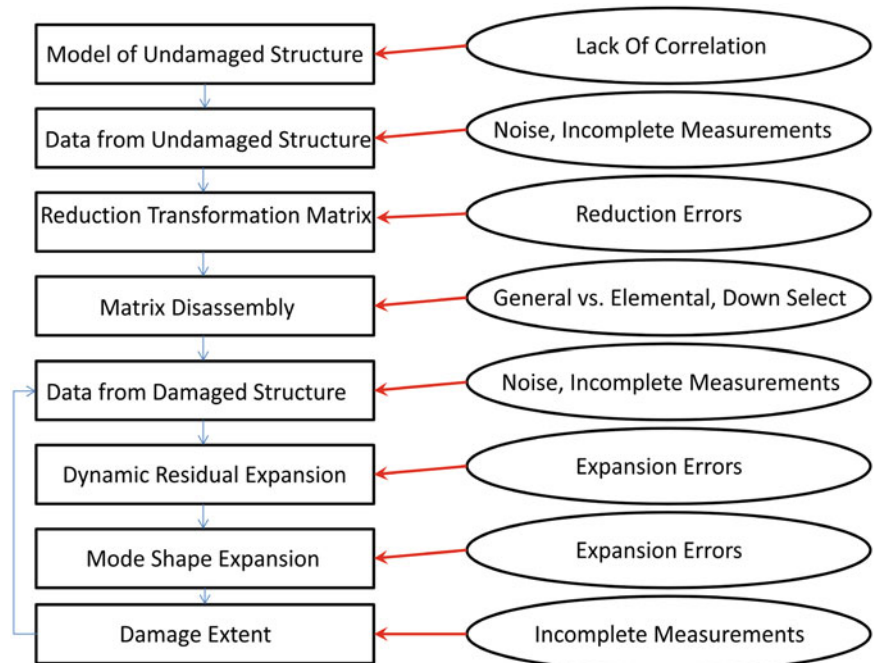


**Fig. 14.7** Technical issues associated with the original procedure

### ***14.5.2 Data from Undamaged Structure***

The issues from this step in the process include the expected measurement noise and the inevitable lack of a complete measurement set (both spatially and with respect to the critical modes of the structure). As was suggested earlier, this process appears to be fairly robust with respect to noise and the a primary reason to develop this procedure was to attack the incomplete measurement problem.

### ***14.5.3 Reduction Transformation Matrix***

The lack of ability for a reduced system to reproduce the relevant aspects of the full system is a common and well-known problem. The original procedure is likely suffering from reduction errors affecting the system changes that are due to damage through the dynamic residuals and expansion steps that follow. Dealing with the reduction issues is one of the areas of near term work that should be undertaken.

### ***14.5.4 Matrix Disassembly***

The matrix disassembly step proposed in the original process was a general approach that broke the stiffness matrix up into simple springs. This did retain the proper coupling in the end but could allow some non-physical stiffnesses to result. A more rigorous and potentially robust approach would be to disassemble based on the actual element coupling used in building the models. This is certainly technically viable but may be beyond the implemented state-of-the-art for many commercial-scale finite element programs. A second issue at this step involves the need to down select from the huge number of potential simple springs in the disassembled matrix to the set that will be used for creating basis vectors. There is certainly the issue that damage information may be missed or incorrect, however it is technically useful to understand which parts of the structure cannot be monitored for damage given the selected measurement set. There is some additional study that is needed to derive a set of targeted metrics (as opposed to the MAC values) that will help sort the simple springs (or disassembled elements) that will be used for damage monitoring and assessment.

### ***14.5.5 Data from Damaged Structure***

The issues associated with this step are the same as were already mentioned in the Data from Undamaged Structure step.

### ***14.5.6 Dynamic Residual Expansion***

The issues in this step revolve around the necessary expansion of the limited measured data set to the larger unmeasured data set. Since the inability to measure every Degrees-Of-Freedom (DOFs) in the model is a physical constraint, it is unlikely that much progress can be made on these issues in the near term. However, since this step in the process is critically dependent on the reduction/expansion transformation used, there is some hope for minor near-term improvements that can be realized by improving and tailoring the transformation process used as well as selecting the basis vectors from the disassembly process.

### ***14.5.7 Mode Shape Expansion***

Many of the same issues that plague the dynamic residual expansion exist in this step as well, namely the physical constraint of unmeasured DOFs. In fact the expansion of the mode shapes will be dependent on the expansion of the dynamic residuals in the previous step. Hence, improving and understanding that process is likely to be a precursor to understanding the errors in the mode shape expansion step. Additionally, there is a need to further study the effectiveness of the novel expansion technique provided in the original work.

### 14.5.8 Damage Extent

The MRPT-based damage extent based approach follows directly from the expanded residuals and mode shapes produced in the previous steps. However, it has been seen that selection of the proper set of basis vectors for the expansion steps is critical to producing unambiguous results in this step. Hence, the issues associated with this step are largely dependent issues on the problems in implementing the previous steps. This does suggest that the damage extent results will be useful as a metric for the integrated effects of all the previous steps and sensitivity studies involving the application of the entire process are called for as a near term activity.

## 14.6 Summary and Conclusions

The procedure reviewed in this work integrates several technologies into an integrated procedure to perform damage location and extent estimation. Of significant importance is the integration of model order reduction and mode shape expansion into the location and extent algorithm. The end result is a hybrid approach that utilizes an analytical model and experimental data to perform rank constrained damage identification. The procedure utilizes minimum rank perturbation theory, spring disassembly, and Ritz vector calculation to couple these technologies. As a result, the issue of determining damage-affected modes is supplanted by determining a truncation order for a set of localized basis vectors. An application to experimental data in the original work proved to be successful in locating the damage. However, this same application pointed out the need to acquire enough modes to discriminate between the residual basis vectors that drive the rest of the process. Earlier studies suggested that this process is fairly robust with respect to noise. The experimental application also suggested that a sparse analytical model could improve the basis vector selection process.

The technical issues associated with the process reviewed herein need to be systematically addressed by mitigating or understanding the effects. Development work to create targeted reduction techniques, generic disassembly, and basis vector selection processes is needed. Understanding and improving the expansion processes are also called for. Other active sensor sets and damage cases should be exercised to understand the experimental potential and sensitivities of this process more completely.

## References

1. Guyan RJ (1965) Reduction of stiffness and mass matrices. *AIAA J* 3(2):380
2. Irons BM (1965) Structural eigenvalue problems: elimination of unwanted variables. *AIAA J* 3(5):961, 962
3. Kidder RL (1973) Reduction of structural frequency equations. *AIAA J* 11(6):892
4. O'Callahan J, Avitabile P, Riemer R (1989) System equivalent reduction/expansion process (SEREP). In: Proceedings of the 7th international modal analysis conference, Las Vegas, NV. Society of Experimental Mechanics, Bethel, CT, pp 29–37
5. Zimmerman DC, Smith SW, Kim H-M, Bartkowicz T (1996) An experimental study of structural damage detection using incomplete measurements. *J Vib Acoust* 118(4):543–550
6. James GH, Zimmerman DC (1996) Reduction/expansion studies for damage identification of continuous aerospace structures. In: Proceedings of the 15th international modal analysis conference, Orlando, FL. Society of Experimental Mechanics, Bethel, CT, pp 1772–1778
7. Imregun M, Ewins DJ (1993) An investigation into mode shape expansion techniques. In: Proceedings of the 11th international modal analysis conference, Kissimmee, FL. Society of Experimental Mechanics, Bethel, CT, pp 168–175
8. Smith SW, Baker RJ, Kaouk M, Zimmerman DC (1993) Mode shape expansion for visualization and model correlation. In: Meirovitch L (ed) Proceedings of the 9th VPI&SU symposium, Virginia Polytechnic Institute and State University, Blacksburg, VA, pp 385–396
9. Levine-West M, Kissil A, Milman M (1994) Evaluation of mode shape expansion techniques on the micro-precision interferometer truss. In: Proceedings of the 12th international modal analysis conference, Honolulu, HI. Society of Experimental Mechanics, Bethel, CT, pp 212–218
10. Gafka GK, Zimmerman DC (1996) Structural damage detection via least squares dynamic residual force minimization with quadratic measurement error inequality constraint. In: Proceedings of the 14th SEM international modal analysis conference, Dearborn, MI. Society of Experimental Mechanics, Bethel, CT, pp 1278–1284
11. James GH, Zimmerman DC (1997) Utilization of large experimental/analytical data sets for structural health monitoring of aerospace structures. In: Proceedings of the 15th international modal analysis conference, Orlando, FL. Society of Experimental Mechanics, Bethel, CT, pp 1765–1771
12. Doebling SW, Peterson LD, Alvin KF (1995) Experimental determination of local structural stiffness by disassembly of measured flexibility matrices. see also AIAA Paper 95-1090. *J Vib Acoust* 120:949–957
13. Doebling SW (1995) Measurement of structural flexibility matrices for experiments with incomplete reciprocity. Ph.D. dissertation, Aerospace Engineering Sciences Department, University of Colorado, Boulder, CO

14. Doebling SW (1996) Damage detection and model refinement using elemental stiffness perturbations with constrained connectivity. AIAA Paper 96-1307
15. Robinson NA, Peterson LD, James GH, Doebling SW (1996) Damage detection in aircraft structures using dynamically measured static flexibility matrices. In: Proceedings of the 12th international modal analysis conference, Dearborn, MI. Society of Experimental Mechanics, Bethel, CT, pp 857–865
16. Cao TT, Zimmerman DC (1997) A procedure to extract Ritz vectors from dynamic testing data. In: Proceedings of the 15th international modal analysis conference, Orlando, FL. Society of Experimental Mechanics, Bethel, CT, pp 1036–1040
17. Kaouk M (1993) Structural damage assessment and finite element model refinement using measured modal data. Ph.D. dissertation, Aerospace Engineering, Mechanics, and Engineering Science Department, University of Florida, Gainesville, FL
18. Kaouk M, Zimmerman DC (1994) Structural damage assessment using a generalized minimum rank perturbation theory. AIAA J 32(4):836–842
19. Simmermacher T, Zimmerman DC, Mayes RL, Reese GM, James GH (1995) The effects of finite element grid density on model correlation and damage detection of a bridge. AIAA Paper 95-1075
20. James G, Zimmerman D, Cao T (1997) Development of a coupled approach for structural damage detection with incomplete measurements, AIAA Paper 97-0362. In: Proceedings of the 35th aerospace sciences meeting, Reno, NV, 6–9 Jan 1997
21. James G, Zimmerman D, Cao T (1998) Development of a coupled approach for structural damage detection with incomplete measurements. AIAA J 36(12):2209–2217
22. James GH, Carne TG, Hansche BD, Mayes RL, Reese GM, Simmermacher T (1995) Health monitoring of operational structures – initial results. AIAA Paper 95-1072
23. Zimmerman DC, Kaouk M (1998) Structural health assessment using a partition and element model update. J Chin Soc Mech Eng 19(1):115–124
24. Kashangaki TAL (1992) Ground vibration tests of a high fidelity truss for verification of on orbit damage location techniques. NASA TM-107626

# Chapter 15

## Efficient and Robust Solution of Inverse Structural Dynamic Problems for Vibration Health Monitoring

Keng C. Yap<sup>†</sup>

**Abstract** Vibration health monitoring of structures involves solving inverse structural dynamic problems that are often mathematically ill-conditioned. Many solution approaches have been developed, of which dynamic residual minimization yielded some of the most computationally attractive algorithms. Minimum Rank Perturbation Theory (MRPT) offers a closed form solution of model matrix perturbation using only a subset of the measured modes equal to the rank of perturbation. The initial formulation of the theory assumed symmetric model matrices in the equations of motion, but was later extended to deal with skew-symmetric matrices. The development led to the discovery of a new matrix property known as “null-symmetry”, which helped explain how MRPT preserves symmetry and skew-symmetry in its solution. To handle incomplete measurements, an iterative algorithm based on MRPT was developed using repeated substitution of the dynamic model reduction transformation to achieve convergence. However, the algorithm can become unstable, and hence does not guarantee convergence. Driven by the limitation, dynamic least squares method was developed to solve for a robust set of parameter perturbations in a least square sense regularized by the reduced dynamic residual constraint. The algorithm is capable of estimating mass and stiffness parameters simultaneously under noise and uncertainty without repeatedly solving the eigenproblem.

**Keywords** Vibration health monitoring • Modal analysis • Structural damage characterization/detection • Inverse eigenproblem • Minimum rank perturbation theory • Null-symmetry • Dynamic residual minimization • Least squares • Quadratic inequality

---

<sup>†</sup> A year 2000 doctoral graduate of the University of Houston’s Cullen College of Engineering. This analytical work was performed as part of the dissertation research at the university in 1997–2000, and presented at a memorial session of the 31st International Modal Analysis Conference in tribute to the late Dr. David Zimmerman.

K.C. Yap (✉)  
Deepwater Innovation, Research & Development, Shell International Exploration & Production Inc.,  
3333 Highway 6 South, Houston, TX 77082-3101, USA  
e-mail: [keng.yap@shell.com](mailto:keng.yap@shell.com)



## Nomenclature

<b><math>B</math></b>	Dynamic residual matrix	<b>Subscripts</b>	<b>Accents</b>
<b><math>C</math></b>	Damping matrix	$h$	$\cdot$ Time derivative
<b><math>G</math></b>	Gyroscopic matrix	$d$	$\sim$ Reduced
<b><math>H</math></b>	Circulatory matrix	$x$	
<b><math>K</math></b>	Stiffness matrix	$y$	
<b><math>M</math></b>	Mass matrix	$i$	
$\mathcal{N}$	Orthonormal basis of null space	$j$	
<b><math>T</math></b>	Model reduction transformation	$\lambda^2$	
$\mathbf{q}(t)$	Position vector over time $t$	$\phi$	
$\Phi$	Mode shape matrix	<b>Superscripts</b>	
$\Lambda^2$	Diagonal matrix of eigenvalues	*	Hermitian
$\Delta$	Perturbation of a matrix	$T$	Transpose
$\varepsilon$	Dynamic residual constraint tolerance		

### 15.1 Introduction

Inspection and monitoring techniques using non-destructive evaluation (NDE) approach are becoming increasingly important as engineers strive to manage the risk of operating critical structures over a long period of time where the structures' performance may become compromised, e.g., due to change in operating conditions which the structures were designed for. These techniques provide valuable information about the structural integrity required for continuing safe operation. Vibration-based techniques offer an NDE capability for large-scale health monitoring and damage detection of structures<sup>1</sup>. They have found industrial applications in various engineering infrastructures, including ageing aircraft, space vehicles, bridges, buildings, and offshore platforms (Fig. 15.1). These techniques exploit the difference between pre- and post-damage vibration signature to assess the structural changes (e.g., in material and geometric properties, boundary conditions, and system connectivity), usually with the aid of a finite element model (FEM). Most of them use vibration signature characterized by the modal parameters (natural frequencies, damping ratios, and mode shapes), while some use directly the frequency response functions or time-domain responses. Modern modal testing equipment and instrumentation allow these vibration signatures to be measured efficiently and cost-effectively.

Vibration health monitoring techniques have evolved and matured over the past 40 years [1–3]. The aerospace community began experimenting with vibration-based damage identification in the late 1970s in conjunction with NASA's Space Shuttle Program. It was found that vehicle component damage could be identified by standard ground modal testing. As a result, NASA procured a dedicated Shuttle Modal Inspection System (SMIS) to inspect critical structural components such as the control surfaces, vertical tail, and wings [4]. The successful operation of the system led to the continuing use of vibration health monitoring for the International Space Station and potentially for future reusable launch vehicles, and as well as the widening applications in the aviation industry. At about the same time in 1970s, the oil and gas industry conducted research



Fig. 15.1 Example applications of vibration health monitoring

<sup>1</sup> In practice, vibration health monitoring is often followed by a secondary local NDE method for prove-up of possible damages.

and development to monitor the vibration signature of offshore oil platforms using ambient (sea and wind) excitation [1]. Examples include BP Forties [5–7], Amoco Montrose [7], Occidental Claymore [7], and Shell SP-62C [8]. The general finding from these studies is that dynamic response spectrum can be used to assess structural integrity, as changes in modal properties due to structural damage tend to be larger than normal variations not attributed to damage (e.g., changes of mass on the decks and changes in the tides). In 1980, Shell conducted modal testing of SP-62C, an eight-legged diagonally-braced jacket platform in the Gulf of Mexico, to benchmark the FEM. A numerical study using the FEM showed that numerous damage scenarios can be indicated by changes in the resonant frequencies [8].

## 15.2 Analysis

Vibration health monitoring of structures consists of two procedures: (i) model refinement and (ii) damage characterization. Model refinement is intended to improve the FEM to better predict the dynamic characteristics of the as-built structure, while damage characterization has the objective of assessing the damage location and extent of the structure. However, they are closely related in the sense that both procedures generate information regarding the discrepancy between the analytical model and the experimental data, and they involve solving inverse structural dynamic problems that are often mathematically ill-conditioned. Survey papers [1–3] provide an overview of various methods used in these procedures.

### 15.2.1 Minimum Rank Perturbation Theory (MRPT)

Among the many solution approaches for model refinement and damage characterization, dynamic residual minimization yielded some of the most computationally attractive algorithms. In fact, based on the Minimum Rank Perturbation Theory (MRPT), this approach can yield a closed form solution of the model matrix perturbation using only a subset of the measured modes equal to the perturbation rank of perturbation [9, 10]. The work in [10] explored the use of MRPT in simultaneous update of property matrices for damped and undamped systems. The theory has been extended to address problems of having no analytical model [11], the direct use of frequency response functions [12], and the use of multiple vibration and static test data sets [13]. A subspace selection algorithm was introduced to improve the numerical conditioning in the presence of experimental noise [13]. The development of an element-by-element approach successfully reduced the required number of measured modes [14]. The theory was generalized to include the skew-symmetric matrices in the equations of motion, which led to the discovery of a new matrix property known as “null-symmetry” that helped explain how MRPT preserves symmetry and skew-symmetry in its solution [15]. Assuming the FEM for a structural system exists, the general equations of motion under free vibration can be represented by

$$\mathbf{M}\ddot{\mathbf{q}}(t) + [\mathbf{C} + \mathbf{G}]\dot{\mathbf{q}}(t) + [\mathbf{K} + \mathbf{H}]\mathbf{q}(t) = 0, \quad (15.1)$$

where matrices  $\mathbf{M}$ ,  $\mathbf{C}$ ,  $\mathbf{K} \in \mathbb{R}^{n \times n}$  are symmetric, while matrices  $\mathbf{G}$ ,  $\mathbf{H} \in \mathbb{R}^{n \times n}$  are skew-symmetric. With an FEM of the healthy structure correlated with the experimental data, e.g., using a model refinement procedure, we can assume that the model satisfies the following eigenequation:

$$\mathbf{M}_h \boldsymbol{\Phi}_h \boldsymbol{\Lambda}_h^2 + [\mathbf{C}_h + \mathbf{G}_h] \boldsymbol{\Phi}_h \boldsymbol{\Lambda}_h + [\mathbf{K}_h + \mathbf{H}_h] \boldsymbol{\Phi}_h = 0. \quad (15.2)$$

For a damaged structure where the damage is manifested in the perturbation of the system matrices, we have the following perturbed eigenequation:

$$\mathbf{M}_d \boldsymbol{\Phi}_d \boldsymbol{\Lambda}_d^2 + [\mathbf{C}_d + \mathbf{G}_d] \boldsymbol{\Phi}_d \boldsymbol{\Lambda}_d + [\mathbf{K}_d + \mathbf{H}_d] \boldsymbol{\Phi}_d = 0, \quad (15.3)$$

where  $\mathbf{M}_d = \mathbf{M}_h - \Delta\mathbf{M}$ ,  $\mathbf{C}_d = \mathbf{C}_h - \Delta\mathbf{C}$ ,  $\mathbf{G}_d = \mathbf{G}_h - \Delta\mathbf{G}$ ,  $\mathbf{K}_d = \mathbf{K}_h - \Delta\mathbf{K}$ ,  $\mathbf{H}_d = \mathbf{H}_h - \Delta\mathbf{H}$ . Grouping the perturbations to one side of the equation, we get

$$\mathbf{M}_h \boldsymbol{\Phi}_d \boldsymbol{\Lambda}_d^2 + [\mathbf{C}_h + \mathbf{G}_h] \boldsymbol{\Phi}_d \boldsymbol{\Lambda}_d + [\mathbf{K}_h + \mathbf{H}_h] \boldsymbol{\Phi}_d = \Delta\mathbf{M} \boldsymbol{\Phi}_d \boldsymbol{\Lambda}_d^2 + [\Delta\mathbf{C} + \Delta\mathbf{G}] \boldsymbol{\Phi}_d \boldsymbol{\Lambda}_d + [\Delta\mathbf{K} + \Delta\mathbf{H}] \boldsymbol{\Phi}_d. \quad (15.4)$$

The left side of the equation is defined as the dynamic residual matrix,  $\mathbf{B}$ . Letting  $\mathbf{D} = \mathbf{C} + \mathbf{G}$  and  $\mathbf{R} = \mathbf{K} + \mathbf{H}$ , the dynamic residual matrix can be written as

$$\mathbf{B} \equiv \mathbf{M}_h \boldsymbol{\Phi}_d \boldsymbol{\Lambda}_d^2 + \mathbf{D}_h \boldsymbol{\Phi}_d \boldsymbol{\Lambda}_d + \mathbf{R}_h \boldsymbol{\Phi}_d. \quad (15.5)$$

Thus,

$$\Delta \mathbf{M} \Phi_d \Lambda_d^2 + \Delta \mathbf{D} \Phi_d \Lambda_d + \Delta \mathbf{R} \Phi_d = \mathbf{B}_M \Lambda_d^2 + \mathbf{B}_D \Lambda_d + \mathbf{B}_R. \quad (15.6)$$

If two of the three perturbations ( $\Delta \mathbf{M}$ ,  $\Delta \mathbf{D}$ ,  $\Delta \mathbf{R}$ ) are known, the problem can be simplified into one of the following cases:

$$(i) \Delta \mathbf{M} \Phi_d = \mathbf{B}_M, \text{ where } \mathbf{B}_M = [\mathbf{M}_h \Phi_d \Lambda_d^2 + \mathbf{D}_d \Phi_d \Lambda_d + \mathbf{R}_d \Phi_d] \Lambda_d^{-2}, \quad (15.7)$$

$$(ii) \Delta \mathbf{D} \Phi_d = \mathbf{B}_D, \text{ where } \mathbf{B}_D = [\mathbf{M}_d \Phi_d \Lambda_d^2 + \mathbf{D}_h \Phi_d \Lambda_d + \mathbf{R}_d \Phi_d] \Lambda_d^{-1}, \quad (15.8)$$

$$(iii) \Delta \mathbf{R} \Phi_d = \mathbf{B}_R, \text{ where } \mathbf{B}_R = \mathbf{M}_d \Phi_d \Lambda_d^2 + \mathbf{D}_d \Phi_d \Lambda_d + \mathbf{R}_h \Phi_d. \quad (15.9)$$

In all cases, we need to solve a matrix inverse problem in the form of

$$\mathbf{A} \mathbf{X} = \mathbf{Y}, \quad (15.10)$$

where  $\mathbf{A}$  is the unknown perturbation matrix,  $\mathbf{X}$  is the mode shape matrix, and  $\mathbf{Y}$  is the dynamic residual matrix. Since matrix  $\mathbf{A}$  is real but generally non-symmetric, matrices  $\mathbf{X}$  and  $\mathbf{Y}$  are generally complex. Matrix  $\mathbf{A}$  is assumed rank deficient, i.e., matrices  $\mathbf{X}$ ,  $\mathbf{Y} \in \mathbb{R}^{n \times p}$ , where the number of measured modes,  $p$ , is typically far less than the model degrees-of-freedom  $n$ . The rank deficiency renders the problem under-determined and cannot be solved by matrix inversion; additional constraint is needed to define a unique solution. Taking the pseudoinverse of  $\mathbf{X}$  offers one way to solve for  $\mathbf{A}$ :

$$\mathbf{A} = \mathbf{Y} [\mathbf{X}^* \mathbf{X}]^{-1} \mathbf{X}^*. \quad (15.11)$$

This produces a unique minimum rank solution which is of minimum norm, but it destroys the system matrix structure (sparsity and symmetry). In contrast, the MRPT solution preserves both the symmetry and skew-symmetry of system matrix structure:

$$\mathbf{A} = \mathbf{Y} [\mathbf{Y}^* \mathbf{X}]^{-1} \mathbf{Y}^*, \quad (15.12)$$

so long as matrix  $\mathbf{A}$  is null-symmetric. By definition, a square matrix  $\mathbf{A}$  is null-symmetric if its null-space is invariant to the transpose or Hermitian operator, i.e.,  $\mathcal{N}(\mathbf{A}) = \mathcal{N}(\mathbf{A}^*)$  [15]. Examples of null-symmetric matrices include normal matrices, which include symmetric and skew-symmetric matrices.

As a numerical example, consider these symmetric and skew-symmetric matrices:

$$\mathbf{A}_1 = \begin{bmatrix} 5 & -2 & 0 & 0 \\ -2 & 5 & 0 & 0 \\ 0 & 0 & 0 & 0 \\ 0 & 0 & 0 & 0 \end{bmatrix}, \quad \mathbf{A}_2 = \begin{bmatrix} 0 & -2 & 0 & 0 \\ 2 & 0 & -3 & 0 \\ 0 & 3 & 0 & 0 \\ 0 & 0 & 0 & 0 \end{bmatrix}. \quad (15.13)$$

The sum of the two matrices is

$$\mathbf{A} = \mathbf{A}_1 + \mathbf{A}_2 = \begin{bmatrix} 5 & -4 & 0 & 0 \\ 0 & 5 & -3 & 0 \\ 0 & 3 & 0 & 0 \\ 0 & 0 & 0 & 0 \end{bmatrix}. \quad (15.14)$$

Matrix  $\mathbf{A}$  is not normal, hence not symmetric or skew-symmetric, but is null-symmetric because its orthonormal basis of null space is transpose invariant, i.e.,

$$\mathcal{N}(\mathbf{A}) = \mathcal{N}(\mathbf{A}^*) = \begin{bmatrix} 0 \\ 0 \\ 0 \\ 1 \end{bmatrix}. \quad (15.15)$$

Since matrix  $\mathbf{A}$  is of rank 3, matrix  $\mathbf{X}$  is arbitrarily generated with three linearly independent columns:

$$\mathbf{X} = \begin{bmatrix} 0.18 + 0.39i & -0.36 + 0.53i & -0.12 - 0.62i \\ -0.65 + 0.72i & -0.29 - 0.37i & 0.87 - 0.23i \\ 0.33 - 0.14i & 0.10 - 0.18i & -0.24 - 0.30i \\ 0.82 + 0.31i & -0.54 + 0.84i & -0.36 + 0.27i \end{bmatrix}. \quad (15.16)$$

Matrix  $Y$  is computed from  $Y = AX$ :

$$Y = \begin{bmatrix} 3.50 - 0.93i & -0.64 + 4.13i & -4.08 - 2.18i & \\ -4.24 + 4.02i & -1.75 - 1.31i & 5.07 - 0.25i & \\ -1.95 + 2.16i & -0.87 - 1.11i & 2.61 - 0.69i & \\ 0 & 0 & 0 & 0 \end{bmatrix}. \quad (15.17)$$

We have now set up the matrix inverse problem for demonstration. Based on MRPT, the solution is estimated as

$$\hat{A} = Y [Y^* X]^{-1} Y^* = \begin{bmatrix} 5 & -4 & 0 & 0 \\ 0 & 5 & -3 & 0 \\ 0 & 3 & 0 & 0 \\ 0 & 0 & 0 & 0 \end{bmatrix}. \quad (15.18)$$

The symmetric and skew-symmetric parts of the solution are calculated as

$$\hat{A}_1 = \frac{\hat{A} + \hat{A}^*}{2} = \begin{bmatrix} 5 & -2 & 0 & 0 \\ -2 & 5 & 0 & 0 \\ 0 & 0 & 0 & 0 \\ 0 & 0 & 0 & 0 \end{bmatrix}, \hat{A}_2 = \frac{\hat{A} - \hat{A}^*}{2} = \begin{bmatrix} 0 & -2 & 0 & 0 \\ 2 & 0 & -3 & 0 \\ 0 & 3 & 0 & 0 \\ 0 & 0 & 0 & 0 \end{bmatrix}. \quad (15.19)$$

As expected,  $\hat{A} = A$ , and  $\hat{A}_1 = A_1$ ,  $\hat{A}_2 = A_2$ . Pseudoinverse would have resulted in the following erroneous solution:

$$\hat{A} = Y [X^* X]^{-1} X^* = \begin{bmatrix} 4.59 - 0.69i & -2.86 - 0.86i & -0.01 - 1.90i & 0.02 - 0.58i \\ 0.50 + 0.51i & 4.19 + 0.98i & -2.59 + 1.64i & 0.11 + 0.51i \\ -0.06 + 0.52i & 2.08 - 0.00i & -0.73 + 0.98i & -0.24 + 0.29i \\ 0 & 0 & 0 & 0 \end{bmatrix}. \quad (15.20)$$

### 15.2.2 Iterative MRPT

After obtaining the model update matrix from MRPT, model parameters can be further estimated from the matrix, e.g., using ordinary least squares [16]. Although in theory any matrix update method can be extended in a similar manner to estimate the model parameters, most parameter estimation algorithms attempt to solve a parameter optimization problem, where the objective function is formulated based on modal data matching or dynamic residual optimization. Modal data matching involves iterative minimization of a nonlinear error function of frequencies and mode shapes [17–20]. Dynamic residual optimization involves an objective function defined by the norm of the dynamic residual matrix, without requiring repeated evaluation of the eigensolutions or eigensensitivities. When all of the model degrees-of-freedom (DOFs) are measured, the objective function is linear with respect to the design parameters. However when the measured DOFs are incomplete, model reduction or modal expansion introduces nonlinearity to the objective function. Approximate techniques have been proposed by researchers [20, 21], but in general they do not produce numerically exact solutions even in a noise free situation.

The MRPT approach combined with least squares parameter estimation was extended in an iterative framework to deal with incomplete measured DOFs [22]. Assuming a linear conservative system where the perturbed stiffness matrix is the only unknown, Eq. (15.9) can be further simplified into

$$\Delta K \Phi_d = B, \quad (15.21)$$

where the dynamic residual matrix is given by

$$B = M_d \Phi_d A_d^2 + K_h \Phi_d, \quad (15.22)$$

As the stiffness perturbation matrix  $\Delta \mathbf{K} \in \mathbb{R}^{n \times n}$  is expected to be symmetric, the MRPT solution can be obtained by

$$\Delta \mathbf{K} = \mathbf{B} [\mathbf{B}_d^T \boldsymbol{\Phi}_d]^{-1} \mathbf{B}_d^T. \quad (15.23)$$

A subspace selection algorithm can be used to extract the most relevant and significant information from all the residual vectors [13]. After computing the perturbation matrix, the estimated stiffness matrix that represents the experimental structure can be calculated as

$$\mathbf{K}_d = \mathbf{K}_h - \Delta \mathbf{K}. \quad (15.24)$$

The perturbed stiffness matrix,  $\mathbf{K}_d$  can be expressed as linear combination of the elemental matrices,

$$\mathbf{K}_d = \sum_{j=1}^N x_j \mathbf{K}_h, \quad (15.25)$$

where  $x_j$  is the stiffness parameter and  $N$  is the number of parameters. By rearranging Eq. (15.25) into a linear matrix equation, we can estimate the unknown parameters using least squares. When the measured DOFs are incomplete, model reduction of Eq. (15.21) would result in

$$\Delta \tilde{\mathbf{K}} \tilde{\boldsymbol{\Phi}}_d = \tilde{\mathbf{B}}, \quad (15.26)$$

where  $\Delta \tilde{\mathbf{K}} \in \mathbb{R}^{m \times m}$  is the reduced stiffness matrix perturbation ( $m < n$ ). Each  $i$ th column of the reduced dynamic residual matrix is given by

$$\tilde{\mathbf{b}}_i = \lambda_{d_i}^2 \tilde{\mathbf{M}}_{d_i} \tilde{\boldsymbol{\phi}}_{d_i} + \tilde{\mathbf{K}}_{h_i} \tilde{\boldsymbol{\phi}}_{d_i}, \quad (15.27)$$

where  $\tilde{\mathbf{M}}_{d_i}, \tilde{\mathbf{K}}_{h_i} \in \mathbb{R}^{m \times m}$  are the reduced mass and stiffness matrices for each mode,

$$\tilde{\mathbf{M}}_{d_i} = \mathbf{T}_i^T \mathbf{M}_d \mathbf{T}_i, \quad \tilde{\mathbf{K}}_{h_i} = \mathbf{T}_i^T \mathbf{K}_h \mathbf{T}_i \quad (15.28)$$

obtained from transformation  $\mathbf{T}_i$ , which projects the measured experimental mode shapes to the full, i.e.,  $\boldsymbol{\phi}_{d_i} = \mathbf{T}_i \tilde{\boldsymbol{\phi}}_{d_i}$ . If Guyan reduction [23] were to be used, transformations  $\mathbf{T}_i$  are the same, i.e.,  $\mathbf{T} = \mathbf{T}_i$ , and  $\tilde{\mathbf{M}}_d = \tilde{\mathbf{M}}_{d_i}, \tilde{\mathbf{K}}_d = \tilde{\mathbf{K}}_{d_i}$ . Assuming that the rank of the dynamic residual matrix is preserved after model reduction, MRPT would yield solution

$$\Delta \tilde{\mathbf{K}} = \tilde{\mathbf{B}} [\tilde{\mathbf{B}}^T \boldsymbol{\Phi}_d]^{-1} \tilde{\mathbf{B}}^T. \quad (15.29)$$

The reduced perturbed stiffness matrix can be calculated as

$$\tilde{\mathbf{K}}_d = \mathbf{T}^T \mathbf{K}_h \mathbf{T} - \Delta \mathbf{K}. \quad (15.30)$$

The stiffness parameters can then be estimated from

$$\mathbf{K}_d = \sum_{j=1}^N x_j \mathbf{T}^T \mathbf{K}_{h_j} \mathbf{T}. \quad (15.31)$$

In order to satisfy the reduced eigenequation of the perturbed system, the transformation must be computed from the perturbed model, i.e.,  $\mathbf{T} = \mathbf{T}_d$ , which is unknown. Often, the original model is used instead, by letting  $\mathbf{T} = \mathbf{T}_h$ , which is known. As a result, the solution is only an approximation, and the accuracy depends on the validity of the assumption that  $\mathbf{T}_h \approx \mathbf{T}_d$ . The conjecture of the iterative MRPT algorithm is that the estimated parameters would yield more accurate transformation, which in turn produces better parameter estimates, and the iteration would proceed toward convergence. A noise-free simulated damage characterization study was performed to test the algorithm [22]. The study found non-monotonic convergence and sometimes even divergence, and numerically non-exact solutions. The inconsistent performance of the algorithm was mainly due to instability in the repeated substitution of the model reduction transformation, while the rank of the reduced dynamic residual matrix cannot be estimated reliably.

### 15.2.3 Dynamic Least Squares

The iterative MRPT algorithm was further developed into the more effective and stable dynamic least squares (DLS) method. The improved formulation directly estimates the model parameters in the reduced inverse eigenproblem without explicitly calculating the model matrix perturbation [22]. Rewriting Eq. (15.3) mode-by-mode for a linear conservative system,

$$\lambda_{d_i}^2 \mathbf{M}_d \boldsymbol{\phi}_{d_i} + \mathbf{K}_d \boldsymbol{\phi}_{d_i} = 0. \quad (15.32)$$

Using dynamic reduction [24] with transformation matrix  $\mathbf{T}_i$  for each mode,

$$\lambda_{d_i}^2 \tilde{\mathbf{M}}_{d_i} \tilde{\boldsymbol{\phi}}_{d_i} + \tilde{\mathbf{K}}_{d_i} \tilde{\boldsymbol{\phi}}_{d_i} = 0, \quad (15.33)$$

where the reduced model matrices are given by (15.28). We can express the model matrices as the linear combination of their elemental matrices, and separate the parameters into the unknown mass  $x_M$  and stiffness  $x_K$  parameters, and the known mass  $y_M$  and stiffness  $y_K$  parameters,

$$\sum x_M + \sum y_M + \sum x_K + \sum y_K = 0, \quad (15.34)$$

where the summation terms are given by

$$\sum x_M = \lambda_{d_i}^2 \sum_{k_{xM}=1}^{N_{xM}} x_M^{k_{xM}} \tilde{\mathbf{M}}_{h_i}^{k_{xM}} \tilde{\boldsymbol{\phi}}_{d_i}, \quad \sum x_K = \sum_{k_{xK}=1}^{N_{xK}} x_K^{k_{xK}} \tilde{\mathbf{K}}_{h_i}^{k_{xK}} \tilde{\boldsymbol{\phi}}_{d_i}, \quad (15.35)$$

$$\sum y_M = \lambda_{d_i}^2 \sum_{k_{yM}=1}^{N_{yM}} y_M^{k_{yM}} \tilde{\mathbf{M}}_{h_i}^{k_{yM}} \tilde{\boldsymbol{\phi}}_{d_i}, \quad \sum y_K = \sum_{k_{yK}=1}^{N_{yK}} y_K^{k_{yK}} \tilde{\mathbf{K}}_{h_i}^{k_{yK}} \tilde{\boldsymbol{\phi}}_{d_i}. \quad (15.36)$$

Grouping the unknown terms to one side and the known terms to the other, we obtain

$$\sum x_M + \sum x_K = - \left[ \sum y_M + \sum y_K \right]. \quad (15.37)$$

Rewriting the equation in an augmented matrix form for all modes, the problem comes down to solving

$$\mathbf{B}_x \mathbf{x}_d = -\mathbf{B}_y \mathbf{y}_d \quad (15.38)$$

for the unknown damage model parameters  $\mathbf{x}_d$ , where  $\mathbf{x}_d = [\mathbf{x}_M \ \mathbf{x}_K]^T$ ,  $\mathbf{y}_d = [\mathbf{y}_M \ \mathbf{y}_K]^T$ , and

$$\mathbf{x}_M = [x_M^1 \ \dots \ x_M^{N_{xM}}], \quad \mathbf{x}_K = [x_K^1 \ \dots \ x_K^{N_{xK}}], \quad (15.39)$$

$$\mathbf{y}_M = [y_M^1 \ \dots \ y_M^{N_{yM}}], \quad \mathbf{y}_K = [y_K^1 \ \dots \ y_K^{N_{yK}}]. \quad (15.40)$$

Matrices  $\mathbf{B}_x = [\mathbf{B}_{xM} \ \mathbf{B}_{xK}]$  and  $\mathbf{B}_y = [\mathbf{B}_{yM} \ \mathbf{B}_{yK}]$  contain the following

$$\mathbf{B}_{xM} = \begin{bmatrix} \mathbf{b}_{xM1} \\ \vdots \\ \mathbf{b}_{xMm} \end{bmatrix}, \quad \mathbf{B}_{xK} = \begin{bmatrix} \mathbf{b}_{xK1} \\ \vdots \\ \mathbf{b}_{xKm} \end{bmatrix}, \quad (15.41)$$

$$\mathbf{B}_{yM} = \begin{bmatrix} \mathbf{b}_{yM1} \\ \vdots \\ \mathbf{b}_{yMm} \end{bmatrix}, \quad \mathbf{B}_{yK} = \begin{bmatrix} \mathbf{b}_{yK1} \\ \vdots \\ \mathbf{b}_{yKm} \end{bmatrix}, \quad (15.42)$$

**Fig. 15.2** Cantilevered beam model

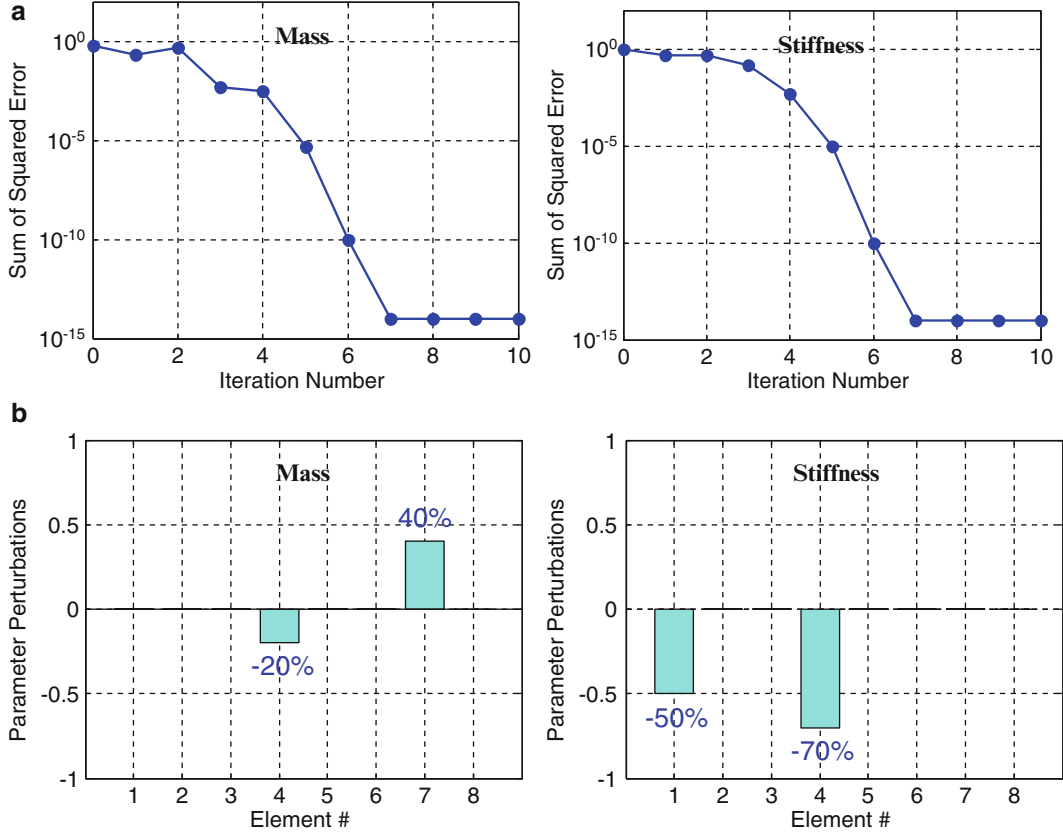
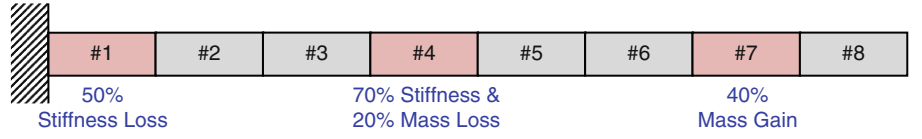


**Fig. 15.3** Simulated parameter estimation results. (a) Parameter error over iteration. (b) Final parameter perturbations

where

$$\mathbf{b}_{x_{M_i}} = \begin{bmatrix} b_{x_{M_i}}^1 \cdots b_{x_{M_i}}^{N_{xM}} \end{bmatrix}, \quad \mathbf{b}_{x_{K_i}} = \begin{bmatrix} b_{x_{K_i}}^1 \cdots b_{x_{K_i}}^{N_{xK}} \end{bmatrix}, \quad (15.43)$$

$$\mathbf{b}_{y_{M_i}} = \begin{bmatrix} b_{y_{M_i}}^1 \cdots b_{y_{M_i}}^{N_{yM}} \end{bmatrix}, \quad \mathbf{b}_{y_{K_i}} = \begin{bmatrix} b_{y_{K_i}}^1 \cdots b_{y_{K_i}}^{N_{yK}} \end{bmatrix}, \quad (15.44)$$

and

$$b_{x_{M_i}}^{k_{xM}} = \lambda_{d_i}^2 \tilde{\mathbf{M}}_h^{k_{xM}} \tilde{\boldsymbol{\phi}}_{d_i}, \quad b_{x_{K_i}}^{k_{xK}} = \tilde{\mathbf{K}}_h^{k_{xK}} \tilde{\boldsymbol{\phi}}_{d_i}, \quad (15.45)$$

$$b_{y_{M_i}}^{k_{yM}} = \lambda_{d_i}^2 \tilde{\mathbf{M}}_h^{k_{yM}} \tilde{\boldsymbol{\phi}}_{d_i}, \quad b_{y_{K_i}}^{k_{yK}} = \tilde{\mathbf{K}}_h^{k_{yK}} \tilde{\boldsymbol{\phi}}_{d_i}. \quad (15.46)$$

As in the iterative MRPT algorithm, the true model reduction transformations  $\mathbf{T}_{d_i}$  are unknown, thus  $\mathbf{T}_{h_i}$  is used instead. In a noise-free simulated problem, ordinary least squares can be used to solve (15.38) for  $\mathbf{X}_d$ . However when noise is present, the ill-posed inverse problem needs to be regularized. An effective scheme is to relax the satisfaction of Eq. (15.38) using a linear least squares formulation with quadratic inequality constraint (LSQI) [25]:

$$\min_{\mathbf{x}_d} \|\mathbf{x}_d - \mathbf{x}_h\|_2 \quad \text{subject to} \quad \|\mathbf{B}_x \mathbf{x}_d + \mathbf{B}_y \mathbf{y}_d\|_2 \leq \varepsilon, \quad (15.47)$$

where  $\mathbf{x}_h$  is the vector of healthy model parameters and  $\varepsilon$  is a positive constant representing the level of noise or uncertainty tolerance. The generalized singular value decomposition (GSVD) is usually used to analyze the LSQI problem [25]. If the constraint is active, a secular equation is solved using root-finding strategy such as bisection or Newton's method. Otherwise, the solution is obtained from minimizing the ordinary unconstrained least squares.

A numerical simulation study based on a cantilever beam as shown in Fig. 15.2 was performed with multiple mass and stiffness perturbations [22]. The unknown parameter set consists of five stiffness parameters (elements #1–#5) and five mass parameters (elements #4–#8). The results are shown in Fig. 15.3. All unknown mass and stiffness parameters were estimated accurately. The convergence was linear in the beginning, and became quadratic after five iterations.

Following the successful results of the numerical simulation, an experimental study based on the NASA eight-bay truss structure (Fig. 15.4a) was conducted. The truss was designed to model the International Space Station truss components and possible damage scenarios, so as to provide a convenient experimental testbed for various model refinement and damage characterization algorithms [26]. The mass and stiffness matrices of the truss structure were constructed based on a linear conservative model assumption with damping neglected. The model consists of 104 rod elements that connect 32 unconstrained nodes and four constrained nodes (Fig. 15.4b). Lumped mass model was used. Each unconstrained node has three DOFs in the  $x$ -,  $y$ -, and  $z$ -directions, resulting in a total of 96 DOFs. The first five modes of vibration were measured from modal testing. The analytical mode shapes and frequencies are shown in (Fig. 15.4c). Although the actual experiment placed accelerometers at all DOFs, it was decided to use only a subset of the data to simulate incomplete measurement. It was assumed that sensors were placed only in the  $x$ - and  $z$ -directions at the locations shown.

In model refinement, six mass parameters at the two nodes as shown in Fig. 15.4b were updated to account for the unmodeled actuator mass effects. The refined model was then used as baseline for damage characterization. The figure also shows the damage locations for a subset of the cases studied. All damage cases were created by removing the corresponding structural member, except that case P was created by buckling. Two members were removed in case O. In damage characterization, it was assumed that damage only affects the stiffness parameter and not mass. Face diagonal elements were excluded due to having virtually zero eigensensitivity. The final damage perturbations are shown in Fig. 15.5. The damage location in each case was successfully identified as the largest perturbation, with some small spurious perturbations elsewhere. The amount of damage was estimated at -1.0 for cases D and K, while it was underestimated to some small extent for the other cases.

When dealing with real experimental data, it would be necessary to replace the ordinary least squares estimation with the more robust LSQI estimation. In this study, the uncertainty tolerance  $\varepsilon$  in Eq. (15.47) was determined using the L-curve method [27]. For each value of  $\varepsilon$ , the solution converged to a pair of constraint and objective values that were plotted on the ordinate and abscissa respectively. Using different  $\varepsilon$  values, an L-shaped curve was formed. The objective and constraint were best compromised by selecting the  $\varepsilon$  value at the corner or point of largest curvature. In the events where instability occurred as  $\varepsilon$  was decreased, the smallest possible  $\varepsilon$  from a stable run was used. An example L-curve is shown in Fig. 15.6.

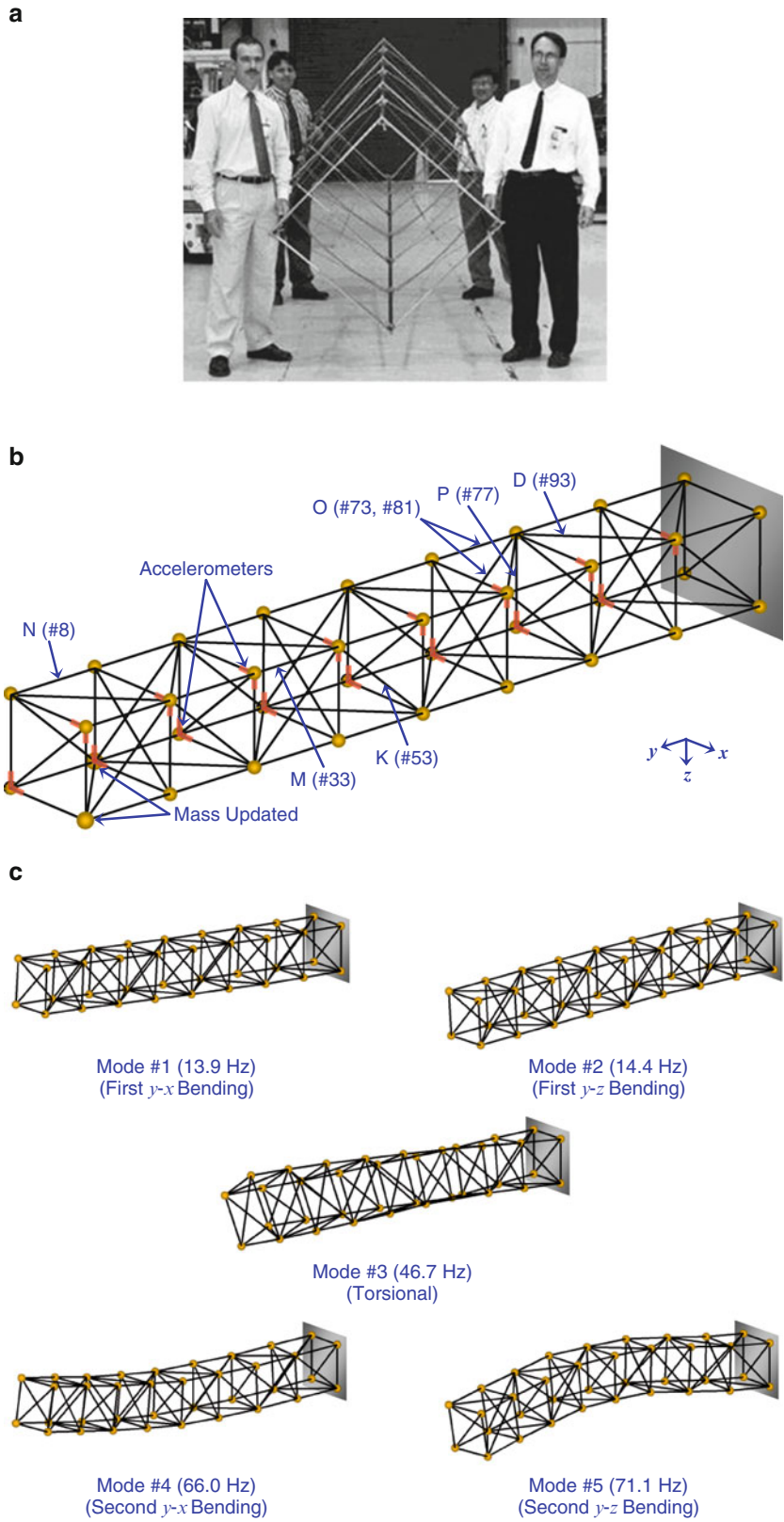
### 15.3 Conclusions

Among the solution approaches for vibration health monitoring of structures, dynamic residual minimization yielded some of the most computationally attractive algorithms. Minimum Rank Perturbation Theory (MRPT) offers a closed form solution of model matrix perturbation using only a subset of the measured modes equal to the rank of perturbation. The formulation of the theory was extended to include both symmetric and skew-symmetric model matrices in the equations of motion. The development led to the discovery of a new matrix property known as “null-symmetry” that helped explain how MRPT preserves symmetry and skew-symmetry in its solution. An iterative scheme combined with ordinary least squares parameter estimation was developed for MRPT to obtain FEM-consistent damage parameters under incomplete measurements.

This iterative algorithm was further developed into the more efficient and robust dynamic least squares method, which provided direct parameter estimation of the reduced inverse eigenproblem, bypassing the explicit computation of the model matrix perturbation. In each iteration, the method solves a linear least squares subproblem subject to a relaxed quadratic residual constraint. The formulation also allows the convenient use of dynamic reduction. The method does not require re-analysis of eigensolution or gradient, and is capable of simultaneously estimating multiple mass and stiffness parameters. A simulation study showed that the results are numerically exact in the absence of noise. Results based on actual experimental data further demonstrated the ability of the approach to identify the damage location and extent under noise and uncertainty.



**Fig. 15.4** NASA eight-bay truss. (a) Test structure. (b) Structural configuration. (c) Analytical modes of vibration



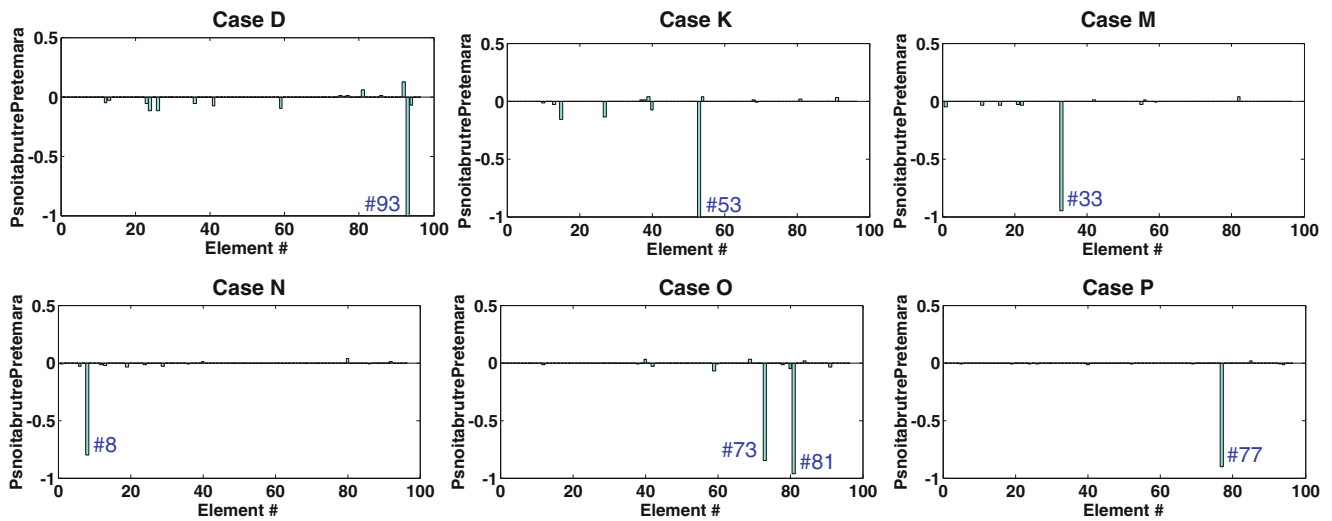
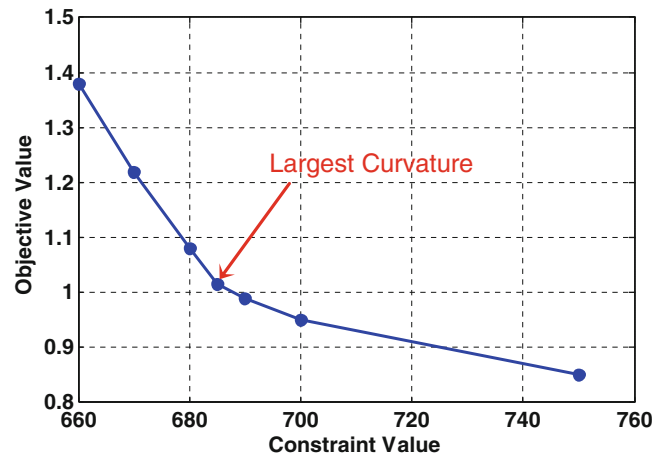


Fig. 15.5 Damage stiffness parameter perturbations

Fig. 15.6 L-curve for case D



**Acknowledgements** The analytical work presented in this paper was previously performed at the University of Houston in 1997–2000 through the support of the mechanical engineering department. Under the advice of the late professor David Zimmerman, the work was completed and subsequently published in conference proceedings and journals. The author, as well as many in the engineering community, were deeply saddened by the untimely passing of Dr. Zimmerman on April 10, 2012. This paper is dedicated to his significant contributions, profound insights, and adept knowledge in the field of modal analysis.

## References

1. Doebling SW, Farrar CR, Prime MB, Shevitz DW (1996) Damage identification and health monitoring of structural and mechanical systems from changes in their vibration characteristics: a literature review. Los Alamos National Laboratories LA-13070-MS
2. Mottershead JE, Friswell MI (1993) Model updating in structural dynamics – a survey. *J Sound Vib* 167(2):347–375
3. Zimmerman DC, Smith SW (1992) Model refinement and damage detection for intelligent structures. In: Tzou HS, Anderson GL (eds) *Intelligent structural systems*. Kluwer Academic, Amsterdam, pp 403–452
4. Hunt DL, Weiss SP, West WM, Dunlop TA, Freesmeyer S (1990) Development and implementation of a shuttle modal inspection system. In: *The 8th international modal analysis conference (IMAC)*, Kissimmee, FL
5. Loland O, Dodds JC (1976) Experience in developing and operating integrity monitoring system in north sea. In: *The 8th annual offshore technology conference*. Houston, TX, pp 313–319
6. Whitton TR, Dodds CJ (1983) Monitoring offshore structures by vibration techniques. In: *Design in offshore structures conference*. London, UK, pp 93–100
7. Nataraja R (1983) Structural integrity monitoring in real seas. In: *The 15th annual offshore technology conference*. Houston, TX, pp 221–228

8. Coppolino RN, Rubin S (1980) Detectability of structural failures in offshore platforms by ambient vibration monitoring. In: The 12th annual offshore technology conference. Houston, TX, pp 101–110
9. Kaouk M, Zimmerman DC (1993) Evaluation of the minimum rank update in damage detection: an experimental study. In: The 11th international modal analysis conference (IMAC), Orlando, FL, pp 1061–1068
10. Kaouk M, Zimmerman DC (1994) Structural damage assessment using a generalized minimum rank perturbation theory. *AIAA J* 32(4): 836–842
11. Kaouk M, Zimmerman DC (1995) Structural damage detection using modal data and no original analytical model. In: The 12th international modal analysis conference (IMAC), Honolulu, HI, pp 731–737
12. Zimmerman DC, Simmermacher T, Kaouk M (1995) Structural damage detection using frequency response functions. In: The 13th international modal analysis conference (IMAC), Nashville, TN, pp 179–184
13. Zimmerman DC, Simmermacher T (1995) Model correlation using multiple static load and vibration tests. *AIAA J* 33(11):2182–2188
14. Zimmerman DC, Kaouk M (1997) Structural health assessment using a partition and element model update technique. *J Chinese Soc Mech Eng* 19(1):115–124
15. Yap KC, Zimmerman DC (1999) Damage detection of gyroscopic systems using an asymmetric minimum rank perturbation theory. In: The 17th international modal analysis conference (IMAC), Kissimmee, FL, pp 1368–1372
16. Dos Santos JMC, Zimmerman DC (1996) Damage detection using minimum rank update theory and parameter estimation. In: *AIAA/ASME/AHS adaptive structures forum*, Salt Lake City, UT, pp 168–175
17. Flannigan CC (1987) Test/analysis correlation using design sensitivity and optimization. SAE paper 871743
18. Martinez D, Red-Horse J, Allen J (1991) System identification methods for dynamic structural models of electronic packages. In: The 32nd structures, structural dynamics, and materials (SDM) conference, Baltimore, MD, pp 2336–2346
19. Zimmerman DC, Yap KC, Hasselman T (1997) Evolutionary approach for model refinement. *MSSP J* 13(4):609–625
20. Farhat C, Hemez FM (1993) Updating finite element dynamic models using an element-by-element sensitivity methodology. *AIAA J* 31(9):1702–1711
21. Abdalla M, Grigoriadis KM, Zimmerman DC (1998) Enhanced damage detection using linear matrix inequalities. In: The 16th international modal analysis conference (IMAC), Santa Barbara, CA, pp 144–150
22. Yap KC, Zimmerman DC (2000) Dynamic least squares parameter estimation of structures. In: The 18th international modal analysis conference (IMAC), San Antonio, TX, pp 1513–1520
23. Guyan RJ (1965) Reduction of stiffness and mass matrices. *AIAA J* 3(2):380
24. Kidder RL (1973) Reduction of structural frequency equations. *AIAA J* 11(6):892
25. Bjork A (1996) Numerical methods for least squares problems. SIAM, Philadelphia, PA
26. Kashangaki TAL (1992) Ground vibration tests of a high fidelity truss for verification of on-orbit damage location techniques. NASA-LaRC technical Memorandum 107626
27. Hansen PC, O’Leary DP (1993) The use of the L-Curve in the regularization of discrete ill-posed problems. *SIAM J* 14(6):1487–1503

# Chapter 16

## Finite Element-Based Damage Detection Using Expanded Ritz Vector Residuals

Stuart G. Taylor, George Khoury, Michael D. Todd, and David C. Zimmerman

**Abstract** The incomplete measurement problem poses a significant obstacle for both model correlation and structural health monitoring (SHM). In practice, information about the health of a structure must be ascertained using measurement data from only a limited number of sensors. Several approaches to this problem have been proposed. One approach involves a reduced order model, such as that obtained using methods such as the Guyan reduction, the Improved Reduced System Model, or the System Equivalent Reduction Process. A second approach, which this work considers, involves an expansion of the test data to match a higher-fidelity model. This work presents a damage detection method utilizing Ritz vectors and the Method of Expanded Dynamic Residuals (MEDR). Ritz vectors have several advantages over eigenvectors for application to damage detection, including lower sensitivity to noise, and, as a result of their load-dependent nature, a greater sensitivity to localized damage. The MEDR restricts identified damage locations to those where there is physical connectivity, which eliminates the “smearing” that plagues direct expansion methods, and provides a physically meaningful estimate of the damage location. LA-UR-12-25460.

**Keywords** Ritz vectors • Damage detection • Matrix disassembly • NASA 8-bay truss • Expanded residuals

### 16.1 Introduction

Structural damage detection is an important issue for large civil structures, airplane wings, car frames, and any structure that regularly undergoes fatigue or impact loading. Damage detection becomes especially important when human lives are at stake, but improved damage detection methods would have financial benefits as well. Early detection of faults would allow repairs or replacements to be made before the damage becomes too costly to repair. Certain expensive components, such as carbon-fiber composite airplane wings, might enjoy a longer service life, rather than being replaced on an expensive time-based maintenance schedule.

Damage detection is often approached as a finite element model updating problem, either through updating the stiffness matrix or by physical parameter updating. Several methods for updating the mass and stiffness property matrices have been proposed, including the Minimum Rank Perturbation Theory (MRPT) [1]. Without a priori knowledge of the damage location, physical parameter updating requires intense manual interaction and heavy reliance on engineering

---

S.G. Taylor (✉)

Graduate Research Assistant, Los Alamos National Laboratory, Engineering Institute, Los Alamos, NM, USA

Department of Structural Engineering, University of California, San Diego, La Jolla, CA, USA

e-mail: [sgtaylor@lanl.gov](mailto:sgtaylor@lanl.gov)

G. Khoury

Department of Mechanical Engineering, University of Houston, Houston, TX, USA

e-mail: [gckhoury@uh.edu](mailto:gckhoury@uh.edu)

M.D. Todd

Professor and Vice Chair, Department of Structural Engineering, University of California, San Diego, La Jolla, CA, USA

e-mail: [mdtodd@mail.ucsd.edu](mailto:mdtodd@mail.ucsd.edu)

D.C. Zimmerman

Professor, Department of Mechanical Engineering, University of Houston, Houston, TX, USA

experience. Genetic Algorithms can be used to provide accurate convergence for the nonlinear optimization problem posed by physical parameter updating, but knowledge of the damage location would significantly improve the results and reduce the time required for the algorithm to converge.

Several difficulties present themselves in the damage detection problem. One difficulty to overcome is the incomplete measurements problem, wherein it is desired to detect damage based on a finite element model using physical measurements taken at only a small subset of the degrees of freedom present in the full model. Various model reduction techniques have been developed to help address the incomplete measurements problem, including the Guyan static reduction [2], sometimes referred to as a static condensation, the Improved Reduced System [3], and the System Equivalent Reduction Expansion Process (SEREP) [4]. However, a study that attempted to utilize mode shape expansion methods for damage detection with reduced measurements showed that direct expansion of measured mode shapes is ineffective [5].

The Method of Expanded Dynamic Residuals (MEDR) [6] couples the concept of the damage residual in MRPT with the of stiffness matrix disassembly [7] to arrive at an expanded damage residual vector, which is used to determine the location of damage using limited measurement points. With the damage location identified, the task of determining damage is significantly simplified. Several studies exist to address the issue of damage extent given knowledge of the damage location. One such study proposed a method for reduced model updating using Ritz vectors to compute the stiffness change [8].

MEDR was originally developed using measured mode shapes. In this work, Ritz vectors are applied to MEDR to provide a comparison between the application of Ritz vectors and mode shapes to MEDR in the face of significant signal noise. Load-dependent Ritz vectors [9] are an alternative to mode shapes that contain information about the dynamics of a structure. The first Ritz vector is the structure's deflection under a static load, and the subsequent Ritz vectors are defined recursively based on the structure's mass and stiffness properties.

The prime advantage of Ritz vectors over mode shapes in damage detection is that, rather than each vector describing the structure's behavior at a given frequency, each Ritz vector describes some aspect of the structure's behavior across a broad frequency range. Ritz vectors can be used to detect local structural damage, which is generally a high frequency phenomenon, using only the first few global Ritz vectors. Ritz vectors are also less sensitive to noise than measured mode shapes, and confidence in extracted Ritz vectors can be further increased by the application of accuracy indicators [10].

An important step in the development of Ritz vectors and their application to damage detection was the development of a method to extract Ritz vectors from dynamic testing data. After characterizing the effects of noise on measured Ritz vectors [11] and applying them to structural damage detection [12], Cao and Zimmerman showed that, using a state-space system realization, Ritz vectors extracted from dynamic testing data agree with analytically calculated Ritz vectors [13, 14]. Cao, Zimmerman, and James applied this method to identify Ritz vectors using Space Shuttle data [15], and later combined Ritz properties with modal strain for experimental damage detection [16]. Jeancolas and Zimmerman [17], Boxoen and Zimmerman [10], and Taylor and Zimmerman [18] continued to develop improvements to Ritz vector extraction, with further applications to damage detection [19, 20]. More recently, Khoury and Zimmerman have developed pre-test planning methods to aid in the extraction of load dependent Ritz vectors [21].

## 16.2 Mathematical Preliminaries

### 16.2.1 Analytical Ritz Vectors

A discrete  $n$ -degree-of-freedom ( $n$ -DOF) single-input undamped system model can be expressed as

$$\mathbf{M}\ddot{\mathbf{x}}(t) + \mathbf{K}\mathbf{x}(t) = \mathbf{b}u(t), \quad (16.1)$$

where  $\mathbf{M}$  and  $\mathbf{K}$  are the  $(n \times n)$  mass and stiffness matrices, respectively,  $\mathbf{x}(t)$  is an  $(n \times 1)$  position vector,  $\mathbf{b}$  is an  $(n \times 1)$  force influence vector, and  $u(t)$  is the force input signal. The first Ritz vector is the deflection of the structure under a unit static load; it is the mass-normalized static solution to Eq. (16.1), given by

$$\bar{\mathbf{v}}_1 = \mathbf{K}^{-1}\mathbf{b} \quad \mathbf{v}_1 = \bar{\mathbf{v}}_1/\Gamma \quad \Gamma_1^2 = \bar{\mathbf{v}}_1^T\mathbf{M}\bar{\mathbf{v}}_1. \quad (16.2)$$

Subsequent Ritz vectors are computed in a recursive algorithm that includes the inertial. Each subsequent Ritz vector is computed as

$$\bar{\mathbf{v}}_i = \mathbf{K}^{-1}\mathbf{M}\mathbf{v}_{i-1}. \quad (16.3)$$

Upon computation, each Ritz new vector is orthogonalized using a Gram-Schmidt orthogonalization process and mass normalized as

$$\begin{aligned}\hat{\mathbf{v}}_i &= \bar{\mathbf{v}}_i - \sum_{j=1}^{i-1} (\mathbf{v}_j^T \mathbf{M} \bar{\mathbf{v}}_i) \mathbf{v}_j \\ \mathbf{v}_i &= \hat{\mathbf{v}}_i / \Gamma_i \Gamma_i^2 = \hat{\mathbf{v}}_i^T \mathbf{M} \hat{\mathbf{v}}_i.\end{aligned}\quad (16.4)$$

### 16.2.2 Ritz Damage Residual

Damage location can be estimated using a model updating technique and a Ritz vector-based damage residual matrix. The primary assumptions that this work applies for such a method are that (1) a finite element model given by mass and stiffness  $\mathbf{M}$  and  $\mathbf{K}$ , with negligible damping accurately describes the structure of interest in an undamaged state; that (2) any damage to the structure only affects the stiffness property of the model; and that (3) the damaged structure continues to behave in a linear fashion described by an unknown stiffness matrix,  $\mathbf{K}_d = \mathbf{K} - \Delta\mathbf{K}$ . For a healthy system, Eq. (16.3) can be rewritten as the following equilibrium equation:

$$\mathbf{K}\bar{\mathbf{z}}_i - \mathbf{M}\mathbf{z}_{i-1} = \mathbf{0}.\quad (16.5)$$

The Ritz vectors are written in Eq. (16.5) with a ‘z’ to indicate that they are experimental Ritz vectors. The experimentally extracted Ritz vectors will satisfy Eq. (16.5) only if the structure remains in a healthy state. If the system becomes damaged, the equilibrium condition becomes

$$(\mathbf{K} - \Delta\mathbf{K})\bar{\mathbf{z}}_i - \mathbf{M}\mathbf{z}_{i-1} = \mathbf{0}.\quad (16.6)$$

If the Ritz vectors are extracted from a damaged structure, the right hand side of Eq. (16.5) becomes nonzero, and it is defined as the dynamic residual vector as

$$\mathbf{d} \equiv \mathbf{K}\bar{\mathbf{z}}_i - \mathbf{M}\mathbf{z}_{i-1} = \Delta\mathbf{K}\bar{\mathbf{z}}_i,\quad (16.7)$$

If the test DOFs are the same as those for the model, the DOFs affected by damage will appear as nonzero elements of  $\mathbf{d}$ . Given  $n$  DOFs and  $m$  Ritz vectors, Eq. (16.7) can be formulated as

$$\mathbf{B}_d \equiv \mathbf{K}\bar{\mathbf{Z}} - \mathbf{M}\mathbf{Z} = \Delta\mathbf{K}\bar{\mathbf{Z}},\quad (16.8)$$

where  $\mathbf{B}_d$  is the  $n \times (m-1)$  damage residual matrix. The stiffness change can then be obtained using minimum rank perturbation theory (MRPT) as

$$\Delta\mathbf{K} = \mathbf{B}_d (\mathbf{B}_d^T \bar{\mathbf{Z}})^{-1} \mathbf{B}_d^T.\quad (16.9)$$

In the noise-free case, the formulation given in Eq. (16.9) would be sufficient, as each column of  $\mathbf{B}_d$  would contain identical information. Practical implementations would implement a noise-resistant solution using the Singular Value Decomposition (SVD) as in [10].

### 16.2.3 Experimental Ritz Vectors

Although the preceding analytical formulation is useful, in order for damage detection using Ritz vectors to be practical, the vectors must be obtainable from dynamic testing data. Cao and Zimmerman [14] presented an algorithm using a system realization to extract Ritz vectors. The Eigenvalue Realization Algorithm (ERA) [22] uses dynamic testing data to identify a discrete time system model of the form

$$\begin{aligned}\mathbf{x}(k+1) &= \hat{\mathbf{A}}\mathbf{x}(k) + \hat{\mathbf{B}}\mathbf{u}(k) \\ \mathbf{y} &= \hat{\mathbf{C}}\mathbf{x}(k),\end{aligned}\quad (16.10)$$

where  $\hat{\mathbf{A}}$ ,  $\hat{\mathbf{B}}$ , and  $\hat{\mathbf{C}}$  are the discrete time system matrices. In practice these system matrices can be converted to continuous time using a zero-order hold method. The resulting continuous-time state-space representation  $[\mathbf{A}, \mathbf{B}, \mathbf{C}]$  can be used to

extract experimental Ritz vectors utilizing the improved Ritz vector extraction method [18], which orthonormalizes Ritz vectors in physical coordinates to produce non-orthonormalized Ritz vectors that are consistent with those produced by the Wilson algorithm. This method is necessary for accurate damage residual estimates using experimental Ritz vectors.

In the improved Ritz vector extraction method, the first Ritz vector in state-space is computed as

$$\bar{\mathbf{x}}_1 = -\mathbf{A}^{-1}\mathbf{B}. \quad (16.11)$$

This vector is immediately transformed to physical coordinates and mass-normalized as

$$\begin{aligned} \bar{\mathbf{z}}_1 &= \mathbf{C}\bar{\mathbf{x}}_1 \\ \mathbf{z}_1^T \mathbf{M} \mathbf{z}_1 &= 1. \end{aligned} \quad (16.12)$$

The first orthonormalized Ritz vector in state space is obtained by transforming the normalized Ritz vector back into state-space as

$$\mathbf{x}_1 = \mathbf{C}^+ \mathbf{z}_1, \quad (16.13)$$

where the ‘+’ is the pseudo-inverse operator. Subsequent Ritz vectors are computed and transformed to physical coordinates directly as

$$\bar{\mathbf{z}}_i = -\mathbf{C}\mathbf{A}^{-2}\mathbf{x}_{i-1}, \quad (16.14)$$

where they are orthogonalized and mass-normalized as

$$\begin{aligned} \mathbf{z}_i &= \bar{\mathbf{z}}_i - \sum_{j=1}^{i-1} (\mathbf{z}_j^T \mathbf{M} \bar{\mathbf{z}}_i) \mathbf{z}_j \\ \mathbf{z}_i^T \mathbf{M} \mathbf{z}_i &= 1. \end{aligned} \quad (16.15)$$

At each step, the orthonormalized Ritz vectors are obtained in state-space as

$$\mathbf{x}_i = \mathbf{C}^+ \mathbf{z}_i. \quad (16.16)$$

#### 16.2.4 Matrix Disassembly

Matrix disassembly is a process that decomposes a structural matrix into a matrix representation of the connectivity between DOFs and a matrix containing the magnitude information [7]. This application of matrix disassembly reduces any stiffness matrix into a set of equivalent springs. For a truss structure, this disassembly is exact, but for structures made up of more complicated elements, the disassembly is only approximate. Although some advanced applications utilize a disassembly of the stiffness matrix into the elemental stiffness matrices, the matrix disassembly method produces a general technique that can be applied to any model without detailed knowledge into the actual elements used. In. The matrix  $\mathbf{C}$  is an  $(n \times m)$  matrix, where  $n$  is the matrix dimension of  $\mathbf{K}$ , and  $m$  is equal to the total number of unique entries in  $\mathbf{K}$ . If  $\mathbf{K}$  is symmetric, this number amounts to the number of nonzero entries in the upper triangular portion of the matrix. The diagonal matrix  $\mathbf{P}$  is calculated as

$$\begin{aligned} \mathbf{P}(i, i) &= \sum_{j=1}^n \mathbf{K}(i, j) \quad i = 1 : n \\ \mathbf{P}(i, i) &= \mathbf{K}(j, k) \quad i = (n + 1) : m. \end{aligned} \quad (16.17)$$

The  $(n \times m)$  matrix  $\mathbf{C}$  can be written as  $[\mathbf{C}_1 \ \mathbf{C}_2]$ , where  $\mathbf{C}_1$  is the identity matrix. The elements of the  $n \times (m - 1)$  matrix  $\mathbf{C}_2$  are defined according to the element locations of the unique entries of the stiffness matrix  $\mathbf{K}$ . For each element  $\mathbf{K}(j, k)$  used to define the element  $\mathbf{P}(i, i)$  with  $i = (n + 1) : m$ , the  $i$ th column of  $\mathbf{C}$  is given as

$$\begin{aligned} \mathbf{C}(j, i) &= 1 \quad i = (n + 1) : m \\ \mathbf{C}(k, i) &= -1 \quad i = (n + 1) : m. \end{aligned} \quad (16.18)$$

### 16.2.5 Damage Residual Estimation with Reduced Measurements

If an  $(n \times p)$  transformation matrix  $\mathbf{T}$ , where  $n$  is the number of model DOFs and  $p$  is the number of measurement DOFS, relates the reduced measurement system to the full system as

$$\mathbf{x}_{full} = \mathbf{T}\mathbf{x}_{red}, \quad (16.19)$$

then the damage residual matrix of Eq. (16.8) can be rewritten as

$$\mathbf{B}_d = \mathbf{K}\mathbf{T}\bar{\mathbf{Z}}_r - \mathbf{M}\mathbf{T}\mathbf{Z}_r. \quad (16.20)$$

This work utilizes the transformation matrix  $\mathbf{T}$  derived from the Guyan model reduction [2]. Premultiplying Eq. (16.20) by  $\mathbf{T}^T$ , the reduced damage residual matrix can be defined as

$$\mathbf{B}_{d,r} = \mathbf{K}_r\bar{\mathbf{Z}}_r - \mathbf{M}_r\mathbf{Z}_r, \quad (16.21)$$

where  $\mathbf{B}_{d,r} = \mathbf{T}^T\mathbf{B}_d$ ,  $\mathbf{K}_r = \mathbf{T}^T\mathbf{K}\mathbf{T}$ , and  $\mathbf{M}_r = \mathbf{T}^T\mathbf{M}\mathbf{T}$ .

If one assumes that the connectivity information is invariant with respect to the damage, then the changes in the disassembly detailed in the previous section would be contained in the diagonal magnitude matrix  $\mathbf{P}$ . The connectivity matrix would be an invariant that could be used as a linearly dependent set of basis vectors to approximate the true damage residual. Choosing a reduced target vector,  $\mathbf{u}_{tar}$ , to be the first left singular vector of the reduced damage residual matrix  $\mathbf{B}_{d,r}$  the reduced target vector and the full target vector, similarly defined as the first left singular vector of the full damage residual matrix  $\mathbf{B}_d$ , can ideally be related as

$$\mathbf{u}_{red} = \mathbf{T}^T\mathbf{u}_{full}, \quad (16.22)$$

where the unknown full target vector is approximated as a linear combination of the columns of the connectivity matrix  $\mathbf{C}$ , as

$$\mathbf{u}_{full} = \mathbf{C}\mathbf{ff}, \quad (16.23)$$

where  $\mathbf{ff}$  is a vector of constants defining the contribution of each column. The reduced target vector can then be related to the full target vector through the connectivity matrix as

$$\mathbf{u}_{red} = \mathbf{T}^T\mathbf{C}\mathbf{ff}. \quad (16.24)$$

Choosing the values for  $\mathbf{ff}$  that best satisfy (16.24) permits the approximation of the full target vector using (16.23). The number of columns of  $\mathbf{C}$  will exceed its rank, so many of the components of  $\mathbf{ff}$  must be zero. The full combinatorial optimization problem that arises in choosing the nonzero elements of  $\mathbf{ff}$  would be infeasible even for modestly sized models, so a ‘‘best subspace’’ selection algorithm [23] is implemented to select the columns of  $\mathbf{C}$  that minimize

$$\min_{\text{wrt } \gamma} \varepsilon = (\mathbf{T}^T\mathbf{c}_i - \gamma\mathbf{u}_{tar})^T (\mathbf{T}^T\mathbf{c}_i - \gamma\mathbf{u}_{tar}). \quad (16.25)$$

At each selection of a column of  $\mathbf{C}$  to include, the target vector  $\mathbf{u}_{tar}$  is updated to remove the portion provided by that column, as

$$\mathbf{u}_{tar}^i = \frac{1}{\gamma}\mathbf{T}^T\mathbf{c}_i - \mathbf{u}_{tar}^{i-1}. \quad (16.26)$$

The process can be repeated until the error  $\varepsilon$  in Eq. (16.25) drops below some threshold. Once the nonzero elements of  $\mathbf{ff}$  are identified, the full damage residual vector can be estimated as

$$\mathbf{u}_{full} = \mathbf{C}\mathbf{ff}^*, \quad (16.27)$$

where  $\mathbf{ff}^*$  is the least squares solution to (16.24) using only the identified nonzero elements.



## 16.3 Numerical Examples

### 16.3.1 Description of Test Model

The NASA 8-bay truss was part of the Dynamic Scale Model Technology Program at NASA Langley Research Center [24]. This truss has been used extensively for damage location and extent studies [25]. A schematic of the 96-DOF cantilevered truss is shown in Fig. 16.1, with several experimental damage cases highlighted. Zimmerman and Bartkowicz [6] applied MEDR to several of these damage cases using measured mode shapes. The case considered in this work is case H, in which the longeron connecting DOFs 62 and 74 was removed.

This work seeks to demonstrate the efficacy of Ritz vector-based methods using examples that are relevant to the community, which is the motivation for choosing the NASA 8-bay truss for an example case. While some works have computed Ritz vectors using measured flexibility matrices, [26], the benefits of Ritz vectors cannot fully be realized if they are limited to spanning the space of the measured modes. As such, experimental Ritz vector extraction requires time-domain data; however, at the time of this writing, the only data available from tests conducted on this structure were the measured modes. In order to make a valid comparison between the application of mode shapes and Ritz vectors to MEDR, each vector set was obtained using the simulated system response. In an effort to remain true to the original experimental test bed, no more than the first five modes of vibration are used in this work, because individual members' local modes of vibration made it impossible to experimentally measure beyond the fifth global mode.

### 16.3.2 Damage Residual Estimation

The impulse response of the damaged truss system was simulated using the mass and stiffness for the damaged case, and ERA was used to identify a state-space model of the structure. The full analytical model of the damaged structure was used to generate the impulse response because this data is closest to what would be measured in an actual test, but the output from only 10 sensors were utilized, their locations chosen using a QR decomposition method to maximize linear independence of the selected DOFs. Applying the MEDR, estimates of the full damage residual vector were separately obtained using mode shapes and Ritz vectors. Estimates of the full damage residual vector were obtained each for the mode shapes and Ritz vectors. The estimates were normalized to unit length. The results are shown in Fig. 16.2, which contains two bar plots. The upper plot shows the absolute value of the damage residual estimates obtained using the ERA-identified mode shapes, while the lower plot shows the estimates obtained using the extracted Ritz vectors. The actual damaged DOFs (62 and 74) are indicated with asterisks.

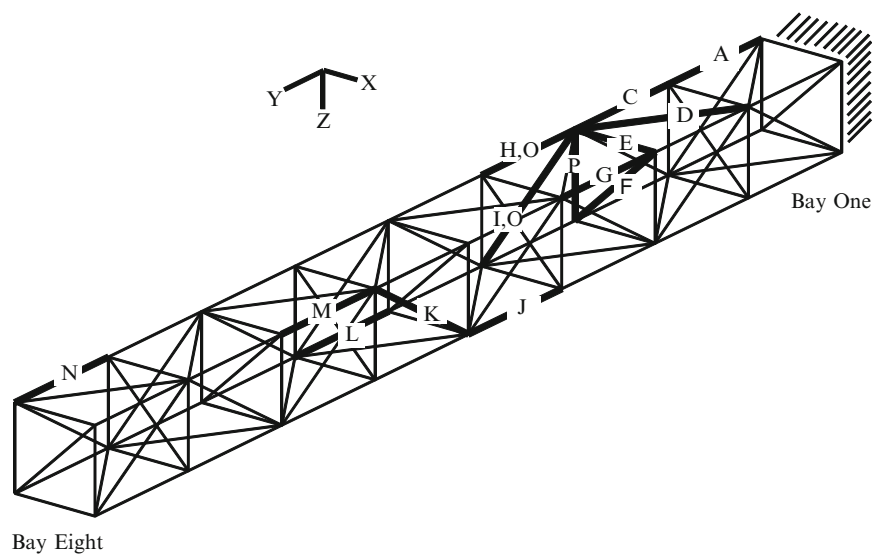
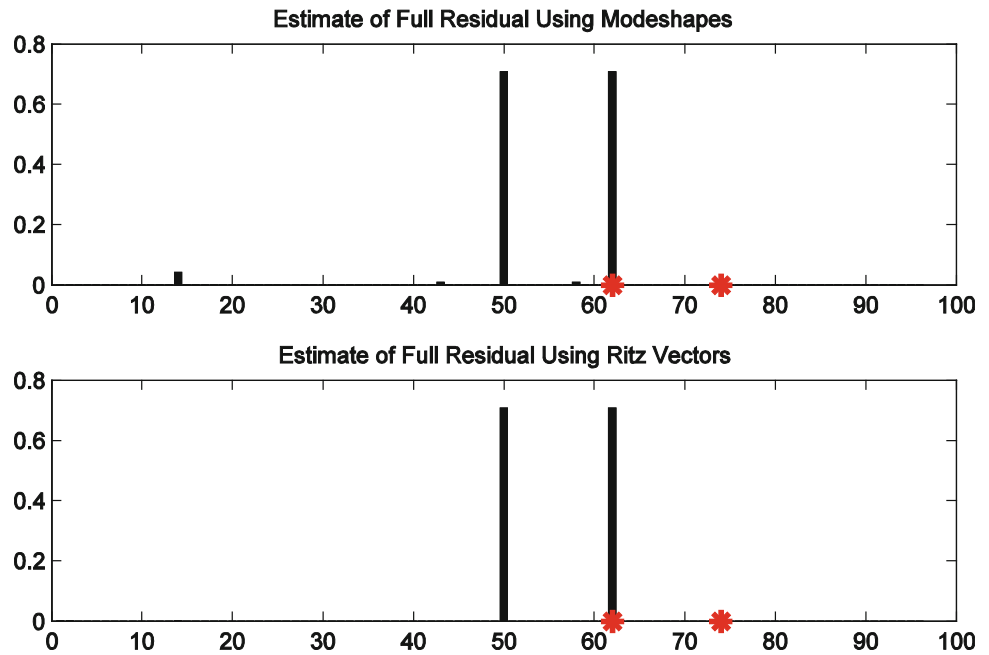


Fig. 16.1 NASA eight-bay truss

**Fig. 16.2** Normalized estimates of the full damage residual in the noise-free case



For the noise-free case, the results obtained using mode shapes and Ritz vectors are nearly identical to one another. This result is expected, because Ritz vectors should see no advantage over mode shapes in the absence of noise. Note that in both cases, DOFs 50 and 62 were indicated as damaged, rather than DOFs 62 and 74, as was the case. This results from the fact that, for particular reduced sensor sets, certain damage cases are indistinguishable from one another. In this case, removing the longeron connecting DOFs 50 and 62 has exactly the same effect on the reduced dynamic system behavior as removing the longeron connecting DOFs 62 and 74.

The process was repeated for noisy data, where the signals at the 10 output DOFs were corrupted with 5% RMS noise. The noisy data was generated as

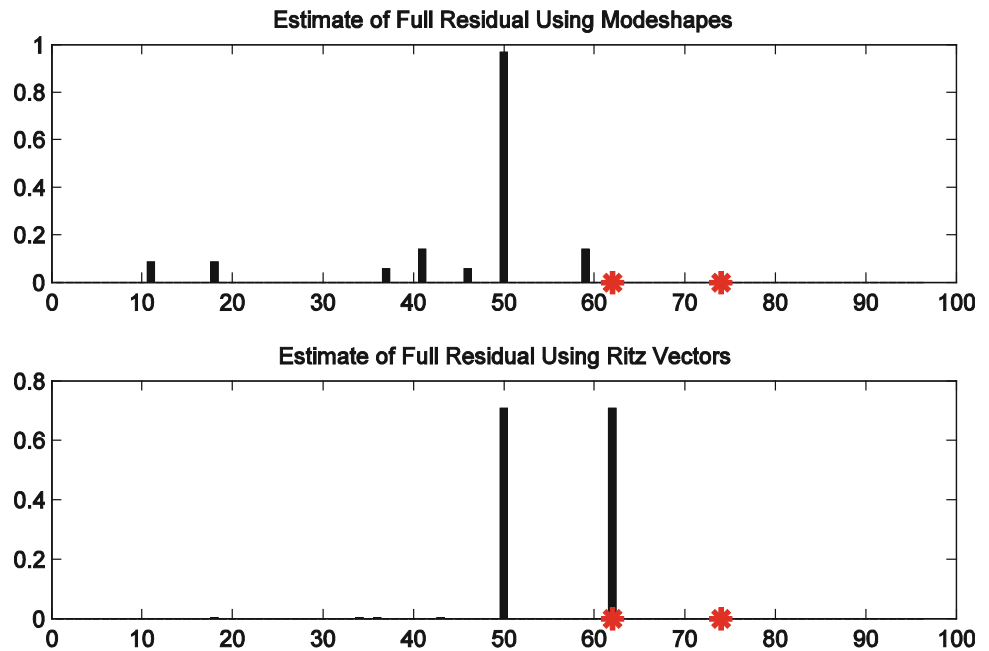
$$\mathbf{y}_n = \mathbf{y} + \frac{x}{100} \text{RMS}(\mathbf{y}) \cdot \mathbf{r}, \quad (16.28)$$

where  $\mathbf{y}_n$  is the corrupted time response vector,  $\mathbf{y}$  is the noise-free time response vector, and  $x$  is a scalar that determines the noise level, expressed as a percentage of the root-mean-square (RMS) value of the noise-free signal. The vector  $\mathbf{r}$  is generated from a pseudo-random uniform distribution over  $[-1, 1]$ .

Using identified mode shapes and extracted Ritz vectors from the noisy data, the MEDR was applied once more to obtain estimates of the full damage residual vector. The absolute values of the normalized damage residual estimates are shown in Fig. 16.3, where the upper plot shows the estimates obtained using mode shapes, and the lower plot shows the estimates obtained using Ritz vectors. The residual estimate using mode shapes primarily indicates DOF 50, while the estimate using Ritz vectors indicates DOFs 50 and 62, as in the noise-free case. While the mode shapes' result indicating DOF 50 is not entirely incorrect, because the damage cases are indistinguishable by the reduced model, the mode shapes do appear to be more significantly affected by the presence of noise.

In the next example it was assumed that 12 sensors were available, their locations having again been chosen using the QR decomposition method. The response of each DOF was corrupted with 5% RMS noise as above, and ERA was used to identify five separate state-space systems utilizing 8, 9, 10, 11 and 12 of the available sensors. The MEDR was then applied to obtain estimates of the full damage residual. In Figs. 16.4 and 16.5 there are each five plots: one for each estimate obtained using the different sensor sets. Figure refch16:fig16.4 contains the damage residual estimates obtained using mode shapes, while Fig. 16.5 contains the estimates obtained using Ritz vectors. The correct damaged DOFs, 62 and 74, are indicated with asterisks. In this case, the three DOFs 50, 62, and 74 could all be indicated, because more columns of the connectivity matrix were utilized in computing the residual estimates. Observing Fig. 16.4, only the sensor set with 9 sensors indicates

**Fig. 16.3** Normalized estimates of the full damage residual in the noisy case



the correct damaged DOFs, although for the sensor sets with 10 and 12 sensors, DOF 50 is indicated. It is clear that while the mode shapes are capable of indicating the correct damaged DOF, particular sensor sets allow them to become overwhelmed by signal noise. Observing Fig. 16.5, it is apparent that, while the presence of noise affects the results, the Ritz vectors are able to produce a more consistently correct estimate of the damage location across the range of sensor sets.

## 16.4 Summary

The method of expanded dynamic residuals was found to be robust to noise, even with a significantly reduced measurement set. The application of both measured mode shapes and extracted Ritz vectors successfully located damage for the test cases considered, although in the case considered, the extracted Ritz vectors provided a more consistently correct result in comparison to mode shapes. In noisy cases, varying the reduced sensor set affected the ability to obtain consistently correct results using mode shapes. However, in spite of some incorrect estimates provided by particular sensor sets, the application of the singular value decomposition to several estimates obtained using slightly different sensor sets successfully located the correct damaged degrees of freedom. By comparison, the application of Ritz vectors yielded the correct damaged degrees of freedom for each sensor set considered. Because multiple estimates may not be required when using Ritz vectors and MEDR, it would be more advisable to utilize Ritz vectors in this application.

It is difficult to extend directly the results obtained using expanded residuals to compute the damage extent in terms of a stiffness update matrix. Methods such as the minimum rank perturbation theory require system vectors (either mode shapes or Ritz vectors) at the full system DOFs in order to obtain a quantifiable stiffness property change. Rather than seeking an update matrix, once the damage location is known, damage extent can more easily be determined using parameter updating methods and optimization schemes such as genetic algorithms. However, Ritz vectors lend themselves very well to static reduction, with the first Ritz vector being the static deflection itself.

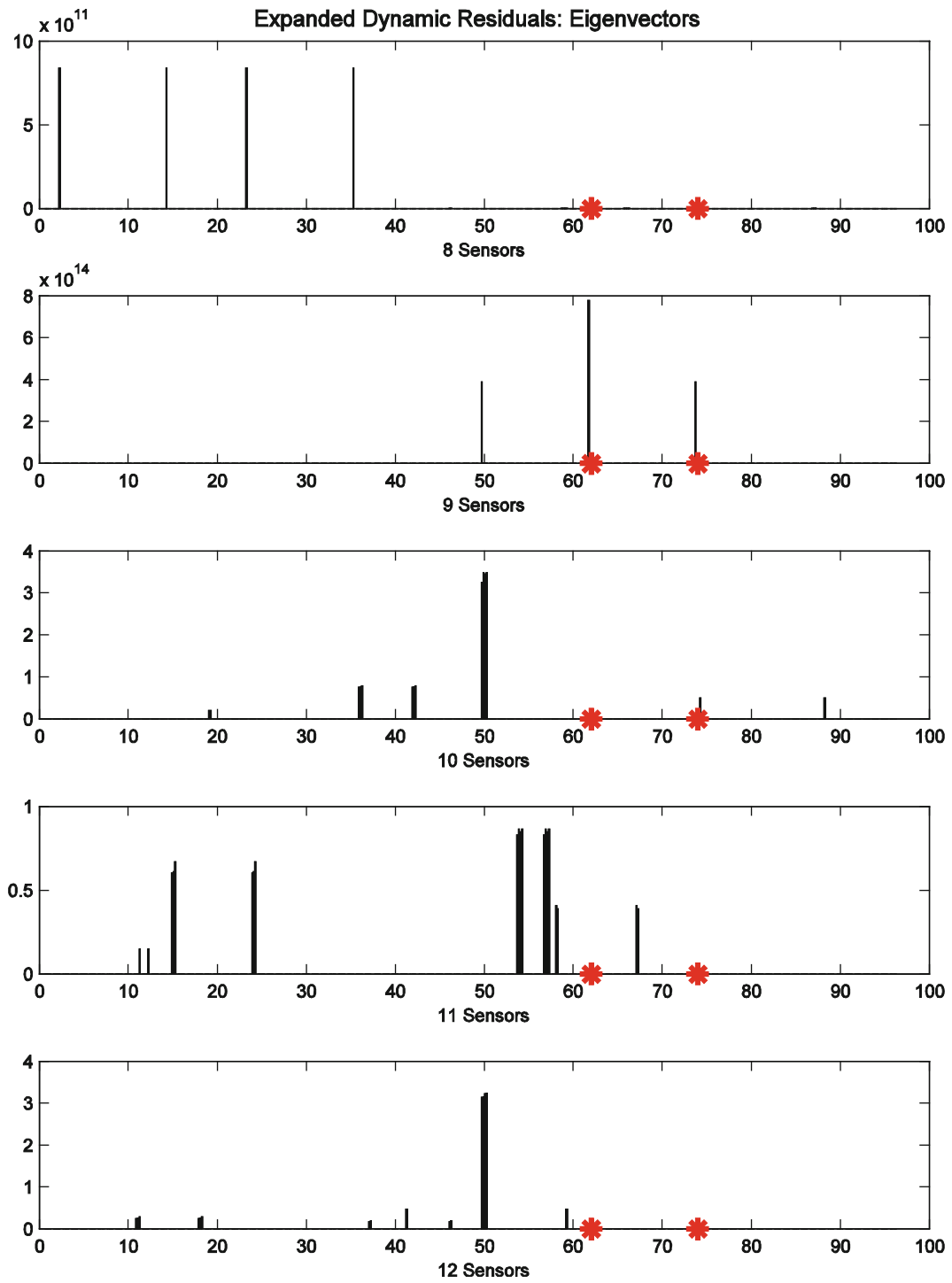
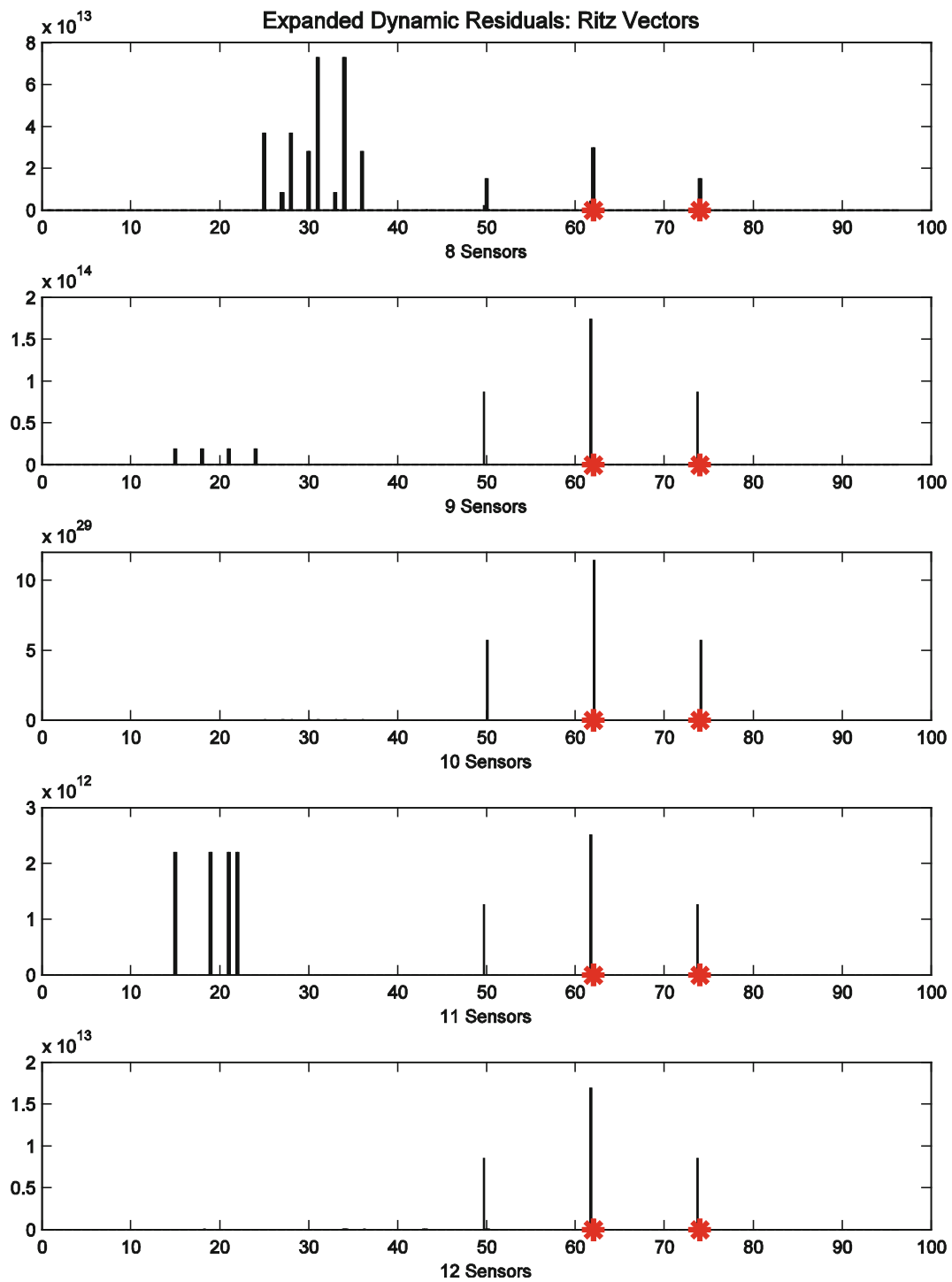


Fig. 16.4 Damage residual estimates for different sensor sets using eigenvectors



**Fig. 16.5** Damage residual estimates for different sensor sets using Ritz vectors

## References

1. Kaouk M, Zimmerman D (1994) Structural damage assessment using a generalized minimum rank perturbation theory. *AIAA J* 32:836–842
2. Guyan R (1965) Reduction of stiffness and mass matrices. *AIAA J* 3:380
3. O'Callahan J (1989) A procedure for an improved reduced system (IRS) model. In: International modal analysis conference, Las Vegas, NV
4. O'Callahan J, Li P (1996) SEREP expansion (system equivalent reduction expansion procedure). In: IMAC XIV – 14th international modal analysis conference, Dearborn, MI, pp 1258–1264
5. Zimmerman DC, Smith SW, Kim HM, Bartkowicz TJ (1996) An experimental study of structural damage detection using incomplete measurements. *J Vib Acoust*, 118(4):543–550
6. Zimmerman DC, Kim HM, Bartkowicz TJ, Kaouk M (2001) Damage detection using expanded dynamic residuals. *J Dyn Syst Meas Control* 123:699–705
7. Peterson L, Doebbling S, Alvin K (1995) Experimental determination of local structural stiffness by disassembly of measured flexibility matrices. 2756–2766
8. Burton TD, Farrar CR, Doebbling SW (1998) Two methods for model updating using damage Ritz vectors. In: International modal analysis conference, Santa Barbara, CA
9. Wilson E, Yuan M, Dickens J (1982) Dynamic analysis by direct superposition of Ritz vectors. *Earthq Eng Struct Dyn* 10:813–821
10. Boxoen T, Zimmerman DC (2003) Advances in Ritz vector identification. *J Struct Eng* 129:1131–1140
11. Zimmerman D, Cao T (1997) Effects of noise on measured Ritz vectors. In: DETC'97, Sacramento, CA, pp 1–8
12. Cao TT, Zimmerman DC (1997) Application of load dependent Ritz vectors in structural damage detection. In: Society of photo-optical instrumentation engineers, Bellingham, WA, pp 1319–1324
13. Cao TT, Zimmerman DC, James G (1998) Identification of Ritz vectors from ambient test data. In: International modal analysis conference, Santa Barbara, CA, pp 1609–1614
14. Cao TT, Zimmerman DC (1999) Procedure to extract Ritz vectors from dynamic testing data. *J Struct Eng* 125:1393–1400
15. Cao TT, Zimmerman DC, James GH (1999) Identification of Ritz vectors from the space shuttle vertical stabilizer assembly test article. In: International modal analysis conference, Kissimmee, FL, pp 2005–2010
16. Zimmerman DC, James GH, Cao T (1999) An experimental study of damage detection using modal, strain, and Ritz properties. In: Society of photo-optical instrumentation engineers, Santa Clara, CA, pp 586–592
17. Jeancolas H, Zimmerman D (2002) Improving the accuracy of measured Ritz vectors. In: International modal analysis conference, Los Angeles, CA pp 802–808
18. Taylor SG, Zimmerman DC (2010) Improved experimental Ritz vector extraction with application to damage detection. *J Vib Acoust* 132:011012
19. Taylor SG, Zimmerman DC (2005) Damage detection in a cargo bay frame using Ritz vectors. In: International modal analysis conference, Orlando, FL
20. Taylor SG, Zimmerman DC (2007) Structural health monitoring using Ritz vectors and expanded residuals. In: International modal analysis conference, Orlando, FL
21. Khoury GC, Zimmerman DC (2011) Development of pretest planning methodologies for load dependent Ritz vectors. In: Proulx T (ed) Rotating machinery, structural health monitoring, shock and vibration, vol 8. Springer, New York, pp 1–13
22. Juang JN, Pappa RS (1985) An eigensystem realization algorithm for modal parameter identification and model reduction. *J Guid* 8:620–627
23. Lallemant G, Piranda J (1989) Localization methods for parametric updating of finite element models in elastodynamics. In: International modal analysis conference, Kissimmee, FL, pp 690–695
24. McGowan PE, Edighoffer HH, Wallace JW (1989) Development of an experimental space station model for structural dynamics research. In: Shock and vibration symposium, Virginia Beach, VA
25. Kashangaki TA (1992) Ground vibration tests of a high fidelity truss for verification of on orbit damage location techniques. NASA Langley Research Center 107626
26. Sohn H, Law K (2001) Extraction of Ritz vectors from vibration test data. *Mech Syst Signal Process* 15:213–226

# Chapter 17

## Proportional Damping from Experimental Data

Brian Schwarz and Mark Richardson

**Abstract** Damping forces are typically ignored during the Finite Element Analysis (FEA) of mechanical structures. In most real structures, it can be assumed that there are several damping mechanisms at work, but they may be difficult to identify, and even more difficult to model.

Since both mass & stiffness matrices are available during an FEA, a common method of modeling viscous damping is with a *proportional* damping matrix. That is, the viscous damping matrix is assumed to be a *linear combination* of the mass & stiffness matrices. Therefore, in order to model viscous damping with a *proportional* damping matrix, the two constants of proportionality must be determined.

In this paper, a least-squared-error relationship between *experimental* modal frequency & damping and the proportional damping *constants of proportionality* is developed. An example is included in which experimental modal parameters are used to calculate the constants of proportionality. The modal parameters of an FEA model with proportional damping are then compared with the original experimental modal parameters.

**Keywords** Viscous damping • Proportional damping • Modal damping • Finite element analysis • Experimental modal parameters

### 17.1 Introduction

All experimental resonant vibration data is characterized by a *decaying sinusoidal response* when all forces are removed from the structure. The overall response is modeled as a *summation* of contributions, each term due to a mode of vibration. Each modal contribution is itself a *decaying sinusoidal* function. The decay envelope for each mode is modeled with a decreasing exponential function, and the decay constant in the exponent is called the modal *damping coefficient*. It is also called the *half power point*, or *3 dB point* damping.

### 17.2 Viscous Damping

It is commonly assumed that displacement of the surrounding air by the surfaces of a vibrating structure is a *dominant* damping mechanism at work in most structures, at least those in earth's atmosphere. It is also assumed that this mechanism can be adequately modeled using a linear viscous damping model.

A linear viscous damping model, in which the damping or dissipative forces are proportional to the surface velocity, is used as the time domain model for this type of damping.

The time domain linear differential equations of motion for a vibrating structure with viscous damping are written as;

$$[M] \{\ddot{x}(t)\} + [C] \{\dot{x}(t)\} + [K] \{x(t)\} = \{f(t)\} \quad (17.1)$$

---

B. Schwarz (✉) • M. Richardson  
Vibrant Technology, Inc., Scotts Valley, CA, USA  
e-mail: [brian.schwarz@vibetech.com](mailto:brian.schwarz@vibetech.com); [mark.richardson@vibetech.com](mailto:mark.richardson@vibetech.com)

where:

- [M] = mass matrix (n by n)
- [C] = viscous damping matrix (n by n)
- [K] = stiffness matrix (n by n)
- $\{\ddot{x}(t)\}$  = accelerations (n-vector)
- $\{\dot{x}(t)\}$  = velocities (n-vector)
- $\{x(t)\}$  = displacements (n-vector)
- $\{f(t)\}$  = external forces (n-vector)
- n = number of degrees-of-freedom of the model

Equation (17.1) is a *force balance* between the *internal* (*inertial*, *dissipative*, and *restoring*) forces on the left-hand side and the *externally applied* forces on the right-hand side.

Equation (17.1) describes the *linear*, *stationary*, *viscously damped*, dynamic behavior of a structure. The mass [M] & stiffness [K] matrices are typically synthesized from the physical properties and geometry of the structure, using an FEA software program. However, in most FEA practice today, the viscous damping matrix [C] is assumed to be zero. That is, damping is ignored altogether.

The frequency domain version of this equation is commonly used as the basis for determining the modes of a structure. Modes are solutions to the *homogeneous* form of this equation, shown as Eq. (17.2) below [3, 4];

$$\begin{aligned} ([M] p^2 + [C] p + [K]) \{\phi\} &= \{0\} \\ p &= -\sigma + j\omega \end{aligned} \quad (17.2)$$

Each *non-trivial* solution of this matrix equation consists of a pole location, p (also called an *eigenvalue*) and a mode shape,  $\{\phi\}$  (also called an *eigenvector*). Each complex pole is made up of both the *damping decay constant* ( $\sigma$ ) and the *damped natural frequency* ( $\omega$ ).

### 17.3 Proportional Damping Matrix

A proportional damping matrix is assumed to be a *linear combination* of the mass & stiffness matrices. That is, the viscous damping forces are *assumed* to be proportional to the inertial and restoring forces in the structure [2].

$$[C] = \alpha [M] + \beta [K] \quad (17.3)$$

- $\alpha$  = constant of mass proportionality
- $\beta$  = constant of stiffness proportionality

Once  $\alpha$  &  $\beta$  have been determined, all of the matrices in Eq. (17.2) are known, and the modes of the damped structure can be calculated. The question now becomes; “*How can  $\alpha$  &  $\beta$  be determined for a real structure?*”

### 17.4 Proportional Damping Coefficients

Modal frequency & damping estimates are routinely determined from experimental data using modern modal testing and analysis methods. Experimental forced vibration data is commonly obtained in the form of a set of Frequency Response Functions (FRFs). An FRF is a special form of a Transfer Function. Its numerator is the Fourier spectrum of a structural *output* (acceleration, velocity, or displacement response), and its denominator is the Fourier spectrum of the *input* (the force that caused the response).

Modal frequency & damping estimates are obtained from one or more FRFs by *curve fitting* them, using an analytical model that includes frequency & damping as unknown parameters. A set of modal frequency & damping estimates can therefore be obtained for all modes in the frequency band of the FRF measurements.

These experimental frequency & damping estimates can then be used to calculate the proportional damping matrix coefficients,  $\alpha$  &  $\beta$ . The relationship between modal frequency & damping and  $\alpha$  &  $\beta$  is derived from Eq. (17.2).



Substituting Eq. (17.3) into Eq. (17.2) and re-arranging terms gives;

$$\begin{aligned}
 ([\mathbf{M}] p^2 + (\alpha [\mathbf{M}] + \beta [\mathbf{K}]) p + [\mathbf{K}]) \{\phi\} &= \{0\} \\
 ([\mathbf{M}] (p^2 + \alpha p) + [\mathbf{K}] (\beta p + 1)) \{\phi\} &= \{0\} \\
 ([\mathbf{M}] ((-\sigma + j\omega)^2 + \alpha (-\sigma + j\omega)) + [\mathbf{K}] (\beta (-\sigma + j\omega) + 1)) \{\phi\} &= \{0\} \\
 ([\mathbf{M}] ((\sigma^2 - \omega^2 - j2\sigma\omega) + (-\alpha\sigma + j\alpha\omega)) + [\mathbf{K}] (\beta (-\sigma + j\omega) + 1)) \{\phi\} &= \{0\} \\
 ([\mathbf{M}] ((\sigma^2 - \omega^2 - \alpha\sigma) + j(-2\sigma\omega + \alpha\omega)) + [\mathbf{K}] ((-\sigma\beta + 1) + j\beta\omega)) \{\phi\} &= \{0\}
 \end{aligned} \tag{17.4}$$

If the damping term were removed from Eq. (17.2), it would be the homogeneous equation of motion for an *un-damped* structure. Notice that Eq. (17.4) also has the same form as an equation for an *un-damped* structure. A known property of the mode shapes  $\{\phi\}$  of an *un-damped* structure is that they are *real-valued*. Modes with *real-valued* mode shapes are also called *normal modes* [2].

Because  $\{\phi\}$  is real-valued, the real and imaginary parts of Eq. (17.4) are not coupled. Therefore, the *real* and *imaginary* parts of Eq. (17.4) can be written as separate equations;

$$\begin{aligned}
 ([\mathbf{M}] (\sigma^2 - \omega^2 - \alpha\sigma) + [\mathbf{K}] (-\sigma\beta + 1)) \{\phi\} &= \{0\} \\
 ([\mathbf{M}] (-2\sigma\omega + \alpha\omega) + [\mathbf{K}] \beta\omega) \{\phi\} &= \{0\}
 \end{aligned} \tag{17.5}$$

Putting these equations into the standard form for an *un-damped* structure;

$$\begin{aligned}
 \left( \frac{(\sigma^2 - \omega^2 - \alpha\sigma)}{(-\sigma\beta + 1)} [\mathbf{M}] + [\mathbf{K}] \right) \{\phi\} &= \{0\} \\
 \left( \frac{(-2\sigma + \alpha)}{\beta} [\mathbf{M}] + [\mathbf{K}] \right) \{\phi\} &= \{0\}
 \end{aligned} \tag{17.6}$$

Both of these equations must be satisfied for a proportionally damped structure. The eigensolution to these equations has *unique* poles (or eigenvalues), and the coefficients of the mass matrix can be equated to each of the poles. The equation for one of the poles of the *un-damped* structure is;

$$\frac{(\sigma^2 - \omega^2 - \alpha\sigma)}{(-\sigma\beta + 1)} = \frac{(-2\sigma + \alpha)}{\beta} = -\Omega^2 \tag{17.7}$$

where;

$$\Omega^2 = (\sigma^2 + \omega^2) = \text{an } \textit{un-damped} \text{ natural frequency squared.}$$

This gives us a single equation with two unknowns ( $\alpha$  &  $\beta$ ) in it;

$$2\sigma = \alpha + \beta\Omega^2 \tag{17.8}$$

or

$$2\sigma = \alpha + \beta(\sigma^2 + \omega^2) \tag{17.9}$$

Equation (17.9) can be used together with estimates of frequency & damping for *two or more* modes to compute the proportional damping constants,  $\alpha$  &  $\beta$ .

## 17.5 Least-Squared-Error Solution

Given a set of modal frequencies & damping for **n modes** ( $n \geq 2$ ), then **n equations** can be written;

$$2 \begin{Bmatrix} \sigma_1 \\ \sigma_2 \\ \vdots \\ \sigma_n \end{Bmatrix} = \begin{bmatrix} 1 & \Omega_1^2 \\ 1 & \Omega_2^2 \\ \vdots & \vdots \\ 1 & \Omega_n^2 \end{bmatrix} \begin{Bmatrix} \alpha \\ \beta \end{Bmatrix} \tag{17.10}$$

This is an *over-specified* set of linear equations. The least-squared-error solution of these equations is written as;

$$2 \begin{bmatrix} 1 & 1 & \dots & 1 \\ \Omega_1^2 & \Omega_2^2 & \dots & \Omega_n^2 \end{bmatrix} \begin{Bmatrix} \sigma_1 \\ \sigma_2 \\ \vdots \\ \sigma_n \end{Bmatrix} = \begin{bmatrix} 1 & 1 & \dots & 1 \\ \Omega_1^2 & \Omega_2^2 & \dots & \Omega_n^2 \end{bmatrix} \begin{bmatrix} 1 & \Omega_1^2 \\ 1 & \Omega_2^2 \\ \vdots & \vdots \\ 1 & \Omega_n^2 \end{bmatrix} \begin{Bmatrix} \alpha \\ \beta \end{Bmatrix} \quad (17.11)$$

or;

$$2 \begin{Bmatrix} \sum_{i=1}^n \sigma_i \\ \sum_{i=1}^n \sigma_i \Omega_i^2 \end{Bmatrix} = \begin{bmatrix} N & \sum_{i=1}^n \Omega_i^2 \\ \sum_{i=1}^n \Omega_i^2 & \sum_{i=1}^n (\Omega_i^2)^2 \end{bmatrix} \begin{Bmatrix} \alpha \\ \beta \end{Bmatrix} \quad (17.12)$$

Equation (17.12) can be solved for  $\alpha$  &  $\beta$  with the following matrix equation;

$$\begin{Bmatrix} \alpha \\ \beta \end{Bmatrix} = 2 \begin{bmatrix} N & \sum_{i=1}^n \Omega_i^2 \\ \sum_{i=1}^n \Omega_i^2 & \sum_{i=1}^n (\Omega_i^2)^2 \end{bmatrix}^{-1} \begin{Bmatrix} \sum_{i=1}^n \sigma_i \\ \sum_{i=1}^n \sigma_i \Omega_i^2 \end{Bmatrix} \quad (17.13)$$

Equation (17.13) is the desired relationship between the frequency & damping estimates for multiple modes and the proportional damping matrix coefficients,  $\alpha$  &  $\beta$ .

Least-squared-error estimates of  $\alpha$  &  $\beta$  can be calculated using any number (2 or greater) of experimental modal frequencies & damping and Eq. (17.13). These estimates can then be used to add a proportional damping matrix to an FEA model.

If the *damped* FEA model is then solved for its modes, the following question arises; “How well do the modal frequencies & damping of the damped FEA model match the experimental modal parameters from which the damped model was derived?” This question is addressed with the following examples.

## 17.6 Beam Structure

We will consider the modes of the beam structure shown in Fig. 17.1, also called the Jim Beam. This beam consists of three aluminum plates fastened together with cap screws. The top plate is fastened to the back plate with three screws, and the bottom plate is also fastened to the back plate with three screws.

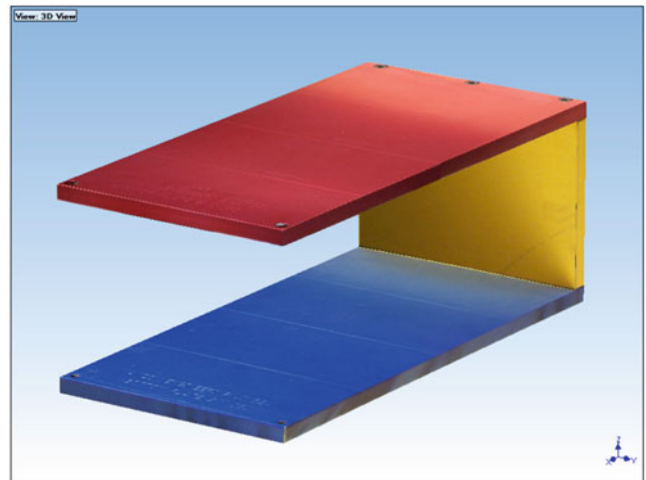


**Fig. 17.1** Jim beam structure

**Table 17.1** Un-damped FEA & damped EMA modes

Mode	FEA freq. (Hz)	FEA damp. (Hz)	EMA freq. (Hz)	EMA damp. (Hz)	Mode shape MAC
1	61.405	0.0	96.944	5.6347	0.74
2	143.81	0.0	164.95	3.1125	0.96
3	203.71	0.0	224.57	6.5223	0.96
4	310.62	0.0	347.56	5.1552	0.95
5	414.4	0.0	460.59	11.502	0.93
6	442.6	0.0	492.82	4.6424	0.96
7	583.44	0.0	635.18	14.247	0.94
8	1,002.2	0.0	1,108.2	4.964	0.90
9	1,090.8	0.0	1,210.5	7.1292	0.88
10	1,168.3	0.0	1,322.6	7.2498	0.84
11	1,388.2	0.0	1,555.1	17.112	0.84

### 17.6.1 Modal Frequency and Damping

The modal frequency & damping for the first 11 (lowest frequency) *un-damped* FEA modes and the Experimental Modal Analysis (EMA) modes of the Jim Beam are listed in Table 17.1. The FEA frequencies were obtained as the eigenvalues of an *un-damped* FEA model [1]. Because the FEA model was *un-damped*, the FEA modes have no damping. The EMA parameters were estimated by *curve fitting* a set of experimentally derived FRFs.

Each FEA modal frequency is less than its corresponding EMA frequency, indicating that the FEA model was *less stiff* than the actual Jim Beam structure. However, the Modal Assurance Criterion (MAC) values between the mode shape pairs indicate that the FEA and EMA mode shapes are comparable. Two mode shapes are strongly correlated if their MAC value is *0.90 or greater*.

A modal model consisting of 11 modes is called a *truncated* modal model because *all* of the modes of the actual Jim Beam are not present in the model. In principle, all real structures have an *infinite* number of modes, but because all FEA models contain a *finite* number of DOFs, they will only yield a finite number of modes, or a *truncated* modal model. Similarly, because FRF measurements are made over a *finite* frequency band, all experimentally derived modal models are *truncated* models.

## 17.7 Two Extreme Cases

Two extreme cases are possible with the coefficients  $\alpha$  &  $\beta$ , namely,  $\alpha > 0, \beta = 0$  and  $\alpha = 0, \beta > 0$ .

### Case #1 ( $\beta = 0$ )

If  $\beta = 0$ , then viscous damping is *only proportional* to the mass distribution, and Eq. (17.8) reduces to;

$$\alpha = 2\sigma \quad (17.14)$$

Assume that the Jim Beam is proportionally damped, and that its proportional damping matrix coefficients are;  $\alpha = 2\pi$ ,  $\beta = 0$ . Then Eq. (17.14) says that *all* modes of the beam will have the *same* modal damping;

$$\sigma = \pi \text{ rad/sec} = 0.5 \text{ Hz.}$$

The coefficients  $\alpha = 2\pi$ ,  $\beta = 0$  were used to create a proportional damping matrix from the mass & stiffness matrices of the *un-damped* FEA model for the Jim Beam, and the *damped* FEA model was solved for its modes. The expected result (all modes with damping = 0.5 Hz), is shown in Table 17.2.

### Case #2 ( $\alpha = 0$ )

If  $\alpha = 0$ , then viscous damping is *only proportional* to the stiffness distribution, and Eq. (17.8) reduces to;

$$\beta\Omega = \frac{2\sigma}{\Omega} = 2\zeta \quad (17.15)$$

where  $\zeta = \frac{\sigma}{\Omega}$  is the *percent of critical* damping of a mode.

**Table 17.2** Proportionally damped FEA modes ( $\alpha = 2\pi$ ,  $\beta = 0$ )

Mode	Un-damped FEA freq. (Hz)	Un-damped FEA damp. (Hz)	Damped FEA freq. (Hz)	Damped FEA damp. (Hz)	Mode shape MAC
1	61.405	0.0	61.403	0.49975	1.00
2	143.81	0.0	143.81	0.49975	1.00
3	203.71	0.0	203.71	0.49975	1.00
4	310.62	0.0	310.62	0.49975	1.00
5	414.4	0.0	414.4	0.49975	1.00
6	442.6	0.0	442.6	0.49975	1.00
7	583.44	0.0	583.44	0.49975	1.00
8	1,002.2	0.0	1,002.2	0.49975	1.00
9	1,090.8	0.0	1,090.8	0.49975	1.00
10	1,168.3	0.0	1,168.3	0.49975	1.00
11	1,388.2	0.0	1,388.2	0.49975	1.00

**Table 17.3** Damped FEA modes ( $\alpha = 0$ ,  $\beta = 0.0000518$ )

Mode	Un-damped FEA freq. (Hz)	Un-damped FEA damp. (Hz)	Damped FEA freq. (Hz)	Damped FEA damp. (Hz)	Damped FEA damp. (%)
1	61.405	0.0	61.402	0.61361	0.99928
2	143.81	0.0	143.77	3.3657	2.3403
3	203.71	0.0	203.6	6.7533	3.3151
4	310.62	0.0	310.23	15.702	5.0549
5	414.4	0.0	413.46	27.946	6.7437
6	442.6	0.0	441.45	31.879	7.2026
7	583.44	0.0	580.81	55.396	9.4947
8	1,002.2	0.0	988.81	163.46	16.31
9	1,090.8	0.0	1,073.5	193.63	17.751
10	1,168.3	0.0	1,147	222.11	19.012
11	1,388.2	0.0	1,352.3	313.61	22.591

Assume that the FEA model of the Jim Beam is proportionally damped, and  $\alpha = 0$ . Equation (17.15) says that for a given value of  $\beta$ , the *percent of critical damping* of each mode is proportional to its *un-damped* frequency. For  $\zeta = 1\%$  for the first mode (with frequency 61.4 Hz), Eq. (17.15) gives  $\beta = 0.0000518$ .

The coefficients  $\alpha = 0$ ,  $\beta = 0.0000518$  were used to create a proportional damping matrix from the mass & stiffness matrices of the *un-damped* FEA model, and the *damped* FEA model was solved for its modes. The results are shown in Table 17.3. Notice that the 61.4 Hz mode has the expected 1% damping, and also that the *percent of critical damping increases* as the modal frequency of the other modes increases.

The list of EMA damping values in Table 17.1 shows a wide range of values, from 3.11 to 17.11 Hz. Clearly, neither of the two extreme proportional damping cases exists in the Jim Beam;  $\beta = 0$  which gives modes with the *same* damping, or  $\alpha = 0$  which give modes with *percent of critical damping* that *increases* with increasing frequency.

Nevertheless, all of the EMA frequency & damping estimates in Table 17.1 can be used in Eq. (17.13) to calculate least-squared-error estimates of  $\alpha$  &  $\beta$ . These estimates can in turn be used to create a proportionally *damped* FEA model for the Jim Beam.

## 17.8 Using EMA Frequency and Damping

The EMA frequency & damping for the 11 modes in Table 17.1 were used to calculate  $\alpha$  &  $\beta$  for the Jim Beam using Eq. (17.13). The least-squared-error estimates of  $\alpha$  &  $\beta$  were;

$$\alpha = 76.6972, \beta = 8.0835 e - 7$$

**Table 17.4** Damped FEA modes  
( $\alpha = 76.6972, \beta = 8.0835 \text{ e-}7$ )

Mode	Damped FEA freq. (Hz)	Damped FEA damp. (Hz)	EMA freq. (Hz)	EMA damp. (Hz)	Mode shape MAC
1	61.1	6.1129	96.944	5.6347	0.73
2	143.68	6.1559	164.95	3.1125	0.97
3	203.62	6.2088	224.57	6.5223	0.96
4	310.56	6.3484	347.56	5.1552	0.96
5	414.35	6.5395	460.59	11.502	0.93
6	442.55	6.6008	492.82	4.6424	0.96
7	583.4	6.9678	635.18	14.247	0.94
8	1,002.2	8.6542	1,108.2	4.964	0.92
9	1,090.8	9.125	1,210.5	7.1292	0.90
10	1,168.2	9.5695	1,322.6	7.2498	0.86
11	1,388.2	10.997	1,555.1	17.112	0.84

**Table 17.5** Damped FEA modes  
( $\alpha = 76.4183, \beta = 1.0202 \text{ e-}6$ )

Mode	Damped FEA freq. (Hz)	Damped FEA damp. (Hz)	EMA freq. (Hz)	EMA damp. (Hz)	Mode shape MAC
1	61.102	6.0933	96.944	5.6347	0.73
2	143.68	6.1475	164.95	3.1125	0.97
3	203.62	6.2142	224.57	6.5223	0.96
4	310.56	6.3904	347.56	5.1552	0.96
5	414.35	6.6316	460.59	11.502	0.93
6	442.55	6.7091	492.82	4.6424	0.96
7	583.4	7.1723	635.18	14.247	0.94
8	1,002.2	9.3007	1,108.2	4.964	0.92
9	1,090.8	9.8949	1,210.5	7.1292	0.90
10	1,168.2	10.456	1,322.6	7.2498	0.86
11	1,388.2	12.258	1,555.1	17.112	0.84

These coefficients were used to create a proportional damping matrix from the mass & stiffness matrices of the *un-damped* FEA model. This model was solved for its modes, and the modal frequency & damping of the *damped* FEA model of the Jim Beam are shown in Table 17.4.

The modal damping values of the *damped* FEA model do exhibit monotonically increasing values with frequency, indicating their stronger proportionality to the stiffness matrix than to the mass matrix. This is similar to extreme Case #2. Even though the FEA damping values don't *closely match* the EMA damping values, they are *in the range* of the EMA values. This is a desirable property for making the FEA model useful for modeling the dynamics of the real structure.

## 17.9 Using FEA Frequency and EMA Damping

Each FEA frequency in Table 17.1 is *less than* the frequency of its corresponding EMA frequency, indicating that the FEA model is *less stiff* than the real Jim Beam, as tested. To determine the influence of modal frequency on the calculation of  $\alpha$  &  $\beta$  values, the FEA frequencies were used instead of the EMA frequencies in Eq. (17.13). For this case, the least-squared-error estimates of  $\alpha$  &  $\beta$  were:

$$\alpha = 76.4183, \beta = 1.0202 \text{ e} - 6$$

These estimates were then used to create a proportional damping matrix from the mass & stiffness matrices of the *un-damped* FEA model. The modal parameters of the *damped* FEA model are again compared with the EMA parameters of the Jim Beam in Table 17.5.

The modal damping values of the *damped* FEA model are monotonically increasing with frequency, again indicating proportionality more like extreme Case #2. These FEA damping values are *closer* to the EMA values than when the EMA frequencies are used, but the differences between the two solutions are *not significant*. The mode shape MAC values for this case are identical to the case where the EMA frequencies were used to estimate  $\alpha$  &  $\beta$ .

## 17.10 Conclusions

An equation was derived for calculating estimates of the proportional damping matrix coefficients  $\alpha$  &  $\beta$  from experimental modal frequency & damping. The equation for obtaining the  $\alpha$  &  $\beta$  estimates was derived as a least-squared-error solution to an over-specified set of linear equations, where  $\alpha$  &  $\beta$  are functions of modal frequency & damping alone.

These coefficients can be used to create a *damped* FEA model for a structure, which is more clearly useful for simulation studies than an *un-damped* model. This approach provides a straightforward way to add a viscous damping matrix to any FEA model, and solve for its FEA modes which include realistic values of modal damping.

The damping values of a two differently *damped* FEA models were compared with the EMA damping estimates for the same structure. Although the FEA modal damping didn't match well on a mode-by-mode basis with all of the EMA estimates, the damping values of matching mode pairs were *similar in value*.

The strongest reason for this disparity in FEA versus EMA values is that the proportional damping matrix is *restricted* by the distribution of mass & stiffness in the FEA model. On the other hand, the damping *mechanisms* that influenced the experimental damping values were most likely *distributed differently* than the mass & stiffness.

In fact, the Jim Beam structure was tested while resting on a foam rubber pad, which clearly would have greater damping influence on the lower plate than on the other two plates. Therefore, *depending on their mode shape deformations* on the lower plate, some modes would be more strongly influenced than others by the damping provided from the foam base. This alone could account for the wide range of modal damping values (3.11–17.11 Hz) among the EMA modes. Because it was modeled using the mass & stiffness of the FEA model, the modal damping of the damped FEA model not only increased monotonically with frequency, but also had less range of values (6.09–12.2 Hz).

From our example, it can be concluded that a proportionally damped FEA model doesn't necessarily yield modes with damping that perfectly match experimental damping values. Nevertheless, this approach is a useful and straightforward way to add *realistic viscous damping* to a *un-damped* FEA model. A *damped* FEA model, using proportional viscous damping derived from experimental data, is a lot closer to modeling the dynamics of a real structure than an *un-damped* FEA model.

## References

1. Richardson SC, Richardson MH (2008) Using photo modeling to obtain the modes of a structure. In: Proceedings of the international modal analysis conference, Orlando, FL
2. Craig RR Jr, Kurdila AJ (2006) Fundamentals of structural dynamics. Wiley, Hoboken
3. McConnell KG (1995) Vibration testing theory and practice. Wiley, New York
4. Ewins DJ, Inman DJ (eds) (2001) Structural dynamics @ 2000: current status and future directions. Research Studies Press, Taunton

# Chapter 18

## Superior Damping of Hybrid Carbon Fiber Composites Grafted by ZnO Nanorods

A. Alipour Skandani, N. Masghouni, and M. Al-Haik

**Abstract** The elevated specific strength of fiber reinforced plastics (FRP) is the prominent drive for their ever-growing applications. Their inadequate vibrational damping properties prevent them from replacing conventional metal alloys for certain structural applications. In this study we attempt to utilize a low temperature hydrothermal synthesis to grow ZnO nanorods on the surface of woven carbon fibers and implement the resulting hybridized fibers in an epoxy matrix composite. X-ray diffraction and scanning electron microscopy are carried out to study the morphology of the surface-grown nanorods and their adhesion to the substrate carbon fibers. Two-layered hybrid composite laminas are tested for their structural damping properties using dynamic mechanical analysis (DMA). It is observed that the ZnO nanorods can enhance the damping figure of merit of the composites by 40 % without a major delineation in the storage modulus. The enhanced damping performance can be attributed to the additional surfaces manifested by the presence of the ZnO nanorods and, consequently, augmenting the sliding and frictional mechanisms. Furthermore, ZnO as piezoelectric material has the energy scavenging advantages over other 1D nanostructures which ultimately constitutes the fabricated hybrid composites as a multifunctional structural material for energy harvesting applications.

**Keywords** Hybrid composite • ZnO • Damping • Hydrothermal growth

### 18.1 Introduction

The rationale of implementing 1D nano-structures such as ZnO nanorods over microfibers can be well understood considering their contribution to a wide range of applications such as smart materials for energy scavenging [1, 2], improved mechanical behavior by better matrix to fiber adhesion [3–5], gas sensors [6], field emission [7], photo-electrochemical cells [8], surface polarity shielding [9] and improved damage growth resistance [10]. ZnO nanorods – when incorporated with fiber reinforced polymer composites (FRPs) – can be utilized for improving the structural properties as well as adding piezoelectric capabilities for these composites. The typical energy dissipation mechanism of FRPs is due to fiber and matrix elastic/viscoelastic behaviors, respectively, which allow traditional FRPs to possess relatively low vibration attenuation capabilities [11–13]. To reconcile this shortcoming and still be able to benefit from their superior static mechanical properties, a multitude of research is directed towards improving the vibration damping properties of FRPs while retaining their light weight, in plane properties and other advantageous properties unchanged or even improved. So far the most common methods developed for this purpose comprise embedding a viscoelastic layer between the laminates with the outlay of lowering the strength and stiffness [14], fiber/surface treatment [15], addition of nano-fillers [14, 16] and matrix modification via incorporating viscoelastic particles [17].

The prime factors of increasing the energy loss in the filler modified composites are slippage and frictional mechanisms in the filler/matrix interfaces. Consequently, increasing the interfacial area by implementing nano-scaled high aspect ratio fillers (e.g. carbon nanotubes, CNTs) are reported to produce pronounced energy dissipations [18, 19, Based on the results obtained by the authors of this article]. How efficient these nano-fillers act toward increasing the damping is a function of their fraction, morphology and distribution in the matrix. Carbon nanotubes are some of the most difficult fillers to disperse in the matrix

---

A.A. Skandani (✉) • N. Masghouni • M. Al-Haik  
Department of Engineering Science and Mechanics, Virginia Tech, Blacksburg, VA 24061, USA  
e-mail: aalipour@vt.edu; mnejib@vt.edu; alhaik@vt.edu

due to the secondary Van der Waals forces existing amongst the tubes. However, they exhibited the maximum damping improvement when they were well dispersed and their volume fraction exceeded the mechanical percolation threshold of the composite [Based on the results obtained by the authors of this article]. The quality of the CNTs dispersion dictated the improvement of damping where published literatures reported considerable discrepancies from 0 to 700 % [20, 21]. Various mechanical routes such as sonication [22], calendaring [23] and prolonged shear mixings [Based on the results obtained by the authors of this article] were utilized to obtain reasonable dispersion of CNTs within polymer matrices.

Whiskerization is a grafting technique in which secondary reinforcing material can be grown on the surface of the primary reinforcement fibers utilizing different chemical or physical routes. Interfacial reinforcement through whiskerization by growing a secondary reinforcing material directly on the fiber surface is proven to have several advantages over other surface modification methods [5]. Composites made by whiskerization of CNTs on the designated surfaces yields the best result where up to 1,400 % improvement in damping is reported in some cases [Based on the results obtained by the authors of this article, 24].

Zinc Oxide, due to its wide band-gap (3.37 eV) and the absence of inversion symmetry in its wurtzite structure represents a large electromechanical coupling [25]. The tendency of directional growth stems from the better stability of the  $\pm(0001)$  polar surfaces which facilitates the zinc oxide embryos growth in a direction perpendicular to these planes. The outcome of such directional growth leads to different 1D and 2D nano-structures of ZnO such as nanowires, nanorods, flower-like and cabbage-like structures, tubes and rings [25, 26]. Some of the common methods of synthesizing nanorods and nanowires of ZnO are chemical vapor deposition (CVD) [27], electrodeposition [26], hydrothermal and templated growth [28]. Most of these deposition techniques can be performed on a ZnO, or equivalent material in terms of the lattice parameters, pre-existing layer. Hence, ZnO nanorods can grow on top of any surface simply by pre-coating that surface by a thin layer of ZnO.

The degradation of carbon fibers when exposed to high temperatures was reported [20, 29] which makes it essential to utilize synthesis methods with lower temperatures requirement. Among the common methods for synthesizing ZnO nanorods, hydrothermal synthesis is a solution-based growth method which can be conducted at temperatures as low as 60–90 °C. The growth takes place in aqueous solution of zinc acetate  $\text{Zn}(\text{O}_2\text{CCH}_3)_2$  or zinc nitrate  $\text{Zn}(\text{NO}_3)_2$  as the source for  $\text{Zn}^{2+}$  ions in water and nonionic cyclic tertiary amine (HMTA) where  $\text{H}_2\text{O}$  molecules provides  $\text{O}^{2-}$  ions [26].

Different mechanical tests were performed on single fibers or nonwoven fibers coated individually with ZnO nanorods [3–5, 30, 31]. The conducted tests on single coated fibers are not feasible to characterize the real structural composites as FRPs utilize bundles of woven fibers rather than single fibers and the bundles are usually coated with a polymer sizing for the sake of handling and health issues. In this study we attempt to apply ZnO nanorods into FRPs with woven architecture and regular grades of sizing utilizing a hydrothermal growth technique. The corresponding hybrid composites were investigated for vibration damping within a frequency range close to that encountered in real structural applications. Also, the effects of the moisture in general and hydrothermal growth solution in particular were probed.

## 18.2 Experiment

### 18.2.1 Sample Preparation

ZnO nanorods growth was conducted on commercial high strength PAN-based plain-woven carbon fabric (AS2C supplied by HEXCEL Inc.) with 3k bundles as the substrate. An 80 nm ZnO thin film was coated on the carbon fabrics using a magnetron sputtering system (ATC Orion high vacuum sputtering system, AJA International Inc.) to serve as initiator of the crystallization and growth of ZnO nanorods. Growth solution comprised 20 mM zinc acetate hexahydrate ( $\text{Zn}(\text{O}_2\text{CCH}_3)_2 \cdot 6\text{H}_2\text{O}$ ) and hexamethylenetetramine (HMTA) dissolved in deionized (DI) water. A  $13 \times 13 \text{ cm}^2$  carbon fiber coupons were cut and sputtered with 80 nm films of ZnO on both sides and then suspended in a sealed container filled with the growth solution and kept at 80 °C for 12 h. To investigate the effect of the solution on the final properties of the samples, a separate set of samples with 80 nm ZnO film was prepared and exposed to a solution that does not contain zinc acetate employed; 20 mM HMTA/DI water solution for 12 h at 80 °C. Also a reference set of samples (based on raw carbon fibers) were prepared using intact carbon fabrics.

Vacuum-assisted compression mold was utilized to fabricate the composite based on the three different fibers configuration, separately. The mold used for the fabrication consisted of two aluminum parts with a flexible rubber sheet separating them. The setup comprised a vacuum bag, peel ply, release fabric, stacked carbon fabrics which were impregnated with the epoxy resin (using a roller), another peel ply film, perforated release film, and breather cloth, consecutively. The epoxy resin was Aeropoxy™ manufactured by PTM&W Industries, Inc. The two layers layup was placed inside the bottom half of the mold which is connected to the vacuum line and the top part that has an airway (which is lastly connected to compressed



air line) remained empty. While the layup was being vacuumed, compressed air (70 psi) was applied to it by the means of flexible separator. To seal the mold from the ambient, it was placed in a hydraulic press (operated at 30 tons). Simultaneous use of the vacuum, compressed air, and press assures degassing of the resin while the carbon fabrics were kept intact under high pressure. The composites were left for 24 h to ensure full curing of the epoxy.

### 18.2.2 Sample Characterization

To study the size and morphology of the grown nanorods and how the coated fibers were affected by the solution environment, Scanning Electron Microscopy (LEO (Zeiss) 1550 field-emission SEM) was employed. Also SEM was used to study delamination and possible nanorods detachment after the composite fabrication process. To make sure the obtained rods are fully crystalline and have acceptable purity, X-ray diffraction (Philips Xpert Pro with Cu-K $\alpha$  lamp and Ni filter) was employed on all three configurations of samples.

### 18.2.3 Dynamic Mechanical Analysis (DMA)

The specimens were removed from the mold after 24h curing at room temperature and prepared for DMA testing following the ASTM D4056-06 standard. Rectangular samples of 12  $\times$  60  $\times$  0.4 mm were cut and tested using DMA Q800 (TA Instruments, Inc). A dual cantilever loading condition is applied following ASTM D5418-07 in constant frequency of 1 Hz, elastic strain range of 0.0025–0.0125% and room temperature.

## 18.3 Results and Discussion

### 18.3.1 SEM and XRD

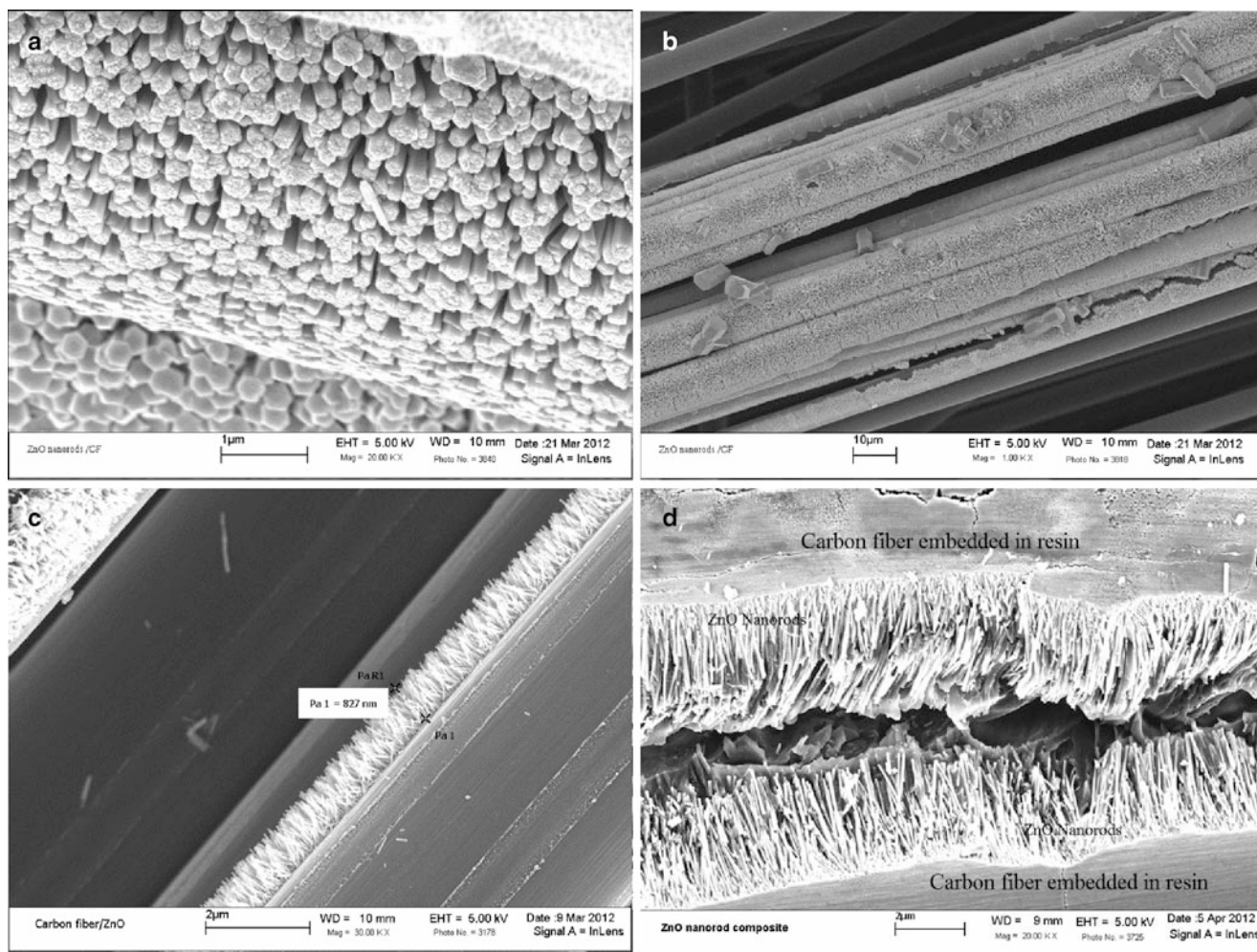
Figure 18.1a provides an SEM micrograph of hydrothermally grown ZnO nanorods on top of AS2C carbon fibers. It can be seen that they are aligned perpendicular to the fibers and covered over the entire fiber surface while maintaining a uniform length and distribution. Figure 18.1b, c illustrate the growth over a bundle of fibers and the typical length of rods. Figure 18.1d illustrates the inter-laminar space of bilayer composite where it can be seen that nanorods are well aligned and still attached to the upper and lower fibers despite the vacuum and pressure applied during the composite molding process. The average length of these nanorods lies within 1  $\mu$ m (as shown in Fig. 18.1c).

As mentioned earlier, to investigate the effect of growth media, ZnO coated carbon fabrics were exposed to similar concentration solution (without zinc acetate) and kept at the same temperature and time interval. Figure 18.2 shows the SEM micrographs of the growth solution exposed samples, it can be seen that coatings and underlying sizing are peeled off and removed in parts.

It can be interpreted from the XRD patterns plotted in Fig. 18.3 that only the sample with complete exposure to the growth solution containing 20 mM of zinc acetate depicts presence of crystalline ZnO. Sharp characteristic peaks of ZnO in sample with surface-grown nanorods reveal the high purity and crystallinity of the hydrothermally grown ZnO nanorods. Meanwhile, the samples coated with the ZnO thin film (with no exposure to zinc acetate hexahydrate hexahydrate) do not show any evidence of the zinc oxide due to amorphous nature of the sputtered layer.

### 18.3.2 DMA

Dynamic mechanical analysis tests is one of the most convenient methods to annex the viscoelastic properties of materials including storage modulus ( $E'$ ) as measure of dynamic stiffness, loss modulus ( $E''$ ) as a measure for energy dissipation and the tangent of phase angle between stress and strain vectors  $E'/E''$  ( $\tan(\delta) = \frac{E''}{E'}$ ) representing the damping coefficient.



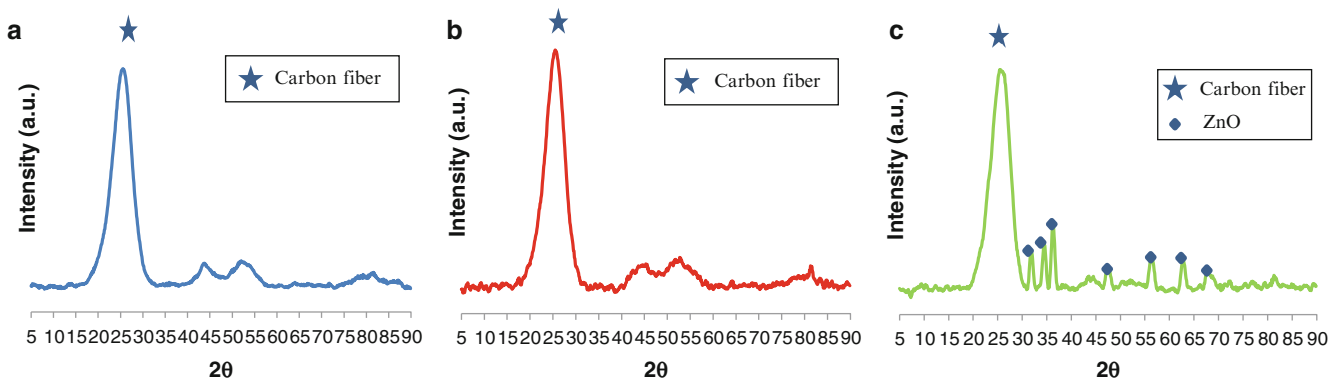
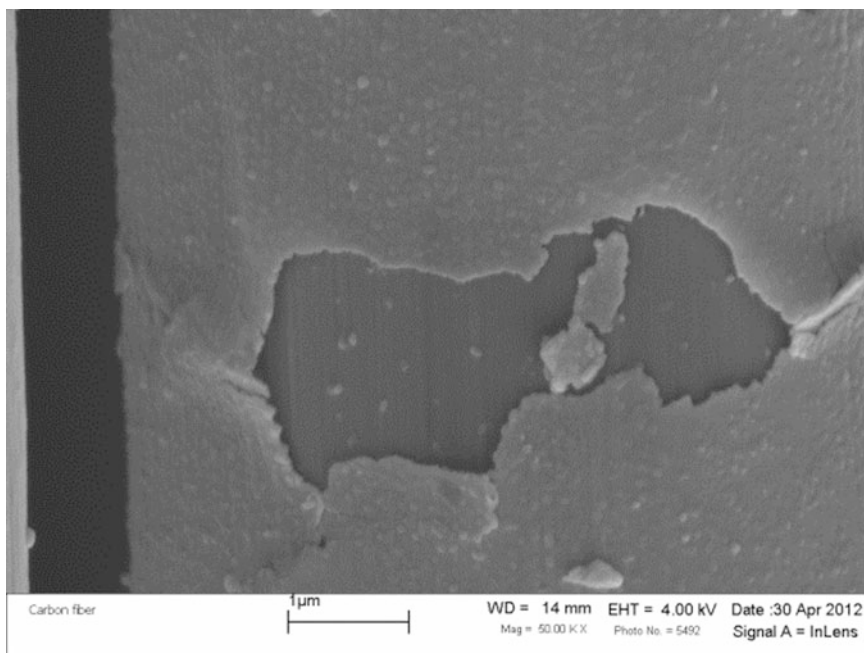
**Fig. 18.1** SEM micrograph of hydrothermally grown ZnO nanorods (a) over a single fiber and (b) over bundle of fibers (c) typical length of grown fibers (d) fibers attachments after hand layup process

Figure 18.4 presents the results of the storage moduli and damping coefficients ( $\tan(\delta)$ ) for all samples at 1 Hz frequency and strain range of 0.0025–0.0125% at ambient temperature.

Also, the applied stress is plotted versus strain in Fig. 18.4a to ensure that the DMA tests were carried out within the elastic range as dissipation mechanisms due to plastic deformation vary significantly from its elastic counterparts. The storage modulus is shown to be independent of the strain at which the DMA test was conducted whereas the damping coefficient varies significantly with strain. Considering storage modulus to be a representative of material's stiffness one can conclude that the presence of ZnO nanorods roughly retains the composite's stiffness (5% decrease at most) while it improves the damping coefficient by almost 40% over the composites based on the raw carbon fibers.

The slight reduction in stiffness can be further discussed in terms of the peeled off sizing of the carbon fibers under the growth solution condition (Fig. 18.2). Despite the drop in the stiffness, the hydrothermal synthesis route is far less damaging to the fiber in comparison with high temperature synthesis methods [Based on the results obtained by the authors of this article]. On the other hand, the enhanced damping achieved by ZnO nanorod whiskerization is mainly caused by frictional and slippage mechanisms in the presence of high surface area/high aspect ratio nanorods. Furthermore, based on several other reports on the damping properties of ZnO particulates embedded in polymer matrices, piezoelectric effect of ZnO converts a considerable portion of mechanical energy into electricity [32–34]. This electro-mechanical conversion of energy is a secondary contributor to the vibrational damping of fabricated hybrid nano composites.

**Fig. 18.2** The SEM micrographs of sample exposed to growth solution without zinc acetate



**Fig. 18.3** XRD patterns for (a) raw carbon fiber, (b) sputtered carbon fiber and (c) carbon fiber with surface-grown ZnO

### 18.4 Conclusion

In this study it was shown that conventional carbon fiber composites can be modified via hydrothermally growing ZnO nanorods at low temperatures on the inter laminar spaces. X-ray diffraction and scanning electron microscopy showed that the grown ZnO nanorods are uniformly distributed, fully crystalline and retain good attachment to the fiber substrate even after the composite processing. Furthermore, the DMA testing affirmed that the surface grown ZnO substantially improve the dynamic properties of the hybrid composite with caveat of lowering the in-plane elastic properties slightly. Frictional sliding mechanisms of high surface area/high aspect ratio ZnO distributed uniformly over the carbon fibers together with electromechanical coupling of ZnO nanorods are the primary mechanisms for their enhanced vibration attenuation.

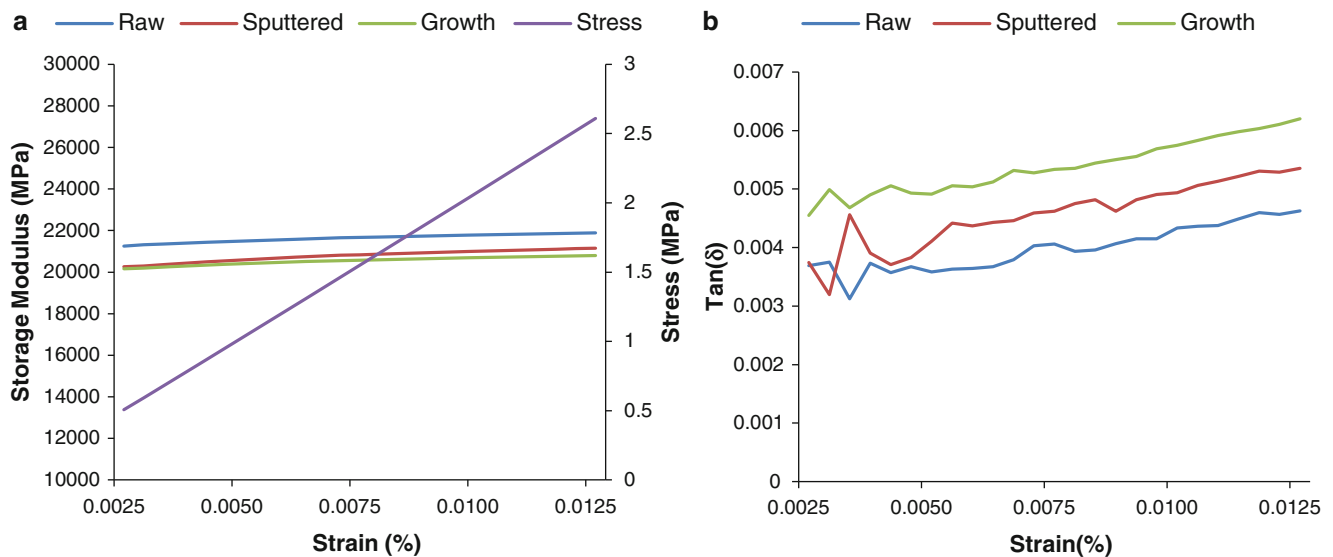


**Fig. 18.4** (a) Storage modulus and stress (b)  $\tan(\delta)$  for composites made out of raw (non-processed), sputtered (ZnO coated and soaked in solution) and growth (with surface grown ZnO nanorods) woven carbon fibers

## References

- Qin Y, Wang X, Wang ZL (2008) Microfibre-nanowire hybrid structure for energy scavenging. *Nature* 451(7180):809–813
- Wang ZL, Song J (2006) Piezoelectric nanogenerators based on zinc oxide nanowire arrays. *Science* 312(5771):242–246
- Galan U, Lin Y, Ehlert GJ, Sodano HA (2011) Effect of ZnO nanowire morphology on the interfacial strength of nanowire coated carbon fibers. *Compos Sci Technol* 71(7):946–954
- Galan U, Ehlert GJ, Lin Y, Sodano HA (2009) Effect of morphology of ZnO nanowire arrays on interfacial shear strength in carbon fiber composites. *Mater Res Soc Symp Proc* 1174:1105–1101
- Ehlert GJ, Lin Y, Galan U, Sodano HA (2011) Interaction of ZnO nanowires with carbon fibers for hierarchical composites with high interfacial strength. *J Solid Mech Mater Eng* 4(11):1687–1698
- Tonezzer M, Lacerda RG (2010) Integrated zinc oxide nanowires/carbon microfiber gas sensors. *Sens Actuat B-Chem* 150(2):517–522
- Jo SH, Banerjee D, Ren ZF (2004) Field emission of zinc oxide nanowires grown on carbon cloth. *Appl Phys Lett* 85(8):1407
- Unalan HE, Wei D, Suzuki K, Dalal S, Hiralal P, Matsumoto H et al (2008) Photoelectrochemical cell using dye sensitized zinc oxide nanowires grown on carbon fibers. *Appl Phys Lett* 93(13):133116
- Na J-S, Gong B, Scarel G, Parsons GN (2009) Surface polarity shielding and hierarchical ZnO nano-architectures produced using sequential hydrothermal crystal synthesis and thin film atomic layer deposition. *ACS Nano* 3(10):3191–3199
- Zhou W, Jin HB (2011) Acoustic emission based flexural characteristics of glass fiber reinforced composites embedded with ZnO nanowhiskers. *J Compos Mater* 46(3):291–299
- Shankar K, Lakkad SC (1982) Damping in fibre reinforced plastics. *J Mater Sci Lett* 1:53–57
- Adams RD, Maheri MR (2003) Damping in advanced polymer–matrix composites. *J Alloy Compd* 355(1–2):126–130
- Chandra R, Singh SP, Gupta K (2002) Micromechanical damping models for fiber-reinforced composites: a comparative study. *Compos Part A-Appl Sci Manuf* 33(6):787–796
- Hudnut SW, Chung DDL (1995) Use of submicron diameter carbon filaments for reinforcement between continuous carbon-fiber layers in a polymer-matrix composite. *Carbon* 33(11):1627–1631
- Chung DDL (2003) Structural composite materials tailored for damping. *J Alloy Compd* 355(1–2):216–223
- Vlasveld DPN, Bersee HEN, Picken SJ (2005) Nanocomposite matrix for increased fibre composite strength. *Polymer* 46(23):10269–10278
- Dutra RCL, Soares BG, Campos EA, Silva JLG (2000) Hybrid composites based on polypropylene and carbon fiber and epoxy matrix. *Polymer* 41(10):3841–3849
- Sun L, Gibson RF, Gordaninejad F, Suhr J (2009) Energy absorption capability of nanocomposites: a review. *Compos Sci Technol* 69(14):2392–2409
- Zhou X, Shin E, Wang KW, Bakis CE (2004) Interfacial damping characteristics of carbon nanotube-based composites. *Compos Sci Technol* 64(15):2425–2437
- Thostenson ET, Chou TW (2004) Aligned multi-walled carbon nanotube-reinforced composites: processing and mechanical characterization. *J Phys D Appl Phys* 35(16):L77–L80
- Rajoria H, Jalili N (2005) Passive vibration damping enhancement using carbon nanotube-epoxy reinforced composites. *Compos Sci Technol* 65(14):2079–2093
- Jin L, Bower C, Zhou O (1998) Alignment of carbon nanotubes in a polymer matrix by mechanical stretching. *Appl Phys Lett* 73(9):1197–1199
- Gojny FH, Wichmann MHG, Kopke U, Fiedler B, Schulte K (2004) Carbon nanotube-reinforced epoxy-compo sites: enhanced stiffness and fracture toughness at low nanotube content. *Compos Sci Technol* 64(15):2363–2371

24. Suhr J, Koratkar N, Koblinski P, Ajayan P (2005) Viscoelasticity in carbon nanotube composites. *Nat Mater* 4(2):134–137
25. Baruah S, Dutta J (2009) Hydrothermal growth of ZnO nanostructures. *Sci Technol Adv Mater* 10(1):013001
26. Xu S, Wang ZL (2011) One-dimensional ZnO nanostructures: solution growth and functional properties. *Nano Res* 4(11):1013–1098
27. Xiang B, Wang P, Zhang X, Dayeh SA, Aplin DPR, Soci C et al (2007) Rational synthesis of p-Type zinc oxide nanowire arrays using simple chemical vapor deposition. *Nano Lett* 7(2):323–328
28. Vayssieres L (2003) Growth of arrayed nanorods and nanowires of ZnO from aqueous solutions. *Adv Mat* 15(5):464–466
29. Zhang Q, Liu J, Sager R, Dai L, Baur J (2009) Hierarchical composites of carbon nanotubes on carbon fiber: influence of growth condition on fiber tensile properties. *Compos Sci Technol* 69(5):594–601
30. Lin Y, Shaffer JW, Sodano HA (2010) Electrolytic deposition of PZT on carbon fibers for fabricating multifunctional composites. *Smart Mater Struct* 19(12):124004
31. Lin Y, Ehlert G, Sodano HA (2009) Increased interface strength in carbon fiber composites through a ZnO nanowire interphase. *Adv Funct Mater* 19(16):2654–2660
32. Sumita M, Gohda H, Asai S, Miyasaka K (1991) New damping materials composed of piezoelectric and electro-conductive, particle-filled polymer composites: effect of the electro mechanical coupling factor. *Makromol Chem Rapid Commun* 12:657–661
33. Liu Z, Wang Y, Huang G, Wu J (2008) Damping characteristics of chlorobutyl rubber/poly(ethyl acrylate)/piezoelectric ceramic/carbon black composites. *J Appl Polym Sci* 108(6):3670–3676
34. Alipour Skandani A, Masghouni N, Case SW, Leo DJ, Al-Haik M (2012) Enhanced vibration damping of carbon fibers-ZnO nanorods hybrid composites. *Appl Phys Lett* 101(7):073111

# Chapter 19

## Advanced Identification Techniques for Operational Wind Turbine Data

Simone Manzato, Jonathan R. White, Bruce LeBlanc, Bart Peeters, and Karl Janssens

**Abstract** During a field test campaign, Sandia National Laboratories acquired operational data both in parked and rotating conditions on a modified MICON wind turbine with the Sensored Rotor 2 experiment. The objective of the test campaign was to acquire data to develop advanced system identification and structural health monitoring techniques. The data includes wind speed, tower deformations, low and high speed shaft rotational speed measurements as well as accelerations and strains on different locations of the blades. Applying Operational Modal Analysis on such data represents a difficult task due to the strong influence of rotor harmonics on the measured data. Accurately identifying and removing the harmonics is required to perform modal parameter identification. In this paper, data acquired with the turbine in both parked and operating conditions will be analyzed and the modal results compared. Several harmonic removal techniques will be applied on the operational data and their efficiency to solve this specific problem analyzed. In addition, a new enhanced identification technique will be applied, that improves the parameter estimation accuracy in the case of very noisy data and also provides uncertainty bounds of the parameters.

**Keywords** Wind turbine • Operational • Parked • Modal analysis • Harmonic removal

### 19.1 Introduction

In this paper, Operational Modal Analysis in combination with harmonic removal techniques will be applied to wind turbine field data, with the structure both in parked and operating conditions. The main objective of the paper is to evaluate how these techniques perform in solving this specific problem, which poses significant issues to the industrial and research communities. This work provides a baseline to understand how currently used signal processing and identification techniques can be improved to provide more reliable modal parameter estimates. The dynamic behavior of structures is a prime factor to determine their structural stability, reliability and lifespan. Operational Modal Analysis (OMA) is a powerful tool to identify eigenparameters of structures randomly excited by force inputs that cannot be measured. This information can then be used to improve numerical models to predict the dynamics of new designs, to identify the dynamic characteristics of prototypes, and to monitor the system while in operation.

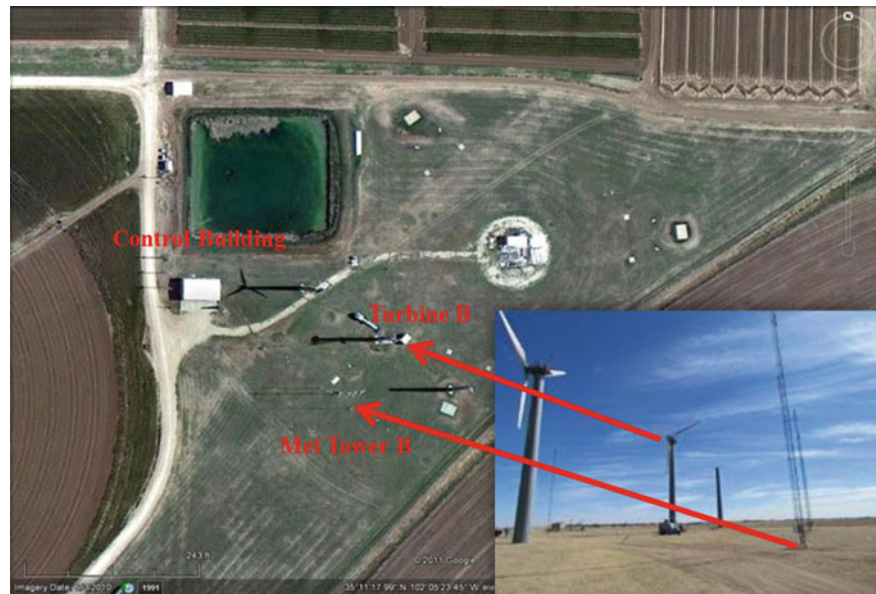
OMA provides an interesting procedure to investigate the dynamic properties of structures while in operation. First proposed in the 1980s with the Natural Excitation Technique (NExT), it was specifically developed to tackle the problem of dynamic analysis of wind turbines [1]. Following this first application, the potential of output-only system identification for structures in operating conditions was fully realized and applied to a variety of civil structures as well as aerospace and automotive applications [2–4]. However, OMA methods are based on a set of assumptions that need to be considered when applying them to practical cases. One of the problems of wind turbine analysis is that most of these assumptions are violated due to the inherent structural response and conditions [1, 5].

---

S. Manzato (✉) • B. Peeters • K. Janssens  
LMS International, Interleuvenlaan 68, B-3001 Leuven, Belgium  
e-mail: [simone.manzato@lmsintl.com](mailto:simone.manzato@lmsintl.com); [bart.peeters@lmsintl.com](mailto:bart.peeters@lmsintl.com); [karl.janssens@lmsintl.com](mailto:karl.janssens@lmsintl.com)

J.R. White • B. LeBlanc  
Sandia National Laboratories, Wind Energy Technologies, Albuquerque, NM, USA  
e-mail: [jonwhit@sandia.gov](mailto:jonwhit@sandia.gov); [blebla@sandia.gov](mailto:blebla@sandia.gov)

**Fig. 19.1** Layout of Bushland test site with the tested turbine and meteorological tower highlighted



A first limiting constraint of OMA is that the structure must be excited by steady state random white noise in the frequency band where the modal parameters are sought. This implies that if harmonic excitations are present in addition to random forces, standard OMA procedure cannot be applied. This is the case for wind turbines where, together with the turbulent random wind, the rotation of the blades will introduce sharp peaks in the response signals due to the rotational sampling of the inflow. In some applications the harmonic response components can be considered as virtual modes in identification, but if the amplitude of these components is much higher than the underlying structural response or if the harmonic frequencies are close to the natural ones, standard OMA approaches may break down [6, 7]. In addition to this, as discussed in [5], periodic aerodynamic effects related to the blade rotation and significant correlation between input forces introduce additional issues that cannot be solved with standard tone removal techniques.

A second critical OMA assumption is that the system must be linear time invariant [8]. This imposes that the structure should not change, or change only slightly, during the entire test duration. Wind intensity, variation of rotor speed, blade pitch and yaw angle all cause the turbine to change significantly, modifying both stiffness and damping properties. A possible way of overcoming these problems is to limit the analysis to portions of time signals where the properties don't change significantly. However, the typical frequency range of interest for this application requires that the analyzed signals are long enough to allow a confident estimation of the modal parameters [9].

In this paper, the analysis will focus on the problems related to blade rotation, including harmonics and periodic aerodynamic effects. The Sensored Rotor 2 experiment will be presented in Sect. 19.2. Section 19.3 will describe the harmonic removal techniques applied on the operational data. Section 19.4 will then discuss the baseline modes identified for the turbine in parked conditions and that will be then used as reference for the operational analysis, which are presented and discussed in Sect. 19.5. The last section will then discuss the comments and conclusions of the analysis performed.

## 19.2 The Micon 65/13M Wind Turbine and Field Test Description

The United States Department of Agriculture (USDA), under contract with US Department of Energy/Sandia National Laboratories (SNL), operated a set of research Micon 65/13M Wind Turbines at the Conservation and Production Research Laboratory (CPRL) in Bushland, TX [10]. The three fixed-pitch fixed-speed wind turbines erected on the site (Fig. 19.1) were modified (Micon 65/13 "M") throughout their lifetimes with upgrades to the rotor, brake, yaw, instrumentation and generator systems.

Turbine B, which is the object of this investigation and is shown in Fig. 19.2, was equipped with three 9 m CX-100 Sensor Rotor 2 blades [11, 12]. SNL fabricated these sensed rotor blades to investigate load monitoring and damage detection capabilities of accelerometers, strain gauges and Fiber Bragg Grating sensors. A SNL team installed these sensors onto the rotor blades. To measure the signals coming from these sensors, a rugged and robust hub-mounted data acquisition system was developed. National Instrument Compact-RIO data acquisition systems in the rotor hub acquired the signals from the

**Fig. 19.2** Micon 65/13M  
Turbine B



machine and transmitted them wirelessly to the control building in Fig. 19.1. Information on wind direction and speed and ambient temperature were collected in the meteorological tower and transmitted as well to the control building, where an SNL Accurate Time-Linked Acquisition System (ATLAS) combined all of the data and precisely time-synchronize it based on GPS time stamps.

In this paper, two different datasets were considered. The first one includes data continuously collected at 50 Hz with the turbine in parked condition on July 8th 2011. In addition, 7 h of continuous measurement with the turbine in operating condition, collected on August 15th 2011, were also analyzed. From the whole dataset SNL provided, only a limited number of channels were included in the analysis. For each blade, two triaxial and two uniaxial accelerometers were considered, with the triaxials positioned on the pitch axis and uniaxial close to the trailing edge. In addition, the translational accelerations from an inertial measurement unit within the nacelle and the signal from two strain gauges on the tower bottom, measuring side-to-side and fore-aft motions, were included. To correlate the reading with the environmental conditions, the signals from the anemometer and the wind vane were included as well. Figure 19.3 shows the complete instrumentation of a Sensor Rotor 2 blade, while in Fig. 19.4 the locations and orientations of the accelerometers used in this analysis are graphically represented.

To validate the results obtained in this paper, the results of an experimental test campaign previously performed and presented in [13] are considered as a reference. A list of the results obtained with an impact test on the full structure is provided in Table 19.1.

### 19.3 Harmonic Component Removal Techniques

As already discussed in the Introduction, an inherent problem of application of OMA to operational wind turbines is the violation of the assumption concerning the operational excitation forces [5]. Although the excitation coming from the turbulent wind flow has a broadband uniform spectrum, in other words it is distributed over the entire structure and is uncorrelated, the effect of the blade rotation cannot be neglected. This was clearly observed in Fig. 19.5. The light spectrum was computed from one of the acceleration of the blade with the turbine in parked condition. The peaks were associated to the modal response of the structure to the turbulent wind excitation. Subsequently, the black spectrum was computed for the same channel but with the turbine in operation. The vertical cursor indicates the fundamental harmonic associated with the rotational speed (around  $0.93 \text{ Hz} = 55 \text{ rpm}$ ) and its multiples. While the structural response should remain almost the same, it was observed that, when in operating condition, the response was dominated by effects of the blade rotation. To overcome this problem, different techniques have been proposed in the past to separate periodic and random signals components, so that



**Fig. 19.3** Sensor Rotor 2 blade instrumentation

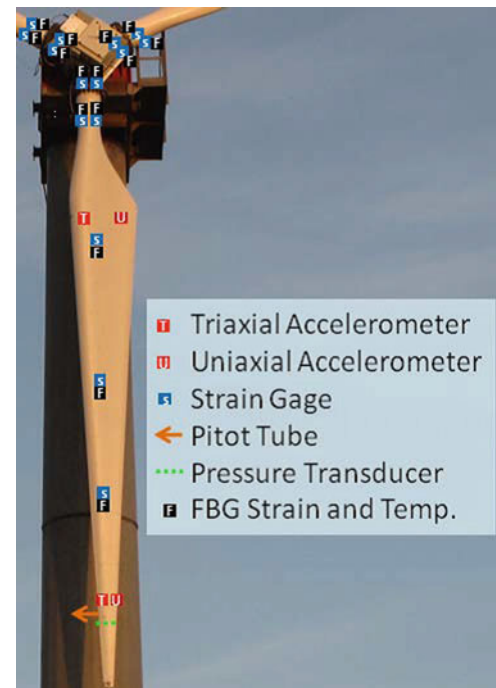
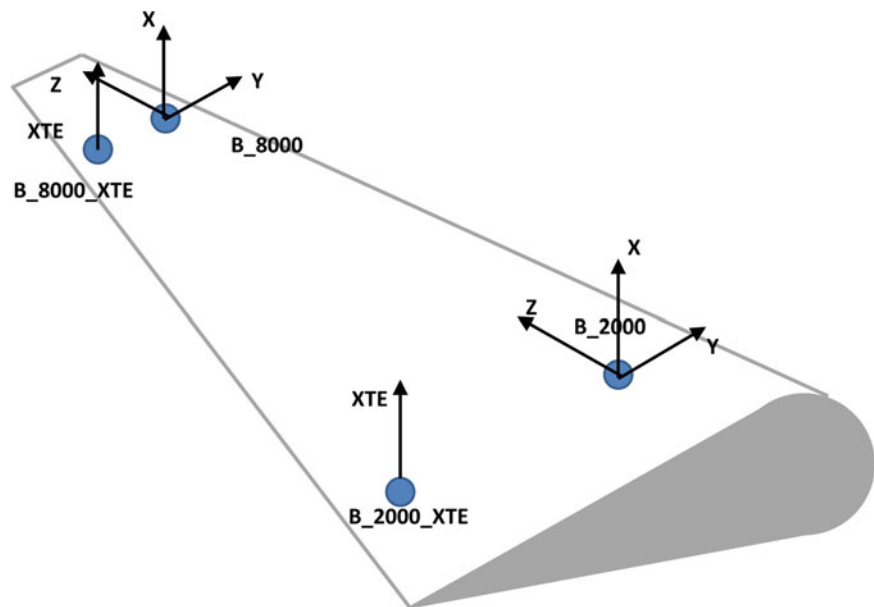


**Fig. 19.4** Blade accelerometer positions and orientation



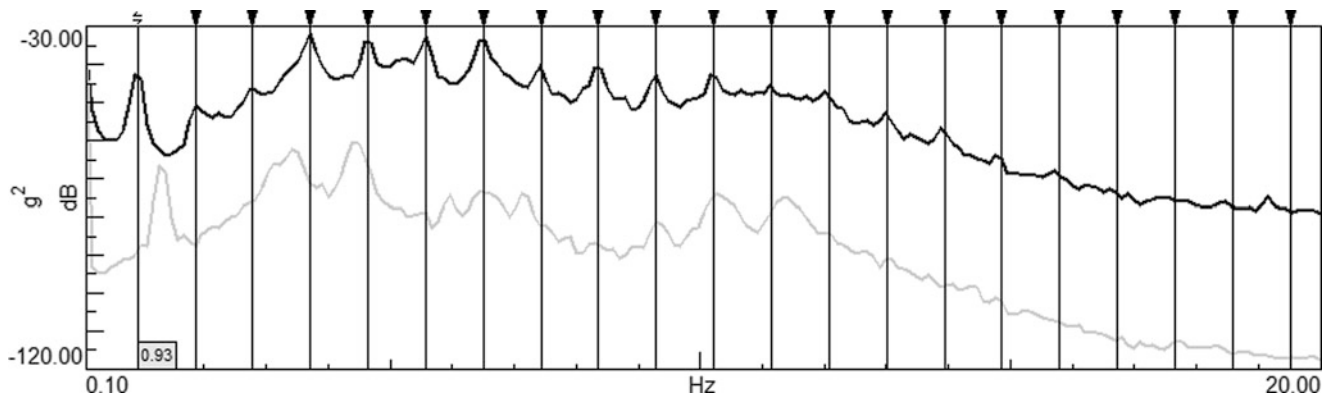
OMA can then be applied only on the latter [14]. In this section two methodologies were presented, while their performance in identifying and removing the harmonic components from operational wind turbine data will be discussed in a following section.

### 19.3.1 Time Synchronous Averaging

The first analyzed method was the Time Synchronous Averaging (TSA) technique, which was one of the most widely applied in the dynamic analysis of rotating machineries. Different implementations of this technique can be applied, depending on the particular case and information available, as described in [15]. In this paper, the one presented in [6] was used, which was based on double angular resampling as described in [16]. The applied procedure can be summarized in four steps:

**Table 19.1** Full-scale modal test results

Mode	Frequency (Hz)	Description
1	1.30	First side-side tower
2	1.34	First fore-aft tower
3	3.19	First rotor torsion
4	3.26	First flap antisymmetric (about vertical axis)
5	3.45	First flap antisymmetric (about horizontal axis)
6	4.51	First flap symmetric
7	5.35	First edge symmetric, in-phase
8	5.51	First edge symmetric, out-phase
9	6.57	Second flap antisymmetric (about vertical axis), tower in-phase
10	7.17	Second flap antisymmetric (about horizontal axis), tower in-phase
11	10.01	Second flap antisymmetric (about vertical axis), tower out-phase
12	10.34	Second flap antisymmetric (about horizontal axis), tower out-phase
13	11.49	Second flap symmetric
14	15.41	Second rotor torsion

**Fig. 19.5** Comparison of power spectra of a blade acceleration in parked (*light*) and operational (*dark*) conditions

1. Measure or estimate the fundamental harmonic of the rotational phenomenon;
2. Upsample the acceleration signals and resample them in the angle domain using a constant angular speed increment;
3. Apply sliding window (angle) synchronous averaging to separate discrete (harmonic) and random (broadband response) components;
4. Restore the signal in the time domain.

The filtered signal was then used with all existing OMA methods. The effect of TSA was equivalent to a comb filter, isolating the harmonics of the periodic frequency which could then be subtracted from the original signal. A fundamental requirement to properly applying this method and obtaining a good harmonic removal was the availability of an accurate rotational speed profile, either from a direct measurement or from estimation techniques. This method was demonstrated to efficiently work in cases where the peaks were very sharp, such as in the analysis of in-flight helicopter data or engine run-ups [6]. However, in a previous work from the authors [17], this methodology was applied to simulated wind turbine data. It was concluded that the method was not suitable to remove the harmonics in this specific case, due to the thick tails of the harmonic peaks which were also discussed in [5]. In this work, the method was applied to the experimental data to verify that the simulated and measured data behaved similarly, although similar results were expected.

### 19.3.2 Removing Harmonics by Cepstrum Editing

The second applied methodology consisted in editing the acquired signals in the cepstrum domain. The concept of cepstrum was first introduced in the 1960s and was applied to detect echoes in seismic signals [18]. The paper also explains the terminology used in the cepstrum domain and was basically coined by reversing the first syllable of the equivalent quantities in the frequency domain. We will then refer to “cepstrum” instead of “spectrum”, “quefrequency” instead of “frequency”, “lifter”

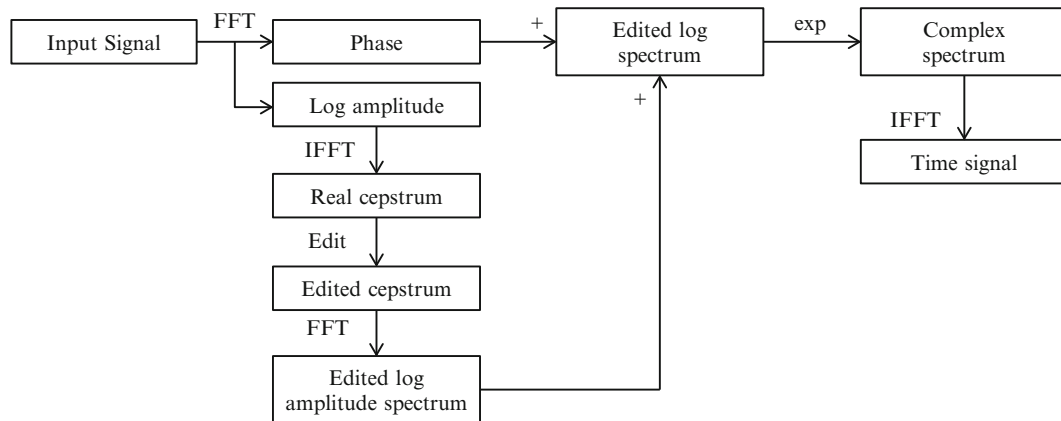


**Fig. 19.6** Methodology of cepstral method for removing selected families of harmonics and/or sidebands from time signals [20]

instead of “filter”, “rahmonic” instead of “harmonic” and so on. The cepstrum can be computed from the spectrum of a time signal as:

$$C(t) = FFT^{-1} [\log(X(f))] \quad (19.1)$$

Where, if the spectrum  $X(f)$  is complex, i.e.:

$$X(f) = FFT(x(t)) = A(f) \exp(j\phi(f)) \quad (19.2)$$

so that

$$\log(X(f)) = \ln(A(f)) + j\phi(f) \quad (19.3)$$

then the result is the complex cepstrum. If the phase in Eq. (19.3) is then set to zero, the so-called “real cepstrum” is obtained.

In recent studies, the possibility to use the cepstrum directly for Operational Modal Analysis [19] or as a preprocessing tool to eliminate periodic components, such as harmonics, from the measured signals [20] was discussed. The two methodologies presented in [20] and applied to helicopter in-flight data was used in this paper.

The procedure proposed to achieve editing of the signals using the real cepstrum to modify amplitude information in the log spectrum is shown in Fig. 19.6. By combining the edited log spectrum (as real part) with the original phase (as imaginary part), the complex spectrum can be obtained by exponentiation. By inverse transforming this spectrum, the time signals were then retrieved and used for OMA identification.

Both pre-processing techniques presented in [20] were applied here in sequence. First, a notch lifter was applied in the quefrequency domain to remove specific rhomonics from the signals. Each notch was centered at the inverse of the fundamental frequency of the rotor and all its multiples. The fundamental frequency was considered as the average of the rotational speed profile over the total measurement time, and to account for small speed variations notches with a broader band were selected. After the rhomonics were removed, a low-pass exponential lifter was defined. This removed everything above a certain quefrequency in the cepstrum and was based on the fact all modal information were relegated to the low quefrequency region, starting at zero quefrequency. Moreover, the damping introduced by multiplying the cepstrum to the exponential window was subtracted from the values found from the results of OMA.

## 19.4 Analysis of Data in Parked Conditions

To obtain a set of modal parameters to be used as reference for the operational analysis, the data acquired in parked conditions was analyzed first. In these conditions, the main OMA applicability issues were not present since the turbine was not rotating and the excitation coming from the wind was considered as broad-band random white noise. To obtain a first correlation, the results were compared with the one obtained from the modal survey presented in [13] and listed in Table 19.1. During the analysis, only acceleration data was used, even though initially strain gauges were used to capture tower bending. However, a quantization error was found in the data and, when converting the signals to the frequency domain, harmonics of the first bending tower modes were found. To avoid this problem, this data was not included in the processing.

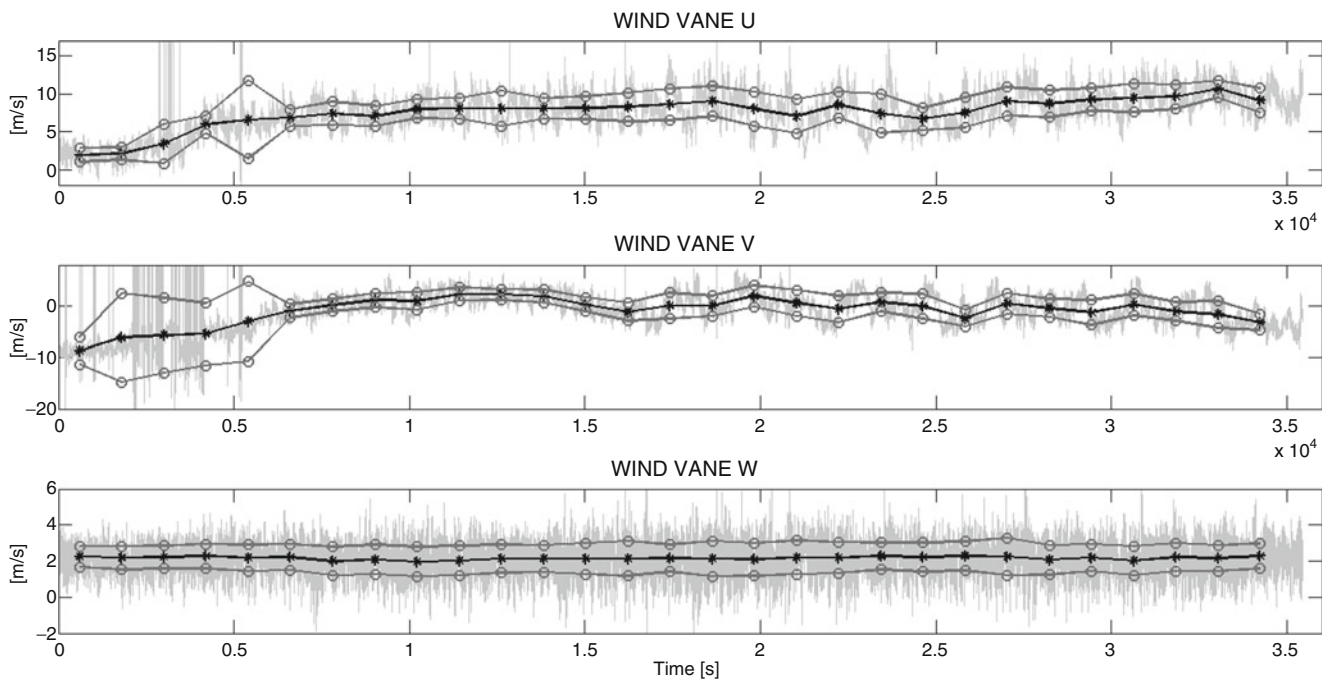


Fig. 19.7 Wind speed velocity components from the wind vane sensor. Light grey: time data. Black: mean value. Dark grey: standard deviation

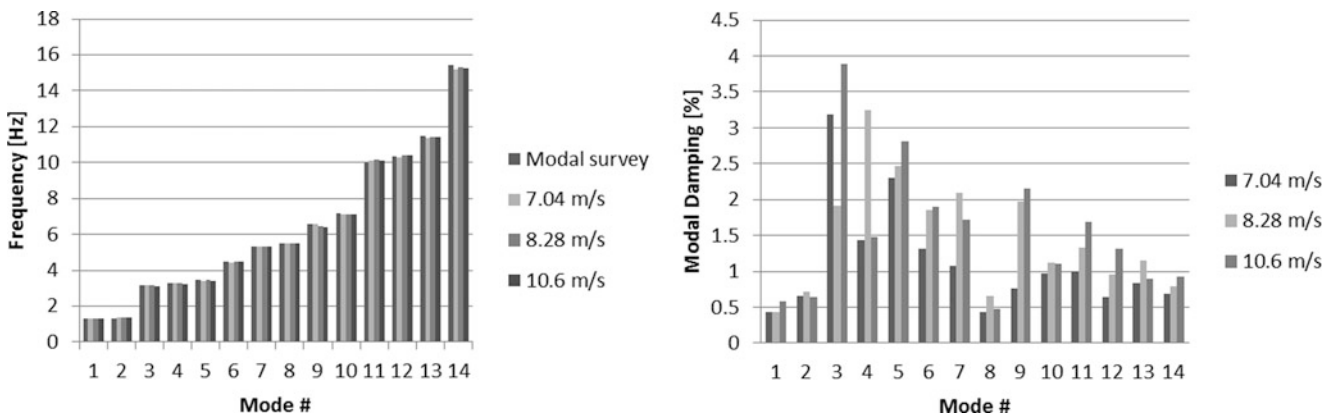


Fig. 19.8 Comparison of modal parameters for 20 min section with different mean wind speed

The parked-turbine data was a continuous 10 h measurement. During this period of time the environmental conditions changed significantly; therefore, the readings from the meteorological station were analyzed first. In Fig. 19.7, the three components of the wind speed coming from the wind vane are shown. In light grey the actual measured data is presented. As can be observed, wind variations were significant in a small time scale, so one should be careful in selecting the time section to analyze. To have an initial idea on the wind conditions, the 10-h measurements were split in section of 20 min each and the mean value and standard deviation were computed. In the initial part of the measurements numerous bit drop-outs were observed, so the mean and standard deviation values were corrupted. To understand the influence of wind intensity on the modal parameter estimation, three sections with different average wind intensity and small standard deviation were selected.

To process the data, the standard Operational PolyMAX [4] method available in the LMS Test.Lab software was used. As can be observed in Fig. 19.8, all natural frequencies from the modal survey were properly identified with only the wind exciting the structure. As expected, the average wind speed was not influencing the estimated frequency values. On the other hand, a big scatter was observed for the damping values. In general, stronger wind should result in higher damping values (greater aerodynamic damping contribution), but due to the instantaneous wind variations the identification cannot be considered as very reliable. In general, even for a constant wind speed, very long time data would be necessary because

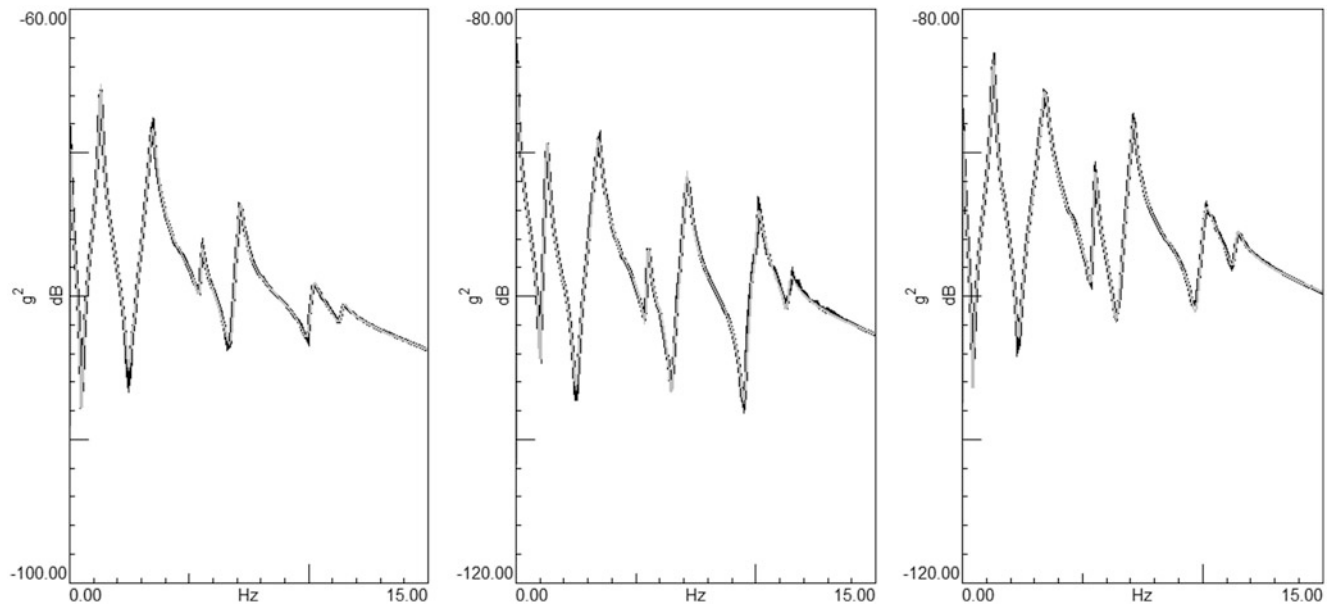


Fig. 19.9 Original (black) versus synthesized (grey) autopowers for different average wind speeds (Left: 8.28; Center: 7.04; Right: 10.6 m/s)

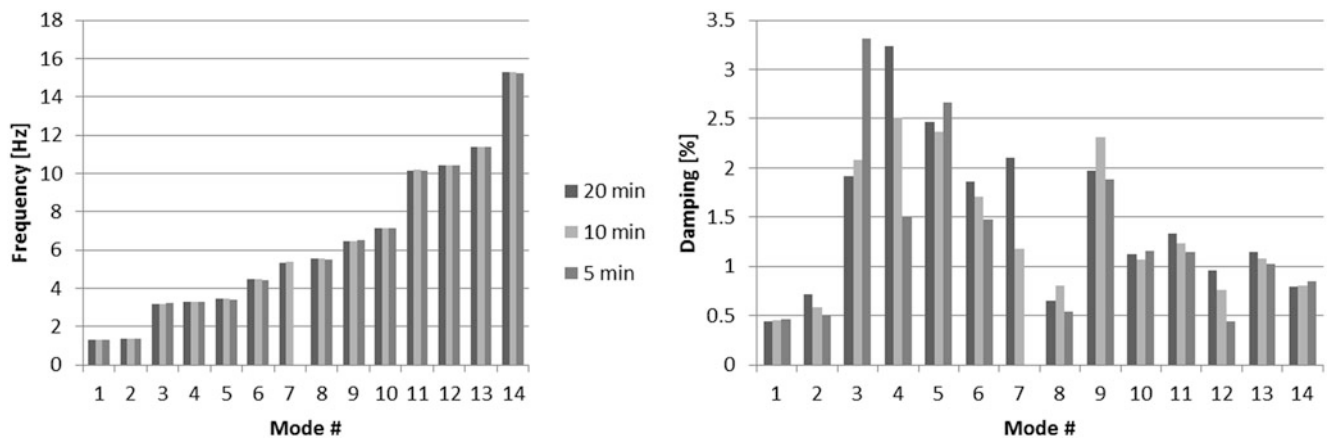


Fig. 19.10 Influence of time window length on modal parameter estimates

of the low frequency of the main modes (in general, the lower the frequency the longer the data necessary to identify). The quality of the modal estimation could only be assessed by comparing the original auto- and cross-powers with the synthesized one. In Fig. 19.9, the results for the processing performed at different average wind speeds are presented. The quality of the synthesis was very high and the overall error between original and synthesized spectra was always below 2% (except one case which is 2.5%) for all the spectra.

To verify the influence of the processing window on the modal estimation, the data from the section with 8.28 m/s average wind speed was cut in smaller sections, respectively of 10 and 5 min. The frequencies and damping values obtained for the different sections are shown in Fig. 19.10. While the frequency estimates were very consistent between the different runs, the damping estimates were more scattered, but still of the same order of magnitude of those presented in Fig. 19.8 for different wind speeds. However, during the processing, the stabilization diagram became less clear and mode 7 was not identified using the 5 min window.

Finally, the same processing was repeated by using the new PolyMAX Plus [21, 22] algorithm on the time data. The results were comparable with the original algorithm, mainly because of the very clean acquired data. This new method was known to provide a better estimation when the data was noisy, which was not the case here for the parked condition analysis.

## 19.5 Analysis of Operational Data

With the analysis performed in the previous section, a list of modes corresponding to those identified during the modal survey was found. Although modal damping changes significantly depending on the time window used and the environmental conditions, the identified values were used to understand the actual amount of damping introduced by aerodynamic effects during rotation. To allow a proper estimation of the modal parameters, the periodic components associated both to the aerodynamic effects and rotor harmonics discussed in the Introduction needed to be properly removed. First, the raw data was analyzed to verify how the identification technique performed with it. As for the previous analysis, only the accelerometers on the blades and the nacelle were included. In parked conditions, all the sensors gave the signal in the same reference frame. When the blades started rotating, the associated sensors gave accelerations in a local frame, which was rotating, while the tower and nacelle sensors still produced the results in a ground-fixed frame. In some cases, it was desirable to keep the response in the measured frame, thus studying the tower and blade response in their local frames. In other situations, one might be interested in the full tower-nacelle-rotor coupled behavior. In this case, methods such as the Coleman Transformation have been developed to express all signals in the same fixed frame [23].

In this preliminary analysis, all data was treated together, without any coordinate transformation. A 20 min-data section was processed, with the turbine rotating at a constant average speed. The typical OMA preprocessing procedure was applied, where first the correlations were computed and then the spectra estimated. The auto-power spectra for the two selected references are shown in Fig. 19.11. The signal in the lag-wise direction was clearly dominated by the first rotor harmonic, while the flap-wise one had a higher response at the higher harmonics. Together with the spectra, the natural frequencies of the modes identified in the parked condition analysis were marked in Fig. 19.11. It was observed that the modal response was mostly masked by the rotor harmonics. Moreover, the modes from 3 to 7 Hz were all close to harmonic components, so it was difficult to properly identify them.

Using the same processing settings applied for the parked turbine analysis, the stabilization diagram in Fig. 19.12 was obtained, from which the modes in Table 19.2 were identified.

In both cases, it was clearly observed that most of the identified modes corresponded to multiples of the rotor fundamental harmonic. Additionally, the damping associated with the harmonic peaks was observed. While the first harmonic was identified as a mode with a very small damping, almost all of the others showed values which were comparable with those shown in Fig. 19.8. The modal shapes obtained were discussed based on the results in Fig. 19.13. The autoMAC (auto Modal Assurance Criterion) matrix on the right shows that the correlation between the different modes is low, so that the identified modes are orthogonal. However, by analyzing their animations, only the two reported in Fig. 19.13, namely the first and second symmetric flap-wise mode, can be clearly distinguished. For all the other modes, the shape could be attributed to one of the modes in Table 19.1, but this was due to the fact that the identified peaks corresponded to harmonics rather than resonance. Because of this, the identified shapes were closer to Operational Deflection Shapes at a specific frequency rather than true mode shapes. A further validation of the identified model was obtained by comparing the identified modes with those in parked conditions. The results are not shown but, only the first symmetric flap-wise mode showed a significant correlation between the two analysis ( $MAC = 71\%$ ).

The harmonic and periodic component removal techniques presented in Sect. 19.3 were applied and the results analyzed. For the Time Synchronous Averaging technique, both the case where the true speed profile was used for the angular resampling and the case where only the average speed is included is were considered. For the cepstrum editing, a simple

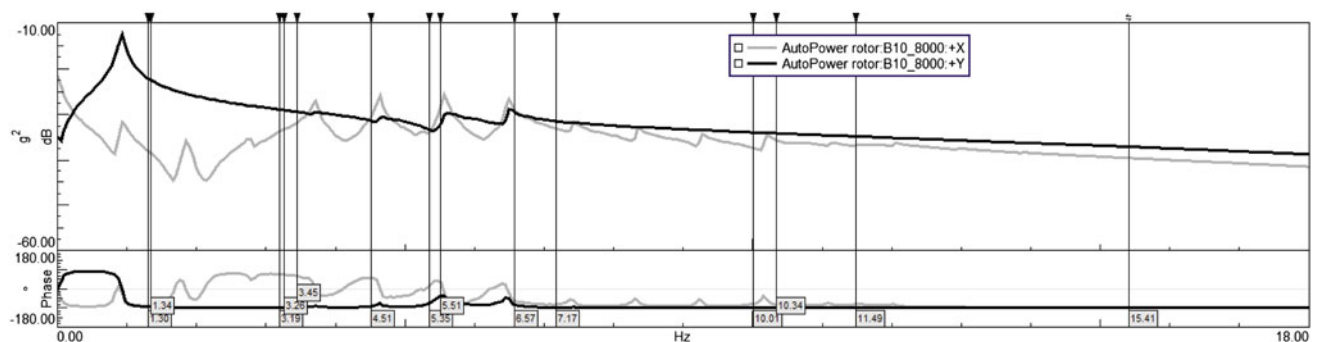


**Fig. 19.11** Computed auto-powers for measured accelerations in flap-wise and lag-wise directions. Vertical lines represent the parked turbine modes

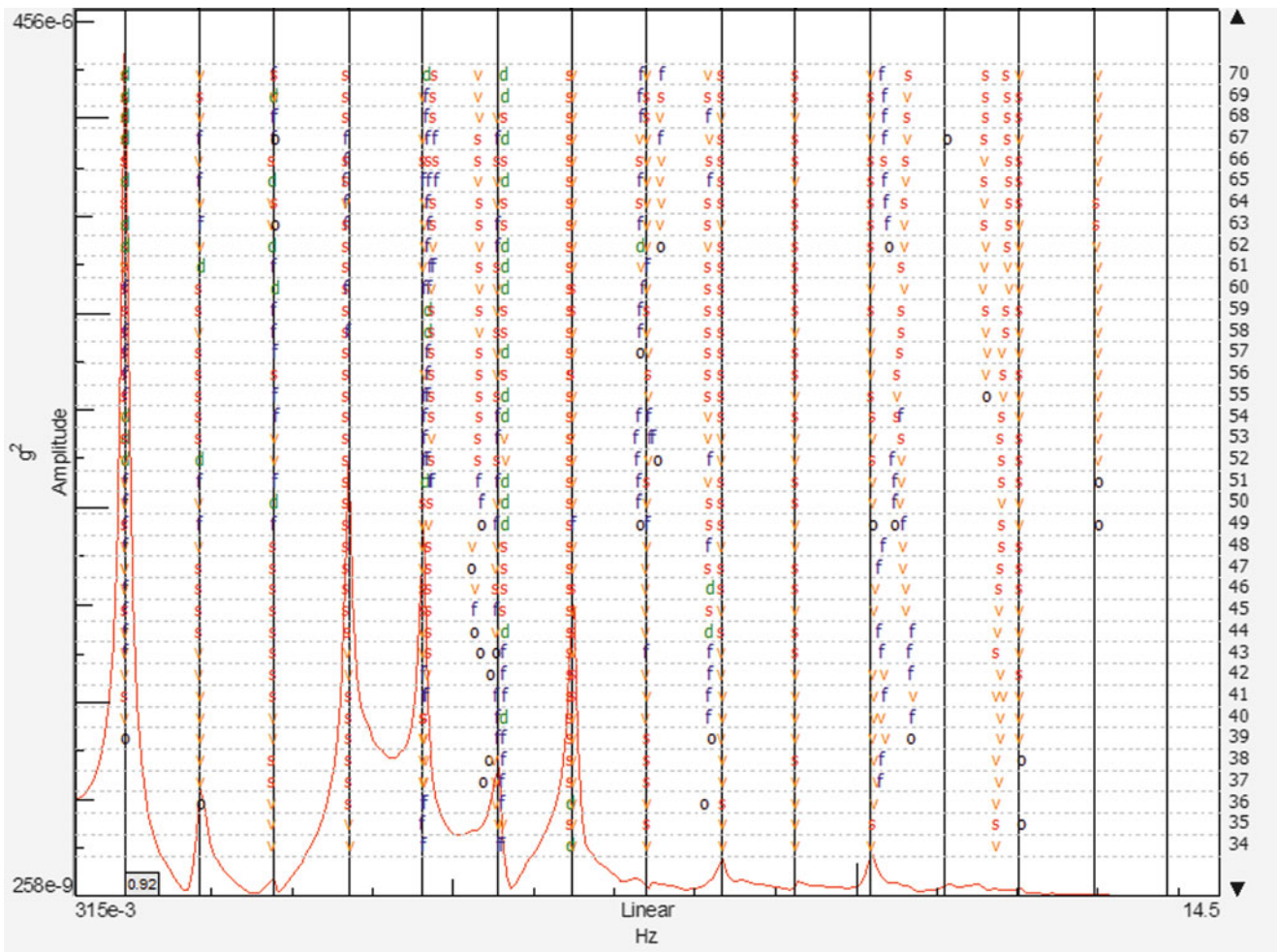


Fig. 19.12 Stabilization diagram for unfiltered data. Vertical lines correspond to harmonic components

Table 19.2 Identified modes from unfiltered operational data with the corresponding harmonic number

$f_n$ (Hz)	$\xi$ (%)	$f_n$ (Hz)	$\xi$ (%)
0.926 [1P]	0.03	7.407 [8P]	0.30
1.867 [2P]	1.08	8.195	1.96
2.774 [3P]	1.33	8.335 [9P]	0.11
3.678 [4P]	4.89	9.262 [10P]	0.09
4.656 [5P]	3.11	10.236 [11P]	0.72
4.747	3.20	10.602	1.25
5.312	2.40	11.821	2.96
5.641 [6P]	2.00	12.035 [13P]	0.12
6.454 [7P]	3.67	12.978 [14P]	0.27

notching lifter in combination to an exponential low pass lifter were used. The results of the periodic component removal can be observed in Fig. 19.14.

From the autospectra comparison, it was observed how, in general, Time Synchronous Averaging was not able to remove the periodic components from the original signals. This method was known to perform well when harmonic components appeared at discrete frequencies or under very small speed fluctuations. This was not the case for the analyzed data where, as can be observed in Fig. 19.14, the harmonic peaks are characterized by thick tails [5]. The modal models identified by applying TSA versus the one from the original data are compared in Fig. 19.15. The identified modes are exactly the same as those reported in Table 19.2 and the only that can be clearly identified remain the first and second symmetric flapwise bending modes (indicated by first SF and second SF in the x-axis label).

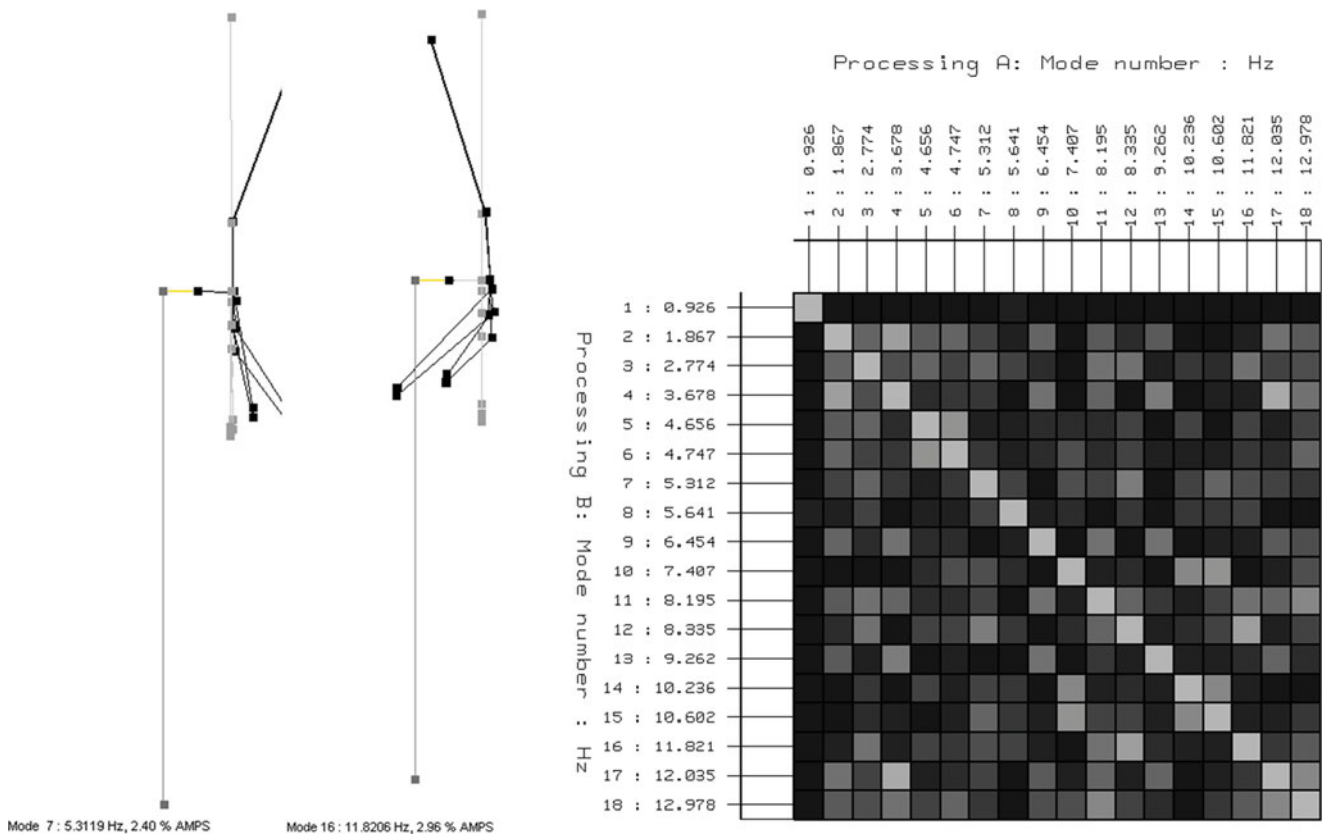


Fig. 19.13 First (left) and second (center) symmetric flap-wise modes; (right) identified modal set autoMAC

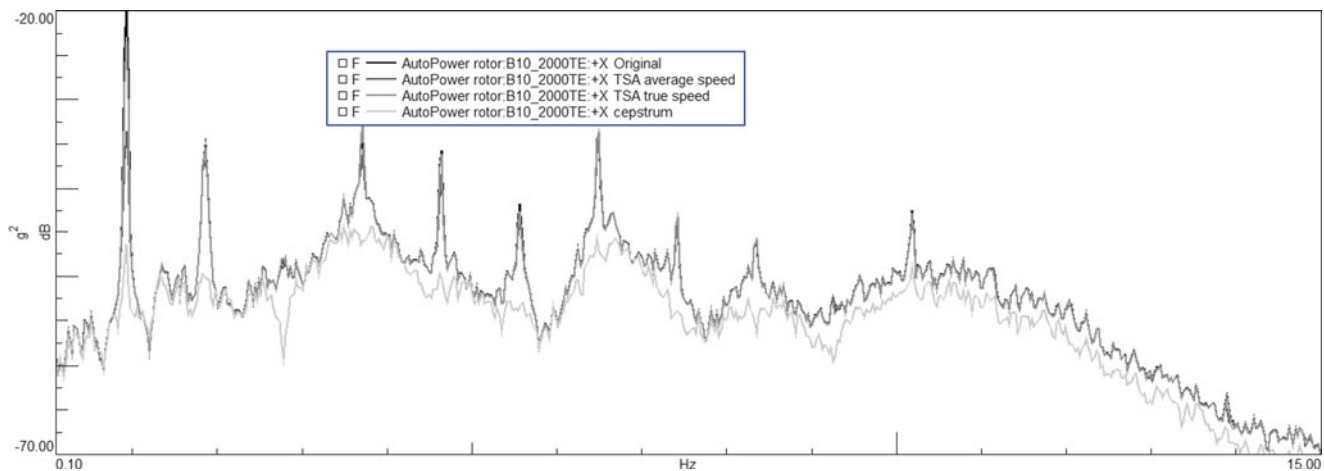
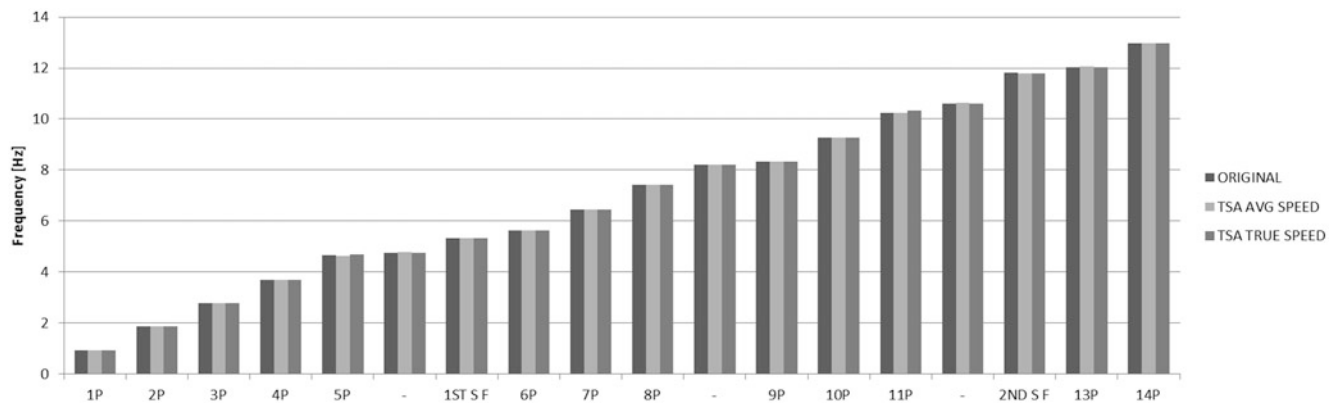


Fig. 19.14 Effect of different harmonic removal techniques on the autopower spectrum of an acceleration signal

On the other hand, the advantage of using cepstrum editing was clearly visible in Fig. 19.14. This technique allowed not only separating the harmonic components from a random signal, but in general any periodic phenomena which were included in the data. Thus, the presence of the thick tails should not be a limit for this method. Although from the autospectrum in Fig. 19.14 it was clear that some of the harmonic components were not completely removed (i.e. the 1P component), the number of modes which were identified here was higher. Moreover, from the mode shape animation, the lag-wise component which was present in the previously identified modes did not appear anymore. An overview of the identified modes is given in Table 19.3. Although some of the modes still corresponded to harmonic components or to numerical poles introduced by the filtering, a much higher number of modes than before were clearly distinguished. The correlation in terms of MAC with





**Fig. 19.15** Comparison between modal frequencies from original and TSA filtered data

**Table 19.3** Identified modes after cepstrum editing

Description	Frequency (Hz)
1P	0.930
-	2.065
First shaft torsion	2.381
-	2.947
First flap antisymmetric (about vertical axis)	3.556
-	3.921
-	4.788
First flap symmetric	4.911
-	5.502
First edge symmetric, in-phase	5.722
Second flap antisymmetric (about vertical axis)	6.449
-	9.250
Second flap antisymmetric (about vertical axis)	10.600
Second flap antisymmetric (about horizontal axis)	11.134
Second flap symmetric	11.743
-	12.017

the parked condition as still poor except for few modes, but this was explained by the different operating condition of the turbine. In Fig. 19.16, the stabilization diagram from which the poles are selected is shown. The vertical dark lines correspond to multiples of the rotational speed. If compared to the one in Fig. 19.12, much less of the stable poles found correspond to harmonic components. This explained why more modes correlated well with the analysis of the parked condition.

In general, it can be concluded that editing the cepstrum was a good procedure to remove not only harmonic but also periodic components from the acquired accelerations in operating, which was not the case for standard tonal component removal techniques such as time Synchronous Averaging.

Finally, a graphical comparison between the corresponding modes identified in parked and operating conditions is presented in Fig. 19.17. For most of the blade modes, an increase in the natural frequency was observed, which can be related to the stiffening effect due to the centrifugal force introduced by the blade rotation. The only mode which showed a lower frequency in operating condition was the torsional mode of the main shaft. To keep the turbine in parked conditions, the brake was applied to lock the transmission shaft. The reduction in the frequency of the associated mode was then explained by the removal of the brake, which reduced the torsional stiffness of the driveline. A similar analysis would also be interesting for the damping values, to understand how the aerodynamic damping affects the global analysis in operating conditions. In parked conditions, the variability of damping for different processing sets was already significant (see Figs. 19.8 and 19.10). In operational conditions, the stabilization diagram was much less clear and there were less poles that showed a stable evolution; additionally, the harmonic removal techniques still need to be fine-tuned and optimized to be able to only remove the periodic components while leaving the underlying structural response unmodified.

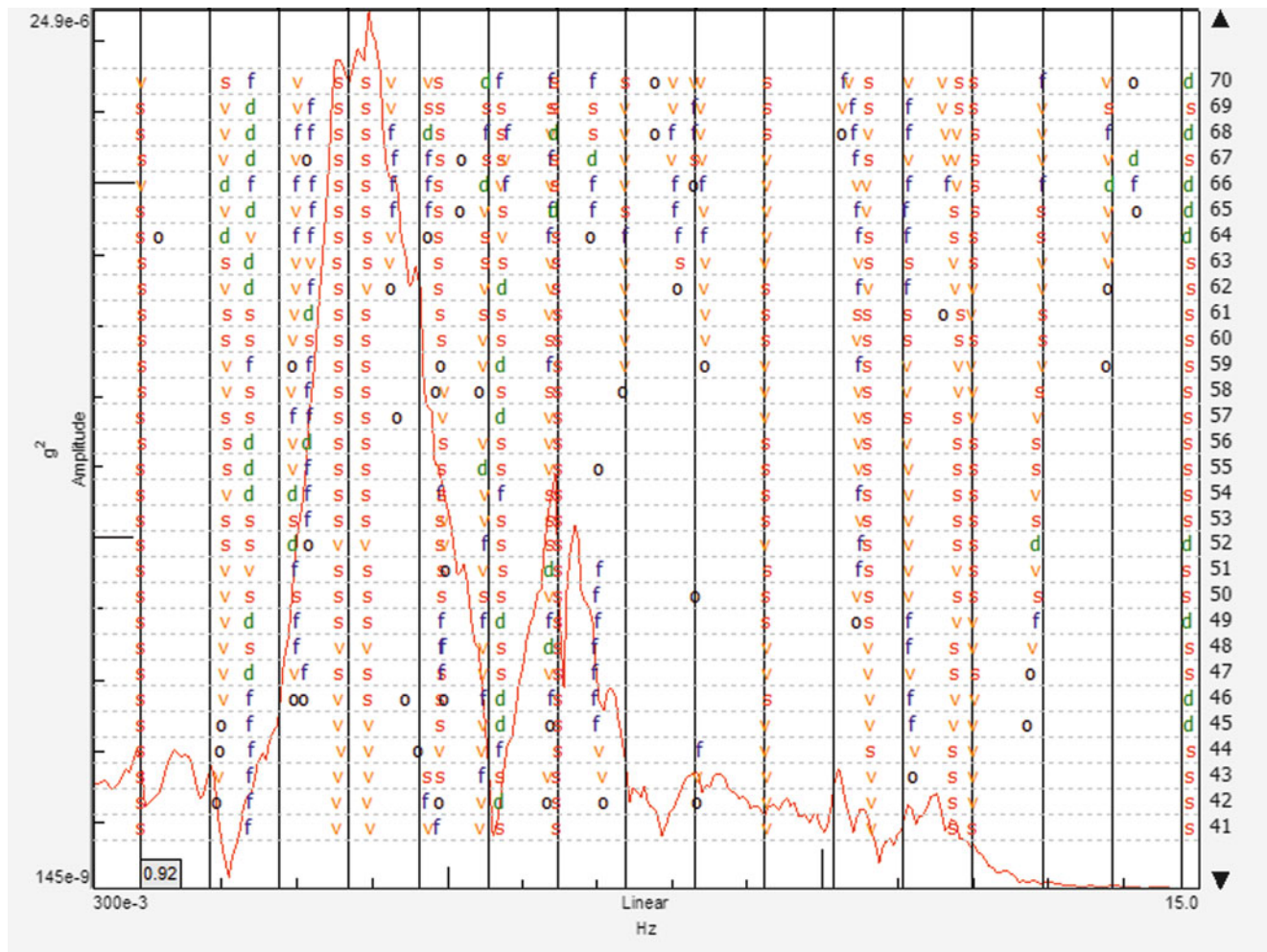
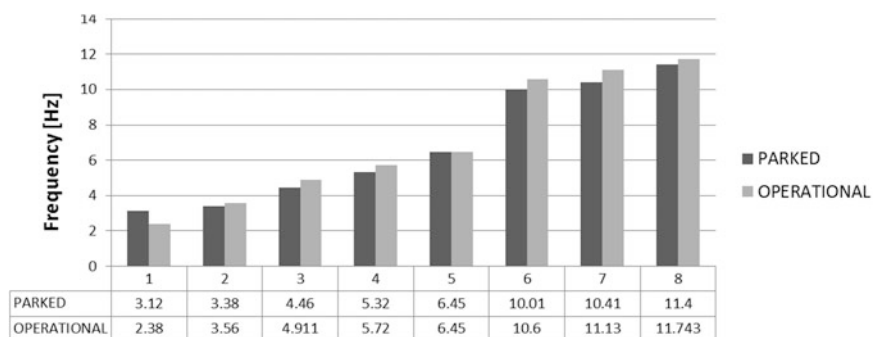


Fig. 19.16 Stabilization diagram for cepstrum edited data

Fig. 19.17 Comparison of identified frequencies between parked and operational measurement



## 19.6 Conclusions and Way Forward

In this paper, data acquired by Sandia National Laboratories during a field test campaign on a modified MICON wind turbine were analyzed. The data includes accelerations on the blades and nacelles, strains on the blades and tower as well as rotor speed and azimuth angle for the machine in parked and operating condition. These signals were synchronized with the wind speed and direction acquired on a meteorological tower, so that the environmental conditions could be correlated with the structural response. First, the data from parked condition was analyzed to understand which processing parameters were influencing the modal identification procedure the most. The full time histories were cut in smaller segments of 20, 10 and

5 min and the modal parameters obtained were compared with those acquired by Sandia National Laboratories during an impact hammer test of the turbine. Using different time blocks for the analysis, it was observed that while the identified natural frequencies were the same, the damping values vary significantly. Since the damping estimates should improve if longer time segments are selected, the 20-min analysis was chosen as a reference. However, one needs to be careful with such a long analysis time that the environmental and operating conditions did not vary significantly in order to comply with the stationarity assumption of Operational Modal Analysis. In the second part of the paper, the data from the operating conditions were also analyzed and particular attention was given to the harmonic and periodic components appearing in the measured data and related to the blade rotation. As expected, by identifying the raw measured data, the majority of the identified modes corresponds to harmonic components. Only few of the poles represent physical natural frequencies of the structure. Different harmonic removal techniques were then applied to the data to investigate their performance. First, a standard Time Synchronous Averaging procedure based on double resampling was applied. The method was developed to solve discrete harmonic components or slowly varying ones and it was not able to deal with the fat-tailed peaks which were present in the signal spectra. A method based on filtering the signal in the cepstrum domain was then applied. In this domain, all periodic components in the spectrum appeared as discrete harmonics, which were easily removed by notching. The signal was then transformed back in the time domain. A simple procedure was applied in this analysis, which showed some significant improvements in removing the effect of the rotating blades from the signal thereby allowing better identification of the structural modes of the system. In the future, the procedure will be further refined by applying different lifters (filters in cepstrum domain) and varying the length of the processing window. Different pre-processing methodologies, such as the Coleman coordinate transformation or more advanced periodic identification techniques will also be investigated, with the final objective of developing an automated operational modal analysis for wind turbine analysis. Finally, only acceleration signals were included in this paper, limiting the analysis to the blades and the nacelle. More advanced techniques will then be sought to also include strain signals, thus providing a better spatial description and a more global structural response.

**Acknowledgements** Sandia National Laboratories is a multi-program laboratory managed and operated by Sandia Corporation, a wholly owned subsidiary of Lockheed Martin Corporation, for the U.S. Department of Energy's National Nuclear Security Administration under contract DE-AC04-94AL85000.

The research presented was performed in the framework of the IWT 120029 project OPTIWIND: Serviceability Optimisation of the Next Generation Offshore Wind Turbines. Finally, the authors would also like to kindly acknowledge Professor R.B. Randall from the University of New South Wales in Australia for his precious support.

## References

1. Carne TG, James III GH (2010) The inception of OMA in the development of modal testing for wind turbines. *Mech Sys Signal Process* 24:1213–1226
2. Peeters B, Guillaume P, Van der Auweraer H, Cauberghe B, Verboven P, Leuridan J (2004) Automotive and aerospace applications of the PolyMAX modal parameters estimation method. In: *Proceedings of IMAC XXII*, Dearborn, MI
3. Peeters B, Dammekens F, Magalhães F, Van der Auweraer H, Caetano E, Cunha A (2006) Multi-run operational modal analysis of the Guadiana cable-stayed bridge. In: *Proceedings of IMAC XXIV*, St. Louis, MO
4. Peeters B, Van der Auweraer H, Vanhollebeke H, Guillaume P (2007) Operational modal analysis for estimating the dynamic properties of a stadium structure during a football game. *Shock Vib* 14(4):283–303
5. Tcherniak D, Chauhan S, Hansen MH (2010) Applicability limits of operational modal analysis to operational wind turbines. In: *Proceedings of IMAC XXVII*, Jacksonville, FL
6. Peeters B, Cornelis B, Janssens K, Van der Auweraer H (2007) Removing disturbing harmonics in operational modal analysis. In: *Proceedings of IOMAC*, Copenhagen, Denmark
7. Mohaveny P (2005) Operational modal analysis in the presence of harmonic excitation. PhD dissertation thesis, Technische Universiteit Delft
8. Heylen W, Lammens S, Sas P (1997) Modal analysis theory and testing. Katholieke Universiteit Leuven, Leuven
9. Hansen MH, Thomsen K, Fuglsang P (2006) Two methods for estimating aeroelastic damping of operational wind turbine modes from experiments. *Wind Energy* 9:179–191
10. White JR (2009) Operational monitoring of horizontal axis wind turbines using inertial measurements. PhD dissertation, Purdue University
11. White JR, Adams DE, Rumsey MA (2010) Modal analysis of CX-100 rotor blade and micon 65/13 wind turbine. In: *Proceedings of IMAC XXVII*, Jacksonville, FL
12. Berg D, Berg J, Wilson D, White J, Resor B, Rumsey M (2011) Design, fabrication, assembly and initial testing of a SMART rotor. In: *Proceedings of the 29th ASME wind energy symposium*, Orlando, FL, Jan 2011
13. Adams DE, White JR, Rumsey M, Farrar C (2011) Structural health monitoring of wind turbines: method and application to HAWT. *Wind Energy* 14:603–623
14. Randall RB (2002) State of the art in monitoring rotating machinery. In: *Proceedings of ISMA 2002*, Leuven, Belgium
15. Bechhoefer E, Kingsley M (2009) A review of time synchronous averaging algorithms. In: *Proceedings of the annual conference of the prognostic and health management society*, San Diego, CA

16. Groover CL, Trethewey MW, Maynard KP, Lebold MS (2005) Removal of order domain content in rotating equipment signals by double resampling. *Mech Syst Signal Process* 19:483–500
17. Manzato S, Moccia D, Peeters B, Janssens K, White JR (2012) A review of harmonic removal methods for improved operational modal analysis of wind turbines. In: *Proceedings of ISMA 2012, Leuven, Belgium*
18. Bogert BP, Healy MJR, Tukey JW (1963) The quefrency analysis of time series for echoes: cepstrum, pseudo-autocovariance, cross-cepstrum and shape cracking. In: *Proceedings of the symposium on time series analysis, New York*, pp 209–243
19. Randall RB (2009) Cepstral methods of operational modal analysis. In: *Encyclopedia of structural health monitoring*. Wiley, Chichester
20. Randall RB, Peeters B, Antoni J, Manzato S (2012) New cepstral methods of signal pre-processing for operational modal analysis. In: *Proceedings of ISMA 2012, Leuven, Belgium*
21. El-Kafafy M, Guillaume P, Peeters B, Marra F, Coppotelli G (2012) Advanced frequency-domain modal analysis for dealing with measurement noise and parameter uncertainty. In: *Proceedings of IMAC XXX, Jacksonville, FL*
22. Peeters B, El-Kafafy M, Guillaume P (2012) The new PolyMAX Plus method: confident parameter estimation even in very noisy cases. In: *Proceedings of ISMA 2012, Leuven, Belgium*
23. Bir G (2008) Multiblade coordinate transformation and its application to wind turbine analysis. In: *Proceedings of the 2008 ASME wind energy symposium, Reno, Nevada*

# Chapter 20

## Tracking and Removing Modulated Harmonic Components with Spectral Kurtosis and Kalman Filters

Jean-Luc Dion, Cyrille Stephan, Gaël Chevallier, and Hugo Festjens

**Abstract** This work describes an automatic method for removing modulated sinusoidal components in signals. The method consists in using the Optimized Spectral Kurtosis for initializing Series of Extended Kalman Filters.

The first section is an introduction to vibration applications with Kalman Filters and modulated sinusoids. The detection process with OSK is described in the second section. The third section concerns the tracking algorithm with SEKF for amplitude and frequency modulated sinusoidal components. The last section deals with the complete process illustrated with an experimental application on a rotating machine.

**Keywords** Kurtosis • Detection • Extended Kaman filter • Frequency modulation • Amplitude modulation • Operational modal analysis

### Acronyms

ARMA	Auto Regressive – Moving Average
DOF	Degree Of Freedom
EKF	Extended Kalman Filter
SEKF	Series of Extended Kalman Filters
OMA	Operational Modal Analysis
OSK	Optimized Spectral Kurtosis
PBF	Pass Band Filter
PSD	Power Spectral Density

## 20.1 Introduction

In the field of Operating Modal Analysis (OMA) applied on structures like helicopters or large structures in energy production, vibration signals are composed with random sources and periodic signals due to rotating machines which can not be shut down. It is a well-known problem that these harmonic components introduce mistakes in experimental modes extraction by OMA algorithms. The present paper intended to solve this problem by tracking and removing modulated sinusoidal signals in noisy records. The previous work has focused on the detection of sinusoidal components [1]. The present work aims to remove these sinusoidal components by using Series of Extended Kalman Filter [2].

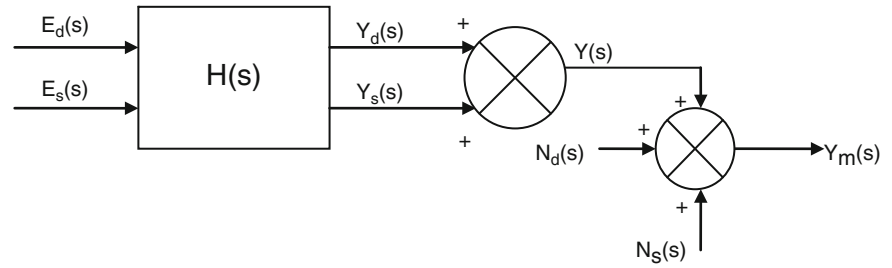
---

J.-L. Dion (✉) • G. Chevallier • H. Festjens

Laboratoire d'Ingénierie des Systèmes Mécaniques et des Matériaux (LISMMA) – EA 2336, SUPMECA Paris 3, rue Fernand Hainaut, 93407 Saint Ouen, France, Tel: 33(0)1 49 45 29 12, Fax: 33(0)1 49 45 29 10  
e-mail: [jean-luc.dion@supmeca.fr](mailto:jean-luc.dion@supmeca.fr); [gael.chevallier@supmeca.fr](mailto:gael.chevallier@supmeca.fr); [hugo.festjens@supmeca.fr](mailto:hugo.festjens@supmeca.fr)

C. Stephan  
ONERA, Châtillon, France  
e-mail: [cyrille.stephan@onera.fr](mailto:cyrille.stephan@onera.fr)

**Fig. 20.1** Block diagram of the studied problem. Measured signals  $Y_m(s)$  are composed of stochastic and deterministic signals. The aim of the study is to remove the deterministic part in  $Y_m(s)$



In the field of vibrations, several works have already used Kalman filters for identification, detection, health monitoring or tracking order. In identification and detection processes, Kalman Filters are performed for the localization of cracks on rotating machines [3], for stiffness identification [4] or vibration force estimation [5,6]. Some health monitoring methods for structures and rotating machines are based on Kalman Filters with varying Auto Regressive identification parameters [7–11]. Kalman Filters are also used in active vibration control [12–15] with real-time algorithms and non-stationary signals on smart structures. Other works use Kalman filters to improve time-frequency analysis and order tracking techniques [16–20]. Order Tracking techniques for rotating machines are often based on Vold-Kalman Filter [21, 22]. Recent techniques aim to improve the Vold Kalman Filtering for resampling techniques, high frequency resolution in Fourier analysis and crossing orders detection [23–30]. Most of these works are based on shaft speed information, as an instantaneous frequency is often measured by tachometers.

The whole process of measurement from an excitation source to measured signals can be depicted in a diagram (see Fig. 20.1). In the rest of this paper, the structure is supposed to have a linear dynamic behavior. Then in a limited bandwidth, the relation between inputs and outputs can be fully captured by its transfer function  $H(s)$ , defined in the Laplace domain.

This structure is supposed to be excited by two kinds of input. The first one is created by a random source which delivers a white noise. Thus it is a stochastic input named  $E_s(s)$ . The second one is created by an unbalanced rotating machine. Contrary to the first input, it delivers a signal whose amplitude and frequency are slowly modulated. As the signal slowly changes over time, it has a phase and is deterministic. It is named  $E_d(s)$ , for deterministic input. Both inputs are not measured.

For a linear structure, the response  $Y(s)$  of the structure can be separated into its stochastic and deterministic parts:

$$Y(s) = Y_s(s) + Y_d(s) \quad (20.1)$$

where  $Y_s(s) = H(s)E_s(s)$  is the response due to the stochastic input  $E_s(s)$  and  $Y_d(s) = H(s)E_d(s)$  is the response due to the deterministic input  $E_d(s)$ .

As errors are unavoidable in measurements, they have to be taken into account too. As for inputs, two kinds of observation noise can distort signals. The first one is a random noise  $N_s(s)$  which come from electronic flaws. Its probability law is usually supposed to be Gaussian  $p(t) = N(0, W)$  and is characterized in the frequency domain by a flat density of spectral amplitudes, i.e. its energy is uniformly distributed among frequencies.

The second possible noise often results of an electrical field which produces a periodic component at a stable frequency, but with modulated amplitude. Unfortunately this electrical field is also caught by sensors. For instance, in Europe the spurious harmonic components at  $n \cdot 50$  Hz are well known by experimental engineers. This added noise  $N_d(f)$  is deterministic and is noticeable in signals as narrow components around its fundamental frequency and its harmonics. From a structural point of view, they look like spurious low-damped modes. Unfortunately, this noise cannot be accurately predicted because it highly depends on each experiment and on each sensor technology. This kind of noise is seldom taken into account, although it can seriously alter signals if structural responses are weak.

In conclusion, the observed signals result in the sum of these noises added to structural responses:

$$Y_m(t) = Y(t) + N_d(t) + N_s(t) \quad (20.2)$$

that can be also separated into its stochastic and deterministic parts:

$$Y_m(t) = Y_s(t) + N_s(t) + Y_d(t) + N_d(t) \quad (20.3)$$

As a rule, OMA are designed for only stochastic input and noise measurement. It is a strong assumption for these algorithms and is seldom respected. As a result, deterministic components in responses can strongly false results given by OMA algorithms.

The purpose of the proposed method is to identify the deterministic part  $Y_d(t)$  and to subtract it from  $Y_m(t)$ . It will give an approximation of the stochastic response which would be obtained if  $E_d$  and  $N_d$  were missing. Then this approximation could be possibly used for OMA identification techniques, although here the focus will be made on the filtering process. Here the term filtering means that the deterministic component of  $Y_d(t)$  is going to be filtered from the available signals  $Y_m(t)$ , without previous knowledge of the structure of  $Y_d(t)$ .

In the present study, the detection and the tracking of sinusoidal components are performed without the knowledge of frequencies of periodic signal or of a transfer function  $H(s)$ . Studied signals are assumed to be composed of random noise and modulated sinusoidal components. Indeed, measured signals on rotating engines in operational conditions are:

$$s(t) = b(t) + \sum_k p_k(t)$$

$$\text{With } b(t) = Y_s(t) + N_s(t) \text{ and } \sum_k p_k(t) = Y_d(t) + N_d(t) \quad (20.4)$$

The first term  $b(t)$  is assumed to be mainly composed with the structural response under random excitation. The second terms  $p_k(t)$  come from engines in operation and from spurious harmonic components of the electric power supply. The signals  $p_k(t)$  are deterministic and assumed to be both amplitude and frequency modulated. The  $k$ th pseudo periodic source is assumed to be composed of  $N$  modulated sines:

$$p_k(t) = \sum_{i=1}^N a_{i,k}(t) \cos \left( 2\pi i \left( f_{0,k}t + \Delta f_k \int_0^t m_k(\theta) d\theta \right) + \varphi_{i,k} \right) \quad (20.5)$$

where:

- $a_{i,k}(t)$  the amplitude for the  $k$ th source and the  $i$ th sinusoid
- $f_{0,k}$  the central fundamental frequency of the  $k$ th source
- $\Delta f_k$  the frequency deviation of the  $k$ th source
- $m_k$  the reduced frequency modulation of the  $k$ th source with  $MAX\{|m_k|\} \leq 1$
- $\varphi_{i,k}$  the phase of the  $k$ th source and the  $i$ th sinusoid

In the proposed technique, the frequency modulation is assumed to occur slowly in a short range of variation.

$$\frac{d}{dt} \left( \Delta f_k \int_0^t m_k(\theta) d\theta \right) \ll f_{0,k} \text{ With } |m_k(t)| < 1 \text{ and } \Delta f_k \ll f_{0,k} \quad (20.6)$$

Two signals are sketched in the time domain in Fig. 20.2: signal A is a frequency and amplitude modulated sinusoid (Fig. 20.2 upper left) and signal B is a narrow bandwidth random noise (Fig. 20.2 lower left). Both signals share the same spectrum magnitude (Fig. 20.2 right), although they have different phase spectras. Thus, for a given PSD or spectrum magnitude where phase information is lost, the original temporal signal can not be identified: it could be either a modulated sinusoid (deterministic) or a random noise (stochastic).

As a result, in the case of structural behavior identification, dynamic responses based on “output only” techniques have to be free of such modulated sinusoidal signals. Thus, the purpose is to remove sinusoidal components, such as unbalanced rotating machines speed or electrical current components, from the original signal. The method is built upon two main steps.

First, all sinusoidal components are detected with an Optimized Spectral Kurtosis (OSK) [1]. Thus, the number of sinusoidal components is identified by the OSK. This process is described in Sect. 20.2.

Secondly, an EKF is built per detected central frequency. Then a set of EKFs is obtained and called a Series of Extended Kalman Filters (SEKF). Its size is defined by the number of identified frequencies. State variables and variances in the EKF are firstly identified with OSK data in order to initialize the SEKF process. This step is developed in Sect. 20.4.1.

Finally, each detected periodic signal is tracked and suppressed from the original signal with the help of a SEKF. These steps are developed in Sect. 20.3 from a theoretical point of view, and numerical applications are exposed in Sect. 20.4.

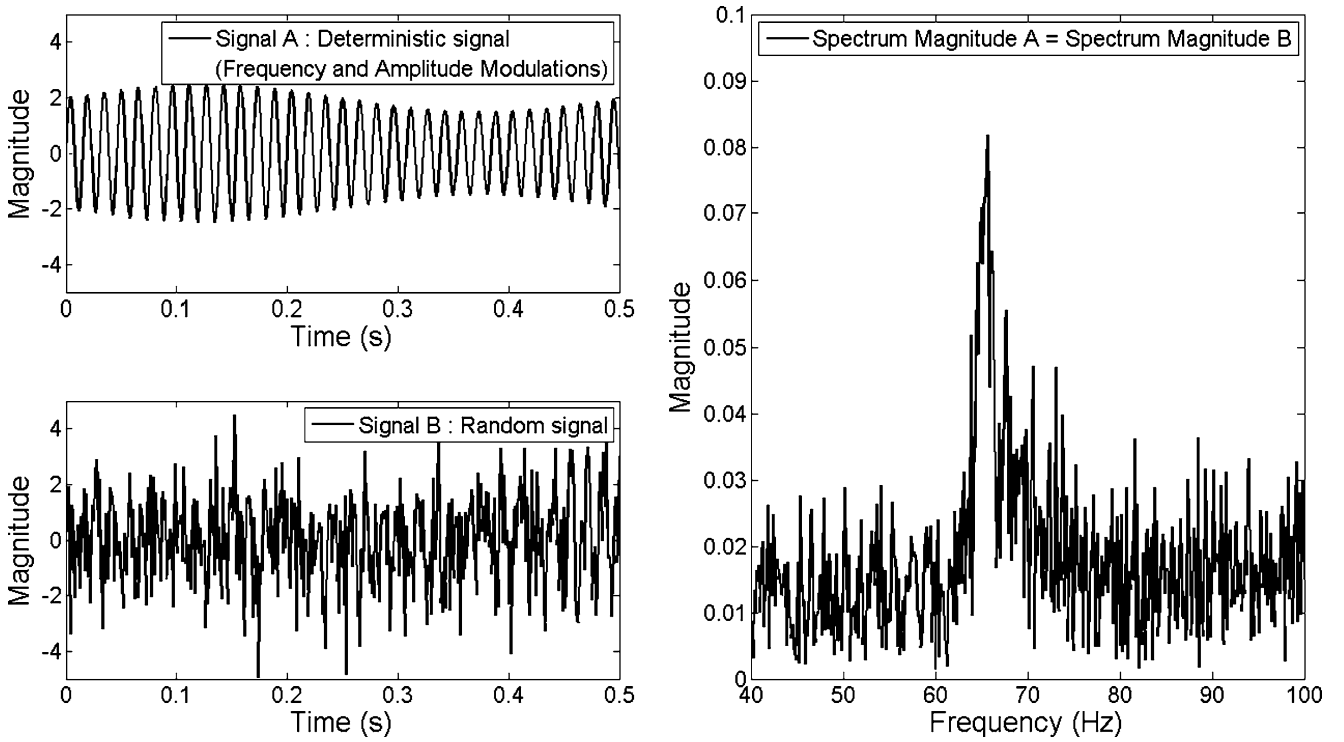


**Fig. 20.2** Example of frequency and amplitude modulations of a sinusoid (Signal A: *upper left*), random noise in a narrow bandwidth (Signal B: *lower left*): both signals have the same spectrum magnitude (*right*)

## 20.2 Detection of Modulated Sinusoidal Components

### 20.2.1 Definition of the Optimized Spectral Kurtosis Method

The detection of sinusoidal components is based on combining two kinds of information: statistical and spectral as developed in a previous work [1]. The OSK consists in establishing a spectral description of Kurtosis.

First, the signal is filtered with a narrow Pass Band Filter (PBF) centered on the studied frequency.

Secondly, the Kurtosis of the filtered signal is computed and the numerical result defines the assumed nature of the signal (included in the spectral bandwidth). In the  $i$ th Pass Band, the  $i$ th Kurtosis is defined by:

$$K_i = E \left[ \left( \frac{Xf_i - \mu}{\sigma} \right)^4 \right] \quad (20.7)$$

where  $Xf_i$  is the  $i$ th filtered signal obtained from the  $i$ th PBF,  $\mu = E[X]$ ,  $\sigma^2 = E[(X - \mu)^2]$  and  $E(X)$  is the statistical expectation of  $X$ .

The complete spectral description of Kurtosis is obtained by translating the PBF along the entire frequency bandwidth. In order to obtain an accurate spectral resolution, the used PBF is a sixth order Cauer Filter [31] for Real Time Computation but could also be performed with an ideal PBF for Post-Processing Computation. In the case of a real time computation, statistical expectations are computed with the following linear recursive technique:

$$E_k[Y] = \left( 1 - \frac{1}{k} \right) E_{k-1}[Y] + \frac{1}{k} y_k \quad (20.8)$$

where  $y_k$  is the new data (realization of process  $Y$ ),  $E_{k-1}[Y]$  the old expectation of  $Y$  and  $E_k$  the new expectation of  $Y$ .



**Fig. 20.3** Picture of the bench test. Diagram of the experiment

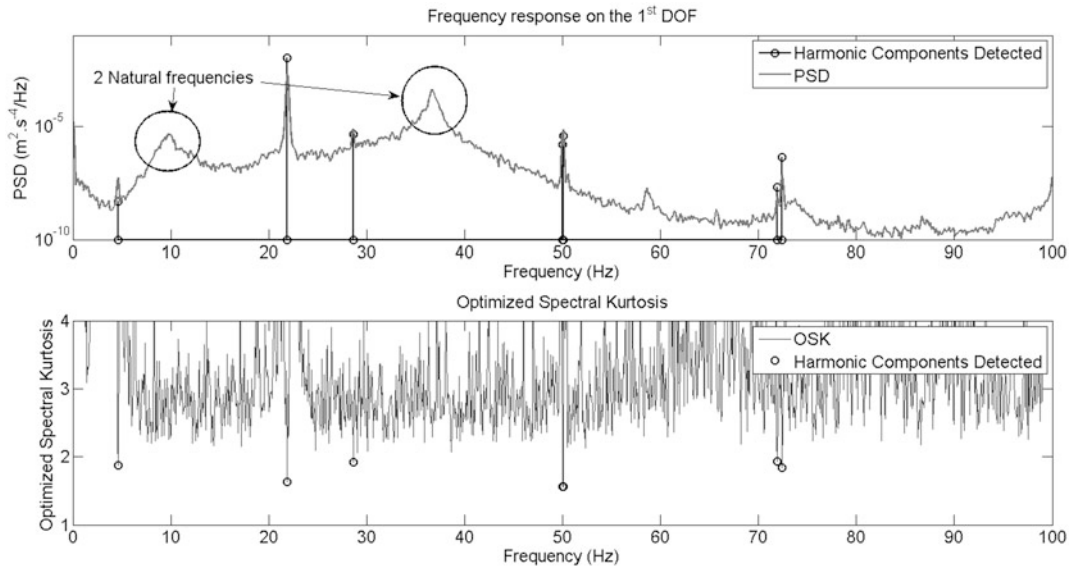
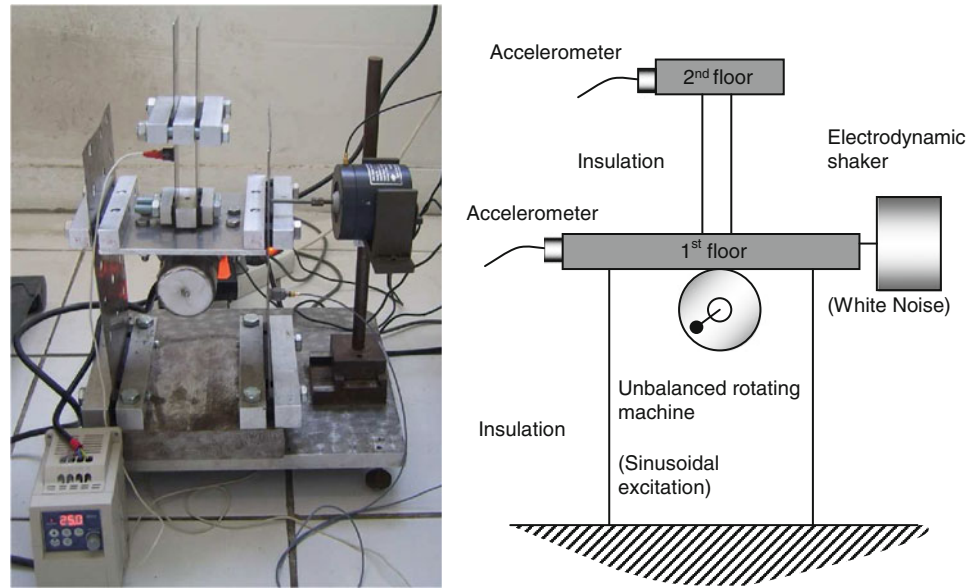


**Fig. 20.4** Detection of sinusoidal components using Spectral Kurtosis. One frequency expected but 5 frequencies detected [1]

### 20.2.2 Testing of the OSK on an Experimental Bench

In order to test the OSK and SEKF in a real experiment, a test bench is set up (Fig. 20.3). The experiment is composed of two masses insulated with flexible blades. The mechanical system can be described as a two DOF system in the bandwidth 0–100 Hz. The system natural frequencies are 9.7 and 36.7 Hz. The structure is simultaneously excited with a white noise by the electrodynamic shaker and an amplitude and frequency modulated signal thanks to an unbalanced rotating machine closed to 1,320 rpm (Fig. 20.3).

Figure 20.4 shows PSD and the OSK applied on a 131 s record of the accelerometer of the first floor with 262,144 ( $2^{18}$ ) samples. The sampling frequency is 2,000 Hz, the filter bandwidth is around 0.15 Hz, detection is defined for a Spectral Kurtosis lower than two. Detected sinusoidal components are highlighted with “o” markers on both graphs when the OSK is below two [1].

The results shown in Fig. 20.4 highlight expected observations. Frequency  $f_b = 22$  Hz is well detected as a sinusoidal component and not as a structural response. The corresponding OSK at 22 Hz is lower than two. Duly, both structural eigen

modes (9.7 and 36.7 Hz) are not identified as sinusoidal components. Nevertheless, other components, not initially foreseen, are identified as sinusoidal components: the electric network frequency  $f_r = 50$  Hz, a low frequency around 5 Hz and two frequencies:  $f_r - f_b = 28$  Hz and  $f_r + f_b = 72$  Hz.

These components are very small but are parts of the signal. The first one is due to the electric power frequency used for the electric motor. The last two are due to the magnitude modulation between the rotation frequency of the engine and its electric power frequency. These components are 100 to 100,000 times smaller than the main excitation at  $f_b = 22$  Hz.

Measurements have been realized with a piezoelectric accelerometer. Due to this technology, low frequencies are not studied in the present work (even if a 5 Hz component is detected).

The next step consists in removing these components from the original signal.

## 20.3 Tracking of Modulated Sinusoidal Components

The filtering of modulated sinusoidal components into a composite signal cannot be carried out by classical spectral analysis methods. ARMA filters [31] are not able to separate sinusoidal components and random noise into a same frequency bandwidth. Liftering techniques in cepstral analysis [32] and curve smoothing introduce important distortions in phase spectrum. Instantaneous phases of modulated signals should be accurately determined in order to be tracked. The Extended Kalman Filter has been retained for this purpose.

### 20.3.1 Discrete State Space Formulation of an Amplitude and Frequency Modulated Sinusoid

The goal of this paragraph is to derive a state space formulation which is relevant on a short time scale.

A sinusoid whose amplitude and frequency are modulated over time can be described in the complex domain as an analytic signal:

$$x(t) = a(t) \exp(j\phi(t)) \quad (20.9)$$

where  $a(t)$  is the instantaneous complex amplitude and  $\Phi(t)$  is the instantaneous phase. The discrete form of  $x(t)$  at the time step  $tn = n\Delta t$  is  $x_n = x(n\Delta t)$ . The complex variable  $x_n$  can be divided into its real and imaginary parts  $x_n = x_{1,n} + jx_{2,n}$ . A sinusoid that slightly varies over time can be approximated by:

$$x_n = a_n \exp(j(2\pi f_n n \Delta t)) \quad (20.10)$$

where  $f_n$  is the instantaneous frequency.

As the parameters  $f_n$  and  $a_n$  of the sinusoid slightly vary over time, they are almost equal between two consecutive time steps. Then a transition formulation can be given from  $x_n$  to  $x_{n+1}$ :

$$x_{n+1} \approx a_n \exp(j(2\pi f_n n \Delta t)) \times \exp(j(2\pi f_n \Delta t)) \quad (20.11)$$

This approximation is only true if modulations of  $a_n$  and  $f_n$  are slower than the period of the sinusoid. This constraint is assumed to be verified. Then a linear transition is obtained between the imaginary part  $x_{2,n}$  and real part  $x_{1,n}$  of  $x_n$  and  $x_{n+1}$ :

$$\begin{aligned} x_{1,n+1} &= x_{1,n} \cdot \cos(2\pi f_n \Delta t) - x_{2,n} \cdot \sin(2\pi f_n \Delta t) \\ x_{2,n+1} &= x_{1,n} \cdot \sin(2\pi f_n \Delta t) + x_{2,n} \cdot \cos(2\pi f_n \Delta t) \end{aligned} \quad (20.12)$$

or written in a matrix form

$$\begin{pmatrix} x_{1,n+1} \\ x_{2,n+1} \end{pmatrix} = \begin{bmatrix} \cos(2\pi f_n \Delta t) & -\sin(2\pi f_n \Delta t) \\ \sin(2\pi f_n \Delta t) & \cos(2\pi f_n \Delta t) \end{bmatrix} \begin{pmatrix} x_{1,n} \\ x_{2,n} \end{pmatrix} \quad (20.13)$$

The instantaneous amplitude  $a_n$  is given by

$$a_n = \sqrt{x_{1,n}^2 + x_{2,n}^2} \quad (20.14)$$

As  $a_n$  and  $f_n$  should be allowed to vary over time, it is proposed here to use the following non linear state space formulation:

$$X_{n+1} = \Phi(X_n) + W_n \quad (20.15)$$

where  $X_n = (x_{1,n} x_{2,n} x_{3,n})^T$  and  $W_n$ , the process noise. A state variable  $x_{3,n} = 2\pi f_n \Delta t$  was added to track the evolution of the instantaneous frequency  $f_n$ . The transition between two time steps is composed by a sum of two parts: the stationary part and the evolutionary part.

The stationary part links two successive points of a stationary sinusoid by  $\Phi(\cdot)$ . Then  $\Phi(\cdot)$  is assumed as the non-linear transition function and is given by  $\Phi(X_n) = F_n X_n$ :

$$\text{where } F_n = \begin{pmatrix} \cos(x_{3,n}) & -\sin(x_{3,n}) & 0 \\ \sin(x_{3,n}) & \cos(x_{3,n}) & 0 \\ 0 & 0 & 1 \end{pmatrix} \quad (20.16)$$

The two first components are related to the complex amplitude and are obtained by the previous linear relation. The third component  $x_{3,n+1} = x_{3,n}$  constrains the frequency not to change strongly between two time steps.

Up to now, the non-stationary behavior of the sinusoid was not modeled because it is not possible to express an exact equation for this evolution. We suppose that  $W_n$  is a random variable whose probability law is Gaussian:  $W_n = N(0, Q)$ , where  $Q$  is its variance matrix. Then the variations of amplitude and frequency are allowed by random values of  $W_n$ .

In a first glance, it could seem strange to choose a random variable for an effect which is generally deterministic. For instance, the variation of frequency excitation of an engine is mainly deterministic. Anyway, this state space does not need to represent accurately the evolution of a sinusoid on a long period, but only step by step. Then on a short time scale, a random evolution of  $a_n$  and  $f_n$  is enough to model a non-stationary sinusoid.

For a signal composed of  $M$  modulated sinusoidal components, the size of the state function is  $3M$ .

$$F_n(X_n) = \begin{bmatrix} \cos(x_{3,n}) & -\sin(x_{3,n}) & 0 & \dots & 0 & 0 & 0 \\ \sin(x_{3,n}) & \cos(x_{3,n}) & 0 & \dots & 0 & 0 & 0 \\ 0 & 0 & 1 & & 0 & 0 & 0 \\ \vdots & \vdots & & \ddots & 0 & 0 & 0 \\ 0 & 0 & 0 & \dots & \cos(x_{3+3(M-1),n}) & -\sin(x_{3+3(M-1),n}) & 0 \\ 0 & 0 & 0 & \dots & \sin(x_{3+3(M-1),n}) & \cos(x_{3+3(M-1),n}) & 0 \\ 0 & 0 & 0 & \dots & 0 & 0 & 1 \end{bmatrix} \quad \text{and } X_n = \begin{pmatrix} x_{1,n} \\ x_{2,n} \\ x_{3,n} \\ \vdots \\ x_{1+3(M-1),n} \\ x_{2+3(M-1),n} \\ x_{3+3(M-1),n} \end{pmatrix} \quad (20.17)$$

This state space formulation is non linear: the transition function  $\Phi(X_n)$  is varying over time and depends on the frequency modulation.

In reality, only the real part  $x_{1,n}$  of the analytic signal  $x_n$  can be observed. Unlike the transition phase, the observation phase is completely linear

$$\begin{aligned} Z_n &= [1 \ 0 \ 0] X_n + V_n \\ Z_n &= x_{1,n} + V_n \end{aligned} \quad (20.18)$$

for one sinusoid and slightly more complex for  $M$  sinusoids

$$\begin{aligned} Z_n &= [1 \ 0 \ 0 \ \dots \ 1 \ 0 \ 0] X_n + V_n \\ Z_n &= x_{1,n} + \dots + x_{1+3(M-1),n} + V_n \end{aligned} \quad (20.19)$$

where  $V_n$  is a noise observation random process.

Finally, a nonlinear discrete state space model has been derived to model the transition and observation of sinusoid components mixed with random processes

$$\begin{cases} X_{n+1} = \Phi(X_n) + W_n \\ Z_{n+1} = H X_{n+1} + V_{n+1} \end{cases} \quad (20.20)$$

where  $\Phi(\cdot)$  is the nonlinear transition function given by  $\Phi(X_n) = F(X_n) X_n$  and  $H(\cdot)$  is the observation matrix given by:

$$H = [1 \ 0 \ 0 \ \dots \ 1 \ 0 \ 0]. \quad (20.21)$$

### 20.3.2 Application to the Extended Kalman Filter

Kalman filtering refers to a family of algorithms that track the temporal evolution of a dynamic model based on noised measurements:

$$\begin{cases} X_{n+1} = f(X_n, W_n) \\ Z_{n+1} = h(X_{n+1}, V_{n+1}) \end{cases} \quad (20.22)$$

described here in the discrete time domain. An efficient solution in terms of means and covariances can be derived when  $f(\cdot)$  and  $h(\cdot)$  are linear. Indeed it estimates the state probability distribution by its two first moments. Unfortunately, they are no longer sufficient to characterize the distribution in the nonlinear case. Then some approximations have to be done in order to find a practical solution.

The extended Kalman filtering is an extension of the classical Kalman filtering to problems with state dynamics governed by nonlinear state transformations. Although it is not required here, it should be noticed that it can also handle a nonlinear transformation from state variables to measurement variables. It generally exhibits a good robustness because it uses linear approximation over small ranges of state space. Without any input control, the state model is defined by the first equation in system (20.22) where  $W_n$  is the process noise assumed to be Gaussian with zero mean with a variance matrix  $Q$ . The observation model is described by the second equation in system (20.22) where  $HX_{n+1}$  is the observation function and  $V_{n+1}$  the observation noise assumed to be Gaussian and zero mean with a variance  $R$ . State and observation noises are assumed to be uncorrelated. The Extended Kalman Filter [2] is defined using predict and update phases. The predict phase gives an a priori estimate of the state and covariance based on previous time step  $t_n$ :

$$\text{Predicted state } \hat{X}_{n+1|n} = \hat{F}_{n|n} \hat{X}_{n|n} \quad (20.23)$$

$$\text{Predicted estimated covariance } \hat{P}_{n+1|n} = \tilde{F}_{n|n} \hat{P}_{n|n} \tilde{F}_{n|n}^T + Q \quad (20.24)$$

And the update phase corrects the deviation of these estimations based on new observation at time step  $t_{n+1}$ :

$$\text{Innovation } \tilde{Y}_{n+1|n} = Z_{n+1} - H \hat{X}_{n+1|n} \quad (20.25)$$

$$\text{Innovation covariance } S_{n+1} = H \hat{P}_{n+1|n} H^T + R \quad (20.26)$$

$$\text{Kalman gain } K_{n+1} = \hat{P}_{n+1|n} H^T (S_{n+1})^{-1} \quad (20.27)$$

$$\text{Updated state estimate } \hat{X}_{n+1|n+1} = \hat{X}_{n+1|n} + K_{n+1} \tilde{Y}_{n+1|n} \quad (20.28)$$

$$\text{Updated estimate covariance } \hat{P}_{n+1|n+1} = (I - K_{n+1} H) \hat{P}_{n+1|n} \quad (20.29)$$

As the transition function  $\Phi$  is non-linear but differentiable, it is well locally approximated thanks to its

$$\text{Jacobian : } \tilde{F}_{n|n} = \left( \nabla_X (F(X) X)^T \right) \Big|_{X=\hat{X}_{n|n}} \quad (20.30)$$

In the case of  $M$  modulated components, the first order derivative is required:

$$\nabla X_n = \left( \frac{\partial}{\partial X_{1,n}} \frac{\partial}{\partial X_{2,n}} \cdots \frac{\partial}{\partial X_{3M-1,n}} \frac{\partial}{\partial X_{3M,n}} \right)^T \quad (20.31)$$

and the approximation becomes a banded block matrix:

$$\tilde{F}_n = \begin{bmatrix} \tilde{F}_{n,1} & 0 & \dots & 0 \\ 0 & \tilde{F}_{n,2} & \ddots & \vdots \\ \vdots & \ddots & \ddots & 0 \\ 0 & \dots & 0 & \tilde{F}_{n,M} \end{bmatrix} \quad (20.32)$$

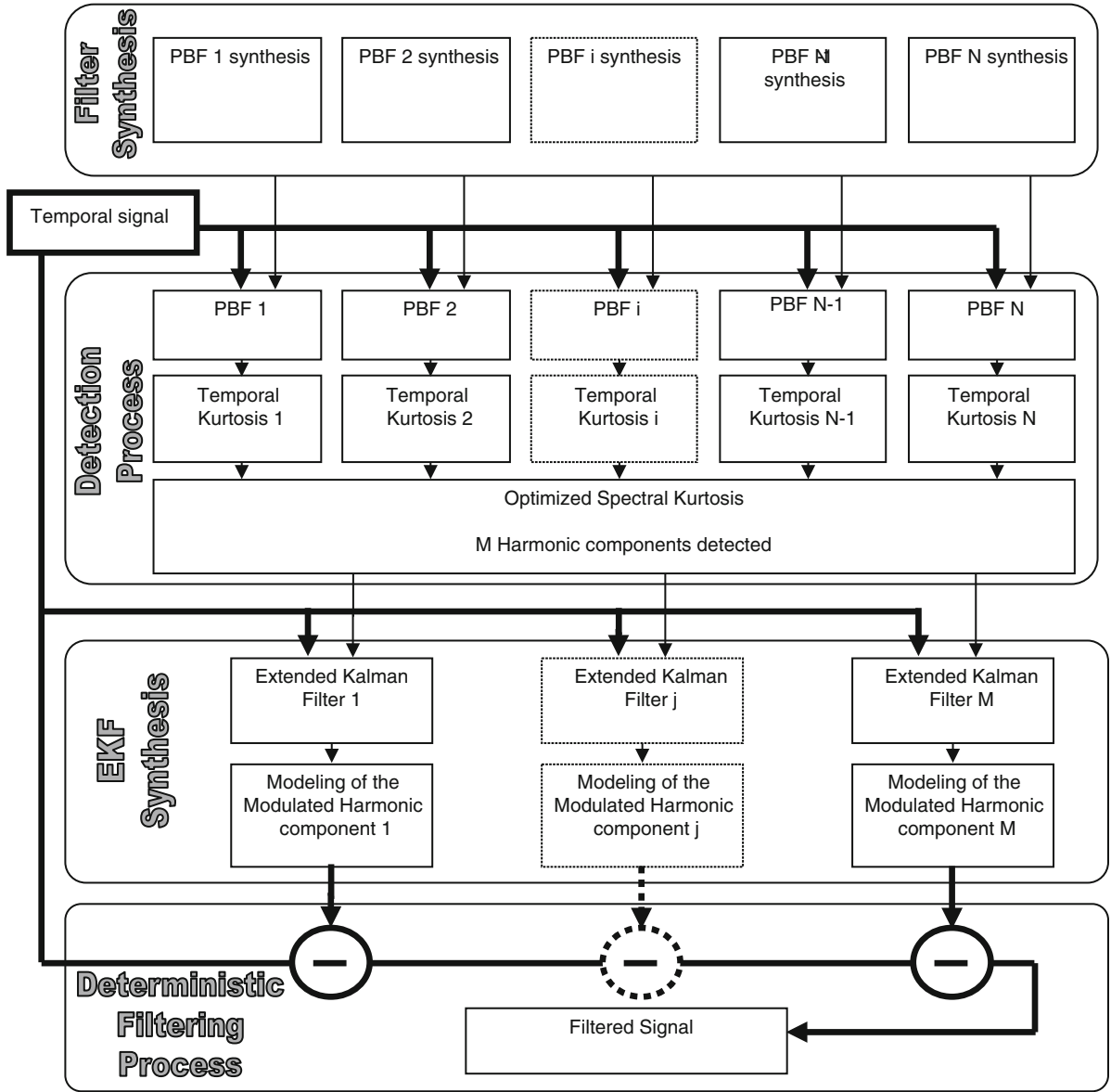


**Fig. 20.5** Block diagram of the method. Four main steps in filtering process: filter synthesis ( $N$  filters computed off line), sinusoidal components detection with OSK (real time or post-process of  $M$  components), Extended Kalman filtering (real time or post-process of  $M$  Kalman filters), filtering process (real time or post-process of  $M$  modulated sinusoids)

where an elementary block is given by

$$\tilde{F}_{n,i} = \begin{bmatrix} \cos(\hat{x}_{3i,n}) & -\sin(\hat{x}_{3i,n}) & -\hat{x}_{1+3(i-1),n} \sin(\hat{x}_{3i,n}) & -\hat{x}_{2+3(i-1),n} \cos(\hat{x}_{3i,n}) \\ \sin(\hat{x}_{3i,n}) & \cos(\hat{x}_{3i,n}) & \hat{x}_{1+3(i-1),n} \cos(\hat{x}_{3i,n}) & -\hat{x}_{2+3(i-1),n} \sin(\hat{x}_{3i,n}) \\ 0 & 0 & & 1 \end{bmatrix} \quad (20.33)$$

This state matrix is composed of  $3M$  equations which could be described as  $M$  independent systems of 3 equations. The complete EKF can be expanded in a series of  $M$  elementary EKM which could be computed in a same step or in  $M$  independent steps. This point of view allows parallel computation of all EKM cells. The complete process is described in the block diagram in next section, Fig. 20.5.

## 20.4 OSK and SEKF in Operation

In this section, the aim is to propose a method for the filtering process of experimental signals as described in the block diagram (Fig. 20.5).

The filtering process consists in removing detected and tracked sinusoidal components. The efficiency of the method is due to the fact that the OSK allows an accurate initialization of the SEKF. The combination of OSK and SEKF techniques could be performed into two different ways for real time computation or for post-processing computation. These two ways are illustrated in Fig. 20.6.

In order to test the method, the previous Series of EKF have been applied on signals obtained with the test bench described in Sects. 20.2.1 and 20.2.2. Previous results obtained in Sect. 20.2.3 have highlighted 4 modulated components. The tracking of two of them is presented in this section. The first frequency (22 Hz) corresponds to the rotation of the engine and is amplitude and frequency modulated. The second frequency corresponds to the electric power frequency (50 Hz) and is only amplitude modulated.

### 20.4.1 Initializing the Series of Extended Kalman Filters

An important step for EKF is the estimation of initial parameters conditions. The first unknown parameter is the suitable size of the SEKF. In a second step, for each EKF, several parameters and their variances have to be estimated. The efficiency of the filtering process strongly depends on the quality of estimated initial parameters.

For each EKF, the initial values of nine parameters have to be set:

- Three parameters used for the sinusoidal component modeling,
- Three parameters variances (one per parameter),
- Three process noise variances (one per parameter).

The observation noise variance is defined for the complete SEKF.

For the proposed filtering method based on a SEKF composed of  $M$  EKF,  $9M + 2$  initial conditions have to be estimated. The very first parameter is the number  $M$  of EKF. This parameter is defined by the OSK and equal to the number of narrow bandwidths in which detection occurs. The second one is the observation noise variance. The three parameters used to define each sinusoidal component depends on the amplitude, the frequency and the phase of this component.

The estimated amplitude  $\tilde{A}_j$  of the  $j$ th detected component is determined from the DSP  $\hat{\gamma}_k$  or the FFT  $\hat{s}_k$  results:

$$\tilde{A}_j \simeq 2 \underset{k|f_j=f_k}{\hat{s}} \simeq \sqrt{\Delta f \underset{k|f_j=f_k}{\hat{\gamma}}} \tag{20.34}$$

These two estimators overestimate the actual value of  $A$ . The higher the frequency is modulated, the larger the overestimation.

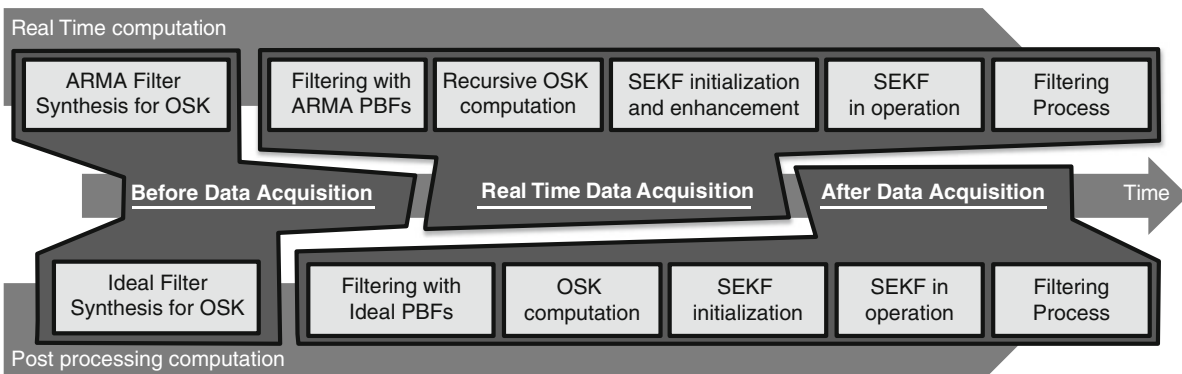


**Fig. 20.6** Chronogram of the 2 different ways for combining and computing OSK and SEKF: for real time computation and for post processing computation

The estimated frequency  $\tilde{f}_j$  is determined from the OSK and equal to the center frequency  $f_k$  of the narrow bandwidth  $\Delta f_j$  in which the detection occurs.

The phase is not estimated and always set in the present method to 0. This lack of estimation is quickly vanished by the specific efficiency of the Kalman Method for this kind of parameter [17].

The  $j$ th sinusoidal component modeling is also estimated:

$$\begin{cases} x_{1+3(j-1),0} = \tilde{A}_j \\ x_{2+3(j-1),0} = 0 \\ x_{3+3(j-1),0} = \Delta t 2\pi f_j \end{cases} \quad (20.35)$$

Due to the statistical properties of sinus functions, the estimated variances  $\tilde{\sigma}_{1+3(j-1)}^2, \tilde{\sigma}_{2+3(j-1)}^2$  of the first two parameters are:

$$\begin{cases} P_{1+3(j-1),0} = \sigma_{1+3(j-1),0}^2 = \frac{1}{2} \tilde{A}_j^2 \\ P_{2+3(j-1),0} = \sigma_{2+3(j-1),0}^2 = \frac{1}{2} \tilde{A}_j^2 \end{cases} \quad (20.36)$$

These estimators underestimate actual variances. The larger the amplitude modulation, the bigger the variance underestimation. For robustness reasons in numerical applications, these parameters are chosen four times bigger.

The estimation of the third variance  $\tilde{\sigma}_{3+3(j-1)}^2$  is based on the bandwidth  $\Delta f_j$  in which the detection  $j$  occurs:

$$P_{3+3(j-1),0} = \sigma_{3+3(j-1),0}^2 = (2\pi \Delta f_j \Delta t)^2 \quad (20.37)$$

The two first process noise variances  $Q_{1+3(j-1)}$  and  $Q_{2+3(j-1)}$  tend to zero since the modeling of amplitude modulated component is linear. The third process noise variance deals with the frequency modulation and depends on the ‘‘velocity’’ of the frequency modulation. The chosen estimation is:

$$Q_{3+3(j-1)} = \left( \frac{2\pi \Delta f_j \Delta t}{f_j T} \right)^2 \quad (20.38)$$

This approximation can be seen as a linear frequency evolution along  $\Delta f_j$  during the observation time  $T$ .

The observation noise variance  $R$  is simply chosen equal to the observed signal variance. This approximation is relevant as long as the studied signal is mainly stochastic, i.e. the energy of sinusoid components is weak compared to the total energy of the signal.

#### 20.4.2 Numerical Results and Filtering Efficiency

The SEKF was performed on the previous experiment with two tracked sinusoids previously detected by the OSK. The first component is around 22 Hz and the second around 50 Hz. For each component, the amplitude modulation is determined with the instantaneous amplitude:

$$a_n = \sqrt{x_{1,n}^2 + x_{2,n}^2} \quad (20.39)$$

This amplitude could also be obtained by the complex analytic signal composed of the observed signal (real part) and its Hilbert transform (imaginary part).

The frequency modulation is determined by the instantaneous frequency:

$$f_n = \frac{x_{3,n}}{2\pi \Delta t} \quad (20.40)$$

The SEKF provides an analytic signal  $\{x_{1,n}, x_{2,n}\}$  per sinusoid from the original signal. Thus one tracked signal is obtained per sinusoid. Spectral amplitudes of these tracked signals show the main components at 22 and 50 Hz and lateral modulated bands (Fig. 20.7).

The first tracked signal concerns the effect of engine rotation. It is characterized by its frequency and amplitude modulations. As it can be observed on the Fig. 20.8, its instantaneous frequency fluctuates between 21.8 and 22 Hz.

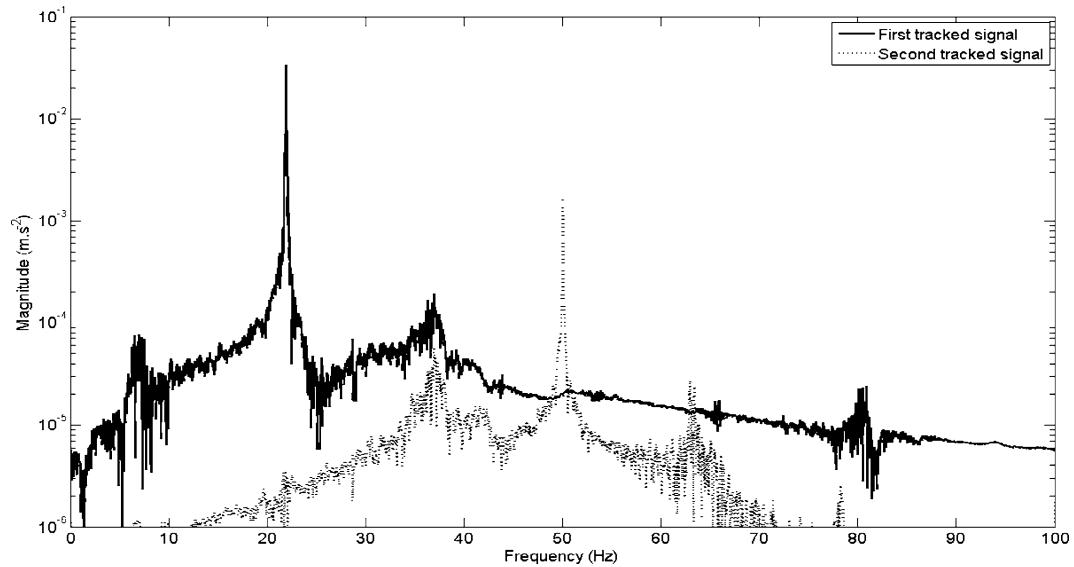


**Fig. 20.7** Spectrums of two tracked signals. Symmetric lateral bands are due to modulation effects on spectrums

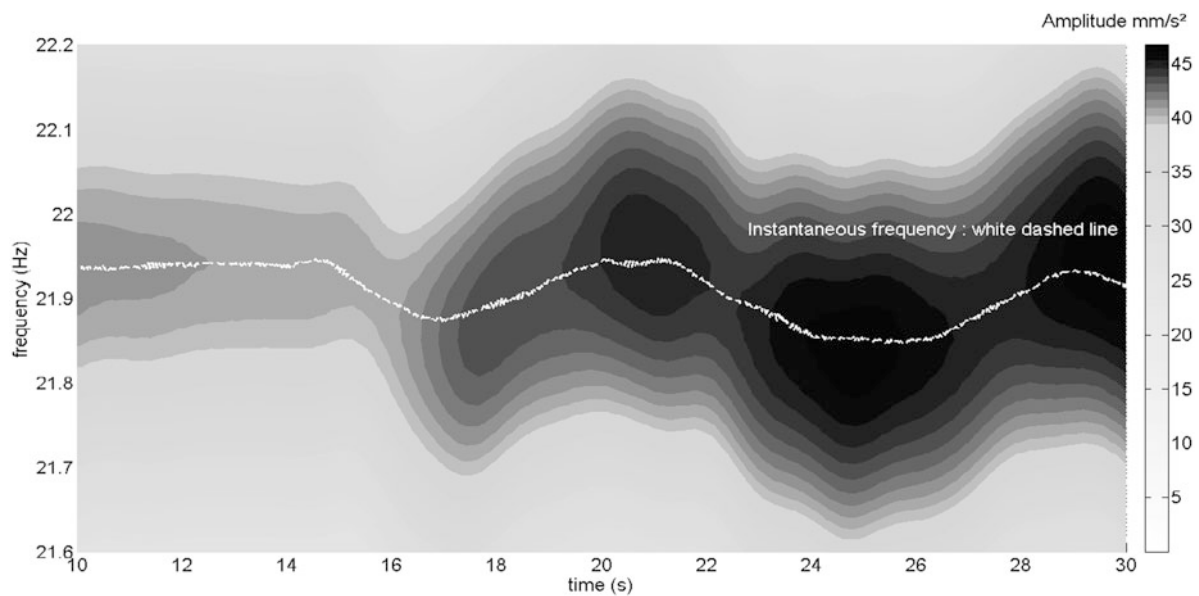


**Fig. 20.8** Time-frequency representation of the first tracked signal. Magnitude and frequency modulation are identified with a good accuracy (instantaneous frequency is identified with 4 significant digits)

The second tracked signal is due to the electrical network and is only amplitude-modulated. This property could have been foreseen since the 50 Hz due to the network is absolutely stable in frequency.

The very last step, the effective filtering process, is simply realized in removing the tracked signals from the initial signal in the time domain. Figure 20.9 shows spectral amplitudes before and after the filtering process and for two tracked components (22 and 50 Hz). Although the filtering process removes the 50 Hz component with efficiency, it does not show the same behaviour on the 22 Hz component. This lower efficiency could be explained by the frequency evolution of 22 Hz which makes the tracking harder. However, this component is twenty times lower after the filtering process, which is still a significant improvement.



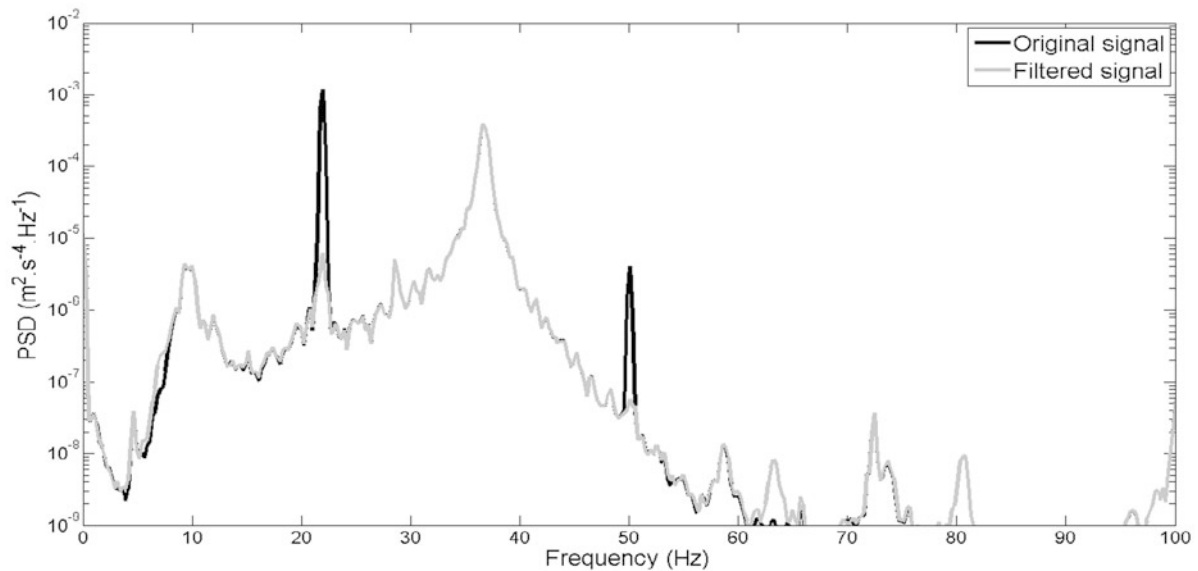


**Fig. 20.9** Spectrums before and after the filtering process. The two modulated sinusoidal components are successfully removed

## 20.5 Conclusion

An important difficulty in the application of Kalman filters is the initialization of state variables and variances. The most important rule of the OSK is to initialize the computation of SEKF. The combination of the Optimized Spectral Kurtosis and Series of Extended Kalman Filters allows a robust computational technique in tracking sinusoidal components. The filtering process can be performed during or after the real time data acquisition. The complete signal filtering can be performed automatically, even if the size of the SEKF is defined by the OSK. Inside the limits of our numerical and experimental tests, the combination of OSK and SEKF allows a robust and efficient way for removing modulated sinusoidal components in signals. The tested method is limited by the frequency modulation rate. Those limits are a new challenge for our work in progress, especially for non smooth non linear systems.

## References

1. Dion J-L, Tawfiq I, Chevallier G (2012) Sinusoidal component detection: Optimized Spectral Kurtosis for operational modal analysis. *Mech Syst Signal Process* 26:24–33
2. Kalman RE (1960) A new approach to linear filtering and prediction problems. *Trans Am Soc Mech Eng Ser D – J Basic Eng* 82:35–45
3. Seibold S, Weinert K (1996) A time domain method for the localization of cracks in rotors. *J Sound Vib* 195:57–73
4. Wang Z, Yan W, Shao Y (2009) Three-step method for stiffness identification of inter-story shearing structures under ambient excitation. *Tsinghua Sci Technol* 14:69–74
5. Ma C-K, Lin D-C, Chang J-M (1999) Estimation of forces generated by a machine mounted upon isolators under operating conditions. *J Frankl Inst* 336:875–892
6. Ma C-K, Ho C-C (2004) An inverse method for the estimation of input forces acting on non-linear structural systems. *J Sound Vib* 275:953–971
7. Zhan YM, Jardine AKS (2005) Adaptive autoregressive modeling of non-stationary vibration signals under distinct gear states. Part 1: modeling. *J Sound Vib* 286:429–450
8. Zhan Y, Mechefske CK (2007) Robust detection of gearbox deterioration using compromised autoregressive modeling and Kolmogorov–Smirnov test statistic. Part I: compromised autoregressive modeling with the aid of hypothesis tests and simulation analysis. *Mech Syst Signal Process* 21:1953–1982
9. Zhan Y, Mechefske CK (2007) Robust detection of gearbox deterioration using compromised autoregressive modeling and Kolmogorov–Smirnov test statistic. Part II: experiment and application. *Mech Syst Signal Process* 21:1983–2011
10. Shao Y, Mechefske CK (2009) Gearbox vibration monitoring using extended Kalman filters and hypothesis tests. *J Sound Vib* 325:629–648
11. Wang G, Luo Z, Qin X, Leng Y, Wang T (2008) Fault identification and classification of rolling element bearing based on time-varying autoregressive spectrum. *Mech Syst Signal Process* 22:934–947
12. Al-Zaharah IT (2006) Suppressing vibrations of machining processes in both feed and radial directions using an optimal control strategy: the case of interrupted cutting. *J Mater Process Technol* 172:305–310

13. Dong X-J, Meng G, Peng J-C (2006) Vibration control of piezoelectric smart structures based on system identification technique: numerical simulation and experimental study. *J Sound Vib* 297:680–693
14. Marzbanrad J, Ahmadi G, Zohoor H, Hojjat Y (2004) Stochastic optimal preview control of a vehicle suspension. *J Sound Vib* 275:973–990
15. Yoshimura T, Edokoro K, Ananthanarayana N (1993) An active suspension model For rail/vehicle systems with preview and stochastic optimal control. *J Sound Vib* 166:507–519
16. Bai M, Huang J, Hong M, Su F (2005) Fault diagnosis of rotating machinery using an intelligent order tracking system. *J Sound Vib* 280: 699–718
17. Blough JR (2003) Development and analysis of time variant discrete Fourier transform order tracking. *Mech Syst Signal Process* 17:1185–1199
18. Guo Y, Tan KK (2009) Order-crossing removal in Gabor order tracking by independent component analysis. *J Sound Vib* 325:471–488
19. Pan M-C, Chiu C-C (2006) Investigation on improved Gabor order tracking technique and its applications. *J Sound Vib* 295:810–826
20. Pan M-C, Liao S-W, Chiu C-C (2007) Improvement on Gabor order tracking and objective comparison with Vold–Kalman filtering order tracking. *Mech Syst Signal Process* 21:653–667
21. Vold H, Leuridan J (1993) High resolution order tracking at extreme slew rates, using Kalman tracking filters SAE Paper No. 931288
22. Vold H, Herlufsen H (1997) Multi axle order tracking with the Vold–Kalman tracking filter *Sound Vib* 31(5):30–34
23. Guo Y, Tan KK (2010) High efficient crossing-order decoupling in Vold–Kalman filtering order tracking based on independent component analysis. *Mech Syst Signal Process* 24:1756–1766
24. Pan M-C, Lin Y-F (2006a) Further exploration of Vold–Kalman-filtering order tracking with shaft-speed information–I: theoretical part, numerical implementation and parameter investigations. *Mech Syst Signal Process* 20:1134–1154
25. Pan M-C, Lin Y-F (2006b) Further exploration of Vold–Kalman-filtering order tracking with shaft-speed information–II: engineering applications. *Mech Syst Signal Process* 20:1410–1428
26. Pan M-C, Wu C-X (2007) Adaptive Vold–Kalman filtering order tracking. *Mech Syst Signal Process* 21:2957–2969
27. Wang KS, Heyns PS (2011a) An empirical re-sampling method on intrinsic mode function to deal with speed variation in machine fault diagnostics. *Appl Soft Comput* 11:5015–5027
28. Wang KS, Heyns PS (2011b) The combined use of order tracking techniques for enhanced Fourier analysis of order components. *Mech Syst Signal Process* 25:803–811
29. Wang KS, Heyns PS (2011c) Application of computed order tracking, Vold–Kalman filtering and EMD in rotating machine vibration. *Mech Syst Signal Process* 25:416–430
30. Pan M-C, Wu C-X (2010) Extended angular-velocity Vold–Kalman order tracking. *J Dyn Syst Meas Control* 132(3) doi:10.1115/1.4001326
31. Parks TW, Burrus CS (1987) Digital filter design. Wiley, New York. Chapter 7
32. Randall RB (2001) Cepstrum analysis. In: Ewins D, Rao SS, Braun S (eds) *Encyclopedia of vibration*. Elsevier, Oxford, pp 216–227

# Chapter 21

## Vibration Reduction of Brush Cutter

Nobuyuki Okubo, Hiroyuki Nakagawa, Kohei Furuya, and Takeshi Toi

**Abstract** Brush cutter powered by engine has been widely used on a daily basis for mowing of road shoulders and gardens. People who regularly operate brush cutter are at risk of developing Raynaud's disease due to large vibration. Such vibration disorder can be prevented by reducing the handle vibration by good use of structural modification. In this study we focused on rubber bushes which support the drive shaft in pipe to transmit the engine power to the cutting blade. First the dynamic characteristics of the brush cutter such as Operational Deflection Shape are grasped and then the hardness and the placement of rubber bushes are optimized to reduce the handle vibration effectively.

**Keywords** Brush cutter • Vibration reduction • Rubber bush • Structural modification • Engine rotation

### 21.1 Introduction

The brush cutter powered by an engine is a widely used agricultural machine for not only forest operation but also mowing of road shoulders and gardens on a daily basis. However people who regularly operate brush cutter are at risk of developing Raynaud's disease due to large vibration and consequently the working hours are restricted by law [1]. Recently the law is revised to suppress the working hours according to the vibration acceleration level of the machine [2]. Since the less vibration at handle the longer working hours can be allowed, more vibration reduction is strongly demanded.

The vibration of brush cutter under operating condition is generated at the frequency of engine rpm together with higher harmonics independently to the vibration characteristic of the brush cutter, namely the forced vibration due to engine rpm different from its natural frequency. Therefore in order to reduce the vibration under operating condition, the dominant natural frequency and associated mode shape which contribute significantly should be found.

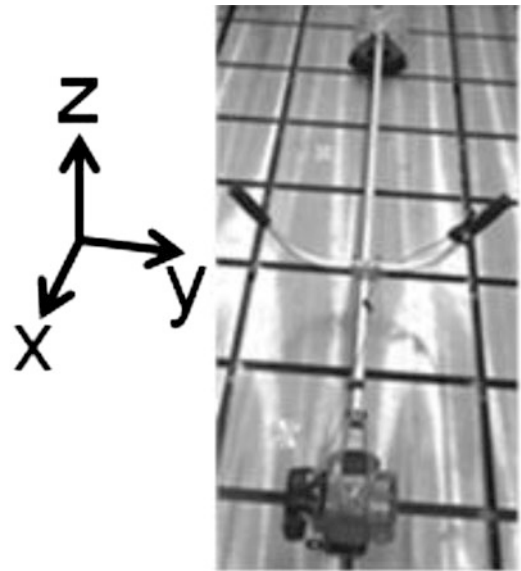
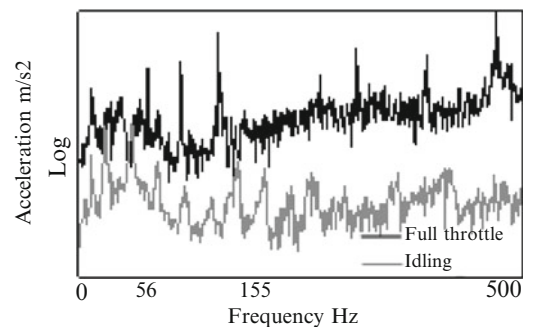
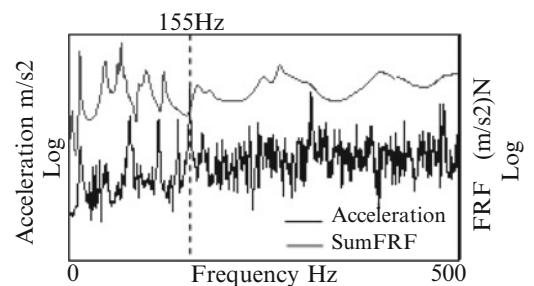
In this paper, first the dynamic characteristics of the brush cutter are grasped and then the contribution of each mode to Operational Deflection Shape (hereafter denoted as ODS) is analyzed to focus the attention for appropriate structural modification [3]. The rubber bushes which support the drive shaft in the pipe to transmit the engine rotation to the cutting blade is dealt with for optimized vibration reduction.

### 21.2 Dynamic Characteristics of Brush Cutter

The measurement of ODS and Frequency Response Function (hereafter denoted as FRF) are carried out and then the vibration evaluation is conducted to find out the specific frequency to improve. Finally the most contributing mode is taken into account to discuss the structural modification.

---

N. Okubo (✉) • H. Nakagawa • K. Furuya • T. Toi  
CAMAL, Chuo University, 1-13-27 Kasuga, Bunkyo-ku, Tokyo, Japan 112-8551  
e-mail: [okubo@mech.chuo-u.ac.jp](mailto:okubo@mech.chuo-u.ac.jp); [furuya@gifu-u.ac.jp](mailto:furuya@gifu-u.ac.jp); [toi@mech.chuo-u.ac.jp](mailto:toi@mech.chuo-u.ac.jp)

**Fig. 21.1** Brush cutter**Fig. 21.2** Measurement of operational vibration**Fig. 21.3** Relation between the acceleration and the summed FRF

### 21.2.1 Measurement of ODS and FRF

Figure 21.1 shows the brush cutter under consideration. The measurement of ODS of the brush cutter is carried out under full throttle (9,300rpm) and idling (3360rpm) operation in free-free boundary supported by flexible ropes. The typical acceleration measured is shown in Fig. 21.2 where several peaks are observed. The first order of engine rotation corresponds to 155 Hz under full throttle and 56 Hz under idling respectively and these are clearly observed together with the harmonic orders, which indicates the forced vibration by engine rotation. The idling vibration is much less than the full throttle and therefore only full throttle is taken into account in this study.

Then the modal testing is conducted where an impact hammer is used for excitation in z direction and three axis acceleration pickups are used for response vibration under the same free-free boundary condition. Figure 21.3 shows the relation between the acceleration under full throttle and the summed FRF, where the peaks at the first order of engine rotation, namely 155 Hz together with harmonic orders are dominant and do not match the natural frequencies that confirms the forced vibration by engine rotation.

**Fig. 21.4** Input signal

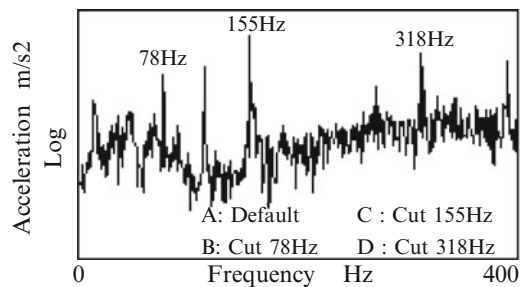
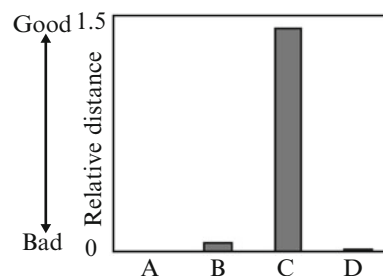


**Fig. 21.5** Setup for vibration evaluation



**Fig. 21.6** Relative distance



### 21.2.2 Vibration Evaluation

Under full throttle operation the acceleration at the first order of engine rotation, namely 155 Hz is the largest but the human feeling of unpleasant is depend on the frequency and so the vibration evaluation is conducted as follows.

As indicated in Fig. 21.4, four patterns are edited: pattern A is the original, pattern B 78 Hz component is cut, pattern C 155 Hz and pattern D 318 Hz respectively. The set up for vibration evaluation is shown in Fig. 21.5, where the handle is gripped tightly by the jury and the electromagnetic exciter provides the vibration pattern A to D and then the jury answers “Which is less vibration?” for the paired comparison.

The result of vibration evaluation is shown in Fig. 21.6 where the relative distance from the original A is indicated. It can be seen that pattern C where 155 Hz component is cut is evaluated the most improved pleasant compared with the original.

### 21.2.3 Mode Contribution

The ODS is consisted of linear combination of individual mode shape with associated the modal contribution coefficient. Therefore once the ODS of the brush cutter is measured and the natural frequencies and the mode shapes are detected by FRF, the mode contribution coefficient can be determined as,

$$\gamma_i(\omega) = (\phi_i^T \phi_i)^{-1} \phi_i^T x(\omega) \tag{21.1}$$

where  $\gamma_i(\omega)$  is the  $i$ th mode contribution coefficient,  $\phi_i$   $i$ th mode shape,  $x(\omega)$  ODS and  $\omega$  the specific frequency, in this case 155 Hz.

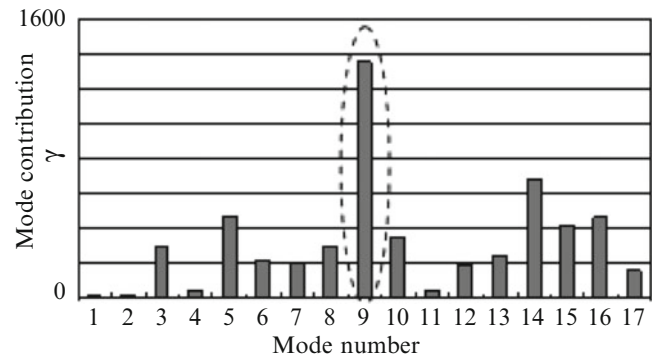
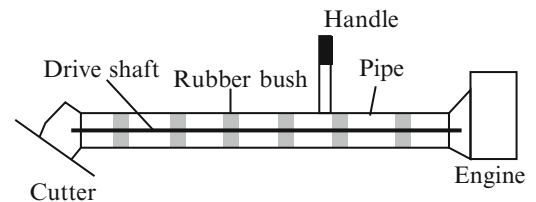
**Fig. 21.7** Mode contribution**Fig. 21.8** Structure of brush cutter

Figure 21.7 shows the result of the mode contribution coefficient and 9th mode at 166 Hz is found the most contributing mode that should be modified to achieve the vibration reduction of the brush cutter.

## 21.3 Dynamic Characteristic of Brush Cutter

As the target of structural modification, the rubber bush is focused and therefore the modeling of the rubber bush and also the brush cutter are conducted as follows.

### 21.3.1 Structure of the Brush Cutter

Figure 21.8 shows the structure of the brush cutter under consideration, which is consisted of engine, cutter, pipe, handle and so on. In the pipe, the drive shaft which transmits the engine rotation to the cutter blade rotation is supported by six rubber bushes, usually placed in even interval. It is easy to change the hardness and the placement of the rubber bushes and therefore in order to reduce the vibration, these are the design variable of the structural modification.

### 21.3.2 Rubber Bush Hardness

Figure 21.9 shows the rubber bush used in the brush cutter which is forced into the pipe and stayed by its friction between the rubber bush and the pipe. The hardness number of rubber bush is available, #30, #40, #50, #60, #70 and #80 in order to soft, that #30 is the softest. The standard is #60.

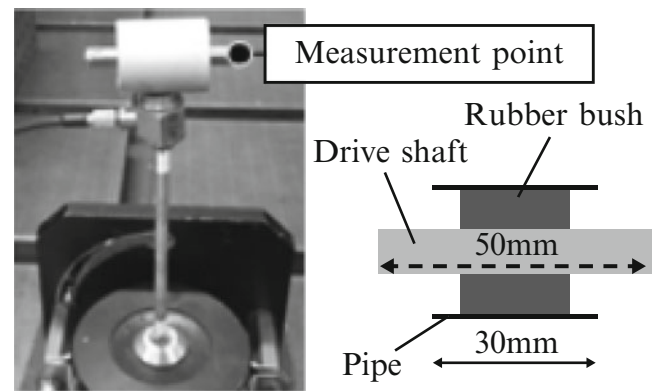
In order to determine the vibration property of the rubber bush, the measurement is carried out as shown in Fig. 21.10 where one rubber bush is forced into a 30 mm length pipe with a 50 mm length drive shaft. The outside of the pipe is excited by an electromagnetic exciter with burst random signal and a small acceleration pickup is used to measure the response.

Table 21.1 indicates the first natural frequency measured with respect to the hardness number and the larger number the higher natural frequency is observed.

**Fig. 21.9** Rubber bush



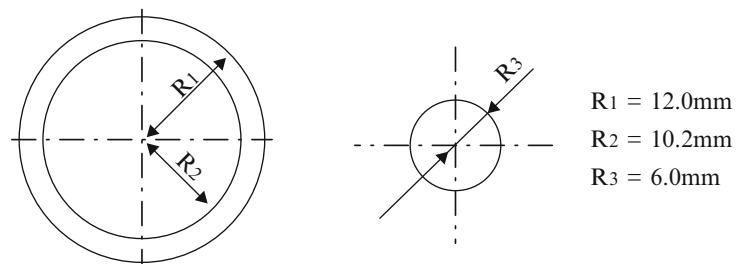
**Fig. 21.10** Setup to measure rubber bush vibration property



**Table 21.1** Natural frequency (experiment)

Hardness	Natural frequency (Hz)
30	1,231
40	1,641
50	2,308
60	2,340
70	2,851
80	2,902

**Fig. 21.11** Cross-section shape



### 21.3.3 Rubber Bush Modeling

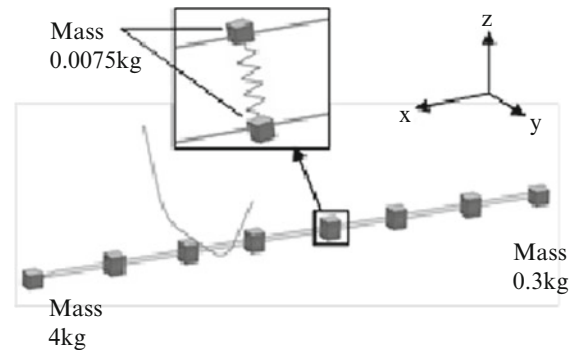
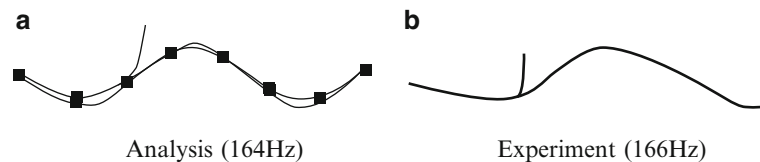
The rubber bush can be modeled by a scalar spring while the pipe and the drive shaft by a simple beam element. The mass of rubber bush is divided half and added to the pipe and the drive shaft connected. Figure 21.11 shows the cross section of the pipe and the drive shaft and Table 21.2 indicates the material properties. By use of these data and the measured first natural frequency, the spring constant of each rubber bush is determined as indicated in Table 21.3 together with calculated natural frequency which agrees well.

**Table 21.2** Material properties

	Density (kg/m <sup>3</sup> )	Young's modulus (GPa)	Poisson's ratio ( <i>ν</i> )
Pipe	2,300	57.5	0.330
Drive shaft	7,400	220.0	0.288

**Table 21.3** Spring constant and natural frequency

Hardness	Spring constant (m/N)	Natural frequency (Hz)
30	5.0E + 05	1,256
40	9.0E + 05	1,682
50	1.7E + 06	2,300
60	1.8E + 06	2,366
70	2.6E + 06	2,829
80	2.7E + 06	2,881

**Fig. 21.12** FEM**Fig. 21.13** Comparison of mode shapes

### 21.3.4 Brush Cutter Modeling

The total brush cutter FE modeling is shown in Fig. 21.12 where the handle is expressed by beam element and the engine and the cutting blade by lumped mass 4 and 0.3 kg connected rigidly. Based on this model the target mode is calculated as shown in Fig. 21.13 which shows a good agreement compared with measured natural frequency and mode shape

## 21.4 Structural Modification

In this study two structural modifications on rubber bush: hardness and placement are taken into consideration based on FE model of the brush cutter mentioned above and verified by experiments.

### 21.4.1 Rubber Bush Hardness Optimization

The hardness of six rubber bushes which are evenly spaced is so optimized as to realize the minimum of the largest FRF value for the frequency range of interest in this case between 130 and 190 Hz based on the identified FE model shown in Fig. 21.14, where the reference point is at engine and the response point at handle. The hardness of six rubber bushes, K1–K6 can be modified in the range of #30 to #80 corresponding to identified spring constant as described above.

The final result of optimization is shown in Table 21.4 and Fig. 21.15 shows the FRF comparison of before and after the optimization. Although slight the vibration can be reduced in the frequency range.



**Fig. 21.14** FEM for optimization

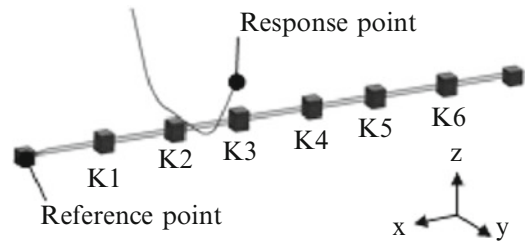


**Table 21.4** Corresponding hardness

Spring	Spring constant (m/N)	Hardness
K1	5.0E + 05	30
K2	5.0E + 05	30
K3	2.7E + 06	80
K4	2.7E + 06	80
K5	2.7E + 06	80
K6	2.7E + 06	80

**Fig. 21.15** FRF of the stiffness optimized model

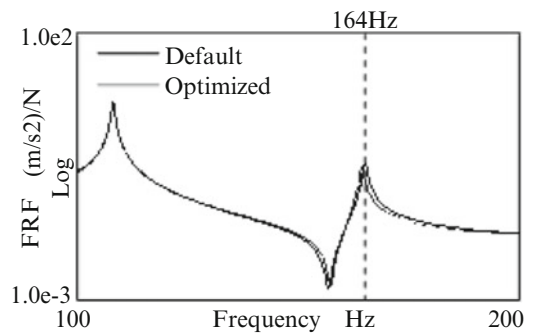
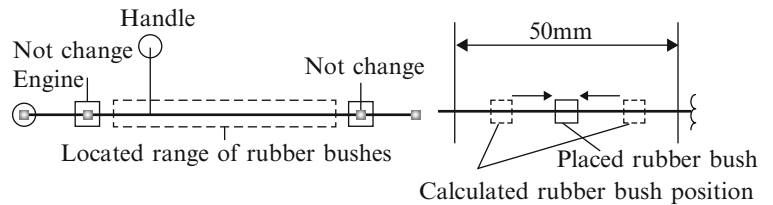


**Fig. 21.16** Placement modification method



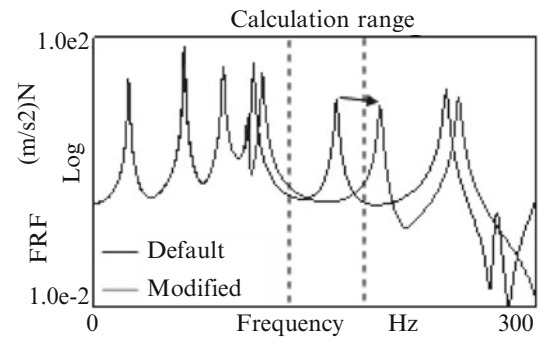
### 21.4.2 Rubber Bush Placement Optimization

The interval of six rubber bush is even for the original instead the variable interval is taken into consideration to realize the vibration reduction. Figure 21.16 shows the scheme for optimization of placement modification where the two both end rubber bushes are fixed due to safety and not to prevent the fundamental function. Therefore the placement for four rubber bushes is modified as follows.

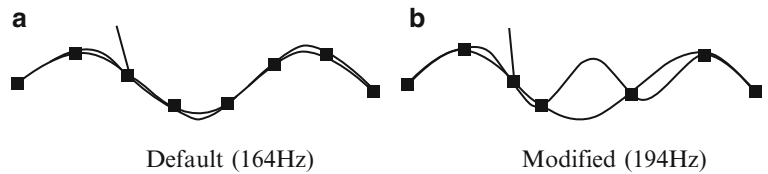
The distance between two both end rubber bushes is divided into 90 candidate placement points with 10 mm interval and then randomly four rubber bushes placement points are chosen and the FRF between the engine and the handle are calculated to determine the largest FRF value for 130 and 190 Hz range. One thousand trials are carried out to seek the minimum of the largest FRF value. When two adjacent rubber bushes are mutually close within 50 mm interval, these are replaced by one rubber bush at the middle point. Note that the hardness of rubber bushes are constant #60.

Figure 21.17 shows the result of optimized FRF compared with the original where 164 Hz mode is shifted significantly higher to 194 Hz and away from 130 to 190 Hz range like almost valley. The comparison of mode shape with the original 164 Hz and modified 194 Hz is shown in Fig. 21.18 and the reason why so large natural frequency shift is achieved is interpreted by the fact that the phase relation of deflection between the pipe and the drive shaft at one interval is completely changed from in phase to out of phase such as counter balance.

**Fig. 21.17** FRF of the modified model



**Fig. 21.18** Comparison of mode shapes



**Fig. 21.19** Comparison of modified acceleration

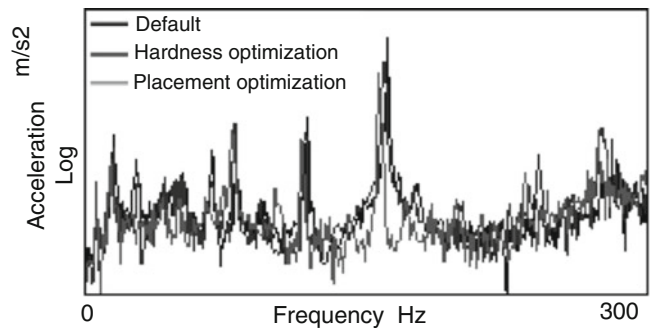
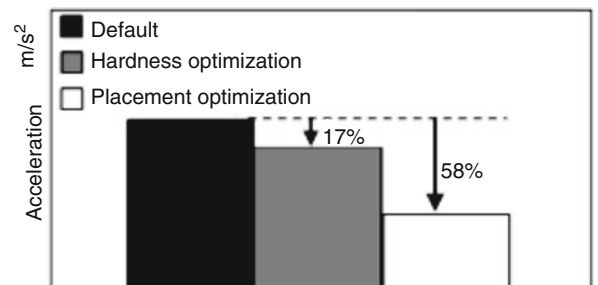


**Fig. 21.20** Result of vibration reduction



### 21.4.3 Experimental Verification

The optimized brush cutter is then actually operated under full throttle under the same free-free boundary condition. Figure 21.19 shows the acceleration comparison at right handle of the original, the hardness optimization and the placement optimization. Further based on frequency compensation by ISO 5349-1, the total vibration reduction is estimated 17% by the hardness optimization and 58% by the placement optimization as shown in Fig. 21.20

## 21.5 Conclusions

- 1 The most contributing vibration mode of the brush cutter to unpleasant feeling under full throttle is identified which should be improved.
- 2 Based on the identification of rubber bush hardness, the FE model of the brush cutter is created and the optimization of rubber bush hardness is conducted to reduce the vibration.

- 3 By the modification of placement of rubber bushes, optimized uneven interval can be found to realize the vibration reduction significantly.
- 4 These proposed modifications are experimentally verified to confirm the predicted vibration reduction of the brush cutter under full throttle operation.

## References

1. Iwata I (1990) Hand-arm vibration syndrome and its prevention *AST J* 46(2):150–156
2. Ministry of Health, Labor and Welfare(2009) Guideline for prevention against vibration injury by vibration tool except chainsaw 710(2)
3. Neyrinkck F et al (1992) Operational analysis and problem identification of a high performance racing engine In: *Proceedings of IMAC-X San Diego, CA*, pp 1399–1405

## Chapter 22

# Design of a Test Setup for Measuring Dynamic Stiffness of Vibration Isolators

Canan Uz, Gokhan O. Ozgen, and Ender Cigeroglu

**Abstract** In this paper, design efforts to develop a custom test setup for measuring dynamic stiffness of vibration isolators are presented. The setup is designed to conduct dynamic stiffness measurements for various static preload values and over a certain (target) frequency range. Direct Method has been selected among the methods defined by standards found in the literature. In order to investigate the effect of basic design parameters of the test setup on its overall performance, an equivalent eight degree of freedom lumped parameter model of the test setup is used which takes into account the basic dimensions and materials used for main structural components of the proposed setup design as well as the inertial characteristics of the isolators. Using the equivalent model, virtual tests are performed and the accuracy of the test setup is studied for various testing scenarios. A major work that is conducted as part of this work is to come up with a procedure that will enable tuning of the setup parameters such that the percent error on measured dynamic stiffness of various types of isolators are minimized for the case when various levels of error are present in measured displacement and force amplitudes.

**Keywords** Dynamic stiffness measurement • Error analysis • Vibration isolator • Virtual test • Complex stiffness measurement

### 22.1 Introduction

Vibration isolators are used to reduce the transfer vibrational energy between the structural systems [1]. For effective use of an isolator in a specific vibration isolation application, its stiffness and damping properties has to be experimentally characterized as a function of frequency (in some cases also as a function of temperature). Hence, it is important to design a test setup that can accurately measure the stiffness and damping of vibration isolators. In this paper, efforts on the structural design of a test setup capable of measuring dynamic stiffness (frequency dependent elastic stiffness and damping, sometimes also called complex stiffness) of vibration isolators of various sizes are presented. Test setup will be designed to have an effective measurement frequency range as wide as possible. Test setup is also expected to have a preload feature.

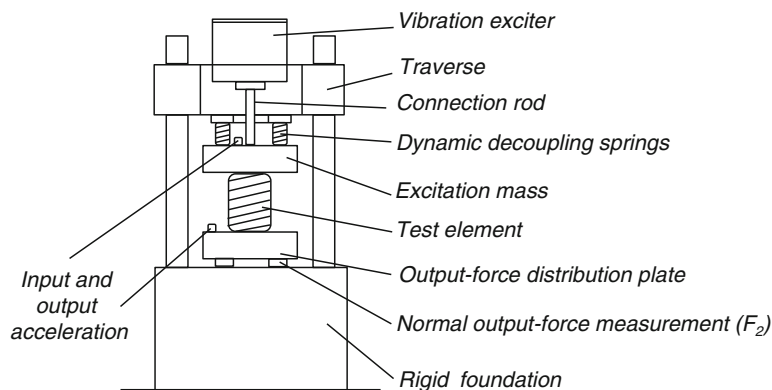
There are several test methods defined in ISO standards using various test procedures, measurement quantities, and test setup configurations. Effective frequency range of measurements for each of these methods also varies. The Direct Method defined in ISO 10846-2 [2] will be used in the test setup that will be designed as result of the activities reported in this paper. Focus of this paper is the mechanical design of this test setup to be developed. In most of the studies given in literature, when designing similar test setups, the main supporting structure of the setup is assumed to behave rigidly. However, the setup main structure in fact usually has vibration modes in the measurement frequency range which may adversely affect measurement accuracy. For example, Dickens et al. [3] investigated modal behavior of a similar test setup and the effect of structural modes on measurement results via harmonic response analysis.

Main objective of this paper is to investigate the measurement accuracy of the test setup to be designed. As a first step towards achieving this objective, modal analysis of the test setup is performed using a simple mathematical model of the test setup so that the effect of structural dynamics of the test setup on its measurement accuracy can be addressed. As a result of this analysis, modal frequencies and mode shapes of the setup that exist in the target frequency range of measurements

---

C. Uz • Gokhan O. Ozgen (✉) • E. Cigeroglu  
Department of Mechanical Engineering, Middle East Technical University, Ankara 06800, Turkey  
e-mail: [uzcanan@yahoo.com](mailto:uzcanan@yahoo.com); [gozgen@metu.edu.tr](mailto:gozgen@metu.edu.tr); [ender@metu.edu.tr](mailto:ender@metu.edu.tr)

**Fig. 22.1** Representative test setup for Direct Method for axial loading



are identified. In the next step, harmonic analysis is performed to simulate various test scenarios. Simulated tests enable the investigation of the effect of measurement errors that inherently exist in the test procedure. For example, there exists possible error in amplitude and phase of the response and force measurements, due to sensor calibration, cross axis sensitivity, and temperature dependence of transducer sensitivities. Author's past experience shows that these input measurement errors can lead to errors in measured dynamic stiffness around structural resonances of the test setup. Following sections present the development of the mathematical model and the results of the virtual tests that are performed.

## 22.2 Conceptual Design of the Test Setup

Three major test methods defined in ISO (International Standards Organization) standards are the Direct Method, the Driving Point Method, and the Indirect Method [2, 4–6]. Among these three methods, the Direct Method has the widest effective frequency range. In the Direct method, a controlled (generally harmonic) force is applied to one end of the isolator while the other end is fixed to the foundation of the test setup. Dynamic stiffness of the isolator (elastic and damping properties of the isolator as a function of frequency, sometimes also called the complex stiffness) is estimated by measuring the force transmitted to the foundation through the isolator and the net dynamic deflection on the isolator. The dynamic stiffness of the isolator is simply estimated as the ratio of the harmonic amplitudes of transmitted force and the net deflection across the isolator for each frequency of excitation. A possible setup configuration for the Direct Method is given in Fig. 22.1. The upper frequency limit of the Direct Method can be as high as 500 Hz while for lower frequency limit is around 1 Hz [2].

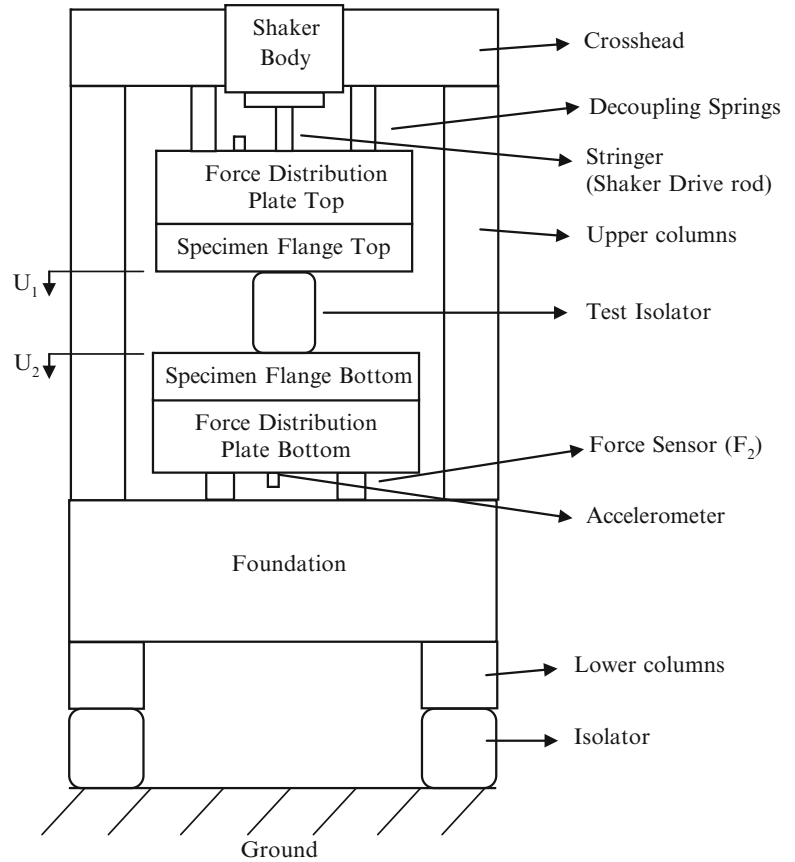
Conceptual design, which is used in the test setup being considered in this paper, is given in Fig. 22.2. This representative conceptual model is a fixture having the Crosshead as the upper cross member at the top, the Rigid Foundation at the bottom and the (Electrodynamics) Shaker as the actuator with the Shaker body mounted on the Crosshead. There exist force distribution plates and specimen flanges at input and output ends of the Test Isolator to distribute force evenly. Top Force Distribution Plate is connected to the Crosshead by decoupling springs. Decoupling springs are used for applying static preload on the Test Isolator by moving the Crosshead relative to the Test Isolator. Columns are for supporting the crosshead; on the other hand, lower columns and isolators are located below the Foundation are for adjusting rigid or soft connection of the fixture to the ground. Input force is applied by the Shaker to the Top Force Distribution Plate as harmonic excitation, and force transmitted to the Foundation through the Test Isolator is measured by force sensors at the Bottom Force Distribution Plate/Foundation interface. Accelerations are measured with accelerometers which are placed on force distribution plates.

In the Direct Method [2], frequency dependent dynamic stiffness can be calculated from:

$$k_{2,1} = \frac{F_2}{U_1} = i\omega \frac{F_2}{V_1} = -\omega^2 \frac{F_2}{A_1}, \quad (22.1)$$

where,  $k_{2,1}$  is the dynamic transfer stiffness of the test isolator (or resilient element) being tested,  $F_2$  is the harmonic amplitude of force transmitted to the rigid foundation,  $\omega$  is frequency in rad/s,  $U_1$  is the harmonic amplitude of the displacement of the input side of the isolator,  $V_1$  is the harmonic amplitude of the velocity at the input side of the isolator,

**Fig. 22.2** Conceptual model of the test setup



and  $A_1$  is the harmonic amplitude of the acceleration at the input side of the isolator. The dynamic transfer stiffness which is a complex number has an amplitude  $|k_{2,1}|$  and phase angle  $\phi_{2,1}$ . Loss factor,  $\eta$  of the Test Isolator can be calculated from [2]:

$$\eta = \tan \phi_{2,1} = \text{Im}(k_{2,1})/\text{Re}(k_{2,1}) \quad (22.2)$$

### 22.3 Mathematical Model of the Test Setup

A mathematical model of the test setup, which can be seen in Fig. 22.3, is developed to analyze mode shapes, modal frequencies of the test setup given in Fig. 22.2. Same model will also be used to perform virtual tests on the test setup by performing harmonic response analysis on the mathematical model. A similar mathematical model can also be found in Ref. [7]. In fact, mathematical model developed in this paper is based on the discrete model in Ref. [7] with some modifications and developments in order to define the specific physical model of the mathematical model given in Fig. 22.3.

Some of the physical components that form the test setup, which are the Crosshead, Foundation, Top Force Distribution Plate, Bottom Force Distribution Plate, Top Specimen Flange and Bottom Specimen Flange, are all modeled as rectangular solids. Some other physical components of the test setup, which are columns, lower columns, isolators, and Test Isolator, are modeled as cylindrical solids. Finally, decoupling springs are modeled as helical springs.

In the mathematical model, inertia of solid components is defined using rigid masses lumped at connection points of main components of the test setup in the physical model. For each solid element, total mass is calculated from  $A \times L \times \rho$ , where  $A$  is the cross sectional area,  $L$  is the length, and  $\rho$  is the mass density. Massless linear springs are used to represent the elastic characteristics of the physical components. Derivation of effective lumped masses and spring constants for each component are given in the following sections.

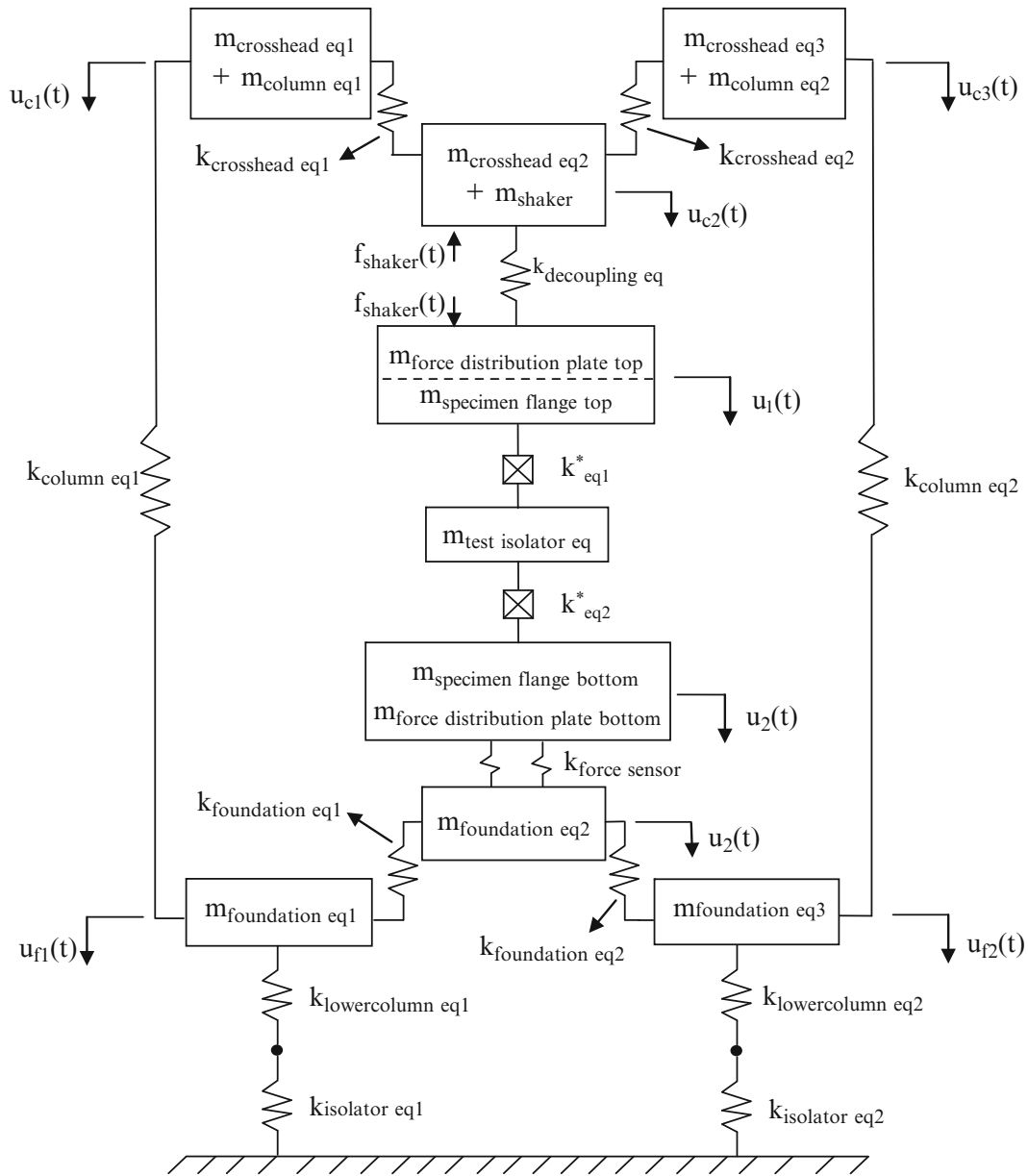


**Fig. 22.3** Equivalent eight degree of freedom lumped parameter model of the conceptual model of the test setup

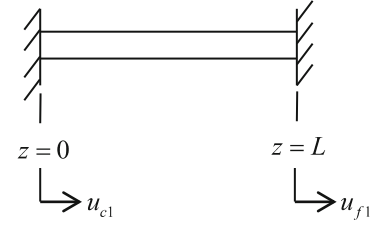
### 22.3.1 Equivalent Model of Upper Columns

Equivalent column mass is distributed to the upper ends which is one third of total mass of the column and embedded to the partitioned mass of the Crosshead at the ends as seen in Fig. 22.3. For equivalent mass calculation of a single column, trial function that satisfies geometric boundary conditions in Fig. 22.4 can be given as:

$$u(z) = u_{c1} + \frac{z}{L}(u_{f1} - u_{c1}), \tag{22.3}$$

where,  $u_{c1}$  is displacement of upper end (the end connected to the Crosshead),  $u_{f1}$  is displacement of the lower end of the Column (the end connected to the Foundation) which is also valid for  $u_{c3}$  and  $u_{f2}$ . These are consistent with displacements in Fig. 22.3.

**Fig. 22.4** Fixed-fixed bar to demonstrate column



Substituting the trial function given in Eq. (22.1) into the kinetic energy equivalency equation,

$$T = \int_0^L \frac{1}{2} \frac{m_{column}}{L} \left( \dot{u}_{c1} + \frac{z}{L} (\dot{u}_{f1} - \dot{u}_{c1}) \right)^2 dz = \frac{1}{2} m_{eq} \dot{u}_{c1}^2 + \frac{1}{2} m_{eq} \dot{u}_{f1}^2, \quad (22.4)$$

Equivalent mass expression of upper columns now can be found as:

$$m_{eq} = \frac{1}{3} \frac{m_{column} (\dot{u}_{c1}^2 + \dot{u}_{c1} \dot{u}_{f1} + \dot{u}_{f1}^2)}{\dot{u}_{c1}^2 + \dot{u}_{f1}^2}. \quad (22.5)$$

where for  $u_{f1} = 0$ ,  $m_{eq} = m_{column}/3$  at  $z = u_{c1}$ , and for  $u_{f1} = u_{c1}$ ,  $m_{eq} = m_{column}/2$  both at  $z = u_{c1}$ , and  $z = u_{f1}$ .

Since foundation side is the base side with minimum motion, its displacement is expected to have a very small amplitude during the actual test. Hence, effective mass of a column element can be approximately distributed to the upper ends; i.e., to DOFs  $u_{c1}$ , and  $u_{c3}$ , as one third of its mass. Therefore,  $m_{column\ eq1} = m_{column\ eq2} = m_{column}/3$ . Equivalent stiffness can be calculated using  $k_{column\ eq1} = k_{column\ eq2} = EA_{column}/L_{column}$ , where  $E$  is Young's modulus.

### 22.3.2 Equivalent Model of the Crosshead and the Foundation

In order to model major deformation modes of these components, which are transverse bending deflection, vibrational characteristics of the Crosshead and Foundation are represented by three lumped masses of one third of the total mass and two flexural stiffness elements (see Fig. 22.3 for the DOFs to which the masses are lumped).

$$m_{crosshead\ eq1} = m_{crosshead\ eq3} = m_{crosshead}/3 + m_{column}/3, \quad (22.6)$$

$$m_{crosshead\ eq2} = m_{crosshead}/3 \quad (22.7)$$

$$m_{foundation\ eq1} = m_{foundation\ eq2} = m_{foundation\ eq3} = m_{foundation}/3, \quad (22.8)$$

For equivalent stiffnesses of the Crosshead and Foundation,  $k_{crosshead\ eq1}$ ,  $k_{crosshead\ eq2}$ ,  $k_{foundation\ eq1}$ ,  $k_{foundation\ eq2}$  are considered as twice the bending stiffness of the Crosshead and Foundation, i.e.

$$k_{crosshead\ eq1} = k_{crosshead\ eq2} = 2EI_{crosshead}/L_{crosshead}^3, \quad (22.9)$$

and

$$k_{foundation\ eq1} = k_{foundation\ eq2} = 2EI_{foundation}/L_{foundation}^3, \quad (22.10)$$

where,  $I$  is area moment of inertia, and  $E$  is Young's modulus.

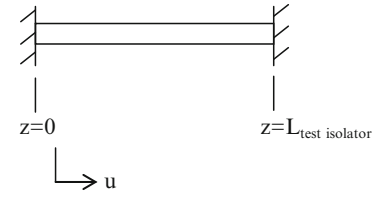
### 22.3.3 Equivalent Model of the Test Isolator

Test Isolator mass is also included in the model to see the effects of axial resonances of the test specimen. Test Isolator mass is lumped to the center of the specimen by calculation from kinetic energy equivalence which is three eighths of its total mass. For equivalent mass calculation of the Test Isolator, it is modeled as a spring which is fixed-fixed at its two ends and subject to only longitudinal deformation. Boundary conditions for the fixed-fixed case also be seen in Fig. 22.5 and are as follows

$$u(0, t) = u(L_{test\ isolator}, t) = 0, \quad (22.11)$$



**Fig. 22.5** Fixed-fixed bar to demonstrate Test Isolator



where,  $z$  and  $t$  are spatial and time variables respectively. Separation of variables method can be applied to solve for longitudinal displacement, i.e.

$$u(z, t) = x(t)U_r(z). \quad (22.12)$$

The trial function that satisfies geometric boundary conditions in Eq. (22.11) for a fixed-fixed bar is:

$$U_r(z) = \sin\left(\frac{r\pi z}{L_{test\ isolator}}\right) \quad r = 1, 2, \dots, \quad (22.13)$$

where,  $U_r(z)$  is the  $r$ th eigenfunction,  $x(t)$  is the generalized coordinate which is a time function,  $z$  is the location, and  $L$  is the length of the bar. From the equation of kinetic energy equivalence, along with the trial function given in Eq. (22.13), equivalent mass of the Test Isolator can be calculated. For the first mode, equivalence of kinetic energy becomes:

$$T = \int_0^L \frac{1}{2} \frac{m_{test\ isolator}}{L_{test\ isolator}} \left(\sin\left(\frac{\pi z}{L}\right)\right)^2 \dot{x}^2 dz = \frac{1}{2} m_{test\ isolator\ eq} \dot{x}^2 \quad (22.14)$$

Thus, from Equation Eq. (22.14),

$$m_{test\ isolator\ eq} = m_{test\ isolator}/2 \text{ at } z = L_{test\ isolator}/2. \quad (22.15)$$

Therefore, test isolator mass is located at the center with equivalent mass of  $m_{test\ isolator}/2$ . Equivalent stiffnesses of the Test Isolator,  $k_{eq1}^*$ , and  $k_{eq2}^*$  should add up to its total stiffness, i.e.

$$k_{eq1}^* = k_{eq2}^* = 2EA_{test\ isolator}/L_{test\ isolator} \quad (22.16)$$

### 22.3.4 Equivalent Model of Force Distribution Plates, Specimen Flanges, and the Shaker

The Shaker, force distribution plates, and specimen flanges, are modeled as rigid bodies. Thus, only their total mass values are used in the mathematical model.

### 22.3.5 Equivalent Model of Lower Columns and Isolators Below the Test Setup

Lower columns and isolators are connected in series and no inertia is defined at their connection DOFs. Equivalent stiffnesses are derived as extensional stiffnesses for these components, i.e.

$$k_{lower\ column\ eq1} = k_{lower\ column\ eq2} = EA_{lower\ column}/L_{lower\ column} \quad (22.17)$$

$$k_{isolator\ eq1} = k_{isolator\ eq2} = EA_{isolator}/L_{isolator} \quad (22.18)$$

### 22.3.6 Equivalent Model of Decoupling Springs

For each Decoupling Spring, equivalent stiffness  $k_{decoupling\ eq}$  is calculated from  $2Gd^4/8d^3N_a$ , where  $G$  is the shear modulus,  $d$  is the wire diameter,  $D$  is the coil diameter, and  $N_a$  is the number of active coils. Their masses are neglected.

## 22.4 Investigation of Modal Characteristics of the Test Setup

As mentioned in Sect. 22.2, error in estimated dynamic stiffness of the Test Isolator is likely to be amplified at frequencies close to the structural resonances of the test setup. Since the output of the test procedure; i.e., dynamic stiffness estimation, can be adversely affected from resonance related error amplification, modal characteristics of the system should be well investigated. Eigenvalues associated with natural frequencies, and eigenvectors associated with mode shape information of the test setup are found by modal analysis performed on the model (see Fig. 22.3) using MATLAB.

The physical components that form the test setup are given in the first column of Table 22.1. The first row of Table 22.1 is comprised of the geometrical parameters and material properties that would describe each component of the test setup in detail. By using the specific set of geometrical and material parameters, Design Set 1, given in Table 22.1, mode shapes (see Fig. 22.6) and natural frequencies of the setup for that particular design configuration are determined (see Table 22.2). Description of the structural modes of Design Set 1 is given in Table 22.3. Modal analysis results obtained from the model using MATLAB are also verified by comparing them with results obtained from finite element analysis performed on the same mathematical model using NASTRAN.

## 22.5 Virtual Tests on the Test Setup

In order to simulate an actual dynamic stiffness measurement test performed using the test setup, two harmonic forces with equal magnitude but opposite directions are applied at the two nodes as seen in Fig. 22.3. These forces represent the interaction of the Shaker with the test setup in terms of forces which are acting on the Top Force Distribution Plate and Crosshead. Harmonic analyses are performed in MATLAB to find the harmonic amplitude of the force transmitted to the Foundation, and harmonic amplitudes of responses of interest in the eight DOF system. (The harmonic analysis results are also verified by comparing the results for the same Design Set 1 with results obtained from NASTRAN for the same model and boundary conditions).

For all simulated tests, harmonic analysis is performed with a frequency increment of 0.5 Hz in a frequency range of 0–1,000 Hz. The upper frequency limit in simulated tests is decided by considering the capabilities of commercially available test systems. The upper frequency for commercial test systems which can be used to characterize isolators using the Direct Method varies from 50 up to 200 Hz. There exist systems which can characterize isolators up to 1,000 Hz such as the MTS Model 831.50 high frequency elastomer test system which has a frequency range of 0.01–1,000 Hz. Taking the highest performing test system, upper frequency limit for the virtual tests performed in this paper is taken as 1,000 Hz.

For harmonic motion, force and displacements can be defined using harmonic amplitudes such as  $f_{trans} = F_{trans}e^{i\omega t}$ ,  $u_1 = U_1e^{i\omega t}$ , and  $u_2 = U_2e^{i\omega t}$  where,  $F_{trans}$  is the harmonic amplitude of the force transmitted to the Foundation through the Bottom Force Distribution Plate,  $U_1$  is the harmonic amplitude of the displacement of the Test Isolator at the actuator side, and  $U_2$  is the harmonic amplitude of the displacement of the Test Isolator at the Foundation side.

In dynamic stiffness formulation, there are some crucial points. In the relevant standard [2], the motion of the Foundation side is assumed to be very low thus  $u_2$  is taken as zero in the standard, i.e.

$$k^* = \frac{F_{trans}}{U_1} \quad (22.19)$$

**Table 22.1** Geometrical parameters and material properties of the test setup (Design Set 1)

Thickness [cm]	Length [cm]	Width [cm]	Diameter [cm]	Wire diameter [cm]	Active coils [cm]	E [GPa]	$\rho$ [g/cm <sup>3</sup> ]	G [GPa]	
Crosshead	10	35	25	N/A	N/A	N/A	200	7,800	N/A
Foundation	20	35	20	N/A	N/A	N/A	200	7,800	N/A
Columns	N/A	25	N/A	10	N/A	N/A	200	7,800	N/A
Lower columns	N/A	5	N/A	15	N/A	N/A	200	7,800	N/A
Isolator	N/A	5	N/A	5	N/A	N/A	10 <sup>6</sup>	1,103	N/A
Decoupling spring	N/A	8	N/A	5	0.5	5	N/A	7,800	80
Top force D. Pl.	2	6	6	N/A	N/A	N/A	200	7,800	N/A
Top Sp. flange	2	6	6	N/A	N/A	N/A	200	7,800	N/A
Bottom force D. Pl.	2	10	10	N/A	N/A	N/A	200	7,800	N/A
Bottom specimen Fl.	2	10	10	N/A	N/A	N/A	200	7,800	N/A
Test Isolator	N/A	7	N/A	5	N/A	N/A	10	1,103	N/A

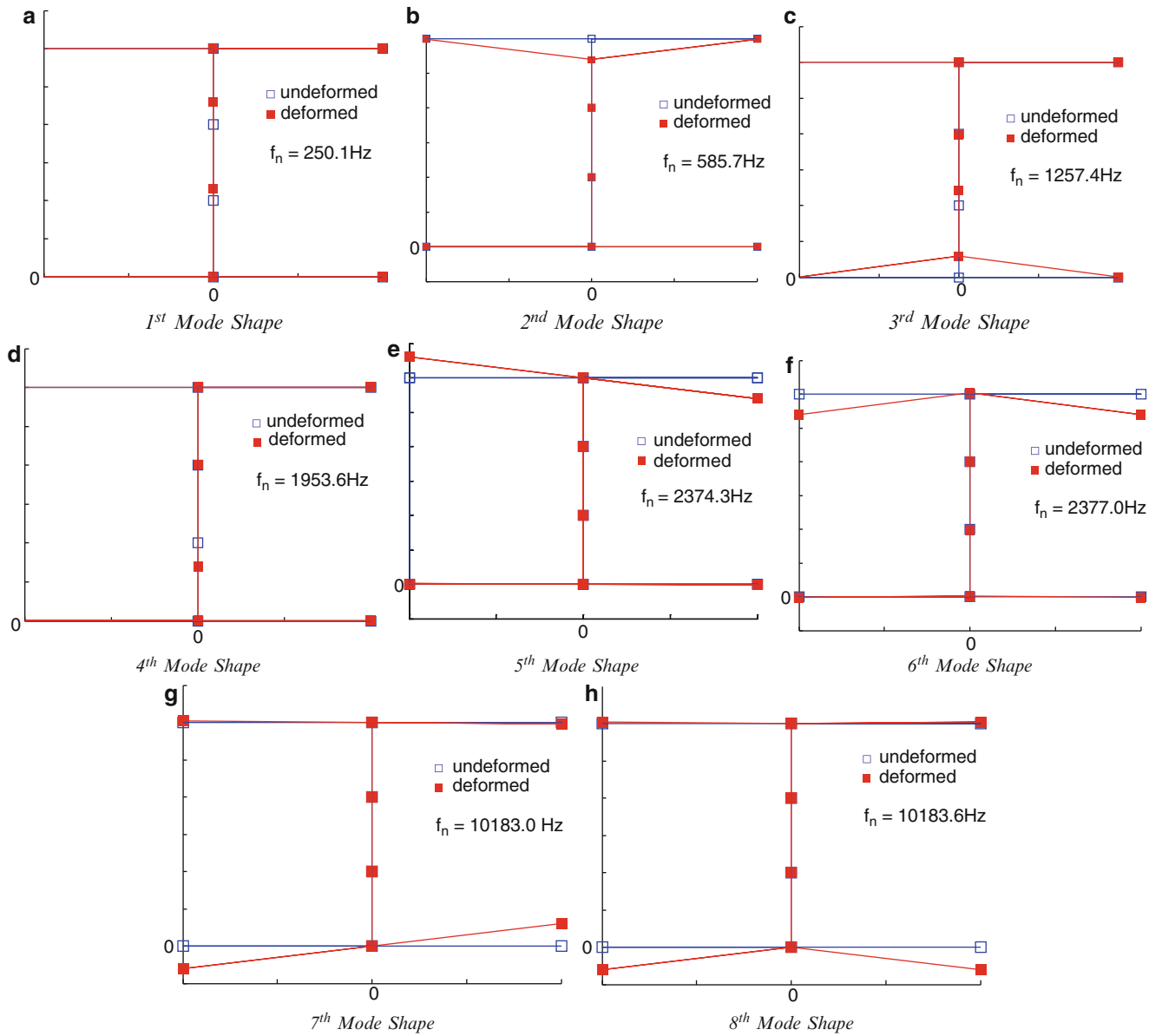


**Fig. 22.6** Mode shapes and natural frequencies for the configuration defined in Design Set 1 (see Table 22.1). (a) through (h) are for modes 1 through 8

**Table 22.2** Natural frequencies of the test setup for the design configuration defined in Design Set 1 (see Table 22.1)

	1st	2nd	3rd	4th	5th	6th	7th	8th
Natural frequency [Hz]	250.1	585.7	1,257.4	1,953.6	2,374.4	2,377.0	10,183.0	10,183.6

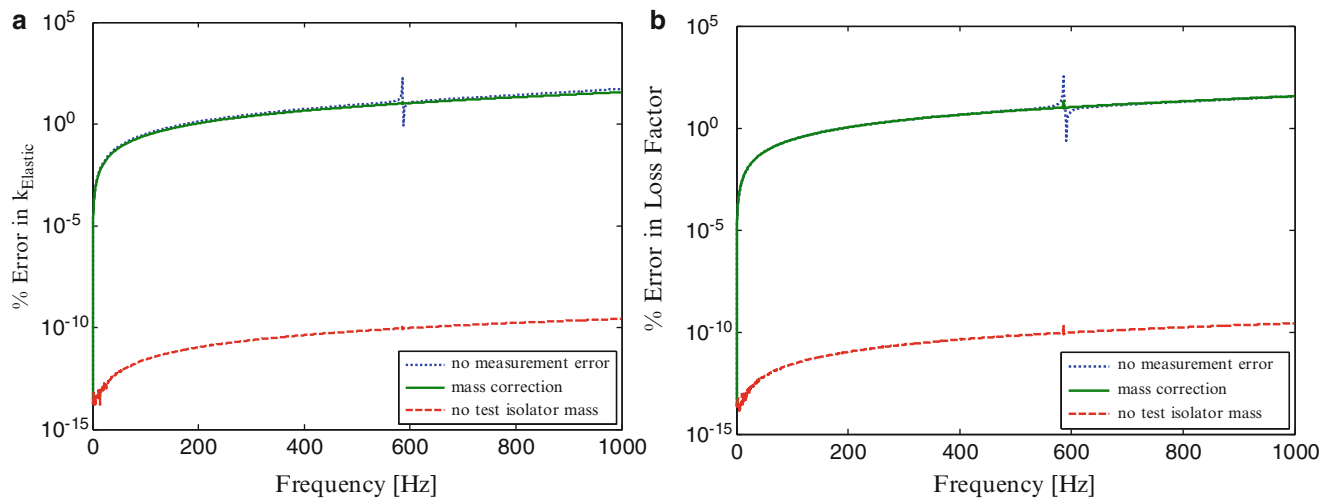
Assuming  $U_2$  as zero does not appropriately represent the actual deformation in the Test Isolator, thus this DOF ( $u_2$ ) is also taken into consideration in this study. Dynamic stiffness formulation used in this paper is

$$k^* = \frac{F_{trans} - \omega^2(m_{fdp.bot} + m_{sf.bot})U_2}{U_1 - U_2}, \quad (22.20)$$

where,  $\omega$  is angular frequency,  $m_{fdp.bot} + m_{sf.bot}$  is sum of the masses of the Bottom Force Distribution Plate and Bottom Specimen Flange,  $k^*$  is the dynamic stiffness of the Test Isolator. Dynamic stiffness can be defined in terms of elastic stiffness (real part of dynamic stiffness) and the loss factor such that  $k^* = k_{elastic}(1 + i\eta)$ , where  $\eta$  is loss factor. Note that

**Table 22.3** Description of mode shapes for the configuration defined in Design Set 1 (see Table 22.1)

Mode number	Description of the corresponding mode
First mode	Axial motion of the Test Isolator and plate on top of it dominates the mode shape
Second mode	Crosshead bending response dominates the mode shape
Third mode	Foundation bending response dominates the mode shape. Also, test specimen moves axially
Fourth mode	Only the Test Isolator has a motion in axial direction
Fifth mode	Column extensional motion dominates the mode shape. Upper ends of the column go up and down. There is a tilting in the Crosshead
Sixth mode	Crosshead bending deflection dominates the mode shape
Seventh mode	Column extensional motion dominates the mode. Lower ends of the column go up and down. Tilting of the foundation is also observed
Eighth mode	Foundation bending deflection dominates the mode shape

**Fig. 22.7** Percent maximum error in the calculated dynamic stiffness vs. frequency for the case when no measurement errors exist: (a) maximum percent error in elastic stiffness, (b) maximum percent error in loss factor

in Eq. (22.20), inertial force of the Bottom Force Distribution Plate and the Bottom Specimen Flange are subtracted from force transmitted to the Foundation (which is the actual measured force) in order to calculate the exact force transmitted directly through the Test Isolator.

Numerical values given in Table 22.1 is the design parameter set (Design Set 1) used in the test simulations performed. Results of these simulated tests are given and discussed in the next two sections.

### 22.5.1 Test Simulations with No Measurement Error Present

First, virtual tests are performed for the case when no measurement errors are present in measured displacements and forces. The purpose of this case study is to see if there are any inherent errors in dynamic stiffness estimation procedure used in the Direct Method. In the simulated test, measured parameters are harmonic amplitudes  $U_1$ ,  $U_2$ , and  $F_{trans}$ . The results of virtual tests are presented as the error percentages in elastic part of stiffness and the loss factor where the real values are known and measured values can be computed using Eq. (22.20).

Three cases were simulated for the basic test scenario of “no measurement errors are present”. These cases are:

- *Case 1:* Mass correction (mass decrease) of the Bottom Force Distribution Plate and Bottom Specimen Flange is not made. Equivalent mass of the Test Isolator is included at the center of the specimen. Percent error distributions in measured dynamic stiffness components can be seen in Fig. 22.7 (plot with blue line);
- *Case 2:* This simulation is performed for the case where mass correction of the Bottom Force Distribution Plate and Bottom Specimen Flange is made in order to more accurately estimate the force transmitted through the Test Isolator.

**Table 22.4** Natural frequencies of the test setup when the Crosshead thickness is decreased by half (Design Set 2)

	1st	2nd	3rd	4th	5th	6th	7th	8th
Natural frequencies [Hz]	250.12	273.66	1,257.45	1,953.63	3,041.58	3,041.77	10,192.33	10,192.98

**Table 22.5** Natural frequencies of the test setup when the column diameters are decreased by half (Design Set 3)

	1st	2nd	3rd	4th	5th	6th	7th	8th
Natural frequencies [Hz]	250.12	554.52	1,257.24	1,357.47	1,375.09	1,953.63	10,008.94	10,009.64

Percent error distribution in measured dynamic stiffness components can be seen Fig. 22.7 (green line). As it can clearly be seen in this figure, error spikes around 600 Hz observed in case 1 is eliminated due to the mass correction.

- *Case 3:* Finally, mass of the Test Isolator is taken as zero (i.e. as if a massless isolator is tested in the virtual test). Percent error distribution in estimated dynamic stiffness components can be seen in Fig. 22.7 (red line). It can be seen that the inertia of the specimen is a big contributor to the error in measured dynamic stiffness (inherent to the test procedure). Since there is a drastic decrease in error levels when tested specimen is massless.

### 22.5.2 Test Simulations with Measurement Errors Present

Virtual tests are also performed for the case when there is finite error in magnitudes and phase angles of measured response and force amplitudes. For the first set of simulations, an error of 1% is applied to the magnitudes of the measured harmonic amplitudes  $U_1$ ,  $U_2$ , and  $F_{trans}$ . Magnitude error is applied to each quantity both as negative and positive deviations from the actual value (since adding or subtracting the error from the actual value may have a different effect on the observed error in the calculated dynamic stiffness for the Test Isolator). For each error scenario, error in estimated quantities (elastic stiffness and loss factor) is calculated as a function of frequency. Maximum value of the error in calculated quantities, which is caused by the artificially added error in the magnitudes of the measured quantities, is recorded for each frequency and then this maximum error value is plotted to assess the error amplification characteristics of the design set of interest. Same procedure is applied to the case when the measured quantities have errors in their phase angles. The amount of error introduced to phase angles of measured quantities is taken as a constant value of  $0.18^\circ$  (0.1% of 3.14 radians i.e.  $0.001\pi$ ). The same error is applied to phases of all measured quantities one quantity at a time, but the error in the calculated dynamic stiffness components are only recorded for the particular measurement error scenario where error in the calculated quantity is a maximum at that particular frequency. Maximum error in the calculated quantities due to errors present in phase angles of measured quantities are also plotted as a function of frequency.

Main objective of these error simulations is to address the following questions:

- How does error in calculated dynamic stiffness depend on the error present in measured displacements and force?
- How does error amplification characteristics of the setup change if either one of the geometrical variables or mass, stiffness, and damping in the system is varied?

First design configuration used is the Design Set 1 defined in Table 22.1. In addition to this design configuration two additional design configurations are also studied. Among these two, Design Set 2 is obtained by decreasing the thickness of the Crosshead member by half. The other one is the Design Set 3, which is obtained by decreasing column diameters used in Design Set 1 by half. Both design sets are essentially slightly modified versions of Design Set 1. Natural frequencies of the test setup for Design Set 2 and Design Set 3 are given in Tables 22.4 and 22.5, respectively.

For this three design sets, plots of maximum error in the calculated dynamic stiffness quantities are given in Figs. 22.8 and 22.9. Figure 22.8 includes the maximum percent error distribution in calculated dynamic stiffness due to 1% error in magnitudes of measured quantities (see Fig. 22.8a for error in elastic stiffness and see Fig. 22.8b for error in loss factor). Figure 22.9 includes the maximum percent error distributions in calculated dynamic stiffness components due to  $0.18^\circ$  phase angle error in measured quantities (Fig. 22.9a for error in elastic stiffness and Fig. 22.9b for error in loss factor). All these plots show that error distributions have general trends with some spikes which locally amplify the error. When the frequencies, at which the spikes in error plots are observed, are investigated it can be seen that the spikes actually correspond to the second natural frequencies of the test setup for the corresponding design sets (i.e.  $f_2 = 585.7$  Hz for Design Set 1 and  $f_2 = 273.66$  Hz for Design Set 2,  $f_2 = 554.52$  Hz for Design Set 3). For Design Set 2, spikes are not that pronounced (can be hardly seen in the error plots) but when zoomed in to the 270 Hz region the error amplification effect can be observed.

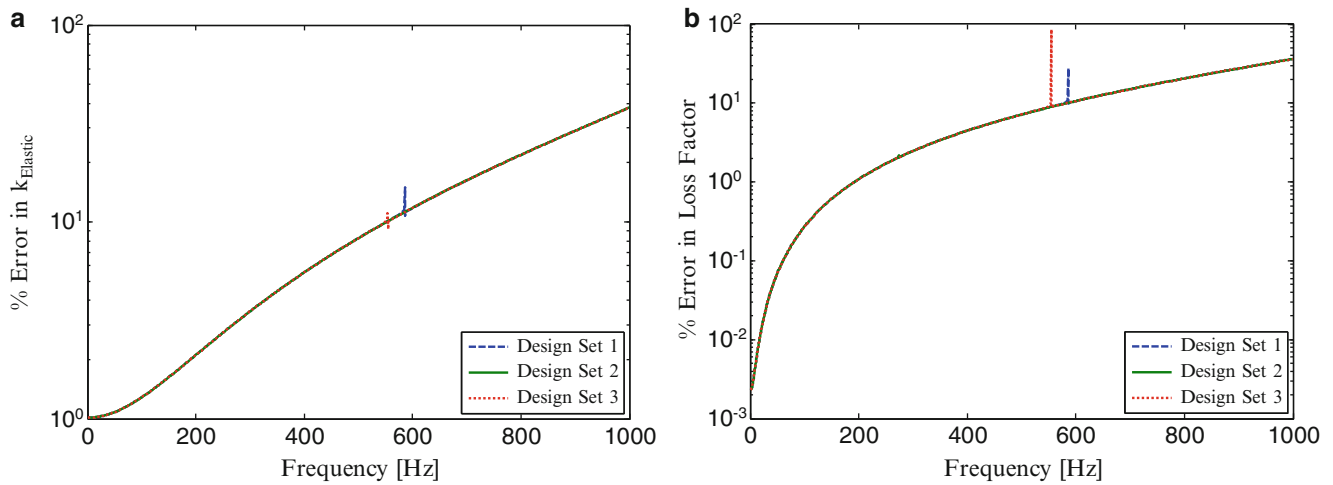


**Fig. 22.8** Percent maximum error in the calculated dynamic stiffness vs. frequency for 1% error in magnitudes of measured displacement and force quantities for three design sets: (a) maximum percent error in elastic stiffness, (b) maximum percent error in loss factor

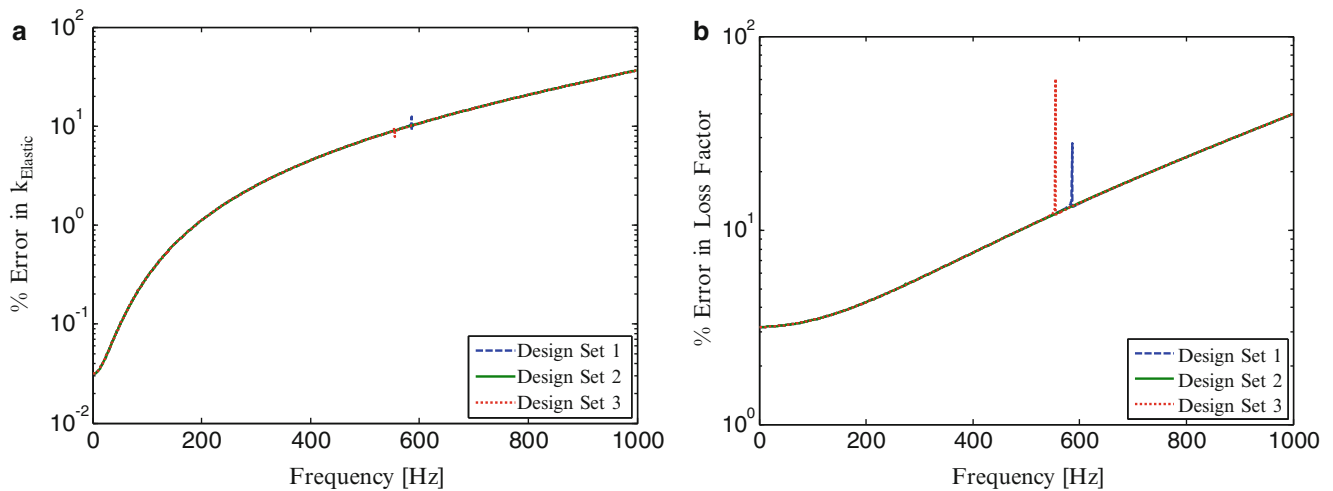


**Fig. 22.9** Percent maximum error in the calculated dynamic stiffness vs. frequency for  $0.18^\circ$  phase angle error in measured displacement and force amplitudes for three design sets: (a) maximum percent error in elastic stiffness, (b) maximum percent error in loss factor

When the mode shape descriptions in Table 22.3 are investigated, it can be concluded that the second mode of the test setup is dominated by the bending deformation of the Crosshead (ordering of modes remain same for all three design sets being studied). This indicates that the bending response of the Crosshead may potentially amplify error in calculated dynamic stiffness components. Still, error amplification at this second resonance region is rather local and does not affect the general frequency dependent distribution of error in calculated dynamic stiffness components too much.

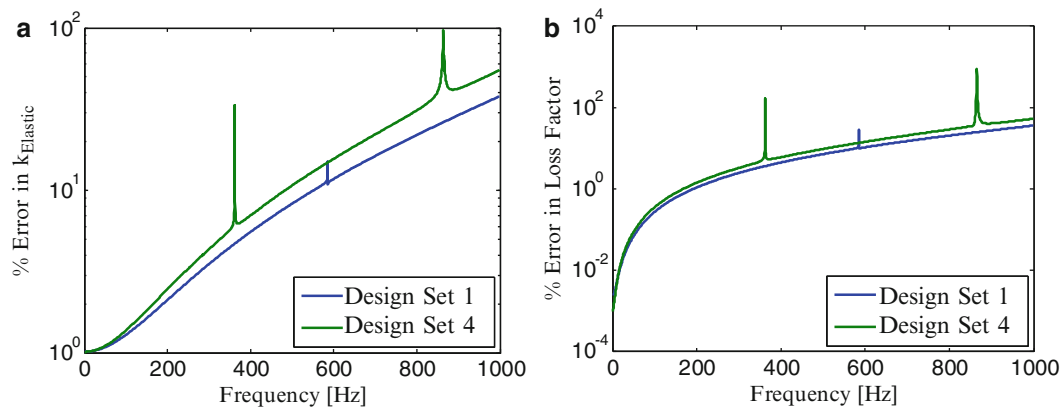
Another thing worth mentioning is that the error in calculated dynamic stiffness for the case when there is constant error in magnitudes of measured quantities, minimum error in the calculated elastic stiffness is almost always equal to the percent error in the measured quantity. Error in the elastic stiffness actually starts from a value very close to the percent error in magnitudes of the measured quantities, and slowly increases with increasing frequency (see Fig. 22.8a). This indicates that the upper frequency limit of the test setup may be determined by studying how rapidly error in estimated elastic stiffness increases as a function of frequency. However, for the error in loss factor, when measurement errors are present only in magnitudes of measured quantities, lowest percent error is not necessarily at same level same as the percent error in the magnitudes of measured quantities (see Fig. 22.8b). It can be concluded that compared to elastic stiffness estimation, loss factor estimation is less sensitive to errors that are present in magnitudes of measured quantities. The opposite is also true, i.e. loss factor estimation is more sensitive to measurement errors compared to elastic stiffness estimation, when the measurement errors are present only in phase angles of measured quantities (see Fig. 22.9).

**Table 22.6** Geometrical parameters and material properties of the test setup for a different design configuration (Design Set 4)

Thickness [cm]	Length [cm]	Width [cm]	Diameter [cm]	Wire diameter [cm]	Active coils [cm]	E [GPa]	$\rho$ [g/cm <sup>3</sup> ]	G [GPa]	
Crosshead	12	50	30	N/A	N/A	N/A	200	7,800	N/A
Foundation	30	50	35	N/A	N/A	N/A	200	7,800	N/A
Columns	N/A	30	N/A	10	N/A	N/A	200	7,800	N/A
Lower columns	N/A	5	N/A	15	N/A	N/A	200	7,800	N/A
Isolator	N/A	5	N/A	8	N/A	N/A	10 <sup>6</sup>	1,103	N/A
Decoupling spring	N/A	6	N/A	4	0.5	5	N/A	7,800	80
Force D. Pl. top	4	12	12	N/A	N/A	N/A	200	7,800	N/A
Sp. flange top	2	12	12	N/A	N/A	N/A	200	7,800	N/A
Force D. Pl. bottom	7.5	20	20	N/A	N/A	N/A	200	7,800	N/A
Specimen Fl. bottom	2.5	20	20	N/A	N/A	N/A	200	7,800	N/A
Test Isolator	N/A	8	N/A	5	N/A	N/A	10	1,103	N/A

**Table 22.7** Natural frequencies for the test setup for the configuration given in Table 22.6 (Design Set 4)

	1st	2nd	3rd	4th	5th	6th	7th	8th
Natural frequencies [Hz]	96.7	362.5	864.8	1,573.7	1,575.1	1,958.9	5,267.9	5,269.1

**Fig. 22.10** Percent maximum error in the calculated dynamic stiffness vs. frequency for 1% error in magnitudes of measured displacement and force quantities for Design Sets 1 and 4: (a) maximum percent error in elastic stiffness, (b) maximum percent error in loss factor

A fourth design set is also defined and studied to see the error characteristics of a relatively different design configuration compared to Design Set 1. Parameters for this new design configuration, Design Set 4, are given in Table 22.6. Almost all geometrical parameters are chosen different compared to the parameters defined for Design Set 1. Natural frequencies of the test setup for this configuration are given in Table 22.7. One thing to notice is that the third natural frequency of the test setup for this configuration now lies within the frequency range used in the error analysis (i.e.  $f_3 < 1,000$  Hz). This mode (see Table 22.3 for mode shape descriptions) is dominated by the bending response of the Foundation. Looking at the plots of percent error (in calculated dynamic stiffness terms) for Design Set 4 (along with Design Set 1), it can be seen that error in dynamic stiffness is also amplified around the third natural frequency of the setup (see Figs. 22.10 and 22.11). The general trend of the error plots still remains relatively unaffected. It can be concluded that natural frequencies of the bending deformation modes of the transverse members of the setup should be kept as large as possible to have the least effect on error amplification in the measurement frequency range. Note that in the error simulations for Design Set 4 same measurement errors are used as the error simulations performed for Design Sets 1, 2 and 3 (i.e. 1% error introduced to magnitudes of measured quantities and  $0.18^\circ$  error introduced to phases of measured quantities).

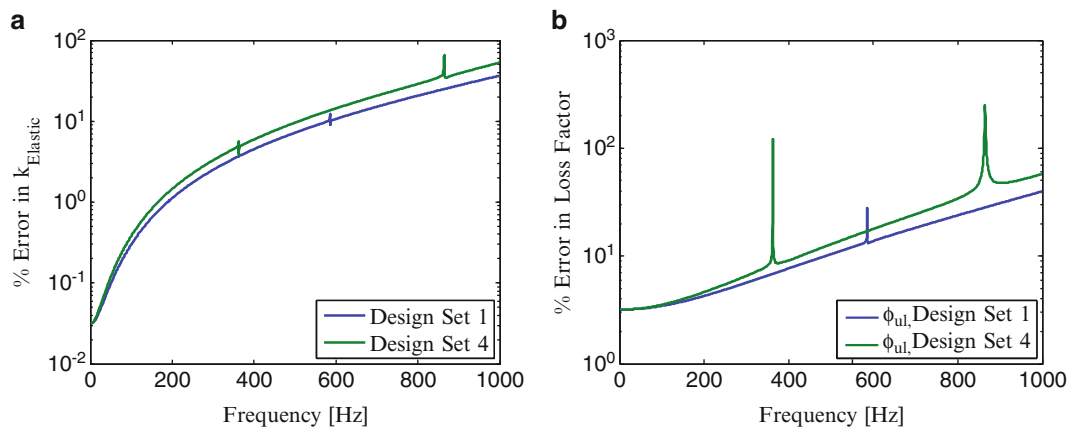


**Fig. 22.11** Percent maximum error in the calculated dynamic stiffness vs. frequency for  $0.18^\circ$  phase angle error in measured displacement and force amplitudes for Design Sets 1 and 4: (a) maximum percent error in elastic stiffness, (b) maximum percent error in loss factor

## 22.6 Conclusion

Design efforts for a custom vibration isolator test system using the Direct Method are reported in this paper. Main focus was investigating the error characteristics of the test setup. Main objective was to answer the question “how accurately the dynamic stiffness can be estimated when there are measurement errors in measured displacement and force quantities?”. The simple analytical model developed is shown to be a good tool for detailed investigation of determining how the measurement errors are transferred to the error in calculated dynamic stiffness of the Test Isolator for various design configurations. The developed mathematical model and the procedure for virtual test simulations used in this paper can be utilized to estimate the upper frequency of the test setup and come up with a set of design parameters (geometrical dimensions and material properties) of the test setup that will have the most favorable error characteristics (least sensitivity of estimated dynamic stiffness to measurement errors present in measured quantities).

## References

1. Rivin EI (2003) Passive vibration isolation. New York, ASME Press
2. ISO 10846-2, Acoustics and vibration – laboratory measurement of vibro-acoustic transfer properties of resilient elements, Part 2: Direct method for determination of the dynamic stiffness of resilient supports for translatory motion
3. Dickens JD, Norwood CJ (1997) Design of a test facility for vibration isolator characterization. *Acoust Aust* 25(1):23–28
4. ISO 10846-1, Acoustics and vibration – laboratory measurement of vibro-acoustic transfer properties of resilient elements, Part 1: Principles and guidelines
5. ISO 10846-3, Acoustics and vibration – laboratory measurement of vibro-acoustic transfer properties of resilient elements, Part 3: Indirect method for determination of the dynamic stiffness of resilient supports for translatory motion
6. ISO 10846-5, Acoustics and vibration – laboratory measurement of vibro-acoustic transfer properties of resilient elements, Part 5: Driving point method for determination of the low-frequency transfer stiffness of resilient supports for translatory motion
7. Jones David IG (2001) Handbook of viscoelastic vibration damping, 7.8.1 frequency domain response. John Wiley & Sons Inc, 432 Elizabeth Ave, Somerset, NJ, 08817, pp 247–255



## Chapter 23

# An Impact Excitation System for Repeatable, High-Bandwidth Modal Testing of Miniature Structures

Bekir Bediz, Emrullah Korkmaz, and O. Burak Ozdoganlar

**Abstract** Recent advances in various micro-manufacturing techniques have enabled utilization of miniature devices in numerous applications. However, testing, modeling, and predicting performance of these structures still poses various challenges. Experimental modal analysis techniques have been widely used to obtain the dynamic characteristics of structures; however, having very high natural frequencies, small vibration amplitudes, and high compliance, miniature structures require additional care during modal testing. Although recent developments in sensor technology enabled to obtain accurate high frequency vibration measurements during modal testing of miniature structures, excitation of miniature structures without any damage and within high frequency range in a reproducible manner is still being investigated. This paper presents design, development, and performance evaluation of a custom-made impact excitation system that enables repeatable, high bandwidth, single-hit impacts, and controllable impact force for modal testing of miniature structures. The system is equipped with a miniature force sensor attached to a custom designed flexure and an automated release mechanism driven by an electromagnet. The excitation bandwidth and the impact force exerted to the test structure can be controlled through control parameters: initial displacement given to the flexure and gap between the impact tip and the test surface.

**Keywords** Modal testing • Impact excitation • High bandwidth excitation • Repeatable excitation • Miniature structures

### 23.1 Introduction

Miniature devices offer several advantages including reduction in space, material and energy requirements, and improved efficiency over large-scale components. Therefore, the demand for miniature components has been increasing recently [1, 2]. However, testing, modeling, and predicting performance of these miniature structures still poses significant challenges due to their small size, mass, fragility, and compliance [3–6]. Therefore, accurate dynamic characterization of these structures is highly needed for reliable design and performance evaluation.

Experimental modal analysis techniques have been widely used to obtain the dynamic characteristics of structures, as well as to verify numerical and analytical models [7–9]. For the majority of modal testing techniques, the structure is excited via a known (or measured) forcing function and the response is recorded using motion sensors such as accelerometers or laser Doppler vibrometry (LDV) [7, 10]. Thereby, a description of the system characteristics (input-output relationship) is obtained in the form of Frequency Response Functions (FRFs) calculated using power and cross spectral density functions. Having very high natural frequencies, small vibration amplitudes, and high compliance, miniature structures require additional care during modal testing [11]. Therefore, both excitation and measurement methods need to be appropriate for the required high frequency range [12]. With the recent developments in metrology and sensor technology, it is possible to obtain accurate high frequency vibration (response) measurements during modal testing of miniature structures [3, 7, 12]. However, excitation of miniature structures that provides inputs covering the high frequency range with controlled force amplitudes in a reproducible manner is still being investigated.

---

B. Bediz • E. Korkmaz • O.B. Ozdoganlar (✉)  
Department of Mechanical Engineering, Carnegie Mellon University, Pittsburgh, PA 15213, USA  
e-mail: [bbediz@andrew.cmu.edu](mailto:bbediz@andrew.cmu.edu); [ekorkmaz@andrew.cmu.edu](mailto:ekorkmaz@andrew.cmu.edu); [ozdoganlar@cmu.edu](mailto:ozdoganlar@cmu.edu)

Impact excitation, which is one of the common methods in modal testing of macro-scale structures is promising for experimental modal analysis of miniature structures [7, 13] since it is easy to implement, requires shorter measurement durations due to its transient characteristics, and prevents altering the dynamic characteristics of the miniature structures [14, 15]. However, the conventional impact hammers cannot be used in testing miniature structures due to its size and limited excitation bandwidth. With the recent advances in sensor technology, miniature impact hammers, which are capable of exciting required high frequencies, have been employed in modal testing. Yet, large amplitude of forces applied to the structure and repeatability issues need to be addressed for effective testing of miniature structures using miniature impact hammers [3, 5, 6, 16, 17]. Due to the aforementioned challenges of excitation methods, it is desirable to develop a setup to enable adjusting the amplitude of impact force to prevent any damage to the structure while simultaneously obtaining sufficient excitation bandwidth and single-hit impacts in a repeatable manner.

This paper presents design, development, and performance evaluation of an impact excitation system for repeatable and high-bandwidth modal testing of miniature structures. The system is equipped with a miniature force sensor attached to a custom designed flexure and an automated release mechanism driven by an electromagnet. The excitation bandwidth and the impact force exerted to the structure can be controlled by adjusting the initial displacement given to the impact excitation system and the gap between the impact load cell tip and the test surface. To show the effectiveness of the presented design, modal tests are performed on a cast iron block. It is shown that the presented impact excitation setup excites the structure with sufficient bandwidth and repeatable single-hit impacts.

## 23.2 Design and Construction of the Impact Excitation System

The schematic model of the designed impact excitation system (IES) is shown in Fig. 23.1. To measure the impact force exerted to the structure, an impact load cell (sensitivity 22.5 mV/N) that is attached to a custom designed flexure, is used. To provide initial deflection to the flexure (to excite the structure), a tubular electromagnet (ELMATU019017) is used. Both the electromagnet and the flexure are connected to an aluminum frame via manual positioners. With the aid of the manual positioners, the initial deflection (dictated by  $x_0$ ) given to the flexure and also the initial gap ( $g_0$ ) between the test surface and the impact hammer tip can be controlled (see Fig. 23.1).

As mentioned earlier, the designed impact excitation system should excite the structure in a repeatable and controllable manner with impacts capable of exciting higher frequencies. To address the repeatability issue, a flexure design that provides smooth, continuous, and repeatable displacements (without going into nonlinear regimes) that can be predicted accurately [18, 19] is used. More importantly, the tailor made flexure makes the system to be compliant in only one axis; therefore limits the motion in other axes (e.g., torsional motions or bending motions in other direction). Apart from the flexure design, a tubular electromagnet that eliminates the variability arising from a manual user is utilized. By cutting of the voltage supplied to the electromagnet, the flexure is released.

To achieve controllable impacts, the impact momentum, which is a function of both impact velocity and mass, needs to be controlled carefully [20–22]. To control the impact velocity, manual positioners are used between the aluminum frame and both the flexure and the electromagnet. The manual positioners enable controlling the amount of initial displacement ( $x_0$ ) given to the flexure and the distance ( $g_0$ ) between the impact load cell tip and the test surface.

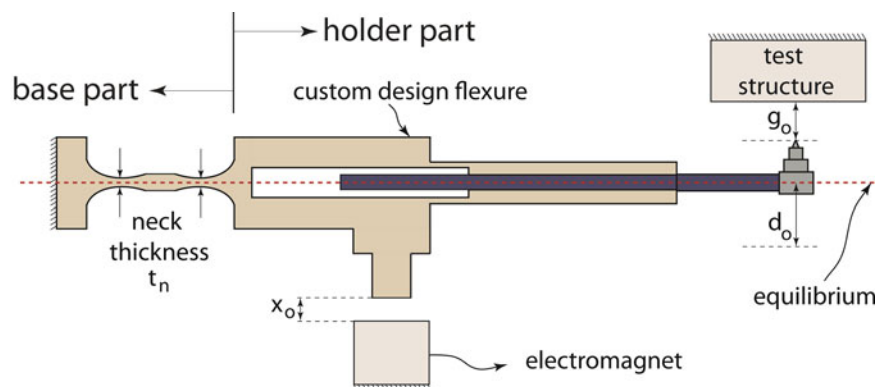


**Fig. 23.1** Schematic model of the impact excitation system

### 23.3 Model Development

To satisfy the test requirements (impact force amplitudes and excitation bandwidths), the control parameters ( $x_0$  and  $g_0$ ) need to be determined attentively. Especially for fragile miniature structures (or for compliant structures), excessive impact force levels may cause damage on the test structure. To address this issue, a dynamic model of the IES, that includes the analytical model of the flexure and the impact load cell system and the impact dynamics model, is constructed.

#### 23.3.1 Analytical Model of the Impact Excitation System

Spectral-Tchebychev (ST) approach is used to construct the analytical model of the flexure and impact load cell system [23, 24]. In the modeling process, to simultaneously achieve numerical efficiency and modeling accuracy, the IES divided into substructures (whose geometric parameters are either uniform or can be expressed as continuous functions) and one-dimensional (for holder substructures) and three-dimensional (for the base (curved) sections of the flexure) ST models used together. For simplicity, the plastic handle of the impact load cell inside the flexure is neglected. For each substructure, the integral boundary value problem (IBVP) is derived using the extended Hamilton's principle. Afterwards, to obtain the overall system's dynamic model, the individually modeled substructures are coupled using the component mode synthesis (CMS) approach.

For the 1D model, the IBVP can be expressed as (using Timoshenko beam assumptions),

$$\int_0^L \left[ \rho A \frac{\partial^2 u}{\partial t^2} \hat{u} + \rho I_x \frac{\partial^2 \psi_y}{\partial t^2} \hat{\psi}_y + \rho A \frac{\partial^2 v}{\partial t^2} \hat{v} + \rho I_y \frac{\partial^2 \psi_x}{\partial t^2} \hat{\psi}_x + \rho A \frac{\partial^2 \omega}{\partial t^2} \hat{\omega} + \rho I_p \frac{\partial^2 \psi_z}{\partial t^2} \hat{\psi}_z + E I_x \frac{\partial \psi_y}{\partial z} \frac{\partial \hat{\psi}_y}{\partial z} \right. \\ \left. + k_s G A(z) \left( \frac{\partial u}{\partial z} - \psi_y \right) \left( \frac{\partial u}{\partial z} - \hat{\psi}_y \right) + E I_y \frac{\partial \psi_x}{\partial z} \frac{\partial \hat{\psi}_x}{\partial z} + k_s G A(z) \left( \frac{\partial v}{\partial z} - \psi_x \right) \left( \frac{\partial v}{\partial z} - \hat{\psi}_x \right) + \right. \\ \left. E A \frac{\partial \omega}{\partial z} \frac{\partial \hat{\omega}}{\partial z} + G J_s \frac{\partial \psi_z}{\partial z} \frac{\partial \hat{\psi}_z}{\partial z} \right] dz = \int_0^L \{F_q\}^T \{\hat{q}\} dz, \quad (23.1)$$

where  $\{\hat{q}\}^T = \{\hat{u} \hat{\omega} \hat{\psi}_x \hat{\psi}_y \hat{\psi}_z\}^T$  are the functions representing the variation terms. Here,  $\rho$  is the density,  $A(z)$  is the cross-sectional area,  $I$ 's are the second area moments,  $J_s$  is the polar moment of inertia,  $E$  is the modulus of elasticity,  $G$  is the shear modulus, and  $k_s$  is the shear constant. For the 3D model, the IBVP is obtained 3D linear elasticity equations and can be expressed as

$$\int_{t_1}^{t_2} \int_0^L \int_{Area} \left[ \rho \{\ddot{q}\}^T \{\hat{q}\} - \{q\}^T [B]^T [B_C] \{\hat{q}\} + \{F_q\}^T \{\hat{q}\} \right] dx dy dz = 0, \quad (23.2)$$

where  $\{F_q\} = \{F_x F_y F_z\}^T$ . In arriving the IBVP given in Eq. (23.2), the stress-strain (constitutive) equations are  $\{\sigma\} = [C] \{\varepsilon\}$ , where  $[C]$  is the constitutive matrix, and the strain-displacement relations are  $\{\varepsilon\} = [B] \{q\}$ , where  $[B]$  is the differential operator matrix.

Next, to discretize the IBVPs given in Eqs. (23.1) and (23.2),  $q$ 's are expanded using 1D-ST and 3D-ST techniques as,

$$q_i \cong \sum_{n_i=1}^{N_z} a_{q_i}(t) T_{n_i-1}(z), \quad (23.3)$$

$$q_i(\xi, \eta, \zeta, t) \cong \sum_{l=1}^{N_\xi} \sum_{m=1}^{N_\eta} \sum_{n=1}^{N_\zeta} a_{q_i}(t) T_{l-1}(\xi) T_{m-1}(\eta) T_{n-1}(\zeta), \quad (23.4)$$

for 1D-ST and 3D-ST approaches, respectively, where  $q_i$  is the generalized coordinate,  $T$ 's are the scaled Tchebychev polynomials, and  $a_{q_i}$  are the time-dependent expansion coefficients. Both approaches result in

$$\underline{q}(M \ddot{\underline{q}} + K \underline{q} - F) = 0, \quad (23.5)$$

where  $[M]$  and  $[K]$  are the mass and stiffness matrices, respectively, and  $\{F\}$  is the forcing vector. The reader is referred to [23–25] since the derivation includes many intricate details, including a cross-section mapping (for the 3D-ST case) to simplify the solution domain.

**Table 23.1** Comparison of natural frequencies of the IES

Mode no	ST (Hz)	Exp. (Hz)	% Diff.	Damping ratio ( $\zeta$ )
1	23.0	23.1	-0.22	0.0086
2	287.5	289.3	-0.63	0.0411
3	532.0	533.8	-0.33	0.0217

To validate the analytical model of the flexure and the impact load cell system and also to determine the damping characteristics of the system (i.e. to determine the modal damping matrix,  $[C]$ ) that is necessary for simulating the tip motion of the IES, an experimental study is carried out to extract the modal parameters of the IES. The excitation is provided via the designed IES and the response is measured using an LDV. The modal parameters are extracted using a curve fitting algorithm (rational fraction polynomial method) and are given in Table 23.1. It is observed that the maximum difference between the simulation and the experimentation is 0.63 % (the average difference is 0.39 %) for the 2nd mode. These small differences between the simulation and experimentation results are mainly due to the small differences between the modeled and actual geometry, neglecting a portion of the stem part of miniature impact hammer, and the non-uniform material properties.

### 23.3.2 Impact Dynamics Model

To simulate the motions during impact, Hertz theory of contact is used [20, 21]. According to the Hertz theory, the impact (contact) force including the hysteresis damping can be expressed as [26],

$$F_{impact} = K\delta^n \left\{ 1 + \frac{3(1-e^2)}{4} \frac{\dot{\delta}}{U_o} \right\}, \quad (23.6)$$

where  $e$  represents the coefficient of restitution,  $U_o$  represents the impact velocity,  $\delta$  represents indentation amount,  $r_i$  and  $r_j$  represents the radii of the colliding bodies at the impact region, and  $K$  represents the contact stiffness expressed as

$$K = \frac{4}{3\pi(k_i + k_j)} \left\{ \frac{r_i r_j}{r_i + r_j} \right\}^{\frac{1}{2}}. \quad (23.7)$$

Here,  $k_i$  and  $k_j$  are related to the material properties of the colliding bodies and calculated as

$$k_l = \frac{1 - \nu_l^2}{\pi E_l}, \quad (23.8)$$

where  $\nu$  is the poisson's ratio and  $E$  is the elastic modulus of the colliding bodies.

### 23.3.3 Simulating the Tip Motion of the Impact Load Cell

Combining the analytical model of the flexure and impact load cell system and the impact dynamics model, the tip motion of the IES can be simulated to predict the impact force magnitude and bandwidth. However, initially it is necessary to decompose the overall motion of the IES into sub-motions. Figure 23.2 summarizes the three sub-motions of the IES experiences during testing.

In the first part (see Fig. 23.2a), the voltage supplied to the electromagnet to hold the IES in a deflected motion is cut off to release flexure. However, the electromagnetic field and force cannot become zero immediately. Therefore, until the electromagnetic field collapses completely, there is short period of time that the electromagnet continues to pull the flexure. Also, due to the eddy current issues, the flexure experiences a (decaying) magnetic damping since it moves within the collapsing magnetic field [27]. As a result, the motion can be found as a superposition of response due to displacement initial condition and electromagnetic force. To determine the decaying force profile of the electromagnet (both as a function of time and position), a force sensor (Kistler, 9256C1) is used. The (decaying) magnetic damping is determined through a curve fitting approach using an initial condition experiment where the response of the flexure is measured using an LDV.

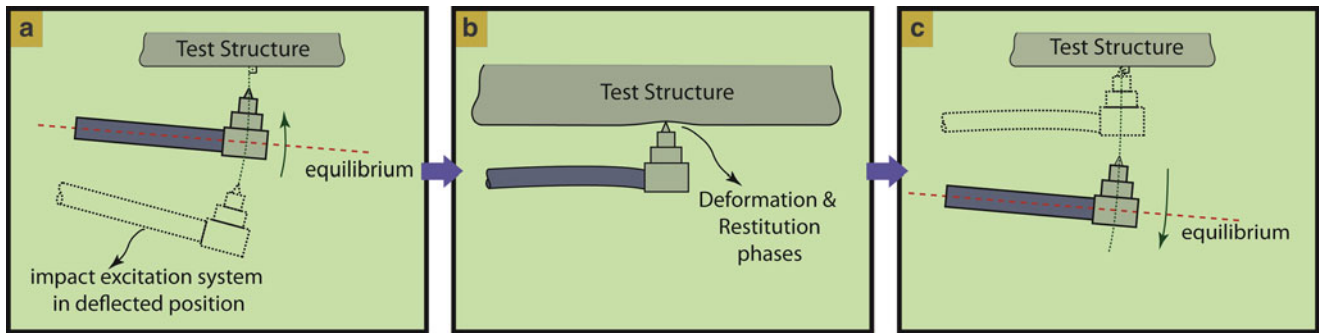


Fig. 23.2 Three different motions that the IES experiences during modal testing

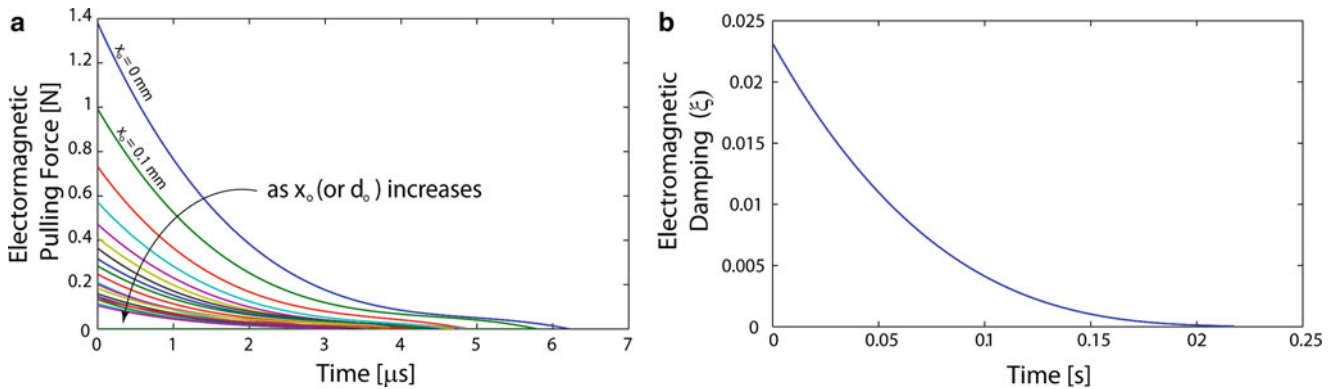


Fig. 23.3 (Decaying) (a) Force and (b) damping profile exerted by the electromagnet after it is shut off (when the electromagnet is connected to a 6 V DC supply)

Figure 23.3 shows both the decaying force profile of the electromagnet and the (decaying) magnetic damping experienced by the IES. Therefore, until the impact (hit) occurs, the tip motion can be calculated using the forced vibration of the flexure and the impact load cell system.

The second part (see Fig. 23.2b) is the impact period which is composed of deformation and restitution sub-periods. In this period, the IES moves under the effect of the impact force that can be calculated using Eqs. 23.6, 23.7 and 23.8. After the hit occurs, impact load cell tip is separated from the test structure's surface and moves freely due to the initial conditions (see Fig. 23.2c). Note that the initial conditions (both displacement and velocity initial conditions) in this step should be determined from the forced vibration response simulation performed in the second part.

To determine the tip motion of the impact load cell in all three parts, MATLAB<sup>®</sup> *ode* function is implemented using the analytical model of the flexure and the impact load cell system and the impact dynamics model. Figure 23.4 shows a sample result for the tip motion of the IES.

## 23.4 Performance Evaluation of the Impact Excitation System

To validate the constructed model to predict the tip motion and evaluate the performance of the IES, a case study is performed on a cast iron block as seen in Fig. 23.5. The experimental setup lies on a vibration isolation table (Newport RS 4000 with tuned damping). The excitation is provided via the designed IES and the response is measured using an LDV system (Polytecs MSA-400) with two fiber optic laser sources. Each fiber optic laser source splits into a pair of channels; therefore both relative and absolute measurements can be performed.

Since a cast iron block (which does not have an impact force limitation) is used to validate the constructed model, the model is validated for 20 different sets of control parameters. Figure 23.6 shows the impact force profiles and the corresponding impact spectra of the experimentation and simulation results for two selected sets of control parameters. It is observed that for all the selected parameter sets, the simulation results are in excellent agreement with those obtained from experimentation.

**Fig. 23.4** Sample simulated motion of the impact load cell tip

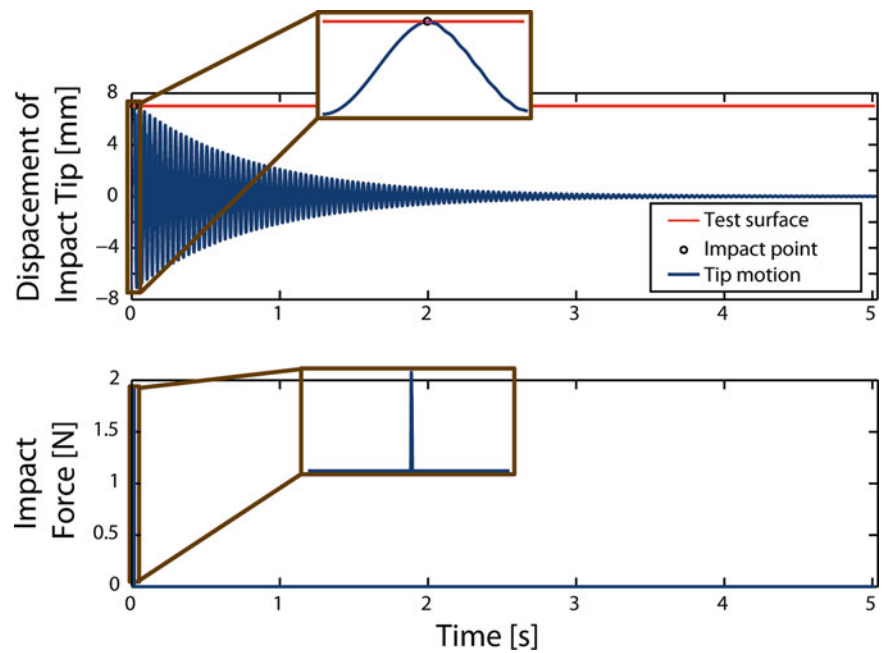
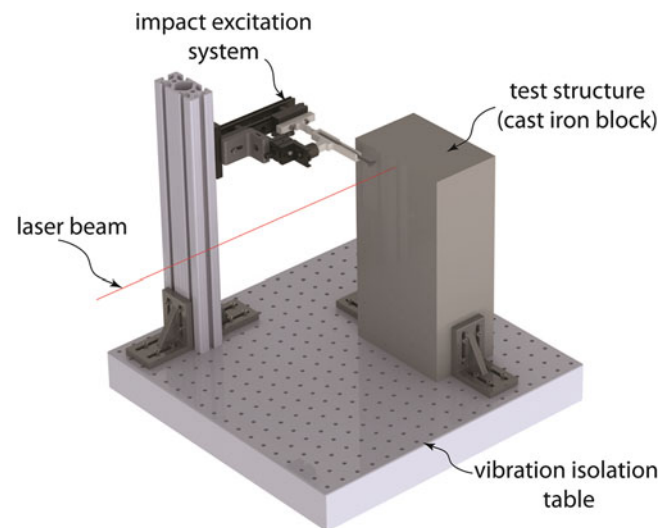


**Fig. 23.5** Impact testing on a cast iron block



To evaluate the performance of the IES, another important feature is to assess its repeatability in terms of (i) variability in impact (hitting) location, (ii) variability in impact force amplitudes and excitation bandwidth, and (iii) coherence values in modal testing. First, to determine the variability in hitting location (i.e. the precision of the IES), a pressure paper, that changes color with pressure is attached to the surface of the test block. 50 consecutive impacts are performed and the traces (of the impact tip) on the pressure paper are then analyzed using a microscope. Furthermore, to show the superiority of the IES with respect to manual hits, a similar experimentation is repeated hitting the structure manually with a hand held miniature impact hammer (that has the same impact tip geometry). To compare the impact regions, an image processing algorithm is used to calculate the area of the total impact region that encloses the impact points. It is observed that an impact area of  $0.25 \text{ mm}^2$  can be achieved with the designed IES (see Fig. 23.7a). On the other hand, with manual impacts, the impact region is calculated as  $10.94 \text{ mm}^2$  (see Fig. 23.7b).

Secondly, to test the variability in impact force magnitudes and compare with manual hits, 50 consecutive hits are performed both with IES and hand-held miniature impact hammer and the response is measured with an LDV to calculate the coherence values. Figures 23.8 and 23.9 show the obtained impact force profiles and the distribution of the impact force

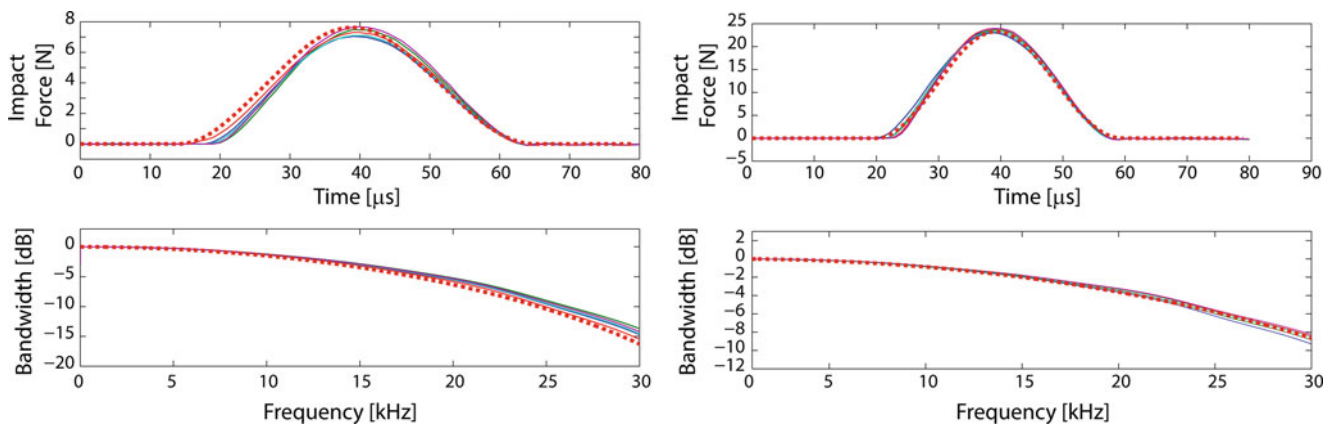
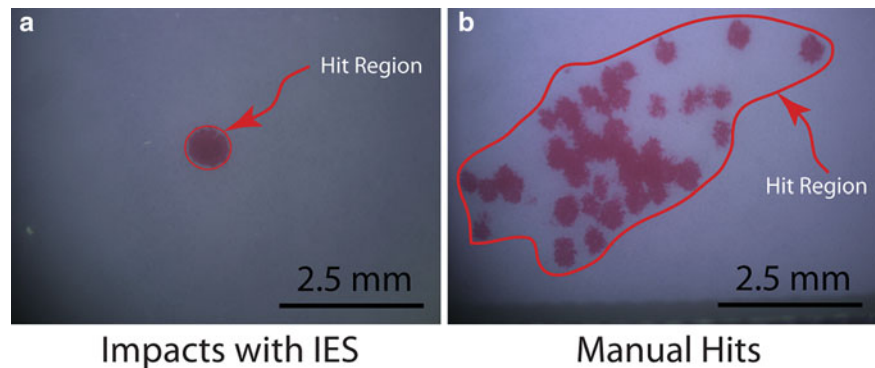


**Fig. 23.6** Impact force profiles and the corresponding input spectra for the selected parameters (*solid lines* – experimental data (5 hits are performed for each set), *red (dotted) line* – simulation data)

**Fig. 23.7** Impact location variability obtained (a) using the designed IES and (b) with manual hits



amplitudes, and the coherence plots obtained after 50 consecutive hits, respectively. Although, all of the 50 consecutive hits are single hit impacts for the experiments with the designed IES, only 32 out of 50 hits are single hit impacts for the tests performed manually. Therefore, to calculate the coherence values, only the response and input data for single hits are used. From Fig. 23.8, it is observed that the designed IES enables repeatable impacts in terms of impact force amplitude and bandwidth. The standard deviations are calculated as 0.54 and 8.82 N for impact force amplitudes and 0.43 and 4.19 kHz for impact bandwidths, by exciting the structure with the IES and manual hits, respectively. Furthermore, the coherence values obtained using the IES, is above 0.95 for the 20 kHz frequency range, even at the anti-resonance regions (see Fig. 23.9).

## 23.5 Summary and Conclusions

This paper presents an extensive study on design, development, and performance evaluation of an impact excitation system for repeatable and high-bandwidth modal testing of miniature structures. In this study, the constructed impact excitation system is tested on a cast iron block to investigate the variability in impact location, magnitude and bandwidth and compared with the experiments performed with hand-held miniature impact hammer. Coherence plots obtained from the modal test are also presented. Furthermore, to guide the selection of control parameters ( $x_0$  and  $g_0$ ), a dynamic model of the impact excitation system is constructed and validated through the performed experiments. It has been shown that the constructed dynamic model is accurate to predict the impact force amplitudes and bandwidths. Therefore, for modal testing of miniature (or compliant) structures, to prevent any damage to the test structure, the control parameters can be determined prior to the experimentation. In conclusion, the designed impact excitation system enables repeatable and high-bandwidth modal testing while controlling impact force amplitudes and bandwidths.

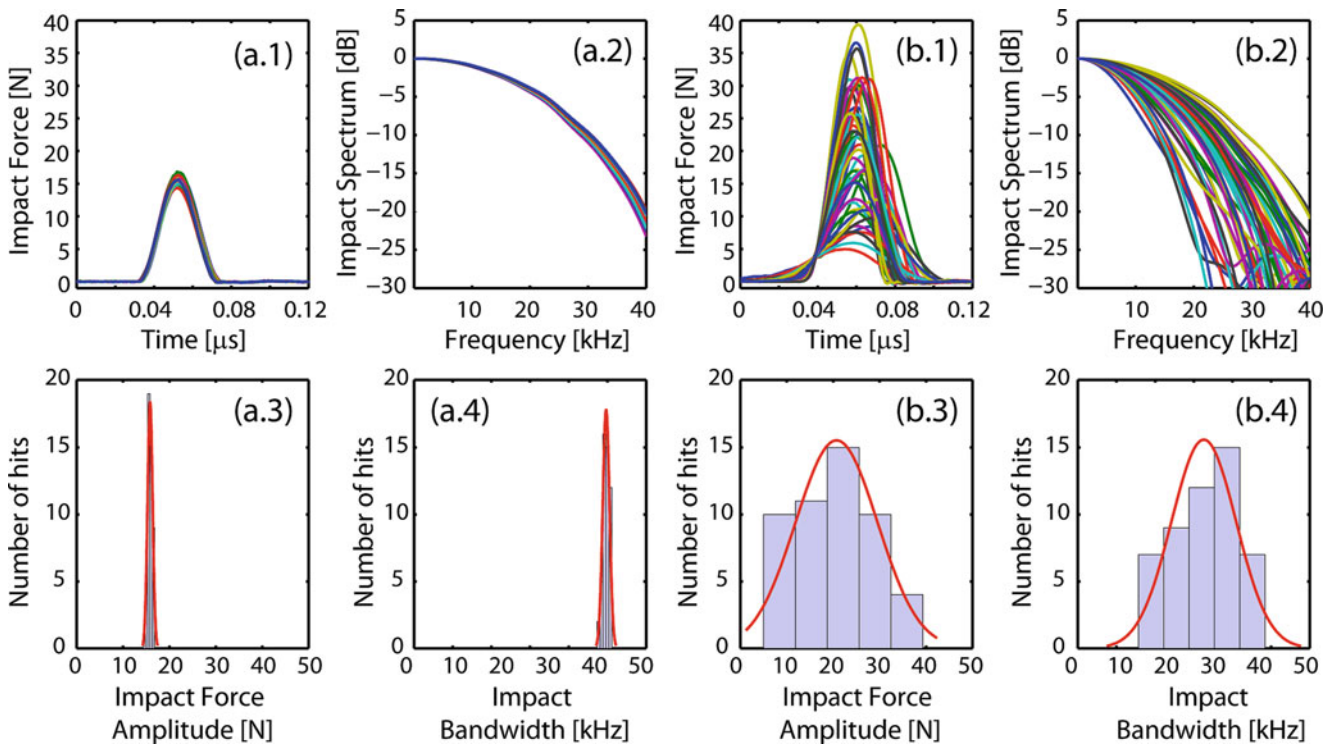
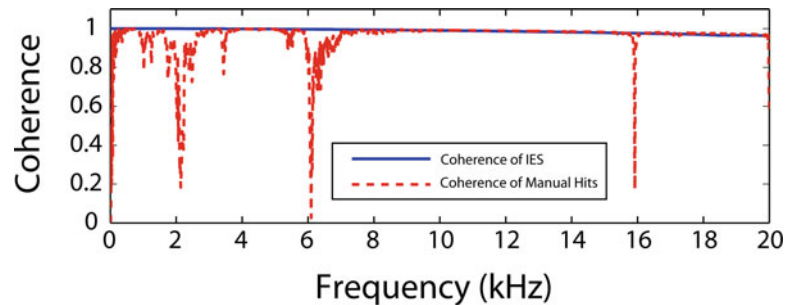


**Fig. 23.8** Impact force amplitude and bandwidth variability obtained (a) using the designed IES and (b) with manual hits

**Fig. 23.9** Coherence plots (obtained only averaging the test in which single-hits are obtained)



## References

- Salomon P (2005) Nexus market analysis report for MEMS and micro-systems, [http://www.meminfo.jp/whitepaper/WP18\\_MEX.pdf](http://www.meminfo.jp/whitepaper/WP18_MEX.pdf)
- Ehmann FK, Bourell D, Culpepper ML, Hodgson TJ, Kurfess TR, Madou M et al (2005) International assessment of research and development in micromanufacturing. World Technology Evaluation Center, Baltimore, Maryland, <http://www.wtec.org/micromfg/report/Micro-report.pdf>.
- Ozdoganlar OB, Hansche BD, Carne TG (2005) Experimental modal analysis for microelectromechanical systems. *Soc Exp Mech* 45(6):498–506
- Lin RM, Wang WJ (2006) Structural dynamics of microsystems—current state of research and future directions. *Mech Syst Signal Process* 20:1015–1043
- Filiz S, Tulsian A, Kota N, Ozdoganlar OB (2008) Obtaining the speed-dependent dynamics of an ultra-high-speed miniature spindle through experimental modal analysis. In: *Proceedings of the 3rd International conference on micromanufacturing*, Pittsburgh, PA
- Chou YF, Wang LC (2001) On the modal testing of microstructures: its theoretical approach and experimental setup. *J Vib Acoust* 123:104–109
- Ewins D (1984) *Modal testing: theory and practice*. Research Studies Press LTD., Letchworth, Hertfordshire, UK
- Ramsey KA (1983) *Experimental modal analysis, structural modifications and FEM analysis on a desktop computer*. Sound Vib 33–41
- Hermans L, Van Der Auweraer H (1999) *Modal testing and analysis of structures under operational conditions: Industrial applications*. *Mech Syst Signal Process* 13:193–216
- Schwarz BJ, Richardson MH (1999) *Experimental modal analysis*, CSI Reliability Week, Orlando, FL
- Filiz S, Ozdoganlar OB (2008) Microendmill dynamics including the actual fluted geometry and setup errors – Part II: model validation and application. *J Manuf Sci Eng* 130(3):1113
- Sriram P, Craig JJ, Hanagud S (1990) A scanning laser Doppler vibrometer for modal testing. *Int J Anal Exp Modal Anal* 5:155–167
- Agilent (2000) *How-To Guides/Manuals Agilent Application Note 243-3 ~ the Fundamentals of Modal Testing (5954-7957E)*, 05-2000



14. Corelli D, Brown DL (1984) Impact testing considerations. In: Proceedings of the 2nd international modal analysis conference, Orlando, FL
15. Olsen N (1984) Excitation functions for structural frequency response measurements. In: Proceedings of the 2nd international modal analysis conference, Orlando, FL
16. Burdess JS, Harris AJ., Wood D, Pitcher RJ, Glennie D (1997) A system for the dynamic characterization of microstructures. *J Microelectromech Syst* 6(4):322–328
17. Wu TW, Lee CK, Wang RH (1993) Micro-impact technique and its applications. *Materials Research Society Symposium*, pp 133–139
18. Smith ST, Chetwynd DG (2005) *Foundations of ultra-precision mechanism design*, Gordon and Breach Science Publishers, New York, NY, USA
19. Gary PJ (1954) *Flexure Devices. Pivots, Movements, Suspensions*, British Scientific Instruments Research Association, Chislehurst
20. Akay A, Hodgson TH (1978) Acoustic radiation from the elastic impact of a sphere with a slab. *Appl Acoust* 11:285–304
21. Guban D (2000) Inelastic collision and the Hertz theory of impact. *Am J Phys* 68:920–924
22. Gilardi G (2002) Literature survey of contact dynamics modeling. *Mech Mach Theory* 37:1213–1239
23. Yagci B, Filiz S, Romero LA, Ozdoganlar OB (2009) A spectral-Tchebychev technique for solving linear and nonlinear beam equations. *J Sound Vib* 321:375–404
24. Filiz S, Bediz B, Romero LA, Ozdoganlar OB (2012) A spectral-Tchebychev solution for three-dimensional vibrations of parallelepipeds under mixed boundary conditions. *J Appl Mech* 79(5):051012
25. Bediz B, Kumar U, Schmitz TL, Ozdoganlar OB (2012) Modeling and experimentation for three-dimensional dynamics of endmills. *Int J Mach Tools Manuf* 53:39–50
26. Lankarani H (1994) Continuous contact force models for impact analysis in multibody systems. *Nonlinear Dyn* 5:193–207
27. Kraus JD, Fleisch DA (1999) *Electromagnetics: with applications*. McGraw Hill, New York

# Chapter 24

## Replicating Aerodynamic Excitation in the Laboratory

P.M. Daborn, P.R. Ind, and D.J. Ewins

**Abstract** Many structures experience random vibration caused by the rapid flow of air over the external surface of the structure. One example of this “aerodynamic excitation” occurs when missiles fly through the atmosphere en-route to target in powered flight, or slung to the undercarriage of an aircraft. In most cases, it is necessary to carry out laboratory testing in order to qualify the design of the structure and to assess the pedigree of the manufacturing and assembly process. The laboratory test should replicate, as closely as possible, the damage potential of the in-flight environment. The traditional method of replicating the aerodynamic induced vibration in the laboratory is to rigidly attach the structure to a large electrodynamic shaker and to subject the structure to random vibration. This testing methodology is inadequate and non-representative for two main reasons: (1) the excitation mechanisms are very different, i.e. through a distinct region when attached to a shaker compared to distributed excitation over the entire outer surface in-flight, (2) The boundary conditions are very dissimilar, i.e. attachment to a very high mechanical impedance shaker compared to “free” flight. There is much evidence to show that this testing methodology often leads to overly severe tests. Furthermore, the test program can be costly and time-consuming as tests are often carried out sequentially in three orthogonal axes. In addition, tests have to be repeated with different response control accelerometers as it is impossible to maintain in-flight responses all over the structure simultaneously due to the two reasons given previously. This paper details research carried out to replace the traditional rigid shaker approach to one with the structure “freely” supported and excited at multiple locations simultaneously using Multi Input Multi Output (MIMO) vibration control. The research focusses on analytical models in Matlab and Ansys to carry out “virtual tests” in order to demonstrate issues with the current testing methodology and to highlight the benefits of a new approach. Results from the analytical models show significant improvements in degree-of-replication and would result in faster and more cost effective laboratory testing.

**Keywords** Virtual testing • Aerodynamic • Random vibration • Matlab • Ansys • Piezoelectric exciters • Laser Doppler vibrometry • Electrodynamic shaker • Finite element model • Power spectral density • Multi input multi output (MIMO) • Frequency response function • Missile

### 24.1 Introduction

A watershed period of aerospace research and development occurred during the 1960s, often referred to as the Apollo era, providing major advances in the field of structural dynamics [1]. In recent decades, the development of computational modelling has accelerated far more rapidly than testing procedures, which often still have their methodologies rooted in the 1960s and 1970s [2–4]. Today, testing is often perceived as slow, inefficient and costly when compared with analytical methods and some focused efforts are required to redress the balance [5–7]. A comment that is often heard is “test versus

---

P.M. Daborn (✉) • D.J. Ewins  
Bristol Laboratory for Advanced Dynamics Engineering (BLADE), Aerospace Engineering,  
University of Bristol, Queen’s Building, University Walk, Bristol BS8 1TR, UK  
e-mail: [aepmd@bristol.ac.uk](mailto:aepmd@bristol.ac.uk); [philip.daborn@awe.co.uk](mailto:philip.daborn@awe.co.uk)

P.R. Ind  
Structural Dynamics, AWE Aldermaston, Reading, Berks RG7 4PR, UK

analysis”, implying that they are opposing activities, although much evidence exists which supports the notion that the two used in tandem can be much greater than the sum of their parts [8–11].

One of the major deficiencies with current laboratory testing practices is the replication in the laboratory of aerodynamic excitation as seen by structures flying through the atmosphere. It should be noted that aerodynamic excitation is just one form of distributed excitation, of which there are many. This paper focusses on aerodynamic excitation, however the details of this research could easily be transferred to other forms of distributed excitation.

One typical example of aerodynamic excitation is a missile en-route to target in powered flight or slung to the undercarriage of an aircraft. In most cases, it is necessary to carry out laboratory testing in order to qualify the design of the structure and to assess the pedigree of the manufacturing and assembly process. The laboratory test should replicate, as closely as possible, the damage potential of the in-flight environment. The traditional method of replicating the aerodynamic induced vibration in the laboratory is to rigidly attach the structure to a large electrodynamic shaker and to subject the structure to random vibration. This testing methodology is inadequate and non-representative for two main reasons: (1) the excitation mechanisms are very different, i.e. through a distinct region when attached to a shaker compared to distributed excitation over the entire outer surface in-flight, (2) The boundary conditions are very dissimilar, i.e. attachment to a very high mechanical impedance shaker compared to “free” flight. There is much evidence to show that this testing methodology often leads to overly severe tests [12–15]. Furthermore, the test program can be costly and time-consuming as tests are often carried out sequentially in three orthogonal axes. In addition, tests have to be repeated with different response control accelerometers as it is impossible to maintain in-flight responses all over the structure simultaneously due to the two reasons given previously.

This paper demonstrates the issues with current methods of replicating aerodynamic excitation in the laboratory and offers an alternative approach that may result in significant benefits in terms of quality and efficiency of the laboratory test. This research is heavily reliant on “virtual testing”, i.e. simulating the test in an analytical model prior to testing and the use of a simple case study is an ideal way to understand some of the necessary concepts.

### 24.2 10 DOF Case Study: Applying Aerodynamic Excitation

Consider the simple free-free 10 DOF system shown in Fig. 24.1 and algebraically constructed in Matlab.

This system replicates a structure, such as a missile, in flight and all calculations associated with the system are carried out in the frequency domain. Each system mass is 10 kg giving a total mass of 100 kg and virtual accelerometers ( $a_1$  and  $a_2$ ) have been placed on masses 1 and 7. The spring stiffness values ( $k_n$ ) have been selected to achieve three flexural resonances under 2,000 Hz and to ensure asymmetry. Modal damping ( $\eta_r$ ) of 5 % has been applied to all modes. In order to replicate the distributed aerodynamic excitation over the surface of the structure, force PSDs have been applied to each of the system masses. The magnitude of the force PSDs can be seen in Fig. 24.2 and these were selected to be  $3 \text{ N}^2/\text{Hz}$  as this resulted in realistic test specifications later in the case study.

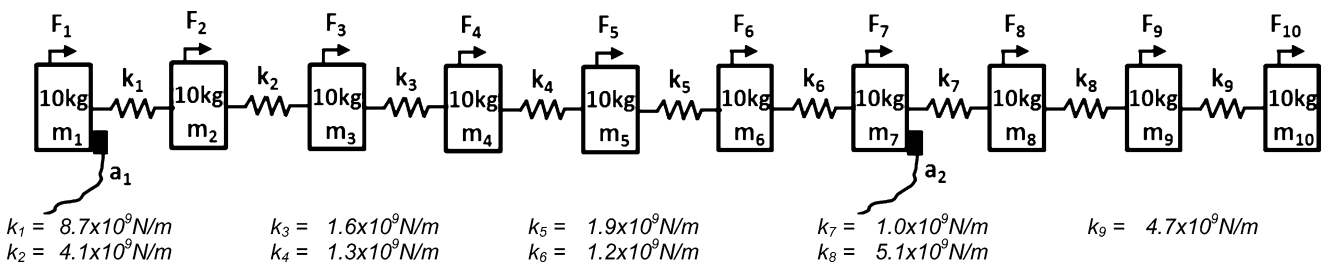
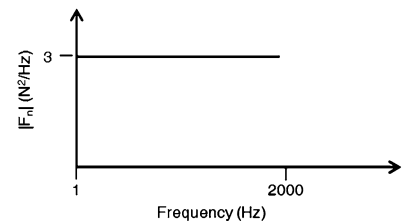
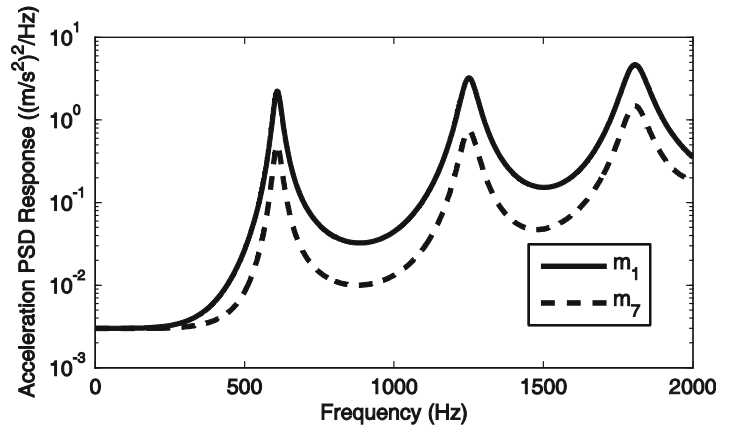


Fig. 24.1 Simple 10 DOF spring mass system with distributed excitation

Fig. 24.2 Magnitude of force PSDs applied to each of the system masses



**Fig. 24.3** Response of masses 1 and 7 to distributed excitation



It is assumed that the force PSDs are a flat spectrum from 1 to 2,000 Hz – for the purposes of this case study, it is not necessary to accurately replicate aerodynamic excitation, only to apply a **distributed** excitation to the system. The forces were generated such that there was random correlation between the forces applied to the different masses. Random correlation of the forces seemed to be the most appropriate approach to take for this simple case study and no account is taken of the degree of correlation that is likely to be seen in true aerodynamic excitation, e.g. higher degree of correlation between closely spaced masses. The acceleration response PSDs of the system masses ( $[S_{xx}(\omega)]$ ) were calculated at each spectral line ( $\omega$ ) using the standard Multiple Input Multiple Output (MIMO) equation below:

$$[S_{xx}(\omega)]_{10 \times 10} = [\alpha(\omega)]_{10 \times 10} [S_{ff}(\omega)]_{10 \times 10} [\alpha(\omega)]_{10 \times 10}^H \quad (24.1)$$

Where  $[S_{ff}(\omega)]$  is a matrix of the auto power spectral density elements of the applied force,  $[\alpha(\omega)]$  is a matrix of acceleration frequency response elements and  $[ ]^H$  denotes the Hermitian transpose. The diagonal values of the  $[S_{ff}(\omega)]$  were set to be  $3 \text{ N}^2/\text{Hz}$  and the off-diagonal values were set to be zero, i.e. the mean average value of an infinite number of repetitions of two randomly correlated forces. The acceleration matrix was generated using the following equation:

$$[\alpha(\omega)] = [\phi] \begin{bmatrix} \ddots & & & & \\ & \frac{-\omega^2}{\omega_r^2 - \omega^2 + i\eta_r\omega_r} & & & \\ & & \ddots & & \\ & & & \ddots & \\ & & & & \ddots \end{bmatrix} [\phi]^T \quad (24.2)$$

Where  $[\phi]$  is the matrix of eigenvectors of the system,  $\omega_r$  is the natural frequency of the  $r$ th mode,  $\eta_r$  is the modal damping value of the  $r$ th mode. The natural frequencies and eigenvectors were calculated by eigenvalue decomposition of the mass and stiffness matrices of the system in Matlab.

Assume that acceleration measurements were taken at masses 1 and 7 by the virtual accelerometers ( $a_1$  and  $a_2$  in Fig. 24.1), these will be called the “true” aerodynamic response measurements and are the target to be aimed for in any laboratory test and are shown in Fig. 24.3. The MIMO equations used to calculate these curves are detailed in Sect. 24.4.

### 24.3 Virtual Shaker Test

Ideally a structure which is subjected to aerodynamic excitation in-flight would be subjected to a wind tunnel test in order to replicate the environment in the laboratory. However, wind tunnels are not easily accessible to most establishments, are expensive to use and may not be able to excite the structure to adequate levels. With this in mind, the use of shaker testing is still the most common method of qualifying a system for aerodynamic environments and is likely to remain so for the foreseeable future.

The rationale for selecting accelerometer locations is often based on convenience or read back to previous trials data and not on a scientific basis. For instance, mass 1 may be selected as it is a convenient mounting position and will be used as shaker control location in a subsequent shaker test. The response measured at mass 1 would typically be enveloped when generating the test specification for the laboratory test. This is to ensure that the test level will always be more severe

**Fig. 24.4** Typical envelope of aerodynamic response (mass 1)

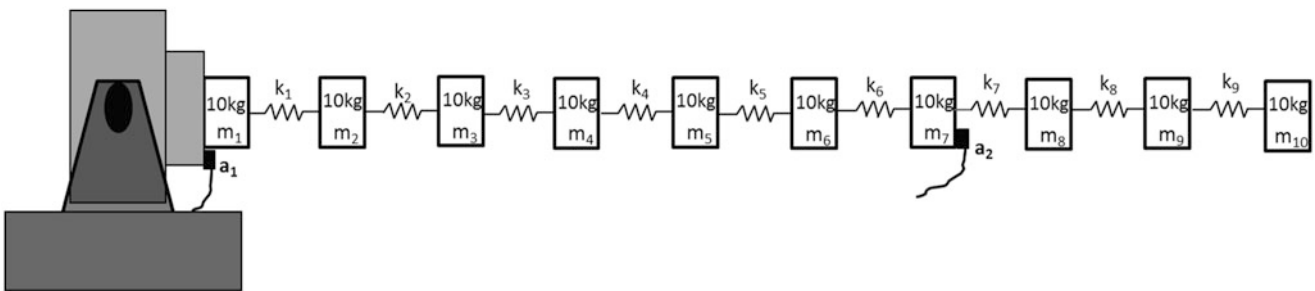
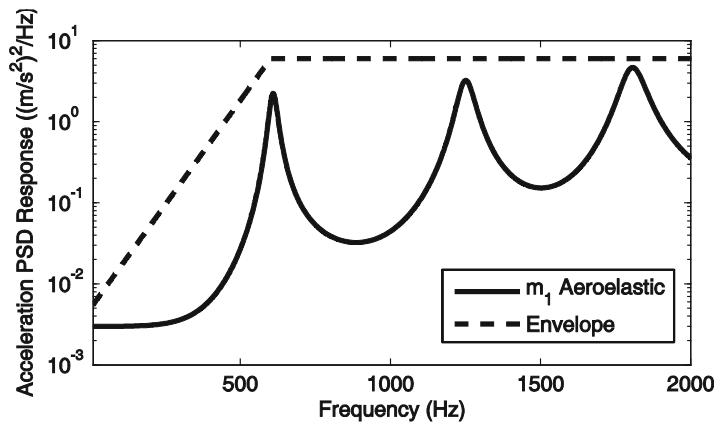
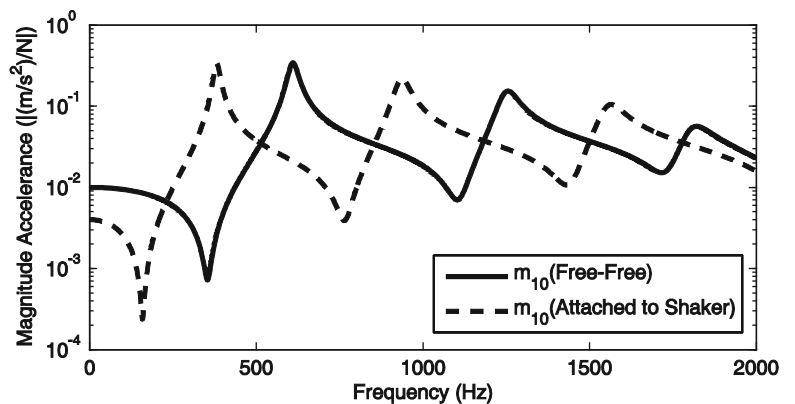


**Fig. 24.5** Structure attached to shaker in laboratory test

**Fig. 24.6** Drive point FRFs for mass 10 in free-free and attached to shaker configurations



than the in-flight environment, especially when considering the unit-to-unit variability of the structure, the variability in the environment severity and the fact that attaching the structure to the shaker alters the dynamics of the structure. A typical envelope of the aerodynamic response can be seen in Fig. 24.4.

The next step is to attach the structure to an electrodynamic shaker in the laboratory as shown in Fig. 24.5.

In this case study, mass 1 is rigidly attached to an adaptor plate (50 kg), which in turn is rigidly attached to the shaker armature (100 kg) to form one large rigid mass of 160 kg. The process of attaching the structure to the shaker significantly alters the dynamics of the structure – this can be seen by the drive point FRFs of mass 10 for the two configurations as shown in Fig. 24.6.

It can be seen from the figure above that the frequencies of the resonances and anti-resonances have shifted significantly.

The next step in a typical laboratory random vibration test is to excite the structure with the shaker and to control the level of vibration to the envelope at mass 1 as shown in Fig. 24.4. This random vibration test was simulated in Matlab with perfect control, i.e. the mass 1 response matches exactly the envelope in Fig. 24.4. The response at mass 7, compared to the original aerodynamic response, is shown in Fig. 24.7.

**Fig. 24.7** Acceleration response PSD of mass 7 (aerodynamic and attached to shaker)

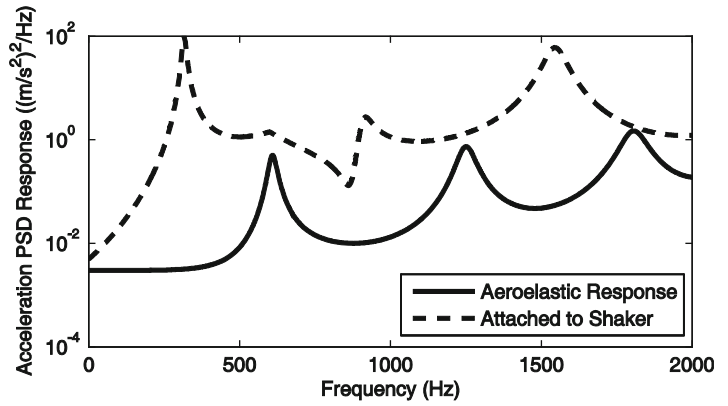
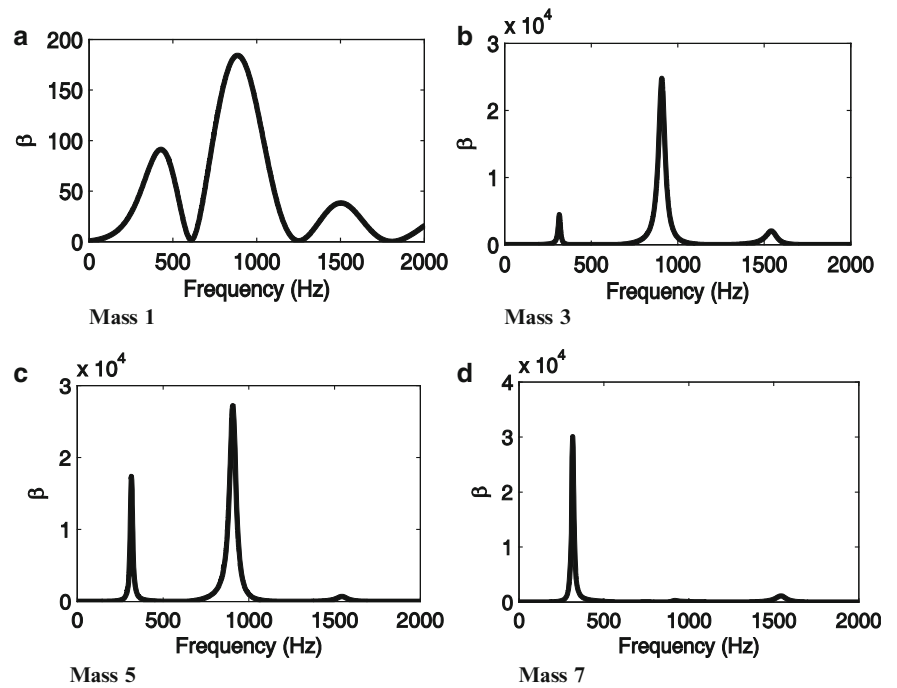


**Fig. 24.8** Degree of overttest/undertest for masses 1, 3, 5 and 7 in virtual shaker test controlled to mass 1 envelope



It can be seen that the laboratory test, carried out to match the envelope, is a significant overttest when compared to the original aerodynamic excitation. Furthermore, the degree of overttest is significantly different across the bandwidth and for different masses. The degree of overttest/undertest across the bandwidth can be calculated by Eq. (24.3):

$$\beta(\omega) = (({}_nS_{xx}^L(\omega) - {}_nS_{xx}(\omega)) / {}_nS_{xx}(\omega)) \tag{24.3}$$

Where  ${}_nS_{xx}^L(\omega)$  and  ${}_nS_{xx}(\omega)$  are the acceleration PSD response for system mass  $n$  at frequency  $\omega$  for the MIMO laboratory and the aerodynamic environments respectively.  $\beta$  is unit-less and is shown for four of the system masses (1, 3, 5 and 7) in Fig. 24.8 where the degree of overttest is significant for large portions of the bandwidth and particularly at resonances of the coupled structure/shaker system. A positive  $\beta$  value indicates that the virtual laboratory test has a higher PSD response than the aerodynamic PSD response and vice versa. A zero  $\beta$  value indicates that the virtual laboratory test and the aerodynamic responses are identical in magnitude.

The overttest in the virtual laboratory test is caused by two main factors; (1) the enveloping procedure, (2) the alteration of the structural dynamics by rigidly attaching the structure to the shaker. In order to ascertain the relative contribution of each, a virtual laboratory test was run with mass 1 controlled to the aerodynamic response level shown in Fig. 24.3 i.e. ensure mass 1 behaves as it does in the aerodynamic environment with no enveloping. The overttest values for four of the system masses (masses 1, 3, 5 and 7) can be seen in Fig. 24.9.

**Fig. 24.9** Degree of overttest/undertest for masses 1, 3, 5 and 7 in virtual shaker test controlled to mass 1 aerodynamic response

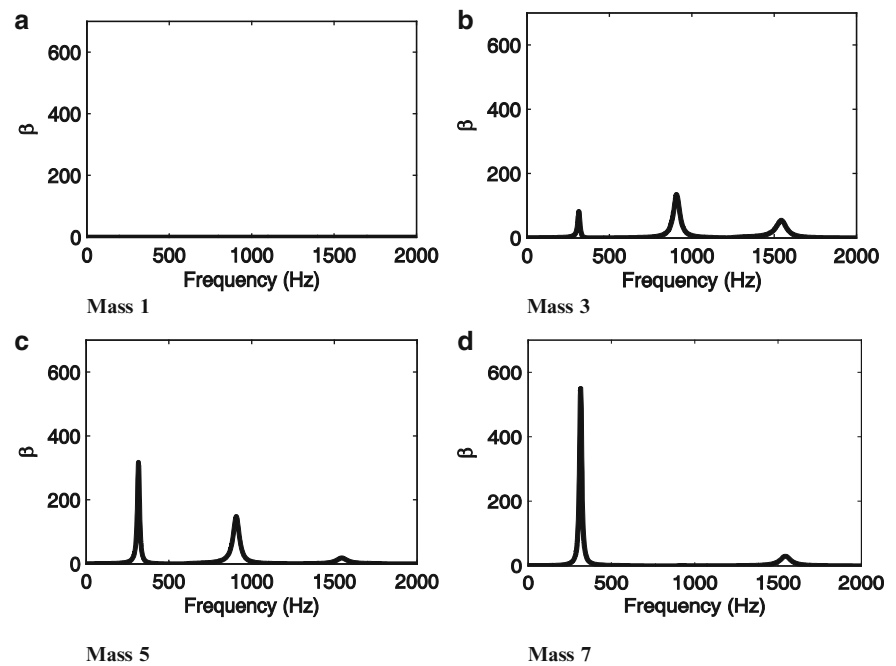


**Table 24.1** g-rms values of all systems masses for aerodynamic excitation and the virtual shaker test

Mass #	Aerodynamic excitation (g-rms)	Virtual shaker test (g-rms)		g-rms overttest (%)	
		Controlled to envelope of mass 1	Controlled to aerodynamic response of mass 1	Controlled to envelope of mass 1	Controlled to aerodynamic response of mass 1
1	3.3	9.6	3.3	191	0
2	1.6	17.6	2.6	1000	63
3	1.8	19.0	2.8	956	56
4	1.7	18.1	2.2	965	29
5	1.7	17.1	2.3	906	35
6	2.0	16.1	2.9	705	45
7	1.8	10.4	2.3	478	28
8	1.2	12.9	1.6	975	33
9	1.4	14.8	1.9	957	36
10	1.6	16.0	2.1	900	31

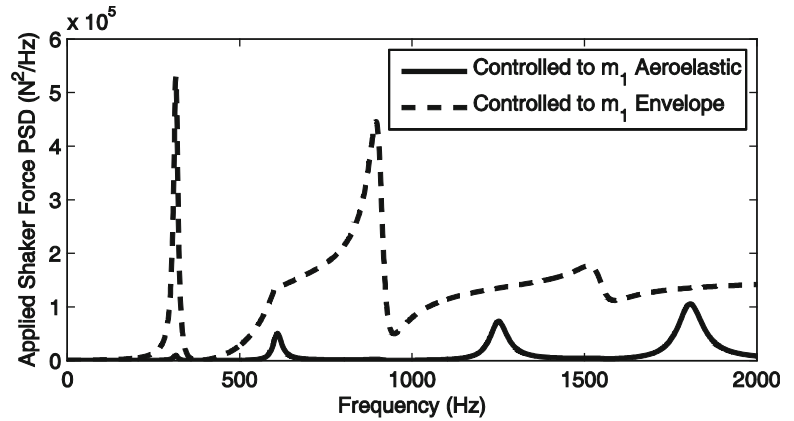
It can be seen from Fig. 24.9 that for the system masses, with the exception of mass 1, that at certain spectral lines the overttest can be considerable, especially at the resonances of the coupled structure/shaker system.

It is possible to determine the acceleration root mean square (rms) value of any given mass by calculating the area under the response PSD curve and taking the square root. These values were calculated for the original aerodynamic excitation and for the virtual shaker test controlled to both mass 1 envelope and mass 1 aerodynamic response and are shown in Table 24.1 where rms values have been calculated in acceleration units of  $g$ .

It can be seen from the table above that the g-rms overttest for the virtual shaker test is far greater when it is controlled to the envelope of mass 1. It can be concluded that the dominant cause of the g-rms overttest is the enveloping procedure. However, it is the act of rigidly coupling the structure to the shaker that causes considerable overttests at individual spectral lines, often the structure is subjected to excitation levels on the shaker that are many orders-of-magnitude higher than the aerodynamic excitation would cause.

It is possible to determine the force applied to the structure in the aerodynamic excitation environment and the virtual shaker test. In the aerodynamic environment, the force rms values can be determined by the summation of the  $3 \text{ N}^2/\text{Hz}$  force PSDs applied to each of the 10 masses and yields a value of  $775 \text{ Nrms}$ . In the virtual shaker test, it is possible to determine the force applied by the shaker to the coupled shaker armature/adaptor plate/mass 1 system. The force PSD applied by the shaker for the two virtual shaker tests can be seen in Fig. 24.10. It can be seen that there are significant peaks at the anti-resonances of the coupled structure/shaker system. The Nrms values of these two virtual shaker tests are approximately

**Fig. 24.10** Force PSD applied by the shaker in the virtual shaker tests



4,000 Nrms (controlled to aerodynamic) and 15,000 Nrms (controlled to envelope). These values are significantly higher than the force values applied in the original aerodynamic excitation. This mismatch in force imparted, which is related to the energy imparted, is usually a natural warning that something is incorrect in the test setup. In this instance, the warning is indicating that it is not ideal to replicate distributed excitation with a discreet excitation at one (or few) locations and to significantly alter the structural dynamics by attaching the structure to a massive and rigid shaker.

It has been shown that the current methods for replicating aerodynamic excitation in the laboratory are not ideal and the following section discusses a different approach which may result in significant improvements.

## 24.4 A New Approach to Replicating Aerodynamic Excitation in the Laboratory

Consider the same 10 DOF system suspended in the laboratory by elastic bungee (Fig. 24.11). All calculations assume that there is negligible effect from the suspension, i.e. the structure is freely floating in space with no gravitational effects. This is the configuration often employed to replicate structures freely floating in space, e.g. modal tests to validate finite element (FE) models and is far more representative of a structure in-flight when compared to rigidly attaching the structure to a large shaker. The structure is excited by three small electrodynamic shakers Q(1), Q(2) and Q(3) at masses 2, 4 and 8 respectively and the acceleration is measured by accelerometers P(1) and P(2) at masses 1 and 7 respectively. The shakers and accelerometers are not located in optimal positions, they are only located for reasons of convenience. Discussion regarding the number and positions of P and Q is given later in this paper. It is assumed that the shakers impart a force to the structure without affecting the dynamics of the structure.

This setup shall employ Multiple Input Multiple Output (MIMO) control, i.e. the multiple inputs (force<sup>1</sup> applied by the shakers, Q) shall be optimally controlled to achieve desired multiple outputs (acceleration at accelerometers, P). This test setup shall be referred to as the MIMO laboratory test. The first step in the process of carrying out a MIMO laboratory test is to obtain the aerodynamic response at P. For this case study, this can be done by a reduced version of Eq. (24.1) and is given below:

$$[S_{xx}(\omega)]_{P \times P} = [\alpha(\omega)]_{P \times N} [S_{ff}(\omega)]_{N \times N} [\alpha(\omega)]_{N \times P}^H \quad (24.4)$$

Where  $N$  is the number of DOFs aerodynamically excited, in this case 10. The leading diagonal elements of  $[S_{xx}(\omega)]_{P \times P}$  are the two PSD curves shown in Fig. 24.3. It is possible to determine the optimal shaker force PSDs (Q) in a least squares sense, to achieve the desired aerodynamic accelerations (P) by the following equation:

$$\left[ S_{ff}^L(\omega) \right]_{Q \times Q} = [\alpha(\omega)]_{Q \times P}^+ [S_{xx}(\omega)]_{P \times P} [\alpha(\omega)]_{P \times Q}^{+H} \quad (24.5)$$

<sup>1</sup> In a physical MIMO laboratory test, it is likely that the inputs would be the voltage to the shakers instead of the force to the structure.



**Fig. 24.11** 10 DOF system freely suspended in laboratory

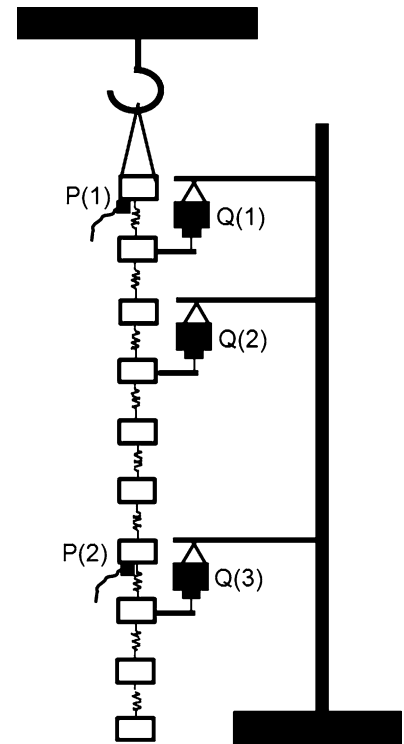
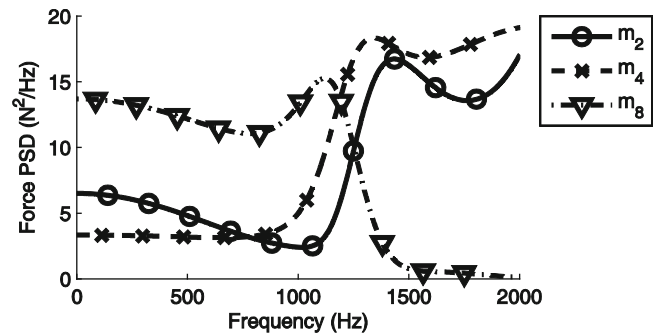


**Fig. 24.12** Virtual MIMO laboratory test force PSDs



Where  $[S_{ff}^L(\omega)]$  is a matrix of the auto power spectral density elements of the applied force in the MIMO test and  $[ ]^+$  denotes the Moore-Penrose pseudo inverse.  $[S_{ff}^L(\omega)]$  was calculated for the three excitation DOFs in the 10 DOF system and the leading diagonal elements are shown in Fig. 24.12.

The total force rms values of the three force PSDs above is approximately 400 Nrms. This is far lower than the values calculated earlier for the virtual shaker test which gave values of approximately 4,000 Nrms (controlled to aerodynamic) and 15,000 Nrms (controlled to envelope). Furthermore, it is approximately half the value of the original aerodynamic excitation and shows that it is possible in the laboratory to give a structure the “same ride” as it would see in-flight, even by applying less total force. This is possible as the force in the laboratory is applied in an intelligent manner.

With the force PSDs in Fig. 24.12, it is then possible to calculate the acceleration PSD response ( $[S_{xx}^L(\omega)]_{P \times P}$ ) at the accelerometer DOFs (P) in the MIMO laboratory test using the following equation:

$$[S_{xx}^L(\omega)]_{P \times P} = [\alpha(\omega)]_{P \times Q} [S_{ff}^L(\omega)]_{Q \times Q} [\alpha(\omega)]_{Q \times P}^H \tag{24.6}$$

Prior to the calculation using Eq. (24.6), the off diagonal terms of  $[S_{ff}^L(\omega)]$  were set to zero. This is appropriate for a test involving lots of averages of a randomly correlated signal. The acceleration response PSDs were calculated and are plotted with the original aerodynamic responses at the same DOFs in Fig. 24.13.

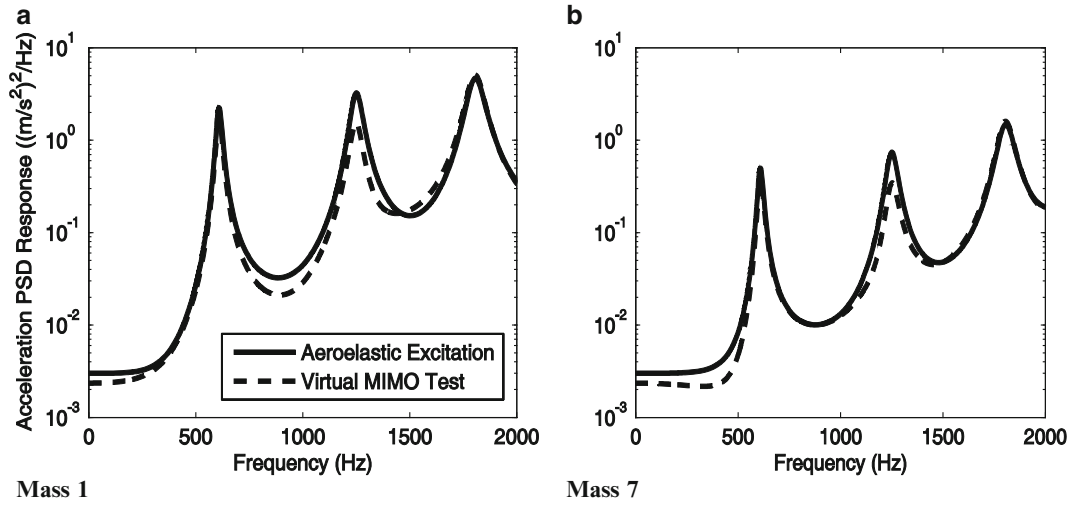


Fig. 24.13 Acceleration PSD response in aerodynamic environment and virtual MIMO test for measured DOFs (P). (a) Mass 1. (b) Mass 7

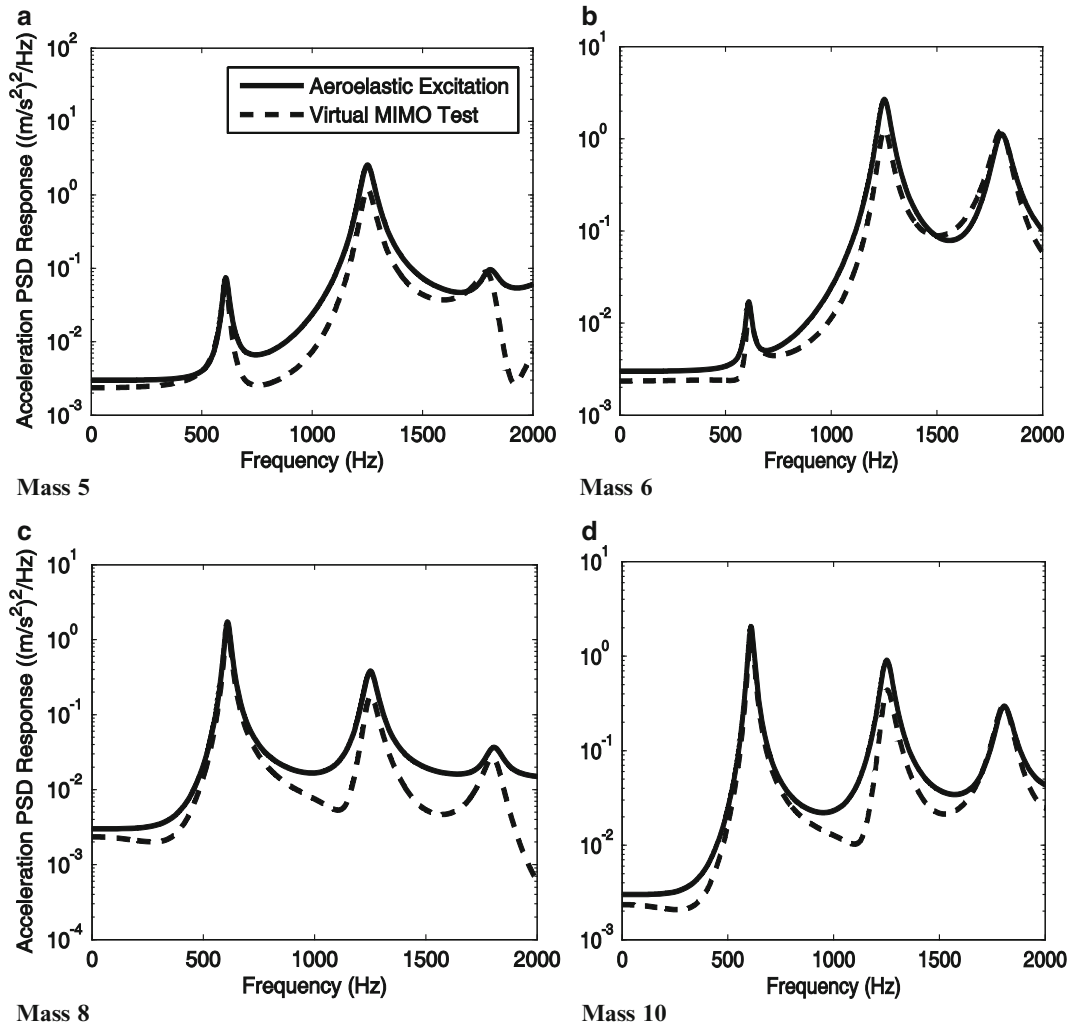
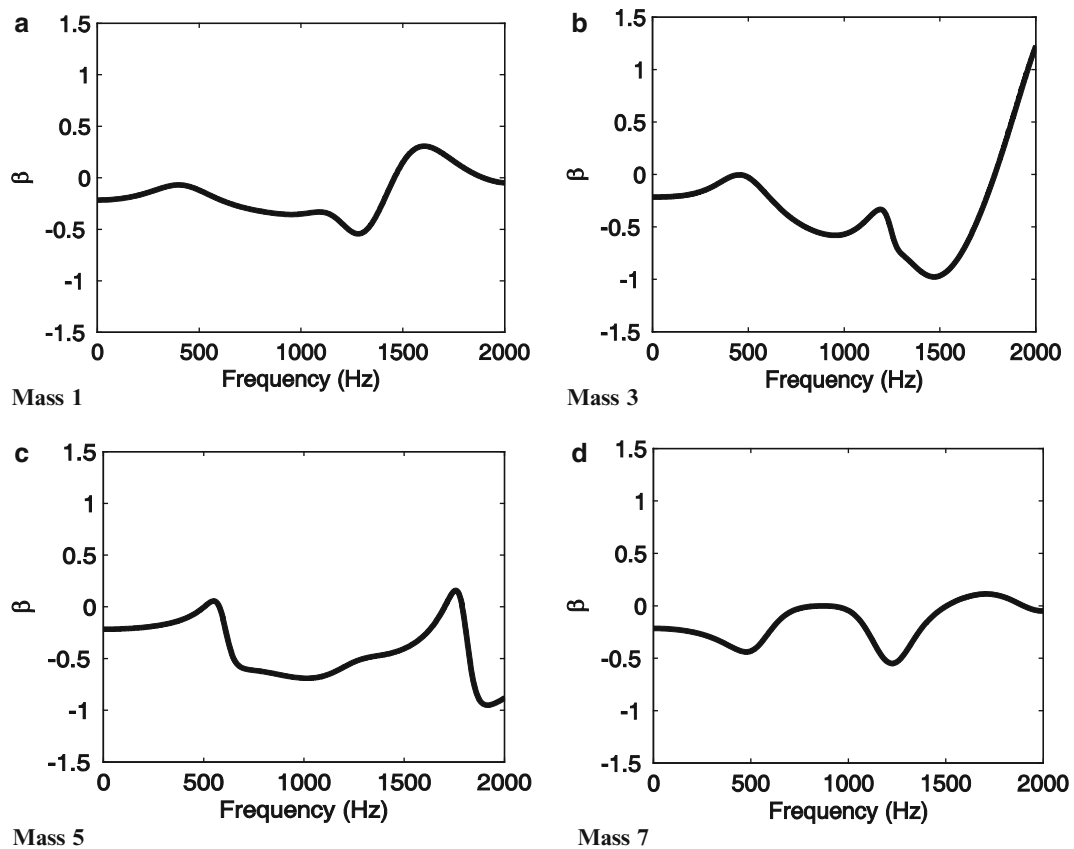


Fig. 24.14 Acceleration PSD response in aerodynamic environment and virtual MIMO test for non-measured DOFs. (a) Mass 5. (b) Mass 6. (c) Mass 8. (d) Mass 10



**Fig. 24.15** Degree of overtest/undertest for masses 1, 3, 5 and 7 in virtual MIMO laboratory test

**Table 24.2** g-rms values of virtual MIMO test and aerodynamic excitation

Mass #	Aerodynamic excitation (g-rms)	Virtual MIMO test (g-rms)	Difference (%)
1	3.3	3.3	0
2	1.6	1.6	0
3	1.8	1.8	0
4	1.7	1.7	0
5	1.7	1.6	-6
6	2.0	2.0	0
7	1.8	1.8	0
8	1.2	1.1	-8
9	1.4	1.3	-7
10	1.6	1.5	-6

It can be seen that the PSD response in the virtual MIMO laboratory test closely replicates the aerodynamic excitation for the two masses with accelerometers (P). It is possible to determine the response of DOFs not included in the MIMO calculation, i.e. DOFs other than P. Four of these responses (masses 5, 6, 8 and 10) are shown in Fig. 24.14

It can be seen that the general profile of the virtual MIMO test follows that of the aerodynamic excitation, however it is generally of a lower severity level. The degree of overtest/undertest across the bandwidth for four of the system masses (1, 3, 5 and 7) is shown in Fig. 24.15

It can be seen that the level of overtest/undertest across the bandwidth is within  $\pm 150\%$ . This is a significant improvement compared to traditional shaker methods (Figs. 24.8 and 24.9) where the level of overtest can be many orders of magnitude. The g-rms values of the virtual MIMO test were calculated and are given in Table 24.2. They show that the g-rms values from the aerodynamic environment are extremely well matched by the virtual MIMO test. For some of the DOFs, there is slight undertest, both in terms of the g-rms values and across the bandwidth (Figs. 24.13 and 24.14). In a true physical test, it is standard practice to add a factor of safety to ensure that there is no undertesting, e.g. raise the severity levels by 3 dB.

## 24.5 Selection of Excitation Locations

The selection of optimal excitation locations (Q) is critical to the success of the MIMO technique. It is not particularly important for the 10 DOF system as the calculations are very fast and the number of possible permutations is relatively low. Significant research has been carried out on FE models of structures with thousands of DOFs and the author has tried numerous different methods of selecting the excitation locations based on the relevant<sup>2</sup> eigenvectors – these methods include:

- (I) Intuitive selection
- (II) The Optimum Drive Point (ODP) calculation
- (III) Low off-diagonal auto-Modal Assurance Criterion (MAC) values
- (IV) Triangular decomposition (LU)
- (V) Orthogonal-triangular decomposition (QR)

It is beyond the scope of this paper to discuss in detail the research into each of the techniques above. Details on how to calculate the ODP and MAC values can be found in [16], for the LU, QR and correlation coefficient the reader is directed to standard matrix mathematics textbooks or the Matlab reference page.

The use of LU and QR decomposition had only limited success. Intuitive selection of the locations was occasionally successful but it does not always yield an optimal set of excitation locations and has no scientific basis. The conclusion of the research is that the most beneficial method of selecting excitation locations relies on the combination of the ODP, MAC and correlation coefficient calculations.

A DOF with a high ODP value indicates that this DOF is a leading candidate for exciting, to some level, all the relevant resonances so the first step to selecting optimal excitation locations is to calculate the ODP values for all the DOFs and sub-select those with high values. The second step is to select DOFs which give rise to low off-diagonal auto-MAC values for the relevant eigenvectors as this increases the probability that the exciters are able to excite the modes independently. The research showed that in most instances, two excitation locations are required for each direction of significant motion. The reasons for this are unclear and further research is required in this area.

The technique detailed above has been applied to a Dummy Air Launched Missile modelled in Ansys and solved for its modeshapes and natural frequencies. The modal model was exported into Matlab and distributed excitation (replicating aerodynamic excitation) was applied in all three Cartesian directions. The MIMO excitation locations selected by the calculations in Eqs. (24.4), (24.5) and (24.6) can be seen in Fig. 24.16 where it has selected four excitation locations exciting in the transverse directions (X,Y) as this is the plane of the two bending modes (first and second bending) within the chosen bandwidth (0–700 Hz).

## 24.6 Selection of Response Locations

As with the excitation locations, the selection of optimal response locations (P) is critical to the success of the MIMO technique. Research by the author has concluded that there are three criteria that must be satisfied if optimal response locations are to be selected:

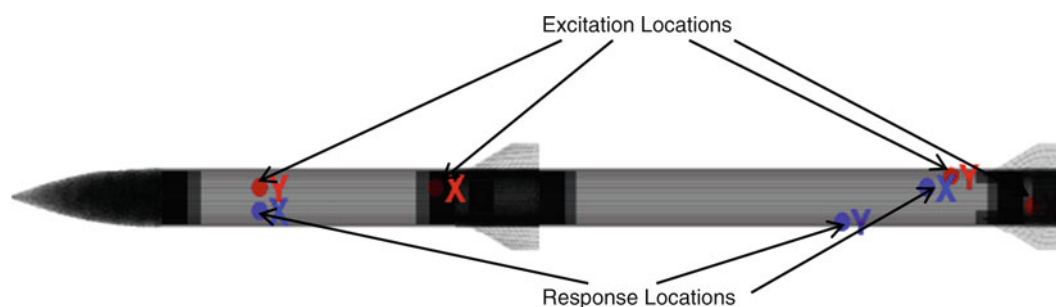


**Fig. 24.16** Excitation locations and response locations selected by MIMO technique for dummy air launched missile

<sup>2</sup> The relevant eigenvectors are those of resonances within the bandwidth and those which are outside the bandwidth but still have a significant effect.

- (I) The DOFs selected must have a high ODP value
- (II) The DOFs selected must result in a low condition number of the FRF matrix (across the bandwidth) to be inverted/pseudo-inverted
- (III) The inverse/pseudo-inverse of the FRF matrix must contain values that are low in magnitude

It is beyond the scope of this paper to discuss at great length the research carried out in order to determine the above criteria but some details follow. Adhering to criteria I prevents selection of DOFs which have low responses which would cause issues with the data in the physical tests as the measurements would be swamped by noise, making it difficult to invert the matrices in the MIMO calculations. Adhering to criteria II increases the probability of inverting the FRF matrix at each spectral line and prevents ill conditioning. Criteria III stems from the discovery that when poor locations were selected, the resulting force PSDs contained very high spikes. These spikes are unnecessarily high and would be unachievable in the laboratory.

It was undesirable to select response locations that were near excitation locations. This is because the resulting FRFs have a profile similar to that of a drive point FRF, i.e. lots of anti-resonances. Anti-resonances are undesirable both in terms of adhering to criteria III and from a practical perspective, i.e. large forces are required by the shakers in order to achieve the desired response. Conversely, most practical MIMO control systems prefer response locations near to excitation locations as it makes it easier to control – further investigation is required about the practicalities of having response locations distant from excitation locations in a physical MIMO test.

The number of response DOFs to be used is dependent on the application and MIMO hardware limitations, e.g. it may be necessary to have one response location for every excitation resulting in square matrices in the MIMO calculations.

## 24.7 Discussion

The process of carrying out a virtual test in order to optimise a random vibration test is iterative and will always rely on engineering judgement to “fine tune” some of the details. As an example, the Dummy Air Launched Missile model had many tens of thousands of DOFs. These were reduced to only the external surface where aerodynamic excitation could occur and where shakers could be attached. In addition, the mesh on the external surface was too fine and caused the calculations to become too large so these DOFs had to be further reduced in a simple decimating fashion. With this in mind, carrying out a virtual test for the Dummy Air Launched Missile took only a few minutes on a standard desktop PC.

The number of shakers employed is a balancing act between exciting the relevant resonances and making the test configuration too complicated. It should be relatively easy to apply sufficient energy with relatively small electrodynamic shakers for most applications. This is highlighted by the fact that for the relatively harsh envelope environment (Fig. 24.4) for a 100 kg structure (10 DOF system, Fig. 24.1) the total force rms value required is approximately 400 Nrms. In the example given earlier (Fig. 24.12), this is shared between three shakers. A single “modal type” shaker can deliver a force of approximately 300 Nrms, which is more than adequate for most applications.

Comparison between aerodynamic and MIMO response curves have only been carried out by visual comparison in this paper. As part of the research it has been necessary to make multiple iterations and so it has been beneficial to utilise the Frequency Response Assurance Criterion (FRAC) [16] to make a quantitative comparison between the set of PSD curves from the aerodynamic excitation and the virtual MIMO test. This is a more scientific way of making the comparison and can be carried out on multiple curves simultaneously.

The virtual testing reported in this paper has utilised analytical models to generate the FRF matrices. It is possible to use test-based FRFs if no model is available. In fact, it may be preferable to use test-based FRFs as they will have the true response of the tested structure whereas the model will almost certainly contain errors. It may be necessary to utilise Scanning Laser Doppler Vibrometry (SLDV) to obtain enough test FRFs to allow sufficient virtual testing to be carried out. Another benefit of test-based FRFs are that they can be tailored to include only locations where shakers and transducers can be physically located and avoid the inevitable redundant data associated with an FE model.

It is standard practice to carry out a flight trial of a structure, such as a missile, in its actual environment as part of the qualification process. Often the location of instrumentation such as accelerometers is based purely on convenience or comparison to previous flight trials. If the virtual testing process can be employed prior to a flight trial, then placement of accelerometers can be optimised and be located at positions specified by Eqs. (24.4), (24.5) and (24.6).

In a typical qualification test procedure, the structure will be excited in three orthogonal directions sequentially. With a MIMO test, this is not necessary as multiple shakers can excite the structure in all relevant directions simultaneously. This could potentially save a significant amount of time associated with testing and rigging activities.

When carrying out a physical MIMO test, it may be beneficial to use a mixture of shaker sizes simultaneously. It may be more appropriate to have some large shakers to apply the low frequency excitation and some smaller shakers to apply the high frequency excitation. In addition, using piezoelectric patches or stack actuators may be ideal for exciting the high frequency excitation and would be far simpler to use than rigging up electrodynamic shakers.

It is only in recent years that the technology associated with physical MIMO vibration controllers has matured sufficiently, allowing the concept of a MIMO random vibration test, as detailed in this paper, to be considered viable. In addition, recent advances in computing, FE modelling and SLDV allows virtual testing to be an integral part of the process and can allow a transition away from the traditional rigid shaker testing for replicating aerodynamic excitation.

## 24.8 Conclusions

This paper has demonstrated issues with the common methods of replicating aerodynamic excitation in the laboratory. These issues come in two main forms:

- (I) Quality of replication
- (II) Efficiency of the test

A new and simple approach based on MIMO vibration control of multiple shakers has been demonstrated that could yield significant benefits in both of the areas above and utilises technology which has only recently become available. The new approach could help alter the perception of environmental testing, which some see as slow, inefficient and non-representative, to a perception of tests that are highly representative of in-service environments and which are carried out in an efficient manner. The use of virtual testing and modern technology could allow testing practices to close the gap in capability on computer modelling. A little thought up front could result in far better, faster and cost-effective tests, where less time is wasted post-test investigating spurious results and redundant data.

## 24.9 Further Work

Currently, no physical testing has been carried out as part of this research. It is unknown if current MIMO vibration controllers can achieve the desired results or if one has to be developed. An LMS MIMO vibration controller is currently being acquired and it is proposed that research is carried out to ascertain its suitability for the MIMO testing methodology detailed in this paper. If a new system has to be developed then this may take significant time. In addition, mature MIMO vibration controllers will have mechanisms in place to deal with inverting near singular matrices and abort limits to protect the structure which may make development of a new system highly complicated. Once a suitable system is in place, physical testing can be carried out on the Dummy Air Launched Missile. The dummy missile shall be subjected to a wind tunnel test at the University of Bristol and this shall be replicated with a MIMO vibration test in the laboratory. The results for the two shall then be compared and an assessment made about the viability of using the MIMO technique to replicate distributed aerodynamic excitation.

None of the calculations in this paper have included noise. It is imperative that the sensitivity of the calculations to noise be understood as there may be significant levels of noise in physical test measurements.

## References

1. Himelblau H, Kern DL, Manning JE, Piersol AG, Rubin S (2001) Dynamic environmental criteria. NASA Technical Handbook (NASA-HDBK-7005)
2. Kroeger RC, Hasslacher GJ III (1965) Relationship of measured vibration data to specification criteria. *Acoust Soc Am* 37(1):43–53
3. Piersol AG (1966) The development of vibration test specifications for flight vehicle components. *J Sound Vib* 4(1):88–115
4. Piersol AG (1974) Criteria for the optimal selection of aerospace component vibration test levels. *Proc Inst Environ Sci* 88–94
5. Ewins DJ (2006) A future for experimental structural dynamics. In: *Proceedings of ISMA 2006: international conference on noise and vibration, Leuven*
6. Smallwood DO (2000) The correct balance between analysis and test. *J Sound Vib* 34(4):6–7
7. Wilkinson P (2007) The changing role of physical testing in vehicle development programmes. *J Terramechanics* 44:15–22
8. Kammer DC (1991) Sensor placement for on-orbit modal identification and correlation of large space structures. *J Guid Control Dyn* 14(2):251–259

9. Jarvis B (1991) Proceedings of the 9th IMAC, Florence, Italy, 1:402–408
10. Daborn PM (2006) Development of a new modal test planning algorithm. In: Proceedings of ISMA 2006: international conference on noise and vibration, Leuven
11. Lobitz DW, Gregory DL, Smallwood DO (2001) Comparison of finite element predictions to measurements from the Sandia microslip experiment. In: Proceedings of IMAC XIX, Kissimmee, FL
12. Salter JP (1964) Taming the general-purpose vibration test. *Environ Eng* 33(2-4):211–217
13. Witte AF, Sandia National Laboratories, Albuquerque (1970) Realistic vibration tests. *Instrum Technol* 45–48
14. Soucy Y, Cote A (2002) Reduction of overtesting during vibration tests of space hardware. *Can Aeronaut Space J* 48(1):77–86
15. Scharton TD (1995) Vibration-test force limits derived from frequency-shift method. *J Spacecr Rockets* 32:312–316
16. Ewins DJ (2000) *Modal testing – theory, practice and application*, 2nd edn. Research Studies Press Ltd, Baldock

# Chapter 25

## A Systematic Approach to Modal Testing of Nonlinear Structures

A. delli Carri and D.J. Ewins

**Abstract** The application of experimental modal analysis methods to nonlinear structures (sometimes referred to as “nonlinear modal testing” – NLMT) is not a new field, but only in the past few years has it become mature enough to be approached in a systematic way. Many methods have been developed over the years for dealing with nonlinearities in structural dynamics, but nonlinearity is an extremely complex phenomenon with so many aspects and consequences that it is not possible to have a single method capable to deal with all of them. Rather than taking a holistic approach, it is perhaps useful for the engineer to have a set of mathematical tools to analyse separate subsets of the whole problem, i.e. one being within the scope of each individual investigation. The main objective of this paper is to provide a modular framework from which the engineer can choose the most appropriate method to retrieve information about an examined nonlinearity, based on the type of information needed and the available data set. This is achieved by performing a breakdown of the nonlinear modal analysis process into four main stages: detection, localisation, characterisation and quantification – each of these providing a different level of insight into the problem. A review of currently-available algorithms applicable for these four categories is presented, as well as their application to two simple case studies.

**Keywords** Review • Nonlinear modal testing • Reverse path • Nonlinear characterisation • Nonlinear localisation

### 25.1 Introduction

In recent years, due to wide applicability of the well-developed modal analysis approach, the spotlight has naturally turned to the identification of nonlinear systems. The need to broaden this technology is not purely academic, it is increasingly driven by industrial needs for a deeper knowledge of their dynamical systems in order to achieve the best results in terms of automation, monitoring, control and validation.

To tackle this problem, a wide variety of methods have been presented over the years, each exploiting some physical principle or mathematical property in order to have a better understanding of the system under investigation. Each of these methods deals with nonlinearity in a specific way, but since nonlinear phenomena are extremely complex, there is no one method universally applicable and totally reliable, as is the case in classical modal analysis for linear systems. Rather than taking a holistic approach then, it is useful to look at these methods as a mathematical toolbox that can help the engineer to construct as full a picture as s/he needs to solve individual problems.

---

A. delli Carri (✉)  
University of Bristol, Bristol, UK

AgustaWestland UTC  
e-mail: [a.dellicarri@bristol.ac.uk](mailto:a.dellicarri@bristol.ac.uk)

D.J. Ewins  
University of Bristol, Bristol, UK

Imperial College London, London, UK  
e-mail: [d.ewins@bristol.ac.uk](mailto:d.ewins@bristol.ac.uk)



**Table 25.1** Each capability of the methods is checked: detection (*D*), characterisation (*C*), localisation (*L*), quantification (*Q*). Lastly, any reference reporting an experimental use of the method (*E*) is included

Method	Excitation	Response	D	C	L	Q	E	Notes
Hg	Any (2)	Any	<input type="checkbox"/>			<input type="checkbox"/>		SDOF only
HT	Any	Any	<input type="checkbox"/>					Indirect detection. May fail in experimental tests
RP	Broadband	Disp	<input type="checkbox"/>	<input type="checkbox"/>	<input type="checkbox"/>	<input type="checkbox"/>	[1]	Subject to numerical issues
SVD	Any	Disp, vel, acc	<input type="checkbox"/>	<input type="checkbox"/>	<input type="checkbox"/>	<input type="checkbox"/>		Massive request of input data
CFRF	Stepped sine	Disp (any)	<input type="checkbox"/>			<input type="checkbox"/>	[2]	SDOF only
NNM	Harmonic (n)	Disp (acc)	<input type="checkbox"/>	<input type="checkbox"/>		<input type="checkbox"/>	[3]	SDOF only, complex theory, Peculiar test
RFS	Any	Disp, vel, acc	<input type="checkbox"/>	<input type="checkbox"/>		<input type="checkbox"/>	[4]	SDOF only, massive request of input data
NOFRFs	Broadband (2)	Acc			<input type="checkbox"/>		[5]	Complex theory, only works for inline DOFs
•	•	•	•	•	•	•	•	•

As the final objective would be the application and implementation of these methods in an industrial environment, we need to establish some criteria for their assessment.

First, we must choose between Single Degree Of Freedom (SDOF) and Multiple Degrees Of Freedom (MDOF) methods. SDOF methods must be repeatedly applied to each mode of the system and could present some problems for the identification of closely spaced modes. Also, these methods do not take into account the interactions between modes, which are particularly important in the nonlinear field. To overcome these problems, one should use MDOF methods wherever possible, notwithstanding the major accosts of much greater computational burden.

Another important criterion for industrial applications is the specific input data requirements of each of the methods: some may not be suitable for practical application because of their need for non-standard data requirements (e.g. accelerations **and** velocities **and** displacements), in a certain format (time histories, frequency spectra) or using a very specific excitation method (sine step, more than one excitation level).

Speaking of identification, the basic concept that applies is that for every system there is considered to be an underlying linear model (ULM) – which is usually the model that applies at zero displacement response – added to which there are non-linear elements. The identification of these elements is the primary goal of the methods discussed here. Each method can extract different information about the nonlinear system. We can categorise this information into four distinct levels of depth in the understanding of the phenomenon:

- Detection: is there nonlinearity?
- Localisation: where is the nonlinearity?
- Characterisation: which type of nonlinearity is it?
- Quantification: what are the nonlinear parameters?

A further, and very important, criterion is the existence of documented application of each of the methods to real-life structures. In the industrial environment, a method is not a good method if it cannot be applied. The application is not always straightforward because the mathematics that forms the basis of the algorithms could be of very difficult implementation. Also, mathematicians and engineers have different priorities about the modelling of a phenomenon – the former are interested in exact solutions whereas the latter are for simplicity over accuracy – so the methods could be more or less industrially applicable depending on the provenance.

This work aims to provide a good summary of all the methods that deal with nonlinear systems at some level. Since there are so many, this paper has to be considered as a first iteration of this larger work. Table 25.1 shows the nonlinearity identification methods proposed for consideration for inclusion in this first iteration, alongside the criteria previously discussed.

## 25.2 Brief Review of Some of the Methods Available in Literature

In this section, some of the methods presented in Table 25.1 will be reviewed, emphasizing the principles and practicalities as well as the need for specific data requirements.

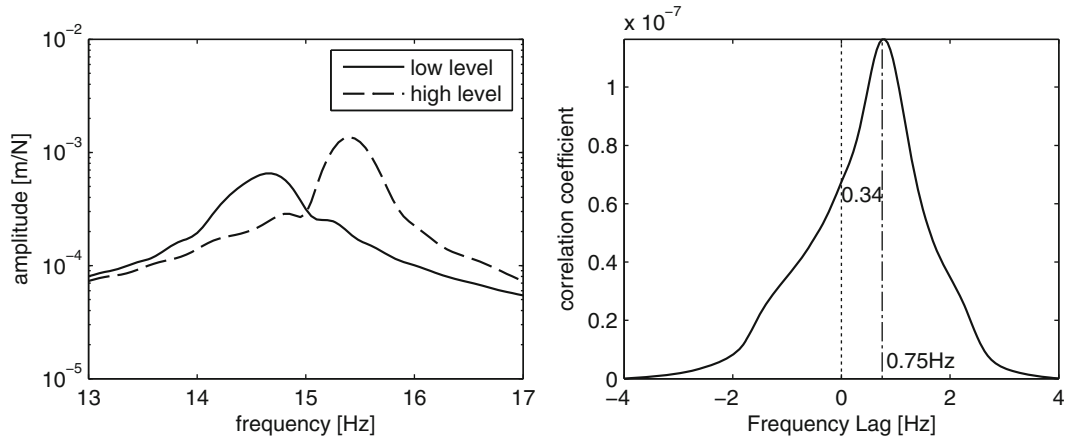


**Fig. 25.1** The Homogeneity method overlays two FRFs at different level of excitation (*left*). Their correlation function (*right*) indicates the shift in frequency of the peak as well as the nonlinearity index

### 25.2.1 Homogeneity Method (*Hg*)

The homogeneity method is by far the simplest and most intuitive of the methods. It is based on a direct comparison of 2 FRFs and relies on the fact that the FRFs of a linear system are independent of the input amplitude. This is called *homogeneity* of the system, and it can be summarised in the well-known Eq. (25.1) of the superposition principle:

$$H \cdot \{cF\} = cH \cdot \{F\} \quad (25.1)$$

In contrast to linear systems, the FRF of a nonlinear system is dependent on the input force magnitude (e.g. a system with a cubic hardening nonlinearity will experience an increase of the resonance frequencies with increasing input force).

The largest challenge when using the homogeneity condition for detection is quantifying the FRF distortion and providing a measure of the nonlinearity level with physical meaning. To achieve this result, an index  $l$ , based on the normalised cross correlation between the two FRFs at lag zero is used:

$$R(\Delta\omega) = \int_{-\infty}^{+\infty} H_{high}(\omega) H_{low}(\omega + \Delta\omega) d\omega$$

$$l = R^2(0) \quad (25.2)$$

By looking at the cross-correlation function in Fig. 25.1 it is also possible to retrieve the value of the frequency shift  $\Delta\Omega$  between the two FRFs:

$$R(\Delta\Omega) = 1 \quad (25.3)$$

The homogeneity method must be applied to a single mode in order to return a reliable result, therefore for systems featuring multi degrees of freedom this method must be repeated for each mode of vibration and each degree of freedom.

As this method uses such a simple approach, it has no requirements for specific data. Any form of FRF can be used (receptance, mobility, accelerance) with any kind of excitation.

### 25.2.2 Hilbert Transform Method (*HT*)

The detection theory based on the Hilbert transform is a classical approach, which dates back to the beginning of the 1980s. The Hilbert transform is an integral transform similar to the Fourier transform. In contrast to the Fourier transform, the Hilbert transform maps functions into the same domain (frequency into frequency and time into time). The Hilbert transform of an FRF defined in [6] has the interesting property of being invariant for linear systems:

$$\mathcal{H}[H(\omega)] = H(\omega) \quad (25.4)$$

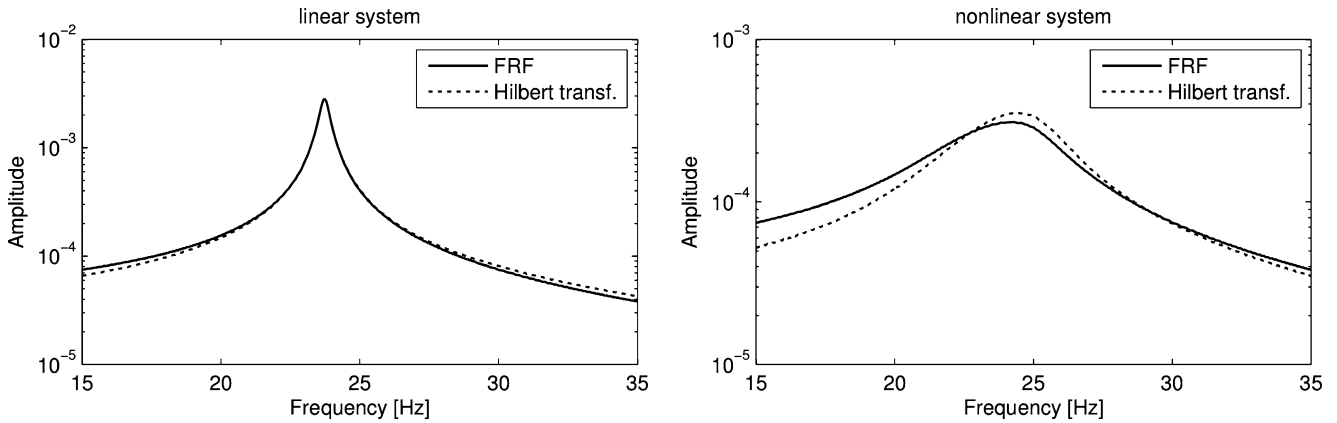


**Fig. 25.2** Hilbert transform method applied to a linear system (*left*) and a nonlinear one (*right*). The nonlinearity in the system causes the Hilbert transform of the FRF to be distorted

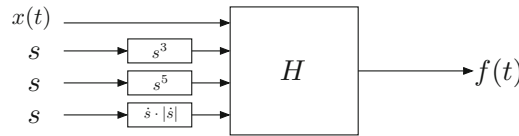


**Fig. 25.3** The reverse path method feeds back the nonlinear forces and exploits the coherence of the MISO analysis as a quality indicator for the estimation of the underlying linear system (H)

The Hilbert transform of a FRF from a nonlinear system will return a distorted version of the original FRF (Fig. 25.2). This distortion can be used for detection and can be quantified in a similar manner as described for the homogeneity method, using the cross correlation (25.2).

The Hilbert transform method is appealing because it is fairly simple to implement and it requires only one excitation series. One of the drawbacks of this method is that it is an indirect method for detection of nonlinearities, since it really detects non-causality [6], which is not necessarily due to nonlinearities. As for the homogeneity method, care should be taken when selecting excitation level. In a practical setting, the excitation level should be towards the high end of the operating range in order to ensure detection. Several ways of extending the use of the Hilbert transform have been exploited over time, more information can be found in [7].

### 25.2.3 Reverse Path Method (RP)

The reverse path method treats the nonlinearities as force feedback terms acting on an underlying linear system. The parameter estimation is performed in the frequency domain using conventional Multiple-Input-Single-Output (MISO) techniques and estimates of both the underlying linear properties and the nonlinear coefficients are obtained from a single analysis. The method is known as Reverse Path since the input and output quantities are reversed (Fig. 25.3). The Reverse Path method has proven to work well in experimental environments [1] and has been applied to various mechanical systems with zero-memory nonlinearities, indicating that the method is robust and well suited for use in engineering applications.

The method relies on the multiple coherence function (25.5) as an index for the goodness of estimation. This coherence function is a linear relationship that measures the causality between output and input signals, and it ranges between 0 (no correlation) and 1 (the output is completely caused by the input). The coherence function for a nonlinear system will always be less than 1 because of the linear nature of the coherence. The Reverse Path method feeds back some guessed responses as nonlinear inputs to the underlying linear system in order to improve the coherence function (Fig. 25.4).

$$\gamma_m^2 = \frac{\mathbf{G}_{XF} \mathbf{G}_{FF}^{-1} \mathbf{G}_{XF}^H}{\mathbf{G}_{XX}} \tag{25.5}$$

**Fig. 25.4** The overall improved coherence obtained by feedback of a cubic term indicates that the nonlinearity has been characterised successfully

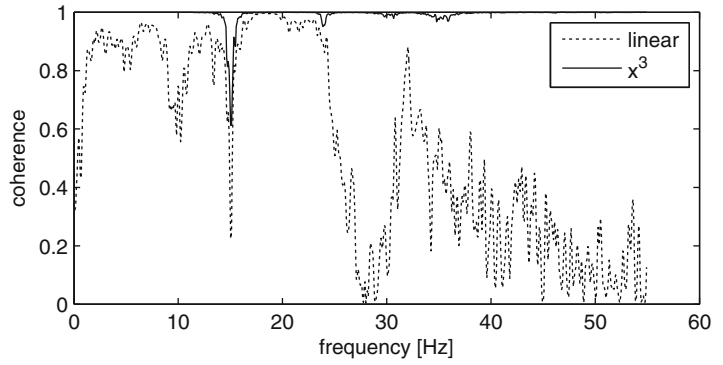
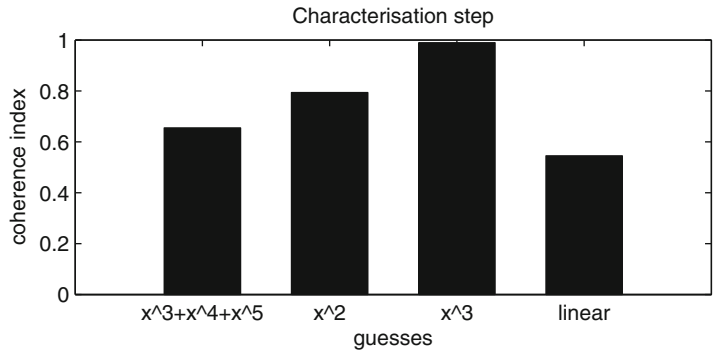


**Fig. 25.5** By testing a standard set of guesses for the nonlinear terms it is possible to find the best functional form and location of the nonlinearity



The “guessing” step permits the user to exploit any knowledge of where or what type of nonlinearity might be present (Fig. 25.5), and once the best coherence has been achieved, one can use the selected guesses to quantify their coefficients. The Reverse Path method needs time histories of both forces and displacements, acquired using a broadband excitation. Acceleration may be used instead of displacement but it would change the guessing step in a non-trivial way.

### 25.2.4 Singular Value Decomposition Method (SVD)

The method based on singular value decomposition is also referred to as the SVD method and is applicable to discrete MDOF systems where acceleration, velocity, displacement and force time histories are available for all DOFs. The method is based on estimating parameters in a least squares sense. For a single degree of freedom system featuring cubic stiffness nonlinearity, a matrix equation describing the DOF behaviour can easily be constructed:

$$\begin{bmatrix} \ddot{x}_1 & \dot{x}_1 & x_1 & x_1^3 \\ \ddot{x}_2 & \dot{x}_2 & x_2 & x_2^3 \\ \vdots & \vdots & \vdots & \vdots \\ \ddot{x}_N & \dot{x}_N & x_N & x_N^3 \end{bmatrix} \cdot \begin{bmatrix} m_1 \\ c_1 \\ k_1 \\ k_{NL} \end{bmatrix} = \begin{bmatrix} f_1 \\ f_2 \\ \vdots \\ f_N \end{bmatrix} \tag{25.6}$$

$\mathbf{A} \cdot \mathbf{C} = \mathbf{F}$

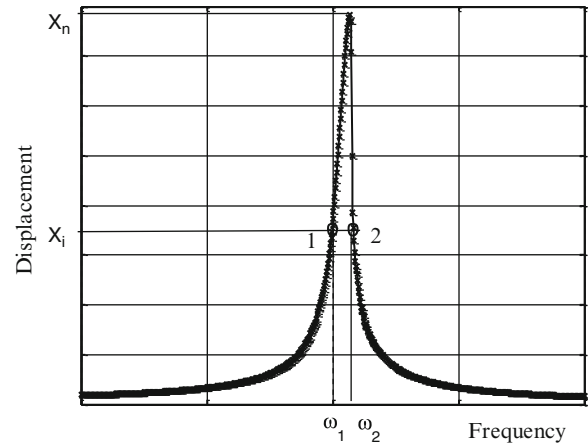
The above equation is over determined since the number of data points is generally larger than the number of parameters necessary to define the characteristics. Finally, the parameters can be fitted using a least squares model, minimizing the length of the residual vector

$$\|\mathbf{e}\| = \|\mathbf{AC} - \mathbf{F}\| \tag{25.7}$$

Using the Singular Value Decomposition of matrix  $\mathbf{A}$

$$\mathbf{A} = \mathbf{U}\mathbf{\Sigma}\mathbf{V}^T \tag{25.8}$$

**Fig. 25.6** Qualitative plot of a FRF with hardening nonlinearity



Models identified by the SVD method will tend to be over specified and not all terms will be significant, therefore some methods for evaluating the identified terms were introduced in [8]. Virtually any excitation would be suitable for an SVD characterisation-quantification. The major lack of practicality of this method is in the fact that all kind of responses (accelerations, velocities, displacements) have to be recorded, making this method just a theoretical added value for the engineer.

### 25.2.5 Complex Frequency Response Function Method (CFRF)

The so-called Complex Frequency Response Function method is also an SDOF method and it is based on the collection of standard FRF measurements obtained with a stepped sine excitation. By measuring a specific FRF at pairs of frequencies (each pair having one point below and one above the resonance frequency) such that the displacement response amplitude is the same for each pair), it is possible to extract modal parameters which correspond to each of the different displacement levels. The displacement response for a nonlinear system with hardening stiffness is qualitatively shown in Fig. 25.6.

Each point of the curve, e.g. points 1 and 2 corresponding to the displacement amplitude  $X_i$ , has a real and an imaginary part. The relationship between amplitude and frequency is

$$X_i = \frac{A_r + iB_r}{\omega_{ri}^2 - \omega_{li}^2 + i\eta_{ri}\omega_{ri}^2} = R_{1i} + jI_{1i}$$

$$X_i = \frac{A_r + iB_r}{\omega_{ri}^2 - \omega_{2i}^2 + i\eta_{ri}\omega_{ri}^2} = R_{2i} + jI_{2i} \quad (25.9)$$

in which  $A_r$  and  $B_r$  are the real and imaginary parts of the modal constant respectively,  $\omega_{ri}$  and  $\eta_{ri}$  are the natural frequency and the modal loss factor at the given amplitude  $X_i$  for the mode  $r$  (considered to be the dominating mode). From (25.9) it is possible to extract the natural frequency and the modal loss factor for that particular amplitude of displacement and applying that to  $n$  different amplitude levels  $X_i$  with  $i = 1 \dots n$  enables to reconstruct the variation of the natural frequency and/or modal loss factor with the response amplitude. These will be constant for a linear system but will show a consistent trend in presence of nonlinearity whether this is in the stiffness and/or in the damping. This method is implemented in the CODE for Nonlinear identification from measured Response To vibratiOn (CONCERTO) owned by AgustaWestland SpA [2].

### 25.2.6 Nonlinear Normal Modes Experimental Technique (NNM)

The NNM method, applied in [3], relies entirely on the invariance principle that states: “if the motion is initiated on one specific nonlinear normal mode, the remaining nonlinear normal modes remain quiescent for all time.”

Following this principle, one can extract the nonlinear normal modes one at the time performing a phase resonance test (i.e. harmonic excitation) for each mode. The test is performed in two steps (Fig. 25.7). First, there is a step of modal

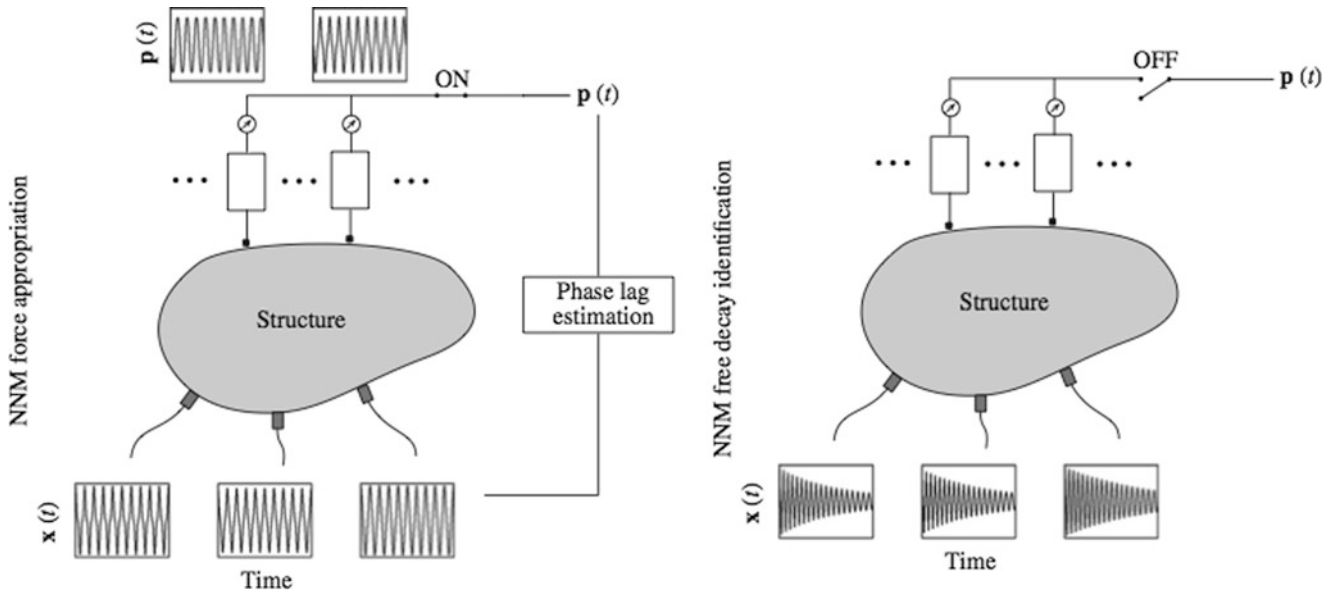


**Fig. 25.7** Nonlinear normal modes experimental methodology. Once the nonlinear normal mode have been appropriated by mean of a multi-harmonic excitation (*left*), the shakers are turned off and the decaying signal is acquired (Image taken by Peeters [9])

appropriation of the nonlinear mode under investigation: then, once the appropriation has been fulfilled, the excitation is turned off and the decaying signal is measured. According to the invariance property, the motion started in the appropriated nonlinear normal mode remains in that manifold even when decaying. The extraction of the NNM is finally performed using the Wavelet Transform.

### 25.2.7 Restoring Force Surface Method (RFS)

The method known as the Restoring Force Surface method, RSF method is described in [4]. In its basic form, this only applicable to SDOF systems and will provide a three-dimensional representation of the system in terms of the three parameters: displacement, velocity and force. The method is essentially based on Newton’s second law:

$$m\ddot{x}(t) + g(x(t), \dot{x}(t)) = f(t) \tag{25.10}$$

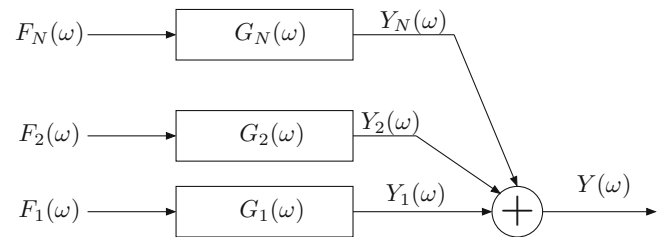
where  $f(t)$  is the applied force and  $g(*)$  represents the restoring and dissipative forces, linear and nonlinear. If the system is excited and data are measured at  $N$  points, (25.10) can be rearranged such that the restoring force can be calculated for each data point:

$$g(x(t), \dot{x}(t)) = \sum_{i=0}^m \sum_{j=0}^n \alpha_{ij} x_i \dot{x}_j \tag{25.11}$$

The RSF surface provides information related to restoring forces in the excited range. To characterise and quantify the nonlinear effects two cross sections are taken – one at  $\dot{x} = 0$ , showing the restoring force and another at  $x = 0$ , showing the dissipative force.

The method is powerful but suffers from two major drawbacks: (i) a lot of information is needed to retrieve a good fit of the surface (i.e. accelerations, velocities, displacements and the total mass of the system) and (ii) the visualization is non-trivial for multi degree of freedom systems, as the surface turns into a hyper surface (i.e. dimension of twice the DOFs involved).

**Fig. 25.8** Composition of the output signal using NOFRFs



### 25.2.8 Nonlinear Output FRFs Method (NOFRFs)

The NOFRFs method is described in [5]. It relies on the Volterra series to calculate “higher order FRFs” that are a generalization of classical linear FRFs and possess similar qualities as their linear counterparts, like homogeneity and the ability to express any output as a product of the NOFRF with the input, as shown in Fig. 25.8.

Another useful property that can be exploited to locate nonlinearities is the following: suppose the system under study has a nonlinearity associated with the  $j$ -th DOF, then the fraction of the first order NOFRF will not be equal to all higher order NOFRFs if  $i \geq (j - 1)$ , thus localising the source of nonlinearity. An obvious drawback associated with this detection method is that it requires calculation of the NOFRFs associated with all degrees of freedom.

In [5] promising simulated results are presented and the method seems to be rather easy to implement due to the matrix formulation. Unfortunately, due to the formulation, this method is only applicable whenever it is possible to have the tested DOFs in a straight line in order to analyse them pair by pair. A small region of the structure under investigation suspected to be the source of nonlinearity may be selected for the purpose, but this weakness makes this method much less appealing for practical engineering applications.

## 25.3 Testing the Methods

In order to assess the different methods and techniques, two numerical models and one experimental rig are presented:

- Case N1: single degree of freedom featuring cubic spring and quadratic damping nonlinearities (Fig. 25.9)
- Case N2: 3 degrees of freedom featuring non-grounded cubic and quadratic spring nonlinearities (Fig. 25.16)

In the following sections, the results of some of the algorithms presented in Sect. 25.2 will be presented, extracting all the information according to Table 25.1 to assess the quality of the methods.

### 25.3.1 Case N1

The first system under investigation is a simple SDOF system featuring cubic stiffness and quadratic damping nonlinearities [Figure]; the parameters are depicted in Table 25.2. The excitation is a sinusoidal chirp signal in the bandwidth 0–40 [Hz] at low (0.01 [N]) and high (10 [N]) force levels. The response signal is in the form of a displacement time history; simulation time is 60 [s] and all the signals have a SNR of 53 [dB].

#### 25.3.1.1 Detection

The *homogeneity method* applied to both low and high force levels returns a clear picture of the nonlinear system. Exploiting the cross-correlation function it is possible to estimate the shift in peak frequency (Fig. 25.10) to be of 0.55 [Hz] in 25. The nonlinearity index defined in (25.2) is not reliable since it does not take into account the damping nonlinearity due to the normalised nature of the cross-correlation function.

The *Hilbert transform method* in Fig. 25.11 struggles to detect the nonlinearity because of the massive damping. Although some distortion in the FRF can be spotted, it may not be of any help in case of noisy real experimental data.

**Fig. 25.9** Numerical case N1 featuring cubic stiffness and quadratic damping nonlinearities

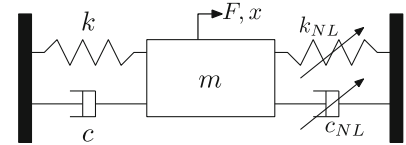


**Table 25.2** Parameters for numerical case N1

$m$	45	Kg
$k$	1e6	N/m
$c$	100	Ns/m
$k_{NL}$	6e13	N/m <sup>3</sup>
$c_{NL}$	2e5	N*s <sup>2</sup> /m <sup>2</sup>

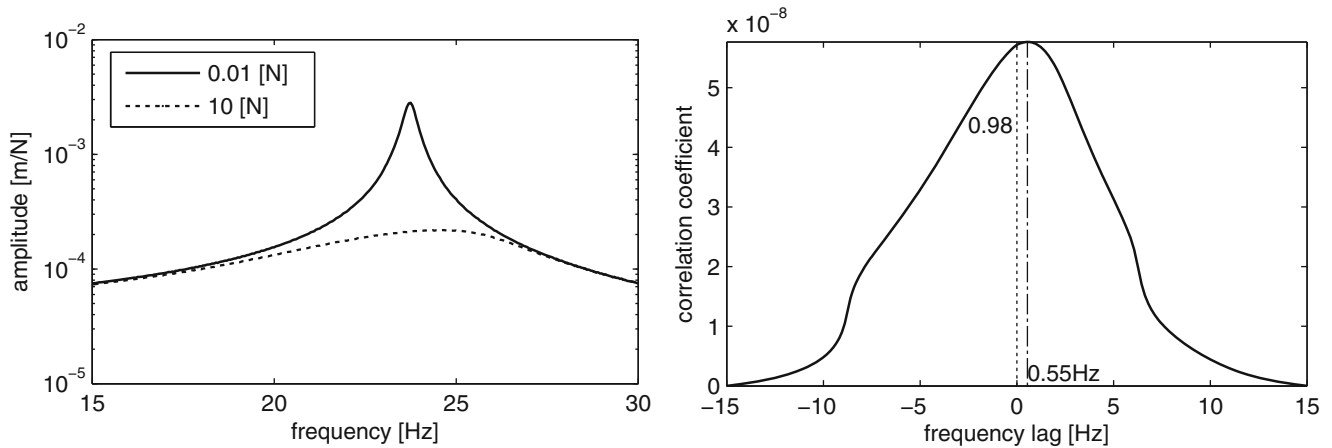
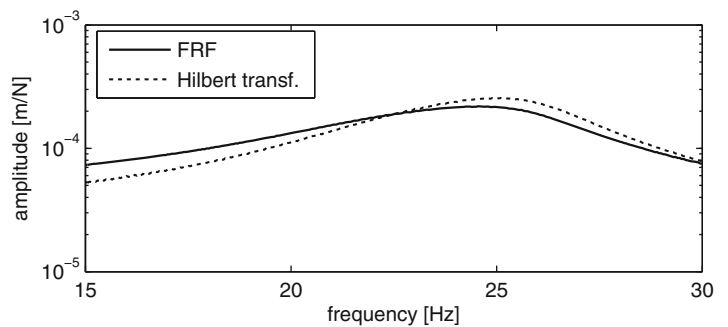


**Fig. 25.10** Homogeneity method applied to Case N1. The overlaid FRFs (*left*) show the massive damping of the nonlinear case. The correlation function (*right*) indicates the peak frequency shift and the nonlinearity index

**Fig. 25.11** Hilbert transform method applied to Case N1. The massive damping causes the distortion in the FRF to be not very important and hard to detect



### 25.3.1.2 Characterisation

While the localisation methods have no relevance on a single degree of freedom system, the *reverse path method* actually managed to characterise both the nonlinearities successfully. First, a set of guesses for the nonlinearities' functional forms is chosen, the nonlinear restoring forces are then calculated and fed back to the system. Figure 25.12 shows the improvement of the coherence index for each guess. The maximum improvement is achieved when both the cubic stiffness and quadratic damping nonlinearities are present (Fig. 25.13).



**Fig. 25.12** Reverse path method, guessing step for characterisation. For coherence estimation, the stiffness nonlinearity is more important than the damping one. When both are included the coherence is maximised

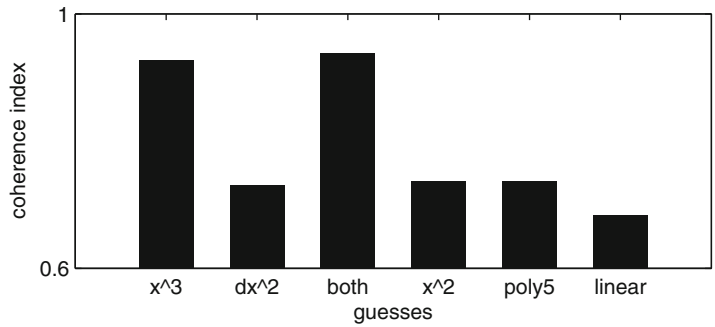


**Fig. 25.13** The overall improvement of the coherence function with respect to the linear case is clearly visible

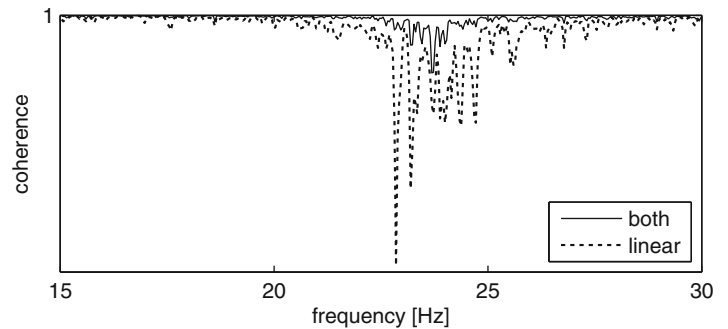
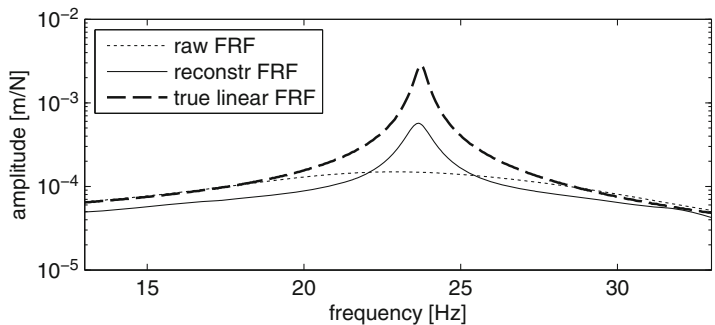


**Fig. 25.14** The estimated underlying linear system is correct in terms of modal frequency. The damping estimation is much less accurate



### 25.3.1.3 Quantification

The *reverse path method* was able to reconstruct the underlying linear system and to estimate the order of magnitude of the stiffness nonlinearity correctly. The estimation of the nonlinear damping coefficient proved to be beyond the capability of this method, as can clearly be seen in Fig. 25.14. It is noteworthy to observe that, in spite of the poor linear damping estimation, the method still managed to reconstruct a fair linear FRF with a pronounced peak that retains the underlying linear resonant frequency, whereas the raw FRF exhibits a hardly-noticeable peak due to the heavy damping.

Thanks to the demand for a huge quantity of input data (accelerations, velocities, displacements) the *SVD method* quantified the nonlinear stiffness with a fair accuracy over a limited range of displacement. The nonlinear damping estimation proved to be less accurate (Fig. 25.15).

### 25.3.2 Case N2

The second numerical case in Fig. 25.16 is represented by three masses, each moving in a single direction in which nonlinearities are placed between the first and the third mass (quadratic spring) and between the second and the third mass (cubic spring). A summary of the system parameters is found in Table 25.3.

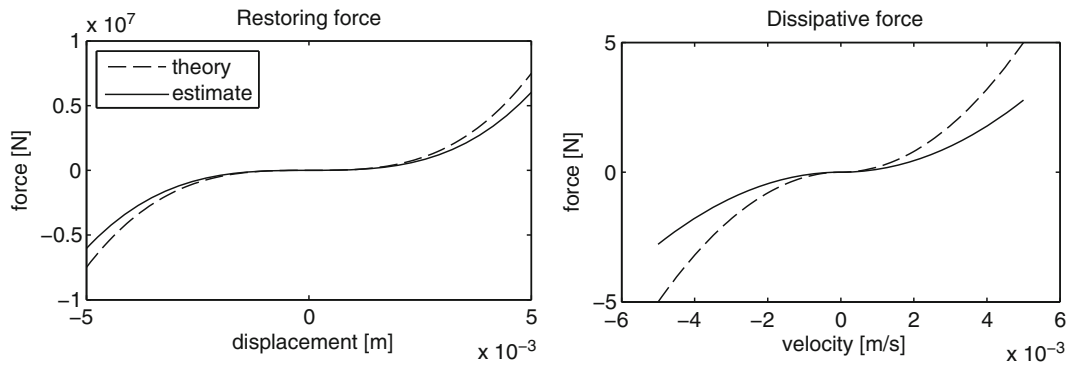


**Fig. 25.15** SVD quantification. The restoring force (*left*) coefficient has been adequately estimated, while some discrepancies can clearly be seen for the dissipative force coefficient (*right*)

**Fig. 25.16** Numerical case N2 featuring non-grounded cubic and quadratic stiffness nonlinearities

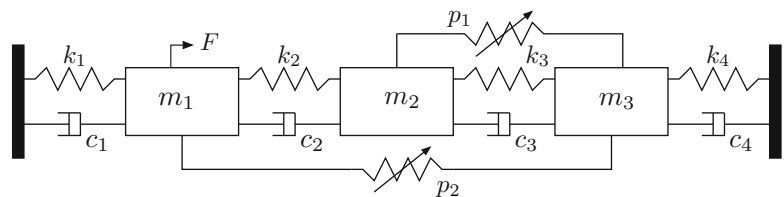


**Table 25.3** Parameters for numerical case N2

Mass		Stiffness			Damping			
$m_1$	250	Kg	$k_1$	5e6	N/m	$c_1$	500	Ns/m
$m_2$	450	Kg	$k_2$	3e6	N/m	$c_2$	560	Ns/m
$m_3$	750	Kg	$k_3$	7e6	N/m	$c_3$	680	Ns/m
			$k_4$	1e7	N/m	$c_4$	100	Ns/m
			$p_1$	4e16	N/m <sup>3</sup>			
			$p_2$	6e10	N/m <sup>2</sup>			

The system was excited using a sinusoidal chirp signal in the bandwidth 0–55 [Hz] both at low and high force levels (0.01–10 [N]). The response signal is in the form of displacements; simulation time is 60 [s] and all the signals have a SNR of 53 [dB].

**25.3.2.1 Detection**

As the *homogeneity method* is a SDOF method, it has to be applied multiple times to provide useful data. The lack of nonlinear damping makes the nonlinearity index (25.2) far more reliable in this case. The method proves to be very sensitive, identifying even a small amount of frequency shift for the first mode (Fig. 25.17). When excited at large amplitude, the nonlinearity of the second mode of vibration is very severe, and the second resonant peak bends to cover the third one. The resulting cross-correlation function in Fig. 25.18 shows that the peak has moved of almost 7 [Hz], making the third mode impossible to distinguish. Consequently, the homogeneity method could not be applied to the third mode under such extreme conditions.

The *Hilbert transform method* exhibits a small distortion of the FRF for the first peak and a larger one for the other two Fig. 25.19. However, it fails to give some more information or insights about the nonlinear system under investigation.

**25.3.2.2 Localisation**

The *reverse path method* exploits the coherence functions to identify the worst-behaving DOF and to use it as a first guess in a combined localisation-characterisation step. When the best coherence is achieved for all the DOFs, the selected degree of

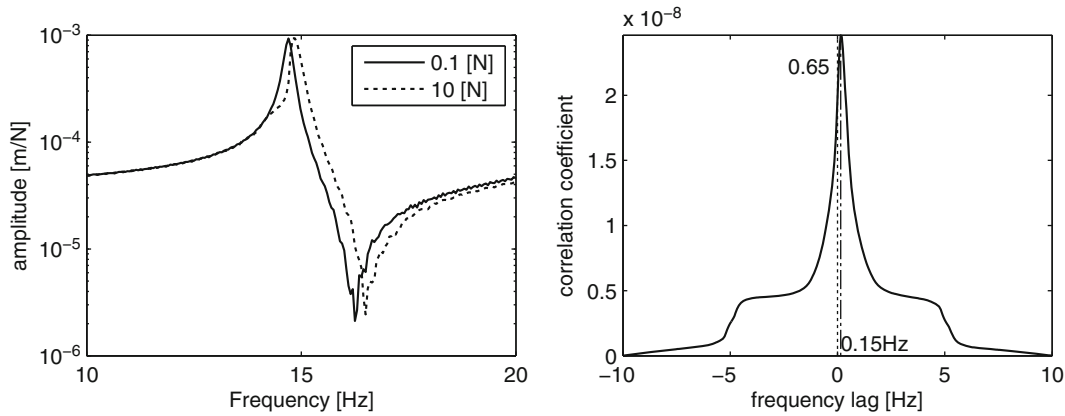


Fig. 25.17 Homogeneity method for the first mode of vibration

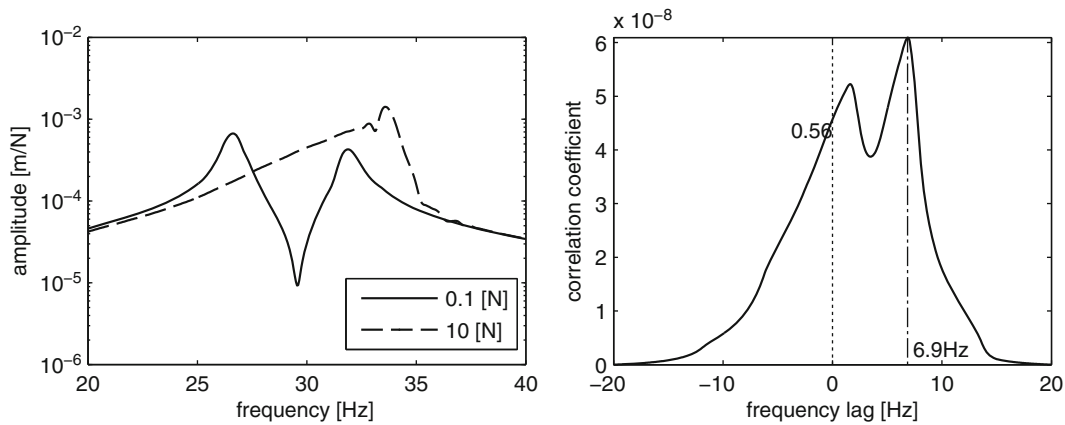


Fig. 25.18 Homogeneity method for the second mode of vibration. The close modes and the severe nonlinearity make harder to detect the frequency shift of the peak (right)

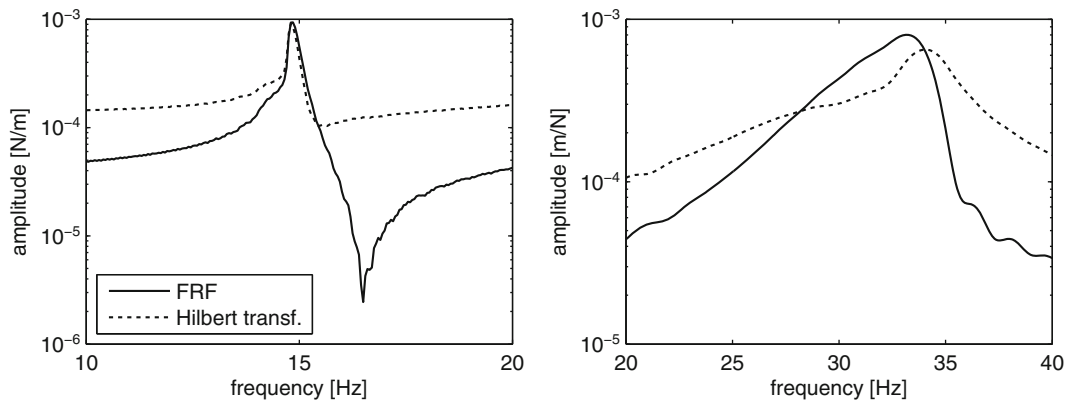
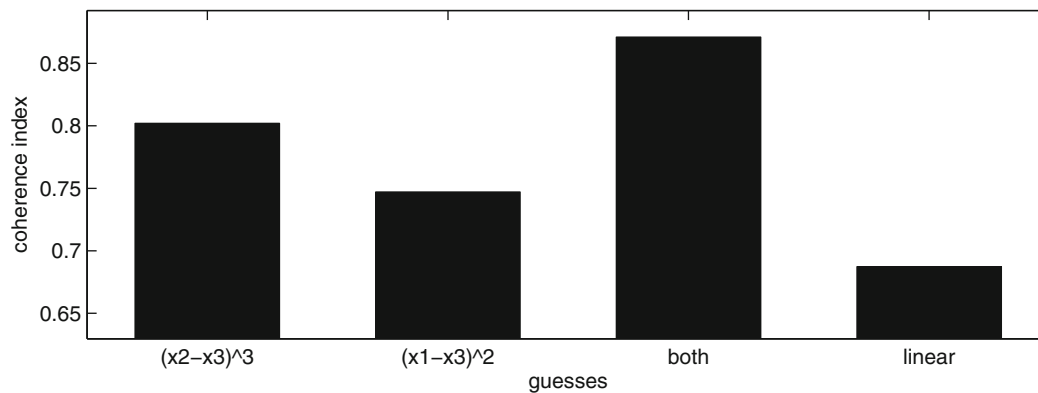
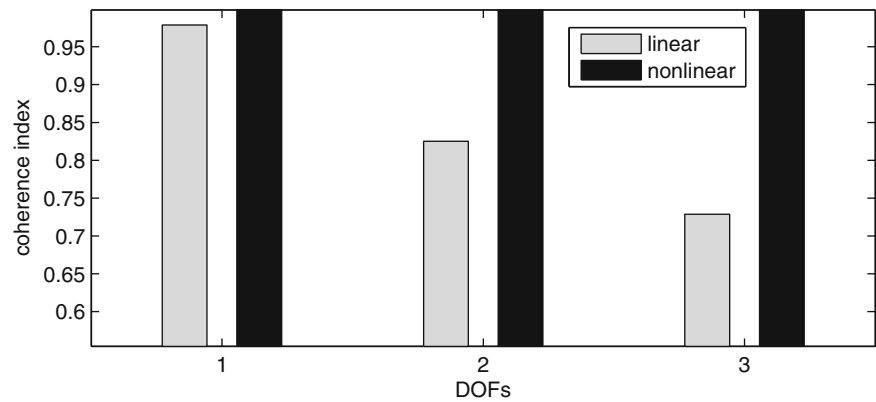


Fig. 25.19 Hilbert transform method applied to the first (left) and the second (right) mode of vibration

freedom is the one that shows the best overall improvement. If the maximum coherence has not been achieved, the procedure is repeated and a new DOF is selected as source of nonlinearity. The iterations stop when the coherence index reaches its maximum for all DOFs (Fig. 25.20).

The *NOFRFs method* suffers for the very definition of its algorithm: in order for the method to work, the DOFs must be on a straight ideal one-dimensional line. Also, the method is unable to deal with multiple nonlinearities, so this method is constrained to a very specific class of engineering problems such crack detection and structural health monitoring.

**Fig. 25.20** Reverse path method, localisation step. It is clearly visible that the best overall improvement of the coherence can be seen for DOF #3, which is also the DOF with two nonlinear elements attached



**Fig. 25.21** Reverse path method, characterisation step. The best overall improvement in the coherence function can be observed when both nonlinearities are considered

### 25.3.2.3 Characterisation

The results of the characterisation step of the *reverse path method* are shown in Fig. 25.21. The coherence improvement over the linear estimate is remarkable, and one can also notice that the most important nonlinearity is the cubic one, which contributes more than the other terms to the total improvement.

### 25.3.2.4 Quantification

Once characterised and localised, the nonlinearities can be fed back into the system in a reverse path fashion and a MISO analysis performed. This leads to an estimation of the underlying linear system and to the quantification of the nonlinear coefficients. As one can see in the left side of Fig. 25.22, the reconstructed FRFs look better than the raw FRFs but are still far from being perfect. The source of these errors is to be found in numerical issues due to the inversion of matrices containing very small numbers (ill-conditioned matrices), which leads to unreliable results. There are some ways to improve the estimation by pre-conditioning the matrices or by using some tricks in order to avoid a proper inversion, but they are still under investigation. Using a random excitation with a fairly long block size greatly helps minimizing these kinds of errors (Fig. 25.22 – right), resulting in much better estimates for the underlying linear system and, consequently, the nonlinear coefficients.

## 25.4 Conclusions and Future Work

Of all the algorithms for nonlinear identification tested so far, the *CFRF method*, *homogeneity method* and the *reverse path method* have proven to be robust enough to be used in an experimental environment, although both of them suffers from

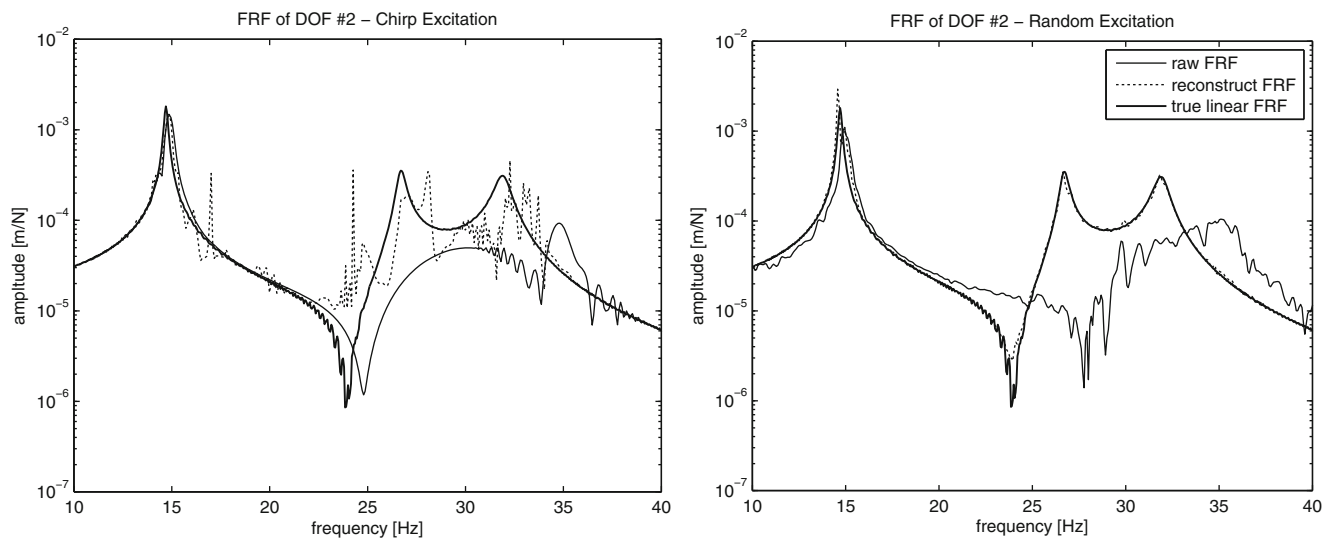


**Fig. 25.22** The underlying linear system estimation suffers by numerical illness when the system is excited with a chirp signal (*left*). The issues are not present when the system is excited with a random signal (*right*)

minor issues. The *homogeneity method* is suitable just for detection of nonlinear behaviour, but it can be helpful for the engineer who is looking for a quick way to make sure the structure he is testing is actually linear. Also, this detection method is capable to give some insights about the frequency shift of the peaks, which sometimes may be valuable information. The *reverse path method* is a full-featured algorithm that could be easily broke down in modules to perform just characterisation, just localisation or just quantification. Its weakest point seem to be the trial-and-error methodology of the guessing step which, combined with the fact there is no unique solution to the nonlinear problem, may lead to erroneous estimations. Lastly, some numerical issues have been raised that need further investigations. It has been noticed that these numerical issues tend to disappear when exciting the structure stochastically using a random or pseudo-random input signal, leading to much better estimates.

Since the landscape is full of algorithms designed to deal with nonlinear systems at any level, this paper is meant to be the first iteration of a work aimed to explore the principles and practicalities of all of them, explicating the need for specific data, their strong and weak spots. The idea is to test all the known algorithms with various numerical and, most of all, experimental tests in order to populate table [table] and make it an exhaustive and up to date picture of the nonlinear identification panorama.

**Acknowledgements** The authors wish to acknowledge, with thanks, the sponsorship by AgustaWestland SpA of the research which has resulted in this paper, and specifically to recognise the support and collaboration of Attilio Colombo and Vincenzo Barraco.

## References

1. Magneval M (2011) Simulation and experimental methods for characterization of nonlinear mechanical systems. Blekinge Institute of Technology, Sweden
2. Carrella A, Ewins DJ (2011) Identifying and quantifying structural nonlinearities in engineering applications from measured frequency response functions. *Mech Syst Signal Process* 25(3):1011–1027
3. Peeters M, Kerschen G, Golinval JC (2011) Dynamic testing of nonlinear vibrating structures using nonlinear normal modes. *J Sound Vib* 330(3):486–509
4. Kerschen G, Lenaerts V, Golinval J-C (2003) Vtt benchmark: application of the restoring force surface method. *Mech Syst Signal Process* 17(1):189–193
5. Peng ZK, Lang ZQ, Billings SA (2007) Crack detection using nonlinear output frequency response functions. *J Sound Vib* 301(3–5):777–788
6. Feldman M (2011) Hilbert transform in vibration analysis. *Mech Syst Signal Process* 25(3):735–802
7. Huang TL, Ren WX, Lou ML (2011) Identification of MDOF non-linear uncoupled dynamical systems using Hilbert transform and empirical mode decomposition method. *Adv Mater Res* 255–260:1676–1680
8. Mohammad KS, Worden K, Tomlinson GR (1992) Direct parameter estimation for linear and non-linear structures. *J Sound and Vib* 152:471–499
9. Peeters M, Kerschen G, Golinval JC (2011) Modal testing of nonlinear vibrating structures based on nonlinear normal modes: experimental demonstration. *Mech Syst Signal Process* 25(4):1227–1247

# Chapter 26

## Fiber Optics Sensing of Stressing and Fracture in Cylindrical Structures

Shen-en Chen, Benjamin Smith, and Peng Wang

**Abstract** The SCARC (Simulated Carbon Ash Retention Cylinder) model is being developed to model rock stressing, and fracture development, when underground ground voids are backfilled with mine wastes. SCARC specimens are hollow tubes, cast with cementitious materials, and are filled with different blends of mine wastes, such as tailing and post-processed slurry. To monitor the strain history of the concrete cylinder, fiber optical sensors are wrapped around the tube exteriors. This distributed fiber optic layout consists of eight FBG strain gages in a single loop, permanently affixed to the SCARC cylinder. The fiber optic sensors monitor the material expansion characteristics of the initial filling stage of the waste material, and perpetually monitor the induced strain over a 24 h period. The initial experiment, of SCARC specimens, indicates that fiber optic sensors can successfully monitor, and accurately report, the strain history of the cylinder, as well as detect the fracture location within the cylinder, by the distributed sensor array. The results indicate the potential of fiber optics as embedded sensors for monitoring the backfilling of waste into abandoned mines, which is suggested as a mine stabilization technology.

**Keywords** Fiber-optic • Sensor • Mine • Anthropogenic • Sequestration

### Nomenclature

$\lambda$	Bragg wave length
$n$	Effective index
$\Lambda$	Grating pitch
$\alpha$	Mass density
$\beta$	outer diameter
$\Delta T$	inner diameter
$\Delta \varepsilon$	Natural frequency
$t$	time

### 26.1 Introduction

To deplete coal fire generation byproducts, ash concrete application and technology have been studied since the early 1930s. With concerns about global warming, and the reduction of anthropogenic CO<sub>2</sub> emissions, there is a growing interest in using concrete to reduce greenhouse gases. Researchers have found that concrete naturally sequesters CO<sub>2</sub> through carbonation over a long period of time [1,2]. Unlike geological sequestration, carbonation permanently bonds CO<sub>2</sub> with the cementitious material. These findings are significant because they demonstrated the potential of *anthropogenic sequestration* of CO<sub>2</sub>, rather than a compulsory reliance of geological sequestration.

---

S. Chen (✉) • B. Smith • P. Wang  
Department of Civil and Environmental Engineering, University of North Carolina at Charlotte, 9201 University City Boulevard,  
Charlotte, NC 28223-0001, USA  
e-mail: [schen12@uncc.edu](mailto:schen12@uncc.edu); [bhsmith@uncc.edu](mailto:bhsmith@uncc.edu); [pwang@uncc.edu](mailto:pwang@uncc.edu)

**Fig. 26.1** Conceptual CO<sub>2</sub> competitive sequestration for physiochemical sorption

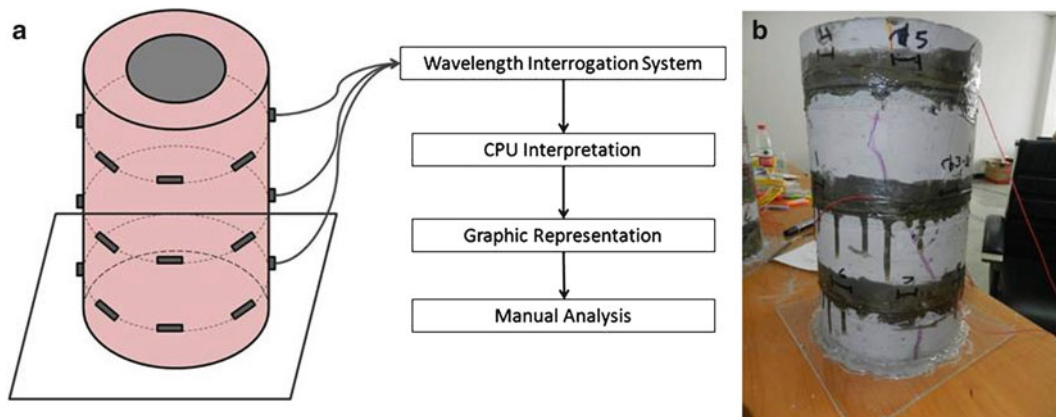
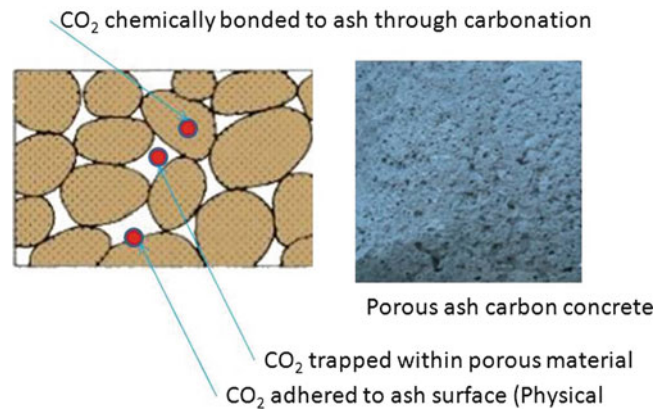


**Fig. 26.2** SCARC experimental setup (a) SCARC experimental setup (patent pending). (b) SCARC specimen

The proposed strategy suggests combining ash concrete with active carbonation to concurrently reduce both CO<sub>2</sub> and fly ash. The ash carbon concrete (ACC) can be “designed” to maximize the CO<sub>2</sub> storage capacity, including the option to increase the pore volume. By injecting CO<sub>2</sub> into ACC, two processes are activated for CO<sub>2</sub> storage: (1) chemical absorption and (2) physical adsorption. Physical adsorption occurs when CO<sub>2</sub> saturates the pore space and adheres to the matrix surface. The strength of ACC is inversely correlated to the pore space and the CO<sub>2</sub> storage capacity. Thus, ACC can be “designed” to have “competitive sequestration”, which means we can increase either chemical absorption or physical adsorption by altering its pore space. Figure 26.1 shows the envisioned competitive sequestration within the porous cementitious material.

To determine the effects of material expansion on rock materials, the SCARC (simulated carbon ash retention cylinder) experiment is proposed. SCARC consists of a hollow geo-formed cylinder with ACC fillings. The exterior of the cylinder is wrapped with three layers of fiber optic FBG sensors. Each layer consists of eight strain gages, which measure the ACC expansion induced stressing, and potential fracturing, of the cylinder. The very simplistic FBG sensor arrangement allows the capture of both strain and fracture behavior of SCARC cylinder. Figure 26.2 shows the setup of the FBG sensors (Fig. 26.2a) and the SCARC specimen (Fig. 26.2b).

The SCARC experiment can be used to generate design mixes that can allow engineers/scientists to determine the optimal blending needs for region-specific applications to maximize the sequestration and ash reduction potentials. In this paper, we will discuss the preliminary results of the SCARC experiments, in terms of strain measurement and crack detection using the FBG strain sensors.

## 26.2 Scarc Specimen

During the ACC maturation, and subsequent CO<sub>2</sub> injection process, the material expands and induces pressure to the adjacent material. The expansion will subsequently subside as the CO<sub>2</sub> is gradually absorbed into the material through carbonation (chemical sequestration). Hence, to monitor the pressurization process, SCARC (Simulated Carbon Ash Retention Cylinder)

is created as the reaction vessel to quantify the material expansion as the cylinder swells, in terms of hoop stress. To make the cylinder material compatible with the ACC, ceramic-based (i.e. cement) material is used. For other ACC applications such as abandoned mine backfilling, SCARC can be made with geomaterial, such as rock or synthetic rock materials. The dimensions of the cylinder are 29.0 cm in height, 15.5 cm in outside diameter and 9 cm inside diameter. The design of the cylinder thickness is critical – since ceramic materials may be weak in tension, the expansive ACC may force the wall to fracture. The same mechanisms can happen in field applications where pressurization due to ACC expansion and/or CO<sub>2</sub> injection can force the containment unit to crack.

Cracking of the ceramic containment unit is not critical for the trapped CO<sub>2</sub>, since the greenhouse gas is kept within the cement matrix, it will not cause massive escape. However, the cracking may have long term implications to secondary and even tertiary gas storage and need to be monitored. Optical Fiber Bragg Grating (FBG) strain sensors are used in this study with the dual purpose of measuring the strain deformation and detecting crack development locations.

### 26.3 FBG Strain Sensing and Crack Detection

Fiber optical sensors have been used in structural health monitoring of large civil structures and substructure systems [3–8]. The basic principle of using FBG-based sensor is to monitor the Bragg wave length shift due to changes in the sensor (i.e. strain or temperatures):

$$\lambda = 2n\Lambda \tag{26.1}$$

Where:  $n$  is the effective index of the fiber core and  $\Lambda$  is the grating pitch [8]. The Bragg wave length shift resulting from strain deviations,  $\Delta\varepsilon$ , and thermal deviations,  $\Delta T$ , are defined as follows:

$$\Delta\lambda = \alpha\Delta\varepsilon + \beta\Delta T \tag{26.2}$$

Where:  $\alpha$  is related to the effective strain optic constant and  $\beta$  is related to the thermal expansion coefficient. The thermal variation during ACC fabrication is dependent on the heat of hydration generated during cement curing and is ignored in current study. Heat of hydration can deviate about 50 °C [9]; however, since pressurized CO<sub>2</sub> can have lowered temperature, the heat effect is difficult to quantify and ignored in the current study – It is possible, and temperature measurements should be included in future studies. Since temperature is ignored, the Bragg wave length shift is interpreted as a simple function of induced strain:

$$\Delta\lambda = \alpha\Delta\varepsilon \tag{26.3}$$

$\alpha$  is a function of the effective strain optic constant that can be determined when fabricating the FBG strain sensors. The fiber optic cables with eight strain sensors in consecutive orders are epoxied to the cylinder surface (Fig. 26.3). The sensors serve as both strain measurement in the hoop direction and localized crack detectors. During initial ACC expansion, the

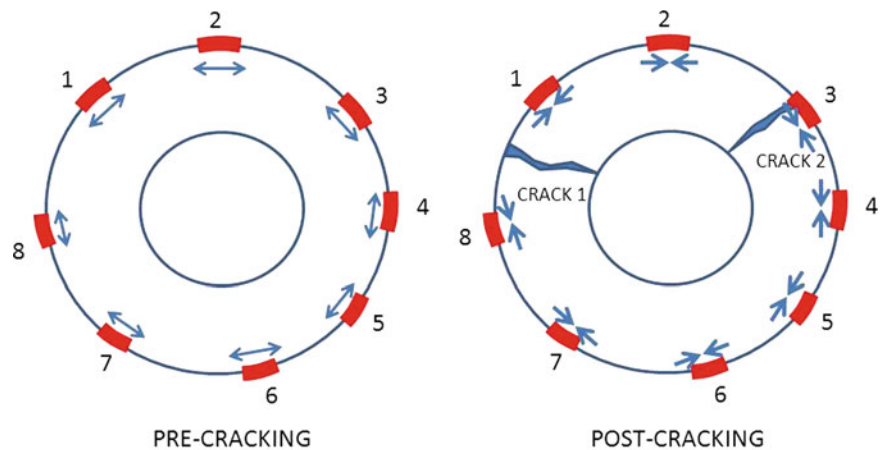


**Fig. 26.3** FBG strain measurements and crack detection

Crack 1: ch1 – 8 readings  
Crack 2: ch1 – 2 readings



multiplexed the cylinder will experience significant tension. The maximum tensile stress is at inner surface and results in fully penetrating rupture failures. When the tension stress overcomes the ceramic material rupture strength, the material will crack. Large cracking would result in material shrinkage and possibly cause sensor failures. The orientation nature of the sensors allow damage detection based on readings, or failure, of monitored sensors through wavelength readings. As an example, in Fig. 26.3, the initial crack (crack 1) occurs between sensors 1 and 8, hence, the outer surface rapidly develops compressive characteristics, as all the sensors will report. After crack 2 occurs, the fiber will be either severely elongated, at sensor 3, or broken. Following the development of crack 2, if the only sensors registering readings are sensors 1 and 2, the crack is assumed to be between 2 and 3. Typically, sensors remain useful even after specimen cracking because the tensile elastic properties of the fiber are greater than that of the ceramic material, so the fibers are even able to garner useful information post-fracture.

## 26.4 Experiment

To evaluate basic material properties of the cement used to construct the SCARC specimen, three cylinders were cast and subsequently crushed using controlled loading machines, following ASTM C39 [10]. The results are presented in Table 26.1. The average computed elastic modulus is 4.7 GPa. The SCARC specimen was first made with pure cement (white architectural cement), and the FBG sensors were attached to the cured cylinder. To prevent the specimen from leaking, the cylinder is attached to a plexiglass plate at the base. Additionally, the fixation prevents swelling at the base. As a result, the cracking will start from the top of the cylinder. Initial sensor wave length measurements were made and then the expansive ACC was introduced to the voided region of the cylinder. The sensor readings are continued after the ACC is introduced. Table 26.2 shows the initially calibrated wavelength measurement channel partitions.

## 26.5 Results and Discussion

Figure 26.4a shows the top view of the SCARC specimen, following the introduction of the ACC material. Notice that the ACC has expanded, vertically, beyond the cylinder by approximately 2 cm. Figure 26.4b shows the first large crack (marked with ink pen) on the cylinder. In the ensuing 24 h period, the initial cracks expand, propagate vertically, and spawn horizontal cracks.

The sensor locations are shown in Fig. 26.5. Channel 1 is for the top ring with eight sensors, channel 2 is the middle ring with sensors 1–6, channel 3 recorded middle ring sensor 7, and channel 4 recorded the bottom ring eight sensors. Only seven sensors were functional from the middle ring, indicating that sensor 8 was damaged during the application process. The sensor readings and results, from the first 5 h (approximately 20,000 s), are shown in Fig. 26.6. The graphs indicate the specimen developing tension (positive strain), on the exterior surface, until 1 h 40 min (5,000 s), when a significant crack forced all the sensor regions into compression. The strain readings of the bottom ring contain more variability than the top two ring sensor readings because of the fixity at the base. This indicates that the FBG sensors are very sensitivity to the strain condition, which is a function of the boundary condition. After initial cracking, as predicted, the specimen started to experience contraction (shrinkage), which is shown as negative strains, and subsequent strain relief.

**Table 26.1** The results of the cylinder compression tests

Cylinder	Compressive stress (MPa)	Approximate Young's modulus (GPa)
1	33.92	5.38
2	32.32	4.46
3	36.3	4.25
Average	34.18	4.7

**Table 26.2** Wavelength interrogation ranges

Sensor	1	2	3	4	5	6	7	8
Interrogation wavelength (nm)	1,524–1,528	1,528–1,531	1,531–1,535	1,535–1,539	1,539–1,543	1,543–1,547	1,547–1,551	1,551–1,555

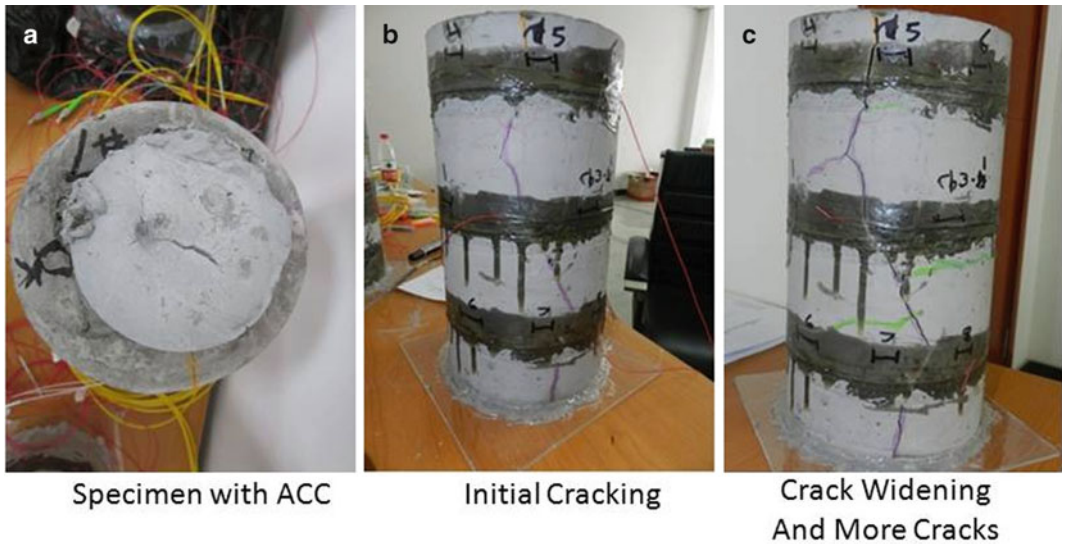
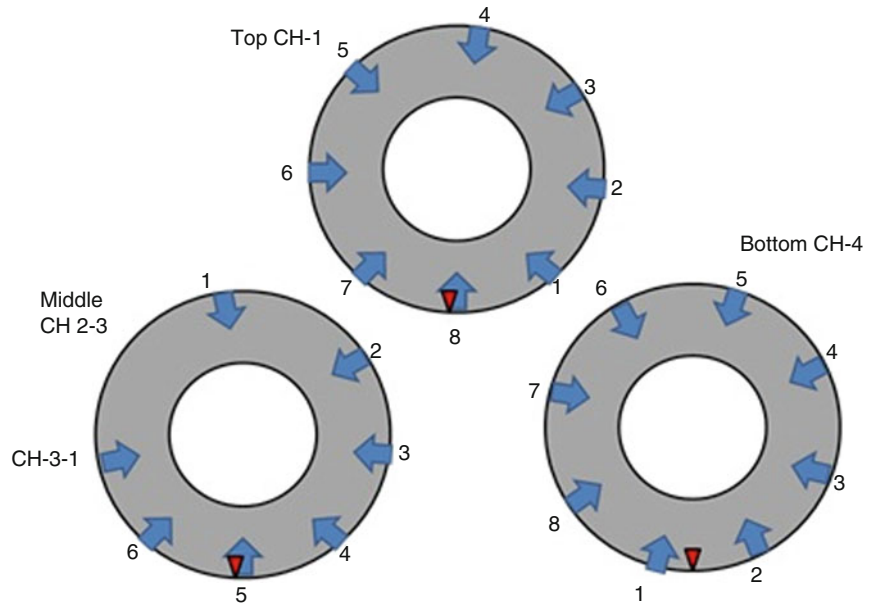


**Fig. 26.4** SCARC Specimen: (a) the In-filled ACC expansion within the cylinder; (b) initial cracking of the cylinder; (c) crack widening after 24 h

**Fig. 26.5** Sensor locations



## 26.6 Discussion

In Fig. 26.6, it is shown that the specimen ruptured at approximately 220 micro-strain, at sensor 5 of top ring. To understand the mechanics of the hoop stress transformation, a simple forensic analysis of the data from the SCARC specimen was performed, which provides a practical correlation between the crack behavior and the temporal strain, as well as demonstrating patterns for crack prediction. It must be understood that the reported strain values are gleaned from the FBG wavelength interrogation, and are capable of conveying deceptive circumferential strain values. For example, an FBG sensor may report a strain well over the tensile capabilities of the investigated material because of cracking that imparts large tensile force onto a delaminated fiber; if the intact FBG spans a crack, the reported strain is irrelevant to the surface material.

The expansive material (ACC) was introduced into the cylinder at at 9:33:47 AM, and evidenced first external cracking at 10:36 AM. This converts to the crack being visually recognized approximately 3,700 s after material introduction. The first crack, caused by the expansive mixture, was revealed at the bottom of the SCARC specimen, very close to sensor 3 of channel 4. Figure 26.7 shows the simple visual correlation for the validation of the first cracking. This indicates that sensor 3,

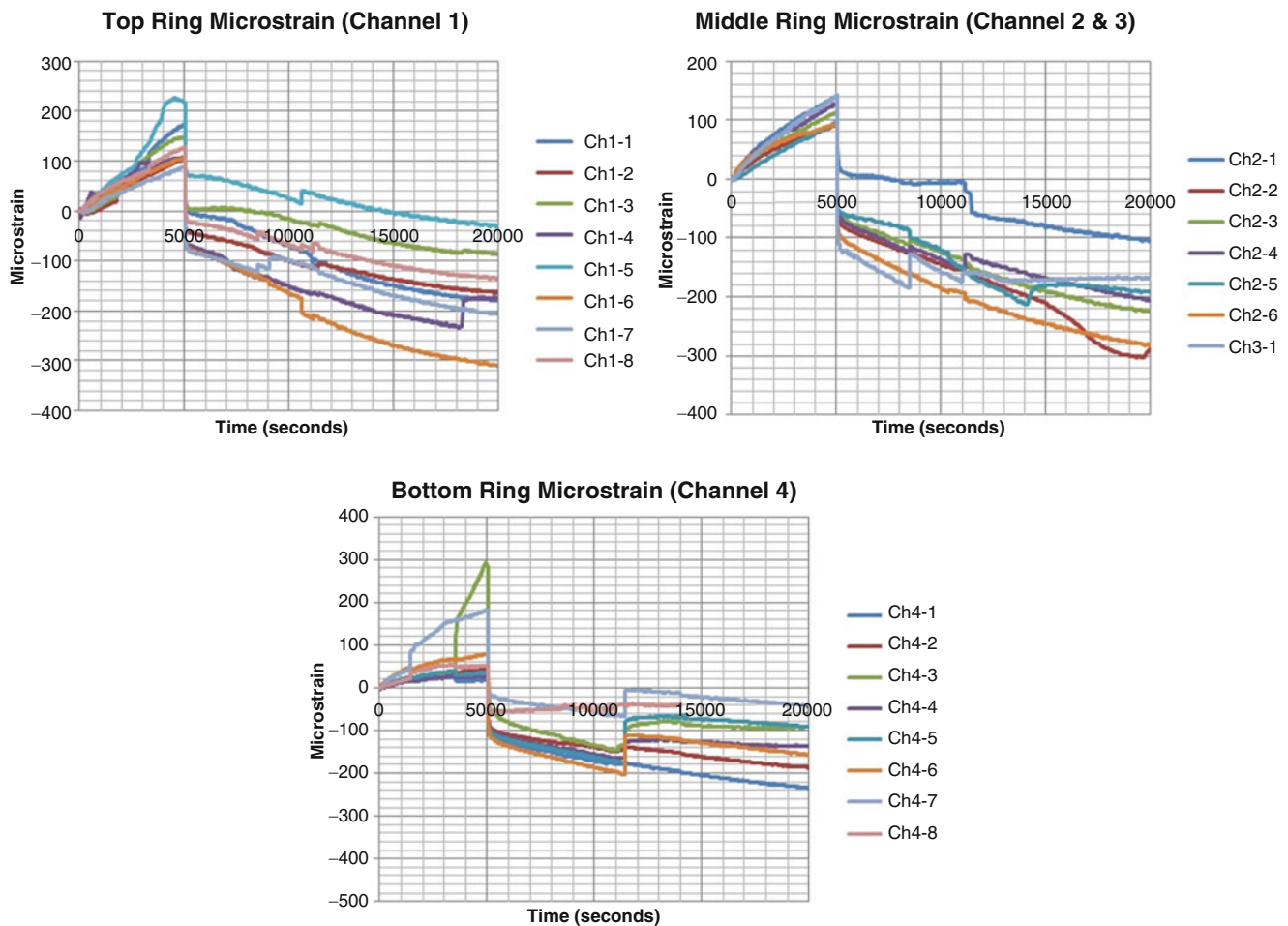


**Fig. 26.6** Strain history of the SCARC specimen for the first 5 h

of channel 4, (Ch4-3) was a prime location for major crack development. The major tensile strain jump, just following 3,500 s, indicates that there is significant local tension, resulting in the crack directly under Ch4-3. Hence, the FBG sensors correctly measured the strain and cracking history of the SCARC specimen. Future studies will use this advantage in the form of an active monitoring, and cracking predicting, system.

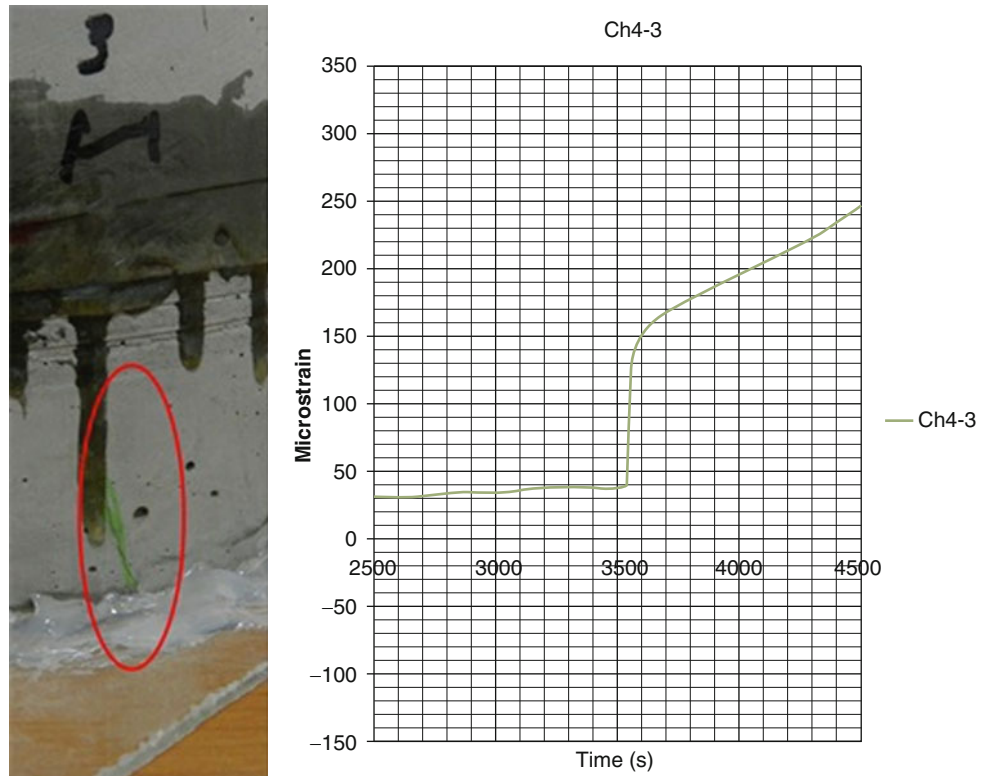
## 26.7 Conclusion

For this study, the use of FBG strain sensors to evaluate and monitor, a SCARC specimen was demonstrated. The conclusions drawn from this study are:

1. Using FBG sensors is a reactive way to accurately monitor circumferential behavior of the SCARC specimen following introduction of expansive material to the voided volume.
2. Manual interpretations of crack behavior indicate that the FBG sensors accurately predicted the cracking behavior of the SCARC specimen.
3. The strain reports provide an effective way to measure crack opening and propagation over long periods of time.

It is recommended that the following future studies are conducted: (1) Thermo-sensitivity study of the FBG sensors, and (2) longer term monitoring using the FBG sensors. The results of the testing were able to provide significant data regarding the circumferential strain behavior, but certain studies must be conducted to ensure result accuracy. The manual interpretation is the most tedious portion of the interrogation process and should be supplemented with basic automation. The importance of large-scale testing relates to the dimension-dependent variables; for example, the expansive material, AAC, would have a

**Fig. 26.7** Cracking correlations by visual inspection and strain value interrogation



better material representation in a larger sample because it would allow the formation of a fully developed material matrix. From the data reports, and manual interpretations, this study shows that FBGs are effective for monitoring the strain behavior of the SCARC specimen, and should be implemented in further studies.

**Acknowledgements** We would like to acknowledge the financial support from the National Natural Science Foundation of China via grant No. 5095011345 and the Division Chief, Bureau of International Cooperation, Dr. Liyao Zhou. We would like to acknowledge the financial support of the State Key Laboratory of Geomechanics and Deep Underground Engineering at Chinese University of Mining Technology. We also acknowledge Professor Bin Shi from Nanjing University and Drs. Guangqin Wei, M. Wang of Nanzee Sensing Technology, Suzhou, China, for their technical supports. We also acknowledge Professors Xiexing Miao, Zhengfu Bian, Qiyen Feng, Xianbiao Mao, Shaogang Lei, Chunde Piao of The Chinese University of Mining Technology for facilitating our study in China.

## References

1. Pade C, Guimaraes M (2007) The CO<sub>2</sub> uptake of concrete in a 100 year perspective. *Cem Concr Res* 37:1384–1356
2. Haselbach L (2009) Potential fore carbon dioxide absorption in concrete. *J Environ Eng* 135:465–472
3. Gliši B, Inaudi D (2007) *Fibre optic methods for structural health monitoring*. Wiley
4. Li HN, Li DS, Song GB (2004) Recent applications of fiber optic sensors to health monitoring in civil engineering. *Eng Struct* 26:1647–1657
5. Friebele EJ (1998) Fiber Bragg Grating strain sensors: present and future applications in smart structures. *Opt Photon News* 9(8):33–37
6. Shi B, Xu H, Chen B, Zhang D, Ding Y, Cui H, Gao J (2003) A feasibility study on the application of fiber-optic distributed sensors for strain measurement in the Taiwan Strait Tunnel Project. *Mar Georesour Geotechnol* 21(3–4):333–343
7. Morey WW, Meltz G, Glenn WH *Fiber Bragg Grating sensors*. In: *Proceedings of the SPIE fiber optic and laser sensors VII*, vol 1169, p 98, Boston
8. Hao J, Leng J, Wei Z (2007) Non-destructive evaluation of composite pressure vessel by using FBG sensors. *Chin J Aeronaut* 20:120–123
9. Portland Cement Association (1997) *Portland cement, concrete and heat of hydration*. *Concr Technol Today* 18(2):1–7

# Chapter 27

## Real-Time Damage Identification in Nonlinear Smart Structures Using Hyperchaotic Excitation and Stochastic Estimation

Shahab Torkamani, Eric A. Butcher, and Michael D. Todd

**Abstract** Among numerous damage identification techniques, those which are used for online data-driven damage identification have received considerable attention recently. One of the most widely-used vibration-based time-domain techniques for nonlinear system identification is the extended Kalman filter, which exhibits a good performance when the parameter to be identified is a constant parameter. However, it is not as successful in identification of changes in time-varying system parameters, which is essential for real-time identification. Alternatively, the extended Kalman-Bucy filter has been recently proposed due to its enhanced capabilities in parameter estimation compared with extended Kalman filter. On the other hand, when applied as the excitation in some attractor-based damage identification techniques, chaotic and hyperchaotic dynamics produce better outcomes than does common stochastic white noise. The current study combines hyperchaotic excitations and the enhanced capabilities of extended Kalman-Bucy filter to propose a real-time approach for identification of damage in nonlinear structures. Simulation results show that the proposed approach is capable of online identification and assessment of damage in nonlinear elastic and hysteretic structures with single or multiple degrees-of-freedom using noise-corrupted measured acceleration response.

**Keywords** Smart structures • Real-time damage identification • Hyperchaos • Stochastic estimation • Kalman-Bucy filter

### 27.1 Introduction

Damage identification in structures can be divided into active (on-line) and passive (off-line) approaches. The active approach needs actuation (or excitation) of monitored structures and real-time measurements and analysis of the resulting response. While the passive approach is satisfactory for traditional structures, it is not as desirable for some modern structures, and in particular, “smart structures” which contain active components or layers. For such smart structures, the identification algorithm needs to provide instantaneous updates of the mechanical properties of the structure to the active components to adaptively perform functions of sensing and actuation required. For the online identification of damage, various time-domain approaches have been used in the literature with different degree of success. A few examples include least-squares estimation [1–3], different filter approaches including the extended Kalman filter [4–7],  $H_\infty$  filter [8], Monte Carlo filter [9], etc. The Monte Carlo method is capable of dealing with nonlinear systems with even non-Gaussian uncertainties. However, it is computationally expensive due to requiring a large number of sample points. Since the application of least squares estimation (LSE) for nonlinear structural system identification requires displacement and velocity measurements, which may not always be readily available. The extended Kalman filter (EKF) is perhaps the most widely-used vibration-based time-domain techniques for identification of nonlinear systems. While the EKF has good performance when the parameter to be identified is a constant parameter, it is not as successful in identification of changes in time-varying system parameters

---

S. Torkamani (✉) • E.A. Butcher

Department of Mechanical and Aerospace Engineering, New Mexico State University, Las Cruces, NM 88003-8001, USA  
e-mail: [shahab@nmsu.edu](mailto:shahab@nmsu.edu); [eab@nmsu.edu](mailto:eab@nmsu.edu)

M.D. Todd

Department of Structural Engineering, University of California San Diego, La Jolla, CA 92093-0085, USA  
e-mail: [mdtodd@mail.ucsd.edu](mailto:mdtodd@mail.ucsd.edu)

[10]. A common technique used in the literature for identification of time-varying parameters is an extension of the LSE approach. This technique makes use of a constant [11, 12] or time-dependent [13] forgetting factor in LSE. This approach has some drawbacks and shows good performance in some cases; however, it exhibits poor results when the stiffness of the structure has an abrupt change [10]. An adaptive tracking technique based on EKF to identify structural parameters is proposed in [10], which is particularly suitable for tracking the abrupt changes of the system parameters with the purpose of online evaluation of the structural damages.

The extended Kalman-Bucy filter is an alternative filtering approach that has been recently reintroduced due to its enhanced capabilities in parameter estimation compared with the extended Kalman filter [14]. On the other hand, an aspect of damage identification which is shown to be crucial from a detectability standpoint is the excitation. When applied as the excitation in some attractor-based damage identification techniques, chaotic and hyperchaotic dynamics can often produce better outcome rather than the common stochastic white noise [15–21]. The current study combines hyperchaotic excitations and the enhanced capabilities of extended Kalman-Bucy filter to develop a feasible real-time technique for identification of damage which can be used in nonlinear smart or self-healing structures. Simulation results show that the proposed approach is capable of real-time identification and assessment of damage in nonlinear elastic and hysteretic structures with single or multiple degree-of-freedom using noise-corrupted acceleration response.

## 27.2 Methodology

### 27.2.1 Stochastic Estimation Problem

In a general parametric identification problem (cf. non-parametric identification) it is assumed that the form of the model is known only approximately due to imperfect knowledge of the dynamical model that describes the motion and/or imperfect knowledge of parameters. The goal is to obtain the best estimate of the state as well as of model parameters based on measured data that has a random component due to observation errors. In addition, a second source of stochastic excitation typically appears in the state dynamics as so-called process noise. Both the stochastic excitation and the measurement noise are assumed to be additive in this paper. The optimal continuous-time filtering problem in the general form considered in this paper can be written as a set of Ito stochastic differential equations as

$$\begin{aligned} d\mathbf{x}(t) &= \mathbf{f}(\mathbf{x}(t), \mathbf{a}(t), t) dt + \mathbf{G}(\mathbf{x}(t), t) d\boldsymbol{\beta}(t) \\ d\mathbf{z}(t) &= \mathbf{h}(\mathbf{x}(t), \mathbf{a}(t), t) dt + \mathbf{J}(t) d\boldsymbol{\eta}(t), \end{aligned} \quad (27.1)$$

where  $\mathbf{x}(t) \in \mathbb{R}^n$  is the state process,  $\mathbf{z}(t) \in \mathbb{R}^q$  is the measurement process,  $\mathbf{a}(t) \in \mathbb{R}^r$  is a vector of unknown parameters,  $\mathbf{f}$  is the drift coefficient,  $\mathbf{G}$  is the diffusion coefficient,  $\mathbf{h}$  is the measurement model function,  $\mathbf{J}(t)$  is an arbitrary time-varying functions independent of  $\mathbf{x}$ , and  $\boldsymbol{\beta}(t)$  and  $\boldsymbol{\eta}(t)$  are independent Brownian motion additive stochastic processes with  $E[d\boldsymbol{\beta}(t)] = E[d\boldsymbol{\eta}(t)] = 0$ ,  $E[d\boldsymbol{\beta}(t)d\boldsymbol{\beta}^T(t)] = \mathbf{Q}dt$  and  $E[d\boldsymbol{\eta}(t)d\boldsymbol{\eta}^T(t)] = \mathbf{R}dt$  where  $E[\ ]$  represents the expectation operator. Note that in this paper the system is considered to be excited by additive noise only. Therefore, hereafter we will treat stochastic differential equations with the diffusion coefficient only depending on  $t$  and not the process  $\mathbf{x}$ . Under this condition the filtering problem can also be formulated in terms of the stationary zero-mean Gaussian white noise processes formally defined as  $\mathbf{v}(t) = d\boldsymbol{\beta}(t)/dt$ ,  $\mathbf{w}(t) = d\boldsymbol{\eta}(t)/dt$  and differential measurement  $\mathbf{y}(t) = d\mathbf{z}(t)/dt$  as [22]

$$\begin{aligned} \dot{\mathbf{x}}(t) &= \mathbf{f}(\mathbf{x}(t), \mathbf{a}(t), t) + \mathbf{G}(t) \mathbf{v}(t) \\ \mathbf{y}(t) &= \mathbf{h}(\mathbf{x}(t), \mathbf{a}(t), t) + \mathbf{J}(t) \mathbf{w}(t), \end{aligned} \quad (27.2)$$

where  $\mathbf{v}(t)$  and  $\mathbf{w}(t)$  are assumed to be both mutually independent and independent from the state and observation with constant covariance matrices of  $\mathbf{Q}$  and  $\mathbf{R}$ , respectively, i.e.  $\mathbf{v} \sim N(0, \mathbf{Q})$  and  $\mathbf{w} \sim N(0, \mathbf{R})$ . Here in this paper, the stochastic term  $\mathbf{v}(t)$  (the “process noise”) functions as an approximation for the influence of the unknown dynamics of the process model. The time evolution of the states of the system and the unknown parameters of the stochastic model are to be identified using measurements of the output corrupted by the measurement noise term  $\mathbf{w}(t)$ .

The Ito and standard forms in Eqs. (27.1) and (27.2) are only equivalent, however, because the process and measurement noise are restricted to be additive and not multiplicative. Also, note that  $\mathbf{a}(t)$  can be a constant or time-varying vector and it is assumed to be Heaviside function later in this study. Equation (27.2) defines a continuous-time state-space optimal

filtering model. The purpose of the optimal continuous-time filtering problem is to recursively obtain estimates of the states and parameters from the mean, median, or mode of the time-varying conditional probability density

$$p(\mathbf{x}(t) | \{\mathbf{y}(\tau) : 0 \leq \tau \leq t\}). \quad (27.3)$$

To see how the filtering problem can be represented in the context of system identification, once again consider Eq. (27.2). As mentioned before, the assumed model of the system consists of the nonlinear function  $f$  which is a function of the state vector  $\mathbf{x}(t)$  and parameters  $\mathbf{a}(t)$ . Suppose that  $\mathbf{a}(t)$  is unknown but is assumed to be piecewise constant. The Kalman-Bucy filter can be used to simultaneously estimate the states  $\mathbf{x}(t)$  and the parameters  $\mathbf{a}(t)$ . The standard method employs the so-called state augmentation method, in which the parameter vector  $\mathbf{a}(t)$  is included in an augmented state vector  $\mathbf{X}(t) = [\mathbf{x}(t), \mathbf{a}(t)]^T$  while being constrained to have a predefined rate of change (zero here), i.e.

$$\begin{aligned} \dot{\mathbf{X}} &= \mathcal{F}(\mathbf{X}, t) + \mathcal{G}(t) \mathbf{v}(t) = \begin{Bmatrix} f(\mathbf{x}(t), \mathbf{a}(t), t) \\ 0 \end{Bmatrix} + \begin{Bmatrix} \mathbf{G}(t) \\ 0 \end{Bmatrix} \mathbf{v}(t) \\ \mathbf{y}(t) &= \mathcal{H}(\mathbf{X}, t) + \mathbf{J}(t) \mathbf{w}(t). \end{aligned} \quad (27.4)$$

The parameter vector  $\mathbf{a}(t)$  is assumed to initially have a Gaussian distribution with mean  $\mathbf{a}_0$  and covariance  $\mathbf{P}_0$ . Note that there is no noise term in the equation for the unknown parameter dynamics. The reason is that the parameters are already assumed to be stationary. Therefore, the augmented state method along with optimal filtering problem provides a pertinent approach for simultaneous estimation of the state and parameters of a (possibly) nonlinear system.

### 27.2.2 The Extended Kalman-Bucy Filter

The nonlinear optimal filtering problem described via the Ito differential form of Eq. (27.1) is considered, where the nonlinear process and measurement function are now functions of the augmented state  $\mathbf{X}$  (as in Eq. (27.4)), and  $\mathbf{J}(t)$  is the identity matrix. In order for the Kalman-Bucy filter to be applicable to the nonlinear system, the dynamics need to be locally linearized. Rather than linearizing about a reference trajectory, the extended Kalman-Bucy filter employs a linearization about the state estimate itself. It can be derived by taking the expectation of the dynamic model and adding a feedback term consisting of the measurement residual times an (as yet) unknown gain matrix, i.e.

$$d\hat{\mathbf{X}}(t) = E[\mathcal{F}(\mathbf{X}, t)] dt + \mathbf{K}(t) [d\mathbf{z}(t) - E[\mathcal{H}(\mathbf{X}, t)] dt]. \quad (27.5)$$

Defining the observer error as  $\mathbf{e}(t) = \mathbf{X}(t) - \hat{\mathbf{X}}(t)$ , the differential observation error is obtained as

$$d\mathbf{e}(t) = d\mathbf{X}(t) - d\hat{\mathbf{X}}(t) = \mathcal{F}(\mathbf{X}, t) dt - E[\mathcal{F}(\mathbf{X}, t)] dt - \mathbf{K}(t) [\mathcal{H}(\mathbf{X}, t) dt - E[\mathcal{H}(\mathbf{X}, t)] dt] + d\mathbf{B}(t), \quad (27.6)$$

where  $d\mathbf{B}(t) = \mathcal{G}(t) d\boldsymbol{\beta}(t) - \mathbf{K}(t) d\boldsymbol{\eta}(t)$  is a Brownian motion process with

$$E[d\mathbf{B}(t) d\mathbf{B}(t)^T] = [\mathcal{G}(t) \mathbf{Q}(t) \mathcal{G}(t)^T + \mathbf{K}(t) \mathbf{R}(t) \mathbf{K}(t)^T] dt. \quad (27.7)$$

Defining  $\tilde{\mathbf{F}}(t)$  and  $\tilde{\mathbf{H}}(t)$  to be the Jacobian matrices

$$\tilde{\mathbf{F}}(t) \sim := \left. \frac{\partial \mathcal{F}(\mathbf{X}, t)}{\partial \mathbf{X}} \right|_{\mathbf{X}=\hat{\mathbf{X}}}, \quad \tilde{\mathbf{H}}(t) := \left. \frac{\partial \mathcal{H}(\mathbf{X}, t)}{\partial \mathbf{X}} \right|_{\mathbf{X}=\hat{\mathbf{X}}}. \quad (27.8)$$

and linearizing about the current estimate yields

$$\begin{aligned} \mathcal{F}(\mathbf{X}, t) &= \mathcal{F}(\hat{\mathbf{X}}, t) + \tilde{\mathbf{F}}(t) (\mathbf{X} - \hat{\mathbf{X}}) + r_f(\mathbf{X}, \hat{\mathbf{X}}, t) \\ \mathcal{H}(\mathbf{X}, t) &= \mathcal{H}(\hat{\mathbf{X}}, t) + \tilde{\mathbf{H}}(t) (\mathbf{X} - \hat{\mathbf{X}}) + r_h(\mathbf{X}, \hat{\mathbf{X}}, t), \end{aligned} \quad (27.9)$$

from which  $E[\mathcal{F}(\mathbf{X}, t)] = \mathcal{F}(\hat{\mathbf{X}}, t) + E[r_f(\mathbf{X}, \hat{\mathbf{X}}, t)]$  and  $E[\mathcal{H}(\mathbf{X}, t)] = \mathcal{H}(\hat{\mathbf{X}}, t) + E[r_h(\mathbf{X}, \hat{\mathbf{X}}, t)]$ :  $r_f(\mathbf{X}, \hat{\mathbf{X}}, t)$  and  $r_h(\mathbf{X}, \hat{\mathbf{X}}, t)$  represent the remaining higher order terms. Truncating the Taylor series after the first order terms yields the differential observation error as

$$d\mathbf{e}(t) = \left[ \tilde{\mathbf{F}}(t) - \mathbf{K}(t)\tilde{\mathbf{H}}(t) \right] \mathbf{e}(t) dt + d\mathbf{B}(t). \quad (27.10)$$

The error covariance matrix can be obtained by differentiating  $E[\mathbf{e}(t)\mathbf{e}(t)^T]$  using the Ito differential rule to obtain

$$d\mathbf{P}(t) = \left[ \tilde{\mathbf{F}}(t) - \mathbf{K}(t)\tilde{\mathbf{H}}(t) \right] \mathbf{P}(t) dt + \mathbf{P}(t) \left[ \tilde{\mathbf{F}}(t) - \mathbf{K}(t)\tilde{\mathbf{H}}(t) \right]^T dt + \mathcal{G}(t)\mathbf{Q}(t)\mathcal{G}(t)^T dt + \mathbf{K}(t)\mathbf{R}(t)\mathbf{K}(t)^T dt. \quad (27.11)$$

The optimal gain matrix  $\mathbf{K}(t)$  which leads to a minimum variance estimator can be obtained by minimizing the cost function  $J = \text{Trace}(d\mathbf{P}(t))$  with respect to  $\mathbf{K}(t)$  as

$$\frac{\partial}{\partial \mathbf{K}(t)} [\text{Trace}(d\mathbf{P}(t))] = -2\mathbf{P}(t)\tilde{\mathbf{H}}(t)^T + 2\mathbf{K}(t)\mathbf{R}(t)^T = 0, \quad (27.12)$$

which yields the  $\mathbf{K}(t)$  matrix as

$$\mathbf{K}(t) = \mathbf{P}(t)\tilde{\mathbf{H}}(t)^T \mathbf{R}(t)^{-1}. \quad (27.13)$$

Therefore the propagation of the estimate is obtained as

$$d\hat{\mathbf{X}}(t) = \mathcal{F}(\hat{\mathbf{X}}, t) dt + \mathbf{K}(t) \left[ dz(t) - \mathcal{H}(\hat{\mathbf{X}}, t) dt \right], \quad (27.14)$$

while the following Riccati differential equation is obtained which propagates the error covariance  $\mathbf{P}(t)$ .

$$d\mathbf{P}(t) = \tilde{\mathbf{F}}(t)\mathbf{P}(t) dt + \mathbf{P}(t)\tilde{\mathbf{F}}(t)^T dt + \mathcal{G}(t)\mathbf{Q}(t)\mathcal{G}(t)^T dt - \mathbf{K}(t)\tilde{\mathbf{H}}(t)\mathbf{P}(t) dt. \quad (27.15)$$

The estimator so obtained is the extended Kalman-Bucy filter. Unlike the discrete-time extended Kalman filter, the prediction and measurement update steps are combined in the continuous-time extended Kalman filter.

### 27.2.3 Tuned Hyperchaotic Excitation

Traditionally, broadband random signals have been widely used for exciting structures. The reason is that the broadband nature of noise ensures a full modal response, ideal for frequency domain approaches to system identification or feature extraction. The motivation for the use of a chaotic signal as the excitation mechanism in damage detection is due to various unique features intrinsic to a chaotic signal. Chaotic signals also tend to possess broadband frequency spectra. However, unlike noise, chaos is deterministic and intrinsically low-dimensional (a stochastic process is infinite-dimensional). In fact many chaotic systems can be as low as three-dimensional when described as a continuous time process. In addition, a chaotic system is defined by a positive Lyapunov exponent (LE) implying extreme sensitivity to small changes in system parameters. The subtlety of damage-induced changes to a structure further motivates this choice as the mechanism of excitation.

Hyperchaos can be defined as chaotic behavior where at least two Les are positive. Having all the advantages that make a chaotic signal suitable for being used as an excitation, it is shown in [20,21] that a hyperchaotic signal is even more sensitive to subtle changes in damage severity as a result of the trajectory being permitted to more fully explore the entire phase space. Thus, hyperchaotic oscillators can be an alternative excitation mechanism in damage detection when extra sensitivity to damage is required. However, in order for hyperchaotic excitation to have the best performance the excitation should be tuned for the structure. There are two tuning criteria based on attractor dimensionality. First, the Lyapunov spectrum of the oscillator must overlap that of the structure. This ensures that changes to the Les of the structure, i.e. by damage, will alter the dimension of the filtered signal. Second, the dominant exponent associated with the oscillator must be minimized for a



given degree of overlap in order to maintain the lowest possible dimensionality. By employing the Kaplan-York conjecture in attractor dimensionality, these criteria become

$$\begin{aligned} |\lambda_M^C| &> |\lambda_1^L| \\ |\lambda_1^L| &> \sum_{r=1}^p \lambda_r^C, \end{aligned} \quad (27.16)$$

where  $\lambda_i^C$  are the exponents associated with the  $M$ -dimensional hyperchaotic system,  $\lambda_j^L$  are the exponents of the  $N$ -dimensional structure, and  $p$  is the number of positive Lyapunov exponents of the  $M$ -dimensional oscillator.

As mentioned before, the proposed approach takes advantage of the optimal filtering problem as the estimation technique for real-time identification of damage in structural systems. Therefore, the process equation in the optimal filtering problem of Eq. (27.4) is considered as

$$\mathbf{f}(\mathbf{x}(t), \mathbf{a}(t), t) = \boldsymbol{\varphi}(\mathbf{x}(t), \mathbf{a}(t)) + \mathbf{b}\mathbf{u}(t), \quad (27.17)$$

where  $\boldsymbol{\varphi}()$  describes the nonlinear structure of interest,  $\mathbf{u}()$  is the hyperchaotic excitation force, and the constant coefficient  $\mathbf{b}$  determines which component of  $\mathbf{u}()$  to be used as the excitation and which degree-of-freedom of the structure is to be excited. Any of the hyperchaotic nonlinear systems may be used as an excitation. We use a hyperchaotic version of the well-known Lorenz oscillator shown below, i.e.

$$\begin{aligned} \dot{u}_1 &= (\sigma(u_2 - u_1) + u_4)\delta \\ \dot{u}_2 &= (ru_1 - u_2 - u_1u_3 - u_5)\delta \\ \dot{u}_3 &= (u_1u_2 - bu_3)\delta \\ \dot{u}_4 &= (du_4 - u_1u_3)\delta \\ \dot{u}_5 &= (ku_2)\delta, \end{aligned} \quad (27.18)$$

which exhibits hyperchaotic behavior with three positive LEs for  $\sigma = 10, \rho = 28, \beta = \frac{8}{3}, d = 2, k = 10$  [23]. Note that if we eliminate states  $u_4$  and  $u_5$  from the first three states of the oscillator above, the resulting 3-dimensional oscillator is the well-known Lorenz oscillator which exhibits chaotic behavior (one positive LE) for  $\sigma = 10, \rho = 28, \beta = \frac{8}{3}$ . The bandwidth control parameter  $\delta$  is used to tune the LEs of the excitation based on the tuning criteria of Eq. (27.16). Values of  $\delta$  that are less than unity decrease the bandwidth of the input, while values greater than unity increase the bandwidth. In order to eliminate transient dynamics when using the hyperchaotic oscillator as an excitation, the oscillator is initiated at a point on the attractor. The matrix  $\mathbf{b}$  throughout this paper is chosen in a way that the first component  $u_1$  of the chaotic/hyperchaotic Lorenz oscillators is used for the excitation.

## 27.3 Simulation Results

### 27.3.1 S-DOF Hysteretic Nonlinear Structure

Consider a single degree of (SDOF) nonlinear hysteretic Bouc–Wen system subject to the excitation  $f_{exc}(t)$

$$m\ddot{x}(t) + c\dot{x}(t) + kr(t) = f_{exc}(t) \quad (27.19)$$

where  $r(t)$  is the Bouc–Wen hysteretic component with

$$\dot{r} = \dot{x} - \beta|\dot{x}||r|^{\alpha-1}r - \gamma\dot{x}|r|^\alpha \quad (27.20)$$

The system parameters  $m = 1, c = 0.3, k = 9, \beta = 2, \gamma = 1, \alpha = 2$  are chosen for the simulation. Considering  $\mathbf{z} = [x, \dot{x}, r]^T$  the  $\boldsymbol{\varphi}$  function in Eq. (27.17) that forms the process function  $\mathbf{f}$  of the filtering problem for this system is

$$\boldsymbol{\varphi}(\mathbf{z}(t)) = \left\{ \begin{array}{c} z_2(t) \\ (1/m)(-kz_3(t) - cz_2(t)) \\ z_2(t) - \beta|z_2(t)||z_3(t)|^{\alpha-1}z_3(t) - \gamma z_2(t)|z_3(t)|^\alpha \end{array} \right\}, \quad (27.21)$$

Time-varying damage is implemented as a 50% abrupt reduction in the stiffness and damping coefficients of the system at time  $t = 50$  s. The mass of the system is assumed to be known throughout this simulation. The filtering sequence is initiated with values of the state and parameters ( $k, c$ ) which are 50% deviated from the true values. Three types of excitation  $\mathbf{u}(t)$  including white noise, chaotic Lorenz excitation and hyperchaotic Lorenz excitation (Eq. 27.18) are applied to the system under identical measurement and process noise covariance ( $\mathbf{R}, \mathbf{Q}$ ) with identical initial error covariance  $\mathbf{P}$ . The measurement function  $\mathbf{h}$  is considered to be the identity function i.e. both displacement  $r$  and velocity  $\dot{x}$  are measured. The extended Kalman-Bucy filter is used for real-time identification of the stiffness  $k$  and the damping coefficient  $c$  of the system. The value of  $\delta = 0.542$  can be shown to satisfy the tuning criteria for both the chaotic Lorenz oscillator and hyperchaotic Lorenz oscillator of Eq. (27.18) and is used for this simulation. The results of the identified parameters with each of the three excitations are shown in Fig. 27.1. As is clear from the figure, in the case of random excitation the change in system parameters is not sensed. However, when chaotic and hyperchaotic excitations are applied the approach successfully identifies the change. Note that in the case of hyperchaotic excitation the filter converges to the true value of the parameter faster than for the case of chaotic excitation.

In the second simulation the proposed approach is applied for real-time identification of a 10% stiffness reduction in the hysteretic system of Eq. (27.19). The system parameters are considered as mentioned previously and the hyperchaotic Lorenz oscillator of Eq. (27.18) is used for the excitation. The value of  $\delta = 0.1$  is used for this simulation which can be shown to satisfy the tuning criteria of Eq. (27.18) for the hyperchaotic Lorenz oscillator and the nonlinear system of Eq. (27.19). Since measurements of displacement  $r$  and velocity  $\dot{x}$  may not always be readily available, a more common acceleration measurement is considered here. Acceleration measurements in this simulation are provided by using the measurement function  $\mathbf{h}$  based on the Eq. (27.19) as

$$\mathbf{h}(x(t), t) = \frac{1}{m} (f_{\text{exc}}(t) - c\dot{x}(t) - k r(t)) \quad (27.22)$$

Note that the excitation force in Eq. (27.22) is assumed to be easily measurable via force transducers. The filtering sequence is initiated with values of the state and unknown parameters ( $k, c$ ) which are 50% deviated from the true values. As is clear from Fig. 27.2, the approach is capable of real-time identification of the 10% stiffness reduction at time  $t = 250$  s with good accuracy and fast convergence from measurements of acceleration in the presence of noise.

Although measuring acceleration is more realistic and practical than measuring both velocity  $\dot{x}$  and displacement  $r$ , the  $\mathbf{h}$  function that is used for measuring acceleration is still not quite realistic for some modern structures. The arguable part is that the values of system parameters  $m, k$  and  $c$  used in the  $\mathbf{h}$  function are assumed to be known a priori. This is only realistic in the case that the mechanical properties of the structure can be measured or identified before the occurrence of damage. However, if the structure under consideration is a smart structure, then the identification algorithm needs to provide instantaneous updates of the mechanical properties of the structure to some embedded or layered actuators in order for the structure to adaptively perform functions of sensing and actuation. Therefore, the measurement function of Eq. (27.22) is not applicable to a smart structures. Consequently, in the third simulation the measurement function  $\mathbf{h}$  is modified to incorporate the estimated values of the system parameters instead of the true values. Assuming the vector of unknown parameters in Eq. (27.2) to be composed of parameters  $m, k$  and  $c$ , i.e.  $\mathbf{a} = [m, k, c]$ , the modified measurement function is

$$\mathbf{h}(x(t), \mathbf{a}(t), t) = \frac{1}{\mathbf{a}_1(t)} (f_{\text{exc}}(t) - \mathbf{a}_3(t)\dot{x}(t) - \mathbf{a}_2(t)r(t)), \quad (27.23)$$

where  $\mathbf{a}(t)$  is identical to what used as the augmented state  $\mathbf{X}(t)$  in Eq. (27.4) when forming the process function  $\mathcal{F}(\mathbf{X}, t)$  in the process of using the EKB filter. The EKB filter estimates are thus simultaneously used in the measurement function  $\mathbf{h}$  to relate the measured acceleration to the states of the system ( $\dot{x}$  and  $r$ ). Note that in this simulation  $m, k$  and  $c$  are all assumed to be unknown.

Again, the value of  $\delta = 0.1$  is used for this simulation and the filtering sequence is initiated with values of the state and parameters ( $m, k$  and  $c$ ) 50% deviated from the true values. Figure 27.3 shows the simulation results. As is clear from the figure, in this simulation a stiffness reduction of 10% at time  $t = 250$  is accurately identified online in the nonlinear hysteretic system without any prior knowledge of the system parameters and by sole measurement of the acceleration response and the excitation force. In fact, the proposed technique first accurately identifies the values of the parameters from noise-corrupted measurements of the acceleration response within the first 250 s of excitation, and then successfully monitors the change in the system by identifying the parameter that has changed, the amount of change, and the instant of occurrence of the change. Therefore, the proposed adaptive identification technique is capable of real-time sensing of mechanical properties ( $m, k$  and  $c$ ) in a S-DoF nonlinear smart structure.

**Fig. 27.1** Comparing damage identification with (a) random, (b) chaotic and (c) hyperchaotic excitations in nonlinear system of Eq. (27.19) estimated from noise-corrupted measurement using extended Kalman-Bucy filter (damage defined as a 50% stiffness and damping reduction at  $t = 50$  s).  $Q = 1 \times 10^{-8}I$ ,  $R = 1 \times 10^{-8}I$ ,  $P_0 = 1 \times 10^{-6}I$

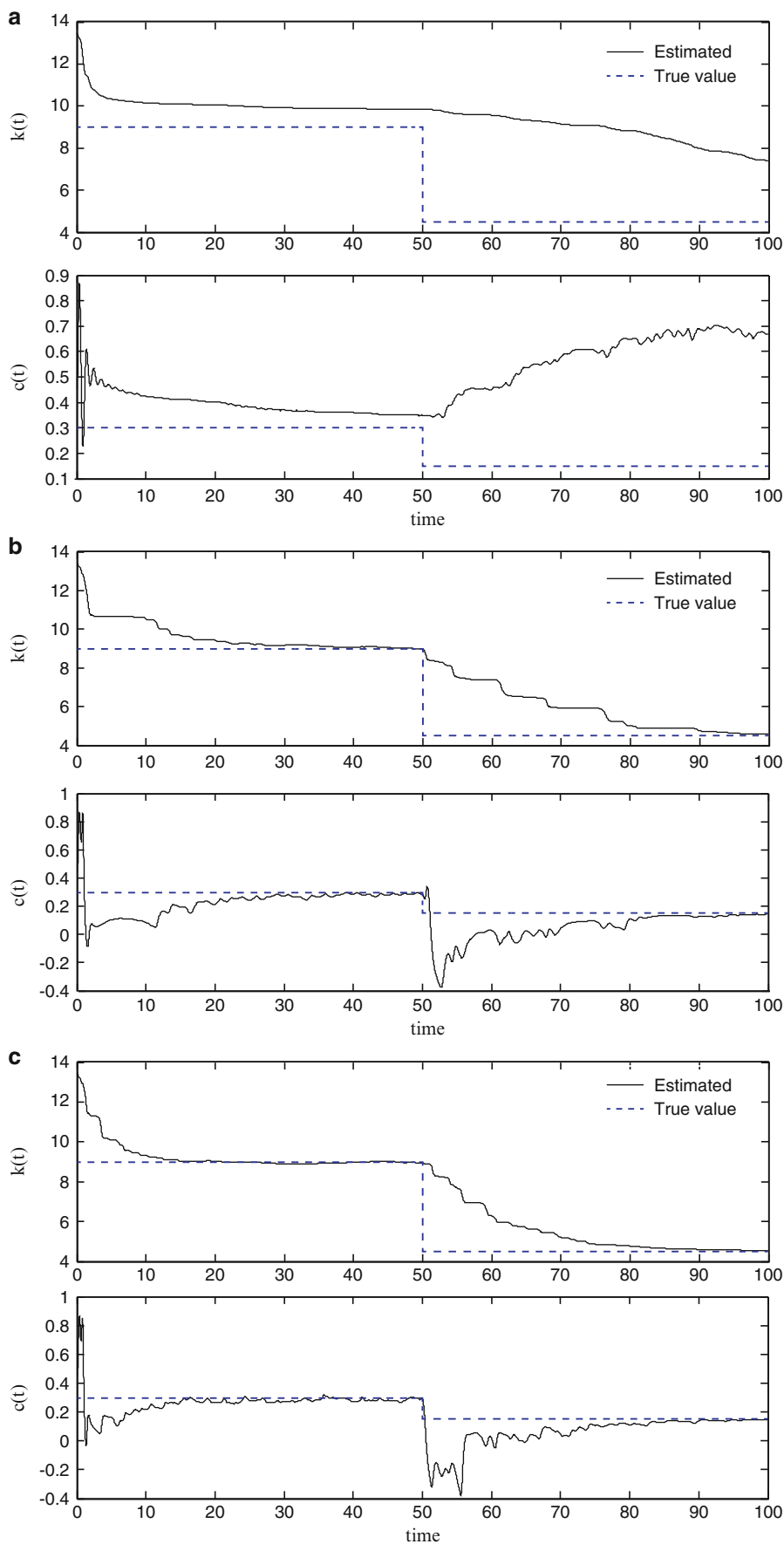


**Fig. 27.2** Identification of 10% change in the stiffness of the nonlinear hysteretic system of Eq. (27.19) from acceleration measurements (Eq. 27.22) using hyperchaotic excitation and extended Kalman-Bucy (EKB) filter ( $Q = 1 \times 10^{-4}I$ ,  $R = 1 \times 10^{-4}I$ ,  $P_0 = 1 \times 10^{-4}I$ )

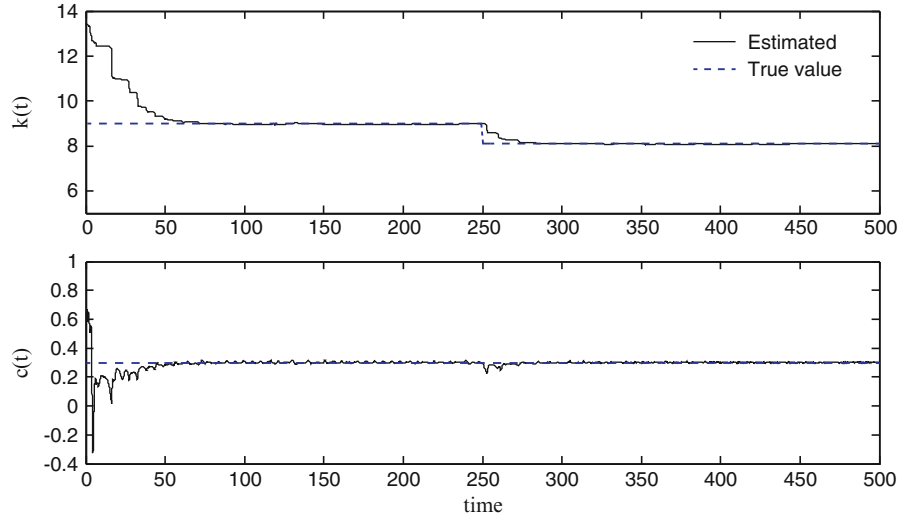
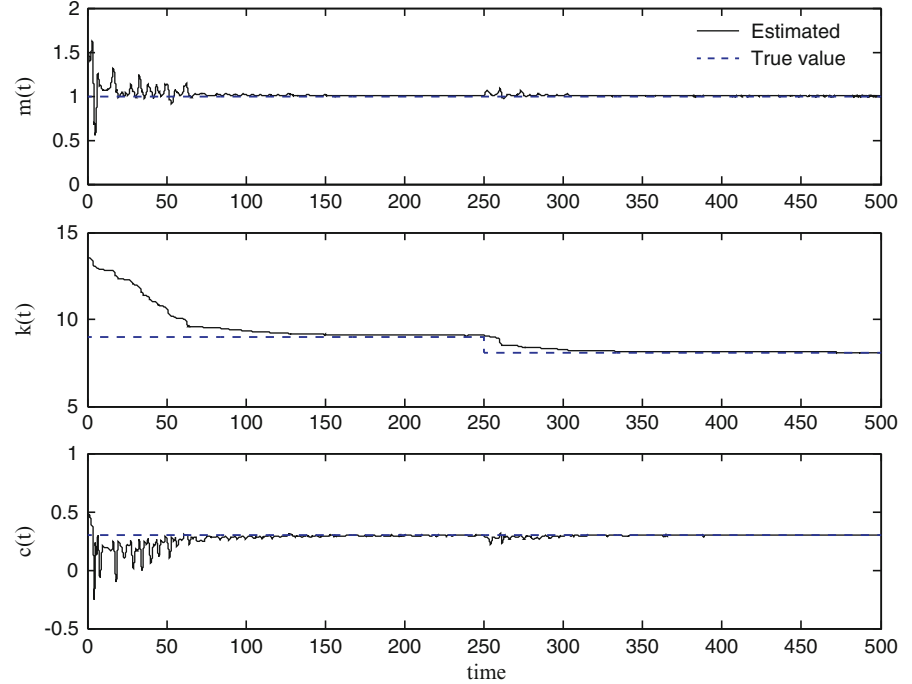


**Fig. 27.3** Identification of 10% change in the stiffness of the nonlinear hysteretic system of Eq. (27.19) from acceleration measurements (Eq. 27.22) using hyperchaotic excitation and extended Kalman-Bucy (EKB) filter ( $Q = 1 \times 10^{-4}I$ ,  $R = 1 \times 10^{-4}I$ ,  $P_0 = 1 \times 10^{-4}I$ )



### 27.3.2 Four-Story Shear-Beam Structure

Consider an idealized four-story linear shear-beam type building with floor masses  $m_i$ , inter-story stiffnesses  $k_i$ , and inter-story viscous damping coefficients  $c_i$  where  $i = 1, \dots, 4$ . The structure is modeled with a linear spring–mass–damper system where the first spring is connected to the ground. The masses, spring stiffnesses and damping coefficients forming the  $M$ ,  $K$  and  $C$  matrices are set to  $m_i = 5$ ,  $k_i = 8$  and  $c_i = 0.5$ . Considering the state-space vector  $\mathbf{z} = [\mathbf{x}(t), \dot{\mathbf{x}}(t)]^T$ , the  $\varphi$  function of Eq. (27.17) for this system is the linear function

$$\varphi(\mathbf{z}(t)) = \mathbf{A}\mathbf{z}(t) = \begin{bmatrix} 0 & \mathbf{I} \\ -\mathbf{M}^{-1}\mathbf{K} & -\mathbf{M}^{-1}\mathbf{C} \end{bmatrix} \mathbf{z}(t) \quad (27.24)$$

Damage is introduced as a 10% stiffness reduction in the third spring of the system occurring at time  $t = 350$  s. In order to implement the proposed real-time damage identification technique, the fourth mass is excited with the hyperchaotic Lorenz excitation of Eq. (27.18) with a value of  $\delta = 0.1$  which can be shown to satisfy the tuning criteria of Eq. (27.16). It is assumed

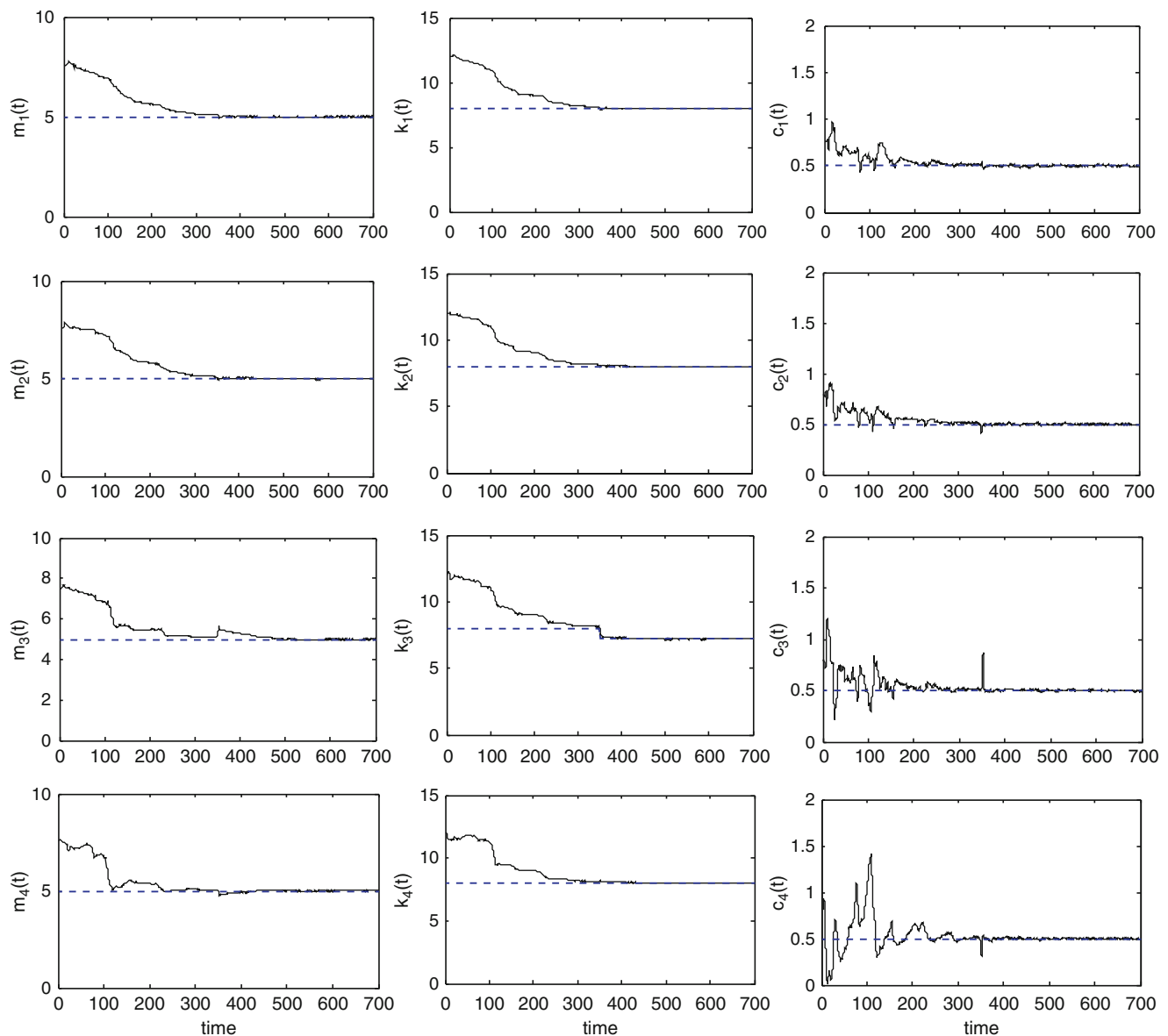


**Fig. 27.4** Identification of 10% change in the stiffness 4-DoF linear system of Eq. (27.24) from acceleration measurements (Eq. 27.23) using hyperchaotic excitation and extended Kalman-Bucy (EKB) filter ( $\mathbf{Q} = 1 \times 10^{-3}\mathbf{I}$ ,  $\mathbf{R} = 1 \times 10^{-2}\mathbf{I}$ ,  $\mathbf{P}_0 = 1 \times 10^{-2}\mathbf{I}$ )

that only the excitation force and the acceleration of the masses are measured. Thus, since the states of the system consist of velocity  $\dot{\mathbf{x}}$  and displacement  $\mathbf{x}$ , an appropriate measurement function is required to enable acceleration measurement. For the first simulation, a measurement function similar to that of Eq. (27.22) is considered by replacing  $\mathbf{m}, \mathbf{k}$  and  $\mathbf{c}$  respectively with  $\mathbf{M}, \mathbf{K}$  and  $\mathbf{C}$  matrices. All 12 components of the  $\mathbf{M}, \mathbf{K}$  and  $\mathbf{C}$  matrices are considered as unknown parameters to be identified. The filtering sequence is initiated with values of the state and unknown parameters 50% deviated from the true values. The system is excited for 700s by the hyperchaotic Lorenz excitation and the parameters are identified using the current approach. The real-time values of all 12 parameters of the 4-DoF system are depicted in Fig. 27.4. The identified parameters converge to the true value within the first 300s. Upon the occurrence of damage, the identified values of some parameters experience a disturbance without losing convergence. The identified stiffness of the third spring clearly monitors the 10% reduction at time  $t = 350$  s.

In the fourth simulation, a measurement function similar to that of Eq. (27.23) is used. Again, all 12 components of the  $\mathbf{M}, \mathbf{K}$  and  $\mathbf{C}$  matrices are considered as unknown parameters and the estimated values of those parameters are employed in the measurement function to relate the acceleration measurements to the states of the process. The same damage scenario occurring at time  $t = 300$  s is applied with the same excitation strategy as used in the previous simulation. The filtering

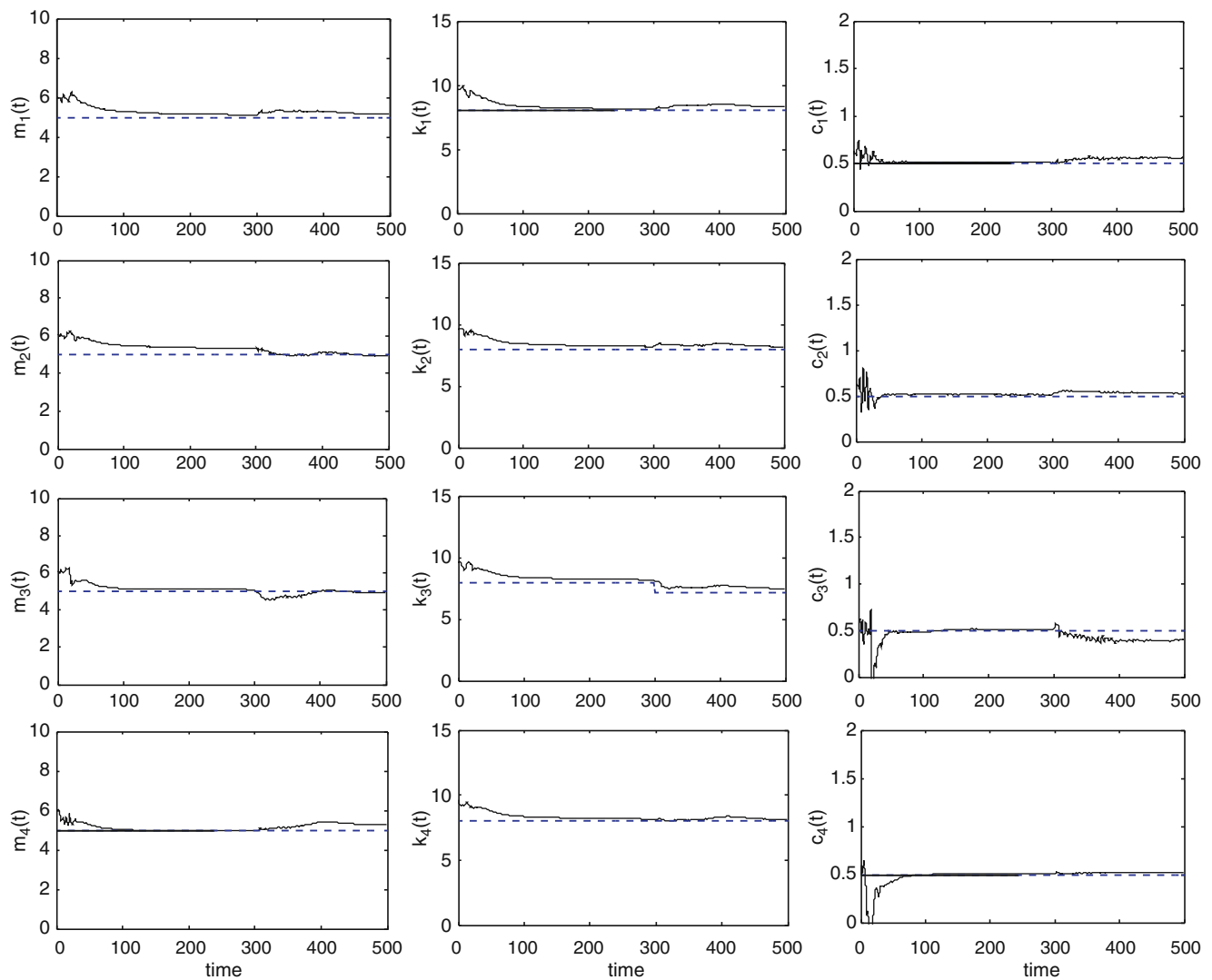


**Fig. 27.5** Identification of 10% change in the stiffness 4-DoF linear system of Eq. (27.24) from acceleration measurements (Eq. 27.23) using hyperchaotic excitation and extended Kalman-Bucy (EKB) filter ( $Q = 1 \times 10^{-3}I$ ,  $R = 1 \times 10^{-2}I$ ,  $P_0 = 1 \times 10^{-2}I$ )

sequence is initiated with values of the state and unknown parameters 20% deviated from the true values. Figure 27.5 demonstrates the results. As seen in the figure, the identified parameters converge to the true value with good accuracy (except for  $m_2$  which only has an acceptable accuracy) within the first 300 s. Upon the occurrence of damage, the identified values of some parameters experience a disturbance and, given enough time they will retrieve convergence. The identified stiffness of the third spring monitors 10% reduction at time  $t = 300$  s. The simulation results show that the technique needs a longer excitation than just 500 s for a better accuracy. Therefore, using the proposed technique, a stiffness reduction of the 10% at time  $t = 300$  s is identified in the 4-DoF system without any prior knowledge of the system parameters and by sole measurement of the acceleration response and the excitation force.

## 27.4 Conclusions

The current study combines hyperchaotic excitation, which has been previously shown to produce improved outcome when applied as the excitation in some attractor-based damage identification techniques, with the stochastic estimation technique of extended Kalman-Bucy filter, which has been recently reintroduced due to its enhanced estimation capabilities over similar filtering techniques. As a result, a novel feasible technique for identification of damage in nonlinear structures is developed

that can be used in smart or self-healing structures for real-time identification of damage. Simulation results performed on single- and multi-DoF linear and nonlinear structural systems show that the proposed technique is capable of identifying modal parameters of structures from noise-corrupted measurements of acceleration response. The current technique is also capable of monitoring changes in the identified parameters by determining the parameter that has changed, the amount of change, and the instant of occurrence of the change. Therefore, the proposed adaptive identification technique is capable of real-time monitoring of damage based on the response of the system to a hyperchaotic probe. The results in this study are obtained with a fixed integration time step of 0.01 s. Considering the continuous-time nature of the filtering algorithm used in this approach, more accurate estimates are expected to be achieved by using smaller time steps for integration.

## References

1. Lin J, Betti R, Smyth AW (2001) Online identification of nonlinear hysteretic structural system using a variable trace approach. *Earthq Eng Struct Dyn* 30:1279–1303
2. Smyth AW, Masri SF, Chassiakos AG, Caughey TK (1999) Online parametric identification of MDOF nonlinear hysteretic systems. *ASCE J Eng Mech* 125:133–142
3. Yang JN, Lin S (2004) Online identification of nonlinear hysteretic structures using an adaptive tracking technique. *Int J Nonlinear Mech* 39:1481–1491
4. Shinozuka M, Yun C, Imai H (1982) Identification of linear structural dynamic systems. *ASCE J Eng Mech* 108:1371–1390
5. Shinozuka M, Ghanem R (1995) Structural system identification. II: experimental verification. *ASCE J Eng Mech* 121:265–273
6. Ghanem RG, Shinozuka M (1995) Structural-system identification. I: theory. *ASCE J Eng Mech* 121(2):255–264
7. Hoshiya M, Saito E (1984) Structural identification by extended Kalman filter. *ASCE J Eng Mech* 110:1757–1771
8. Sato T, Qi K (1998) Adaptive  $H_\infty$  filter: its application to structural identification. *ASCE J Eng Mech* 124(11):1233–1240
9. Yoshida I (2001) Damage detection using Monte Carlo filter based on non-Gaussian noise. In: *Proceedings of structural safety and reliability, ICOSSA 2001*. Swet & Zeitinger, Lisse, 8 pp
10. Yang JN, Lin S, Huang H, Zhou L (2006) An adaptive extended Kalman filter for structural damage identification. *Struct Control Health Monit* 13:849–867
11. Loh CH, Lin CY, Huang CC (2000) Time domain identification of frames under earthquake loadings. *ASCE J Eng Mech* 126(7):693–703
12. Loh CH, Tou IC (1995) A system identification approach to the detection of changes in both linear and nonlinear structural parameters. *J Earthq Eng Struct Dyn* 24:85–97
13. Åström KJ (1980) Self-tuning regulators: design principles and applications. In: Narendra KS, Monopoli RV (eds) *Applications of adaptive control*. Academic, New York, pp 1–68
14. Torkamani S (2013) Hyperchaotic and delayed oscillators for system identification with application to damage assessment. PhD dissertation, New Mexico State University
15. Nichols JM, Trickey ST, Todd MD, Virgin LN (2003) Structural health monitoring through chaotic interrogation. *Meccanica* 38:239–250
16. Nichols JM, Todd MD, Virgin LN, Nichols JD (2003) On the use of attractor dimension as a feature in structural health monitoring. *Mech Syst Signal Process* 17:1305–1320
17. Olson C, Todd MD, Worden K, Farrar C (2007) Improving excitations for active sensing in structural health monitoring via evolutionary algorithms. *J Vib Acoust* 129:784–802
18. Olson CC, Todd MD (2010) On the convergence of multiple excitation sources to a global optimum excitation in active sensing for structural health monitoring. *Struct Control Health Monit* 17:23–47
19. Olson CC, Overbey LA, Todd MD (2009) The effect of detection feature type on excitations bred for active sensing in structural health monitoring. *J Intell Mater Struct Syst* 20:1307–1327
20. Torkamani S, Butcher EA, Todd MD, Park GP (2011) Hyperchaotic probe for damage identification using nonlinear prediction error. *Mech Syst Signal Process* 29:457–473
21. Torkamani S, Butcher EA, Todd MD, Park GP (2011) Detection of system changes due to damage using a tuned hyperchaotic probe. *Smart Mater Struct* 20:025006
22. Jazwinski AH (1970) *Stochastic processes and filtering theory*. Academic, New York
23. Guosi Hu (2009) Generating hyperchaotic attractors with three positive Lyapunov exponents via state feedback control. *Int J Bifurcation Chaos* 19:651–660

# Chapter 28

## Damage Detection Based on Electromechanical Impedance Principle and Principal Components

Mario Anderson de Oliveira, Jozue Vieira Filho, Vicente Lopes Jr., and Daniel J. Inman

**Abstract** This paper presents a novel time domain approach for Structural Health Monitoring (SHM) systems based on Electromechanical Impedance (EMI) principle and Principal Component Coefficients (PCC), also known as loadings. Differently of typical applications of EMI applied to SHM, which are based on computing the Frequency Response Function (FRF), in this work the procedure is based on the EMI principle but all analysis is conducted directly in time-domain. For this, the PCC are computed from the time response of PZT (Lead Zirconate Titanate) transducers bonded to the monitored structure, which act as actuator and sensor at the same time. The procedure is carried out exciting the PZT transducers using a wide band chirp signal and getting their time responses. The PCC are obtained in both healthy and damaged conditions and used to compute statistics indexes. Tests were carried out on an aircraft aluminum plate and the results have demonstrated the effectiveness of the proposed method making it an excellent approach for SHM applications. Finally, the results using EMI signals in both frequency and time responses are obtained and compared.

**Keywords** SHM • Damage detection • Time-domain analysis • Electromechanical impedance • Principal component coefficients

### 28.1 Introduction

Researches in Structural Health Monitoring (SHM) have been conducted in the last years focusing the importance of economic and security aspect for mechanical, aerospace and civil structures. As a consequence, the SHM systems have become an important way to increase the safety and reduce maintenance costs in a variety of such systems [1, 2]. Typically, conventional inspection tests are based on either visual inspection or other types of Non-Destructive Evaluation (NDE) methods [3]. Visual inspection methods are very limited because they depend of the visual acuity and experience of the inspector. On the other hand, other types of NDE can be used to detect small cracks that would be imperceptible to the human eye. Among several NDE techniques, Electromechanical Impedance (EMI) and Lamb wave based methods have been exploited on academic and industrial researches. Both techniques are notable by using the small and lightweight piezoelectric

---

M.A. de Oliveira (✉)

Department of Electrical and Electronic, Federal Institute of Education, Science and Technology of Mato Grosso, Campus Cuiabá, Cuiabá, Mato Grosso, Brazil

Department of Electrical Engineering, Universidade Estadual Paulista, Ilha Solteira, São Paulo, Brazil  
e-mail: [mario.oliveira@cba.ifmt.edu.br](mailto:mario.oliveira@cba.ifmt.edu.br)

J. Vieira Filho

Department of Electrical Engineering, Universidade Estadual Paulista, Ilha Solteira, São Paulo, Brazil  
e-mail: [jozue@dee.feis.unesp.br](mailto:jozue@dee.feis.unesp.br)

V. Lopes Jr

Department of Mechanical Engineering, Universidade Estadual Paulista, Ilha Solteira, São Paulo, Brazil  
e-mail: [vicente@dem.feis.unesp.br](mailto:vicente@dem.feis.unesp.br)

D.J. Inman

Department of Aerospace Engineering, University of Michigan, Ann Arbor, MI, USA  
e-mail: [daninman@umich.edu](mailto:daninman@umich.edu)



wafer active sensor bonded to the structure to be monitored. When the structure is excited through PZTs in an appropriate frequency range it is possible to identify structural damages by analyzing their responses and computing some statistical indexes [4]. For that, both methodologies need to previously know the response signal from the structure in healthy condition (baseline). Thus, the development of new techniques and methods of prognosis and identification of structural failures can provide more efficiency and also cost reduction in different applications [5, 6]. With the growing demand for new services in the area of structural analysis, researches in SHM have been developed in order to extrapolate the academic world and reach the most sophisticated practical SHM systems.

Thus, this paper proposes a novel method for damage detection based on EMI principle applied to SHM using the Principal Component Coefficients (PCC). Differently of traditional EMI which use the Frequency Response Function (FRF), this approach uses the response signals in time-domain to calculate the PCC. A chirp signal is used to excite the structure through PZT transducers and the same transducers are used as a sensor to get the response from the structure. The Root Mean Square Deviation (RMSD) indexes are directly calculated from the PCC. The proposed method was applied to an aircraft aluminum plate, and the results were compared with the traditional EMI technique based on FRF.

## 28.2 Theoretical Base

### 28.2.1 Principal Component Analysis

The main characteristic of Principal Component Analysis (PCA) is its capability to reduce amount of data. However, PCA is considered a factorial method because the reduction of variables do not happen by simply selecting some variables, but by construction of new synthetic variables obtained by linear combination of initial variables by means of factors. The new set of variables occurs with the least possible loss of information, and this also seeks to eliminate some variables that have little information about the original data. The use of the Principal Component Analysis (PCA) applied to SHM can be found in several works in the literature. In [7], PCA algorithm was used as a preprocessing module to reduce the data dimensionality and eliminate the unwanted noises on EMI based method. In [8] the authors used PCA to distinguish changes in the measured features due to environmental variations. In [9] the authors used PCA to eliminate environmental factors in damage detection applied to an outlier. In [10] the authors proposed PCA to reduce dimensionality in damage identification problem, more specifically detecting and locating impacts in a part of a commercial aircraft wing flap. In [11], PCA was used in a vibration problem for data reduction in a time-series obtained from a benchmark structure.

The calculation of Principal Components (PC) is described as follows. Given a data set represented by the matrix  $\mathbf{X} = [x_{i1} x_{i2} \dots x_{ij}]$  where  $i = 1, 2, 3, \dots, M$ ;  $j = 1, 2, 3, \dots, N$  which  $M$  is the total number of observations and  $N$  number of variables, we form the covariance matrix ( $\mathbf{C}$ ) with dimension  $N \times N$  as following Eq. (28.1) [12],

$$\mathbf{C} = \sum_{i=1}^M \mathbf{X}_i \mathbf{X}_i^T \quad (28.1)$$

where  $T$  represents transposition. If  $\mathbf{C}$  is a square matrix and  $\mathbf{I}$  represent the identity matrix, then the scalars  $\lambda_1, \lambda_2, \dots, \lambda_N$  must satisfy the Eq. (28.2),

$$|\mathbf{C} - \lambda \mathbf{I}| = 0 \quad (28.2)$$

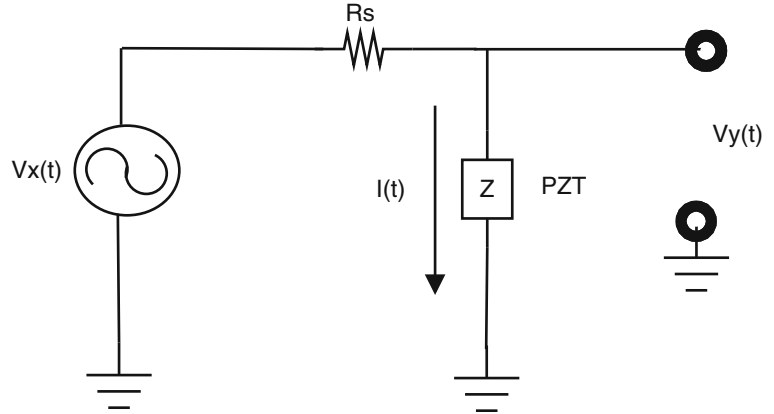
where,  $\lambda$  is known as eigenvalues of  $\mathbf{C}$ . Considering the covariance matrix  $\mathbf{C}$  and  $\lambda$  as an eigenvalues of  $\mathbf{C}$ , thus eigenvector ( $\mathbf{E}$ ) can be calculated according to Eq. (28.3)

$$\mathbf{C}\mathbf{E} = \lambda\mathbf{E} \quad (28.3)$$

where, the dimension of  $\mathbf{E}$  is  $N \times N$  as well. The strategy to obtain the PC ( $\mathbf{Z}$ ) is to form the linear combinations of original variables. For this, they are determined taking the elements of  $\mathbf{X}$  and calculating the coefficients of  $\mathbf{Z}$  according to Eq. (28.4) [13].

$$\mathbf{Z} = \mathbf{X}\mathbf{E} \quad (28.4)$$

**Fig. 28.1** Circuit used to excite PZT and get response signal



The Principal Component Coefficients (PCC) quantify the influence of each variable  $x_{i,1}, x_{i,2}, \dots, x_{i,j}$  have on the each principal components ( $z_{i,1}, z_{i,2}, \dots, z_{i,j}$ ) (Eq. 28.4). In the PCC matrix ( $\mathbf{W}$ ), the rows correspond to variables, columns to component. The PCC of each variable above the component principal can be calculated from the Eq. (28.5) [12],

$$\mathbf{W} = \frac{e_{i,j}}{\sqrt{\text{Var}(x_{i,j})}} \quad (28.5)$$

where  $e_{i,j}$  represents an element of eigenvector matrix  $\mathbf{E}$  and  $\text{Var}(x_{i,j})$  represents the variance of  $x_{i,j}$ . In this work, the PCC will be used as input to calculate the RMSD indexes.

### 28.2.2 Electromechanical Impedance Principle

The technique based on the Electromechanical Impedance (EMI) applied to SHM was originally proposed by Liang et al. [14] and improved by several other authors. Currently, EMI has been studied in several fronts and application including signal processing, statistics methods and new circuits for excitation/reception of signals from the set PZT/structure. Its basic principle considers a PZT bonded to a structure which is excited in an appropriated frequency range (acting as an actuator) to generate a response based on the structure condition (acting as a sensor). In general, the results from these measurements are used to determine the Frequency Response Function (FRF) in both healthy and damaged conditions and then statistical indexes are computed to detect structural damage [4].

The proposed method is based on the basic idea of the EMI, but the analysis is carried out in time-domain without computing the FRF. The time-domain analysis based on the electromechanical impedance principle is recent and it was proposed by Vieira Filho et al. [15], in which the authors proposed to detect damages using multilevel wavelet decomposition. Posteriorly, the authors proposed a new method in which the time response of the PZT provides information on the electromechanical impedance variation when a monitored structure is damaged [16]. The results showed that the EMI does not need to be computed and damage could be detected using only the time response from the PZT. Time-domain applications can be carried out considering the excitation circuit of the couple PZT/structure as presented in Fig. 28.1 [17].

From Fig. 28.1, the module of electromechanical impedance  $|Z|$  is given by Eq. (28.6)

$$|Z| = \frac{V_y}{(V_x - V_y)_P} R_s \quad (28.6)$$

where,  $P$  represents peak,  $I(t)$  represents the current through the PZT,  $V_x$ , and  $V_y$  represent excitation and response voltages, respectively.  $R_s$  is used to limit the current through the PZT. From Eq. (28.6), it is possible to determine structural damages using only the response signals from the couple PZT/structure because these signals are correlated with the mechanical impedance of structure. In this work the damage detection is carry out using the measurement response signal in time-domain ( $V_y$ ) to procedure the calculation of PCC. This analysis provides a damage detection system fast and efficient.

### 28.3 Methodology and Experimental Setup

The proposed method is based on the electromechanical impedance principle which uses PZT transducers attached to the host structure. For this, from the circuit presented in the Fig. 28.1 a chirp signal from DC 0–125 kHz was used to excite the set PZT/structure. At the same time, the response signal of structure is sampled at 1.25 Msample/s. The resistance  $R_s$  was fixed at 1 k $\Omega$ . The system presented in Fig. 28.2 is used to excite and receive the response signals from the structure. The multifunctional Data Acquisition (DAQ) is controlled by LabVIEW® [17].

Practical tests were carried out using an aircraft aluminum plate as illustrated in Fig. 28.3. Firstly, five piezoelectric transducers (S1, S2, S3, S4 and S5) were bonded to the plate. Then, six removable damages (A, B, C, D, E and F) were simulated by using a magnet in the structure at different distances from the actuator/sensors.

The first step of the experiment consists on exciting each PZT and getting its response keeping the structure undamaged. A couple of signals were obtained at different times for each sensor and used to calculate a simple arithmetic mean and other ones were stored as baseline (BL). Posteriorly, damages (A, B, C, D, E and F) were simulated separately and individual responses were acquired from each PZT sensor (S1, S2, S3, S4 and S5). Figure 28.4 presents time-domain responses from sensor S4 in both healthy and damage (D) conditions. Note that the variation between the two signals, in healthy and damaged conditions, is almost imperceptible. The previously described procedure is repeated for each simulated damage and healthy condition (H), which make possible to acquire a set of response.

Afterward, the data obtained from each sensor (S1, S2, S3, S4 and S5) are grouped in eight matrices considering the baseline (BL), all damages (A, B, C, D, E and (F)) and healthy condition (H). As an example, Eqs. (28.7)–(28.9) show three of these matrices.

$$\mathbf{BL} = [x_{BLi,S1} \ x_{BLi,S2} \ x_{BLi,S3} \ x_{BLi,S4} \ x_{BLi,S5}] \quad (28.7)$$

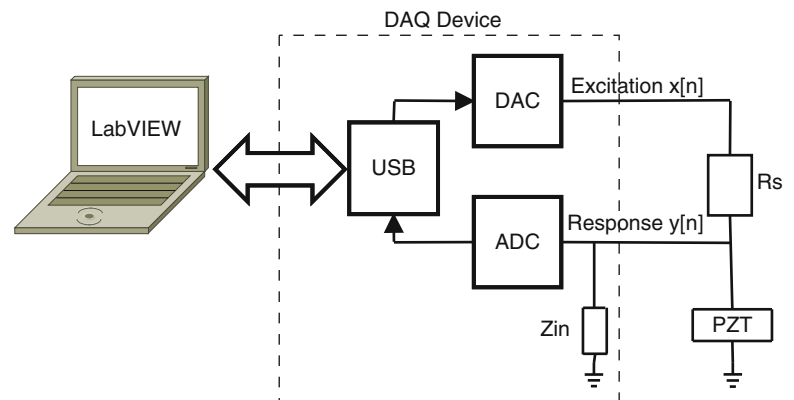
$$\mathbf{A} = [x_{Ai,S1} \ x_{Ai,S2} \ x_{Ai,S3} \ x_{Ai,S4} \ x_{Ai,S5}] \quad (28.8)$$

$$\mathbf{H} = [x_{Hi,S1} \ x_{Hi,S2} \ x_{Hi,S3} \ x_{Hi,S4} \ x_{Hi,S5}] \quad (28.9)$$

In these equations,  $i = 1, 2, 3, \dots, 262144$ ,  $x_{BLi,S1}$  represent signals from sensor 1 (S1) for the baseline,  $x_{Ai,S3}$  represent the signal from sensor 3 (S3) considering damage A, and thus for the other indexes. Summarizing, all baselines (for all sensors) are grouped to determinate the baseline matrix  $\mathbf{BL}$  (Eq. 28.7). Similarly, six other matrices are grouped considering the respective signals for all damages (A, B, C, D, E and F) and another for healthy structure ( $\mathbf{H}$ ). The matrices are organized in five columns and 262,144 rows. Summarizing, eight matrices are formed and will be used to calculate PCC.

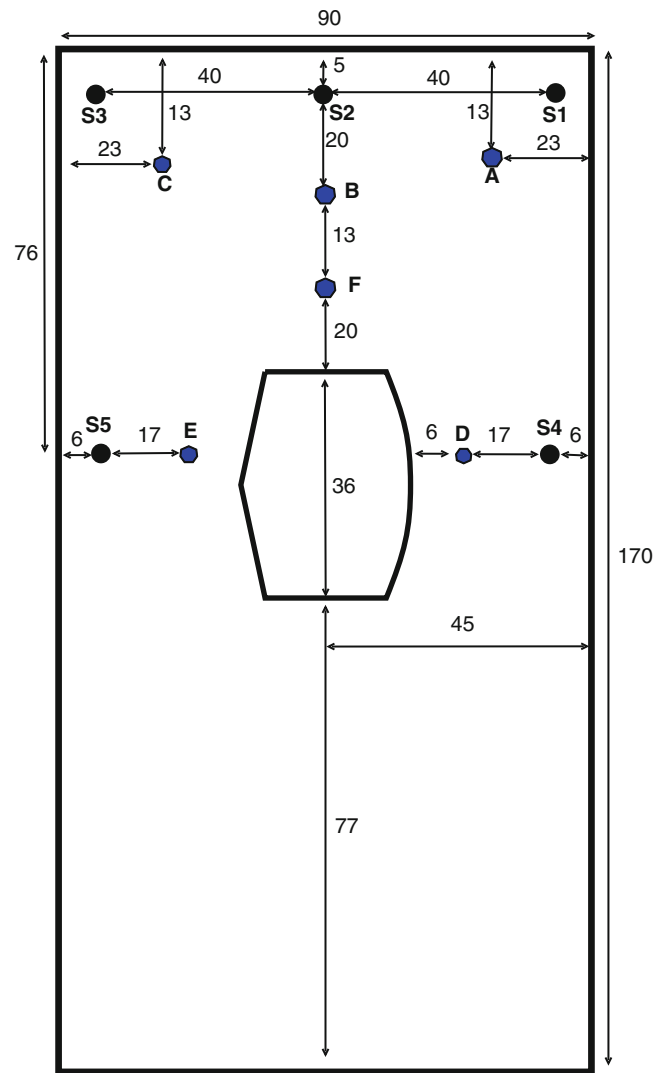
### 28.4 Results

Figure 28.5 shows a picture of the aircraft aluminum plate used in this experiment, which is 170 × 90 × 0.2 cm of size. The PZT wafers were bonded to the plate using “super glue”. The damages were simulated using a magnet with diameter and height around 2 cm and about 31 g weighted.



**Fig. 28.2** Schematic picture of the measurement system

**Fig. 28.3** Schematic of plate containing the PZT and damage positions (dimensions in centimeters)



**Fig. 28.4** Time signal response for sensor S4 at healthy and damaged conditions

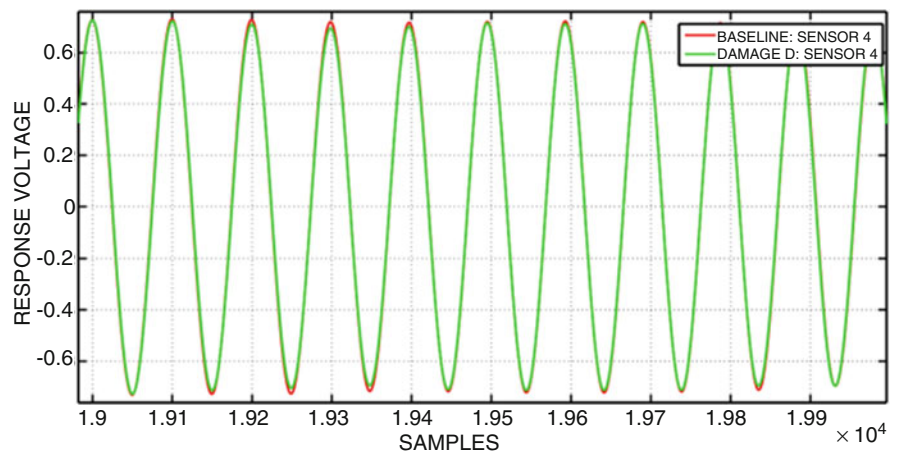
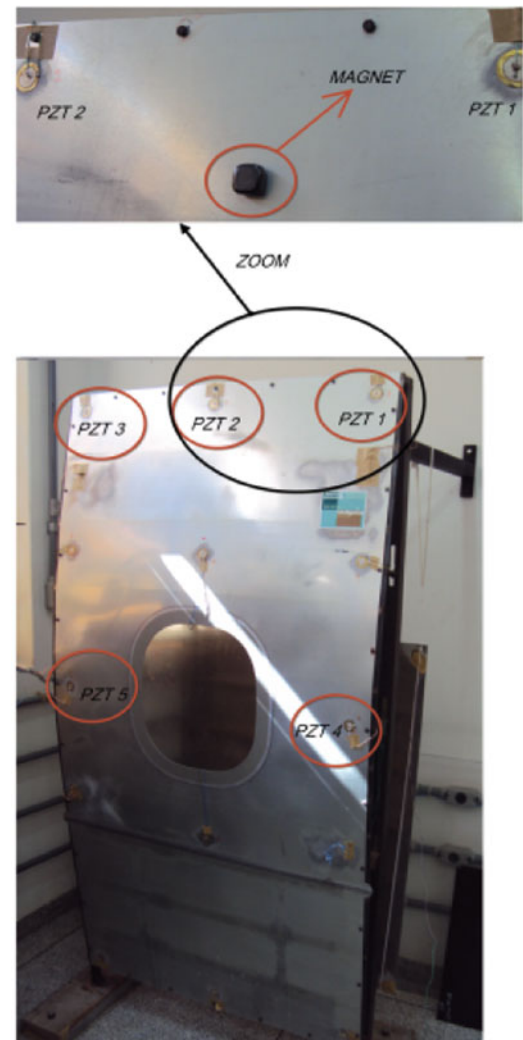


**Fig. 28.5** Aircraft aluminum plate with PZT transducers bonded



The matrices of data organized as show in (Eqs. 28.7–28.9) were used to calculated the PCC according to (Eq. 28.5) for all conditions (healthy and damages A, B, C, D, E and F) and for all sensors. Then, the first three principal components were added to the RMSD indexes, in all conditions, as follows:

$$\text{RMSD} = \sqrt{\frac{(P_a - P_b)^2}{(P_b)^2}} \quad (28.10)$$

In (Eq. 28.10),  $P_a$  and  $P_b$  represent the addition of the first three PC obtained from the analyzed structure and the baseline, respectively. Figure 28.6 shows the results for the set of sensors.

The analysis of results presented in the Fig. 28.6 is extremely difficult because there are great differences among the RMSD indexes. So, to simplify the analysis and compare results, the RMSD indexes will be normalized considering the healthy condition as a reference for each sensor.

### 28.4.1 Comparison Between PCC and EMI

In order to compare the traditional EMI based on the FRF with the proposed method, the FRF was computed according to the system proposed in [17]. So, using the real part of EMI, the RMSD indexes were calculated as follows:

$$\text{RMSD} = \sum_1^n \sqrt{\frac{(E_{n,a} - E_{n,b})^2}{(E_{n,b})^2}} \quad (28.11)$$

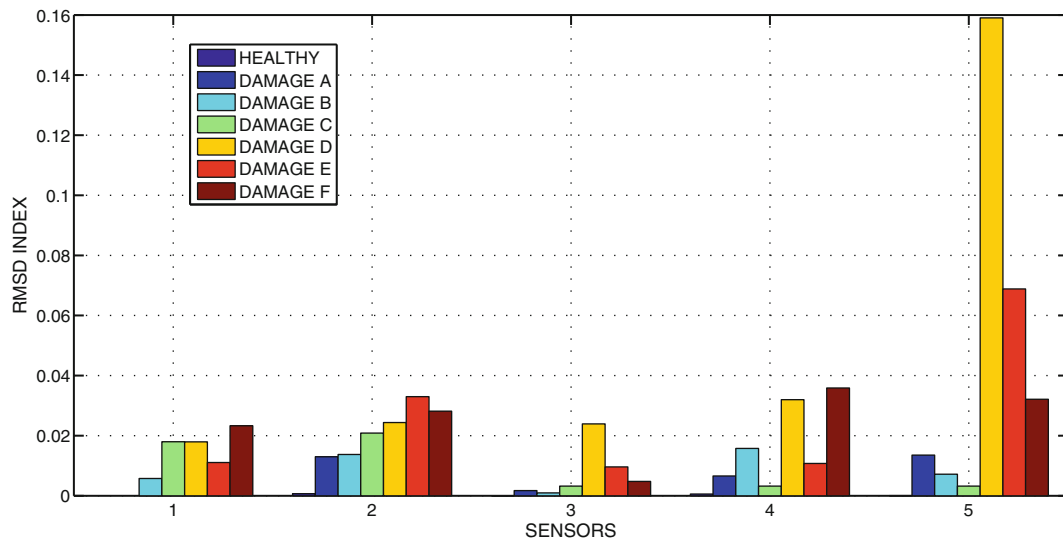


Fig. 28.6 RMSD indexes for PCC

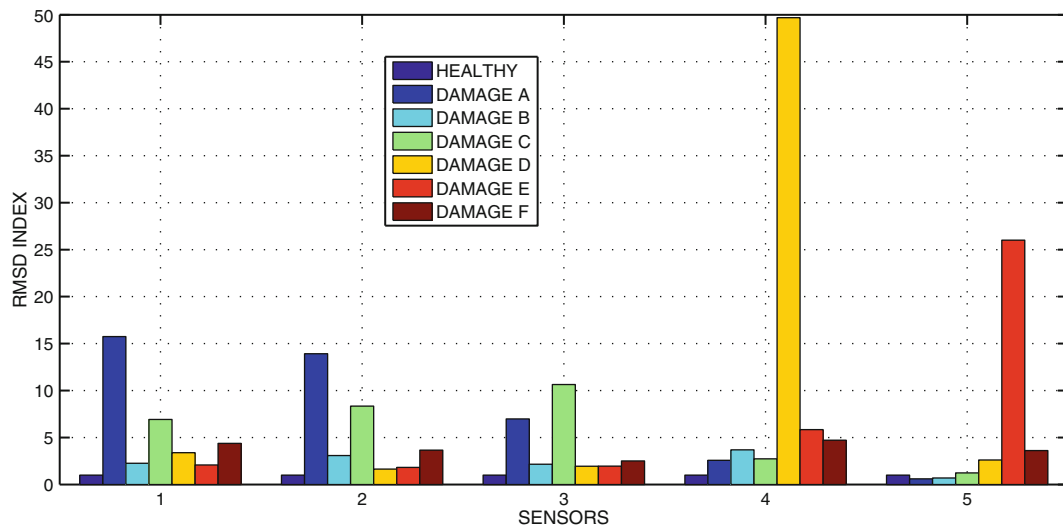


Fig. 28.7 Normalized RMSD indexes for EMI

were  $n = 1 \dots N$ ,  $E_{n,a}$  and  $E_{n,b}$  represent the EMI for the analyzed structure and baseline, respectively. As a way to improve the analysis of the results, the RMSD indexes for both techniques (EMI and PCC) were normalized considering the healthy condition as a reference for each sensor. Then, the normalized RMSD indexes for real part of EMI considering all conditions (healthy and damages A, B, C, D, E and F) and all sensors (S1, S2, S3, S4 and S5) were obtained (Fig. 28.7).

Figures 28.8, 28.9 and 28.10 show a comparison plotting in the same picture the normalized RMSD indexes for both techniques (EMI and PCA) considering all sensors (S1, S2, S3, S4 and S5).

Although both methods have presented excellent results for damage detection, it can be seen that the sensitivity of the proposed method is extremely more significant than the traditional method using FRF/EMI. Of course, this is very important because higher RMSD simplify practical SHM applications.

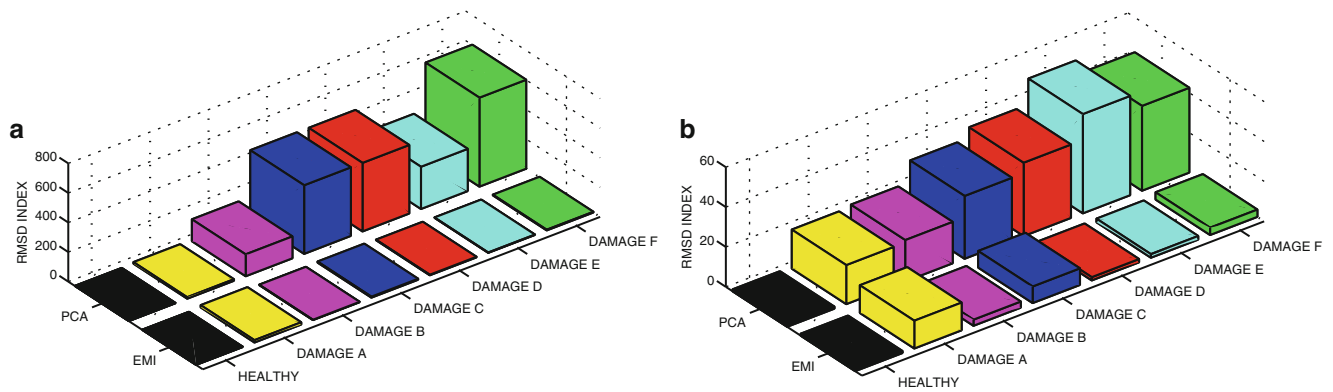


Fig. 28.8 Normalized RMSD results for: (a) sensor S1, (b) sensor S2

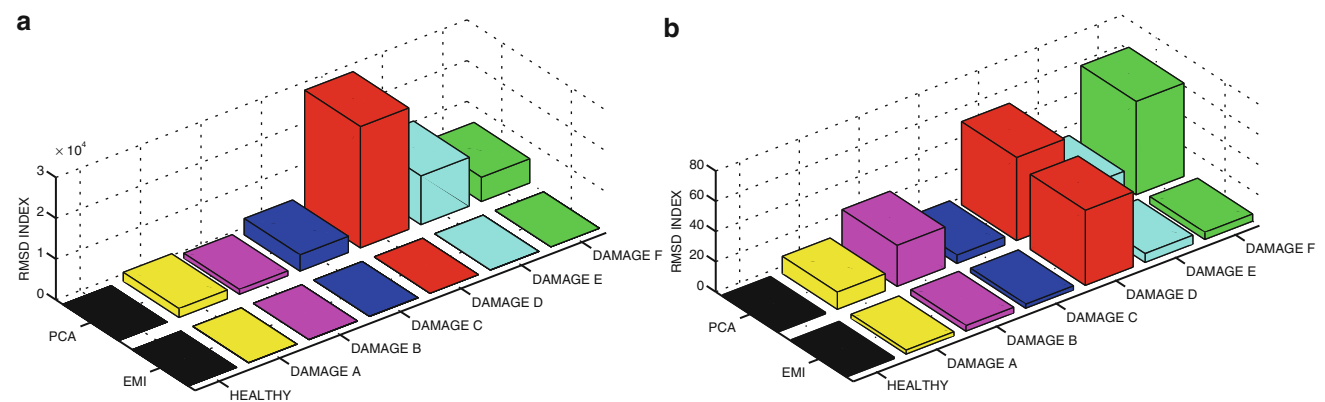
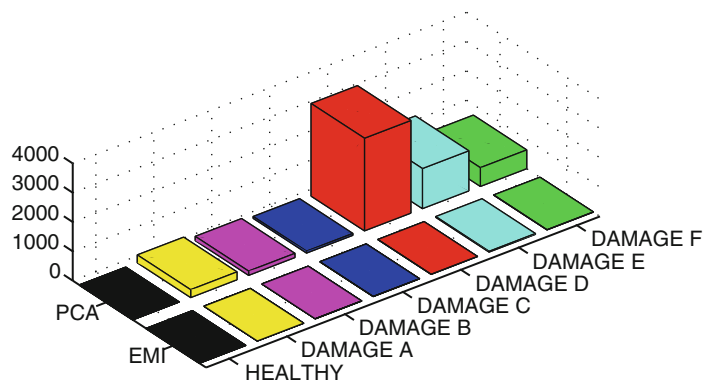


Fig. 28.9 Normalized RMSD results for: (a) sensor S3, (b) sensor S4

Fig. 28.10 Normalized RMSD results for sensor S5



### 28.5 Conclusion

This work presented a novel method for damage detection in structures by exploiting the electromechanical impedance principle. The method is based on time-domain signal analysis and uses Principal Component Coefficients (PCC) to improve the sensitivity of RMSD indexes. Experimental tests were carried out on an aircraft aluminum plate and data were analyzed employing the traditional RMSD indexes. The results show a very sensitive approach for detecting damage when compared with traditional EMI method based on the FRF. Also, this high sensitivity can make the proposed method conveniently in applications for which the traditional EMI present low sensitivity such as composite materials for instance.

**Acknowledgements** The authors would like to thank Capes Foundation, Ministry of Education of Brazil (DINTER 23038.034330/2008-32), FAPESP (grant 2011/20354-6), CNPq and FAPEMIG (through the INCT-EIE).

## References

1. Worden K, Dulieu-Barton JM (2004) Overview of intelligent fault detection in system and structures. *Struct Health Monit* 3:85–98
2. Lopes VL Jr, Park G, Cudney HH, Inman DJ (2000) Impedance-based structural health monitoring with artificial neural networks. *J Intell Mater Syst Struct* 11:206–214
3. Boller C, Staszewski WJ (2004) Health monitoring of aerospace structures: smart sensor technologies and signal processing, an introduction to damage prognosis. In: Staszewski WJ, Boller C, Tomlinson G (eds) *Aircraft structural health and usage monitoring*. John Wiley & Sons, Hoboken, 2:29–73
4. Park G, Sohn H, Farrar C, Inman DJ (2003) Overview of piezoelectric impedance-based health monitoring and path forward. *Shock Vib Dig* 35:451–463
5. Park G, Inman DJ (2007) Structural health monitoring using piezoelectric impedance measurements. *Philos Trans R Soc* 365:373–392
6. Boller C (2001) Ways and options for aircraft structural health management. *Smart Mater Struct* 10:432–439
7. Park S, Lee JJ, Yun CB, Inman DJ (2008) Electro-mechanical impedance-based wireless structural health monitoring using PCA-data compression and k-means clustering algorithms. *J Intell Mater Syst Struct*, Lancaster, 19(4):509–520
8. Yan A-M, Kerschen G, Boe PD, Golinval J-C (2007) Structural damage diagnosis under varying environmental conditions – part I: a linear analysis. *Mech Syst Signal Process* 19:847–864
9. Manson G (2002) Identifying damage sensitive, environment insensitive features for damage detection. In: *Proceedings of the third international conference on identification in engineering systems*, Swansea, 15–17 Apr 2002
10. Mujica LE, Vehi J, Ruiz M, Verleysen M, Staszewski W, Worden K (2008) Multivariate statistics process control for dimensionality reduction in structural assessment. *Mech Syst Signal Process* 22:155–171
11. Silva S, Junior MD, Lopes VL Jr, Brennan MJ (2008) Structural damage detection by fuzzy clustering. *Mech Syst Signal Process* 22(7):1636–1649
12. Jolliffe IT (2002) *Principal component analysis*, 2nd edn. Springer, New York
13. Rencher AC (2002) *Methods of multivariate analysis*, 2nd edn. Wiley, New York
14. Liang C, Sun FP, Rogers CA (1994) Coupled electromechanical analysis of adaptive material systems – determination of the actuator power consumption and system energy transfer. *J Intell Mater Syst Struct* 5:12–20
15. Vieira Filho J, Baptista FG, Inman DJ (2011) Time-domain analysis of piezoelectric impedance-based structural health monitoring using multilevel wavelet decomposition. *Mech Syst Signal Process* 25:1550–1558
16. Vieira Filho J, Baptista FG, Farmer J, Inman DJ (2011) Time-domain electromechanical impedance for structural health monitoring. In: *8th International conference on structural dynamics (Eurodyn 2011)*, Leuven, Belgium
17. Baptista FG, Vieira Filho J (2010) A new impedance measurement system for PZT-based structural health monitoring. *IEEE Trans Instrum Meas* 58:3602–3808



# Chapter 29

## Enhanced Modal Wavelet Analysis for Damage Detection in Beams

Mario Algaba, Mario Solís, and Pedro Galvín

**Abstract** The wavelet transform has proven to be a useful mathematical tool to detect changes in the mode shapes of a structure and therefore to detect damage. The authors have proposed a damage detection methodology based on the wavelet analysis of the difference of mode shapes corresponding to a reference state and a potentially damaged state. The wavelet coefficients of each mode shape difference are added up to obtain an overall graphical result along the structure. The coefficients are weighted according to changes in natural frequencies to emphasize the mode shapes most affected by damage. This paper is focused on the enhancement of the damage sensitivity of the methodology. It presents new results when applying a curve fitting approach to reduce experimental noise effect in mode shapes as well as a interpolation technique to virtually increase the geometric sample frequency of the wavelet transform input signal. The enhanced methodology is applied to experimentally tested steel beams with different crack location and depth. The paper analyses the results when considering different number of measuring points. Successful results are obtained using a small number of sensors and mode shapes.

**Keywords** Wavelet analysis • Modal analysis • Hybrid method • Damage detection • Beams

### 29.1 Introduction

Detection, location and evaluation of damage are a major challenge in structural engineering to enhance performance, efficiency and reliability of structures. Unlike classical non destructive methods, vibration based damage detection methodologies provides global information and can work without a priori knowledge of damage location. These methodologies are based on the analysis of the dynamic response of the structures either to service loads (Operational Modal Analysis, OMA) or applied known forces (Experimental Modal Analysis, EMA). The presence of damage must be inferred from changes in the measured response, and more specifically from the analysis of damage detection parameters based on modal properties.

The wavelet transform is a promising mathematical tool to detect changes in the response of a structure. It is considered that the pioneering application of wavelet transform to SHM was published in 1994 [1]. Since then, wavelet transform applications to damage detection have been widely developed [2–4].

Wavelet transform was originally designed for the analysis of non stationary signals in the time domain. However, it can also be applied to space defined signals. When using a spaced based wavelet analysis, static deflection or mode shapes of the structure can be used. If a modal analysis is performed, then wavelet analysis can be applied to mode shape vectors or difference in mode shapes to detect changes induced by damage [5–10]. Some reviews of different proposals of using wavelet analysis for damage detection can be found in [2, 3].

This paper applies a wavelet based damage detection method proposed by the authors for beam structures, in which modal parameters and wavelet analysis are combined [11]. It is based on the continuous wavelet transform of the difference of mode shapes between an undamaged and a damaged state. Changes in natural frequencies are used to weight the difference in mode shapes. Addition of the wavelet coefficients obtained for all the mode shapes are used as a global damage detection parameter.

---

M. Algaba • M. Solís (✉) • P. Galvín  
Grupo de Estructuras, Escuela Técnica Superior de Ingeniería, Universidad de Sevilla,  
Camino de los Descubrimientos s/n, 41092, Sevilla, Spain  
e-mail: [msolis@us.es](mailto:msolis@us.es); [marioalgaba@gmail.com](mailto:marioalgaba@gmail.com); [pedrogalvin@us.es](mailto:pedrogalvin@us.es)

A quadratic curve fitting approach has been introduced to reduce experimental noise effect on mode shapes. Moreover, a cubic spline interpolation scheme allows the application of the methodology even if a small number of measuring points is available, or if those points are not uniformly spaced along the structure.

The paper reviews firstly some basic concepts about wavelet analysis. After that, the proposed enhanced methodology and the experimental campaign on several beams are presented. Finally, the damage detection methodology is applied to the tested beams and results are discussed.

## 29.2 Continuous Wavelet Transform Background

The Continuous Wavelet Transform (CWT) of a function  $f(x)$  can be defined as:

$$CWT_f(u, s) = \frac{1}{\sqrt{s}} \int_{-\infty}^{+\infty} f(x) \cdot \Psi^* \left( \frac{x-u}{s} \right) \cdot dx \quad (29.1)$$

Where  $\Psi^*$  indicates the complex conjugate of the wavelet function, although wavelet function is not always complex. The wavelet function is translated and dilated or stretched through translation parameters ' $u$ ' and scale parameter ' $s$ ' respectively. Therefore,  $CWT_f(u, s)$  indicates how similar is the original function  $f(x)$  to the wavelet function at a specific location (given by  $u$ ) and for a certain frequency or pseudofrequency (given by scale  $s$ ).

A good candidate to be wavelet function should have zero average and finite length (compact support)

$$\int_{-\infty}^{\infty} \Psi(x) dx = 0 \quad (29.2)$$

and its Fourier transform to the frequency domain ( $\omega$ ) should also fulfil the wavelet admissibility condition.

$$\int_0^{\infty} \frac{|\Psi(\omega)|^2}{\omega} d\omega < \infty \quad (29.3)$$

An important feature of a wavelet function is its number of vanishing moments. If a wavelet function has  $N$  vanishing moments, then:

$$\int_{-\infty}^{\infty} x^k \Psi(x) dx = 0 \quad \text{for } k = 0 \dots N - 1 \quad (29.4)$$

For any polynomial of smaller order than the number of vanishing moments, the wavelet transform will give null values. Therefore, the number of vanishing moments indicates how sensitive is the wavelet to low order signals, and it can be chosen so as to take only into account the components of the signal above certain order value.

The sensitivity of the wavelet transform to changes induced by damage depends on the wavelet family and the number of vanishing moments of the wavelet function. The choice of these parameters should be based on a mathematical analysis of the nature of the signal to be studied as well as the expected effect of damage. However, this mathematical analysis is not always clear a priori and in most applications these parameters are chosen depending on previous results or on trial and error [2].

In this paper, the well-known Daubechies [12] wavelet family with two vanishing moments has been used. For the beams analysed in this paper, a higher number of vanishing moments proved to be less sensitive to damage. That may suggest that the effect of damage induces a change of order two in mode shapes that should not be neglected.

## 29.3 Modal-Wavelet Analysis Applied to Damage Detection

Firstly, an experimental or operational modal analysis of the structure is required to obtain information about mode shapes and natural frequencies. Mode shape vectors will be used as input signals for the wavelet analysis.

Therefore, the well known edge effect in wavelet analysis has to be addressed. This effect is especially important when applied to space based signals, and is somehow similar to the leakage effect on Fourier analysis due to the finite and non stationary nature of the input signal. The wavelet transform is defined for an infinite integration interval, whereas the original signal is defined over a finite interval. When the wavelet transform is performed, there is a singular behavior at the beginning and end of the signal. The signal starts and finishes at those points, so there is a significant local change there, unless the signal trends softly in an asymptomatic way to a constant value, which will never be the case for a mode shape.

This unstable behavior of the wavelet coefficients in the vicinity of the beginning and the end of the analysed signal is known as the edge effect, and it is a serious drawback of the wavelet transform when the damage is close to the beginning or end of the signal. Moreover, the high values of wavelet coefficients near those regions of the signal can mask the structural damage effect on the wavelet transform along the structure.

This paper applies an antisymmetric extension of the signal, of the same length of the original signal, at both ends to avoid edge effects. The wavelet analysis will be performed on the extended signal so the edge effects will appear at the beginning and at the end of the extended signals. The interesting results will only be those related to the original signal that will be free of edge effects.

Another important issue when analysing mode shapes is the reduction of experimental noise effect. The experimental mode shapes will always be affected by noise, so they will always show some kind of irregularities. This undesirable behavior will affect the wavelet analysis and it could eventually mask the effect of damage. In order to reduce this effect, a smoothing technique has been introduced to enhance the damage detection sensibility. Thus, local peaks induced by experimental noise are eliminated without affecting any local trend that could have been induced by damage since damage is not expected to produce only a local peak as it is the case of experimental noise. The softening technique proposed in this paper uses ‘mslowess’ built-in function of MatLab software [13]. It consists of a weighted quadratic least squares approach performed at every location of the original mode shape considering a span including 10 neighbouring points centered at that location.

Wavelet transform requires a high number of measurement points to obtain a meaningful scalogram. This implies that a high number of measuring points uniformly distributed in space is required for modal analysis. When there are not many measuring points available, new “virtual” measuring points should be obtained. For that purpose, a cubic spline interpolation technique [10, 14] has been introduced to enhance the performance of the damage detection methodology.

The wavelet transform requires that the components of the input signal are equally spaced. When the measuring points are not uniformly distributed, the interpolation technique can be used to solve this problem. Besides, it can be useful if measuring points, clearly identified as noisy samples, must be disregarded because they provide undesirable peaks for the mode shapes. Moreover, the interpolation process smoothes the resulting mode shape by itself, so the previously described smoothing technique is not necessary when interpolation is applied.

Once the extended and smoothed mode shapes have been obtained, the wavelet analysis is applied. Firstly, the extended difference mode shapes  $\Phi_{diff,ext}$  is computed from the difference between the smoothed extended  $\Phi_{s,ext,d}$  and undamaged  $\Phi_{s,ext,u}$  mode shapes.

$$\Phi_{diff,ext} = (\Phi_{s,ext,d} - \Phi_{s,ext,u}) \quad (29.5)$$

Then, a CWT of each extended mode shape difference is done to give information about changes in mode shapes. The CWT for the  $i$ th mode shape can be written as:

$$CWT_{\Phi_{diff,ext}}^i(u, s) = \frac{1}{\sqrt{s}} \int_{-\infty}^{+\infty} \Phi_{diff,ext}^i(x) \cdot \Psi^* \left( \frac{x-u}{s} \right) \cdot dx \quad (29.6)$$

At this point, only the CWT coefficients that corresponds to the original signal, and therefore to the real structure, are analysed. The coefficients corresponding to the antisymmetric extension of the signal at both ends are disregarded.

The CWT of each mode shape difference can be used to detect damage. The instabilities in the CWT coefficients, especially for higher scales, could indicate the location of damage. A ridge or increasing values with scale in the CWT coefficients could be interpreted as a structural damage effect [5, 8, 14]. The absolute values of the coefficients can be used to obtain a more precise and clear detection of singularities.

Finally, in order to simplify the analysis of the CWT for each mode shape and to draw an overall result for damage detection, the absolute values of CWT coefficients of each mode shape are added up to obtain a global wavelet parameter for damage detection  $CWT_{sum}$ . This global parameter may also reduce the effect of noise that is present in a specific mode shape, whereas it will always accumulate the effect of damage for all mode shapes.

In addition, the coefficients for each mode shape are weighted according to its corresponding change in natural frequencies. This operation is used to emphasize the most sensitive mode shapes to damage. It is assumed that those modes that exhibit a higher frequency change are more sensitive to damage and therefore changes in those mode shapes are more significant, whereas the mode shapes that do not change their natural frequencies are almost disregarded.

The weighted addition of the coefficients can be written as

$$CWT_{sum}(u, s) = \sum_{i=1}^N CWT_{\phi_{diff}}^i(u, s) \cdot \left(1 - \frac{\omega_u^i}{\omega_d^i}\right)^2 \tag{29.7}$$

where  $\omega_u^i$  and  $\omega_d^i$  stand for the natural frequencies of mode shape  $i$  for the undamaged and the damaged state respectively.

### 29.4 Experimental Testing

Five steel I-beams have been tested to apply the proposed methodology. The beams of length  $L = 1,280$  mm, height  $h = 100$  mm, width  $b = 50$  mm, web thickness  $h_w = 4.5$  mm, flange thickness  $h_f = 6.8$  mm and mass per unit length  $m = 8.1$  kg/m have been damaged by a saw cut in the scenarios described in Table 29.1. The cuts are 1 mm width approximately.

The experimental program involved dynamic characterization of the specimens by modal analysis. An impact force was applied at one end of the beams by an instrumented impact hammer, and the response was measured at 65 points distributed along the beam every  $d = 20$  mm using piezoelectric accelerometers with nominal sensitivity of 100 mV/g and a low frequency limit of 2 Hz. The beams were hung in two soft springs at both ends with  $k_s = 145.8$  N/m stiffness, approaching a free-free boundary condition (Fig. 29.1). Eleven accelerometers were distributed in seven experimental set ups to eventually obtain 65 measuring points. The reference signal for the set ups was the applied impact force. For each set-up, several impacts were performed in order to eventually obtain average values and reduce the experimental noise effect. Impact response was acquired during 30 s per channel per set-up. The data were sampled to 16,384 Hz.

The wavelet based damage detection methodology has been applied using only the first three vertical bending mode shapes of the beams. These mode shapes are in the frequency range between 300 and 1,800 Hz.

Table 29.2 presents the three natural frequencies that have been identified for each damage scenario together with the Modal Assurance Criteria values (MAC) obtained between each damaged mode and the corresponding undamaged one.

**Table 29.1** Damage scenarios

Scenario	0	1	2	3	4
Cutting location	Undamaged	0.5 L	0.5 L	0.25 L	0.25 L
Cup depth		30 mm	20 mm	30 mm	20 mm

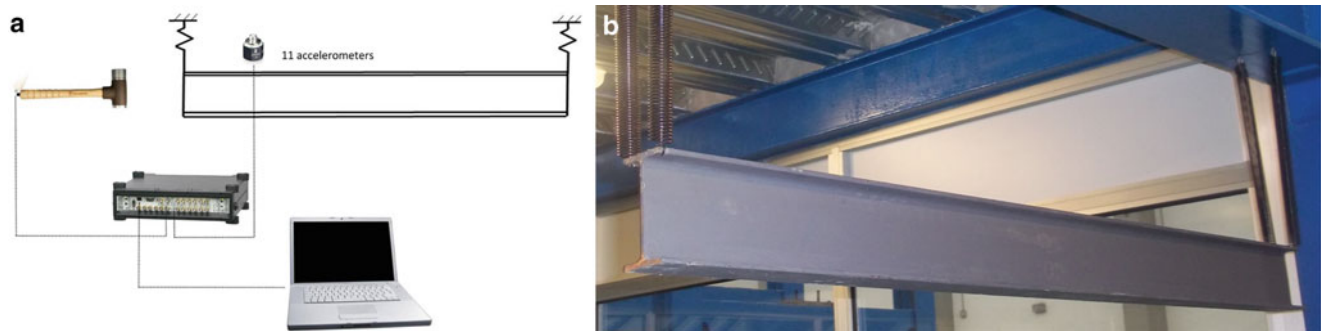


**Fig. 29.1** (a) Experimental configuration and (b) test set-up in the laboratory

**Table 29.2** Experimental natural frequencies for each damage scenario/MAC values for each mode compared to the reference state

Mode\Scenario	0	1	2	3	4
1	415.65	300.96/0.99258	362.28/0.99795	364.75/0.96874	397.27/0.99413
2	1,032.7	1,027.35/0.99874	1,030.15/0.99829	822.99/0.89465	932.71/0.96742
3	1,786.75	1,473.96/0.93651	1,634.17/0.98433	1,557.21/0.84222	1,663.19/0.95711

Natural frequencies and MAC values decrease as the damage is more severe. Nevertheless, MAC values are always close to one, indicating that mode shapes are similar to those obtained for the undamaged state.

### 29.5 Results

The wavelet damage detection methodology is employed to detect and locate damage in the tested beams. The number of required measuring points is also analysed in this section.

In next figures, the absolute values of the addition of CWT coefficients are presented for different scales along the beam. Increasing values of the CWT coefficients at a certain location could be interpreted as damage effect. Noise effect usually produces a more irregular trend with scale.

Figures 29.2 and 29.3 show the cumulative CWT coefficients for scenarios with the crack located at 0.5 and 0.25L respectively, obtained from the response at 65 points. Figures 29.4 and 29.5 show the same results from the response at 13 points.

The proposed methodology clearly identifies crack location for all studied situations from the response in 65 points. Increasing values of the coefficients are clearly observed for higher scales at crack location. The smoothing technique is successfully applied over the mode shapes. No effect of noise is observed in the scalograms, and the effect of damage is dominant and can be clearly identified. It should be noted that this effect is obviously clearer for more severe damage, so Figs. 29.2a and 29.3a show a more clear result than Figs. 29.2b and 29.3b, respectively.

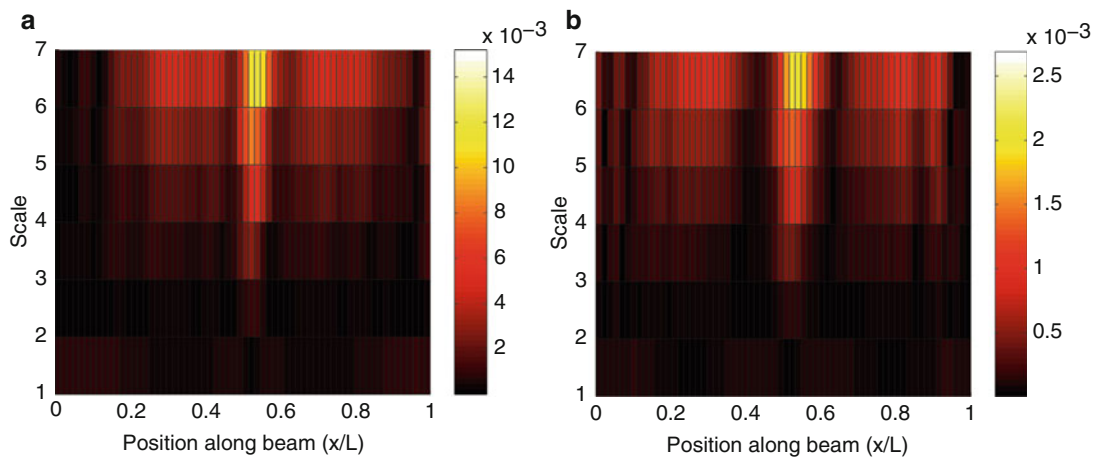


Fig. 29.2 Weighted addition of CWT coefficients of mode shape difference for scenarios 1 (a) and 2 (b) obtained from the response at 65 points

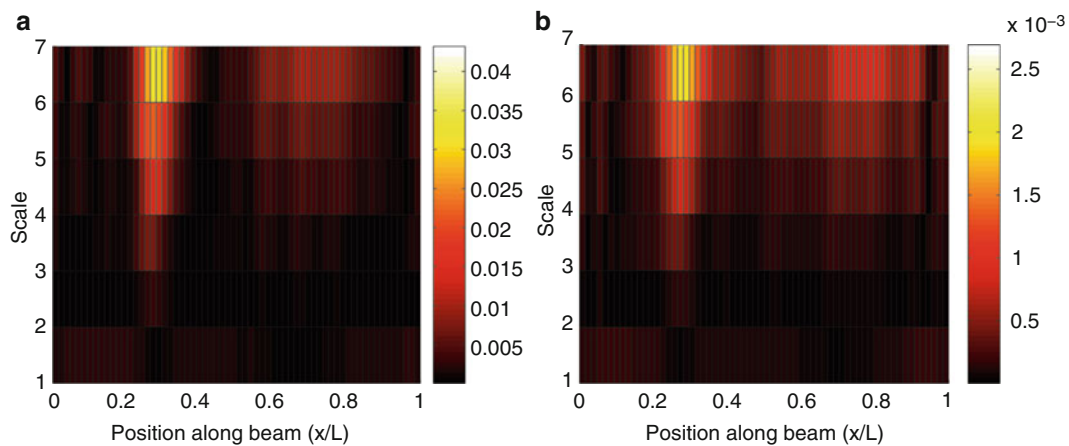
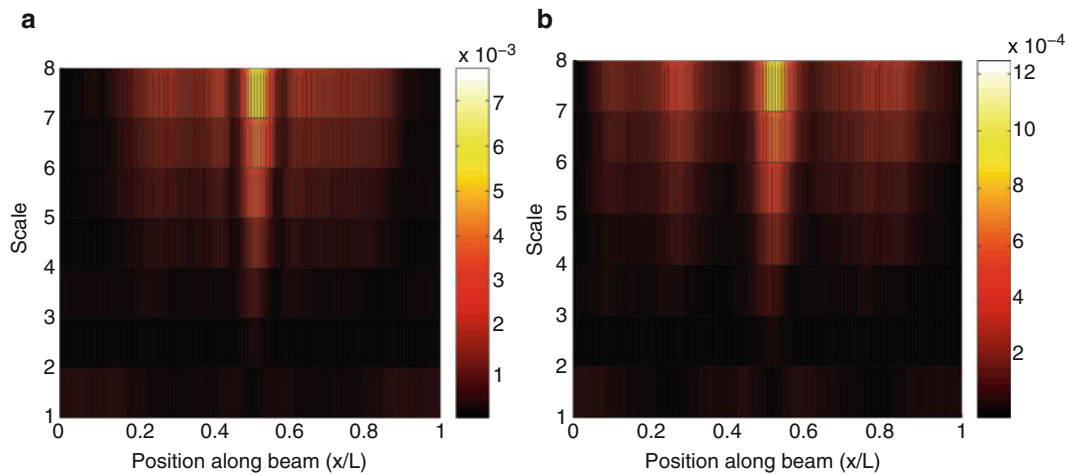
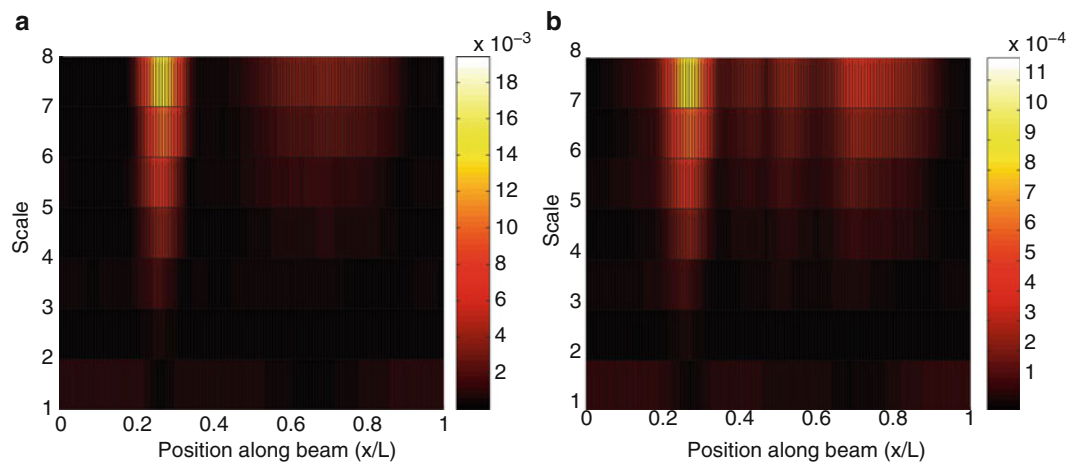


Fig. 29.3 Weighted addition of CWT coefficients of mode shape difference for scenarios 3 (a) and 4 (b) obtained from the response at 65 points



**Fig. 29.4** Weighted addition of CWT coefficients of mode shape difference for scenarios 1 (a) and 2 (b) obtained from the response at 13 points



**Fig. 29.5** Weighted addition of CWT coefficients of mode shape difference for scenarios 3 (a) and 4 (b) obtained from the response at 13 points

If 13 measuring points are taken out of the 65 previously considered, then selected points are not exactly uniformly spaced. Moreover, they are a small amount of measuring points. Therefore, the interpolation technique was applied and an overall number of 128 “virtual” (interpolated) measuring points were obtained. Figures 29.4 and 29.5 show how damage can be identified and located for every scenario considered, as in the previous analysis for 65 points. However, the results are not so clear. It is obvious that less information is available with less number of measuring points, and results are likely to be less sensitive to damage. It can be observed that a maximum value at damage locations for 13 measuring points is lower than those obtained for 65 points. As the numbering of measuring points is reduced, the smoothed mode shapes are less sensitive to damage. In spite of this, the interpolation technique allows a good and realistic approach of mode shapes and the effect of damage still being dominant in the scalograms. This is an important achievement from a practical point of view, since the number of measuring points is four times lower and consequently experimental time and budget is saved.

## 29.6 Conclusions

This paper applies a combined modal-wavelet analysis for crack location in beams proposed by the authors. It is an important issue for damage detection to reduce the effect of experimental noise in mode shapes, so noise effect is not considered as actual damage and false positives are avoided. For that purpose, this paper enhances the damage detection technique by introducing a smoothing technique based on a quadratic weighted regression for a moving span of ten points. Moreover,

a cubic spline interpolation has also been introduced, so new mode shape data points can be obtained when a small number of sensors are used. Thus, enough number of points are available for the input signal of the wavelet transform. This interpolation also serves as a smoothing process when applied.

The enhanced methodology has been applied to steel beams with induced cracks at different locations and severities. It has proven to be sensitive to damage even using a rather small number of sensors and mode shapes.

**Acknowledgements** This work has been supported by the Ministerio de Educación y Ciencia of Spain (project BIA2010-14843). The financial support is gratefully acknowledged.

## References

1. Surace C, Ruotolo R (1994) Crack detection of a beam using the wavelet transform. In: Proceedings of the 12th international modal analysis conference, Honolulu, pp 1141–1147
2. Taha MMR, Noureldin A, Lucero JL, Baca TJ (2006) Wavelet transform for structural health monitoring: a compendium of uses and features. *Struct Health Monit* 5(3):267–295
3. Kim H, Melhem H (2004) Damage detection of structures by wavelet analysis. *Eng Struct* 26(3):347–362
4. Ren WX, Sun Z (2008) Structural damage identification by using wavelet entropy. *Eng Struct* 30(10):2840–2849
5. Rucka M, Wilde K (2006) Application of continuous wavelet transform in vibration based damage detection method for beams and plates. *J Sound Vib* 297(3–5):536–550
6. Zhong S, Oyadiji SO (2007) Crack detection in simply supported beams without baseline modal parameters by stationary wavelet transform. *Mech Syst Signal Process* 21(4):1853–1884
7. Zhong S, Oyadiji SO (2011) Detection of cracks in simply-supported beams by continuous wavelet transform of reconstructed modal data. *Comput Struct* 89(1–2):127–148
8. Douka E, Loutridis S, Trochidis A (2003) Crack identification in beams using wavelet analysis. *Int J Solids Struct* 40(13–14):3557–3569
9. Chang C, Chen L (2005) Detection of the location and size of cracks in the multiple cracked beam by spatial wavelet based approach. *Mech Syst Signal Process* 19(1):139–155
10. Radzienski M, Krawczuk M, Palacz M (2011) Improvement of damage detection methods based on experimental modal parameters. *Mech Syst Signal Process* 25(6):2169–2190
11. Algaba M, Solís M, Galvín P (2012) Wavelet based mode shape analysis for damage detection. In: Proceedings of the SEM IMAC XXX conference, Jacksonville, FL, 30 Jan–2 Feb 2012
12. Daubechies I (1988) Orthonormal bases of compactly supported wavelets. *Comm Pure Appl Math* 41(7):909–996
13. The Mathworks, Matlab (2011)
14. Douka E, Loutridis S, Trochidis A (2003) Crack identification in beams using wavelet analysis. *Int J Solids Struct* 40(13–14):3557–3569

# Chapter 30

## Linear Projection Techniques in Damage Detection Under a Changing Environment

Salma Mozaffari Kojidi, Michael Döhler, Dionisio Bernal, and Yang Liu

**Abstract** The merit of linear projections as a way to improve the resolution in damage detection under changing environmental conditions is examined. It is contended that if the data from the reference condition is balanced, in the sense that the number of feature vectors available for the various temperatures is similar, then projections, such as those in Principal Component Analysis and Factor Analysis, will not improve performance. Projections, however, help to control the false positive rate when the reference data set is not balanced. Analysis and simulation results suggest that previous claims on the merit of projection as a way to improve damage detection resolution under environmental variability may be too optimistic.

**Keywords** Structural health monitoring • Damage detection • Environmental variability • Factor analysis • Principal component analysis

### 30.1 Introduction

A difficulty in the use of SHM in civil engineering structures stems from the fact that any characterization used to describe the reference state is not a point in feature space but a hyper-volume (HV) whose boundaries depend on temperature, humidity, and other environmental variables. Making the reference state characterization conditional on a set of environmental variables reduces the dimension of the HV and this is the most effective way to treat environmental fluctuations, when feasible [1–3]. The possibility of performing detection without measurements of the environment, however, is of interest for cases where the formulation of an environmental model is deemed impractical.

If the environment is not compensated for, one expects that resolution will suffer because the reference state HV is large. A closer look, however, shows that not only the size, but also the shape of the HV enters the problem. Namely, if there are narrow dimensions in the HV, and the damage has a substantial projection in these directions, then reasonable resolution can still be realized. Since existence of narrow dimensions is a necessary condition for good performance, a question is how to check for their existence. A general answer is not trivial, because these dimensions can be curved in hyper-space, but for the simple case of constant directions, in feature space, they exist when there are small singular values in the covariance matrix of the data. Numerous claims have been made in the literature indicating that projection of the data in the subspace of the narrow dimensions followed by novelty detection in this subspace leads to improved performance. In this paper we examine the merit (or lack of) of these projections.

---

S.M. Kojidi (✉) • M. Döhler • D. Bernal  
Department of Civil and Environmental Engineering, Center for Digital Signal Processing, Northeastern University,  
360 Huntington Ave., Boston, MA 02115, USA  
e-mail: [mozaffarikoj.s@husky.neu.edu](mailto:mozaffarikoj.s@husky.neu.edu); [m.doehler@neu.edu](mailto:m.doehler@neu.edu); [bernal@neu.edu](mailto:bernal@neu.edu)

Y. Liu  
School of Transportation Science and Engineering, Harbin Institute of Technology, Harbin 150090, China  
e-mail: [ly7628@hit.edu.cn](mailto:ly7628@hit.edu.cn)



## 30.2 Basic Scheme

The maximum likelihood estimate of the state of nature, given an observation  $x$ , is that for which the probability density of  $x$  is highest. In damage detection it is often the case that only the probability density associated with the healthy state can be estimated and classification is reduced to deciding whether the point belongs to the reference state or not. This one class classification problems are carried out by selecting (in principle) some limit of the probability density below which the point is classified as “novel”. In practice density is seldom computed explicitly and a surrogate is used instead. The Square Mahalanobis Distance (SMD) [4], which is proportional to the probability density when the distribution is multidimensional Gaussian, is perhaps most widely used. The SMD is defined as:

$$d_x^2 = (x - \mu)^T \Sigma_x^{-1} (x - \mu) \quad (30.1)$$

where  $\mu \in \mathbb{R}^n$  and  $\Sigma_x$  are the mean vector and covariance matrix of the reference data, respectively. In this study we compare the performance of novelty detection based on the SMD in two instances: (1) when the distance is computed in the original space of the data and (2) when the distance is computed after the feature is projected to minimize the environmentally related variance. The SMD in the original space is given by Eq. 30.1 and in the projected space by Eq. 30.2

$$d_\varepsilon^2 = (\varepsilon - \bar{\varepsilon})^T \Sigma_\varepsilon^{-1} (\varepsilon - \bar{\varepsilon}) \quad (30.2)$$

where  $\bar{\varepsilon}$  and  $\Sigma_\varepsilon$  are the mean vector and covariance matrix of the projected reference data. We begin by summarizing the PCA and FA techniques.

### 30.2.1 Principal Component Analysis

Let  $X = \{x_1, \dots, x_m\}$ , where  $x_i \in \mathbb{R}^n$ , and  $I = 1, \dots, m$  be a data matrix where each column is a realization of a random process. An estimate of the covariance of the process is, by definition

$$\Sigma_x = \frac{1}{m} \sum_{i=1}^m (x_i - \mu)(x_i - \mu)^T \quad (30.3)$$

where  $\mu$  is the mean vector. Recognizing that the covariance is symmetric, the singular value decomposition (SVD) gives

$$\Sigma_x = ULU^T \quad (30.4)$$

where  $U$  is an orthogonal matrix with vectors  $u_1, \dots, u_n$  as its columns and  $L$  is a diagonal matrix of singular values  $l_1, \dots, l_n$  ( $l_1 > \dots > l_n$ ). It often happens in practice that only a small numbers of singular values are large (relative to the rest) and the associated left side singular vectors are the principal components. In damage detection under environmental variability the projection is not in the principal components but in their complement, namely, the components that are associated with small singular values since these correspond to the smallest variability in the data. Formally, assuming that the last  $(n - q)$  singular values are to be retained one has

$$U = [U_1 \ U_2] \quad L = \begin{bmatrix} L_1 & 0 \\ 0 & L_2 \end{bmatrix} \quad (30.5)$$

where  $L_1 \in \mathbb{R}^{q \times q}$ ,  $L_2 \in \mathbb{R}^{(n-q) \times (n-q)}$ ,  $U_1 \in \mathbb{R}^{n \times q}$ ,  $U_2 \in \mathbb{R}^{n \times (n-q)}$  and the projected feature vector is

$$\varepsilon = U_2^T x \quad (\varepsilon \in \mathbb{R}^{n-q}) \quad (30.6)$$

Use of PCA in damage detection under environmental variability appears in [5].

### 30.2.2 Factor Analysis

In factor analysis it is assumed that the data vector  $x$  is generated by

$$x = \mu + \Lambda\xi + \varepsilon \quad (30.7)$$

where  $\mu \in R^n$  is the mean of the data,  $\xi \in R^q$  are the latent (unobserved) factors where  $q < n$  and  $\varepsilon \in R^n$  is the residual or unique factor. It is evident by inspection that the decomposition in Eq. 30.7 is not unique. Two constraints that restrict the solution space are imposed: namely, one requires that: (1) the covariance of the factors is the identity and (2) the covariance of the residual  $\Psi$  is diagonal. With these constraints the covariance of the model in Eq. 30.7 is

$$\Sigma_x = \Lambda\Lambda^T + \Psi \quad (30.8)$$

The most common approach to obtain  $\Lambda$  and  $\Psi$  from data is to use the Expectation Maximization algorithm [6]. In the literature the relevant equations appear as functions of the data but examination shows that the data itself is not relevant and that the equations reduce to

$$\Lambda = \Sigma_x \beta^T [I - \beta\Lambda + \beta\Sigma_x \beta^T]^{-1} \quad (30.9)$$

$$\Psi = \text{diag}\{(I - \Lambda\beta)\Sigma_x\} \quad (30.10)$$

where the *diag* operator sets all the off-diagonal elements of a matrix to zero, and  $\beta$  is:

$$\beta = \Lambda^T (\Psi + \Lambda\Lambda^T)^{-1} \quad (30.11)$$

Eq.'s 30.9, 30.10 and 30.11 are solved iteratively as follows: (a) select initial values for  $\Lambda$  and  $\Psi$ , (b) compute  $\beta$  from Eq. 30.11, (c) compute new values of  $\Lambda$  and  $\Psi$  from Eqs. 30.9 and 30.10, and repeat from (b) until convergence. The solution is unique for  $\Psi$  and for the product  $\Lambda\Lambda^T$  (which implies that the span of  $\Lambda$  is uniquely determined). In the FA model the term  $\Lambda\xi$  in Eq. 30.7 is assumed to contain most of the changes in the feature due to the environmental changes. The premise in FA is that when the system is damaged, the temperature effects no longer fit in the same span  $\Lambda$  and this would be observable by inspecting the residual. To obtain the residuals, one computes the factors and uses Eq. 30.7. There are two main approaches to compute the factors: one is to use a weighted least squares solution, which is known as Bartlett's factor score

$$\tilde{\xi} = (\Lambda^T \Psi^{-1} \Lambda)^{-1} \Lambda^T \Psi^{-1} x \quad (30.12)$$

and the other, known as the Thomson's score, is

$$\tilde{\xi} = \Lambda^T (\Psi + \Lambda\Lambda^T)^{-1} x \quad (30.13)$$

Given the factors the residuals follow as

$$\varepsilon = \mu + \Lambda\tilde{\xi} - x \quad (30.14)$$

Use of FA for damage detection under environmental variability can be found in [7].

## 30.3 Projection

When projection is used, one trades the feature  $x$  for the residual  $\varepsilon$ . Assume that the residual is linearly related to the feature by an invertible linear transformation,  $P$ , namely

$$\varepsilon = Px \quad (30.15)$$

In this case the SMD on  $\varepsilon$  and  $x$  are identical, namely:

$$d_\varepsilon^2 = (\varepsilon - \bar{\varepsilon})^T \Sigma_\varepsilon^{-1} (\varepsilon - \bar{\varepsilon}) = (x - \mu)^T P^T (P \Sigma_x P^T)^{-1} P (x - \mu) = (x - \mu)^T \Sigma_x^{-1} (x - \mu) = d_x^2 \quad (30.16)$$

and it follows that if the SMD is used to decide on the novelty, a rank preserving transformation of the data vector is superfluous.

### 30.3.1 Novelty Detection Using PCA

In PCA the projected vector is calculated using Eq. 30.6. Since  $U_2$  is a tall matrix, PCA is not a rank preserving transformation. To examine the relation between the SMD in the original and projected spaces we note that

$$\Sigma_\varepsilon = U_2^T \Sigma_x U_2 = L_2 \quad (\Sigma_\varepsilon \in \mathbb{R}^{(n-q) \times (n-q)}) \quad (30.17)$$

so the SMD on  $\varepsilon$  is:

$$\begin{aligned} d_\varepsilon^2 &= (\varepsilon - \bar{\varepsilon})^T \Sigma_\varepsilon^{-1} (\varepsilon - \bar{\varepsilon}) = (U_2^T x - U_2^T \mu)^T L_2^{-1} (U_2^T x - U_2^T \mu) \\ &= [U_2^T (x - \mu)]^T L_2^{-1} U_2^T (x - \mu) = (x - \mu)^T U_2 L_2^{-1} U_2^T (x - \mu) \end{aligned} \quad (30.18)$$

Expressing the covariance in Eq. 30.1 in terms of its SVD, with a partition into significant and small singular values, (subscripts 1 and 2), one gets:

$$\begin{aligned} d_x^2 &= (x - \mu)^T U_1 L_1^{-1} U_1^T (x - \mu) + (x - \mu)^T U_2 L_2^{-1} U_2^T (x - \mu) \\ d_x^2 &= (x - \mu)^T U_1 L_1^{-1} U_1^T (x - \mu) + d_\varepsilon^2 \end{aligned} \quad (30.19)$$

which shows that the SMD of the original data and of the projected data differ by the first term on the *rhs* of Eq. 30.19. Defining  $y_1 = U_1^T (x - \mu)$  and  $y_2 = U_2^T (x - \mu)$ , which are the projections of  $(x - \mu)$  to orthogonal subspaces  $U_1$  and  $U_2$ , Eq. 30.19 becomes:

$$d_x^2 = y_1^T L_1^{-1} y_1 + y_2^T L_2^{-1} y_2 \quad (30.20)$$

where  $y_2^T L_2^{-1} y_2 = d_\varepsilon^2$ . Consider performance under the null hypothesis. If there are an approximately equal number of data vectors for each of the temperature conditions, then the data matrix can be said to be ‘‘balanced’’, indicating that the mean vector  $\mu$  is at the ‘‘center of gravity’’ of the data and the SMD in Eq. 30.20 can be expected to provide a good indicator of how likely any vector  $x$  is. In contrast, if the data for a certain temperature distribution is poorly represented, vectors from this distribution will be ‘‘far from the mean’’, and the SMD will classify them (incorrectly) as novelty. Projection can help the Type I error in these cases but detection of damage with strong projections in the  $U_1$  direction is then difficult.

### 30.3.2 Novelty Detection Using FA

In FA the covariance of the factors is assumed to be the identity and the covariance of residuals is diagonal. To examine self-consistency assume that the factors are computed using Thompson’s score, in this case one finds that

$$\begin{aligned} \varepsilon &= x - \Lambda \tilde{\xi} = x - \Lambda \Lambda^T (\Lambda \Lambda^T + \Psi)^{-1} x = \left( (\Lambda \Lambda^T + \Psi) (\Lambda \Lambda^T + \Psi)^{-1} - \Lambda \Lambda^T (\Lambda \Lambda^T + \Psi)^{-1} \right) x \\ &= (\Lambda \Lambda^T + \Psi - \Lambda \Lambda^T) (\Lambda \Lambda^T + \Psi)^{-1} x = \Psi \Sigma_x^{-1} x \end{aligned} \quad (30.21)$$

therefore:

$$cov(\varepsilon) = \Psi \Sigma_x^{-1} \Psi \quad (30.22)$$

so  $cov(\varepsilon) \neq \Psi$ . Taking  $P_{Th} = \Psi \Sigma_x^{-1}$ , it follows that  $\varepsilon = P_{Th} x$  and since  $P_{Th}$  is full rank the SMD on  $\varepsilon$  and  $x$  are identical, making the computation of  $\varepsilon$  superfluous for damage detection purposes.

Using Bartlett’s estimation for the factors, the residual is found to be:

$$\begin{aligned} \varepsilon &= x - \Lambda \xi = x - \Lambda (\Lambda^T \Psi^{-1} \Lambda)^{-1} \Lambda^T \Psi^{-1} x \\ &= \left( I - \Lambda (\Lambda^T \Psi^{-1} \Lambda)^{-1} \Lambda^T \Psi^{-1} \right) x \end{aligned} \quad (30.23)$$

The question then is whether the term in the parenthesis in Eq. 30.23 is full rank, to make a determination we factor

$$\Psi^{-1/2} \Lambda = QR \quad (30.24)$$

where  $Q \in \mathbb{R}^{n \times q}$  has orthonormal columns ( $Q^T Q = I$ ) and  $R \in \mathbb{R}^{q \times q}$  is an invertible matrix. Then the residual becomes:

$$\begin{aligned}\varepsilon &= \left( I - \Psi^{\frac{1}{2}} Q R (R^T Q^T Q R)^{-1} R^T Q^T \Psi^{-\frac{1}{2}} \right) x \\ &= \left( \Psi^{\frac{1}{2}} \Psi^{-\frac{1}{2}} - \Psi^{\frac{1}{2}} Q Q^T \Psi^{-\frac{1}{2}} \right) x \\ &= \Psi^{\frac{1}{2}} (I - Q Q^T) \Psi^{-\frac{1}{2}} x\end{aligned}\quad (30.25)$$

Define  $P_B = \Psi^{\frac{1}{2}} (I - Q Q^T) \Psi^{-\frac{1}{2}}$ , then  $\varepsilon = P_B x$ . In this case, the rank of  $P_B$  is  $(n - q)$ , which is not full rank and one gathers that the SMD of the projection is not the same as that of the original data. We note that the covariance of  $\varepsilon$  becomes

$$\text{cov}(\varepsilon) = P_B \Sigma_x P_B^T \quad (30.26)$$

which, again, is not equal to  $\Psi$ . To have an invertible full rank covariance matrix the residual must be projected into a lower dimensional space. To do so let  $Q_2 \in \mathbb{R}^{n \times (n-q)}$  be orthonormal to  $Q$  in Eq. 30.24, such that  $[Q \ Q_2]$  is an orthogonal matrix of size  $n \times n$ . Then,  $(I - Q Q^T) = Q_2 Q_2^T$ . Defining a new environment-independent vector by normalizing  $\varepsilon$  by  $\Psi^{-1/2}$ , projecting it into the subspace defined by  $Q_2$ , and using Eq. 30.25:

$$\begin{aligned}\tilde{\varepsilon} &= Q_2^T \Psi^{-\frac{1}{2}} \varepsilon = Q_2^T \Psi^{-\frac{1}{2}} \left[ \Psi^{\frac{1}{2}} (I - Q Q^T) \Psi^{-\frac{1}{2}} x \right] \\ &= Q_2^T (Q_2 Q_2^T) \Psi^{-\frac{1}{2}} x = Q_2^T \Psi^{-\frac{1}{2}} x\end{aligned}\quad (30.27)$$

where  $\tilde{\varepsilon} \in \mathbb{R}^{n-q}$ , and its covariance in the reference condition is

$$\Sigma_{\tilde{\varepsilon}} = Q_2^T \Psi^{-\frac{1}{2}} \Sigma_x \Psi^{-\frac{1}{2}} Q_2 \quad \Sigma_{\tilde{\varepsilon}} \in \mathbb{R}^{(n-q) \times (n-q)} \quad (30.28)$$

where the term  $\Psi^{-\frac{1}{2}} \Sigma_x \Psi^{-\frac{1}{2}}$  can be simplified using Eqs. 30.24 and 30.8:

$$\begin{aligned}\Psi^{-\frac{1}{2}} \Sigma_x \Psi^{-\frac{1}{2}} &= \Psi^{-\frac{1}{2}} (\Lambda \Lambda^T + \Psi) \Psi^{-\frac{1}{2}} \\ &= \Psi^{-\frac{1}{2}} \Lambda \Lambda^T \Psi^{-\frac{1}{2}} + I = Q R R^T Q^T + I\end{aligned}\quad (30.29)$$

Substituting Eqs. 30.29 in 30.28 and recalling that  $Q_2^T Q = 0$  (or  $Q^T Q_2 = 0$ ), yields:

$$\Sigma_{\tilde{\varepsilon}} = Q_2^T (Q R R^T Q^T + I) Q_2 = 0 + Q_2^T I Q_2 = I \quad (30.30)$$

This covariance is full rank in the space of  $\tilde{\varepsilon}$ . Thus, the SMD on  $\tilde{\varepsilon}$  to the reference data set after projection is defined as

$$d_{\tilde{\varepsilon}}^2 = (\tilde{\varepsilon} - \tilde{\bar{\varepsilon}})^T (\tilde{\varepsilon} - \tilde{\bar{\varepsilon}}) \quad (30.31)$$

where  $\tilde{\bar{\varepsilon}} = Q_2^T \Psi^{-1/2} \mu$ . To inspect how the Mahalanobis of this projection compares to that in the original space we note that

$$\begin{aligned}d_x^2 &= (x - \mu)^T \Sigma_x^{-1} (x - \mu) \\ &= (x - \mu)^T \Psi^{-\frac{1}{2}} \left( \Psi^{-\frac{1}{2}} \Sigma_x \Psi^{-\frac{1}{2}} \right)^{-1} \Psi^{-\frac{1}{2}} (x - \mu) \\ &= (x - \mu)^T \Psi^{-\frac{1}{2}} (Q R R^T Q^T + I)^{-1} \Psi^{-\frac{1}{2}} (x - \mu) \\ &= (x - \mu)^T \Psi^{-\frac{1}{2}} \left( [Q \ Q_2] \begin{bmatrix} R R^T + I & 0 \\ 0 & I \end{bmatrix} \begin{bmatrix} Q^T \\ Q_2^T \end{bmatrix} \right)^{-1} \Psi^{-\frac{1}{2}} (x - \mu) \\ &= (x - \mu)^T \Psi^{-\frac{1}{2}} Q (R R^T + I)^{-1} Q^T \Psi^{-\frac{1}{2}} (x - \mu) + (x - \mu)^T \Psi^{-\frac{1}{2}} Q_2 Q_2^T \Psi^{-\frac{1}{2}} (x - \mu) \\ &= (x - \mu)^T \Psi^{-\frac{1}{2}} Q (R R^T + I)^{-1} Q^T \Psi^{-\frac{1}{2}} (x - \mu) + (\tilde{\varepsilon} - \tilde{\bar{\varepsilon}})^T (\tilde{\varepsilon} - \tilde{\bar{\varepsilon}}) \\ &= (x - \mu)^T \Psi^{-\frac{1}{2}} Q (R R^T + I)^{-1} Q^T \Psi^{-\frac{1}{2}} (x - \mu) + d_{\tilde{\varepsilon}}^2\end{aligned}\quad (30.32)$$

which shows that the SMD of the original data and of the projected data differ by the first term on the *rhs* of Eq. 30.32. All one can say by looking at Eq. 30.32 is that the first term in Eq. 30.32 is negligible compared to the second when  $(RR^T + I) \gg I$ , since then  $(RR^T + I)^{-1} \ll I$  and this appears to be usually the case.

### 30.3.3 Summary

The basic observations from the analytical examination are:

1. If the data matrix is balanced, no advantage is expected from projection (in either PCA or FA).
2. If the data matrix is unbalanced, projection can improve the Type I error rate, but this may lead to some degradation in the Type II error performance (both in PCA or FA).
3. When using FA, the factors need to be computed with Bartlett’s score, otherwise the projection is rank preserving and thus superfluous for a Mahalanobis distance computation.

## 30.4 Simulation Example

This example is set up to validate the analytical observations. Consider a mass-spring system with eight equal masses and initial stiffness  $k_0$  as shown in Fig. 30.1.

The spring stiffness is assumed to be a function of temperature as:

$$k = k_0 \left( 1 + \frac{0.005}{20^3} T^3 \right) \tag{30.33}$$

where  $T$  is the temperature in Celsius and  $k_0$  is the stiffness at  $T = 0^\circ\text{C}$ . The temperature is assumed to have a yearly seasonal fluctuation that is harmonic plus a random component as shown in Fig. 30.2. The temperature in each spring is taken as the value from the ambient temperature plus an additional increment taken from a Gaussian distribution with zero mean and  $0.5^\circ\text{C}$  standard deviation. The feature vector consists of the first three frequencies, which, in the simulations are contaminated with white noise with a standard deviation of 0.2 % of the mean of the frequency. Damage is simulated as a 10 % reduction in each one of the springs (one at a time).

The first year is used to formulate the reference model (the threshold is set for the 5 % type I error), a second year is used for validation and in the third year damage is introduced. We consider two reference state models, namely, one where the data matrix is balanced, obtained by sampling three times a day, and a second that is not balanced, obtained by sampling three times a day when the ambient temperature is below zero and once a day when it’s above. In both cases the second year

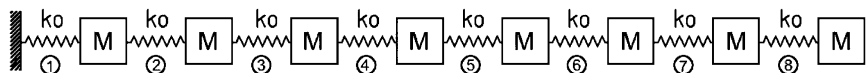


Fig. 30.1 Mass-spring system

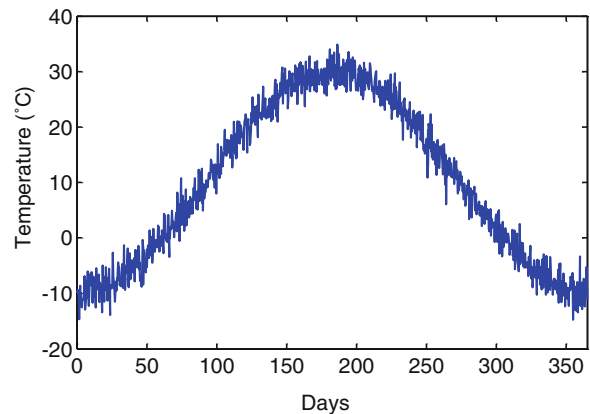


Fig. 30.2 Yearly temperature variation

**Table 30.1** Type I error and power of the test – balanced reference data

	Type I error (%)	Power of the test (%) (10% damage on springs #1–8 one at a time)							
		#1	#2	#3	#4	#5	#6	#7	#8
No projection	4	84	98	94	98	53	97	98	78
Projection (PCA, $p = 1$ )	5	41	99	91	15	8	12	87	48
Projection (PCA, $p = 2$ )	6	45	99	93	92	40	98	80	57

**Table 30.2** Type I error and power of the test – unbalanced reference data

	Type I error (%)	Power of the test (%) (10% damage on springs #1–8 one at a time)							
		#1	#2	#3	#4	#5	#6	#7	#8
No Projection	14	–	–	–	–	–	–	–	–
Projection (PCA, $p = 1$ )	8	74	98	93	40	16	11	65	38
Projection (PCA, $p = 2$ )	6	79	99	96	90	51	98	61	46

is used for validation and in the third damage is considered. Sampling in the second and the third year is three times per day. Results are presented in Table 30.1 for a balanced reference and in Table 30.2 for the unbalanced case. The Type I error is the number of false positives on the second year validation data, the Power of the Test (POT) is the percent of the times that damage is identified in the third year, when it is present, and  $p$  is the dimension of the projection space.

As anticipated, the Type I error is essentially the same whether one projects the data or not in the balanced data case and performance in the damaged state is superior when operating with the original data. The large improvement in the Type II error (in some cases) when  $p$  goes from 1 to 2 is due to the fact that in this case the feature vector is only of dimension 3. Results for the case where the data is not balanced show that the Type I error without projection is unacceptable. In this case we do not report the POT since it would be misleading. Results for FA are not presented but proved analogous to the ones shown for the PCA projections.

### 30.5 Concluding Remarks

The analysis presented suggests that projections do not improve performance if the data for the reference condition is balanced. The analyses and results do not support the claims that have been made in the literature about the gains in resolution attained by projection when the features vary with environmental conditions. The essential point is that feasibility depends on whether there are narrow dimensions, not on whether one projects the data. Indeed, it is contended that if the reference data is balanced, so the mean and the covariance are representative, then projection leads to a deterioration of the detector performance.

With regards to damage detection in real structures subjected to environmental changes it is essential to recognize that the problem becomes increasingly difficult as the size of the structure increases. This is so because the environmental effects act on the complete structure while damage is local. As the size increases, therefore, the importance of changes due to damage compared to changes due to environmental fluctuations decreases.

**Acknowledgements** This research was supported by NSF grant 1000391 under the Hazard Mitigation and Structural Engineering Program. This support is gratefully acknowledged.

### References

1. Worden K, Sohn H, Farrar CR (2002) Novelty detection in a changing environment: regression and interpolation approaches. *J Sound Vib* 258(4):741–761
2. Peeters B, De Roeck G (2000) One year monitoring of the Z24 bridge: environmental influences versus damage effects. In: Proceedings of the IMAC-XVIII, San Antonio, TX, pp 1570–1576
3. Sohn H, Farrar CR, Hunter NF, Worden K (2001) Structural health monitoring using statistical pattern recognition techniques. *J Dyn Syst Meas Control* 123:706
4. Hotelling H (1947) *Multivariate Quality Control Illustrated by Air Testing of Sample Bombsights*, Selected Techniques of Statistical Analysis, C Eisenhart, et al., Editors, McGraw-Hill, New York.

5. Yan A-M, Kerschen G, De Boe P, Golinval J-C (2005) Structural damage diagnosis under varying environmental conditions – Part I: a linear analysis. *Mech Syst Signal Process* 19:847–864
6. Rubin D, Thayer D (1982) EM algorithms for ML factor analysis. *Psychometrika* 47(1):69–76
7. Kullaa J (2003) Is temperature measurement essential in structural health monitoring. In: *Proceedings of the 4th international workshop on structural health monitoring*, Stanford, CA, pp 717–724

# Chapter 31

## Modal Reduction Based on Accurate Input-Output Relation Preservation

M. Khorsand Vakilzadeh, S. Rahrovani, and T. Abrahamsson

**Abstract** An eigenmode based model reduction technique is proposed to obtain low-order models which contain the dominant eigenvalue subspace of the full system. A frequency-limited interval dominance is introduced to this technique to measure the output deviation caused by deflation of eigenvalues from the original system in the frequency range of interest. Thus, the dominant eigensolutions with effective contribution can be identified and retained in the reduced-order model. This metric is an explicit formula in terms of the corresponding eigensolution. Hence, the reduction can be made at a low computational cost. In addition, the retained low-order model does not contain any uncontrollable and unobservable eigensolutions. The performance of the created reduced-order models, in regard to the approximation error, is examined by applying three different input signals; unit-impulse, unit-step and linear chirp.

**Keywords** Modal analysis • Frequency-limited dominance metric • Unit-impulse response • Model reduction • Linear system dynamics

### 31.1 Introduction

Many model order reduction techniques were developed during the last decades in order to balance the accuracy and simplicity of the systems; see [1–3] for overviews. Eigenvalue based model reduction techniques, such as dynamic condensation, component mode synthesis and modal truncation, continue to receive attention due to their low computational cost and applicability for very large systems [4, 5]. These approaches produce reduced-order models from the knowledge of the system's dominant eigenvalues. This feature is of interest in applications like vibration analysis. To obtain accurate reduced-order models, it is necessary to determine the dominant eigenvalue subset which keeps the most important features of the system.

In the simplest form, the nearest eigenvalues to the imaginary axis are considered as the dominant eigenvalue subset [6]. The shortcoming of this approach is that the retained modes can be selected from the uncontrollable or unobservable eigenvalue subspace of the original system. Thus, the created reduced-order model is not minimal. In [4], the original system is divided to several sub-systems which are in the balanced form. In each sub-system, eigenvalues with largest Hankel singular values, which is the squared root of the eigenvalues of the product of the observability and controllability gramians, are considered as the dominant ones. Acknowledging the importance of the degrees of controllability and observability of an eigenvalue, Rommes [7, 8] utilized a dominance metric which is the corresponding residue over the real part of the eigenvalue.

One of the key features of the system is its input-output behavior. Many studies developed metrics to conserve this feature of the original system. Skelton proposed *component cost analysis* method for first order continuous-time systems [9, 10]. This method assigns a cost function to the components of the system which can be interpreted as the mean-squared output norm while input is a zero mean white noise with unit intensity. This method is not applicable to very large systems since the solution of a Lyapunov equation is required for the computation of the components cost. Later, Lastman et al. [11] introduced a metric which measures the impulse response energy of the system. They claimed that their approach is very

---

M.K. Vakilzadeh (✉) • S. Rahrovani • T. Abrahamsson  
Department of Applied Mechanics, Chalmers University of Technology, SE-412 96, Gothenburg, Sweden  
e-mail: [sadeghr@chalmers.se](mailto:sadeghr@chalmers.se); [khorsand@chalmers.se](mailto:khorsand@chalmers.se); [thomas.abrahamsson@chalmers.se](mailto:thomas.abrahamsson@chalmers.se)



similar to the component cost analysis of Skelton. However, the computation of the participation matrix involved in their formulation is very complex and time-consuming. Another drawback of their approach is that the assigned metric to each of the eigensolutions of a complex conjugate pair is different. A metric based on the unit-step response was proposed by Aguirre [12]. This metric is a simple formulation for both transfer function and state-space representation of the system.

This study introduces a frequency-limited interval modal dominance index for continuous-time systems with both under-damped and over-damped eigenvalues in order to quantitatively measure the contribution of each eigensolution to the squared norm of the system output deviation resulted from the deflation of each eigensolution. Thus, the non-dominant eigensolutions with less output contribution can be identified and eliminated to obtain the appropriate reduced order model. The main advantage of this index is that it is on explicit form in terms of the corresponding eigensolution and the frequency bound of interest. In addition, the retained low-order model does not contain any uncontrollable and unobservable eigensolutions. Investigation of a numerical example illustrates the performance of the proposed dominance metric.

## 31.2 Method

### 31.2.1 Modal Truncation

The first step is to describe the modal truncation strategy which is used to retain the dominant candidate part of the system. Consider a linear, time invariant and stable continuous-time system with the following state-space representation:

$$\begin{aligned}\dot{x}(t) &= Ax(t) + Bu(t) \\ y(t) &= Cx(t) + Du(t)\end{aligned}\quad (31.1)$$

where  $x(t) \in \mathbb{R}^{n_x}$  is the state vector,  $u(t) \in \mathbb{R}^{n_u}$  is the input vector and  $y(t) \in \mathbb{R}^{n_y}$  is the system output. The state-space representation of the full system can be transformed to the diagonal form, as shown below

$$\begin{aligned}\dot{z}(t) &= \Lambda z(t) + \hat{B}u(t) \\ y(t) &= \hat{C}z(t) + Du(t)\end{aligned}\quad (31.2)$$

with the solutions of the eigenvalue problem  $A\Phi = \Phi\Lambda$  one obtains

$$\begin{aligned}x(t) &= \Phi z(t), \\ \Lambda &= \text{diag}(\lambda_1, \lambda_2, \dots, \lambda_{n_x}) = \Phi^{-1}A\Phi, \\ \hat{B} &= \Phi^{-1}B = [\hat{b}_1 \ \hat{b}_2 \ \dots \ \hat{b}_{n_x}]^T, \\ \hat{C} &= C\Phi = [\hat{c}_1 \ \hat{c}_2 \ \dots \ \hat{c}_{n_x}].\end{aligned}$$

where  $z(t) \in \mathbb{R}^{n_x}$  is the modal coordinate vector, and  $\Phi$  and  $\Lambda$  are the right eigenvector and the eigenvalue matrices, respectively.  $\lambda_i, \phi_i$  are, respectively, the eigenvalue and eigenvector corresponding to the  $i$ th mode of the full system. Now, let the partitioning of the diagonalized state-space representation, Eq. (31.2), be established as

$$\begin{aligned}\begin{bmatrix} \dot{z}_1 \\ \dot{z}_2 \end{bmatrix} &= \begin{bmatrix} \Lambda_1 & 0 \\ 0 & \Lambda_2 \end{bmatrix} \begin{bmatrix} z_1 \\ z_2 \end{bmatrix} + \begin{bmatrix} \hat{B}_1 \\ \hat{B}_2 \end{bmatrix} u \\ y &= [\hat{C}_1 \ \hat{C}_2] \begin{bmatrix} z_1 \\ z_2 \end{bmatrix} + Du\end{aligned}\quad (31.3)$$

where  $z_1$  contains the  $n_r$  modal coordinates to be retained in the low-order system and  $\Lambda_1$  is a diagonal matrix which involves the  $n_r$  dominant eigenvalues of the full system. Thus, the truncated system can be written as  $\Sigma_r = (\Lambda_1, \hat{B}_1, \hat{C}_1, D)$ .

The low-order model obtained by modal truncation has some guaranteed properties. First, the  $H_\infty$ -norm of the difference between the full model and the low-order model has an *a priori* upper bound. In diagonalized form, the difference between the transfer functions of the full model,  $G$ , and the reduced-order model,  $G_r$ , can be written as [3, 13]

$$G(s) - G_r(s) = \sum_{i=n_r+1}^{n_x} \frac{\hat{c}_i \hat{b}_i}{s - \lambda_i}\quad (31.4)$$

Thus, the  $H_\infty$ -norm of the error system is upper bounded by the following expression:

$$\|G(s) - G_r(s)\|_\infty = \sup_{s \in i\mathbb{R}} [\bar{\sigma}(G(s) - G_r(s))] \leq \sum_{i=n_r+1}^{n_x} \frac{\bar{\sigma}(\hat{c}_i \hat{b}_i)}{|\operatorname{Re}(\lambda_i)|} \quad (31.5)$$

where  $\bar{\sigma}(\cdot)$  is the largest singular value of a matrix and  $\operatorname{Re}(\cdot)$  is the real part of a complex variable. Secondly, the eigenvalues of the low-order model is a subset of the eigenvalues of the original model and therefore they keep their physical interpretations [3]. Consequently, modal truncation preserves the stability property of the full system.

In the next section, a similarity matrix is defined to transform the eigenvectors, corresponding to equal or nearly close eigenvalues, to the range and null space of the loading in order to decrease the size of the controllable and observable eigenvalue subspace.

### 31.2.2 Multiple Eigenvalues

Modes with eigenfrequencies within the frequency spectrum of the loading contribute substantially to the system response. However, the spatial distribution of the load is also of importance inasmuch as a particular spatial distribution of loading cannot excite eigenmodes which are orthogonal to the load. This well-known fact is utilized in this study to treat the special case that the degree of multiplicity of an eigenvalue is higher than the dimension of the range space of the loading, i.e., for eigenvalues with multiplicity larger than the columns rank of  $\hat{B}$  in Eq. (31.2).

Let the partition of Eq. (31.2) associated to the multiple eigenvalue  $\lambda_j$ ,  $j = 1, 2, \dots, n_m$  where  $n_m$  is larger than  $n_u$ , be arranged as follows

$$\dot{z}_j = \Psi_{j:} A \Phi_{:j} z_j + \hat{B}_{j:} u \quad (31.6)$$

Here  $\Psi$  is the left eigenvector matrix,  $(j:)$  denotes the  $j$ th block row of the matrix and  $(:j)$  is the  $j$ th block column of a matrix. The matrix  $\hat{B}_{j:}$ , which is a rectangular matrix of dimension  $n_m \times n_u$ , can be decomposed into a unitary matrix  $Q$  and upper triangular matrix  $R$ . It follows that, at least, the  $n_m - n_u$  last rows of the  $R$  are zero. Thus, the QR decomposition of the  $\hat{B}_{j:}$  can be written as

$$\hat{B}_{j:} = Q \begin{bmatrix} R_1 \\ 0 \end{bmatrix} \quad (31.7)$$

Introduce the transformation  $z_j = Q z'_j$  to Eq. (31.6), which leads to

$$\dot{z}'_k = (Q^T \Psi_{j:}) A (\Phi_{:j} Q) z'_k + Q^T Q \begin{bmatrix} R_1 \\ 0 \end{bmatrix} u \quad (31.8)$$

Therefore, the last  $n_m - n_u$  modes of the set would not be excited by the load. The corresponding eigenvectors can be replaced by  $\Phi_{:j} Q$ . It follows from the orthogonality property of  $Q$ , i.e.  $Q^T Q = I$ , that the state-space equations are still diagonalized after transformation.

### 31.2.3 Modal Dominancy Approach

At this point, the reduction strategy is available to yield the low-order model. It remains to be determined which set of eigensolutions to be used in the reduced-order model in order to conserve the input-output behavior of the full system to as large extent as possible. To this end, let the  $i$ th modal coordinate of the diagonalized state-space equation be described by

$$\begin{aligned} \dot{z}_i &= \lambda_i z_i + \hat{b}_i u \\ \Delta y_i &= \hat{c}_i z_i \end{aligned} \quad (31.9)$$

where  $u(t) \in \mathbb{R}^{n_u}$  is a unit-impulse and  $\Delta y_i \in \mathbb{R}^{n_y}$  is the contribution to the system output due to the  $i$ th mode. In this study, the following metric, or dominance index, is defined to measure the contribution of the  $i$ th modal coordinate to the full system output

$$M_i = \int_0^{\infty} (\Delta y_i^H \Delta y_i) dt \quad (31.10)$$

where  $(\cdot)^H$  is the Hermitian transpose of a matrix. According to Parseval's theorem for a causal system, this metric can be transformed into the frequency domain as

$$M_i = \int_{-\infty}^{+\infty} (\Delta Y_i(\omega)^H \Delta Y_i(\omega)) d\omega \quad (31.11)$$

However, to more accurately predict the behavior of the created low-order model, the frequency information of the input can be taken into the account by adjusting the limits of integration to the interval  $[\omega_1, \omega_2]$  as follows

$$M_i = \int_{\omega_1}^{\omega_2} (\Delta Y_i(\omega)^H \Delta Y_i(\omega)) d\omega \quad (31.12)$$

Utilizing the Laplace transformation, the input-output relation can be written as

$$\Delta Y_i(s) = \hat{c}_i (s - \lambda_i)^{-1} \hat{b}_i U(s) \quad (31.13)$$

It is assumed that the input is a unit-impulse signal, such that  $U(s) = 1$ . Substitution of Eq. (31.13) into Eq. (31.12) leads to

$$M_i = \int_{\omega_1}^{\omega_2} \hat{b}_i^H \frac{1}{j\omega - \lambda_i} \hat{c}_i^H \hat{c}_i \frac{1}{j\omega - \lambda_i} \hat{b}_i d\omega \quad (31.14)$$

$$M_i = \hat{b}_i^H \hat{c}_i^H \hat{c}_i \hat{b}_i \left[ \frac{1}{|\operatorname{Re}(\lambda_i)|} \arctan \left( \frac{\omega}{|\operatorname{Re}(\lambda_i)|} \right) \right]_{\omega_1 - |\operatorname{Im}(\lambda_i)|}^{\omega_2 - |\operatorname{Im}(\lambda_i)|} \quad (31.15)$$

where  $\operatorname{Im}(\cdot)$  denotes the imaginary part of variable. Based on this metric, a new limited frequency interval dominance definition can be introduced.

**Definition** For a given threshold value  $\varepsilon \geq 0$  and frequency interval  $[\omega_1, \omega_2]$ , let  $n_r$  be the number of metrics for which  $M_k > \varepsilon$  for  $k = 1, \dots, n_r$ . Subsequently, the full model has  $n_r$  dominant and  $n_x - n_r$  non-dominant eigensolutions.

A nice feature of this metric is that the dominant eigenvalue subspace is both controllable and observable.

### 31.2.4 Improved Modal Truncation Algorithm

This section presents a complete summary of the proposed modal based model reduction technique for generating an approximated model which contains dominant eigenvalues of the original system based on the new metric. The algorithm is as follows:

- Step 1. Given the stable system  $(A, B, C, D)$  of Eq. (31.1).
- Step 2. Solve eigenvalue problem  $A\Phi = \Phi\Lambda$  for matrix  $A$ .
- Step 3. Transfer the system to modal decomposed form of Eq. (31.2).
- Step 4. Find multiple eigenvalues with dimension of multiplicity larger than column rank of  $B$ .
- Step 5. Do a QR decomposition of  $\hat{B}$  to make a subset of the eigenvectors found in step 4 being orthogonal to the load.
- Step 6. Set the frequency range of interest according to the frequency information of the input signal.
- Step 7. Compute the metric correspond to each modal coordinate by Eq. (31.15).
- Step 8. Rearrange the modal coordinates as they appear in order:

$$M_1 \geq M_2 \geq \dots \geq M_{n_x}$$

- Step 9. Set the threshold for dominance analysis and compute the low-order model order.
- Step 10. Do modal truncation.

It is worthy to be mentioned that this algorithm is applicable for large systems with both over- and under-damped eigenvalues.

### 31.3 Numerical Example

In the first part of this section, the physical description and the obtained finite element model of a large scale problem, described in [1], are presented. The input signals which are utilized to assess the performance of the created low-order models are described in the second part.

#### 31.3.1 Aluminum Plate Model

A finite element model of a 0.5 m wide square aluminum plate with thickness 1 mm, density 2,700 kg/m<sup>3</sup>, Young's modulus 70 GPa and Poisson's ratio 0.33, is set up using 4-noded shell elements. A 16 × 16 elements mesh is used to discretize the model. The origin of its coordinate system is to the bottom-left. The plate is subjected to input signal at coordinate (0.125, 0.25) m. The displacement of the vertical motion of the plate captured at three nodes of coordinates (0.125, 0.25) m, (0.25, 0.25) m and (0.125, 0.125) m. The plate is also subjected to free edge boundary conditions with fixed translation only at the four corner nodes. Classical Rayleigh viscous damping of  $V = \alpha M + \beta K$  is assigned to the model, where  $M$  is the mass matrix,  $K$  is the stiffness matrix and  $\alpha = 10^{-3}$ ,  $\beta = 10^{-6}$ . After second-order diagonalization, the damping coefficient of 50 modes was increased to 1.1, to ensure that the system includes both real and complex conjugate eigenvalues.

A Guyan reduction scheme is applied to the model to eliminate massless rotational degrees of freedom. This leads to a state-space model of order 1710. Figure 31.1 depicts the eigenvalue spectrum of the resulted full model. The full model is stable since all eigenvalues have negative real part.

#### 31.3.2 Time Domain Input Signals

Three candidate signals, generated by MATLAB, are considered in this study to assess the quality of the reduced-order model obtained by the proposed modal reduction method; unit-impulse, unit-step and linear chirp. The unit impulse function, often referred to as Dirac delta function, is zero all over the time except at zero. The impulse response of the continuous-time state-space model of Eq. (31.1) is equivalent to unforced response to initial condition  $B$  for single input systems. It can be shown that unit-impulse has unit spectrum in the entire frequency range. Another considered input signal is unit-step with the following description,

$$u(t) = \begin{cases} 1 & t \geq 0 \\ 0 & t < 0 \end{cases} \quad (31.16)$$

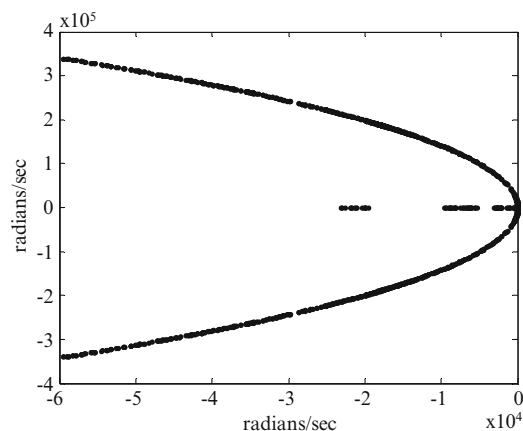


**Fig. 31.1** Eigenvalue spectrum of full model of aluminum plate

**Fig. 31.2** Frequency spectrum of linear chirp

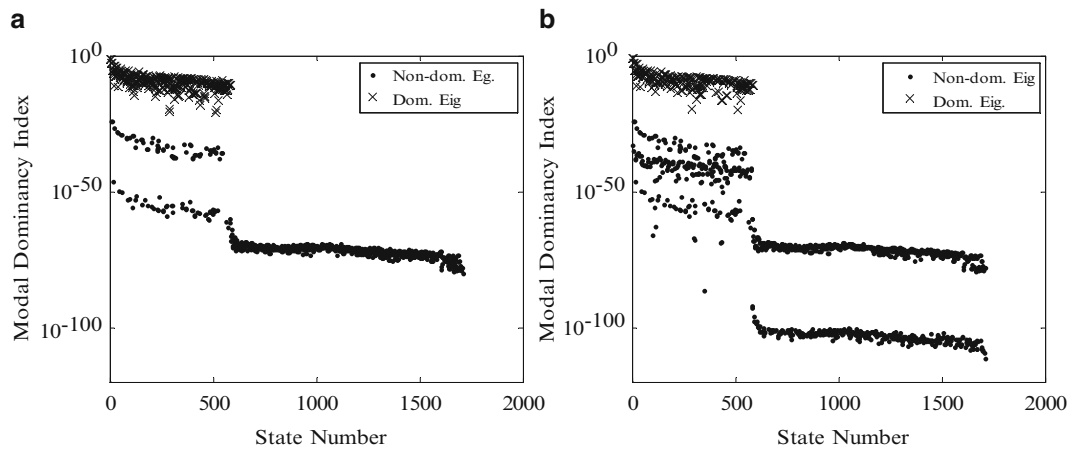
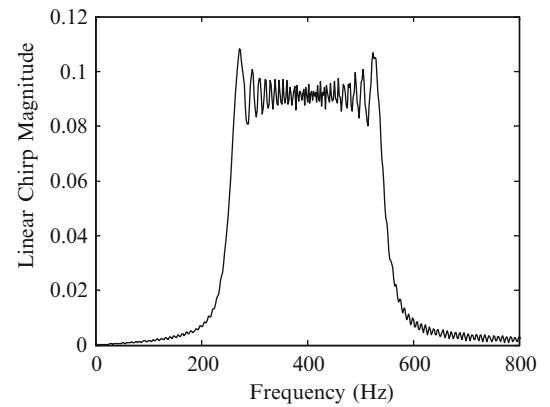


**Fig. 31.3** Contribution of modal coordinates into dominance index of Eq. (31.15); (a) without and (b) with QR factorization in case of multiple eigensolutions

The unit-step response of the system is utilized in this study to investigate the transient and, mainly, the steady-state error due to truncation.

A linear chirp is a signal which its instantaneous frequency linearly changes with time. To consider the performance of the proposed limited frequency range reduction technique, it is assumed that its instantaneous frequency varies linearly between 250 Hz at the initial time and 550 Hz at the final time. Figure 31.2 shows the spectrum of the utilized linear chirp in this study.

### 31.4 Results and Discussion

The proposed modal truncation algorithm is tested on an illustrative example of Aluminum plate for different input signals and displacement as its output to show its full capabilities to create a low-order model. The proposed dominance index corresponding to each eigensolution is computed by Eq. (31.15) and depicted in Fig. 31.3. In Fig. 31.3a the QR factorization is not used in case of multiple eigenvalues, the number of most dominant eigensolutions is 444. Then, we repeated to compute the modal dominance index containing the QR factorization in case of equal or nearly close eigenvalues and results are depicted in Fig. 31.3b. As shown, the contribution of some eigensolutions to the modal dominance metric decreased in this figure since QR factorization transforms part of eigensolutions to the null space of B matrix, spatial distribution of loading. Thus, the number of most dominant eigenvalues is decreased to 288.

In order to examine the performance of the suggested modal truncation algorithm, reduced-order models are yielded by utilizing the 100, 50 and 20 most dominant eigensolutions of the full system while the frequency range of interest is unlimited, semi-infinite dominance analysis, in Eq. (31.15). Figure 31.4 demonstrates that the eigenvalue spectra of the resulted low-order models are subsets of the eigenvalue spectrum of the full system. It also confirms that the proposed reduction algorithm is applicable for systems which have both real, over-damped, and complex, under-damped, eigenvalues.

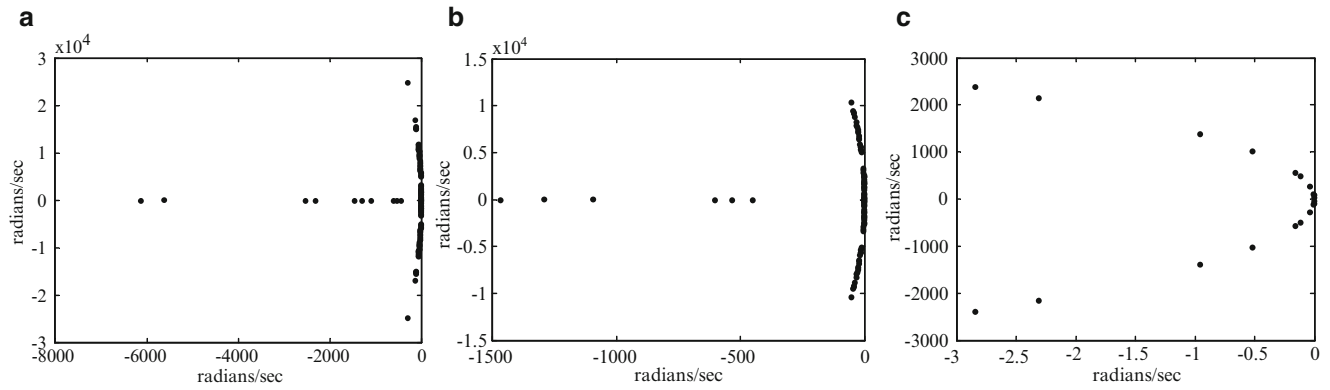


**Fig. 31.4** Eigenvalue spectrum of low-order models of plate, with different model orders, obtained by proposed modal approach; (a)  $n_r = 100$ , (b)  $n_r = 50$ , (c)  $n_r = 20$

**Table 31.1** Numerical results of the computed reduced-order models for three different inputs; the Frobenius norm of full system output is 29.33, 1.209, 0.0219 for the three signals and the  $H_\infty$ -norm of the full system is 28.4118

Reduced model order	Unit impulse response		Unit step response		Linear chirp	
	RHN of error system (%)	RFN of error system (%)	RHN of error system (%)	RFN of error system (%)	RHN of error system (%)	RFN of error system (%)
$k = 150$	$2.7e - 5$	0.16	$2.7e - 5$	0.04	$2.7e - 5$	1.29
$k = 100$	$8.7e - 5$	0.52	$8.7e - 5$	0.11	$8.7e - 5$	3.30
$k = 20$	0.014	3.8	0.014	0.87	0.014	61.28

Three different input signals are applied to the obtained reduced-order models to show their efficiency in the sense of the resulting approximation error due to unit-impulse, unit-step and linear chirp loadings. Table 31.1 shows the results for different input signals. In this table, the resulting error is analyzed based on Relative  $H_\infty$ -Norm (RHN) of the error system, i.e.,

$$\frac{\|G - G_r\|_\infty}{\|G\|_\infty} \quad (31.17)$$

for a frequency domain analysis and Relative Frobenius Norm (RFN) of the approximation error, i.e.,

$$\frac{\|e(t)\|_F}{\|y(t)\|_F} = \frac{\|y(t) - y_r(t)\|_F}{\|y(t)\|_F} = \frac{\sqrt{\sum_{i=1}^{n_y} \sum_{j=1}^m |e_{ij}|^2}}{\sqrt{\sum_{i=1}^{n_y} \sum_{j=1}^m |y_{ij}|^2}} \quad (31.18)$$

for a time domain analysis, where  $y_r(t)$  is the output of the reduced-order model. This table expectedly shows that the amount of error for both RHN, frequency domain analysis, and RFN, time domain analysis, is growing by decreasing the low-order model order.

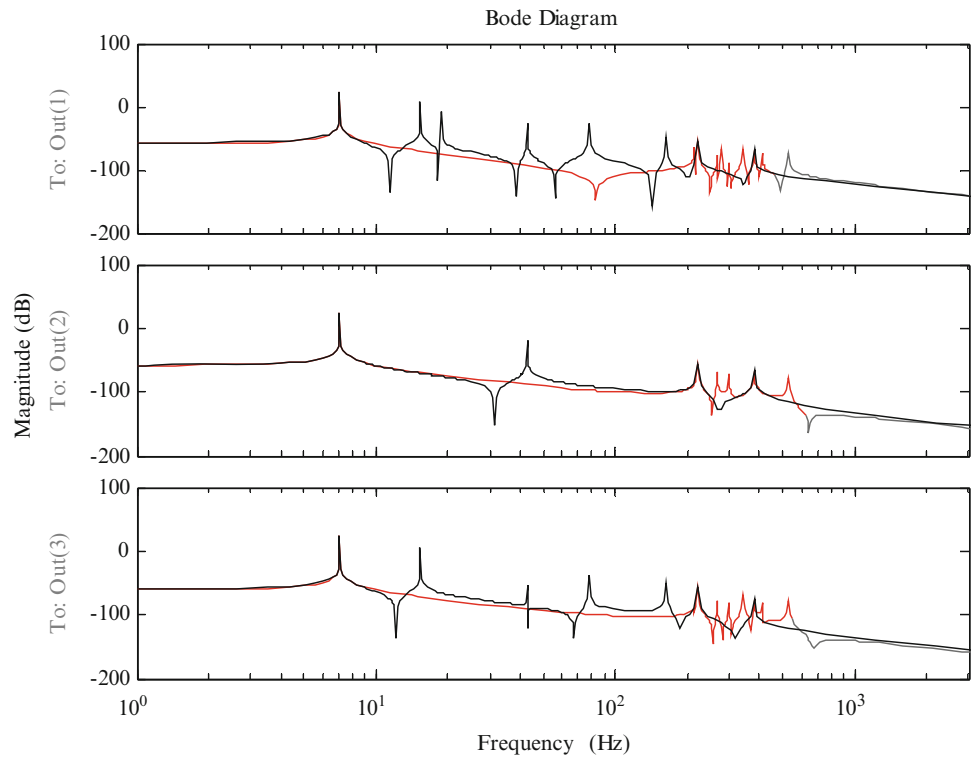
In frequency domain analysis, at a first glance it can be noticed that the created low-order models produce a satisfactory approximation error, which has considered to be less than 0.02% of the  $H_\infty$ -Norm of the original system. It should also be noted that, for a given model order, the RHN is obviously constant for different inputs inasmuch as RHN only depends on the resulted low-order model and not on the realization of the input signal.

In time domain analysis, to compare the transient and steady-state response of the reduced-order models to the response of the full system, we excited the Aluminum plate with unit-impulse and unit-step signals, respectively. However, Table 31.1 shows that for these inputs the created low-order models by the proposed modal truncation algorithm yielded satisfactory approximation error. It justifies the fact that although the proposed dominance index is based on the contribution of the eigensolutions to the unit-impulse response, the created reduced-order models properly approximated the steady-state response of the original system. On the other hand, the RFN error resulted based on linear chirp is much higher than the transient and steady-state errors for a given model order when the proposed reduction algorithm including the semi-infinite modal dominance index which means that the frequency information of the input signal is not involved in

**Table 31.2** Results of the computed reduced-order models with and without limited-frequency range truncation when input is linear chirp; The Frobenius norm of the full system output is 29.33, 1.209, 0.0219 and the  $H_\infty$ -norm of the full system is 28.4118

Reduced-model order	Semi-infinite frequency range dominance analysis		Limited-frequency range dominance analysis	
	RHN of error system (%)	RFN of error system (%)	RHN of error system (%)	RFN of error system (%)
$k = 150$	$2.7e - 5$	1.29	$3.56e - 4$	0.82
$k = 100$	$8.7e - 5$	3.30	$3.56e - 4$	2.58
$k = 20$	$1.4e - 2$	61.28	9.90	29.39

**Fig. 31.5** The bode diagram of reduced-order model of order 20 with frequency-restricted (*red line*) and semi-infinite (*black line*) dominance analysis



the modal dominance analysis part. Thus, we repeated the reduction algorithm to the given low-order model orders for the specified linear chirp signal while the frequency range of interest is bounded to the interval [200, 600] Hz, see Fig. 31.1.

Table 31.2 shows the results obtained with frequency-restricted and semi-infinite dominance analysis when input is the same, linear chirp. For a given model order, the amount of RHN error is increased while the amount of the RFN error is decreased in the case that the frequency information of the input signal is utilized in the modal dominance analysis. To interpret this phenomenon, the magnitude part of the bode diagram for reduced model order of 20 with and without utilizing the limited-frequency range reduction algorithm is depicted in Fig. 31.5. Using the frequency information of the input signal benefits us to keep the modes which are more substantial in that frequency interval. Thus we could expect to improve the response in the frequency range of interest while the deviation of the frequency response becomes worse in the rest of frequency range as shown in the Fig. 31.5. It should also be noted that the Frobenius norm is an overall measure of the output deviation from the response of the original system while the  $H_\infty$ -norm of error system is a measure of the largest amplitude of the error in the frequency domain. On the other hand, since the reduction process is always accompanied by a loss of information, it is crucial that it approximates well the input-output behavior of the system. Therefore, this suggests that the Frobenius norm of the error, as a measure of the overall behavior of the system, is more relevant to the worst deviation from the frequency response of the original system in a certain frequency. Figure 31.5 also shows that the first dominant eigenvalue is still of importance although it is not located in the specified frequency range of interest.

In addition to the input signal, the character of the response parameter also affects the input-output relation of a system. Thus, the efficiency of the proposed modal dominance index is examined for three different types of response parameters; displacement, velocity and acceleration using a semi-infinite modal dominance index while the QR factorization is also

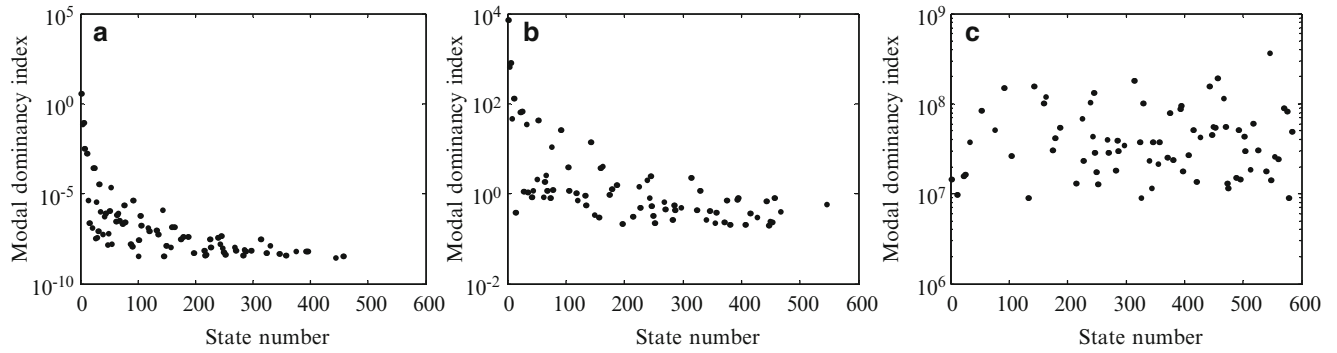


**Fig. 31.6** Contribution of modal coordinates into the proposed dominance index with (a) displacement, (b) velocity and (c) acceleration as system output

**Table 31.3** Results of the computed reduced-order models for three different inputs; The Frobenius norm of full system output is  $3.3e7$ ,  $5.7e3$  and  $29.3$ , and the  $H_\infty$ -norm of the full system is  $5.5e4$ ,  $1.2e3$  and  $28.4118$  for displacement, velocity and acceleration output, respectively

Reduced-model order	Displacement output		Velocity output		Acceleration output	
	RHN of error system (%)	RFN of error system (%)	RHN of error system (%)	RFN of error system (%)	RHN of error system (%)	RFN of error system (%)
$k = 100$	$1.3e - 4$	0.80	0.09	30.34	100.00	38.15
$k = 50$	$1.2e - 3$	1.97	0.11	47.91	100.00	63.15

involved. Figure 31.6 shows the 150 most dominant eigenvalues using the proposed modal dominance metric for different types of response parameters. This figure depicted how the acceleration responses are weighted by the squared power of the frequency compared to displacement responses. Thus, the system output is mostly dominated by eigensolutions in the mid frequency range.

Table 31.3 illustrates the approximation error resulted from yielding low-order models with 100 and 50 states. For a given model order, the low-order model created based on the displacement output has less approximation error in comparison to the velocity and acceleration output. This table also shows that selection of acceleration as the response parameter caused to 100% relative  $H_\infty$ -Norm of error system while the relative Frobenius norm error is 38.15 and 68.15% when the model order is 100 and 50, respectively.  $H_\infty$ -Norm of error system measures the highest value of the error caused by the truncation procedure while the Frobenius norm is a measure of the overall error over the time domain. Although the  $H_\infty$ -Norm is a common norm to analyze the approximation error in the model reduction applications, these results suggest that measurement of the overall behavior of the low-order model is more relevant. Therefore, the metric proposed here, which holds information on modal dynamics based on the input-output relation, is relevant.

For simplicity of our discussion, we assumed that the full system is non-defective. However, in case of a defective system with incomplete eigenvector basis, the full system can be transformed into the Jordan block diagonal form and the contribution of each block can be separately investigated for input-to-output relation.

This paper does not discuss the residualization methods to compensate for reduced states. The residualization technique, presented in [1], can be utilized to preserve the frequency response gain of the original system at either end of the frequency range of interest. Residual mass and stiffness terms could be employed to adjust for the reduction of low and high frequency eigensolutions, see [14].

## 31.5 Concluding Remarks

A new criterion is proposed to improve available modal dominance analysis methods. The proposed index is a frequency-limited interval input-output relation which measure and ranks the contribution of each eigensolution to the impulse response of the system. The eigensolutions with large indices would be retained during model reduction procedure. It was shown that the created reduced-order models, based on this index, are minimal and their eigensolutions are fully controllable and observable. Three different input signals are applied to the produced low-order models to analyze their



sensitivity to the type of input. The resulted approximation error for linear chirp showed that semi-infinite modal dominance index is not capable to yield reduced-order models which capture the input-output behavior of the original system as well as the frequency-restricted dominance criterion.

## References

1. Antoulas AC (2005) Approximation of large-scale dynamical. Society for Industrial and Applied Mathematics, Philadelphia
2. Noor AK (1994) Recent advances and applications of reduction methods. *Appl Mech Rev* 47(5):125–146
3. Eرسال T, Fathy HK, Rideout DG, Louca LS, Stein JL (2008) A review of proper modeling techniques. *J Dyn Syst Measur Control Trans ASME* 130(6):0610081–06100813. doi:10.1115/1.2977484
4. Varga A (1995) Enhanced modal approach for model reduction. *Math Modell Syst* 1(2):91–105. doi:10.1080/13873959508837010
5. Qu ZQ (2004) Model order reduction techniques: with application in finite element analysis. Springer, New York
6. Davison E (1966) A method for simplifying linear dynamic systems. *Auto Control IEEE Trans* 11(1):93–101. doi:10.1109/tac.1966.1098264
7. Rommes J, Martins N (2007) Computing transfer function dominant poles of large-scale second-order dynamical systems. *SIAM J Sci Comput* 30(4):2137–2157. doi:10.1137/070684562
8. Rommes J, Martins N (2006) Efficient computation of multivariable transfer function dominant poles using subspace acceleration. *IEEE Trans Power Syst* 21(4):1471–1483. doi:10.1109/tpwrs.2006.881154
9. Skelton RE, Yousuff A (1983) Component cost analysis of large scale systems. *Int J Control* 37(2):285–304
10. Skelton RE (1980) Cost decomposition of linear systems with application to model reduction. *Int J Control* 32(6):1031–1055
11. Lastman GJ, Sinha NK, Rozsa P (1984) On the selection of states to be retained in a reduced-order model. *IEE Proc D: Control Theory Appl* 131(1):15–22
12. Aguirre LA (1993) Quantitative measure of modal dominance continuous systems. In: Anon (ed) Proceedings of the 32nd IEEE conference on decision and control, Part 3 (of 4), San Antonio, TX. IEEE, pp 2405–2410 doi: 10.1109/CDC.1993.325629
13. Green M, Limebeer DJN (1995) Linear robust control, reprint edn. Prentice Hall, Englewood Cliffs
14. Ewins DJ (2001) Modal testing: theory, practice and application. Res Stud Press, Letchworth

# Chapter 32

## Fast Precise Algorithm of Computing FRF by Considering Initial Response

J.M. Liu, W.D. Zhu, M.Ying, and S. Shen

**Abstract** At present, the common algorithm of computing FRF is averaging method in frequency domain. This algorithm is precise method for impact exciting or burst random exciting, but not for continuous exciting, for the initial response cannot be considered. In continuous exciting test, increasing data length which permits increasing averaging times is needed to alleviate the error of FRF caused by the initial response. The initial response is caused by the previous frame of exciting force. Thus, in this work an algorithm model is put forward by considering the initial response. For each averaging computation in frequency domain, the data of two frames force and one frame response, aligned in right end, are used. The initial response is caused by the first frame force. When the FRFs of MISO are known, the IRFs (Impulse Response Function) are obtained by IFFT transform of FRFs. The theoretical response of this point except the first frame can be computed out by the convolution of forces and IRFs. The RMS of error series between theoretical response and measured response, divided by the RMS of measured response, reflects the preciseness of FRF. The smaller is the value, the better. The speed of common averaging method in frequency domain is fast, but with bad FRF preciseness when data is short. The FRF preciseness of least square devolution method in time domain is best, but with the slowest computation speed and unpractical. The preciseness of FRF with new algorithm is very near to the devolution method but the computation time can be shortened greatly. Applying the new algorithm in continuous exciting MIMO test, the test time can be greatly shortened. The new algorithm can also be applied to impact MIMO test, with multi impacts acting in different points at the same time. In the paper, real test and simulating data are used to verify the new algorithm, and the new algorithm is also compared with the time domain iteration method which is put forwarded before.

**Keywords** FRF • Preciseness • Iteration algorithm • Frequency domain • IRF

### 32.1 Introduction

For continuous exciting modal test, the averaging algorithm in frequency domain to obtain FRF will cause error.

In averaging method, first assuming the number of FFT points is  $N$ , which corresponds to analyzing time  $T = N/SF$ . Here  $SF$  is sampling frequency. The time wave corresponding to FRF is unit impulse response function (UIRF). To assure the preciseness of FRF, the  $N$  must be big enough, to ensure the amplitude of UIRF decreasing greatly after time  $T$ . For example, the amplitude decreases over 1,000 times, illustrated as Fig. 32.1.

The discrete force waves  $F(i)$  ( $i = 1, 2, \dots, N$ ) from 1 to  $N$  point, will cause response wave  $y(i)$  from point 1 to  $N$  and response wave  $y'(i + N)$  from point  $N + 1$  to  $2N$ .  $y'(i + N)$  can be looked as the initial response wave corresponding to the next frame force wave from point  $N + 1$  to  $2N$ .

---

J.M. Liu (✉) • M.Ying • S. Shen  
China Orient Institute of Noise & Vibration, Beijing 100085, China  
e-mail: [liujm@coinv.com](mailto:liujm@coinv.com); <http://www.coinv.com>; [Yingm@coinv.com](mailto:Yingm@coinv.com); [Shens@coinv.com](mailto:Shens@coinv.com)

W.D. Zhu  
University of Maryland, Baltimore county, Baltimore, MD 20250, USA  
e-mail: [wzhu@umbc.edu](mailto:wzhu@umbc.edu)

**Fig. 32.1** The FFT number should satisfied amplitude decreasing

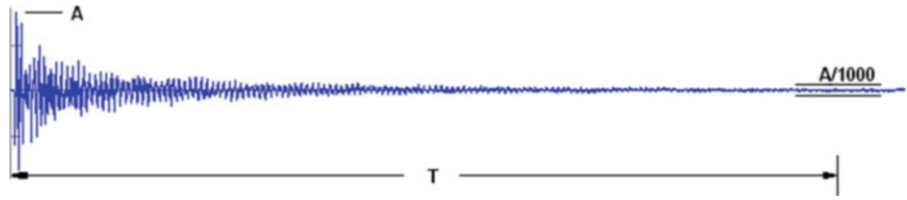
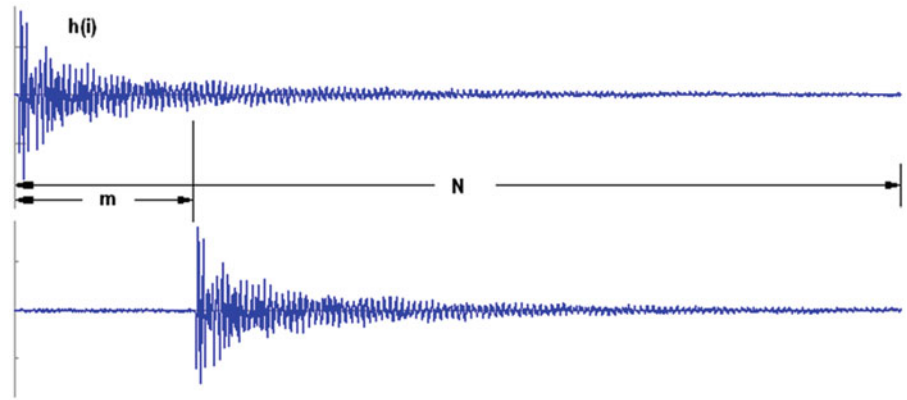


**Fig. 32.2** The response wave caused by 2 unit impulses delayed m points



For continuous exciting, assuming the force wave is  $F1(i)$  ( $i = 1, 2, \dots, N$ ) from point 1 to  $N$  and  $F2(i + N)$  ( $i = 1, 2, \dots, N$ ) from point  $N + 1$  to  $2N$ , the discrete response wave from point  $N + 1$  to  $2N$  will be  $y'_1(i + N)$  adding  $y_2(i + N)$ , that is  $r(i + N) = y'_1(i + N) + y_2(i + N)$ .

It can be proved that when  $F1(i) = F2(i)$ , the FRF obtained by averaging in frequency domain method between discrete wave  $F2(i + N)$  from point  $N + 1$  to  $2N$  and discrete response wave  $r(i + N)$  from point  $N + 1$  to  $2N$  is theoretical FRF.

Assuming UIRF is  $h(i)$  ( $i = 1, 2, \dots, N$ ),  $h(i) = 0$  ( $i > N$ )

The corresponding FFT spectrum is the theoretical FRF, the complex  $H(i\Delta f)$  ( $i = 0, 1, 2, \dots, N/2$ ). Here  $\Delta f = SF/N$ .

Assuming  $F2(i)$  is the unit impulse in point  $m$ , for  $F1(i) = F2(i)$ , so exciting force are unit impulse in point  $m$  and unit impulse in point  $m + N$ . The relationship of the response wave from point  $N + 1$  to  $2N$  produced by force  $F2(i)$  and  $F2(i + N)$  with the UIRF  $h(i)$ , is illustrated as Fig. 32.2. In this figure, the above is the wave of UIRF  $h(i)$ , the below is the response wave. In response wave, the forward  $m$  points are caused by  $F2(i)$ , that is the unit impulse in point  $m$ , are the wave of  $h(i)$  from point  $N - m + 1$  to  $N$ . The backward  $N - m$  points are caused by  $F2(i + N)$ , that is the unit impulse in point  $m + N$ , are the wave of  $h(i)$  from point 1 to  $N - m$ .

The FFT spectrum of  $F2(i)$ , the unit impulse in point  $m$ , is unit impulse delayed by  $m$  points, is complex,  $X(i\Delta f) = e^{j(-2\pi(i\Delta f)m/SF)} = e^{j(-2\pi im/N)}$  ( $i = 0, 1, 2, \dots, N/2$ )

The response wave  $r(i)$ , illustrated in Fig. 32.2, is UIRF  $h(i)$  delayed by  $m$  points. Here the response wave is periodic function,  $r(i) = r(i + N)$ . The corresponding FFT spectrum is complex

$$Y(i\Delta f) = H(i\Delta f) e^{j(-2\pi im/N)} \quad (i = 0, 1, 2, \dots, N/2)$$

Let the  $F2(i)$  come back to common wave.

For the linear system, the complex FFT spectrum of wave  $F2(i)$  is

$$X(i\Delta f) = \sum_{m=1}^N F_2(m) e^{j(-2\pi im/N)} \quad (i = 0, 1, 2, \dots, N/2)$$

When  $F1(i) = F2(i)$ , the complex FFT spectrum of  $r(i)$  is

$$Y(i\Delta f) = H(i\Delta f) \sum_{m=1}^N F_2(m) e^{j(-2\pi im/N)} \quad (i = 0, 1, 2, \dots, N/2)$$

So  $Y(i\Delta f)/X(i\Delta f) = H(i\Delta f) \quad (i = 0, 1, 2, \dots, N/2)$

That ends the proving.

For continuous exciting test, the cause of error of FRF in frequency domain averaging method can be found. Assuming UIRF length is limited to  $N$ , here  $N$  is the FFT point number for FRF analysis. The response wave  $r(i + N)$  ( $i = 1, 2, \dots, N$ ) from point  $N + 1$  to  $2N$  is totally determined by force wave  $F1(i)$  and  $F2(i + N)$ . Force wave  $F1(i)$  produces initial response. In frequency domain averaging method, the FRF is decided by FFT spectrum of  $F2(i)$  and  $r(i)$ , the force wave  $F1(i)$  which produces the initial response is not be used. It has been proved, when  $F1(i) = F2(i)$ ,  $r(i + N) = y'_2(i + N) + y_2(i + N)$ , or

$$r(i) = y'_2(i) + y_2(i) \quad (32.1)$$

There is no error for frequency domain averaging method to obtain FRF.

But in practical,  $r(i + N) = y'_1(i + N) + y_2(i + N)$ , or it can be written as

$$r(i) = y'_1(i) + y_2(i) \quad (32.2)$$

Here  $y'_1(i)$  is the initial response caused by  $F1(i)$ .

If  $y'_1(i) \neq y'_2(i)$ , that is  $F1(i) \neq F2(i)$ , will produce error. The error is produced by wave  $y'_1(i) - y'_2(i)$ , which can be looked as random wave. If averaging times is not enough, the error will be big. By increasing the test data length to increase the averaging times, the error can be decreased.

For multi trigger impact shocking or burst random exciting, the sampling does not start until initial response is zero, that is  $y'_1(i) = 0$ . The lasting time of exciting force is short for each trigger, when sampling ends, the response wave will decrease to zero, that is  $y'_2(i) = 0$ . In this way, the FRF obtained by the method of averaging in frequency domain is precise. When sampling ends, if the left response wave does not decreased to zero, by adding exponent window, the influence of  $y'_2(i)$  will be decreased. When parameters identification is completed, the damping ration needs to be corrected to detract the exponent window influence [1].

By Eq. (32.1), the convolution speed can be accelerated. Assuming force wave  $F2(i)$  and UIRF  $h(i)$  are known, to compute  $y'_2(i)$  and  $y_2(i)$ , only the convolution to compute  $y_2(i)$  is needed. The sum of  $y'_2(i) + y_2(i)$  can be computed out by IFFT of response spectrum, the response spectrum can be computed out by frequency domain method. Compared with the computation time in time domain convolution, the time spending in frequency domain computation can be neglected. By this way, the computing speed will be accelerated almost two times. This skill can be applied to compute response wave of continuous exciting, to evaluate the FRF preciseness.

When FRF is known, UIRF can be obtained by IFFT of FRF. From the convolution of UIRF and continuous exciting force, the continuous theoretical response wave except forward  $N$  points can be computed out. The fitting extent of theoretical response wave and measured response wave reflects the preciseness of FRF evaluation. By spectrum analysis of response error series and measured response wave, the new coherence function can be defined which can reflect the FRF evaluation preciseness in different spectrum lines' position [2].

The preciseness of FRF evaluation can be reflected by fitting coefficient

$$fit = y_{rms} / \sqrt{e_{rms}^2 + y_{rms}^2} \quad (32.3)$$

The greater is the value, the better.

Where  $y_{rms}$  and  $e_{rms}$  are roots of mean square of measured response wave and error series separately. For continuous exciting, the forward  $N$  points are ignored.

The error coefficient

$$error = e_{rms} / y_{rms} \quad (32.4)$$

It can also be used to reflect the FRF evaluation preciseness, the smaller is the value, the better.

The relationship of fitting coefficient with error coefficient is

$$fit = \frac{1}{\sqrt{1 + error^2}} \quad (32.5)$$

The new coherence function is defined as

$$\gamma^2(f) = P_y(f) / (P_e(f) + P_y(f)) \quad (32.6)$$

$P_y(f)$  and  $P_e(f)$  are power spectrum of measured response wave and error series wave in frequency spectrum line  $f$  separately. This definition is also suitable for MIMO test.

The relationship of fitting index with new coherence function is

$$fit = \sqrt{\sum P_y(f) / (\sum P_y(f) / \gamma^2(f))} \tag{32.7}$$

Where  $\sum$  means the sum of all spectrum lines. If  $\sum$  means only part of the spectrum lines, the fitting coefficient of part frequency domain district can be obtained by Eq. (32.7).

For multi impact shocking or burst random exciting, it is proved that tradition coherence function is [2]

$$\gamma_c^2(f) = (P_y(f) - P_e(f)) / P_y(f) \tag{32.8}$$

The relationship of it with new coherence function is

$$\gamma^2(f) = 1 / (2 - \gamma_c^2(f)) \tag{32.9}$$

For  $\gamma_c^2(f) > 0$ , there is  $\gamma^2(f) > 0.5$ .

### 32.2 Fast Precise Algorithm of Computing FRF by Considering Initial Response in Continuous Exciting Test

Known the cause of FRF error in frequency domain averaging method for continuous exciting test, a new algorithm is put forward which considers the initial response.

Assuming the FFT point number is N and the length of UIRF is shorter than N, the force wave from point 1 to 2N will totally determine the response wave from point N + 1 to 2N.

In traditional frequency domain averaging method, the same time model is applied for each averaging, illustrated as Fig. 32.3. The N points exciting and response wave are located at the same time district.

In practical, for continuous exciting test, if only initial response wave is considered, each averaging can applied model illustrated in Fig. 32.4. In this model, the exciting and response points number both are N, but not in the same time. The next point after exciting force ending is the first point of response wave.

The most reasonable model should be illustrated as Fig. 32.5. In each averaging, there are 2N exciting points and N response wave points, aligned in right end.

For continuous exciting, the lest square devolution method in time domain, get the best UIRF [2], but the computation time is too long for practical use. In Ref. [2], the time domain iteration algorithm is put forward. Based on Fig. 32.5 model, the frequency domain iteration algorithm is put forward here.

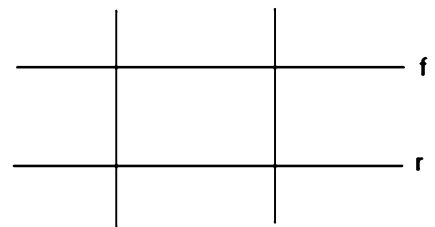


Fig. 32.3 Traditional averaging model

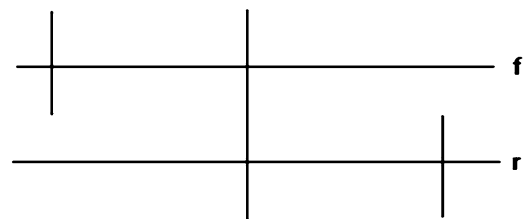
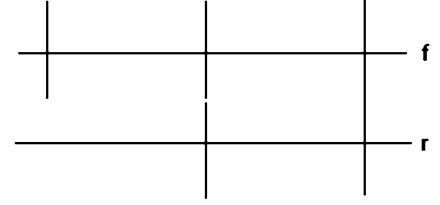


Fig. 32.4 Only considering initial response model

**Fig. 32.5** New algorithm model

First the model of Fig. 32.3, that is the traditional frequency domain averaging method, is used to obtain the initial FRF. Then, for the error series of response wave, the model of Fig. 32.4 is used, to compute the correcting FRF. To obtain the afterward correcting FRF, the model of Figs. 32.3 and 32.4 will be used alternatively. After five times iteration, the FRF preciseness will be very near to the least square devolution algorithm in time domain.

The traditional MIMO FRF algorithm is introduced as bellowing [3]:

The response of one point is caused by multi exciting force in MIMO test, for response wave in point  $m$ , there is

$$\sum_{r=1}^p F_r(s) H_{rm}(s) = Y_m(s) \quad (32.10)$$

Where  $p$  is exciting points number.  $F_r(s)$  is the force spectrum of exciting point  $r$ .  $H_{rm}(s)$  is the FRF between response point  $m$  and exciting point  $r$ .  $Y_m(s)$  is the response spectrum of response point  $m$ .  $s = j\omega$ ,  $\omega$  is circle frequency.

The FRF is obtained by averaging, for  $k$ th averaging

$$\left[ F_1^k(s) F_2^k(s) \cdots F_p^k(s) \right]_{1 \times p} \left[ H_{1m}(s) H_{2m}(s) \cdots H_{pm}(s) \right]_{p \times 1}^T = Y_m^k(s) \quad (32.11)$$

$k = 1, 2, \dots, n$ , total averaging times number is  $n$ , here  $\bullet^T$  is transpose.

Equation (32.11) can be written as

$$F^k(s)_{1 \times p} H(s)_{p \times 1} = Y_m^k(s) \quad (32.12)$$

For  $n$  times averaging, there is

$$\left[ F^1(s) F^2(s) \cdots F^n(s) \right]_{n \times p}^T H(s)_{p \times 1} = \left[ Y_m^1(s) Y_m^2(s) \cdots Y_m^n(s) \right]_{n \times 1}^T \quad (32.13)$$

Simplified as

$$F(s)_{n \times p} H(s)_{p \times 1} = Y(s)_{n \times 1} \quad (32.14)$$

The FRFs of all exciting point can be obtained at one time by least square method

$$\left[ H_{1m}(s) H_{2m}(s) \cdots H_{pm}(s) \right]_{p \times 1}^T = \left[ F^H(s) F(s) \right]_{p \times p}^{-1} F^H(s)_{p \times n} Y(s)_{n \times 1} \quad (32.15)$$

Where  $\bullet^H$  is conjugate transpose.

New algorithm is introduced as bellow:

According to model of Fig. 32.5, choose overlapping coefficient and averaging times.

According to model of Fig. 32.3, compute FRF. For each response,  $H_{rm}(s)$  ( $r = 1, 2, \dots, p$ ) will be obtained. Turn the FRF to UIRF by IFFT, convolute with  $p$  points exciting force, the theoretical continuous response wave  $y_{rm}(i)$ , ( $r = 1, 2, \dots, p$ ),  $i = N + 1, N + 2, \dots, l$  will be obtained. Here  $l$  is total points number of sampling points. To let the error series of response wave to be convergent always, to solve the coefficients  $k_r$  which is waiting for determining,  $r = 1, 2, \dots, p$ , there is

$$\left[ y_{1m} y_{2m} \cdots y_{pm} \right]_{(l-N) \times p} \left[ k_1 k_2 \cdots k_p \right]_{p \times 1}^T = \left[ y_m \right]_{(l-N) \times 1} \quad (32.16)$$

$$\begin{aligned} & \left[ k_1 k_2 \cdots k_p \right]_{p \times 1}^T \\ & = \left( y_{1m} y_{2m} \cdots y_{pm} \right)_{p \times p}^T \left[ y_{1m} y_{2m} \cdots y_{pm} \right]_{p \times (l-N)}^{-1} \left[ y_{1m} y_{2m} \cdots y_{pm} \right]_{p \times (l-N)}^T \left[ y_m \right]_{(l-N) \times 1} \end{aligned} \quad (32.17)$$

The real FRF is  $k_r H_{rm}(s)$ , the error series of response wave is

$$[y_m]_{(l-N) \times 1} - [y_{1m} \ y_{2m} \ \dots \ y_{pm}]_{(l-N) \times p} [k_1 \ k_2 \ \dots \ k_p]^T_{p \times 1} \tag{32.18}$$

The error series can be used to obtain the correcting FRF according to the model of Fig. 32.4, the process is similar to above, the energy of error series will decreased further. The new FRF is the original FRF adding correcting FRF.

The model of Figs. 32.3 and 32.4 will be applied alternatively. After four or five times iteration, the precise of FRF will very near to the best FRF evaluation.

Single point random impact shocking (SISO) and multi points' random impact shocking (MISO) both are very high efficient test methods [4]. Especially the test method of multi points' random impact shocking, is a new exciting method for MIMO test, deserves to be widely used. If in computing FRF, the new algorithm is used, the FRF preciseness will be improved greatly, the test time can also be shortened.

The algorithm introduced in Ref. [2] is named as the time domain iteration algorithm. The algorithm in this paper is named as the frequency domain iteration algorithm.

### 32.3 Examples

#### 32.3.1 A Real Test Example for Continuous Random Impact Shocking

An educational beam with both ends pinned connection, is illustrated as Fig. 32.6, to obtain the FRF between point A and point B.

Three exciting method are used.

The first method is multi trigger impacting. Exciting point is A, for hammer to knock in vertical direction. Accelerometer is fixed in point B for measuring vertical direction. Five times impacting are recorded. The sampling frequency is 12,800 Hz, FFT point number is 8192. The analyzing frequency range is 0–1,000 Hz. The analysis result is illustrated as Fig. 32.7. In the figure, the above part is FRF amplitude with log style, middle part is FRF phase, below part is coherence function and new coherence function. Fitting coefficient is fit = 99.92%. Error coefficient is error = 3.95%.

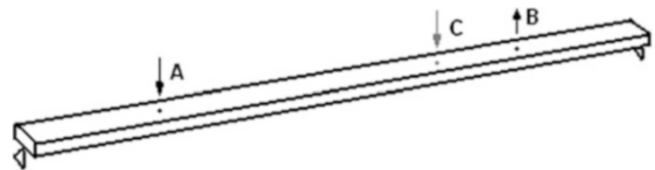


Fig. 32.6 Exciting points and response point

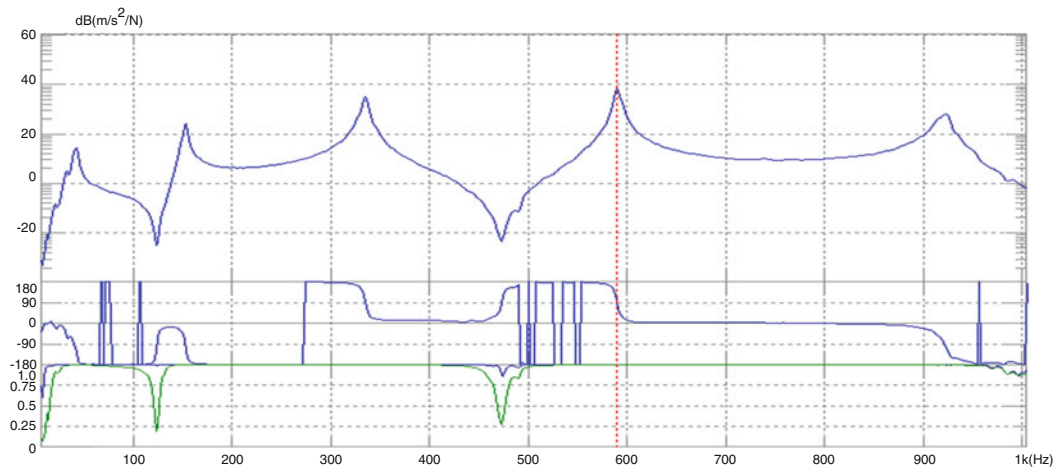
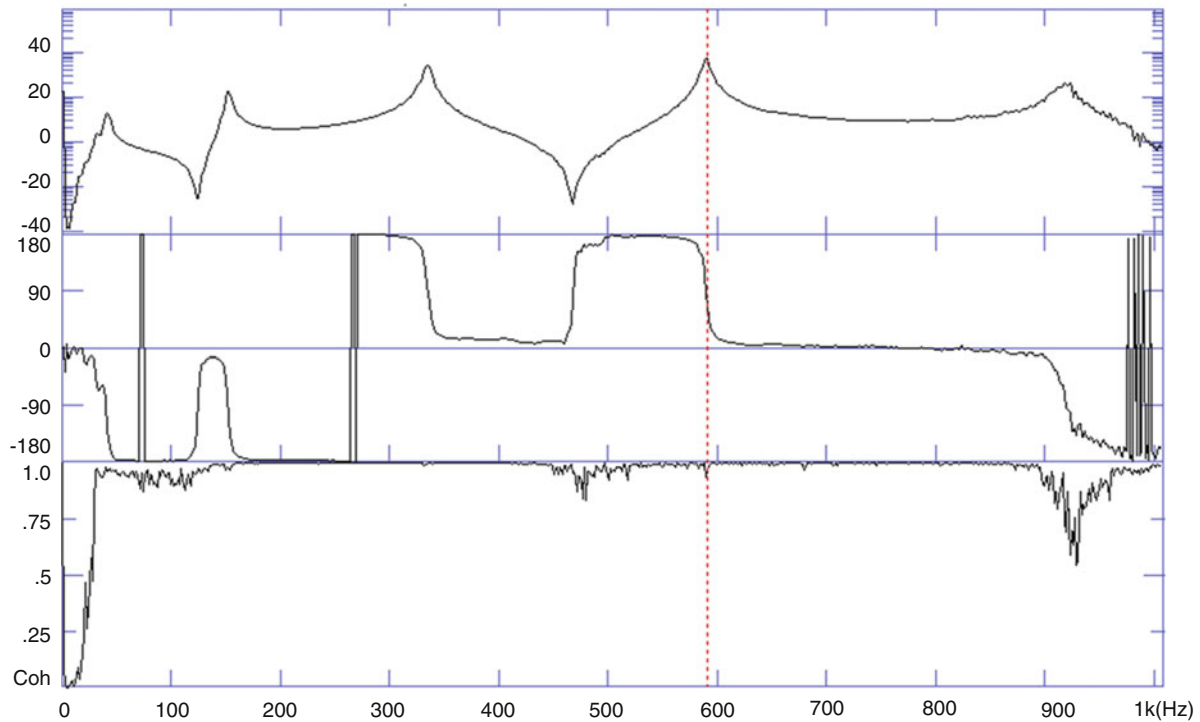


Fig. 32.7 FRF of multi trigger impacting



**Fig. 32.8** FRF of SISO random impacting

**Table 32.1** FRF analysis of SISO test with random impacting

Method	Fit (%)	Error (%)	Computation time (s)
Common	99.65	8.38	1.47
Frequency domain iteration	99.91	4.38	17.26
Time domain iteration	99.74	7.21	12.72

The second method is SISO, one point continuous random impacting. Exciting point is A, for harmer to knock. Accelerometer is fixed in point B. The sampling frequency is 12,800 Hz, sampling length is 51,200, 4 s. For traditional frequency domain averaging algorithm, FFT point number is 8192, adding Hanning window, overlap coefficient is 75%. The analyzing frequency range is 0–1,000 Hz. The analysis result is illustrated as Fig. 32.8. In the figure, the above part is FRF amplitude with log style, middle part is FRF phase, below part is new coherence function.

The results of three different FRF algorithms are listed in Table 32.1.

The third method is MISO, two points continuous random impacting. Exciting points are point A and point C, for two harmers to knock, but with different rhythms. Accelerometer is fixed in point B. Obtaining the FRF of AB and AC at the same time. The sampling frequency is 12,800 Hz, sampling length is 51,200, 4 s. For traditional frequency domain averaging algorithm, FFT point number is 8192, adding Hanning window, overlap coefficient is 75%. The analyzing frequency range is 0–1,000 Hz. The analysis result is illustrated as Fig. 32.9. In the figure, the above part is FRF amplitude with log style and FRF phase of AC, middle is FRF amplitude with log style and FRF phase of AB, below part is new coherence function.

The results of three different FRF algorithms are listed in Table 32.2.

From Tables 32.1 and 32.2, it can be found that for random impacting test, the frequency time domain iteration algorithm is effective in improve the preciseness of FRF evaluation, but the time domain iteration algorithm is not in good effective.

The peaks of FRF between point A and point B obtained by different test methods and algorithms are list in Table 32.3. Including the frequency, amplitude, phase and new coherence function of each peak.



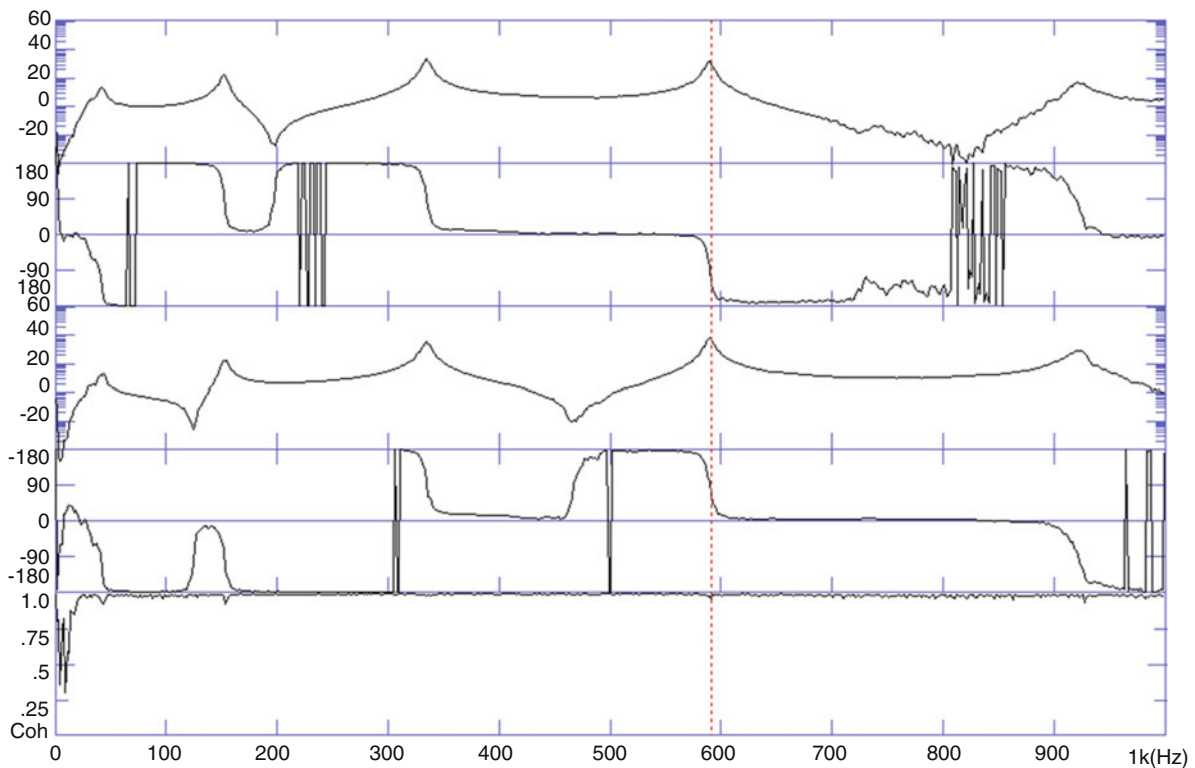


**Fig. 32.9** FRF of MISO random impacting

**Table 32.2** FRF analysis of MISO test with random impacting

Method	Fit (%)	Error (%)	Computation time (s)
Common	99.51	9.58	2.83
Frequency domain iteration	99.95	3.01	17.50
Time domain iteration	99.77	6.84	21.80

In Table 32.3, new method is frequency domain iteration algorithm, common method is frequency domain averaging. The result of new method is closer to multi trigger than common method. The new methods of SISO and MISO both are effective.

### 32.3.2 A Real SISO Test Example for Continuous Random Exciting

This example had been used in Ref. [2], here it is mainly used for comparing the frequency domain iteration algorithm with the time domain iteration algorithm.

Consider a model bridge frame in Fig. 32.10 under narrow band white noise excitation in the horizontal Y direction; the shaker in the vertical Z direction in Fig. 32.10 was not used. In modal testing, the structure was excited three times, and each time the input force and the responses of seven output points were measured. There are  $60 \times 1024 = 61440$  sampling points in the input and output data series. The sampling frequency is 512 Hz.

In Tables 32.4, 32.5 and 32.6, the traditional frequency domain averaging, frequency domain iteration, time domain iteration and least square devolution, four algorithms are compared for one point FRF computation. The FFT point number in Table 32.4 is 1024, in Table 32.5 is 2048 and in Table 32.6 is 4096.

**Table 32.3** The peaks in FRF between point A and point B

No.	Method	f (Hz)	H (m/ss/N)	Phase	New coherence
1	Multi trigger	42.1875	5.34	-126.60	1.0
	SISO common	42.1875	4.70	-125.01	0.98
	SISO new	42.1875	5.55	-127.02	1.0
	MIMO common	42.1875	5.30	-127.11	0.97
	MIMO new	42.1875	6.82	-119.24	0.99
2	Multi trigger	153.1250	16.09	-121.23	1.0
	SISO common	153.1250	14.45	-112.87	0.97
	SISO new	153.1250	17.12	-117.07	1.0
	MIMO common	153.1250	16.18	-112.77	0.98
	MIMO new	153.1250	17.44	-118.26	1.0
3	Multi trigger	334.3750	57.30	95.75	1.0
	SISO common	334.3750	50.20	99.70	0.99
	SISO new	334.3750	57.27	97.03	1.0
	MIMO common	334.3750	65.54	97.64	0.99
	MIMO new	334.3750	63.47	99.51	1.0
4	Multi trigger	589.0625	86.02	95.60	1.0
	SISO common	589.0625	76.03	93.17	0.99
	SISO new	589.0625	81.58	94.99	1.0
	MIMO common	589.0625	92.91	94.29	0.99
	MIMO new	589.0625	90.10	95.13	1.0
5	Multi trigger	920.3125	24.92	-94.45	0.99
	SISO common	920.3125	20.33	-87.45	0.75
	SISO new	920.3125	22.95	-92.11	0.75
	MIMO common	920.3125	28.43	-85.98	0.98
	MIMO new	920.3125	27.61	-89.07	0.98

From Tables 32.4, 32.5 and 32.6, it is obvious that the number of FFT is very important to the preciseness of FRF evaluation, the cause has been discussed in the beginning of introduction part. The number of FFT should be big enough, otherwise, even with the least square devolution algorithm, the error is still large. For narrow band white noise exciting, the effect of frequency iteration and time iteration are almost the same. Both iteration algorithms can greatly increase the preciseness of FRF evaluation, with the computation time far less than the least square devolution algorithm.

## 32.4 Conclusions

For random continuous exciting test, using the traditional frequency domain averaging method without considering the initial response to obtain FRF, the error is large. The least square devolution in time domain can obtain the most precise FRF evaluation, but involved time-consuming inversion of matrix with large size, is unpractical.

The preciseness of FRF evaluation can be quantified by comparing the theoretical and measured response wave fitting extent. The coherence function can also be defined by this way.

The frequency domain iteration algorithm to compute FRF put forward here, with 2 frames force wave, 1 frame response wave, aligned in right end, as the base model, can take into account the initial response, the computation process is concise.

The random impacting, including MIMO, is practical. For traditional frequency domain averaging algorithm, only if the FFT point number is big enough, and the data length is long enough, the preciseness of FRF can be ensured. If the new algorithm of this paper is used, the preciseness of FRF can reach the level of multi trigger impacting test. Here the effect of time domain iteration is not so well as the frequency domain iteration.

For continuous white noise exciting, both iteration algorithms are effective. The preciseness of iteration algorithms is very near to least square devolution algorithm, but the computation time can be shorten 10 ~ 100 times.

**Fig. 32.10** (a) A model bridge frame excited by a horizontal shaker, and (b) the measurement setup

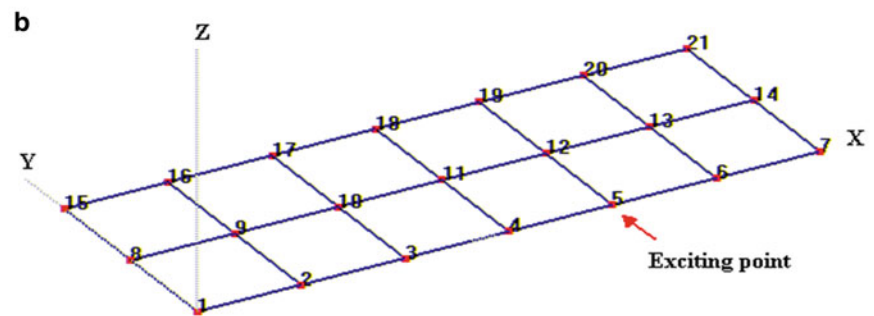


**Table 32.4** FFT number 1024, points 60 \* 1024, overlap 50%, averaging times 117, Adding Hanning window

Algorithm	Fit (%)	Error (%)	Time (s)
Common	84.82	62.46	0.297
Frequency iteration	95.01	32.83	2.719
Time iteration	95.38	31.51	2.046
Devolution	95.75	30.14	66.0

**Table 32.5** FFT number 2048, points 30 \* 2048, overlap 50%, averaging times 57, Adding Hanning window

Algorithm	Fit (%)	Error (%)	Time (s)
Common	88.87	52.60	0.531
Frequency iteration	98.35	18.42	5.156
Time iteration	98.35	18.35	3.868
Devolution	98.57	17.09	230.406

**Table 32.6** FFT number 4096, points 5 \* 4096, overlap 50%, averaging times 27, Adding Hanning window

Algorithm	Fit (%)	Error (%)	Time (s)
Common	92.06	42.43	1.000
Frequency iteration	98.87	15.14	9.984
Time iteration	98.87	15.16	7.641
Devolution	99.04	13.98	830.578

**References**

1. Fladung W, Rost R (1997) Application and correction of the exponential window for frequency response functions. *Mech Syst Signal Process* 11(1):23–36
2. Liu JM, Zhu WD, Lu QH, Ren GX (2011) An efficient iterative algorithm for accurately calculating impulse response functions in modal testing. *J Vib Acoust* 133(6). doi:10.1115/1.4005221
3. Heylen W, Lammens S, Sas P (1998) *Modal analysis theory and testing*. Katholieke Universiteit Leuven, Leuven
4. Napolitano KL, Yoder NC, Brillhart RD (2012) A comparison of multiple impact testing methods. In: *Proceeding of the SEM IMAC XXX conference*, Jacksonville, FL, 30 Jan –2 Feb 2012

# Chapter 33

## Development of Full Space System Model Modes from Expansion of Reduced Order Component Modal Information

Christopher Nonis, Louis Thibault, Timothy Marinone, and Peter Avitabile

**Abstract** Model reduction is a technique commonly used to reduce the computation time of structural dynamic models. The results of the reduced model can then be expanded to full space using the transformation matrix developed in the reduction process. This work focuses on expanding the mode shapes of system models that are comprised of reduced component models. Typically, this expansion requires the full space system model to be computed in order to obtain the system model transformation matrix needed to perform the expansion. Computing the full space system model to determine the expansion matrix does not save computation time and therefore defeats the purpose of using model reduction.

This paper proposes using the expansion matrices of the individual components to expand the assembled system model modes. In this work, System Equivalent Reduction Expansion Process (SEREP) is used for reduction and expansion. The accuracy of the expanded system model is shown to be dependent on the modes retained in the reduced component models. Recent work on Variability Improvement of Key Inaccurate Node Groups (VIKING) has shown that over specifying the number of modes used in the reduction/expansion process that span the space of the system model modes significantly improves the results. The VIKING technique is the basis for the expansion process developed in this work. Multiple analytical cases are presented to show how the selection of component modes affects the expansion results. The analytical cases demonstrate that accurate system model expansion results can be obtained when a sufficient set of component modes that span the space of the system model modes are used.

**Keywords** Expansion • SEREP • Component model • System model • Reduction

### Nomenclature

SEREP	System Equivalent Reduction Expansion Process
VIKING	Variability Improvement of Key Inaccurate Node Groups
DOF	Degrees of Freedom
SDM	Structural Dynamic Modification
MAC	Modal Assurance Criterion
POC	Pseudo Orthogonality Check

### 33.1 Introduction

Model reduction is a commonly used tool to reduce the computation time of structural dynamic models. The purpose of model reduction is to lower the number of degrees of freedom, DOF, while preserving the dynamic characteristics. After a reduced model simulation is computed, the results can be expanded back to the full number of degrees of freedom. There are

---

C. Nonis (✉) • L. Thibault • T. Marinone • P. Avitabile

Structural Dynamics and Acoustic Systems Laboratory, University of Massachusetts Lowell, One University Avenue, Lowell, MA 01854, USA  
e-mail: [chrisnonis@gmail.com](mailto:chrisnonis@gmail.com); [louishtibault@gmail.com](mailto:louishtibault@gmail.com); [timothy.marinone@gmail.com](mailto:timothy.marinone@gmail.com); [peter\\_avitabile@uml.edu](mailto:peter_avitabile@uml.edu)

numerous schemes for the reduction/expansion process. In this paper, System Equivalent Reduction Expansion Process (SEREP) [1] is used because this technique exactly preserves the dynamics of the model regardless of which degrees of freedom are retained.

This paper investigates how SEREP can be used to expand system models that are comprised of reduced component models. To expand this model the traditional way using SEREP, the system model transformation matrix would be used. To find the system model transformation matrix, the full DOF mode shapes must be computed for the full system model. This procedure is counterproductive because the purpose of model reduction is to avoid computing the full DOF model. This paper shows that the system modes can be expanded using the transformation matrices of the original unmodified component modes. To perform the expansion, the system shapes are separated into component shapes and expanded on a component by component basis using the component transformation matrices.

This expansion technique has been developed from Variability Improvement of Key Inaccurate Node Groups (VIKING) [2]. VIKING is a technique that was developed to expand experimental mode shapes using a finite element model that may not be perfectly correlated to test data. The VIKING paper [2] showed that over specifying the number of modes used in the reduction/expansion process that span the space of the system model modes significantly improves the expansion results. Therefore, if the modes used to reduce the component span the space of the component's shapes in the system modes, accurate results can be achieved. The error in the expanded shapes results from mode truncation, not from the expansion process. To prove this, the expanded shapes are compared to a full space Structural Dynamic Modification (SDM) model that uses the same modes. In the full space SDM model, expansion error is not an issue because the model is computed at full space. The reduced/expanded shapes were shown to be the equivalent to the SDM model, which proves the expansion is exact and truncation error is the real problem.

## 33.2 Theoretical Background

### 33.2.1 Equations of Motion for Multiple Degree of Freedom System

The general equation of motion for a multiple degree of freedom system written in matrix form is

$$[M_1] \{\ddot{x}\} + [C_1] \{\dot{x}\} + [K_1] \{x\} = \{F(t)\} \quad (33.1)$$

Assuming proportional damping, the eigensolution is

$$[[K_1] - \lambda [M_1]] \{x\} = \{0\} \quad (33.2)$$

The results of the eigensolution yield the eigenvalues (natural frequencies) and eigenvectors (mode shapes). The eigenvectors are arranged in column fashion to form the modal matrix  $[U_1]$ . Usually a subset of modes is included in the modal matrix to save computation time. Exclusion of modes results in truncation error which can be serious if key modes are excluded. Truncation error will be discussed in further detail in the structural dynamic modification section.

The physical system can be transformed to modal space using the modal matrix as

$$[U_1]^T [M_1] [U_1] \{\ddot{p}_1\} + [U_1]^T [K_1] [U_1] \{p_1\} = [U_1]^T \{F(t)\} \quad (33.3)$$

In modal space,  $p$  is the principal coordinate.

Scaling to unit modal mass yields

$$[I_1] \{\ddot{p}_1\} + [\Omega_1^2] \{p_1\} = [U_1^n]^T \{F(t)\} \quad (33.4)$$

where  $[I_1]$  is the identity matrix and  $\Omega_1$  is the diagonal natural frequency matrix. More detailed information on the equations of motion of a multiple degree of freedom system is contained in *Twenty Years of Structural Dynamic Modification – A Review* [3].

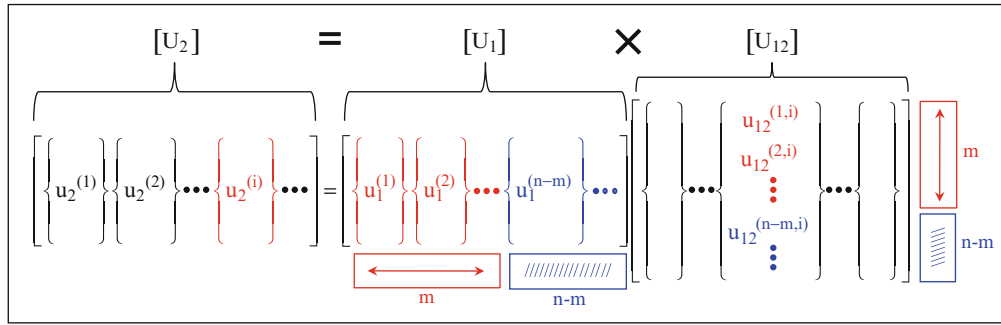


Fig. 33.1 Structural dynamic modification, mode contribution identified using  $U_{12}$  [2]

### 33.2.2 Structural Dynamic Modification

Structural Dynamic Modification, SDM, is a technique that uses the original mode shapes and natural frequencies of a system to estimate the dynamic characteristics after a modification of mass and/or stiffness is made. First, the change of mass and stiffness are transformed to modal space as shown

$$[\Delta \bar{M}_{12}] = [U_1]^T [\Delta M_{12}] [U_1] \tag{33.5}$$

$$[\Delta \bar{K}_{12}] = [U_1]^T [\Delta K_{12}] [U_1] \tag{33.6}$$

The modal space mass and stiffness changes are added to the original modal space equations to give

$$\left[ \begin{bmatrix} \ddots & & \\ & \bar{M}_1 & \\ & & \ddots \end{bmatrix} + [\Delta \bar{M}_{12}] \right] \{\ddot{p}_1\} + \left[ \begin{bmatrix} \ddots & & \\ & \bar{K}_1 & \\ & & \ddots \end{bmatrix} + [\Delta \bar{K}_{12}] \right] \{p_1\} = [0] \tag{33.7}$$

The eigensolution of the modified modal space model is computed and the resulting eigenvalues are the new frequencies of the system. The resulting eigenvector matrix is the  $[U_{12}]$  matrix, which is used to transform the original modes to the new modes is given as

$$[U_2] = [U_1] [U_{12}] \tag{33.8}$$

The new mode shapes are  $[U_2]$ . The new mode shapes are formed from linear combinations of the original mode shapes. The  $[U_{12}]$  matrix shows how much each of the  $[U_1]$  modes contributes to forming the new modes (Fig. 33.1).

Unless  $[U_1]$  includes all of the original system modes, there will be truncation error due to the missing modes. The severity of truncation error depends on which modes are missing from  $[U_1]$ . Some original system modes are more important than others for forming the new modes. A  $[U_{12}]$  calculated using all the original system modes would show the correct contributions of all modes. More detailed information on SDM is contained in Twenty Years of Structural Dynamic Modification – A Review [3].

### 33.2.3 Physical Space System Modeling

To form a physical system model, the mass and stiffness matrices of each component are assembled in stacked form into the system mass and stiffness matrices. To account for the static and dynamic coupling between components, mass and stiffness terms are added to the off diagonal, linking the corresponding degrees of freedom

$$\begin{bmatrix} [M_A] & \\ & [M_B] \end{bmatrix} \{\ddot{x}\} + \begin{bmatrix} [K_A] & \cdots & K_{tie} \\ & \ddots & \vdots \\ & & [K_B] \\ K_{tie} & \cdots & & \end{bmatrix} \{x\} = F(t) \quad (33.9)$$

The eigensolution of the mass and stiffness system matrices yields the system's natural frequencies and modes shapes. The mode shapes of each component are arranged in the eigenvectors as

$$[U_{sys}] = \begin{bmatrix} U_A \\ U_B \end{bmatrix} \quad (33.10)$$

### 33.2.4 General Reduction/Expansion Technique

Model reduction is used to reduce the number of degrees of freedom in an analytical model to reduce computing time while attempting to preserve the full DOF characteristics. The relationship between the full space and reduced space model can be written as

$$\{X_n\} = \begin{Bmatrix} X_a \\ X_d \end{Bmatrix} = [T] \{X_a\} \quad (33.11)$$

where subscript 'n' signifies the full set of DOF (n DOF), 'a' signifies the reduced set of DOF (a DOF) and 'd' is the deleted DOF. The transformation matrix [T] relates the full set of DOF to the reduced set of DOF.

The transformation matrix is used to reduce the mass and stiffness matrices as

$$\begin{aligned} [M_a] &= [T]^T [M_n] [T] \\ [K_a] &= [T]^T [K_n] [T] \end{aligned} \quad (33.12)$$

The eigensolution of these 'a' set mass and stiffness matrices are the modes of the reduced model. These modes can be expanded back to full space using the transformation matrix

$$[U_n] = [T] [U_a] \quad (33.13)$$

If an optimal 'a' set is not selected when using methods such as Guyan Condensation [4] or Improved Reduced System Technique [5], the reduced model may not perfectly preserve the dynamics of the full space model. If System Equivalent Reduction Expansion Process (SEREP) is used, the dynamics of selected modes will be perfectly preserved regardless of the 'a' set selected.

### 33.2.5 System Equivalent Reduction Expansion Process (SEREP)

The SEREP modal transformation relies on the partitioning of the modal equations representing the system DOFs relative to the modal DOFs [1]. The SEREP technique utilizes the mode shapes from a full finite element solution to map to the limited set of master DOF. SEREP is not performed to achieve efficiency in the solution but rather is intended to perform an accurate mapping matrix for the transformation. The SEREP transformation matrix is formed using a subset of modes at full space and reduced space as

$$[T_u] = [U_n] [U_a]^g \quad (33.14)$$

When the SEREP transformation matrix is used for model reduction/expansion as outlined in the previous section, the reduced model perfectly preserves the full space dynamics of the modes in  $[U_n]$  [1].

### 33.2.6 Modal Assurance Criterion (MAC)

Modal Assurance Criterion is a correlation tool commonly used to compare mode shapes. MAC compares two vectors ( $u_i$  and  $e_j$ ) and calculates a value from 0 to 1 that quantifies the degree of similarity between the vectors. The equation is

$$MAC_{ij} = \frac{\left[ \{u_i\}^T \{e_j\} \right]^2}{\left[ \{u_i\}^T \{u_i\} \right] \left[ \{e_j\}^T \{e_j\} \right]} \quad (33.15)$$

A MAC value of 1 signifies perfect correlation and 0 signifies no correlation.

### 33.2.7 Pseudo Orthogonality Check

Pseudo Orthogonality Check is a mass weighted orthogonality tool used to compare mode shapes and is given as

$$POC = [U]^T [M] [E] \quad (33.16)$$

The POC is mass weighted. If the shapes are scaled to unit modal mass, POC ranges from 0 to 1, similar to MAC.

## 33.3 Methodology

The procedure for expanding reduced system models using limited sets of component modal information is four steps as follows.

- Reduce models of system components individually using SEREP. Connection degrees of freedom must be retained during reduction in all cases for the assembly process. The modes selected for reduction are very important for minimizing truncation error (Fig. 33.2).
- Assemble component mass and stiffness matrices into system mass and stiffness matrices and link connection DOF (Fig. 33.3).
- Perform eigensolution on system mass and stiffness matrices to calculate frequencies and mode shapes (Fig. 33.4).
- Partition the system mode shapes into matrices of shape information for each component.

Use the SEREP transformation matrices of each component to expand the component shape matrices to full space (Fig. 33.5).

The results of this expansion process are the system mode shapes at the full set of DOF whose accuracy is only affected by mode truncation error that occurred during the reduction process. This will be demonstrated by the following cases.

#### Component A:

$$\text{SEREP Reduction} \\ [M_{aA}] = [T_{uA}]^T [M_{nA}] [T_{uA}]$$

$$[K_{aA}] = [T_{uA}]^T [K_{nA}] [T_{uA}]$$

#### Component B:

$$\text{SEREP Reduction} \\ [M_{aB}] = [T_{uB}]^T [M_{nB}] [T_{uB}]$$

$$[K_{aB}] = [T_{uB}]^T [K_{nB}] [T_{uB}]$$

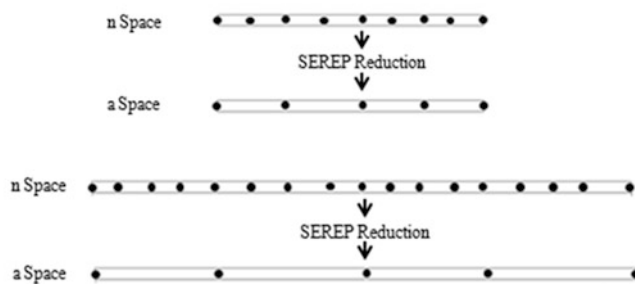
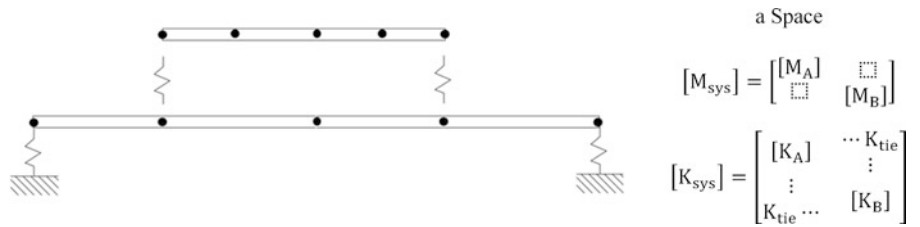


Fig. 33.2 Reduce system components using SEREP



**Fig. 33.3** Assemble reduced components to form system



**Fig. 33.4** Perform eigensolution to calculate frequencies and mode shapes

yields:

$$\begin{bmatrix} [K_A] & \dots & K_{tie} \\ \vdots & & \vdots \\ K_{tie} & \dots & [K_B] \end{bmatrix} - \lambda \begin{bmatrix} [M_A] & \dots \\ \vdots & [M_B] \end{bmatrix} \{x\} = \{0\}$$

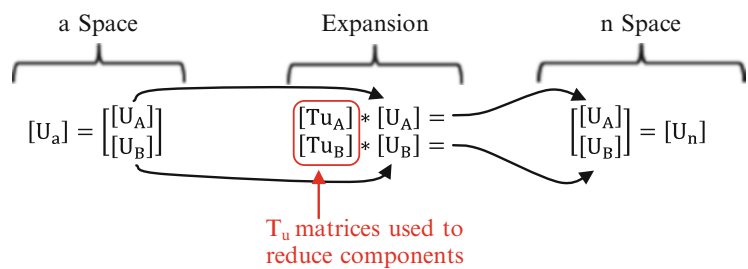
Natural Frequencies

$$\begin{bmatrix} \omega_1^2 & \dots & \dots \\ \dots & \omega_2^2 & \dots \\ \dots & \dots & \ddots \end{bmatrix}$$

System Mode Shapes

$$[U_a] = \begin{bmatrix} [U_A] \\ [U_B] \end{bmatrix}$$

**Fig. 33.5** Expand reduced system shapes using component transformation matrices



### 33.4 Model Description

Three simple beam models were used to demonstrate this expansion technique. All of the models were two beam systems connected in various configurations. The beams were modeled using 2D Euler Bernoulli beam elements. Only bending modes were calculated. Figure 33.6 shows the two beam model in the three configurations at reduced space. In all three configurations, the bottom beam is connected to ground at each end by a 1,000 lb/in. translational spring. In configurations #1 and #2, the beams are connected with two translation springs. In Configuration #3 the beams are connected with translation and rotational springs. Details of the model are shown in Table 33.1.

### 33.5 Cases Studied

In order to evaluate the expansion methodology, each of the specific models were developed at full space to obtain a solution for reference for the models developed. All cases were reduced and expanded following the procedure outlined in the methodology section. For comparison, a full space physical model and a structural dynamic modification model were also developed and compared. The SDM model is comprised of the full DOF using the same modes used for reduction. MAC and POC are used to compare mode shapes. The specific cases studied are:

- Case 1: Five Modes from Component A & Five Modes from Component B with Symmetric Mounting
- Case 2: Ten Modes from Component A & 10 Modes from Component B with Symmetric Mounting
- Case 3: Five Modes from Component A & Five Modes from Component B with Asymmetric Mounting
- Case 4: Seven Modes from Component A & Seven Modes from Component B with Translation and Rotational Mounting

**Fig. 33.6** Configurations of two beam system model

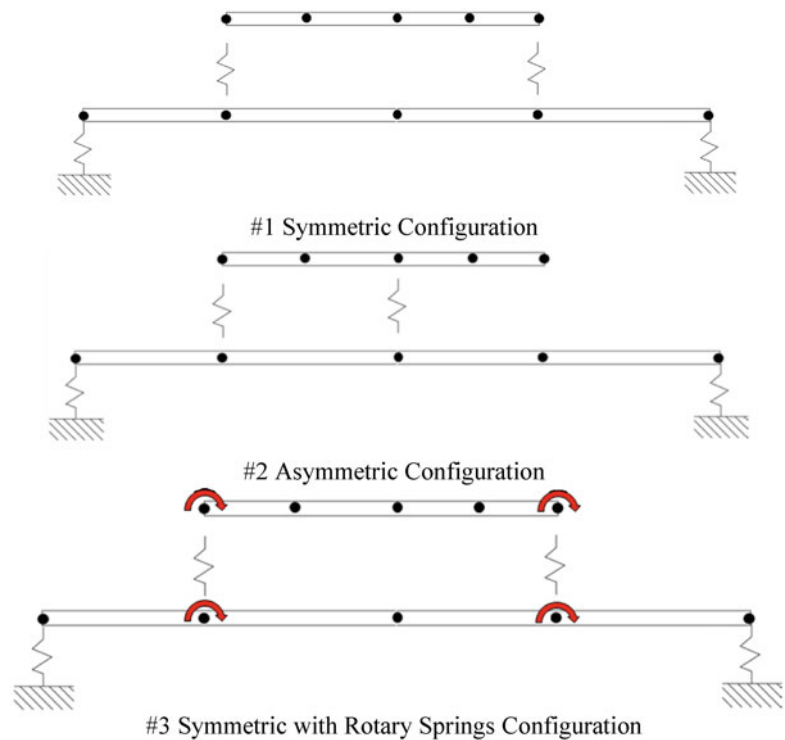


**Table 33.1** Two beam system model parameters

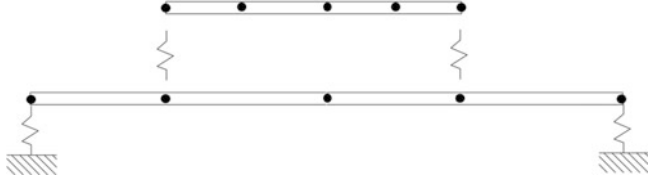
Parameter	Top beam	Bottom beam
Length	50 in.	140 in.
Height	1.5 in.	1.5 in.
Width	3 in.	3 in.
Wall thickness	3/16 in.	3/16 in.
Area moment of inertia	0.5323 in. <sup>4</sup>	0.5323 in. <sup>4</sup>
Elastic modulus	10*10 <sup>6</sup> psi	10*10 <sup>6</sup> psi
Density	0.1 lbm in. <sup>3</sup>	0.1 lbm in. <sup>3</sup>
Nodes	15	15
Beam elements	14	14
Full space DOF	30	30
Connector spring stiffness	1*10 <sup>6</sup> lbf in.	
Connector rotary spring stiffness (for config. #3)	1*10 <sup>6</sup> in.-lbf rad	
Ground support spring stiffness	1,000 lbf/in.	

These cases are described in the following sections.

### Case 1: Five Modes from Component A & Five Modes from Component B with Symmetric Mounting

In Case #1, both beams were reduced to five translation DOF using the first five modes of each component beam to form the system model. The expanded results are compared to the full space physical and SDM models in Table 33.2 and Fig. 33.7. The table is broken down into the left and right sides as discussed next; the left side compares the full space physical system model results and the right side presents comparison checks to confirm accuracy of results.

On the left side, the full space system model lists the results obtained from a full space physical model and is referred to as the reference solution. Based on the  $[U_{12}]$  matrix generated for this case (not shown for brevity), only six system modes are expected to be accurately; This is due to the fact that the five component modes of each component only accurately span that space of the system model. The  $[U_{12}]$  from the structural dynamic modification system modeling process identifies this and these results are anticipated. Table 33.2 shows that the first six system modes are accurately represented by the structural dynamic modification system model as evidenced by the accurate frequency prediction ( $< 2.00\%$  difference). The reduced

**Table 33.2** Case 1, expanded results compared to full space physical and SDM model**Case 1:**


Mode	Full space system model comparison					Structural dynamic modification comparison				
	Frequency (Hz)					Frequency (Hz)				
	Full physical 'n' space	Expanded SDM from 'a' space	% Diff	MAC	POC	SDM at 'n' space	Expanded SDM from 'a' space	% Diff	MAC	POC
1	7.3	7.2	0.01	1.000	1.000	7.2	7.2	0.00	1.000	1.000
2	29.5	29.5	0.02	1.000	1.000	29.5	29.5	0.00	1.000	1.000
3	58.7	58.7	0.01	1.000	1.000	58.7	58.7	0.00	1.000	1.000
4	81.7	83.36	2.00	0.997	0.998	83.36	83.36	0.00	1.000	1.000
5	83.3	83.37	0.10	1.000	0.999	83.37	83.37	0.00	1.000	1.000
6	132.8	132.8	0.00	1.000	0.999	132.8	132.8	0.00	1.000	1.000
7	191.8	316.4	65.0	0.073	0.253	316.4	316.4	0.00	1.000	1.000
8	273.8	680.8	148	0.064	0.252	680.8	680.8	0.00	1.000	1.000
9	306.2	4,461.2	1,356	0.002	0.058	4,461.2	4,461.2	0.00	1.000	1.000
10	398.7	4,977.3	1,148	0.000	0.000	4,977.3	4,977.3	0.00	1.000	1.000

order system model mode shapes are expanded to full space using the original unmodified individual component modes as described in this paper. These expanded system model modes are then checked with the full space reference model using both MAC and POC; these two columns of values on the left side of the table clearly show that the expansion of the reduced order system model using the original unmodified component modes are an accurate representation of the mode shapes. Any modes beyond the six system model modes are not accurately predicted because the modes of the component models do not span the space of the higher order system modes and therefore do not accurately predict those frequencies.

The results on the right side of the table are presented as a check to make sure that the results are as expected. The SDM results are those obtained using the full space modal model and are compared to the expanded results; these two results must produce identical results for both the accurately predicted system modes as well as the truncated higher frequency results. The MAC and POC also substantiate this. This perfect correlation shows there is no distortion when expanding from a space to n space; the only source of error for the modal models is mode truncation.

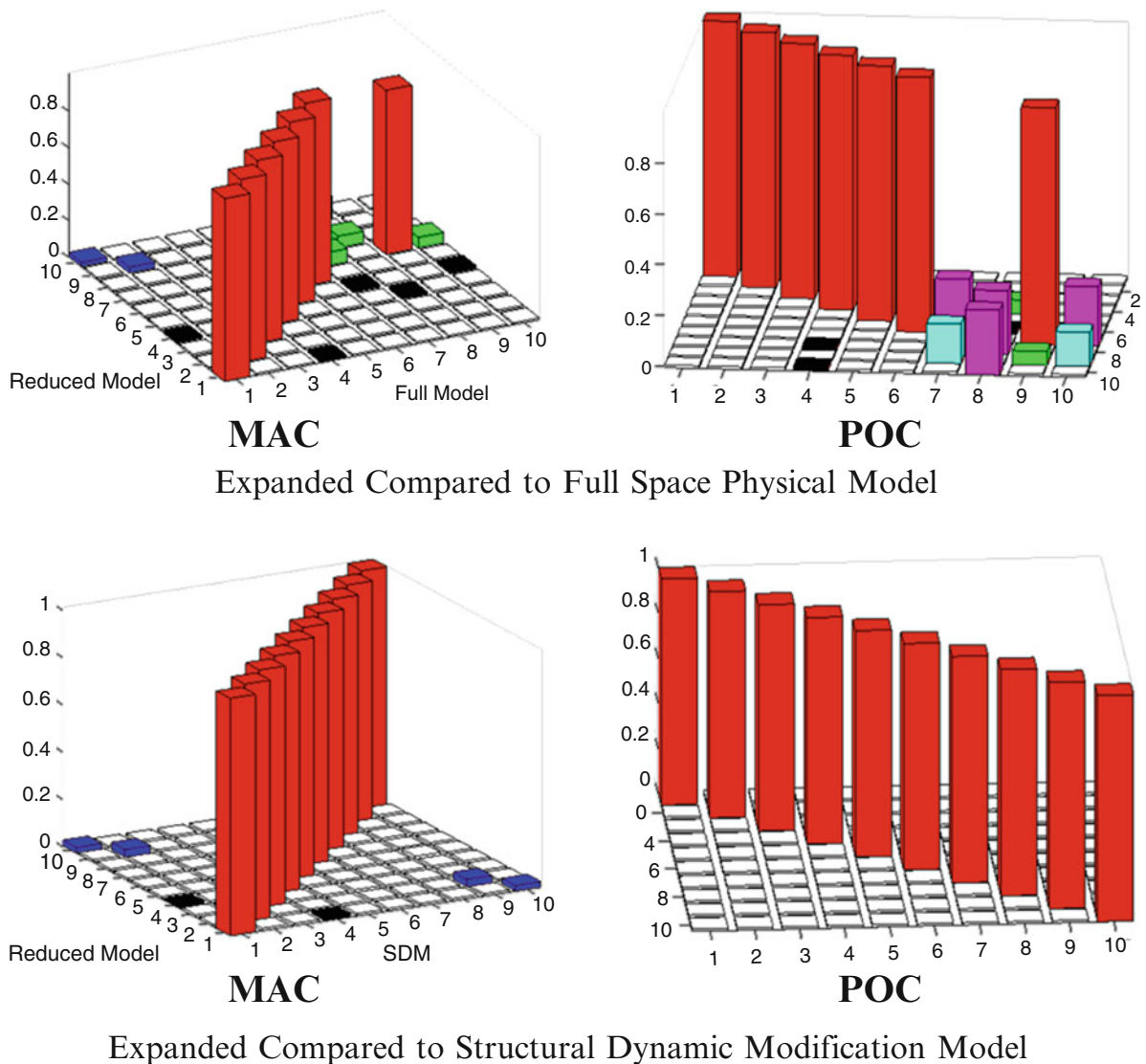
The results of this case clearly show that if the original unmodified component modes are sufficient to span the space of the reduced order system model to predict accurate system model frequencies, then these same component modes are also sufficient to be used as expansion matrices to obtain the full system model combined response; but this is only true for the system modes that can be accurately represented by the individual component modes.

### Case 2: 10 Modes from Component A & 10 Modes from Component B with Symmetric Mounting

In Case 1, the first six system modes were accurately represented by five component modes for each individual component. These five component modes are only capable of predicting the first six system model modes accurately. To show that truncation limits the number of accurate system modes, Case 2 uses 10 component modes for each of the individual components and based on the  $[U_{12}]$  then the system model can only predict the first 12 system model modes accurately. Table 33.3 and Fig. 33.8 show these results. Case 2 shows that more system modes are accurately predicted due to the inclusion of more component modes to describe each reduced order component.

### Case 3: Five Modes from Component A & Five Modes from Component B with Asymmetric Mounting

Similar to Case 1, the beams were reduced to five translation DOF using the first five modes but the main difference lies in the fact that the components were connected at different locations to make an asymmetric configuration; this was done

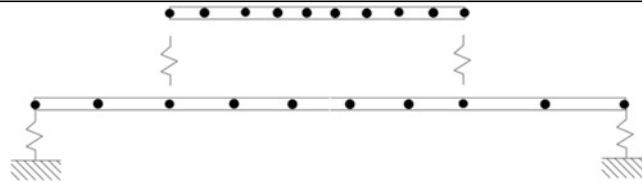


**Fig. 33.7** Case 1, expanded results compared to full space model and SDM

as an additional case to assure that accurate results could still be obtained. Expanded results are compared to the full space physical and SDM models in Table 33.4 and Fig. 33.9 and show expected results. All the same observations for Case 1 can be stated for this case and are not repeated here.

**Case 4: Seven Modes from Component A & Seven Modes from Component B with Translation and Rotational Mounting**

For Case 4, both beams were reduced to seven DOF using the first seven modes of each beam. The same five translation DOF are used plus rotational DOF at each connection point. This case was performed to show that the methodology is not restricted to only translational connection strategies. The expanded results are compared to the physical and SDM model results in Table 33.5 and Fig. 33.10. Again, as in all the previous cases, the same comments and observations can be made for this case.

**Table 33.3** Case 2, expanded results compared to full space physical and SDM model**Case 2:**

Mode	Full space system model comparison					Structural dynamic modification comparison				
	Frequency (Hz)					Frequency (Hz)				
	Full physical 'n' space	Expanded SDM from 'a' space	% Diff	MAC	POC	SDM at 'n' space	Expanded SDM from 'a' space	% Diff	MAC	POC
1	7.3	7.3	0.00	1.000	1.000	7.3	7.3	0.00	1.000	1.000
2	29.5	29.5	0.00	1.000	1.000	29.5	29.5	0.00	1.000	1.000
3	58.7	58.7	0.00	1.000	1.000	58.7	58.7	0.00	1.000	1.000
4	81.7	81.9	0.21	1.000	1.000	81.9	81.9	0.00	1.000	1.000
5	83.3	83.3	0.01	1.000	1.000	83.3	83.3	0.00	1.000	1.000
6	132.8	132.8	0.00	1.000	1.000	132.8	132.8	0.00	1.000	1.000
7	191.8	191.8	0.03	1.000	1.000	191.8	191.8	0.00	1.000	1.000
8	273.8	273.9	0.06	1.000	1.000	273.9	273.9	0.00	1.000	1.000
9	306.2	307.6	0.44	1.000	1.000	307.6	307.6	0.00	1.000	1.000
10	398.7	398.7	0.01	1.000	1.000	398.7	398.7	0.00	1.000	1.000
11	514.2	515.0	0.15	1.000	0.999	515.0	515.0	0.00	1.000	1.000
12	649.0	649.7	0.10	0.999	1.000	649.7	649.7	0.00	1.000	1.000
13	674.4	694.7	3.02	0.945	0.967	694.7	694.7	0.00	1.000	1.000
14	840.4	1,206.6	43.6	0.000	0.000	1,206.6	1,206.6	0.00	1.000	1.000
15	1,011.6	1,837.4	81.6	0.000	0.000	1,837.4	1,837.4	0.00	1.000	1.000

### 33.5.1 Observations for All Cases

Results of all the case studies shows that expanding system model modes using the component transformation matrices yields exactly the same results as a full space structural dynamic modification model, assuming the same modes are used.

In the full space SDM model, mode truncation is the only source of error. There is no expansion error because the SDM is done at full space. The SDM and expansion results were shown to be equivalent; therefore mode truncation is the only source of error in this technique. Truncation error is introduced when reducing the component models.

Comparison to the full space model shows that lower order modes can be calculated accurately; higher order modes are significantly affected by mode truncation and cannot be predicted accurately, as expected. If more modes were desired, more modes would need to be used in the reduction of the components.

**Case 1: Five Modes from Component A & Five Modes from Component B with Symmetric Mounting**

**Case 2: 10 Modes from Component A & 10 Modes from Component B with Symmetric Mounting**

**Case 3: Five Modes from Component A & Five Modes from Component B with Asymmetric Mounting**

**Case 4: Seven Modes from Component A & Seven Modes from Component B with Translation and Rotational Mounting**

## 33.6 Conclusion

The technique proposed in this work uses the expansion matrices of uncoupled component models to expand the modes of an assembled system model. Expansion to the full space assembled system can be performed to define full space characteristics.

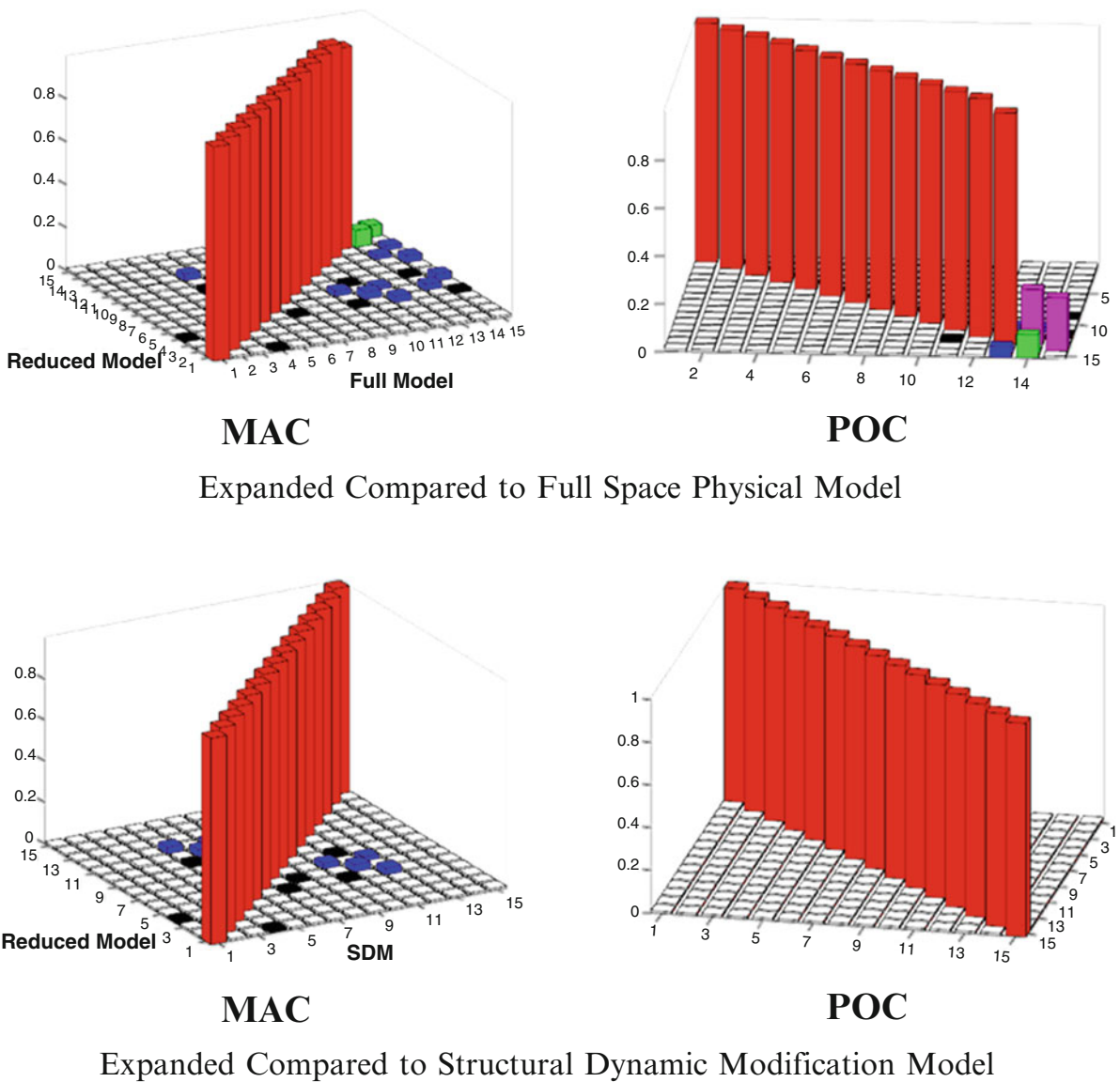


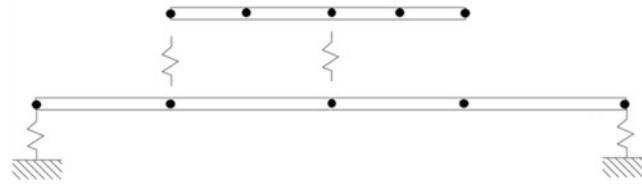
**Fig. 33.8** Case 2, expanded results compared to full space model and SDM

Several beam system model cases were presented to demonstrate the validity of the expansion approach developed in this work. This approach works provided that the original unmodified component modes retained in the reduction process are sufficient to span the space of the final system model in order to obtain accurate system modes. The expansion matrices developed in the reduction process, which contains the same modal information as in the reduced models, are also sufficient to be used as expansion matrices to obtain full system model characteristics; but this is only true for the system modes that can be accurately represented by the individual component modes. This allows for full system level identification of modal characteristics without the need for developing the expansion matrices using the fully assembled full space system model.

**Acknowledgements** Some of the work presented herein was partially funded by Air Force Research Laboratory Award No. FA8651-10-1-0009 “Development of Dynamic Response Modeling Techniques for Linear Modal Components”. Any opinions, findings, and conclusions or recommendations expressed in this material are those of the authors and do not necessarily reflect the views of the particular funding agency. The authors are grateful for the support obtained.

**Table 33.4** Case 3, expanded results compared to full space physical and SDM model

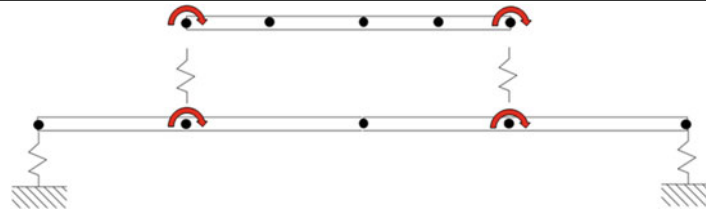
**Case 3:**



Mode	Full space system model comparison					Structural dynamic modification comparison				
	Frequency (Hz)					Frequency (Hz)				
	Full physical 'n' space	Expanded SDM from 'a' space	% Diff	MAC	POC	SDM at 'n' space	Expanded SDM from 'a' space	% Diff	MAC	POC
1	6.8	6.8	0.02	1.000	1.000	6.8	6.8	0.00	1.000	1.000
2	29.1	29.2	0.16	0.999	0.999	29.2	29.2	0.00	1.000	1.000
3	47.6	48.1	1.00	0.999	0.999	48.1	48.1	0.00	1.000	1.000
4	73.1	74.4	1.74	0.995	0.997	74.4	74.4	0.00	1.000	1.000
5	90.8	91.5	0.74	0.994	0.998	91.5	91.5	0.00	1.000	1.000
6	134.1	134.4	0.26	0.998	0.999	134.4	134.4	0.00	1.000	1.000
7	196.2	371.2	89.18	0.017	0.115	371.2	371.2	0.00	1.000	1.000
8	265.5	648.3	144.16	0.055	0.180	648.3	648.3	0.00	1.000	1.000
9	358.0	2,762.3	671.67	0.005	0.061	2,762.3	2,762.3	0.00	1.000	1.000
10	399.9	4,766.9	1,092.13	0.019	0.079	4,766.9	4,766.9	0.00	1.000	1.000

**Table 33.5** Case 4, expanded results compared to full space physical and SDM model

**Case 4:**



Mode	Full space system model comparison					Structural dynamic modification comparison				
	Frequency (Hz)					Frequency (Hz)				
	Full physical 'n' space	Expanded SDM from 'a' space	% Diff	MAC	POC	SDM at 'n' space	Expanded SDM from 'a' space	% Diff	MAC	POC
1	8.3	8.4	1.7	1.000	1.000	8.4	8.4	0.00	1.000	1.000
2	30.4	30.8	1.1	1.000	1.000	30.8	30.8	0.00	1.000	1.000
3	60.4	60.6	0.3	1.000	1.000	60.6	60.6	0.00	1.000	1.000
4	86.4	87.9	1.7	0.999	0.999	87.9	87.9	0.00	1.000	1.000
5	131.0	132.2	0.9	0.918	0.954	132.2	132.2	0.00	1.000	1.000
6	140.5	165.0	17.5	0.877	0.948	165.0	165.0	0.00	1.000	1.000
7	197.2	201.0	2.0	0.994	0.997	201.0	201.0	0.00	1.000	1.000
8	278.7	283.6	1.8	0.993	0.996	283.6	283.6	0.00	1.000	1.000
9	387.2	446.0	15.2	0.918	0.955	446.0	446.0	0.00	1.000	1.000
10	402.1	803.6	99.9	0.000	0.000	803.6	803.6	0.00	1.000	1.000

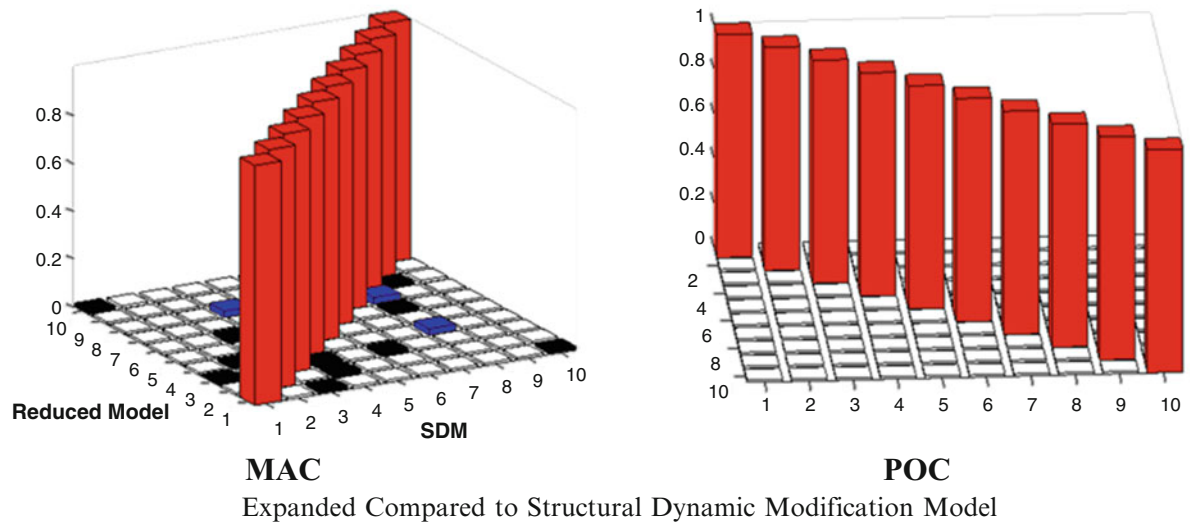
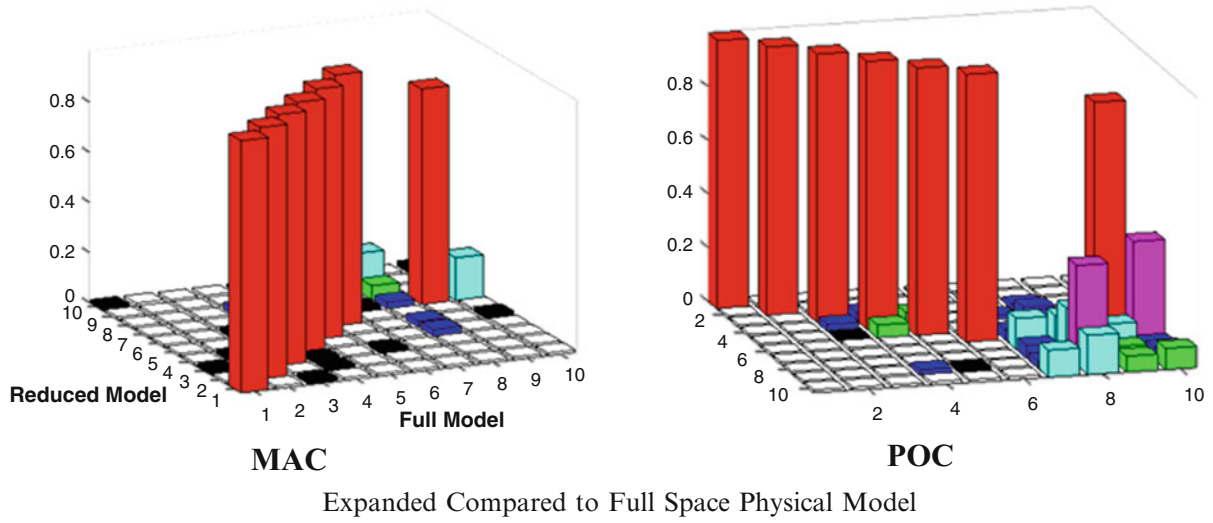
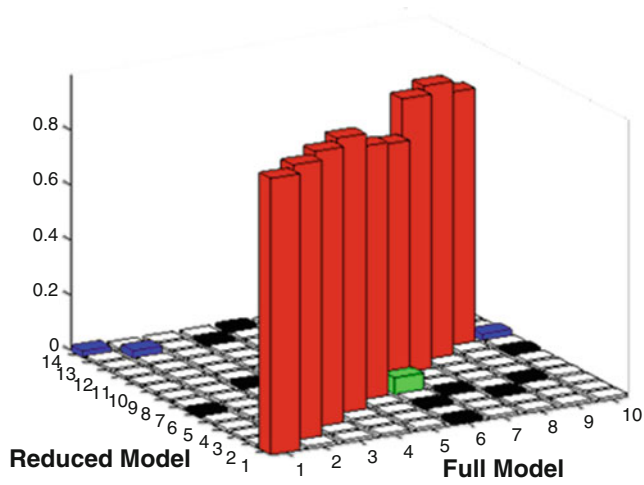
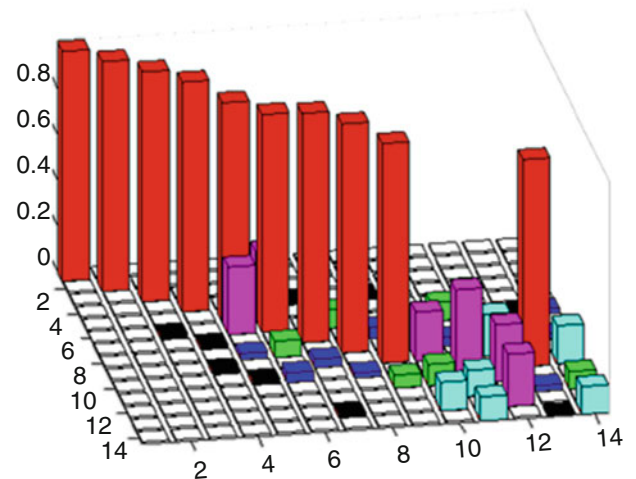


Fig. 33.9 Case 3, expanded results compared to full space model and SDM



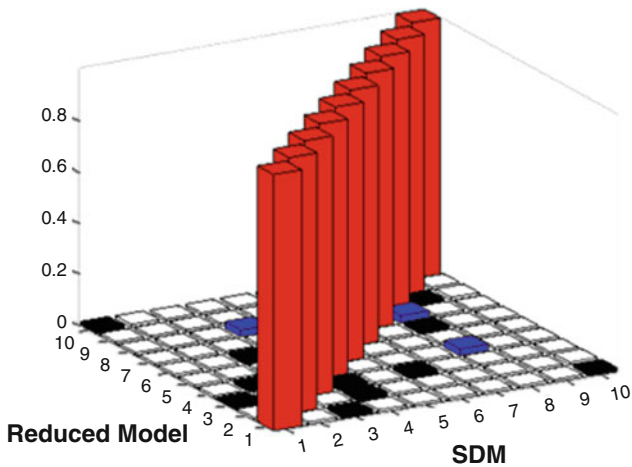


**MAC**

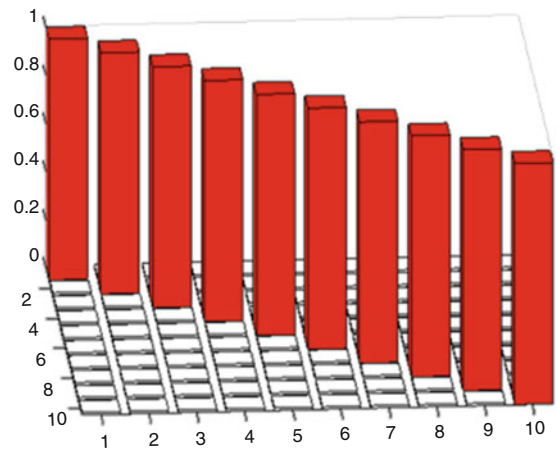


**POC**

Expanded Compared to Full Space Physical Model



**MAC**



**POC**

Expanded Compared to Structural Dynamic Modification Model

**Fig. 33.10** Case 4, expanded results compared to full space model and SDM

## References

1. O'Callahan JC, Avitabile P, Riemer R (1989) System equivalent reduction expansion process. In: Proceedings of the 7th international modal analysis conference, Las Vegas, Nevada, Feb 1989
2. Thibault L, Butland A, Avitabile P (2012) Variability Improvement of Key Inaccurate Node Groups – VIKING. In: Proceedings of the 13th international modal analysis conference, Jacksonville, FL
3. Avitabile P (2002) Twenty years of structural dynamic modification – a review. In: Proceedings of the 20th international modal analysis conference, Los Angeles
4. Guyan RJ (1965) Reduction of stiffness and mass matrices. *AIAA J* 3(2):380
5. O'Callahan JC (1989) A procedure for an Improved Reduced System (IRS) model. In: Proceedings of the 7th international modal analysis conference, Las Vegas, Nevada, Feb 1989

# Chapter 34

## Damage Localization from the Image of Changes in Flexibility

Dionisio Bernal

**Abstract** A recently introduced theorem on the localization of damage from changes in flexibility is reviewed. The theorem states that the image of the change in the flexibility matrix resulting from damaged is a basis for the influence lines of the stress resultants at the damaged locations. The theorem is the dual of the damage locating vector theorem, which states that the vectors in the kernel lead to stress fields that are zero over closed regions that contain the damage. Extension of the theorem to cases where flexibility matrices cannot be extracted from vibration data is realized by replacing the flexibility change with a surrogate. Performance of the image based localization approach is examined in simulations and in an experimental setting.

**Keywords** Damage localization • Damage locating vectors • Influence lines • Identification • Flexibility

### 34.1 Introduction

A systematic approach to interrogate changes in flexibility,  $\Delta F$ , regarding damage location is presented in [1]. In this reference it is shown that the kernel is such that the vectors in its span, treated as loads, lead to stress fields that are zero over closed regions that contain the damage. Since the image and the kernel are complementary subspaces, i.e., both are known when one is specified, the information on damage location contained in the kernel must also be encoded in the image. Clarification of the form of this encoding has been recently presented in the form of a theorem [2]. The theorem, designated as the Influence Line Damage Localization (ILDL) theorem states that the image of the flexibility change is a basis for the influence lines of the stress resultants that coincide with the locations of damage. When  $\Delta F$  is exact the information in the kernel and the image are, of course, equivalent, but this is not so in the real case where the matrix is approximate. While one anticipates that improved robustness can be realized by combination of the two “approximate subspace estimates”, this paper is not about the blending these estimates but is restricted to outlining the theory and exemplifying the approach based on the estimated image. The paper presents the proof of the ILDL theorem and shows how the theory can be extended to the situation where flexibility matrices cannot be extracted because only output signals are available. Illustration of the approach in simulations and in an experimental setting is included.

### 34.2 Influence Line Damage Localization Theorem

Let the structure be linear and the individual damage locations such that the relevant stress resultant over the damage is constants for arbitrary loading in sensor coordinates.

**ILDL Theorem:** *The image of the change in the flexibility in sensor coordinates,  $\Delta F$ , is a basis for the influence lines of the stress resultants at the damage locations.*

---

D. Bernal (✉)  
Professor, Civil and Environmental Engineering Department, Center for Digital Signal Processing,  
Northeastern University, Boston, MA 02115, USA  
e-mail: [bernal@neu.edu](mailto:bernal@neu.edu)

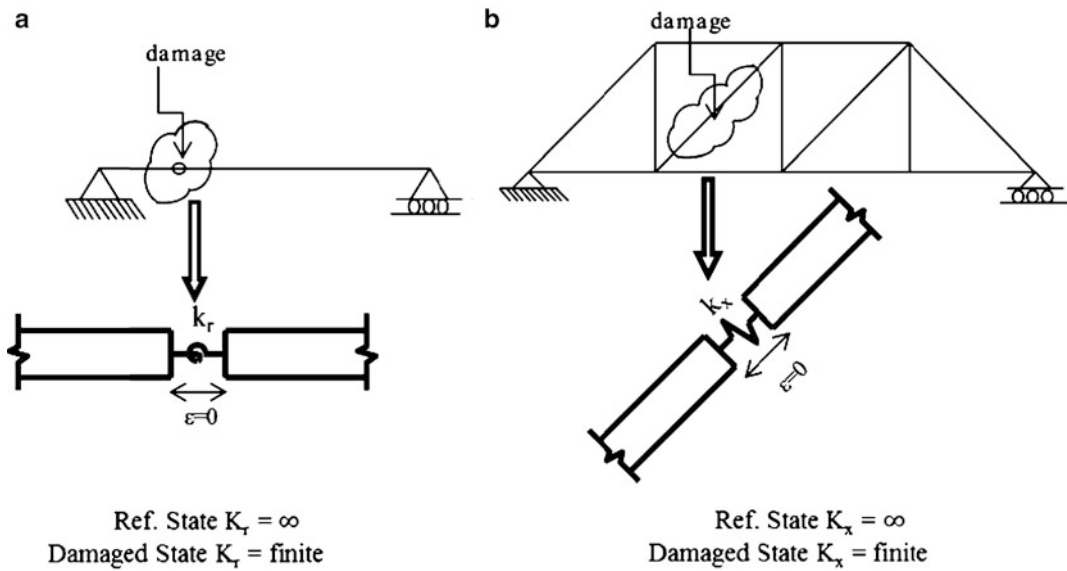


Fig. 34.1 Idealization of damage as local discontinuity

*Proof.* Let  $\Omega$  be the structural domain,  $\Omega_{RE}$  a version where the internal constraints associated with the stress resultant at the locations of damage are removed and let  $\Omega_{RE}(\bullet)$  indicate that the system is loaded, at the locations where the releases are introduced, with the vector  $(\bullet)$ . Let the displacement field be designated as  $y$  and the stress resultants at the locations of the damage as  $q$ , with an added tilde designating, for any quantity, the damaged state. A direct consequence of linearity is that

$$\delta = \tilde{y} - y \Rightarrow \Omega_{RE}(\tilde{q} - q) \tag{34.1}$$

The next step is recognizing that  $\delta$  is (or can be viewed) as discontinuous at the location of damage. In the case of flexural members it is evident that one can model the damage as a lumped rotational spring that switches from an infinite constant to some finite value and the discontinuity is at the damage location. In the case of a truss bar the stress resultant is constant and the damage location, within a given bar, is fictive. For conceptual consistency, however, one thinks there is an axial spring located at some arbitrary point along the damaged bar (Fig. 34.1).

With the discontinuity at the damaged locations as  $\varphi_j$  and a unit load applied on the domain (the direction at each arbitrary point being predetermined) one has from the principle of virtual work, taking  $\delta$  as a virtual deformation pattern

$$1 \cdot \delta_1 - \sum_{j=1}^p q_j \cdot \varphi_j = \int_{\Omega} \sigma_1^T \varepsilon_2 dV \tag{34.2}$$

where  $q_j$  is the stress resultant, due to the unit load, at the damaged position  $j$ , the subscript 1 in  $\delta$  is used to indicate that this is the value at the location of the unit load and the negative sign arises because the  $q_j$  forces are internal. On the *rhs* the subscript 1 refers to “the body in equilibrium” and 2 to the virtual deformation pattern. Reversing the “real” and the “virtual” systems one has

$$0 = \int_{\Omega} \sigma_2^T \varepsilon_1 dV \tag{34.3}$$

Since the structure is linear  $\sigma = \Gamma \varepsilon$ , with  $\Gamma$  being a material’s properties matrix and, given that work is a scalar quantity the right side of Eqs. 34.2 and 34.3 are equal and thus

$$\delta_1 = \sum_{j=1}^p q_j \cdot \varphi_j \tag{34.4}$$

where  $p$  is the number of damaged locations. Let the flexibility in the damage and the undamaged states be  $F_D$  and  $F_U \in \mathbb{R}^{m \times m}$  and  $\ell \in \mathbb{R}^{m \times 1}$  be an arbitrary loading in the coordinates in which the flexibility is described. The difference in the deformations at the coordinates is then

$$\delta = F_D \ell - F_U \ell = \Delta F \cdot \ell \quad (34.5)$$

Assuming the rank of  $\Delta F$  is  $z < m$  one has

$$\Delta F = [U_1 \ U_2] \begin{bmatrix} s_1 & \\ & 0 \end{bmatrix} [U_1 \ U_2]^T \quad (34.6)$$

where  $s_1$  are the  $z$  non-zero singular values. From Eqs. 34.5 and 34.6 one has

$$\delta = U_1 \cdot v \quad v = s_1 U_1^T \ell \quad (34.7a,b)$$

which shows that  $\delta$  is in the span of  $U_1$ ; this result, together with Eq. 34.4 completes the proof.

### 34.2.1 Practical Implementation of the Influence Line Damage Localization (ILDL) Theorem

It follows from the ILDL theorem that potential damage locations can be obtained by computing the influence lines for all candidate locations and determining which ones are in the span of  $\Delta F$ . Note that we used the term potentially damaged, instead of damaged, because conditions exist for which two or more stress resultants have the same influence line sampled at the sensor locations, making these locations inseparable from changes in flexibility. The subspace angle between the influence line  $q_j$  and the image  $U_1$ , which is a direct measure of how well  $q_j$  fits into  $U_1$  (with zero being a perfect fit) can be computed as

$$\theta_j = \cos^{-1} \left\| \left( \frac{U_1^T q_j}{\|q_j\|} \right) \right\| \quad (34.8)$$

Localization can be carried out, therefore, by finding the stress resultants for which the subspace angle is zero (small in practice).

### 34.3 Extension to the Output Only Case

While flexibility matrices cannot be extracted from the data when the input is stochastic the ILDL approach can be extended to this situation by noting that it is not the change in flexibility per se that is needed but a matrix with the same image. Therefore, any matrix of the form

$$\Delta Q = \Delta F \cdot T \quad (34.9)$$

with  $T$  full rank will do. It is shown in [3] and [4] that a viable  $\Delta Q$  can be taken as

$$\Delta Q \cong R_D - R_U \quad (34.10)$$

where

$$R = C [I \cdot s - A]^{-1} H^{-*} L \quad (34.11)$$

with

$$H = \begin{bmatrix} C \cdot A \\ C \end{bmatrix} \quad \text{and} \quad L = \begin{bmatrix} I \\ 0 \end{bmatrix} \quad (34.12a,b)$$

**Fig. 34.2** Truss used in the numerical examples

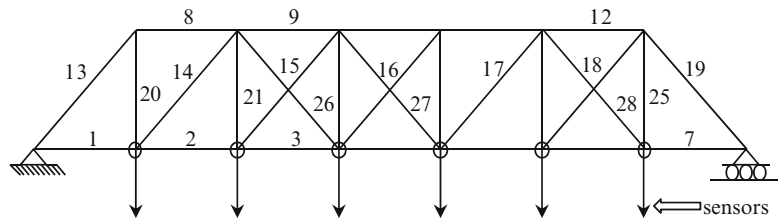
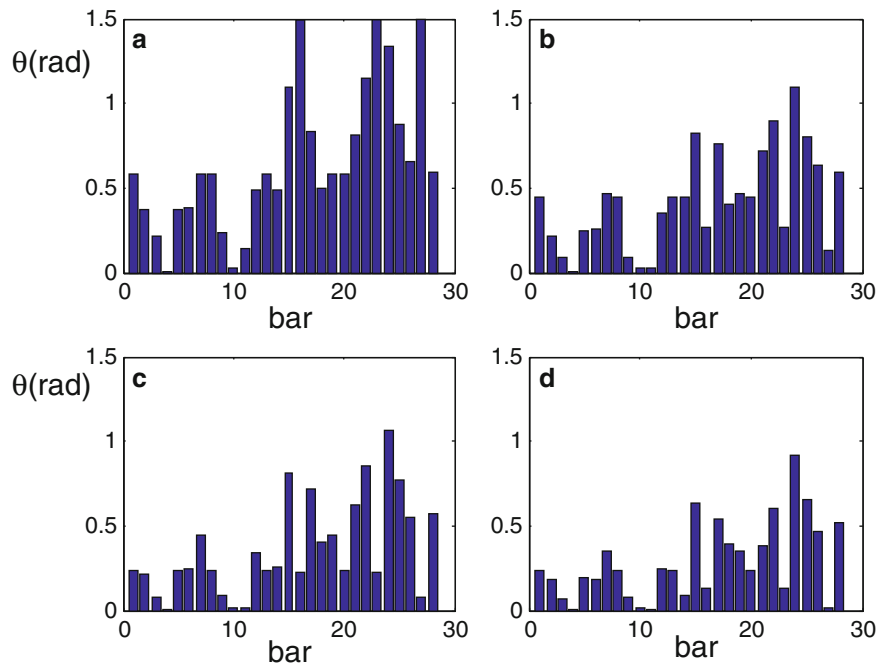


**Fig. 34.3** Subspace angle between sampled influence lines and the estimated image of  $\Delta F$  for assumed image dimensions of (a) = 1, (b) = 2, (c) = 3 and (d) = 4



where A and C are the transition and state to output matrices in continuous time for the reference (undamaged) or damaged state (depending on which R is being computed). We note that in the original reference [4] the expressions presented correspond to the case where the measurements are displacements. Due to mathematical cancellations not previously realized, however, the expressions shown can be used independently of the type of measurement taken.

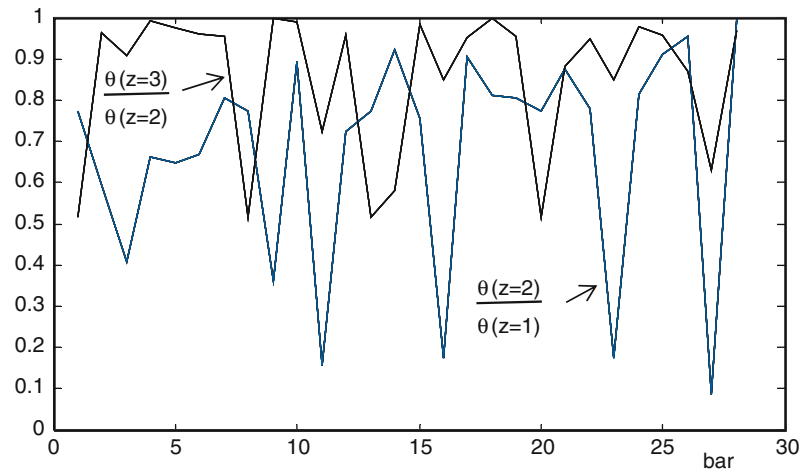
### 34.4 Numerical Example

*Example #1* Consider the truss in Fig. 34.2 with equal areas and sensors measuring in the vertical direction at each one of the nodes of the lower chord. Let damage be 10% loss of stiffness in bars 4 and 27.

To consider the effect of modal truncation the flexibility matrices are computed assuming only the first four modes (based on an identity mass matrix). The normalized singular values of  $\Delta F$  are then  $\{1, 0.0409, 0.0253, 0.0147, 0.0034, 0.0001\}$ . The effective image dimension is not evident so we compute it for assumed values of 1, 2, 3 and 4 and plot the results in Fig. 34.3.

As can be seen, for an assume dimension = 1 one finds bar#4 in the set of potentially damaged bars (for any threshold) but bar 27 (second bar from the end) is missed since the true dimension of the image in this case (using exact matrices) is two. Looking at dimension = 2 one can see that bar 27 is now also small. Stopping at this point the set of potentially damaged bars (at some reasonable threshold) would include the two true damaged bars as well as 9, 10 and 11, which are difficult to discriminate given only four modes. Inspecting the results for dimensions 3 and 4 confirms the previous observations. The results in Fig. 34.4 suggest an adaptive approach to decide on the optimal estimate of the image dimension. Namely, starting with one (or some larger value if deemed appropriate) one computes the subspace angles for increasing dimensions and stops when the reduction in any bar from dimension v to v + 1, is no more than some threshold, 0.2 suggested tentatively.

**Fig. 34.4** Ratio of subspace angles for the results in Fig. 34.3 as the assumed dimension of the image increases



The decision on the potentially damaged set is then made by inspecting the results at the largest dimension. For the results in Fig. 34.3 the ratio of the angles for dimensions two and one, and three and two, are shown in Fig. 34.4. As can be seen, the results indicate clearly that dimension two is appropriate.

### 34.5 Experimental Illustration

A cantilever beam tested by Brüel & Kjaer in Copenhagen is shown in Fig. 34.5. The beam was excited by a shaker located as shown and the response was monitored by 27 accelerometers, 18 horizontal and nine vertical ones. We operate with output signals only. Due to the configuration and the direction of the excitation the response in the vertical direction is minimal so the nine vertical accelerometers are not included in this analysis. Moreover, the 18 accelerometers measuring in the horizontal direction were replaced by nine virtual sensors with signals taken as the mean of the pairs that are at equal distance from the root. Damage was introduced by drilling a 10 mm hole, 80 mm from the fixed end (420 mm from the tip). The frequencies and damping ratios of all the identified modes are listed in Table 34.1. As can be seen, the changes in frequency, which are random variables, are very small and in several modes are increases, indicating that the shift introduced by damage was small compared to the realizable accuracy.

From the identification results and the expression in Eqs. 34.9–34.12a,b one finds that the normalized singular values of  $\Delta R$  are  $\{1, 0.013, 0.0015, 0.0005, 0.0001, 0, 0, 0, 0\}$ ; so the effective dimension of the image appears to be one. The subspace angles for image dimensions of 1 and 2, for 50 equally spaced points are depicted in Fig. 34.6. As can be seen, the location of the minimum subspace angle for dimension one is essentially exact and for dimension two remains close to the correct location.

### 34.6 Conclusions

The influence line damage localization theorem reviewed in this paper is the dual of the DLV theorem and, together with it, provides a complete description of how damage localization information is encoded in flexibility changes. Namely, the kernel contains loads that lead to zero stress fields over the damage and the image is a basis for the influence lines of the stress resultants at the damage locations.

**Acknowledgements** The research reported in this paper was carried with support from NSF under grant CMMI-1000391, this support is gratefully acknowledged.

**Fig. 34.5** Beam tested by B&K in Copenhagen

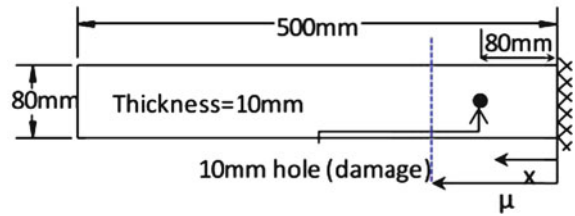
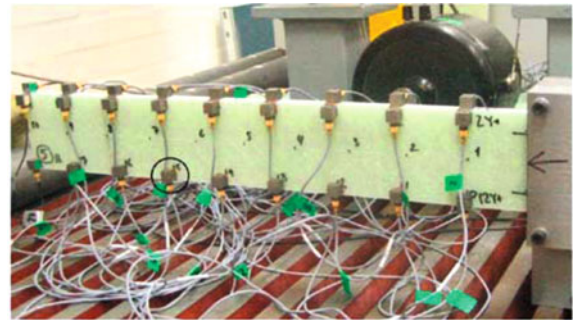
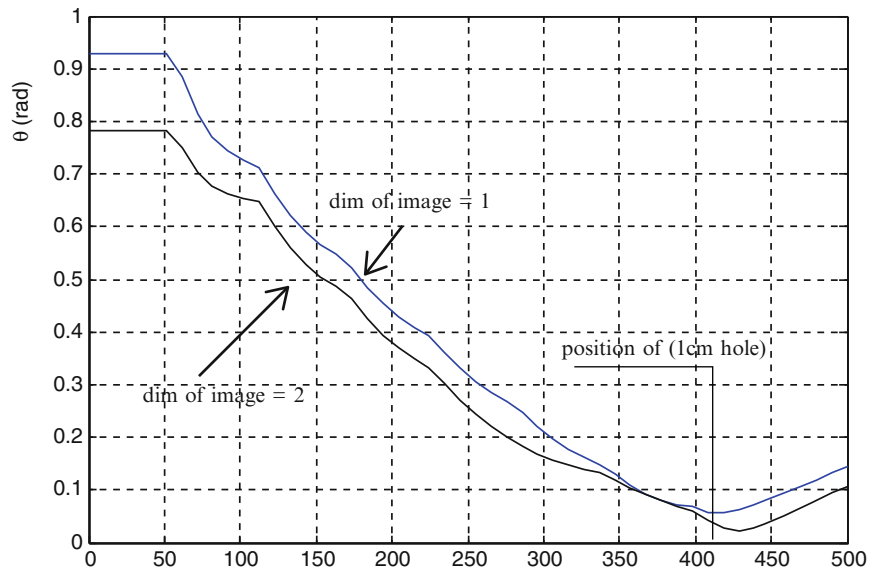


**Table 34.1** Identified frequencies and damping ratios for the beam in Fig. 34.5

Reference state		Damaged state	
Frequency (Hz)	Damping ratio (%)	Frequency (Hz)	Damping ratio (%)
15.91	2.09	15.74	1.62
96.69	0.65	96.69	0.69
191.97	1.39	191.32	1.49
265.58	0.72	265.96	0.70
289.87	3.14	292.79	3.20
337.33	0.79	337.82	0.98
502.24	2.07	498.48	1.97
526.18	0.80	523.99	0.84
560.63	1.32	557.26	1.28
838.38	1.83	838.35	1.56
919.11	2.28	921.21	2.41
1,170.80	1.06	1,173.30	1.00
1,236.00	2.18	1,231.80	2.34

**Fig. 34.6** Subspace angles between the influence lines and the image of ΔR for the beam in Fig. 34.5





## Reference

1. Bernal D (2002) Load vectors for damage localization. *J Eng Mech* 128(1):7–14
2. Bernal, D. (2013). Damage Quantification from the Image of Changes in Flexibility. *J Eng Mech* 10.1061/(ASCE)EM.1943-7889.0000617 (Feb. 28, 2013)
3. Bernal D (2012) A null space strategy for damage localization. *Experimental Vibration Analysis for Civil Engineering Structures (EVACES)*, Varenna, Italy, (1), pp 1–10
4. Bernal D (2006) Flexibility-based damage localization from stochastic realization results *J Eng Mech ASCE* 132:651–658

# Chapter 35

## Spectral Element Method for Cable Harnessed Structure

Jiduck Choi and Daniel J. Inman

**Abstract** This paper presents a predictive model of a cable-harnessed structure through using the Spectral Element Method (SEM) and this is compared to a finite element approach. SEM is an element-based method that combines the generality of the finite element method with the accuracy of spectral techniques. The exact dynamic stiffness matrices are used as the element matrices in the Finite Element Method (FEM). Thus it is possible to generate the meshes on geometric domains of concern. The spectral element can be assembled in the same terminology of the FEM. After assembly and application of the boundary conditions, the global matrix can be solved for response of model, repeatedly at all discrete frequencies because the dynamic stiffness matrices are computed at each frequency. Here we model a cable-harnessed structure as a double beam system. The presented SEM model can define location and number of connections very conveniently. Comparison is conducted between the FEM and SEM for several cases. The results show that the proposed SEM approach can be used as the exact solution of cable harnessed structures.

**Keywords** FEM • SEM • Spectral element method • Double beam system • Cable harnessed structure

### 35.1 Introduction

In satellite applications modeling is extremely important in order to predict behavior during launch and in orbit. Today detailed finite element models of satellites are accurate and agree well with experimental data. However once the satellites are hung with cable harnesses the ability to model the system dynamics has eluded modeling engineers. Here we investigate in a simple way the effects of adding cables to a simple structure with the goal of developing an understanding of the physics of cables interacting with a structure. The goal of this research is to obtain the predictive and precise model of the cable harnessed structure.

To obtain a simplified model of cable harnessed structure, the total system can be considered as a double beam system with both beams connected by spring connection at specific locations to emulate the effect of attaching cables to the structure.

The response of single Euler-Bernoulli beam is a classical example of a distributed system. And exact solution of this beam can be obtained in various ways [1]. However, when secondary beam is attached to the main beam by means of several spring connections, obtaining the solution of system can be more complicated. Several authors have investigated double-beam systems elastically combined by a distributed spring in parallel. Seelig and Hoppman II [2], worked out the solution of differential equation of elastically connect parallel beams. Rao [3] considered the free response of several Timoshenko beam systems. Gürgöze [4, 5] dealt with the derivation of the frequency equation of a clamped-free Euler Bernoulli beam with several spring-mass systems attached in mid of span by means of the Lagrange multipliers method. Vu et al. [6] presented an exact method for the vibration of a double-beam system subject to harmonic excitation. The system consists of a main beam

---

J. Choi

Ph.D. Candidate, Department of Mechanical Engineering, Virginia Tech, 100S Randolph Hall, Blacksburg, VA 24061, USA  
e-mail: [jdchoi@vt.edu](mailto:jdchoi@vt.edu)

D.J. Inman (✉)

“Kelly” Johnson Collegiate Professor, Department Chair, Department of Aerospace Engineering, University of Michigan, FXB Building, 1320 Beal Ave, Ann Arbor, MI 48109, USA  
e-mail: [daninman@umich.edu](mailto:daninman@umich.edu)

with an applied force, and an auxiliary beam, with a distributed spring  $k$  and dashpot  $c$  in parallel between the two beams. Wu and Chou [7] considered the beam connected with two degrees-of-freedom systems at specific location.

Doyle [8] and Lee [9] describe the spectral element method very well. Doyle introduced the basic formulation of spectral element matrix by Euler-Bernoulli beam. And Lee summarized the various ways to derive the spectral element matrix for structural elements such as Euler beam, Timoshenko beam and plate. Lee also presented several practical applications of SEM. Many authors used the dynamic stiffness approach very closely related to the SEM. Banerjee [10] and Chen [11] used dynamic stiffness matrix for the beam with attached two degree-of-freedom system. Li and Hua [12, 13] considered elastically connected two and three parallel beams by dynamic stiffness analysis. Jiao et al. [14] investigated the Euler beam with an arbitrary cross section. However, most of papers only considered the clamped-free or fixed-fixed or simply supported boundary conditions. Thus the free-free boundary condition is considered and tried for both single beam and double beam in this paper. And the procedure of modeling the cable-harnessed system with the SEM is presented. Through the SEM approach, we can obtain the extremely high accurate result with a minimum number of DOFs. And it can be considered as a numerical exact solution because the SEM is based on the exact solutions of the governing differential equation of the element. Thus the SEM results are compared with FEM results and exact solution in single Euler Bernoulli beam model to validate the accuracy. Then the SEM approach has extended to double beam system. Furthermore, various connections will be considered by presented SEM model.

### 35.2 The SEM for Euler-Bernoulli Beam with a Free-Free Boundary Condition

A single beam can be considered as Euler-Bernoulli beam or a long slender beam if width and thickness is 10 times less than length [1]. For Euler beam, the shear deformation can be neglected. Thus we can only consider the transverse displacement. The bending moment of beam and shear force can be defined by

$$M(x, t) = EI(x) \frac{\partial^2 w(x, t)}{\partial x^2}, \quad V(x, t) = -\frac{\partial M(x, t)}{\partial x} = -EI(x) \frac{\partial^3 w(x, t)}{\partial x^3} \quad (35.1)$$

If  $EI(x)$  and  $A$  are assumed to be constant and the no external force exists, the free vibration of beam is governed by

$$EI \frac{\partial^4 w(x, t)}{\partial x^4} + \rho A \frac{\partial^2 w(x, t)}{\partial t^2} = 0 \quad (35.2)$$

Assume the solution of Eq. (35.2) in spectral form to be

$$w(x, t) = \frac{1}{N} \sum_{n=0}^{N-1} W_n(x) e^{i\omega_n t} \quad (35.3)$$

Substitute Eq. (35.3) into (35.2), then we get the eigenvalue problems at the specific frequency  $\omega = \omega_n$  such as

$$EI \frac{\partial^4 W(x)}{\partial x^4} - \omega^2 \rho A W(x) = 0 \quad (35.4)$$

Assume the general solution of Eq. (35.4) as

$$W(x) = A \cos \beta x + B \sin \beta x + C \cosh \beta x + D \sinh \beta x \quad (35.5)$$

Substituting Eq. (35.5) into (35.4) yields the following dispersion relation equation by

$$\beta^4 - \frac{\rho A \omega^2}{EI} = 0 \quad (35.6)$$

The nodal displacement and slope at both ends can be expressed by

$$\{d\} = \begin{pmatrix} W(0) \\ \frac{\partial W}{\partial x}(0) \\ W(L) \\ \frac{\partial W}{\partial x}(L) \end{pmatrix} = \begin{bmatrix} 1 & 0 & 1 & 0 \\ 0 & \beta & 0 & \beta \\ \cos \beta L & \sin \beta L & \cosh \beta L & \sinh \beta L \\ -\beta \sin \beta L & \beta \cos \beta L & \beta \sinh \beta L & \beta \cosh \beta L \end{bmatrix} \{a\} \quad (35.7)$$

where  $\{a\} = [A \ B \ C \ D]^T$  and

$$[D(\omega)] = \begin{bmatrix} 1 & 0 & 1 & 0 \\ 0 & \beta & 0 & \beta \\ \cos \beta L & \sin \beta L & \cosh \beta L & \sinh \beta L \\ -\beta \sin \beta L & \beta \cos \beta L & \beta \sinh \beta L & \beta \cosh \beta L \end{bmatrix} \quad (35.8)$$

And the transverse shear force and bending moments at the nodal points are given by

$$\{f\} = \begin{Bmatrix} V(0) \\ M(0) \\ -V(L) \\ -M(L) \end{Bmatrix} = EI \begin{bmatrix} 0 & -\beta^3 & 0 & \beta^3 \\ \beta^2 & 0 & -\beta^2 & 0 \\ -\beta^3 \sin \beta L & \beta^3 \cos \beta L & -\beta^3 \sinh \beta L & -\beta^3 \cosh \beta L \\ -\beta^2 \cos \beta L & -\beta^2 \sin \beta L & \beta^2 \cosh \beta L & \beta^2 \sinh \beta L \end{bmatrix} \{a\} \quad (35.9)$$

where

$$[F(\omega)] = EI \begin{bmatrix} 0 & -\beta^3 & 0 & \beta^3 \\ \beta^2 & 0 & -\beta^2 & 0 \\ -\beta^3 \sin \beta L & \beta^3 \cos \beta L & -\beta^3 \sinh \beta L & -\beta^3 \cosh \beta L \\ -\beta^2 \cos \beta L & -\beta^2 \sin \beta L & \beta^2 \cosh \beta L & \beta^2 \sinh \beta L \end{bmatrix} \quad (35.10)$$

From the Eqs. (35.8), (35.9) and (35.10), the relation  $f$  and  $d$  can be obtained such as

$$[S]\{d\} = \{f\}, \quad [S] = [F][D]^{-1} \quad (35.11)$$

Finally, the spectral element matrix of Euler Bernoulli Beam is given by

$$[S] = EI \begin{bmatrix} S_{11} & S_{12} & S_{13} & S_{14} \\ S_{12} & S_{22} & S_{23} & S_{24} \\ S_{13} & S_{23} & S_{33} & S_{34} \\ S_{14} & S_{24} & S_{34} & S_{44} \end{bmatrix} \quad (35.12)$$

where

$$\begin{aligned} \eta &= \frac{1}{1 - \cos(\beta L) \cosh(\beta L)} \\ S_{11} &= S_{33} = \eta(\beta L)^3 (\cos(\beta L) \sinh(\beta L) + \sin(\beta L) \cosh(\beta L)) \\ S_{22} &= S_{44} = \eta\beta L^3 (-\cos(\beta L) \sinh(\beta L) + \sin(\beta L) \cosh(\beta L)) \\ S_{12} &= -S_{34} = \eta\beta^2 L^3 \sin(\beta L) \sinh(\beta L) \\ S_{13} &= -\eta(\beta L)^3 (\sin(\beta L) + \sinh(\beta L)) \\ S_{14} &= -S_{23} = \eta\beta^2 L^3 (-\cos(\beta L) + \cosh(\beta L)) \\ S_{24} &= \eta\beta L^3 (-\sin(\beta L) + \sinh(\beta L)) \end{aligned} \quad (35.13)$$

After obtaining the spectral element matrix, we can assemble elements to generate the global spectral matrix. And we apply the boundary conditions to the global system. The global system can be expressed by

$$[S_g]\{d_g\} = \{f_g\} \quad (35.14)$$

Owing to usage of the exact dynamic stiffness matrix to formulate the spectral element matrix, we can solve exactly the system characteristics with minimum number of element matrix. Especially, single Euler-Bernoulli beam with free-free boundary condition case, we can obtain the exact solution with only one element and no application of boundary condition. Now, we can calculate the natural frequencies by solving the eigenvalue problem for spectral element model given by

$$[S_g]\{d_g\} = 0 \quad (35.15)$$

**Table 35.1** Natural frequencies (Hz) of exact solution, SEM and FEM

Mode	$\omega_{exact}$	$\omega_{spec.}$	$\omega_{FEM}$ n = 10	$\omega_{FEM}$ n = 30	$\omega_{FEM}$ n = 50
1	0	0	0.00001	0.00009	0.0002
2	11.1794	11.1794	11.1798	11.1794	11.1794
3	30.8165	30.8165	30.8242	30.8166	30.8165
4	60.4127	60.4127	60.4683	60.4135	60.4128
5	99.8654	99.8654	100.1052	99.8687	99.8658
6	149.5272	149.1817	149.9387	149.1928	149.1831
7	208.3612	208.3612	210.2857	208.3915	208.3652
8	277.4040	277.4040	281.5237	277.4749	277.4134

Similar to the regular eigenvalue problem, we need to consider that determinant of spectral element matrix  $[S_g]$  is zero,  $\det(S(\omega_{NAT})) = 0$ , to find the natural frequencies. However, the spectral element matrix consists of transcendental functions such as sine, cosine, hyperbolic cosine (cosh), and hyperbolic sine (sinh). We cannot use the linear eigensolver such as 'eig' in MATLAB. The several approaches to find the eigenvalues are summarized by Lee [9]. The determinant of global stiffness matrix  $[S_g]$  can be simplified as

$$\det[S_g] = \frac{E^4 I^4 \beta^8 (\cos(2\beta L) - \cos(\beta L) \cosh(\beta L)) \sin^2(\beta L) \sinh^2(\beta L)}{4(-1 + \cos(\beta L) \cosh(\beta L))^3} \quad (35.16)$$

The conventional and spectral beam elements will be compared using a simple example. A free vibration of free-free beam will be analyzed using both types of elements. The material used in the example is aluminum with elastic modulus of  $7 \times 10^{10}$  N/m<sup>2</sup> and density of 2,700 kg/m<sup>3</sup>. The dimensions of beam are  $1.2192 \times 0.0254 \times 0.003175$  m. From the characteristic equation of free-free beam [1],  $\cos(\beta L) \cosh(\beta L) = 1$ , the exact natural frequencies are calculated. And the root-finding algorithms [15] are used to find the  $\omega_n$  in SEM.

Table 35.1 shows the natural frequencies of free-free beam. The SEM results are identical to exact solution. And the FEM results go closer to SEM and exact solution as the number of elements is increased. This tendency also can be notified by means of the receptance versus frequency graph in Fig. 35.1. In Fig. 35.1a, FEM gives 3 good natural frequencies. The number of elements is increased to 10 in Fig 35.1b. And the 5 natural frequencies are almost identical with SEM frequencies. Considering the high frequency range, the more elements are necessary to obtain the good results.

### 35.3 The SEM for Double Beam with a Free-Free Boundary Condition

Most of papers considered the double beam such that two beams are connected with distributed spring connections, not in specific location. In this paper, we can define the exact number and locations of connections. Through this approach, the effect of number and locations of connection can also be identified.

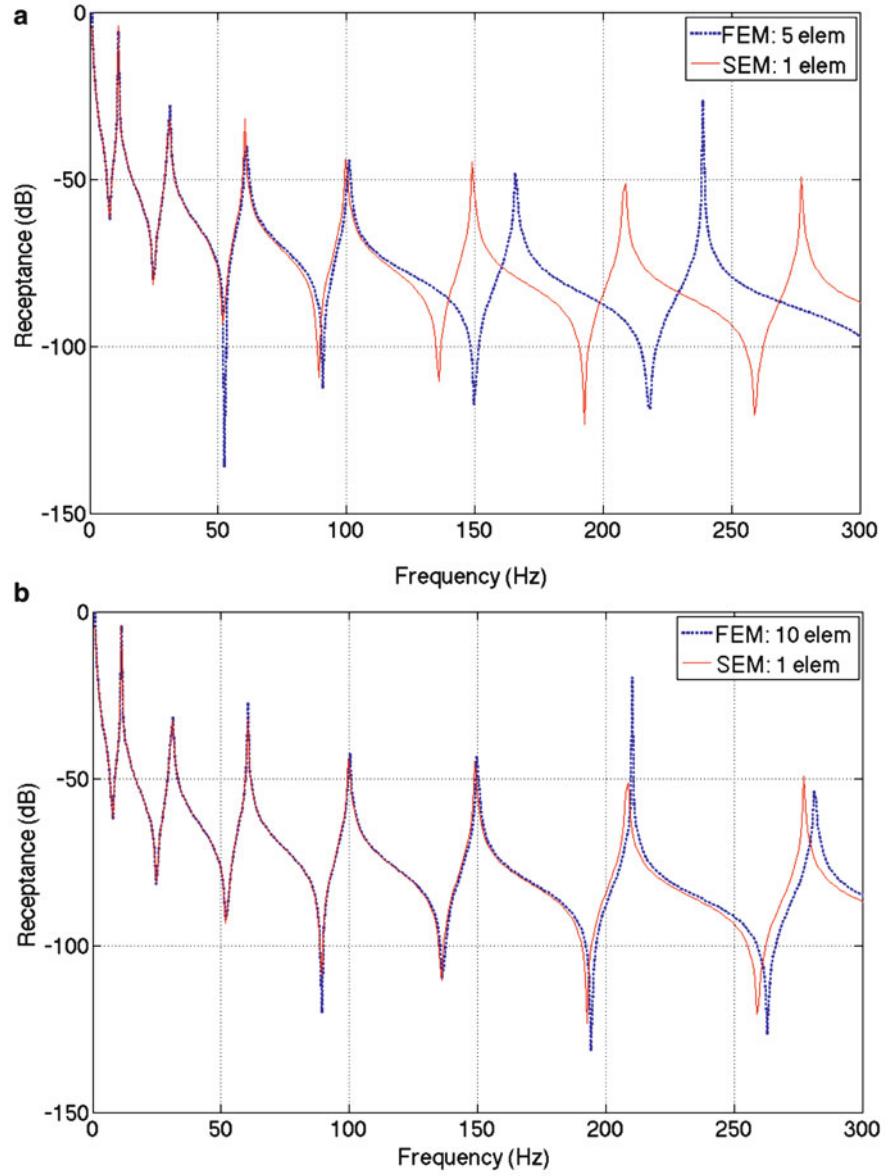
Considering the double beam system in Fig. 35.2 each beam is  $2N$  d.o.f system. And the spring connection exists between  $i$ th nodes of beam 1 and beam 2. For beam 1 and beam 2, we can formulate the global stiffness matrix by means of Eq. (35.12). From the relation between nodal displacement and force, the combined global stiffness matrix without spring connection can be shown as

$$\begin{bmatrix} S_{g,1} & 0 \\ 0 & S_{g,2} \end{bmatrix} \begin{Bmatrix} \{d_{g,1}\} \\ \{d_{g,2}\} \end{Bmatrix} = \begin{Bmatrix} \{f_{g,1}\} \\ \{f_{g,2}\} \end{Bmatrix} \quad (35.17)$$

where

$$\begin{aligned} \{d_{g,1}\} &= [W_{1,1} \ \Theta_{1,1} \ \cdots \ W_{i,1} \ \Theta_{i,1} \ \cdots \ W_{N,1} \ \Theta_{N,1}]^T \\ \{d_{g,2}\} &= [W_{1,2} \ \Theta_{1,2} \ \cdots \ W_{i,2} \ \Theta_{i,2} \ \cdots \ W_{N,2} \ \Theta_{N,2}]^T \\ \{f_{g,1}\} &= [V_{1,1} \ M_{1,1} \ \cdots \ V_{i,1} \ M_{i,1} \ \cdots \ V_{N,1} \ M_{N,1}]^T \\ \{f_{g,2}\} &= [V_{1,2} \ M_{1,2} \ \cdots \ V_{i,2} \ M_{i,2} \ \cdots \ V_{N,2} \ M_{N,2}]^T \end{aligned} \quad (35.18)$$

**Fig. 35.1** Comparison of SEM and FEM by means of Receptance graph.  
**(a)** Receptance of SEM (1 element) and FEM (5 elements).  
**(b)** Receptance of SEM (1 element) and FEM (10 elements)



The global stiffness matrix  $S_{g,1}$  and  $S_{g,2}$  are  $2N \times 2N$  matrices and the global displacement and force vector  $d_{g,1}$ ,  $d_{g,2}$ ,  $f_{g,1}$  and  $f_{g,2}$  are  $2N \times 1$  vectors. If the force  $f_k$  is working on between  $i$ th nodes of beam 1 and beam 2 due to the spring connection,  $f_k$  can be given by

$$f_k = k(W_{i,1} - W_{i,2}) \quad (35.19)$$

The total combined system can be expressed as

$$\begin{cases} [S_{g,1}] \{d_{g,1}\} + f_k = \{f_{g,1}\} \\ [S_{g,2}] \{d_{g,2}\} - f_k = \{f_{g,2}\} \end{cases} \quad (35.20)$$

Fig. 35.2 Double beam model

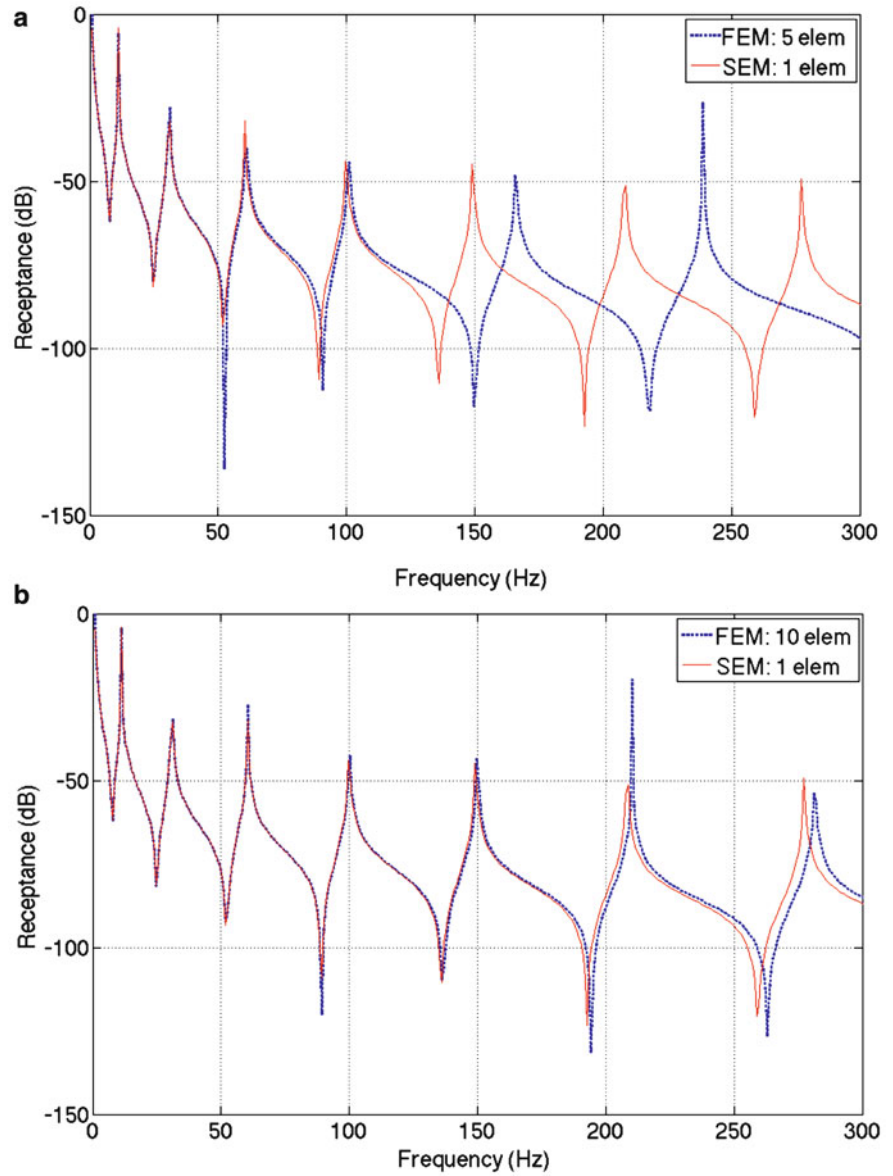


Table 35.2 Material properties of two beams

	E(N/m <sup>3</sup> )	I(m <sup>4</sup> )	A(m <sup>2</sup> )	ρ(kg/m <sup>3</sup> )	L (m)
Beam1	7 × 10 <sup>10</sup>	6.7746 × 10 <sup>-11</sup>	8.0645 × 10 <sup>-5</sup>	2,700	1.2192
Beam2	2.333 × 10 <sup>10</sup>	2.7098 × 10 <sup>-12</sup>	4.03225 × 10 <sup>-5</sup>	540	1.2192

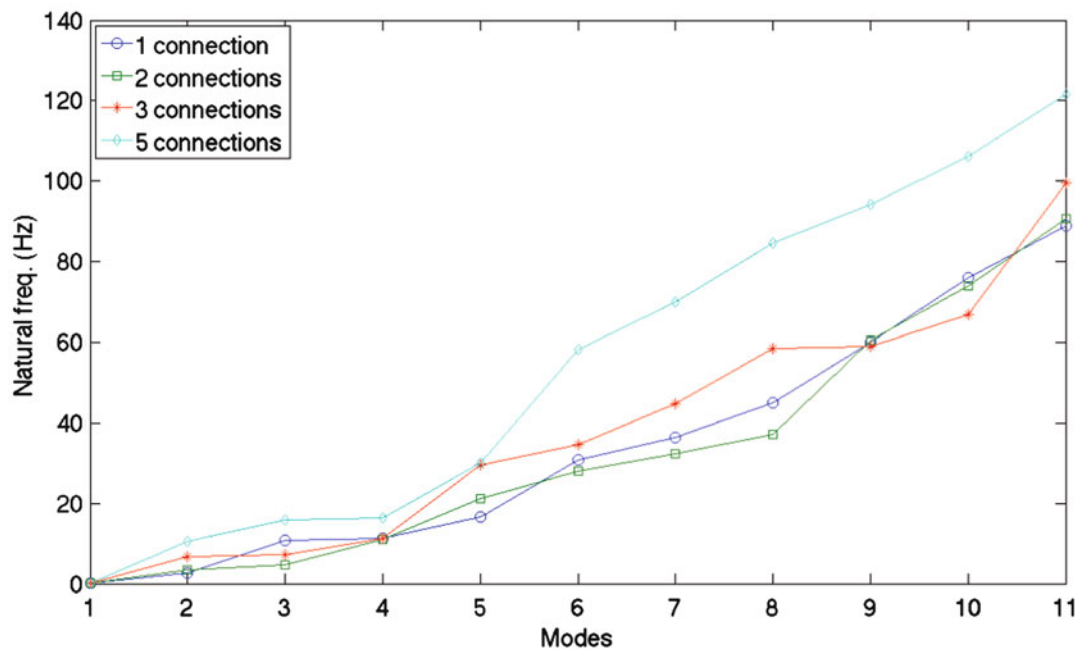
Let's introduce the locator vector  $\{L_i\}$ . The vector  $\{L_i\}$  is  $4N \times 1$  vector correspondent with  $[d_{g,1} \ d_{g,2}]^T$ . The  $2i-1$ th component of  $\{L_i\}$  is 1 and the  $2N + 2i-1$ th component of  $\{L_i\}$  is -1 and the remainders are zero.

$$\begin{bmatrix} S_{g,1} & 0 \\ 0 & S_{g,2} \end{bmatrix} \begin{Bmatrix} d_{g,1} \\ d_{g,2} \end{Bmatrix} + \sum_{i=1}^p k_i \{L_i\} \{L_i\}^T \begin{Bmatrix} d_{g,1} \\ d_{g,2} \end{Bmatrix} = \begin{Bmatrix} f_{g,1} \\ f_{g,2} \end{Bmatrix} \tag{35.21}$$

where  $p$  is the total number of connections. The FEM and SEM will be compared using a double beam example. A free vibration of free-free double beam will be analyzed for several connection cases. The material properties of both beams are summarized in Table 35.2. And the spring constant  $k$  is  $10^5$  N/m. And the root-finding algorithms [15] are utilized to find the  $\omega_n$  in the SEM.

**Table 35.3** Natural frequencies (Hz) for double beam with several connections

Mode	1 spring connection		2 spring connections		3 spring connections		5 spring connections	
	FEM 128	SEM 2	FEM 120	SEM 3	FEM 128	SEM 4	FEM 120	SEM 6
1	0.0024	0.0213	0.0027	0.0124	0.0025	0.0119	0.0006	0.0053
2	2.6341	2.6341	3.3250	3.3250	6.8085	6.8085	10.5753	10.5753
3	10.7977	10.7977	4.6189	4.6189	7.1844	7.1844	15.7602	15.7603
4	11.2526	11.2526	10.9921	10.9921	11.1687	11.1687	16.2981	16.2982
5	16.5676	16.5679	21.1613	21.1613	29.5254	29.5254	30.1176	30.1176
6	30.8166	30.8166	27.9176	27.9176	34.6464	34.6464	58.0927	58.0927
7	36.4657	36.4648	32.4038	32.4037	44.8028	44.8028	69.8780	69.8780
8	44.9628	44.9938	37.1127	37.1016	58.4510	58.4506	84.7031	84.7031
9	59.9995	59.9995	60.3813	60.3813	58.8538	58.8545	94.2957	94.2947
10	76.0828	76.0828	73.9227	73.9226	66.7777	66.7782	106.1145	106.1145
11	88.7920	88.8003	90.6776	90.6776	99.6240	99.6240	121.6623	121.6622

**Fig. 35.3** Natural frequencies of 11 modes for each connection case

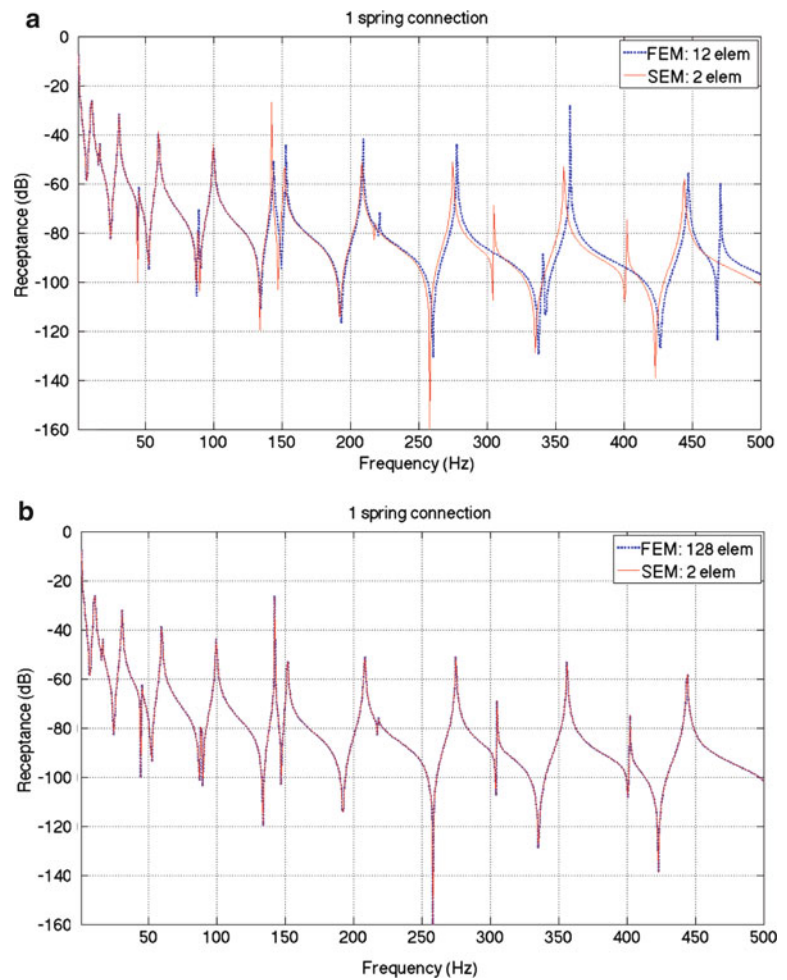
The double beam system with 1, 2, 3, and 5 connections has simulated by means of material properties in Table 35.2. The result from 1st ~ 11th modes are summarized in Table 35.3. The SEM uses minimum number of element to obtain the exact natural frequencies. As the connections are added, the natural frequencies increase as in Fig. 35.3.

In (a) of Fig. 35.4 ~ 35.7, the small number of elements are used in the FEM, the difference between the FEM and the SEM goes bigger in higher frequency range. About 10 times more number of elements are used in (b) of Fig. 35.4 ~ 35.7. Frequencies by the FEM are very close with the SEM results.



**Fig. 35.4** Receptance versus frequency graph of double beam with 1 connections.

(a) Receptance of SEM (2 element) and FEM (12 elements) (b) Receptance of SEM (2 element) and FEM (128 elements)

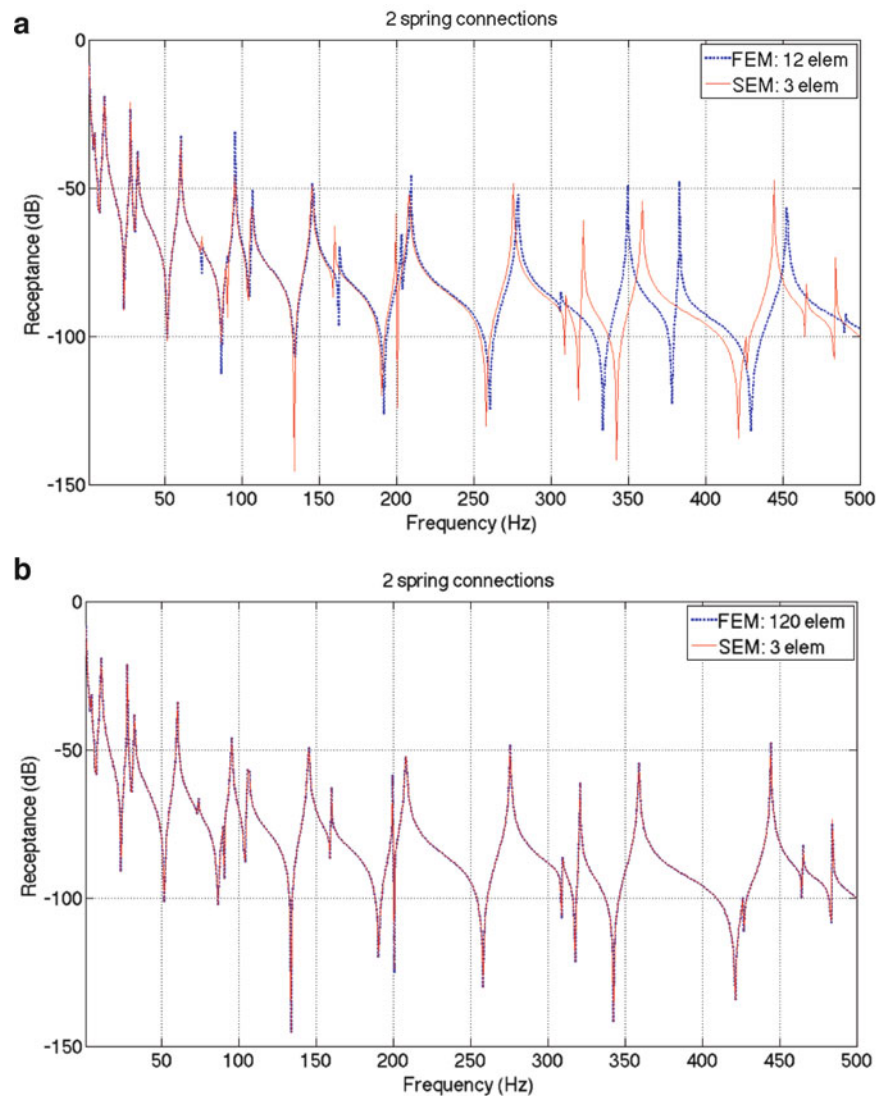


### 35.4 Conclusion

The SEM is presented as the numerical exact solution to predict the response of a cable harnessed structure. The single and double beam cases are considered to validate the exactness of the SEM. In all cases, the comparisons are performed by means of calculated natural frequencies and the receptance graphs. The SEM shows the exact solution, requiring fewer elements than the FEM, with the minimum number of degree-of-freedom. Moreover, the SEM allows us to define the locations very conveniently. Through this convenience, the effect of number of connections is also investigated. As the number of connections increases, the natural frequencies increase. The effectiveness and accuracy of the proposed SEM are demonstrated with several numerical examples.

**Fig. 35.5** Receptance versus frequency graph of double beam with 3 connections.

(a) Receptance of SEM (3 element) and FEM (12 elements). (b) Receptance of SEM (3 element) and FEM (120 elements)



## References

1. Inman DJ (2008) Engineering vibration 4th edition Pearson Prentice Hall, Upper Saddle River
2. Seelig JM, Hoppmann WH II (1964) Normal mode vibrations of systems of elastically connected parallel bars *J Acoust Soc Am* 36(1):93–99
3. Rao SS (1974) Natural vibrations of systems of elastically connected Timoshenko beams *J Acoust Soc Am* 55(6):1232–1237
4. Gürgöze M (1996) On the eigenfrequencies of a cantilever beam with attached tip mass and a spring-mass system *J Sound Vib* 190(2):149–162
5. Gürgöze M (1998) On the alternative formulations of the frequency equation of a Bernoulli-Euler beam to which several spring-mass systems are attached in-span *J Sound Vib* 217(3):585–595
6. Vu HV, Ordonez AM, Karnopp BH (2000) Vibration of a double-beam system *J Sound Vib* 229(4):807–822
7. Wu JS, Chou HM (1998) Free vibration analysis of a cantilever beam carrying any number of elastically mounted point masses with the analytical-and-numerical-combined method. *J Sound Vib* 213(2):317–332
8. Doyle JF (1997) Wave propagation in structures: spectral analysis using fast discrete Fourier transforms Springer, New York
9. Lee U (2009) Spectral element method in structural dynamics Wiley, Singapore/Hoboken
10. Banerjee JR (2003) Dynamic stiffness formulation and its application for a combined beam and a two degree-of-freedom system *J Vib Acoust* 125(3):351–358
11. Chen DW (2006) The exact solution for free vibration of uniform beams carrying multiple two-degree-of-freedom spring-mass systems *J Sound Vib* 295(1–2):342–361
12. Li J, Hua H (2007) Spectral finite element analysis of elastically connected double-beam systems *Finite Elem Anal Des* 43(15):1155–1168
13. Li J, Hua H (2008) Dynamic stiffness vibration analysis of an elastically connected three-beam system *Appl Acoust* 69(7):591–600
14. Jiao S, Li J, Hua H, Shen R (2008) A spectral finite element model for vibration analysis of a beam based on general higher-order theory *Shock Vib* 15(2):179–192
15. Burden RL, Faires JD (2005) Numerical analysis Thomson Brooks/Cole, Belmont

**Fig. 35.6** Receptance versus frequency graph of double beam with 3 connections.

(a) Receptance of SEM (4 element) and FEM (12 elements).

(b) Receptance of SEM (4 element) and FEM (120 elements)

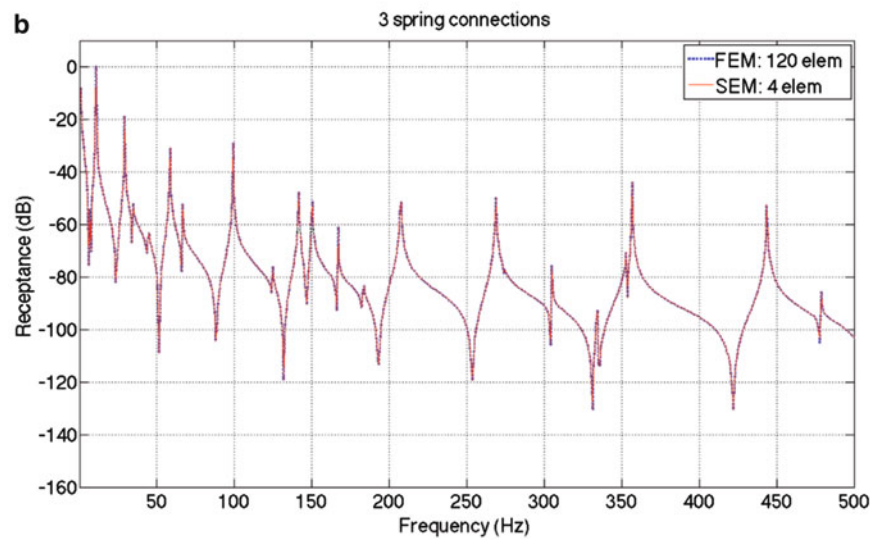
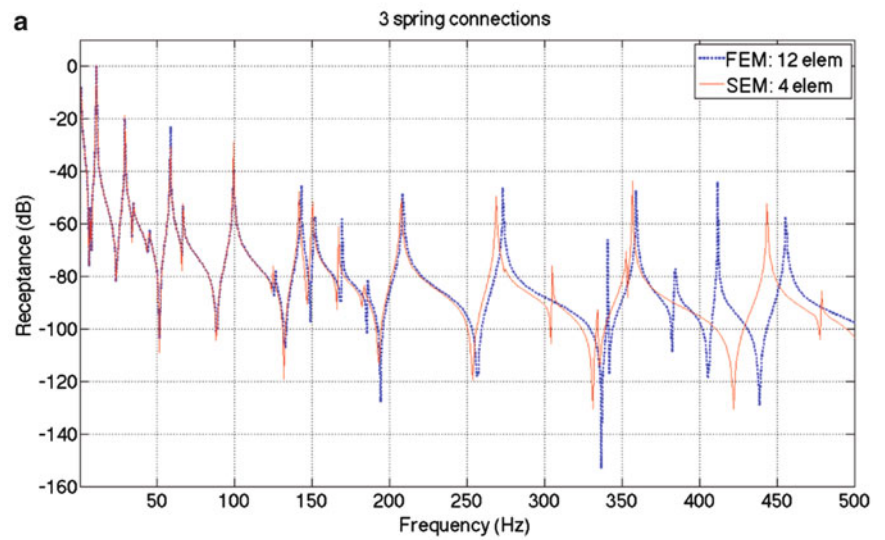
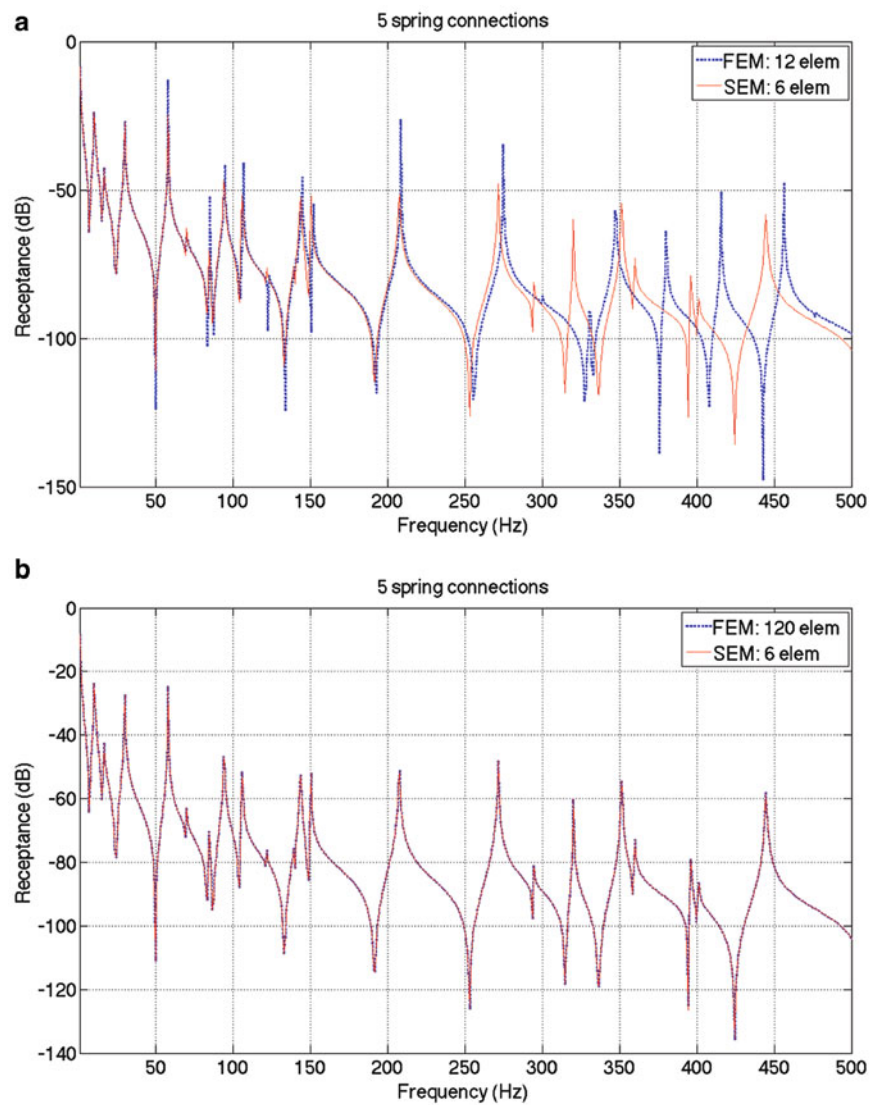


**Fig. 35.7** Receptance versus frequency graph of double beam with 5 connections. (a) Receptance of SEM (6 element) and FEM (12 elements). (b) Receptance of SEM (6 element) and FEM (120 elements)



# Chapter 36

## Analytic Formula Derivation for a Rolling Tire with a Ring Model

Jongsuh Lee, Peter Kindt, Bert Pluymers, Paul Sas, and Semyung Wang

**Abstract** This paper analyzes the dynamic characteristics of a rolling tire with a modal approach. A ring model is adopted to model a tire and this model is substituted in a general transfer function and considers the rolling condition to make a transfer function of a rolling tire in the Laplace domain and an corresponding impulse response function in the time domain. From this transfer function it is clearly confirmed that the shifting effect, the so-called Doppler Effect, shifts not only the natural frequencies but also the damping ratios.

**Keywords** Rolling tire • Ring model • Fixed reference frame • Mode summation method • Doppler shifting

### 36.1 Introduction

Interior noise, vibrations and passenger's harshness are getting more importance as the car's quality is improving. Automobile companies have organized the NVH group where they are conducting studies focusing on these issues. It is identified that the vibration occurring in low frequency region ( $< 500$  Hz) affects vehicle interior noise and vibration level due to interaction between the tire and the road while it is moving on the road [1, 2]. Therefore, studies of tire/road interaction have been also carried out as well, as itself of a tire. There are many approaches to understand the dynamic characteristics of a rolling tire, which are from a case regarding a tire as a ring model, a pneumatic tire case [3], a ring model case on an elastic foundation with distributed spring in radial and tangential directions [4] and to rotating case [5]. Many of these approaches create a tire model with numerical analysis methods [4, 6], Lopez et al. [7] apply modal analysis method to analyze the dynamic characteristics of it. Kindt et al. [1, 2] analyze the dynamic characteristics of a rolling tire in operating condition with the Operational Modal Analysis (OMA) method with a newly proposed experimental setup which consists of two identical tires, one is for driving, while the other one is for measuring, this setup is more simpler than existing setups which use a large drum. In addition, influential factors (rotating speed, inflation pressure, cleat height, etc.) are investigated by experiments.

In this research a tire is analyzed by a ring model under the assumption that the tire is measured by a non-contact sensor (Euler reference), a laser vibrometer and an analytic formula is derived for analyzing the dynamic characteristics while the tire/ring is rotating. Every term of this formula is investigated to interpret the physical meaning of it.

---

J. Lee • S. Wang (✉)  
Gwangju Institute of Science and Technology (GIST), 261 Cheomdan-gwagiro (Oryong-dong),  
Buk-gu, Gwangju, 500-712, Republic of Korea  
e-mail: [leejongsuh@gist.ac.kr](mailto:leejongsuh@gist.ac.kr); [smwang@gist.ac.kr](mailto:smwang@gist.ac.kr)

P. Kindt  
Goodyear Innovation Center, Colmar-Berg, Luxembourg  
e-mail: [peter\\_kindt@goodyear.com](mailto:peter_kindt@goodyear.com)

B. Pluymers • P. Sas  
Katholieke Universiteit Leuven, Leuven, Belgium  
e-mail: [bert.pluymers@mech.kuleuven.be](mailto:bert.pluymers@mech.kuleuven.be); [paul.sas@mech.kuleuven.be](mailto:paul.sas@mech.kuleuven.be)

## 36.2 Theory

### 36.2.1 Brief Introduction of a Rotating Ring

Over the past few decades, a considerable number of studies have been conducted on the rolling tire with a ring model. In this article, the same model is used to investigate the changes of dynamic characteristics during rotating condition. First of all, natural frequency of a non-rotating ring is represented by  $\omega_n$  and modeshape shows standing wave. Once the ring starts rotating in counterclockwise direction, the natural frequency can be divided into  $\omega_{n1}$  and  $\omega_{n2}$  (bifurcation effect). The modeshape of each mode will respectively form a travelling wave in the opposite and same direction to the rotation of the ring [8]. These are called backward and forward mode. Here, subscript 1 refers to the backward mode and subscript 2 refers to the forward mode. There are two coordinate axes to deal with a rotating ring. One is a co-axis reference frame, which uses a local coordinate axis during rotation. It is used to describe the dynamic characteristics of a rolling tire which is measured by accelerometer attached on the tire. Another one is a fixed reference frame, which uses absolute coordinate in order to describe dynamic characteristics during rotation. It is possible to apply this coordinate frame to a rolling tire which is measured by a non-contact sensor, Laser Vibrometer. It is observed that the natural frequencies are shifted by angular velocity while considering a fixed reference frame for measurement. This phenomenon is called Doppler shift. Previous researches have explained the Doppler shift in the following ways.

$$u_3(\theta, t) = A_3 e^{j(n\theta + \omega_n t)} \quad (36.1)$$

Where,  $u_3$  is the modeshape in radial direction,  $A_3$  is the modal participation constant,  $n$  is individual mode number, and  $\theta$  is the location of radial direction. The modeshape shown in Eq. 36.1 is for a co-axis reference frame. Absolute coordinate is introduced to transform the axis frame to a fixed reference frame and the shape of the absolute coordinate is given as.

$$\Psi = \Omega t + \theta \quad (36.2)$$

Here,  $\Psi$  is the absolute coordinate,  $\Omega$  is the angular velocity. The result of substituting Eq. 36.2 in Eq. 36.1 will give that the modeshape of a fixed reference frame.

$$u_3(\Psi, t) = A_3 e^{j[n\Psi + (\omega_n - n\Omega)t]} \quad (36.3)$$

Equation 36.3 includes a shifting parameter, in comparison with Eq. 36.1, for natural frequency, which is represented by combination of mode number and angular velocity. As shown in Eq. 36.3, Doppler shifting is described by transformation of a coordinate frame and its results make it possible to understand the response measured in a fixed reference frame. Analytic formula, however, has not been studied to represent dynamic behavior changes in a fixed reference frame. It will be shown in the next chapter that the parameter included in the derived formula is related to the Doppler shifting.

### 36.2.2 Derive a Formula of a Rotating Ring with Mode Summation Method

Each mode of structure is composed of natural frequency, damping ratio and modeshape. Summation of each mode is used to estimate and analyze the dynamic characteristics of the structure [9]. For instance, given an analytic model, which is made up of  $N$  number of modes, each mode is assumed second order system and then is compared with frequency response function obtained by experiment. Each parameter, in analytic model, by minimizing the difference between the analytic model and the experiment result can be estimated and the estimated parameters can be compared with numerical model to verify the reliability of the analytic model [10]. The form of an analytic model commonly used is as below.

$$H(s) = \sum_{n=1}^N F \frac{\phi_n \phi'_n}{s^2 + 2\zeta_n \omega_n s + \omega_n^2} \quad (36.4)$$

$H$  is the transfer function of the system and  $s$  is a parameter in Laplace domain.  $\zeta_n$  and  $\omega_n$  are the modal damping and the natural frequency of  $n$ th mode respectively.  $\phi_n$  and  $\phi'_n$  are the modeshape information at measured position and the modeshape information at applied force position, respectively. This formula is the starting point for the experimental modal analysis method. Many methodologies have been introduced and these are applied to frequency domain based on Eq. 36.4.

In this study, an analytic model for a rotating ring is derived from Eq. 36.4. As shown in previous chapter, for a rotating case each mode is separated in backward and forward mode with respect to direction of rotation. Once, this concept is applied to in a co-axis reference frame, then, Eq. 36.4 is transformed as below.

$$H(s) = H_1(s) + H_2(2) = \sum_{n=0}^N F \frac{\phi_{n1}(\theta_s) \phi_{n1}(\theta_f)}{s^2 + 2\zeta_{n1}\omega_{n1}s + \omega_{n1}^2} + \sum_{n=1}^N F \frac{\phi_{n2}(\theta_s) \phi_{n2}(\theta_f)}{s^2 + 2\zeta_{n2}\omega_{n2}s + \omega_{n2}^2} \quad (36.5)$$

Where

$$\phi_{n1}(\theta) = A_{n1}e^{jn\theta}, \quad \phi_{n2}(\theta) = A_{n2}e^{-jn\theta} \quad (36.6)$$

Equation 36.5 depicts that the respective frequency response function of a rotating ring depends on the direction of rotation of the modeshape (i.e. backward and forward), where subscript 1 represents backward mode and 2 represents forward mode. Each formula of each mode has same form as Eq. 36.4.  $\theta_s$  and  $\theta_f$ , which are included in the numerator, represent the circumferential direction at sensor position and the applied force position respectively. Modeshape of each mode are depicted in Eq. 36.6. As shown in Eq. 36.5,  $H_1$  and  $H_2$  have similar form. For simple derivation, only the backward case is considered in deriving process. First of all, the Eq. 36.5 is expressed in time domain by using inverse Laplace transform.

$$h_1(t) = \sum_{n=0}^N \frac{F}{\omega_{d1}} A_{n1}^2 e^{jn\theta_f} e^{jn\theta_s} e^{-\zeta_{n1}\omega_{n1}t} \sin(\omega_{d1}t) \quad (36.7)$$

Equation 36.7 shows the expression of impulse response function (IRF) in time domain.

For the fixed reference frame, that is, for the case where laser vibrometer is used to measure response of vibration, the measurement point is changed with respect to time. Therefore, the sensor position can be considered by function of time.

$$\theta_s = \theta_0 - \frac{2\pi}{T}t \quad (36.8)$$

Where  $T(= 1/\Omega)$  is the measured time,  $\theta_0$  is the location from where the measurement was started. Because the ring was assumed to rotate in the counterclockwise direction, it includes a  $-$  sign. Once Eq. 36.8 is substituted into Eq. 36.7, by the previous assumption, co-axis reference frame is transformed into a fixed reference frame (Eq. 36.9).

$$h_1(t) = \sum_{n=0}^N \frac{F}{\omega_{d1}} A_{n1}^2 e^{jn\theta_f} e^{jn(\theta_0 - \frac{2\pi}{T}t)} e^{-\zeta_{n1}\omega_{n1}t} \sin(\omega_{d1}t) \quad (36.9)$$

Equation 36.9 shows combined spatial information derived by modeshape with time information derived by time domain. Note that Eq. 36.9 combines the time information which is derived in time domain with spatial information which is derived by modeshape. Rearranging this equation with respect to the time and spatial domain, we obtained.

$$h_1(t) = \sum_{n=0}^N \frac{F}{\omega_{d1}} B_{n1} e^{-j\frac{2n\pi}{T}t} e^{-\zeta_{n1}\omega_{n1}t} \sin(\omega_{d1}t) \quad (36.10)$$

Where,

$$B_{n1} = A_{n1}^2 e^{jn(\theta' + \theta_0)} \quad (36.11)$$

Where  $e^{-j\frac{2n\pi}{T}t}$ , in Eq. 36.10, is expanded by Euler's formula.

$$h_1(t) = \sum_{n=0}^N \frac{F}{\omega_{d1}} B_{n1} \left\{ \cos \frac{2n\pi}{T}t - j \sin \frac{2n\pi}{T}t \right\} \sin(\omega_{d1}t) e^{-\zeta_{n1}\omega_{n1}t} \quad (36.12)$$

Equation 36.12 is expanded and applied trigonometric identity to the result. Then,

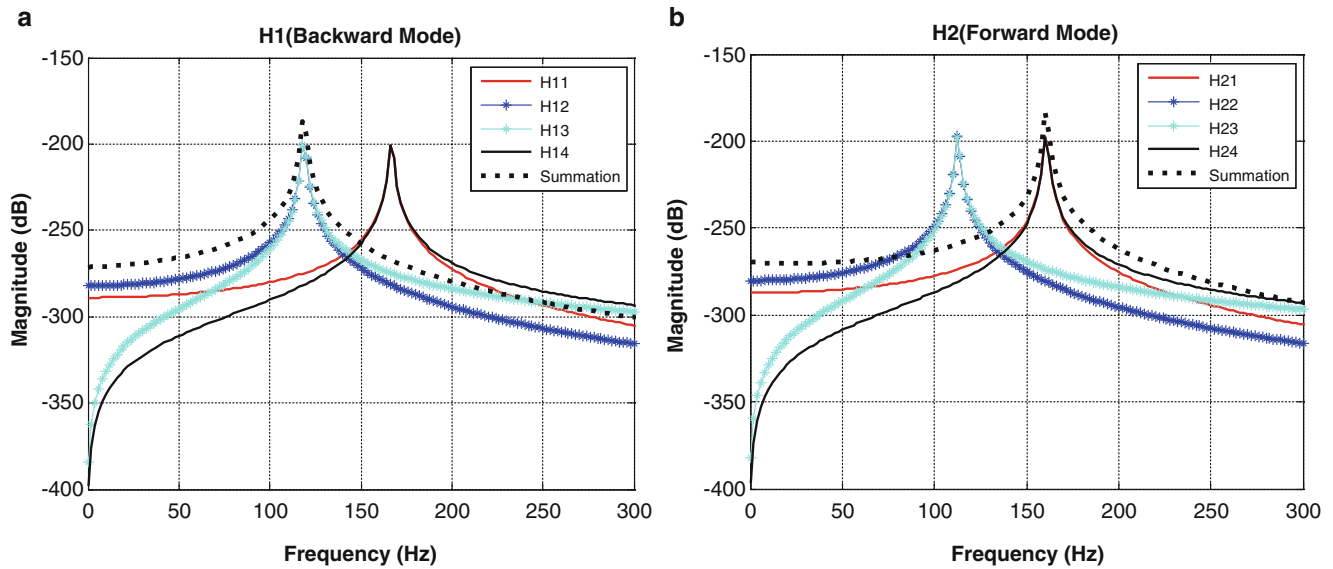


**Fig. 36.1** (a) Every each component of H1 and summation of those, (b) every each components of H2 and summation of those

$$h_1(t) = \sum_{n=0}^N \frac{F}{2\omega_{d1}} B_{n1} \left\{ \sin\left(\omega_{d1} + \frac{2n\pi}{T}\right)t + \sin\left(\omega_{d1} - \frac{2n\pi}{T}\right)t - j \cos\left(\omega_{d1} - \frac{2n\pi}{T}\right)t + \cos\left(\omega_{d1} + \frac{2n\pi}{T}\right)t \right\} e^{-\zeta_{n1}\omega_{n1}t} \quad (36.13)$$

Applying Laplace transform to Eq. 36.13, the transfer function of the backward mode in a fixed reference frame is obtained (Eq. 36.14).

$$H_1(s) = \sum_{n=0}^N \frac{F}{2\omega_{d1}} B_{n1} \left\{ \begin{array}{l} \frac{\omega_{d1} + \frac{2n\pi}{T}}{(s + \zeta_{n1}\omega_{n1})^2 + (\omega_{d1} + \frac{2n\pi}{T})^2} + \frac{\omega_{d1} - \frac{2n\pi}{T}}{(s + \zeta_{n1}\omega_{n1})^2 + (\omega_{d1} - \frac{2n\pi}{T})^2} \\ j \left( \frac{s + \zeta_{n1}\omega_{n1}}{(s + \zeta_{n1}\omega_{n1})^2 + (\omega_{d1} - \frac{2n\pi}{T})^2} - \frac{s + \zeta_{n1}\omega_{n1}}{(s + \zeta_{n1}\omega_{n1})^2 + (\omega_{d1} + \frac{2n\pi}{T})^2} \right) \end{array} \right\} \quad (36.14)$$

In the same manner, the forward mode is induced as below.

$$H_2(s) = \sum_{n=1}^N \frac{F}{2\omega_{d2}} B_{n2} \left\{ \begin{array}{l} \frac{\omega_{d2} + \frac{2n\pi}{T}}{(s + \zeta_{n2}\omega_{n2})^2 + (\omega_{d2} + \frac{2n\pi}{T})^2} + \frac{\omega_{d2} - \frac{2n\pi}{T}}{(s + \zeta_{n2}\omega_{n2})^2 + (\omega_{d2} - \frac{2n\pi}{T})^2} \\ j \left( \frac{s + \zeta_{n2}\omega_{n2}}{(s + \zeta_{n2}\omega_{n2})^2 + (\omega_{d2} - \frac{2n\pi}{T})^2} - \frac{s + \zeta_{n2}\omega_{n2}}{(s + \zeta_{n2}\omega_{n1})^2 + (\omega_{d2} + \frac{2n\pi}{T})^2} \right) \end{array} \right\} \quad (36.15)$$

Equations 36.14 and 36.15 represent the transfer functions for backward mode and forward mode, sum of these two equations is the analytic model which can be compared with frequency response function which is the result of experiment

### 36.2.3 Interpretation of the Derived Formula

Equations 36.14 and 36.15 have more complex form in comparison with the Eq. 36.4 which is the starting point of derivation of the formula. These two equations, for backward mode and for forward mode, are composed of four bases, out of which two parts have an increment of  $\frac{2n\pi}{T}$  in original resonance frequency while the other two parts have a decrement of  $\frac{2n\pi}{T}$  in



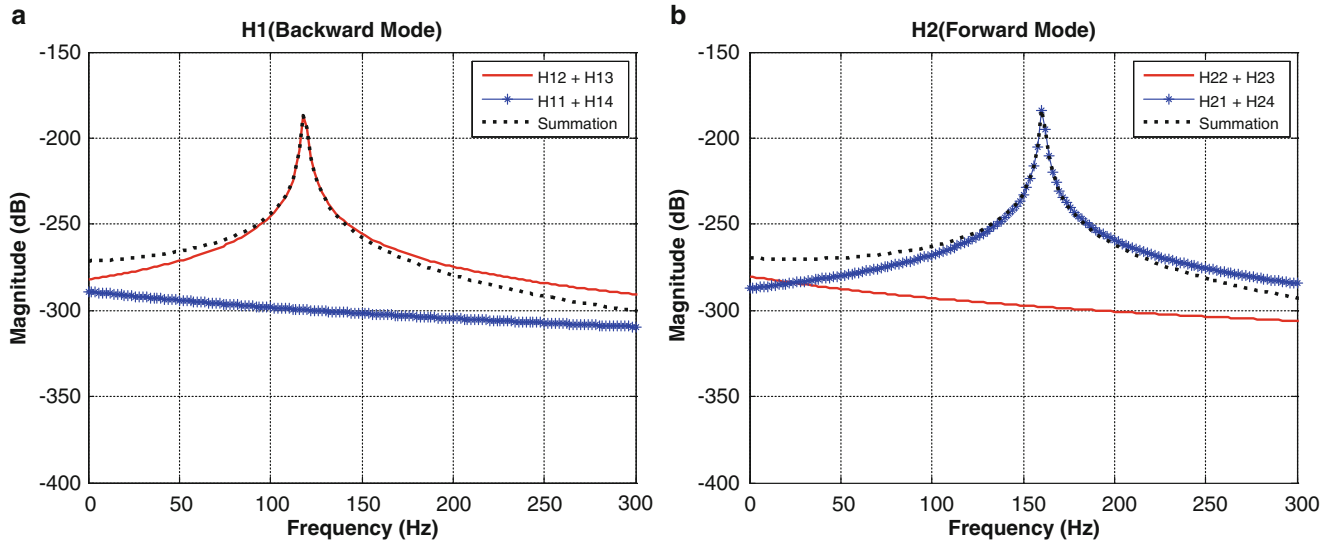


**Fig. 36.2** (a) Sum of two components located on same frequency of a peak value and sum result of each component of H1, (b) sum of two components located on same frequency of a peak value and sum result of each component of H2

original resonance frequency. Each Eqs. 36.14 and 36.15, can be divided into real and imaginary part. For the Eq. 36.14, the first part of real term is referred as  $H_{11}$  and the second part of real term is referred as  $H_{12}$ , while the first part of imaginary term is referred as  $H_{13}$  and the second part of imaginary term is referred as  $H_{14}$ . In the same manner, every basis in Eq. 36.15 is referred as  $H_{21}$ ,  $H_{22}$ ,  $H_{23}$  and  $H_{24}$ .

The first and fourth basis of H1, H2 are plotted by solid lines, while the second and third basis are plotted by combination of solid line and star and the summation results are plotted by bold dotted line as shown in Fig. 36.1. In the figure, it is observed that every basis has its peak. Two bases of those for the each mode have peak values at the same place with the summation results which is appeared by summation of all the bases of each mode. In other two bases, however, it is observed that the peaks are located at different places to the summation results. Examining H1 and H2 separately, the second and third bases of peak of H1 are located on the same place with summation result of H1, while, the other bases are located on rather increasing frequency compared to the summation result (Fig. 36.1a). Contrary to H1, the first and fourth bases of peak of H2 are located on the same place with summation result of H2, while, the other bases are located on rather decreasing frequency compared to summation result (Fig. 36.1b). For the purpose of investigating more clear relationship between each basis and summation result for each distinct mode, every basis is rearranged with respect to the location of the peak and their sums are plotted in Fig. 36.2.

Figure 36.2a, in which there are three lines shown for H1, these three lines can be distinguished by the locations of the peaks or by the sum of all bases. The summation result is expressed by bold dot, sum of H12 and H13 is expressed by solid line and sum of H11 and H14 is expressed by combination of solid line and star. As expected, the sum result of H12 and H13 is similar with the sum result of all the bases of H1, but sum of H11 and H14, of which peaks are located on higher place than the result of all summation, shows monotonic decreasing tendency. Figure 36.2b is for H2, as same with Fig. 36.2a, sum of all bases is expressed by bold dot and sum of H21 and H24 is expressed by combination of solid line and star. As expected, that the sum of H21 and H24, of which peaks are located on the same place with the summation result of all bases, shows similar behavior with the sum results, but sum of H22 and H23, of which peaks are located on lower place than the place of all summation result, shows monotonic decreasing tendency. Thus, it has been confirmed that both H1 and H2 have element for having a peak and element for being monotonically decreasing tendency, these two elements are summarized as below.

$$H_{1s} = H_{12} + H_{13}, \quad H_{2s} = H_{21} + H_{24} \tag{36.16}$$

$$H_{1h} = H_{11} + H_{14}, \quad H_{2h} = H_{22} + H_{23} \tag{36.17}$$

Where, Eq. 36.16 represents elements, for each mode, H1 and H2, composing peak value, these elements are referred by subscript s. In the similar manner, Eq. 36.17 represents elements showing

Monotonic decreasing part (denoted by subscript h) has considerably smaller values than peak part (denoted by subscript s) as shown in Fig. 36.2. Given results estimated by applying experimental modal analysis (EMA) method (e.g. LSCF, ITD and etc.) to experimental measurement of a rolling tire are the values regarding indicated by subscript s of Eq. 36.16, on

the contrary, the values, even though these are included in experimental measurement, are not likely to be estimated by traditional EMA method. Therefore, in this paper, the part represented by Eq. 36.16, which can be estimated from modal estimation method, is called “Shown part” and the part even though it is included in experimental measurement result but does not appear is called “Hidden part”. As shown in Fig. 36.2. Shown part has a peak value and from this fact, it makes it possible to predict the shown part affecting to vibration in radial direction of a rotating ring. Also shown in the figure, most of the components in frequency of the hidden part are allocated on low frequency region, it affects the envelope of vibration in time domain. The shape of the low frequency of the hidden part is affected by the curvature of the measurement node during rotation. Consequently, it is induced that the hidden part is related to modeshape. Within Eqs. 36.14 and 36.15, the hidden part of each H1 and H2 pushes respective natural frequency as much as  $\frac{2n\pi}{T}$  to  $-$  direction and  $+$  direction. Due to this fact, the resonance frequency of backward mode, when a rotating tire is measured in a fixed reference, is decreased by  $\frac{2n\pi}{T}$  than the resonance frequency for a co-axis frame. Similarly, it is shown that the resonance frequency of forward mode is increased by same amount. It should be noted that because it can explain the phenomenon that the resonance frequency is changed depending on the direction of the mode and this phenomenon is called Doppler Effect. Next, the phenomenon, which is observed by Fig. 36.2, about the shown part and the hidden part are verified by a formula for H1 and H2. H1 is only used to derive the equation for the same reason as given in the first chapter. To begin with, the shown part and the hidden part in Eq. 36.14 are expressed together (Eq. 36.18)

$$H_1 = \sum_{n=0}^N \frac{F}{2\omega_{d1}} B_{n1} \left\{ \frac{\left(\omega_{d1} + \frac{2n\pi}{T}\right) + j(s + \zeta_{n1}\omega_{n1})}{(s + \zeta_{n1}\omega_{n1})^2 + \left(\omega_{d1} + \frac{2n\pi}{T}\right)^2} + \frac{\left(\omega_{d1} - \frac{2n\pi}{T}\right) - j(s + \zeta_{n1}\omega_{n1})}{(s + \zeta_{n1}\omega_{n1})^2 + \left(\omega_{d1} - \frac{2n\pi}{T}\right)^2} \right\} \quad (36.18)$$

There are common terms include in Eq. 36.18. These terms can be represented by more simple forms.

$$H_1 = \sum_{n=0}^N \frac{F}{2\omega_{d1}} B_{n1} \left\{ \frac{\omega_{hn1} + ja_{n1}(s)}{a_{n1}(s)^2 + \omega_{hn1}^2} + \frac{\omega_{sn1} - ja_{n1}(s)}{a_{n1}(s)^2 + \omega_{sn1}^2} \right\} \quad (36.19)$$

Where

$$\omega_{hn1} = \left(\omega_{d1} + \frac{2n\pi}{T}\right), \omega_{sn1} = \left(\omega_{d1} - \frac{2n\pi}{T}\right) \quad \text{and} \quad a_{n1}(s) = (s + \zeta_{n1}\omega_{n1}) \quad (36.20)$$

In Eq. 36.19, the first term inside the brace is the hidden part and the second one is the shown part. The elements composing of these parts are summarized in Eq. 36.20. If the each of parts is multiplied by the complex conjugate of numerator to the numerator and the denominator at the same time, then, each of the original denominators can be cancelled out, and only the complex conjugate terms remained. Substituting  $s = j\omega$  to the remained equation is as follows.

$$H_1(j\omega) = \sum_{n=0}^N \frac{F}{2\omega_{d1}} B_{n1} \left\{ \frac{1}{\omega_{hn1} + \omega + j\zeta_{n1}\omega_{n1}} + \frac{1}{\omega_{sn1} - \omega + j\zeta_{n1}\omega_{n1}} \right\} \quad (36.21)$$

As same with Eq. 36.19, the first term inside the brace of Eq. 36.21 is the hidden part and the second one is the shown part. As you can see from Eq. 36.21, the denominator of the hidden term is increased when the variable increases due to the  $+$  sign of the  $\omega$ . Otherwise, the shown part has minimum value, when  $\omega$  is close to the resonance frequency of the shown part,  $\omega_{sn1}$ , due to the  $-$  sign. Therefore, you can see that the hidden part has a monotonically decreasing tendency and the shown part has maximum value (peak value) at the resonance frequency. The results shown in Fig. 36.2a. are proved from Eq. 36.21.

### 36.3 Conclusion

The transfer function of a rotating ring model is derived for the purpose of analyzing the dynamic characteristics of a rolling tire by the mode summation method. Generally, a rotating ring can be expressed by two axis frames. One is the co-axis frame and the other one is the fixed reference frame. The derived transfer function is for the case of the fixed reference frame. The phenomenon that each of the resonance frequencies of each mode, backward and forward mode, is shifted to the ‘ $-$ ’ and ‘ $+$ ’ direction when a rotating ring is expressed in a fixed reference frame, is clearly explained by the derived formula. This phenomenon is called the Doppler shifting and is observed in response data which is measured by a laser vibrometer on a rolling tire. This paper shows that each mode has a different travelling wave direction. The hidden and the shown part, which

are included in each mode, are introduced in this paper. The transfer function of a rotating ring is expressed depending on the travelling wave direction and also depending on the hidden and shown part. The physical meaning of each part is interpreted.

**Acknowledgements** The authors would like to thank the EU Seventh Framework Programma (FP7/2010) for its support under the TIRE-DYN project (grant agreement no 251211) and LMS International for co-financing the research stay of the first author in Leuven.

## References

1. Kindt P, Sas P, Desmet W (2009) Measurement and analysis of rolling tire vibrations. *Opt Lasers Eng* 47(3–4):443–453
2. Kindt P, Berckmans D, De Coninck F, Sas P, Desmet W (2009) Experimental analysis of the structure-borne tyre/road noise due to road discontinuities. *Mech Syst Signal Process* 23:2557–2574
3. Kung LE, Soedel W, Yang TY (1986) On the dynamic response at the wheel axle of a pneumatic tire. *J Sound Vib* 107(2):195–213
4. Kung LE, Soedel W, Yang TY (1986) Free vibration of a pneumatic tire-wheel unit using a ring on an elastic foundation and a finite element model. *J Sound Vib* 107(2):181–194
5. Kindt P, Sas P, Desmet W (2009) Development and validation of a three-dimensional ring-based structural tyre model. *J Sound Vib* 326: 852–869
6. Brinkmeier M, Nackenhorst U, Petersen S, Estorff OV (2008) A finite element approach for the simulation of tire rolling noise, a finite element approach for the simulation of tire rolling noise. *J Sound Vib* 309:20–39
7. Lopez I, Blom PEA, Roozen NB, Nijmeijer H (2007) Modelling vibrations of deformed rolling tyres – a modal approach. *J Sound Vib* 307:481–494
8. Soedel W (2004) *Vibrations of shells and plates*, 3rd edn. Marcel Dekker, New York
9. Ewins DJ (2000) *Modal testing: theory and practice*, 2nd edn. Research studies, Baldock
10. Heylen W, Lammens S, Sas P (1997) *Modal testing theory and testing*. Katholieke Universiteit Leuven, Belgium

# Chapter 37

## Nonlinear Identification of the Viscous Damping of the Resistor for Nuclear Plants

Giancarlo Galli, Francesco Braghin, and Edoardo Sabbioni

**Abstract** A procedure for the nonlinear modal analysis of a resistor is presented in this paper. The identification process aims at assessing the viscous damping factor of the structure including the nonlinear terms in the frequency response function with the harmonic balance method. For this purpose a simplified single DOF system has been adopted to describe the nonlinear behavior. A good agreement between numerical and experimental results has been achieved.

**Keywords** Structural safety • Nonlinear dynamics • Nonlinearity modeling • Modal analysis • Harmonic balance

### Nomenclature

$\Omega$	Excitation frequency
$\xi$	Viscous damping factor
$\omega$	Natural frequency of the system
$A$	Modal constant
$H$	Frequency response function
$S$	Spectrum
$k_1$	Mass-normalized linear stiffness
$k_3$	Mass-normalized cubic stiffness
$r_1$	Mass-normalized linear viscous damping

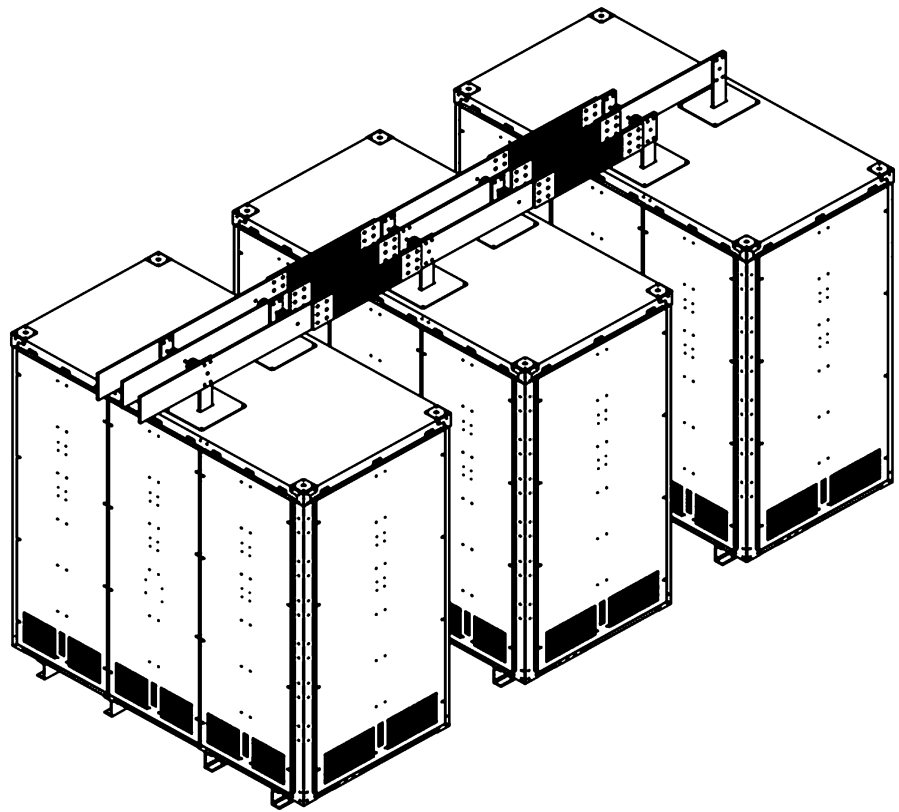
### 37.1 Introduction

The safety of nuclear plants is nowadays a key-issue in the field of energy production. In particular it's necessary to ensure the operational continuity of the system and of its auxiliary components even in presence of extreme events such as hurricanes or earthquakes. This task has been remarkably complicated by the fact that, due to the request of weight and cost reduction, structures have become more slender and therefore their fatigue life is strongly affected by their dynamic behavior.

The prototype of a resistor for the dissipation of the electric charge of a supermagnet in a nuclear plant is analyzed in this paper. In particular its structural safety in the case of a seismic event has been evaluated with an extensive experimental modal analysis aimed at assessing the viscous damping factor of the structure. Since the typical acceleration levels of an earthquake are such as to excite the nonlinearities of the structure, the present paper describes a methodology to include these effects in the frequency response function.

---

G. Galli • F. Braghin (✉) • E. Sabbioni  
Department of Mechanical Engineering, Politecnico di Milano, Via la Masa 1, 20158 Milano, Italy  
e-mail: [giancarlo.galli@polimi.it](mailto:giancarlo.galli@polimi.it); [francesco.braghin@polimi.it](mailto:francesco.braghin@polimi.it); [edoardo.sabbioni@polimi.it](mailto:edoardo.sabbioni@polimi.it)

**Fig. 37.1** Complete resistor

## 37.2 Tested Structure

The complete resistor consists of three modules linked by three bars on the top, as shown in Fig. 37.1. Each module has the same configuration and presents the following main components:

- A frame composed by riveted beams,
- Covering panels to protect internal parts,
- Two internal suspended columns with the resistors.

Since the top bars slightly couple the dynamic behavior of the modules, their presence has been neglected and the experimental tests have concerned a single module.

## 37.3 Experimental Tests

The modal parameters of the resistor have been assessed imposing a slowly increasing sweep vibration at its base according to the *Calculate amplitude test method* of the standard IEC 60068-3-3:1991 [1].

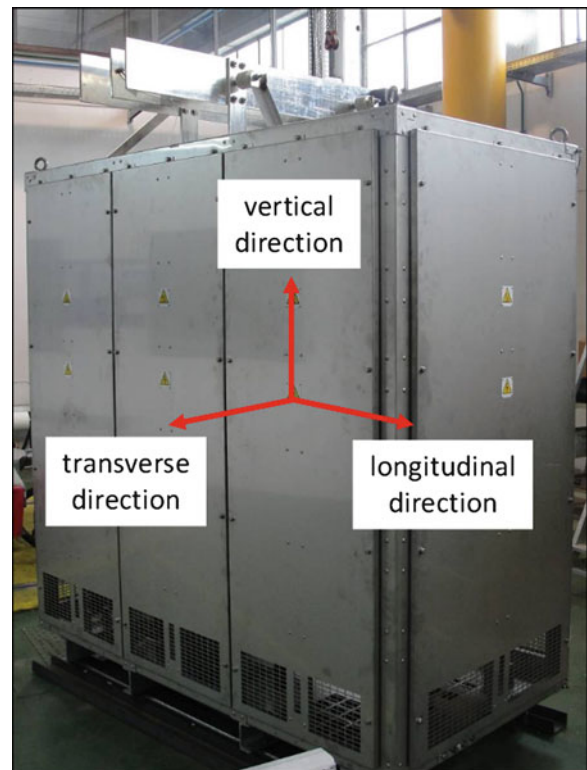
It should be noted that, as the structure presents two geometric symmetries and a load symmetry (the imposed displacement is equal at each ground connection), the standard allows to perform the complete analysis with the superposition of three simple mono-axial tests along the main horizontal directions (Fig. 37.2): longitudinal and transverse.

Eventual interactions of the responses along different directions can be corrected with proper geometric factors.

Each test consists of a sweep excitation from 1 to 35 Hz whose vibration amplitudes have been calculated according to the standard IEC 60068-3-3:1991 for the generic seismic class.

Finally, in order to obtain reliable measurements with high coherence function [2], each test has been repeated 12 times.

**Fig. 37.2** Resistor's test directions



### 37.4 Experimental Set-Up

Tests have been performed on a bench constituted by two table shakers moved by servo-hydraulic actuators controlled in acceleration and able to force the structure both in the horizontal and vertical plane (see Fig. 37.3).

The dynamic response of the resistor have been measured with accelerometers at seven different points in order to get a complete description of the eigenmodes. Each measuring point is indicated with the code TP followed by a progressive number (from Figs. 37.4 to 37.7). The TP1 accelerometer has been placed on the table shaker to obtain the reference displacement.

Since the maximum sweep frequency is equal to 35 Hz, the signals have been acquired with a sampling frequency of 1 kHz and low-pass filtered at 300 Hz to avoid aliasing.

### 37.5 Viscous Damping Assessment

The standard requires to calculate the maximum value of the viscous damping factor for each test. To do this, the following discussion will consider only the most significant resonances of the system.

The signals have been processed according to the sliding discrete Fourier transform algorithm [3] and applying the following steps:

- Windowing of the signals using a sliding short-time Hanning window centered about the considered time instant,
- Computation of the spectra applying the FFT algorithm to extract the harmonic component synchronous with the instantaneous excitation frequency,
- Calculation of auto-spectra and cross-spectra averaging 12 tests,
- Estimation of the frequency response functions and coherence functions considering the imposed acceleration at the base of the structure as the excitation.

In order to reduce the leakage effect, the length of the Hanning window was changed to be as close as possible to an integer multiple of the instantaneous excitation period. Moreover the  $H_3$  estimator has been adopted because it is referred to as the most suitable for nonlinear systems [4].

**Fig. 37.3** Vertical and horizontal table shakers

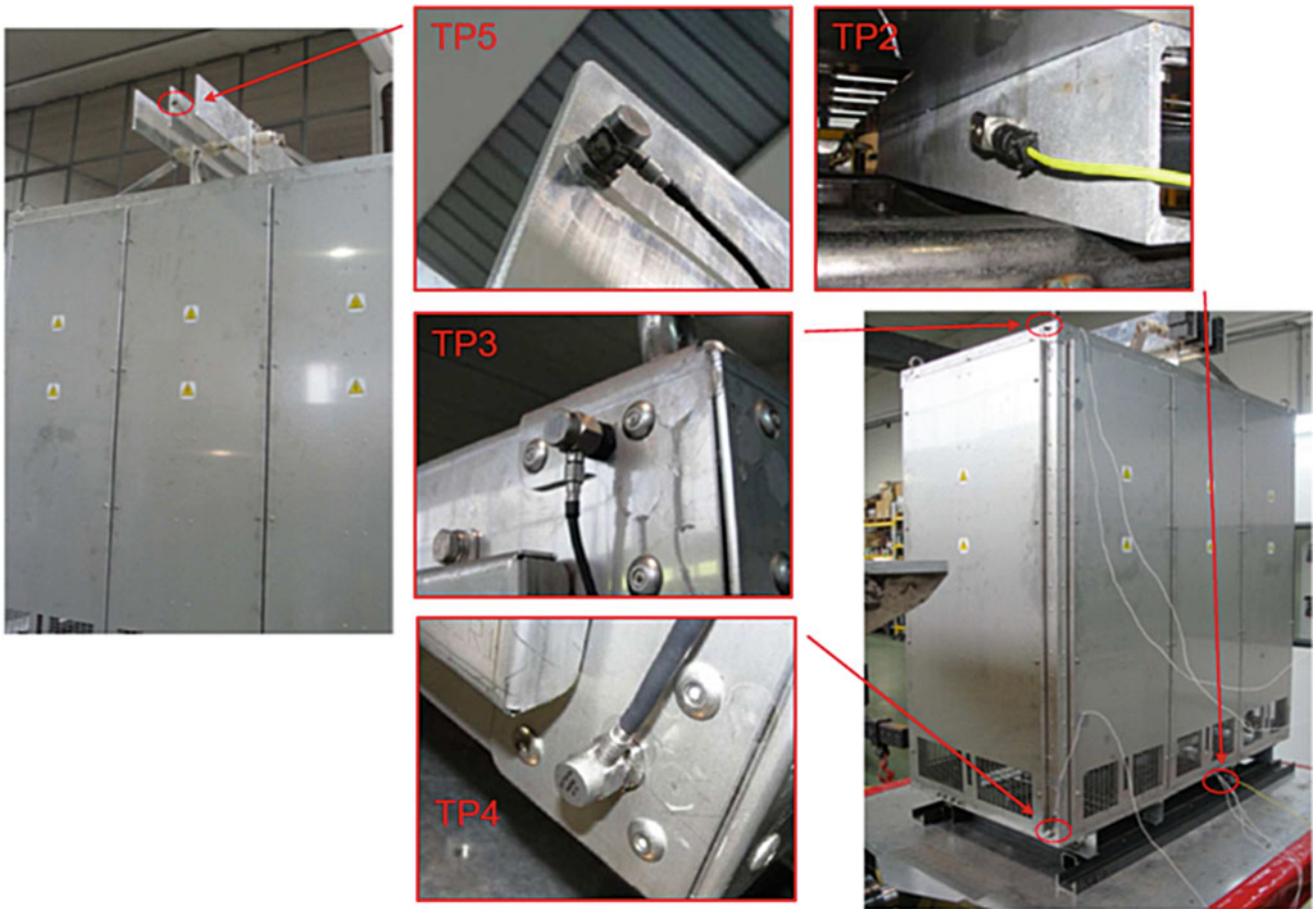


**Fig. 37.4** Measuring points for the longitudinal test (part 1)

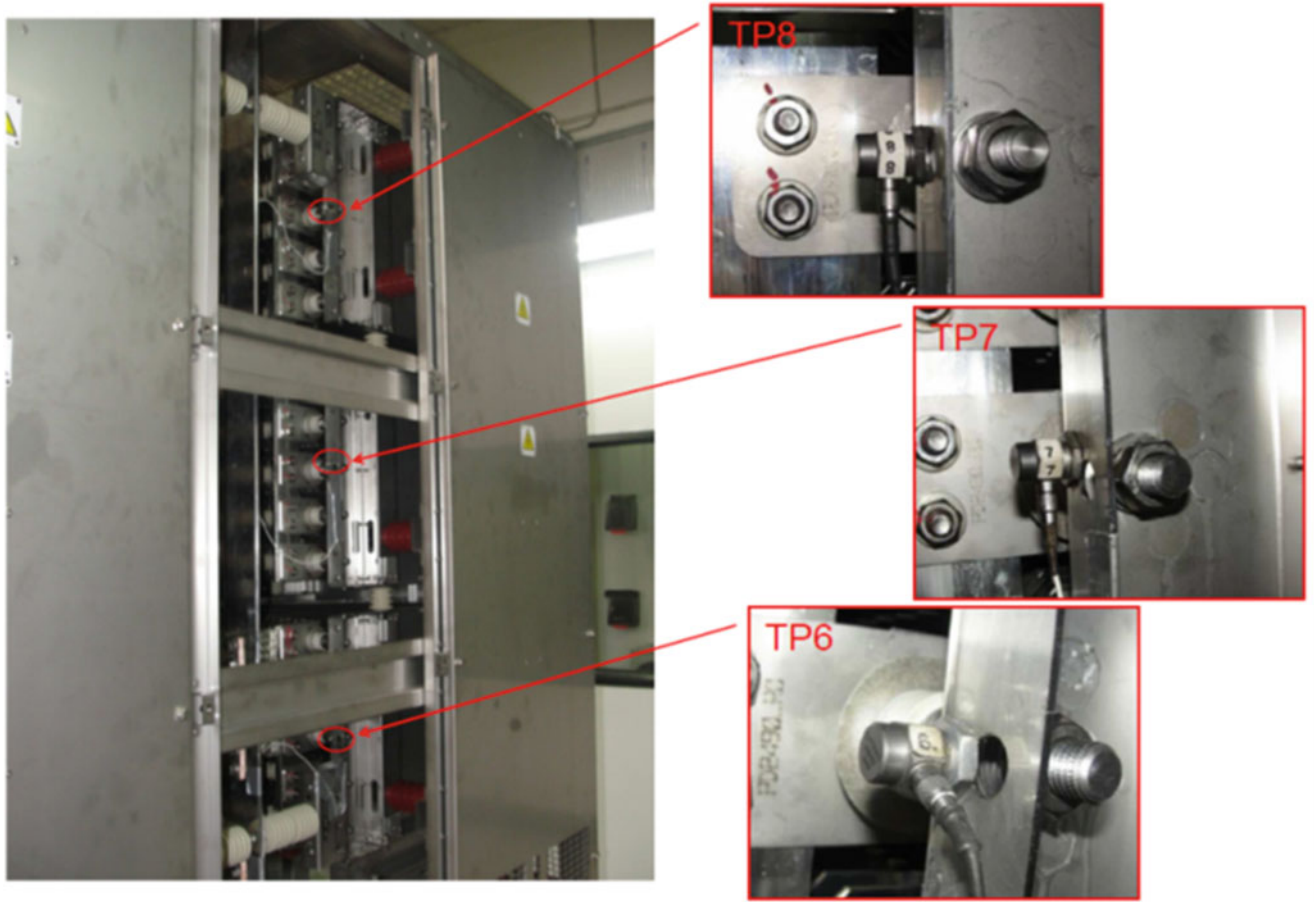


**Fig. 37.5** Measuring points for the longitudinal test (part 2)

As an example, Fig. 37.8 shows the results of the post-process of channel TP4 for the transverse test. In particular the amplitude of the frequency response function (displayed on the top) presents three resonance peaks at approximately 5, 11 and 13 Hz. It should be noted that the value of the coherence function is decreasing in correspondence of the first two resonances. In order to understand the source of this phenomenon tests with lower sweep speeds have been performed but the same frequency response function has been obtained. Therefore this effect has been associated to a discrete nonlinearity inside the tested structure.

The nonlinear behavior has been explained with the geometry of the attachments to the table shaker that is realized with four U channels welded to the resistor's frame and connected to the ground with a screw (Fig. 37.9). The vibration cycle of the U channels can be ideally divided in two phases:

- Traction phase where the lower plate of the U channels bend and, in case of large amplitude motion, can be subjected to a nonlinear deformation that is commonly modeled with a cubic stiffness term [5],
- Compression phase where the lower plate is pushed against the table shaker and the force is transmitted through the vertical plate.

It was decided to model the connection with an equivalent cubic stiffness.

In order to account for this nonlinearity in the identification process, a simplified single DOF model has been adopted where  $x$  is the response of system and  $z$  is the imposed displacement at the base (Fig. 37.10)

The subscripts  $j$  and  $s$  relate to the mass-normalized viscoelastic properties respectively of the joint and the structure

The equation of motion of the simplified single DOF system of Fig. 37.10 is

$$\ddot{x} + (r_{1s} + r_{1j}) \dot{x} + (k_{1s} + k_{1j}) x + k_{3j} (x - z)^3 - r_{1j} \dot{z} - k_{1j} z = 0 \quad (37.1)$$

where  $k_{3j}$  is the nonlinear cubic stiffness of the joint.





**Fig. 37.6** Measuring points for the transverse test (part 1)

The frequency response function of the mass displacement with respect to the ground displacement has been obtained applying the harmonic balance method approximating the solution with a single harmonic:

$$H_{xz}(\Omega) = \frac{X}{Z} = \frac{i\Omega r_{1j} + k_{1j} + \frac{3}{4}k_{3j} |X - Z|^2}{-\Omega^2 + i\Omega(r_{1s} + r_{1j}) + (k_{1s} + k_{1j}) + \frac{3}{4}k_{3j} |X - Z|^2} \quad (37.2)$$

where  $i$  is the imaginary unit and capital letters relate to the complex vibration amplitudes.

This method is generally incorrect because the response of a forced nonlinear system contains several harmonics that are multiple of the excitation frequency. However it can be demonstrated that the amplitudes of the super harmonics are relatively small compared to fundamental one if the mechanical energy is sufficiently low and internal resonances don't occur, as shown in [6] using numerical simulations.

Comparing Eq. 37.2 with the classical frequency response function of a forced single DOF linear system (Eq. 37.3) [7], the following relations can be obtained

$$H_{XF}(\Omega) = \frac{1}{-\Omega^2 + i2h\omega\Omega + \omega^2} \quad (37.3)$$

$$\omega = \sqrt{k_{1s} + k_{1j} + \frac{3}{4}k_{3j} |X - Z|^2} \quad (37.4)$$

$$\xi = \frac{r_{1s} + r_{1j}}{2\omega} \quad (37.5)$$

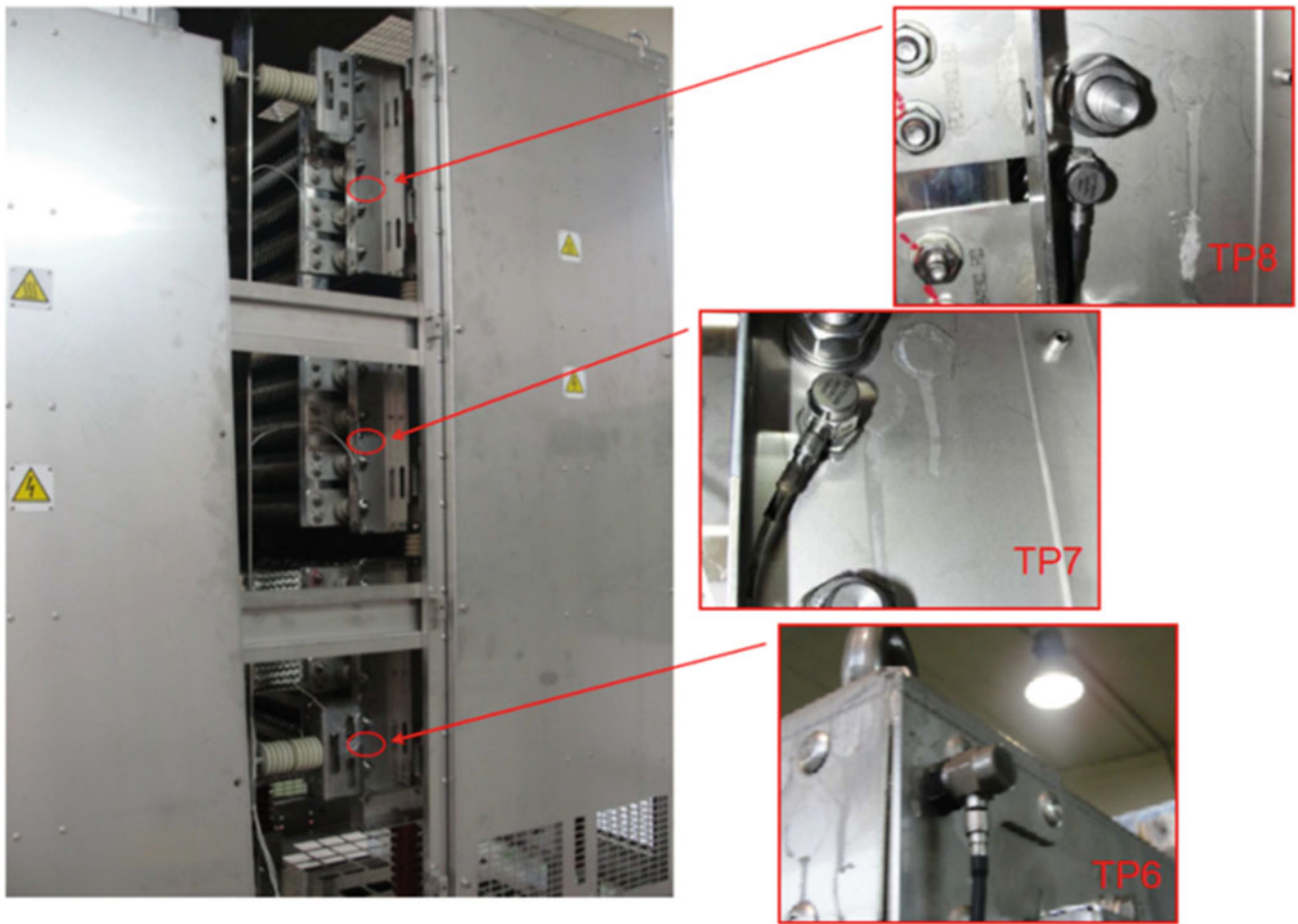


**Fig. 37.7** Measuring points for the transverse test (part 2)

**Fig. 37.8** Frequency response function (*top*) and coherence function (*bottom*) of channel TP4 during the transverse test

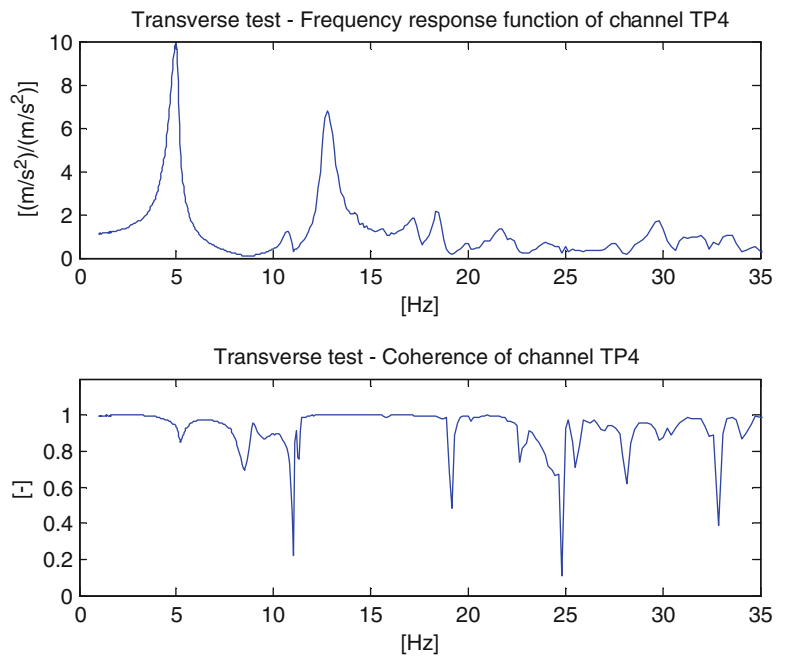


**Fig. 37.9** Geometry of the resistor in correspondence with the attachments to the table shaker

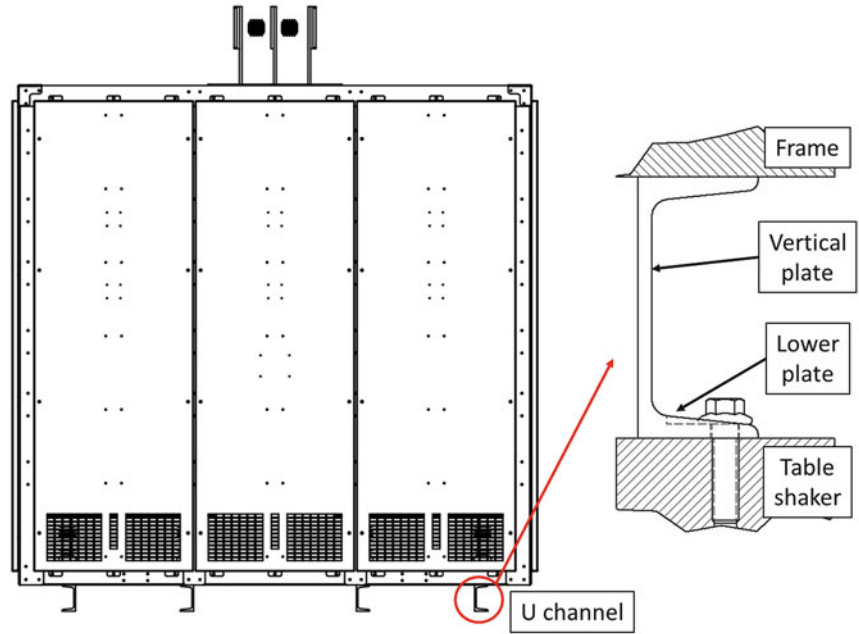
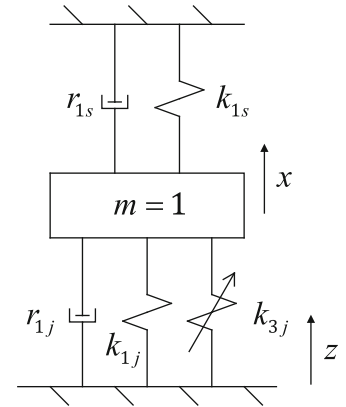


**Fig. 37.10** Simplified model for the resistor's nonlinear dynamics



In agreement with the simplified model, channels TP4 (accelerometer just above an U channel) and TP1 (accelerometer on the table shaker) are the most suitable to represent respectively the output and the input and they have been used for the viscous damping assessment.

Moreover, since the resonance peaks are sufficiently separated, the behavior of the resistor can be approximated as the superposition of several single DOF systems, each one representing a resonance.

Therefore the complete frequency resonance function is defined by

$$H_{TP4,TP1}(\Omega) = \frac{S_{TP4}}{S_{TP1}} = \sum_{m=1}^N A_m \frac{i\Omega r_{1j,m} + k_{1j,m} + \frac{3}{4} \frac{k_{3j,m}}{\Omega^4} |S_{TP4} - S_{TP1}|^2}{-\Omega^2 + i\Omega (r_{1s,m} + r_{1j,m}) + (k_{1s,m} + k_{1j,m}) + \frac{3}{4} \frac{k_{3j,m}}{\Omega^4} |S_{TP4} - S_{TP1}|^2} \quad (37.6)$$

where  $N$  is the number of considered resonances and  $A_m$  is the modal parameter that weights the influence of the excitation on the  $m$ -th mode. The nonlinear term associated to the cubic stiffness has been divided by  $\Omega^4$  because the spectra  $S_{TP4}$  and  $S_{TP1}$  refer to acceleration signals.

The modal parameters and the mass-normalized viscoelastic properties have been assessed minimizing the mean square error between the numerical and experimental frequency response functions in the neighborhood of the resonance peaks where the response is mainly dominated by a single mode. For this purpose the Gauss–Newton algorithm [8] has been adopted. Obviously, in the case of a linear mode,  $k_{3j,m} = 0$ .

**Fig. 37.11** Comparison of the experimental (*continuous line*) and numerical (*dots*) frequency response functions of channel TP4 for the longitudinal test

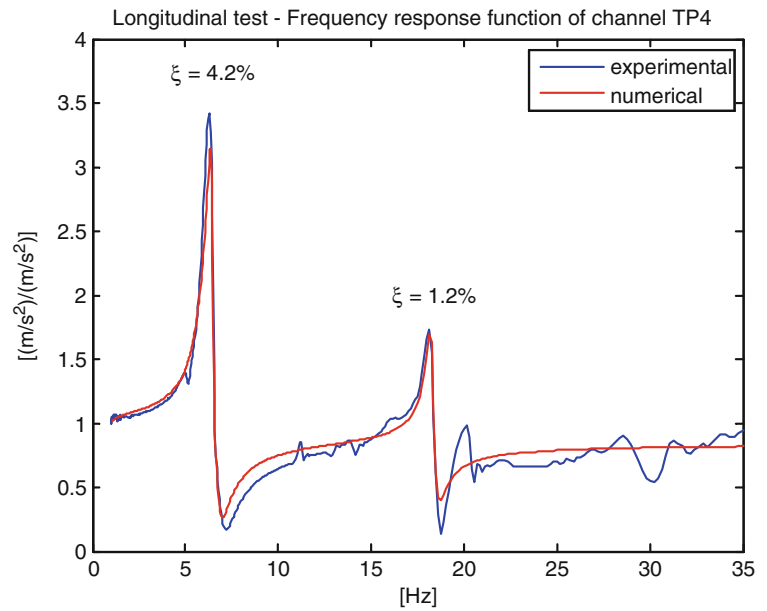


**Fig. 37.12** Comparison of the experimental (*continuous line*) and numerical (*dots*) frequency response functions of channel TP4 for the transverse test

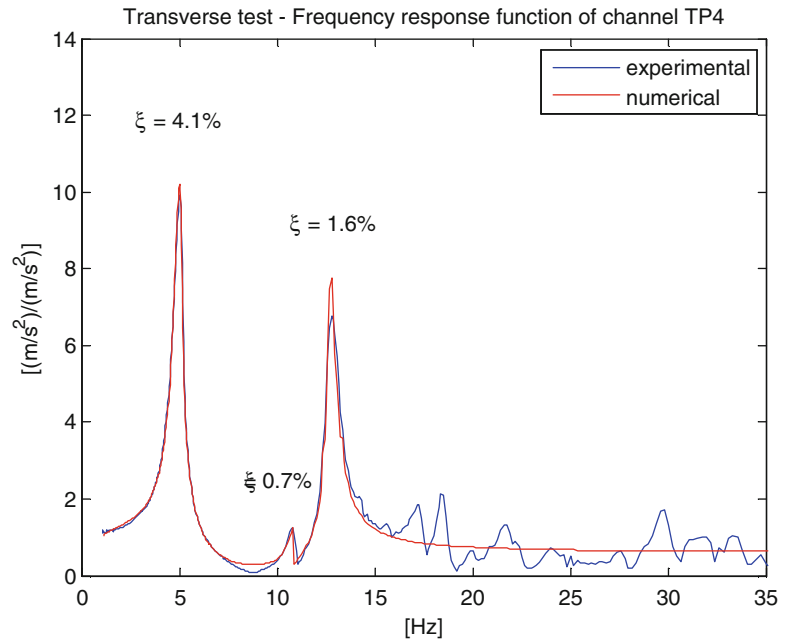


**Table 37.1** Maximum values of the viscous damping factor for each test type

Test type	$\xi_{max}$ (%)
Longitudinal	4.2
Transverse	4.1

Figures 37.11 and 37.12 show the comparison of the experimental and numerical frequency response functions of channel TP4 respectively for the longitudinal (using two modes) and transverse (using three modes) tests. Above each resonance peak the value of the correspondent viscous damping factor is displayed according to Eqs. 37.4 and 37.5.

The numerical results approximate very well the experimental measurements.

Table 37.1 summarizes the maximum values of the viscous damping factor for longitudinal and transverse tests.

## 37.6 Conclusions

The dynamic behavior of a resistor has been characterized in order to predict its fatigue life. Significant nonlinear effects were observed during the experimental tests. In order to obtain an accurate assessment of modal parameters, a great effort has been devoted to the detection and modeling of the nonlinearity. This analysis, combined with the harmonic balance method, led to the definition of the frequency response function whose parameter have been identified minimizing the mean square error between numerical and experimental data with a least square algorithm.

The numerical and experimental frequency response functions have presented a good agreement confirming that the adopted simplified model is suitable to describe the nonlinear dynamics of the tested system.

## References

1. Standard IEC 60068-3-3 (1991) Environmental testing – part 3: guidance – seismic test methods for equipment
2. Bendat JS, Piersol AG (1993) Engineering applications of correlation and spectral analysis. Wiley, New York
3. Jacobsen E, Lyons R (2003) The sliding DFT. *IEEE Signal Process Mag* 20(2):74–80
4. Worden K, Tomlinson GR (2001) Nonlinearity in structural dynamics – detection, identification and modelling. Institute of Physics Publishing, Bristol
5. Amabili M (2008) Nonlinear vibrations and stability of shells and plates. Cambridge University Press, Cambridge
6. Kerschen G, Peeters M, Golinval JC, Vakakis AF (2009) Nonlinear normal modes, part I: A useful framework for the structural dynamicist. *Mech Syst Signal Process* 23(1):170–194
7. Ewins JD (2001) Modal testing: theory and practice. Wiley, New York
8. Björck A (1996) Numerical methods for least squares problems. SIAM, Philadelphia

# Chapter 38

## Effect of Spin Speed on Stability Lobes in High Speed Machining

Hasan Yılmaz and Ender Cigeroglu

**Abstract** In milling and turning processes high speed rotation is used to decrease operation time; as a result, the cost of machining operation is as well reduced. In order to estimate the stability lobes and determine optimum cutting conditions, tool point Frequency Response Function (FRF) is required. Euler and Timoshenko beam models are employed in literature in order to obtain tool point FRF of spindle-holder-tool assemblies. However, due to the high speed rotation of spindle, it is also necessary to consider gyroscopic effects for the determination of tool point FRF. In this paper, spindle-holder-tool assembly is modeled by Timoshenko beam theory considering gyroscopic effects as well. Considering the analytical modal solution available in literature and structural coupling methods, FRF of the tool point is obtained. A case study is performed on an example of spindle-holder-tool assembly, which is as well modeled by finite elements in order to verify the results obtained by the continuous model. Next, using the continuous model, stability lobes are obtained for different spin speeds and the effect of gyroscopic forces are studied.

**Keywords** Spinning • Timoshenko beam • Chatter • Vibrations • Gyroscopic effects • High speed machining • Stability lobes

### 38.1 Introduction

High speed machining is employed in milling or turning operation in order to decrease machining time as well as the cost of the operation. As a result of this dynamics of the spinning system is crucial to satisfy design requirements, especially for mass production. Inaccurate modeling of spindle-holder-tool dynamics may cause chatter which results in poor surface quality in the work piece. Regenerative chatter in orthogonal cutting was first explained by Tobias [1] and Tlustý [2]. Milling stability analysis is different than orthogonal cutting process which includes time dependent geometry and variables. Budak [3, 4] developed an analytical solution for milling stability lobe diagram. Altintas [5] explained constructing stability lobes for both orthogonal and milling cutting operations using specified Frequency Response Functions (FRF). Tool point FRF of the system is required to construct milling stability lobe diagrams. FRF of the tool point can be either found by experiments or analytical modeling of the spindle-holder-tool assembly. Experimental methods require significant amount of time and it is not practical to repeat the experiments considering the possible changes in the elements of the system. Therefore, in this paper, in order to predict the tool point FRF, an analytical model of the spindle-holder-tool assembly is constructed. In this model, the spindle-holder-tool assembly is modeled by series of beams, each one of which is modeled as a free-free spinning Timoshenko beam, and coupled by using FRF coupling method. Analytical solution for the spinning Timoshenko beam model for various boundary conditions is given by Zu [6]. Using the analytical natural frequencies and mode shapes

---

H. Yılmaz  
Middle East Technical University, 06800 Ankara, Turkey

Aselsan MGEO, 06750 Ankara, Turkey  
e-mail: [e144746@metu.edu.tr](mailto:e144746@metu.edu.tr)

E. Cigeroglu (✉)  
Middle East Technical University, 06800 Ankara, Turkey  
e-mail: [ender@metu.edu.tr](mailto:ender@metu.edu.tr)

of the free-free beam given by Zu [6], end point receptances of each segment are obtained which are coupled to give the tool point FRF. In order to include the effects of bearings at various locations on the spindle, springs and dampers are added to the model by utilizing Özgüven's structural modification method [7]. Moreover, spindle-holder and holder-tool assemblies are coupled by using elastic coupling elements.

## 38.2 Analytical Model

### 38.2.1 Spinning Timoshenko Beam Model

In the modeling of spindle, a spinning Timoshenko beam model having free-free boundary conditions is employed. Non-dimensional partial differential equations of motion are given as follows [6]:

$$\frac{\partial^2 u}{\partial t^2} + \frac{KG}{\rho l^2} \left( l \frac{\partial \psi}{\partial \zeta} - \frac{\partial^2 u}{\partial \zeta^2} \right) = F, \quad (38.1)$$

$$\frac{\partial^2 \psi}{\partial t^2} - i \frac{\Omega J_z}{\rho I} \frac{\partial \psi}{\partial t} - \frac{E}{\rho l^2} \frac{\partial^2 \psi}{\partial \zeta^2} + \frac{KAG}{\rho I l} \left( l \psi - \frac{\partial u}{\partial \zeta} \right) = 0, \quad (38.2)$$

where  $u$  is the transverse displacement,  $\psi$  is the rotation of the cross-section and  $F$  is the applied transverse force. In these equations,  $l$  is beam length,  $\rho$  is density,  $I$  is transverse moment of inertia,  $J_z$  is polar mass moment of inertia,  $E$  is Young's modulus,  $G$  is shear modulus,  $A$  is cross-sectional area,  $\Omega$  is spin speed,  $\kappa$  is shear correction factor and  $\zeta$  is the non-dimensional axial position. Solution of Eqs. (38.1) and (38.2) can be written in the following form [6]

$$U(\zeta) = A_1 \cosh(s_1 \zeta) + A_2 \sinh(s_1 \zeta) + A_3 \cos(s_2 \zeta) + A_4 \sin(s_2 \zeta), \quad (38.3)$$

$$\Psi(\zeta) = A'_1 \sinh(s_1 \zeta) + A'_2 \cosh(s_1 \zeta) + A'_3 \sin(s_2 \zeta) + A'_4 \cos(s_2 \zeta), \quad (38.4)$$

where  $A_1, A'_1, s_1$  and  $s_2$  are related parameters which are given in [6] in detail. Using free-free boundary conditions and substituting Eqs. (38.3) and (38.4) into Eqs. (38.1) and (38.2), natural frequencies and mode shapes of free-free spinning beam is obtained. Solutions for this BC's and other desired BC's are given in [6].

Equations (38.1) and (38.2) can be written in matrix form as follows

$$[M] \{\dot{W}(x, t)\} - [K] \{W(x, t)\} = \{F\}, \quad (38.5)$$

$$\{W\} = \{\dot{U}(x, t) U(x, t) \dot{\Psi}(x, t) \Psi(x, t)\}^T, \quad (38.6)$$

$$\{F\} = \{0 \ F \ 0 \ 0\}^T, \quad (38.7)$$

where  $[M]$  and  $[K]$  matrices are given as follows

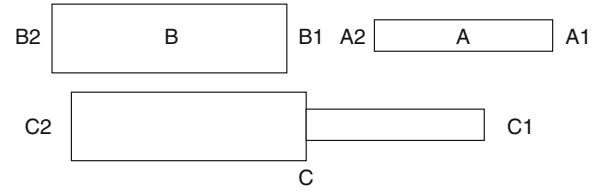
$$[M] = \begin{bmatrix} 0 & \rho A & 0 & 0 \\ \rho A & 0 & 0 & 0 \\ 0 & 0 & 0 & \rho I \\ 0 & 0 & \rho I & -i \Omega J_z \end{bmatrix}, \quad [K] = \begin{bmatrix} \rho A & 0 & 0 & 0 \\ 0 & \frac{KAG}{l^2} \frac{\partial^2}{\partial \zeta^2} & 0 & -\frac{KAG}{l} \frac{\partial}{\partial \zeta} \\ 0 & 0 & \rho I & 0 \\ 0 & \frac{KAG}{l} \frac{\partial}{\partial \zeta} & 0 & \frac{E}{l} \frac{\partial^2}{\partial \zeta^2} + KAG \end{bmatrix}. \quad (38.8)$$

Using the modal expansion theorem, solution of this system can be written in terms of its mode shapes as

$$\{W(x, t)\} = \sum_{r=-N}^N z_r(t) \{W_r(x)\}, \quad (38.9)$$

where  $z_r$  is the modal coefficient of the  $r$ th mode. Multiplying each side of Eq. (38.5) by  $\{W_s\}^T$ , integrating over the length and using the orthogonality conditions, the following equation of motion is obtained,

$$M_r \dot{z}_r(t) - K_r z_r(t) = Q_r(t) \quad (38.10)$$

**Fig. 38.1** Coupling of beams

where  $M_r$ ,  $K_r$  and  $Q_r(t) = U_r(L)F(t)$  are the modal mass and modal stiffness and the modal forcing for the  $r$ th mode. Solution of this uncoupled differential equation for harmonic forcing becomes as follows

$$z_r(t) = \frac{U_r(x)F e^{i\omega t}}{M_r(i\omega - \lambda_r)} \quad (38.11)$$

Total response of the beam becomes as follows,

$$W(x, t) = \sum_{r=-N_m}^{N_m} \frac{W_r(x)U_r(x)F e^{i\omega t}}{M_r(i\omega - \lambda_r)} \quad (38.12)$$

where  $N_m$  is the number of modes used in the modal expansion. Using the mass normalized eigenfunctions, receptances of the end points of the free-free beam can be obtained. Receptance functions are denoted as  $H_{jk}$ ,  $N_{jk}$ ,  $L_{jk}$ ,  $P_{jk}$ .  $H_{jk}$  and  $L_{jk}$  represent linear displacement receptance of point  $j$  due to a unit force and moment applied at point  $k$ , respectively. Similarly,  $N_{jk}$  and  $P_{jk}$  represent angular displacement receptance of point  $j$  due to a force and moment applied at point  $k$ , respectively. Small structural damping is assumed as  $(1 + i\gamma)$ . Using Eq. (38.12) these receptances can be defined as

$$H_{jk} = \sum_{r=-N}^N \frac{U_r(x_j)U_r(x_k)}{i\omega - \lambda_r(1 + i\gamma)}, N_{jk} = \sum_{r=-N}^N \frac{\Psi_r(x_j)U_r(x_k)}{i\omega - \lambda_r(1 + i\gamma)}, L_{jk} = \sum_{r=-N}^N \frac{U_r(x_j)\Psi_r(x_k)}{i\omega - \lambda_r(1 + i\gamma)}, P_{jk} = \sum_{r=-N}^N \frac{\Psi_r(x_j)\Psi_r(x_k)}{i\omega - \lambda_r(1 + i\gamma)}, \quad (38.13)$$

where  $\gamma$  is the loss factor for structural damping, which is assumed to be a very small value in the case studies considered.

### 38.2.2 Coupling of Beams

After obtaining the receptances of each beam element utilizing sufficient number of modes, these beams are coupled to each other in order to obtain the combined receptance of the tool point. Figure 38.1 shows coupling of two beam segments. Receptance matrices for beams A and B can be found utilizing Eq. (38.13) at the two extreme points. The coupled structure is represented as beam C.

Receptance matrix of the coupled structure can be found as follows [8]:

$$\begin{aligned} [C_{11}] &= [A_{11}] - [A_{12}] [[A_{22}] + [B_{11}]]^{-1} [A_{21}], \\ [C_{12}] &= [A_{12}] [[A_{22}] + [B_{11}]]^{-1} [B_{12}], \\ [C_{21}] &= [B_{21}] [[A_{22}] + [B_{11}]]^{-1} [B_{21}], \\ [C_{22}] &= [B_{22}] - [B_{21}] [[A_{22}] + [B_{11}]]^{-1} [B_{12}], \end{aligned} \quad (38.14)$$

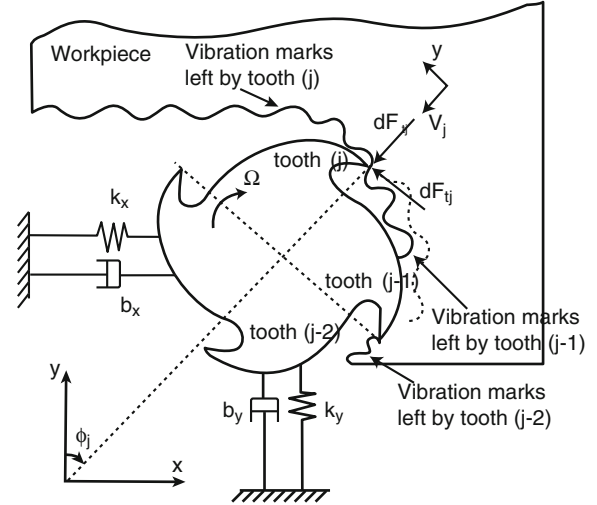
where  $[A_{11}]$  is given as follows

$$[A_{11}] = \begin{bmatrix} H_{A1A1} & L_{A1A1} \\ N_{A1A1} & P_{A1A1} \end{bmatrix}, \quad (38.15)$$

and  $[B_{11}]$  can be found in a similar fashion. It should be noted that, in order to support the spindle, bearings are used at different locations. Effect of bearings are included into the model as translational/rotational spring and damper elements by using Özgüven's structural modification method [7]. Although impedance coupling can as well be used to include spring and damper elements, it is computationally expensive due to inversion of higher order matrices. In addition to the bearing,



**Fig. 38.2** Cross sectional view of an end mill showing differential forces [4]



elastic elements can as well be added to various locations, especially between holder and tool connections. In order to include these elastic elements the following equations are used

$$\begin{aligned} [C_{11}] &= [A_{11}] - [A_{12}] \left[ [A_{22}] + [K_{AB}]^{-1} + [B_{11}] \right]^{-1} [A_{21}], \\ [C_{12}] &= [A_{12}] \left[ [A_{22}] + [K_{AB}]^{-1} + [B_{11}] \right]^{-1} [B_{12}], \\ [C_{21}] &= [B_{21}] \left[ [A_{22}] + [K_{AB}]^{-1} + [B_{11}] \right]^{-1} [B_{21}], \\ [C_{22}] &= [B_{22}] - [B_{21}] \left[ [A_{22}] + [K_{AB}]^{-1} + [B_{11}] \right]^{-1} [B_{12}], \end{aligned} \quad (38.16)$$

$$[K_{AB}] = \begin{bmatrix} k_y^{AB} + i\omega c_y^{AB} & 0 \\ 0 & k_\theta^{AB} + i\omega c_\theta^{AB} \end{bmatrix}, \quad (38.17)$$

where  $[K_{AB}]$  is composed of translation and rotational stiffness and damping elements.  $k_y^{AB}$  and  $k_\theta^{AB}$  are translational and rotational stiffnesses, and  $c_y^{AB}$  and  $c_\theta^{AB}$  are translational and rotational damping coefficients of the flexible connection. It can be seen that Eq. (38.16) is very similar to Eq. (38.14) where the only difference is due to  $[K_{AB}]$  term added into the equations.

### 38.2.3 Stability Lobes

The first analytical formulation for milling operation is obtained by Budak [3, 4]. In the milling dynamics, two orthogonal degrees of freedom are assumed in the cutting operation as shown in Fig. 38.2.

Equation of motion for milling is given below as,

$$\{F\} e^{i\omega_c t} = \frac{1}{2} a K_t \begin{bmatrix} \alpha_{xx} & \alpha_{xy} \\ \alpha_{yx} & \alpha_{xx} \end{bmatrix} [G(i\omega_c)] \{F\} e^{i\omega_c t}, \quad (38.18)$$

where  $a$  is axial depth of cut,  $K_t$  is cutting force coefficient,  $[\alpha]$  is the matrix of average directional cutting coefficients and  $[G(i\omega_c)]$  is the summation of tool point FRF and workpiece FRF matrices identified in the orthogonal cutting directions. For simplicity only tool point FRF matrices is used in this paper and workpiece is assumed as a rigid.  $[G(i\omega_c)]$  and  $[\alpha]$  is given as

$$[G(i\omega_c)] = \begin{bmatrix} G(i\omega_c)_{xx} & G(i\omega_c)_{xy} \\ G(i\omega_c)_{yx} & G(i\omega_c)_{yy} \end{bmatrix}, \quad (38.19)$$

$$\begin{aligned}
\alpha_{xx} &= \frac{1}{2} [\cos 2\phi - 2K_r\phi + K_r \sin 2\phi]_{\phi_{st}}^{\phi_{ex}}, \\
\alpha_{xy} &= \frac{1}{2} [-\sin 2\phi - 2\phi + K_r \cos 2\phi]_{\phi_{st}}^{\phi_{ex}}, \\
\alpha_{yx} &= \frac{1}{2} [-\sin 2\phi + 2\phi + K_r \cos 2\phi]_{\phi_{st}}^{\phi_{ex}}, \\
\alpha_{yy} &= \frac{1}{2} [-\cos 2\phi - 2K_r\phi - K_r \sin 2\phi]_{\phi_{st}}^{\phi_{ex}}.
\end{aligned} \tag{38.20}$$

Average directional cutting factors depend on  $K_r$ ,  $\phi_{ex}$  and  $\phi_{st}$  which are radial cutting constant, entry angle and exit angle, respectively. Entry and exit angles are related to the cutting type (e.g. end milling, down milling and up milling).

Equation (38.18) has a non-trivial solution if

$$\det[[I] + (\Lambda) ([A_0] [G(i\omega_c)])] = 0, \tag{38.21}$$

where

$$\Lambda = -\frac{N}{4\pi} a K_t (1 - e^{i\omega_c T}), [A_0] = \frac{N}{2\pi} \begin{bmatrix} \alpha_{xx} & \alpha_{xy} \\ \alpha_{yx} & \alpha_{yy} \end{bmatrix}. \tag{38.22}$$

For orthogonal cutting condition off-diagonal terms  $G(i\omega_c)_{yx}$  and  $G(i\omega_c)_{xy}$  can be taken as zero. Then, using Eq. (38.21) eigenvalue  $\Lambda$  can be found as

$$\Lambda = -\frac{1}{2a_0} \left( a_1 \pm \sqrt{a_1^2 - 4a_0} \right), \tag{38.23}$$

where

$$\begin{aligned}
a_0 &= G(i\omega_c)_{xx} G(i\omega_c)_{yy} (\alpha_{xx}\alpha_{yy} - \alpha_{xy}\alpha_{yx}), \\
a_1 &= \alpha_{xx} G(i\omega_c)_{xx} + \alpha_{yy} G(i\omega_c)_{yy}.
\end{aligned} \tag{38.24}$$

FRFs at the tool point have complex values; hence,  $\Lambda$  is a complex number. Since depth of cut must be a real value,  $\Lambda$  is decomposed into real and imaginary components as  $\Lambda = \Lambda_R + i\Lambda_I$ . After some manipulations, to get only real valued depth of cut, real and imaginary part of  $\Lambda$  should have the following proportion

$$\kappa = \frac{\Lambda_I}{\Lambda_R} = \frac{\sin \omega_c T}{1 - \cos \omega_c T}, \tag{38.25}$$

where  $T$  is spindle period and  $\omega_c$  is chatter frequency. Equation (38.25) can be related with the spindle speed  $n$  as follows [4],

$$\begin{aligned}
\omega_c T &= \varepsilon + 2k\pi, \\
\varepsilon &= \pi - 2\psi, \\
\psi &= \tan^{-1} \kappa, \\
n &= \frac{60}{N_t T}.
\end{aligned} \tag{38.26}$$

$\varepsilon$  is phase shift between inner and outer modulations,  $k$  is the corresponding vibration waves with in period, and  $N_t$  is the tooth number. Finally stable limiting depth of cut is found from Eq. (38.22) as,

$$a_{lim} = -\frac{2\pi\Lambda_R}{NK_t} (1 + \kappa^2). \tag{38.27}$$

Eqs. (38.27) and (38.26) can be employed to find the related spindle speed for a given depth of cut or limiting depth of cut for a given spindle speed.

### 38.2.4 Spindle Geometry

For a case study, the spindle-holder-tool model given by Erturk [8, 9] is used in this study. The material and geometrical properties of the spindle-holder-tool assembly are given in Table 38.1. At four locations, springs and dampers are added to simulate bearings. Location of each bearing and the corresponding stiffness values are given in Table 38.2.

**Table 38.1a** Spindle dimensions [9]

Segment number	1	2	3	4	5	6	7	8	9	10
Length (mm)	26	26	26	38	100	66	75	30	40	40
Outer diameter (mm)	66	66	66	66	76	70	62	58	58	58
Inner diameter (mm)	54	48	40	32	32	32	32	32	32	32

**Table 38.1b** Holder dimensions [9]

Segment number	1	2	3	4	5	6
Length (mm)	22	19	24	26	26	26
Outer diameter (mm)	72	60	70	54	48	40
Inner diameter (mm)	16	16	16	16	16	16

**Table 38.1c** Tool dimensions [9]

Segment number	1	2
Length (mm)	50	57
Outer diameter (mm)	14	26
Inner diameter (mm)	0	0

**Table 38.1d** Material properties [9]

$\rho$ (density)	7,800 kg/m <sup>3</sup>
$\nu$ poisson ratio)	0.3
$\gamma$ damping factor)	0.003
E (Young's modulus)	200 Gpa

**Table 38.2a** Bearing and interface properties [9]

	Translational stiffness (N/mm)	Rotational stiffness (N/mm)
Front bearings (for each)	$7.5 \times 10^5$	–
Rear bearings (for each)	$2.5 \times 10^6$	–
Spindle holder interface	$5 \times 10^7$	$1.5 \times 10^6$
Holder tool interface	$2 \times 10^7$	$1.5 \times 10^6$

**Table 38.2b** Bearing locations [9]

Bearing no	Bearing 1	Bearing 2	Bearing 3	Bearing 4
Distance (mm)	26	78	387	427

**Table 38.3** Comparison of natural frequencies for zero spin speed

	Analytical model	ANSYS	% difference wrt FEM
Mode 1	71.6	71.6	0.0
Mode 2	193.8	193.8	0.0
Mode 3	870.3	867.5	0.3
Mode 4	1,430	1,424.3	0.4
Mode 5	1,764	1,752.6	0.6

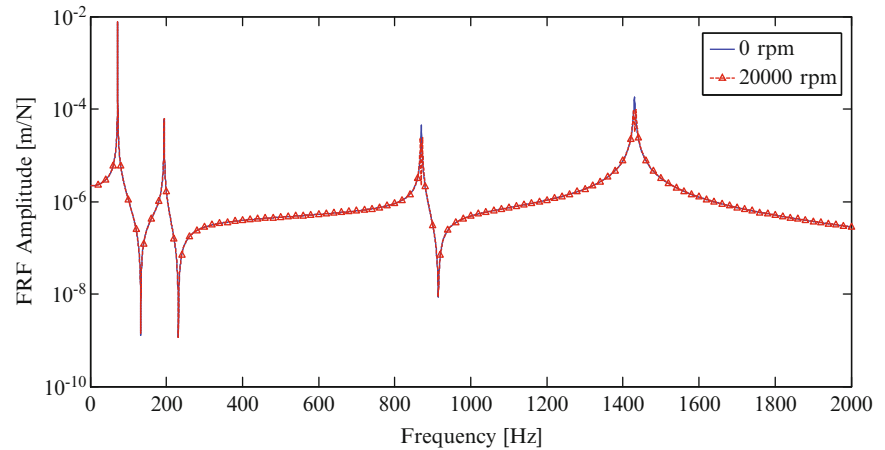
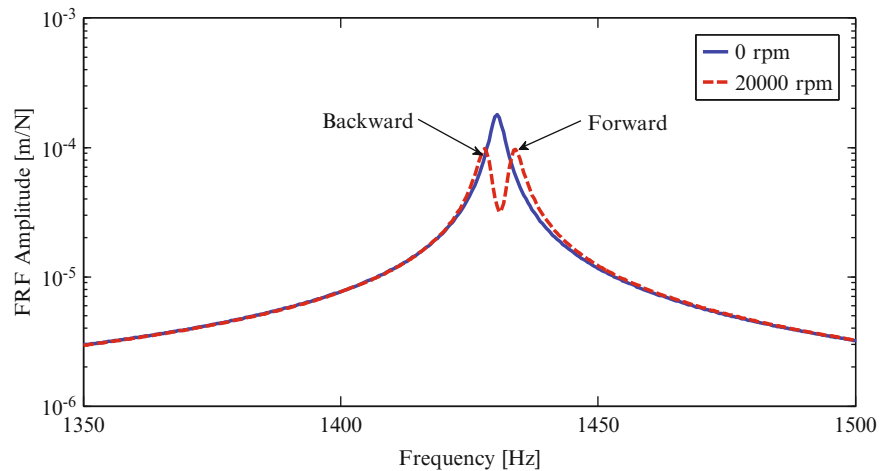
### 38.2.5 Results

After constructing the spindle-holder-tool assembly for specified geometrical and connection parameters, case study is performed considering different spindle speeds. First, spindle speed is taken as zero and corresponding natural frequencies and FRF of the tool point is obtained using the analytical model. Then spindle speed is increased to 20,000rpm and comparison is made with respect to zero spin speed. Stability lobes are constructed for both cases and change in the depth of cut is observed between two cases. In addition, finite element model (FEM) of the system is constructed in ANSYS and the results obtained are compared with results of the analytical model. In ANSYS, beam 188 element which uses Timoshenko beam model is used to model the spindle and combine 14 element is used to model bearing stiffness and damping.

Table 38.3 gives the comparison of natural frequencies obtained by the analytical method and FEM for zero spin speed. Natural frequencies are obtained from the frequency response function which is determined by using 0.1 Hz increments in the finite element software. It is observed that the results for zero spinning speed are very close to the results obtained from the FEM. It should be noted that the maximum error compared to FEM is less than 1% in the first five modes.

**Table 38.4** Comparison of forward and backward natural frequencies

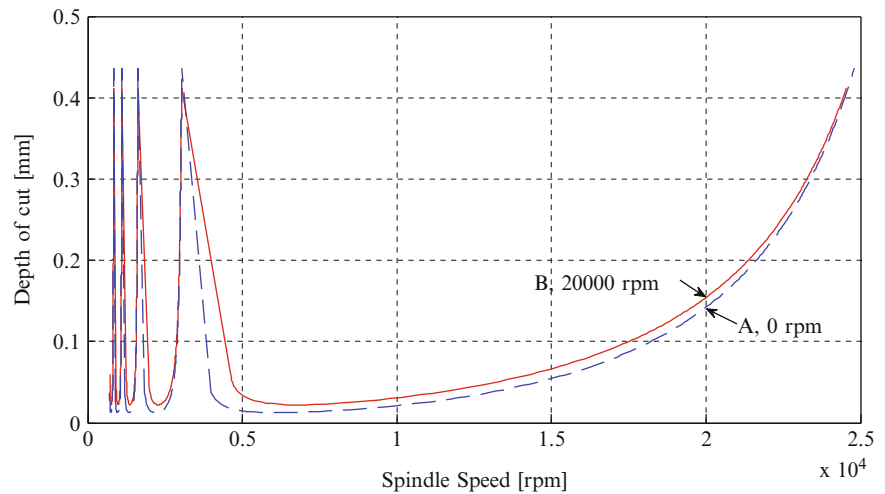
	Backward analytical	Forward analytical	Backward FEM	Forward FEM	% dif. forward	% dif. backward
Mode 1	71.3	71.3	70.3	72.9	1.4	2.2
Mode 2	193.8	193.8	190.2	197.7	1.9	2.0
Mode 3	867.5	872.7	862.9	871	0.5	0.2
Mode 4	1,428	1,433.8	1,422.2	1,425.8	0.4	0.6
Mode 5	1,751.5	1,774.3	1,734.9	1,769.5	0.9	0.3

**Fig. 38.3** Comparison of tool point FRF at 20,000 and 0 rpm**Fig. 38.4** Separation of forward and backward modes

Dynamic characteristics of rotating beams change with respect to spinning speed. Natural frequencies split as backward and forward natural frequencies. As spinning speed increases, difference between backward and forward natural frequencies increases as well. In Table 38.4, comparison of natural frequencies between analytical method and FEM at 20,000 rpm spin speed is given. In the analytical solution, the first two modes do not change, since they correspond to the rigid body modes of the spindle around bearings. In contrast, finite element solution splits them as forward and backward modes. If the elastic modes starting with the third mode are considered, analytical solutions also splits as backward and forward modes and their comparison with results of the FEM gives a maximum error less than 1%. Comparison of tool point FRF at 20,000 and 0 rpm, calculated by the analytical method, is given in Fig. 38.3. It can be seen that two FRFs are very close to each other in general. If close investigation is done on the natural frequencies, forward and backward separation can be observed as shown in Fig. 38.4. The effect of separation of forward and backward frequencies on FRF is dominant only around the natural frequencies; whereas, other parts of the FRF are similar to the zero spin speed case.

Stability lobe for the given case study is constructed by considering the rotational speed of the tool. The spindle speed is 20,000 rpm; hence depth of cut at 20,000 rpm is the main focus point in the stability lobe diagram. Depth of cut at 20,000 rpm

**Fig. 38.5** Comparison of stability lobes at zero and 20,000 rpm



is investigated for by including and excluding the effects of the spin speed. Cutting parameters are taken from [5]. The results obtained are given in Fig. 38.5. It is observed that depth of cut increases from 10% at 20,000 rpm spindle speed if spin speed effects are included. As a result of this depth of cut can be increased which also increases the material removal rate.

### 38.3 Conclusions

Effect of spindle speed on the dynamics of milling operation is investigated in this paper. A Timoshenko beam model is used to model different cross sectioned beams and receptance coupling method is employed to construct the complete spindle model. Spring and dampers are added to various locations using structural modification method in order to include the effect of bearings used. It is observed that, addition of spindle speed into the model, natural frequencies of the spindle split into two parts as forward and backward natural frequencies. The results obtained for the elastic modes are in good agreement with the finite element solution. Using the analytical model developed stability lobes are obtained for spin speed of 0 and 20,000 rpm which are compared with each other. It is observed that 10% increase in depth of cut is obtained by including the gyroscopic effects into the formulation.

### References

1. Tobias SA, Fishwick W (1958) The chatter of lathe tools under orthogonal cutting conditions. *Trans ASME* 80:1079–1088
2. Tlustý J, Poláček M (1963) The stability of machine tools against self-excited vibrations in machining. In: *Proceedings of ASME international research in production engineering*, Pittsburg, pp 465–474
3. Budak E (2006) Analytical models for high performance milling. Part I: cutting forces, structural deformations and tolerance integrity. *Int J Mach Tools Manuf* 46:1478–1488
4. Budak E (2006) Analytical models for high performance milling. Part II: process dynamics and stability. *Int J Mach Tools Manuf* 46:1489–1499
5. Altintas Y (2000) *Manufacturing automation*, s.l. Cambridge University Press
6. Zu JW, Han PS (1992) Natural frequencies and normal modes of a spinning timoshenko beam with general boundary conditions. *J Appl Mech* 59:197–204
7. Özgüven HN (1987) A new method for harmonic response of non-proportionally damped structures using undamped modal data. *J Sound Vib* 117:313–328
8. Ertürk A (2006) *Dynamic modeling of spindle-tool assemblies in machining centers*. MSc thesis, METU Mechanical Engineering Department
9. Ertürk A, Özgüven HN, Budak E (2006) Analytical modeling of spindle-tool dynamics on machine tools using Timoshenko beam model receptance coupling for the prediction of tool point FRF. *Int J Mach Tools Manuf* 46:1901–1912

# Chapter 39

## Chatter Reduction in Turning by Using Piezoelectric Shunt Circuits

Ufuk Yigit, Ender Cigeroglu, and Erhan Budak

**Abstract** In this paper, the effect of piezoelectric shunt damping (PSD) on chatter vibrations in turning process is studied. Chatter is a self-excited type of vibration that develops during machining due to process-structure dynamic interactions resulting in modulated chip thickness. Chatter is an important problem, since it results in poor surface quality, reduced productivity and reduced tool life. The regenerative chatter results from phase differences between two subsequent passes of the cutting tool and occurs earlier than mode coupling chatter in most cases. In regenerative chatter theory, stability limit in the cutting process is inversely proportional to the negative real part of frequency response function (FRF) of the cutting tool-workpiece assembly. If the negative real part of the FRF at the cutting point can be decreased, depth of cut, in other words productivity rates, will increase. In piezoelectric shunt damping method, an electrical impedance is connected to a piezoelectric transducer which is bonded to the main structure. In this study, resistive – inductive – capacitive shunt circuit is used, whose elements are optimized with genetic algorithm to minimize the real part of the FRF for certain target frequencies. Afterwards, the effect of the optimized piezoelectric shunt damping on the absolute stability limit of the cutting process is investigated.

**Keywords** Chatter • Absolute stability limit • Piezoelectric shunt damping • Genetic algorithm • Turning

### 39.1 Introduction

Chatter is a self-induced vibration problem that results from the variation of chip thickness in cutting conditions. The mechanism of chatter instability for different machining processes was explained in detail by Tobias [1] and Tlustý [2]. Chatter can be recognized by rapid increase in noise during the cutting process, due to which, high cutting forces could develop resulting in poor surface quality, reduced tool life and unacceptable tolerance values on machined part. Two main types of chatter are defined as mode coupling and regeneration of waves [1, 2]. Stability limit in regenerative chatter can be expressed as

$$b_{\text{lim}} = -\frac{1}{2K_f \text{Re}[G(\omega)]}, \quad (39.1)$$

where  $K_f$  is the cutting force coefficient.  $\text{Re}[G(\omega)]$  is the real part of the frequency response function (FRF) at the cutting point and  $b_{\text{lim}}$  is the chip width. Note that, in order to have a physically meaningful chip width,  $\text{Re}[G(\omega)]$  should have negative values. Therefore, negative values of cutting point FRF define the stability limit in the cutting process. The minimum of these chip thickness values is determined by  $\text{Re}[G(\omega)]_{\text{min}}$  which is called the critical limit of stability

---

U. Yigit • E. Cigeroglu (✉)  
Middle East Technical University, 06800, Ankara, Turkey  
e-mail: [uyigit@metu.edu.tr](mailto:uyigit@metu.edu.tr); [ender@metu.edu.tr](mailto:ender@metu.edu.tr)

E. Budak  
Sabanci University, Orhanli 81474 Tuzla, Istanbul, Turkey  
e-mail: [ebudak@sabanciuniv.edu](mailto:ebudak@sabanciuniv.edu)

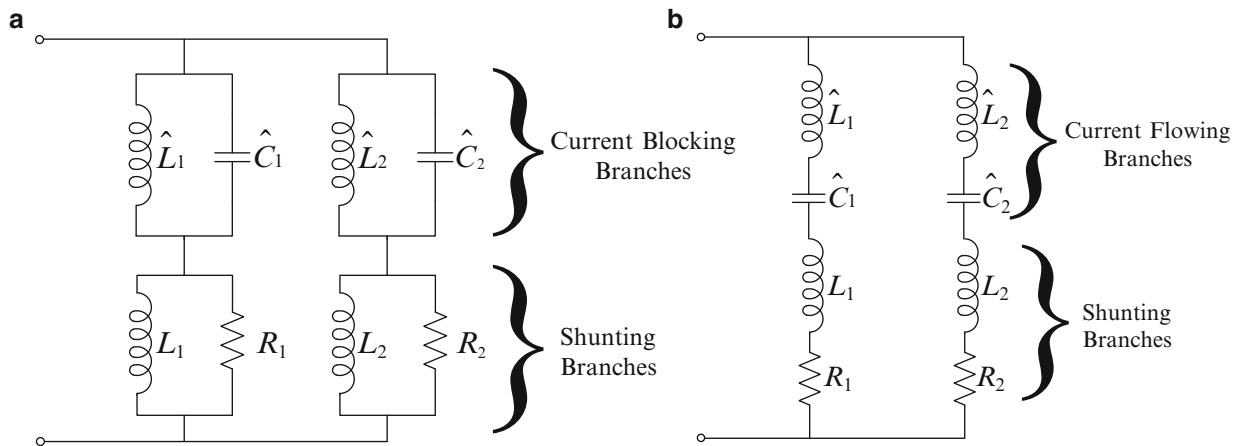
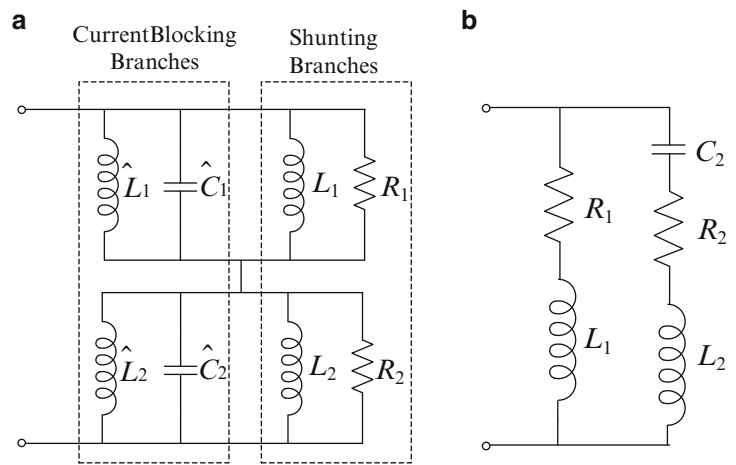


**Fig. 39.1** (a) Two mode shunt damping current blocking circuit, (b) Two mode shunt damping current flowing circuit

**Fig. 39.2** (a) Two mode shunt damping series-parallel circuit, (b) Two mode shunt damping Hollkamp's circuit



$$b_{lim,cr} = -\frac{1}{2K_f \text{Re}[G(\omega)]_{min}}. \quad (39.2)$$

Regenerative chatter is the main reason for the chatter instability in orthogonal cutting processes such as turning and boring. As stated before, regenerative chatter is dominant for lathe operations; therefore, mode coupling mechanism is beyond the scope of this paper.

Piezoelectric shunt damping (PSD) has become a popular technique for vibration suppression in the last decades. In literature, Hagood and von Flotow [3] interpreted that shunted piezoelectrics have a similar working principle to a tuned mass damper. They found that if inductance of the shunt circuit is set to  $(1/\omega_r^2 C_p)$  value, the vibration in the  $r$ th mode of the system will be reduced critically.

The main issue in PSD is damping multiple modes with one piezoceramic by using relatively complicated circuits. There are different types of shunt circuits developed for this purpose. Wu [4, 5] used current blocking circuit which can be seen in Fig. 39.1a. In this circuit, to reduce vibration in multiple modes, shunt circuits are added in parallel. For each mode, an isolator circuit is added in series to the corresponding shunt circuit and current blocking branches are tuned to a different mode than shunting branches. Secondly, the current flowing circuit was investigated by Behrens et al. [6] which is shown in Fig. 39.1b. Unlike current blocking circuits, current flowing branches allow current flows at shunting branch frequencies. Another alternative for the shunt circuits is the series-parallel circuit studied by Fleming et al. [7] as shown Fig. 39.2a. These circuits share the working principle of current flowing circuits and reduce the inductance requirement in shunting circuits dramatically. The last shunt circuit to mention was proposed by Hollkamp [8] which can be seen in Fig. 39.2b. In this circuit, when a tuning of a new mode is desired, all the circuit parameters have to be recalculated. The main advantage of this circuit type is that it has much fewer circuit components compared to others. Detailed comparison of the studies [4–8] can be found in Moheimani and Fleming [9].

The circuits and tuning methods proposed in the literature [4–8] are based on magnitude of the vibrations; however, this approach is not suitable for chatter applications. The more accurate approach is to optimize the circuit parameters according to the negative real part of the cutting point FRF.

## 39.2 Theory

In this study, distributed parameter beam model is used. This model was proposed by Erturk and Inman [10] and the equation for the transverse displacement of the cantilever beam with electromechanical coupling information is obtained as

$$w(x, t) = \sum_{r=1}^{\infty} \left[ \left( \phi_r(L_b) - \chi_r \frac{\sum_{s=1}^{\infty} \frac{j\omega\kappa_s\phi_s(L_b)}{\omega_s^2 - \omega^2 + j2\zeta_s\omega_s\omega}}{Y(\omega) + j\omega C_p + \sum_{s=1}^{\infty} \frac{j\omega\kappa_s\chi_s}{\omega_s^2 - \omega^2 + j2\zeta_s\omega_s\omega}} \right) \frac{\phi_r(x) F_0 e^{j\omega t}}{\omega_r^2 - \omega^2 + j2\zeta_r\omega_r\omega} \right], \quad (39.3)$$

where  $\phi_r(x)$  is the mass normalized eigenfunction for the  $r$ th undamped natural frequency.  $\omega_r$  and  $\zeta_r$  are the undamped natural frequency and damping ratio of the corresponding mode shape, respectively.  $C_p$  is the internal capacitance of the bimorph,  $F_0$  and  $\omega$  are the amplitude and frequency of the tip force excitation and  $j$  is the unit imaginary number.  $Y(\omega)$  is the admittance of the shunt circuit and  $L_b$  is the length of the beam.  $\chi_r$  and  $\kappa_r$  are modal electromechanical coupling terms which are defined by Erturk and Inman [11] as

$$\chi_r = \vartheta \left. \frac{d\phi_r(x)}{dx} \right|_{x=L}, \quad (39.4)$$

$$\kappa_r = \bar{e}_{31} h_{pc} \widetilde{b} \left. \frac{d\phi_r(x)}{dx} \right|_{x=L}, \quad (39.5)$$

where  $\vartheta$  is piezoelectric coupling term.  $\bar{e}_{31}$  is the effective piezoelectric stress component and  $h_{pc}$  and  $b$  are the distance between neutral axis and the center of each piezoceramic layer and width of the piezoceramic layers.

Receptance of the beam at the tip point can be determined from Eq. (39.3) as

$$\alpha(L_b) = \sum_{r=1}^{\infty} \left[ \left( \phi_r(L_b) - \chi_r \frac{\sum_{s=1}^{\infty} \frac{j\omega\kappa_s\phi_s(L_b)}{\omega_s^2 - \omega^2 + j2\zeta_s\omega_s\omega}}{Y(\omega) + j\omega C_p + \sum_{s=1}^{\infty} \frac{j\omega\kappa_s\chi_s}{\omega_s^2 - \omega^2 + j2\zeta_s\omega_s\omega}} \right) \frac{\phi_r(L_b)}{\omega_r^2 - \omega^2 + j2\zeta_r\omega_r\omega} \right]. \quad (39.6)$$

In order to calculate the receptance for the cantilever beam,  $\phi_r(x)$  is selected as

$$\phi_r(x) = \sin(\beta_r x) - \sinh(\beta_r x) - \left[ \frac{\sin(\beta_r L) + \sinh(\beta_r L)}{\cos(\beta_r L) + \cosh(\beta_r L)} \right] (\cos(\beta_r x) - \cosh(\beta_r x)), \quad (39.7)$$

which is the  $r$ th eigenfunction of the cantilever beam, where  $\beta_r = 1.875, 4.694, 7.855, 10.996, \dots$ . Undamped natural frequencies can be calculated as follows

$$\omega_r = \beta_r^2 \sqrt{\frac{YI}{mL^4}}, \quad (39.8)$$

where  $m$  is the mass per unit length,  $YI$  is the bending stiffness term for the composite cross section.

## 39.3 Case Study

In the case study considered, the first two natural frequencies of the cantilever beam, representing the tool given in Fig. 39.3, are damped in order to decrease the negative real part of the FRF at the tip point. From this point to the end of this article FRF refers to the tip point. Dimensions of the beam are selected as  $120 \times 20 \times 20$  mm. Two millimeter, where thick PZT-5A piezoceramics are attached on the top and bottom layers of the beam as shown. Note that piezoceramics are polarized



**Fig. 39.3** Cantilever beam excited from the tip point

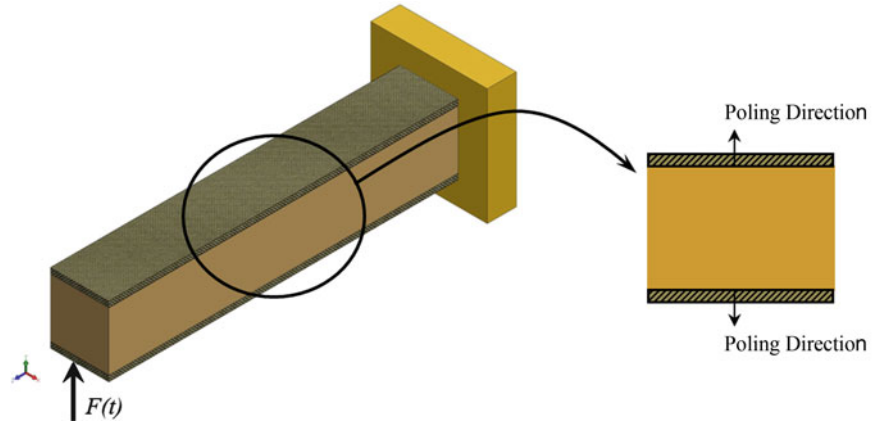


**Table 39.1** Optimized circuit parameters (damping of two modes)

Fitness/cost function	Optimized circuit parameters				
	$R_1 (\Omega)$	$L_1$ (H)	$C_2$ (nF)	$R_2 (\Omega)$	$L_2$ (H)
Negative real part minimization	74	0.481	21.7	439	0.029
Maximum amplitude minimization	82	0.549	18.3	658	0.090

**Table 39.2** Options of genetic algorithm different from the default values

Genetic algorithm option	Values
PopulationSize	500
EliteCount	300
TolFun	1e - 16
StallGenLimit	200
HybridFcn	@fmincon
Generation	300
Fitnesslimit	1e - 10
Initial population	Linearly distributed between lower and upper bounds

at reverse directions, which results in a connection in series of PZT patches. Piezoelectric coupling term for the series connection can be obtained as given in Erturk [11]:

$$\vartheta_s = \frac{\bar{e}_{31}b}{2\tilde{h}_p} \left[ \left( \tilde{h}_p + \frac{\tilde{h}_s}{2} \right)^2 - \frac{\tilde{h}_s^2}{4} \right], \quad (39.9)$$

where  $\tilde{h}_p$  and  $\tilde{h}_s$  are thicknesses of piezoceramic and substructure. The shunt circuit chosen in this case study is the same as the one given in Fig. 39.2b and the admittance of the shunt circuit is obtained as

$$Y(\omega) = \frac{1}{R_1 + jL_1\omega} + \frac{jC_2\omega}{jC_2R_2\omega - C_2L_2\omega^2 + 1}. \quad (39.10)$$

Damping coefficients of the beam are selected such that have nearly equal FRF amplitude in the first two modes in short circuit conditions:  $\zeta_1 = 0.008$ ,  $\zeta_2 = 0.0001$ , where the corresponding resonant frequencies are  $\omega_1 = 1144$  Hz,  $\omega_2 = 7171$  Hz. In the calculation of the displacement given by Eq. (39.6), four eigenfunctions are used.

The genetic algorithm tool of Matlab® is employed for the optimization of the shunt circuit parameters, details of which can be obtained from Optimization Toolbox User's Guide of MATLAB [12]. Optimized shunt circuit parameters are given in Table 39.1 considering two objective functions: minimization of the maximum absolute value of the negative real part of receptance and minimization of the maximum FRF amplitude. The options of the genetic algorithm, which are different than the default values, are given in Table 39.2.

Before the optimization procedure, the minimum value of the FRF's real part is  $-1.186 \times 10^{-6}$  m/N. When cost function of the genetic algorithm was tuned for negative real part, this value decreased to  $-3.758 \times 10^{-7}$  m/N. However, when the

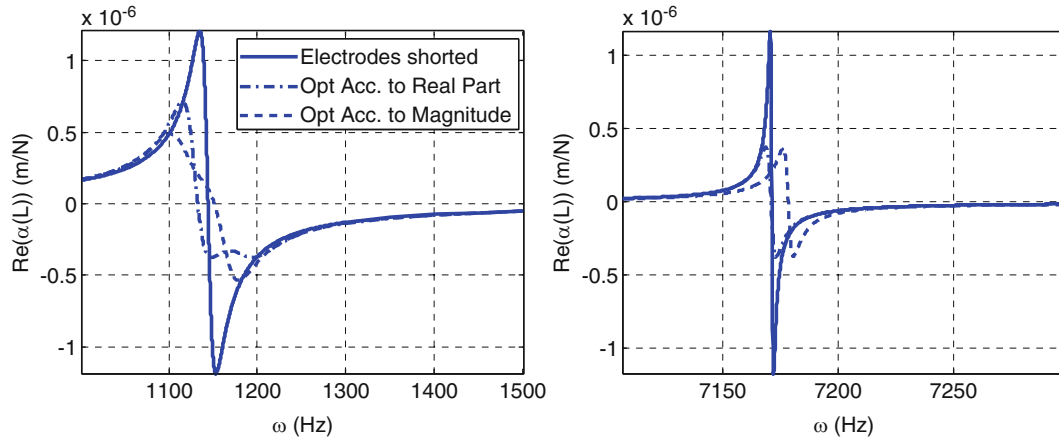


Fig. 39.4 Real part of receptance of the tip point around the first two natural frequencies

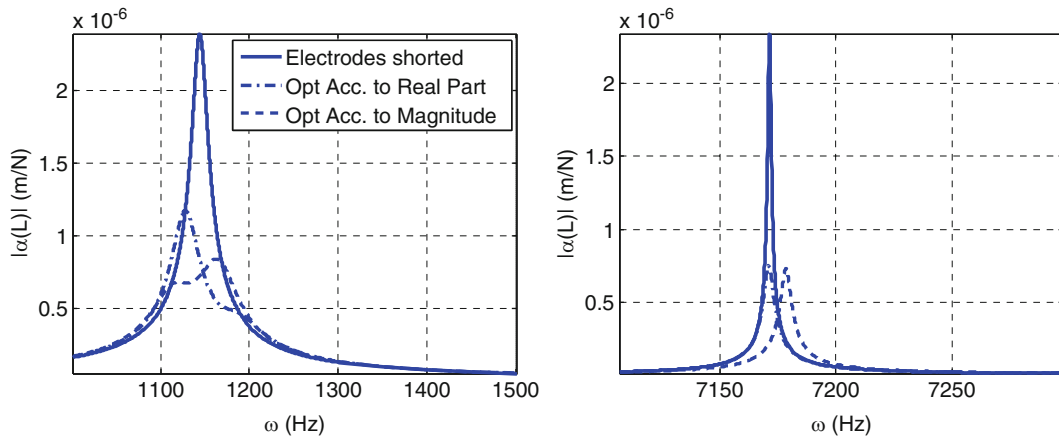


Fig. 39.5 Amplitude of receptance of the tip point around the first two natural frequencies

Table 39.3 Stability limits

	Electrodes shorted	Real part optimization	Amplitude optimization
Maximum value of FRF (m/N)	2.39E-06	1.17E-06	8.41E-07
Minimum value of real part of FRF (m/N)	-1.19E-06	-3.758E-07	-5.37E-07
$b_{lim,cr}$ (mm)	0.53	1.66	1.16
Increase in stability limit	-	216%	121%

optimization is done according to the maximum amplitude of FRF, the minimum value of the negative part of receptance is obtained as  $-5.37 \times 10^{-7}$  m/N. FRFs of the beam around the first two natural frequencies are given in Figs. 39.4 and 39.5.

The absolute stability limit for this beam can be calculated by using Eq. (39.2). A typical value for the cutting force coefficient can be taken as  $K_f = 800$  MPa for mild steel work material. In Table 39.3, the absolute stability limits are given for the both optimizations. Increase in the chatter free depth of cut is 216% in the case when optimization is based on the negative real part of the receptance, and 121% when the optimization basis is the amplitude of receptance.

Note that with this approach, no analytical solution for the inductance value can be obtained. Moreover, the number of parameters to be optimized depends on the number of modes required to be damped; hence, for these reasons, genetic algorithm is employed for the optimization.

Provided that the second branch of the circuit given in Fig. 39.2b is removed, i.e. the shunt circuit damps only the first mode, the inductance of the required inductor becomes  $L = 1.12$  H, whereas, the previous methods given in literature [4–8] suggest that the inductor of the first shunting circuit should be  $L = 1.21$  H, independent of the number of modes to be damped. However, as seen in Table 39.4, due to the utilization of genetic optimization and considering the real part of the

**Table 39.4** Comparison of circuit parameters

–	Circuit parameters			
	Damping only the first mode		Two mode damping	Decrease in required inductance
Fitness/cost function	R( $\Omega$ )	L (H)	L <sub>1</sub> (H)	–
Negative real part minimization	781	1.12	0.481	57%
Maximum amplitude Minimization	845	1.21	0.549	55%

receptance, the inductor of the first shunting circuit  $L_1 = 0.48 H$  is less than half of the single mode shunt circuit case. This is particularly important, since it is practically hard to obtain high inductance values.

### 39.4 Conclusion

The stability limits of turning operations are determined by the frequency response functions at the cutting point. Increasing the damping of cutting point receptance will provide an improvement in chatter free material removal rate, thus productivity of the process. For this purpose, piezoelectric shunt damping is an advantageous passive damping system in terms of cost effectiveness, low weight and efficient space usage. In this paper, different from previous studies, optimization of the electrical components of shunt circuits is performed considering the negative real part of the frequency response function. It is observed that the absolute stability limit of the operation was tripled in the optimum case. It should be emphasized that the inductor components are the most critical components in the design of shunt circuits. Due to the need for high inductance values, synthetic inductors have to be used. Utilizing genetic optimization and considering multiple modes, the inductance requirement with respect to the tuning methods in current blocking, current flowing, and series-parallel circuits is decreased, significantly.

**Acknowledgements** The authors would like to thank Dr. Alper Erturk for his contribution in the selection of this research topic.

### References

1. Tobias SA (1965) Machine tool vibration. Wiley, New York, pp 143–337
2. Tlustý J (2000) Manufacturing processes and equipment. Prentice Hall, Upper Saddle River, pp 559–579
3. Hagood NW, von Flotow A (1991) Damping of structural vibrations with piezoelectric materials and passive electrical networks. *J Sound Vib* 146(2):243–268
4. Wu SY (1998) Method for multiple mode shunt damping of structural vibration using a single PZT transducer. In: Proceedings of the SPIE symposium on smart structures and materials – smart structures and intelligent systems, San Diego, pp 159–167
5. Wu SY (1998) Piezoelectric shunts for simultaneous vibration reduction and damping of multiple vibration modes, U.S. patent 5,783,898
6. Behrens S, Moheimani SOR, Fleming AJ (2003) Multiple mode current flowing passive piezoelectric shunt controller. *J Sound Vib* 266(5): 929–942
7. Fleming AJ, Moheimani SOR, Behrens S (2003) Reducing the inductance requirements of piezoelectric shunt damping circuit. *Smart Mater Struct* 12(1):57–64
8. Hollkamp JJ (1994) Multimodal passive vibration suppression with piezoelectric materials and resonant shunts. *J Intell Mater Syst Struct* 5:49–57
9. Moheimani SOR, Fleming AJ (2006) Piezoelectric transducer for vibration control and damping. Springer, Berlin, pp 73–92
10. Erturk A, Inman DJ (2008) Piezoelectric shunt damping for chatter suppression in machining processes In: Proceedings of the ISMA 2008 international conference on noise and vibration engineering, Leuven
11. Erturk A, Inman DJ (2011) Piezoelectric energy harvesting, Wiley, Chichester, pp 49–97
12. The MathWorks, Inc., (2012) Optimization toolbox user's guide, version 6.2, Natick

# Chapter 40

## Damage Quantification from the Column Space of Flexibility Changes

Dionisio Bernal

**Abstract** On the premise that damage is localized, as opposed to distributed, it follows that difference in the displacement field between the damaged and the reference state due any loading in sensor coordinates is in a subspace whose span is defined by the influence lines of the stress resultants at the damage locations. It is shown that the scaling factors for which the bases vectors combine to give the displacement difference are the amplitude of discontinuities collocated with the damage and that these discontinuities, together with the stress resultant at the same locations, provide means to evaluate the damage severity. The solution proves to be an attractive fixed point.

**Keywords** Health monitoring • Damage quantification • Flexibility changes • Column space • Influence lines

### 40.1 Introduction

Once identified and located the severity of damage can be evaluated by parameterizing the damage in a physically meaningful manner and selecting the value of the parameters to minimize some cost function that measures distance between model and measurements. The complexity of the damage parameterization can vary widely and an overview of various models that have been examined in the literature can be found in [1,2]. This paper is concerned with the quantification of damage severity using experimentally extracted changes in flexibility,  $\Delta F$ . The approach is developed on the premise that the damage is spatially localized, as opposed to distributed. The theory requires that the number of sensors be larger than the number of independent damage locations but within this constraint the approach applies without modification to single or multiple damage cases. Damage is modeled as the switch from infinite to finite in the constants of springs of zero length collocated with the damage, a setting in which quantification proves tantamount to determining the spring constants. A more detailed presentation of the material reviewed in this paper appears in [3].

### 40.2 Damage Discontinuities and the Displacement Field Difference

Let the displacement field be designated as  $y$  and the stress resultants at the locations of damage as  $q$ , with an added tilde designating, for any quantity, the damaged state. It is understood that references made to load distributions and displacements in subsequent discussions refer to sensor defined coordinates. We begin by taking  $\delta$  to be the difference between the displacements of the damaged and the undamaged states due to some loading  $\ell$ , namely

$$\delta = \tilde{y} - y \quad (40.1)$$

---

D. Bernal (✉)  
Professor, Civil and Environmental Engineering Department, Center for Digital Signal Processing,  
Northeastern University, Boston, MA 02115, USA  
e-mail: [bernal@neu.edu](mailto:bernal@neu.edu)

Let the structural domain  $\Omega$  (in the reference state) with a unit load applied at sensor coordinate  $k$  be treated as a body in equilibrium. Taking  $\delta$  as a virtual deformation pattern and recalling that this displacement field has discontinuities  $\varphi$  at the damage locations one has, from the virtual work principle

$$1 \cdot \delta_k - \sum_{j=1}^p q_{j,k} \cdot \varphi_j = \int_{\Omega} \sigma_1^T \varepsilon_2 dV \quad (40.2)$$

where  $q_{j,k}$  is the stress resultant at the  $j$ th location when the unit load is at location  $k$ ,  $\delta_k$  is the difference of the displacement fields at the location and in the direction of the unit load and the discontinuity  $\varphi_j$  is at damage location  $j$ , the minus sign coming from the fact that the second term on the *lhs* is from internal forces. On the *rhs* of Eq. 40.2 the subscript “1” refers to the body in equilibrium and “2” to the virtual deformation pattern. Reversing the “real” and the “virtual” systems gives

$$0 = \int_{\Omega} \sigma_2^T \varepsilon_1 dV \quad (40.3)$$

and since the structure is assumed linear during the data collection,  $\sigma = \Gamma \varepsilon$ , with  $\Gamma$  being a material’s properties matrix. From this relation and given that work is a scalar quantity one concludes that the right side of Eqs. 40.2 and 40.3 are equal and, therefore, that

$$\delta_k = \sum_{j=1}^p q_{j,k} \cdot \varphi_j \quad (40.4)$$

Taking

$$q_j = [q_{j,1} \ q_{j,2} \ \dots \ q_{j,p}]^T \quad \text{and} \quad \delta = \{\delta_1 \ \delta_2 \ \dots \ \delta_m\}^T \quad (40.5a,b)$$

where  $p$  and  $m$  are the number of stress resultants that perform work on the discontinuities and the number of sensors, respectively, it follows that

$$\delta = [q_1 \ q_2 \ \dots \ q_p] \cdot \begin{Bmatrix} \varphi_1 \\ \varphi_2 \\ \vdots \\ \varphi_p \end{Bmatrix} = Q \cdot \varphi \quad (40.6)$$

where  $q_j$  is the influence line of the stress resultant that does work on the discontinuity at damage location  $j$ . Equation 40.6 shows that the difference in the deformation field between the damage and the reference state, for any load in sensor coordinates, is a linear combination of the influence lines of the stress resultants at the damage locations and, in addition, that the scaling coefficients are the collocated discontinuities. As can be seen, the influence lines in  $Q$  refer to the structure in the reference state, not the damaged one.

### 40.3 Localization

With  $\ell \in \mathbb{R}^{m \times 1}$  as a loading in sensor coordinates that is not in the null space of the change in flexibility,  $\Delta F \in \mathbb{R}^{m \times m}$  it follows, by definition, that

$$\delta = \Delta F \cdot \ell \quad (40.7)$$

Comparison of Eqs. 40.6 and 40.7 show that the column space of the change in the flexibility is the same as that of  $Q$ . Damage can be localized, therefore, by determining which locations have stress resultants whose influence lines fit in the column space of  $\Delta F$ . A measure of fit is provided by the subspace angle between the  $q_j$ ’s and  $U_1$  (the image of  $\Delta F$ ) which can be computed as [4]

$$\theta_j = \cos^{-1} \left\| \left( \frac{U_1^T q_j}{\|q_j\|} \right) \right\| \quad (40.8)$$

More detailed discussion on the localization can be found in [5].

## 40.4 Quantification

To interrogate  $\Delta F$  regarding the severity of damage let the load  $\ell$  in Eq. 40.7 be taken as the singular vector associated with the  $j$ th non-zero singular value. From the properties of the SVD it follows that

$$Q\varphi = u_j s_j \quad (40.9)$$

where  $u_j$  is the  $j$ th singular vector. Assuming that  $Q$  is full column rank one can solve for the discontinuities uniquely (in a least square sense) as

$$\varphi = Q^{-*} u_j s_j \quad (40.10)$$

where  $-*$  stands for pseudo-inversion. The discontinuities in Eq. 40.10 depend on the load used to compute them and, therefore, are not by themselves descriptions of damage severity. Together with the magnitude of the collocated stress resultants, however, they permit the definition of a physically significant damage metric. To illustrate let the stress resultant due to  $u_j$  at the  $k$ th damage location, in the damaged state, be  $\tilde{z}_k^j$  and  $\varphi_k^j$  the discontinuity at location  $k$ , also due to the load  $u_j$ . With  $\eta_k$  as the extent over which the stress resultant is (or can be assumed) constant it follows that

$$\frac{\tilde{z}_k^j \eta_k}{\tilde{R}_k} - \frac{z_k^j \eta_k}{R_k} = \varphi_k^j \quad (40.11)$$

where  $R_k$  is the relevant cross sectional stiffness (EA for axial deformations and EI for bending). Taking  $\beta$  as the ratio of the damaged to the undamaged stiffness, namely

$$\tilde{R}_k = \beta_k R_k \quad (40.12)$$

one gets, substituting Eqs. 40.12 in 40.11

$$\beta_k = \frac{1}{1 + \alpha_k^j} \quad \alpha_k^j = \frac{\varphi_k^j R_k}{z_k^j \eta_k} \quad (40a.13a,b)$$

where  $\eta_k$  in a truss is the length of bar  $k$  and in flexural members is the distance over which the damage is smeared, a reasonable value being  $d/2$  on each side of each damage location, where  $d$  = depth of the member (based on the long used value for plastic hinge idealizations). Needless to say, in simulations  $\eta_k$  in a flexural member should be taken as the length over which the flexural stiffness is reduced in the model. As can be seen from Eq. 40a.13a,b, the solution for the severity of damage is a fixed point [6].

### On the Need for the Iterated Solution of Eq. 40a.13a,b

It is of interest to examine how much error is likely introduced if the iterations needed to obtain the exact value of  $\beta$  are not carried out. A linear estimation can be obtained by differentiating Eq. 40a.13a,b with respect to  $\alpha_k^j$ , doing so and performing some simple rearranging gives

$$\frac{d\beta_k}{\beta_k} = (\beta_k - 1) \frac{d\alpha_k^j}{\alpha_k^j} \quad (40.13)$$

which shows that if  $\beta_k$  is not far from one the relative error in the damage severity is small. For example, for a 20% loss of stiffness  $\beta = 0.8$  so, if the stress resultant in the reference state is (for example) 30% away from the exact result, the error in  $\beta$  is only around 6%. In most practical cases, therefore, the stress resultants from the reference state provide sufficiently accurate damage quantification results. We close by pointing out that although in the theoretical development any pair  $\{u_j, s_j\}$  from the image of  $\Delta F$  can be used in Eq. 40.10, in practice  $\Delta F$  is modally truncated and  $j = 1$  yields the best results.

## 40.5 Inseparable Locations

In a multiple damage scenario the locations that can be uniquely identified from  $\Delta F$  are those where the relevant stress resultants are linearly independent. A set of damage locations (or elements) where there is proportionality in stress resultants for arbitrary loading in sensor coordinates forms an inseparable set – a term originally presented and discussed in [7]. The best that can be done when the sensors and the damage lead to inseparable locations (short of bringing information not contained in  $\Delta F$ ) is to obtain an upper bound by replacing the inseparable set by one of its elements and rotating the selection.

## 40.6 Numerical Section

### 40.6.1 Example

Consider the beam depicted in Fig. 40.1.

Damage is simulated as a loss of flexural stiffness of 25 and 40% in two segments, each having a length of 1% of the length of the span and located so that their right side is at 34% and 70% of the span, measured from the left support. The flexibility matrix in the reference and the damaged states is computed for five sensors located at  $0.16L$ ,  $0.32L$ , etc., assuming that the mass matrix is proportional to the identity and that only the first five modes could be identified. Influence lines for the bending moment were computed at the center of each of 100 equal size elements, so the damaged elements are #34 and #70. The singular values of  $\Delta F$ , normalized to a maximum of unity are  $\{1, 0.0868, 0.0015, 0.0005, 0\}$ , from where one can select and image dimension of 2. The subspace angles are plotted in Fig. 40.2, from where the set of potentially damaged elements is clearly identified as being  $\{34$  and  $70\}$ . To illustrate the ability of the quantification to discriminate undamaged elements we include element 10 in the potentially damaged set. The results of the iterations in the quantification are depicted in Table 40.1. As can be seen, the approach discriminates sharply and provides an accurate assessment of the damage severity.

**Fig. 40.1** Beam with damage in two locations

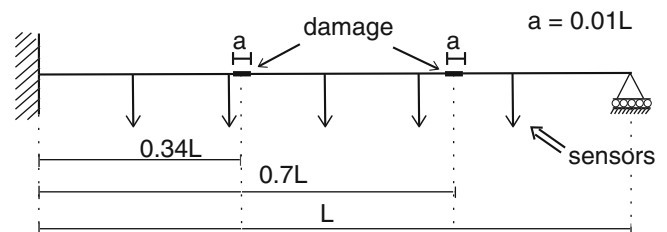


**Fig. 40.2** Subspace angle for the beam of the example (flexibility change based on five modes) damage located in elements 34 and 70

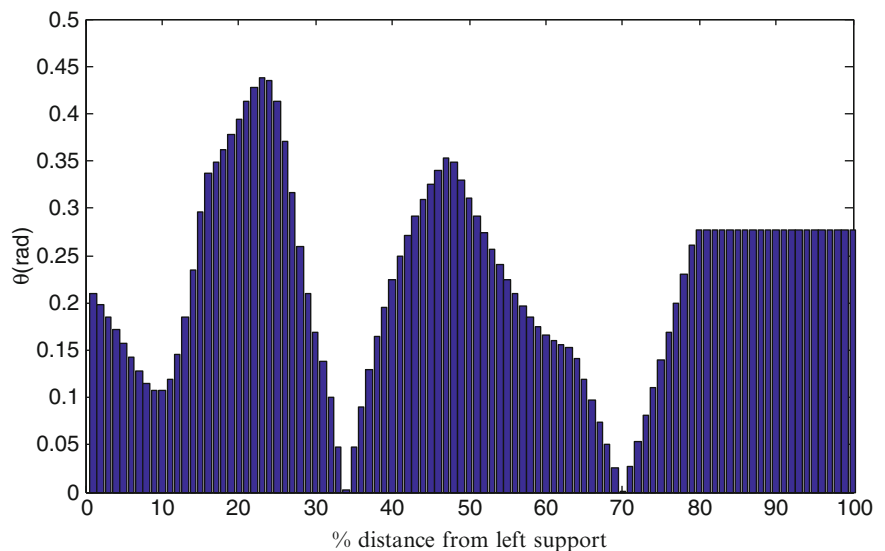


**Table 40.1** Iteration results in the quantification of damage for the example

Cycle	$z_{34}$	$z_{70}$	$z_{10}$	$\beta_{34}$	$\beta_{70}$	$\beta_{10}$
0	5.770	20.653	-19.018	0.763	0.602	0.994
1	5.743	20.640	-19.621	0.760	0.601	0.994
% damage (exact in parenthesis)	-	-	-	24 (25)	39.9 (40)	-

## 40.7 Conclusions

Previous research on extracting damage information from changes in flexibility matrices had shown how the information on localization is encoded in the kernel and in the image. Namely, the kernel contains a basis for load vectors that lead to zero stress over closed regions that contain the damage while the image is a basis for the influence lines of stress resultants associated with the damage locations. This paper illustrates that the severity information is also encoded in  $\Delta F$  and that its extraction requires, as one expects, use of the non-zero singular values. It is shown that the exact solution for the severity is a fixed point. Errors incurred when iterations are bypassed, however, are shown to be small for practical damage levels.

**Acknowledgements** The research reported in this paper was carried with support from NSF under grant CMMI-1000391, this support is gratefully acknowledged.

## References

- Ostachowicz W, Krawczuk M (2001) On modelling of structural stiffness loss due to damage. In DAMAS: 4th international conference damage assessment of structures, Cardiff, pp 185–199
- Friswell MI, Penny JET (2002) Crack modeling for structural health monitoring. *Struct Health Monit Int J* 1:139–148
- Bernal, D. (2013). Damage Quantification from the Image of Changes in Flexibility. *J Eng Mech* 10.1061/(ASCE)EM.1943-7889.0000617 (Feb. 28, 2013).
- Golub GH, Van Loan CF (1996) *Matrix computations*, 3 edn. The Johns Hopkins University Press, Baltimore
- Bernal, D. (2013). Damage Quantification from the Image of Changes in Flexibility. *J Eng Mech* 10.1061/(ASCE)EM.1943-7889.0000617 (Feb. 28, 2013).
- Granas A, Dugundji J (2003) *Fixed point theory*. Springer, New York
- Bernal D (2002) Load vectors for damage localization. *J Eng Mech* 128(1):7–14



# Chapter 41

## State Estimate of Wind Turbine Blades Using Geometrically Exact Beam Theory

Stuart G. Taylor, Darby J. Luscher, and Michael D. Todd

**Abstract** As wind turbine blades fatigue, the blade's dynamic response to loading may be expected to change. The kinematic quantities that exhibit significant changes are important for wind turbine blade operation from the perspective of measurement, estimation, and performance or even life cycle prediction. A state estimate providing accurate information on these features would lead to better estimates of remaining fatigue life and provide valuable information to the turbine control systems for the purpose of maximizing total energy output of a wind turbine system. In this work, we implement an observer for state estimation of nonlinear systems using the system Jacobian to correct the system output by updating the force input to a reference model in an iterative Newton-Raphson scheme. We apply this method to a surrogate wind turbine blade modeled using a geometrically exact beam theory to estimate its state given available measurements. *LA-UR-12-25441*.

**Keywords** Nonlinear observer • State estimation • Geometrically exact beam theory • Newton-Raphson

### 41.1 Introduction

As wind turbines become a larger source of renewable energy in the United States, manufacturers are increasing the length of the turbine blades, often made of composite materials, to increase power output per turbine. As a result of severe wind loadings and material level flaws in composite structures, blade failure is becoming a more common occurrence in the wind industry. Monitoring the structural health of the turbine blades is particularly important, because they account for 15–20% of the total turbine cost, and often require complete replacement. Blade damage can also cause secondary damage to the wind turbine system due to the rotating imbalance created by blade failure.

For structural prognostics, an estimate of the forces being transmitted through the blades to the nacelle would be particularly useful. Researchers have been tackling the inverse problem of input estimation for several decades [1, 2], with some recent interest focusing on estimation input loads to wind turbine towers [3] and blades [4]. One method to estimate transmitted loads using a structural model is to first estimate the dynamic state of the structure (the displacements and velocities at each node) and subsequently compute the resultant force and moment at the blade root. This method would require a model that can accurately describe the behavior of the rotor blade in a wide variety of operating modes and be sufficiently fast-running that (near) real-time state estimates could be obtained given operational measurements.

In this work, we implement an observer for state estimation of nonlinear systems using the system Jacobian to correct the system output by updating the force input to a reference model in an iterative Newton-Raphson scheme. The example

---

S.G. Taylor (✉)

Graduate Research Assistant, Engineering Institute, Los Alamos National Laboratory, Los Alamos, NM, USA

Department of Structural Engineering, University of California, San Diego, La Jolla, CA, USA

e-mail: [sgtaylor@lanl.gov](mailto:sgtaylor@lanl.gov)

D.J. Luscher

Technical Staff Member, Theoretical Division, Los Alamos National Laboratory, Los Alamos, NM, USA

e-mail: [djl@lanl.gov](mailto:djl@lanl.gov)

M.D. Todd

Professor and Vice Chair, Department of Structural Engineering, University of California, San Diego, La Jolla, CA, USA

e-mail: [mdtodd@mail.ucsd.edu](mailto:mdtodd@mail.ucsd.edu)

considered is an upright cantilevered beam modeled using *NLBeam* [5], a finite element research code developed at LANL that implements a geometrically nonlinear generalized Timoshenko beam theory [6–8]. This method is well-suited to modeling wind turbine rotor blades [9], permitting coupled material behavior with fully 3D displacements, while enabling a sufficiently simple representation of the rotor blade (compared to a high-fidelity conventional finite element representation of a composite structure), that useful, near real-time state estimates are realistic.

## 41.2 State Observers

### 41.2.1 Review

State observers for physical systems are ordinarily employed to enable the implementation of full state feedback control. In these cases, the ideal control signal would be calculated given the state of the plant, but the state is often not measurable or is otherwise inaccessible. State observers are implemented to recover an estimate of the system state using a reference model and available measurements. Some observers can be considered optimal in certain ways for linear systems given certain assumptions specific to the method. Other observers are approached as a pole-placement problem, in which the designer must balance performance with rejection of noise or other disturbances in choosing the placement of the observer poles.

A linear, time-invariant (LTI) system can be expressed in state space as

$$\begin{aligned}\dot{\underline{x}} &= \mathbf{A}\underline{x} + \mathbf{B}\underline{u} \\ \underline{y} &= \mathbf{C}\underline{x} + \mathbf{D}\underline{u},\end{aligned}\quad (41.1)$$

where  $\mathbf{A}$  is the system state matrix,  $\underline{x}$  is the state vector,  $\mathbf{B}$  is the input influence matrix,  $\underline{u}$  is the system input vector,  $\mathbf{C}$  is the output influence matrix,  $\underline{y}$  is the system output vector, and  $\mathbf{D}$  is the feed forward matrix. **Boldface** indicates matrix quantities, underlines indicate vector quantities, and the overdot represents differentiation with respect to time. Consider a state observer with a reference model being identical to the plant, having observer gain  $\mathbf{K}_e$ . The system representing the error is then

$$\left(\dot{\underline{\hat{x}}} - \dot{\underline{\hat{x}}}\right) = (\mathbf{A} - \mathbf{K}_e\mathbf{C})(\underline{x} - \underline{\hat{x}}), \quad (41.2)$$

where the hats indicate quantities relating to the reference model. The dynamics of the error vector are determined by the poles of the error state matrix  $(\mathbf{A} - \mathbf{K}_e\mathbf{C})$ . If the error state matrix is stable, the error will tend to zero regardless of the system initial conditions, but the speed of the observer response may not be fast enough for effective control. If the pair  $(\mathbf{A}, \mathbf{C})$  is observable, then  $\mathbf{K}_e$  can be chosen to arbitrarily place the poles of the error state matrix and ensure that the state estimate will be a reasonably real-time estimate of the true state [10]. If the plant is exactly represented by the reference model, and when there is white noise with known distributions present in the input and/or the output signals, the Kalman filter [11] provides an optimal estimate of the state, balancing between reliance on the measurement versus the prediction. However, the reference model is inevitably an inexact representation of the plant; consider a reference model

$$\begin{aligned}\dot{\underline{\hat{x}}} &= \widehat{\mathbf{A}}\underline{\hat{x}} + \widehat{\mathbf{B}}\underline{\hat{u}} \\ \underline{\hat{y}} &= \mathbf{C}\underline{\hat{x}} + \mathbf{D}\underline{\hat{u}},\end{aligned}\quad (41.3)$$

where  $\widehat{\mathbf{A}} = \mathbf{A} + \Delta\mathbf{A}$  and  $\widehat{\mathbf{B}} = \mathbf{B} + \Delta\mathbf{B}$ . In this formulation, it is still assumed that the output influence and feed forward matrices are known and identical for both the plant and the reference systems. Then the corresponding error system is

$$\left(\dot{\underline{\hat{x}}} - \dot{\underline{\hat{x}}}\right) = (\mathbf{A} - \mathbf{K}_e\mathbf{C})(\underline{x} - \underline{\hat{x}}) - (\Delta\mathbf{A}\underline{\hat{x}} + \Delta\mathbf{B}\underline{u}). \quad (41.4)$$

Note that any claims of optimality or stability made for Eq. (41.2) are jeopardized by the disturbance terms  $\Delta\mathbf{A}$  and  $\Delta\mathbf{B}$  in Eq. (41.4). If the noise is unknown or the model is inexact, but the system is observable, the observer design would become a pole-placement problem [12] with the pole locations chosen to maintain stability and performance. If the plant is nonlinear, the disturbance terms effectively become functions of time, and some form of adaptive observer would be required.

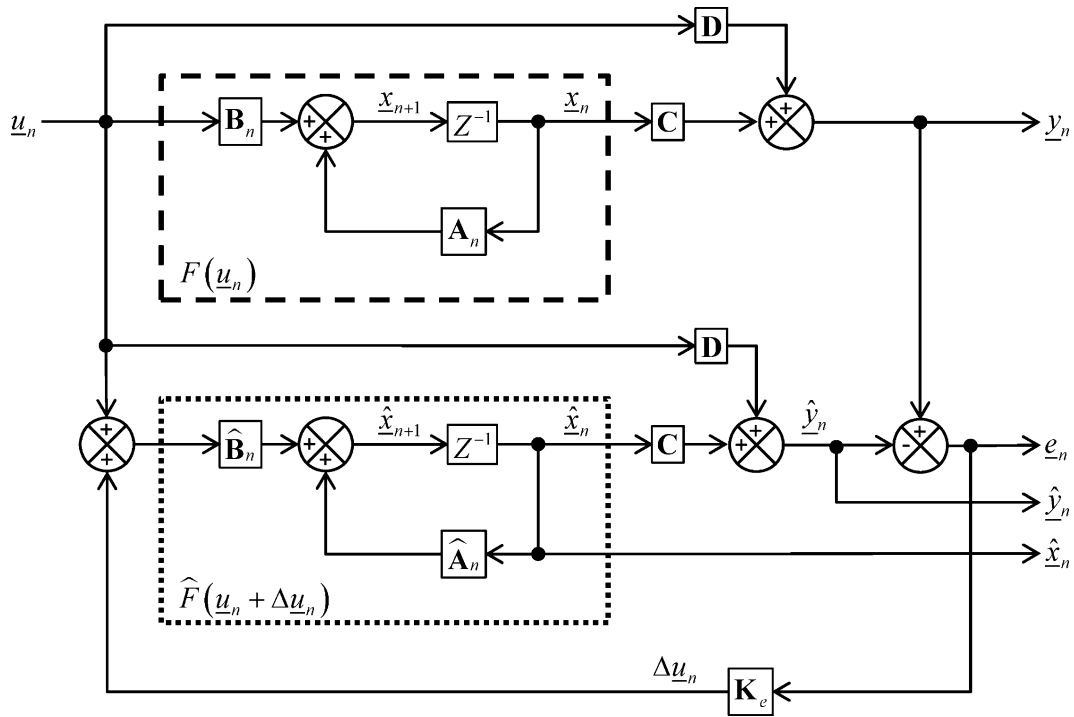


Fig. 41.1 Block diagram of a general observer for a discrete system

### 41.2.2 Newton-Raphson Force Correction Observer

Here, an observer is presented that is intended to improve state estimates for nonlinear systems that are not fully observable. The force correction observer adjusts the force input to a reference system using the system Jacobian to eliminate the measurable model output error in an iterative Newton-Raphson scheme by finding the root of an error expression in terms of the input force correction. The efficacy of this observer is predicated on an assumption that the reference model is “close enough” to the system being observed that, in driving the output error to zero, the state estimate error will also be driven toward zero. However, for nonlinear, non-fully observable systems, there is no guarantee that eliminating the output error will eliminate the state estimation error.

#### 41.2.2.1 Discrete, LTI Reference Model

A general block diagram for a discrete system with a force correction observer is shown in Fig. 41.1, where the plant has an inaccessible state  $\underline{x}_n$  and a measurable output  $\underline{y}_n$ , while the reference model has an accessible state  $\hat{\underline{x}}_n$  and an output  $\hat{\underline{y}}_n$ . The reference system for the observer can be expressed in discrete time as

$$\begin{aligned}\hat{\underline{x}}_{n+1} &= \hat{\mathbf{A}}_n \hat{\underline{x}}_n + \hat{\mathbf{B}}_n \underline{u}_n \\ \hat{\underline{y}}_{n+1} &= \mathbf{C} \hat{\underline{x}}_{n+1} + \mathbf{D} \underline{u}_{n+1},\end{aligned}\quad (41.5)$$

where the subscript  $n$  corresponds to the  $n$ th time point in a temporally discretized representation. The general plant and observer systems shown inside the dashed and dotted lines in Fig. 41.1 can be written for simplicity as  $\underline{x}_n = F(\underline{u}_n)$  and  $\hat{\underline{x}}_n = \hat{F}(\underline{u}_n)$ , respectively. For  $\mathbf{C} = \mathbf{I}$  and  $\mathbf{D} = \mathbf{0}$ , the error signal in Fig. 41.1 can be written as

$$\underline{e}_n = F(\underline{u}_n) - \hat{F}(\underline{u}_n). \quad (41.6)$$

In general, if  $F(\underline{u}_n)$  represents an inaccessible system, and  $\widehat{F}(\underline{u}_n)$  is an accessible reference system intended to approximate  $F(\underline{u}_n)$ , then  $\widehat{F}(\underline{u}_n) \neq F(\underline{u}_n)$ . An updating scheme is proposed whereby the input to  $\widehat{F}(\underline{u}_n)$  is replaced by  $\hat{\underline{u}}_n = \underline{u}_n + \Delta\underline{u}_n$  with the goal of driving an updated error signal to zero; this error is given by

$$\hat{\underline{e}}_n(\Delta\underline{u}_n) = F(\underline{u}_n) - \widehat{F}(\hat{\underline{u}}_n). \quad (41.7)$$

The goal of driving the updated error to zero is equivalent to finding the root of the right hand side (RHS) of Eq. (41.7), thereby identifying an input perturbation  $\Delta\underline{u}_n$  that eliminates the output error. Setting the RHS of Eq. (41.7) to zero and expanding the reference model in the vicinity of the actual input  $\underline{u}_n$  with a Taylor series gives

$$\widehat{F}(\hat{\underline{u}}_n) = \widehat{F}(\underline{u}_n) + \frac{\partial \widehat{F}(\underline{u}_n)}{\partial \underline{u}} \Delta\underline{u}_n + H.O.T. \quad (41.8)$$

Neglecting higher-order-terms (H.O.T.) and substituting Eqs. (41.8) into (41.7) leads to

$$\hat{\underline{e}}_n(\Delta\underline{u}_n) = F(\underline{u}_n) - \left( \widehat{F}(\underline{u}_n) + \frac{\partial \widehat{F}(\underline{u}_n)}{\partial \underline{u}} \Delta\underline{u}_n \right). \quad (41.9)$$

Combining Eqs. (41.6) and (41.9), setting  $\hat{\underline{e}}_n$  to zero and solving for  $\Delta\underline{u}_n$  gives

$$\Delta\underline{u}_n \approx \left[ \frac{\partial \widehat{F}(\underline{u}_n)}{\partial \underline{u}} \right]^{-1} \underline{e}_n. \quad (41.10)$$

Equation (41.10) is an exact solution to Eq. (41.8) for a linear plant and linear reference model. For nonlinear models, this linearized solution provides the Newton step for successive iterative corrections to the perturbed input  $\hat{\underline{u}}_n$ .

#### 41.2.2.2 Nonlinear Reference Model

Noting that, for nonlinear models, multiple iterations will be required to drive the updated error to zero at the conclusion of every time step, we express the updated error at the  $k$ th iteration of the observer for the  $n$ th time step as  $\hat{\underline{e}}_{n,k} = \underline{x}_n - \hat{\underline{x}}_{n,k}$ . Doing the same for the  $(k+1)$ th increment as  $\hat{\underline{e}}_{n,k+1} = \underline{x}_n - \hat{\underline{x}}_{n,k+1}$  enables an expression for the change in error over the  $(k+1)$ th iteration as

$$\begin{aligned} \hat{\underline{e}}_{n,k+1} - \hat{\underline{e}}_{n,k} &= (\underline{x}_n - \hat{\underline{x}}_{n,k+1}) - (\underline{x}_n - \hat{\underline{x}}_{n,k}) \\ &= \hat{\underline{x}}_{n,k} - \hat{\underline{x}}_{n,k+1}. \end{aligned} \quad (41.11)$$

Similar to the procedure followed above, we will use a first-order Taylor series approximation of the model output at the  $n$ th time step in the vicinity of the  $k$ th estimate for the updated input force, as

$$\hat{\underline{x}}_{n,k+1} \approx \hat{\underline{x}}_{n,k}(\hat{\underline{u}}_{n,k}) + \frac{\partial \hat{\underline{x}}_{n,k}}{\partial \underline{u}}(\hat{\underline{u}}_{n,k}) \Delta \hat{\underline{u}}_{n,k}, \quad (41.12)$$

where  $\hat{\underline{u}}_{n,k+1} = \hat{\underline{u}}_{n,k} + \Delta \hat{\underline{u}}_{n,k}$ . Substituting the approximation of the model state from Eq. (41.12) into the error expression of Eq. (41.11) yields

$$\begin{aligned} \hat{\underline{e}}_{n,k+1} - \hat{\underline{e}}_{n,k} &= \hat{\underline{x}}_{n,k} - \left( \hat{\underline{x}}_{n,k}(\hat{\underline{u}}_{n,k}) + \frac{\partial \hat{\underline{x}}_{n,k}}{\partial \underline{u}}(\hat{\underline{u}}_{n,k}) \Delta \hat{\underline{u}}_{n,k} \right) \\ &= -\frac{\partial \hat{\underline{x}}_{n,k}}{\partial \underline{u}}(\hat{\underline{u}}_{n,k}) \Delta \hat{\underline{u}}_{n,k}. \end{aligned} \quad (41.13)$$

Setting  $\hat{\underline{e}}_{n,k+1} = \underline{0}$  and solving Eq. (41.13) for  $\Delta\hat{\underline{u}}$ , the Newton correction to the perturbed input array is

$$\Delta\hat{\underline{u}}_{n,k} = \left[ \frac{\partial \hat{\underline{x}}_{n,k}}{\partial \underline{u}} (\hat{\underline{u}}_{n,k}) \right]^{-1} \hat{\underline{e}}_{n,k}. \quad (41.14)$$

For a nonlinear finite element discretization of the reference model equations of motion, the spatially-discrete form of the equations of motion can be expressed as

$$\widehat{\underline{R}}(\underline{x}, \dot{\underline{x}}, \ddot{\underline{x}}) = \underline{0}, \quad (41.15)$$

and they are satisfied through a nonlinear solution scheme at every time step to within some tolerance. The discrete finite element equations of motion expressed in Eq. (41.15) as an array of nodal residuals can be expressed in a temporally discrete fashion by taking into account the discrete time integration scheme relating velocity and acceleration to changes in displacement over a time step and the state of the model at a previous time step (including previous acceleration in this definition of state). This formulation permits us to write

$$\widehat{\underline{R}}(\underline{x}_n; \{\underline{x}_{n-1}, \dot{\underline{x}}_{n-1}, \ddot{\underline{x}}_{n-1}\}) = \underline{0}, \quad (41.16)$$

where the nodal residual vector  $\widehat{\underline{R}}_n$  is conveniently decomposed into contributions from internal stresses ( $\widehat{\underline{R}}_n^{int}$ ), inertia ( $\widehat{\underline{R}}_n^{dyn}$ ), and external forces ( $\widehat{\underline{R}}_n^{ext}$ ) as

$$\widehat{\underline{R}}(\underline{x}_n; \{\underline{x}_{n-1}, \dot{\underline{x}}_{n-1}, \ddot{\underline{x}}_{n-1}\}) = \widehat{\underline{R}}_n^{int} + \widehat{\underline{R}}_n^{dyn} + \widehat{\underline{R}}_n^{ext} = \underline{0}. \quad (41.17)$$

In this representation, the external force corresponds to the model inputs (i.e.  $\widehat{\underline{R}}_n^{ext} = -\underline{u}$ ), so the equations of motion are satisfied when

$$\widehat{\underline{R}}_n^{int} + \widehat{\underline{R}}_n^{dyn} = \underline{u}_n. \quad (41.18)$$

Note that  $\left[ \frac{\partial \hat{\underline{x}}}{\partial \underline{u}} \right]^{-1} = \left[ \frac{\partial \underline{u}}{\partial \hat{\underline{x}}} \right]$ ; then from Eq. (41.18), the Jacobian we seek in the update scheme for the input perturbation given in Eq. (41.14) is

$$\left[ \frac{\partial \underline{u}_n}{\partial \hat{\underline{x}}_n} \right] = \left[ \frac{\partial \widehat{\underline{R}}_n^{int}}{\partial \hat{\underline{x}}_n} \right] + \left[ \frac{\partial \widehat{\underline{R}}_n^{dyn}}{\partial \hat{\underline{x}}_n} \right]. \quad (41.19)$$

The partial derivatives in Eq. (41.19) are computed and used by *NLBeam* to solve the nonlinear equations of motion at every time step. They are often called the tangent stiffness and inertial matrices, respectively, where  $\mathbf{K}_{n,k}^{int} = \left[ \frac{\partial \widehat{\underline{R}}_n^{int}}{\partial \hat{\underline{x}}_n} \right]$  and  $\mathbf{K}_{n,k}^{dyn} = \left[ \frac{\partial \widehat{\underline{R}}_n^{dyn}}{\partial \hat{\underline{x}}_n} \right]$ . Adopting this notation, and substituting Eq. (41.19) into Eq. (41.14), the  $k$ th correction to the input perturbation at the  $n$ th time step is

$$\Delta\hat{\underline{u}}_{n,k} = \left( \mathbf{K}_{n,k}^{int} + \mathbf{K}_{n,k}^{dyn} \right) \hat{\underline{e}}_{n,k}. \quad (41.20)$$

In practice, acceleration measurements are much more easily obtained than displacement measurements, so the observer should be adapted for acceleration outputs. Expressing the error vector in terms of the translational accelerations at the  $k$ th and the  $(k + 1)$ th iteration permits us to write, after Eq. (41.11),

$$\hat{\underline{e}}_{n,k+1} - \hat{\underline{e}}_{n,k} = \ddot{\underline{x}}_{n,k}^{(t)} - \ddot{\underline{x}}_{n,k+1}^{(t)}, \quad (41.21)$$

where the superscript  $(t)$  indicates that only translational DOFs are utilized in computing the error vector. Following the same procedure as above, we will express  $\ddot{\underline{x}}_{n,k+1}^{(t)}$  as a first-order Taylor series expanded about  $\hat{\underline{u}}_n$  and set  $\hat{\underline{e}}_{n,k+1} = \underline{0}$  to obtain

$$\hat{\underline{e}}_{n,k} = \left( \frac{\partial \ddot{\underline{x}}_{n,k}^{(t)}}{\partial \underline{u}} (\underline{u}_{n,k}) \right) \Delta\hat{\underline{u}}_{n,k}. \quad (41.22)$$

Solving Eq. (41.22) for  $\Delta \hat{u}_{n,k}$  will require inverting the expression in the parentheses; by the chain rule, we may write

$$\frac{\partial \ddot{\hat{x}}_{n,k}^{(t)}}{\partial u} = \frac{\partial \ddot{\hat{x}}_{n,k}^{(t)}}{\partial \hat{x}_{n,k}^{(t)}} \frac{\partial \hat{x}_{n,k}^{(t)}}{\partial u} \tag{41.23}$$

From the Newmark time integration scheme implemented in the nonlinear FE solver,  $\frac{\partial \ddot{\hat{x}}}{\partial \hat{x}} = \frac{1}{\beta \Delta t^2} \mathbf{I}$  (where  $\beta$  is a parameter of the integration scheme). Then, similar to above, the solution to Eq. (41.22) is

$$\Delta \hat{u}_{n,k} = \beta \Delta t^2 \left( (\mathbf{K}_{n,k}^{int})^{(t)} + (\mathbf{K}_{n,k}^{dyn})^{(t)} \right) \hat{e}_{n,k}, \tag{41.24}$$

where the superscript  $(t)$  indicates that only the columns of the Jacobian corresponding to translational DOFs are employed in computing the force correction.

### 41.3 Physical Structure and Plant Model

In the examples presented below, the system being observed is an upright cantilevered aluminum beam with properties as given in Table 41.1.

The beam is depicted in Fig. 41.2 as: (a) the physical beam; (b) the plant model, a 21-node (10-element) geometrically nonlinear generalized Timoshenko beam model implemented in *NLBeam*; (c) a 5-node (2-element) *NLBeam* reference model;

Table 41.1 Beam parameters

Parameter	Symbol	Value	Units
Length	L	0.8839	M
Elastic modulus	E	68.9	GPa
Cross sectional area	A	83.4	mm <sup>2</sup>
Area moment of inertia	I	74.8	mm <sup>4</sup>

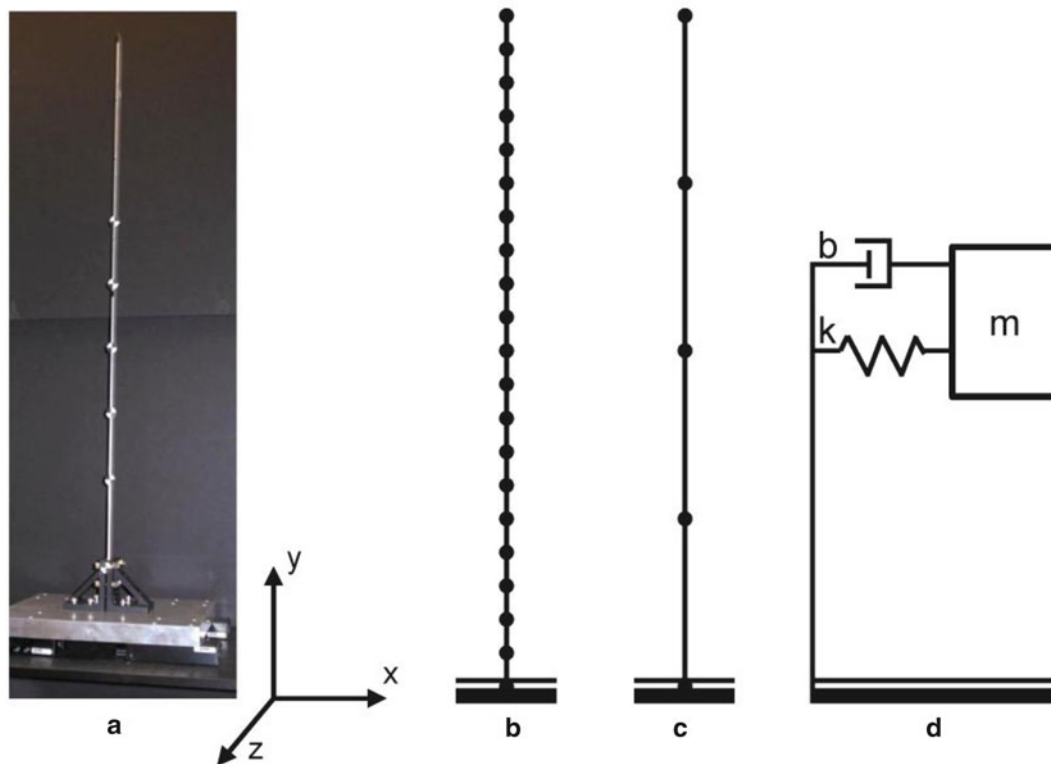


Fig. 41.2 Diagrams of upright cantilever beams with base excitation

and (d) a 3-node (2-element) Euler-Bernoulli beam reference model. The elements implemented in *NLBeam* are 3-noded elements with quadratic interpolation functions, so the 10-element model has 21 nodes. The equations of motion are solved in *NLBeam* using an implicit Newmark time integration scheme, which for the plant model was implemented with parameters  $\beta = 0.5625$  and  $\gamma = 1$ . These values, defined in the customary manner for Newmark integration [13], were based on a numerical damping value of  $\alpha = 0.5$ , where  $\alpha$  is a numerical analog to percent critical damping, and

$$\gamma = \left(\frac{1}{2} - \alpha\right)\beta = \frac{1}{4}(1 - \alpha)^2 \quad (41.25)$$

The system input was a sinusoidal base displacement at  $\sim 3.9673$  Hz. This frequency was chosen to be a bin-centered sinusoid at a sampling frequency of 1,250 Hz and a record length of 8,192 points. In this case, the frequency stepping would be  $\sim 0.1526$  Hz. The excitation frequency is chosen to be a bin-centered sinusoid near 4 Hz, while the beam's first resonance was at 3.745 Hz. The excitation frequency was chosen to be sufficiently close to the beam's first resonance that large amplitude motion could be obtained without inducing an unstable response. Because the frequencies were within two bins of each other, the bin-centeredness of the excitation was intended to ease the frequency-domain separation of the excitation and first resonance of the beam. This selection aids in the exploration of a "beating" phenomenon reported in a parallel study. The excitation consisted of 8,192 points of the above-mentioned sinusoid (from 0 to 6.5528 s), followed by nothing for the duration of a 10-s record. The beam was then allowed to free-decay, so that the damping differences could be seen more clearly and the observers' performance in the absence of structural inputs could be observed.

## 41.4 Numerical Examples

### 41.4.1 *NLBeam* Plant with LTI SDOF Reference Model

#### 41.4.1.1 Reference Model Description

The beam was modeled as a single-degree-of-freedom (SDOF) system as shown in Fig. 41.2d. The stiffness was first computed using Euler-Bernoulli beam theory as  $k = (12EI)/L^3$ , and the sprung mass was taken as the mass of the beam,  $m = \rho AL$ . Then, the stiffness value was adjusted so that the natural frequency of the system matched the first resonance of the *NLBeam* model, 3.745 Hz. The value of the damper was selected to achieve 0.2% critical damping. Denoting the motion of the base and of the mass in the x-direction  $x_0$  and  $x_1$ , respectively, the system EOM are

$$m\ddot{x}_1 + b\dot{x}_1 + kx_1 = b\dot{x}_0 + kx_0, \quad (41.26)$$

where  $m$  is the mass in kg,  $b$  is the damping constant in N/(m/s), and  $k$  is the stiffness in N/m. Cast in the form of Eq. (41.1), with the base displacement and velocity as the system inputs, the mass acceleration as the system output, the observer system state space matrices are

$$\mathbf{A} = \begin{bmatrix} 0 & 1 \\ -\frac{k}{m} & -\frac{b}{m} \end{bmatrix} \quad \mathbf{B} = \begin{bmatrix} 0 & 0 \\ \frac{k}{m} & \frac{b}{m} \end{bmatrix} \quad \mathbf{C} = \begin{bmatrix} -\frac{k}{m} & -\frac{b}{m} \end{bmatrix} \quad \mathbf{D} = \begin{bmatrix} \frac{k}{m} & \frac{b}{m} \end{bmatrix}$$

$$\underline{\dot{x}} = \begin{bmatrix} x_1 \\ \dot{x}_1 \end{bmatrix} \underline{u} = \begin{bmatrix} x_0 \\ \dot{x}_0 \end{bmatrix}. \quad (41.27)$$

Note that this system is both controllable and observable. Applying Eq. (41.10) to the discrete representation of this system given in Eq. (41.5), where  $\mathbf{C} \neq \mathbf{I}$  and  $\mathbf{D} \neq \mathbf{0}$ , the one-step correction to the input can be estimated as

$$\Delta \underline{u}_n = \left(\widehat{\mathbf{CB}}_n\right)^{-1} \underline{e}_{n+1}. \quad (41.27)$$

### 41.4.1.2 Results

The results for the SDOF reference model are shown in Fig. 41.3. In Fig. 41.3a, the system acceleration outputs are plotted together for the plant model, the reference model, the Kalman filter output, and the Newton-Raphson observer output. In Fig. 41.3b, the tip displacement (m) is plotted for the same systems. These plots show that, on the scale presented, the outputs of both observers overlay the plant output exactly. Note that there are transient responses at 0 and 6.5528 s, corresponding to the start and end of the excitation. In Fig. 41.3c–e, the displacement (m) error envelope is plotted in order to present more clearly the observers' state estimation performance. The envelope is obtained as the magnitude of the error analytic signal, computed using the Hilbert transform. This presentation is chosen over the raw error signal so that several error signal envelopes can be plotted together without confusion. With the SDOF model tuned to the first resonance of the *NLBeam* model, the prediction error is on the order of 1 cm, or about 50% of the maximum measured displacement. For the Kalman filter and the Newton-Raphson observer, the error was on the order of 0.5 mm, except when the observers were tracking transient events, and the error spiked to around 1 cm in each case. This inability to track transient events is a limitation of the SDOF reference model; a more spectrally rich reference model, such as an Euler-Bernoulli beam model or the perturbed *NLBeam* reference model discussed below, would be able to track the transient more quickly and reduce the magnitude of the spike in the observer error.

## 41.4.2 *NLBeam* Plant with *NLBeam* Reference Model

### 41.4.2.1 Reference Model Description

The *NLBeam* reference model was a perturbed version of the plant model. The perturbation was introduced by reducing the number of elements from 10 to 2 and decreasing the numerical damping in the simulation by choosing  $\alpha = 0.25$ , so that, from Eq. (41.25),  $\beta = 0.39$  and  $\gamma = 0.75$ . The observer results for two cases are plotted in Fig. 41.4. In the first case (N-R All Disp), as a verification step for the nonlinear implementation of the Newton-Raphson observer, all displacement measurements (including translations and rotations) were utilized to compute the force correction using Eq. (41.20) at each iteration. Because the reference model had only five nodes and the plant model had 21 nodes, the measurements were a subset of the available outputs from the plant model, chosen to correspond exactly to the DOFs of the reference model. In the second case (N-R Tip Acc), only a single measurement was utilized: the tip acceleration in the x-direction. The force correction at each iteration was computed for the acceleration measurement using Eq. (41.24). In the full measurement field verification step, four iterations of the Newton-Raphson update step were used at each time step, while in the acceleration measurement case, eight iterations were used. Although a better practice would be to define a convergence criterion to determine the number of iterations required, these numbers were determined to be sufficient for the examples considered.

## Results

The results for the *NLBeam* reference model are shown in Fig. 41.4. In Fig. 41.4a, b, the system outputs (tip acceleration in  $\text{m/s}^2$ ) and tip displacement (m) are plotted for the plant model, the reference model, the Newton-Raphson observer verification step with all displacement measurements (NR All Disp), and the Newton-Raphson observer implementation with only the tip acceleration (NR X-Tip Acc). The prediction error envelopes for all five nodes are plotted in Fig. 41.4c. The error for Node 1 was zero, because that node was driven by the displacement input boundary condition. The errors at the other nodes were on the order of 0.5 cm, compared to the  $\sim 2$  cm displacement at the tip of the beam. The error envelopes at each node using the Newton-Raphson observer using all displacement measurements are shown in Fig. 41.4d; the errors in this case were on the order of the machine precision. This result is expected, because using all measurements, Eq. (41.20) will be the unique solution to Eq. (41.13) that drives the error signal toward zero at each iteration. The error envelopes at each node using only the tip acceleration are shown in Fig. 41.4e. With the exception of Node 1, the observer errors are well above machine precision, because none of the displacements were measured directly; however, the error signals are about two orders of magnitude below the reference model prediction errors, with an overall observer error of less than 1%. The transient spikes at the start and the end of the excitation signal are still present, but their impact on the error is significantly diminished compared to the SDOF reference model.



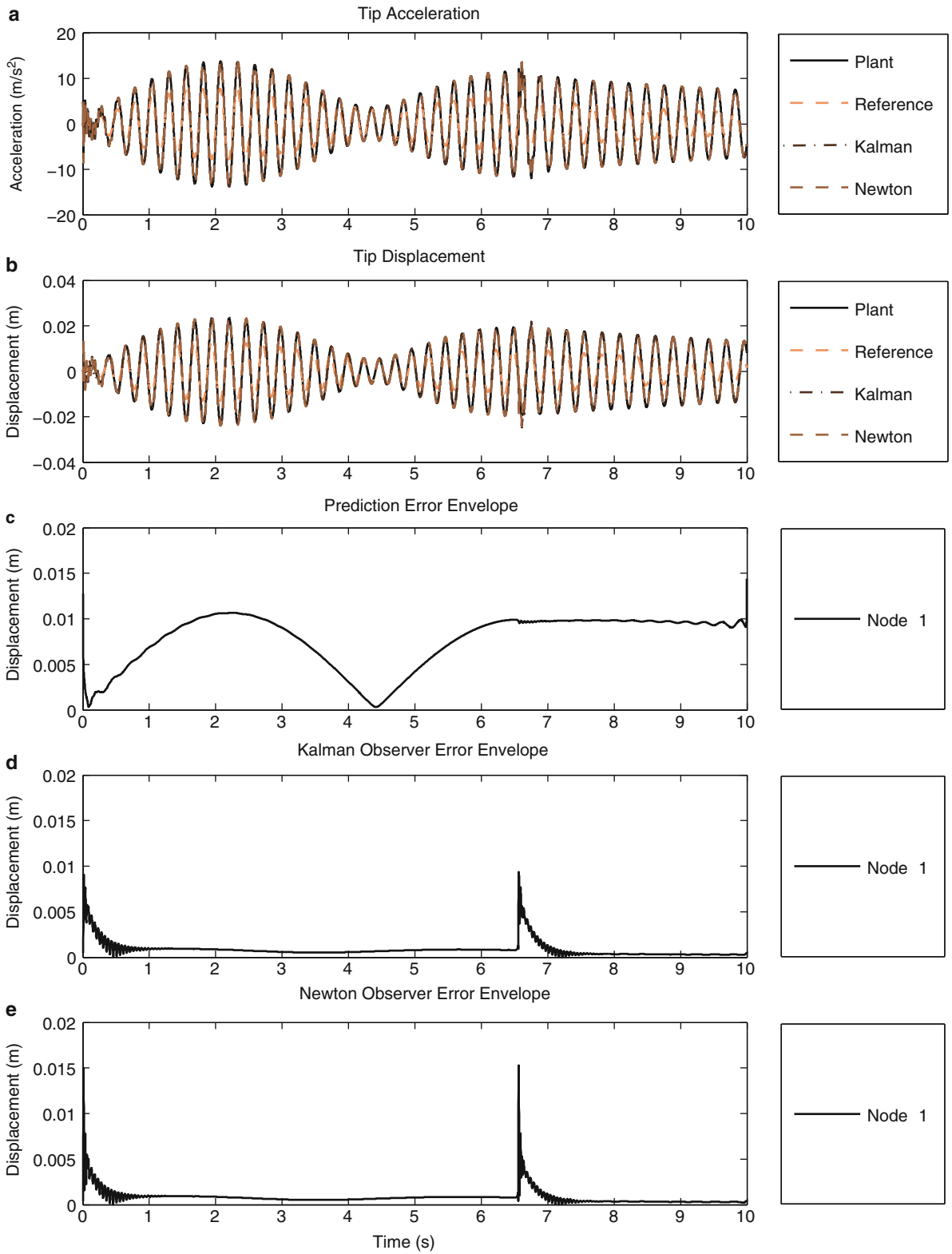


**Fig. 41.3** Kalman filter results for SDOF reference system

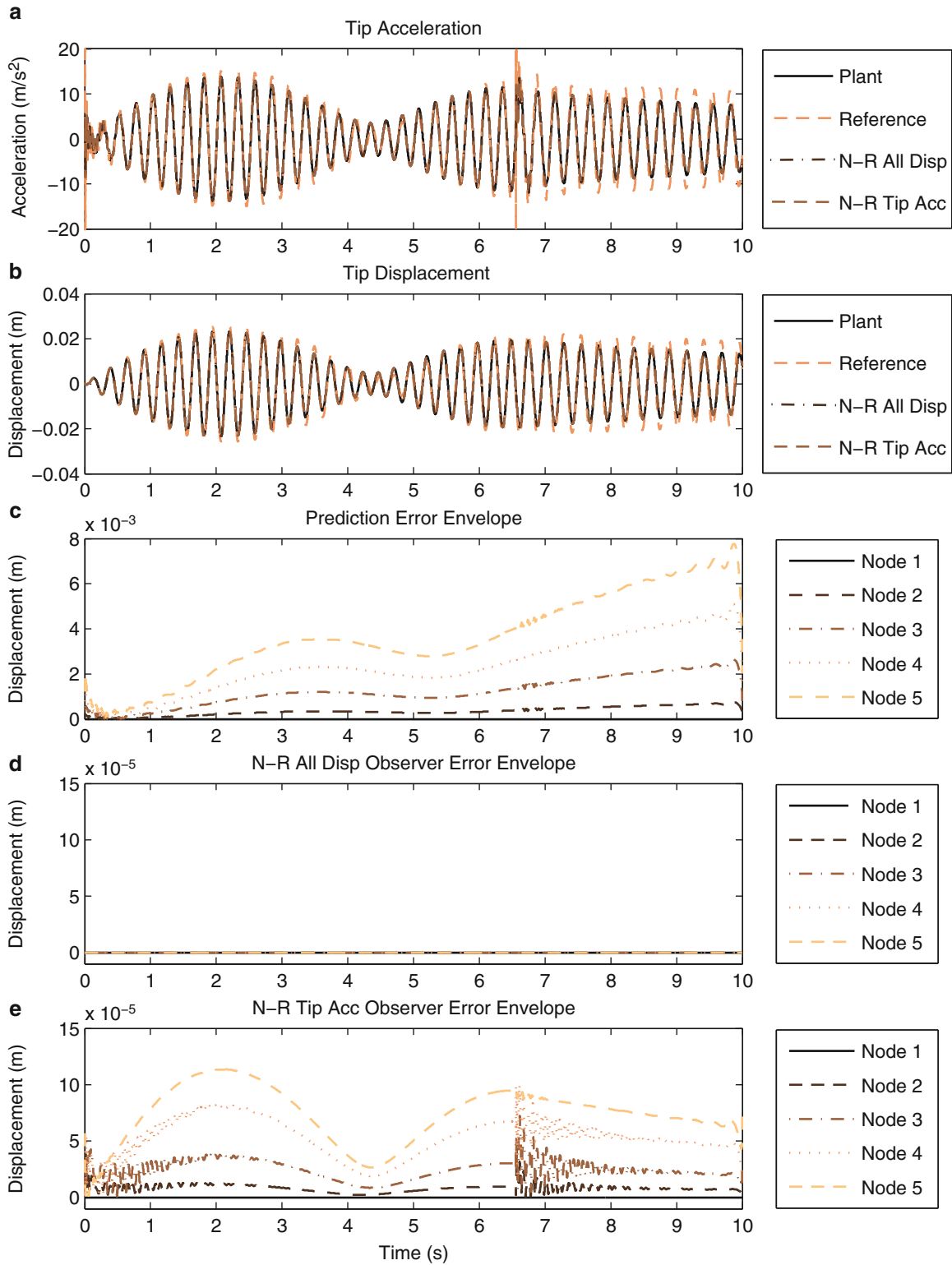


**Fig. 41.4** Observer results for *NLBeam* reference system

## 41.5 Summary

In this paper, a Newton-Raphson force correction observer has been introduced and demonstrated for a linear and nonlinear numerical example. The observer was implemented in a numerical example using a geometrically nonlinear beam code developed for modeling of wind turbine blades. The observer is designed to take advantage of the availability of the system Jacobian matrices from the *NLBeam* solver at each time step. The form of the Newton-Raphson observer was verified using synthesized full-field displacement measurement data from an *NLBeam* plant and a perturbed version of the same *NLBeam* model as the reference model. The Newton-Raphson observer was further tested using a single acceleration measurement to observe displacement at the reference model nodes, demonstrating the numerical ability of the observer to generate a state estimate given acceleration measurements at a subset of nodes.

For implementation of the Newton-Raphson observer on a real-world structure, such as a wind turbine rotor blade, necessary future work includes: (1) an assessment of the observer's performance in the face of noise on the inputs and/or outputs; (2) an assessment of the observer's stability, in particular given that the error system state matrix effectively changes as the system Jacobian changes at each time step and iteration; and (3) experimental validation with the ability to measure the system state being observed (e.g. a beam/surrogate rotor blade with simultaneous displacement and acceleration measurements with the root force/moment couple).

## References

1. Bartlett JFD, Flannelly WG (1979) Model verification of force determination for measuring vibratory loads. *J Am Helicopter Soc* 24:10–18
2. Liu J-J, Ma C-K, Kung IC, Lin D-C (2000) Input force estimation of a cantilever plate by using a system identification technique. *Comput Methods Appl Mech Eng* 190:1309–1322
3. Hernandez AV, Swartz RA, Zimmerman AT (2011) A framework for embedded load estimation from structural response of wind turbines. *Rotating Mach Struct Health Monit Shock Vib* 5:295–305
4. White JR, Adams DE, Rumsey MA (2009) Operational load estimation of a smart wind turbine rotor blade. In: *Proceedings – SPIE the international society for optical engineering*, San Diego, pp 72952D-12
5. Luscher DJ, Ellis G (2011) Part II: plant-scale aeroelastically-coupled wind turbine response from geometrically exact beam theory. In: *Intelligent wind turbine LDRD mid-project review*, Los Alamos National Laboratory
6. Simo JC, Vu-Quoc L (1986) A three-dimensional finite-strain rod model. part II: computational aspects. *Comput Methods Appl Mech Eng* 58:79–116
7. Jelenic G, Crisfield MA (1999) Geometrically exact 3D beam theory: implementation of a strain-invariant finite element for statics and dynamics. *Comput Methods Appl Mech Eng* 171:141–171
8. Hodges DH (2006) *Nonlinear composite beam theory*, American Institute of Aeronautics and Astronautics, Reston
9. Hodges DH, Yu W (2007) A rigorous, engineer-friendly approach for modelling realistic, composite rotor blades. *Wind Energy* 10:179–193
10. Ogata K (2002) *Modern control engineering*. Prentice Hall, Upper Saddle River
11. Kalman RE (1960) A new approach to linear filtering and prediction problems. *J Basic Eng* 82:35–45
12. Laub AJ, Wette M (1984) Algorithms and software for pole assignment and observers. UCRL-15646
13. Belytschko T, Hughes TJR (1983) *Computational methods for transient analysis*, vol 1. North-Holland, Amsterdam

# Chapter 42

## Damage Index Matrix: A Novel Damage Identification Method Using Hilbert-Huang Transformation

Ali Zarafshan and Farhad Ansari

**Abstract** As novel construction materials become more economically and technically available throughout the globe, the structures become more complex. Therefore, an unexpected failure of these structures causes catastrophic economical and fatal losses. Over the past decades, a number of vibration based damage detection techniques have been developed to avoid unexpected failure in structures. These damage detection methods identify presence, location and magnitude of developed damage in the structure associated to change of modal properties such as natural frequency, mode shape and modal damping. An essential limitation of these techniques is that they are majorly sensitive to high intensity of damage only and do not correctly respond to minor to intermediate damage severities. This research proposed a novel damage detection methodology based on application of Hilbert-Huang Transform (HHT) on the acceleration response of the structure. HHT consists of Empirical Mode Decomposition followed by Hilbert Transform of the signal. The method develops a Damage Index Matrix for the structure by connecting energy index of the instrumented structural points. Viability of the proposed method is demonstrated through numerical examples and laboratory experiments. The method was able to locate both single and multiple damage scenarios in numerical models as well as laboratory experiment.

**Keywords** Damage detection • Hilbert-Huang Transform • Structural Health Monitoring • Smart Structures • NDT

### 42.1 Introduction

Development of novel construction materials and techniques has led to the creation of large civil infrastructures. An unexpected failure of these structures causes catastrophic economical and fatal losses. In order to avert the sudden collapse of the structure, detecting the damage in its early development state seems vital. Structural Health Monitoring (SHM) techniques have been shown to be promising for structural damage detection. SHM process involves installing sensors on the structure, acquiring the structural responses by means of sensors and analyzing real-time or recorded data in order to detect the location and extent of the damage. There are several SHM systems installed on civil structures to detect faults during their service lives. These systems have been introduced and discussed by Chen [1]. Damage detection techniques can be referred to as local and global methods. Local damage detection methods including visual inspection and Non-Destructive Testing (NDT) are more likely to detect the damage in the structure. However, the application of these methods to civil infrastructures is time-consuming and expensive. On the other hand global damage detection methods which are based on the modal properties of the structure have achieved growing attention in recent decades. An effective global damage identifying technique is valuable to insure safety of the structure.

Over the past decades, a number of vibration based damage detection techniques have been developed. The idea of these methods is to correlate the change in physical properties of the damaged structure to measurable changes in modal properties. Modal properties include natural frequency, mode shape and modal damping of the structure. Fast Fourier Transform (FFT) based methods are among the most commonly used techniques to identify modal properties of the structure from ambient vibration data. Littler and Ellis [12] deduced that FFT based methods can overestimate the modal damping. In addition, these

---

A. Zarafshan (✉) • F. Ansari  
Department of Civil and Materials Engineering, University of Illinois at Chicago,  
842 W. Taylor Street, (M/C) 603, Chicago 60607, USA  
e-mail: [azaraf2@uic.edu](mailto:azaraf2@uic.edu); [fansari@uic.edu](mailto:fansari@uic.edu)

methods are not sensitive to slight to moderate amount of damage in complex structures. Comprehensive literature study of several damage detection methods can be found in [6] and [5]. Vibration based methods are not able to overcome all the problems in detecting various types of damages. An essential limitation of these methods is that the changes in modal properties such as natural frequency and modal damping caused by damage are usually very small. It is possible that these changes covered by the alterations resulted from service and ambient conditions. For this reason, most successful damage identification methods using frequency are verified only in controlled laboratory scale rather than testing of real structures in their operating environment. Shortcoming and advantages of several damage identification techniques have been studied by Talebinejad [18]. Their findings demonstrated that only high intensity damage is detectable by these methods.

With the intent of precise damage identification, having the proper technique to analyze the response of the structure is crucial. Huang [8] introduced Hilbert-Huang transform (HHT) to process non-stationary, nonlinear data. HHT consists of Empirical Mode Decomposition (EMD) followed by Hilbert Transform (HT) of the signal. EMD is a fully data driven technique and decomposes the signal into a combination of oscillatory Intrinsic Modes Functions (IMF). Then, Hilbert transform is applied to each IMF decomposing it into time-frequency domain. This process was illustrated by Donnelly and Rogers [4] through several numerical examples. The HHT technique has been successfully utilized in the areas of modal parameter identification and damage detection. Yang [21] applied the HHT approach to the vibration response of a single degree of freedom structure. They proposed a method to identify the modal damping and natural frequency of system based on the regression analysis of data. Chen [2] applied HHT technique on the recorded vibration response data of the Tsing Ma Bridge during typhoon Victor in order to obtain natural frequencies and modal damping ratios of the bridge. The results showed the suitability of the HHT method in finding the damping of the bridge structure. Kreschen [9] related the outcome of the HHT to slow-flow dynamic of the system to outline the novel slow-flow identification method.

Applicability of HHT for the purpose of damage detection has been subject of many researches. Quek [16] employed the Hilbert-Huang Transform of the real signals to detect anomalies in beams and plates. The results indicate that HHT is sensitive to local signal distortion. Loutridis [13] used empirical mode decomposition to detect damage in an experimental gear system mechanism. An empirical curve derived to relate the energy of the vibration signals to the crack magnitude in a single gear. Zhu and Law [22] studied nonlinear characteristics of the reinforced concrete beam by means of applying HHT to the vibration data of a reinforced concrete beam. They proposed a damage indicator for the beam structures based on acceleration – frequency eclipse. Tang [19] proposed a damage index based on ratio of equivalent damping ratio and evaluated the damage index using the HHT and FFT spectra. The results indicated that while structural response is in elastic zone, the index change is insignificant.

The method described herein pertains to the development of damage detection technique based on application of HHT on the acceleration response of the structure. The method develops a Damage Index Matrix (DIM) over the structure by connecting energy index of the instrumented structural points. Energy index of each point is constructed from contents of instantaneous energy over the recorded response time. In the following sections, first the concepts of EMD and HT are briefly introduced. Then, concept of energy index and assembly of damage index matrix is explained based on the HHT technique. The application of proposed method is demonstrated through numerical examples and laboratory experiments as well.

## 42.2 Empirical Mode Decomposition

Huang et al. [8] proposed application of EMD technique to decompose the time-series data into Intrinsic Mode Functions (IMF). An IMF is an oscillatory function that satisfies two conditions: (1) Number of zero crossings is zero or at most differs by one from number of extrema and (2) local maxima and minima envelopes have the running value of zero in every single point. In contrast to the Fourier functions, these IMFs can be non-stationary and have time dependent amplitude and frequencies. In fact IMF is the generalized form of a simple harmonic function. EMD process is also known by the sifting procedure. To decompose a signal, one can identify and then connect all the local maxima by a cubic spine line to establish the maximum envelope. The procedure can be repeated to produce the minimum envelope as well. The mean of maximum and minimum envelopes, noted as  $m(t)$  is subtracted from the data to establish the first component,  $h_1(t)$  as:

$$X(t) - m_1(t) = h_1(t) \quad (42.1)$$

However, even in case of perfect fitting, after the first round of sifting, new local maximum can be developed from slight swelling in data. In this order, sifting procedure has to be repeated to shrink the uncovered signal to an IMF. Following sifting processes, the  $h_1(t)$  is used as the source data resulting in:

$$h_1(t) - m_{11}(t) = h_{11}(t) \quad (42.2)$$

Repeated for  $k$  times,  $h_{1k}$  becomes an IMF. the low amplitude signals in the data. Number of sifting processes should be limited to insure that the physical meaning of the IMF is maintained. Huang et al. [8] suggested stoppage criterion for this purpose by restricting the size of standard deviation, where SD, for two successive sifting processes was defined as:

$$SD = \frac{\sum_{T=0}^t |h_{1(k-1)}(t) - h_{1k}(t)|^2}{h_{1(k-1)}^2(t)} \quad (42.3)$$

As stated in [8] SD values between 0.2 and 0.3 provide suitable decomposition. However, this stoppage criterion must be used with caution. Setting excessively stringent criterion may result in many sifting and appearance of counterfeit IMF's. Quek et al. [16] suggested an alternative stoppage criterion as follows:

$$SD = \frac{\sum_{T=0}^t |h_{1(k-1)}(t) - h_{1k}(t)|^2}{\sum_{T=0}^t h_{1(k-1)}^2(t)} \quad (42.4)$$

Once the stoppage criterion is satisfied,  $h_k(t)$  is considered as the IMF. First IMF is denoted as  $C_1(t)$  and contains the shortest period elements of the time-series. Separating  $C_1(t)$  from the original signal results in:

$$X(t) - C_1(t) = r_1(t) \quad (42.5)$$

After subtracting the first IMF, the residual,  $r_1(t)$ , still conveys components of data with longer periods. The EMD procedure is repeated and residue at each step is treated as the new data to extract all subsequent IMFs. As a result of this procedure, signal  $X(t)$  is decomposed into a series of IMFs,  $C_j(t)$  and a residual.

$$r_{n-1}(t) - C_n(t) = r_n(t) \quad (42.6)$$

The procedure is stopped when the residue,  $r_n$ , becomes a monotonic function or trend that no additional IMF can be extracted from. Substitution of Eq. 42.6 into Eq. 42.5, and expansion of Eq. 42.5 results in the following form for the original data:

$$X(t) = \sum_{N}^{j=1} C_j(t) + r_n(t) \quad (42.7)$$

Although EMD technique is an adaptive process, it may encounter some difficulties. In each step, mean envelope is calculated as the average of maximum and minimum envelopes. Therefore mean values at each time step are not an actual data mean. Including the residual as an additional component, Eq. 42.7 is expressed as:

$$X(t) = \sum_{N+1}^{j=1} C_j(t) \quad (42.8)$$

The square of the original signal,  $X^2(t)$ , can be expressed as the multiplication of Eq. 42.8 by itself:

$$X^2(t) = \sum_{N+1}^{j=1} C_j^2(t) + \sum_{N+1}^{j=1} \sum_{N+1}^{i=1} C_j(t)C_i(t) \quad (42.9)$$

If decomposition is complete and resultant IMFs are orthogonal, the second part of the right hand side of the Eq. 42.9 must be zero. To measure the soundness of decomposition, Huang et al. defined an Index of Orthogonality [8], denoted by IO, as:

$$IO = \sum_0^T \left( \sum_{N+1}^{j=1} \sum_{N+1}^{i=1} \frac{C_j(t)C_i(t)}{X^2(t)} \right) \quad (42.10)$$

The IO value is usually employed to measure accuracy of signal decomposition. Loutridis [13] states that IO values between 0.01 and 0.001 are fine. This criterion is used to ensure precise decomposition of the data in both numerical and experimental examples. Furthermore, it is possible that first extracted IMF covers a wide frequency range and as a result mono component characteristics cannot be achieved. To overcome this obstacle and insure mono component IMFs, several methods have been suggested. Peng [15] proposed an improved HHT method by applying Wavelet Package Transform (WPT) as a preprocessor to the signal. Applied to the data, WPT decomposes the signal into several narrow band signals. However, this method involves quite number of calculations. Huang [7] proposed imposing an intermittency frequency condition during the EMD

process. This insures that resulting IMF contains only frequencies higher than the imposed frequency. On the other hand, when signal to noise ratio is low, the number of required siftings could be large. This case is commonly encountered when response of the structure is being monitored in presence of unwanted ambient vibrations. To simplify the process and to lessen the computations, an alternative method based on the band pass filter is proposed by Yang et al. [21]. In this study, former method is employed and experimental test data are passed through a band pass filter to avoid unwanted frequencies due to noise.

### 42.3 Hilbert Transform

Having the time-series data transformed into the finite IMFs, Hilbert transform can be applied on each IMF. The Hilbert transform (HT) for any time-series,  $Y(t)$ , defined by:

$$H(x(t)) = Y(t) = \frac{1}{\pi} P.V \int_{-\infty}^{\infty} \frac{x(\tau) d\tau}{t - \tau} \quad (42.11)$$

Where  $P.V \int$  identifies an extension of the Cauchy principal value integral [10]. Hilbert transform of the time-series  $X(t)$  is the complex conjugate pair of data. Complex analytical signal can be formed as:

$$Z(t) = x(t) + iY(t) = A(t)e^{i\theta(t)} \quad (42.12)$$

Instantaneous amplitude and phase of the signal are respectively described by:

$$A(t) = \sqrt{x^2(t) + y^2(t)} \quad (42.13)$$

$$\theta(t) = \text{Arctan} \left( \frac{Y(t)}{x(t)} \right) \quad (42.14)$$

Equations 42.13 and 42.14 express the  $X(t)$  in a polar system, in terms of time dependent amplitude and phase. In addition, instantaneous frequency can be defined as:

$$\omega(t) = \frac{d\theta(t)}{dt} \quad (42.15)$$

The Oliviera and Barroso [14] have explained that notion of instantaneous frequency is only applicable to the mono component data. The extracted IMFs are monotonic functions with symmetric local mean and therefore instantaneous frequency perception is meaningful.

### 42.4 Proposed Damage Index

Several damage detection methods have been developed based on processing the vibration signals. In these methodologies, an index of damage is defined as the difference between undamaged (healthy) state and damage state of the structure. Loutridis [13] investigated incidence of a crack in a model of gear pair utilizing the HHT. The observation clarified that any fault would alter the local amplitude of one of the calculated IMF's through EMD process. Xu and Chen [20] examined damage identification in terms of change of stiffness in a three storey building model via EMD. Damage location and occurrence time was detected successfully through local abnormalities in the IMFs. Damage location and occurrence time was detected successfully through local abnormalities in the IMFs. In another study, Lin et al. [11] applied HHT method to response of IASC-ASCE benchmark four-storey structure under ambient vibration in order to identify the damage. This approach compared the structural stiffness and damping resulted from HHT technique between healthy and damaged structure. Cheraghi and Taheri [3] successfully identified dynamic characteristics of a 6 DOF mechanical system, such as natural frequency, damping and mode shapes, using the HHT. In a step forward, by comparing these parameters for healthy and damaged structure they developed an EMD energy damage index to identify and to locate the damage. In another study, Rezaei and Taheri [17] experimentally investigated EMD damage index introduced by Cheraghi and Taheri [3], on a cantilever steel pipe. The pipe excited with an impulse hammer and its free end and five sensors recorded its response. They verified the effectiveness of the EMD energy damage index.

The method introduced in this study proposes a damage index matrix based on amplitude of the analytical signal representing vibration data of a structure. When the signal is decomposed into IMFs, first IMF is selected as the principal IMF. Presence of damage in the structure alters the vibration signal in the fault vicinity. Furthermore, due to the fact that any relevant IMF has strong correlation with the signal, the calculated principal IMF is altered for the sensor located close to the damaged zone. This variation affects the local analytical signal structure and its amplitude. Instantaneous amplitude is used to construct instantaneous power, which defined as:

$$E_1(t) = \frac{1}{2} A_1^2(t) \quad (42.16)$$

Where  $A_k(t)$  is the instantaneous amplitude of first IMF. Energy index for  $j$ th sensor location is defined as a scalar value, denoting energy content of the principle IMF as:

$$IDE_j = \int_0^T E_j(t) dt \quad (42.17)$$

Where  $T$  is the duration of observed response. The energy index is constructed for available instrumented points over the structure. The energy indices are developed for undamaged and subsequent damage states of the structure. For each state of structure, an energy index matrix is developed as:

$$[IDE_{ij}]_{st} = [\sqrt{IDE_i \times IDE_j}]_{st} \quad (42.18)$$

In Eq. 42.18, subscript  $st$  denotes the state condition of the structure. The energy index matrix bonds the energy content of the structural points together and provides a comprehensive measure for the whole structure in one step. Therefore, any damage which affects the energy of one monitored degree of freedom, directly affects the other components of energy index matrix. Damage index matrix (DIM) is developed as:

$$[DIM] = \left| \frac{[IDE]_h - [IDE]_d}{[IDE]_h} \right| \times 100 \quad (42.19)$$

Once DIM is computed for each damage state of the structure, presence and magnitude of damage may be assessed by associating high DIM diagonal and immediate off-diagonal elements close to the respective sensors.

## 42.5 Finite Element Validation of Proposed Method

In this section, the proposed damage detection method is evaluated by its application to a numerical model of a three-span steel bridge shown in the Fig. 42.1. The central span is 21.94 m (72 ft) and the other two span lengths are both 14.86 m (48.75 ft). Superstructure of the bridge consists of concrete deck 10.97 m (36 ft) wide and 0.23 m (0.75 ft) thick. Five continues steel girders made of WF 33 × 130 sections (Fig. 42.1) transfer the load from the deck to the interior piers and abutments. Diaphragms made out of WF 16 × 36 sections connect the girders to each other. The Finite Element (FE) model of the structure was developed in ANSYS package using three dimensional solid elements.

Free-vibration response of the structure under the load equal to the weight of H-20 standard truck was recorded for ten points, representing ten sensors. These points were located along the bottom flange of the central girder and are shown

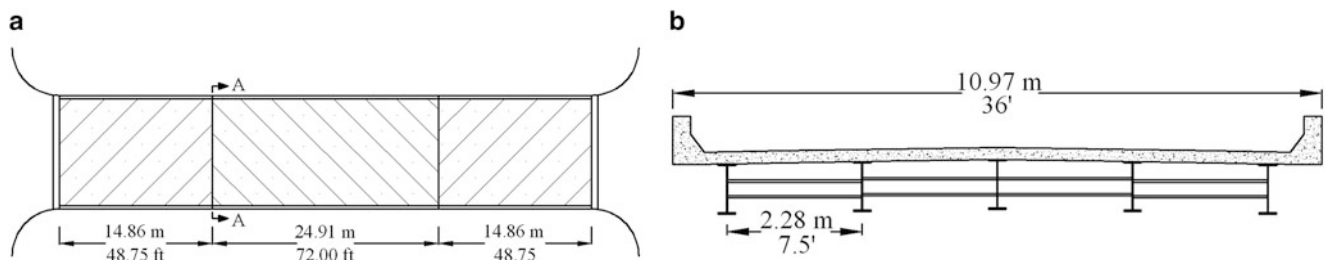
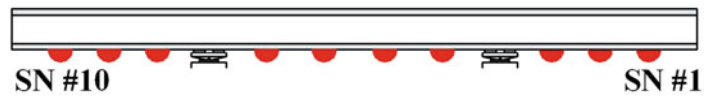


Fig. 42.1 (a) Aerial plan of the bridge and (b) super structure section A-A



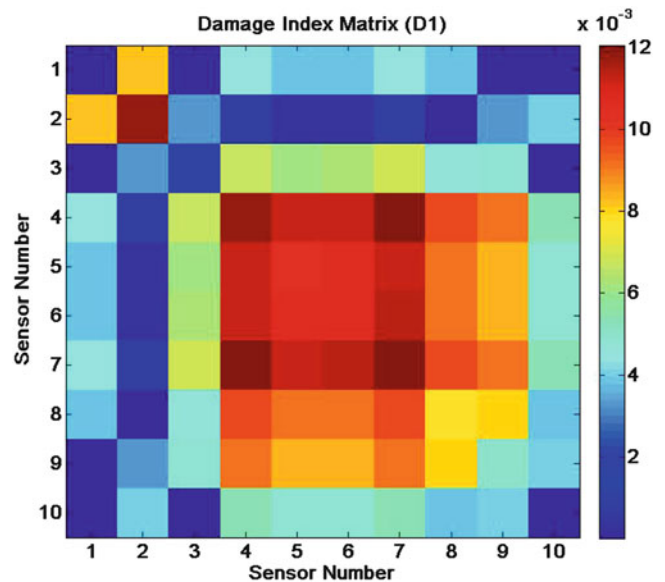
**Fig. 42.2** Sensor location on the central girder



**Table 42.1** Damage scenarios, damage locations and respective damage intensities

Scenario	Damage type	Damage location	Intensity (%)	Noise level (RMS) (%)
D1	Single	9.3 m (30.75 ft)	13.0	10
D2	Single	21.9 m (72 ft)	17.8	10
D3	Single	21.9 m (72 ft)	22.5	10
D4	Multiple	8.9/24.9 m (29.25/81.75 ft)	17.8/17.8	10
D5	Multiple	42.5/21.9 m (139.5/72 ft)	22.5/17.8	10

**Fig. 42.3** Damage Index Matrix for damage scenarios D1



in Fig. 42.2. The data were recorded with sampling frequency of 200 Hz. In addition, to consider the effect of the unwanted ambient vibrations, recorded data polluted with additional noise. Noise magnitude was equal to 10% Root Mean Square (RMS) of the recorded response.

These data were employed to establish the instantaneous energy and energy indices for each state of the structure. Different damage scenarios were simulated by reducing stiffness of the elements in the second steel girder of the bridge, and therefore diminishing the bending stiffness of the whole section. Both single and multiple damage location scenarios were considered in this study. Locations of damages for each scenario are also presented in the Table 42.1.

In first scenario, D1, stiffness of the bridge section reduced by 13% due to a single induced damage point. Computed DIM is shown in Fig. 42.3. Despite this stiffness reduction, no significant discrepancy was observed among the DIM elements. Especially, elements corresponding to the sensors encompassing the damage location had not unraveling values. Therefore, location of damage cannot be located confidently in the structure.

In next two scenarios, D2 and D3, a single point damage at 21.9 m (72 ft) was introduced to the model. For these cases, damage location kept identical, while its magnitude reduced cross section's stiffness at by 17.8 and 22.5%, respectively. As shown in Fig. 42.4a, for damage scenario D2, diagonal elements corresponding to sensors 4 and 5, with the respective values of 7.51 and 5.83, had highest values among the DIM entries. In addition, off-diagonal entries of DIM had distinctive value of 6.68 in locations encompassing the damage. Therefore, DIM was able to identify location of damage between fourth and fifth diagonal entries corresponding to fourth and fifth sensors.

In scenario D3, bending stiffness of the bridge section was reduced further by additional 4.8–17%. Fourth and fifth diagonal entries had the value of 12.65 and 8.96, in that order. Therefore, DIM accurately spots the damage between corresponding fourth and fifth sensors. Comparing damage index matrices for scenarios D2 and D3, it observed that as the severity of the damage increases, the magnitude of DIM values ascends. As presented in Fig. 42.4b, in D3 configuration, amplified damage magnitude augmented the DIM values around the damage location by 61%.

Damage scenarios D4 and D5 were defined to assess the capability of the proposed method in multiple damage detection. For scenario D4, two damaged developed at 8.9 m (29.25 ft) and 24.9 m (81.75 ft), respectively. Damage intensity equal to

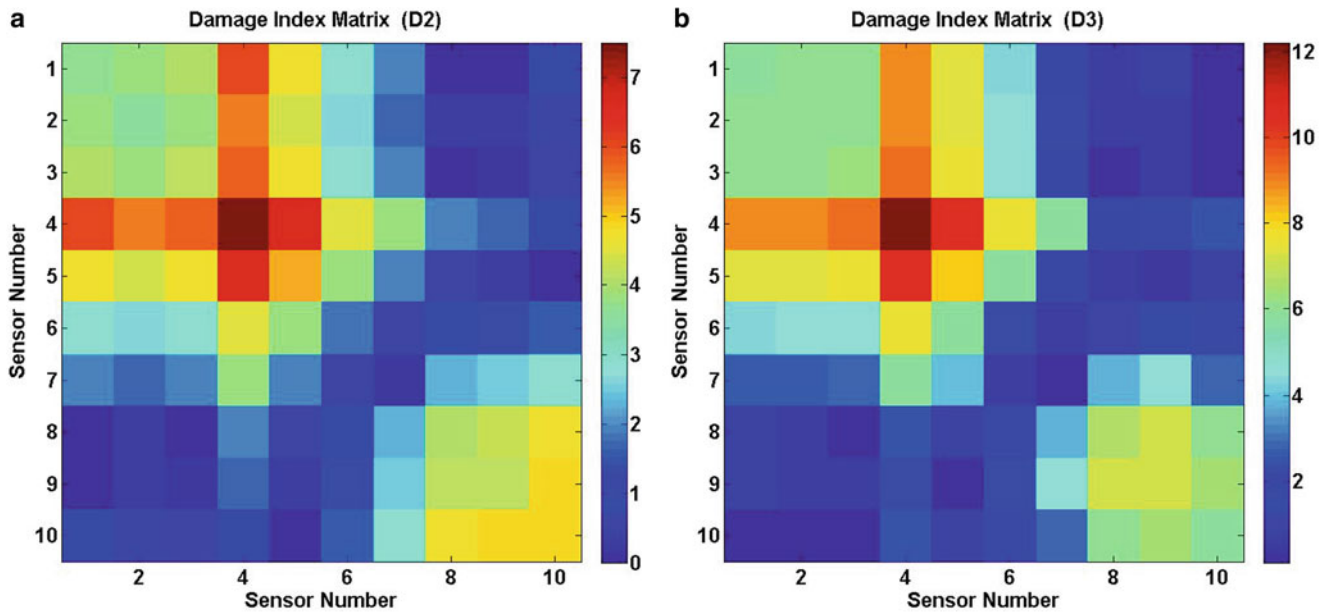


Fig. 42.4 Damage Index Matrix for damage scenario (a) D2 (b) D3

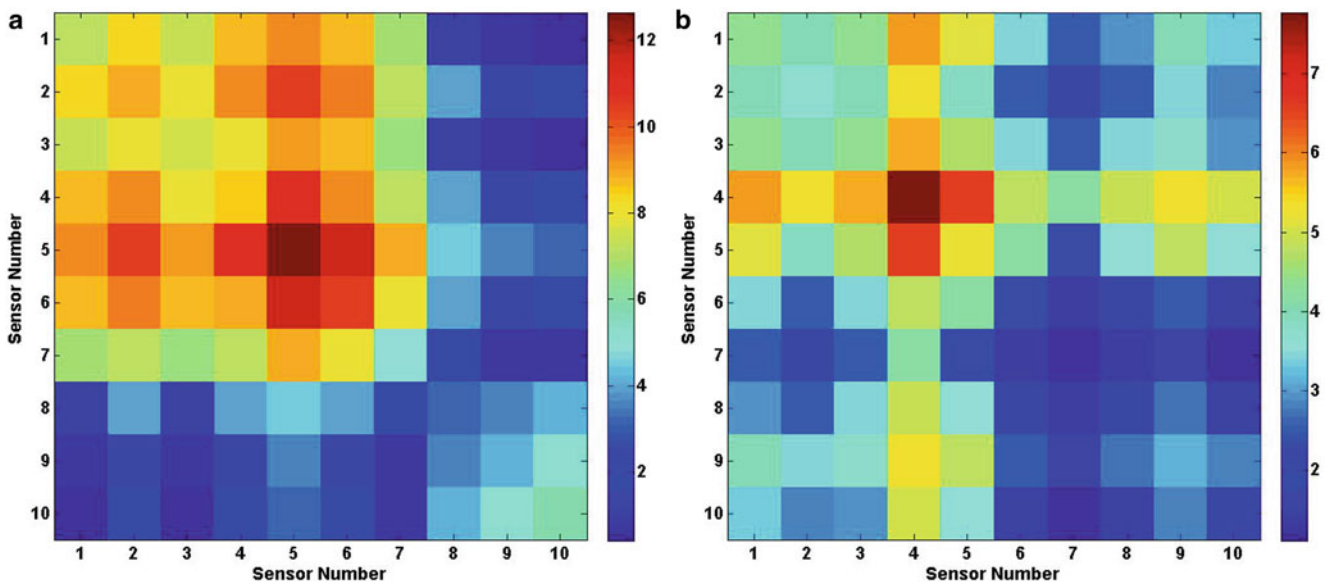


Fig. 42.5 Damage Index Matrix for damage scenario (a) D4 and (b) D5

17.8% reduction of stiffness applied at both locations. As depicted in the Fig. 42.5a, DIM correctly identifies first damage location to be between fifth and sixth. Diagonal and immediate off-diagonal corresponding DIM entries had values of 12.65 and 11.63, respectively. Second damaged location encompassed by first and second sensors. However, DIM diagonal entries associating with these sensors point to the damage location vaguely. Therefore, spotting the damage in this position was not as clear as the discovering the first damage location.

In D5 scenario, two different intensities were considered for damages in the structure. The stiffness of the bridge section lessened by 17.8% at 21.9 m (72 ft) and by 22.5% at 42.5 m (139.5 ft), respectively. DIM representation for this scenario is shown in Fig. 42.5b. Sensor 4 and 5 had values of 7.77 and 5.23, respectively and they distinguish first damage location. Second damage location is also recognizable, due to high values of ninth and tenth diagonal entries, 3.35 and 2.67, respectively.

## 42.6 Experimental Set-Up

An experimental laboratory test performed to verify the analytical results. The experimental set up consists of a three-span wide flange  $W4 \times 13$  beam with two splice spots. The beam is made of steel A572 grade 50 with the yield and ultimate strength of 344.7 MPa (50 ksi) and 448.15 MPa (65 ksi) respectively. The beam rests on two simple supports which provide restrains on the vertical and horizontal axis. Geometry of the experiment is presented in the Fig. 42.6.

Splices, bolted to the beam, were considered fully fixed. Pins were made of hardened alloy steel in compliance with ASME B18.8.2 standard and had shear and yield strength of 1,034.2 MPa (150 ksi) and 1,172.1 MPa (170 ksi), respectively. The bolts chosen according to ASME B18.2.1 standard and had the minimum yield strength and shear strength of 896.3 MPa (130 ksi) and 627.4 MPa (91 ksi), respectively. Bolts and pins with 9.52 mm ( $\frac{3}{8}$  in.) and 12.7 mm ( $\frac{1}{2}$  in.) diameter were employed for both flange and web plate connections. Plates were made out of steel A36 grade. Splice point configuration is shown in the Fig. 42.7.

To simulate the damage in the beam structure, bolts in top flange and pins on the right side of the first splice were removed. This setup presents damage in the current structure condition and simulates the characteristics of the aged structure. To generate free vibration in the structure, an impact loading was applied on the far right end of the beam by means of releasing a 12 Kg (26.45 lb) mass from the beam. Five accelerometers were attached to the structure in various locations and recorded the acceleration response of the mentioned points. These locations are depicted in the Fig. 42.8. Accelerations were recorded from a second before the release of the weight with sampling frequency of 200 Hz for 10 s.

The test was performed three times to ensure integrity of the results. After removing bolts and pins in the second splice, tests were repeated with same loading conditions. Response of the structure was recorded for the same duration with the same sampling frequency as before.

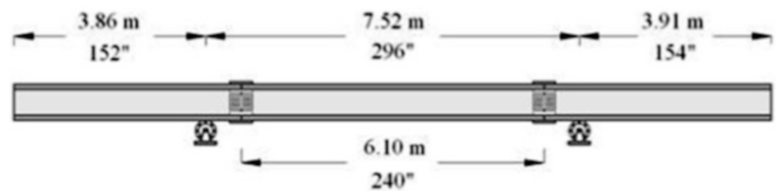


Fig. 42.6 Beam geometry

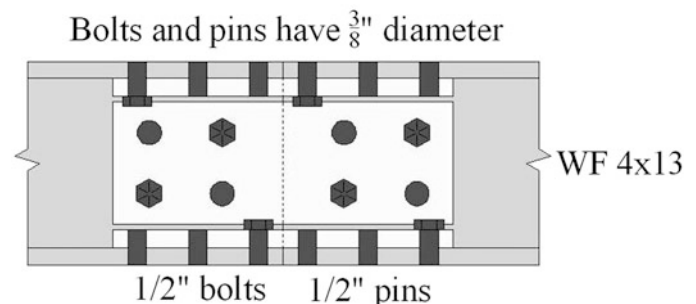


Fig. 42.7 Details of the beam splice

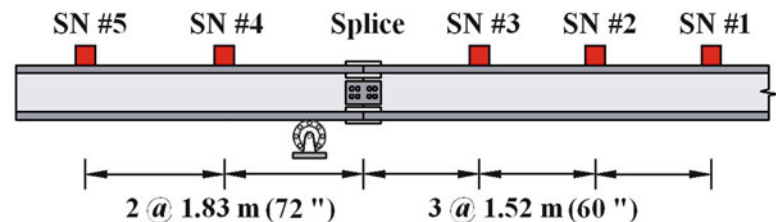


Fig. 42.8 Experimental test sensor locations

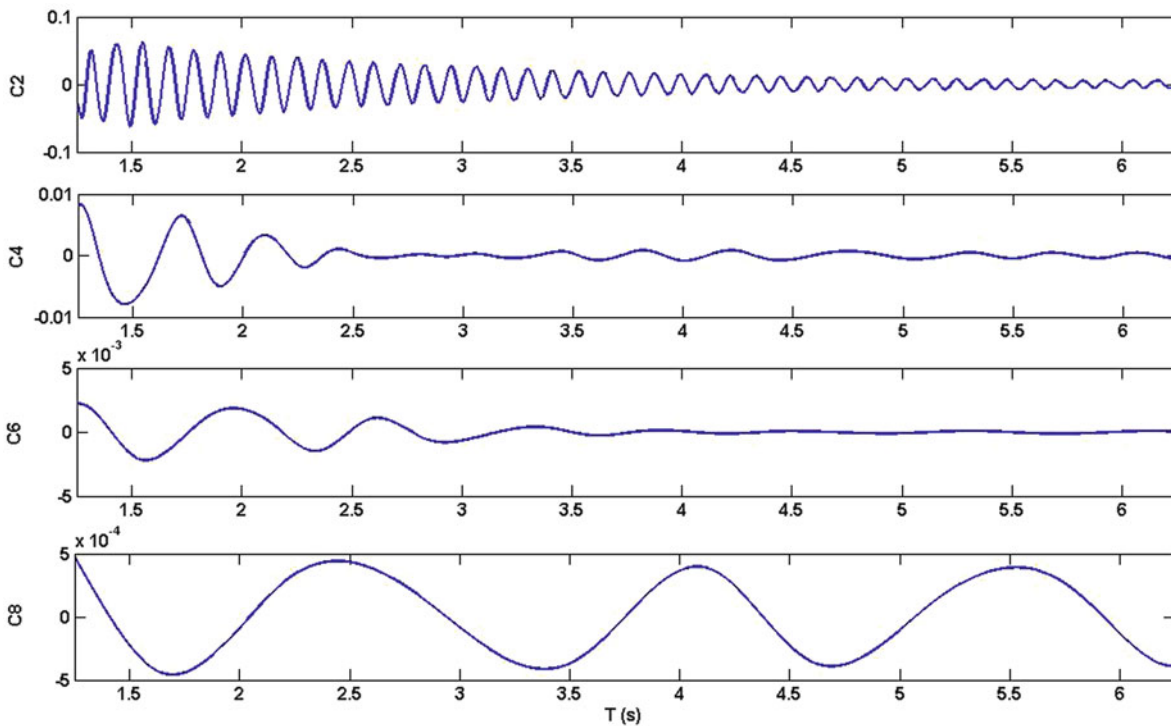


Fig. 42.9 Even IMF's of the first sensor acceleration response

## 42.7 Experimental Results

Free vibration part of the data was selected to be analyzed by applying HHT to the recorded data. Each sensor acceleration data consist of 1,000 data points starting from 0.25 s after load release to prevent high transient response in that duration. The impact loading excites several vibration modes of the structure. Therefore, to isolate a narrow frequency band containing few first natural frequency of the beam, acceleration signals were processed through a band pass filter. Filtered acceleration signals decomposed into IMFs via EMD procedure. Stoppage criterion noted in Eq. 42.3 was employed in individual test sets with the value of 0.15. Selected even decomposed IMFs for the first sensor are shown in the Fig. 42.9.

As discussed earlier, Hilbert transform must be applied to the mono-component data. One way to ensure the efficiency of the EMD process is to check the substantial frequency of the decomposed data. Figure 42.10 depicts the obtained signals from second sensor for the healthy structure and its first and second IMFs, respectively. Fast Fourier Transform (FFT) was applied to these signals. Results are shown precise separation of the data into mono-component signals via EMD process.

In addition to investigating frequency content of the decomposed data, Index of Orthogonality (IO) is an alternative measure which demonstrates the accuracy of decomposition. Resulted IO values for the decompositions calculated for each set of data and results are summarized in the Table 42.2.

Analytical signals transferred into instantaneous amplitude and frequency as discussed in previous section. Energy index matrices constructed for both intact and damaged structure namely prior to and after splice damage development. Figure 42.11 represents constructed DIM and its corresponding entries values. While the mean value of diagonal elements is 3.786, sensor 3 and 4 had values of 4.75 and 5.12. Figure 42.11 evidently demonstrated that constructed DIM properly located the damage between sensor 3 and 4.

## 42.8 Conclusion

Early fault detection in structures insures safety under extreme loading conditions. In past three decades, several vibration based methods have been proposed to identify fault development in the structures. These techniques correlate changes in stiffness and mass of the structure to its modal properties. However, several researchers documented are insensitive to minor

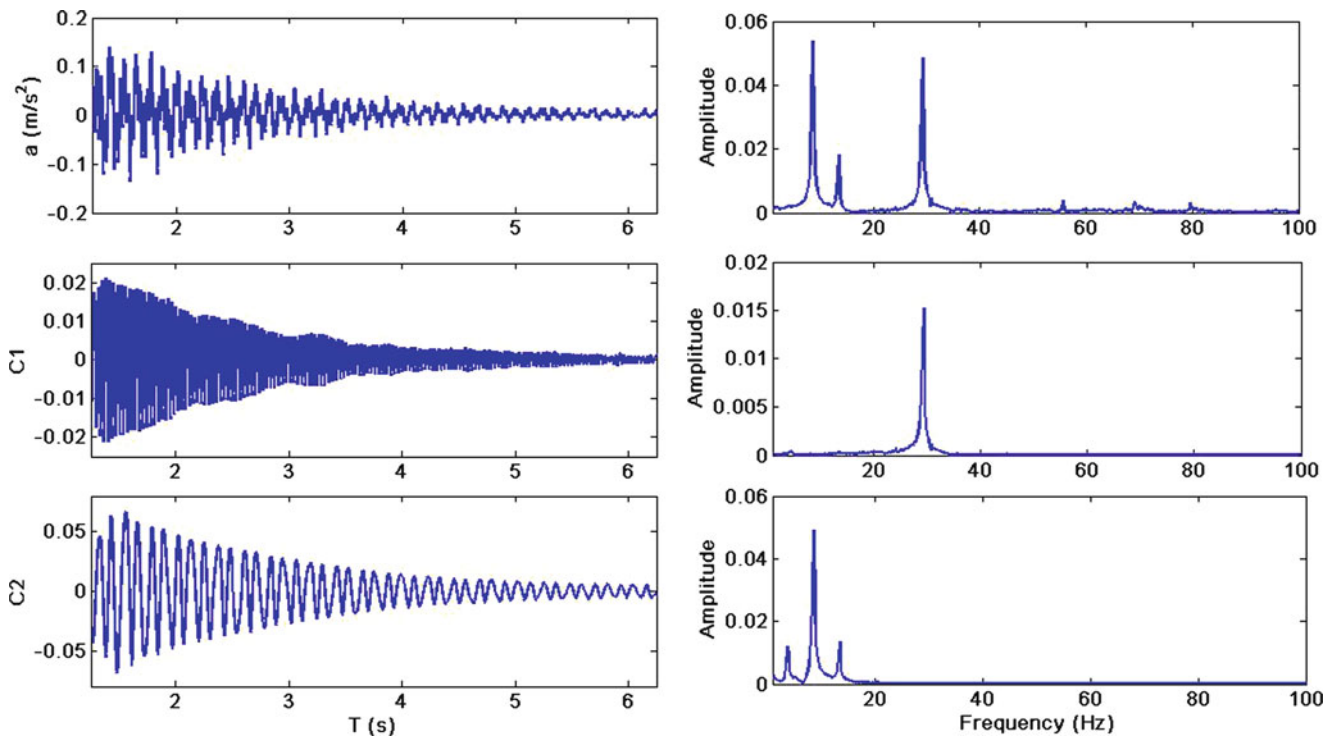


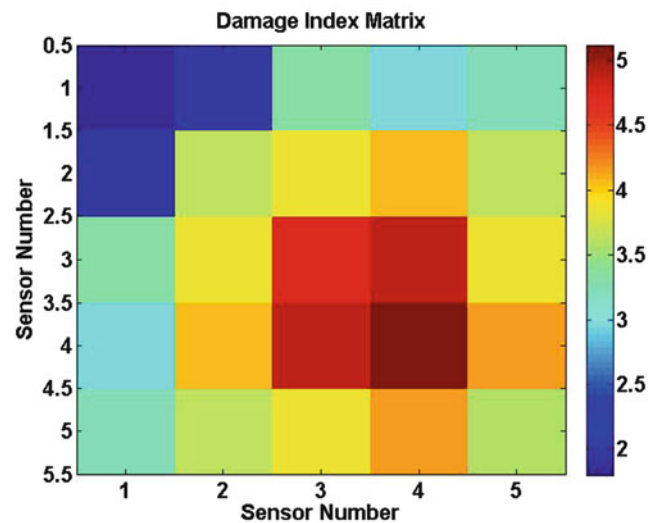
**Fig. 42.10** Vibration signals, its first two IMF's and their respective FFT spectrums

**Table 42.2** Index of Orthogonality for each sensor

Sensor no.	IMFs no.	IO
1	9	0.0014
2	7	0.0017
3	7	0.0013
4	9	0.0016
5	9	0.0038

amount of damage in the structures. Due to this fact, search for a responsive damage detection technique based on structural vibration data is still required. In current study, a novel damage detection method was proposed based on applying Hilbert Huang Transformation to the vibration response of the structure. This approach employs EMD technique to decompose vibration signals into Intrinsic Mode Functions. Then, Hilbert transforms are applied to the resulted IMF's. Instantaneous amplitude and energy of each IMF is computed over the response time for each measured location. Then, energy index of each structural point is constructed from integral over instantaneous energy. For each damage state of the structure, damage index matrix is assembled from energy index of each instrumented point. This procedure is able to trace the damage position by changes in DIM entries. The capability of the proposed method was evaluated by its application to the response of the numerical model of a multi-span bridge. Several damage scenarios, including multiple damage locations, were introduced. Responses of the structure were analyzed by proposed procedure and Damage Index Matrices developed to locate damages. In numerical examples, three single point damage scenarios introduced to the model. Damage intensities in terms of section's bending stiffness reduction by of 13, 17.8 and 22.5% developed in the structure. The method was not successful in spotting the damage with intensity of 13%. However, it observed that as the magnitude of damage increases, amount of damage indices merit ascend and therefore, damage location is detected more precisely. The results indicated technique ability to locate the damage more than 13% in the structure. Two scenarios developed with multiple damage points. Moreover, results of the analysis of structures with multiple damage points confirmed that proposed methodology could be promising tool to identify the occurrence and to locate damages. In the case of dissimilar damage intensities, the method was able to locate the fault spots. In the case of identical damage magnitudes in distinctive locations, the success of the technique was lower and the multiple damage locations cannot be spotted with high confident. A laboratory experiment sat up to confirm the validity of the proposed method. In this test, a multi-span beam instrumented with accelerometer sensors at five points. Damage

**Fig. 42.11** Constructed DIM for the laboratory experiment



developed in the structure by lessening the bending stiffness at a splice point. Free vibration response of the structure was used to establish the DIM. The proposed method was capable to properly identify the damage location.

## References

- Chen J (2009) Application of empirical mode decomposition in structural health monitoring: some experience. *Adv Adapt Data Anal* 1(4):601–621
- Chen J, Xu LY, Zhang RC (2004) Modal parameter identification of tsing ma suspension bridge under typhoon victor: Emd – ht method. *J Wind Eng Ind Aerodyn* 92:805–827
- Cheraghi N, Taheri F (2008) Application of the empirical mode decomposition for system identification and structural health monitoring. *Int J Appl Math Eng Sci* 2:61–72
- Donnelly D, Rogers E (2009) Time series analysis with the hilbert-huang transform. *Am J Phys* 77(12):1154–1161
- Fan W, Qiao P (2011) Vibration-based damage identification methods: a review and comparative study. *Struct Health Monit* 10:83–111
- Farrar CR, Jaureguiz DA (1998) Comparative study of damage identification algorithms applied to a bridge: I experiment *Smart Mater Struct* 7(5):704–719
- Huang NE, Shen Z, Long SR (1999) A new view of nonlinear water waves: the hilbert spectrum. *Annu Rev Fluid Mech* 31:417–475
- Huang NE, Shen Z, Long SR, Wu MC, Shih HH, Zheng Q, Yen NC, Tung CC, Liu HH (1998) The empirical mode decomposition and the hilbert spectrum for nonlinear and non-stationary time series analysis. *Proc R Soc Lond* 454(1971):903–995
- Kerschen G, Vakakis AF, Lee YS, McFarland DM, Bergman LA (2008) Toward a fundamental understanding of the hilbert-huang transform in nonlinear structural dynamics. *J Vib Control* 14(1):77–105
- King FW (2009) *Hilbert transforms, vol 1,2*. Cambridge University Press, Cambridge/New York
- Lin S, Yang YN, Zhou L (2005) Damage identification of a benchmark building for structural health monitoring. *J Smart Mater Struct* 14:162–169
- Littler JD, Ellis BR (1995) Measuring the dynamic characteristics of prototype structures. In: Krishna P (ed) *A state of the art in wind engineering*. New Age International/Wiley, New Delhi, pp 133–154
- Loutridis SJ (2004) Damage detection in gear systems using empirical mode decomposition. *Eng Struct* 26:1833–1841
- Oliveira PM, Barroso V (2000) Definitions of instantaneous frequency under physical constraints. *J Franklin Inst* 337(4):303–316
- Peng ZK, Tse PW, Chu FL (2005) An improved hilbert-huang transform and its application in vibration signal analysis. *J Sound Vib* 286:187–205
- Quek ST, Tua PS, Wang Q (2003) Detecting anomalies in beams and plate based on the hilbert-huang transform of real signals. *Smart Mater Struct* 12:447–460
- Rezaie D, Taheri F (2009) Experimental validation of a novel structural damage detection method based on empirical mode decomposition. *Smart Mater Struct* 18:1–14
- Talebinejad I, Fischer C, Ansari F (2011) Numerical evaluation of vibration-based methods for damage assessment of cable-stayed bridges. *Computer-Aided Civil and Infrastructure Engineering* 26(3): 230–251
- Tang JP, Chiou DJ, Chen CW, Chiang WL, Hsu WK, Chen CY, Liu TY (2011) A case study of damage detection in benchmark buildings using a hilbert-huang transform-based method. *J Vib Control* 17(4):623–636
- Xu YL, Chen J (2004) Structural damage detection using empirical mode decomposition: experimental investigation. *J Eng Mech* 130:1279–1288

21. Yang JN, Ying L, Shuwen P, Huang NE (2003) System identification of linear structures based on hilbert-huang spectral analysis. part 1: normal modes. *Earthquake Eng Struct Dyn* 32:1443–1467
22. Zhu XQ, Law SS (2007) Nonlinear characteristics of damaged reinforced concrete beam from hilbert-huang transform. *ASCE JStruct Eng* 133(8):1186–1191

## Chapter 43

# An Approach to the Moving Load Problem for Multiple Cracked Beam

N.T. Khiem, T.H. Tran, and N.V. Quang

**Abstract** The present report is devoted to present an approach to dynamic analysis of multiple cracked Euler-Bernoulli beam subjected to general moving load. The novelty of the approach consists of using analytical solution of vibration mode of multiple cracked beam in the frequency domain that is straightforward to compute the time response of multiple cracked beam to moving load given generally in a discrete form. The proposed method enables to eliminate the “moving singularity” phenomena that trouble the use of either the conventional modal method or the modern numerical techniques. The theoretical development is illustrated by numerical results.

**Keywords** Moving load problem • Multiple cracked beam • Dynamic response • Spectral approach • Modal method

### 43.1 Introduction

The moving load problem for a long time has attracted a great interest of researchers and engineers because of its importance in structural engineering. Studies on the problem have being advanced simultaneously with development in modeling the object. The simplest model for the problem is the concentrated constant force moving on an Euler-Bernoulli beam that allowed the problem to be solved by using the conventional method of modal superposition or finite element formulation [1, 2]. Then, the moving load model is gradually improved by using the moving mass or vehicles which lead to more complicated mathematical representation of the problem [3,4]. So far the difficulty is necessity to solve the nonlinear differential equations with the time dependent coefficients despite numerous modern numerical techniques have been developed. On the other hand, the more appropriate to practical use model of the structures subjected to the moving load is also adopted [5,6]. Recently, the damaged structures have been studied with purpose not only to predict the dynamic response of the structures to the moving load [7–11] but also to employ the signal measured in the moving vehicle for the baseline structure damage detection [12,13].

There have been occupied different approaches to the problem that can be categorized as follow. The methods of first category are based on solution of the free vibration problem and expansion of the response in a series of the structure eigenfunctions. The methods of this class are acknowledged as the mode superposition or modal method [1–11]. Note that the Green’s function method may be related to the first category because seeking the Green function in a bounded domain is rather equivalent to the free vibration problem [14]. The methods of other category are based on the finite element formulation of structure leading the problem to be solved simply by using the well known numerical procedures [15–19]. Despite the Gibbs phenomenon associated with the moving singularity has been improved by modifying the expansion [14], the modal method is unable to expose the effect of eigen-mode interaction and higher frequency components. The noticeable drawback of the finite element method is requirement of the time consumable scanning current position of the moving load though it is enhanced by involving the dynamic shape functions instead of the static ones [18]. This report is devoted to present a new

---

N.T. Khiem (✉)

Institute of Mechanics and Environment Engineering, VUSTA, 264, Doi Can, Ba Dinh, Hanoi, Vietnam

Institute of Mechanics, VAST, 264, Doi Can, Ba Dinh, Hanoi, Vietnam

e-mail: [ntkhiem@imech.ac.vn](mailto:ntkhiem@imech.ac.vn)

T.H. Tran • N.V. Quang

Institute of Mechanics, VAST, 264, Doi Can, Ba Dinh, Hanoi, Vietnam

e-mail: [tthai@imech.ac.vn](mailto:tthai@imech.ac.vn); [nvquang@imech.ac.vn](mailto:nvquang@imech.ac.vn)



approach to the moving load problem for multiple damaged beam based on the dynamic response obtained directly in the frequency domain for arbitrary load. The proposed approach enables to abolish the limitations of either the modal method or the finite element one. Moreover, once the spectral response has been obtained the time response is easily calculated by using the FFT procedure. The developed herein theory is illustrated by numerical results.

### 43.2 The Governing Equations of Dynamic System

Let's consider a dynamic system that comprises a simply supported Euler-Bernoulli beam and a vehicle moving on the beam, see Fig. 43.1. Suppose that  $E, \rho, A, I, \ell$  are parameters of the beam and  $m, c, k$  – of the vehicle. Moreover, it is assumed also that the beam is cracked at the positions  $e_1, \dots, e_n$  with depth  $a_1, \dots, a_n$  respectively.

By introducing the notations  $w(x, t), y(t), x_0(t)$  respectively for transverse deflection of the beam at section  $x$ , vertical displacement of the vehicle and distance of the vehicle from the left end ( $x = 0$ ) of beam, the governing equations for the system can be derived as follow

$$EI \frac{\partial^4 w(x, t)}{\partial x^4} + \rho A \eta \frac{\partial w(x, t)}{\partial t} + \rho A \frac{\partial^2 w(x, t)}{\partial t^2} = P(t) \delta[x - x_0(t)]; \quad (43.1)$$

$$P(t) = mg + c\dot{z}(t) + kz(t) = m[g - \ddot{y}(t)]; \quad m\ddot{z}(t) + c\dot{z}(t) + kz(t) = -m\ddot{w}_0(t); \quad z(t) = [y(t) - w_0(t)];$$

$$w_0(t) = w[x_0(t), t]. \quad (43.2)$$

Solution of equation (43.2) is subject to the boundary conditions

$$w(0, t) = w''(0, t) = w(\ell, t) = w''(\ell, t) = 0 \quad (43.3)$$

and the compatibility conditions at crack positions

$$w(e_k + 0, t) = w(e_k - 0, t); \quad w''(e_k + 0, t) = w''(e_k - 0, t); \quad w'''(e_k + 0, t) = w'''(e_k - 0, t);$$

$$[w'(e_k + 0, t) - w'(e_k - 0, t)] = \gamma_k w''(e_k, t); \quad \gamma_k = EI\theta(a_k). \quad (43.4)$$

Function  $\theta(a)$  in Eq. (43.4) is defined in the theory of cracked beam [20].

It has to notice here that the model described in Fig. 43.1 includes also the cases of constant moving force and mass investigated in many earlier studies. Namely, for the constant moving force  $P(t) = mg = P_0$  and in the case of moving mass  $P(t) = m[g - \ddot{w}_0(t)]$ . Moreover, it is apparent that  $\ddot{z}(t) + \ddot{w}_0(t) = \ddot{y}(t)$  is the absolute acceleration of the vehicle which can be easily measured on the vehicle. In present report the case of arbitrary given moving load  $P(t)$  is considered to develop a new method termed by spectral approach for the moving load problem. The case is of interest because not only it is essential for the iteration procedure in solving the problem but also it can be used for analysis and identification of beam with measured vibration of vehicle moving on the beam.

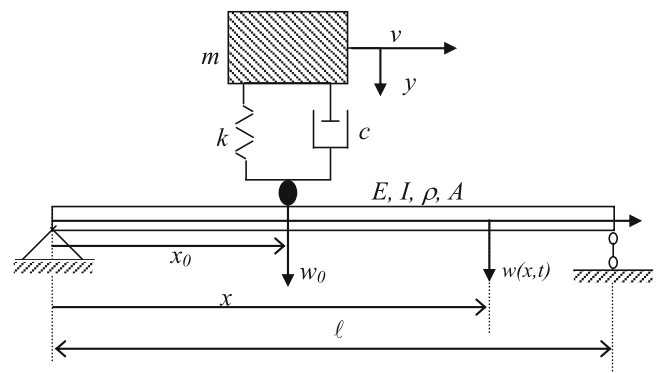


**Fig. 43.1** Dynamic model of beam under moving vehicle

### 43.3 Spectral Response of Cracked Beam to Arbitrary Moving Load

Consider in this section the case of arbitrarily given load  $P(t)$  moving on the beam with constant velocity  $v$ , i.e.  $x_0(t) = vt$ . In this case, the Furrier transform leads Eq. (43.1) to

$$\frac{d^4\phi(x, \omega)}{dx^4} - \lambda^4\phi(x, \omega) = Q(x, \omega); \quad \lambda^4 = (\omega^2 - i\eta\omega)/a^2; \quad a = \sqrt{EI/\rho A}; \quad (43.5)$$

$$\phi(x, \omega) = \int_{-\infty}^{\infty} w(x, t)e^{-i\omega t} dt; \quad Q(x, \omega) = P(x/v)e^{-i\omega x/v}/EIv. \quad (43.6)$$

It is well known that general solution of equation (43.5) is

$$\phi(x, \omega) = \phi_0(x, \omega) + \phi_1(x, \omega), \quad (43.7)$$

where

$$\phi_1(x, \omega) = \int_0^x h(x-s)Q(s, \omega)ds, \quad h(x) = (1/2\lambda^3)[\sinh \lambda x - \sin \lambda x] \quad (43.8)$$

and  $\phi_0(x, \omega)$  is general solution of homogeneous equation

$$\frac{d^4\phi(x, \omega)}{dx^4} - \lambda^4\phi(x, \omega) = 0 \quad (43.9)$$

satisfying the conditions  $\phi_0(0, \omega) = \phi_0''(0, \omega) = 0$ . It can be shown furthermore that solution  $\phi_0(x, \omega)$  of Eq. (43.9) satisfying the compatibility conditions at cracks

$$\begin{aligned} [\phi'(e_k + 0) - \phi'(e_k - 0)] &= \gamma_k \phi''(e_k); \\ \phi(e_k + 0) &= \phi(e_k - 0); \quad \phi''(e_k + 0) = \phi''(e_k - 0); \quad \phi'''(e_k + 0) = \phi'''(e_k - 0), \end{aligned} \quad (43.10)$$

can be expressed in the form

$$\phi_0(x, \lambda) = L_0(x, \lambda) + \sum_{k=1}^n \mu_k K(x - e_k). \quad (43.11)$$

In the latter equation  $L_0(x, \lambda)$  is a particular continuous solution of equation (43.9) satisfying the boundary condition  $L_0(0, \lambda) = L_0''(0, \lambda) = 0$  and

$$\begin{aligned} K(x) &= \begin{cases} 0 & \text{for } x \leq 0 \\ S(x) & \text{for } x > 0 \end{cases}; \quad K''(x) = \begin{cases} 0 & \text{for } x \leq 0 \\ S''(x) & \text{for } x > 0 \end{cases}; \\ S(x) &= (\sinh \lambda x + \sin \lambda x)/2\lambda, \quad S''(x) = \lambda(\sinh \lambda x - \sin \lambda x)/2; \end{aligned} \quad (43.12)$$

$$\mu_j = \gamma_j [L_0''(e_j, \lambda) + \sum_{k=1}^{j-1} \mu_k S''(e_j - e_k)]. \quad (43.13)$$

Representing the function  $L_0(x, \lambda)$  as  $L_0(x) = CL_1(x, \lambda) + DL_2(x, \lambda)$  and substituting it together with Eq. (43.11) into the Eqs. (43.10) one obtains finally

$$\phi(x, \omega) = CL_1(x, \lambda) + DL_2(x, \lambda) + \sum_{k=1}^n \mu_k K(x - e_k) + \phi_1(x, \omega). \quad (43.14)$$

Obviously, the solution (43.14) satisfies boundary conditions at the left end of beam and the unknown constants  $C$ ,  $D$  can be found from the boundary conditions  $\phi(\ell, \omega) = \phi''(\ell, \omega) = 0$  that give

$$CL_1(\ell, \lambda) + DL_2(\ell, \lambda) = -\sum_{k=1}^n \mu_k S(\ell - e_k) - \phi_1(\ell, \omega);$$

$$CL_1''(\ell, \lambda) + DL_2''(\ell, \lambda) = -\sum_{k=1}^n \mu_k S''(\ell - e_k) - \phi_1''(\ell, \omega).$$

Solution of the latter equations is easily obtained in the form

$$C = C_0 + \sum_{k=1}^n C_k \mu_k; \quad D = D_0 + \sum_{k=1}^n D_k \mu_k, \quad (43.15)$$

where

$$C_0 = \frac{[L_2(\ell, \lambda)\phi_1''(\ell, \omega) - L_2''(\ell, \lambda)\phi_1(\ell, \omega)]}{d_0(\lambda)}; \quad D_0 = \frac{[L_1''(\ell, \lambda)\phi_1(\ell, \omega) - L_1(\ell, \lambda)\phi_1''(\ell, \omega)]}{d_0(\lambda)}; \quad (43.16)$$

$$C_k = \frac{[L_2(\ell, \lambda)S''(\ell - e_k) - L_2''(\ell, \lambda)S(\ell - e_k)]}{d_0(\lambda)}; \quad D_k = \frac{[L_1''(\ell, \lambda)S(\ell - e_k) - L_1(\ell, \lambda)S''(\ell - e_k)]}{d_0(\lambda)};$$

$$d_0(\lambda) = L_1(\ell, \lambda)L_2''(\ell, \lambda) - L_1''(\ell, \lambda)L_2(\ell, \lambda). \quad (43.17)$$

Now substituting function  $L_0(x, \lambda)$  with coefficient (43.15) and (43.16) into (43.13) yields

$$[\mathbf{I} - \Gamma(\boldsymbol{\gamma})\mathbf{B}(\lambda, \mathbf{e})]\boldsymbol{\mu} = \Gamma(\boldsymbol{\gamma})\mathbf{b}(\lambda, \mathbf{e}), \quad (43.18)$$

where the following matrices and vectors are introduced

$$\mathbf{B}(\lambda, \mathbf{e}) = [b_{jk}; j, k = 1, \dots, n]; \quad b_{jk} = C_k L_1''(e_j, \lambda) + D_k L_2''(e_j, \lambda) + K''(e_j - e_k);$$

$$\Gamma(\boldsymbol{\gamma}) = \text{diag}\{\gamma_1, \dots, \gamma_n\}; \quad \boldsymbol{\mu} = (\mu_1, \dots, \mu_n)^T; \quad \mathbf{e} = (e_1, \dots, e_n)^T; \quad \boldsymbol{\gamma} = (\gamma_1, \dots, \gamma_n)^T;$$

$$\mathbf{b} = (b_1, \dots, b_n)^T, \quad b_j = C_0 L_1''(e_j, \lambda) + D_0 L_2''(e_j, \lambda), \quad j = 1, \dots, n. \quad (43.19)$$

Equation (43.18) gives

$$\boldsymbol{\mu} = [\mathbf{I} - \Gamma(\boldsymbol{\gamma})\mathbf{B}(\lambda, \mathbf{e})]^{-1} \Gamma(\boldsymbol{\gamma})\mathbf{b}(\lambda, \mathbf{e}) \quad (43.20)$$

that allows for calculating the damage parameters  $\boldsymbol{\mu} = (\mu_1, \dots, \mu_n)^T$  from given crack parameters. So, frequency response of cracked beam to moving load can be represented as

$$\phi(x, \omega) = \alpha_0(x, \omega) + \sum_{k=1}^n \mu_k \alpha_k(x, e, \gamma, \omega), \quad (43.21)$$

where

$$\alpha_0(x, \omega) = C_0 L_1(x, \lambda) + D_0 L_2(x, \lambda) + \phi_1(x, \omega);$$

$$\alpha_k(x, \omega) = C_k L_1(x, \lambda) + D_k L_2(x, \lambda) + K(x - e_k), \quad k = 1, \dots, n. \quad (43.22)$$

Since the static response is defined as solution of equation (43.5) at  $\omega = 0$ ,  $d^4\phi(x, 0)/dx^4 = Q(x, 0)$ , that is

$$\phi(x, 0) = Q_4(x) - Q_4''(\ell)x^3/6\ell + [Q_4''(\ell)\ell/6 - Q_4(\ell)/\ell]x; \quad (43.23)$$

$$Q_4(x) = \int_0^x ds_1 \int_0^{s_1} ds_2 \int_0^{s_2} ds_3 \int_0^{s_3} Q(s, 0) ds. \quad (43.24)$$

For the moving load  $P(t)$  given at the time mesh  $(t_1, \dots, t_M)$  the function  $Q(x, \omega)$  is defined as

$$Q(x_j, \omega) = P(t_j)e^{-i\omega t_j}/EIv; \quad x_j = vt_j; \quad j = 1, \dots, M \quad (43.25)$$

that leads the integral in Eq. (43.8) to be estimated

$$\phi_1(x, \omega) = \int_0^x h(x-s)Q(s, \omega)ds = (1/EI) \sum_{r=1}^M H(x-vt_r)P(t_r)e^{-i\omega t_r} \Delta t_r \quad (43.26)$$

and

$$\phi_1''(x, \omega) = \int_0^x h''(x-s)Q(s, \omega)ds = (1/EI) \sum_{r=1}^M H''(x-vt_r)P(t_r)e^{-i\omega t_r} \Delta t_r, \quad (43.27)$$

where

$$H(x) = \begin{cases} 0; & x \leq 0 \\ h(x); & x \geq 0 \end{cases}; \quad H''(x) = \begin{cases} 0; & x \leq 0 \\ h''(x); & x \geq 0 \end{cases}; \quad \Delta t_r = t_r - t_{r-1}. \quad (43.28)$$

Equations (43.26), (43.27) and (43.28) enable to calculate the coefficients  $C_0, D_0$  defined in expressions (43.16) that lead the frequency response (43.21) to be completely determined for the discrete moving load. Thus, frequency response of multiple cracked beams under moving load with constant speed has been obtained in general formulation. Once the frequency response  $\phi(x, \omega)$  is available the time history response can be evaluated at the discrete time mesh  $t_r = rT/N, r = 0, \dots, N$  in a finite interval of time  $[0, T]$  as

$$w(x, t_r) = (2/T) \sum_{k=0}^{N-1} \phi(x, \omega_k) e^{2i\pi k r/N}; \quad r = 0, \dots, N, \quad (43.29)$$

where  $\omega_k = 2\pi k/T$  and  $F_N = N/T$  is the Nyquist's frequency measured in Hz of the response  $\phi(x, \omega)$ . Accordingly to the Discrete Fourier Transform, among the three parameters  $F_N, T, N$  only two can be initially chosen. For example, if duration of a signal  $T$  is given then  $N$  should be selected to cover a desired frequency band of the signal. In present study the time interval  $T$  is chosen equal  $T = q\ell/v$  with  $q = 1$  or  $2$ . Thus, the Eq. (43.29) is the basic for investigating the time response of beam to moving load by using the so called spectral method. Namely, the Fast Fourier representation can be used to evaluate the deflection and acceleration at the point where the moving load is applied,  $x = x_0(t) = vt$  as

$$w_0(t_j) = w(vt_j, t_j) = (2/T) \sum_{k=0}^{N-1} \phi(vt_j, \omega_k) e^{2i\pi k j/N}, \quad j = 0, \dots, N. \quad (43.30)$$

$$\ddot{w}_0(t_j) = (2/T) \sum_{k=0}^{N-1} \left[ v^2 \frac{\partial^2}{\partial x^2} + 2i\omega_k v \frac{\partial}{\partial x} - \omega_k^2 \right] \phi(vt_j, \omega_k) e^{2i\pi k j/N}, \quad j = 0, \dots, N. \quad (43.31)$$

These deflection and acceleration are called herein convective one. Moreover, knowing the convective acceleration (43.31), the dynamic response of vehicle is computed from Eq. (43.2) as

$$z(t) = z_0(t) - (T/N) \sum_{j=0}^N g(t-t_j) \ddot{w}_0(t_j), \quad (43.32)$$

where

$$z_0(t) = e^{-\zeta t} \left[ z_{00} \cos \omega_0 t + \frac{\dot{z}_{00} + \zeta z_{00}}{\omega_0} \sin \omega_0 t \right]; \quad g(t) = (1/\omega_0) e^{-\zeta t} \sin \omega_0 t; \quad (43.33)$$

$$\omega_0 = \sqrt{4mk - c^2}/2m; \zeta = c/2m; z_{00} = z_0(0); \dot{z}_{00} = \dot{z}_0(0). \quad (43.34)$$

### 43.4 Results and Discussion

First, analytical solution is conducted for the case of harmonic moving load  $P(t) = P_0 e^{i\omega_e t}$  in which  $Q(x, \omega) = (P_0/EIv)e^{-i\hat{\omega}x/v} = Q_0 e^{-i\hat{\omega}x/v}$ ,  $\hat{\omega} = \omega - \omega_e$ . Therefore,

$$\phi_1(x, \omega) = \int_0^x h(x-s)Q(s, \omega)ds = Q_0 e^{-i\hat{\omega}x/v} \int_0^x h(s)e^{i\hat{\omega}s/v} ds = \phi_{10}(\lambda x) - \frac{Q_0 e^{-i\hat{\omega}x/v}}{\lambda^4 - (\hat{\omega}/v)^4}, \quad (43.35)$$

where

$$\phi_{10}(\lambda x) = P_1(\omega) \cosh \lambda x - P_2(\omega) \sinh \lambda x + P_3(\omega) \cos \lambda x - P_4(\omega) \sin \lambda x, \quad (43.36)$$

$$P_1 = \frac{Q_0}{2\lambda^2[\lambda^2 + (\hat{\omega}/v)^2]}; P_3 = \frac{Q_0}{2\lambda^2[\lambda^2 - (\hat{\omega}/v)^2]}; P_2 = \frac{i\hat{\omega}/v Q_0}{2\lambda^3[\lambda^2 + (\hat{\omega}/v)^2]}; P_4 = \frac{i\hat{\omega}/v Q_0}{2\lambda^3[\lambda^2 - (\hat{\omega}/v)^2]}. \quad (43.37)$$

Moreover, in this case one obtains

$$\phi_1''(x, \omega) = \int_0^x h''(x-s)Q(s, \omega)ds = \phi_{10}''(\lambda x) + \frac{(\hat{\omega}/v)^2 Q_0 e^{-i\hat{\omega}x/v}}{\lambda^4 - (\hat{\omega}/v)^4}. \quad (43.38)$$

By choosing the functions  $L_1(x, \lambda) = \sinh \lambda x$ ;  $L_2(x, \lambda) = \sin \lambda x$ , coefficients in (43.15) and (43.16) become

$$C_0 = P_2 - P_1 \coth \lambda \ell + \frac{Q_0 e^{-i\hat{\omega}\ell/v}}{(\lambda^2 + \hat{\omega}^2/v^2) \sinh \lambda \ell}; D_0 = P_4 - P_3 \cot \lambda \ell + \frac{Q_0 e^{-i\hat{\omega}\ell/v}}{(\lambda^2 - \hat{\omega}^2/v^2) \sin \lambda \ell};$$

$$C_k = -\frac{\sinh \lambda(\ell - e_k)}{2\lambda \sinh \lambda \ell}; D_k = -\frac{\sin \lambda(\ell - e_k)}{2\lambda \sin \lambda \ell}, k = 1, \dots, n. \quad (43.39)$$

Finally, an analytical expression of solution (43.21) can be obtained specifically with the following coefficients

$$\alpha_0(x, \omega) = P_1 \cosh \lambda x - \bar{P}_2 \sinh \lambda x + P_3 \cos \lambda x - \bar{P}_4 \sin \lambda x - \frac{Q_0 e^{-i\hat{\omega}x/v}}{\lambda^4 - (\hat{\omega}/v)^4};$$

$$\alpha_k(x, \omega) = C_k \sinh \lambda x + D_k \sin \lambda x + K(x - e_k), k = 1, \dots, n,$$

where  $P_1, P_3, C_k, D_k$  have the expressions (43.37) and (43.39) respectively, and

$$\bar{P}_2 = \frac{Q_0(\cosh \lambda \ell - e^{-i\hat{\omega}\ell/v})}{2\lambda^2(\lambda^2 + \hat{\omega}^2/v^2) \sinh \lambda \ell}; \bar{P}_4 = \frac{Q_0(\cos \lambda \ell - e^{-i\hat{\omega}\ell/v})}{2\lambda^2(\lambda^2 - \hat{\omega}^2/v^2) \sin \lambda \ell}. \quad (43.40)$$

Solution for the case of constant moving load is easily obtained from the solution by setting  $\omega_e = 0$ , i.e.  $\hat{\omega} = \omega$ . Moreover, in the case of no damping, i.e.,  $\eta = 0$  and  $\lambda^4 = (\omega/a)^2$  Eqs. (43.38), (43.39) and (43.40) show that the frequency response is undetermined for the frequency approaching to the natural frequencies of the beam  $\omega_j = a(j\pi/\ell)^2$ ,  $j = 1, 2, 3, \dots$ , and  $\omega = \omega_c$ , where

$$\omega_c = (\omega_e \pm v^2/2a) \pm \sqrt{(v^2/2a)^2 \pm \omega_e v^2/a}. \quad (43.41)$$

The former case implies the phenomena that can be called the natural resonance and the latter case reminds the resonance caused by the moving and harmonic load. Obviously, the trivial value of the speed,  $v=0$ , gives rise the external frequency of the harmonic moving load  $\omega_e$  so that the resonant frequency defined in (43.41) can be referred to as external one. For the constant moving load with  $\omega_e = 0$  the Eq. (43.41) results in two external resonant frequencies  $\omega_{c1} = 0$ ,  $\omega_{c2} = v^2/a$ . As well known the critical speed of the moving load is defined by assuming  $\omega_{c2} = \omega_1$  that yields  $v_c = a\pi/\ell$ .

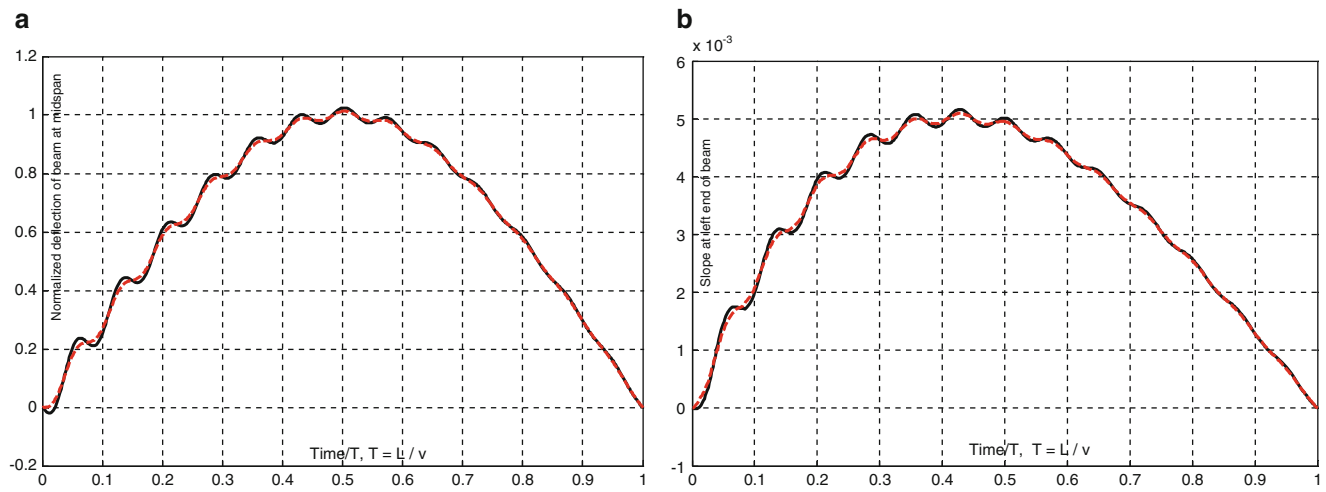


**Fig. 43.2** Comparison of deflection at the midspan (a); slope at the right end (b);  $P_0 = 100\text{ kN}$ ;  $v = 12\text{ m/s}$ . *Solid line* – the present method and the *dash line* – the modal method [1]

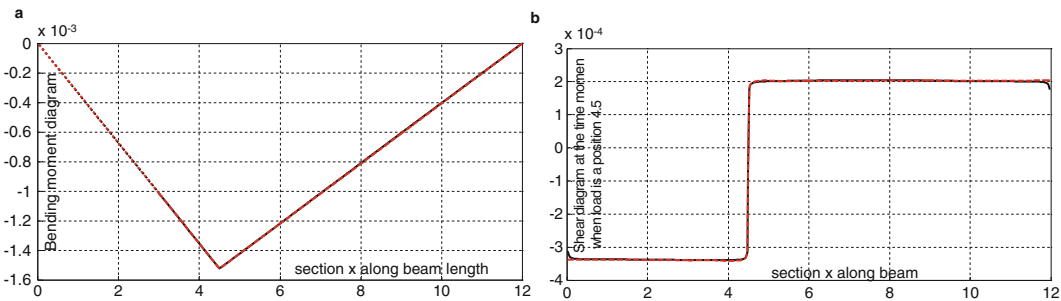


**Fig. 43.3** Comparison bending moment (a) and shear force (b) diagram at the time moment when load is at the position 4.5 m;  $P_0 = 100\text{ kN}$ ;  $v = 12\text{ m/s}$ . *Solid line* – the present method and *dash line* – the modal method [1]

For comparison, numerical computation is performed for the undamaged beam under the constant force studied in [20] by using both the method developed above and the modal method given in Ref. [2]. Numerical results are plotted in Figs. 43.2, 43.3, 43.4, 43.5, 43.6, 43.7 and 43.8. Figure 43.2 shows the deflection at mid-span and slope at the left end of beam versus the time during the load travelling on the beam. Diagrams of bending moment and shear force of the beam at the time moment when the load is at the section 4.5 m are shown in the Fig. 43.3. The convective deflection and acceleration of the beam are presented in the Figs. 43.4 and 43.5. It is observed from the graphics that results obtained by the spectral method and the conventional modal method are almost identical, exceptionally for the bending moment and shear force. It has to notice here that the spectral method developed in this study has ignored the Gibbs phenomenon gathered in computation of the shear of beam under moving load by using the conventional methods. This can be explained by the fact that the response representation (43.30) has included the quasi-static response (43.23) at the zero frequency  $\phi(x, 0)$  which was used by Pesterev et al. [14] and Azizi et al. [19] to avoid the phenomena. A light disagreement between convective accelerations observed in Fig. 43.5 may be caused by that the acceleration (43.32) may include components of extra-resonant frequency compared to the mode superposition method. The Fig. 43.6 represents influence of moving load speed on the midspan normalized deflection of uncracked beam and Figs. 43.7 and 43.8 show the effect of crack depth in combination with speed on the convective deflection of beam. It is obviously that crack adds the high frequency components to the deflection of uncracked beam and increase of crack depth leads to larger deflection of beam.

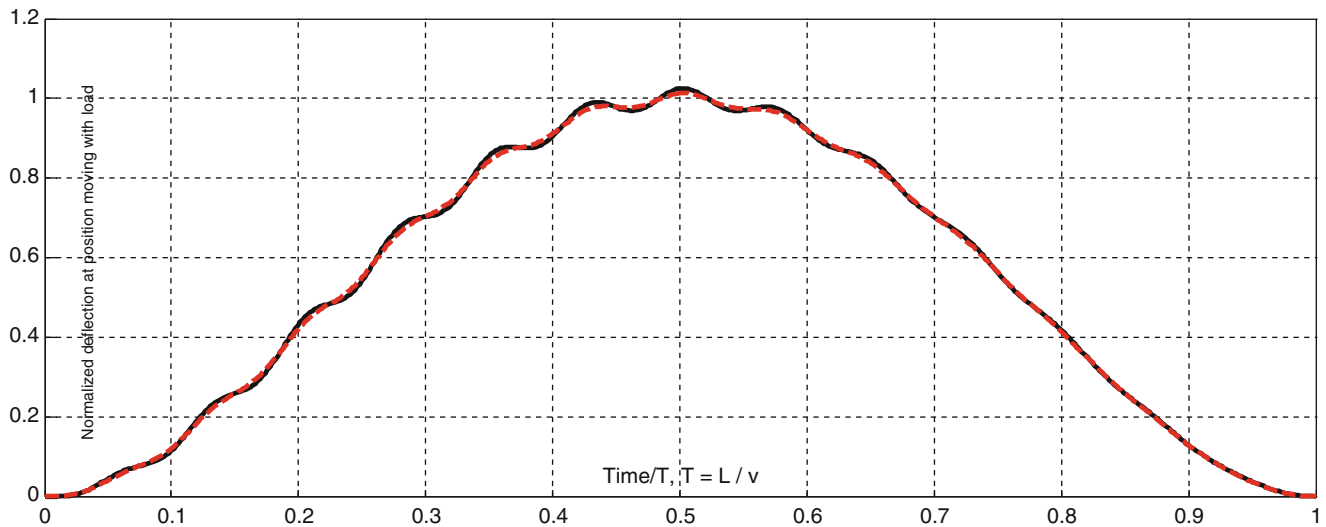


**Fig. 43.4** Comparison of convective deflection of uncracked beam;  $P = 100 \text{ kN}$ ,  $v = 12 \text{ m/s}$ ; *Solid line* – the present method and *dash line* – the modal method [1]

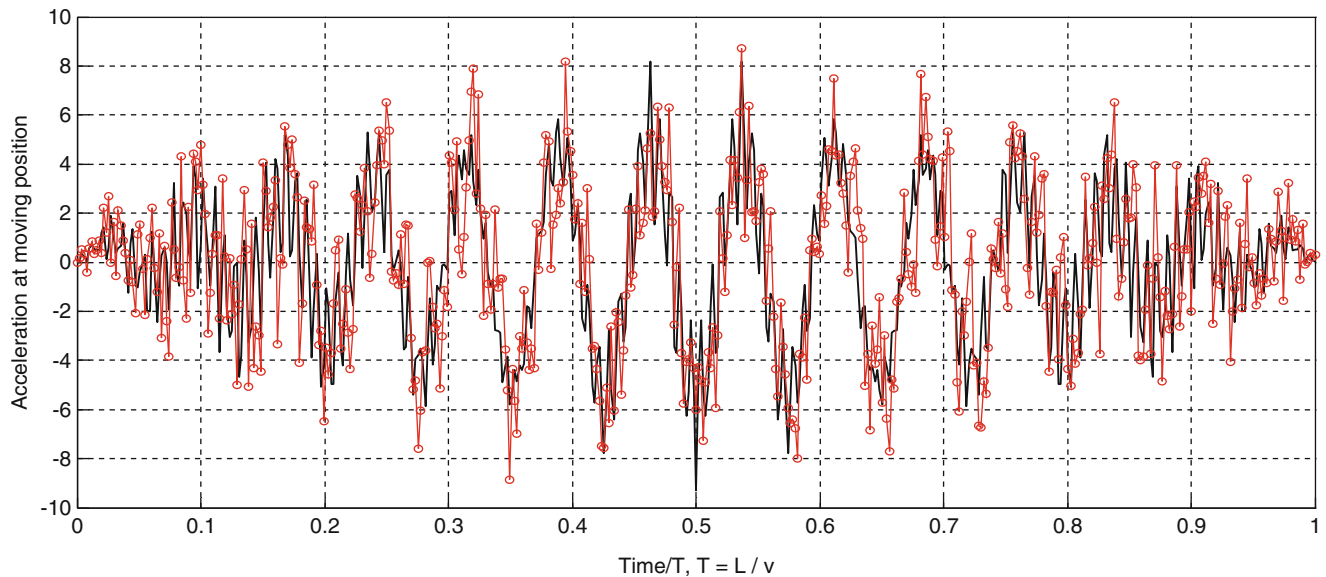


**Fig. 43.5** Comparison of convective acceleration of uncracked beam;  $P = 100 \text{ kN}$ ;  $v = 12 \text{ m/s}$ ; *solid line* – the present method and *dot line with makers* – the modal method [1]

### 43.5 Conclusion

In this report the moving load problem for Euler-Bernoulli beam with multiple cracks has been led to a standard boundary problem for ordinary differential equation of order four that is straightforward to be solved in a closed form. As result the dynamic response of the beam to arbitrary moving load was obtained in an arbitrary frequency domain that makes easily

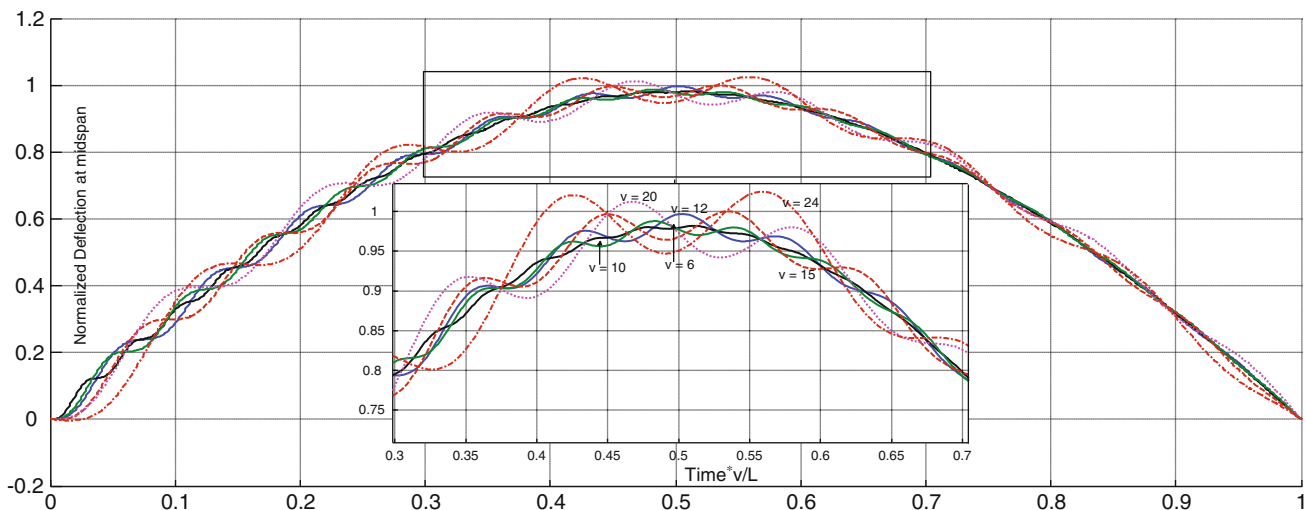


**Fig. 43.6** Normalized deflection at mid-span of uncracked beam for different speeds of moving force ( $v = 6; 10; 12; 15; 20; 24$  m/s)

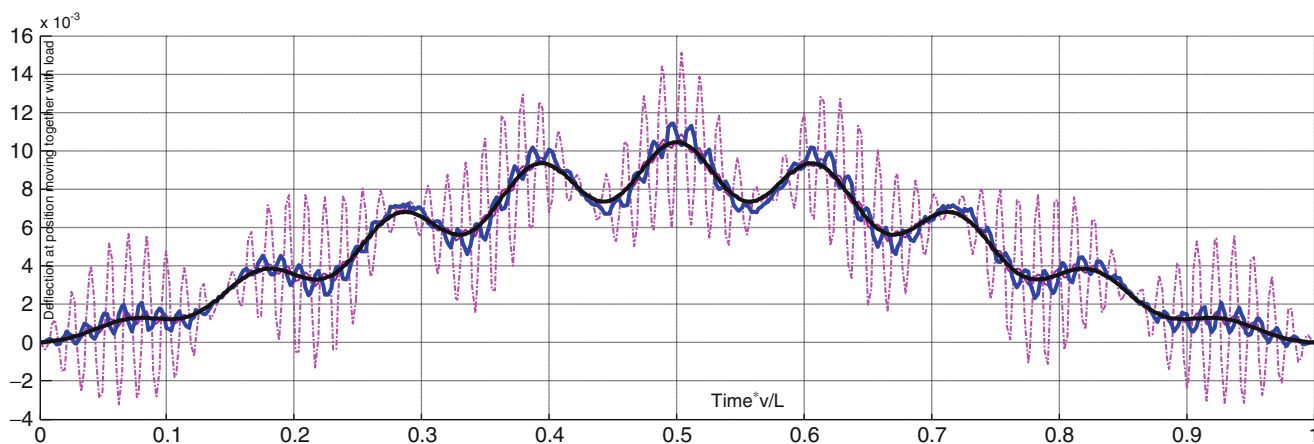


**Fig. 43.7** Convective deflection of cracked beam subjected to a constant load moving with speed 15 m/s. Crack at position 10 m with various depth 0; 5; 10; 20; 30 %

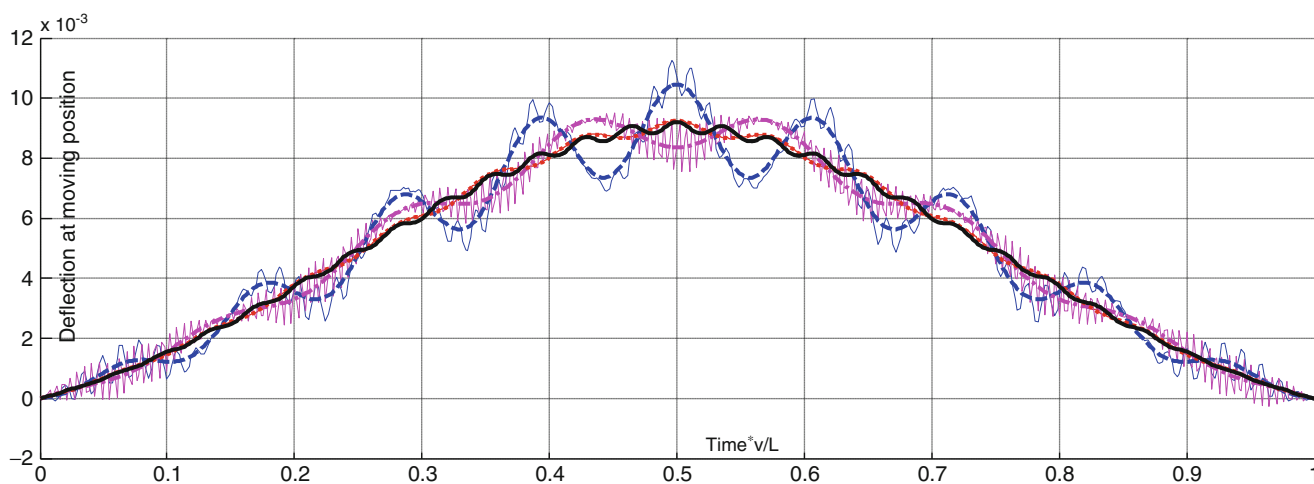


**Fig. 43.8** Convective deflection in different speed (5; 10; 15; 20 m/s) of constant load for beam with two cracks at positions 5 and 10 m of equal depth 20 % compared to that of uncracked beam



to conduct the time history response by using the FFT procedure. The proposed herein approach that can be called spectral method allows for avoiding the moving singularity phenomenon and time consumable tracking current position of the load. Moreover, this method is capable to expose the effect of high frequency components overall beam length that is typically caused by cracks appeared in the beam. The spectral method can be further developed to use for crack detection of beam based on the dynamic signal measured at vehicle moving on the beam.

**Acknowledgements** This work has been completed under support from the NAFOSTED of Vietnam to whom the authors are much thankful.

## References

1. Fryba L (1972) *Vibration of solids and structures under moving loads*. Noordhoff International Publishing, Prague
2. Olsson M (1991) On the fundamental moving load problem. *J Sound Vib* 145(2):299–307
3. Rao GV (2000) Linear dynamics of an elastic beam under moving loads. *J Vib Acoust* 122:281–289
4. Pesterev AV et al (2001) Response of elastic continuum carrying multiple moving oscillators. *J Eng Mech* 127(3):260–265
5. Garinei A (2006) Vibration of simple beam-like modeled bridge under harmonic moving loads. *Int J Eng Sci* 44:778–787
6. Zehsaz M, Sadeghi MH, Ziaei Asl A (2009) Dynamics response of railway under a moving load. *J Appl Sci* 9(8):1474–1481
7. Mahmoud MA, Abou Zaid MA (2002) Dynamic response of a beam with a crack subject to a moving mass. *J Sound Vib* 256(4):591–603
8. Bilello C, Bergman LA (2004) Vibration of damaged beams under a moving mass: theory and experimental validation. *J Sound Vib* 274:567–582
9. Lin H-P, Chang S-C (2006) Forced response of cracked cantilever beams subjected to a concentrated load. *Int J Mech Sci* 48:1456–1463
10. Yang J et al (2008) Free and forced vibration of cracked inhomogeneous beams under an axial force and moving load. *J Sound Vib* 312:166–181
11. Shafiei M, Khaji M (2011) Analytical solution for free and forced vibrations of multiple cracked Timoshenko beam subject to a concentrated moving load. *Acta Mech* 22:79–97 doi:10.1007/s00707-011-0495-x
12. Li J, Law SS (2012) Damage identification of a target substructure with moving load excitation. *Mech Syst Signal Process* 30:78–90
13. Zhang Y, Wang L, Xiang Z (2012) Damage detection by mode shape squares extracted from a passing vehicle. *J Sound Vib* 331:291–307
14. Pesterev AV, Tan CA, Bergman LA (2001) A new method for calculating bending moment and shear force in moving load problems. *Trans ASME: J Appl Mech* 68:252–259
15. Wu JJ, Whittaker AR, Cartmell MP (2000) The use of finite element techniques for calculating the dynamic response of structures to moving loads. *Comput Struct* 78:789–799
16. Martinez-Castro AE, Museros P, Castillo-Linares A (2006) Semi-analytic solution in the time domain for non-uniform multi-span Bernoulli-Euler beams traversed by moving load. *J Sound Vib* 294:278–297
17. Anderson L, Nielsen SRK, Krenk S (2007) Numerical methods for analysis of structure and ground vibration from moving load. *Comput Struct* 85:43–58
18. Henchi K et al (1997) Dynamic behavior of multi-span beams under moving load. *J Sound Vib* 199(1):33–50
19. Azizi N, Saadatpour MM, Mahzoon M (2011) Using spectral element method for analyzing continuous beams and bridges subjected to a moving load. *Appl Math Model* 36:3580–3592. doi:10.1016/j.apm.2011.10.019
20. Chondros TG, Dimaroganas AD (1998) A continuous cracked beam theory. *J Sound Vib* 215:17–34

# Chapter 44

## Detection of Structural Damage Through Nonlinear Identification by Using Modal Testing

Murat Aykan and H. Nevzat Özgüven

**Abstract** Structural damages usually introduce nonlinearity to the system. A previously developed nonlinear identification method is employed to detect crack type structural damage. The method requires the measurement of FRFs at various points in order to locate the damage. The method makes it also possible to determine the extent of damage by identifying the level of nonlinearity. The verification of the method is demonstrated with experimental case studies using beams with different levels of cracks. The approach proposed in this study is very promising to be used in practical systems, but still open to further improvements.

**Keywords** Damage detection • Nonlinear structural dynamics • Nonlinear structures • Nonlinear identification • Nonlinear testing

### 44.1 Introduction

Structural damage is defined as a permanent change in the mechanical state of a structural material that may affect their performance [1]. Common sources of damage in materials and structural components include micro-structural defects (dislocations, voids, inclusions), corrosion (loss of material), residual stress, cracking (fatigue, matrix, ply), fastening fault (weld crack, bolt preload, broken rivet), adhesive fault (de-bonding, delamination, separation), and instability (thermo-mechanical buckling) [1].

Successful damage detection and localization in structures is essential for health monitoring and maintenance. Non-destructive testing methods which can identify damage can be used for this purpose. However, most of the non-destructive methods, such as ultrasonic methods require the suspected location of the damage and that location must be accessible. The methods which use vibration responses usually do not suffer from these limitations.

The basis of vibration response methods is that damage changes the dynamic behavior of the structure. Salawu [2] presented a review on damage detection methods which use the shift in natural frequencies. The measurement of natural frequency changes is very simple but less informative compared to the mode shapes and can lead to wrong crack locations. Thus, methods which use mode shapes and their derivatives for damage detection were developed [3–6]. Recently, Yan et al. [7] presented a review for the advances in vibration based damage detection methods. The recent vibration based methods use the basic dynamic information of structures such as Frequency Response Functions (FRF) [8] and modal parameters [9–13]. Some of the vibration methods use wavelet analysis [14–16] and some use neural network analysis [17, 18]. These methods are based on linear models.

Damage can also add nonlinearity in structural systems which have otherwise linear responses [19]. The most common type of damage which introduces nonlinearity is breathing cracks which behave as bilinear stiffness elements. Many

---

M. Aykan (✉)

Department of Mechanical Engineering, Middle East Technical University, Ankara 06800, Turkey

Defense Systems Technologies Division, ASELSAN Inc., Ankara 06172, Turkey

e-mail: [maykan@aselsan.com.tr](mailto:maykan@aselsan.com.tr)

H.N. Özgüven

Department of Mechanical Engineering, Middle East Technical University, Ankara 06800, Turkey

e-mail: [ozguven@metu.edu.tr](mailto:ozguven@metu.edu.tr)

researchers have investigated different aspects of nonlinear damage identification using different approaches. These approaches include, for example, using nonlinear output FRFs [20], NARMAX modeling [21], using nonlinear characteristics of forced response of structures [22], and bifurcation boundary analysis [23].

Damage detection method presented in this study consists of two main stages. Firstly, existence of damage in the system is detected by performing step sine tests with different loads. Secondly, the location of the damage is determined by using incomplete FRF data. The work presented in this study is mainly an experimental application of the method suggested by Aydoğan [24] which was verified only by simulated data. The approach is based on the nonlinearity identification method developed by Özer et al. [25, 26].

## 44.2 Theory

Representation of nonlinear forces in matrix multiplication form using describing functions has been first given by Tanrıku et al. [27] and employed in identification of structural nonlinearities by Özer et al. [25, 26]. As the basic theory of the identification method is given in detail in reference [25, 26], here only the nonlinearity localization equations are given.

The nonlinear internal forces in the system can be expressed by using describing functions. This approach makes it possible to represent the nonlinear stiffness and damping properties of the system as a response dependent matrix which can easily be included into the dynamic stiffness matrix of the linear system in the frequency domain. From the mathematical expressions of the FRF matrix of the nonlinear system ( $[H^{NL}]$ ) and FRF matrix of the linear part of the system ( $[H]$ ) (see reference [26] for details) the response dependent “nonlinearity matrix”  $[\Delta(x, \dot{x})]$  can be obtained as

$$[\Delta] = [H^{NL}]^{-1} - [H]^{-1} \quad (44.1)$$

where the elements of the nonlinearity matrix are expressed in terms of describing functions  $v$  [27].

Post multiplying both sides of Eq. (44.1) by  $[H^{NL}]$  gives

$$[\Delta] [H^{NL}] = [I] - [Z] [H^{NL}] \quad (44.2)$$

where  $[Z]$  is the dynamic stiffness matrix of the linear part.

In order to localize nonlinearity in a system, a parameter called “nonlinearity index” is used. The nonlinearity index ( $NLI$ ) for an  $p$ th coordinate is defined by taking any  $i$ th column of  $[H^{NL}]$  and the  $p$ th row of  $[\Delta]$  from Eq. (44.2) as follows:

$$NLI_p = \Delta_{p1} \cdot H_{1i}^{NL} + \Delta_{p2} \cdot H_{2i}^{NL} + \dots + \Delta_{pn} \cdot H_{ni}^{NL} \quad (44.3)$$

Here, theoretically,  $i$  can be any coordinate; however, in practical applications it should be chosen as an appropriate coordinate at which measurement can be made and also is close to suspected nonlinear element. Equation (44.3) shows that any nonlinear element connected to the  $p$ th coordinate will yield a nonzero  $NLI_p$ . On the other hand,  $NLI_p$  can be experimentally obtained by using the right hand side of Eq. (44.2), which requires the measurement of the receptances of the system at high and low forcing levels, presuming that low level forcing will yield FRFs of the linear part:

$$NLI_p = \delta_{ip} - Z_{p1} \cdot H_{1i}^{NL} - Z_{p2} \cdot H_{2i}^{NL} - \dots - Z_{pn} \cdot H_{ni}^{NL} \quad (44.4)$$

It should be noted that when there is only friction type of nonlinearity, then low level of forcing will yield  $H^{NL}$  and high level of forcing will approximately give  $H$ .

The main drawback of the method presented in [26] is that in order to calculate  $NLI_p$  from experimental  $H$  values, the whole linear FRF matrix is required (alternatively, theoretically calculated dynamic stiffness matrix can be used). Then it may not be feasible to apply the method with experimentally measured  $H$  values. In a recent study [28] it was proposed to use theoretically predicted values for unmeasured receptances calculated from the measured ones, and it is shown with case studies that this approach yields acceptable results.

In this present study, the damage locations are determined from NLI values calculated from vibration tests. Theoretically, if a nonlinear element is between a coordinate and ground, we would expect to have high NLI value for that coordinate only, and if a nonlinear element is between two coordinates, we would expect to have high NLI values at these two coordinates. In the simulated cantilever beam case studies given in [24], it is concluded that, in order to observe such characteristics we need to measure the rotational coordinates which are affected the most from crack type nonlinearities. If translational coordinates

are measured, then this method gives us an indication of the crack location by yielding a high peak only at the coordinate right after the crack closer to the fixed boundary. When this is the case, further investigations should be carried out by NDT methods around the coordinate with high NLI to pinpoint the crack.

### 44.3 Experimental Studies

#### 44.3.1 Experimental Study 1

For the implementation and validation of the method given above, step sine tests with different load levels are performed with four hollow square beams which are all manufactured from aluminum. The beams have 2.5, 5.5 and 7.5 mm cracks, respectively. In order to see the effect of measurement noise on NLI values calculated from experimental measurements, a fourth beam with no crack is also tested. The cracks are produced by creating an indentation of 1 mm first with a saw and then bending the beam several times until the desired crack is obtained. The test rig manufactured for this study, dimensions and technical details are given in Figs. 44.1 and 44.2, respectively. This test rig is preferred for its simplicity. The test rig consists of a cantilever beam with a crack between 4th and 5th coordinates. The modal test setup configuration with its elements is shown in Fig. 44.3. For step sine testing, a shaker (PCB) is connected to the free end (point 1) of the cantilever beam via

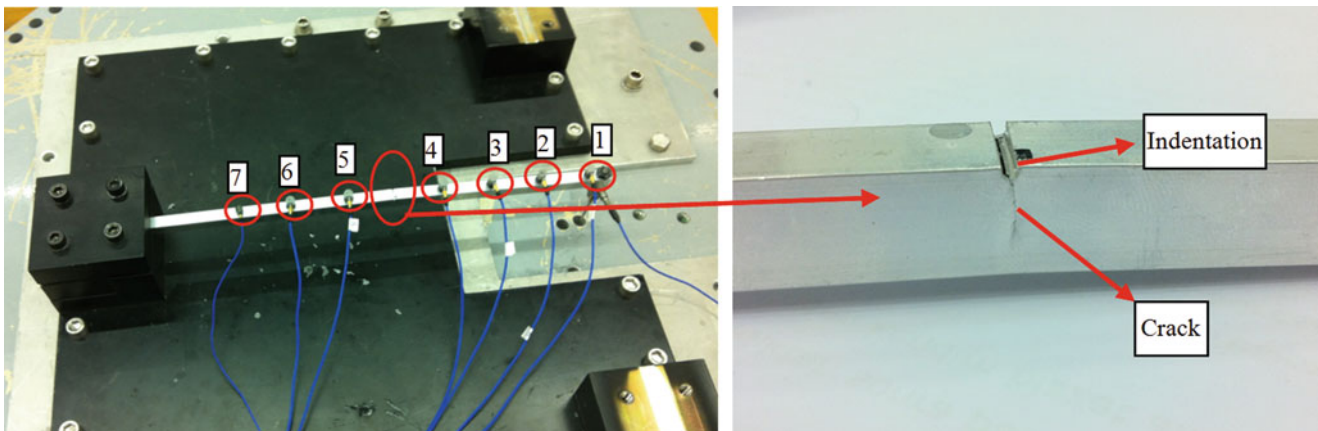


Fig. 44.1 Setup used in the experimental study-1

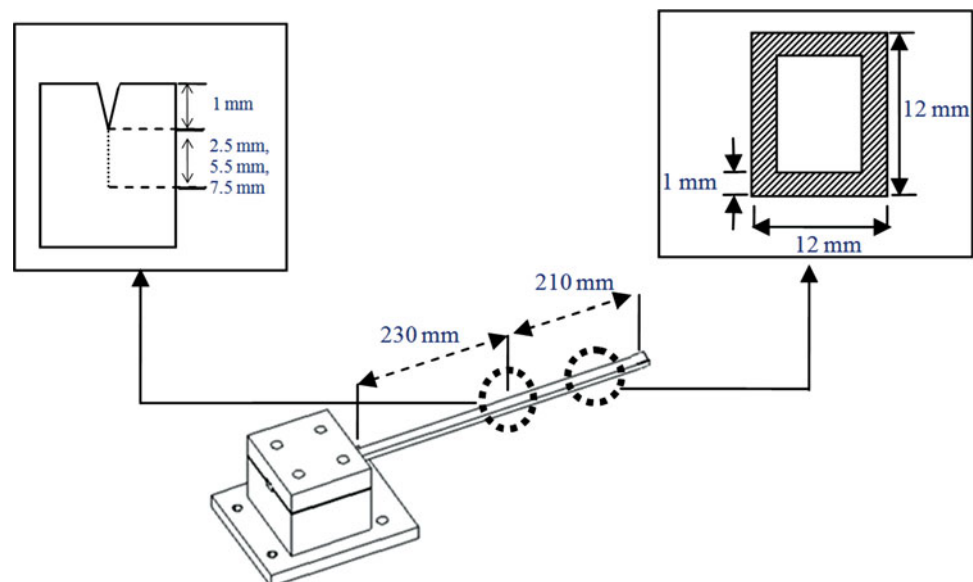
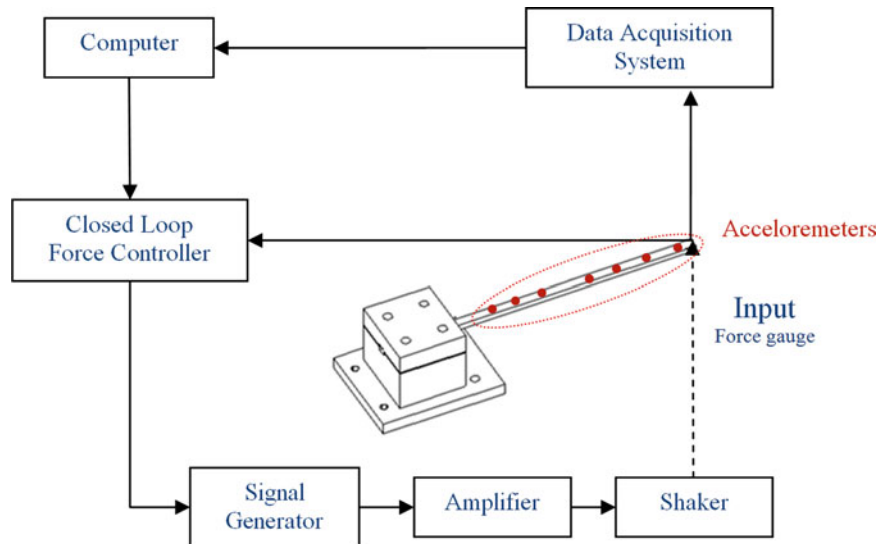
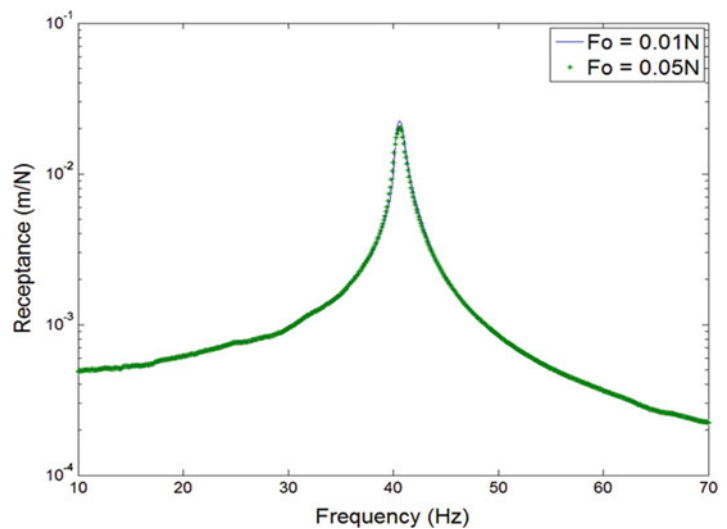


Fig. 44.2 Dimensions of experimental study-1

**Fig. 44.3** Test setup of experimental study-1



**Fig. 44.4** Linear and nonlinear direct point FRFs at 1 (undamaged)



a push-rod with a PCB 208C01 force transducer. The vibration responses are measured using six miniature PCB 352C65 and one PCB 352A24 accelerometers. The frequency resolution is 0.1 Hz. The crack in the system causes changes in the frequency response around resonance frequencies. Ability to observe this phenomenon is closely related to the frequency resolution employed in the harmonic vibration tests. The force closed loop control is achieved by the SCADAS-III data acquisition system.

The modal tests are performed using harmonic forcing with amplitudes of 0.01 and 0.05 N at point 1 and measuring responses from 7 points. The FRFs obtained for the constant amplitude force tests with an undamaged beam and with three different crack lengths ( $h = 2.5, 5.5$  and  $7.5$  mm) are shown in Figs. 44.4, 44.5, 44.6, and 44.7. The FRFs obtained with 0.01 N amplitude harmonic forcing are taken as linear FRFs of the system.

In this experimental study, we measured only the first columns of the linear (0.01 N forcing) and nonlinear receptance (0.05 N forcing) matrices. Then, firstly the missing elements of the linear FRF matrix are calculated by using the approach mentioned in Sect. 44.2, and the NLI values are calculated for each coordinate by using Eq. (44.4). Note that here only translational DOFs are used. The calculated NLI values are shown in Figs. 44.8, 44.9, 44.10, and 44.11. The coordinates which are affected from nonlinearity can be determined from the NLI values obtained for each coordinate. The crack is located between the 4th and 5th coordinates so one expects to find two high peaks at these coordinates. In the simulated case studies given in [24], it is stated that, in order to observe such a chart we have to measure FRFs at the rotational coordinates which are affected the most from the nonlinearity. If translational coordinates are measured, then this method gives us an indication about the crack location by giving a high peak only at the coordinate right after the crack closer to the fixed boundary. The results obtained verify this expectation: We have high peaks at 5th coordinate. However, the NLI values we

**Fig. 44.5** Linear and nonlinear direct point FRFs at 1 ( $h = 2.5$  mm)

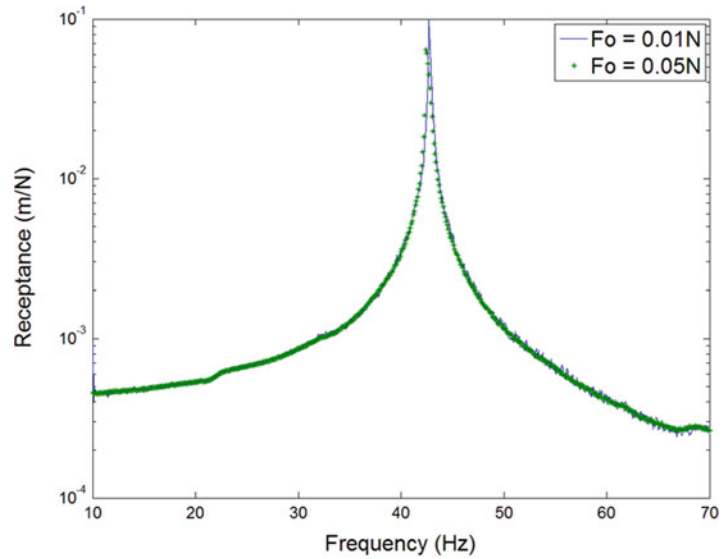
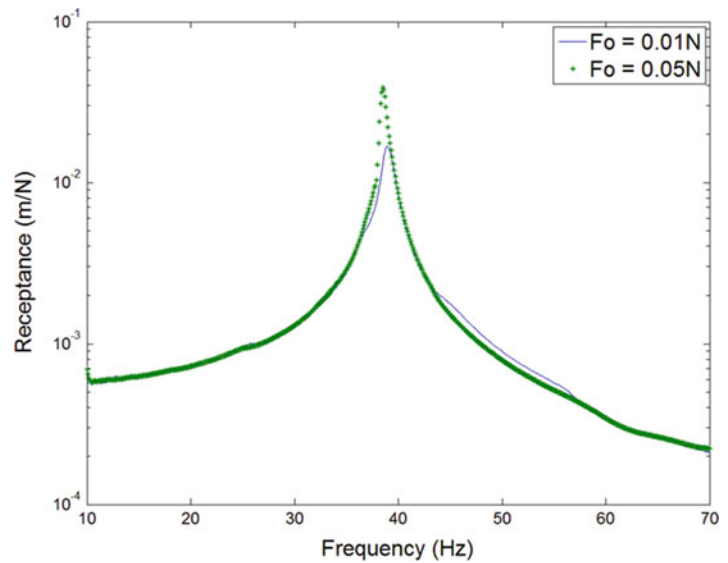


**Fig. 44.6** Linear and nonlinear direct point FRFs at 1 ( $h = 5.5$  mm)



obtain are not much smaller than that of coordinate 5, unless the crack gets deeper (when we have deeper cracks the NLI value of 5th coordinate increases considerably, compared to other NLI values).

### 44.3.2 Experimental Study 2

In the first experimental study step sine testing with a shaker is preferred for the validation of the method. With this case study it is intended to demonstrate that this method can also be used with impact testing. However, it must be noted that the change in the FRFs with different impact levels will not be as much as that observed in closed loop shaker testing since it is more difficult to apply considerably higher force levels in impact testing. In this experimental study, the test specimen is changed to E-Glass reinforced plastic (E-GFRP). The damage is located between the same coordinates but this time the extent of damage is not known since the damage is created by simply bending the sheet. The test rig manufactured for this study, dimensions and technical details are given in Figs. 44.12 and 44.13, respectively. For impact testing, an impact hammer (PCB 086C01) is used and the structure is hit at the 7th coordinate. The vibration responses are measured using six miniature PCB 352C65 and one PCB 352A24 accelerometers. The frequency resolution is 0.3125 Hz. The crack in the system causes changes in the frequency response around resonance frequencies. Ability to observe this phenomenon is closely related to the frequency resolution employed in the harmonic vibration tests.

**Fig. 44.7** Linear and nonlinear direct point FRFs at 1 (h = 7.5 mm)

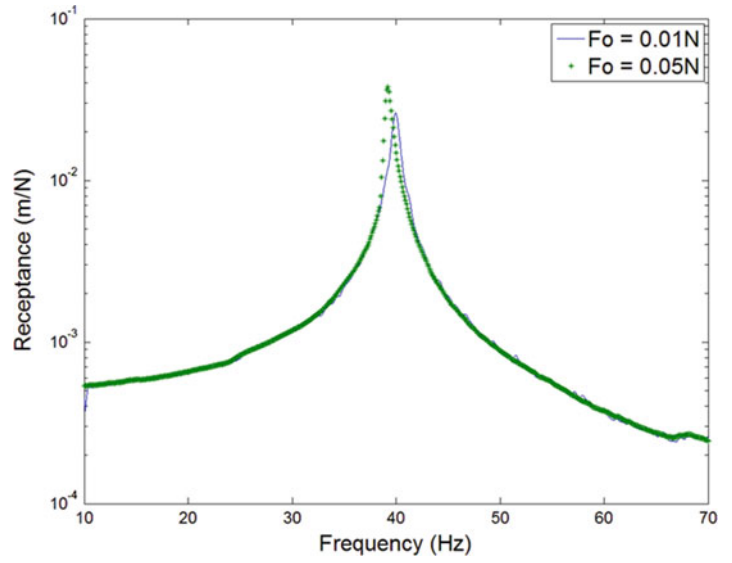


**Fig. 44.8** Uncracked nonlinearity index chart

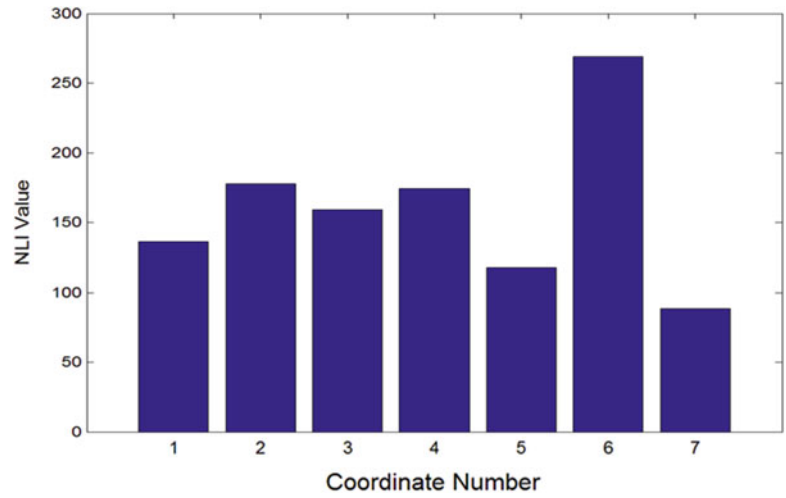


**Fig. 44.9** 2.5 mm nonlinearity index chart

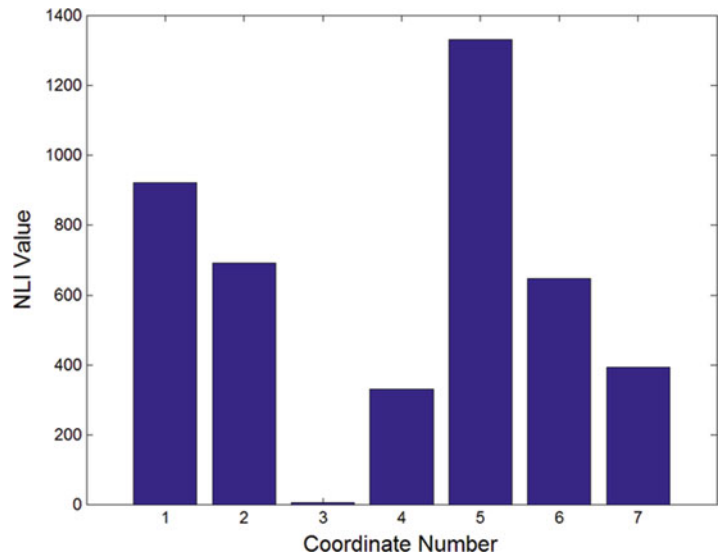


**Fig. 44.10** 5.5 mm nonlinearity index chart

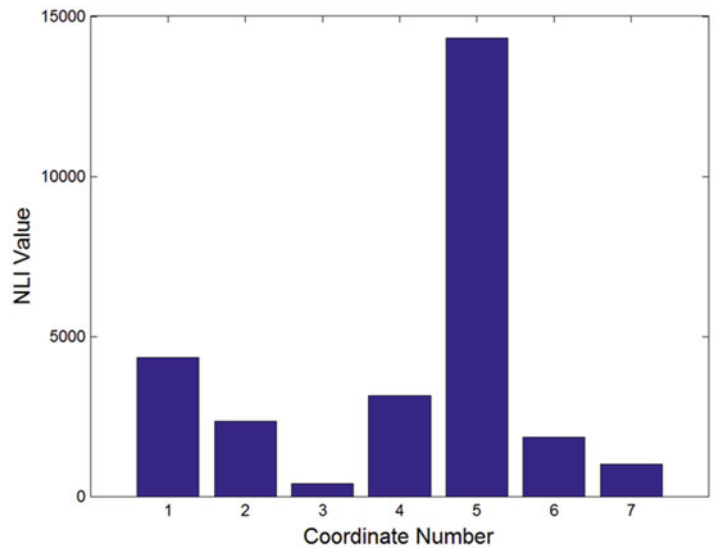


**Fig. 44.11** 7.5 mm nonlinearity index chart

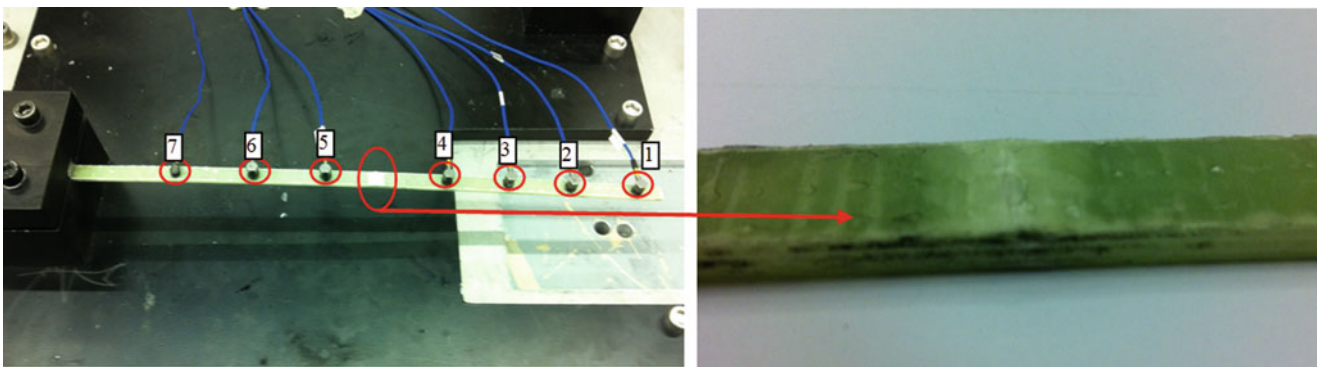
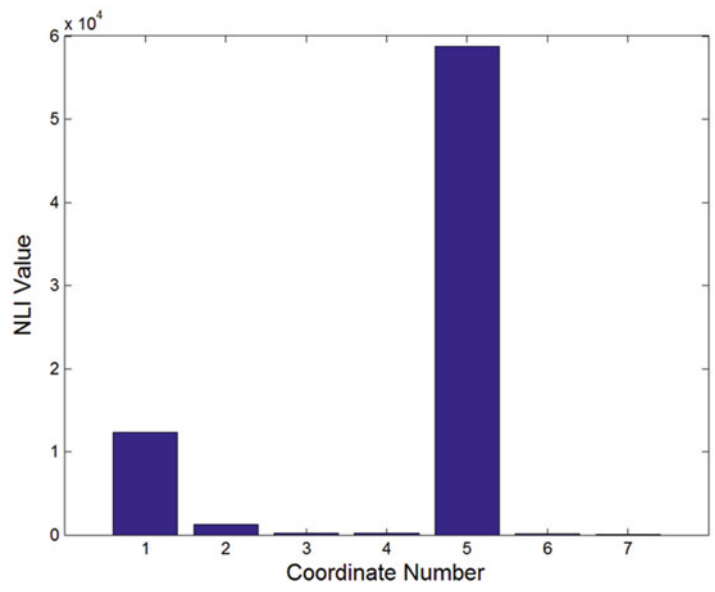


**Fig. 44.12** Setup used in the experimental study-2



**Fig. 44.13** Dimensions of experimental study-2

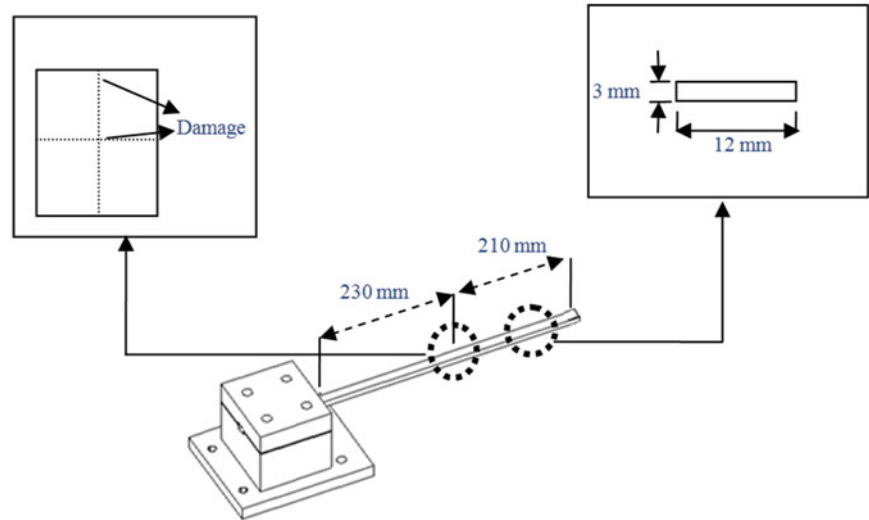
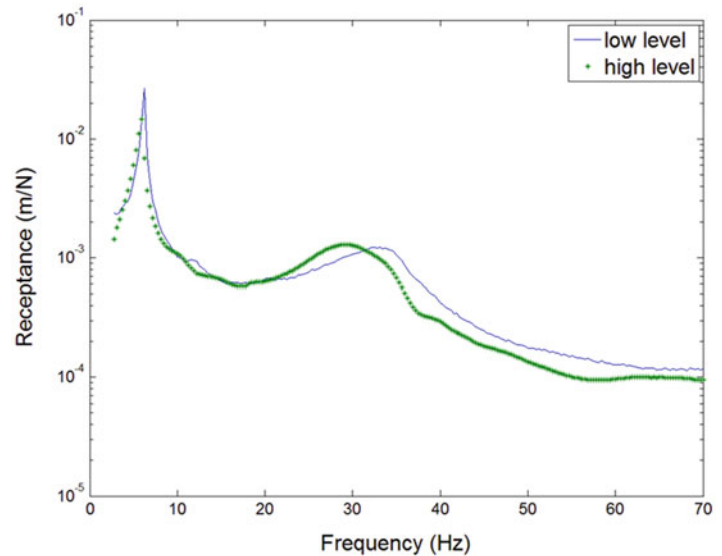


**Fig. 44.14** E-GFRP impact tests, tip point FRF curves



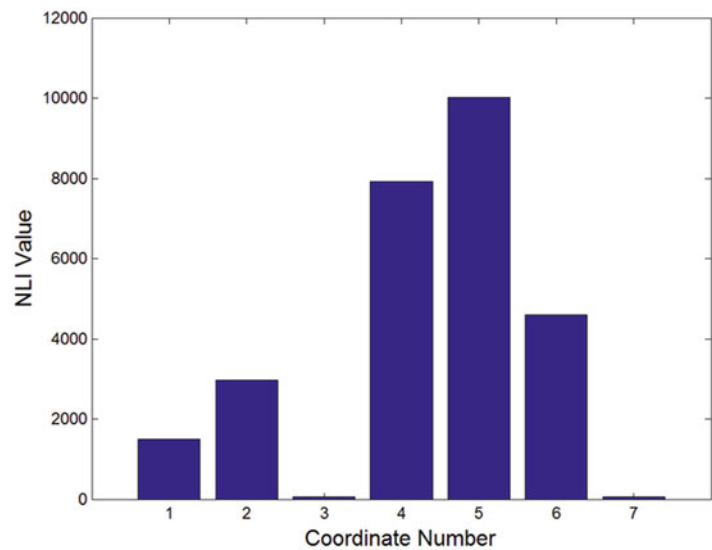
The modal tests are performed by hitting the structure with low and high impact forces. The FRFs obtained for two load levels are shown in Fig. 44.14. The FRFs obtained with low amplitude forcing are taken as linear FRFs of the system.

In this experimental study, we measure only the first columns of the linear (low forcing) and nonlinear receptance (high forcing) matrices. Then, firstly the missing elements of the linear FRF matrix are calculated as discussed in Sect. 44.2, and the NLI values are calculated for each coordinate by using Eq. (44.4). The calculated NLI values are shown in Fig. 44.15. The NLI chart shows the coordinates which are affected from nonlinearity. High NLI values at 4th and 5th coordinates indicate the damage between these coordinates. Relatively high value obtained for NLI at 6th coordinate may be due to the damage that might be extended to that coordinate. However, we observe from the experimental results that the method proposed may yield nonzero NLI values at some other coordinates as well, although they are not adjacent to damaged region. This is most probably due to using only translational FRFs and not including those related with rotational DOF in the computation of NLI values. Fortunately, these nonzero NLI values are not as high as the ones obtained at damaged locations.

## 44.4 Conclusions

It was recently shown [29] with an experimental case study that the method developed by Özer et al. [26] for detecting, localizing and parametrically identifying nonlinearity in MDOF systems is a promising method that can be used in industrial applications. In the study presented here it is shown that the same method can also be used for damage detection and

**Fig. 44.15** E-GFRP nonlinearity index chart



localization for the type of damages which introduce nonlinearity to the structure. The verification of the approach proposed is demonstrated with two experimental studies.

The approach suggested is first applied to an aluminum beam with a breathing crack and it is shown that detection and localization of damage can be achieved by exciting the system from only one point and measuring the responses at all other coordinates (or only at the coordinates around which there might be a crack).

Secondly, it is shown in this study that the same method can also be employed to localize damage by using impact testing, which is more practical. The tests are conducted on a composite sheet and it is concluded that the accuracy in damage localization with impact testing is comparable to that of a shaker testing. Impact testing has many advantages over shaker testing as the most important one being the reduction of setup and test duration. Furthermore, the possibility of damaging the specimen during localization tests is much less in impact testing. The nonzero and relatively high NLI values obtained at coordinates not adjacent to damaged locations are believed to be due to measuring only translational FRFs and not including those related with rotational DOF. Consequently, it can be said that the approach proposed in this study is very promising to be used in practical systems, but still open to further improvements.

## References

- Adams DE (2007) Health monitoring of structural materials and components. Wiley, Chichester
- Salawu OS (1997) Detection of structural damage through changes in frequency: a review. *Eng Struct* 19(9):718–723
- Pandey AK, Biswas M, Samman MM (1991) Damage detection from changes in curvature mode shapes. *J Sound Vib* 145(2):321–332
- Ratcliffe CP (1997) Damage detection using a modified Laplacian operator on mode shape data. *J Sound Vib* 204(3):505–517
- Maia NMM, Silva JMM, Almas EAM (2003) Damage detection in structures: from mode shape to frequency response function methods. *Mech Syst Signal Process* 17(3):489–498
- Whalen TM (2008) The behavior of higher order mode shape derivatives in damaged beam-like structures. *J Sound Vib* 309(3–5):426–464
- Yan YJ, Cheng L, Wu ZY, Yam LH (2007) Development in vibration-based structural damage detection technique. *Mech Syst Signal Process* 21:2198–2211
- Huynh D, He J, Tran D (2005) Damage location vector: a non-destructive structural damage detection technique. *Comput Struct* 83:2353–2367
- Rizos DD, Fassois SD, Marioli-Riga ZP, Karanika AN (2008) Vibration-based skin damage statistical detection and restoration assessment in a stiffened aircraft panel. *Mech Syst Signal Process* 22:3151–3337
- Radzienski M, Krawczuk M, Palacz M (2011) Improvement of damage detection methods based on experimental modal parameters. *Mech Syst Signal Process* 25:2169–2190
- Wang J, Qiao P (2008) On irregularity-based damage detection method for cracked beams. *Solids Struct* 45:688–704
- Huang Q, Gardoni P, Hurlbauss S (2012) A probabilistic damage detection approach using vibration-based nondestructive testing. *Struct Saf* 38:11–21
- Qiao P, Lu K, Lestari W, Wang J (2007) Curvature mode shape-based damage detection in composite laminated plates. *Compos Struct* 80:409–428
- Xiang J, Liang M (2012) A two-step approach to multi-damage detection for plate structures. *Eng Fract Mech* 91:73–86
- Wu N, Wang Q (2011) Experimental studies on damage detection of beam structures with wavelet transform. *Int J Eng Sci* 49:253–261

16. Fan W, Qiao P (2009) A 2-D continuous wavelet transform of mode shape data for damage detection of plate structures. *Int J Solids Struct* 46:4379–4395
17. Bakhary N, Hao H, Deeks AJ (2007) Damage detection using artificial neural network with consideration of uncertainties. *Eng Struct* 29: 2806–2815
18. Yu L, Cheng L, Yam LH, Yan YJ, Jiang JS (2007) Experimental validation of vibration-based damage detection for static laminated composite shells partially filled with fluid. *Compos Struct* 79:288–299
19. Nichols JM, Seaver M, Trickey ST, Todd MD, Olson C, Overbey L (2005) Detecting nonlinearity in structural systems using the transfer entropy. *Phys Rev E* 72:046217
20. Lang ZQ, Park G, Farrar CR, Todd MD, Mao Z, Zhao L, Worden K (2011) Transmissibility of non-linear output frequency response functions with application in detection and location of damage in MDOF structural systems. *Int J Non Linear Mech* 46:841–853
21. Peng ZK, Lang ZQ, Wolters C, Billings SA, Worden K (2011) Feasibility study of structural damage detection using NARMAX modeling of Nonlinear Output Frequency Response Function based analysis. *Mech Syst Signal Process* 25:1045–1061
22. Andraeus U, Baragatti P (2012) Experimental damage detection of cracked beams by using nonlinear characteristics of forced response. *Mech Syst Signal Process* 31:382–404
23. Eftekhari SA, Bakhtiari-Nejad F, Dowell EH (2011) Bifurcation boundary analysis as a nonlinear damage detection feature: does it work? *J Fluids Struct* 27:297–310
24. Aydoğan MÖ (2003) Damage detection in structures using vibration measurements. MSc thesis in Mechanical engineering, Middle East Technical University, Turkey
25. Özer MB, Özgüven HN (2002) A new method for localization and identification of nonlinearities in structures. In: Proceedings of the ESDA2002: 6th biennial conference on engineering systems design and analysis, stanbul, Turkey
26. Özer MB, Özgüven HN, Royston TJ (2009) Identification of structural non-linearities using describing functions and the Sherman–Morrison method. *Mech Syst Signal Process* 23:30–44
27. Tanrıku Ö, Kuran B, Özgüven HN, mregun M (1993) Forced harmonic response analysis of non-linear structures. *AIAA J* 31:1313–1320
28. Aykan M, Özgüven HN (2012) Parametric identification of nonlinearity from incomplete FRF data using describing function inversion. In: Proceedings of the SEM IMAC XXX conference, vol 3, Jacsonville, FL
29. Arslan Ö, Aykan M, Özgüven HN (2011) Parametric identification of structural nonlinearities from measured frequency response data. *Mech Syst Signal Process* 25:1112–1125

# Chapter 45

## Vibration Fatigue Analysis of a Cantilever Beam Using Different Fatigue Theories

Yusuf Eldoğan and Ender Cigeroglu

**Abstract** In this study, vibration fatigue analysis of a cantilever beam is performed using an in-house numerical code. Finite element model (FEM) of the cantilever beam verified by tests is used for the analysis. Several vibration fatigue theories are used to obtain fatigue life of the cantilever beam for white noise random input and the results obtained are compared with each other. Fatigue life calculations are repeated for different damping ratios and the effect of damping ratio is studied. Moreover, using strain data obtained from cantilever beam experiments, fatigue life of the beam is determined by utilizing time domain (Rainflow counting method) and frequency domain methods, which are compared with each other. In addition to this, fatigue tests are performed on cantilever beam specimens and fatigue life results obtained experimentally are compared with that of in-house numerical code. It is observed that the accuracy of the damping ratio is very important for accurate determination of fatigue life. Furthermore, for the case considered, it is observed that the fatigue life result obtained from Dirlik method is considerably similar to that of Rainflow counting method.

**Keywords** Vibration fatigue theories • Rainflow counting • Dirlik method • Probability density function • Frequency domain fatigue theories

### 45.1 Introduction

In vibration environments, if structures are designed only considering static requirements, due to dynamic characteristic of the environment, generally failure occurs. Hence, in order to avoid this kind of failures, dynamic characteristic of the environment and the structure should be considered. If the loading is cyclic, usually such failures occur even though stresses caused by these cyclic loadings are smaller than yield or ultimate strength of the material. These kinds of failures caused by cyclic loadings are called “Fatigue”. However, especially in military environments, generally structures are exposed to random loading; hence, the resulting stresses are not cyclic. In order to avoid fatigue due to random loading, fatigue life of structures should be calculated using vibration fatigue approaches in time and frequency domains.

In the following sections, firstly, brief information about vibration fatigue approaches used in this study is described. These fatigue life estimation approaches are employed in order to determine the fatigue life of an example cantilever beam. In addition to this, fatigue life of the cantilever beam is determined experimentally, by utilizing several cantilever beams and an average fatigue life is determined. The results obtained from different fatigue approaches are compared with each other and also with the experimental data.

---

Y. Eldoğan  
Middle East Technical University, 06800, Ankara, Turkey

ASELSAN MGEO Inc., 06750, Ankara, Turkey  
e-mail: [yeldogan@aselsan.com.tr](mailto:yeldogan@aselsan.com.tr)

E. Cigeroglu (✉)  
Middle East Technical University, 06800, Ankara, Turkey  
e-mail: [ender@metu.edu.tr](mailto:ender@metu.edu.tr)

## 45.2 Theory

In frequency domain, expected fatigue damage,  $E [D]$ , caused by random loading is given as follows [1];

$$E [D] = \sum \frac{n}{N}. \quad (45.1)$$

where,  $n$  and  $N$  are the number of stress cycles applied at a fixed stress amplitude and the number of cycles the material can withstand at applied fixed stress amplitude, respectively.

In order to calculate  $E [D]$ , firstly Probability Density Function (PDF),  $p (S)$ , of rainflow stress ranges should be determined. A typical PDF is shown in Fig. 45.1 [2].

The bin widths,  $dS$  and total number of cycles in the histogram,  $S_i$  should be obtained in order to calculate PDF from a stress range histogram. The opposite work can also be performed using PDF. The area shown in Fig. 45.1,  $p (S) \cdot dS$ , gives the probability of stress ranges between  $S_i - \frac{dS}{2}$  and  $S_i + \frac{dS}{2}$  where  $i$  indicates the number of bin widths.

Finally, multiplying the probability of stress ranges with the total number of cycles,  $S_i$ , in the histogram, the number of total cycles,  $n (S)$ , for a given stress level,  $S$  can be obtained as follows [2]:

$$n(S) = p(S) \cdot dS \cdot S_i. \quad (45.2)$$

In order to use Eq. (45.1),  $n (S)$  is obtained from PDF. For a given stress level,  $S$ , total number of cycles,  $N (S)$ , which cause failure, can be obtained by using Wohler curve formulation, which is defined as:

$$N = C \times S^{-b}. \quad (45.3)$$

In Eq. (45.3),  $b$  is Basquin exponent and  $C$  is a material constant.

Finally, by substituting Eqs. (45.2) and (45.3) into Eq. (45.1), expected fatigue damage,  $E [D]$ , can be found as:

$$E [D] = \sum_i \frac{n_i (S)}{N (S_i)} = \frac{S_i}{C} \int_0^{\infty} S^b \cdot p (S) \cdot dS. \quad (45.4)$$

In frequency domain, Power Spectral Density (PSD) obtained from random time histories is the most widely used expression for the calculation of fatigue life if vibration fatigue theory is used [3].

There are many different techniques that determine the PDF as functions of four spectral moments of the PSD ( $m_0, m_1, m_2, m_4$ ). These spectral moments of the PSD given in Fig. 45.2 are expressed as  $G_k (f_k)$  [1]

$$m_n = \int_0^{\infty} G (f) \times df = \sum_{k=1}^m f_k^n \times G_k (f_k) \times \delta f, \quad (45.5)$$

where  $f$ ,  $G_k (f_k)$  and  $\delta f$  are frequency, PSD and frequency increment, respectively.

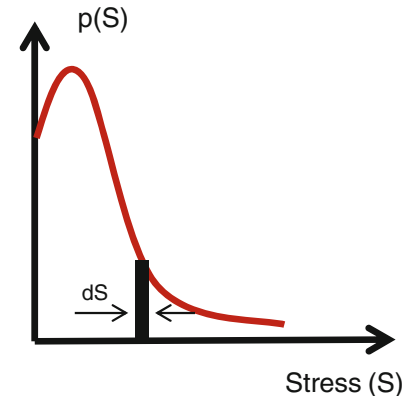
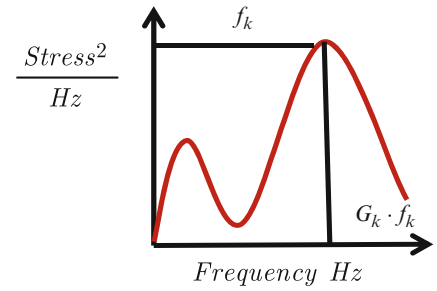


**Fig. 45.1** Probability density function (PDF)

**Fig. 45.2** Power spectral density of stress



In 1954, a very important relationship is developed by S.O Rice [4], for the number of upward mean crossings per second,  $E [P]$ , and peaks per second,  $E [0]$ , in terms of the spectral moments defined by Eq. (45.5) in a random signal. The relationships developed by Rice can be given as follows;

$$E [P] = \sqrt{\frac{m_4}{m_2}}, \quad E [0] = \sqrt{\frac{m_2}{m_0}}. \quad (45.6)$$

By utilizing Eq. (45.6), irregularity factor can be defined as

$$\gamma = \frac{E [0]}{E [P]} = \sqrt{\frac{m_2^2}{m_0 \cdot m_4}}. \quad (45.7)$$

Theoretically, this factor can only take a value in the range of 0–1. If the value is 1, the process is narrow band otherwise; it tends to be white noise. It should be noted that;

$$E [P] \cdot T = S_f, \quad (45.8)$$

where,  $T$  is fatigue life in seconds.

By substituting Eq. (45.8) into Eq. (45.4), expected damage formulation is obtained as

$$E [D] = \sum_i \frac{n_i (S)}{N (S_i)} = \frac{E [P] \cdot T}{C} \int_0^{\infty} S^b \cdot p (S) \cdot dS, \quad (45.9)$$

which can be used in frequency domain applications. By setting  $E [D]$  equal to 1, fatigue life,  $T$ , can be obtained. However, it is worth noting that, while calculating fatigue damage by using Eq. (45.9), an appropriate cut-off value should be used for the upper limit of integration.

Bendat [5] first proposed a frequency domain solution, which gives conservative results for wide-band applications. Therefore, Bendat's solution is also called as a Narrow-Band solution. As a result of this, for Narrow-Band solution, probability density function and expected damage are given as follows:

$$p (S) = \frac{S}{4 \cdot m_0} e^{-\frac{S^2}{8 \cdot m_0}}, \quad (45.10)$$

$$E [D]_{NB} = \sum_i \frac{n_i (S)}{N (S_i)} = \frac{E [P] \cdot T}{C} \int_0^{\infty} S^b \cdot \frac{S}{4 \cdot m_0} e^{-\frac{S^2}{8 \cdot m_0}} \cdot dS. \quad (45.11)$$

In order to solve the problem of getting conservative results from narrow-band solutions, many expressions are investigated. The first expression for expected damage developed by Wirching and Light [6] is

$$E [D] = E [D]_{NB} (a + (1 - a) (1 - \varepsilon)^c), \quad (45.12)$$

where,  $E [D]_{NB}$  is the expected damage determined by narrow-band solutions and

$$a = 0.926 - 0.033b, \quad c = 1.587b - 2.323, \quad \varepsilon = \sqrt{1 - \gamma^2}. \quad (45.13)$$

Later, Tunna [7] replaced the expression of probability density function given in narrow-band solution with the following one

$$p(S) = \frac{S}{4 \cdot \gamma \cdot m_0} e^{\frac{-S^2}{8 \cdot \gamma \cdot m_0}}. \quad (45.14)$$

Expected fatigue damage,  $E[D]$ , given by Eq. (45.9) can be also described as follows

$$E[D] = \frac{E[P] \cdot T}{C} \cdot S_{eq} \quad (45.15)$$

where,  $S_{eq}$  is equivalent stress.

In order to find equivalent stress, Hancock [8] first proposed the following expression

$$(S_{eq})_{Hancock} = \left(2 \cdot \sqrt{2 \cdot m_0}\right) \left[\gamma \cdot \Gamma\left(\frac{b}{2} + 1\right)\right]^{\frac{1}{b}} \quad (45.16)$$

Chaudhuery and Dover [9] used a different expression for equivalent stress

$$(S_{eq})_{CandD} = \left(2 \cdot \sqrt{2 \cdot m_0}\right) \left[\frac{\varepsilon^{b+2}}{2 \cdot \sqrt{\pi}} \cdot \Gamma\left(\frac{b}{2} + 1\right) + \frac{\gamma}{2} \cdot \Gamma\left(\frac{b}{2} + 2\right) + erf(\gamma) \cdot \frac{\gamma}{2} \cdot \Gamma\left(\frac{b}{2} + 2\right)\right]^{\frac{1}{b}}. \quad (45.17)$$

However, the simplest form of equivalent stress is given by Steinberg [10] as

$$(S_{eq})_{Steinberg} = \left[0.683 (2 \cdot \sqrt{m_0})^b + 0.271 \cdot (4 \cdot \sqrt{m_0})^b + 0.043 (6 \cdot \sqrt{m_0})^b\right]^{\frac{1}{b}} \quad (45.18)$$

The best correlation in order to find probability density function is proposed by Dirlik [11] and it is given as

$$p(S) = \frac{\frac{D_1}{Q} \cdot e^{\frac{-Z}{Q}} + \frac{D_2 \cdot Z}{R^2} \cdot e^{\frac{-Z^2}{2 \cdot R^2}} + D_3 \cdot Z \cdot e^{\frac{-Z^2}{2}}}{2 \cdot \sqrt{m_0}}, \quad (45.19)$$

where,

$$D_1 = \frac{2 \cdot (x_m - \gamma^2)}{1 + \gamma^2}, D_2 = \frac{1 - \gamma - D_1 + D_1^2}{1 - R}, D_3 = \frac{1 - D_1 + D_2}{1 - R}.$$

Dirlik investigated this method without using narrow-band solution. This empirical closed form of PDF is obtained by using computer simulations based on Monte Carlo technique [1].

### 45.3 Results

An Aluminum 6061 T6 beam shown in Fig. 45.3 is used for case studies, finite element model (FEM) of which is verified by tests [11].

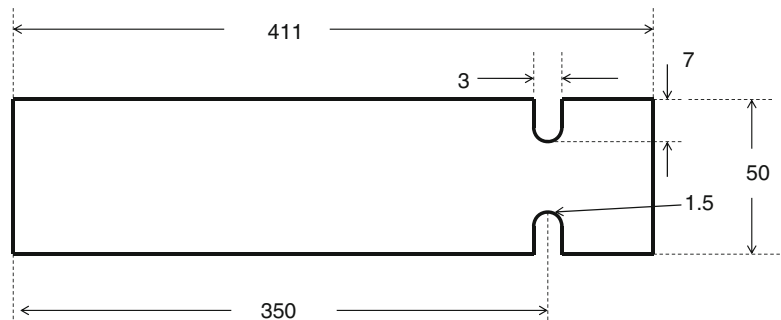


**Fig. 45.3** Dimensions of the cantilever beam

**Fig. 45.4** PSD input acceleration for fatigue analysis

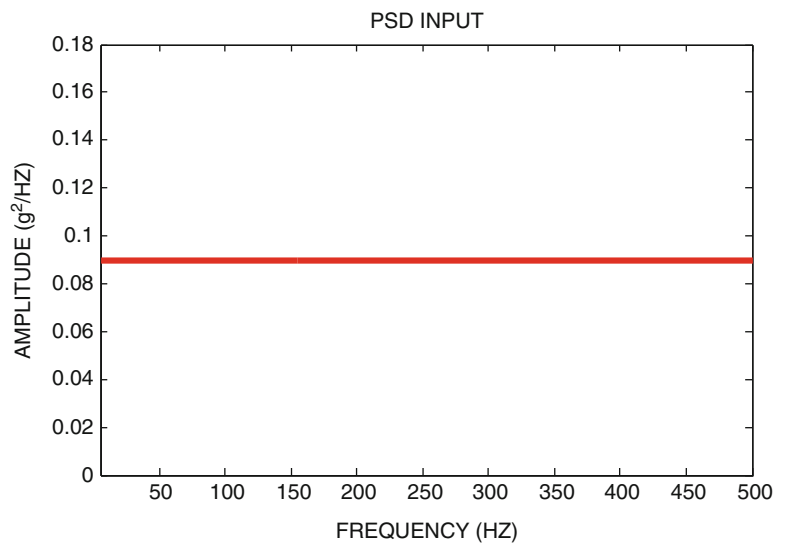


**Fig. 45.5** Experimental setup for cantilever beam fatigue test



## Case Study 1

In this case study, fatigue analyses and tests are performed using the white noise PSD acceleration given in Fig. 45.4 as base input.

Experimental setup is shown in Fig. 45.5 where the beam is fixed to shaker. Since the experimental setup is configured perpendicular to gravity direction, there is no mean component of the stress can be neglected. The test is stopped when the crack is observed and the time from the beginning to the end of the test is accepted to be the fatigue life of the cantilever beam. The test is repeated for seven cantilever beams and the average of the results is accepted as the fatigue life of the beam. The fatigue life results for the seven test items and average of them is given in Table 45.1.

Fatigue life of cantilever beam is calculated using different vibration fatigue theories as mentioned in Theory section. The obtained fatigue life results together with experimentally obtained fatigue life are given in Table 45.2. It can be concluded from the results obtained that Dirlik [11] method generally gives the most accurate results of fatigue life. In addition, comparison of the locations of crack initiation estimated from both finite element and experimental setup is shown in Fig. 45.6, which are in good agreement.



**Table 45.1** Fatigue life of test specimens

Condition	Fatigue life (s)
Test item 1	1,320
Test item 2	1,260
Test item 3	1,250
Test item 4	1,380
Test item 5	1,200
Test item 6	1,400
Test item 7	1,200
Average life	<b>1,287</b>

**Table 45.2** Fatigue life of cantilever beam predicted by different vibration fatigue theories and experiments

Method	Fatigue life (s)	Fatigue life (min)	% difference with experimental
Narrow-band	9.57E+01	1.59E+00	93
Wirching	1.59E+02	2.65E+00	88
Tunna	6.05E+02	1.01E+01	53
Hancock	3.76E-03	6.27E-05	100
Kam and Dover	3.76E-03	6.27E-05	100
Steinberg	3.76E-03	6.27E-05	100
Dirlik	9.84E+02	1.64E+01	24
Experiment	<b>1.29E+03</b>	<b>2.15E+01</b>	-

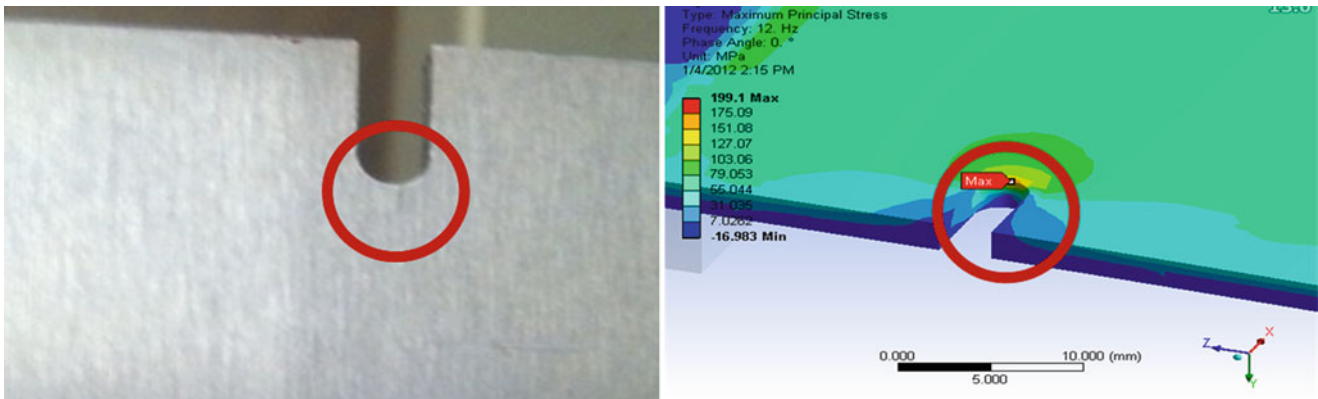


**Fig. 45.6** Locations of the crack initiation for both finite element and manufactured models

**Table 45.3** Fatigue life results of cantilever beam for three different damping ratios

Fatigue theories Frequency domain	Fatigue life (s)				Identified damping ratio
	0.5% damping ratio	1% damping ratio	1.5% damping ratio	2% damping ratio	
Narrow-band	1.47E+02	2.58E+02	4.13E+02	6.73E+02	9.57E+01
Wirching	2.45E+02	4.29E+02	6.87E+02	1.12E+03	1.59E+02
Tunna	1.22E+03	4.26E+03	1.08E+04	2.21E+04	6.05E+02
Hancock	5.04E-03	5.25E-03	5.35E-03	6.60E+00	3.76E-03
Kam and Dover	5.04E-03	5.25E-03	5.35E-03	5.44E-03	3.76E-03
Steinberg	5.04E-03	5.25E-03	5.35E-03	5.44E-03	3.76E-03
Dirlik	1.41E+03	2.90E+03	5.00E+03	8.35E+03	9.84E+02

In addition, in order to observe how the damping ratio affects the fatigue life results of the cantilever beam, four different fatigue life analyses are performed using 0.5, 1, 1.5 and 2% constant damping ratios and the results including that of identified damping ratio are given Table 45.3. It is observed from the results that, damping ratio of the structure affects the fatigue life significantly. Hence, accurate identification of the damping ratios is crucial in the estimation of fatigue life.

**Fig. 45.7** Stress data for  $0.001g^2/Hz$  white noise PSD input at the critical location

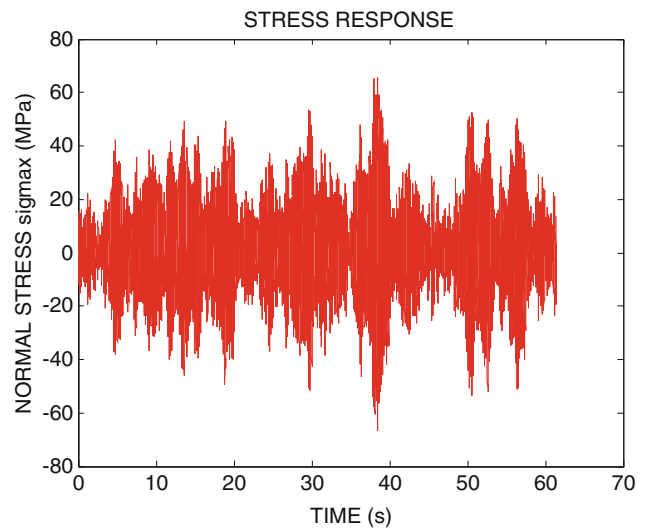
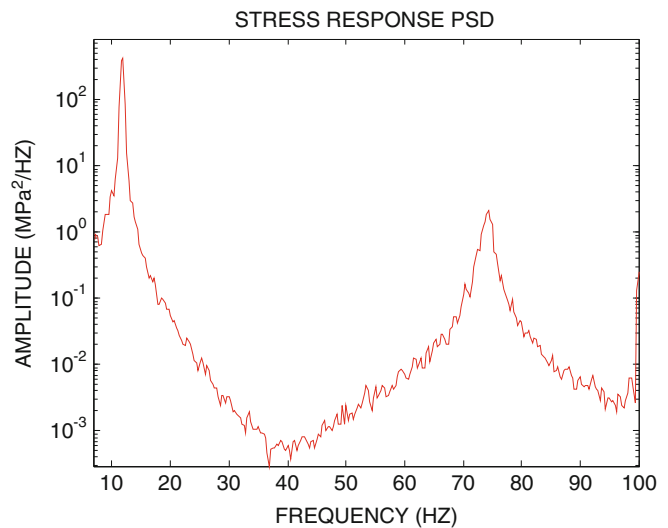


**Fig. 45.8** Stress PSD data for  $0.001g^2/Hz$  white noise PSD input at the critical location



## Case Study 2

In this case study, firstly, rainflow counting algorithm is developed according to ASTM E 1048 85 [13] and it is used in time domain fatigue life calculations. In order to compare the fatigue life results obtained in time and frequency domains, stress history of the location where strain gage is placed on the cantilever beam is obtained both in time and frequency domains. Strain gage cannot be located on the most critical location exactly due to geometric properties of the notch and strain gage; hence, the measured data is used only for comparison of time domain and frequency domain methods. In this case study, strain gage data is obtained by using a  $0.001g^2/Hz$  White Noise PSD input. Using developed rainflow algorithm, rainflow counting of the stress-time history given in Fig. 45.7 is performed and fatigue life is obtained. Then, using the stress PSD data presented in Fig. 45.8, fatigue life is calculated utilizing different fatigue theories and all the results are presented in Table 45.4.

Using the same stress history, it is expected to have similar fatigue life results calculated by time and frequency domain methods. However, when the results in

Table 45.4 are studied, it is observed that Dirlik method gives the closest result to that of Rainflow counting.

**Table 45.4** Fatigue life results calculated in time and frequency domains

Fatigue theories	Fatigue life (s)	Fatigue life (h)
Frequency domain	–	–
Narrow-band	4.14E+09	1.15E+06
Wirching	6.89E+09	1.91E+06
Tunna	9.95E+09	2.76E+06
Hancock	1.72E+07	4.78E+03
Kam and Dover	1.93E+07	5.37E+03
Steinberg	7.08E+06	1.97E+03
Dirlik	1.40E+10	3.89E+06
Time domain	–	–
Rainflow counting	<b>1.43E+10</b>	<b>3.97E+06</b>

## 45.4 Conclusion

In this study, firstly descriptions of vibration fatigue approaches are given which are used for fatigue life predictions. An Aluminum 6061 T6 cantilever beam is used for all case studies. In addition, several fatigue tests are performed in order to compare the results obtained by fatigue life prediction approaches with experimentally obtained fatigue lives. It is observed that fatigue life obtained using Dirlik method is the closest and smaller than the experimental fatigue lives. In addition, by performing fatigue life calculations using different damping ratios, effect of the accurate identification of the damping ratio is brought out to be crucial. Finally, using different loading and strain gage data, fatigue life results are obtained in both frequency and timed domains. For time domain calculations, rainflow counting algorithm is developed and it is observed that the results obtained using Dirlik method and rainflow counting method are very similar to each other.

## References

1. Bishop NWM, Sherratt F (2005) Finite element based fatigue calculations. NAFEMS, Bernau am Chiemsee, Germany
2. Bishop N Fatigue (2000) Analysis of a missile shaker table mounting bracket. Time Los Angeles, USA, 10p
3. Aykan M (2005) Vibration fatigue analysis of equipments used. M.Sc. Thesis, Middle East Technical University, Ankara
4. Rice SO (1954) Mathematical analysis of random noise. In: Wax N (ed) Selected papers on noise and stochastic processes. Dover, New York
5. Bendat JS (1964) Probability functions for random responses. NASA report on contract NAS-4590
6. Wirching PH, Light MC (1980) Fatigue under wide band random loading. J Struct Div 1593–1607. ASCE
7. Tunna JM (1986) Fatigue life prediction for Gaussian random loads at the design stage. Fatigue Fract Eng Mater Struct 9(3):169–184
8. Kam JCP, Dover WD (1988) Fast fatigue assessment procedure for offshore structures under random stress history. Proc Inst Civ Eng 85:689–700
9. Chaudhury GK, Dover WD (1985) Fatigue analysis of offshore platforms subject to sea wave loadings. Int J Fatigue 1(1):13–19
10. Steinberg DS (2000) Vibration analysis for electronic equipment, 3rd edn. Wiley, New York
11. Dirlik T (1985) Application of computers in fatigue analysis. University of Warwick
12. Eldogan Y, Cigeroglu E (2012) Vibration fatigue analysis of a cantilever beam exposed to random loading. In: The 15th international conference on machine design and production, Pamukkale, Denizli, Turkey
13. ASTM Designation E 1049-85 (1997) Standard practices for cycle counting in fatigue analysis 1. Read 85:1–10. Reapproved

# Chapter 46

## Automated Modal Analysis Based on Statistical Evaluation of Frequency Responses

Vahid Yaghoubi and Thomas Abrahamsson

**Abstract** This paper presents a newly developed method for obtaining the modal model with a proper model order from experimental frequency response functions (FRF). The method is a multi-step procedure which commences with the identification of a high-order state-space model, Exhaustive Model (EM), using the full FRF data set. Then, modal states that give small contribution to the output, quantified by a metric associated to the observability grammian, are rejected from the EM resulting in a Reference Model (RM). Competing models, with the same model order as the RM, are then found by bootstrapping realization using same-size fractions of the full FRF. Eigensolutions of the Bootstrapping Models (BMs) are then paired by the eigensolutions of the RM based on high Modal Observability Correlation (MOC) indices. In a second reduction stage, the modal states with low MOC index are rejected from the BMs. Final model is found by an averaging through BMs. Only one threshold quantity, related to observability grammians need to be set by the user. The method thus requires very little user interaction. The method is applied to experimental data used in a previous IMAC Round Robin exercise for experimental modal analysis evaluation.

**Keywords** Modal parameters • Automated modal analysis • Modal observability correlation (MOC) • Frequency response function (FRF) • Bootstrapping

### 46.1 Introduction

Estimating the modal parameters from test data is the special case of system identification. Since 1960, several methods have been developed to numerically estimate the modal parameters with little user interaction. Three state-of-the-art methods for multi-input-multi-output (MIMO) systems being the state-space sub-space based method called N4SID [1], the poly-reference least square complex frequency domain method called PolyMAX [2] and the Poly-Reference Complex Exponential (PRCE) method [3]. With these methods, the user only needs to define the proper model order and the methods estimate the corresponding system parameters very efficiently. However, a key problem is to select the proper model order.

In implementations of identification methods, the user often gets help in this selection by the use of pole stabilization charts or plots that shows drop of Hankel singular values [4]. For the system with well separated modes it is easy to find a good model order by means of inspection of mode indicating functions but for systems with closely spaced or highly damped modes, finding model order by visual inspection is very tedious and results are user dependent.

In this paper a method for obtaining a proper model order is presented. The method is based on the statistical evaluation of an ensemble of state-space models all identified from the same basic set of frequency response functions, but with different realizations based on a bootstrapping scheme. The method is based upon a recently developed correlation metric, called the maximum Modal Observability Correlation (MOC) [5], and a criterion based on the mean value of the maximum correlation number is used for rejection of spurious states. In the following, the theory and rejection method are presented and the method is applied to test data to estimate the proper model order.

---

V. Yaghoubi (✉) • T. Abrahamsson

Department of Applied Mechanics, Chalmers University of Technology, SE-41296 Gothenburg, Sweden  
e-mail: [yaghoubi@chalmers.se](mailto:yaghoubi@chalmers.se); [thomas.abrahamsson@chalmers.se](mailto:thomas.abrahamsson@chalmers.se)

## 46.2 Theory

We base our model order determination on state rejection using statistics from bootstrapping realization from frequency response function estimates. A frequency domain state-space sub-space method, the N4SID method, is used to obtain competing models from bootstrapping data. The N4SID method is a system identification (SYSID) method that establish a mathematical state-space model of a dynamic system from experimental data, *i.e.* it gives the quadruple  $\{A, B, C, D\}$  given measured stimuli and response data  $\{u, y\}$ , see e.g. Ljung [4] or Van Overschee and DeMoor [6]. A particular implementation of the N4SID method that use frequency domain data is given by McKelvey [7]. In particular it does not require data to be evenly sampled over the frequency range of interest. This makes it ideal for a bootstrapping sampling strategy in which multiple realizations of subsets of the available data are used based on the frequency response function data at randomly selected frequencies.

Our reduction method has two steps, *step 1* is Coarse Selection. In this step we will remove some states that have almost no contribution to the output. The resulting model will be referred to as the **Reference Model**. At first, a high order state-space model using the full data set should be found. We use an exhaustive number of states to establish this model, a number that certainly is larger than the true system order. Besides containing the true system states, that model also include noise states and other test imperfection states that we want to exclude from our final model. The reference model is obtained from this exhaustive state order model by model reduction after balanced realization. In that reduction we reject states that has observability and controllability grammians that are lower than a given small threshold number  $t_g$ . For a small  $t_g$  the reduced model is still of high order and is our reference model to which we compare the competing models that are obtained from bootstrapped data.

*Step 2* is fine selection. In this step some states with little contribution to the model will be removed, therefore, kept states have large contribution to the output. In this step, by the use of bootstrapping method, the available data was resampled randomly at the discrete frequencies to form fractional realizations of data. Based on these data the corresponding state-space model  $\{A, B, C, D\}$ , of same order as the reference model, was obtained by SYSID and further subjected to diagonalization and balancing. This model will be referred to as a **Bootstrapped Model**. Bootstrapped models were correlated to the reference model by the use of the Modal Observability Correlation, MOC [5].

$$MOC_{ij} = |\{O_i^{bd}\}^H \{O_j^{bd}\}|^2 / \max(\{O_i^{bd}\}^H \{O_i^{bd}\}, \{O_j^{bd}\}^H \{O_j^{bd}\})^2, \quad (46.1)$$

in which

$$O_i = \begin{bmatrix} C \Psi_i T_2^{ii} \\ C \Psi_i T_2^{ii} \lambda_i \\ C \Psi_i T_2^{ii} \lambda_i^2 \\ \dots \\ C \Psi_i T_2^{ii} \lambda_i^{n-1} \end{bmatrix} \quad (46.2)$$

is the  $i$ th column of the balanced modal observability matrix.  $\Psi_i$  and  $\lambda_i$  is the eigenvector and eigenvalue of the of  $i$ th mode respectively.  $T_2^{ii}$  is a transformation to balance the  $i$ th mode.

Eigenvalues and eigenvectors of the bootstrapping model were paired with the counterparts of the reference model based on maximum correlation numbers. So each reference mode has a cluster of bootstrapped modes and also an index which is the mean of maximum correlation numbers. Based on these indices the modes of reference model and their corresponding clusters are divided into three groups: Physical, Possibly Physical and Spurious.

Since MOC used for correlating bootstrapped models to reference model, the modes with MOC indices more than 90% of the maximum index are the modes that not only keep their properties like eigenvalues and eigenvectors in different realizations but also their contribution to the output are almost the same in all different realizations, therefore, we call these modes physical. Based on the same idea the modes with MOC indices less than 50% of maximum index are called Spurious. The modes in between are possibly physical. To find if the mode in the possibly physical group is physical or spurious, Eq. (46.3) is used to scale their indices.

$$Index_s = \frac{Index^2}{\max(Index^2)} \quad (46.3)$$

This Scaled Index has value between 0 and 1. The modes with the indices more than 0.8 are grouped as physical and less than 0.5 are removed as spurious modes and for the rest, we calculated the drop of their scaled index to find out if they are physical or spurious *i.e.* the modes before the mode with the biggest drop are put in physical region.

### 46.3 Case Studies

In the following, the method presented before will be applied to two case studies, namely Plexiglass Plate and Dryer Cabinet. They were used in a previous IMAC Round Robin exercise for experimental modal analysis evaluation.

#### 46.3.1 Plexiglass Plate

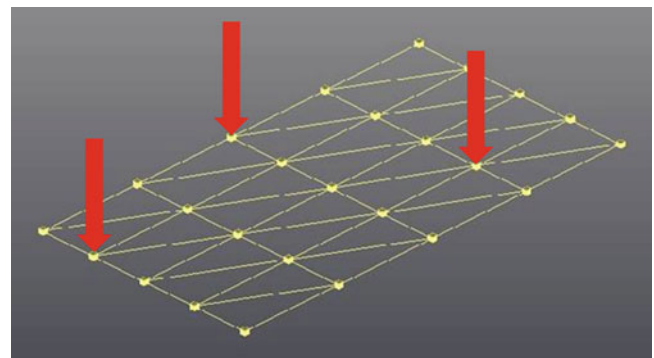
The data of the Plexiglas Plate, shown in Fig. 46.1, is from a test of a plate that measured  $53 \times 32 \times 1.5$  cm. The plate was tested in a free-free condition. Eight triaxial accelerometers were mounted using wax and were roved three times to complete the test. Random excitation from three simultaneous sources was used. A hanning window was applied to reduce leakage. The data set contains FRFs from 3 uncorrelated references and 75 response DOFs. FRFs, coherence functions and geometry are provided as specified in reference [8].

Although the FRF were provided in the frequency range of (0–2,048) Hz. Data for frequency less than 50 Hz and above 900 Hz were not considered as being trustable, so we used only data between these two frequencies.

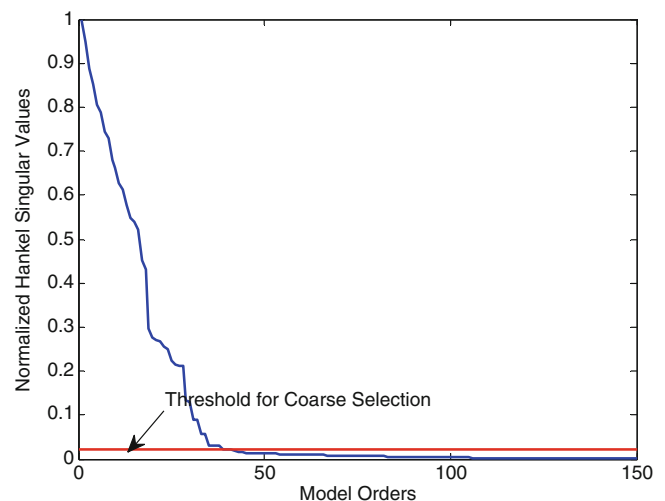
Exhaustive model with the order 150 was first obtained by SYSID using N4SID. As the first reduction step, a reduction of states based on the normalized grammians of the balanced model was made. For Coarse selection step, grammian threshold  $t_g = 0.02$  was used for rejecting states that contribute little to the input-output relation (see Fig. 46.2). This threshold was chosen arbitrarily. In this step, the model order was reduced to 40. The resulting model is referred to as the reference model.

Bootstrapping was made by randomly sampling, with replacement, of the frequency response functions at 60% of the discrete frequencies. The bootstrapping sampling was repeated 10 times with proceeding identification to form an ensemble of 10 state-space models. The models obtained after each bootstrap sample are referred to as bootstrapping models.

**Fig. 46.1** Plexiglass plate with dimension of  $53 \times 32 \times 1.5$  cm, The data set contains FRFs from 3 uncorrelated references and 75 response DOFs (Arrows used only to show the number of inputs not their position) [8]



**Fig. 46.2** Normalized Hankel singular values used for coarse selection (The maximum of the Hankel singular values is used to make normalization)



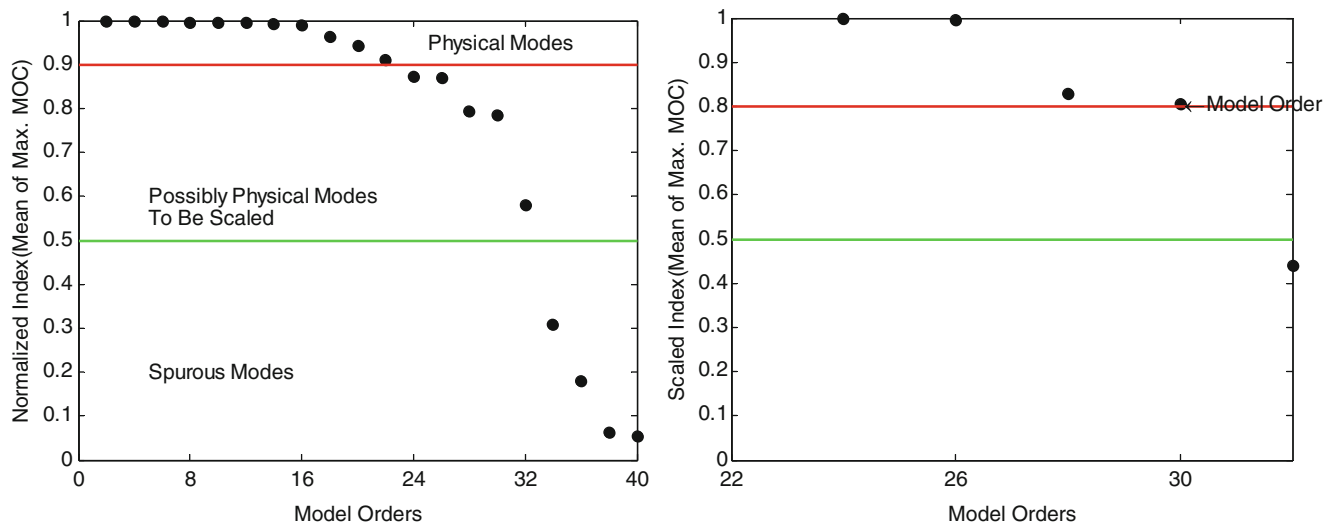


**Fig. 46.3** Illustration of fine selection procedure, (left) MOC values (Normalized based on the maximum MOC value which was 0.9967), The modes with index more than 0.9 are kept as physical modes and the ones less than 0.5 are removed. MOC index of the modes in between are scaled. (Right) Normalized Scaled Index. The modes with the scaled index higher than 0.8 are kept and the ones less than 0.5 are removed

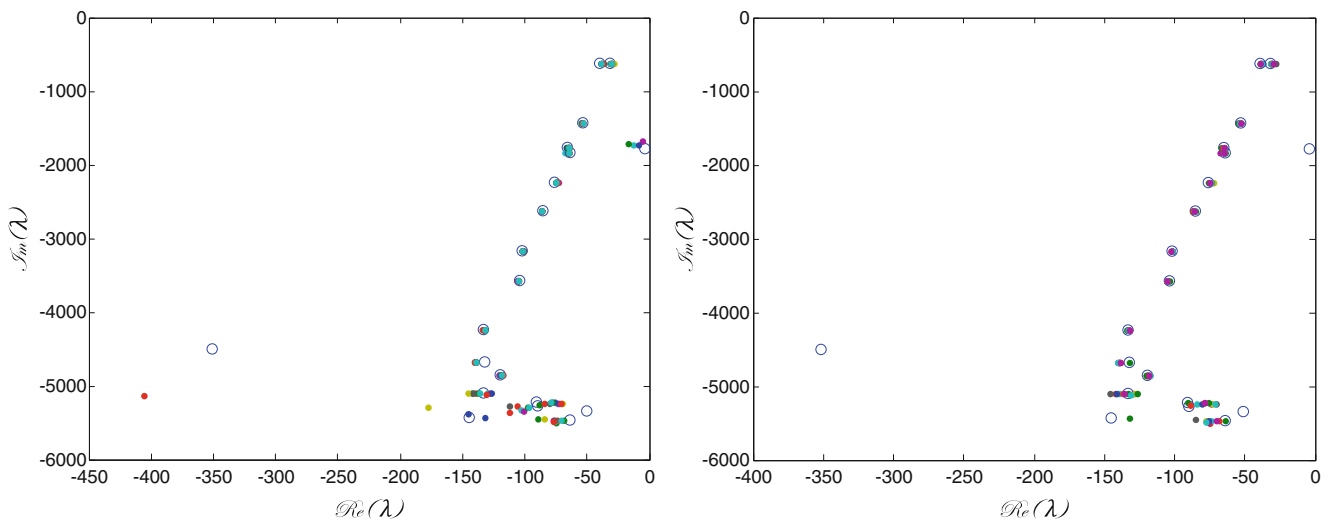


**Fig. 46.4** Root-locus plot showing eigenvalues of models after 10 bootstrapping realizations. “o” stands for the eigenvalues of reference model and colored dots are for eigenvalues of bootstrapped models with each color representing one realization. (Left) before reduction, (Right) after reduction

The mean of maximum MOC magnitude were calculated for all modes of the bootstrapping models and were normalized based on the maximum of them. The left plot in Fig. 46.3 shows the normalized MOC index for all modes. The modes with index less than 0.5 are removed as spurious modes and the modes with index more than 0.9 are kept as physical modes. The modes in between are possibly physical so we scaled their indices based on Eq. (46.3). The scaled indices for the modes in the possibly physical region are presented in right plot of Fig. 46.3. The modes with scaled index more than 0.8 are kept as physical modes and the modes less than 0.5 are removed. Drop of scaled index is the criteria that should be used to select the modes as spurious or physical in the middle region. As a final, a reduced model with 30 states was obtained.

Figure 46.4 indicates root locus plots including the eigenvalues of the reference system and the bootstrapping systems. The left plot shows all system poles before model reduction and the right one displays remaining poles after reduction.

Figure 46.5 demonstrates the stabilization chart of the plexiglass plate with the Complex Mode Indicator Function (CMIF) in background. Blue lines are the poles selected by the method.

**Fig. 46.5** Stabilization chart for the Plexiglass plate the biggest CMIF shown in *black* and the others are shown in *grey lines*. *Blue lines* are location of poles chosen by our method

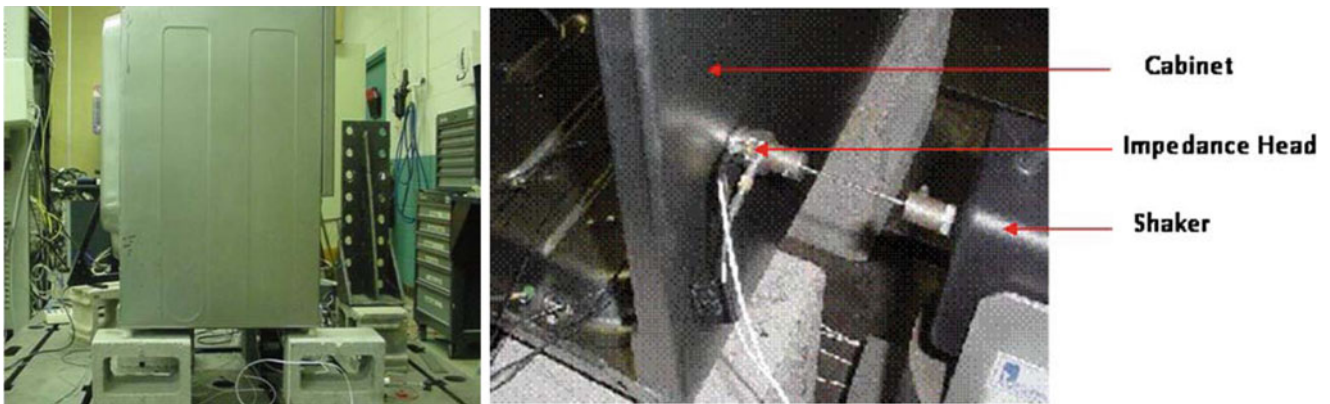
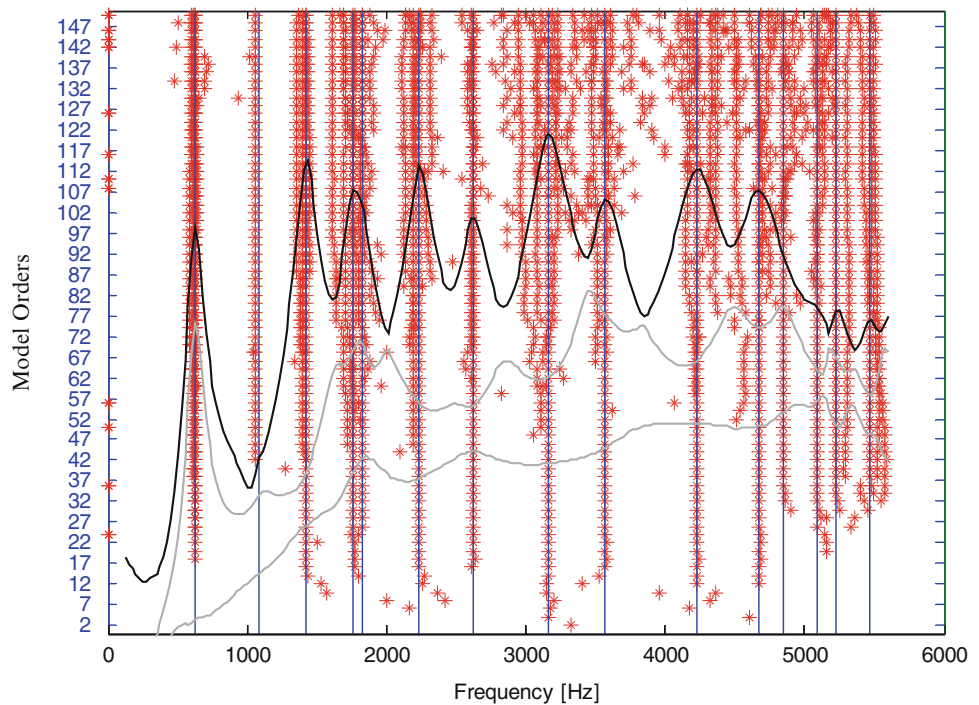


**Fig. 46.6** (Left) Dryer Cabinet with 4 inputs and 4 outputs. (Right) Installation of shakers [8]

### 46.3.2 Dryer

The Dryer data is from a test of a residential clothes dryer cabinet, see Fig. 46.6. The data set contains FRFs from 4 uncorrelated references and 300 response FRFs, the associated coherence functions and the test geometry are provided. Four shakers were used to excite the cabinet in a burst random test for the MIMO test, see Fig. 46.5b. The shaker locations were such that the cabinet was excited relatively uniformly. The shakers were placed one on each side (right, left and back) and one shaker on the base. The response of the base was measured with 29 PCB 352B65 accelerometers (simultaneously). The response locations were spread uniformly over the base on a grid size of approximately 3.5". The force and acceleration measurements at the shaker locations were made with PCB 288D01 impedance heads. A Polytec laser was used to measure the response at the locations on the side and back panels of the cabinet. All response measurements were normal to the panel surfaces, see reference [8].

Exhaustive model with the order of 100 was first obtained by SYSID using N4SID. As the first reduction step, a reduction of states based on the normalized grammians of the balanced model was made. For Coarse selection step, a grammian threshold  $t_g = 0.05$  was selected arbitrarily for rejecting states that contribute little to the input-output relation (see Fig. 46.7). In this step, the model order was reduced to 96. The resulting model is referred to as the reference model.



**Fig. 46.7** Normalized Hankel singular values used for coarse selection (the maximum of the Hankel singular values used to make them normalized)

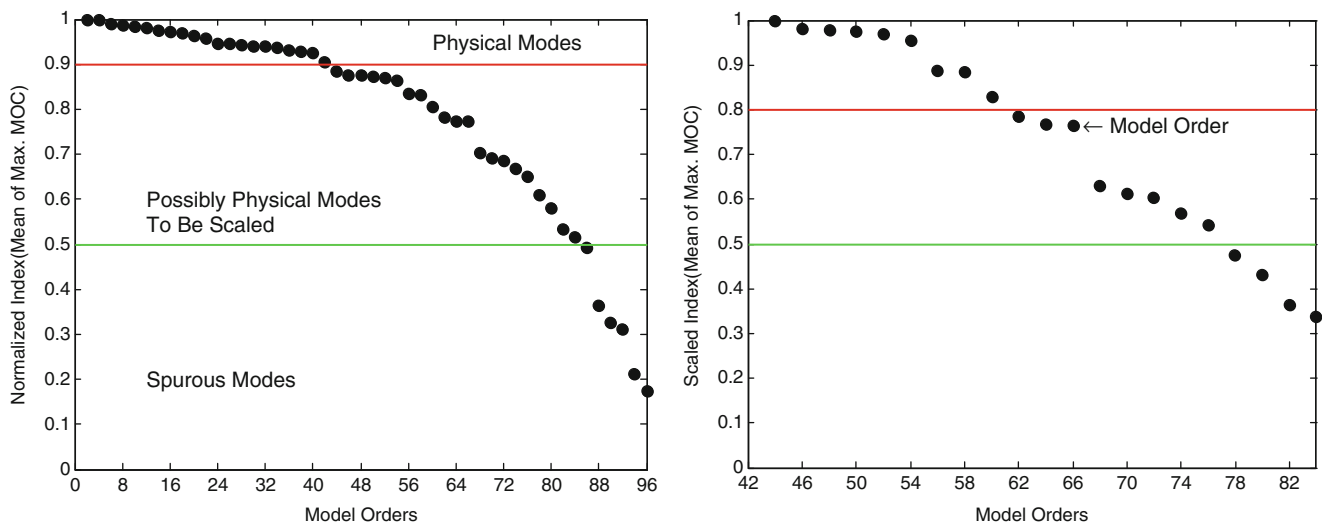
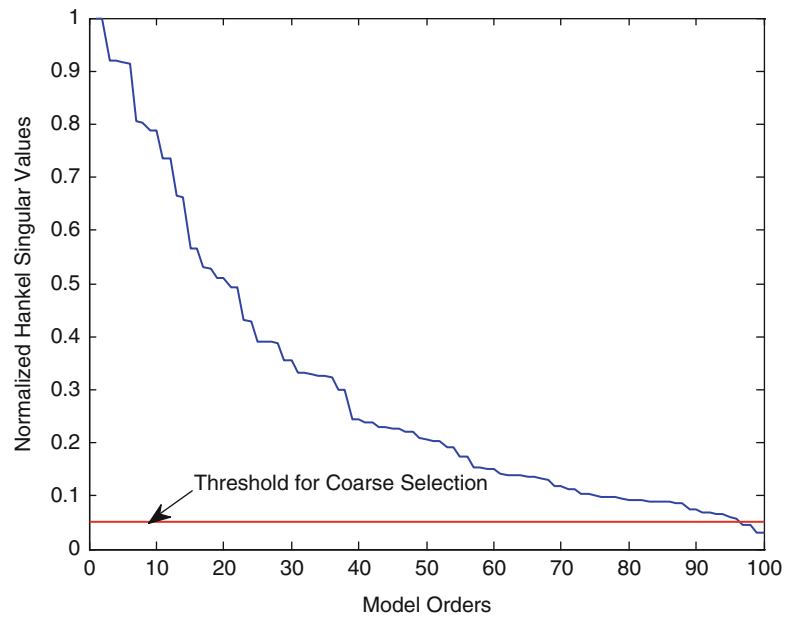


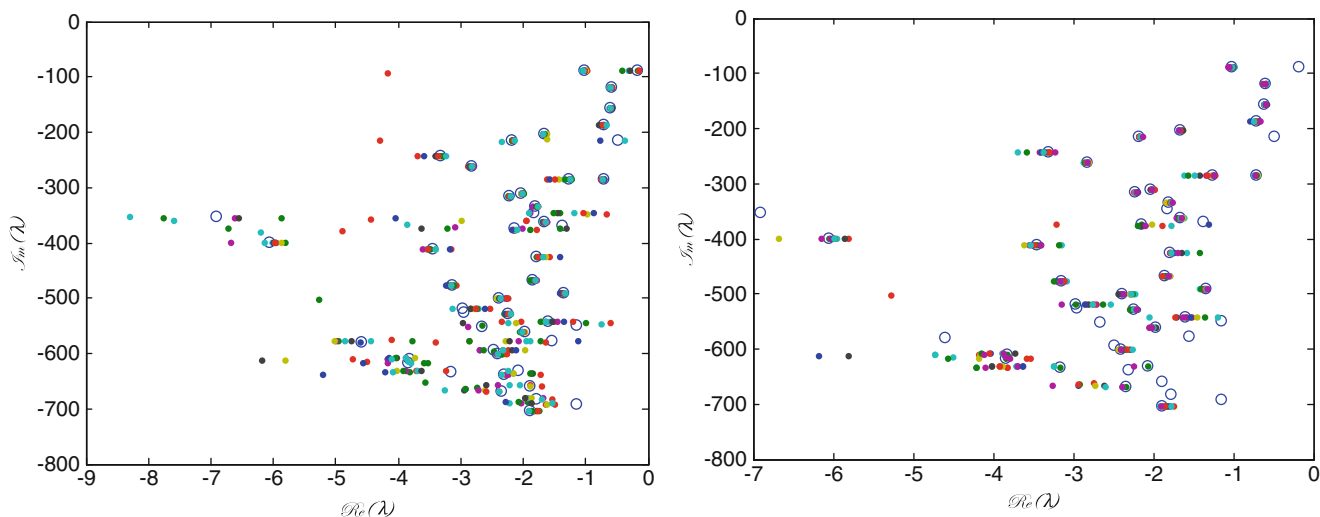
**Fig. 46.8** Illustration of the fine selection procedure, (left) MOC values (Normalized based on the maximum MOC value which was 0.99), The modes with index more than 0.9 are kept as physical modes and the ones less than 0.5 are removed. MOC index of the modes in between are scaled. (Right) Normalized scaled index. The modes with the scaled index higher than 0.8 are kept and the ones less than 0.5 are removed

A Bootstrapping scheme, identical to the scheme used on the plexiglass plate, was used to obtain 10 bootstrapping modes.

Left plot in Fig. 46.8 demonstrates the normalized MOC index for all modes. The same procedure as plexiglass plate is used to keep or remove the modes. Scaled index for the modes in the possibly physical region are presented in right plot of Fig. 46.8. As we can see in Fig. 46.8 the biggest drop of scaled index is in the order of 66. Hence, our method resulted in model order 66 for Dryer.

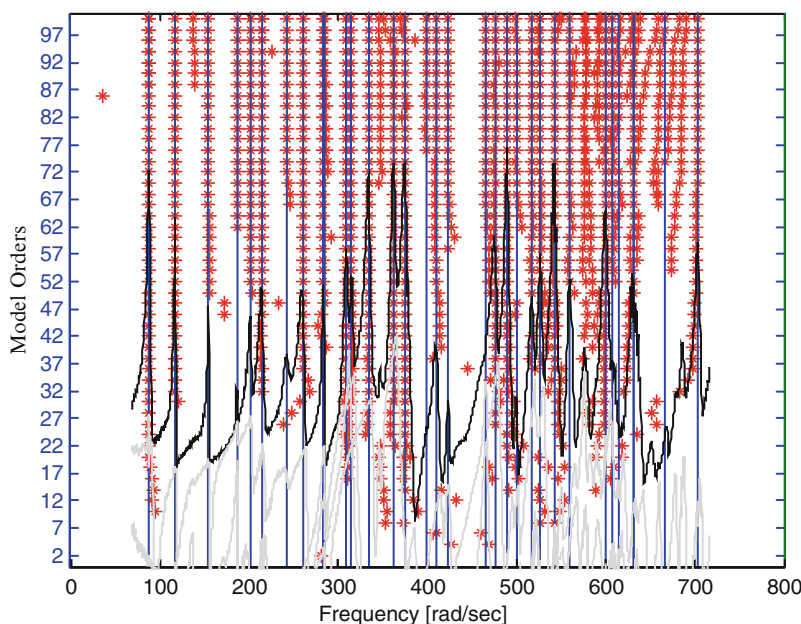
Figure 46.9 indicates the root locus plots of the eigenvalues of the reference system and the bootstrapping systems. The left plot shows all system poles before model reduction and the right one displays remaining poles after reduction.

Figure 46.10 is the stabilization chart of the Dryer with the CMIF in background. Blue lines are the location of poles selected by the method.



**Fig. 46.9** Root-locus plot showing eigenvalues of models after 10 bootstrapping realizations. “o” stands for the eigenvalues of reference model and colored dots are for eigenvalues of bootstrapped models with each color representing one realization. (Left) before reduction, (Right) after reduction

**Fig. 46.10** Stabilization chart for the Dryer with CMIF in the background, the biggest CMIF shown in black and the others are shown in grey lines. Blue lines are the poles chosen by our method



### 46.4 Summary and Conclusion

In this paper, a new method for Automated Modal Analysis based on frequency response statistics has been presented and applied to two application examples. The method started with a big model order and the modes with little contribution to output were removed in two steps, *step 1*, Coarse Selection, leads to in *Reference Model* and *Step 2*, fine selection. In this step, a portion of whole data resampled randomly and realized with the same model order as reference model for several times. These models are *Bootstrapped Models*. We used Modal Observability Correlation (MOC) to correlate bootstrapped models to reference model. The modes with MOC more than 0.9 are kept as physical modes and the ones less than 0.5 are removed. MOC index of the modes in between are scaled based on Eq. (46.3). Then the modes with the scaled index more than 0.8 are kept and the ones less than 0.5 are removed. For the modes in between drop of scaled index are used to keep or remove, i.e. the modes before the mode with the biggest drop are put in physical region.

The method can be used in conjunction with any system identification method that can provide a state-space model of a given order by use of frequency domain data. In the future, this little user-interaction required to set some thresholds will be removed and the method will be presented as Fully Automated method.

## References

1. Verbon P, Parloo E, Guillaume P, Overmiere MV (2001) Autonomous modal parameter estimation based on a statistical frequency domain maximum likelihood approach. Presented at the international modal analysis conference (IMAC XIX), Kissimmee, FL
2. Peeters B, Guillaume P, Van der Auweraer H, Cauberghe H, Verboven B, Leuridan P (2001) Automotive and aerospace application of the PolyMax modal parameter estimation method. In: International modal analysis conference (IMAC), Kissimmee
3. Vold H, Rocklin G (1982) The numerical implementation of a multi-input modal estimation method for mini- computers. In: International modal analysis conference (IMAC I), Orlando
4. Ljung L (1999) System identification-theory for the user, 2nd edn. Prentice Hall PTR, Upper Saddle River
5. Yaghoubi V, Abrahamsson T (2013) The modal observability correlation as a modal correlation metric. Presented at the International Modal Analysis Conference (IMAC XXX), Los Angeles, CA
6. Van Overschee P, DeMoor B (1996) Subspace identification of linear systems: theory implementations, applications. Kluwer, Boston
7. McKelvey T, Akcay H, Ljung L. (1996) Subspace-based multivariable system identification from frequency response data. IEEE Trans Autom Control 41:960–979
8. Modal Parameter Estimation Round Robin, IMAC 2010 (XXVII), Jacksonville, FL [http://www.me.mtu.edu/imac\\_mpe/Dryer%20Data%20Description.htm](http://www.me.mtu.edu/imac_mpe/Dryer%20Data%20Description.htm)

# Chapter 47

## The Modal Observability Correlation as a Modal Correlation Metric

Vahid Yaghoubi and Thomas Abrahamsson

**Abstract** The historical development of the Modal Assurance Criterion (MAC) originated from the need of a correlation metric for comparing experimental modal vectors, estimated from measured data, to eigenvectors that have been determined from finite element calculation. For systems with well separated eigenvalues with many system degrees-of-freedom (DOF) represented in the eigenvectors it is normally easy to distinguish eigenvectors associated to different eigenvalues by low MAC correlation numbers. However, for eigenvectors with a sparse DOF sampling it may be hard to distinguish between vectors by MAC correlation numbers. To reduce the problem of distinguishing between eigensolutions, this paper advocates the use of a new correlation metric based on the observability matrix of the diagonal state-space realization. This is instead of using a metric based on the eigenvectors only.

**Keywords** Auto-correlation • Cross-correlation • Modal assurance criterion (MAC) • Eigenmode • Mode Contribution

### 47.1 Introduction

The historical development of the Modal Assurance Criterion (MAC) originated from the need for a quality assurance indicator for experimental modal vectors that are estimated from measured. MAC is defined as a scalar constant relating the degree of consistency (linearity) between two modal vectors as follows [1],

$$MAC = |\Psi_i^H \Psi_j|^2 / (\Psi_i^H \Psi_i \Psi_j^H \Psi_j), \quad (47.1)$$

Note that the vectors need not come from the same source, but need to be of equal length. For instance the  $i$ th and  $j$ th modes may stem from data from two different tests of the same test object.

For system with well separated eigenvalues with many system degrees-of-freedom (DOF) represented in the eigenvectors it is normally easy to distinguish eigenvectors associated to different eigenvalues by low autoMAC correlation numbers, i.e. correlation between vectors from same source. However, for eigenvectors with a sparse dof sampling or closely spaced eigenvalues it may be hard to distinguish between vectors.

Besides that, since MAC has no information about the frequency correspondence in its formulation, it can sometimes show good correlation between high frequency modes and low frequency modes which is called Spatial Aliasing.

There are some works in the literature that consider the effect of eigenfrequency in the correlations. Fotsch and Ewins changed the way of presenting MAC in order to consider the eigenfrequency [2], and Philips and Allemang presented a correlation metric,  $p_w$ MAC, in which state vectors are used instead of eigenvectors [3] in discrete time systems. By using this correlation metric, distinguishing between the modes with similar eigenvectors but with different eigenvalues is possible, but there is still some problem with distinguishing between the modes with close eigenvalues and similar eigenvectors but with different contribution to the output.

In the following we present new correlations metrics that are based on the observability matrix columns instead of eigenvectors only.

---

V. Yaghoubi (✉) • T. Abrahamsson

Department of Applied Mechanics, Chalmers University of Technology, SE-41296 Gothenburg, Sweden  
e-mail: [yaghoubi@chalmers.se](mailto:yaghoubi@chalmers.se); [thomas.abrahamsson@chalmers.se](mailto:thomas.abrahamsson@chalmers.se)

## 47.2 Theoretical Background

for a linear and time-invariant (LTI) system the state-space model in continuous time can be written as:

$$\dot{x} = \mathbf{A}x(t) + \mathbf{B}u(t), y(t) = \mathbf{C}x(t) + \mathbf{D}u(t) \quad (47.2)$$

Where  $x$  is the  $n$ -dimensional state vector,  $\mathbf{A} \in \mathfrak{R}^{n \times n}$ ,  $\mathbf{B} \in \mathfrak{R}^{n \times m}$ ,  $\mathbf{C} \in \mathfrak{R}^{p \times n}$  and  $\mathbf{D} \in \mathfrak{R}^{p \times m}$ ,  $u$  is the  $m$ -dimensional excitation vector and  $y$  is the  $p$ -dimensional response vector of the system.

The state variables in  $x$  can be linearly transformed according to  $\bar{x}$  :, which state-space matrices pertinent to the transformed coordinate presented in the following

$$\bar{\mathbf{A}} = \mathbf{T}^{-1}\mathbf{A}\mathbf{T}, \bar{\mathbf{B}} = \mathbf{T}^{-1}\mathbf{B}, \bar{\mathbf{C}} = \mathbf{C}\mathbf{T}, \bar{\mathbf{D}} = \mathbf{D} \quad (47.3)$$

Diagonalizing any state-space representation is accomplished by means of a particular similarity transformation specified by the eigenvectors of the state transition matrix  $\mathbf{A}$ . An eigenvector of the square matrix  $\mathbf{A}$  is any vector  $\psi_i$  for which

$$\mathbf{A}\psi_i = \lambda_i \psi_i \quad (47.4)$$

where the eigenvalue  $\lambda_i$  may be complex. In other words, when the matrix  $\mathbf{T}$  of the similarity transformation is composed of the eigenvectors of  $\mathbf{A}$ ,

$$\mathbf{T} = [\psi_1 \dots \psi_n], \quad (47.5)$$

so,

$$\mathbf{A}\mathbf{T} = \mathbf{T}\mathbf{\Lambda}, \quad (47.6)$$

where

$$\mathbf{\Lambda} = \text{diag}(\lambda_1, \lambda_2, \dots, \lambda_n). \quad (47.7)$$

the transformed system will be diagonalized

$$\bar{\mathbf{A}} = \mathbf{T}^{-1}\mathbf{A}\mathbf{T} = \mathbf{T}^{-1}\mathbf{T}\mathbf{\Lambda} = \mathbf{\Lambda} \quad (47.8)$$

Here the diagonal matrix  $\bar{\mathbf{A}}$  having the (complex) eigenvalues of  $\mathbf{A}$  along the diagonal. With the notation of Eq. (47.3),  $\bar{\mathbf{B}}$ ,  $\bar{\mathbf{C}}$  and  $\bar{\mathbf{D}}$  can be easily found. The quadruple  $\{\bar{\mathbf{A}}, \bar{\mathbf{B}}, \bar{\mathbf{C}}, \bar{\mathbf{D}}\}$ , is called diagonal state-space representation. In particular we note that the  $i$ th column of  $\bar{\mathbf{C}}$  is  $\mathbf{C}\psi_i$  which we note being the eigenvector of  $\mathbf{A}$  as projected to the output  $y$ .

## 47.3 Observability Matrix

In experimental modal analysis test setup, the observability of the modal states plays an important role. The observability deals with the possibility to determine the internal states by the knowledge of the selected system outputs  $y$ . A system is said to be observable if, for any possible sequence of states, the current state can be determined in finite time using only information about the outputs. It has been proven that an LTI system is fully observable if the observability matrix  $\mathbf{O}$  has full rank. The observability matrix is formed by the  $\mathbf{A}$  and  $\mathbf{C}$  matrices of the state-space representation as

$$\mathbf{O} = \begin{bmatrix} \mathbf{C} \\ \mathbf{C}\mathbf{A} \\ \mathbf{C}\mathbf{A}^2 \\ \dots \\ \mathbf{C}\mathbf{A}^{n-1} \end{bmatrix} \quad (47.9)$$

It can be seen that the system order  $n$  is part of the observability matrix. The counterpart to observability is the complete state controllability which describe the ability of an external input to move the internal state of a system from any initial state to any other final state in a finite time interval. A system said to be controllable if and only if the system states can be changed arbitrarily by a finite system input. The controllability matrix  $\mathbf{C}$  is defined as

$$\mathbf{C} = [\mathbf{B}\mathbf{A}\mathbf{B}\mathbf{A}^2\mathbf{B} \dots \mathbf{A}^{n-1}\mathbf{B}] \quad (47.10)$$

An LTI system will be controllable if the controllability matrix  $C$  has full rank, i.e.  $\text{rank}(C) = n$ . A balanced realization is characterized by certain symmetry between controllability and observability and is obtained when the state observability and state controllability are equal in a sense. Equality is obtained for a state-space system if the controllability and observability grammians  $W_c$  and  $W_o$  are equal and diagonal. These are

$$W_c = \int_0^{\infty} e^{At} B B^T e^{A^T t} dt \quad (47.11)$$

$$W_o = \int_0^{\infty} e^{A^T t} C^T C e^{At} dt \quad (47.12)$$

When these are equal and diagonal we have

$$W_c = W_o = \Sigma = \text{diag}(\sigma_1, \sigma_2, \dots, \sigma_n) \quad (47.13)$$

in which  $\sigma_i, i = 1, 2, \dots, n$  are called the Hankel singular values. These values are usually put in descending order, i.e.  $\sigma_1 \geq \sigma_2 \geq \dots \geq \sigma_n$ . The Hankel singular values are used as measures that determine how much the system's input-output relation is affected by the corresponding state [4–6]. All controllable and observable systems can be transformed to balanced form by means of a basis change  $\hat{x} = Tx$ , in which  $T$  is the proper non-singular transformation matrix. By the use of Eq. (47.3), any given triple  $\{A, B, C\}$  will be transformed to the triple  $\{\bar{A}, \bar{B}, \bar{C}\}$  that is called the balanced realization.

In our work we bring all realizations to a diagonal balanced form. We do that in sequence such that we first bring it to the decoupled diagonal form. All diagonal states are then individually brought to a balanced form which brings us to the resulting diagonally or modally balanced realization. By that sequence of operations we note that we fix the realization. In particular we note that the columns of  $\bar{C}$  are fixed. Let  $T_1$  be the similarity transformation matrix of the diagonalizing operation and  $T_2$  the diagonal similarity transformation matrix of the balancing operation. Then we have

$$\bar{C} = C T_1 T_2 \quad (47.14)$$

In particular we note that for this matrix, the  $i$ th column being  $C \Psi_i T_2$ , which we see is a projection of the  $i$ th eigenvector of  $A$ . By that we also note that the  $i$ th column  $\mathcal{O}_i$  of the observability matrix becomes

$$\mathcal{O}_i = \begin{bmatrix} C \Psi_i T_2^i \\ C \Psi_i T_2^{ii} \lambda_i \\ C \Psi_i T_2^{ii} \lambda_i^2 \\ \dots \\ C \Psi_i T_2^{ii} \lambda_i^{n-1} \end{bmatrix} \quad (47.15)$$

and thus each column of  $\mathcal{O}$  is associated to quantities of one single eigenmode only.  $T_2^{ii}$  is the  $i$ th diagonal element of  $T_2$ . It should be noted that this modal correlation is only for discrete time systems. For continuous time systems their eigenvalues or matrix  $A$  should be transformed to the discrete form using Eq. (47.16).

$$\lambda_{\text{disc}} = \exp(\lambda_{\text{cont}} \cdot T) \quad (47.16)$$

where  $T$  is arbitrary but ideally is found using Eq. (47.17) to maximize the spread of the discrete time system's eigenvalues within the complex plane unit disc.

$$\max(\text{Im}(\tilde{i})) \cdot T = \pi \quad (47.17)$$

#### 47.4 Modal Observability Correlation

To make the problem of distinguishing between eigenvectors smaller, a new correlation metric based on the observability matrix of the diagonal state-space realization is proposed. We call this metric the Basic Modal Observability Correlation or *bMOC* in short. For this metric we use the columns of the observability matrix of the balanced diagonal realization that we

denote  $\mathcal{O}^{bd}$ . With  $\mathcal{O}_i^{bd}$  being the  $i$ th column of this matrix we define the  $bMOC$  metric between the  $i$ th and  $j$ th columns of the observability matrix to be

$$bMOC_{ij} = |\{\mathcal{O}_i^{bd}\}^H \{\mathcal{O}_j^{bd}\}|^2 / (\{\mathcal{O}_i^{bd}\}^H \{\mathcal{O}_i^{bd}\} \{\mathcal{O}_j^{bd}\}^H \{\mathcal{O}_j^{bd}\}) \quad (47.18)$$

Where  $i$ th and  $j$ th columns of  $\mathcal{O}^{bd}$  relate to the corresponding eigenvectors that are weighted with their associated eigenvalues to increasing power order. A further distinction between modes can be obtained if we use the scaling property of the balanced realization. We note that the controllability and observability balancing of the states makes the columns of the observability matrix fixed. This means that for a modal state that contributes little to the input-output relation, the norm of the corresponding column of the observability matrix is low since the corresponding Hankel singular value is low. On the contrary, for a modal state which contributes much to the input-output relation, the corresponding column norm is large. We use this property to further distinguish between states which have close eigenvalues and similar eigenvectors but that have strong dissimilarities in the input-output contribution to form an enhanced version of the  $bMOC$ , the scaled MOC. This correlation metric was evaluated in a new, autonomous modal identification method [7–9]. We define this to be

$$MOC_{ij} = |\{\mathcal{O}_i^{bd}\}^H \{\mathcal{O}_j^{bd}\}|^2 / \max(\{\mathcal{O}_i^{bd}\}^H \{\mathcal{O}_i^{bd}\}, \{\mathcal{O}_j^{bd}\}^H \{\mathcal{O}_j^{bd}\})^2 \quad (47.19)$$

## 47.5 Case Study

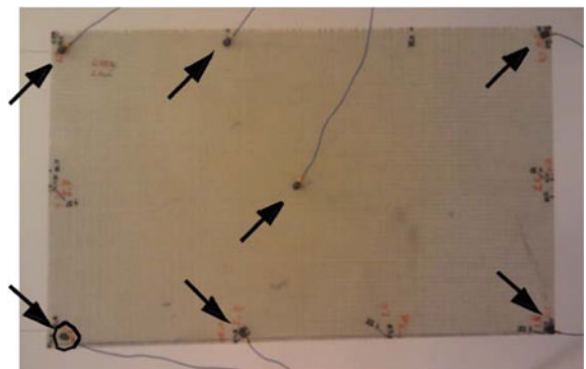
We studied two cases, one case is the data obtained from a Composite Plate and another one is the test data of a Dryer Cabinet. Data for dryer was provided as Round Robin test data at the IMAC XXVII conference in 2009. In the following correlation presentation, the eigenmodes have been arranged in increasing eigenfrequency order.

### 47.5.1 Composite Plate

A composite plate with the dimension of  $540 \times 320 \times 1$  mm with one input and seven outputs was studied. The seven accelerometer sensors and the single actuator were placed as shown in the Fig. 47.1 with sensing and actuation normal to the plate's surface.

The mode sets are from two system identification runs on same data with different identification parameter settings. Figure 47.2 indicates the auto-correlation between the modes and Fig. 47.3 illustrates the cross-correlation between the modes. It can be seen in Fig. 47.3a that eigenmodes 15 and 16 of one set that are related to close eigenvalues makes it hard to distinguish between them from modes of close eigenvalues of modes 14 and 15 of the other set using the MAC correlation metric. Using the same data as before, by augmenting the eigenvectors with the corresponding eigenvalues in the  $bMOC$ , we see in comparison with Fig. 47.3a, the cross-correlation between modes in Fig. 47.3b drop significantly for this correlation metric. However, a further distinction between modes can be obtained if we use the scaling property of the balanced realization, MOC, which is presented in Fig. 47.3c.

**Fig. 47.1** Glass-fibre/epoxy composite plate of  $L \times B \times t = 540 \times 320 \times 1$  mm equipped with accelerometers (at arrows) in laboratory setup. The location of excitation, coincident with one accelerometer, is indicated with a circle. The plate weight is 0.711 kg and it has 30 mm skewness as measured from planar surface to free corner with tree corners fixed to a plane



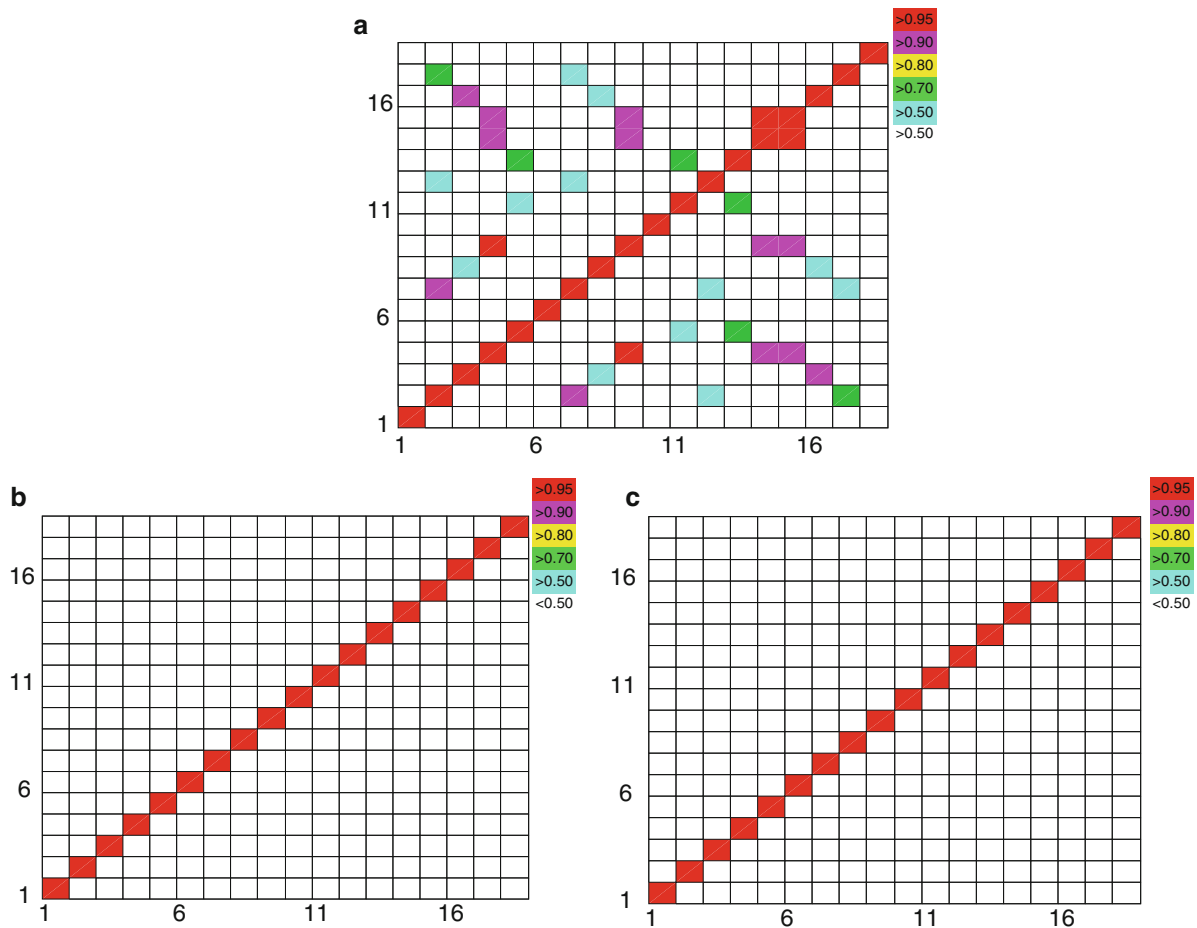


Fig. 47.2 Auto-Correlation between the modes in Composite plate using (a) autoMAC, (b) autobMOC, (c) autoMOC

### 47.5.2 Dryer

The dryer data is from a test of residential clothes dryer cabinet, Fig. 47.4. The data set contains FRFs from 4 uncorrelated references and 300 response FRFs. Four shakers were used to excite the cabinet (burst random) for the MIMO test. The shaker locations were such that the cabinet was excited relatively uniformly. The shakers were placed one on each side (right, left and back) and one shaker on the base.

The response locations were spread uniformly over the base on a grid size of approximately 3.5". The force and acceleration measurements at the shaker locations were made with PCB 288D01 impedance heads. A Polytec laser was used to measure the response at the locations on the side and back panels of the cabinet. All 300 responses measurements were normal to the panel surfaces, see reference [10]

The mode sets are from two system identification runs on same data with different identification parameter settings. Figure 47.5 displays the auto-correlation between the modes and Fig. 47.6 presents the cross-correlation between the modes in dryer cabinet.

## 47.6 Discussion

In the autoMACs (Figs. 47.2a and 47.5a), there are several non-negligible off-diagonal terms that indicate Spatial aliasing. By using autobMOC most of these off-diagonal terms were diminished (Figs. 47.2b and 47.5b) but, since some modes in our model have very close eigenvalues and similar eigenvectors, some high cross-correlation still exist.



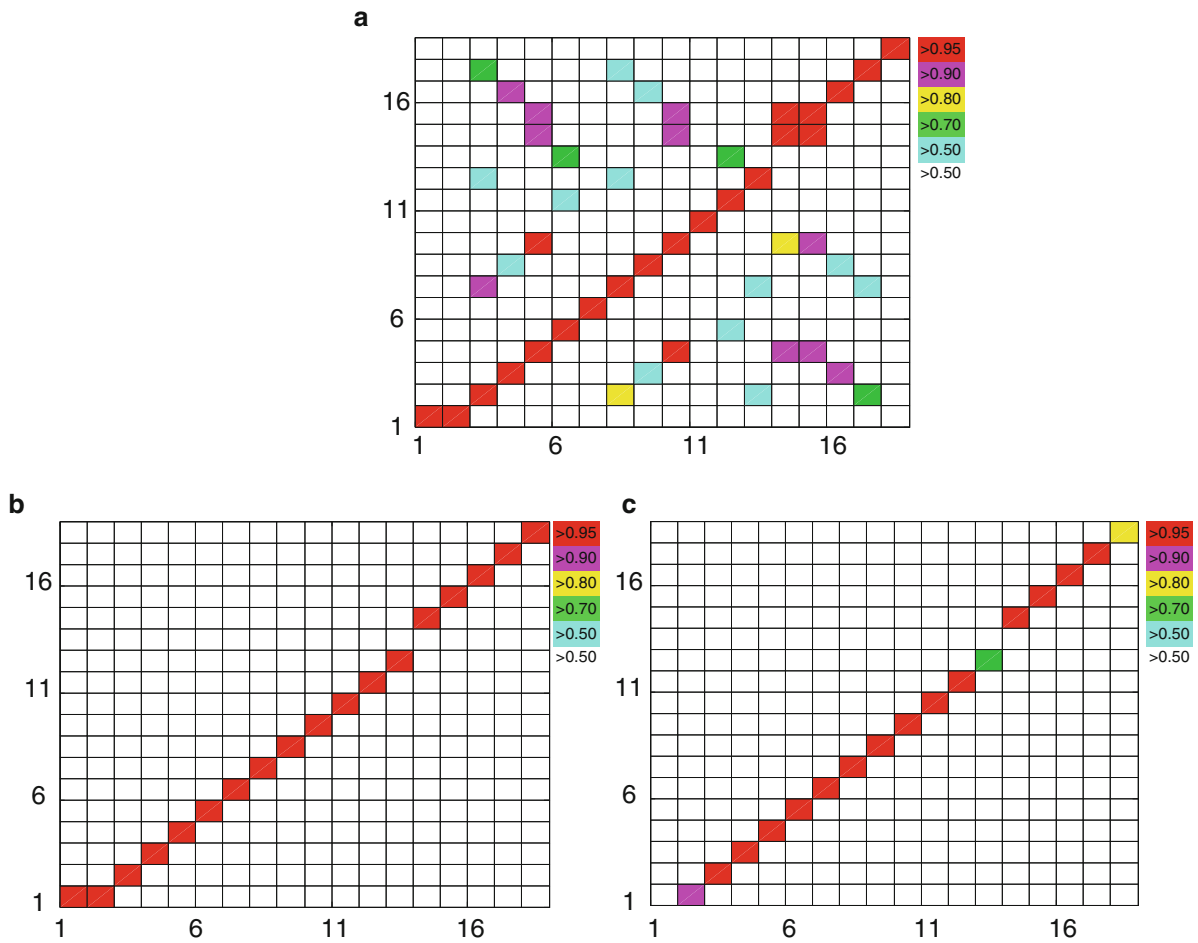


**Fig. 47.3** Cross-Correlation between the modes in Composite plate using (a) MAC, (b) bMOC, (c) MOC

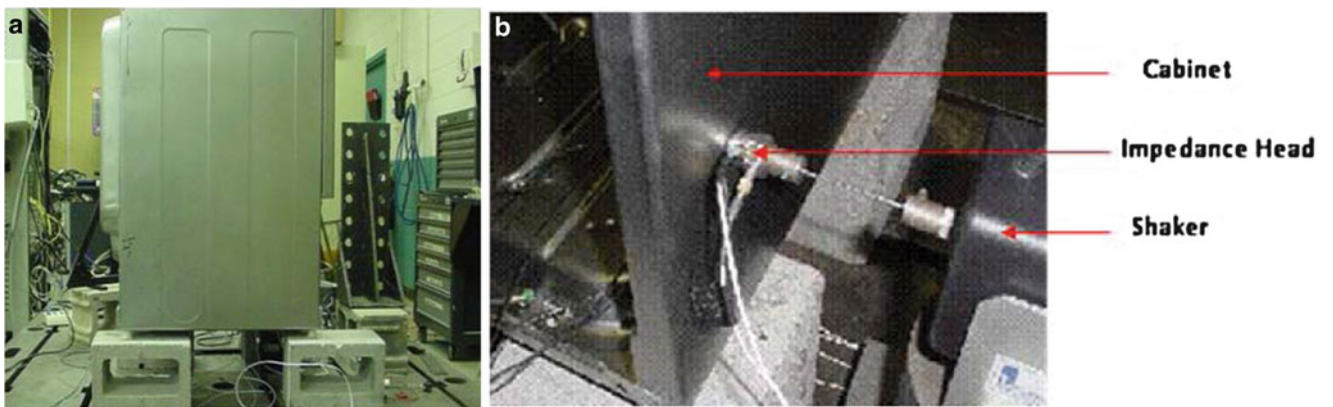


**Fig. 47.4** (a) Dryer cabinet, (b) installation of shaker on the cabinet [10]

As it was shown in Figs. 47.3a and 47.6a, in cross MAC analysis there are many large off-diagonal terms that can be due to spatial aliasing or to genuine correspondence of various modes involved i.e. close eigenvalues or similar eigenvectors; by using bMOC the prementioned reasons for large off-diagonal terms were removed partly (Figs. 47.3b and 47.6b). But there is still some problems with distinguishing the modes with similar eigenvalues and similar eigenvectors but with

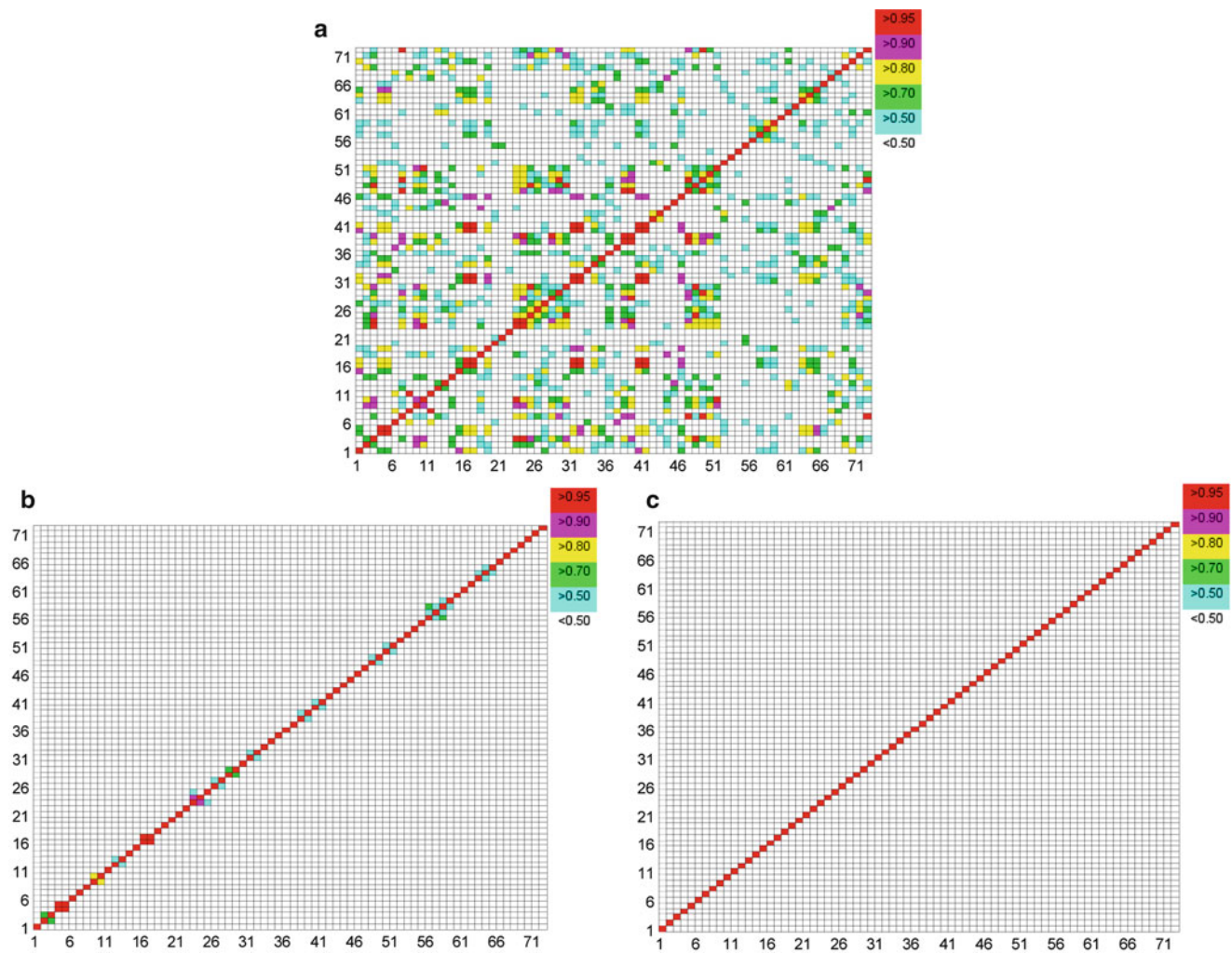


**Fig. 47.5** Auto-Correlation between the modes in Dryer using (a) autoMAC, (b) autobMOC, (c) autoMOC

different contribution to the input-output (I/O) relations that the MAC and bMOC correlation analysis cannot distinguish. By introducing the concept of contribution of each mode in the input-output (I/O) relation in MOC, two modes are called highly correlated to each other if besides having close eigenvalues and similar eigenvectors; they have almost the same contribution in the I/O relation, on the other hand, only the modes that are similar in all aspects, namely eigenvalue, eigenvector and I/O contribution, correlate to each other to high degree (Figs. 47.3c and 47.6c). Therefore, the autoMOC matrix is very likely to be almost diagonal with some very small off-diagonal terms (Figs. 47.2c and 47.5c).

## 47.7 Conclusion

In this paper, two new methods for correlating modes were presented. Besides utilizing eigenvectors and eigenvalues to find correlation between the modes, the effect of contribution of each mode in the input-output relation in correlating modes was introduced. It was shown that by using this effect, only the modes that are very close to each other in all eigenvalue, eigenvector and I/O contribution give have high degree of correlation.

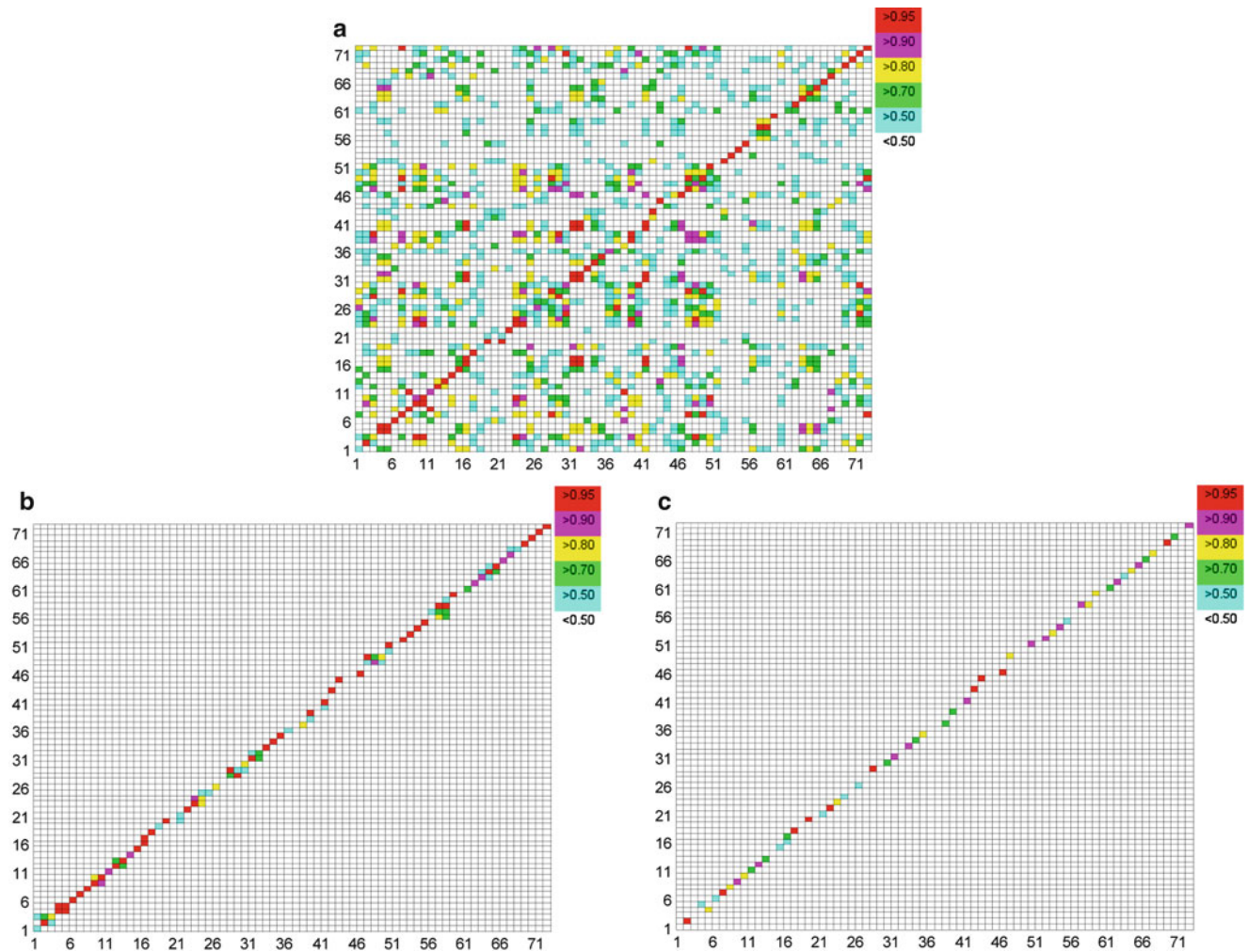


**Fig. 47.6** Cross-Correlation between the modes in Dryer using (a) MAC, (b) bMOC, (c) MOC

## References

1. Allemang RJ (2002) The modal assurance criterion (MAC) – twenty years of use and abuse. In: International modal analysis conference (IMAC XX), Los Angeles, CA, USA
2. Fotsch D, Ewins DJ (2000) Application of MAC in the frequency domain. In: SEM (ed) Proceedings of the international modal analysis conference – IMAC, vol. 2, San Antonio, TX
3. Phillips AW, Allemang RJ (2005) Data presentation schemes for selection and identification of modal parameters. In: International modal analysis conference (IMAC XXIII), Orlando, FL
4. Poonam J. Patil, Mukesh D. Patil (2011) Model order reduction of high order LTI system using balanced truncation approximation. In: International conference on process automation, control and computing (PACC), Coimbatore, India
5. Moore BC (1981) Principal component analysis in Linear system: Controllability, Observability, and Model reduction. *IEEE Trans Autom Control* 26:17–32
6. Moore K (1984) All optimal Hankel norm approximations of linear multivariable systems and their  $L_\infty$  error bound. *Int J Control* 39:1115–1193
7. Yaghoubi V, Abrahamsson T (2012) Automated modal analysis based on frequency response function estimates. In: International modal analysis conference (IMAC XXX), Orlando, FL
8. Yaghoubi V, Abrahamsson T (2013) Automated modal analysis based on statistical evaluation of frequency responses. In: International modal analysis conference, Los Angeles, CA
9. Yaghoubi V, Khorsand Vakilzadeh M, Abrahamsson T (2012) Application of an automated modal analysis based on frequency response function estimates. In: International conference on noise and vibration engineering, Leuven, Belgium
10. [http://www.me.mtu.edu/imac\\_mpe/Dryer%20Data%20Description.htm](http://www.me.mtu.edu/imac_mpe/Dryer%20Data%20Description.htm)

# Chapter 48

## A Modal Test Method Based on Vibro-acoustical Reciprocity

W.D. Zhu, J.M. Liu, Y.F. Xu, and H.Q. Ying

**Abstract** A modal test method that uses sound pressure transducers at fixed locations and an impact hammer roving over a test structure is developed in this work. Since sound pressure transducers are used, the current method deals with a coupled structural-acoustic system. Based on the vibro-acoustic reciprocity, the method is equivalent to the one, where acoustic excitations at fixed locations are given and the resulting acceleration of the test structure is measured. The current method can eliminate mass loading due to the use of accelerometers, which can destroy the existence of repeated or close natural frequencies of a symmetric structure, avoid the effects of a nodal line of a mode and an inactive area of a local mode, and measure all the out-of-plane modes within a frequency range of interest, including global and local ones. The coupling between the structure and the acoustic field in a structural-acoustic system introduces asymmetry in the model formulation. An equivalent state space formulation is used for a structurally damped structural-acoustic system and the associated eigenvalue problem is derived. The biorthonormality relations between the left and right eigenvectors and the relations between the structural and acoustic components in the left and right eigenvectors are proved. The frequency response functions associated with the current method are derived and their physical meanings are explained. The guidelines for using the current method, including the types of structures that are suitable for the method, the positions of the sound pressure transducers, and the orientation of the test structure relative to the transducers, are provided. Modal tests were carried out on an automotive disk brake using the traditional and current methods, where multiple accelerometers and microphones were used to measure its dynamic responses induced by impacts, respectively. The measured natural frequencies and mode shapes by the two methods are almost the same. The differences between the measured natural frequencies using the current method and those from the finite element model of the disk brake are less than 3% for the first 18 elastic modes, and the modal assurance criterion values of the associated mode shapes are all above 90%.

**Keywords** Vibro-acoustic modal test • Vibro-acoustic reciprocity • Experimental modal analysis • Symmetric structure • Model validation

---

W.D. Zhu (✉)

Professor, Department of Mechanical Engineering, University of Maryland, Baltimore County, Baltimore, MD 21250, USA  
e-mail: [wzhu@umbc.edu](mailto:wzhu@umbc.edu)

J.M. Liu

Research Scientist, China Orient Institute of Noise and Vibration, Beijing 100085, China  
e-mail: [jhgo1965@yahoo.com.cn](mailto:jhgo1965@yahoo.com.cn)

Y.F. Xu

Graduate Assistant, Department of Mechanical Engineering, University of Maryland, Baltimore County, Baltimore, MD 21250, USA  
e-mail: [yxu2@umbc.edu](mailto:yxu2@umbc.edu)

H.Q. Ying

Professor, China Orient Institute of Noise and Vibration, Beijing 100085, China  
e-mail: [dasp@coinv.com.cn](mailto:dasp@coinv.com.cn)

## 48.1 Introduction

Experimental modal analysis (EMA) is one of the standard experimental approaches to validate the finite element (FE) model of a structure, where the input to the test structure is in the form of a force and the output from the structure a displacement, velocity, or acceleration response [1, 2]. When the roving hammer technique is used in EMA, a measurement point is fixed on the test structure and an impact hammer roves over the structure. The location of the measurement point is crucial since some mode may not be captured in the test if the measurement point lies on a nodal line of a mode [3] or in an inactive area of a local mode. In order to mitigate the problem, EMA can be conducted using multiple measurement points at different locations. However, it can be difficult to find the proper locations for the measurement points at which all the modes of interest can be captured unless an accurate FE model of the structure is available, providing accurate mode shape information. On the other hand, mass loading due to the use of multiple sensors on the test structure can affect the accuracy of measurement [4], especially for a symmetric structure, whose repeated or close natural frequencies can be destroyed. A laser vibrometer can be used to avoid mass loading in EMA, but it may not be available in many laboratories. Another critical aspect of EMA is the excitation method. A shaker can be connected to the test structure to generate a prescribed excitation force, but the response measurements, especially in the neighborhoods of resonant frequencies, can have low signal-to-noise ratios due to impedance mismatch between the shaker and the test structure [5]. An impact hammer can be used in EMA, but the sensors attached on the structure far away from the excitation point may not capture much vibration. While acoustic excitation can excite the surface of the test structure, it is difficult to measure the acoustic excitation on the surface of the structure. An acoustic modal analysis method was proposed in [6] to measure the modal characteristics of a structure by using an impact hammer and microphones, and the time delay due to the use of microphones was corrected [7]. However, the method does not consider the effects of the structural-acoustic coupling. When acoustic excitation or measurement is involved in a modal test, coupling exists in the corresponding structural-acoustic system, and asymmetry is introduced in the model formulation [8, 9]. As a result, left and right eigenvectors can be defined for the associated eigenvalue problem, and the relations between the structural and acoustic components in the left and right eigenvectors of an undamped coupled system were provided in [10]. The formulation of a damped structural-acoustic system was given for a closed cavity in [11].

In this work, a vibro-acoustic modal test (VMT) method is developed, where an impact hammer roves over the test structure and sound pressure transducers at fixed locations are used to measure its dynamic responses. The formulation of a structurally damped structural-acoustic system in an open environment and the associated eigenvalue problem are provided. The biorthonormality relations between the left and right eigenvectors and the relations between the structural and acoustic components of the left and right eigenvectors are proved. The frequency response functions (FRFs) used in the VMT method are derived, which contain the modal characteristics of the coupled system, and the assumptions used in the acoustic modal analysis in [6, 7] are validated. It is assumed in the VMT method that the natural frequencies and the structural components of the right eigenvectors of the coupled system can be used to approximate the natural frequencies and mode shapes of the structure. Based on the vibro-acoustic reciprocity, the VMT method is equivalent to the one, where acoustic excitation sources are used to excite the test structure and the resulting acceleration is measured, and the guidelines for using the VMT method, including the types of structures that are suitable for the method, the positions of the sound pressure transducers, and the orientation of the test structure relative to the transducers, are provided. The VMT method and EMA were carried out on an automotive disk brake and the experimental results were compared. It is experimentally shown that the VMT method can capture all the out-of-plane modes, including global and local ones, and EMA can miss certain modes. The differences between the measured natural frequencies of the first 18 elastic modes by the VMT method and EMA are less than 1% and the modal assurance criterion (MAC) values [1] of the associated modes are all above 90%. The errors between the measured natural frequencies by the VMT method and the calculated ones from the FE model are less than 3% for the first 18 elastic modes, and the associated MAC values are all above 90%.

## 48.2 Structural-Acoustic System Formulation

### 48.2.1 Eigenvalue Problem

The FE formulation of an undamped, coupled structural-acoustic system has been given in [8, 9] using a displacement-pressure model for a closed cavity. A similar FE formulation has been given in [12] for a coupled fluid-structural system, based on which the FE formulation of a coupled structural-acoustic system in an open environment can be obtained. To apply this formulation, it is assumed that the structure is totally submerged in air and the effects of the boundary of air can

be neglected, which yields the following governing equation:

$$\begin{bmatrix} M_s & 0 \\ M_c & M_a \end{bmatrix} \begin{Bmatrix} \ddot{u}_s \\ \ddot{p}_a \end{Bmatrix} + \begin{bmatrix} K_s & K_c \\ 0 & K_a \end{bmatrix} \begin{Bmatrix} u_s \\ p_a \end{Bmatrix} = \begin{Bmatrix} f_s \\ f_a \end{Bmatrix} \quad (48.1)$$

where  $u_s$  is the  $n$ -dimensional displacement vector of the structure and  $p_a$  is the  $m$ -dimensional sound pressure vector of the acoustic field;  $f_s$  is the  $n$ -dimensional structural force vector and  $f_a$  is the  $m$ -dimensional sound source in the acoustic field;  $M_s$  and  $K_s$  are the  $n \times n$  structural mass and stiffness matrices, respectively;  $M_a$  and  $K_a$  are the  $m \times m$  acoustic mass and stiffness matrices, respectively; and  $M_c$  and  $K_c$  are the coupling matrices of the system of dimensions  $m \times n$  and  $n \times m$ , respectively. Note that  $M_s$ ,  $M_a$ ,  $K_s$ , and  $K_a$  are symmetric. In Eq. (48.1), the upper and lower equations represent the structural and acoustic parts of the system, respectively. The relationship between the two coupling matrices can be expressed by [12]

$$M_c = -K_c^T \quad (48.2)$$

A similar relation between the two coupling matrices has been derived for a closed cavity [8–10]. Assume that viscous damping effects exist in the structural part in Eq. (48.1) and those in the acoustic part can be neglected; no coupling exists between the structural and acoustic damping [13]. Adding structural damping to Eq. (48.1) yields

$$\begin{bmatrix} M_s & 0 \\ M_c & M_a \end{bmatrix} \begin{Bmatrix} \ddot{u}_s \\ \ddot{p}_a \end{Bmatrix} + \begin{bmatrix} C_s & 0 \\ 0 & 0 \end{bmatrix} \begin{Bmatrix} \dot{u}_s \\ \dot{p}_a \end{Bmatrix} + \begin{bmatrix} K_s & K_c \\ 0 & K_a \end{bmatrix} \begin{Bmatrix} u_s \\ p_a \end{Bmatrix} = \begin{Bmatrix} f_s \\ f_a \end{Bmatrix} \quad (48.3)$$

where  $C_s$  is the symmetric structural damping matrix of dimensions  $n \times n$ . In order to determine the natural frequencies and mode shapes of the structural-acoustic system, it is assumed that the system has no excitation, which yields the following equation:

$$\begin{bmatrix} M_s & 0 \\ M_c & M_a \end{bmatrix} \begin{Bmatrix} \ddot{u}_s \\ \ddot{p}_a \end{Bmatrix} + \begin{bmatrix} C_s & 0 \\ 0 & 0 \end{bmatrix} \begin{Bmatrix} \dot{u}_s \\ \dot{p}_a \end{Bmatrix} + \begin{bmatrix} K_s & K_c \\ 0 & K_a \end{bmatrix} \begin{Bmatrix} u_s \\ p_a \end{Bmatrix} = \begin{Bmatrix} 0 \\ 0 \end{Bmatrix} \quad (48.4)$$

Due to the coupling between the structure and the acoustic field, it is difficult to directly solve Eq. (48.4). Let

$$\tilde{M} = \begin{bmatrix} M_s & 0 \\ M_c & M_a \end{bmatrix}, \tilde{C} = \begin{bmatrix} C_s & 0 \\ 0 & 0 \end{bmatrix}, \tilde{K} = \begin{bmatrix} K_s & K_c \\ 0 & K_a \end{bmatrix}, y = \begin{Bmatrix} u_s \\ p_a \end{Bmatrix} \quad (48.5)$$

Equation (48.4) can be written in an equivalent state space form:

$$\begin{bmatrix} -\tilde{K} & 0 \\ 0 & \tilde{M} \end{bmatrix} \begin{Bmatrix} \dot{y} \\ \ddot{y} \end{Bmatrix} + \begin{bmatrix} 0 & \tilde{K} \\ \tilde{K} & \tilde{C} \end{bmatrix} \begin{Bmatrix} y \\ \dot{y} \end{Bmatrix} = \begin{Bmatrix} 0 \\ 0 \end{Bmatrix} \quad (48.6)$$

The solution to Eq. (48.6) is assumed in the form

$$\begin{Bmatrix} y \\ \dot{y} \end{Bmatrix} = \begin{Bmatrix} v e^{\lambda t} \\ \lambda v e^{\lambda t} \end{Bmatrix} \quad (48.7)$$

where  $\lambda$  is an undetermined constant and  $v$  is an  $(n + m)$ -dimensional vector. Let

$$\eta = \begin{Bmatrix} v \\ \lambda v \end{Bmatrix} \quad (48.8)$$

and the following expressions can be obtained:

$$\begin{Bmatrix} y \\ \dot{y} \end{Bmatrix} = \eta e^{\lambda t}, \begin{Bmatrix} \dot{y} \\ \ddot{y} \end{Bmatrix} = \lambda \eta e^{\lambda t} \quad (48.9)$$

Substituting Eq. (48.9) into Eq. (48.6) and canceling  $e^{\lambda t}$  yield

$$\lambda \begin{bmatrix} -\tilde{K} & 0 \\ 0 & \tilde{M} \end{bmatrix} \eta + \begin{bmatrix} 0 & \tilde{K} \\ \tilde{K} & \tilde{C} \end{bmatrix} \eta = \begin{Bmatrix} 0 \\ 0 \end{Bmatrix} \quad (48.10)$$

Let

$$S = \begin{bmatrix} -\tilde{K} & 0 \\ 0 & \tilde{M} \end{bmatrix}, R = \begin{bmatrix} 0 & \tilde{K} \\ \tilde{K} & C \end{bmatrix} \quad (48.11)$$

and Eq. (48.10) can be written as a generalized eigenvalue problem associated with the structural-acoustic system:

$$(\lambda S + R) \eta = 0 \quad (48.12)$$

Due to asymmetry of the matrices  $S$  and  $R$ , there exist right and left eigenvectors of the eigenvalue problem in Eq. (48.12). Let  $\eta_i^r$  be the right eigenvector corresponding to the eigenvalue  $\lambda_i$  of the eigenvalue problem in Eq. (48.12), which satisfies

$$(\lambda_i S + R) \eta_i^r = 0 \quad (48.13)$$

The left eigenvector  $\eta_j^l$  satisfies

$$\eta_j^{lT} (\lambda_j S + R) = 0 \quad (48.14)$$

where the superscript  $T$  denotes the transpose of a matrix, or

$$(\lambda_j S^T + R^T) \eta_j^l = 0 \quad (48.15)$$

It is assumed that all the eigenvalues of the eigenvalue problem in Eq. (48.12) are distinct. Note that while the eigenvalues in Eqs. (48.13) and (48.14) are the same, the corresponding left and right eigenvectors are not the same [14]. Pre-multiplying Eq. (48.13) by  $\eta_j^{lT}$  yields

$$\eta_j^{lT} (\lambda_i S + R) \eta_i^r = 0 \quad (48.16)$$

Post-multiplying Eq. (48.14) by  $\eta_i^r$  yields

$$\eta_j^{lT} (\lambda_j S + R) \eta_i^r = 0 \quad (48.17)$$

Subtracting Eq. (48.17) from Eq. (48.16) yields

$$(\lambda_i - \lambda_j) \eta_j^{lT} S \eta_i^r = 0 \quad (48.18)$$

If  $i \neq j$ , since all the eigenvalues are distinct, by Eq. (48.18), one has

$$\eta_j^{lT} S \eta_i^r = 0 \quad (48.19)$$

Substituting Eq. (48.19) into Eq. (48.16) yields

$$\eta_j^{lT} R \eta_i^r = 0 \quad (48.20)$$

When  $i = j$ , the right and left eigenvectors can be normalized as follows:

$$\eta_i^{lT} S \eta_i^r = 1 \quad (48.21)$$

Using Eq. (48.21) in Eq. (48.16) yields

$$\eta_i^{lT} R \eta_i^r = -\lambda_i \quad (48.22)$$

Equations (48.19)–(48.22) are the biorthonormality relations between the left and right eigenvectors of the system.

Assuming that the structural and acoustic components in the left eigenvector  $\eta_i^l$ , which are  $\phi_{si}^l$  and  $\phi_{ai}^l$ , respectively, can be related to those in the right eigenvector  $\eta_i^r$ , which are  $\phi_{si}^r$  and  $\phi_{ai}^r$ , respectively:

$$\phi_{si}^l = a \phi_{si}^r, \phi_{ai}^l = b \phi_{ai}^r \quad (48.23)$$

then the left eigenvector  $\eta_i^l$  can be expressed by

$$\eta_i^l = \begin{Bmatrix} \phi_{si}^l \\ \phi_{ai}^l \\ \lambda_i \phi_{si}^l \\ \lambda_i \phi_{ai}^l \end{Bmatrix} = \begin{Bmatrix} a \phi_{si}^r \\ b \phi_{ai}^r \\ \lambda_i a \phi_{si}^r \\ \lambda_i b \phi_{ai}^r \end{Bmatrix} \quad (48.24)$$

Substituting Eq. (48.24) into Eq. (48.14) yields

$$\begin{cases} -a\phi_{si}^{rT}\lambda_i K_s + a\phi_{si}^{rT}\lambda_i K_s = 0 \\ -a\phi_{si}^{rT}\lambda_i K_c - b\phi_{ai}^{rT}\lambda_i K_s + a\phi_{si}^{rT}\lambda_i K_c + b\phi_{ai}^{rT}\lambda_i K_s = 0 \\ a\phi_{si}^{rT}K_s + a\phi_{si}^{rT}\lambda_i(\lambda_i M_s + C_s) + b\phi_{ai}^{rT}\lambda_i^2 M_c = 0 \\ a\phi_{si}^{rT}K_c + b\phi_{ai}^{rT}K_a + b\phi_{ai}^{rT}\lambda_i^2 M_a = 0 \end{cases} \quad (48.25)$$

Since the first two equations in Eq. (48.25) are identically satisfied, Eq. (48.25) becomes

$$\begin{cases} a\phi_{si}^{rT}K_s + a\phi_{si}^{rT}\lambda_i(\lambda_i M_s + C_s) + b\phi_{ai}^{rT}\lambda_i^2 M_c = 0 \\ a\phi_{si}^{rT}K_c + b\phi_{ai}^{rT}K_a + b\phi_{ai}^{rT}\lambda_i^2 M_a = 0 \end{cases} \quad (48.26)$$

Due to symmetry of  $K_s$ ,  $K_a$ ,  $M_s$ , and  $M_a$ , taking the transpose of Eq. (48.26) and using Eq. (48.2) in the resulting expressions yield

$$\begin{cases} aK_s\phi_{si}^r + a\lambda_i(\lambda_i M_s + C_s)\phi_{si}^r - b\lambda_i^2 K_c\phi_{ai}^r = 0 \\ -aM_c\phi_{si}^r + bK_a\phi_{ai}^r + b\lambda_i^2 M_a\phi_{ai}^r = 0 \end{cases} \quad (48.27)$$

Expanding Eq. (48.13) using Eqs. (48.8) and (48.11) yields

$$\begin{cases} -\lambda_i K_s\phi_{si}^r - \lambda_i K_c\phi_{ai}^r + \lambda_i K_s\phi_{si}^r + \lambda_i K_c\phi_{ai}^r = 0 \\ -\lambda_i K_a\phi_{si}^r + \lambda_i K_a\phi_{si}^r = 0 \\ K_s\phi_{si}^r + K_c\phi_{ai}^r + \lambda_i(\lambda_i M_s + C_s)\phi_{si}^r = 0 \\ K_a\phi_{ai}^r + \lambda_i^2 M_c\phi_{si}^r + \lambda_i^2 M_a\phi_{ai}^r = 0 \end{cases} \quad (48.28)$$

Since the first two equations in Eq. (48.28) are identically satisfied, Eq. (48.28) becomes

$$\begin{cases} K_s\phi_{si}^r + K_c\phi_{ai}^r + \lambda_i(\lambda_i M_s + C_s)\phi_{si}^r = 0 \\ K_a\phi_{ai}^r + \lambda_i^2 M_c\phi_{si}^r + \lambda_i^2 M_a\phi_{ai}^r = 0 \end{cases} \quad (48.29)$$

Comparing Eqs. (48.27) and (48.29), one has  $a = \kappa$  and  $b = -\frac{\kappa}{\lambda_i^2}$ , where  $\kappa$  can be any non-zero constant. Hence, by Eq. (48.24), the left eigenvector  $\eta_i^l$  can be expressed by

$$\eta_i^l = \begin{Bmatrix} \phi_{si}^l \\ \phi_{ai}^l \\ \lambda_i\phi_{si}^l \\ \lambda_i\phi_{ai}^l \end{Bmatrix} = \kappa \begin{Bmatrix} \phi_{si}^r \\ -\frac{1}{\lambda_i^2}\phi_{ai}^r \\ \lambda_i\phi_{si}^r \\ -\frac{1}{\lambda_i}\phi_{ai}^r \end{Bmatrix} \quad (48.30)$$

For the convenience of discussion, let  $\kappa = 1$ , and one can obtain from Eq. (48.30) the relation between the structural components of the left and right eigenvectors:

$$\phi_{si}^l = \phi_{si}^r \quad (48.31)$$

and that between the acoustic components:

$$\phi_{ai}^l = -\frac{1}{\lambda_i^2}\phi_{ai}^r \quad (48.32)$$



### 48.2.2 FRFs

A sinusoidal force  $F e^{i\omega t}$  with frequency  $\omega$  is applied on the structural part of the system described by Eq. (48.12), where  $F = \{F_s^T \ 0^T\}^T$  is an  $(n + m)$ -dimensional vector, in which  $F_s = \{f_{s1} \ f_{s2} \ \dots \ f_{sn}\}^T$  is an  $n$ -dimensional structural force vector. Assuming a harmonic response of the system with frequency  $\omega$  and canceling  $e^{i\omega t}$  yield

$$(R + i\omega S) \eta = \begin{Bmatrix} 0 \\ F \end{Bmatrix} \quad (48.33)$$

A coordinate transformation is applied on  $\eta$  by letting

$$\eta = \Phi^r q \quad (48.34)$$

where  $\Phi^r = [\eta_1^r \ \dots \ \eta_{(m+n)}^r \ \eta_1^{r*} \ \dots \ \eta_{(m+n)}^{r*}]$ , in which the superscript  $*$  denotes complex conjugation, is a matrix containing the right eigenvectors, and  $q$  is a  $2 \times (n + m)$ -dimensional modal coordinate vector. Substituting Eq. (48.34) into Eq. (48.33), pre-multiplying the resulting expression by  $\Phi^{lT}$ , where  $\Phi^l = [\eta_1^l \ \dots \ \eta_{(m+n)}^l \ \eta_1^{l*} \ \dots \ \eta_{(m+n)}^{l*}]$  is a matrix containing the left eigenvectors, and applying the biorthonormality relations of the left and right eigenvectors in Eqs. (48.19)–(48.22) yield

$$\Lambda q = \Phi^{lT} \begin{Bmatrix} 0 \\ F \end{Bmatrix} \quad (48.35)$$

where  $\Lambda = \text{diag}[-\lambda_1 + i\omega, \dots, -\lambda_{m+n} + i\omega, -\lambda_1^* + i\omega, \dots, -\lambda_{m+n}^* + i\omega]$ . The modal coordinate vector  $q$  can be obtained from Eq. (48.35):

$$q = \Lambda^{-1} \Phi^{lT} \begin{Bmatrix} 0 \\ F \end{Bmatrix} \quad (48.36)$$

Substituting Eq. (48.36) into Eq. (48.34) yields

$$\eta = \Phi^r q = \Phi^r \Lambda^{-1} \Phi^{lT} \begin{Bmatrix} 0 \\ F \end{Bmatrix} \quad (48.37)$$

The ratio of the pressure  $p_{ai}$  measured at point  $i$  in the acoustic field to the applied force  $f_{sj}$  at point  $j$  on the structure is

$$\frac{p_{ai}}{f_{sj}} = \sum_{h=1}^{m+n} \left( \frac{\lambda_h \Phi_{ahi}^r \Phi_{shj}^l}{-\lambda_h + i\omega} + \frac{(\lambda_h \Phi_{ahi}^r \Phi_{shj}^l)^*}{-\lambda_h^* + i\omega} \right) \quad (48.38)$$

Using Eq. (48.31) in Eq. (48.38) yields

$$\frac{p_{ai}}{f_{sj}} = \sum_{h=1}^{m+n} \left( \frac{\lambda_h \Phi_{ahi}^r \Phi_{shj}^l}{-\lambda_h + i\omega} + \frac{(\lambda_h \Phi_{ahi}^r \Phi_{shj}^l)^*}{-\lambda_h^* + i\omega} \right) \quad (48.39)$$

While the matrices  $\tilde{M}$  and  $\tilde{K}$  are non-symmetric, the modal characteristics of the system described by Eq. (48.3) are contained in Eqs. (48.38) and (48.39), and can be extracted from the FRFs in Eqs. (48.38) and (48.39) with the roving hammer technique using a well-developed modal analysis algorithm, such as PolyMax [18].

In the acoustic modal analysis in [6,7], it is assumed that the sound pressure linearly varies with the amplitude of vibration of the test structure at a certain frequency, which is proportional to the amplitude of excitation at an input point. Hence the sound pressure is proportional to the amplitude of excitation at the input point at a certain frequency, which can be validated by Eq. (48.38). It is further assumed in [6,7] that the amplitude of vibration of the test structure at a certain natural frequency varies with the modal coefficient of the input point, and the sound pressure per unit excitation force at the input point at the natural frequency is proportional to the modal coefficient of the input point. In Eq. (48.38), let  $\omega = \omega_k$ , where  $\omega_k$  is

the natural frequency of the  $k$ -th mode of the structural-acoustic system; the sound pressure per unit excitation force at the natural frequency  $\omega_k$  can be approximated by

$$\frac{p_{ai}}{f_{sj}} = \frac{\lambda_k \phi_{aki}^l \phi_{skj}^l}{-\lambda_k + i\omega_k} \quad (48.40)$$

where  $\phi_{skj}^l$  is the modal coefficient of the input point  $j$  for the  $k$ -th mode, and the second assumption in the acoustic modal analysis in [6, 7] can be validated. Note that in the acoustic modal analysis in [6, 7], the measured natural frequencies of the test structure are the ones of the structural-acoustic system, and the measured mode shapes are the structural components of the left eigenvectors of the coupled system; this would also be the case for the VMT method, as illustrated below.

### 48.3 Modal Test Based on Vibro-Acoustic Reciprocity

Based on Eq. (48.38), the VMT method can measure the natural frequencies and the structural components of the left eigenvectors of the coupled system using an impact hammer and one or multiple sound pressure transducers. By Eqs. (48.31) and (48.39), the VMT method can measure the natural frequencies and the structural components of the right eigenvectors of the coupled system. Assuming that the natural frequencies and mode shapes of the structure in the structural-acoustic system described by Eq. (48.3) can be approximated by the natural frequencies and the structural components of the right eigenvectors of the coupled system, respectively, one can use the VMT method to measure the natural frequencies and mode shapes of the structure.

A vibro-acoustic reciprocity can be applied to a structural-acoustic system consisting of a linear elastic structure that is contiguous with air, based on which the transfer function between a structural force applied to the structure and the resulting sound pressure in rest contiguous air can be determined by exciting the structure with an omnidirectional point sound source and measuring the resulting acceleration of the structure [15]. The vibro-acoustic reciprocity is also referred to as Lyamshev reciprocity, and can be expressed by

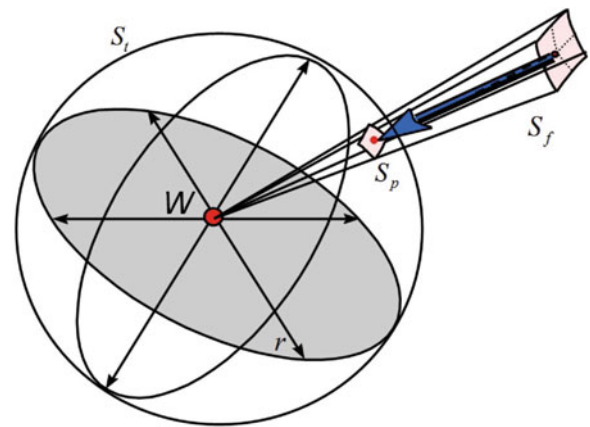
$$\frac{p_{ai}}{f_{sj}} = -\frac{a_{sj}}{\dot{q}_{ai}} \quad (48.41)$$

where  $f_{sj}$  is the applied force to point  $j$  on the structure,  $p_{ai}$  is the measured sound pressure at point  $i$  in air induced by  $f_{sj}$ ,  $\dot{q}_{ai}$  is the volume acceleration of the point sound source at point  $i$  in air, and  $a_{sj}$  is the acceleration of point  $j$  on the structure induced by the point sound source. Note that  $f_{sj}$  and  $a_{sj}$  are in the same direction and  $\dot{q}_{ai}$  represents the strength of the point sound source.

Based on the vibro-acoustic reciprocity, the VMT method is equivalent to the one where one or multiple omnidirectional point sound sources of known strengths are used to excite the structure and the resulting acceleration is measured. When the roving hammer technique is used, the measured mode shapes by the VMT method and EMA are in the directions of impacts. Since the impact directions are usually perpendicular to the surfaces being impacted, the merely in-plane modes cannot be excited by the VMT method and EMA, and only the out-of-plane components of mode shapes can be measured. A difference between the VMT method and EMA lies in the measurements of the dynamic responses of the structure since the former measures the pressure in air and the latter measures the acceleration of the structure. If one sound pressure transducer and one accelerometer are used in the VMT method and EMA, respectively, the FRFs from the former can be considered to be obtained by multiple inputs and a single output as if a point sound source and an accelerometer were used, according to Eq. (48.41), while those from the latter are obtained by a single input and a single output. Assuming that the excitation points are properly selected on the test structure and all the modes within a frequency range of interest can be excited, this difference enables the VMT method to capture all the out-of-plane modes of the structure of interest, including global and local ones, while EMA can miss some of the modes if the positions of the measurement points are improperly selected. The problem can occur when a measurement point in EMA is on a nodal line of a mode or in an inactive area of a local mode, which cannot be captured by the resulting FRFs. This problem will not occur in the VMT method, since the sound pressure transducer is located away from the test structure. Though the value of  $\phi_{ahi}^r$  for a certain mode  $h$  in Eq. (48.39) can be relatively low, it does not vanish in that the pressure measured at the natural frequency  $\omega_h$  by the sound pressure transducer does not vanish unless the excitation point is on a nodal line or in an inactive area of the mode. Use of multiple sound pressure sensors in the VMT method can help improve the measurement quality.

The VMT method is applicable to structures of any shapes when no noise is involved in the measurement of sound pressure. When noise is involved, the method may not be suitable for slender structures and structures with small surface areas. As illustrated in Fig. 48.1, the area of the surface of a structure facing an ideal point sound source is  $S_f$ ; projecting

**Fig. 48.1** Portion of the acoustic power from a point sound source with a power  $W$  transmitted to the area  $S_p$  projected from the surface of a structure facing the point source



the surface to a sphere with the center at the sound source, a constant radius  $r$ , and a surface area  $S_t = 4\pi r^2$  gives a surface with an area  $S_p$ . The portion of the sound power that can reach the structure from the point source with a power  $W$  is  $\beta W$ , where  $\beta = \frac{S_p}{S_t}$  is independent of  $r$ . A structure with a small value of  $\beta$  cannot be well excited by the point source, and the measured transfer functions between the strength of the point sound source and the resulting accelerations on the structure have low signal-to-noise ratios (SNRs). Consequently, based on the vibro-acoustic reciprocity, the measured FRFs in the VMT method using an ideal omnidirectional point sound pressure transducer at the location of the point sound source have low SNRs. Since the value of  $\beta$  is almost inversely proportional to the square of the distance between the sound pressure transducer and the structure, placing the sound pressure transducer close to the structure can increase the value of  $\beta$ . The sound pressure transducers should also be placed on the same side of the impacted surfaces of the structure to increase the SNRs of the measured FRFs. One should adjust the orientation of the structure so that a larger projected surface area can be obtained, which results in a larger  $\beta$ . However, for slender structures such as cables, and structures with small surface areas such as truss structures, the values of  $\beta$  can remain relatively small even if a sound pressure transducer is placed close to them. Hence the VMT method is more suitable for plate-like structures and structures with relatively large surface areas.

## 48.4 Experimental Validation

A case study was performed on an automotive disk brake using both the VMT method and EMA. The experimental results from the two methods were compared and validated using the FE model.

### 48.4.1 Test Setup

The disk brake was placed on foams, as shown in Fig. 48.2a, to simulate the free boundary conditions. For both the VMT method and EMA, the brake was excited at 146 points on the flange and in the bolted area, as shown in Fig. 48.2b, using a PCB 086D80 impact hammer. The excitation direction was perpendicular to the brake surfaces. In order to distinguish some of the modes with close natural frequencies due to almost axial-symmetry of the brake, multiple random impacts [16] were given at every excitation point for 4 s in each test, which results in a frequency resolution of 0.25 Hz, and three tests were averaged to ensure repeatable results with a good coherence. The responses of the brake were measured using one PCB U130D20 and two PCB 130E20 microphones and four PCB 352C66 accelerometers for the VMT method and EMA, respectively; the data were collected using a 36-channel LMS spectrum analyzer. For the VMT method, the three microphones were placed at fixed locations near the brake and pointing towards it, as shown in Fig. 48.2a. For EMA, two sets of tests were conducted; the four accelerometers were attached in one set of tests on the bottom surface of the flange, and in the other set of tests on the bottom surface of the bolted area. Note that the microphones used in the VMT method here are of the free-field type, whose measurements are most accurate when the sound pressure from a single source and a single direction is measured [17]. Since the flange and the bolted area of the brake are flat surfaces, and the microphones were placed not too close to the brake and pointing towards the brake, the measurements of the sound pressure by the microphones can be used in the VMT method by assuming that the sound pressure in the directions perpendicular to those in which the microphones can accurately measure the sound pressure can be neglected.

**Fig. 48.2** (a) Test setup for the VMT method, and (b) excitation points for the VMT method and EMA

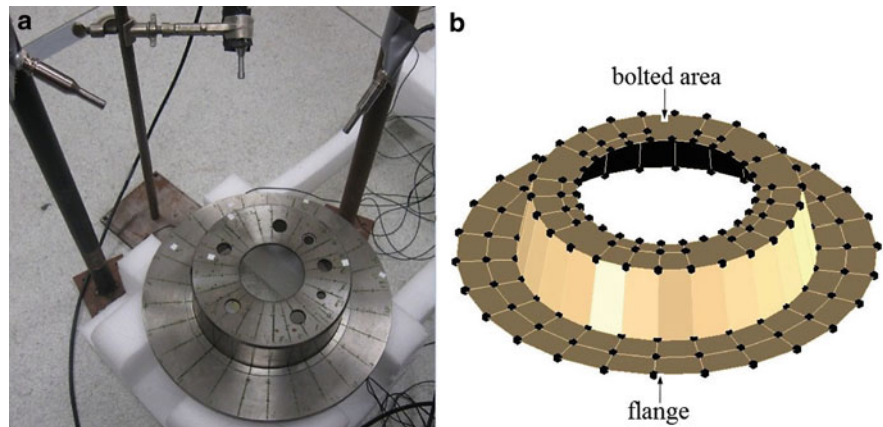


**Table 48.1** Measured natural frequencies of the disk brake by the VMT method and EMA

Mode	VMT frequency (Hz)	EMA frequency (Hz)	Frequency difference (%)
1	1,072.4	1,064.5	0.74
2	1,073.8	1,070.2	0.34
3	1,237.2	1,231.0	0.50
4	1,576.5	1,574.5	0.13
5	1,576.7	1,578.1	-0.09
6	1,617.4	1,608.9	0.53
7	1,620.4	1,612.8	0.47
8	2,004.4	2,003.2	0.06
9	2,115.5	2,113.3	0.10
10	2,115.9	2,114.1	0.09
11	2,428.3	2,412.1	0.67
12	2,429.3	2,421.0	0.34
13	2,591.6	2,591.0	0.02
14	2,600.8	2,600.2	0.02
15	3,504.0	3,503.3	0.02
16	3,504.1	3,503.4	0.02
17	3,918.8	3,918.1	0.02
18	3,940.5	3,938.7	0.05

#### 48.4.2 Results and Discussion

Modal analysis was conducted using PolyMax [18] in the LMS Test.Lab Rev. 9b; the measured natural frequencies and mode shapes of the brake by the VMT method were extracted from three sets of measured FRFs from the three microphones, and those by EMA from eight sets of measured FRFs from the four accelerometers. The highest natural frequency of the rigid body modes of the brake in the tests is 36.75 Hz, which is lower than 10% of the natural frequency of the first elastic mode, and the boundary conditions can be considered to be free [1]. In order to experimentally validate the assumption in Sect. 48.3 that the natural frequencies and mode shapes of the structure can be approximated by the natural frequencies and the structural components of the right eigenvectors of the coupled system, respectively, the natural frequencies of the first 18 elastic modes of the brake from the VMT method and EMA were compared in Tables 48.1 and 48.2, respectively, and the maximum natural frequency difference is 0.74%. The differences between the two sets of measured natural frequencies mainly derive from mass loading introduced by the accelerometers in EMA, since all of the measured natural frequencies from EMA, except that of the fifth elastic mode, are lower than the corresponding ones from the VMT method; the measured natural frequency of the fifth elastic mode from EMA is higher than that from the VMT method due to measurement error. The MAC values of the associated mode shapes, which are the diagonal entries of the MAC matrix [1] in Table 48.2, are all over 90%. Some off-diagonal entries in Table 48.2 are relatively high due to two reasons. One reason is that the number of excitation points is not large enough and some mode shapes cannot be well distinguished from others. The second reason is that the mode shapes were not measured in three dimensions in the tests using the two methods. The impact hammer excited the brake in the direction perpendicular to the surfaces of the flange and the bolted area, and only the out-of-plane mode

**Table 48.2** Entries of the MAC matrix in percent corresponding to the first 18 measured mode shapes of the disk brake by the VMT method and EMA; the horizontal and vertical mode numbers correspond to the measured modes by the VMT method and EMA, respectively

Mode	1	2	3	4	5	6	7	8	9	10	11	12	13	14	15	16	17	18
1	96	49	6	4	4	6	2	1	17	29	11	2	0	0	4	2	1	2
2	41	95	5	2	7	7	4	1	32	28	5	3	0	1	2	3	4	3
3	10	3	98	17	7	5	0	57	5	5	4	3	5	8	1	5	3	8
4	1	2	8	92	34	2	8	9	3	6	1	3	45	22	2	5	3	3
5	0	8	4	29	91	13	13	3	4	2	3	0	18	21	1	3	0	2
6	3	4	2	10	3	91	28	1	2	3	5	10	3	2	2	2	1	1
7	2	7	2	3	9	46	97	1	2	3	3	6	2	3	5	3	1	1
8	1	1	64	9	5	2	1	100	7	3	3	2	7	7	1	1	5	11
9	20	25	6	3	11	4	5	8	90	16	5	4	1	1	4	2	25	2
10	26	37	6	2	2	7	2	4	40	94	4	2	2	3	1	1	15	25
11	9	6	4	2	4	7	2	1	5	6	92	29	3	3	8	7	1	1
12	3	6	3	3	2	6	4	0	2	7	43	96	0	0	6	12	0	1
13	0	0	3	36	20	0	1	2	0	2	5	3	91	11	1	1	5	3
14	0	0	7	17	36	3	5	6	1	3	2	0	28	99	1	1	7	5
15	1	3	3	3	1	3	5	0	1	3	2	5	0	0	95	14	0	1
16	3	2	0	1	2	6	3	0	2	4	6	6	0	0	26	94	1	0
17	1	2	5	4	2	0	0	8	31	9	1	1	11	8	2	2	94	11
18	3	1	7	2	4	0	1	7	9	34	1	0	13	4	0	0	34	97

shapes were measured; one cannot excite the brake in the directions parallel to the surfaces of the flange and the bolted area and the interior points of the brake. If the in-plane components of two distinct modes are not measured, their out-of-plane components can be similar and the corresponding MAC value of the two mode shapes can be relatively high [19].

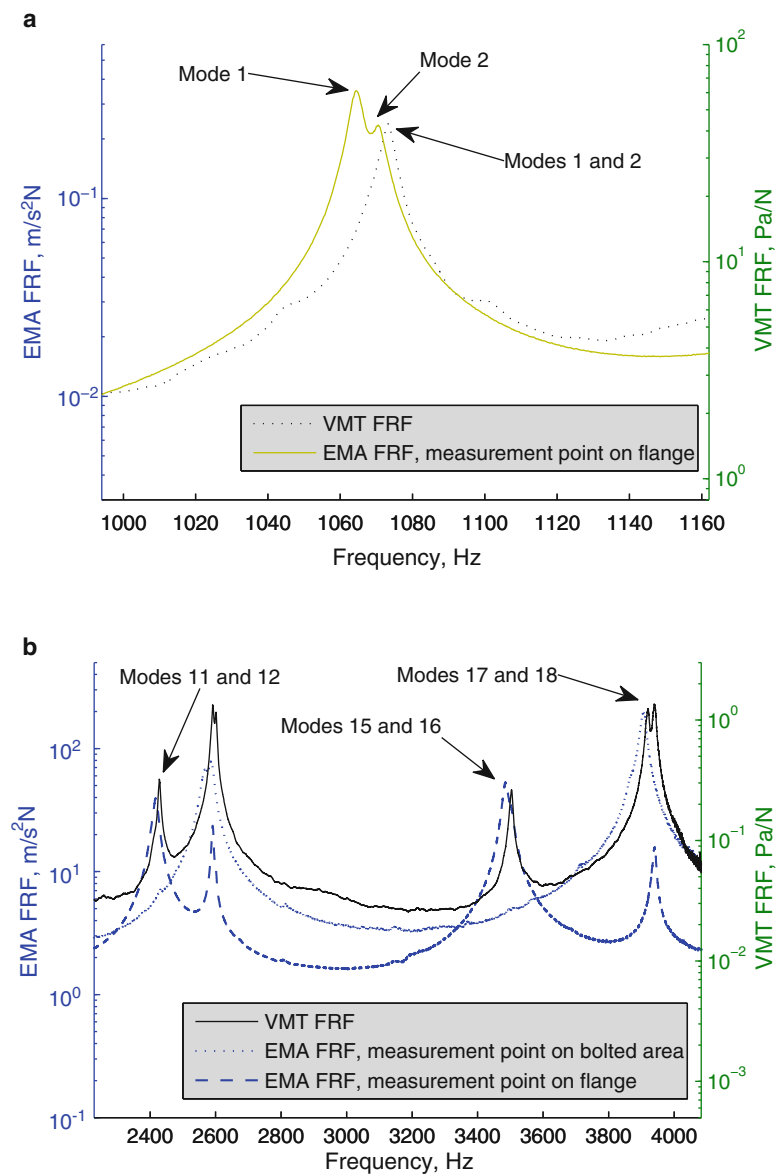
The sums of the measured FRFs in the neighborhoods of the first two elastic modes by the VMT method and EMA are shown in Fig. 48.3a, where the measurements are from a microphone away from the brake and an accelerometer on the flange, respectively. Since the brake is almost axial-symmetric, there are pairs of close frequencies, and the associated peaks in the measured FRFs can be close to each other or overlapped depending on the frequency resolution used. As shown in Fig. 48.3a, there is only one peak that can be observed in the summed FRF from the VMT method, from which two distinct modes can be identified by the modal analysis software and their natural frequency difference is 1.6 Hz. The actual natural frequency difference between the two modes may be smaller than 1.6 Hz and two separate peaks representing the two close natural frequencies may be observed if a higher frequency resolution is used in the test. On the other hand, there are two separate peaks corresponding to the two modes in the summed FRF from EMA due to mass loading from the accelerometers, which increases the natural frequency difference to 5.7 Hz. Hence the VMT method is more suitable for an axial-symmetric structure since it can preserve close natural frequencies of the structure due to axial-symmetry.

The sums of the measured FRFs by EMA, where the measurement points are on the flange and in the bolted area of the brake, and that of the measured FRFs by the VMT method are shown in Fig. 48.3b. As shown in Fig. 48.3b, the peaks corresponding to modes 11 and 12 cannot be identified in the summed FRF for which the measurement point is in the bolted area; the same observation can be made for modes 15 and 16. The reason is that the bolted area is inactive for the four modes, whose vibrations cannot be measured by the accelerometer. On the other hand, the peaks corresponding to the four modes can be clearly identified in the summed FRF by the VMT method. The peaks corresponding to modes 17 and 18 cannot be observed in the two summed FRFs for which the measurement points were on the flange and in the bolted area, respectively. However, the peaks corresponding to the two modes can be clearly identified in the summed FRF from the VMT method, as shown in Fig. 48.3b, since the VMT method can capture all the out-of-plane modes, including global and local ones. In the VMT method, the pressure measured by a microphone is from the vibration of the impacted surface of the brake; the quality of the pressure measurement would not be affected much by the nodal lines and local modes of the brake. If the locations of the microphones and the orientation of the brake relative to the microphones comply with the guidelines in Sect. 48.3, the VMT method would be more efficient than EMA.

In order to validate the experimental results, an intensive FE model of the brake was created using solid tetrahedral elements in the commercial FE software Abaqus 6.9 EF. The brake is made of cast iron Class 25 with an elastic modulus of 113.7 GPa, a Poisson's ratio of 0.28, and a mass density of 7,200 kg/m<sup>3</sup>. The profile and the FE model of the brake are shown in Fig. 48.4. Note that the unit in the profile is mm.

The calculated natural frequencies of the first 18 elastic modes of the brake from the FE model and the measured ones by the VMT method and EMA are shown in Table 48.3. The errors between the measured natural frequencies by the VMT method and EMA and the calculated ones from the FE model are less than 3%, except that the error for the 11th elastic mode

**Fig. 48.3** (a) Summed FRFs by the VMT method and EMA in the neighborhood of the first two elastic modes, and (b) summed FRFs by the VMT method and EMA from 2,250 Hz to 4,050 Hz



by EMA is 3.26%. The calculated three-dimensional mode shapes from the FE model and the measured out-of-plane ones by the VMT method are shown in Table 48.4. Note that the in-plane components of the calculated eighth and ninth elastic mode shapes in Table 48.4 are relatively large compared to their out-of-plane ones. Note also that the eighth through tenth modes from the VMT method and EMA in Table 48.1 correspond to the tenth, eighth, and ninth modes from the FE model, respectively, and the order for the three modes from the VMT method and EMA has been shifted in Tables 48.3 and 48.4 according to that of the FE model. The MAC matrices for the out-of-plane components of the measured mode shapes by the VMT method and EMA and the calculated ones from the FE model are shown in Tables 48.5 and 48.6, respectively; the MAC values of the associated mode shapes are all over 90%.

## 48.5 Conclusion

The VMT method developed here is based on the assumption that the natural frequencies and mode shapes of the test structure can be approximated by the natural frequencies and the structural components of the right eigenvectors of the structurally damped structural-acoustic system, respectively. The coupling between the structure and the acoustic field in a structural-acoustic system introduces asymmetry in the model formulation. The associated eigenvalue problem is derived

**Fig. 48.4** (a) The profile and (b) the FE model of the disk brake

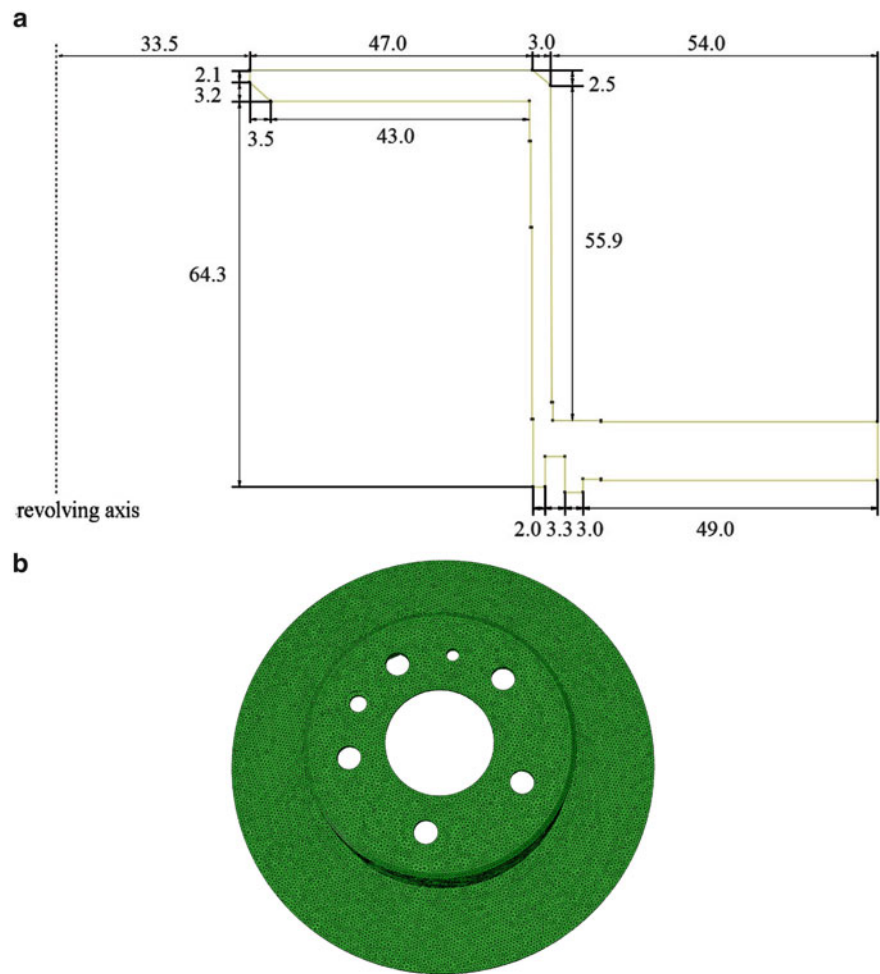


**Table 48.3** Comparison of measured natural frequencies by the VMT method and EMA with the calculated ones from the FE model

Mode	Numerical frequency (Hz)	VMT frequency (Hz)	Error (%)	EMA frequency (Hz)	Error (%)
1	1,062.5	1,072.4	0.93	1,064.5	0.19
2	1,062.7	1,073.8	1.04	1,070.2	0.71
3	1,236.7	1,237.2	0.03	1,231.0	-0.46
4	1,593.3	1,576.5	-1.05	1,574.5	-1.18
5	1,594.0	1,576.7	-1.09	1,578.1	-1.00
6	1,651.1	1,617.4	-2.04	1,608.9	-2.56
7	1,651.3	1,620.4	-1.87	1,612.8	-2.33
8	2,055.3	2,115.5	2.93	2,113.3	2.82
9	2,055.5	2,115.9	2.94	2,114.1	2.85
10	2,061.8	2,004.4	-2.78	2,003.2	-2.84
11	2,493.3	2,428.3	-2.61	2,412.1	-3.26
12	2,493.6	2,429.3	-2.58	2,421.0	-2.91
13	2,656.5	2,591.6	-2.44	2,591.0	-2.47
14	2,666.7	2,600.8	-2.47	2,600.2	-2.49
15	3,601.3	3,504.0	-2.70	3,503.3	-2.72
16	3,601.5	3,504.1	-2.70	3,503.4	-2.72
17	3,995.1	3,918.8	-1.91	3,918.1	-1.93
18	4,015.1	3,940.5	-1.86	3,938.7	-1.90

**Table 48.4** Mode shapes of the first 18 elastic modes of the brake from the FE model and the VMT method

Mode	FE Mode Shape	VMT Mode Shape	Mode	FE Mode Shape	VMT Mode Shape
1			10		
2			11		
3			12		
4			13		
5			14		
6			15		
7			16		
8			17		
9			18		

using an equivalent state space formulation for the coupled system. The biorthonormality relations between the left and right eigenvectors and the relations between the structural and acoustic components in the left and right eigenvectors are proved. The FRFs used in the VMT method are derived, which contain the modal characteristics of the coupled system. Based on the vibro-acoustic reciprocity, the VMT method can measure all the out-of-plane modes and its measurement quality would not be affected by a nodal line of a mode and an inactive area of a local mode of the structure; the guidelines for using the VMT method, including the types of structures that are suitable for the method, the positions of the sound pressure transducers, and the orientation of the test structure relative to the transducers, are provided. Modal tests were carried out on an automotive disk brake using the VMT method and EMA, where multiple microphones and accelerometers were used to measure its dynamic responses induced by impacts, respectively. The differences between the measured natural frequencies of the first 18 elastic modes by the VMT method and EMA are less than 1% and the MAC values of the associated mode shapes are all above 90%. The errors between the measured natural frequencies by the VMT method and those from the FE model are less than 3% for the first 18 elastic modes, and the MAC values of the associated mode shapes are all above 90%. It is shown that the VMT method can not only preserve close natural frequencies of the brake due to axial-symmetry, but also measure all the out-of-plane modes within the frequency range of interest, including global and local ones.



**Table 48.5** Entries of the MAC matrix in percent corresponding to the first 18 calculated mode shapes of the disk brake from the FE model and the measured ones by the VMT method; the horizontal and vertical mode numbers correspond to the calculated and measured modes, respectively

Mode	1	2	3	4	5	6	7	8	9	10	11	12	13	14	15	16	17	18
1	96	15	5	1	3	11	2	2	23	49	6	7	0	0	6	6	1	2
2	29	91	3	4	5	17	8	1	36	45	4	9	0	0	2	4	1	1
3	2	3	99	1	3	1	1	54	4	1	0	5	5	4	1	6	5	6
4	10	2	16	90	32	3	7	7	6	6	7	8	39	4	5	9	2	3
5	8	5	7	9	93	9	11	5	4	7	3	1	5	37	0	3	4	4
6	8	1	3	2	8	92	22	2	1	6	16	3	1	3	6	7	0	0
7	5	6	2	11	13	16	94	1	4	1	3	15	1	4	3	8	0	1
8	0	1	70	3	2	0	0	99	1	0	0	1	5	2	0	1	7	7
9	19	33	7	4	2	6	4	7	91	24	4	1	1	0	2	4	35	11
10	28	20	4	6	2	9	3	3	26	90	5	8	2	3	1	1	20	34
11	1	6	4	2	3	6	1	2	4	2	94	16	6	3	12	18	1	1
12	5	2	2	1	2	8	7	2	2	2	28	92	3	1	11	12	1	0
13	1	0	6	43	19	1	1	7	2	3	1	1	98	13	0	0	5	12
14	0	0	7	28	33	1	0	8	1	3	0	1	33	91	0	0	9	8
15	5	2	1	2	1	4	5	1	2	2	3	10	1	1	94	15	2	1
16	3	3	5	5	3	4	4	2	3	2	10	15	2	1	8	90	1	1
17	1	3	2	3	2	1	0	4	27	6	1	0	6	5	0	1	97	9
18	3	2	9	4	1	0	0	11	6	26	1	1	7	4	1	0	34	93

**Table 48.6** Entries of the MAC matrix in percent corresponding to the first 18 calculated mode shapes of the disk brake from the FE model and the measured ones by EMA; the horizontal and vertical mode numbers correspond to the calculated and measured modes, respectively

Mode	1	2	3	4	5	6	7	8	9	10	11	12	13	14	15	16	17	18
1	95	18	5	2	3	12	4	2	19	51	10	6	0	0	3	3	0	1
2	25	95	3	1	2	12	3	1	41	41	9	6	0	0	1	6	2	1
3	4	3	98	0	4	2	1	48	1	4	3	4	3	5	1	7	5	6
4	2	2	7	90	36	2	2	8	1	4	5	4	41	6	3	5	2	4
5	7	1	3	19	96	11	3	5	3	4	3	1	18	27	2	4	0	1
6	5	10	3	5	7	95	14	1	7	2	8	6	3	4	4	3	1	0
7	4	8	0	8	8	28	93	1	6	1	3	12	1	3	2	4	1	0
8	1	0	71	2	2	0	0	99	1	0	0	1	3	3	0	1	7	7
9	23	38	6	2	9	4	2	7	94	14	6	1	0	0	2	4	31	10
10	24	27	7	3	2	7	4	3	31	90	5	5	1	3	1	3	17	29
11	11	2	3	1	4	7	2	1	3	8	93	8	2	3	12	14	0	1
12	3	1	2	1	1	2	7	1	2	1	29	92	0	0	16	11	0	0
13	0	0	3	34	33	0	0	4	1	1	1	1	91	46	0	0	2	4
14	0	0	6	26	35	0	0	7	1	3	1	0	26	94	0	0	10	7
15	5	1	2	2	2	7	3	1	1	2	8	10	0	0	94	2	0	0
16	1	1	0	1	3	2	3	0	0	2	8	7	0	0	24	90	0	0
17	1	2	6	4	1	0	0	8	29	2	0	0	9	2	0	0	95	18
18	1	2	7	5	1	0	0	8	5	30	0	0	10	1	0	0	33	95

## References

1. Ewins DJ (2001) Modal testing: theory, practice and application, 2nd edn. Wiley, England
2. Van der Auweraer H (2001) Structural dynamics modeling using modal analysis: applications, trends and challenges. In: IEEE instrumentation and measurement technology conference, Budapest, 21–23 May 2001
3. Yang QJ, Lim GH, Lin RM, Yap FF, Pang HLJ, Wang ZP (1997) Experimental modal analysis of PBGA circuit board assemblies. In: IEEE/CPMT electronic packaging technology conference, Singapore
4. Ashory MR (2002) Assessment of the mass-loading effects of accelerometers in modal testing. In: Proceedings of the IMAC XX, Los Angeles, CA
5. Vanlanduit S, Daerden F, Guillaume P (2007) Experimental modal testing using pressurized air excitation. J Sound Vib 299:83–98
6. Allemang R, Shapton W (1978) Using modal techniques to guide acoustic signature analysis. SAE Technical Paper 780106
7. Elwali W, Satakopan H, Shauche V, Allemang R, Phillips A (2010) Modal parameter estimation using acoustic modal analysis. In: Proceedings of the IMAC XXVIII, Jacksonville, FL
8. Craggs A (1969) The transient response of coupled acousto-mechanical systems. NASA Contractor Report: CR 1421

9. Luo J, Gea HC (1997) Modal sensitivity analysis of coupled acoustic-structural systems. *J Vib Acoust* 119:545–550
10. Ma ZD, Hagiwara I (1991) Sensitivity analysis methods for coupled acoustic-structural systems part I: modal sensitivities. *AIAA J* 29(11):1787–1795
11. Wyckaert K, Augusztinovicz F, Sas P (1996) Vibro-acoustical modal analysis: reciprocity, model symmetry, and model validity. *J Acoust Soc Am* 100(5):3172–3181
12. Xing J-T, Price WG (1991) A mixed finite element method for the dynamic analysis of coupled fluid-solid interaction problems. *Proc R Soc* 433(1888):235–255
13. Sung SH, Nefske DJ, Feldmaier DA (2009) A structural-acoustic finite element method for predicting automotive vehicle interior road noise. In: *Proceedings of the ASME 2009 international mechanical engineering congress & exposition, Lake Buena Vista, 13–19 November 2009*
14. Meirovitch L (1997) *Principles and techniques of vibrations*. Prentice Hall, Upper Saddle River
15. Fahy FJ (2003) Some applications of the reciprocity principle in experimental vibroacoustics. *Acoust Phys* 49(2):217–229
16. Zhu WD, Zheng NA, Wong CN (2007) A Stochastic model for the random impact series method in modal testing. *ASME J Vib Acoust* 129:265–275
17. PCB Piezotronics Inc., *Microphone handbook: test and measurement microphones*. PCB Piezotronics, Depew
18. Guillaume P, Verboven P, Vanlanduit S, Van der Auweraer H, Peeters B (2003) A poly-reference implementation of the least-squares complex frequency-domain estimator. *Proceedings of the IMAC XXI, Kissimmee, FL*
19. Heylen W, Lammens S, Sas P (1998) *Modal analysis theory and testing*. Katholieke Universiteit Leuven, Belgium

# Chapter 49

## Reactionless Test to Identify Dynamic Young's Modulus and Damping of Isotropic Plastic Materials

Peter Blaschke and Torsten Schneider

**Abstract** Due to more stringent legal sound regulations and customer demand of quieter products, the acoustic requirements for product design become a major task in the product development. For the requirement for lighter structures, synthetic materials like glass fibers become more prominent in recent designs. For high accurate simulation corresponding material data are needed. But concerning isotropic plastics the Young's modulus and damping are highly frequency- and temperature-dependent. A novel test to determine the frequency- and temperature-dependent Young's modulus and damping of isotropic plastics will be shown in this paper. With a special test facility a sample is excited reactionless by a constant repeatable force during measuring the surface velocity. A novel contactless sample suspension is developed. The modal parameters, response frequency and damping, are extracted from these measurements. With the assistance of FEA simulations the Young's modulus can be adapted step by step to these modal parameters. The Young's modulus can be extracted frequency- and temperature-dependent.

**Keywords** Experimental modal analysis • Dynamic Young's Modulus • Non-linear material • Contactless sample suspension • FEA validation

### Nomenclature

**DMA** Dynamic Mechanical Analysis  
**EMA** Experimental Modal Analysis  
**FEA** Finite Element Analysis  
**FRF** Frequency Response Function  
**NVH** Noise, Vibration, Harshness

### 49.1 Introduction

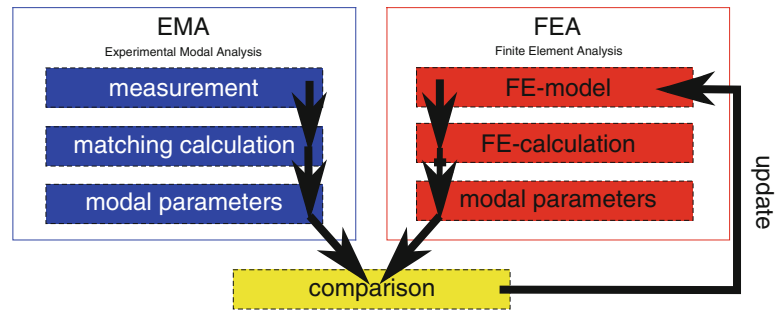
The demand for lighter structures results in structures that are easier to excite. Plastic materials allow new possibilities to reduce weight for the design of established vehicle parts like windshields. Re-thinking the design of these classical elements is part of every strategy for carbon dioxide reduction. Light weight construction, safety and durability are the most important aspects for the manufacturer. For customers is sound quality another significant feature.

Plastic substitutes and conventional materials like glass differ in dynamical characteristics and therefore in acoustical behavior. Decades of design experience with glass acoustics have to be replaced with data of plastic material parameters, which are strongly frequency-dependent. Standardized instrumentation for dynamic mechanical analysis (DMA) is expensive. Another major drawback of classical methods is the necessary clamping of samples. This clamping changes the mechanical state of the sample and introduces contact-surface damping in the range of investigated material damping.

---

P. Blaschke (✉) • T. Schneider  
Technical University of Applied Sciences Wildau, Bahnhofstr., 15745 Wildau, Germany  
e-mail: [peter.blaschke@th-wildau.de](mailto:peter.blaschke@th-wildau.de); [tschneider@th-wildau.de](mailto:tschneider@th-wildau.de)

**Fig. 49.1** Schematic diagram of update process for FEA validation with EMA



The determination (calculation, simulation and measurement) of structural vibrations is one of the main tasks in modern engineering. One major issue in dynamic simulation of noise, vibration and harshness (NVH) is the accuracy of simulation models. These models are based typically on linear material and normal distributed damping. Unfortunately, in almost every industrial structure these assumptions are not fulfilled. Non-linear models, like the viscoelastic Kelvin Voigt model, have been applied for plastic materials (e.g. [1]). However, experimental assessment of the needed parameters is difficult. One solution for this problem is a continuous validation process of simulation models with experimental data in order to improve simulation results (see Fig. 49.1).

## 49.2 Concept of Novel Reactionless DMA System

Dynamic mechanical analysis (DMA) for plastic materials requires three major aspects: first an excitation which covers frequencies up to several kHz.; second the excitation has to be adjustable and reproducible; third the influence of the suspension onto the measured quantities has to be negligible or ideally reactionless.

The first requirement has to be fulfilled because the material has to be excited also in the acoustic frequency range. The second requirement is important for nonlinear materials. Mechanic and dynamic parameters depend in nonlinear materials for example on excitation force amplitude. The third requirement deals with the issue of restraint conditions: clamping introduces errors and uncertainties in conventional DMA test setups during the measurement of Young's modulus and damping. State of the art dynamic mechanic analyzers apply a sinusoidal mechanical force or torque to a clamped sample and measure the resulting displacement. In general, these analyzers are expensive, complex and need experts for handling.

This paper presents a novel measurement solution for DMA. Figure 49.2 illustrates the proposed excitation and suspension elements of the system.

The novel measurement approach is a development on the basis of classical modal analysis with impulse hammer excitation. Typically, manual impulse hammer excitation fulfills just the first requirement (all frequencies have to be excited) of DMA. A solution for the second requirement (adjustability and reproducibility) is a spring-mounted impulse hammer which introduces a constant force with fixed impact point and impact orientation [2]. Blaschke and Mueller-Held presented in [3] a study with an automatic impulse hammer on the basis of the concept by Scheef et al. [2]. The new concept is improved by several enhancements.

By eliminating the influence of differing excitation with an automatic impulse hammer, Blaschke and Mueller-Held could study the influence of different suspensions [3]. They realized free-free boundary conditions with different foams and geometries like feeds, tips, mats and lines. However, the influence of all suspensions was significant for material property identification.

## 49.3 Material and Methods

A prototype of the proposed measurement system is shown in Fig. 49.3. The realized air suspension has a  $1 \times 1$  cm orifices grid. Standard pneumatic tubing and fittings supply air from a compressed air system with minimum pressure of 8 bar. A manually controlled pressure valve is integrated for hovering heights adjustment of samples. It is possible to adjust the magnet's activity with the custom build electrical drive unit. Controls define the interval between succeeding impacts and the duty cycle of electrical activation. The second control is necessary in order to prevent double hits reliably. Special care has been taken to exclude influences of the alternating current from the magnetic system on sensor data.

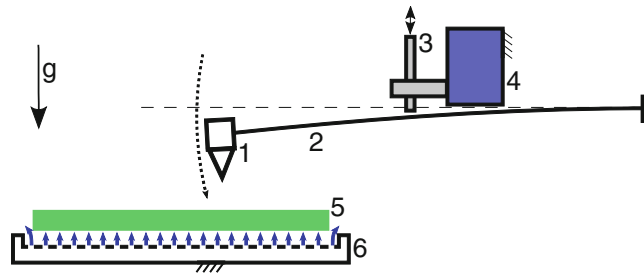
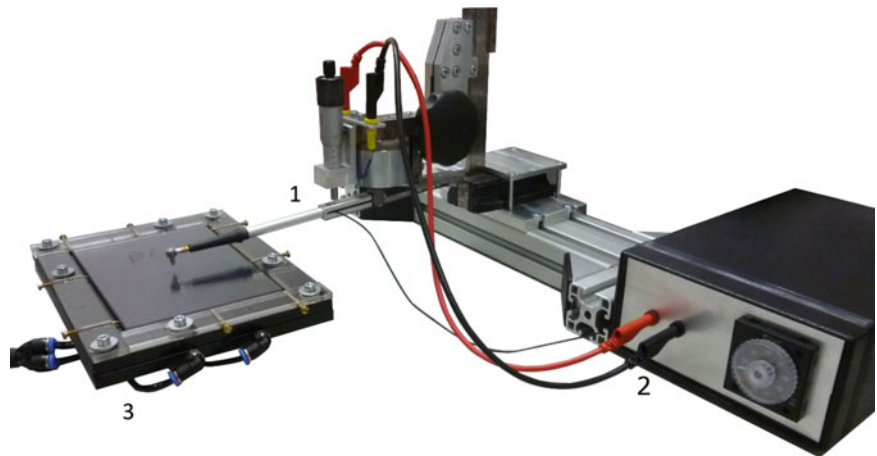


**Fig. 49.2** Schematic diagram of the novel excitation and suspension system for DMA. The impulse hammer (1) is attached to a flat spring (2) and actuated by gravitational acceleration  $g$ . A precision screw (3) fixes the spring's rest position and ultimately the force amplitude of the impulse. The electromagnet (4) prevents double hits and fixes the spring during idle period. The sample (5) hovers over a contactless air suspension system (6)

**Fig. 49.3** Prototype of measurement setup consisting of automated impulse hammer (1), electrical drive unit for the magnet (2) and air suspension system (3)



A miniature instrumented impulse hammer 086E80 (PCB Piezotronics, NY, USA) with custom build elastic handle is mounted at the tip of the flat spring. A single-axis accelerometer 352C33 (PCB Piezotronics, NY, USA) detects the vibration response of the sample (not shown).

Data acquisition and analysis were conducted with LMS SCM01-V4-II at 102.4 kS/s, LMS test.Xpress and LMS Modal analysis software (LMS International, Belgium). FFT block size was 32,768 and input mode H1. Data from impulse hammer was filtered with force window and data from accelerometer with exponential window.

The investigated polycarbonate (Robex, Caleppio, Germany) sample has dimensions of  $150 \times 100 \times 4$  mm. A soft and wavy foam mat suspension serves as comparison case for the air suspension system.

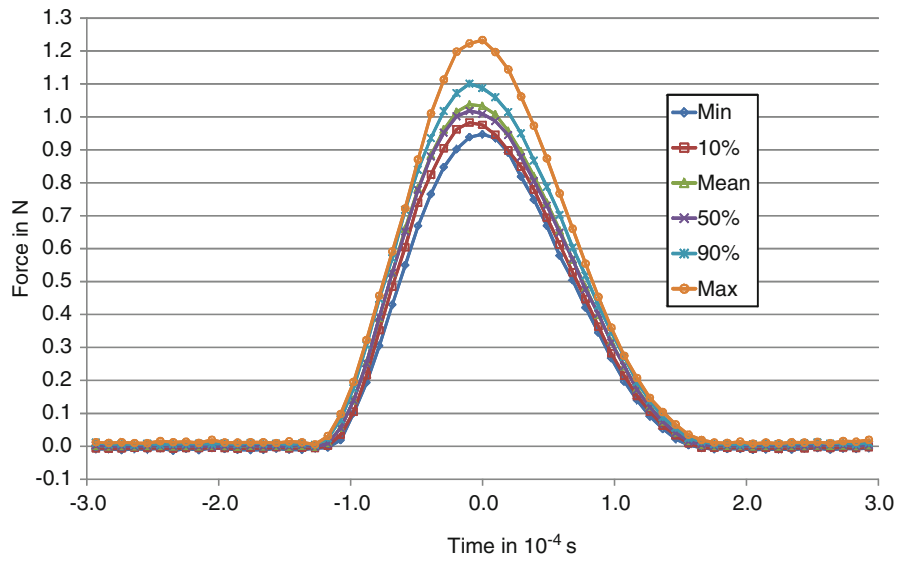
## 49.4 Results

Figure 49.4 shows time resolved plots of impulse hammer data. The measurement setup with polycarbonate sample and air suspension system is shown in Fig. 49.2. The desired value of 1 N at maximum of impact curve was achieved in a range of 0.98 N (10%-quantile) and 1.10 N (90%-quantile) with median 1.02 N (50%-quantile) and mean 1.04 N. All impacts are virtually identical in shape.

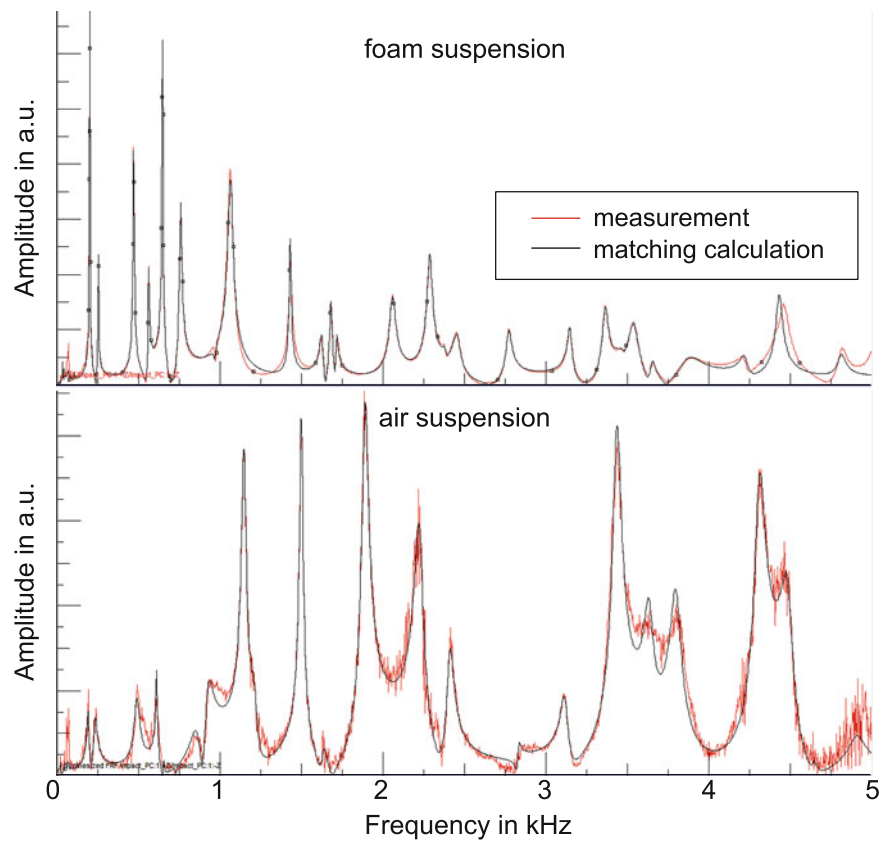
The 1 N-measurements have been conducted with the same polycarbonate sample on foam suspension (graphs not shown). The desired value of 1 N was achieved during 21 impacts in a range of 0.98 N (10%-quantile) and 1.07 N (90%-quantile) with median 1.01 N (50%-quantile) and mean 1.02 N.

Preliminary measurement results with the air suspension prototype are shown Figs. 49.5, 49.6 and 49.7 in comparison with foam suspension results.

**Fig. 49.4** Statistics of impulse hammer data including 21 impacts on polycarbonate sample with air suspension



**Fig. 49.5** Frequency response function of polycarbonate on foam suspension (*top*) and air suspension (*bottom*). Graphs show the measured data together with data from modal matching calculation. Measurements are linearly averaged results of 21 impacts



Frequency response functions (FRF)  $H(\omega) = \ddot{x}(\omega)/F(\omega)$  with  $\ddot{x}(\omega)$  Fourier transform of acceleration response and  $F(\omega)$  Fourier transform of force input, are shown in Fig. 49.5. The graphs show both data sets together with matching calculation for the determination of modal damping parameters. A significant level of noise is observable in the FRF with air suspension in the complete spectrum. This noise results in a significant deviation from the ideal value of 1 in the coherence function shown in Fig. 49.6.

Attempts to determine modal damping parameters from matching calculation have been made. The results of these calculations are presented in Fig. 49.7. The modal damping of the same polycarbonate sample differs between the two suspension cases. First mode modal damping is 24% for air suspension and 7% for foam suspension.

**Fig. 49.6** Coherence function between force input and acceleration response

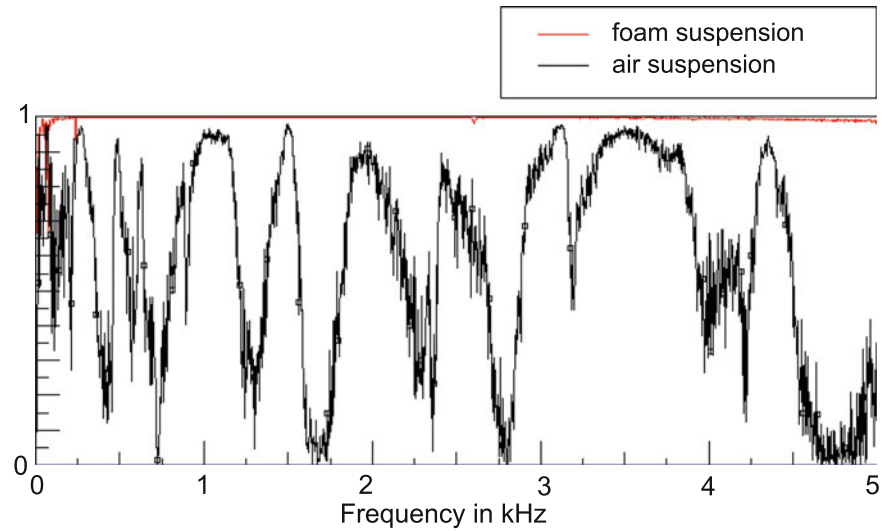
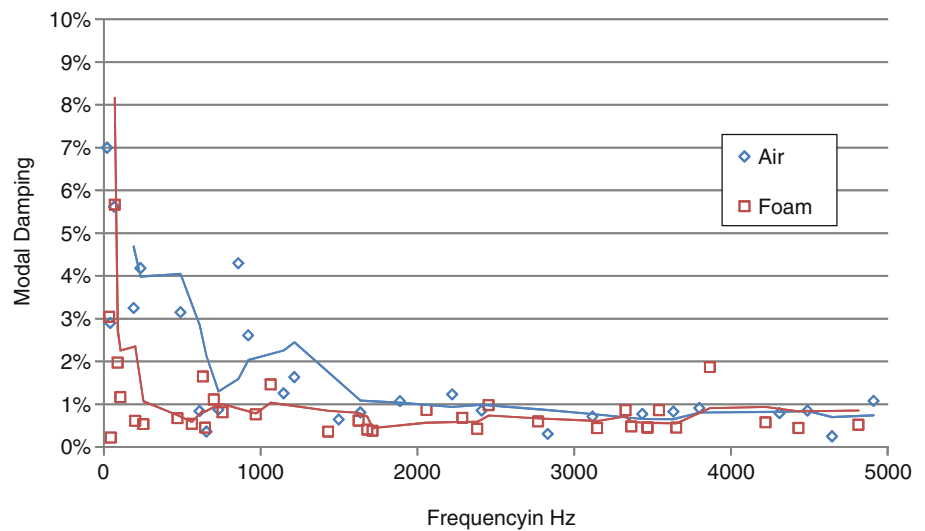


**Fig. 49.7** Modal damping of polycarbonate sample modes up to 5 kHz for air and foam suspension



## 49.5 Conclusion and Further Work

A prototype of the proposed reactionless DMA system has been introduced. With this system, frequency- and temperature-depending dynamic Young's modulus and damping of light weight plastic materials can be extracted and will enable simulations with higher accuracy. Installation of the system in a climate-testing chamber is possible and with it frequency- and temperature-depending dynamic Young's modulus is accessible. With the identification of non-linear properties it will be possible to assist in building non-linear simulation models for tasks like: turbine engines blades, noise and vibration optimization in wind power plants, material identification of innovative light materials like carbon fiber, NVH issues for automotive industry, parameter estimation as basis for active noise control (ANC) and active vibration control (AVC).

The excitation with automatic impulse hammer has an excellent reproducibility. Desired impact forces are possible to set and the system enables automatic testing of samples.

Virtually free-free boundary conditions are necessary in order to validate FEA simulations. The prototype of the air suspension system is able to realize this type of boundary condition. Damping from suspension and contact surfaces are removed from the experiment. However, the removal of suspension damping allows small disturbances to influence the measurement with significant effect (see Fig. 49.5). The coherence between input and response is worse in comparison to classical suspension.

As expected, modal damping is higher in case of contact suspension with foam in comparison with reactionless suspension with air. However, this is only true for the first mode of the polycarbonate sample. For modes between  $10^1$  and  $10^3$  Hz

modal damping with air suspension has higher values (see Fig. 49.7). The experimental data show no conclusive results for frequencies above  $10^3$  Hz.

The presented preliminary data show the difficulties when dealing without suspension damping. Ongoing work focuses on the development and optimization of the air suspension system. Different modifications of the orifices grid and application of porous media will be analyzed.

The influence of the attached accelerometer will be removed from the measurements with the application of microphone and laser scanning vibrometer sensors.

**Acknowledgements** The authors like to thank Artur Zwerschitz for his helpful contribution to manufacturing of the experimental system setup and for assisting the experiments.

## References

1. Catania G, Sorrentino S (2009) Experimental evaluation of the damping properties of beams and thin-walled structures made of polymeric materials. In: Proceedings IMAC-XXVII: conference & exposition on structural dynamics, Orlando, FL, USA
2. Scheef V, Bendel K, Blaschke P (2005) Vorrichtung und Verfahren zur Durchführung einer experimentellen Modalanalyse, Patent, DE10340138A1, 20050324
3. Blaschke P, Mueller-Held B (2009) Identification of dynamic young's modulus and damping of isotropic plastic materials. In: Proceedings IMAC-XXVII: conference & exposition on structural dynamics, Orlando, FL, USA



# Chapter 50

## Real-Time Modal Analysis of Shell-Shaped Objects Using High-Frame-Rate Structured-Light-Based Vision

Hua Yang, Qingyi Gu, Tadayoshi Aoyama, Takeshi Takaki, and Idaku Ishii

**Abstract** In this study, we introduce a real-time vision-based modal testing system to estimate the modal parameters of shell-shaped objects simultaneously using high-frame-rate structured-light-based vision. Based on structured-light-based vision consisting of a DLP LightCrafter projector and a high speed vision platform (IDP Express), the transient three-dimensional (3D) geometry of a vibrating shell-shaped object can be measured in real time at 1,000 fps as the 3D vibrational displacements of 100 points on an object in the audio frequency range. In our system, the modal parameters are estimated simultaneously for the 3D displacements of the shell-shaped object using a fast output-only modal parameter estimation algorithm, SSI-CPAST, on the IDP Express. Therefore, our modal testing system can simultaneously monitor and inspect the input-invariant structural dynamic properties of vibrating shell-shaped objects excited at dozens or hundreds of Hertz. Our system can be applied to real-time vision-based structural damage detection and fatigue testing in various applications. To demonstrate the performance of our vision-based modal testing system, an experiment was performed in real time to estimate the resonant frequencies and mode shapes of steel plates with artificial damage, which were excited at dozens or hundreds of Hertz using a hammer.

**Keywords** Fast modal parameter estimation • High-speed vision • Noncontact measurement • Structured-light-based vision • Visual inspection

### 50.1 Introduction

Modal testing [1] is a well-known structural dynamics analysis method for estimating the modal parameters of vibrating objects. Modal parameters, such as resonant frequencies and mode shapes, are functions of the mass stiffness and damping of vibrating objects, which are treated as input-invariant dynamic properties or features. In the past few decades, modal testing has been used in many engineering fields for estimating structural dynamic properties, such as aeronautical engineering, automotive engineering, and mechanical engineering. In general, contact-type sensors such as accelerometers and strain gauges have been used to measure vibrational responses in traditional modal tests by attaching them to discrete points on vibrating objects. The modal parameters can then be estimated using modal analysis algorithms. In recent years, offline vision-based dynamics analysis methods based on standard commercial cameras [2, 3] or high-frame-rate (HFR) cameras [4, 5] have been used as noncontact-type full-field dynamics measurement technology. However, offline vision-based dynamics analysis methods are limited to mechanical engineering and structural engineering, which are not popular for factory product inspection or dynamic time-variant objects due to the high time consumption of image processing and long-term requirements of the modal parameter estimation procedure. The development of real-time high-speed vision systems that operate at 1,000 fps or more has led to the introduction of online vision-based dynamics analysis methods [6] for damage detection in beam-shaped vibrating objects, which has overcome the limitations of offline vision-based approaches.

In practical applications, shell-shaped objects such as automotive bodies and aircraft wings are basic structures encountered in the engineering field, so it is useful to estimate the dynamic properties of shell-shaped objects in real time during dynamics monitoring or factory inspection. In this paper, we extend the concept of online vision-based dynamics

---

H. Yang (✉) • Q. Gu • T. Aoyama • T. Takaki • I. Ishii  
Department of System Cybernetics, Hiroshima University, Higashi-Hiroshima, 739-8527, Hiroshima, Japan  
e-mail: [yang@robotics.hiroshima-u.ac.jp](mailto:yang@robotics.hiroshima-u.ac.jp)

analysis to shell-shaped objects using real-time structured-light-based vision measurement and fast output-only modal parameter estimation. In our system, three-dimensional (3D) vibrational displacements are determined using HFR structured-light-based vision in real time at 1,000 fps. Simultaneous modal analysis is achieved by implementing a fast output-only modal analysis algorithm on an HFR structured-light-based vision platform. Section 50.2 introduces the output-only modal parameter estimation algorithm, SSI-CPAST, for fast dynamic properties analysis. Section 50.3 describes the 1,000 fps vision-based dynamics analysis system for simultaneously estimating the modal parameters of a shell-shaped object based on the implementation of the SSI-CPAST algorithm on an HFR vision platform with a synchronized structured-light projector. To verify the performance of our system, Sect. 50.4 presents our experimental results using actual shell-shaped plates with artificial cracks.

## 50.2 Fast Output-Only Modal Parameter Estimation

In practical modal testing applications such as mechanical systems or civil infrastructures, it is impossible to measure the forces produced in structures in ambient or operational conditions. In the past decade, output-only modal parameter estimation algorithms have been reported that use only the output vibration response to estimate the dynamic properties of an object responding to an unknown input. Time-domain methods such as the eigensystem realization algorithm (ERA) [7] and the stochastic subspace-based identification (SSI) [8] are very popular and they have already been used in many engineering application fields. Robust but time-consuming numerical tools such as singular value decomposition (SVD) are necessary to estimate the modal parameters in ERA and SSI algorithms. Thus, these time-domain methods are not suitable for online fast output-only modal parameter estimation. To overcome this limitation, we have already proposed a fast output-only modal parameter estimation algorithm SSI-CPAST [6] based on recursive subspace tracking rather than SVD calculation. In this section, the SSI-CPAST algorithm is explained in detail.

The vibration system can be represented as the following discrete time state equations.

$$\mathbf{x}_{k+1} = \mathbf{A} \mathbf{x}_k + \mathbf{w}_k, \quad (50.1)$$

$$\mathbf{y}_k = \mathbf{C} \mathbf{x}_k, \quad (50.2)$$

where  $\mathbf{x}_k (\in R^r)$  is a state variable vector at time  $k$ ,  $\mathbf{y}_k (\in R^N)$  is an observable output vector, and  $\mathbf{w}_k (\in R^r)$  is an input vector at time  $k$  in the case of excitation using zero-mean white noise.  $\mathbf{A} (\in R^{r \times r})$  is a state transition matrix that characterizes the dynamics of the system and  $\mathbf{C} (\in R^{N \times r})$  is an output matrix. Using Hankel vectors and matrices, the discrete time state equations in Eqs. (50.1) and (50.2) can be rewritten as follows.

$$\mathbf{Y}_k = \mathbf{\Gamma}_k \mathbf{X}_k + \mathbf{G}_k \mathbf{W}_k, \quad (50.3)$$

$$\mathbf{\Gamma}_k = \begin{bmatrix} \mathbf{C} \\ \mathbf{C} \mathbf{A} \\ \mathbf{C} \mathbf{A}^2 \\ \vdots \\ \mathbf{C} \mathbf{A}^{u-1} \end{bmatrix}, \quad \mathbf{G}_k = \begin{bmatrix} \mathbf{0} & \mathbf{0} & \dots & \mathbf{0} \\ \mathbf{C} & \mathbf{0} & \dots & \mathbf{0} \\ \mathbf{C} \mathbf{A} & \mathbf{C} & \dots & \mathbf{0} \\ \vdots & \vdots & \ddots & \vdots \\ \mathbf{C} \mathbf{A}^{u-2} & \mathbf{C} \mathbf{A}^{u-3} & \dots & \mathbf{0} \end{bmatrix}, \quad (50.4)$$

where the output Hankel vector  $\mathbf{Y}_k = [\mathbf{y}_k^T, \dots, \mathbf{y}_{k+u-1}^T]^T (\in R^{uN})$  comprises the observable output vectors  $\mathbf{y}_k (\in R^N)$ ; the state Hankel vector  $\mathbf{X}_k = \mathbf{x}_k^T (\in R^r)$  comprises the state sequence  $\mathbf{x}_k$ ; the white noise Hankel vector  $\mathbf{W}_k = [\mathbf{w}_k^T, \dots, \mathbf{w}_{k+u-1}^T]^T (\in R^{ur})$  comprises the white noise vector of  $\mathbf{w}_k$ ; the matrices  $\mathbf{\Gamma}_k (\in R^{uN \times r})$  and  $\mathbf{G}_k (\in R^{uN \times ur})$  denote the observation matrix of the state equation and the block Toeplitz matrix, respectively; and  $u$  is a variable ( $u \geq 1$ ) that indicates the quality of the modal parameters estimated using the SSI-CPAST algorithm. Equation (50.3) indicates that the subspace spanned by the Hankel vector of  $\mathbf{Y}_k$  is equivalent to the subspace spanned by the columns of  $\mathbf{\Gamma}_k$ .

In the SSI-CPAST algorithm, recursive subspace identification (RSI) is used to track the subspace spanned by the columns of  $\tilde{\mathbf{\Gamma}}_k$  for an expanded observation vector  $\mathbf{Y}_k$  instead of SVD calculation, as follows.

$$\tilde{\mathbf{\Gamma}}_k = \tilde{\mathbf{\Gamma}}_{k-1} - (\tilde{\mathbf{\Gamma}}_{k-1} \hat{\boldsymbol{\alpha}}_k) \boldsymbol{\gamma}_k^T + \boldsymbol{\alpha}_k \boldsymbol{\Omega} \hat{\boldsymbol{\alpha}}_k^T \boldsymbol{\Phi}_k, \quad (50.5)$$

$$\boldsymbol{\Phi}_k = \frac{1}{\beta} \boldsymbol{\Phi}_{k-1} (\mathbf{I} - \hat{\boldsymbol{\alpha}}_k \boldsymbol{\gamma}_k^T), \quad (50.6)$$

where the matrix  $\alpha_k = [\mathbf{Y}_k, \mathbf{Y}_{k-\tau}] (\in R^{r \times 2})$ ; and the matrix  $\hat{\alpha}_k = [\mathbf{h}_k, \tilde{\Gamma}_{k-1}^T \mathbf{Y}_{k-\tau}] (\in R^{r \times 2})$ .  $\Omega (\in R^{2 \times 2})$  and  $\mathbf{y}_k (\in R^{2 \times r})$  are expressed as follows.

$$\Omega = \begin{bmatrix} 1 & 0 \\ 0 & -\beta^\tau \end{bmatrix}, \quad (50.7)$$

$$\mathbf{y}_k = \frac{1}{\beta} \Phi_{k-1}^T \hat{\alpha}_k \left( \Omega^{-1} + \frac{1}{\beta} \hat{\alpha}_k^T \Phi_{k-1} \hat{\alpha}_k \right)^{-T}, \quad (50.8)$$

In the SSI-CPAST algorithm, the modal parameters are estimated by replacing the observation matrix  $\Gamma_k$  with the tracked subspace basis matrix  $\tilde{\Gamma}_k$  where the subspaces spanned by the columns of these matrices are equivalent:  $\text{span}(\Gamma_k) = \text{span}(\tilde{\Gamma}_k)$ . The state transition matrix  $\mathbf{A}$  and the output matrix  $\mathbf{C}$  can be estimated using the observation matrix  $\tilde{\Gamma}_k$  according to the following relationship:

$$\mathbf{A} = (\tilde{\Gamma}_{k-1})^+ \cdot \tilde{\Gamma}_k^{(2:u)}, \quad \mathbf{C} = \tilde{\Gamma}_k^{(1:1)}, \quad (50.9)$$

where the observation matrix  $\tilde{\Gamma}_k^{(i:j)} (\in R^{(j-i+1)})$  is defined as  $\tilde{\Gamma}_k^{(i:j)} = [(C\mathbf{A}^{i-1})^T, (C\mathbf{A}^i)^T, \dots, (C\mathbf{A}^{j-1})^T]^T$ .

If the matrix  $\mathbf{A}$  is diagonalizable, the state vector  $\mathbf{x}_k$  and the output vector  $\mathbf{y}_k$  can be expressed in terms of the eigenvectors  $\psi_m$  of  $\mathbf{A}$ , as follows:

$$\mathbf{x}_k = \sum_{m=1}^M a_m \cdot \psi_m e^{s_m(k\Delta t)}, \quad (50.10)$$

$$\mathbf{y}_k = \mathbf{C} \sum_{m=1}^M a_m \cdot \psi_m e^{s_m(k\Delta t)}, \quad (50.11)$$

where the  $m$ -th eigenvalue  $s_m = -\xi_m f_m + j f_m \sqrt{1 - \xi_m^2}$  of  $\mathbf{A}$  is related to the  $m$ -th resonant frequency  $f_m$  and the  $m$ -th damping ratio  $\xi_m$ ;  $\psi_m (\in R^r)$  is the  $m$ -th eigenvector of  $\mathbf{A}$ . The coefficient  $a_m$  indicates the contribution of the  $m$ -th eigenvector.  $\Delta t$  is the sampling interval and  $j$  is the imaginary unit. The  $m$ -th mode shape in the observable space is expressed using the following function  $\phi_m (\in R^N)$ :

$$\phi_m = \mathbf{C} \psi_m. \quad (50.12)$$

## 50.3 System Implementation

### 50.3.1 HFR Structured-Light-Based Vision Platform

To verify the performance of real-time modal analysis of shell-shaped objects, we developed a prototype system to simultaneously estimate the modal parameters of a vibrating cantilever plate by implementing SSI-CPAST on an HFR structured-light-based vision platform that consisted of a high-speed vision system, IDP Express [9], and a high-speed DLP LightCrafter projector. IDP Express consisted of two camera heads, a dedicated Field Programmable Gate Array (FPGA) image processing board (IDP Express board), and a personal computer (PC). The IDP-Express board has been designed to implement various image processing algorithms on FPGAs and it can transfer input images containing  $512 \times 512$  pixels and their processed results to a standard PC memory in real time at 2,000 fps. In this study, the PC specifications were as follows: ASUSTeK P5E motherboard, Intel@Core i7 2.9-GHz CPU, 4 GB of memory, and two 16-lane PCI-e 2.0 buses. The DLP LightCrafter is a compact projector module for HFR light projection. It can project binary patterns of  $840 \times 648$  pixels at 4,000 fps. In this study, we used a  $10 \times 10$  dot matrix pattern that was projected onto the shell-shaped vibrating cantilever plates as a structured-light pattern.

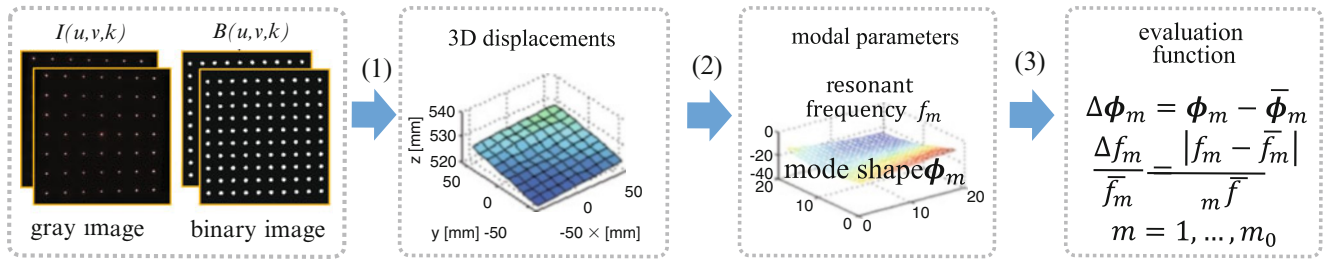


Fig. 50.1 Algorithms implemented in this study

### 50.3.2 The Implemented Algorithms

For the real-time modal analysis of shell-shaped objects, we implemented the following algorithms on the HFR structured-light-based vision platform at 1,000 fps. (1) Measurement of the 3D vibrational displacements of 100 measured points in real time at 1,000 fps using triangulation. (2) Fast output-only modal parameter estimation of 100 measured points in real time at 1,000 fps. (3) Damage inspection based on changes in the observed dynamic properties, as shown in Fig. 50.1.

#### 50.3.2.1 Measurement of 3D Vibrational Displacements

A  $10 \times 10$  dot matrix pattern was projected onto the surface of a shell-shaped object for HFR structured-light-based 3D measurement. The captured 8-bit grayscale  $512 \times 512$  images  $I(u, v, k)$  at time  $k$  were simultaneously transferred to the IDP Express board, where  $u$  and  $v$  denote the column and row pixel positions of the image coordinates. On the IDP Express board, the gray images  $I(u, v, k)$  were binarized into binary images  $B(u, v, k)$  and the centroid position  $(U_{ij}, V_{ij})$  of the  $i$ -th row and  $j$ -th column dot  $P_{ij}$  ( $i, j = 1, \dots, 10$ ) measured points, which were projected onto the image sensor as a  $10 \times 10$  dot matrix pattern, were extracted using a cell-based labeling algorithm, i.e., a fast multi-object feature extraction algorithm [10]. In this study, the binarization and cell-based labeling procedures were accelerated for  $512 \times 512$  images in real time at 1,000 fps or more using FPGA modules on the IDP Express board [10].

Given the relationship between the  $xyz$  coordinate system of the camera system and the direction of the dot-matrix projection, the 3D positions  $(x_{ij}, y_{ij}, z_{ij})^T$  of the  $10 \times 10$  measured points  $P_{ij}$  can be determined in the  $xyz$  coordinate system by the centroid position  $(X_{ij}, Y_{ij})$  of the measured point  $P_{ij}$  as follows:

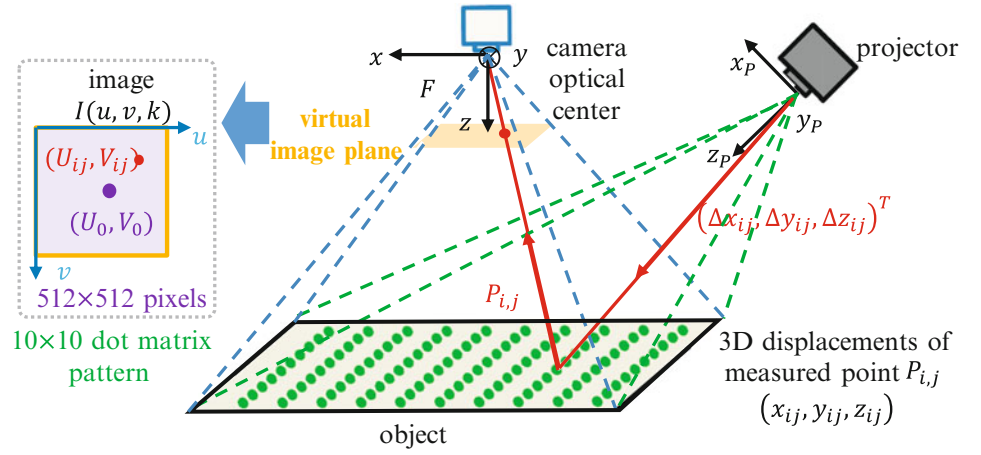
$$x_{ij} = \frac{d(U_{ij} - U_0)z_{ij}}{F^2}, \quad y_{ij} = \frac{d(V_{ij} - V_0)z_{ij}}{F^2}, \quad z_{ij} = \frac{x_p \Delta z_{ij} - z_p \Delta x_{ij}}{\frac{d(U_{ij} - U_0)}{F^2} \Delta z_{ij} - \Delta x_{ij}} \quad (i, j = 1, \dots, 10), \quad (50.13)$$

where  $(U_0, V_0)$  is the centroid pixel position of the image center,  $F$  is the focal length of the camera lens, and  $d$  is the length of one pixel pitch of the image sensor. During triangulation, the optical center of the structured-light projector is located at  $(x_p, y_p, z_p)^T$ , and the  $10 \times 10$  dots are projected in the direction of  $(\Delta x_{ij}, \Delta y_{ij}, \Delta z_{ij})^T$  from the projector, as shown in Fig. 50.2.

#### 50.3.2.2 Fast Output-Only Modal Parameter Estimation

Considering the observation vector  $\mathbf{y}(k)$  as the displacements in the depth direction,  $\mathbf{y}(k) = [z_{1,1}(k), \dots, z_{10,10}(k)]^T (\in \mathbb{R}^{100})$ , the modal parameters of a shell-shaped object can be estimated using a software implementation of the SSI-CPAST algorithm on the HFR structured-light-based vision platform. The observable output vectors  $\mathbf{y}(k)$  can be considered as the output-only vibrational responses to estimate the dynamic properties. For  $m = 1, \dots, m_0$ , the  $m$ -th resonant frequency  $f_m$  and  $m$ -th mode shape  $\phi_m (\in \mathbb{R}^{100})$  are estimated in real time at 1,000 fps. Here  $m_0$  is set to the maximum order of the modal parameters to be estimated.

**Fig. 50.2**  
Structured-Light-Based 3D  
measurement



### 50.3.2.3 Damage Inspection

We compared the estimated modal parameters with reference data and the estimated modal parameters for the shell-shaped object were used to inspect the damage according to the following evaluation functions:

$$\frac{\Delta f_m}{\bar{f}_m} = \frac{|f_m - \bar{f}_m|}{\bar{f}_m}, \quad \Delta \phi_m = \phi_m - \bar{\phi}_m \quad (m = 1, \dots, m_0), \quad (50.14)$$

where  $\bar{f}_m$  and  $\bar{\phi}_m$  denote the  $m$ -th order resonant frequency and mode shape of an undamaged reference shell-shaped object, respectively.  $\Delta f_m$  indicates the deviation from the  $m$ -th order resonant frequency of the reference  $\bar{f}_m$  and the vector  $\Delta \phi_m$  indicates the damage degree and position information.

### 50.3.3 System Configuration

In this study, we simultaneously analyzed 100 measured points in a  $512 \times 512$  image at 1,000 fps to estimate the modal parameters using the SSI-CPAST algorithm where the parameters of the vision system and SSI-CPAST algorithm were set as follows:  $d = 0.01$  mm,  $(U_0, V_0) = (252.3, 246.3)$ ,  $F = 17.4$  mm,  $u = 20$ ,  $N = 100$ ,  $m_0 = 1$ ,  $r = 2$ ,  $\beta = 0.99$ , and  $\tau = 100$ . Using our HFR structured-light-based vision platform, we confirmed the real-time execution of the algorithms using  $512 \times 512$  images at 1,000 fps.

## 50.4 Experiment

To demonstrate the performance of our system, we estimated the modal parameters of cantilever steel plates with cracks during a structural damage inspection where unknown excitation was provided by hammering. Figure 50.3a shows the experimental setup: the camera head of the IDP Express is located 527 mm in front of the cantilever plate; the origin of the  $xyz$  coordinate system was set to the optical center of the camera lens, and the  $xy$ -plane was set in parallel with the image sensor's plane. The DLP LightCrafter is located horizontally at  $(x_p, y_p, z_p) = (8.2, 6.9, \text{and } 120.1)$  mm in the  $xyz$  coordinate system; dot matrix pattern containing  $608 \times 684$  pixels and the matrix was  $10 \times 10$ , which corresponded to the measurement area of  $135 \times 135$  mm on the cantilever plate. Figure 50.3b shows the two steel shell-shaped plates covered with white paper to be inspected *NC* without any cracks and *CI* with 30% damage degree at 152 mm from its end. The cantilever plates were supported only at one end in the experiment. The elastic modulus and density of the steel shell-shaped object were  $1.86 \times 10^{11}$  N/m<sup>2</sup> and  $7.93 \times 10^3$  kg/m<sup>3</sup>, respectively. The width and height of the shell-shaped steel plates were 155 and 182 mm, respectively, and the thickness was 0.28 mm. The size of the fixed area in the middle of the plate at one end was 5 mm  $\times$  15 mm.

**Fig. 50.3** Experimental setup and materials inspected. (a) Experimental setup. (b) Materials

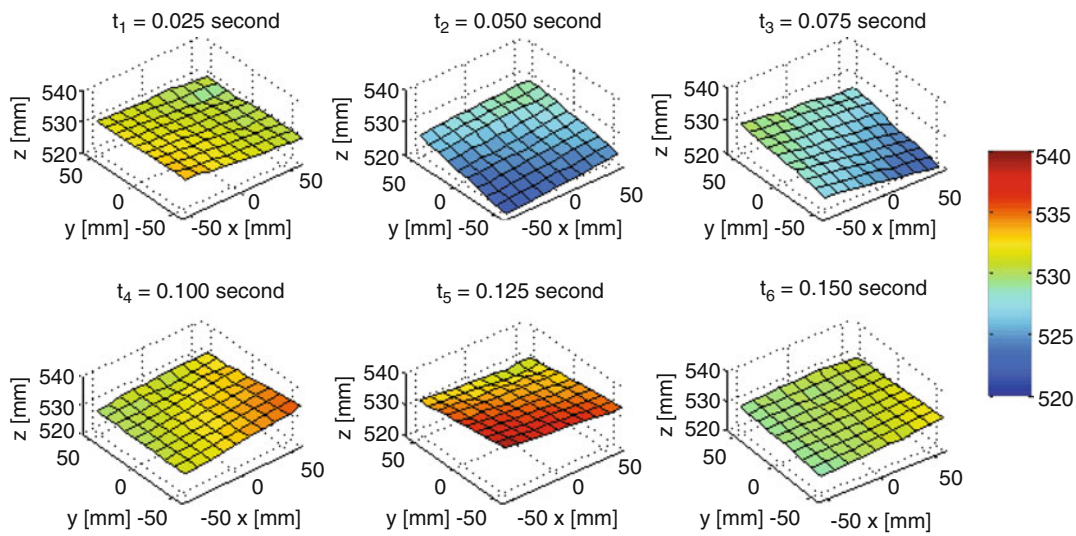
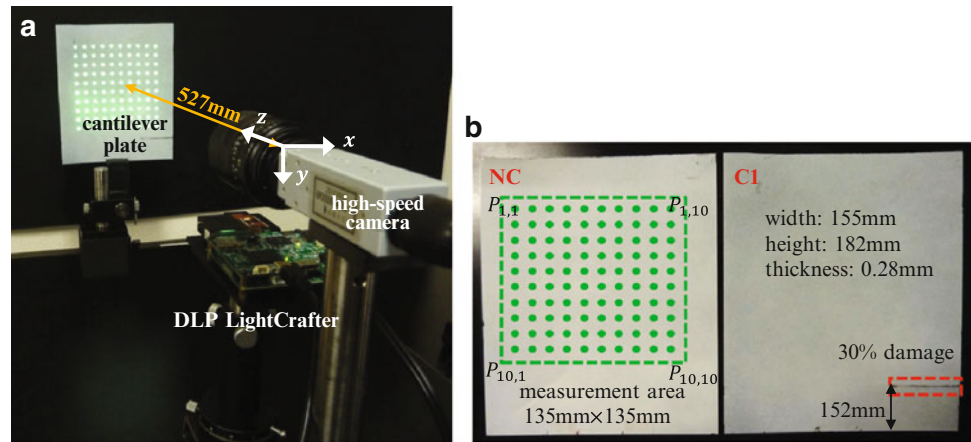


**Fig. 50.4** 3D shape deformation of the NC cantilever beam

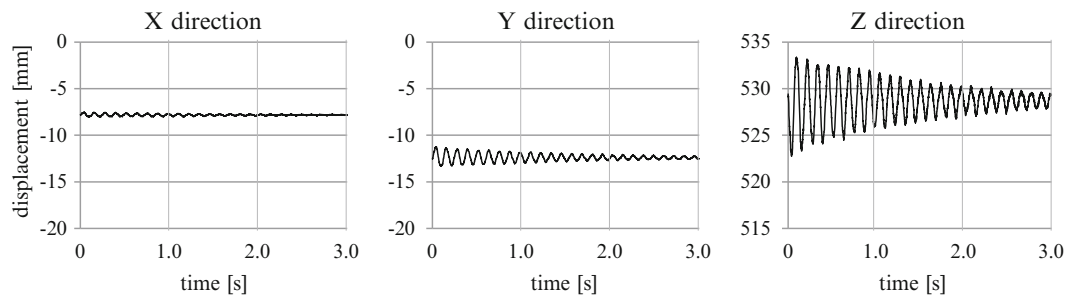


**Fig. 50.5** Temporal changes in the 3D displacement of  $P_{5,5}$

As an example of the shape deformities detected in the cantilever plates with vibration, Fig. 50.4 shows a six color-mapped sequence of the 3D shapes of the NC cantilever plate measured with a  $10 \times 10$  dot matrix pattern projection, which were taken at intervals of 0.025 s. Figure 50.5 shows temporal changes in the 3D displacement of the measured point  $P_{5,5}$  over 3 s. In the  $x$  and  $y$  directions, there were almost no vibrational displacements, whereas displacement in the  $z$  direction at a frequency of seven or eight times per second. The following figures show that our structured-light-based vision system operated at 1,000 fps could measure 3D displacements of shell-shaped objects vibrating at dozens of Hertz.

Figure 50.6a, b show the estimated first-order mode shapes of NC and CI, respectively, when they were excited by hammering. The estimated first-order resonant frequencies of NC and CI were 8.52 and 7.86 Hz, respectively. The first-order resonant frequency of CI decreased by  $\Delta f_1 / f_1 = 8\%$ , compared with NC and this decrease was caused by a crack in

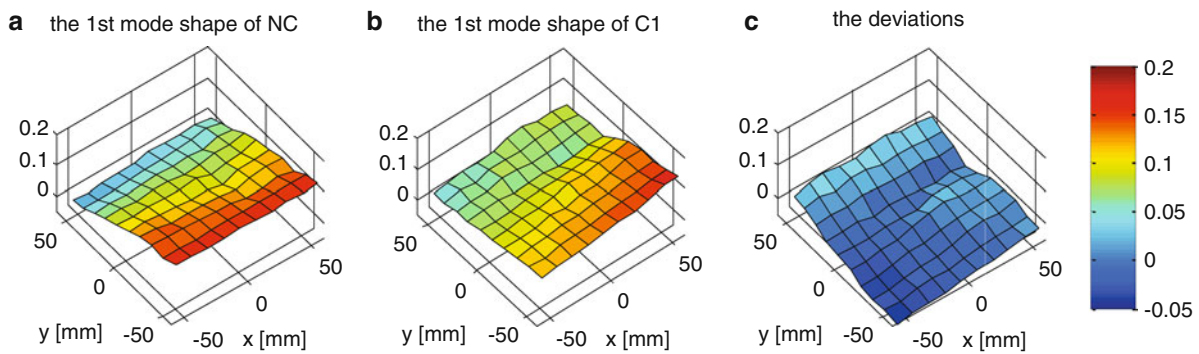


**Fig. 50.6** Estimated mode shapes of cantilever plates

*CI*. Figure 50.6c shows the deviations  $\Delta\phi_1$  of the first-order mode shape of *CI* when the modal parameters of *NC* were set as the reference. The first-order mode shape of *CI* was very different from that of *NC* and this trend increased in the right side of the plate because the 30% crack near the right side of the fulcrum of the cantilever beam greatly affected its spatial dynamics property. These experimental results showed that our system could measure the 3D displacements and estimate the modal parameters of cantilever plates in real time at 1,000 fps to determine any structural damage based on the estimated modal parameters.

## 50.5 Conclusions

In this study, we developed a real-time modal analysis system for inspecting shell-shaped objects based on an HFR structured-light-based vision system. Our system could analyze 3D displacements of 100 measured points on a shell-shaped object in real time at 1,000 fps and simultaneously estimate the modal parameters of shell-shaped objects that experienced unknown excitation in the audio-frequency range. The experimental results demonstrated the performance of our system and showed that it can simultaneously detect changes in the dynamic properties of shell-shaped objects due to cracks, i.e., structural damage.

## References

1. He J, Fu ZF (2001) Modal analysis. Butterworth-Heinemann, Oxford
2. Lee JJ, Fukuda Y, Shinozuka M, Cho S, Yun CB (2007) Development and application of a vision-based displacement measurement system for structural health monitoring of civil structures. *Smart Struct Syst* 3(3):373–384
3. Ji YF, Chang CC (2008) Nontarget stereo vision technique for spatiotemporal response measurement of line-like structures. *J Eng Mech* 134(6):466–474
4. Choi HS, Cheung JH, Kim SH, Ahn JH (2011) Structural dynamic displacement vision system using digital image processing. *NDT & E Int* 44(7):597–608
5. Yang H, Takaki T, Ishii I (2011) A structural damage quantification method for HFR-video-based modal testing. *J Syst Des Dyn* 5(4):624–641
6. Yang H, Takaki T, Ishii I (2011) Simultaneous dynamics-based visual inspection using modal parameter estimation. *J Robot Mechatron* 23(1):180–195
7. Juang JN, Pappa RS (1985) An eigensystem realization algorithm for modal parameter identification and model reduction. *J Guide Control Dyn* 8(5):620–627
8. Peeters B, Roeck GD (1999) Reference-based stochastic subspace identification for output-only modal analysis. *Mech Syst Signal Process* 13(6):855–878
9. Ishii I, Tatebe T, Gu Q, Moriue Y, Takaki T, Tajima K (2010) 2000 fps real-time vision system with high-frame-rate video recording. In: *Proceedings of IEEE international conference on robotics and automation*, Anchorage, pp 1536–1541
10. Gu Q, Takaki T, Ishii I (2012) Fast FPGA-based multi-object feature extraction. *IEEE Trans Circuits Syst Video Technol*. doi:10.1109/TCSVT.2012.2202195 (early access articles)

# Chapter 51

## Field and Numerical Testing of the BWE SchRs4600.50 Dynamic Behavior

Damian Pietrusiak, Przemysław Moczko, and Jerzy Czmochoński

**Abstract** Surface mining machines are the largest mechanical engineering structures. Bucket wheel excavators operating in lignite mines are continually exposed to dynamic loads. Moreover, nearly all structures are over 10 years old. The methods used in design and construction did not cover the dynamic behavior of machines, which resulted in problems in their operation and decreased durability. The tendency to optimize and increase the operational time of machines is currently also visible in the field of surface mining. As a result the machines which have been operating for many years are subject to investigation.

The SchRs (Schaufelradbagger auf Raupenschwenkbar) 4600.50 excavator, which is over 120 m long, 64 m high and weighs approximately 5,000 tons (excluding the dumping bridge), was investigated with regard to vibrations. Operational modal analysis was performed with 15 measurement points in different directions. This approach allowed to determine the variability of the dynamic characteristics of the machine in terms of operational conditions. Simultaneously a numerical model was prepared. Eventually, it was possible to compare and correlate both the numerical and experimental models and to establish the differences based on the operational load acting on the structure.

**Keywords** Bucket wheel excavator • Numerical simulations • Experimental techniques • Modal analysis

### 51.1 Introduction

The SchRs 4600.50 bucket wheel excavator (Fig. 51.1) is the largest lignite mining excavator in Poland. It is over 120 m long and 64 m high and its mass without the discharge bridge exceeds 5,000 tons. It is designed to excavate coal overburden and deposits. The 17.5 m diameter bucket wheel, powered by three 530 kW electric motors, achieves a nominal efficiency of 9,350 m<sup>3</sup>/h. This particular machine has been operating for over 18 years. It is a result of the German engineering thought and was designed for the geological conditions in Germany. In Poland it was introduced in the lignite mine in Bełchatów. The Bełchatów power plant supplies 20% of Poland's electricity needs. Therefore the deposits which are excavated often require the removal of hard overburden layers, stone insertions and interlayer of cohesive rock. In consequence, the bucket wheel excavators operating in the pit are subject to dynamic loads which significantly exceed the limits allowed by the design. As a result a need arose to precisely determine the dynamic characteristics of the machine, which would help to establish its resonance range or to plan its modernization [1, 9]. Due to the fact that the machine is subject to heavy excavating and mass forces during operation, it was decided to perform experimental tests using operational modal analysis [8, 10]. This approach makes it possible to establish the real dynamics of the machine, which are different while operation and in the unloaded state. Additionally a numerical model of the body was built. Based on the experimental tests the correlation between the two models was assessed depending on the operating conditions in which the modal model was identified experimentally. As a result it was possible to establish the usefulness of the numerical model [2] in calculating each particular case of loading.

---

D. Pietrusiak (✉) • P. Moczko • J. Czmochoński

Research Assistant, Institute of Machine Design and Operation, Wrocław University of Technology, Łukasiewicza 7/9, 50-371 Wrocław, Poland  
e-mail: damian.pietrusiak@pwr.wroc.pl; przemyslaw.moczko@pwr.wroc.pl; jerzy.czmochoński@pwr.wroc.pl



**Fig. 51.1** SchRs4600.50 excavator



## 51.2 Numerical Calculations

Based on technical documentation provided by the user a complete geometric model and a discrete model of the SchRs 4600.50 excavator superstructure were created. The model mostly consists of shell elements, which allowed for an accurate representation of many structural joints and other elements of the body. When constructing the model it is very important to properly balance the machine as this has a significant influence on the results of modal analysis, both for the local and global mode shapes. The distribution of masses in the model should be made in accordance with the stability proof, which describes the stability of the machine and all forces and loads affecting the structure. The undercarriage of the excavator was modeled using elastic elements of appropriate stiffness. This method allows for a significant decrease in the size of the model. Unfortunately the stiffness of elastic elements is rough and estimated which creates the risk of error.

Such a model helped to perform preliminary calculations for the excavator body. The main normal mode shapes are shown in Fig. 51.2. By locating them it was possible to determine the measurement points for the experiment on a real machine.

The frequencies of natural vibrations for individual mode shapes identified in the numerical model are presented in Table 51.1. The boundary conditions in the modal numerical model did not include the loads resulting from the digging forces and the dredged material.

## 51.3 Tests on the Machine

Tests were performed using operational modal analysis. In the case of mega machines such as a bucket wheel excavator this research method is the most convenient. The classic approach to identifying the modal model requires that excitation is sufficiently strong, which, in this case, could have proven very difficult to obtain [4, 5]. Additionally, owing to tests performed during operation under load, the dynamic characteristics identified the machine take into account the changes caused by interactions with the excavated material and by the digging forces [3].

Fifteen measuring points (twenty-three channels) were chosen on the SchRs 4600.50 excavator. Depending on the position, the accelerations were recorded in one, two or three directions (Fig. 51.3).

These points were selected on the basis of previous numerical analyses and experience in performing vibration tests and modal analysis. The directions of axes 'x', 'y', and 'z', from a global perspective, represent respectively the transverse, longitudinal and vertical directions relative to the body of the machine. However, in the case of movable elements, i.e. the bucket wheel boom and its jib, the 'y' direction is oriented lengthwise along the given subassembly, thus determining the direction of the 'z' axis. In this case only the 'x' direction remains unchanged with respect to the global system of coordinates.

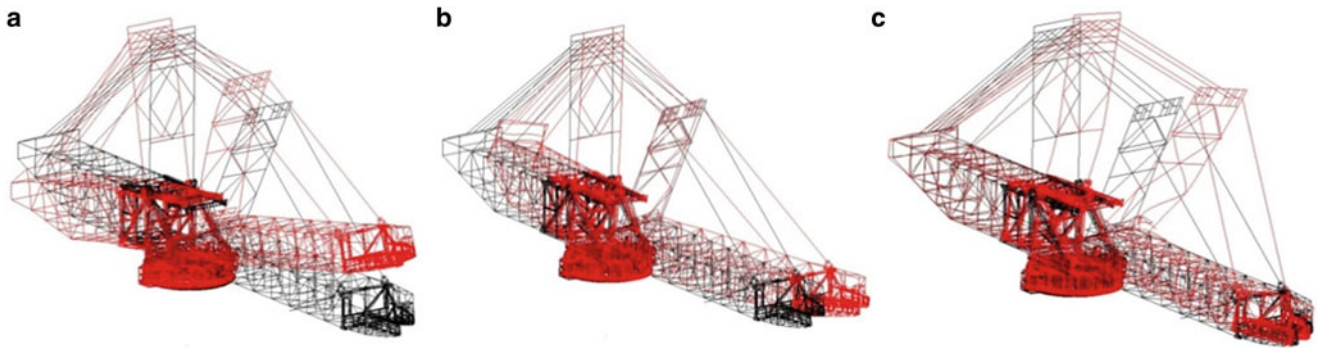
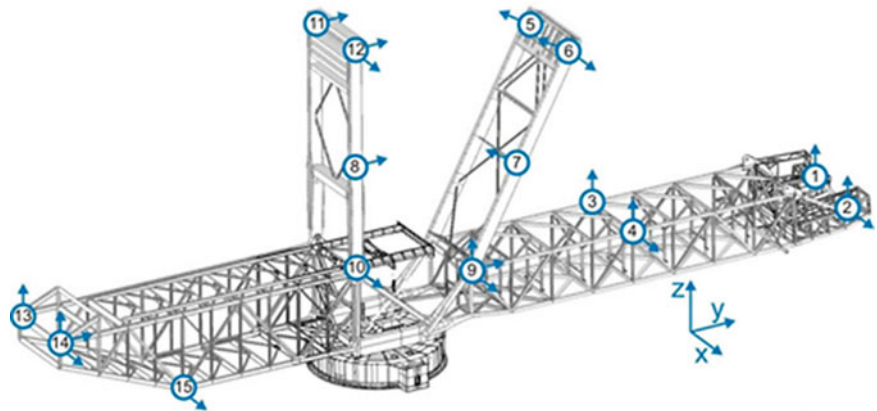


**Fig. 51.2** Three main mode shapes for the SchRs 4600.50 excavator: (a) 0.37 Hz, (b) 0.53 Hz (c) 0.82 Hz

**Table 51.1** Frequencies of natural vibrations of the SchRs 4600.50 excavator determined numerically

Mode shape	Frequency (Hz)
1	0.28
2	0.32
3	0.37
4	0.38
5	0.53
6	0.82
7	0.96
8	1.68

**Fig. 51.3** Measuring points on the SchRs 4600.50 excavator



The tests were run in different operating conditions. There were four cases of working load: upward digging, downward digging, downward digging during overload and machine travel. The time traces of accelerations for point 1 (vertical direction) in the aforementioned cases are illustrated in Fig. 51.4.

The above time traces of accelerations show that the maximum values of vertical acceleration at the end of the bucket wheel boom are approximately 1.5 times higher than in the case of backward digging. This indicates that the excavator is more exposed to dynamic forces and that the digging forces increase. In the case of machine overload the maximum vertical acceleration value at the end of the bucket wheel boom increased threefold in comparison with the case of digging at nominal capacity. During machine travel the vibrations are caused by the inertia forces of the moving excavator. In this case the maximum value of vertical acceleration at the end of the bucket wheel boom was the smallest and was equal to approximately only 0.4 m/s<sup>2</sup>. The vibrations of the machine during overloading were momentary and nonstationary and therefore were not taken into consideration while identifying the modal model.

Experimental studies resulted in the identification of frequencies and normal mode shapes of the excavator. Both the global vibrations of the whole systems as well as the local vibrations of particular booms were taken into account. Table 51.2

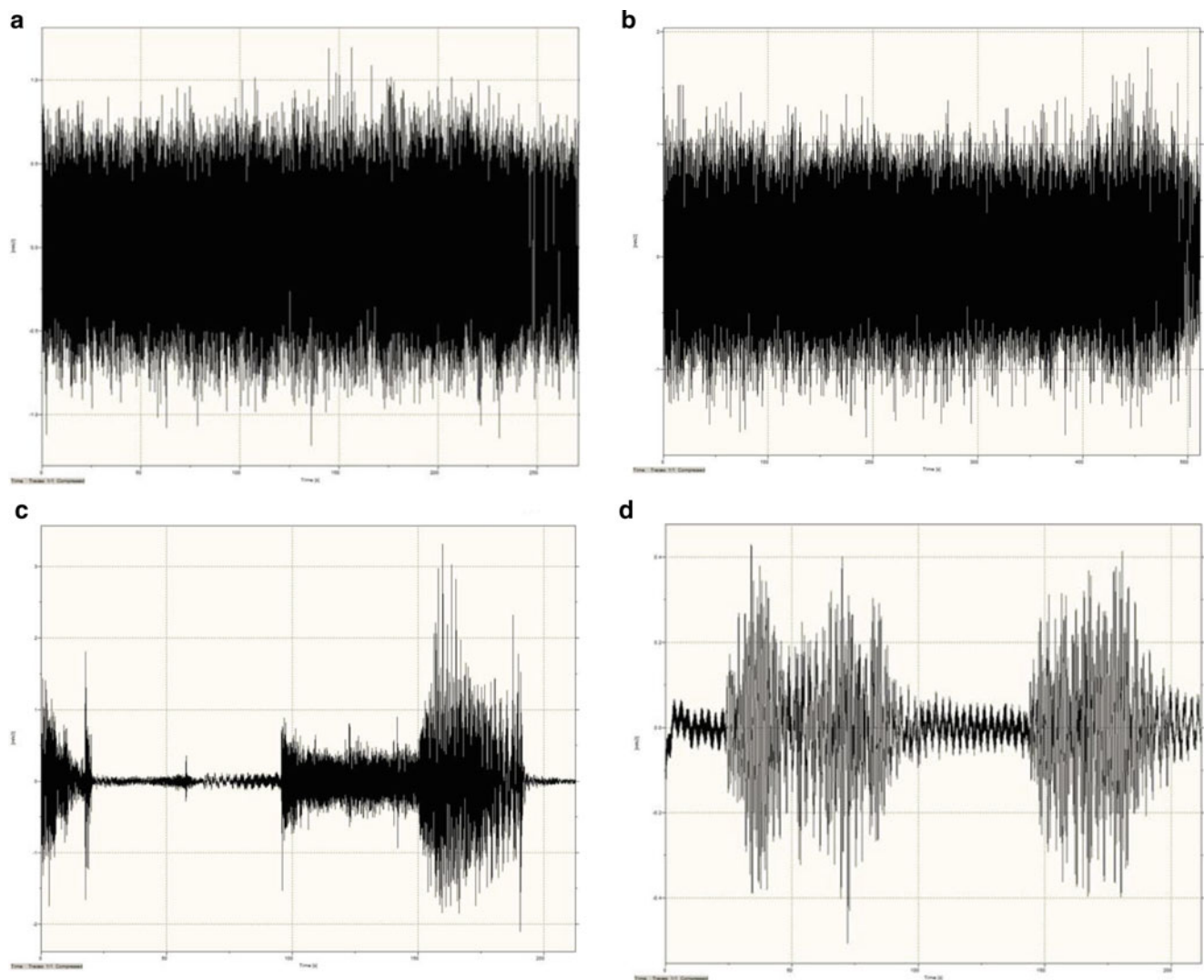


**Fig. 51.4** Time traces of accelerations in vertical direction in point 1 (a) upward digging, (b) downward digging, (c) downward digging with overload, (d) machine travel

**Table 51.2** Natural frequencies of the SchRs 4600.50 excavator identified experimentally

Drive		Normal operation		Downward digging operation	
Mode shape	Frequency (Hz)	Mode shape	Frequency (Hz)	Mode shape	Frequency (Hz)
1	0.36	–	–	1	0.36
2	0.55	2	0.55	2	0.56
3	0.80	–	–	3	1.04
4	1.05	–	–	4	1.08
5	1.18	5	1.08	5	1.13
6	1.55	6	1.58	6	1.57

presents the corresponding global mode shapes and frequencies at which they occurred depending on the type of excitation. It should be underlined that during excavation not all mode shapes are excited. This is mainly caused by the contact of the wheel with the face, which dissipates some of the energy and causes a change in the stiffness of the whole system.

What is also worth noting is the proximity of the frequency at which the second mode shape occurs (Fig. 51.5) and the excitation frequency. In this case it also indicates that the contact of the boom with the excavated material sufficiently dampens the vibrations of this mode shape and as a result it does not pose any major threats to the machine.

## 51.4 Correlation Between the Virtual Model and Experimental Model

The correlation [6,7] was performed on an experimental model based on results of tests on a real machine and on a numerical model. In order to make it similar to the experimental model the numerical model was not modified in any way which could influence the dynamics of the machine. However, it is important to note that the numerical model was based on documentation and stability proof, which were also the basis for constructing the real structure, and therefore, in theory, there should not be any discrepancies between models.

The figures below present MAC matrices which compare the mode shapes obtained during numerical simulations and the corresponding models identified experimentally during machine travel (Fig. 51.7), overburden digging (Fig. 51.8), downward digging of lignite deposits rotating right (Fig. 51.9) and left (Fig. 51.10). Regardless of the cutting direction, no differences in the correlation level were observed during normal operation (upward digging).

The MAC matrix of the numerical and experimental models identified during machine travel (Fig. 51.7) shows the corresponding individual mode shapes with characteristic correlation values along the matrix diagonal.

Among the described cases the best correlation was seen between the numerical model and the experimental model identified during machine travel. The MAC coefficient values (bars) on the matrix diagonal stand out (Fig. 51.7). Their average value is only 0.64 but the observed correlation for most mode shapes indicates a properly built model. Nevertheless this model still requires further analysis and parameters need to be established which would adjust the numerical model to the real one. In the case of the sixth numerical mode shape (0.82 Hz) and the third experimental mode shape (0.80 Hz) the MAC coefficient is 0.85, which indicates a very strong correlation between these mode shapes in both identified models (Fig. 51.6).

In the case of upward digging the correlation of models is insufficient (Fig. 51.8). Correlation is not seen over the whole frequency spectrum (lack of significantly higher values on the matrix diagonal) and only the eighth mode shape of the numerical model (1.68 Hz) corresponds with the fourth (1.53 Hz) and fifth (1.66 Hz) experimental mode shapes. The MAC coefficient for these mode shapes is almost identical. Therefore Table 51.1 lists one mode shape less than the matrix in Fig. 51.7. The results of experimental tests indicated that mode shapes 5 and 6 describe the same system pole. As shown in Fig. 51.7, which presents the correlation with numerical tests of the excavator, these assumptions have proved true. It is necessary to analyze the model in detail and fine-tune it to obtain better correlation results.

In the case of downward digging the correlation between models is also not seen over the whole spectrum but there is a very high value of the MAC coefficient for three mode shapes (Figs. 51.9 and 51.10). Particular attention should be given to

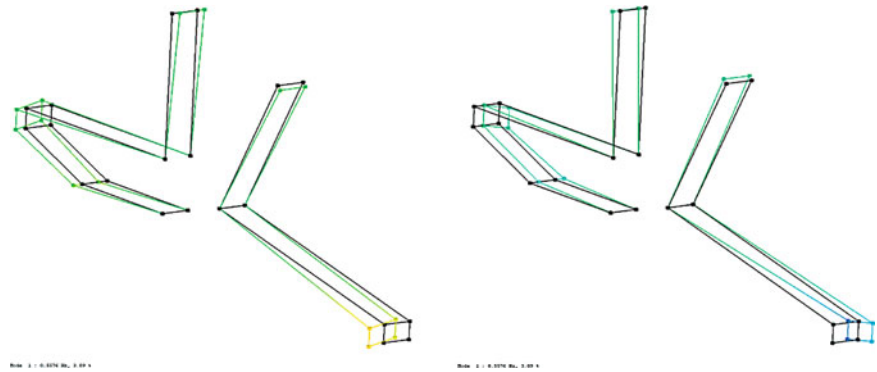


**Fig. 51.5** The second global vibration mode shape of the SchRs 4600.50 excavator

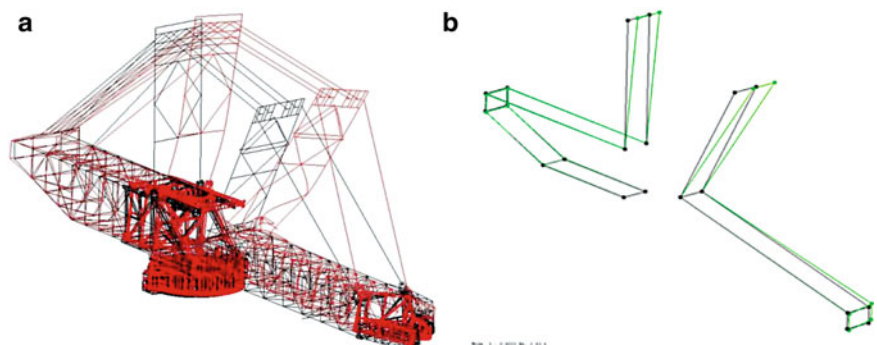


**Fig. 51.6** Numerical mode shape (a) and experimental mode shape (b) with MAC coefficient equal to 0.85

**Fig. 51.7** MAC matrix – excavator travel

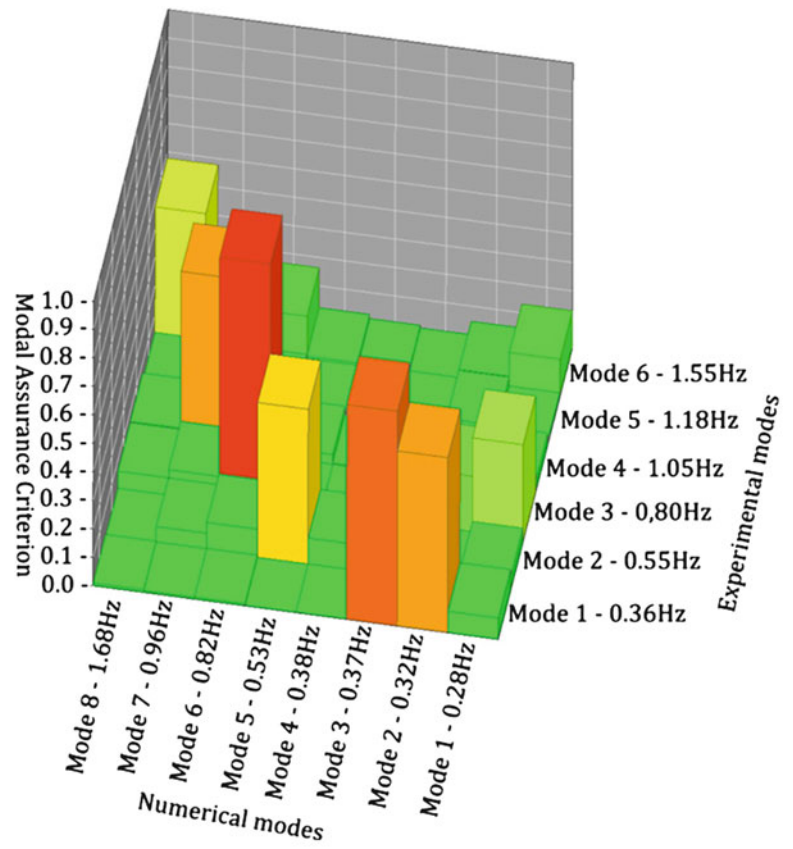


**Fig. 51.8** Upward digging

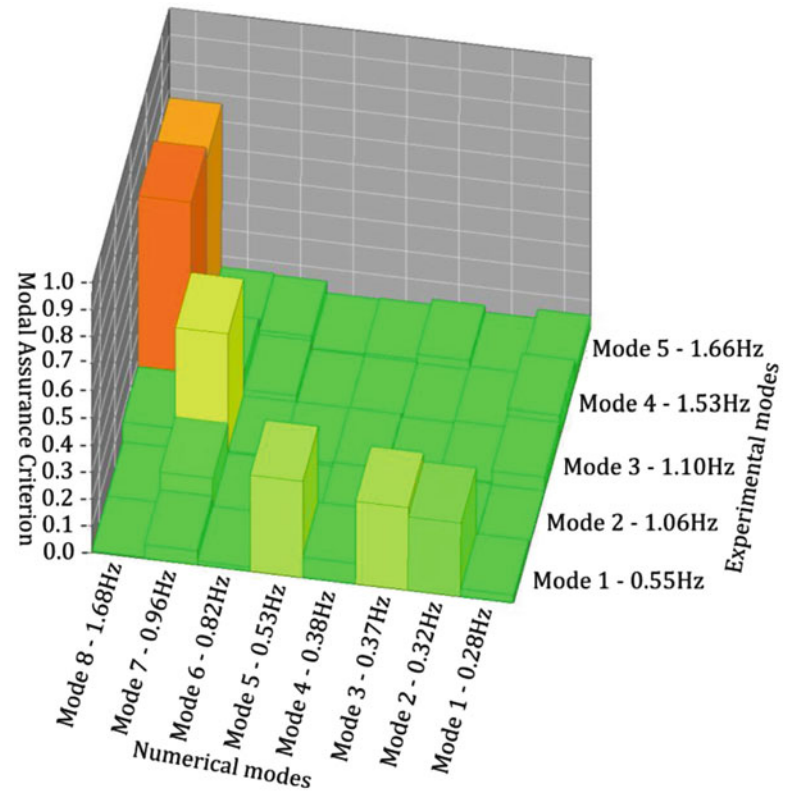


**Fig. 51.9** Downward digging while rotating right

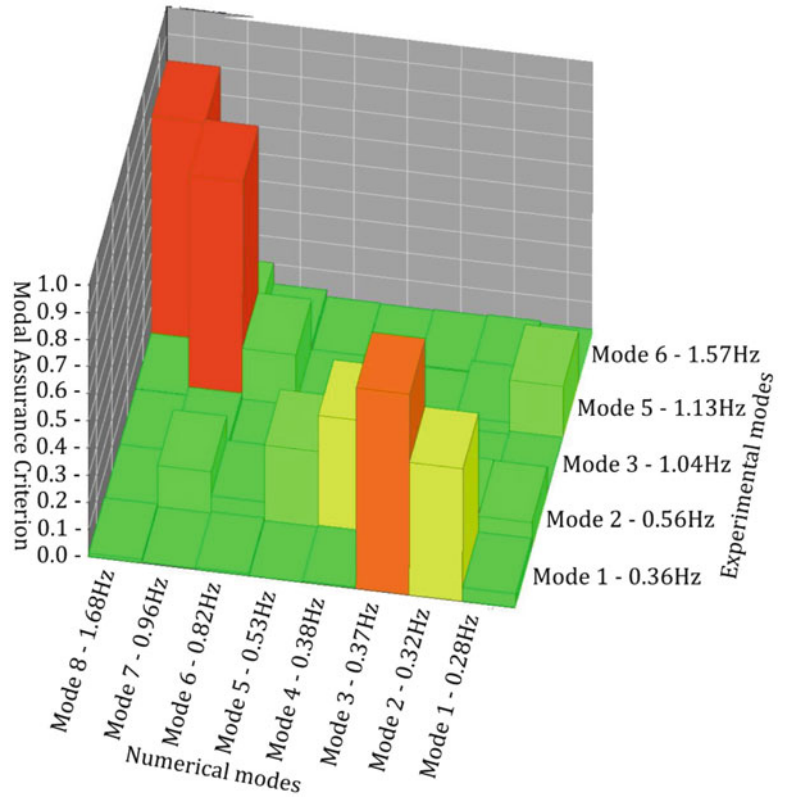


**Fig. 51.10** Downward digging while rotating left

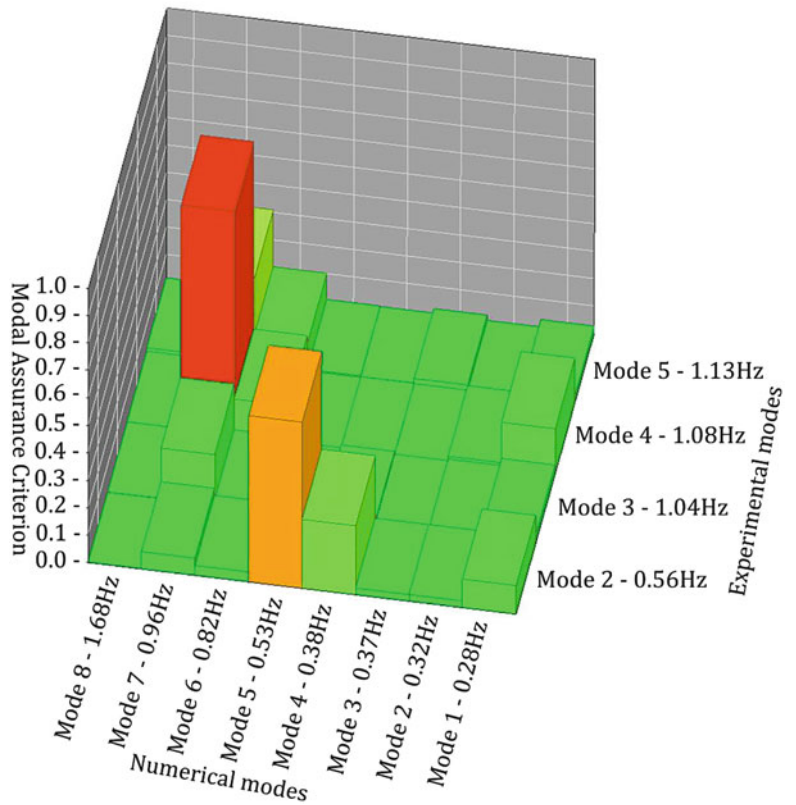
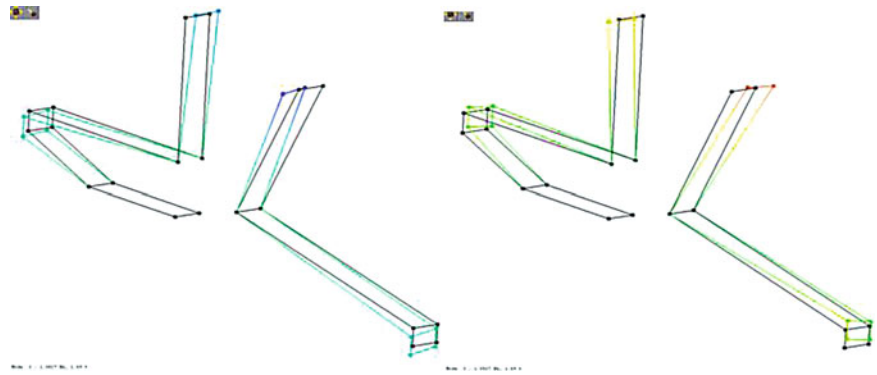


**Fig. 51.11** The fourth experimental mode shape excited during downward digging while rotating left



the sensitivity of the structure to the direction of excitation. When digging while rotating left, certain mode shapes, which were excited when digging while rotating right, were not excited or the excitation was very weak (if we assume the MAC coefficient of the numerical model as the criterion of accuracy). However, there was a very strong excitation of a mode shape (experimental mode shape 4, Figs. 51.10 and 51.11) which was not observed during upward digging or downward digging while rotating right but which occurred while the excavator was travelling.

## 51.5 Summary and Conclusions

The aforementioned results of experimental tests and their correlation with results of numerical tests clearly indicate that the virtual models which are currently built are not perfect. The highest correlation was observed in the case of machine travel. This is due to the fact that boundary conditions which occur during technological movements without working load are best represented in the model.

The representation of boundary conditions occurring during digging is a difficult and complex task. In this case only taking into account the digging forces is not sufficient. The most difficult task, which is the subject of ongoing work, is to take into account the elastic support resulting from the buckets and bucket wheel contacting the excavated slope. Clearly these conditions will also differ depending on the digging method. Downward digging is a less smooth process and is characterized by larger spikes in cutting forces than in the case of upward digging. Each of these methods introduces a different configuration of the machine and a different load spectrum in a different direction. This is clearly seen in the results of experimental tests and in correlation matrices between individual models identified via experiment and numerical simulation.

**Acknowledgement** Research co-financed by the European Union within the European Social Fund.

## References

1. Bosnjak S, Zrnic N (2012) Dynamics, failures, redesigning and environmentally friendly technologies in surface mining systems. *Arch Civil Mech Eng* 12(3):348–359
2. Bosnjak S, Zrnic N, Oguamanam D (2006) On the dynamic modeling of bucket wheel excavators. *FME Trans* 34(4):221–226
3. Bosnjak S, Zrnic N, Petkovic Z (2008) Bucket wheel excavators and trenchers – computer added calculation of loads caused by resistance to excavation. In: Kuzmanovic S (ed) *Machine design*. University of Novi Sad, pp 121–128
4. Gottvald J (2010) The calculation and measurement of the natural frequencies of the bucket wheel excavator SchRs 1320/4x30. *Transport* 25(3):269–277
5. Gottvald J (2011) Measuring and comparison of natural frequencies of bucket wheel excavators SchRs 1320 and K 2000. In: *GEMESSED'11 Proceedings of the 4th WSEAS international conference on Energy and development – environment – biomedicine*, Corfu Island, pp 335–340
6. Heylen W, Lammens S, Sas P (2007) *Modal analysis theory and testing*. Katholieke Universiteit Leuven, Belgium
7. Maia N, Silva J, He J, Lieven N, Lin R, Skingle G, To W-M, Urgueira A (1997) *Theoretical and experimental modal analysis*. Research Studies Press, Taunton
8. Pietrusiak D, Czmochoowski J, Kowalczyk M, Łgwa Ł (2010) Określenie właściwości dynamicznych koparki KWK 1500 metodą eksploatacyjnej analizy modalnej. *Górnictwo Odkrywkowe* 4:45–50
9. Rusinski E, Dragan S, Moczko P, Pietrusiak D (2012) Implementation of experimental method of determining modal characteristics of surface mining machinery in the modernization of the excavating unit. *Arch Civil Mech Eng* 12(4):471–476
10. Rusiński E, Czmochoowski J, Pietrusiak D (2012) Problems of steel construction modal models identification. *Eksploatacja i niezadowność – Maintenance and reliability* 14(1):54–61

# Chapter 52

## Modal Analysis of Rotating Carbon Nanotube Infused Composite Beams

C. DeValve, N. Ameri, P. Tarazaga, and R. Pitchumani

**Abstract** This study presents an operational modal analysis of rotating Carbon Nanotube (CNT) infused composite beams in order to explore the effect of CNT's on the natural frequencies and damping characteristics of the composite structure during rotation. Engineering applications with rotating components made from composites often suffer from excess vibrations because of the inherent high stiffness to weight ratio of the composite material and the oscillating loads from rotation. Previous research has demonstrated that the addition of CNT's to composite resins increases the damping characteristics of the resulting material, and several of these works have suggested that CNT-infused composites may be useful in rotor design as a means of passive vibration suppression. The present work aims to address this suggestion with an experimental investigation using composite beams fabricated with CNT's embedded in an epoxy resin matrix along with several layers of reinforcing carbon fiber fabric. An experimental apparatus is designed and constructed to hold two cantilever composite beams on opposite sides of a rotating central shaft controlled via a DC servo motor and a PID control loop. White noise is generated and added to the input motor RPM signal to randomly excite the base of the structure during rotation, and the Eigensystem Realization Algorithm (ERA) is used to analyze the data measured from the vibrating beam in order to determine the modal parameters of the system. The extracted modal parameters are presented as a function of the angular speed and weight percentage CNT loading in order to gain insight into application areas involving vibration suppression in rotating composite structures such as helicopter rotors and wind turbine blades.

**Keywords** Operational modal analysis • Eigensystem realization algorithm • Carbon nanotube damping • Fiber-reinforced composite • Rotating structure

### 52.1 Introduction

As the implementation of fiber-reinforced composite materials in engineering applications continues to increase, it is important to explore the potential benefits that can be designed into the physics of these materials. Much research has begun to explore the advantages of adding Carbon Nanotubes (CNT's) to the matrix of composite materials, such as strength and stiffness enhancement [1, 2], increased fracture and impact resistance [3, 4], thermal and electrical conductivity improvement [5], and material damping augmentation [6–8]. Damping improvement and the consequent reduction of vibrations is often critical to the successful operation of engineering structures which are composed of composite materials, for instance robotic arms, automotive and aerospace panels, helicopter rotors, and wind turbine blades. Reducing vibrations in rotating composite

---

C. DeValve • R. Pitchumani (✉)

Advanced Materials and Technologies Laboratory, Department of Mechanical Engineering, Virginia Tech, Blacksburg, VA 24061-0238, USA  
e-mail: [cdevalve@vt.edu](mailto:cdevalve@vt.edu); [pitchu@vt.edu](mailto:pitchu@vt.edu)

N. Ameri

Department of Aerospace Engineering, University of Bristol, Senate House, Tyndall Avenue, Bristol BS8 1TH, UK  
e-mail: [nima.ameri@bristol.ac.uk](mailto:nima.ameri@bristol.ac.uk)

P. Tarazaga

Center for Intelligent Material Systems and Structures, Department of Mechanical Engineering, Virginia Tech, Blacksburg, VA 24061-0238, USA  
e-mail: [ptarazag@vt.edu](mailto:ptarazag@vt.edu)



structures such as the aforementioned helicopter rotors or wind turbine blades is essential to maximizing the performance and lifespan of these structures while minimizing their adverse effects on surrounding individuals. Currently, the majority of vibration suppression methods in rotating composite structures consist of complex active techniques that add weight and intricacy to the structure, and therefore a passive means of vibration suppression built into the composite material of these rotors would be beneficial.

Previous research has shown that there is a weak interfacial bond at the CNT-matrix interface when CNT's are incorporated into thermosetting composite matrices [9], which has been sought to be remedied by methods such as CNT surface functionalization [10, 11]. Although this weak interfacial bond may be seen as a material defect, this characteristic can alternatively be exploited since a stick-slip action resulting in energy dissipation can occur at the CNT-matrix interface as the material is put under strain [12, 13]. Experimental measurements have supported this theory by demonstrating that the damping in CNT-reinforced composites increases with increasing strain [6, 7, 14]. Considering that a rotating structure is subject to increased loads and strains due to rotation-induced forces, it is reasonable to infer that the CNT damping mechanism described above has the potential to provide a significant damping enhancement to rotating composite structures during operation when increased strains are present. Building upon this idea, the current work presents an experimental study which investigates the effects of matrix-embedded CNT's on the modal parameters of rotating fiber-reinforced composite systems, using Operational Modal Analysis (OMA) techniques [15, 16] and the Eigensystem Realization Algorithm (ERA) [17] to analyze data measured from rotating cantilever composite beams.

## 52.2 Method

The experimental investigation focuses on rotating fiber-reinforced CNT-infused composites in order to explore the influence of CNT's on the modal properties of functional engineering composite structures. Single-Walled Carbon Nanotubes (SWCNT's) are used in the present study, which were purchased from SES Research (Houston, TX) with >90% purity and dimensions of <2 nm in diameter and 5–15  $\mu\text{m}$  in length. The composite samples were made via hand layup and compression molding, and the cured three-part composites were tested using an in-house developed experimental test setup and a proprietary ERA code developed at the University of Bristol.

### 52.2.1 Composite Fabrication

The thermosetting-matrix fiber-reinforced SWCNT-infused composite samples were fabricated using compression molding techniques in which the resin flows through the thickness of the part as it is being compressed to ensure uniformity of CNT dispersion throughout the sample. The CNT-epoxy mixture was prepared as follows: First, EPON 826 resin (Hexion Specialty Chemicals, Columbus OH) was mixed with Heloxy Modifier 68 (Hexion Specialty Chemicals, Columbus OH) with a ratio of 4:1 by weight in order to reduce the viscosity of the EPON 826 resin. Appropriate amounts of this resin mixture and CNT's were then weighed into a beaker using an Ohaus Explorer Pro balance to achieve the appropriate weight percentage of the CNT's in the final epoxy. The nanotubes were then delicately mixed into the resin by hand using a medical grade utensil in order to ensure that the CNT's were integrated with the resin before transport from the balance. After this brief manual stirring, the resin-CNT combination was blended using a IKA T25 high-shear mixer for 90 s. A Cole-Parmer 500 W ultrasonic processor with the appropriate size probe was then used to process the sample using a pulsed on-off mode with 1 s pulses for a total processing time of 5 min. The appropriate amount of hardener was then added to the sample and immediately incorporated with the CNT-resin sample using manual stirring for 2 min and the high-shear mixer for an additional 90 s. The entire resin sample was then transferred to a larger diameter beaker to increase the exposed surface area of the resin and degassed for 30 min.

The composite beams were fabricated using a hand-layup technique and compression molded using a three-part aluminum mold consisting of a separable top section, a middle spacer frame, and a bottom plate, presented in the left and center portions of Fig. 52.1, along with a finished composite plate shown on the far right-hand side of the figure. The top and bottom mold sections were sealed to the middle spacer using an O-ring fitted to a machined groove in each respective piece. A 3 K plain weave carbon fiber fabric (Fibre Glast Development Corp, Brookville OH), with 12.5 picks and wefts per inch, a nominal thickness of 0.3 mm, and an areal weight of 193  $\text{g}/\text{m}^2$  was used as the reinforcement fabric. Precise amounts of the epoxy-CNT mixture was poured between every two layers of carbon fiber fabric during the hand layup to minimize any filtering of the CNTs from the epoxy during the resin-permeation stage of the compression molding process. The sample was then processed using a programmable hot press from Tetrahedron Associates (San Diego, CA) using the following cure cycle:

**Fig. 52.1** The three part aluminum mold used to fabricate the composite samples, where the top of the mold is shown on the left-hand side of the figure and the center spacer bolted to the bottom plate is shown in the figure's center. On the right-hand side of the figure a finished CNT-infused carbon fiber reinforced composite plate is shown after being cured and removed from the mold

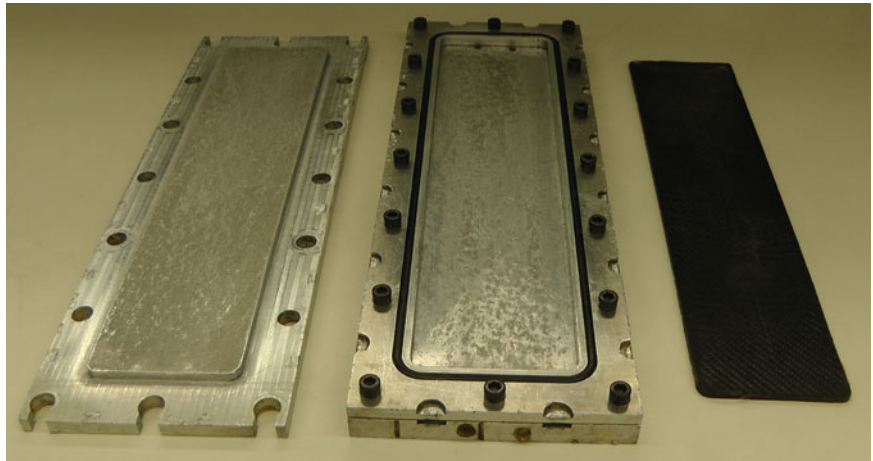
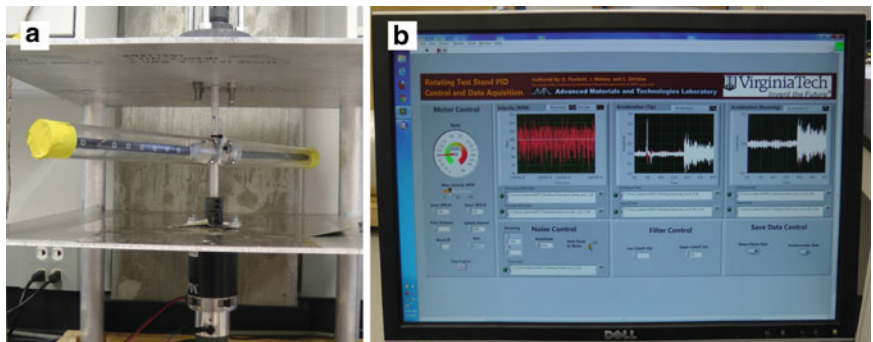


**Fig. 52.2** Depiction of the (a) rotating test rig and (b) Labview™ user control interface



First, the mold was held at 40°C and 40 kN for 1 h. The mold was then held under the same force while the temperature was ramped to 120°C over a 10 min period. After 2 h at 40 kN and 120°C, the mold was then cooled to room temperature in 15 min and the composite specimen was removed from the mold and machined into long slender beams of dimensions 266 × 12.7 × 0.2 mm to be used in the experimental rotating test stand.

### 52.2.2 Rotating Test Stand

An experimental test rig was developed to rotate two cantilever beams up to angular velocities of 500 RPM and simultaneously monitor the vibration of the beams during operation, depicted in Fig. 52.2a. The test rig control interface developed using Labview™ 9.0 is presented in Fig. 52.2b, which also graphically displays the angular speed of the motor and the accelerometer measurements in real time. To rotate the beams, a brushed DC motor (Magmotor, Worcester, MA) was mounted to the underside of a raised aluminum plate and controlled via a PID algorithm developed in Labview. Attached to the central rotating shaft of the motor was a fixture consisting of two clamps on opposite sides of the shaft in order to mount the cantilever beams, where the beams extended lengthwise parallel to the plane of rotation with their primary transverse vibrations also occurring parallel to the plane of rotation. Two accelerometers were attached to one of the beams, the first monitoring the acceleration at the tip of the beam (fixed) where the second (roving) was positioned variably along the length of the beam at precise increments during different experimental measurements. To minimize the effect of inter-sample variation from the roving accelerometer, washers of equal size and mass were attached to the beam at each unused accelerometer node location during the data acquisition. The accelerometers were powered by an external current source, and the signal from the test rig was passed through a liquid mercury slip ring at the top of the rotating test stand and fed through an analog Low-Pass (LP) filter before being recorded by Labview. Vibration measurements were recorded from the test setup at angular speed values from 0 to 500 in 100RPM increments, where 30 s of continuous data sampled at a rate of 1,800 Hz with an equivalent LP filter value was recorded in each case. Uniform white noise of ±10 RPM was added to the constant angular speed signal sent to the motor in order to randomly excite the base of the beam during operation and approach excitation conditions that maximize the effectiveness of OMA analysis techniques. The acquired data was then compiled and analyzed using ERA, detailed in the next subsection.

### 52.2.3 Eigensystem Realization Algorithm (ERA)

In this work, the Eigensystem Realization Algorithm (ERA) is used for the estimation of modal parameters from output-only measurements. ERA is a time-domain technique originally aimed at the evaluation of the dynamic behavior of structures from impulse responses. The discretized state space formulation [18] is defined as follows:

$$\begin{aligned} \mathbf{x}(k+1) &= \mathbf{A}\mathbf{x}(k) + \mathbf{b}(k) \\ \mathbf{y}(k) &= \mathbf{C}\mathbf{x}(k) \end{aligned} \quad (52.1)$$

where  $\mathbf{x}(k)$  is the state vector at the time instant  $t(k) = k\Delta t$ ,  $\mathbf{y}(k)$  is the output vector,  $\mathbf{A}$  and  $\mathbf{C}$  are the state and output matrix respectively and  $\mathbf{b}$  is the input to the system (assumed null after the initial time for an impulse response). The estimation of the modal parameters are evaluated by calculating the eigenvalues and the eigenvectors of the state space matrix  $\mathbf{A}$ . An essential step for the estimation of the state space matrix is the evaluation of the Hankel matrix which collects the impulse response of the system at shifted time steps, written as:

$$\mathbf{H}(k) = \begin{bmatrix} \mathbf{h}_k & \mathbf{h}_{k+1} & \cdots & \mathbf{h}_{k+q-1} \\ \mathbf{h}_{k+1} & \mathbf{h}_{k+2} & \cdots & \mathbf{h}_{k+q} \\ \vdots & \vdots & \ddots & \vdots \\ \mathbf{h}_{k+p-1} & \mathbf{h}_{k+p} & \cdots & \mathbf{h}_{k+q+p-2} \end{bmatrix} \quad (52.2)$$

where  $\mathbf{h}_k$  is a vector that contains the impulse responses at time instant  $k$

The relationship presented in [19] allowed the extension of this technique to the OMA case. Assuming that a system is excited by stationary white noise, it has been shown that the correlation function  $R_{ij}(t)$  between the response signals  $i$  and  $j$  at a time interval of  $t$  is similar to the response of the structure at  $i$  due to an impulse at  $j$ . Assuming damping to be small, this is expressed by the relation

$$R_{ij}(k\Delta t) = \sum_{r=1}^{2N} C_{ij}^{(r)} e^{s_r k\Delta t} \quad (52.3)$$

where  $C_{ij}^{(r)}$  is a constant associated with the  $r$ -th mode for the  $j$ -th response signal (i.e. the reference signal) and  $s_r$  is the system pole. This expression allows the use of techniques such as single-reference or polyreference Least Square Complex Exponential (LSCE) methods, the Ibrahim time-domain method (ITD) and the eigensystem realization algorithm (ERA). Specifically for the ERA case, elements of the matrix in Eq. 52.2 can be substituted with correlation functions and applied to estimate the modal parameters of the system.

## 52.3 Results and Discussion

As the goal of this work is to investigate the effect of matrix-embedded CNT's on the modal parameters of fiber-reinforced composites during rotation with a particular focus on the damping enhancement as a result of the addition of CNT's to the epoxy matrix, the following results present the natural frequencies and damping values of the composite beams found from the ERA analysis as a function of the CNT weight percent loading and angular excitation speed. The following OMA analysis is still in a preliminary development stage and will be expounded in future research.

### 52.3.1 Experimental Test Setup Validation

Extensive work was conducted to validate the rotating experimental test rig by studying the effects of clamping on the modal parameter measurements of various beams. Aluminum was used as a baseline material based on the large quantity of available literature detailing its damping characteristics [20–22], and several beams were machined out of 2024 aluminum to match the dimensions of the composite beams described above. Modal hammer and base excitation tests were performed

**Fig. 52.3** Frequency response of the clamped-free (a) aluminum and (b) composite cantilever beams from the impact hammer tests using a stationary mounted clamp (clamp 1) and the rotating test stand clamp

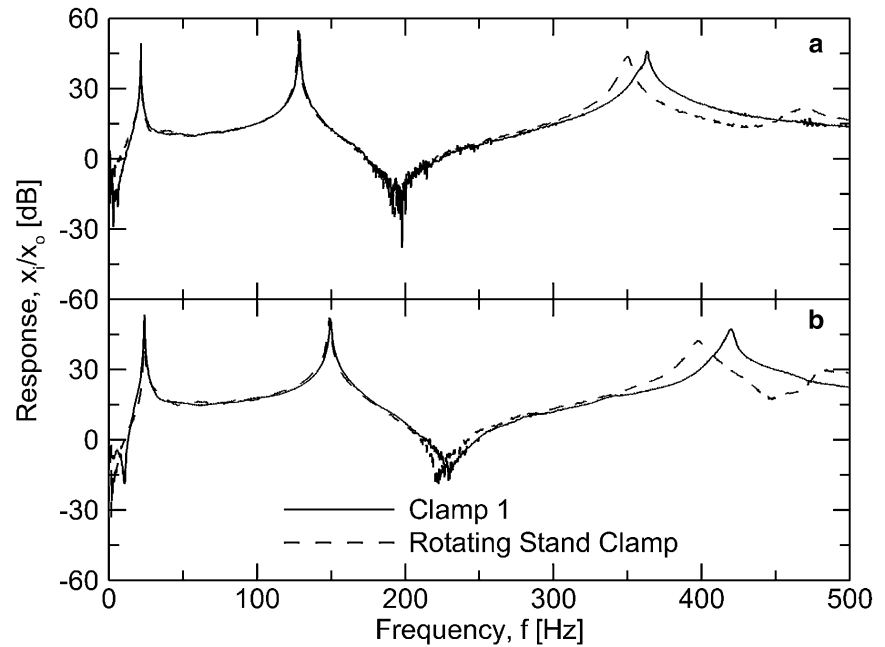
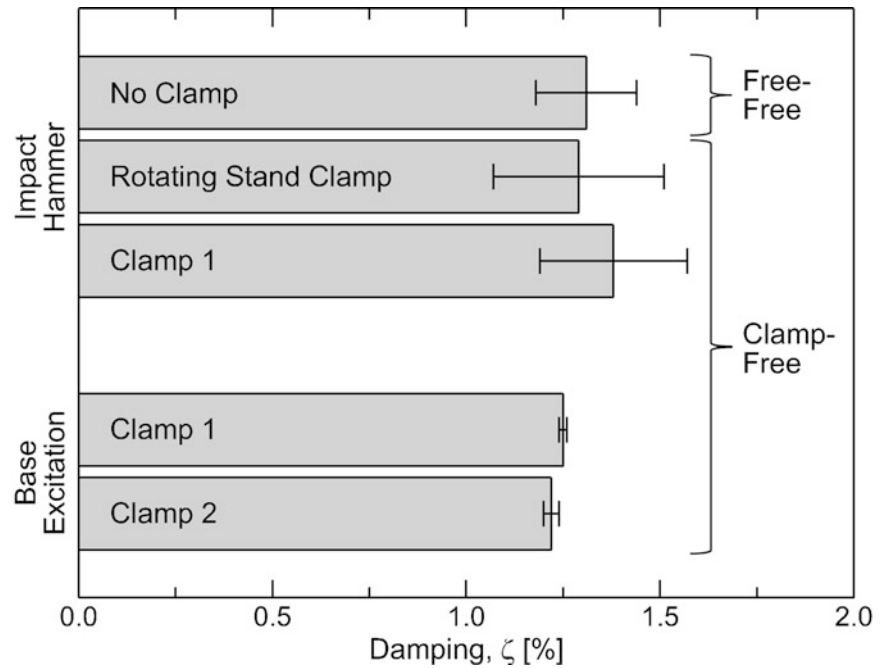


**Fig. 52.4** Comparison of the damping measured in the first mode of the composite beam using various testing conditions



on the beams using free-free and clamped-free boundary conditions with several different clamps. The frequency response of the materials were recorded in each case and the damping in the first mode was calculated as a comparison metric, where the results are presented in Figs. 52.3 and 52.4.

Figure 52.3 presents a frequency response plot for an aluminum beam (Fig. 52.3a) and a composite beam with no CNT's (Fig. 52.3b) obtained from an impact hammer test using an in-house fabricated stationary mounted clamp (denoted as clamp 1) compared to the clamp used on the rotating test stand. The frequency response measurements appear similar in each respective case shown in Fig. 52.3, with the first three natural frequencies occurring at approximately 20, 118, and 334 Hz in the aluminum beam and 21, 125, and 345 Hz in the composite beam with no CNT's. The difference in the first and second natural frequency measurements between the two different clamps equals about 1% for both beams, and a variation of about 5% is seen in the measured third natural frequencies for both beams between the two different clamps, which indicates good agreement between the two different clamping fixtures.

**Table 52.1** Test matrix for rotating test stand clamp validation

Case	Beam type	Boundary conditions	Test method	Clamp
1	Aluminum	Free-free	Modal hammer-Impact	N/A
2		Clamped-free	Modal hammer-Impact	Rotating stand
3				Clamp 1
4			Shaker-base excitation	Clamp 1
5				Clamp 2
6	Composite, 0 wt. % CNT's	Free-free	Modal hammer-impact	N/A
7		Clamped-free	Modal hammer-impact	Rotating stand
8				Clamp 1
9			Shaker-base excitation	Clamp 1
10				Clamp 2

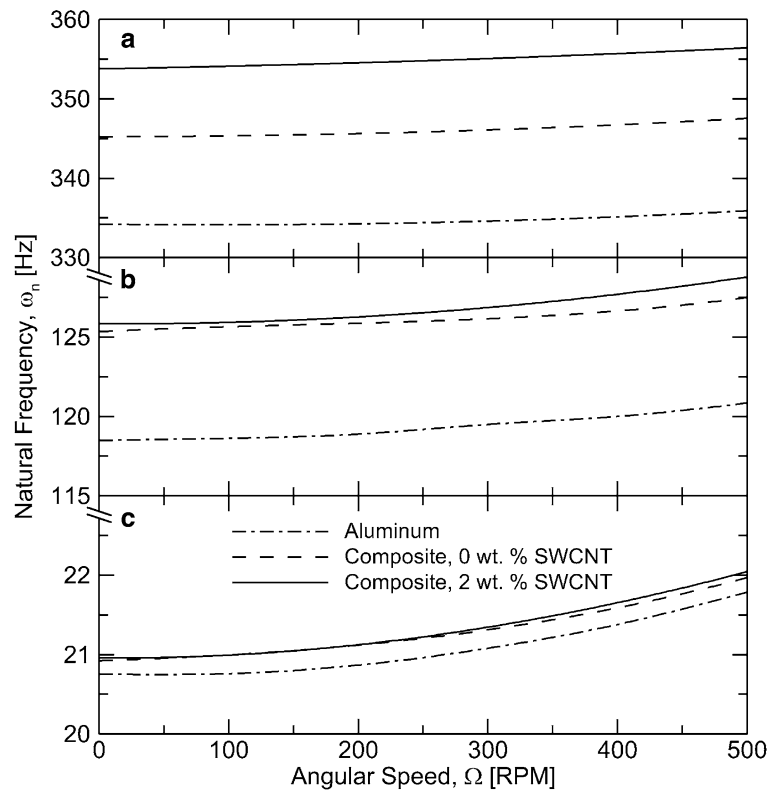
Additional tests were carried out using the same aluminum beam and composite beam with no CNT's to calculate the damping in the first mode of these respective materials and determine the influence from different testing methods and boundary conditions on the computed results, where the full validation test matrix is summarized in Table 52.1 and the results are shown in Fig. 52.4. Although these tests were performed on both the aluminum beam and the composite beam with no CNT's, the trends in each case were similar and therefore only the results for the composite beam are presented in Fig. 52.4 for brevity. The frequency response of the beam in each case was measured and computed using Siglab™, and the test methodology is described as follows: First, the damping was measured using an impact hammer test on a free-free beam to isolate any clamping effects before moving to a clamped-free configuration. Next, the beams were tested as cantilevers by mounting one end in clamp 1 and excited via an impact hammer test, where this same experiment was then repeated using the beam mounted in the rotating test stand clamp. Finally, clamp 1 was mounted to a shaker and the different beams were tested by means of base excitation and compared to the same test using an additional stationary clamp (denoted as clamp 2). From the results in Fig. 52.4, it is evident that the damping in all cases is measured to be approximately 1.25% and there is no statistically significant difference between the results of the free-free tests or any of the clamped-free tests for the composite beam. The standard deviation of the measured damping values for the base excitation results are very small and the standard deviation is relatively larger for the damping measured using the impact hammer tests but still within acceptable limits for the high variation normally found between damping measurements. From the results in Figs. 52.3 and 52.4 it is evident that the clamp used on the rotating test stand produces similar results to the other test clamps and methods, and therefore it is reasonable to assume that the rotating test stand and clamp do not significantly affecting the modal parameters measured from the beams reported throughout the remainder of this study.

### 52.3.2 Operational Modal Analysis

This subsection presents the results of the modal analysis performed on the rotating beams to calculate the natural frequencies and damping values of the different materials as a function of angular speed from 0 to 500 RPM. Using several cantilever beams with dimensions of  $266 \times 12.7 \times 0.2$  mm for each case, three different materials were examined: an aluminum beam serving as the baseline material and two different composite beams reinforced with carbon fiber fabric at a fiber volume fraction of 0.46, the first without CNT's and the second with two weight percent SWCNT's incorporated into the matrix material.

The first three transverse natural frequencies of the different beams as a function of angular speed was first investigated, where the results are presented in Fig. 52.5. The aluminum is shown by a dashed-dot line, the dashed line represents the composite with no CNT's, and the composite infused with two weight percent SWCNT's is denoted using a solid line. To better demonstrate the trends in the natural frequencies of each mode, Fig. 52.5a shows the results from the third mode, the second mode is illustrated in Fig. 52.5b, c presents the results from the first mode. In all three subfigures, it is evident that the natural frequency of each material increases as the angular speed is increased, evidence of the 'spin-stiffening' effect on the beams as a result of centripetal forces acting on the beam at increased rotational speeds [23]. This effect is most noticeable in the first mode shown in Fig. 52.5c, where the natural frequency in each mode increases by more than 1 Hz when the angular speed increases from 0 to 500 RPM. In the subsequent modes shown in Fig. 52.5a, b this trend is less noticeable because of the scale of the graphs, however in the second and third modes of vibration there is an increase in the natural frequency of about 2.5 and 5 Hz, respectively, when the angular speed reaches 500 RPM. It is also apparent that the natural frequency of the composite beams are much larger than the aluminum beam, and the composite beam infused with

**Fig. 52.5** The first three transverse natural frequencies of the aluminum, composite with zero weight percent SWCNT's, and the composite with two weight percent SWCNT's as a function of angular speed. The natural frequencies of the third mode are presented in (a), the second mode in (b), and the first in (c)

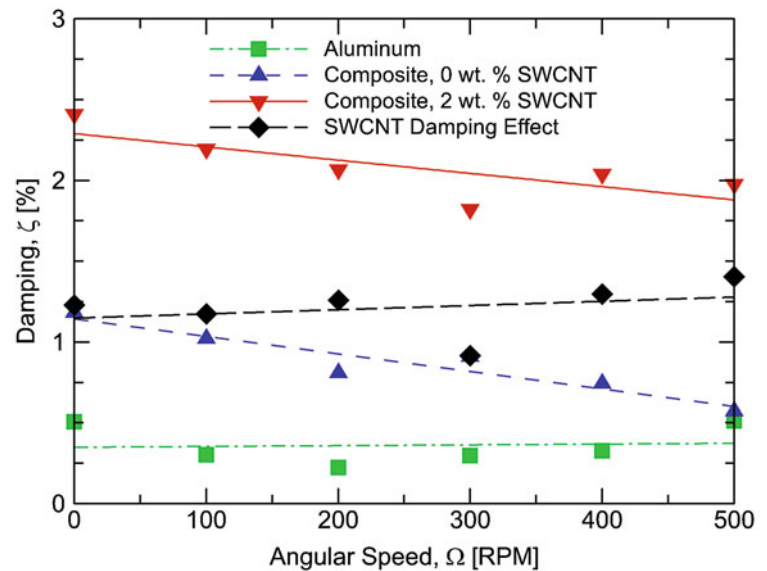


SWCNT's has a higher natural frequency than the composite without CNT's. As carbon-fiber composites are generally stiffer than a similarly shaped aluminum beam, this increase in natural frequency is expected. Additionally, an increase in the natural frequency of the SWCNT-infused composite suggests that the addition of CNT's further enhances the stiffness of the composite beam, a result also observed in previous studies [3, 6]. In general, the results in Fig. 52.5 demonstrate that the beams first three transverse natural frequencies increase with increasing angular speed and that the beams become stiffer when moving from aluminum to composite with no CNT's and from the plain composite to the SWCNT-infused composite material.

Figure 52.6 presents the measured damping in the first mode of all three material cases as a function of the beam's angular speed from 0 to 500 RPM. As in Fig. 52.5, the dashed-dot line represents the aluminum beam, the composite with no CNT's is denoted by a short-dashed line, and the solid line is used to show the composite infused with two weight percent SWCNT's. The raw data points at each incremental angular speed in each case are also shown by the various symbols denoted in the legend of Fig. 52.6, and colors are assigned to each material case to better visualize the data trends. Linear fit lines are used to describe the overall damping trends in each case to better illustrate the damping as a function of angular speed for each material. In the case of the aluminum beam trends shown in Fig. 52.6, the damping remains relatively constant as a function of angular speed and averages approximately 0.35%. The composite beam with no CNT's has a measured damping value of about 1.25% at 0 RPM, but tends to decrease as the angular speed is increased, reducing to almost 0.6% at 500 RPM. The damping in the composite beam with two weight percent SWCNT's also decreases with increasing RPM, but the damping values are much higher than the case without CNT's. At 0 RPM, the damping in the CNT-infused composite is measured to be about 2.4%, and decreases to only 1.9% at 500 RPM. From these values, it is evident that the addition of the CNT's to the composite matrix increases the damping in the composite by an average of 150% throughout the range of tested angular velocities.

In addition, a significant trend is seen when looking at the difference between the measured damping values in the composite beam with and without CNT's versus angular speed, presented in Fig. 52.6 as the long-dashed black fit line with diamond symbols representing the raw data points. This data set is referred to as the 'SWCNT damping effect' since it is representative of the change in damping between the original fiber-reinforced composite material and the identical fiber-reinforced composite material with the addition of CNT's. The damping difference in the composite as a result of the matrix-embedded CNT's increases with increasing angular speed, suggesting that the SWCNT's have an increasing effect on the material damping as the beam is more rapidly rotated. As was mentioned in the introduction section above, several previous studies investigating CNT damping in composites have found that the damping in the CNT-infused composite

**Fig. 52.6** The measured damping in the first transverse mode of the aluminum, composite with zero weight percent SWCNT's, and the composite with two weight percent SWCNT's as a function of angular speed. The difference in the two composite cases with and without CNT's is presented as the 'SWCNT Damping Effect' to visualize the damping increase measured in the fiber-reinforced composite from the SWCNT addition



increases with increasing material strain. This phenomena might explain the trend in Fig. 52.6 which shows an increase in the damping measured in the SWCNT-infused composite at higher angular velocities, as the large rotational loads subject the material to increasing strain as the angular speed is increased. Since the material is under strain from these rotational loads, the additional strain needed to initiate the stick-slip action at the CNT-matrix interface is more attainable from the vibration of the beam and might account for the increased damping measured in the beam at the higher angular speeds. Overall, the trends in Fig. 52.6 imply that the addition of CNT's to the matrix of fiber-reinforced composites enhance the damping in the material in a stationary frame and during rotation, with the CNT damping effects increasing as a function of angular speed. Note that the data presented in Fig. 52.6 is based on preliminary test cases and additional tests will be conducted to further increase the robustness of the inferred trends.

## 52.4 Conclusions

An experimental study was conducted to investigate the effect of Single-Walled Carbon Nanotubes (SWCNT's) on the modal properties of carbon fiber reinforced composite materials during rotation. Operational modal analysis techniques and the eigensystem realization algorithm were applied to analyze vibration measurements recorded from rotating beams excited using an in-house developed experimental test setup utilizing Labview to control and monitor the beams rotation. The results explored the effects of CNT's on the natural frequencies and damping values of aluminum and composite beams as a function of angular speed, and demonstrated that SWCNT's have a beneficial effect on the damping characteristics of rotating composite structures and can further enhance damping at increasingly high angular velocities. This research may be applied to the design of materials used in rotating composite structures such as helicopters blades or wind turbine rotors, where the addition of CNT's to the composite matrix can serve as a means of passive damping augmentation to increase the vibration suppression characteristics of the resulting composite structure.

**Acknowledgements** This research in this paper is funded in part by the National Science Foundation with Grant No. CBET-0934008, and the U.S. Department of Education through a GAANN fellowship to Caleb DeValve through Award No. P200A060289. Their support is gratefully acknowledged.

## References

1. Qian D, Wagner GJ, Liu W, Yu M, Ruoff R (2002) Mechanics of carbon nanotubes. *Appl Mech Rev* 55(6):495–533
2. Thostenson ET, Ren Z, Chou T-W (2001) Advances in the science and technology of carbon nanotubes and their composites: a review. *Compos Sci Technol* 61(13):1899–1912
3. Gojny FH, Wichmann MHG, Köpke U, Fiedler B, Schulte K (2004) Carbon nanotube-reinforced epoxy-composites: enhanced stiffness and fracture toughness at low nanotube content. *Compos Sci Technol* 64(15):2363–2371

4. Kostopoulos V, Baltopoulos A, Karapappas P, Vavouliotis A, Paipetis A (2010) Impact and after-impact properties of carbon fibre reinforced composites enhanced with multi-wall carbon nanotubes. *Compos Sci Technol* 70(4):553–563
5. Bal S, Samal SS (2007) Carbon nanotube reinforced polymer composites—a state of the art. *Bull Mater Sci* 30(4):379–386
6. Johnson RJ, Tang J, Pitchumani R (2011) Characterization of damping in carbon-nanotube filled fiberglass reinforced thermosetting-matrix composites. *J Mater Sci* 46(13):4545–4554
7. Khan SU, Li CY, Siddiqui NA, Kim J-K (2011) Vibration damping characteristics of carbon fiber-reinforced composites containing multi-walled carbon nanotubes. *Compos Sci Technol* 71:1486–1494
8. Kireitseu MV, Tomlinson GR, Ivanenko AV, Bochkareva LV (2007) Dynamics and vibration damping behavior of advanced meso/nanoparticle-reinforced composites. *Mech Adv Mater Struct* 14:603–617
9. Koratkar NA, Suhr J, Joshi A, Kane RS, Schadler LS, Ajayan PM, Bartolucci S (2005) Characterizing energy dissipation in single-walled carbon nanotube polycarbonate composites. *Appl Phys Lett* 87:1–3
10. Che J, Yuan W, Jiang G, Dai J, Lim SY, Chan-Park MB (2009) Epoxy composite fibers reinforced with aligned single-walled carbon nanotubes functionalized with generation 0–2 dendritic poly(amidoamine). *Chem Mater* 21(8):1471–1479
11. Liu L, Barber AH, Nuriel S, Wagner HD (2005) Mechanical properties of functionalized single-walled carbon-nanotube/poly(vinyl alcohol) nanocomposites. *Adv Funct Mater* 15(6):975–980
12. Zhou X, Shin E, Wang KW, Bakis CE (2004) Interfacial damping characteristics of carbon nanotube-based composites. *Compos Sci Technol* 64:2425–2437
13. Lin RM, Lu C (2010) Modeling of interfacial friction damping of carbon nanotube-based nanocomposites. *Mech Syst Signal Process* 24:2996–3012
14. Jang J-S, Varischetti J, Suhr J (2012) Strain dependent energy dissipation in multi-scale carbon fiber composites containing carbon nanofibers. *Carbon* 50(11):4283–4277
15. Reynders E (2012) System identification methods for (operational) modal analysis: review and comparison. *Arch Comput Methods Eng* 19(1):51–124
16. Mohanty P, Rixen DJ (2004) Operational modal analysis in the presence of harmonic excitation. *J Sound Vib* 270(1–2):93–109
17. Mohanty P, Rixen DJ (2006) Modified ERA method for operational modal analysis in the presence of harmonic excitations. *Mech Syst Signal Process* 20:114–130
18. Hermans L, Van der Auweraer H (1999) Modal testing and analysis of structures under operational conditions: industrial applications. *Mech Syst Signal Process* 13(2):193–216
19. James GH, Carne TG, Lauffer JP (1995) The natural excitation technique (NExT) for modal parameter extraction from operating structures. *Int J Anal Exp Modal Anal* 10(4):260–277
20. Granick N, Stern JE (1965) Material damping of aluminum by a resonant-dwell technique. NASA Technical Report, Goddard Space Flight Center, Greenbelt, Maryland.
21. Gibson RF, Plunkett R (1977) A forced-vibration technique for measurement of material damping. *Exp Mech* 17(8):297–302
22. Lee JM, McConnell KG (1975) Experimental cross-verification of damping in three metals. *Exp Mech* 15(9):347–353
23. Wright AD, Smith CE, Thresher RW, Wang JLC (1982) Vibration modes of centrifugally stiffened beams. *J Appl Mech* 49(1):197–202



# Chapter 53

## Modal Analysis and Dynamic Monitoring of a Concentrating Solar Heliostat

Adam Moya, Clifford Ho, Jeremy Sment, Todd Griffith, and Joshua Christian

**Abstract** Heliostats are structures that track the sun and reflect sunlight to a centrally located receiver on top of a tower to produce heat for electricity generation. Commercial power towers can consist of thousands of heliostats that are subject to wind-induced loads, vibration, and gravity-induced sag. This paper presents modal tests of a heliostat located at the National Solar Thermal Test Facility (NSTTF) at Sandia National Labs in Albuquerque, New Mexico. The heliostat was instrumented with 22 accelerometers, 4 strain gauges, and 3 wind anemometers to examine manually and wind-induced vibrations of the structure. Data acquisition software was developed to provide real-time monitoring of the wind velocity, heliostat strain, mode shapes, and natural frequencies which will be used to validate finite element models of the heliostat. The ability to test and monitor full-scale heliostats under dynamic wind loads will provide a new level of characterization and understanding compared to previous tests that utilized scaled models in wind-tunnel tests. Also, the development of validated structural dynamics models will enable improved designs to mitigate the impacts of dynamic wind loads on structural fatigue and optical performance.

**Keywords** Heliostat vibration • Experimental modal analysis • Dynamic wind load • Operational modal analysis • Concentrating solar power

### 53.1 Introduction

Any given commercial power tower consists of hundreds to thousands of heliostats which can range in size and cost with a total installation requirement reaching approximately 40% of the total plant cost [1]. This high cost results in a large effort focused on the development of cheaper or more efficient heliostats. The large number of heliostat structures within a given field introduces an interesting and challenging problem as we consider wind loading effects. Which modes are excited due to a specific wind event, and how they vary as a function of field position needs to be characterized as this could lead to an ultimate goal of a cheaper or more efficient heliostat. To answer this question, a system was developed at Sandia National Laboratories which will provide the data needed for a number of heliostats at the NSTTF in order to characterize its dynamic behavior. Such an analysis tool is currently lacking in the concentrating solar power (CSP) industry as mode shape characterization is often overlooked during the design phase. This paper will present the novel data acquisition system, the instrumented test structures, and some modal verification results by comparing finite element analysis performed in Ansys Mechanical and operational modal analysis performed on one of the NSTTF heliostats.

The dynamic heliostat project presented in this paper is an effort to fully understand the vibration of a heliostat within a real operating environment that is open to the elements. This work further expands on previous analysis [2–4] by introducing a new fully instrumented data monitoring system capable of more detailed modal estimation. Modal identification of these collectors provide a unique opportunity to tie the field of experimental modal analysis to other engineering disciplines often found in solar engineering such as optics or energy optimization. Open to extreme wind gusts peaking up to 50 mpr, the heliostats located at the NSTTF prove to be a great application for operational modal analysis techniques as opposed to

---

A. Moya (✉) • C. Ho • J. Sment • T. Griffith • J. Christian  
Sandia National Laboratories, Concentrating Solar Technologies Department, P.O. Box 5800,  
Albuquerque, NM 87185-1127, USA  
e-mail: [acmoya@sandia.gov](mailto:acmoya@sandia.gov); [ckho@sandia.gov](mailto:ckho@sandia.gov); [dgriffi@sandia.gov](mailto:dgriffi@sandia.gov)

**Fig. 53.1** Aerial photograph of Sandia National Solar Thermal Test Facility (NSTTF)



traditional experimental modal tests. This also provides a chance to verify existing models that are used in the CSP industry for force estimation on interior heliostats and further explore the effect of wind blockage and vortex shedding on the induced vibration of interior and exterior heliostats.

Located in Albuquerque NM, the NSTTF is home to approximately 220 operating heliostats whose sole purpose is research and development. Previous experiments at the NSTTF have sought after a finite element validation technique through the means of static testing [5, 6], however the problem of dynamic model validation proves to be a more difficult task. Current effort has been on completing a real time data acquisition system capable of monitoring vibration, wind, and strain data from a selected block of heliostats that are open to oncoming winds (Fig. 53.1).

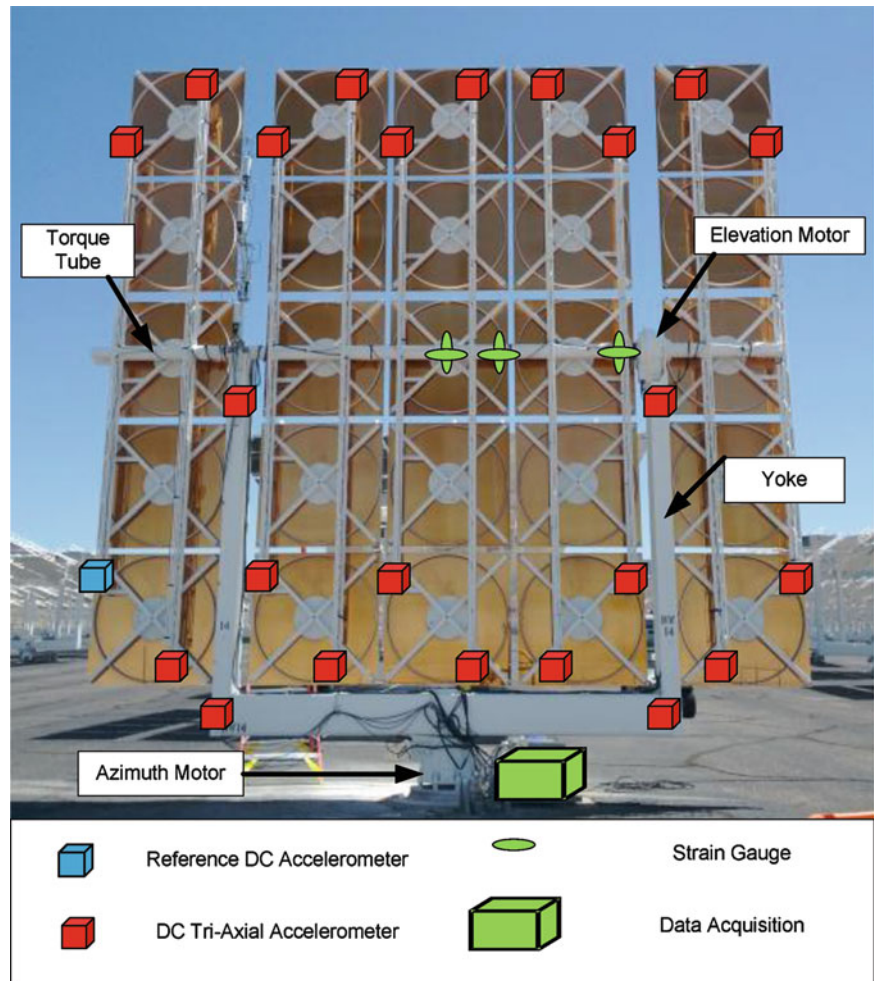
This system will feed useful data for a variety of projects within the NSTTF Solar Program, and ultimately introduce experimental modal analysis as tool for the CSP industry. The dynamic behavior of a heliostat can clearly be seen on a windy day as the beam from any said heliostat will shake off its intended target sometimes missing the tower entirely. Though the vibration magnitudes of these heliostats may be locally small with a displacement on the order of a few millimeters, the reflected beam that may travel up to a mile in to reach its target is extremely offset. This vibration induced error leads to a non-optimum system as the aim point of the heliostat is spread across its intended centroid on the receiver reducing the maximum or intended flux. Wind not only leads to optical losses, but can also lead to structural damage as well. It is common practice at the NSTTF to maneuver the heliostats to a stow position when wind gusts reach above 25 mph in order to prevent any damage or possible injury to personnel. With the monitoring system presented here, we will be able to feed fatigue analysis studies with experimental data with the goal of predicting such damage. For a commercial plant looking to install thousands of heliostats, a test like this could lead to large savings during the design and testing phase. This paper will present the monitoring system deployed at the NSTTF in detail and provide some initial results in terms of operational mode shape measurements and finite element comparisons. The initial goal of this system is to validate and tune a finite element model to important mode shape deformations which then is to be used in ray tracing and other numerical studies.

## 53.2 Test Structure, Instrumentation, and Data Acquisition

The heliostats at the NSTTF consist of 25 individual mirrors that are individually focused to a parabolic shaped based off the distance to the target, and tilted so the normal vector points to a selected centroid on the receiver tower. These mirrors are attached to a “U” shaped structure referred to as the yoke. The yoke rotates about a pedestal housing the azimuth motor and supports the 25 mirrors with a circular torque tube attached to 5 cantilevered truss assemblies. These truss assemblies are rotated via a elevation drive that is mounted to one side of the yoke while the other side is supported via roller bearings. Each truss assembly contains one short truss and one long truss that both support five mirror facets with adjustment bolts used to properly aim each individual mirror. This geometry is shown in Fig. 53.2 along with the locations of sensors installed on a single heliostat.

One heliostat in particular was chosen to instrument heavily in order fully characterize the operational dynamics in terms of mode shapes and natural frequencies. This heliostat deemed the “Well Instrumented Heliostat” is located on the western edge of the field and is the concentration of this study. This heliostat was instrumented with 24 tri-axial DC MEMS accelerometers, 6 piezoelectric strain gauges, and 6 3-dimensional wind anemometers. The accelerometers have

**Fig. 53.2** Well instrumented heliostat sensor layout



a sensitivity of 1,000 mV/g which were selected based off of previous preliminary modal analysis. This preliminary test found this sensitivity to be optimum to capture the modes of interest. These accelerometers are mounted with supplied magnetic mounts onto the extremities of each beam and on the yoke as shown in Fig. 53.2. Another plus from using the DC accelerometers is the low frequency measurement range (0–0.5 Hz) which is normally not measured when piezoelectric accelerometers are used. This low frequency content will aid in the measurement of two rigid body modes that were found within the structure. The six wind anemometers are located on a frontal and rear tripod tower consisting of three different measurement heights strategically selected to properly capture any blockage effects. This experimental setup is all installed remotely with National Instruments hardware and can be used locally with a laptop or remotely in the NSTTF control tower via fiber optic communication.

In addition to the well instrumented heliostat, 11 additional heliostats were instrumented nominally with a more limited set of sensors. The satellite image in Fig. 53.3 shows the locations of these heliostats with respect to the receiver tower. This triangular block of heliostats was selected to best capture incoming wind gusts as well as any reduction in vibration due to the frontal heliostat blockage. These nominal heliostats will not offer the same detailed mode shapes as the well instrumented heliostat, but they will give enough information to decide which modes are excited due to a certain wind event.

Due to the unique remote location requirements of this data collection, a custom configured and stand alone data acquisition system needed to be created. National Instruments hardware was installed in weatherproof containers at each heliostat which houses all sensor connections, National Instruments Compact RIO hardware, and communication hardware. While the well instrumented heliostat transmits data via a high speed fiber optic link, the rest of the heliostats bundles data onto the three phase power line along with heliostat control data. Custom written software syncs the channels to the same reference clock and streams pseudo real time data to the user. The “pseudo real time” refers to blocks of frequency data that get pushed to the acquisition pc based on user specified averaging parameters. For operational modal analysis purposes,

**Fig. 53.3** Vibration monitoring locations at NSTTF © Google 2012

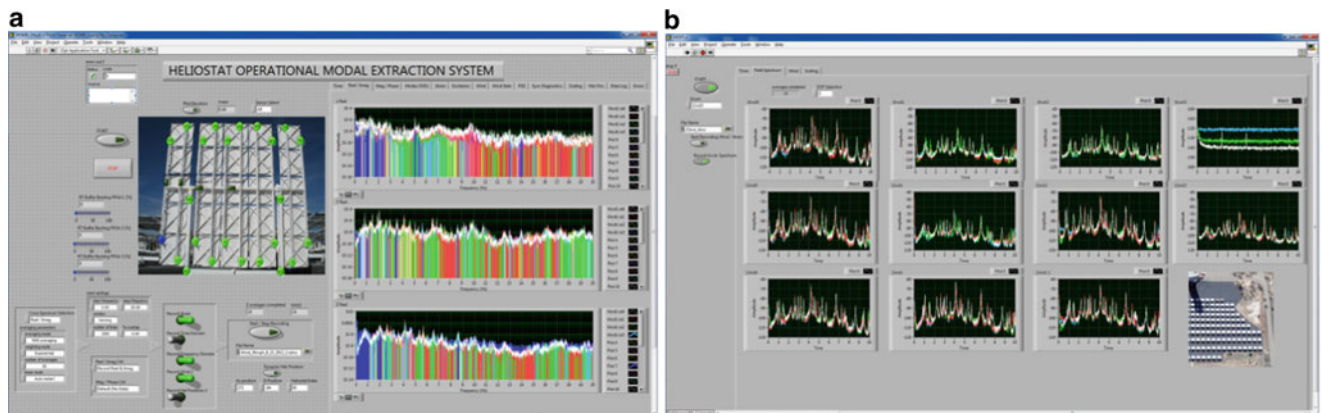
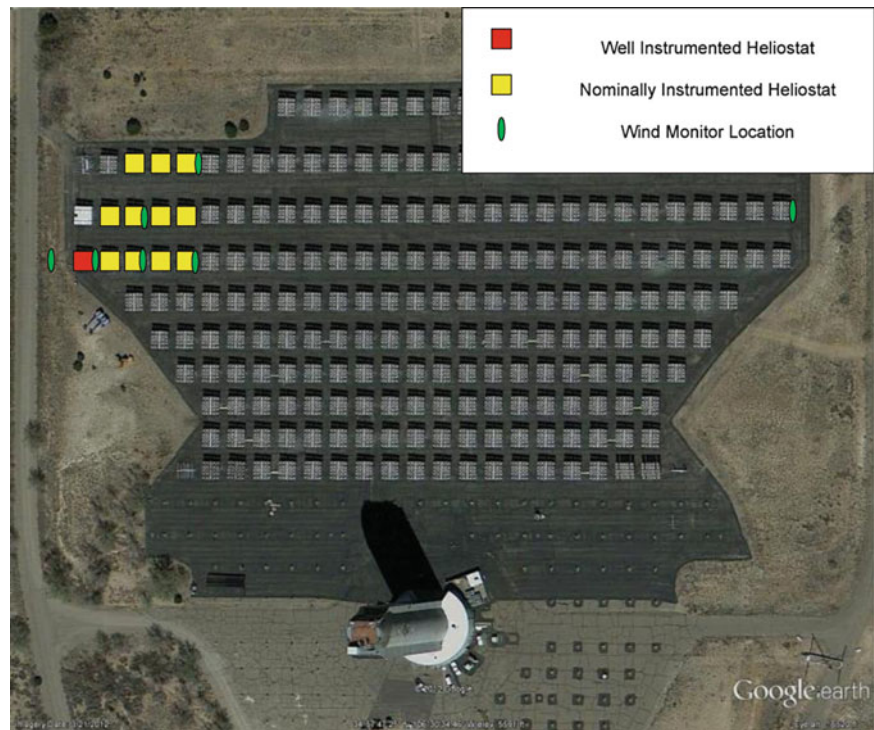


**Fig. 53.4** (a) Example screenshot of OMA cross spectrum on well instrumented heliostat within Labview developed data acquisition program (b) Screen shot of OMA spectrums for nominally instrumented field heliostats during 25+ mph winds

the system streams the accelerometer cross spectrum response data in the frequency domain as well as a time history of acceleration, wind, and strain data. Figure 53.4a, b show screenshots of this system displaying the frequency response from the well instrumented heliostats and the nominal heliostats.

### 53.3 Modal Parameter Estimation

Thanks to previous modeling efforts and preliminary experimental modal testing, finite element predicted shapes are available for aiding in mode shape verification. This model was recently modified from a reconfigurable Solidworks model to run in Ansys Mechanical. This new Ansys model allows for better control over contact conditions as well as faster parallel processing capability. The model will be further verified with newly acquired detailed mode shapes and will be capable of creating deformed mode shapes of the NSTTF heliostat at any configuration or field position. Field position is an important

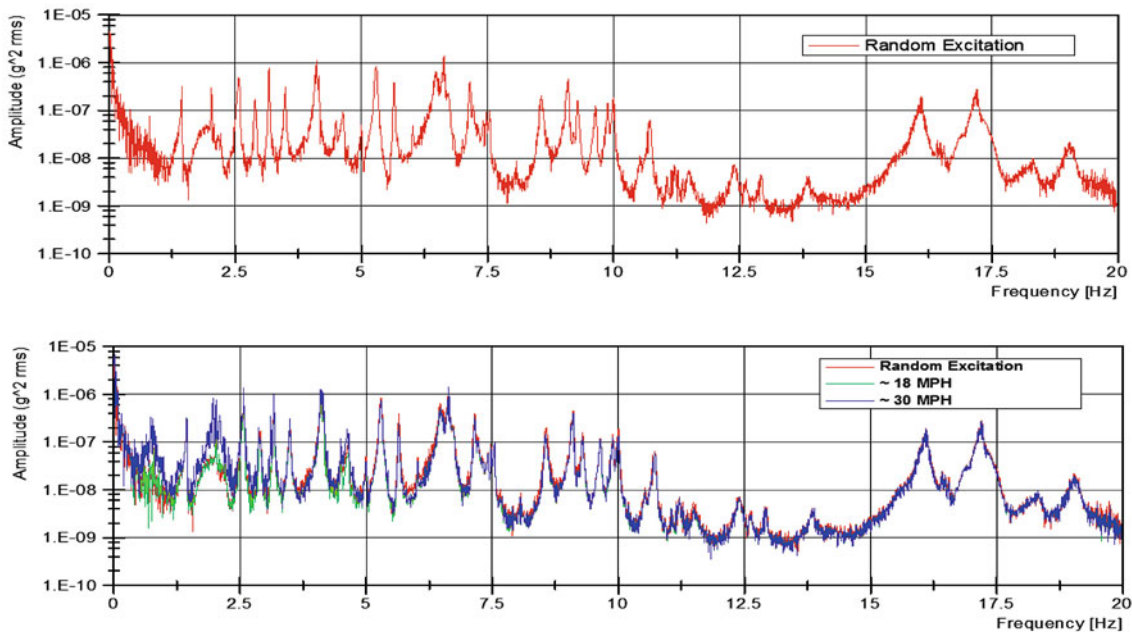


Fig. 53.5 Wind excited data (blue/green) vs. random excitation data (red)

parameter as every heliostat must be initially aimed and focused to its target, thus creating slightly different mirror geometry. These deformed shapes and modal test data will then be used for fatigue analysis and ray tracing studies to demonstrate the importance heliostat vibration can have on power generation and heliostat cost. To verify this model, operational modal analysis was performed on the well instrumented heliostat in three different orientations. The three orientations of current interest are a vertical position or  $90^\circ$  where all mirrors are in plane with the yoke support, a more realistic operational orientation of  $45^\circ$ , and the stow configuration which is  $6^\circ$  with respect to the horizontal.

At the mercy of windy days, a pseudo random input was used to simulate the forcing function of the wind. This random input is introduced with a standard instrumented sledge hammer normally used in experimental modal analysis. This input was provided to the trusses and yoke in order to excite the same modes excited during a wind event. Figure 53.5 displays the cross spectrum of a random excited data set compared to a operational wind excited data set taken during wind events averaging at approximately 18 and 30 mph. Early wind excited data sets show this technique does indeed excite the same modes as a random wind input. The red plot represents cross spectra from random excitation input while the green and blue are the cross spectra from the averaged wind excited data.

To extract the operational mode shapes from the cross spectrum data, a total of 20 data sets per orientation are averaged with frequencies ranging from 0 to 20 Hz with a resolution of 0.00625 Hz. The modes are then isolated from the frequency response data with a modal isolation algorithm in Matlab [7] and plotted next to the finite element counterpart for shape comparison. When plotting mode shapes of such a structure that rotates, it is important to keep track of the orientation as the majority of the sensors rotate at an angle  $\theta$  with respect to the horizontal. A procedure to map the sensor locations in 3 dimensional space is outlined in Fig. 53.6 and Eq. 53.1 below. This equation relates the measured modal response and elevation angle to Cartesian coordinates is used for plotting mode shapes in Matlab. It is easy to see the importance of the elevation angle when plotting mode shapes as the global Y and Z deflections are a function of both the X and Z measurements as well as the elevation angle,  $\theta$ .

Equation 53.1 correlates the static position,  $q_0$  with the deformed position  $q_i$  where  $\phi_i$  is the measured response at the corresponding truss location and  $M_X$  is a arbitrary magnification factor for visualization purposes. Figure 53.6 also shows an example plot of the heliostat in the  $45^\circ$  orientation with the measurement nodes connected for visualization purposes. A comparison of the experimental mode shapes with initial Ansys predictions are presented in this style in the results section below.

$$\vec{q}_i = \begin{Bmatrix} q_{i,x} \\ q_{i,y} \\ q_{i,z} \end{Bmatrix} = \begin{Bmatrix} q_{x0} \\ q_{y0} \\ q_{z0} \end{Bmatrix} + \begin{bmatrix} \phi_{iY} \\ \phi_{iZ} \cos(90 - \theta) - \phi_{iX} \cos(\theta) \\ \phi_{iZ} \sin(90 - \theta) + \phi_{iX} \sin(\theta) \end{bmatrix} \begin{Bmatrix} M_X \\ M_Y \\ M_Z \end{Bmatrix}$$

Equation 53.1 Modal magnitude coordinate relationship used in mode shape plotting

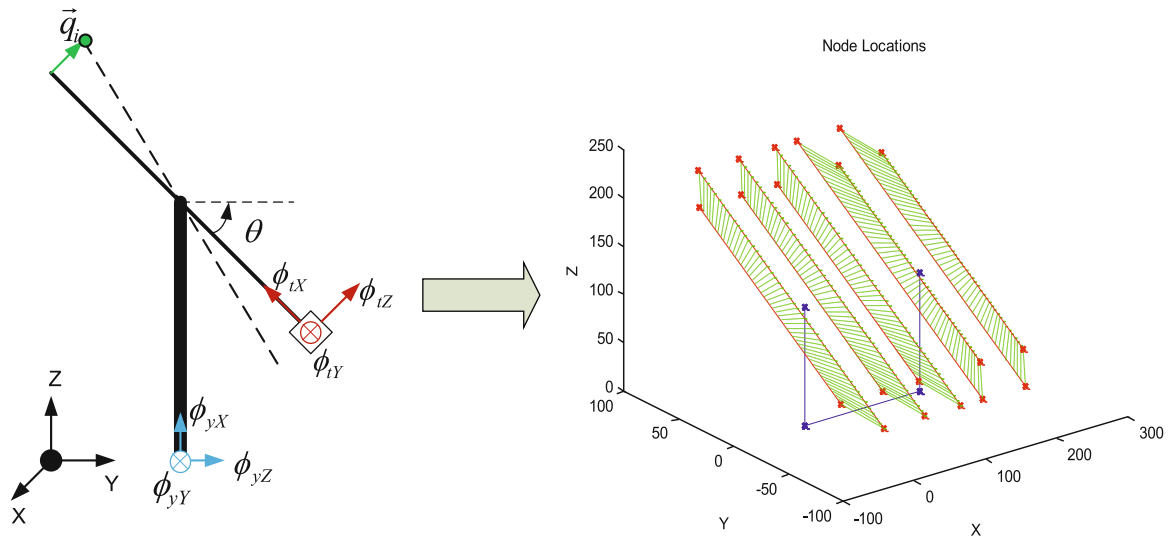


Fig. 53.6 Coordinate description and plot reconstruction of heliostat nodes

### 53.4 Results

It has been shown by both experimental results and the FEA results that there exists two major type of modes labeled as in plane bending modes and out of plane bending or twisting modes. The distinction between these two types of shapes is important as the out of plane modes will present a larger deflection with respect to the reflected beam. To quantify this optical error, the shapes provided by the finite element model are matched with the operational mode shapes that are measured with this new dynamic monitoring system. Once validated, the deformed shape can then be exported to a ray tracing code to determine how much flux is lost at the instance of modal excitation.

With complicated structures such as the NSTTF heliostat, it is easier to isolate mode types or groups in order to better understand the dynamic behavior. In addition to in plane or out of plane motion, we will further break down the mode shapes depending on which portion of the structure is responsible for the motion. This breakdown contains torque tube bending modes, torque tube torsion modes, and yoke bending modes. In addition to these modes, there exists two rigid body modes that occur due to slack or “slop” in the elevation and azimuth motors. These rigid body modes account for rotation about the elevation and azimuth axes and are relatively low at around 0.88 and 1.23 Hz respectively. It was found that the rigid body mode associated with rotation about the azimuth drive varies with heliostat orientation while the elevation mode does not. Early results verify this behavior on both the NSTTF heliostat as well as two commercial heliostats tested at SNL [4]. This is intuitively true as the natural frequency of this mode is dependent on moment of inertia about the vertical axis which is changed as the mirrors rotate. To demonstrate this behavior, the natural frequencies were reconstructed at various orientations using inertia properties from the CAD model. The plot shown in Fig. 53.7 displays the moment of inertia across the relative axis and the reconstructed frequencies using Eq. 53.2 where  $k_\theta$  and  $I_\theta$  are the rotational stiffness and inertia about the drive axis. As expected, we see the shift in the azimuth mode while the elevation mode remains relatively constant.

$$f = \frac{1}{2\pi} \sqrt{\frac{k_\theta}{I_\theta}}$$

#### Equation 53.2 Natural frequency approximation

The above analysis on the rigid body modes provides simplistic yet valuable information to this study as currently the finite element model is simplified with respect to the motors and does not calculate any rigid body modes. The low frequency mode associated with the elevation drive is especially important as early wind excited data sets show excitation of this mode at approximately 0.80 Hz, where as the azimuth rigid body mode must be manually excited. For the majority of the non rigid body modes predicted by the finite element model, there was good agreement between the Ansys predictions and the test data. Table 53.1 below is a list of the first ten predicted and measured modes along with a simple shape description for the vertical orientation data set. These initial frequency results are fairly accurate for the majority of the modes, although some modes do have a rather large discrepancy. These modes will be better matched with the FEA results by tuning the

**Fig. 53.7** Heliostat rotational inertia and rigid body mode frequency vs. elevation angle

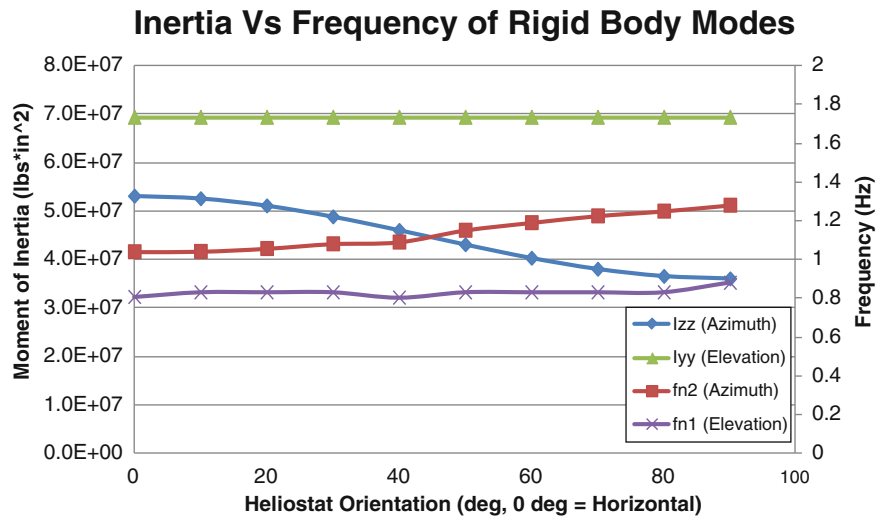


**Table 53.1** Frequency comparison of predicted and measured fundamental frequencies for the vertical orientation

Mode number	OMA Wn (Hz)	Ansys Wn	Shape description
1	1.6589	1.6605	In plane bending of yoke
2	2.2442	2.2875	Out of plane bending of trusses
3	3.1288	3.0968	In plane bending of torque tube
4	3.2416	3.4138	Out of plane twisting of yoke
5	4.1272	3.769	In plane bending of trusses
6	5.6145	4.2717	In plane bending of trusses
7	6.0313	4.4346	In plane bending of trusses
8	3.3521	4.4502	Out of plane truss bending
9	4.6635	4.5977	In plane bending of trusses
10	4.8264	4.703	In plane bending of trusses

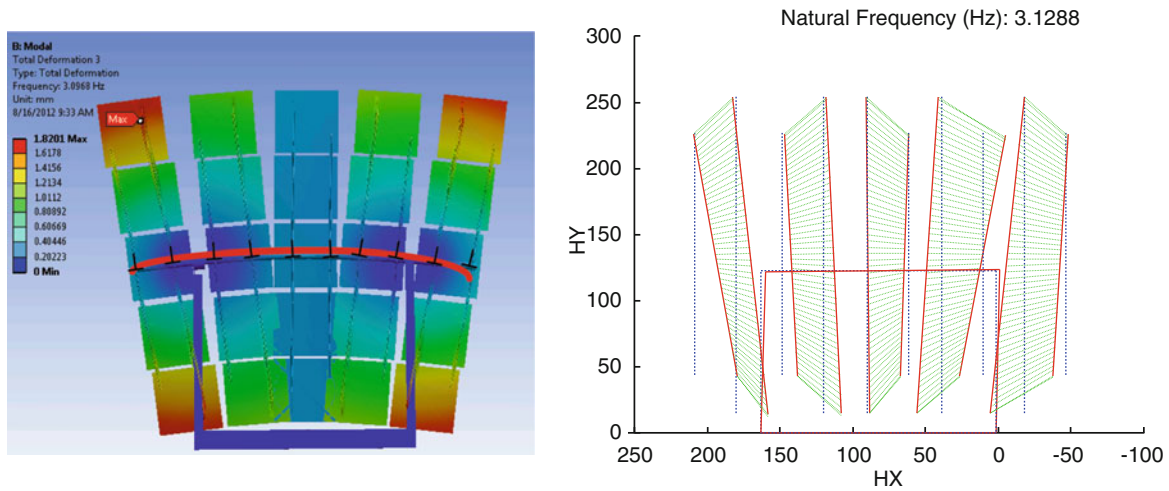


**Fig. 53.8** First torque tube bending mode (Left: Ansys = 3.096 Hz, Right: OMA = 3.1288 Hz)

appropriate spring and material constants in the model in order to shift the frequencies towards their experimental value. The following Figs. 53.8, 53.9, 53.10, and 53.11 contain a few plotted examples of predicted mode shapes versus measured shapes categorized by beam bending modes or beam twisting modes. The red lines or arrows in the finite element solutions were added to help visualize the motion of the structure and to isolate the participating member.

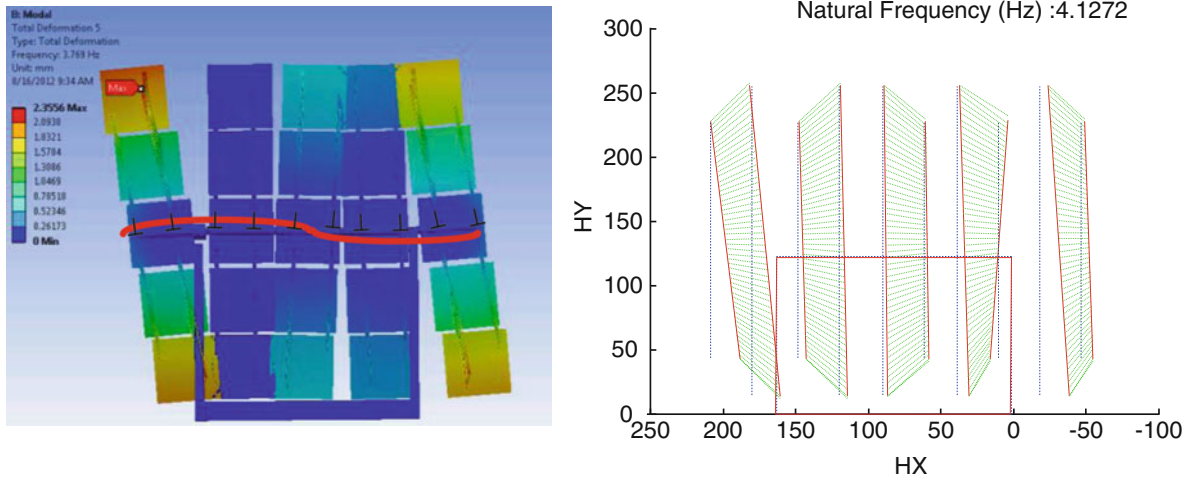


Fig. 53.9 Second torque tube bending mode (Left: Ansys = 3.769 Hz, Right: OMA = 4.1272)

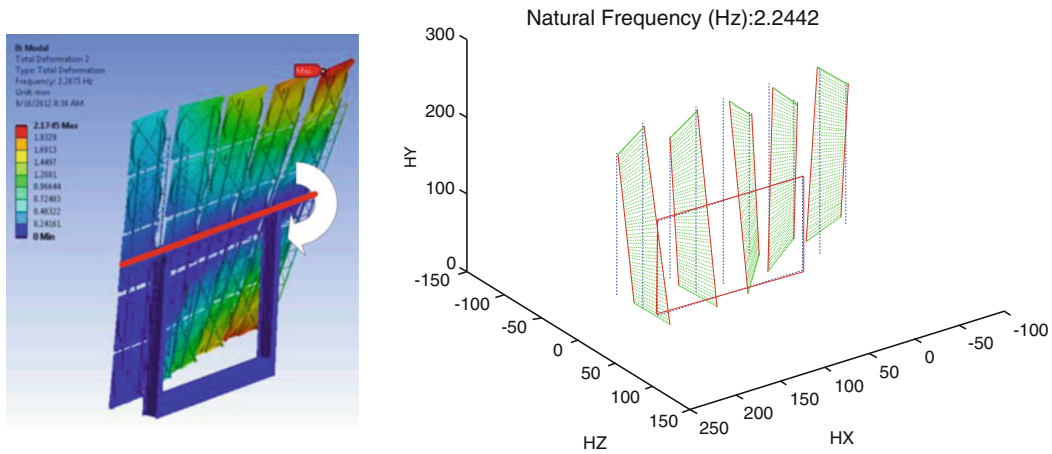


Fig. 53.10 First torque tube torsion mode (Left: Ansys = 2.2875, Right: OMA = 2.2442 Hz)

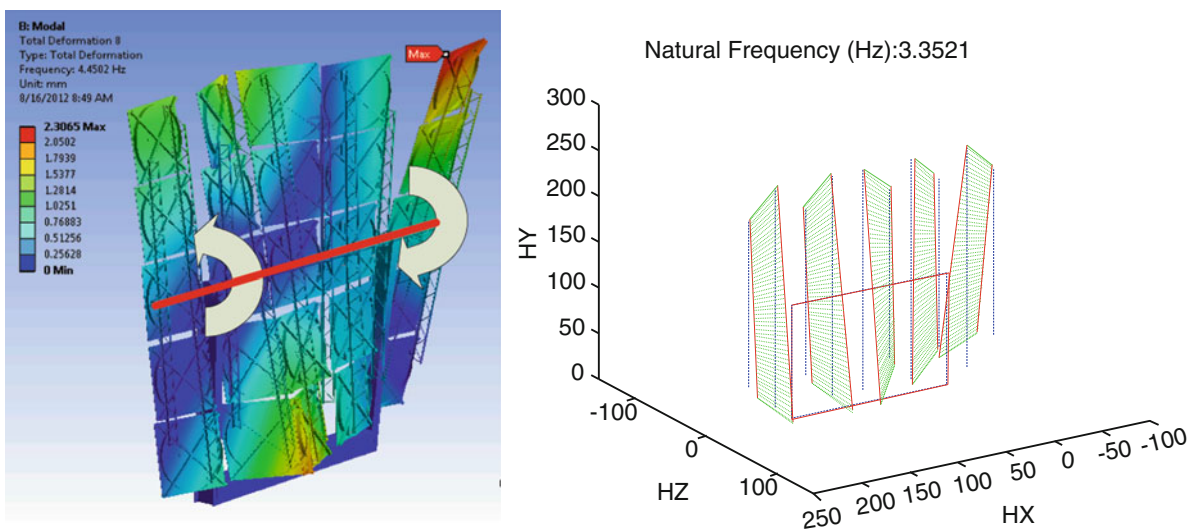


Fig. 53.11 Second torque tube torsion mode (Left: Ansys = 4.4502, Right: OMA = 3.3521 Hz)



## 53.5 Summary and Future Work

The impacts of dynamic wind loads on heliostat vibration has been presented here along with the methodology and instrumentation used. Demonstrated in this paper are some applications and benefits of a real-time modal monitoring system for remote applications such as a CSP heliostat. It was found that the majority of modes excited in a windy environment are under 10 Hz with two low frequency rigid body modes related to the azimuth and elevation motors. These results provide useful information that will ultimately aid in heliostat cost reduction during the design and prototype phase by introducing a test and validation method for modal parameter estimation that is currently lacking in heliostat design. Due to tight time and monetary constraints, the CSP industry has often overlooked or over simplified their dynamic simulation capabilities which leads to less than optimum systems. This current monitoring system presents a methodology for creating and utilizing a validated finite element model of a CSP heliostat and theoretically could be utilized in other CSP collectors such as parabolic troughs or sterling dishes to explore optical losses and dynamic loading due to wind.

The reconfigurable nature of National Instruments hardware and software leaves much room for improvement in the modal identification program. Automated procedures are being added to this monitoring system in order to detect increased wind speed and simultaneously begin logging data so that wind storms are never missed. Other automated tasks are a possibility such as real-time mode shape approximation via frequency domain decomposition (FDD) techniques and real-time force estimation which will back calculate input forces at each measurement node. With these abilities, a well representative finite element model could be made of any CSP structure where vibration may be a concern and ultimately lead to a better design.

The finite element model of the NSTTF heliostat presented has produced fairly accurate shapes, but there is also room for improvement with regard to frequency matching. Their exists rotational spring constants and other contact conditions that can be tuned to better replicate the physical system and possibly include the rigid body modes associated with the two motors. Once this model is tuned to an acceptable limit, the applications open up to more interesting phenomena that will be useful to the CSP industry. After dynamic validation is performed, it will be useful to accurately model the beam dispersion occurring during vibration via ray tracing methods and explore annual power losses using available wind records. Other applications such as fatigue analysis and force reconstruction are also being conducted all with the ultimate goal of a cheaper and more reliable heliostat.

**Acknowledgements** The authors thank Patrick Hunter, Ed Smith, Zach Payne, and Mike Usher for their assistance with the testing and development of the system. The authors would also like to thank Mathew Allen for his assistance at the University of Wisconsin, Madison. Sandia National Laboratories is a multi-program laboratory managed and operated by Sandia Corporation, a wholly owned subsidiary of Lockheed Martin Corporation, for the U.S. Department of Energy's National Nuclear Security Administration under contract DE-AC04-94AL85000.

## References

1. Kolb GJ, Ho CK, Mancini TR, Gary JA (2011) Power tower technology roadmap and cost reduction plan, SAND2011-2419. Sandia National Laboratories, Albuquerque
2. Griffith DT, Ho CK, Moya AC, Hunter PS et al (2012) Modal analysis of a heliostat for concentrating solar power. In: Proceedings of the 30th international modal analysis conference (IMAC XXX), Jacksonville, 30 Jan–2 Feb 2012
3. Griffith DT, Moya A, Ho C, Hunter P (2011) Structural dynamics testing and analysis for design evaluation and monitoring of heliostats. In: Proceedings of the 5th ASME international conference on energy sustainability, Washington, DC, 7–10 Aug 2011. ESFuelCell2011-54222
4. Ho CK, Griffith DT, Moya AC, Sment J, Christian J, Yuan J, Hunter P (2012) Dynamic testing and analysis of heliostats to evaluate impacts of wind on optical performance and structural fatigue. In: Proceedings of SolarPACES 2012 international conference, Marrakech, 11–14 Sept 2012
5. Christian JM, Ho CK (2010) Finite element modelling of concentrated solar collectors for evaluation of gravity loads, bending, and optical characterization. In: Proceedings of the 4th ASME international conference on energy sustainability, Phoenix, 17–22 May 2010. ES2010-90050
6. Moya AC, Ho CK (2011) Modeling and validation of heliostat deformation due to static loading. In: Proceedings of 5th ASME international conference on energy sustainability, Washington, DC, 7–10 Aug 2011. ESFuelCell2011-54216
7. Allen MS (2005) Global and multi-input-multi-output (MIMO) extensions of the algorithm of mode isolation (AMI). In: George W (ed) Woodruff school of mechanical engineering. Georgia Institute of Technology, Atlanta, p 128

# Chapter 54

## Identification of Stability Cutting Parameters Using Laser Doppler Vibrometry

D. Olvera, A. Elías-Zúñiga, M. Pineda, E. Macias, O. Martínez, L.N. López de Lacalle, and C. Rodríguez

**Abstract** High-speed milling operations of thin walls are often limited by the so-called regenerative effect that causes poor surface finishing. To optimize the cutting process in terms of quality surface and productivity, the frequency response function (FRF) of the wall needs to be measured in order to identify the modal parameters of the system which are used to obtain the stability lobes that help identify the optimal system's parameter values to warrant stable cutting conditions. The aim of this work is to experimentally show the variation on the frequency response function (FRF) values obtained by using a laser Doppler vibrometer (LDV) device and accelerometer sensors during a milling operation processes of an aluminum thin-walled workpiece of 1 mm thick and 30 mm height. It is shown that the FRF values variations has strong influence on the stable cutting bounds. To further assess our findings, we used the collected experimental data obtained by using the LDV during milling machine cutting operation processes of several thin-walled workpieces to identify the cutting parameters values that allow us to obtain good quality and acceptable surface finish.

**Keywords** Milling machine operations • Laser Doppler vibrometer (LDV) • Stability lobes • Homotopy perturbation methods

### 54.1 Introduction

High speed machining of a low stiffness structure is a widely used process in the aeronautical industry where thin walls and floors are manufactured. The machining of these kinds of structures may experience regenerative lateral vibrations for some cutting conditions due to the variable dynamics of the system which could result in poor surface finish and lower productivity. See [1] and other references cited therein.

The main purpose of this paper is to discuss some of the dynamic problems associated in collecting experimental data during the machining processes of low-rigidity structures and how inaccurate measurements can lead to misleading interpretations of experimental data and theoretical simulations. For instance, it is well-known that the influence of accelerometer mass on heavy structures has negligible effects on dynamic measurements. However, this could not be the case when the workpiece mass is small. In this work we discuss the effect that the accelerometer mass can have during the experimental determination of the modal parameter of the milling processes, how this affect the prediction of the stability lobes [2] and how the ratio of the thin-walled work piece to the accelerometer is no longer negligible.

For instance, Bravo et al. in [3] studied chatter on thin walls taking into account the rigidities of the workpiece according to the relationship of the wall/tool interaction. They developed three-dimensional stability lobe diagrams that allow to determine stable cutting conditions. Recently, Ozsahin in [2] analyzed the mass-loading effect on the tool frequency response function (FRF). They obtained the FRF by tap testing, exciting the chain (spindle-holder-tool) with an impact hammer and measured

---

D. Olvera • A. Elías-Zúñiga • O. Martínez • C. Rodríguez  
Instituto Tecnológico y de Estudios Superiores de Monterrey, Monterrey, Nuevo León, México

M. Pineda (✉) • E. Macias  
Polytec Inc. Irvine, CA, USA  
e-mail: [aelias@itesm.mx](mailto:aelias@itesm.mx)

L.N. López de Lacalle  
Faculty of Engineering, Mechanical Engineering, University of the Basque Country, UPV/EHU, Bilbao, Basque Country, Spain

the vibrations response with an accelerometer and an LDV, both at the tool tip. Based on their results, they found that the FRF peak value for a carbide end mill 12 mm diameter and 80 mm gauge length has a shift of 167 Hz. They attribute this frequency shift to the accelerometer mass. Laser Doppler Vibrometry is commonly used for a variety of applications where accelerometer mass loading of the sample is either not possible or cumbersome.

Since the accuracy of the FRF affects directly the stability lobes diagram, it is important to study the impact of the accelerometer mass over the stability diagrams to predict accurately the dynamic behavior when milling thin-walled parts.

In order to study the accelerometer mass effect on thin-wall FRFs, we performed several impact tests at different locations over the workpiece thin wall and collected the corresponding FRFs by using a 0.6 g accelerometer and an LDV. Also, we studied the modal behavior variations of the thin-walled work pieces during their machining processes and explored the effects of the cutting path.

At the end of the paper, we showed how these collected FRF data impact the prediction of the stability lobes obtained by using the Enhanced Multistage Homotopy Perturbation Method (EMHPM) [4, 5].

We shall next study the influence of the accelerometer mass on the FRF of a thin-thin walled structure and how the modal parameters must be determined to have stable cutting conditions.

## 54.2 Modal Parameters of Thin-Walled Structure

To assess the influence of accelerometer mass while determining modal parameters of a milling machine operation of thin-walled structures, we used a Polytec Compact Laser vibrometer CLV-2534-2 that allows dynamic measurements without adding mass to the workpiece. These measurements were performed during the milling operation. Prior to that, we selected a DYTRAN 3225F1 0.6 g accelerometer and performed experimental measurements on aluminum 7,075 thin-wall workpiece of 9.23 g with 88 HRB hardness. The dotted line showed in Fig. 54.1 represents the collected frequency response function values. We next used the LDV and performed impact test on the workpiece to obtain the FRF values. The results are showed in Fig. 54.1 by the solid lines. We may notice from Fig. 54.1 that there is a significant variation on the FRF functions obtained by using the accelerometer and LDV. In fact, the laser vibrometer captures two fundamental vibrational modes with peak values at 1,105 and 1,722 Hz. However, the measurements performed with the accelerometer exhibit the same dynamic modes but with peak values at 580 and 1,366 Hz. These differences on the recorded FRF lectures were noticed during experimental tests because of the sound pressure level produced by the thin wall workpiece.

We believe that the 525 Hz shift of the FRF value of the first peak mode is attributed to the effect of the accelerometer mass load. In order to verify our experimental observations, we performed experimental measurements by using the LDV with the accelerometer attached to the workpiece. The results are also shown in Fig. 54.1 by the dashed line. As it may be seen from Fig. 54.1, these results are the same than those collected with the accelerometer. This experimental test confirmed the effects of the accelerometer mass over the FRF values which not only causes a shift of the frequency value of about 48%, but also changes considerably the modal damping of the system. As expected, the effects of the accelerometer mass loading and dampening increase as 1 mm thin wall material is removed from the workpiece during the machining processes. For instance, if we initially use an aluminum block with a thickness of 4.8 mm with the accelerometer attached to it; we recorded a fundamental frequency peak value of 2,531 Hz. When the accelerometer is removed and the laser vibrometer used, we recorded a fundamental frequency peak value of 2,758 Hz. In this case, the system damping parameter values obtained by using the accelerometer is about 0.0195 while the damping value obtained by using the LDV is about 0.0074.

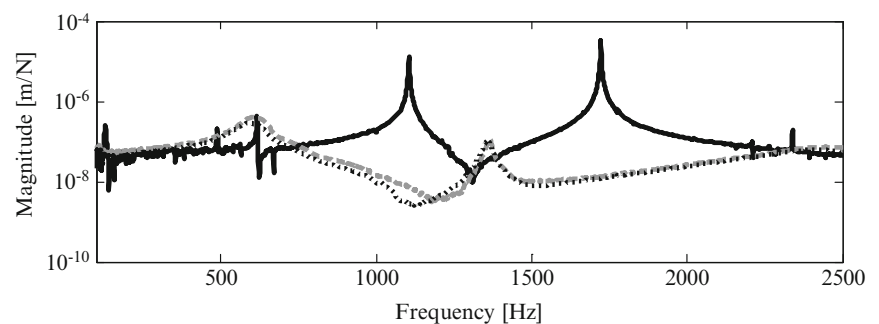


**Fig. 54.1** FRF measured in a workpiece of 1 mm thick, and 30 mm height by using: laser vibrometer (*solid line*), laser vibrometer and accelerometer (*dashed line*), and the accelerometer (*dotted line*)

### 54.3 Time Varying Modal Behavior of the Thin Wall During the Machining Processes

In this section, we briefly discuss how the modal behavior of the workpiece varies along the feed direction and at every stage of the thin wall height. The FRF measurements were performed before and after machining each 5 mm height step from 0 to 30 mm (6 bands) at 4 points along the width of the workpiece thin wall: 5, 17.5, 32.5 and 45 mm from the left to the right side as illustrated in Fig. 54.2. The results obtained at 5 and 17.5 mm are shown in Fig. 54.3. As expected, an almost symmetrical spectral behavior was observed at the locations of 5 and 45 mm and at 17.5 and 32.5 mm along the feed workpiece direction. The thin-walled workpiece was machined using a jump to jump strategy on a Makino F3 machining center with spindle speed up to 30,000 rev/min. We may notice from Fig. 54.2 that the workpiece dynamic behavior exhibits a clear differences during machine operations between its center part and its lateral zones.

These differences on the qualitative behavior of the workpiece zone may be explained from the experimental data showed in Fig. 54.3 where the damping ratios and the stiffness coefficients are not the same in spite of having the same FRF peak values.

The modal parameter values obtained from laser vibrometer measurements now can be used to obtain accurate stability lobes that could warrant stable cutting conditions using frequency [6] or time [7] domain methods. In order to demonstrate the effects accelerometer's mass effects on cutting processes dynamics, we compute the stability lobes by using the Enhanced, Multistage Homotopy Perturbation Method (EMHPPM) for both accelerometer and vibrometer measurements, The stability lobes were computed by the EMHPPM (see Appendix 54.4).

The stability charts plotted in Fig. 54.4 are generated for a 1/2 in. diameter end mill with 2 teeth, a helix angle of 20°, and a radial depth of cut of 0.8 mm. The cutting force coefficients were estimated using the procedure described in [8] as,  $K_t = 1,116 \text{ N/mm}^2$  and  $K_r = 445 \text{ N/mm}^2$ . According to [3], down milling operation is chosen for this study because the relative movement of the thin wall tends to move away from the tool due to the action of the cutting force. This provides a better workpiece surface finish.

As we may see from Fig. 54.4, the accelerometer mass strongly influence the stable depth of cut values on the computed stability lobes. Table 54.1 shows a comparison of the modal parameter values obtained by using both, the FRF accelerometer and the laser vibrometer recorded data. From Table 54.1, it is clearly seen that an accelerometer of 0.6 g attach to the thin wall workpiece has a significant effect over FRF measurements. Besides, it is suspected that the connecting accelerometer

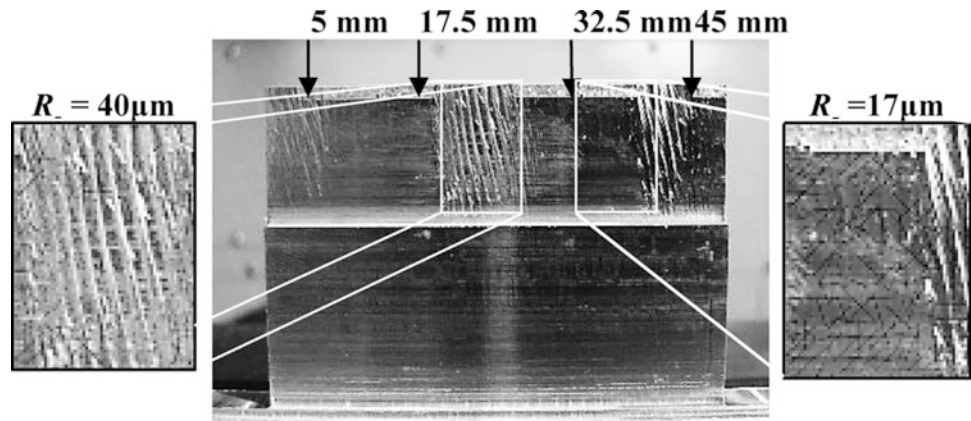


Fig. 54.2 Chatter marks on lateral and center zones

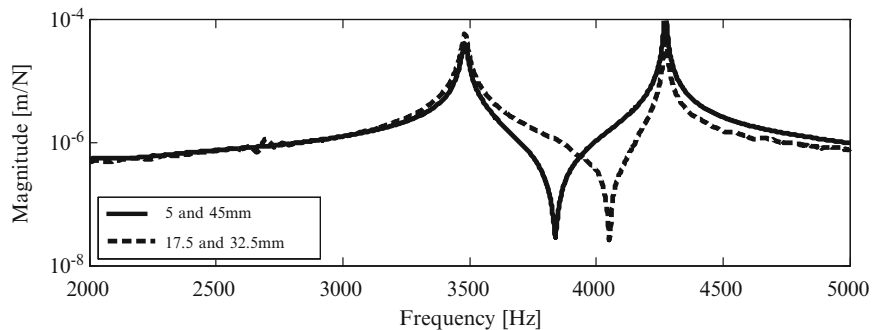
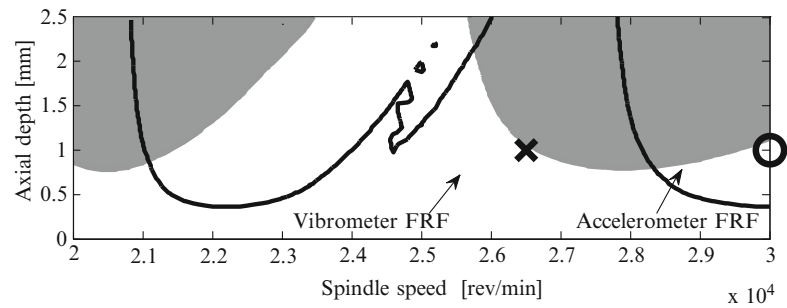


Fig. 54.3 FRF measurements collected in the workpiece at 15 mm height stage by using the LDV

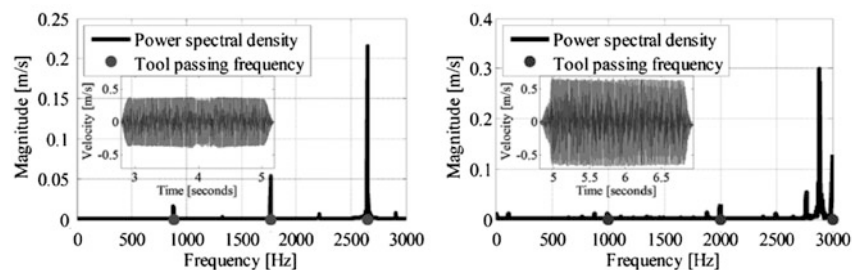
**Fig. 54.4** Stability diagrams for the FRF of a 4.8 mm thick block and 35 mm height using both devices



**Table 54.1** Comparison of modal parameter obtained accelerometer and the LDV FRFs

Height	0 mm	5 mm	10 mm	15 mm	20 mm	25 mm	30 mm
Accelerometer frequency (Hz)	2,531	2,310	1,569	1,146	927	706	580
Accelerometer damping	0.0195	0.0117	0.0105	0.0807	0.0633	0.0603	0.0643
Vibrometer frequency (Hz)	2,758	3,365	3,996	3,481	2,204	1,515	1,105
Vibrometer damping	0.00737	0.00527	0.0129	0.0027	0.00137	0.00151	0.00104
Frequency shift (%)	8	31	61	67	58	53	48

**Fig. 54.5** Experimental data of: (a) (left) stable cutting at 26,500 rpm and (b) (right) unstable cutting at 3,000 rpm



cable could influence the recorded data since the recorded weight of both, the cable and the accelerometer, according to the length needed to perform the experimental test, was varying from 0.6 to 2.1 g. Furthermore if users of milling machines were to use accelerometers only as sensors and calculate stability lobes by EMHPM methods they may assume certain sections to be stable (see Fig. 54.4) when in reality they might be right in the middle of an unstable zone for example 13,000, 16,000 and 21,000 rpm for this particular example.

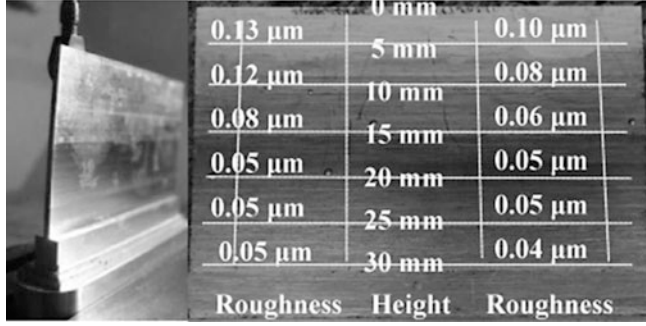
From these stability lobes, we may predict stable or unstable cutting conditions. For instance, Fig. 54.4 shows that at 26,000 rpm, the accelerometer data predicts unstable behavior while the vibrometer device predicts stable one which agrees with experimental observations, see Fig. 54.5a. However, at the spindle speed of 30,000 rpm, the modal data collected from both devices predicts unstable behavior as showed in Fig. 54.5b. In this case, the velocity magnitude recorded at 30,000 rpm is about 0.6 mm per second. Also notice from Fig. 54.5b that at this spindle speed value of 30,000 rpm, the system exhibits a quasi-periodic chatter frequency.

As a conclusion, we believe that care must be exercised in identifying the frequency range apparatus measurements to capture the fundamental dynamic behavior of the system. For instance, we performed measurements in 1 mm thick thin wall workpiece by defining 6 stages of 5 mm height with a width of 50 mm, as showed in Fig. 54.6. We tuned up our apparatus to a maximum value frequency range value of 5,000 Hz. The recorded accelerometer FRF measurements, showed in Table 54.1, exhibit two frequency peak values, while the laser vibrometer recorded only one frequency peak value because of the previously defined maximum apparatus frequency range value.

## 54.4 Conclusion

In this paper, the modal behavior of a thin wall workpiece is analyzed by comparing the corresponding FRF curves obtained by using a 0.6 g accelerometer and an LDV.

**Fig. 54.6** Roughness (Ra) of the thin wall machined with stable cutting conditions



0.13 $\mu\text{m}$	0 mm	0.10 $\mu\text{m}$
0.12 $\mu\text{m}$	5 mm	0.08 $\mu\text{m}$
0.08 $\mu\text{m}$	10 mm	0.06 $\mu\text{m}$
0.05 $\mu\text{m}$	15 mm	0.05 $\mu\text{m}$
0.05 $\mu\text{m}$	20 mm	0.05 $\mu\text{m}$
0.05 $\mu\text{m}$	25 mm	0.05 $\mu\text{m}$
0.05 $\mu\text{m}$	30 mm	0.04 $\mu\text{m}$
Roughness	Height	Roughness

The frequency response functions obtained by using the accelerometer and the laser vibrometer clearly indicate that the FRF peak values are recorded at different frequency values. Hence, the modal stiffness coefficients as well as the modal damping ratios have different magnitudes that strongly influence the dynamic behavior of the system. During the process of determining stable machine operation parameters, we found that stable cutting conditions predicted by using the FRF accelerometer data disagree with physical observations, while the stable cutting conditions found from the laser vibrometer FRF data agree well with reality. In fact, we identified optimum cutting conditions to our thin-walled workpiece which allowed obtaining good quality surface finish of less than  $Ra=0.15 \mu\text{m}$ , as showed in Fig. 54.6.

**Acknowledgement** This work was partially funded by the Tecnológico de Monterrey through the Research Chairs in Intelligent Machines and Nanotechnology and Advanced Materials. We also acknowledge financial support from Polytec Inc.

## Appendix A. THE EMHPM to PREDICT stability lobes for thin walls machining

In order to predict stability in machining operations, the EMHPM was used. This method developed by the authors, permits faster computation times and high accuracy in comparison with literature review. The workpiece under study has a single degree-of-freedom (flexibility only in the  $y$  direction according to the machine tool standard axis nomenclature), with a dynamic model of the following form [9]:

$$\ddot{y}(t) + 2\zeta\omega_n\dot{y}(t) + \omega_n^2y(t) = \frac{K_s(t, z)}{m_m}(y(t) - y(t - \tau)) \quad (54.1)$$

Here,  $m_m$  represents the modal mass,  $\zeta$  is the damping ratio,  $\omega_n$  is the natural angular frequency and  $K_s(t, z)$  is the cutting force over the workpiece in the  $y$ -direction, which is given by:

$$K_s(t, z) = \sum_{j=1}^{z_n} \frac{1}{4k_\beta} [K_{tc} \cos 2\phi_j + K_{rc} (\sin 2\phi_j + 2\phi_j)]_{z_{j,1}(\phi_j)}^{z_{j,2}(\phi_j)} \quad (54.2)$$

where  $z_n$  is the number of teeth,  $K_{tc}$  and  $K_{rc}$  are the tangential and the normal cutting force coefficients,  $k_\beta = 2 \tan \beta / D$ ,  $\beta$  is the helix angle,  $D$  is the tool diameter, and  $\phi_j(z)$  is defined as

$$\phi_j(z) = \phi + (j - 1)2\pi/z_n - k_\beta z_j \quad (54.3)$$

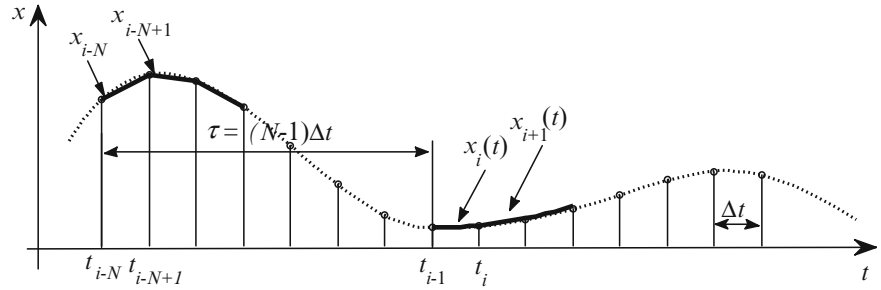
here,  $\phi$  is the immersion angle measured from the  $y$  axis and  $\phi_j$  is the  $j$  tooth angular position. The values of the tangential and normal cutting coefficients can be obtained experimentally [8].

To obtain the stability lobes of Eq. (54.1), a solution procedure based on the EMHPM is proposed. In this methodology, the Eq. (54.1) must be rewritten as:

$$\ddot{y}_i(T) + 2\zeta\omega_n\dot{y}_i(T) + \omega_n y_i(T) \approx \frac{K_{st}}{m_m} (y_i(T) - y_i^\tau(T)) \quad (54.4)$$

where  $K_{st} = K_s(t, a_p)$ , and  $x_i(T)$  denotes de approximate solution of order  $m$  in the  $i$ -th sub-interval that satisfies the initial conditions  $y_i(0) = y_{i-1}$ ,  $\dot{y}_i(0) = \dot{y}_{i-1}$ .

**Fig. 54.7** First order polynomial representation of the time delay subinterval



Next, the Eq. (54.1) is expressed in state space form in accordance with the following matrix form representation

$$\dot{\mathbf{x}}(t) = \mathbf{A}(t)\mathbf{x}(t) + \mathbf{B}(t)(\mathbf{x}(t) - \mathbf{x}(t - \tau)) \quad (54.5)$$

where  $\mathbf{x} = [x, \dot{x}]^T$ ,  $\mathbf{A}(t + \tau) = \mathbf{A}(t)$ ,  $\mathbf{B}(t + \tau) = \mathbf{B}(t)$  and  $\tau$  is the time delay. By following the EMHPM procedure, the Eq. (54.5) can be represented by its equivalent form as

$$\dot{\mathbf{x}}_i(T) - \mathbf{A}_t \mathbf{x}_i(T) \approx \mathbf{B}_t \mathbf{x}_i^\tau(T) \quad (54.6)$$

where  $\mathbf{x}_i(T)$  denotes the  $m$  order solution of Eq. (54.5) in the  $i$ -th sub-interval that satisfies the initial conditions  $\mathbf{x}_i(0) = \mathbf{x}_{i-1}$ ,  $\mathbf{A}_t$  and  $\mathbf{B}_t$  represent the values of the periodic coefficients at the time  $t$ . In order to approximate the delay term  $\mathbf{x}_{-\tau}(T)$  in Eq. (54.6), the period  $[t_0 - \tau, t_0]$  is discretized in  $N$  points that could be equally spaced as shown in Fig. 54.7. Thus, each sub-interval has a time span equal to  $\Delta t = T/(N - 1)$ . Here, it is assumed that the function  $\mathbf{x}_i^\tau(T)$  in the delay sub-interval  $[t_{i-N}, t_{i-N+1}]$  has a first-order polynomial representation of the form:

$$\mathbf{x}_i^\tau(T) = \mathbf{x}_{i-N+1}(T) \approx \mathbf{x}_{i-N} + \frac{N-1}{r}(\mathbf{x}_{i-N+1} - \mathbf{x}_{i-N})T \quad (54.7)$$

To simplify the notation, the term  $\mathbf{x}_i \equiv \mathbf{x}_i(T_i)$  is defined. Next, substituting the Eq. (54.7) into the Eq. (54.6), results

$$\dot{\mathbf{x}}_i(T) = \mathbf{A}_t \mathbf{x}_i(T) + \mathbf{B}_t \mathbf{x}_{i-N} - \frac{N-1}{r} \mathbf{B}_t \mathbf{x}_{i-N} T + \frac{N-1}{r} \mathbf{B}_t \mathbf{x}_{i-N+1} T \quad (54.8)$$

where

$$\mathbf{A}_t = \begin{bmatrix} 0 & 1 \\ -\omega_n^2 + \frac{K_{st}}{m_m} & -2\zeta\omega_n \end{bmatrix}, \mathbf{B}_t = \begin{bmatrix} 0 & 0 \\ -\frac{K_{st}}{m_m} & 0 \end{bmatrix} \quad (54.9)$$

By following our EMHPM procedure, it might be assumed that the homotopy representation of Eq. (54.8) is of the form

$$H(\mathbf{X}_i, p) = L(\mathbf{X}_i) - L(\mathbf{x}_{i0}) + pL(\mathbf{x}_{i0}) - p(\mathbf{A}\mathbf{X}_i + \mathbf{B}\mathbf{x}_{i-N} - \frac{N-1}{r}\mathbf{B}\mathbf{x}_{i-N}T + \frac{N-1}{r}\mathbf{B}\mathbf{x}_{i-N+1}T) \quad (54.10)$$

Later, substituting the  $m$  order expansion of  $\mathbf{X}_i$

$$\mathbf{X}_i(T) = \mathbf{X}_{i0}(T) + p\mathbf{X}_{i1}(T) + \dots + p^m\mathbf{X}_{im}(T) \quad (54.11)$$

in Eq. (54.10) and it is assumed that the initial solution is given by  $\mathbf{x}_{i0} = \mathbf{x}_{i-1}$ . Then, the proposed EMHPM is applied to obtain a set of first order delay differential equations which after solving, we get:

$$\mathbf{X}_{i0} = \mathbf{x}_{i-1}$$

$$\mathbf{X}_{i1} = \mathbf{A}_t \mathbf{x}_{i-1} T + \mathbf{B}_t \mathbf{x}_{i-N} T - \frac{1}{2} \frac{N-1}{r} \mathbf{B}_t \mathbf{x}_{i-N} T^2 + \frac{1}{2} \frac{N-1}{r} \mathbf{B}_t \mathbf{x}_{i-N+1} T^2$$

$$\mathbf{X}_{i2} = \frac{1}{2} \mathbf{A}_t^2 \mathbf{x}_{i-1} T^2 + \frac{1}{2} \mathbf{A}_t \mathbf{B}_t \mathbf{x}_{i-N} T^2 - \frac{1}{6} \frac{N-1}{r} \mathbf{A}_t \mathbf{B}_t \mathbf{x}_{i-N} T^3 + \frac{1}{6} \frac{N-1}{r} \mathbf{A}_t \mathbf{B}_t \mathbf{x}_{i-N+1} T^3$$

⋮

$$\mathbf{X}_{ik} = \frac{1}{k!} \mathbf{A}_t^k \mathbf{x}_{i-1} T^k + \frac{1}{k!} \mathbf{A}_t^{k-1} \mathbf{B}_t \mathbf{x}_{i-N} T^k - \frac{1}{(k+1)!} \frac{N-1}{r} \mathbf{A}_t^{k-1} \mathbf{B}_t \mathbf{x}_{i-N} T^{k+1} + \frac{1}{(k+1)!} \frac{N-1}{r} \mathbf{A}_t^{k-1} \mathbf{B}_t \mathbf{x}_{i-N+1} T^{k+1} \quad (54.12)$$

The  $m$  order approximate solution of Eq. (54.8) is obtained by substituting Eq. (54.12) into Eq. (54.13), this yield:

$$\mathbf{x}_{im}(T) \approx \sum_{k=0}^m \mathbf{X}_{ik}(T) \quad (54.13)$$

To obtain the stability lobes of Eq. (54.1), the Eq. (54.13) is written in the form

$$\mathbf{x}_i(T) \approx \mathbf{P}_i(T)\mathbf{x}_{i-1} + \mathbf{Q}_i(T)\mathbf{x}_{i-N+1} + \mathbf{R}_i(T)\mathbf{x}_{i-N} \quad (54.14)$$

where

$$\begin{aligned} \mathbf{P}_i(T) &= \sum_{k=0}^m \frac{1}{k!} \mathbf{A}_t^k T^k, \\ \mathbf{Q}_i(T) &= \begin{cases} \sum_{k=1}^m \frac{N-1}{(k+1)!} \mathbf{A}_t^{k-1} \mathbf{B}_t T^{k+1} & m \geq 1 \\ \mathbf{0} & m = 0 \end{cases}, \\ \mathbf{R}_i(T) &= \begin{cases} \sum_{k=1}^m \frac{1}{k!} \mathbf{A}_t^{k-1} \mathbf{B}_t T^k - \mathbf{Q}_i & m \geq 1 \\ \mathbf{0} & m = 0 \end{cases}. \end{aligned} \quad (54.15)$$

The approximate solution given by Eq. (54.14) can be written as discrete map by using the following identity:

$$\mathbf{w}_i = \mathbf{D}_i \mathbf{w}_{i-1} \quad (54.16)$$

where  $\mathbf{D}_i$  is a coefficient matrix, and  $\mathbf{w}_{i-1}$  is a vector of the form:

$$\mathbf{w}_{i-1} = [x_{i-1}, \dot{x}_{i-1}, x_{i-2}, \dots, x_{i-N}]^T \quad (54.17)$$

By using Eqs. (54.14) and (54.15), it might be easily showed that the coefficient matrix  $\mathbf{D}_i$  is given by [9]:

$$\mathbf{D}_i = \begin{bmatrix} P_{i,(1,1)} & P_{i,(1,2)} & 0 & 0 & \dots & 0 & Q_{i,(1,1)} & R_{i,(1,1)} \\ P_{i,(2,1)} & P_{i,(2,2)} & 0 & 0 & \dots & 0 & Q_{i,(2,1)} & R_{i,(2,1)} \\ 1 & 0 & 0 & 0 & \dots & 0 & 0 & 0 \\ 0 & 0 & 1 & 0 & \dots & 0 & 0 & 0 \\ \vdots & \vdots & \vdots & \ddots & \vdots & \vdots & \vdots & \vdots \\ 0 & 0 & 0 & 0 & \ddots & 0 & 0 & 0 \\ 0 & 0 & 0 & 0 & \dots & 1 & 0 & 0 \\ 0 & 0 & 0 & 0 & \dots & 0 & 1 & 0 \end{bmatrix} \quad (54.18)$$

Next the transition matrix  $\Phi$  is calculated over the period  $T = (N-1)\Delta t$  by coupling each approximate solution through the discrete map  $\mathbf{D}_i, i = 1, 2, \dots, (N-1)$ , to get:

$$\Phi = \mathbf{D}_{N-1} \mathbf{D}_{N-2} \dots \mathbf{D}_2 \mathbf{D}_1 \quad (54.19)$$

Then, the stability lobes of Eq. (54.1) are determined by computing the eigenvalues of the transition matrix given by Eq. (54.19).



## References

1. Campa FJ (2009) Metodología para la predicción de la estabilidad dinámica en el mecanizado de alta velocidad en suelos delgados (a method to predict and avoid instabilities on the thin floors milling process). Ph.D, University of the Basque Country
2. Özsahin O, Ozguven HN, Budak E (2010) Analysis and compensation of mass loading effect of accelerometers on tool point FRF measurements for chatter stability predictions. *Int J Mach Tools Manuf* 50:585–589
3. Bravo U, Altuzarra O, López de Lacalle LN, Sánchez JA, Campa FJ (2005) Stability limits of milling considering the flexibility of the workpiece and the machine. *Mach Tools Manuf* 45:1669–1680
4. He JH (1999) Homotopy perturbation technique. *Comput Methods Appl Mech Eng* 178:257–262
5. He JH (2003) Homotopy perturbation method: a new nonlinear analytical technique. *Appl Math Comput* 135:73–79
6. Altintas Y, Budak E (1995) Analytical prediction of stability lobes in milling. *CIRP Ann* 44:357–362
7. Insperger T, Mann BT, Stepan G, Bayly PV (2003) Stability of up-milling and down-milling, part 1: alternative analytical methods. *Int J Mach Tools Manuf* 43:25–34
8. Altintas Y (2000) *Manufacturing automation*. Cambridge University Press, Cambridge
9. Insperger T, Stepan G (2004) Updated semi-discretization method for periodic delay-differential equations with discrete delay. *Int J Numer Methods Eng* 61:117–141

# Chapter 55

## System Identification Using Kalman Filters

F. Abid, G. Chevallier, J.L. Blanchard, J.L. Dion, and N. Dauchez

**Abstract** The present study focuses on Model Order Reduction (MOR) methods of non-intrusive nature that can be seen as belonging to the category of system identification techniques. Indeed, whereas the system to analyze is considered as a black box, the accurate modeling of the relationship between its input and output is the aim of the proposed techniques. In this framework, the paper deals with two different methodologies for the system identification of thermal problems. The first identifies a linear thermal system by means of an Extended Kalman Filter (EKF). The approach starts from an a priori guessed analytical model whose expression is assumed to describe appropriately the response of the system to identify. Then, the EKF is used for estimating the model transient states and parameters. However, this methodology is not extended to the processing of nonlinear systems due to the difficulty related to the analytical model construction step. Therefore, a second approach is presented, based on an Unscented Kalman Filter (UKF). Finally, a Finite Element (FE) model is used as a reference, and the good agreement between the FE results and the responses produced by the EKF and UKF methods in the linear case fully illustrate their interest.

**Keywords** Model Order Reduction (MOR) • System identification • Extended Kalman Filter (EKF) • Unscented Kalman Filter (UKF) • Finite Element (FE)

### 55.1 Introduction

The increasing complexity of mathematical models used to predict real-world systems has led to a need for model reduction, which means developing systematic algorithms for replacing large-scaled models with far simpler ones that still accurately capture the most important aspects of the phenomena being modeled. Model reduction techniques can be divided into two main categories. Intrusive methods belong to the first. Their principle is based on projection techniques that map a large number of degrees of freedom (DOFs) to a small number of generalized coordinates using an appropriate reduced-order basis (ROB). They may be called “internal methods” as they require access to the governing equations to project them onto the subspace spanned by the set of ROB vectors. Some of the basic and earliest methods in this category are Guyan (static condensation) [6] and Craig and Bampton reduction [4] that combines the Guyan reduction and modal truncation.

---

F. Abid (✉)

PhD Student, SUPMECA PARIS – LISMMMA, 3 rue Fernand Hainaut, 93407 Saint Ouen, France

VALEO Group Electronics Expertise and Development Services, 2 Rue André Boulle, 94046, Créteil, France

e-mail: [fatma.abid@valeo.com](mailto:fatma.abid@valeo.com)

G. Chevallier • J.L. Dion

Associate Professor, SUPMECA PARIS – LISMMMA, 3 rue Fernand Hainaut, 93407 Saint Ouen, France

e-mail: [gael.chevallier@supmeca.fr](mailto:gael.chevallier@supmeca.fr); [jean-luc.dion@supmeca.fr](mailto:jean-luc.dion@supmeca.fr)

N. Dauchez

Professor, SUPMECA PARIS – LISMMMA, 3 rue Fernand Hainaut, 93407 Saint Ouen, France

e-mail: [nicolas.dauchez@utc.fr](mailto:nicolas.dauchez@utc.fr)

J.L. Blanchard

Engineer, VALEO Group Electronics Expertise and Development Services, 2 Rue André Boulle, 94046, Créteil, France

e-mail: [jean-louis.blanchard@valeo.com](mailto:jean-louis.blanchard@valeo.com)

These classical methods have been commonly used in mechanical engineering problems for many years and can easily be applied to the thermal domain as well. However, they are more suitable for processing linear systems. More recently, modern reduction techniques such as either Singular Value Decompositions (SVD) or Proper Orthogonal Decomposition (POD) were introduced in the last decades. The POD method is an a posteriori powerful technique for model reduction of large-scale non-linear systems and it has been successfully applied for the simulation and control of complex systems [2, 11]. The second category of reduction methods is of non-intrusive nature. This category can be viewed as belonging to the category of system identification techniques aimed at developing models that describe mathematically the dynamic behavior of the real system. System identification techniques drive a model, considered as a black-box, by operating directly only on input data such as command law and output results. In this framework, this paper focuses on two methods based on Kalman filters, namely the Extended Kalman Filter (EKF) and Unscented Kalman Filter (UKF) proposed by Sorenson [12], and Julier and Uhlman [7, 8], respectively. These methods deal with both linear and nonlinear systems. The EKF applies the standard Kalman Filter to nonlinear systems by simply linearizing all the nonlinear models. However, in practice, the use of EKF has two well-known drawbacks [8, 9]. First, linearization can produce highly unstable filters if the assumptions of local linearity are violated. Second, the derivation of the Jacobian matrices is nontrivial in most applications and often lead to significant implementation difficulties, especially when the model construction step starts from a continuous state-space form. However, the UKF is founded on the intuition that it is easier to approximate a Gaussian distribution than it is to approximate an arbitrary nonlinear function [7].

In this study, both the EKF and UKF approaches are used to estimate a linear thermal transient model. To illustrate these methods, a Finite Element (FE) model is considered as a reference. The accuracy of the identified system model is evaluated by comparing its response with the numerical results produced by the FE reference model.

The rest of this paper is organized as follows. Section 55.2 presents the problem statement. The detailed ROM formulation used in identification system technique is given in Sect. 55.3. We also briefly present principles of the EKF and UKF. Section 55.4 contains results for the case study. A sensitivity analysis is conducted to evaluate EKF and UKF performance. Conclusions and future work end this paper.

## 55.2 Problem Statement

In this study, a thermal transient problem is investigated and it is described by a Finite Element FE model of dimension  $n$  (Eq. 55.1). A transient heat flux ( $\phi_{imp}(t)$ ) and a convective condition are considered as boundary conditions. Thermal properties (conductivity  $k$  and heat transfer coefficient  $h$ ) are assumed temperature- and time-independent, and radiative effects are neglected. Initially the system is at a uniform initial temperature  $T_0$  and the surrounding temperature is  $T_{out}$ . Hence, the linear system governing the FE model is:

$$[C]\{\dot{T}\} + [K]\{T\} = \{F\} \quad (55.1)$$

where  $[C]$  and  $[K]$  are the heat capacity and the conductivity matrices. The notation  $\{T\} = [T_1(t) \ T_2(t) \ \dots \ T_n(t)]^T$  stands for the nodal temperature vector,  $\{\dot{T}\} = [\dot{T}_1(t) \ \dot{T}_2(t) \ \dots \ \dot{T}_n(t)]^T$  is the time derivative of the this vector, and  $\{F\} = [\phi_{imp} \ 0 \ 0 \ \dots \ hT_{out}]^T$  designates the heat flux vector of dimension  $n$ .

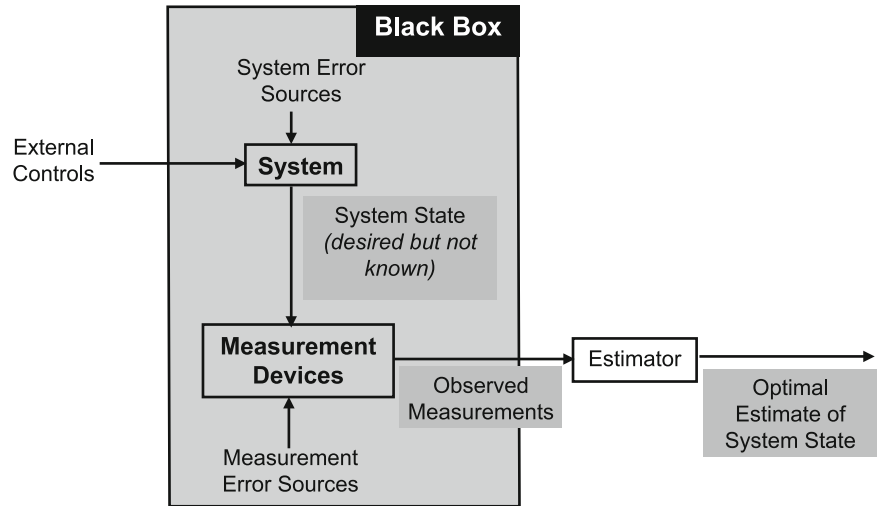
## 55.3 System Identification

### 55.3.1 Generalities

For an identification problem, where the model is considered as a black-box, temperature measurements or part of them are known as well as the forcing term  $\phi_{imp}$ , whereas the model operators are unknown. To deal with this category of problems, system identification technique based on Kalman Filters variants is herein investigated. Both Extended Kalman Filter (EKF) and Unscented Kalman Filter (UKF) are applied in order to identify a reduced-order model (ROM) for the direct linear problem given in Eq. 55.1. The system identification procedure illustrated in Fig. 55.1 is performed in two steps:

- (1) The measurements
- (2) The model construction

**Fig. 55.1** System identification procedure



### 55.3.2 Step 1: Measurements

In the standard (direct) heat transfer problem (55.1), the operators  $[C]$ ,  $[K]$  and  $\{F\}$  are assumed known and  $\{T\}$  is determined through a numerical integration method implemented in Matlab (e.g. Runge-Kutta method). This FE model is considered as a reference and its numerical results are compared to the results of the identified system model to evaluate its accuracy.

### 55.3.3 Step 2: Model Construction

The choice of the model, which consists in selecting a mathematical model to describe the input-output behaviour of the system of interest, is a fundamental step. To begin, the FE reference linear model presented in Eq. (55.1) is first considered. For the purpose of identification, the reference model is transformed into a time-invariant state space form:

$$\begin{cases} \dot{x}(t) = Ax(t) + Bu(t) \\ y(t) = Cx(t) + Du(t) \end{cases} \quad (55.2)$$

where  $x(t)$  is the  $n \times 1$  state vector,  $A$  the  $n \times n$  state transition matrix,  $B$  the  $n \times p$  input-state matrix,  $C$  the  $m \times n$  state-output matrix and  $D$  the  $m \times p$  direct transmission matrix. For physical systems,  $D$  is usually the zero matrix. The vector  $u(t)$  generally groups the applied forces in (55.1) and  $B$  is a matrix which maps the physical locations of the input forces ( $p$ -input vector) to the internal variables of the realization. Similarly,  $y(t)$  are physical sensor measurements (or numerical observations at the DOFs of the reference FE model) yielded by temperature probes, and  $C$  is a matrix which constructs these physical quantities ( $m$ -output vector) from the internal variables  $x(t)$ .

In = addition :

- The system is controllable if and only if the matrix  $\Gamma_{cont} = [B \ AB; A^2B; \dots; A^{n-1}B] \in \mathbb{R}^{n \times np}$  is of rank  $n$ .
- The state  $x(t)$  is observable if and only if the matrix  $\Gamma_{obs} = [C; CA; CA^2; \dots; CA^{n-1}] \in \mathbb{R}^{mn \times n}$  is of rank  $n$ .

#### 55.3.3.1 The Reduced-Order Model (ROM)

Model order reduction is closely related to system identification. It is therefore interesting to keep only the internal variables that capture the essential dynamics of the system. To this purpose, the reference problem (55.1) is represented by a linear reduced-order model (ROM) of dimension  $n_r \leq n$ , in which  $\{x_r\} = [T_{r_1} \ T_{r_2} \ \dots \ T_{r_{n_r}}]^T$  is the new temperature reduced-order state vector. This latter consists of internal variables that are used to describe the dynamic relationships. If an orthonormal basis change  $U$  such that  $U^{-1}AU$  is a diagonal matrix is applied to the system (55.2), this system becomes:

$$\begin{cases} \dot{x}_r(t) = \tilde{A}x_r(t) + \tilde{B}u(t) \\ y(t) = \tilde{C}x_r(t) \end{cases} \quad (55.3)$$

with  $\tilde{A} = U^{-1}AU$ ;  $\tilde{B} = U^{-1}B$  and  $\tilde{C} = CU$ . If only one input  $u(t) = \phi_{imp}(t)$  is applied, the constitutive reduced-order model (ROM) further simplifies into:  $\tilde{A} = \begin{bmatrix} a_1 & & \\ & \ddots & \\ & & a_{n_r} \end{bmatrix}$ ;  $\tilde{B} = \begin{bmatrix} b_1 \\ \vdots \\ b_{n_r} \end{bmatrix}$ ;  $\tilde{C} = \begin{bmatrix} c_{11} & \cdots & c_{1n_r} \\ \vdots & \ddots & \vdots \\ c_{n_r1} & \cdots & c_{n_rn_r} \end{bmatrix}$ . The coefficients  $a_i$ ,  $\{i = 1, \dots, n\}$  depend on the time-constants  $\tau_i$ ,  $\{i = 1, \dots, n\}$  of the reference problem;  $a_i = -\frac{1}{\tau_i}$ .

### 55.3.3.2 Setting of Extended Kalman Filter (EKF)

In this section, the conversion of the continuous ROM (Eq. 55.3) into a discrete representation (Eq. 55.4) is performed using EKF by means of an exponential discretization technique [3](see A.1). The resulting discrete ROM is given by Eq. 55.4:

$$\begin{cases} x_k = \begin{bmatrix} x_{rk} \\ \theta_k \end{bmatrix} = \begin{bmatrix} \tilde{f}_{d_k}(x_{r_{k-1}}, u_{k-1}, \theta_{k-1}) \\ \theta_{k-1} \end{bmatrix} \\ y_k = \tilde{h}_d(x_{rk}, \theta_{k-1}) \end{cases} \quad (55.4)$$

where the  $\tilde{f}_{d_k}$  and  $\tilde{h}_d$  are nonlinear evolution and observation functions at time  $k$ , the  $\theta_k$  a  $n_p$ -stationary parameter vector at time  $k$ ;  $\theta_k = \left[ e^{a_1 T} \cdots e^{a_{n_r} T}, \frac{b_1}{a_1} \cdots \frac{b_{n_r}}{a_2} c_{11} \cdots c_{1n_r} c_{n_r1} \cdots c_{n_rn_r} \right]_k^T$ .

### 55.3.3.3 Setting of Unscented Kalman Filter (UKF)

The continuous ROM in Eq. (55.3) can also be written as:

$$\begin{cases} \dot{x}_r = \tilde{f}(x_r, u) \\ y = \tilde{h}(x_r) \end{cases} \quad (55.5)$$

where  $x_r = [T_{r_1} \cdots T_{r_{n_r}} a_1 \cdots a_{n_r} b_1 \cdots b_{n_r} c_{11} \cdots c_{1n_r} c_{n_r1} \cdots c_{n_rn_r}]^T$  is the extended reduced-state vector, the  $\tilde{f}$  and  $\tilde{h}$  are the nonlinear evolution and observation functions. An implicit numerical integration method (Dormand-Prince method) [5, 10] is used in order to discretize  $\tilde{f}$  and therefore obtain a (discrete-time) recursive ROM. In the case of nonlinear system,  $a_i$ ,  $\{i = 1, \dots, n_r\}$  become time-dependent. To process it, we use the same ROM as in (55.5) and the UKF algorithm is unchanged. Here, the advantage of UKF as regards the implementation simplicity is highlighted with respect to the EKF. This latter methodology actually is not extended to the processing of nonlinear systems due to the difficulty related to the analytical model construction step.

## 55.3.4 Basic Formulation of Kalman Filters

### 55.3.4.1 Extended Kalman Filter (EKF)

In this section, a nonlinear state-space model equivalent to the above model in Eq. (55.4) is considered:

$$\begin{cases} x_k = f_k(x_{k-1}, u_{k-1}) + w \\ y_k = h_k(x_k) + v \end{cases} \quad (55.6)$$

where  $x_k$  is the extended state vector, whose distribution is assumed to be a Gaussian random variable,  $y_k$  the noisy measurement vector,  $u_{k-1}$  the known input at time  $k-1$ ,  $f_k$  and  $h_k$  the nonlinear process and the nonlinear measurement

functions, and  $w$  and  $v$  the process and measurement noise, respectively. These latter are assumed to be uncorrelated zero-mean Gaussian white noises with time-invariant covariance matrices  $Q$  and  $R$ . The idea of the EKF is to linearize the nonlinear process  $f_k$  and measurement function  $h_k$  by a first order Taylor series (Jacobian) at each time step around the most recent estimate of the state vector  $x$ . The resulting EKF algorithm is summarized in B.1.1, [12].

### 55.3.4.2 Unscented Kalman Filter (UKF)

The UKF represents an alternative to the extended Kalman Filter (EKF). The UKF is based on the fact that it is easier to approximate a Gaussian distribution than it is to approximate an arbitrary nonlinear function [7]. Instead of linearization process using Jacobian matrices similarly the EKF approach, the UKF uses a deterministic sampling technique known as the Unscented Transform (UT), proposed by Julier and Uhlmann [7, 8]. The idea of UT is to form  $2n + 1$  samples (or *sigma-points*) that capture exactly the mean and covariance of the original distribution of  $x$ . These *sigma-points* are then propagated through the non-linearity and the mean and covariance of the transformed variable are estimated from them. The UT scheme is illustrated in B.1.2. Consider now the model in (55.6) used in Sect. 55.3.4.1. The distribution of the vector  $x_k$  is assumed to be a Gaussian random variable. The UKF is presented in B.1.3.

## 55.4 Numerical Results

A 10-DOF Finite Element (FE) model simulation is carried out to evaluate the performance of the EKF and UKF methods regarding system identification. The problem is numerically simulated using *ode23*, a Matlab routine implementing a low-order Runge-Kutta method with adaptive step size control. Initial conditions consist of a uniform temperature. The forcing term  $u = \phi_{imp}(t)$  is a square signal applied at DOF 1 (cf. Fig. 55.2 (top)), and Fig. 55.2 (bottom) shows the simulation results. As a first step, the Singular Value Decomposition (SVD) is used in order to determine the minimum number of modes required to capture in the ROM the essential dynamics of the reference model (cf. Fig. 55.3). The Fig. 55.3 (top left and top right) shows that the first two singular values are much greater than the rest (the numerical values are 14,040, 3,314, 885.9, ...). As such, the modal contribution is dominated by the first two modes. Hence, the reference model can be represented by a two-order reduced model.

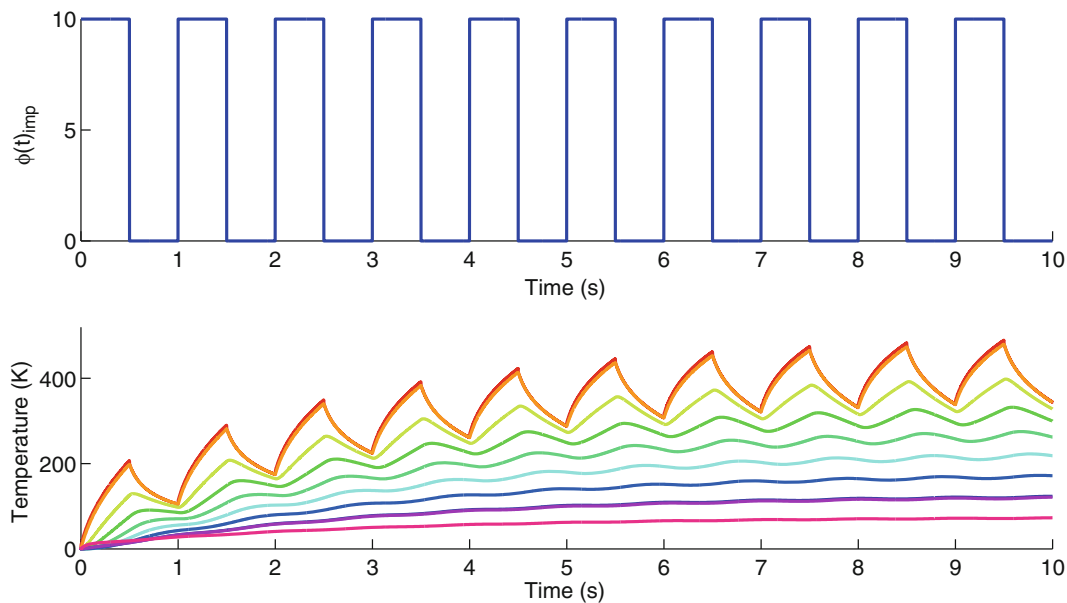
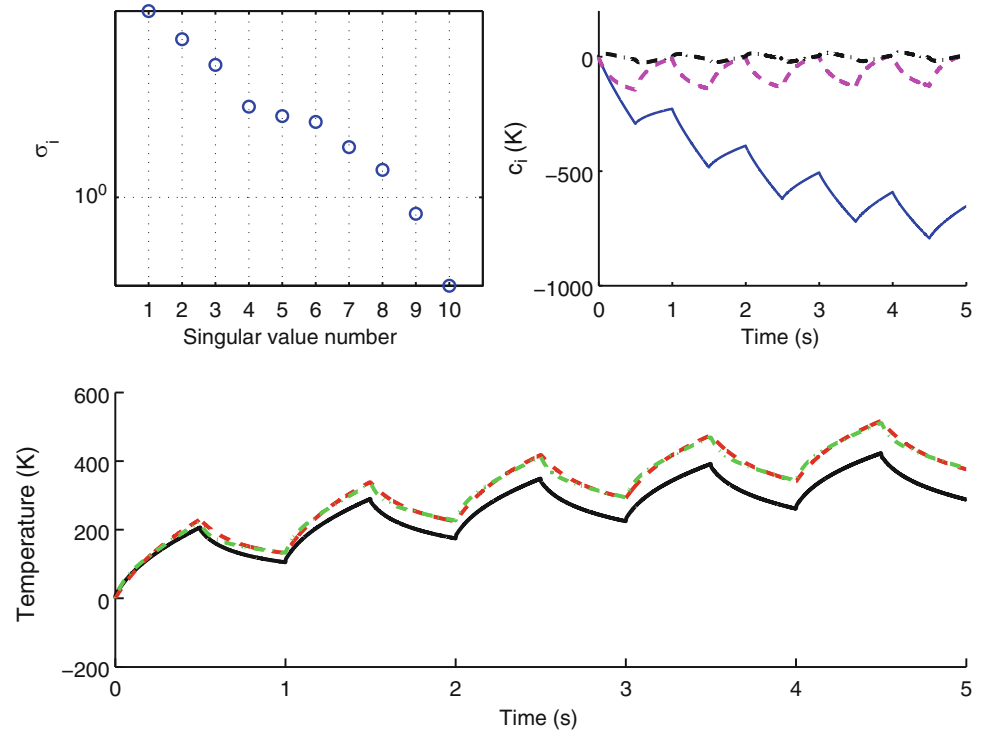


**Fig. 55.2** (Top) The square signal-forcing term of magnitude  $10 \text{ W}\cdot\text{m}^{-1}$  and frequency 1 Hz applied to the reference model at DOF 1; (bottom) Temperature evolution at all DOFs of the reference FE model; from DOF 1 to DOF 10

**Fig. 55.3** SVD computed on the reference FE model; (top left) the singular values (circle); (top right) modal contributions of Proper Orthogonal Mode (POM): POM 1 (solid curve), POM 2 (dashed curve) and POM 3 (dashed-dotted curve); (bottom) Temperature response at DOF 1: FE response (solid curve), SVD with 2 POM (dashed curve) and SVD with 3 POM (dashed-dotted curve)



### 55.4.1 Filtering Step

Now we apply EKF and UKF to the FE reference model. Our goal is to identify the discrete ROM by using known input forcing vector  $u = \phi_{imp}(t)$ , a square signal (see Fig. 55.2 (top)), and available temperature data collected at DOF 1 and 10 of the FE reference model (see Fig. 55.2 (bottom)). For simplicity, the state and observation noise covariance matrices are set as  $Q = \sigma_w^2 I_{n_e \times n_e}$  and  $R = \sigma_v^2 I_{m \times m}$ , where  $\sigma_w^2$  and  $\sigma_v^2$  are the state and observation noise variances. The notations  $I_{n_e \times n_e}$  and  $I_{m \times m}$  denote the  $n_e \times n_e$  and  $m \times m$  identity matrices, and  $n_e = 10$ ,  $m = 2$  stand for the dimension of the extended state vector and observation vector. The initial state estimate covariance is set as  $P_0 = p_0 \text{Diag}(\text{vect})$ , where  $p_0$  is the initial state error variance and  $\text{vect} = [10, 10, 1, 1, 0.01, 0.01, 1, 1, 1, 1]$  a vector of dimension  $n_e$ .

### 55.4.2 Sensitivity Analysis

In this study, we show how: (1) the initial state estimate covariance  $P_0$  representing the confidence in the initial state estimate, (2) state model covariance  $Q$  representing the confidence in the Kalman model and (3) the observation covariance  $R$  representing the confidence in the measurements, affect the performance of both EKF and UKF. The performance of the EKF and UKF can be measured by: (1) comparison of the true observed and estimated temperature and the corresponding terms in  $P$  (not shown here); (2) evolution of the identified parameters and the corresponding terms in  $P$ ; and finally (3) the evolution of the residual term, which is the difference between the predicted and true observed temperatures at DOF of observation (1 and 10 in the reference FE model).

#### 55.4.2.1 Sensitivity to the State Model Covariance

Figures 55.4–55.7, illustrate the sensitivity of EKF and UKF to the state covariance by comparing values from  $\sigma_w = 2 \cdot 10^{-5}$  to  $\sigma_w = 2 \cdot 10^{-9}$  and from  $\sigma_w = 10^{-2}$  to  $\sigma_w = 10^{-11}$ , respectively. Increasing the state model covariance increases the convergence speed (Fig. 55.4) and sensitivity to measurement (a significant decrease of the residual term when  $\sigma_w$  goes from  $10^{-8}$  (dashed-dotted curve; error up to  $\sim 6\%$ ) to  $10^{-5}$  (dashed curve; error up to  $\sim 1.6\%$ ) in Fig. 55.7 (left)). Increasing the state model covariance too far results in parameter identification failure (dashed and solid curves in Fig. 55.6 (left)) and

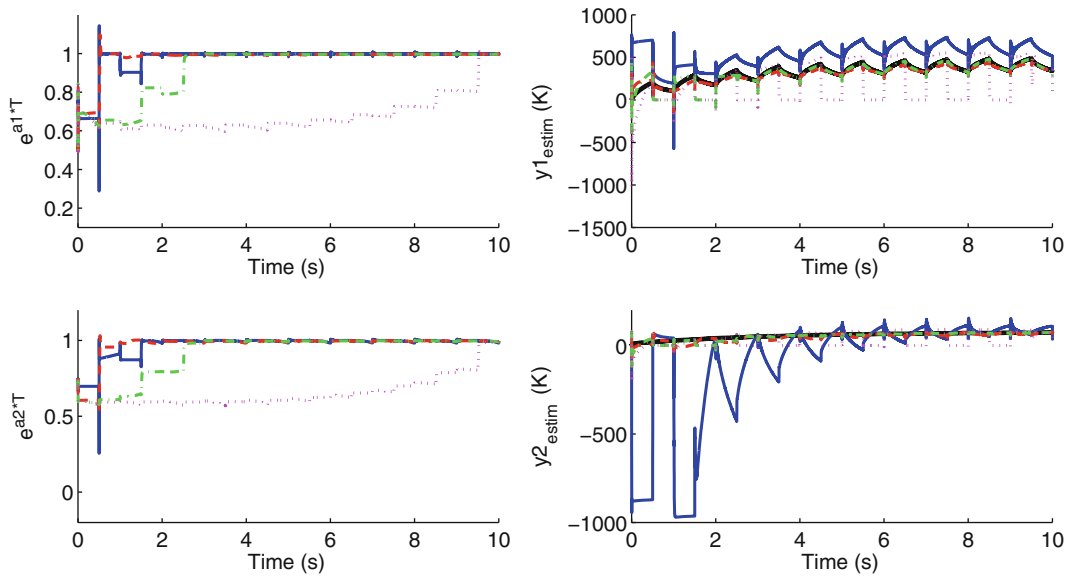


**Fig. 55.4** Sensitivity analysis of EKF to state model covariance ( $\sigma_w$  parameter) for fixed  $\sigma_v = 10^{-3}$  and  $p_0 = 10^{-6}$ : (left) Parameter identification ( $e^{a_1 T}$  (top) and  $e^{a_2 T}$  (bottom)); (right) Temperature evolution at DOF observation 1 (top) and 2 (bottom); FE response (solid curve),  $\sigma_w = 2.10^{-6}$  (solid curve),  $\sigma_w = 10^{-7}$  (dashed curve),  $\sigma_w = 10^{-8}$  (dashed-dotted curve) and  $\sigma_w = 10^{-9}$  (pink dotted curve)

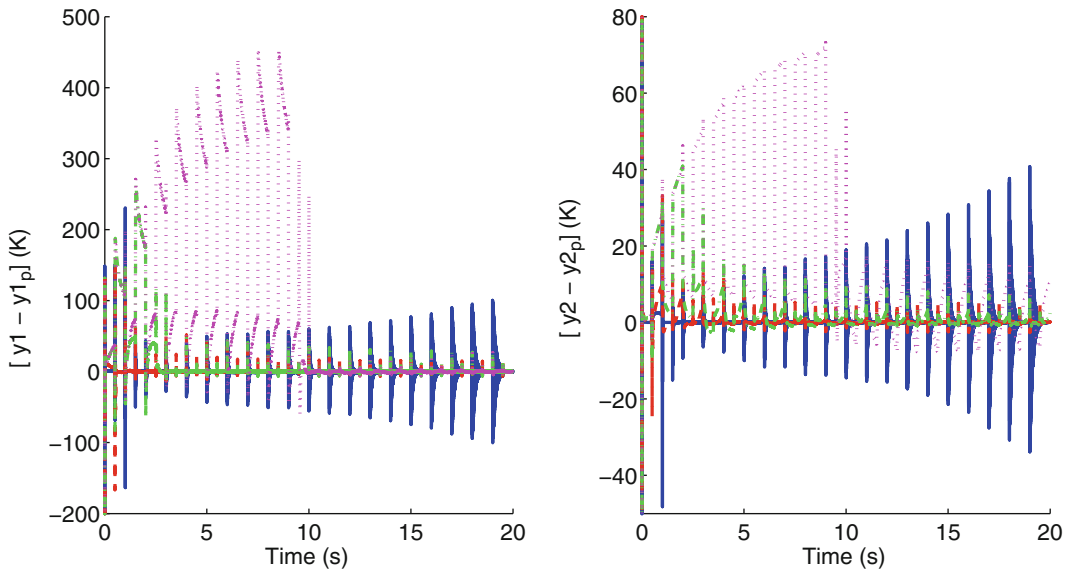


**Fig. 55.5** Sensitivity analysis of EKF to model state covariance ( $\sigma_w$  parameter) for fixed  $\sigma_v = 10^{-3}$  and  $p_0 = 10^{-6}$ : (left) Measurement residual of the estimation at DOF observation 1; and (right) Measurement residual of the estimation at DOF observation 2;  $\sigma_w = 2.10^{-6}$  (solid curve),  $\sigma_w = 10^{-7}$  (dashed curve),  $\sigma_w = 10^{-8}$  (dashed-dotted curve) and  $\sigma_w = 10^{-9}$  (dotted curve)

solution divergence (blue solid curve in Figs. 55.4 and 55.5). In other words, when we are less confident in the Kalman model, the gain  $K$  at update time in both EKF and UKF algorithm is sufficient large and hence observations play a significant role in estimating the state (temperatures) but not in parameter identification.

### 55.4.2.2 Sensitivity to the Observation Covariance

Figures 55.8 and 55.9 illustrate the sensitivity of EKF and UKF to the observation covariance by comparing values from  $\sigma_v = 10^{-1}$  to  $\sigma_v = 10^{-4}$  and from  $\sigma_v = 1$  to  $\sigma_v = 10^{-4}$ , respectively. Decreasing the measurement covariance magnitude



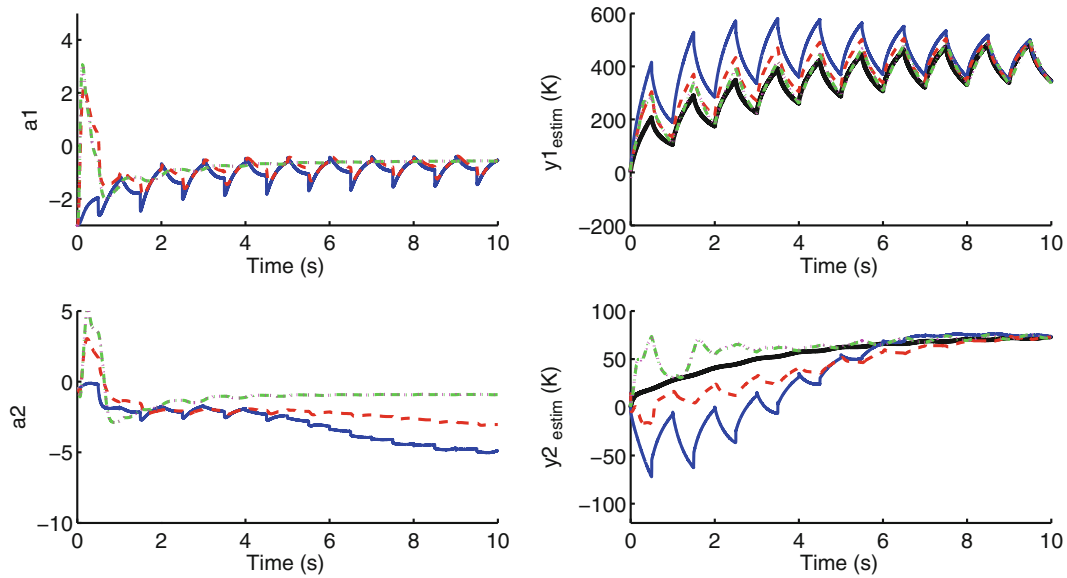


**Fig. 55.6** Sensitivity analysis of UKF to state model covariance ( $\sigma_w$  parameter) for fixed  $\sigma_v = 10^{-2}$  and  $p_0 = 10^{-6}$ : (left) Parameter identification ( $a_1$  (top) and  $a_2$  (bottom)); (right) Temperature evolution at DOF observation 1 (top) and 2 (bottom); FE response (solid curve),  $\sigma_w = 10^{-2}$  (solid curve),  $\sigma_w = 10^{-5}$  (dashed curve),  $\sigma_w = 10^{-8}$  (dashed-dotted curve) and  $\sigma_w = 10^{-11}$  (dotted curve)

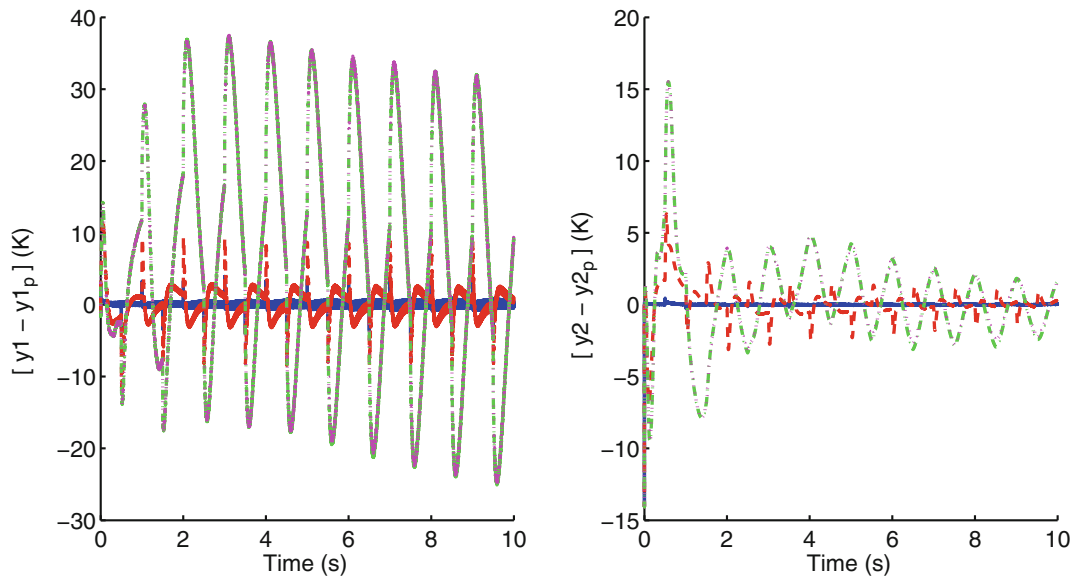


**Fig. 55.7** Sensitivity analysis of UKF to state model covariance ( $\sigma_w$  parameter) for fixed  $\sigma_v = 10^{-2}$  and  $p_0 = 10^{-6}$ : (left) Measurement residual of the estimation at DOF observation 1; and (right) Measurement residual of the estimation at DOF observation 2;  $\sigma_w = 10^{-2}$  (solid curve),  $\sigma_w = 10^{-5}$  (dashed curve),  $\sigma_w = 10^{-8}$  (dashed-dotted curve) and  $\sigma_w = 10^{-11}$  (dotted curve)

increases the convergence speed. Decreasing the magnitude too far results in erratic parameter value (dotted curve;  $e^{a_2 T} > 1$  in Fig. 55.8 (left) and  $a_2 > 1$  in Fig. 55.9 (left)) or the solution fails to converge (dotted curve;  $e^{a_1 T}$  in Fig. 55.8 (left),  $a_1$  in Fig. 55.9 (left)). Conversely, increasing the measurement covariance magnitude too far causes the identified parameters to remain fairly constant at an erratic value (solid curve;  $e^{a_1 T} < 0$  and  $e^{a_2 T} > 1$  in Fig. 55.8 and solid curve;  $a_1, a_2 > 0$  in Fig. 55.9 (left)) and the solution fails to converge (solid curve in Fig. 55.9 (right)).

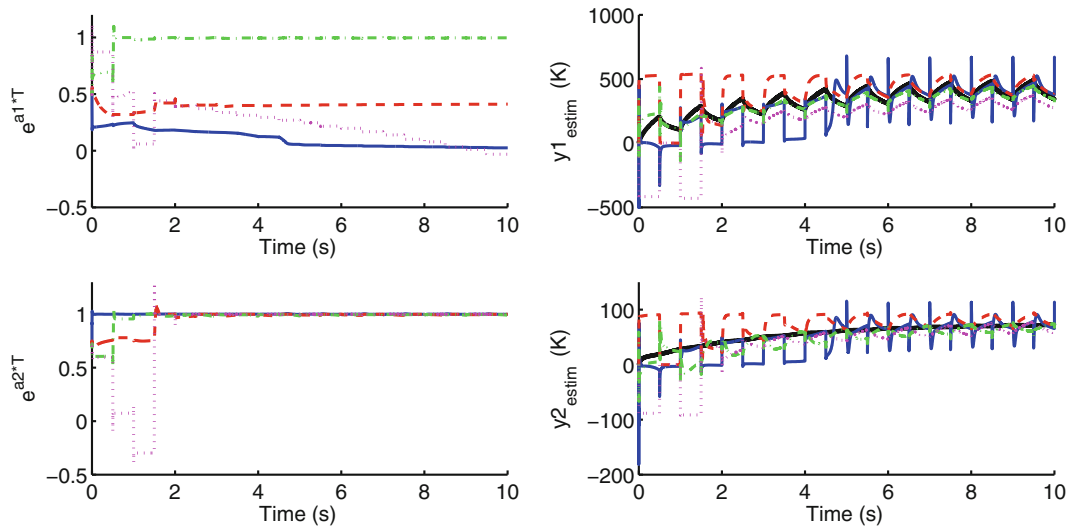


**Fig. 55.8** Sensitivity analysis of EKF to observation noise covariance ( $\sigma_v$  parameter) for fixed  $\sigma_w = 10^{-7}$  and  $p_0 = 10^{-6}$ : (left) Parameter identification ( $e^{a_1T}$  (top) and  $e^{a_2T}$  (bottom)); (right) Temperature evolution at DOF observation 1 (top) and 2 (bottom); FE response (solid curve),  $\sigma_v = 10^{-1}$  (solid curve),  $\sigma_v = 10^{-2}$  (dashed curve),  $\sigma_v = 10^{-3}$  (dashed-dotted curve) and  $\sigma_v = 10^{-4}$  (pink dotted curve)

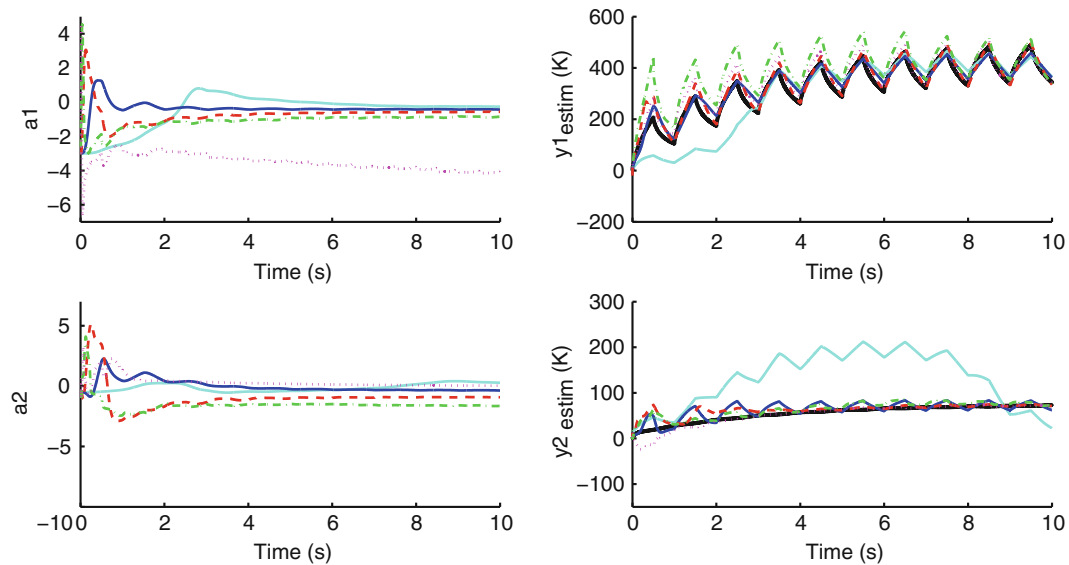


**Fig. 55.9** Sensitivity analysis of UKF to observation noise covariance ( $\sigma_v$  parameter) for fixed  $\sigma_w = 10^{-8}$  and  $p_0 = 10^{-6}$ : (left) Parameter identification ( $a_1$  (top) and  $a_2$  (bottom)); (right) Temperature evolution at DOF observation 1 (top) and 2 (bottom); FE response (solid curve),  $\sigma_v = 10^{-1}$  (solid curve),  $\sigma_v = 10^{-2}$  (dashed curve),  $\sigma_v = 10^{-3}$  (dashed-dotted curve) and  $\sigma_v = 10^{-4}$  (dotted curve)

### 55.4.2.3 Sensitivity to the Initial State Estimate Covariance

Kalman filters diverge (dotted curve in Fig. 55.10 (left)), or converge slowly (dotted curve in Fig. 55.11 (left)), because the initial state covariance is very small. However, if  $p_0$  is very large, the filter converges to an erratic value (solid curve  $e^{a_1T}$ ,  $e^{a_2T} > 1$  in Fig. 55.10 (left); and  $a_2 > 0$  in Fig. 55.11 (bottom left)) or fails to converge (solid curve in Fig. 55.11 (top left);  $a_1$  parameter).

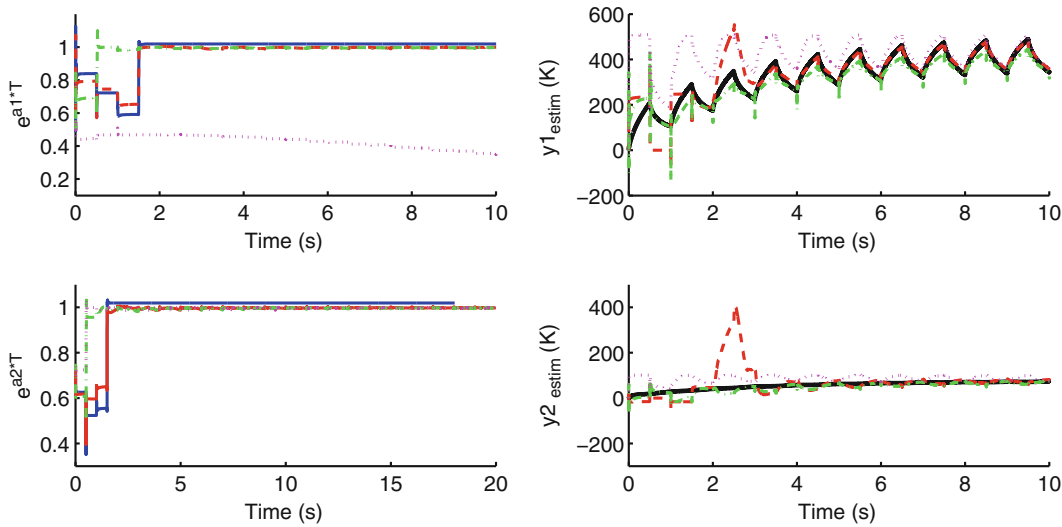


**Fig. 55.10** Sensitivity analysis of EKF to initial state estimate covariance ( $p_0$  parameter) for fixed  $\sigma_w = 10^{-7}$  and  $\sigma_v = 10^{-3}$ : (left) Parameter identification ( $e^{a_1 T}$  (top) and  $e^{a_2 T}$  (bottom)); (right) Temperature evolution at DOF observation 1 (top) and 2 (bottom); FE response (solid curve),  $p_0 = 10^{-4}$  (solid curve),  $p_0 = 10^{-5}$  (dashed curve),  $p_0 = 10^{-6}$  (dashed-dotted curve) and  $p_0 = 10^{-7}$  (dotted curve)

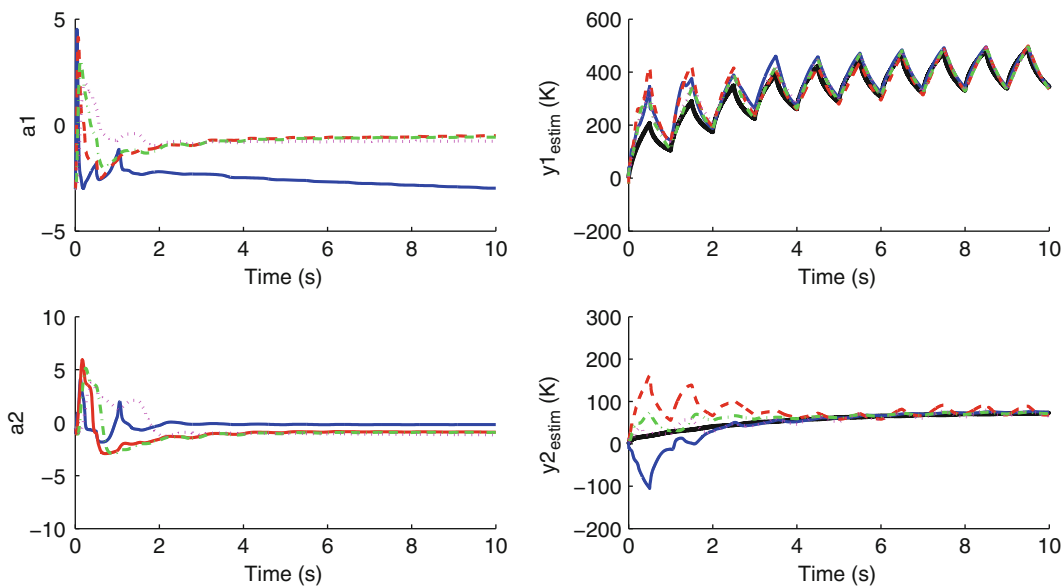


**Fig. 55.11** Sensitivity analysis of UKF to initial state estimate covariance ( $p_0$  parameter) for fixed  $\sigma_w = 10^{-8}$  and  $\sigma_v = 10^{-2}$ : (left) Parameter identification ( $a_1$  (top) and  $a_2$  (bottom)); (right) Temperature evolution at DOF observation 1 (top) and 2 (bottom); FE response (solid curve),  $p_0 = 10^{-4}$  (solid curve),  $p_0 = 10^{-5}$  (dashed curve),  $p_0 = 10^{-6}$  (dashed-dotted curve) and  $p_0 = 10^{-7}$  (dotted curve)

To conclude, the best performance of EKF and UKF is obtained for the following values ( $\sigma_w = 10^{-6}$ ,  $\sigma_v = 10^{-3}$ ,  $p_0 = 10^{-6}$ ) and ( $\sigma_w = 10^{-8}$ ,  $\sigma_v = 10^{-2}$ ,  $p_0 = 10^{-6}$ ), respectively. As the quotient  $\frac{\sigma_w}{\sigma_v}$  is very small, that means more confidence is attributed in the Kalman model, the model adopted for reduction is validated.

### 55.5 Conclusions and Future Work

This paper presents the EKF and UKF methods in order to identify a reduced order model for a linear thermal system based on data produced by a FE numerical model. The sensitivity of these two methods with respect to state model covariance, observation noise covariance, as well as to initial state estimate covariance is analyzed. This analysis shows that these three

Kalman entries significantly impact the filter results and that judicious choices have to be made to guarantee convergence and obtain the best performance and optimal values. This paper illustrates this behavior through the comparison between the FE results and the responses produced by the EKF and UKF. A crucial advantage of the UKF with respect to the EKF is that the implementation of the method for processing a nonlinear system can be done without difficulty by using the same approach for the ROM construction as the one detailed in this paper.

This study has validated both of EKF and UKF methods through a 10-DOF FE linear model. Future studies will deal with larger order FE models, first in the linear and then in the nonlinear domain, using UKF.

## A.1 Model Construction Step Using EKF

The solution of Eq. (55.3) on the time interval  $[t_i t_f]$  is given by [1]:

$$x_r(t_f) = x_r(t_i) e^{\tilde{A}(t_f-t_i)} + \int_{t_i}^{t_f} e^{\tilde{A}(t_f-\tau)} \tilde{B} u(\tau) d\tau \quad (55.7)$$

where the exponential matrix is defined as  $e^{\tilde{A}t} = \sum_{k=0}^{\infty} \frac{1}{k!} (\tilde{A}t)^k$  With  $t_i = t_k$  and  $t_f = t_{k+1}$ , (55.7) becomes:

$$x_r(t_{k+1}) = x_r(t_k) e^{\tilde{A}(t_{k+1}-t_k)} + \int_{t_k}^{t_{k+1}} e^{\tilde{A}(t_{k+1}-\tau)} \tilde{B} u(\tau) d\tau \quad (55.8)$$

Simplifying the notation by writing  $k$  instead of  $t_k$  and supposing  $u(t)$  constant over the sampling interval  $[t_k t_{k+1}]$ , the discrete state space model is written as follows:

$$\left. \begin{aligned} x_{rk} &= \tilde{A}_d x_{rk-1} + \tilde{B}_d u_{k-1} \\ y_{rk} &= \tilde{C}_d x_{rk} \end{aligned} \right\} \tilde{A}_d = e^{\tilde{A}T}; \tilde{B}_d = \int_{t_k}^{t_{k+1}} e^{\tilde{A}(t_{k+1}-\tau)} \tilde{B} d\tau = \int_0^T e^{\tilde{A}\tau} B d\tau; \tilde{C}_d = \tilde{C} \quad (55.9)$$

where  $x_{rk}$  is the state vector of internal variables at time  $k$ ,  $y_k$  the observation vector at time  $k$ ,  $u_{k-1}$  the input data at time  $k-1$ , and  $(\tilde{A}_d \tilde{B}_d \tilde{C}_d)$  the constitutive matrices of the discrete reduced-order model:  $\tilde{A}_d = \begin{bmatrix} e^{a_1 T} & & \\ & \ddots & \\ & & e^{a_{n_r} T} \end{bmatrix}; \tilde{B}_d =$

$$(e^{\tilde{A}_d T} - I) \begin{bmatrix} b_1 \\ \vdots \\ b_{n_r} \end{bmatrix} = \begin{bmatrix} \frac{b_1}{a_1} (e^{a_1 T} - 1) \\ \vdots \\ \frac{b_{n_r}}{a_{n_r}} (e^{a_{n_r} T} - 1) \end{bmatrix}; \tilde{C}_d = \tilde{C} = \begin{bmatrix} c_{11} & \cdots & c_{1n_r} \\ \vdots & \ddots & \vdots \\ c_{n_r 1} & \cdots & c_{n_r n_r} \end{bmatrix}.$$

The objective of our procedure being the identification of parameters, they have to be included in the state vector. The functions  $\tilde{A}_d$  and  $\tilde{C}_d$  are thereby nonlinear and will be denoted  $\tilde{f}_d$  and  $\tilde{h}_d$ , respectively. The discrete model is then given by:

$$\begin{cases} x_k = \begin{bmatrix} x_{rk} \\ \theta_k \end{bmatrix} = [\tilde{f}_d(x_{rk-1}, u_{k-1}, \theta_{k-1})] \\ y_k = \tilde{h}_d(x_{rk}, \theta_{k-1}) \end{cases} \quad (55.10)$$

## B.1 EKF and UKF Algorithms

### B.1.1 Extended Kalman Filter (EKF)

---

#### Extended Kalman Filter algorithm

---

##### Description:

##### 1: Initialization:

State mean and covariance at  $k = 0$ :  $\hat{x}_0 = E[x_0]$  and  $P_0 = E[(x_0 - \hat{x}_0)(x_0 - \hat{x}_0)^T]$

##### 2: Prediction phase

- (a) The process model Jacobian:  $F_k = \frac{\partial f_k}{\partial x} \Big|_{x=\hat{x}_{k-1}}$   
 (b) Predicted state mean and covariance:  $\hat{x}_k^- = f_k(\hat{x}_{k-1}, u_{k-1})$  and  $P_k^- = F_k P_k F_k^T + Q$

##### 3: Correction phase

- (a) Measurement model Jacobian:  $H_k = \frac{\partial h_k}{\partial x} \Big|_{x=\hat{x}_k^-}$   
 (b) Measurement update:  
 Measurement prediction:  $\hat{y}_k = h_k(\hat{x}_k^-)$   
 Innovation (Residual term):  $\tilde{y}_k = y_k - \hat{y}_k$   
 Innovation covariance matrix:  $M_k = cov(\tilde{y}_k) = H_k P_k^- H_k^T + R$   
 (c) Updated state mean and Covariance:  
 Kalman Gain matrix:  $K_k = P_k^- H_k^T M_k^{-1}$   
 State update:  $\hat{x}_k = \hat{x}_k^- + K_k \tilde{y}_k$   
 Covariance update:  $P_k = (I - K_k H_k) P_k^-$
- 

### B.1.2 Unscented Transform (UT)

---

#### Unscented Transform

---

Let  $x \in \mathbb{R}^n$  be a Gaussian random vector and  $y = g(x)$  a general nonlinear function,  $g : \mathbb{R}^n \rightarrow \mathbb{R}^m$ ;  $y = g(x)$ ;  $E[x] = \bar{x}$ ;  $E[(x - \bar{x})(x - \bar{x})^T] = P_{xx}$

##### 1: Decomposition of the distribution in $2n + 1$ sigma-points

$$\{\chi_{i, \omega_i}\}_{i=0 \dots 2n} = UT(\bar{x}, P_{xx})$$

$$\text{where } \chi_0 = \bar{x} ; \omega_0 = \frac{\kappa}{(n+\kappa)}$$

$$\left. \begin{aligned} \chi_i &= \bar{x} + [\sqrt{(n+\kappa)P_{xx}}] ; \omega_i = \frac{1}{2(n+\kappa)} \\ \chi_{i+n} &= \bar{x} - [\sqrt{(n+\kappa)P_{xx}}] ; \omega_{i+n} = \frac{1}{2(n+\kappa)} \end{aligned} \right\} i = 1 \dots n$$

N.B. The term  $[\sqrt{(n+\kappa)P_{xx}}]_i$  represents the  $i$ th column vector of the matrix square root  $(n+\kappa)P_{xx}$  and is derived via the Cholesky factorisation. The parameter  $\kappa$  is a scaling parameter and  $\omega_i$  an associated weight of each *sigma-point*.

---

### B.1.3 Unscented Kalman Filter (UKF)

---

#### Unscented Kalman Filter algorithm

---

##### Description:

##### 1: Initialization:

State mean and covarianc at  $k = 0$ :  $\hat{x}_0 = E[x_0]$  and  $P_0 = E[(x_0 - \hat{x}_0)(x_0 - \hat{x}_0)^T]$

##### 2: Prediction phase

(a) Generation of  $2n + 1$  sigma-points  $\{\chi_{i,k-1}, \omega_i\}_{i=0 \dots 2n} = UT(\hat{x}_{k-1}, P_{x_{k-1}})$

(b) Predicted state:  $\chi_{i,k}^- = f_k(\chi_{i,k-1}, u_{k-1})$  and  $\hat{x}_k^- = \sum_{i=0}^{2n} \omega_i \chi_{i,k}^-$

(c) Predicted covariance:  $P_{x_k}^- = \sum_{i=0}^{2n} \omega_i (\chi_{i,k}^- - \hat{x}_k^-)(\chi_{i,k}^- - \hat{x}_k^-)^T + Q$

##### 3: Correction phase

(a) Measurement update:  $Y_{i,k} = h_k(\chi_{i,k}^-)$

(b) Measurement prediction:  $\hat{y}_k = \sum_{i=0}^{2n} \omega_i Y_{i,k}$

(c) Innovation (Residual term):  $\tilde{y}_k = Y_{i,k} - \hat{y}_k$

(d) Innovation covariance:  $P_{y_k} = \sum_{i=0}^{2n} \omega_i \tilde{y}_k \tilde{y}_k^T + R$

(e) Cross covariance:  $P_{x_k y_k} = \sum_{i=0}^{2n} \omega_i (\chi_{i,k}^- - \hat{x}_k^-)(Y_{i,k} - \hat{y}_k)^T + R$

(f) Updated state mean and Covariance:

Kalman Gain matrix:  $K_k = P_{x_k y_k} P_{y_k}^{-1}$

State update:  $\hat{x}_k = \hat{x}_k^- + K_k \tilde{y}_k$

Covariance update:  $P_{x_k} = P_{x_k}^- - K_k P_{y_k} K_k^T$

---

## References

1. Andrews HC, Patterson CL (1976) Singular value decompositions and digital image processing. *IEEE Trans Acoust Speech Signal Process* 24(1):26–53
2. Berkooz G, Holmes P, Lumley JL (1993) The proper orthogonal decomposition in the analysis of turbulent flows. *Annu Rev Fluid Mech* 25(1):539–575
3. Boyce WE, DiPrima RC (1977) Elementary differential equations and boundary value problems. John Wiley & Sons, New York
4. Craig R, Bampton MCC (1968) Coupling of substructures for dynamic analyses. *AIAA J* 6(7):1313–1319
5. Dormand JR, Prince PJ(1980) A family of embedded runge-kutta formulae. *J Comput Appl Math* 6(1):19–26
6. Guyan RJ (1965) Reduction of stiffness and mass matrices. *AIAA J* 3(2):380–380
7. Julier SJ, Uhlmann JK (1996) A general method for approximating nonlinear transformations of probability distributions. Technical report, University of Oxford, Departement of Engineering Science
8. Julier SJ, Uhlmann JK (1997) A new extension of the kalman filter to nonlinear systems. In: The proceedings of aeroSense: the 11th international symposium on aerospace/defence sensing, simulation and controls, Orlando, Florida, pp 182–193
9. Joseph J, LaViola Jr (2003) A comparison of unscented and extended kalman filtering for estimating quaternion motion. In the proceedings of the 2003 american control conference, Denver, Colorado, pp 2435–2440
10. Mathews JH, Fink KD (2004) Numerical methods using MATLAB. Prentice Hall, Upper Saddle River, New Jersey
11. Moore BC (1981) Principal component analysis in linear systems: controllability, observability, and model reduction. *IEEE Trans Autom Control* 26(1):17–32
12. Sorenson HW (1970) Least-squares estimation: from gauss to kalman. *IEEE Spectr* 7(7):63–68

# Chapter 56

## Identification of Time-Varying Nonlinear Systems Using Differential Evolution Algorithm

Nevena Perisic, Peter L Green, Keith Worden, and Poul Henning Kirkegaard

**Abstract** Online monitoring of modal and physical parameters which change due to damage progression and aging of mechanical and structural systems is important for the condition and health monitoring of these systems. Usually, only the limited number of imperfect, noisy system state measurements is available, thus identification of time-varying systems with nonlinearities can be a very challenging task. In order to avoid conventional least squares and gradient identification methods which require uni-modal and double differentiable objective functions, this work proposes a modified differential evolution (DE) algorithm for the identification of time-varying systems. DE is an evolutionary optimisation method developed to perform direct search in a continuous space without requiring any derivative estimation. DE is modified so that the objective function changes with time to account for the continuing inclusion of new data within an error metric. This paper presents results of identification of a time-varying SDOF system with Coulomb friction using simulated noise-free and noisy data for the case of time-varying friction coefficient, stiffness and damping. The obtained results are promising and the focus of the further work will be on the convergence study with respect to parameters of DE and on applying the method to experimental data.

**Keywords** Differential evolution • Time-varying systems • Coulomb friction • Nonlinear system identification

### 56.1 Introduction

Considering changes of operating conditions, fault propagation, aging, unknown measurement disturbances etc., it is probably valid to say that many mechanical and structural systems are of a nonlinear and/or time-varying nature. For instance, in the case of wind turbines components, it is well known that the mass, damping and stiffness properties change with time, or more precisely with the material degradation. Also, friction affected systems often possess parameters which are dependent on temperature variations, lubricant contaminations or propagation of the fault under the surface of the material. The precise models of time-varying systems with nonlinearities are often necessary to simulate the processes for design, control, monitoring, fault detection, optimization, etc.

Identification of time-varying, nonlinear systems from the limited number of imperfect system state measurements is usually a very challenging task. Some of the conventional, derivative based, identification methods [1] such as the least squares and gradient identification methods are not suitable for this group of problems. In order to be efficient, they require two-time differentiable and uni-modal objective functions with respect to the parameters [2]. For systems nonlinear in parameters, objective functions are nonlinear and may possess more than one global minimum. As a consequence, the efficiency of the algorithm is dependant on the initial conditions. In the case of discontinuous types of nonlinearities, it is not practically feasible to estimate the gradients and Hessian matrices.

---

N. Perisic (✉) • P.H. Kirkegaard

Department of Civil Engineering, Aalborg University, Sohngaardsholmsvej 57, Aalborg 9000, Denmark  
e-mail: [np@civil.aau.dk](mailto:np@civil.aau.dk); [phk@civil.aau.dk](mailto:phk@civil.aau.dk)

P.L. Green • K. Worden

Department of Mechanical Engineering, University of Sheffield, Mappin Street, Sheffield S1 3JD, UK  
e-mail: [p.l.green@sheffield.ac.uk](mailto:p.l.green@sheffield.ac.uk); [k.worden@sheffield.ac.uk](mailto:k.worden@sheffield.ac.uk)

In order to avoid differentiation of the cost function, the group of methods known as derivative-free methods or direct search algorithms are often used for identification of parameters in nonlinear systems. These rely only on the objective function evaluation and selection phase in which it is decided if the proposed next iteration point will be accepted or not. One-point direct searches such as Random Walk [3] and Simulated Annealing [4] involve starting the search from a single initial point. They are able to find the optimal point in situations where the objective function is well known, but when it is insufficiently known, it is very difficult to choose the right standard deviation so as to set the right step size/annealing schedule and to find the global optimum. The other group of direct search methods are known as multi-point because they start the search from different points in the parameter domain. Evolution Strategies [5, 6] and Genetic Algorithms (GAs) [7, 8] are the most popular multi-point direct searches. They are population based, developed on the idea of Darwinian evolution. GA works in a discrete parameter domain using bit strings data format and logical operators to manipulate data. An alternative approach, for the continuous data, is the Differential Evolution (DE) [9] method. DE keeps only a limited number of significant digits by encoding all parameters as floating-point data. Some of the advantages of DE compared to GA includes easier implementation, lower computational complexity and more freedom in designing mutation distribution.

The disadvantage of direct search techniques is that they are developed and used only for identification of systems with time-invariant parameters. The main aim of this work is to present the idea for modification of the DE algorithm such that it can be applied to systems with time-variant parameters. Works where DE and self-adaptive DE were used for identification of memory dependant systems with Bouc-Wen hysteresis model [10, 11] showed very good performance and potential for both deterministic and stochastic identification. Thus, these works are used as a starting point for further generalization of DE.

In this paper, the differential evolution (DE) method is modified to allow identification of time-varying systems. The objective function changes with time to account for the continuing inclusion of new data within an error metric. For the sake of clarity, the performance of the modified differential evolution (M-DE) method is illustrated on the single degree of freedom Eq. (56.4) system with a Coulomb friction damping nonlinearity. The only state assumed measurable is the position, where time-varying friction coefficient, stiffness and damping are assumed to be unknown parameters. The system input is assumed known. The inclusion of new system states, other types of nonlinearities and time-varying parameters should be straightforward, considering the generality of the development.

The paper is organized as follows. Section 56.2 presents the algorithm of the standard DE which is used as a basis of the proposed M-DE algorithm. In the same section, M-DE is described and the main modifications of DE are defined and commented. Section 56.3 shows results of the identification using simulated data of the SDOF system with time-varying parameters. Incapacity of the standard DE to deal with parameter time-variations is shown. M-DE is further tested assuming different initialisation approaches and different measurement noise levels. Obtained results are discussed and future work is suggested.

## 56.2 Differential Evolution for Time-Varying Nonlinear Systems

### 56.2.1 Classical Differential Evolution

DE is a population based optimiser developed on the evolution idea that only the ‘best’ individuals survive successive generations. In this case, term individual is used to refer to a specific parameter vector. The quality of each parameter vector is determined by calculating its cost function which, in this work, is the normalized mean square error function (NMSE). The NMSE compares the measured time series  $y(t)$  with the predicted output  $\hat{y}(t)$  for the specific parameter set  $\hat{\theta}$ .

$$NMSE = \frac{100}{N\sigma_y^2} \sum_{i=1}^N (y(i) - \hat{y}(i|\hat{\theta}))^2 \quad (56.1)$$

The DE algorithm is initiated by sampling multiple parameter vectors from a predefined probability distribution. All initial parameter vectors form the population of the initial generation. The new generation is formed from the initial generation by applying the standard DE operations, i.e. mutation, recombination and selection. The process of forming new generations is repeated until the stopping criterium is satisfied, where mechanisms within DE operations are defined for each specific problems. The DE operations used in this work are specified in the following.

- *Initialization*

The algorithm starts with an initial generation of  $\mathbf{M}$  parameter vectors  $\theta$ , with  $p$  parameters in each vector. Defining the initial values of parameters requires upper and lower bounds in which parameter values are expected to be and predefined



probability density function to seed the initial population.

In this work, a uniform probability distribution is chosen as an initial probability density function (PDF) because it equally covers the search domain. The stiffness, the damping and the friction coefficient are parameters to be identified so  $p$  is equal to 3 where the initial bounds are set around the nominal values of these parameters. The recommended size of the population is 10 times the number of parameters, thus  $\mathbf{M} = 30$ .

- **Mutation**

Mutation is an essential part of the DE as it ensures the variety in the next generation thus increasing the chances that DE finds the local minimum. *Differential mutation* adds a scaled difference of two randomly selected parameter vectors  $\theta_{g,1}$  and  $\theta_{g,2}$  from the generation  $g$  to the target vector  $\theta_T$  which is also randomly selected from the same generation. The new vector is known as a mutant vector  $\theta_M$ , Eq. (56.2).

$$\theta_M = \theta_T + F \cdot (\theta_{g,1} - \theta_{g,2}) \quad (56.2)$$

The scaled parameter  $\mathbf{F}$  is a real positive number which controls the speed of population evolution. From experience it was found that the value of 0.9 provides the optimal estimations with respect of accuracy and convergence speed.

- **Recombination or Crossover**

The aim of recombination or crossover is to build the child or trial vector  $\theta_c$  from the parent vectors which are the mutant vector  $\theta_M$  and the target vector  $\theta_T$ . The trial vector has the same number of parameters as the parent vectors, and it is a combination of characteristics i.e. parameters of the parent vectors.

*Uniform crossover* provides that the probability of passing a certain parameter from different parents to the child vector is equal, i.e. it is 50%. In order to assure that child vector is not equal to the target vector, one randomly chosen parameter is always inherited from the mutant vector.

- **Selection**

Natural selection in DE is performed by comparing the cost of the trial  $\theta_c$  and the target  $\theta_T$  vectors. The one with lower cost is the parameter vector which passes to the next generation. As it was already stated, the cost is defined by NMSE, Eq. (56.1). The values of NMSE under 1% indicate almost perfect estimations, where all values under 5% indicate good estimations.

In order to form the next generation, mutation, recombination and selection are repeated  $\mathbf{M}$  times treating each parameter vector of actual generation as target vector, i.e. until the next generation is filled with  $\mathbf{M}$  parameter vectors. As a stopping criterium of the DE algorithm, the maximal number of generations is defined.

## 56.2.2 Differential Evolution with Time-Varying Cost Function

Theory and practice showed that DE works well under an assumption that the system is time invariant. However, by running the DE on a time-varying system, each identified parameter will be a single value in the whole, observed period of time  $\mathbf{T}$ .

In order to use DE on time-varying systems, the observed time period is divided in  $\mathbf{k}$  shorter, time periods, so the standard DE is iterated  $\mathbf{k}$  times, i.e. the DE algorithm is run individually for each short period of time. Basic DE operations: mutation, recombination and selection, remains the same every time DE is iterated. The main modifications of DE for time-varying systems are in the cost function and the initial conditions for each time-window. This will be explained in the following section.

### 56.2.2.1 Cost Function in DE for Time-Varying Systems

If  $\mathbf{N}$  is the total number of measurements in the period of time  $\mathbf{T}$ , these measurements are in time order split into  $\mathbf{k}$  measurement pools with  $\mathbf{N}/\mathbf{k}$  measured data in each. The objective function depends on the measurement pool, i.e. time when it is calculated. By noting the index of each measurement pool with  $\mathbf{w} \in [1, \mathbf{k}]$ , and the measured data that corresponds to measurement pool  $\mathbf{w}$  by  $y^w(t)$ , the modified, time-dependant objective function is given bellow.

$$NMSE = \frac{100}{(N/k)\sigma_{y^w}^2} \sum_{i=(w-1) \cdot N/k + 1}^{w \cdot N/k} (y(i) - \hat{y}(i|\hat{\theta}^w)) \quad (56.3)$$

Where  $\hat{\theta}^w$  is the estimation of the specific parameter set which corresponds to the measurement pool  $w$ . In this way, sampling frequency of the estimated parameters is increased compared to the case in which the classical DE is applied.

### 56.2.2.2 Initialisation of DE for Time-Varying Systems

Every time the objective function changes in time, DE should be initiated. There are different ways to do the initialisation, and the performances of the following three approaches are tested in this work.

1. *Random uniform initialisation*

The initial generation is chosen randomly, as it would be done in a classical DE.

2. *The last best generation initialisation*

The initial generation for the measurement pool  $w$  is defined to be equal to the best generation obtained from the previous measurement pool  $w - 1$ . In the case when  $w = 1$ , the initialisation is uniform random.

3. *Mutated the last best generation initialisation*

The initial generation for the measurement pool  $w$  is defined to be equal to the best generation obtained from the previous measurement pool  $w - 1$  with additional ‘new blood’. By ‘new blood’ is meant adding some new, mutated parameters to the last best generation using the same idea as in the classical DE for creating the new generation by comparing trial and target vectors. In other words, the last best generation has been altered by mutation, recombination and selection in order to form a new, mutated generation. In this way, the search domain is expanded and the probability that sudden parameter changes will not be missed is increased. In the case when  $w = 1$ , the initialisation is uniform random.

## 56.3 Results of Identification with Simulated Noise-Free and Noisy Data

### 56.3.1 Simulation Set-Up

The model of SDOF, time-varying system with Coulomb friction damping, Eq. (56.4), is developed in Simulink.

$$m\ddot{x}(t) + c(t)\dot{x}(t) + k(t)x(t) + \mu(t)\frac{|\dot{x}(t)|}{\dot{x}(t)} = u(t) \quad (56.4)$$

It is assumed that  $m$  is known mass, and  $k(t)$ ,  $c(t)$  and  $F_d(t)$  are unknown time-varying stiffness, damping and Coulomb friction damping respectively.  $x(t)$ ,  $\dot{x}(t)$  and  $\ddot{x}(t)$  are states of the system, i.e. position, velocity and acceleration signals respectively. The only state of the system assumed measurable is the position  $y(t) = x(t)$ .  $u(t)$  is the known input to the system. Simulated parameter values and time-variations do not have any physical meaning. They are chosen randomly in order to illustrate the performance of the M-DE algorithm.

The time-series are sampled at 2 kHz, so with sampling time of 0.0005 s. Parameters  $k(t)$ ,  $c(t)$  and  $F_d(t)$  linearly increase in time, and the dynamics of the changes are illustrated in Fig. 56.1 with *Reference* lines. In this work, the only available

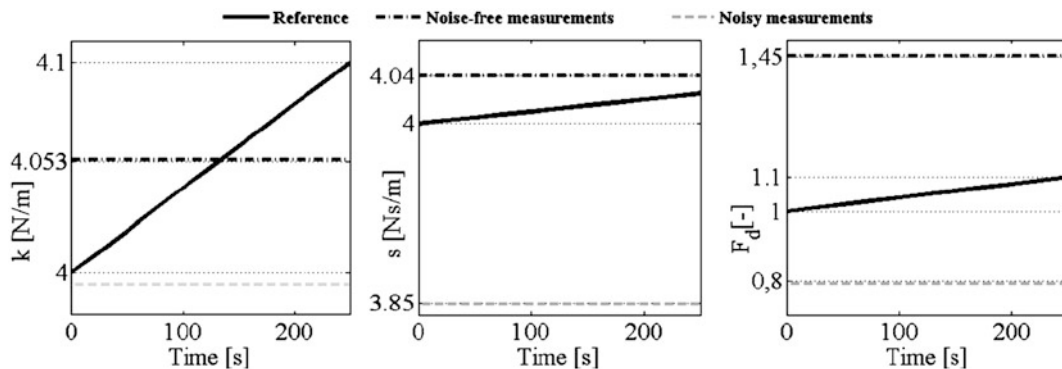


Fig. 56.1 Parameter estimation obtained with DE algorithm using noise-free and noisy measurements with NSR = 20%

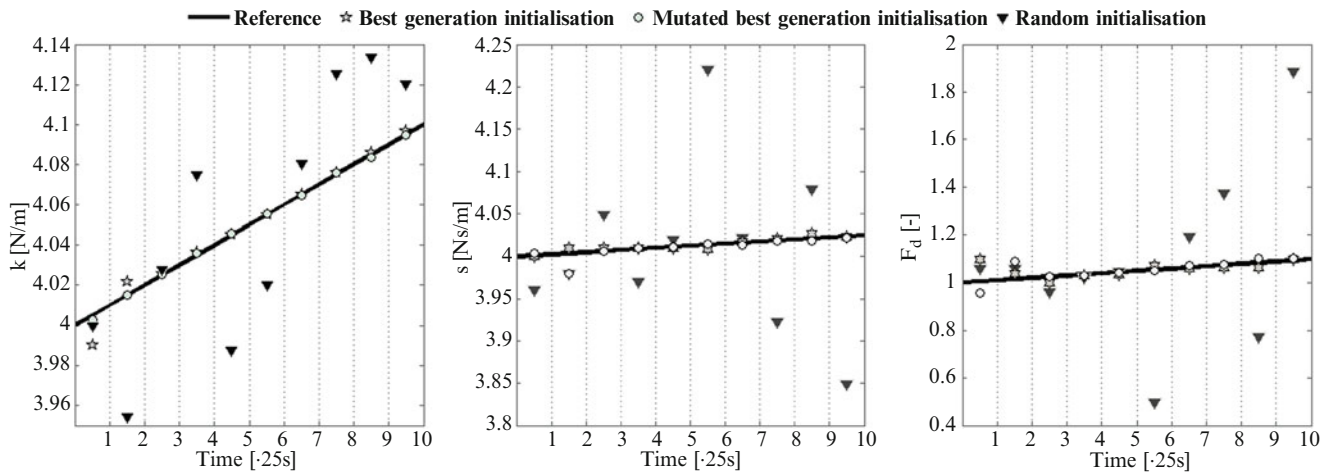


Fig. 56.2 Parameter estimations using M-DE algorithm and noise-free measurements

output signal is the position where the input is the Gaussian white noise. Artificially added measurement noise  $v(t)$  is Gaussian, zero-mean noise with the noise-to-signal (NSR) ratio equal to 1, 5 and 20%. If  $\sigma_v$  and  $\sigma_y$  are standard deviations of the measurement noise and simulated measurement, the NSR is defined by Eq. (56.5).

$$NSR = \frac{\sigma_v}{\sigma_y} \cdot 100[\%] \tag{56.5}$$

The simulation time is 250 s, and in order to apply modified DE for time-varying systems, time-series are divided in 10 measurement pools with equal length of 25 s.

### 56.3.2 Identification of Time-Varying System with Coulomb Friction Nonlinearity Using Classical DE Algorithm

In this section, classical DE is used for the estimation of time-varying  $k(t)$ ,  $c(t)$  and  $F_d(t)$ , thus all simulated data are used for single iteration of DE algorithm. Obtained estimations are constant values, and Fig. 56.1 shows the parameter estimations with the lowest NMSE. Estimations are obtained using noise-free and noisy measurements with NSR equal to 20%. The reason for showing results with high measurement noise is to illustrate that estimation results using DE are not good, irrespective of whether the measurements are perfect or noise contaminated.

### 56.3.3 Identification of Time-Varying System with Coulomb Friction Using Modified DE Algorithm

In order to illustrate the performance of modified DE for time-varying systems, the algorithm is run using noise-free and noisy measurements and assuming three different initialisation scenarios.

#### 56.3.3.1 Results with Noise-Free Measurements

Figure 56.2 shows parameter estimations with the lowest NMSE obtained using M-DE for three different initialisation scenarios. The exact parameter values plotted in Fig. 56.2 are given in Table 56.1.

**Table 56.1** Table of parameter estimations using M-DE algorithm and noise-free measurements

$w$	$\hat{k}_{LNLMSE}^{(1)}$	$\hat{k}_{LNLMSE}^{(2)}$	$\hat{k}_{LNLMSE}^{(3)}$	$\hat{c}_{LNLMSE}^{(1)}$	$\hat{c}_{LNLMSE}^{(2)}$	$\hat{c}_{LNLMSE}^{(3)}$	$\hat{F}_d^{(1)}_{LNLMSE}$	$\hat{F}_d^{(2)}_{LNLMSE}$	$\hat{F}_d^{(3)}_{LNLMSE}$
1	4.004	3.989	3.954	3.960	4.001	4.030	1.060	1.100	0.842
2	3.954	4.022	4.002	3.980	4.010	4.000	1.060	1.040	1.085
3	4.028	4.026	4.024	4.048	4.010	4.000	0.962	1.001	1.052
4	4.075	4.036	4.035	3.970	4.010	4.010	1.020	1.030	1.023
5	3.987	4.045	4.046	4.020	4.010	4.010	1.048	1.036	1.055
6	4.020	4.055	4.054	4.221	4.009	4.021	0.495	1.073	1.023
7	4.080	4.068	4.066	4.022	4.017	4.017	1.192	1.058	1.057
8	4.125	4.076	4.076	3.923	4.021	4.022	1.375	1.066	1.061
9	4.134	4.086	4.084	4.078	4.027	4.022	0.770	1.063	1.080
10	4.120	4.097	4.094	3.850	4.024	4.023	1.887	1.099	1.095

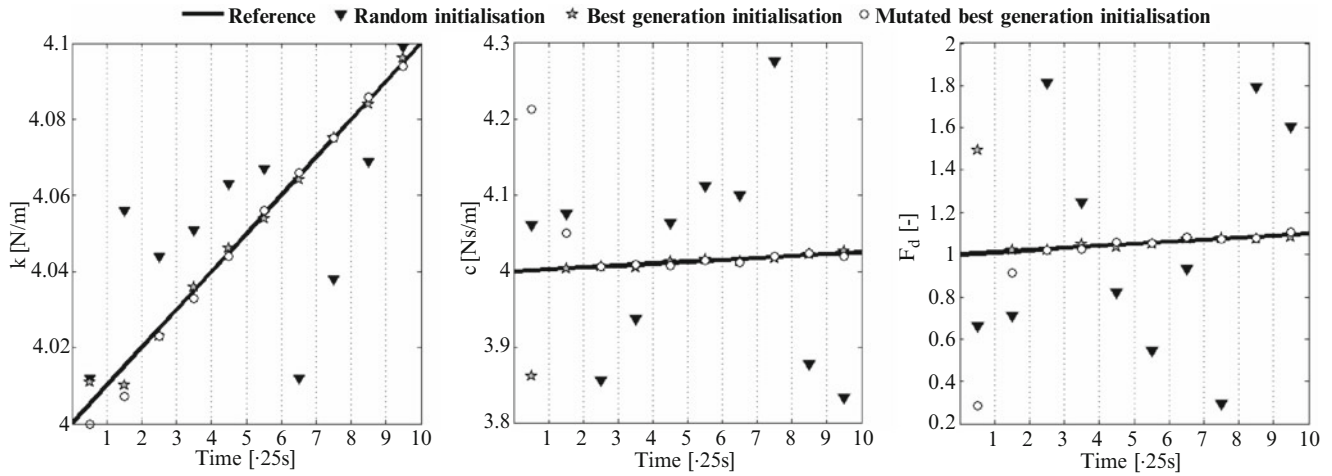


**Fig. 56.3** Parameter estimations using M-DE algorithm and noisy measurements, NSR = 1%

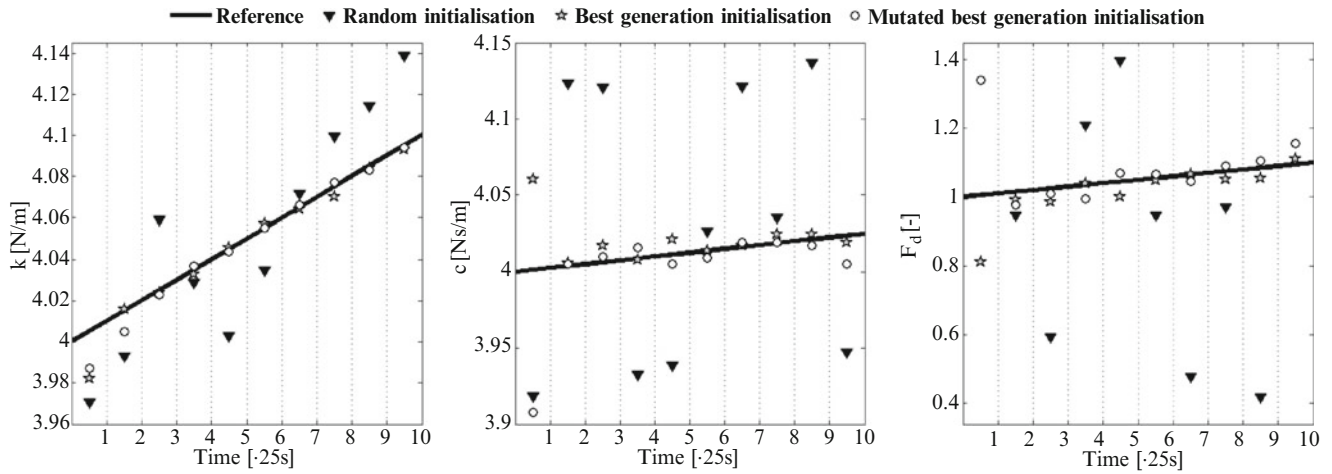


**Fig. 56.4** Parameter estimations using M-DE algorithm and noisy measurements, NSR = 5%

**56.3.3.2 Results with Noisy Measurements**

In order to check how M-DE is dealing with noise, the identification procedure is repeated with artificially added measurement noise. Gaussian, zero-mean noise sequence is directly added to the simulated displacement measurements. The identification is performed for different levels of noise, with NSR equal to 1, 5 and 20%.

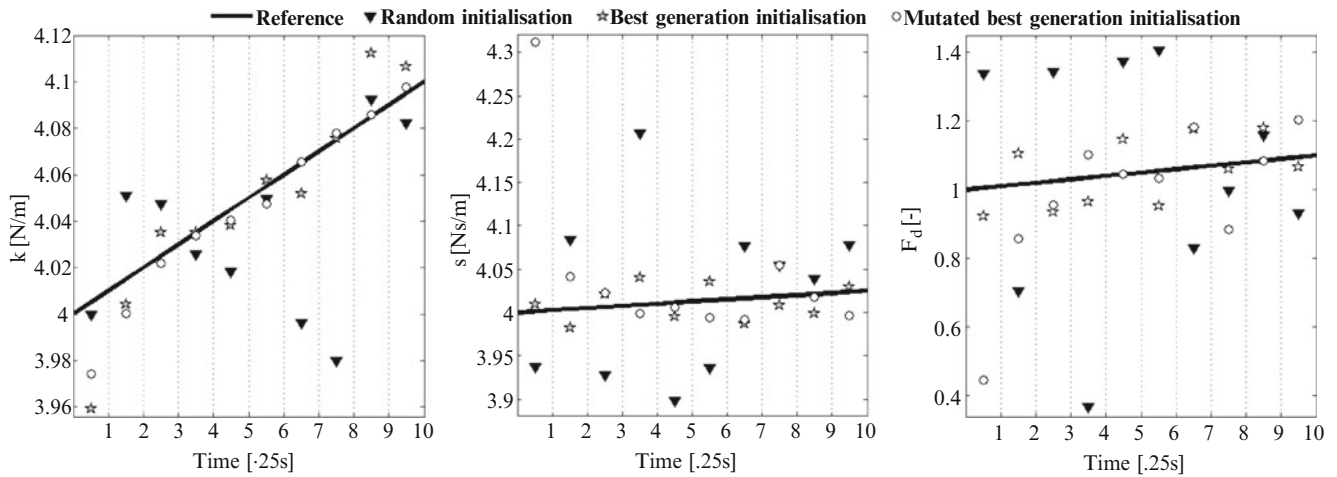


Fig. 56.5 Parameter estimations using M-DE algorithm and noisy measurements, NSR = 20%

The parameter estimations for each of the noise level are given in Figs. 56.3–56.5. Different initialisation procedures are tested for each noise level. The exact values of plotted estimations are given in Tables 56.2–56.4.

### 56.3.3.3 Discussion of the Results

In Fig. 56.1, estimation results of the time-varying parameters using standard DE algorithm are shown. DE finds the single parameter vector with the lowest cost function. In the case of time-varying system, this approach is not appropriate and this can be easily seen from the obtained results.

Table 56.2 Table of parameter estimations using M-DE algorithm and noisy measurements, NSR = 1%

$w$	$\hat{k}_{LN MSE}^{(1)}$	$\hat{k}_{LN MSE}^{(2)}$	$\hat{k}_{LN MSE}^{(3)}$	$\hat{c}_{LN MSE}^{(1)}$	$\hat{c}_{LN MSE}^{(2)}$	$\hat{c}_{LN MSE}^{(3)}$	$\hat{F}_d^{(1)}$	$\hat{F}_d^{(2)}$	$\hat{F}_d^{(3)}$
1	4.012	4.011	4.000	4.061	3.863	4.213	0.664	1.492	0.284
2	4.056	4.010	4.007	4.076	4.003	4.051	0.709	1.019	0.915
3	4.044	4.023	4.023	3.857	4.006	4.006	1.813	1.020	1.022
4	4.051	4.036	4.033	3.938	4.005	4.009	1.246	1.051	1.025
5	4.063	4.046	4.044	4.064	4.013	4.007	0.821	1.035	1.060
6	4.067	4.054	4.056	4.113	4.016	4.014	0.544	1.049	1.053
7	4.012	4.064	4.066	4.100	4.013	4.012	0.934	1.074	1.081
8	4.038	4.075	4.075	4.276	4.017	4.0192	0.295	1.077	1.075
9	4.069	4.084	4.086	3.878	4.023	4.024	1.796	1.071	1.076
10	4.099	4.096	4.094	3.834	4.027	4.020	1.607	1.084	1.109

Performance of the proposed M-DE algorithm is tested for different noise levels and different initialisation approaches. In the case of noise-free measurements, the best performance is achieved by using *the mutated best generation initialisation* with the cost function of order  $10^{-5}\%$ , indicating almost perfect estimations. *The best generation initialisation* provides almost equally good estimation results, where in the case of *the random initialisation*, estimated parameters do not converge to the reference values, but they randomly vary around them. The similar pattern behaviour of M-DE with different types of initialisation is present in the presence of noise. However, in the presence of measurement noise, the cost function gradually increases thus estimations degrade. In the case of measurement signal with NSR = 1%, the cost function is of order  $10^{-2}\%$ , where if the NSR = 5%, the cost function is of order  $10^{-1}\%$  but still lower than 1% which means that estimations are still almost perfect. If the noise level increases, and NSR is 20%, the degradation of estimations is more significant and the cost function is in between 5 and 10%.

**Table 56.3** Table of parameter estimations using M-DE algorithm and noisy measurements, NSR = 5%

$w$	$\hat{k}_{LN MSE}^{(1)}$	$\hat{k}_{LN MSE}^{(2)}$	$\hat{k}_{LN MSE}^{(3)}$	$\hat{c}_{LN MSE}^{(1)}$	$\hat{c}_{LN MSE}^{(2)}$	$\hat{c}_{LN MSE}^{(3)}$	$\hat{F}_d^{(1)}$	$\hat{F}_d^{(2)}$	$\hat{F}_d^{(3)}$
1	3.971	3.982	3.987	3.919	4.060	3.908	1.484	0.812	1.342
2	3.993	4.016	4.005	4.123	4.006	4.005	0.946	0.992	0.978
3	4.059	4.024	4.023	4.121	4.017	4.010	0.596	0.986	1.009
4	4.029	4.033	4.037	3.933	4.008	4.016	1.209	1.039	0.995
5	4.003	4.046	4.044	3.938	4.021	4.005	1.397	1.001	1.070
6	4.035	4.057	4.055	4.027	4.014	4.009	0.948	1.049	1.067
7	4.072	4.064	4.066	4.121	4.017	4.019	0.477	1.066	1.047
8	4.099	4.070	4.077	4.036	4.025	4.019	0.971	1.053	1.089
9	4.115	4.084	4.083	4.137	4.025	4.017	0.419	1.055	1.105
10	4.139	4.093	4.094	3.947	4.019	4.005	1.573	1.112	1.155

**Table 56.4** Table of parameter estimations using M-DE algorithm and noisy measurements, NSR = 20%

$w$	$\hat{k}_{LN MSE}^{(1)}$	$\hat{k}_{LN MSE}^{(2)}$	$\hat{k}_{LN MSE}^{(3)}$	$\hat{c}_{LN MSE}^{(1)}$	$\hat{c}_{LN MSE}^{(2)}$	$\hat{c}_{LN MSE}^{(3)}$	$\hat{F}_d^{(1)}$	$\hat{F}_d^{(2)}$	$\hat{F}_d^{(3)}$
1	4.000	3.959	3.974	4.009	3.937	4.041	1.338	0.924	0.446
2	4.051	4.004	4.001	4.084	3.982	4.312	0.934	1.104	0.858
3	4.048	4.035	4.021	3.928	4.021	4.022	0.705	0.934	0.956
4	4.026	4.034	4.033	4.207	4.039	3.999	1.344	0.963	1.101
5	4.018	4.038	4.040	3.898	3.995	4.005	0.369	1.146	1.045
6	4.050	4.057	4.047	3.936	4.036	3.994	1.374	0.952	1.033
7	3.996	4.051	4.065	4.077	3.987	3.992	1.405	1.178	1.182
8	3.980	4.075	4.077	4.054	4.008	4.054	0.830	1.060	0.885
9	4.092	4.112	4.086	4.039	4.000	4.018	0.998	1.181	1.085
10	4.082	4.106	4.098	4.078	4.029	3.996	1.159	1.065	1.203

## 56.4 Conclusions and Future Work

In this work, the performance of the modified differential evolution method is tested on the single degree of freedom system with Coulomb friction damping nonlinearity given by Eq. (56.4). The only state assumed measurable is the position, where the stiffness, the damping and the friction coefficient are smoothly changing in time (Fig. 56.1).

The initial results of using M-DE show that applying the differential evolution algorithms on time-varying systems, even in the presence of measurement noise, is promising. Parameter estimations in the presence of measurement noise with NSR equal to 1 and 5% are almost perfect if the best generation or the mutated best generation initialisations are used. In the presence of more significant measurement noise with NSR equal to 20%, NMSE increases and has values between 5 and 10%.

The future work will be on convergence study with respect of the optimisation hyperparameters and on applying the method to experimental data within the context of structural health monitoring.

**Acknowledgements** The financial support by the SYSWIND project, funded by the Marie Curie Actions under the Seventh Framework Programme for Research and Technology Development of the EU, is gratefully acknowledged.

## References

1. Ljung L (1987) System identification: theory for the user. Prentice-Hall, Englewood Cliffs, p 519, ISBN 0-13-881640
2. Price KV, Storn RM, Lampinen JA (2005) Differential evolution a practical approach to global optimization. Springer, Berlin/New York
3. Gross D, Harris CM (1985) Fundamentals of queuing theory. Wiley, New York
4. Kirkpatrick S, Gelatt CD, Vecchi MP (1983) Optimization by simulated annealing. Science 220:671–680
5. Rechenberg I (1973) Evolutionstrategie. Frommann-Holzboog, Stuttgart
6. Schwefel HP (1994) Evolution and optimum seeking. Wiley, New York
7. Holland JH (1962) Outline for a logical theory of adaptive systems. J assoc comput mach 8:212–229
8. Goldberg DE (1989) Genetic algorithms in search optimization and machine learning. Addison-Wesley, Reading
9. Storn R, Price KV (1995) Differential evolution – a simple and efficient adaptive scheme for global optimization over continuous spaces. Technical report TR-95-012, ICSI

10. Kyprianou A, Worden K, Panet M (2001) Identification of hysteretic systems using the differential evolution algorithm. *J Sound Vib* 248: 289–314
11. Worden K, Manson G (2011) On the Identification of Hysteretic Systems, Part I: an Extended Evolutionary Scheme. In: *Nonlinear modeling and applications, vol 2 conference proceedings of the society for experimental mechanics series, Proceedings of the 28th IMAC, A Conference on Structural Dynamics, February 1–4, 2010, Jacksonville, Florida, USA, vol 11, pp 67–75*

# Chapter 57

## Experimental Verification and Improvement of Dynamic Characterization Method for Structural Joints

Şerife Tol and H. Nevzat Özgüven

**Abstract** Mechanical connections play a significant role in predicting the dynamic characteristics of assembled structures accurately. Therefore, several methods were developed to determine equivalent dynamic models for joints. In this paper an experimental identification method based on FRF decoupling and optimization algorithm is proposed for modeling structural joints. The method developed is an extension of the method proposed by the authors in an earlier work. In the method proposed in our earlier work FRFs of two substructures connected with a bolted joint are measured, while the FRFs of the substructures are obtained analytically or experimentally. Then the joint properties are calculated in terms of translational, rotational and cross-coupling stiffness and damping values by using FRF decoupling. In this present work, an optimization algorithm is used to update the values obtained from FRF decoupling. The validity and application of the proposed method are demonstrated with experimental case studies. Furthermore, the effects of bolt size on joint dynamics are also studied by making a series of experiments and identifying the joint parameters for each case.

**Keywords** Structural joints • Joint modeling • FRF decoupling • Experimental identification • FRF measurement

### 57.1 Introduction

Many engineering structures are assembled from components by using a variety of connections; such as bolted, riveted, welded and bonded joints. Due to the effect of joints on the dynamic behavior of assembled structures, the importance of joint modeling or the identification of joint dynamic properties has become more and more significant. Reliable dynamic models for structural systems are based on the accurate identification of joint parameters. Since dynamic modeling of joints analytically is very difficult and usually not so accurate, experimental methods are used as an alternative for establishing a mathematical model for a joint.

Experimental methods can be classified as modal based methods and frequency response function (FRF) based methods. In the former class of methods, modal parameters identified from modal testing are utilized in modeling of joints. However, for structures including closely spaced modes or with large modal damping, accurate modal parameters cannot be easily obtained. Moreover, due to the nature of the modal parameter extraction process, results inevitably contain errors to some degree. In order to overcome this shortcoming, FRF based methods have been proposed in the literature.

The basic strategy in most of the FRF based joint identification methods is to use FRFs of individual substructures without joints and also those of the assembled system (structure with joints) to obtain information about the joint properties [1]. In the past decade, there were several researchers who focused on the identification of joint properties using FRF based methods. However, due to the inherent noise in measurements and different sensitivities of the formulations to noise, accuracy of the identification results differs. The reasons for this sensitivity and ways of coping with them are investigated in several studies

---

Ş. Tol

Department of Mechanical Engineering, Middle East Technical University, Ankara 06800, Turkey

George W. Woodruff School of Mechanical Engineering Georgia Institute of Technology, 801 Ferst Drive Atlanta, GA 30332-0405, USA

e-mail: [stol3@gatech.edu](mailto:stol3@gatech.edu)

H.N. Özgüven (✉)

Department of Mechanical Engineering, Middle East Technical University, Ankara 06800, Turkey

e-mail: [ozguven@metu.edu.tr](mailto:ozguven@metu.edu.tr)



[2–10]. For example, Tsai and Chou utilized the substructure FRF synthesis method in the formulation of the joint parameter identification [2]. Wang and Liou [3] improved the work of Tsai and Chou [2]. They avoided inversion of matrices in their algorithm; hence, tried to reduce noise effect in the identification. Hwang [4] used the same formulation and improved the results using an averaging process to exclude highly sensitive regions. Ren and Beards [6] developed a generalized coupling method taking into account the physical restrictions of the real structures, and identified joint parameters with this new method. However, they avoided stiff joints in order to avoid ill-conditioned matrices, and used weighting techniques for better accuracy [1]. Celic and Boltezar [7] improved the method developed by Ren and Beards [1, 6] by including the effects of rotational degrees of freedom (RDOFs). Another approach similar to the one presented in [6] is proposed by Maia et al. [8]. They reformulated the impedance uncoupling technique, and identified joints without using joint related FRFs. However, this method has not been validated with an experimental study. Yang et al. [9] derived identification equations employing substructure synthesis. They modeled a joint in terms of translational and rotational stiffness values and used singular value decomposition to avoid noise effect. However, joint damping was not included in their work.

In this study an experimental identification method based on FRF decoupling and optimization algorithm is proposed for modeling structural joints. The method developed is an extension of the method proposed by the authors in an earlier work [11]. In the method proposed in the earlier work FRFs of two substructures connected with a bolted joint are measured, while the FRFs of the substructures are obtained theoretically or experimentally. Then the joint properties are calculated in terms of translational, rotational and cross-coupling stiffness and damping values by using FRF decoupling. In this present work, an optimization algorithm is proposed to update the values obtained from FRF decoupling. The validity and application of the proposed method are demonstrated with several experimental studies by using beams connected with hexagonal bolts.

## 57.2 Theoretical Formulation

### 57.2.1 Identification of Dynamic Properties of Joints Using FRF Decoupling

Frequency response function coupling is one of the most widely used methods in the literature in analyzing two structures coupled elastically. Consider substructures A, B and their assembly (structure C) obtained by coupling them with a flexible element as shown in Fig. 57.1. The coordinates  $j$  and  $k$  represent joint degrees of freedoms (DOFs), while  $r$  and  $s$  are the ones that belong to the selected points of substructures A and B, respectively, excluding joint DOFs.

By using the elastic coupling equations (explained in more detail in [11]), it is possible to decouple and thus to calculate the complex stiffness matrix representing joint stiffness and damping as shown below:

$$[K*] = [[H_{jr}].[H_{rr}] - [H_{rr}^C]]^{-1} \cdot [H_{rj}] - [H_{jj}] - [H_{kk}]^{-1} \quad (57.1a)$$

$$[K*] = [[H_{ks}].[H_{rs}^C]]^{-1} \cdot [H_{rj}] - [H_{jj}] - [H_{kk}]^{-1} \quad (57.1b)$$

$$[K*] = [[H_{jr}].[H_{sr}^C]]^{-1} \cdot [H_{sk}] - [H_{jj}] - [H_{kk}]^{-1} \quad (57.1c)$$

$$[K*] = [[H_{ks}].[H_{ss}] - [H_{ss}^C]]^{-1} \cdot [H_{sk}] - [H_{jj}] - [H_{kk}]^{-1} \quad (57.1d)$$

As it was discussed in the earlier work of the authors [11] the most accurate results are obtained with Eq. (57.1a). However, from the experimental applicability point of view among the decoupling equations the most practical one is Eq. (57.1d). Equation (57.1a) requires the measurements of FRFs which belong to substructure A at both joint and non-joint DOFs, which

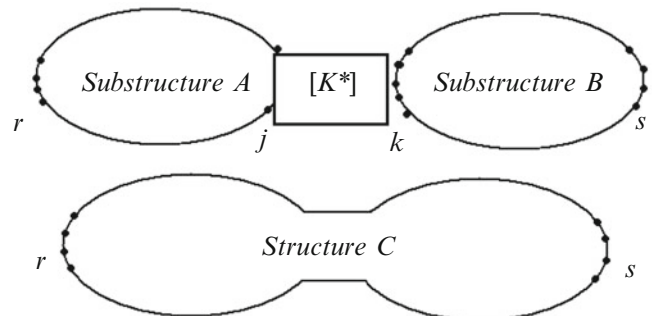
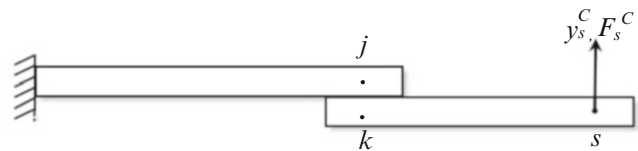


**Fig. 57.1** Elastic coupling of two substructures

**Fig. 57.2** Coupled structure with a bolted joint



is very time consuming and expensive. Furthermore, when Eq. (57.1a) is used it is not possible to obtain cross-coupling FRFs including rotational DOF (RDOF) information between joint and non-joint coordinates. On the other hand, when Eq. (57.1d) is used, only the translational and rotational FRFs at the joint coordinate of the substructure A are required to be measured, since FRFs of the substructure B can be obtained theoretically. Hence, it can be concluded that the most practical decoupling equation is the last one (Eq. (57.1d)). Therefore, being different from our previous study, Eq. (57.1d) is employed in the present study.

Furthermore, in the present study, in order to overcome the difficulties in measuring RDOF related FRFs of the coupled structure in experiments, only translational DOF (TDOF) related ones are measured and used in the identification equation. In this approach only one translational FRF at the tip point (points) of the coupled structure (see Fig. 57.2) is used in the decoupling equation. Hence, in the identification process, the need for the estimation of RDOF related FRFs belonging to the coupled structure is eliminated while keeping joint model unchanged with translational, rotational and cross-coupling elements. It is also observed in the experimental studies that, if the number of TDOF related FRFs is increased, the identification results get better.

Then, the matrix dimensions will be as follows:

$$[K^*] = [[H_{ks}].[H_{ss}] - [H_{ss}^C]]^{-1} \cdot [H_{sk}] - [H_{jj}] - [H_{kk}]^{-1}$$

$$(2 \times 2)(2 \times 1)(1 \times 1)(1 \times 1)(1 \times 2)(2 \times 2)(2 \times 2) \quad (57.2)$$

After calculating the complex joint stiffness matrix, the stiffness and damping values representing the joint dynamics are obtained from the real and imaginary parts of the matrix elements, respectively.

### 57.2.2 Estimation of FRFs for RDOF and Unmeasured Coordinates

Analytically, all elements of an FRF matrix can be calculated easily. However, in real life applications, measuring all the elements of an FRF matrix experimentally, when there are many points under consideration, is very time consuming and expensive; furthermore, it may not be possible in every case due to several different reasons. In the method proposed we need the full receptance matrix for the DOFs we are interested in. In order to obtain complete FRF matrix the structure should be excited from all points we are interested in. However, in testing usually only one column of the FRF matrix is obtained by exciting the structure from a single point and measuring responses at all other points we are interested in. Therefore, we will usually have incomplete data as far as the experimentally measured FRF matrices are considered. In this work, the missing FRF data is obtained by using FRF synthesis after extracting modal parameters by modal testing.

Another difficulty in obtaining experimentally measured FRF matrices is the measurement of RDOF related FRFs which are required in the identification equations. However, the measurement of FRFs related to RDOFs is very difficult and requires special equipment. Therefore, in this study the RDOF related FRFs are estimated by using a procedure based on the well known finite difference formulation proposed by Duarte and Ewins [12]. After measuring three translational FRFs, the RDOF related FRF can be obtained easily.

### 57.2.3 Optimization and Joint Parameter Updating

In this study it is intended to obtain constant joint parameters representing the joint stiffness and joint damping in the whole frequency band of interest, assuming that bolted joints introduce frequency independent stiffness and damping. In our previous study, stiffness and damping values are identified at every frequency in the mode which is sensitive to the joint dynamics by using Eq. (57.1a) and then the average of these identified values is taken as the resultant value [11]. However, in real life applications due to the measurement errors at each level and numerical errors associated with matrix inversion,

the variation of identified values with frequency may be considerable and it may not be easy to decide on the best frequency range to be used even in the mode which is sensitive to joint dynamics for identifying the joint properties correctly. Young et al. proposed a solution for this problem by taking some fit values from the identification curve and using these values to redefine the joint stiffness matrix in a dynamic manner [13]. However, they do not obtain present enhanced results in their work.

In this present study, an optimization algorithm is developed using “fminunc” command of MATLAB to optimize the joint properties such that regenerated and measured FRFs for the bolted assembly match at all the modes in the frequency region of interest. Using the identified joint parameters from Eq. (57.1d) as initial estimates, this algorithm updates the joint parameters by minimizing the sum of the difference between the squares of the actual and regenerated receptance amplitudes calculated at each frequency. The key point for the success of the optimization process lies in starting with a good initial estimate. In fact, one can obtain a set of joint parameters starting with some arbitrary initial estimates and identify joint parameters which may yield the correct FRF curve used in the optimization process. However, when these values are used in a new assembly, the resulting FRFs will not be correct, due to the lacking of a physical basis of the joint dynamic properties. Hence, in order to have a correct dynamic modeling of the joint, it is concluded that, initial estimates used in optimization process for the joint parameters should be close to the actual values, which can be obtained by using the identification method summarized in Sect. 57.2.2 above. The application of the proposed updating method combined with the identification method developed in our previous study [11] is illustrated and the methods are verified with several experiments conducted by using beams connected with hexagonal bolts.

### 57.3 Experimental Studies

In this section three experimental studies are given to verify the method suggested and illustrate the accuracy and applicability of the method in real life applications. In these experiments, the joints obtained connecting two steel beams with M10 × 35, M8 × 35 and M6 × 30 bolts are identified and the models obtained for the connections are used in predicting FRFs either at the points which are not used in identification, or for new assemblies. In all experiments, a cantilever steel beam is used as substructure A, and it is connected to a free-free steel beam (substructure B) with the same cross section.

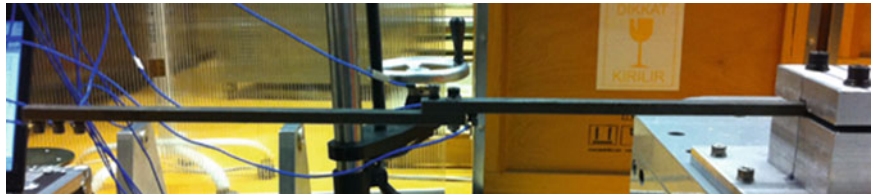
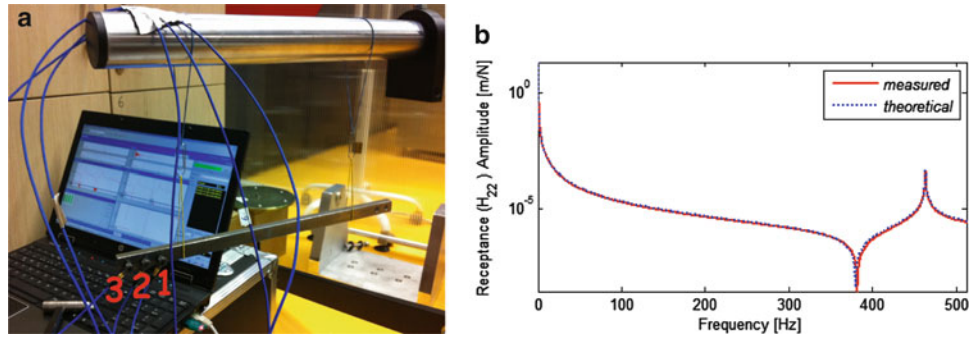
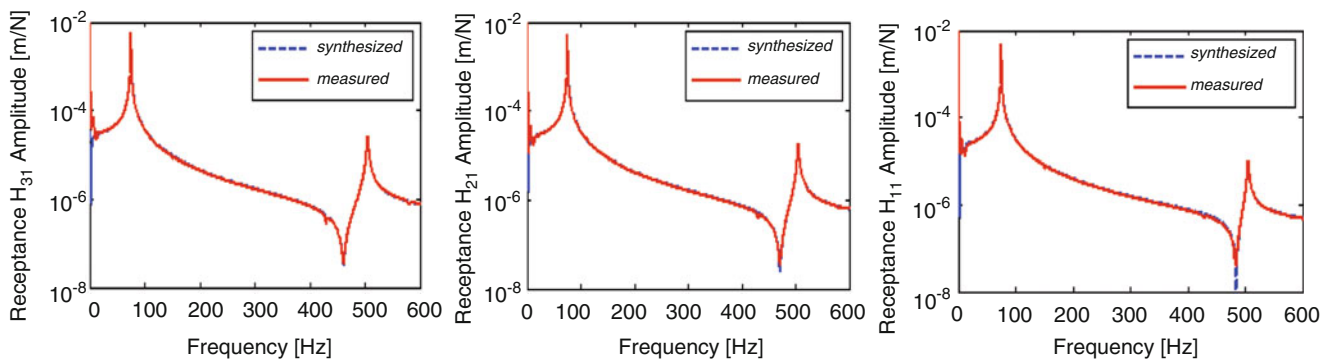
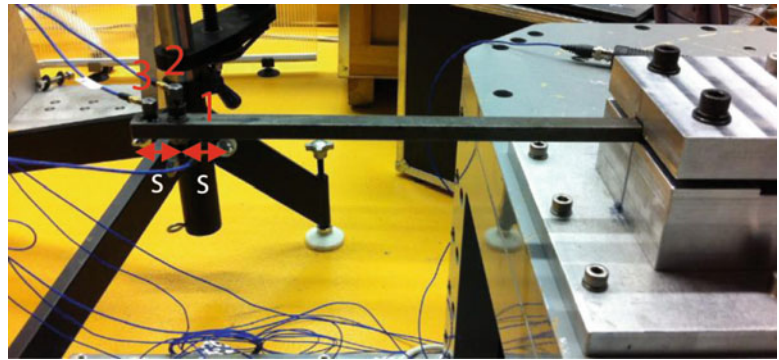
In the first experimental study, the joint obtained connecting two beams with M10 × 35 bolt is identified and the joint model is used to predict the FRFs of another point on the assembled system which is not used in identification computations. The predicted FRFs are compared with experimentally measured ones. In the second experimental study, a similar joint with M8 × 35 bolt is identified and the dynamic model of the joint is used to predict FRFs of a different coupled structure obtained with the same bolt but with a longer steel beam. The predicted FRFs are again compared with experimentally measured ones. Finally, in the last experimental study, a similar joint with M6 × 35 bolt is identified and the dynamic model of the joint is used to predict FRFs of the same beams connected with two M6 × 35 bolts. The predicted FRFs are once again compared with experimentally measured ones.

In the experiments, LMS modal test system, PCB impact hammer, PCB miniature sensors are used. Frequency resolution is selected as 0.25 Hz and the frequency range is set to 512 Hz using soft tip of the impact hammer. For the free-free tests of the substructure B, the frequency range is set to 1,024 Hz using hard tip of the impact hammer. A sufficient pre-trigger level is selected and during the experiments it is assured that all pulses are captured.

#### 57.3.1 Experimental Study I: Beams Connected with M10 × 35 Hexagonal Bolt

In this case study A2-70 M10 × 35 hexagon head bolt is used and the tightening torque is set to 30 Nm. The test set-up used is shown in Fig. 57.3. The dimensions of two stainless steel beams are as follows: Length of substructure A,  $L_A = 0.3$  m; length of substructure B,  $L_B = 0.335$  m; width of the beams: 0.015 m, height of the beams: 0.010 m.

In the experimental identification of the bolted joint, FRFs of substructure A which has fixed-free boundary conditions are measured; while the FRFs of substructure B which has free-free boundary conditions are obtained theoretically by using FE modeling and also employing the measured modal and structural parameters of the beam. In the testing of the substructure B, it is suspended with elastic cords. After exciting the substructure B from the tip point, the tip point FRFs are experimentally obtained as shown in Fig. 57.4 and the modal parameters are identified. From the tests performed on substructure B, the following parameters are obtained: elastic modulus  $E = 1.9210^{11}$  N/m<sup>2</sup>; density  $\rho = 7,604$  kg/m<sup>3</sup>, damping ratio for the first elastic mode = 0.0005. Then, these values are used in the FE model of the free-free beam in calculating the required FRFs of the substructure B ( $[H_{kk}]$ ,  $[H_{ks}]$ ,  $[H_{sk}]$  and  $[H_{ss}]$ ), accurately.

**Fig. 57.3** Single bolt connection**Fig. 57.4** (a) Testing of substructure B, (b) measured and theoretical (after tuning) FRFs at the tip point**Fig. 57.5** Close accelerometers method for substructure A**Fig. 57.6** FRF synthesis for substructure A

In order to estimate the RDOF related FRFs of substructure A, three accelerometer measurements are taken by exciting the system at point 1. The accelerometers are located with spacing,  $s$ , of 0.015 m as shown in Fig. 57.5. After completing the FRF measurements, system identification is performed using the LMS modal analysis software, and required parameters for the FRF synthesis are obtained in terms of upper and lower residuals, modal vectors, natural frequencies and damping ratios. Then, translational FRFs at the tip point of substructure A are obtained as shown in Fig. 57.6.

After obtaining the translational FRFs at the tip point, using the second order finite difference formula, rotational FRFs are estimated at point 2 as shown in Fig. 57.7.

**Fig. 57.7** Rotational FRF estimation for substructure A

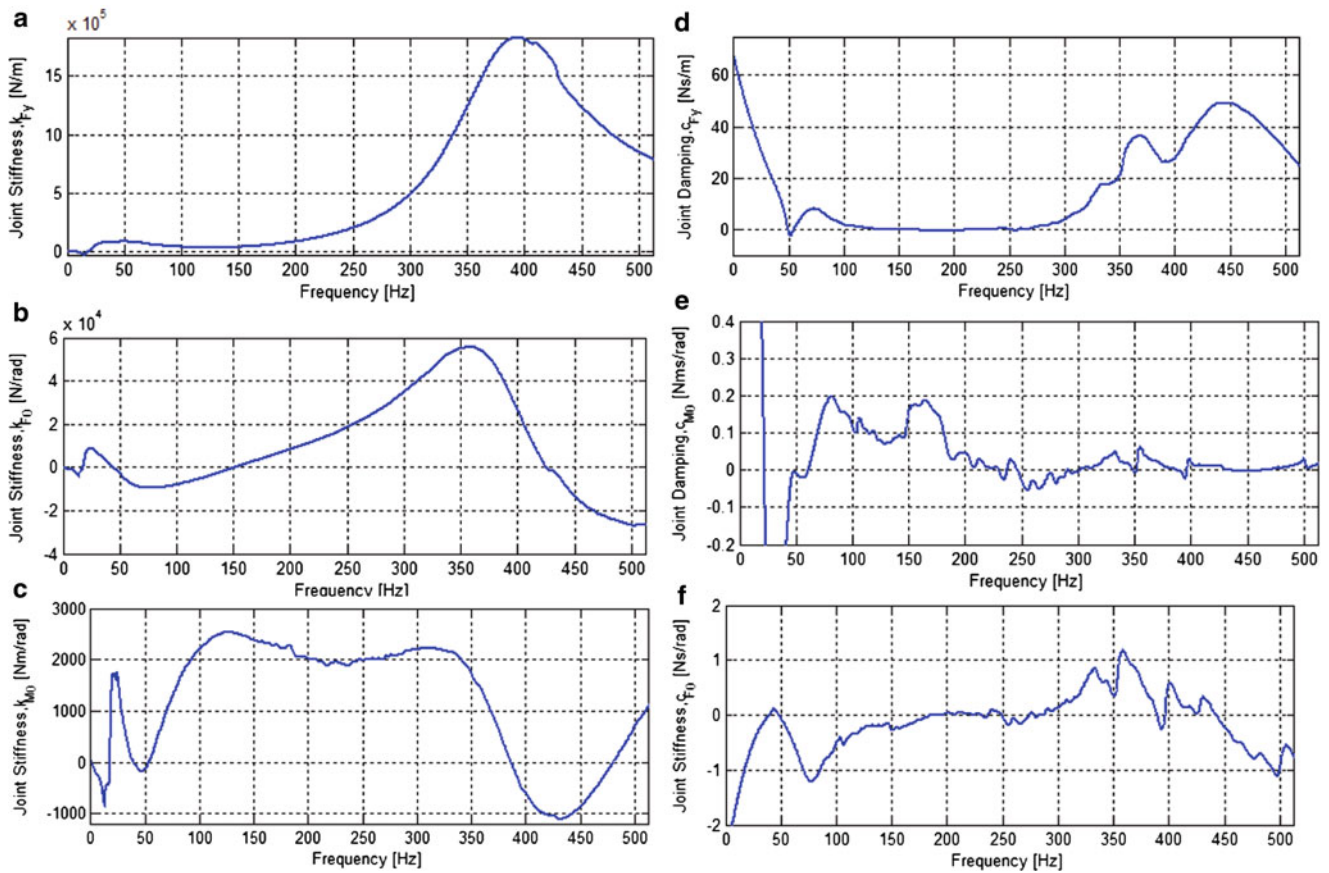
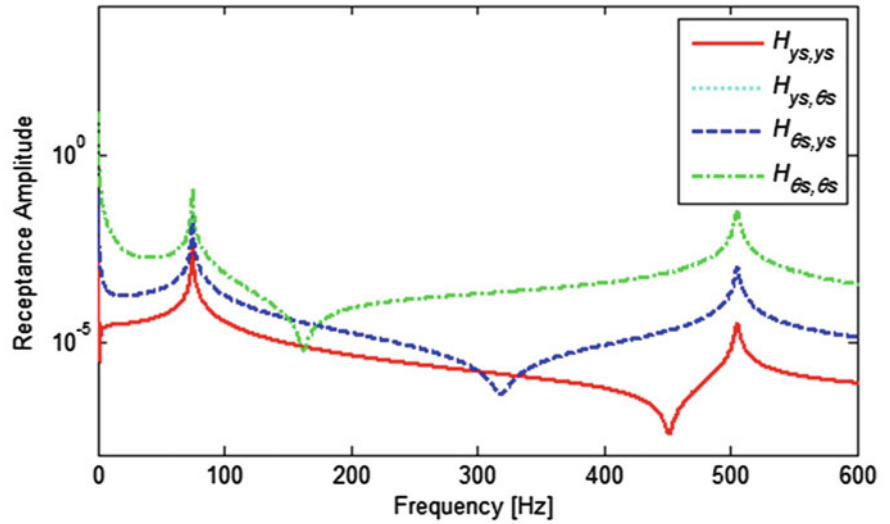


**Fig. 57.8** Identification of joint stiffness and joint damping (a) translational joint stiffness, (b) cross-coupling joint stiffness, (c) rotational joint stiffness, (d) translational joint damping, (e) cross-coupling joint damping, (f) rotational joint damping

In this case study the properties of the bolted joint are extracted with the simplified identification approach, in which only one of the translational direct point FRF measured at the tip point 2 of the structure is used. The identified joint stiffness and damping values are shown in Fig. 57.8. It is seen that the joint properties are changing with frequency and the best frequency range to determine the joint properties are not obvious. When the identification results at some modes of the coupled structure are used in the coupling equations, regenerated FRFs of the coupled structure are found to be exactly the

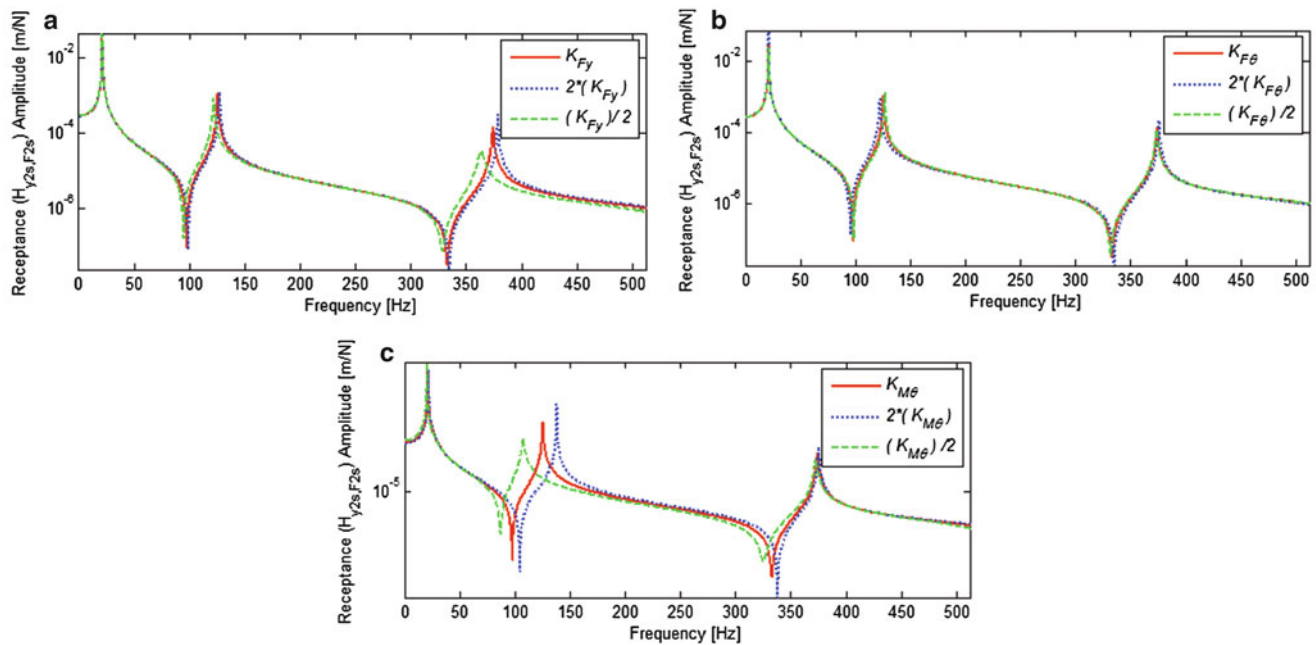


**Fig. 57.9** Sensitivity of the receptance of the coupled structure to (a) translational joint stiffness, (b) cross-coupling joint stiffness, (c) rotational joint stiffness

**Table 57.1** Joint parameters of the M10 × 35 bolted connection

	$k_{Fy}$ (N/m)	$k_{Fθ}$ (N/rad)	$k_{Mθ}$ (N.m/rad)	$c_{Fy}$ (N.s/m)	$c_{Fθ}$ (N.s/rad)	$c_{Mθ}$ (N.m.s/rad)
Initial estimates	$1.71 * 10^6$	$5.12 * 10^4$	$2.5 * 10^3$	34.72	0.646	0.073
Updated	$2.02 * 10^6$	$2.47 * 10^4$	$2.8 * 10^3$	34.41	0.635	0.077

same with the measured FRFs at these modes, but showing differences at other modes, indicating that these values cannot represent the bolted joint accurately at every mode. Yet, it was suggested in the previous work of the authors [11] to use the values identified at the frequencies where FRFs are sensitive to joint dynamics, and take the average of them for the best possible identification. Therefore, first the sensitivity analysis given in Fig. 57.9 is performed before making identification.

From the sensitivity analysis, it is seen that, translational and cross-coupling joint stiffness is effective at the third mode, while rotational stiffness is effective at both second and third modes. Therefore, the values of translational and cross-coupling joint stiffness and damping identified at the third mode and rotational parameters identified at the second mode give the best possible values. Then, these values are used as initial estimates and updated with the algorithm mentioned above. Starting with initial estimates from the identified results at the second mode for rotational parameters, the third mode for translational and cross-coupling parameters, the updated joint parameters are obtained as given in Table 57.1.

By using the updated joint parameters, receptances of the assembled system are regenerated and they are compared with the measured receptances in Fig. 57.10. It can be seen from the comparison that the receptances regenerated by using the updated joint parameters perfectly match with the measured FRFs. It is interesting to note that while some joint parameters do not change much after updating, especially some cross terms change significantly, but the overall effect of updating is very significant at some modes as can be seen from Fig. 57.10.

Finally, by using the updated joint parameters, the FRFs of the coupled structure at points 1 and 3 (see Fig. 57.5), which are not used in the identification of joint properties, are obtained. It can be seen from Fig. 57.11 that the receptances calculated by using the updated joint parameters perfectly match with the measured FRFs. Hence, it can be concluded that, the joint properties are identified accurately.

### 57.3.2 Experimental Study II: Beams Connected with M8 × 35 Hexagonal Bolt

In this experimental study, the properties of a joint with M8 × 35 mm hexagon head bolt are determined. In the identification of the bolted joint parameters, only one of the translational FRF measured at the tip point (point 2) of the coupled structure is

**Fig. 57.10** Regenerated FRF,  $H_{y_2s,F_2s}$ , of the coupled structure using updated joint properties

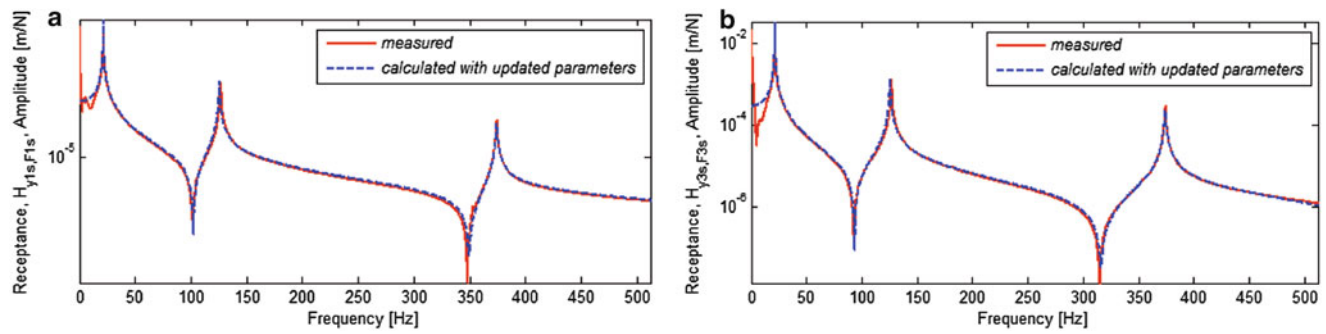
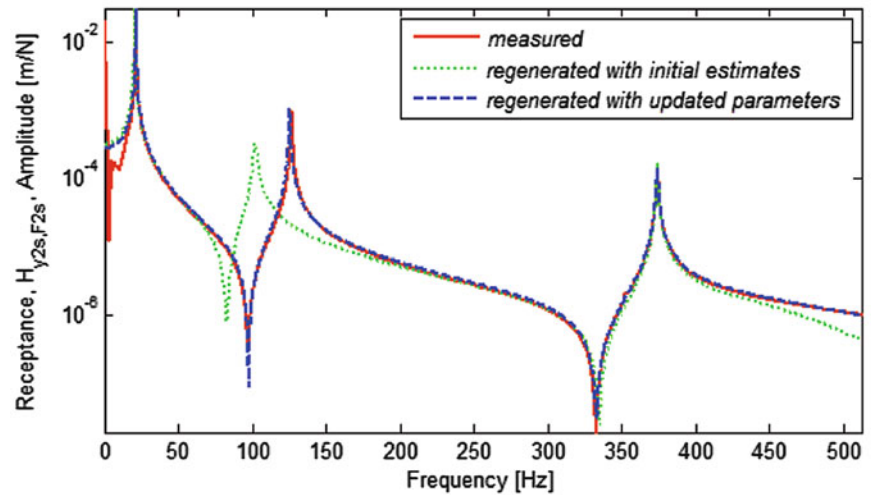


**Fig. 57.11** Calculated FRFs of the coupled structure using updated joint properties (a)  $H_{y_1s,F_1s}$ , (b)  $H_{y_3s,F_3s}$

**Table 57.2** Joint parameters of the M8  $\times$  35 bolted connection

	$k_{F_y}$ (N/m)	$k_{F_\theta}$ (N/rad)	$k_{M_\theta}$ (N.m/rad)	$c_{F_y}$ (N.s/m)	$c_{F_\theta}$ (N.s/rad)	$c_{M_\theta}$ (N.m.s/rad)
Initial estimates	$1.83 \cdot 10^6$	$5.53 \cdot 10^4$	$2.9 \cdot 10^3$	42.2	0.848	0.139
Updated	$2.14 \cdot 10^6$	$2.66 \cdot 10^4$	$3.2 \cdot 10^3$	41.2	0.845	0.119

used. Afterwards, the identified joint parameters are employed to calculate theoretically the FRFs of a different coupled structure constructed with steel beams having the same material and cross sectional dimensions, and the same bolt but different length. Then, the estimated FRFs are compared with the measured ones.

Firstly, again starting with initial estimates from the identified results at the second mode for rotational parameters, at the third mode for translational and cross-coupling parameters, the updated joint parameters are obtained as given in Table 57.2. The initially identified values are also shown in the same table. By using the updated joint parameters, receptances of the assembled system are regenerated and they are compared with the measured receptances in Fig. 57.12. It can be seen from the comparison that the receptances regenerated by using the updated joint parameters perfectly match with the measured FRFs.

After obtaining the joint parameters of the connection with M8 bolt, a different verification study is performed. In this verification study, a new substructure A with a length of 0.35 m (longer than the previous one) is used as shown in Fig. 57.13. By using the measured FRFs of the new substructure A, but joint parameters identified from the previous system (with a shorter substructure A), receptance of the new assembled system at the tip point is calculated, and it is compared with the measured receptance in Fig. 57.13. It can be seen from the comparison that the receptances predicted by using the joint parameters identified from a different assembly perfectly match with the measured FRFs of another assembly. Then it can be concluded that, once the joint properties are identified, it can be used for another structure having the same connection (the same material and cross sectional dimensions for the beams and the same bolt).

**Fig. 57.12** Regenerated FRF,  $H_{y_2s,F_2s}$ , of the coupled structure using updated joint properties

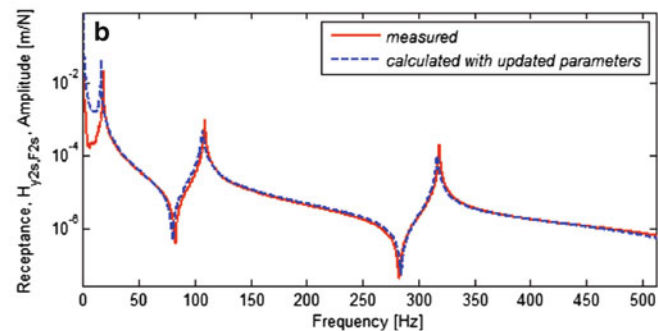
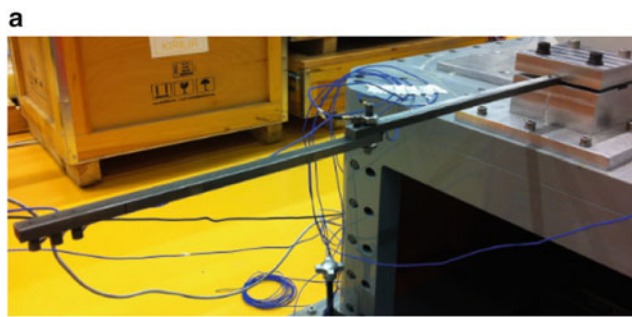
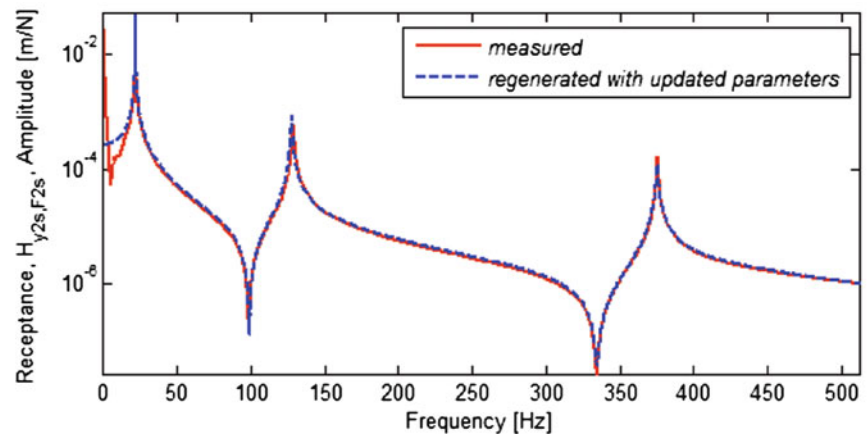


**Fig. 57.13** (a) New assembly with same M8 Bolt, (b) calculated FRF,  $H_{y_2s,F_2s}$ , of the new assembly using updated joint properties

**Table 57.3** Joint parameters of the M6  $\times$  30 bolted connection

	$k_{Fy}$ (N/m)	$k_{F\theta}$ (N/rad)	$k_{M\theta}$ (N.m/rad)	$c_{Fy}$ (N.s/m)	$c_{F\theta}$ (N.s/rad)	$c_{L\theta}$ (N.m.s/rad)
Initial estimates	$2.06 \times 10^6$	$7.40 \times 10^4$	$2.9 \times 10^3$	80.4	2.52	0.139
Updated	$2.27 \times 10^6$	$3.89 \times 10^4$	$3.7 \times 10^3$	75.7	0.94	0.164

### 57.3.3 Experimental Study III: Beams Connected with M6 $\times$ 30 Hexagonal Bolt

In this experimental study, first the dynamic properties of the bolted joint using M6  $\times$  30 mm hexagon head bolt are determined. With the identified joint parameters, the receptances of the same beams coupled with a multiple connection are calculated and compared with the measured ones.

The joint stiffness and damping values identified and updated by using the approach proposed in this study are given in Table 57.3. For initial estimates, identified results at the second mode for rotational parameters, at the third mode for translational and cross-coupling parameters are employed. By using the updated joint parameters, receptances of the assembled system are regenerated and they are compared with the measured receptances in Fig. 57.14. It can be seen from the comparison that the receptances regenerated by using the updated joint parameters perfectly match with the measured FRFs.

Finally, two M6 bolts are used to connect the same substructures, and the receptance of the new system is predicted by using the identified joint parameters and considering that there are two such joints. Comparison of the predicted FRF with the measured one shows a perfect match (Fig. 57.15), indicating that the approach proposed in this study provides a good dynamic model for a bolted joint.

In Fig. 57.16 the receptances of the coupled structure with one and two bolts, as well as with rigid connection are given. It can be seen that bolted joint adds some flexibility to the assembly, and as the number of bolts in the connection increase, assembly becomes more rigid, as expected.



**Fig. 57.14** Regenerated FRF,  $H_{y_2s,F_2s}$ , of the coupled structure using updated joint properties

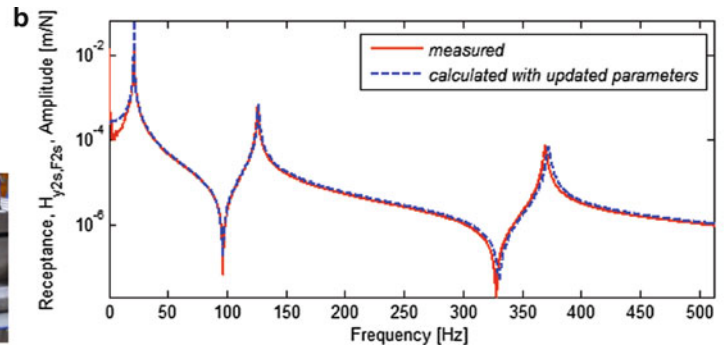
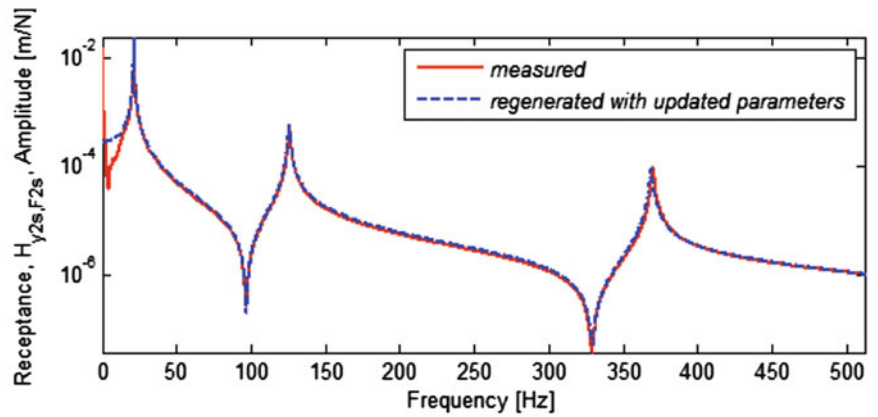
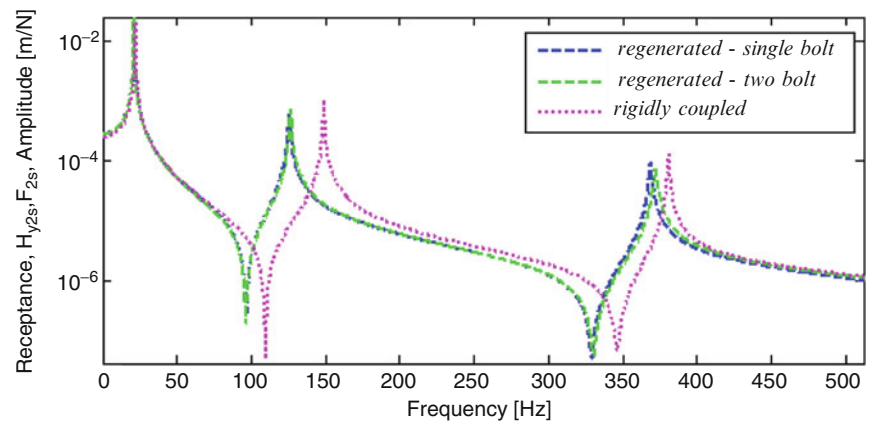


**Fig. 57.15** Connection with two bolts, and calculated FRF ( $H_{y_2s,F_2s}$ ) of the coupled structure using updated joint properties compared with measured one

**Fig. 57.16** FRFs of the coupled structure with single bolt, two bolts and rigid connection



### 57.3.4 Effect of Bolts Size on Dynamic Properties of the Bolted Joint

The comparison of the identified stiffness and damping properties of the joints obtained by using M10, M8 and M6 bolts in this study is given in Fig. 57.17. The figure gives the identified values at each frequency, from which average values are calculated. The updated values found using these average values as initial estimates are presented in Table 57.4.

From the results obtained with the steel beams it can be concluded that as the bolt diameter is decreased stiffness parameters are increased (Table 57.4). However, a more detailed study is required to generalize this observation.

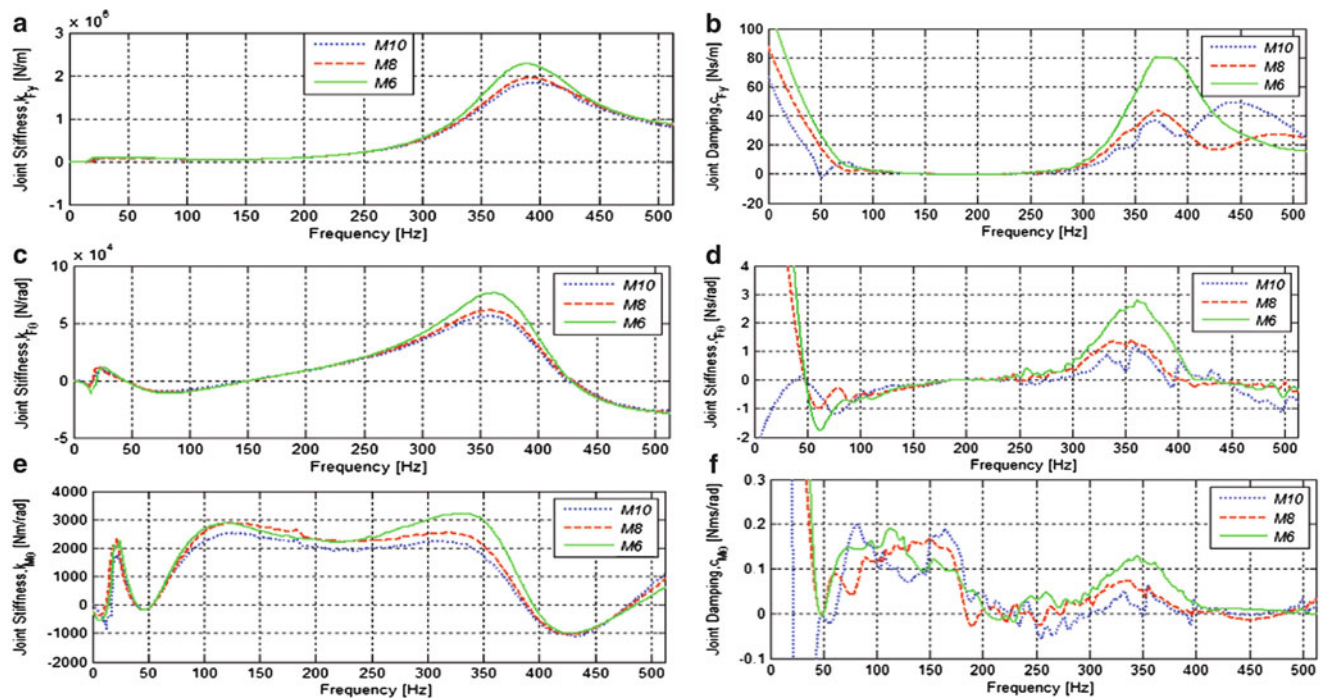


**Fig. 57.17** Identified joint stiffness and joint damping values (a) translational joint stiffness, (b) cross-coupling joint stiffness, (c) rotational joint stiffness, (d) translational joint damping, (e) cross-coupling joint damping, (f) rotational joint damping

**Table 57.4** Comparison of the identified joint parameters (updated values) for joints with different sizes of bolts

	$k_{Fy}$ (N/m)	$k_{F\theta}$ (N/rad)	$k_{M\theta}$ (N.m/rad)	$c_{Fy}$ (N.s/m)	$c_{F\theta}$ (N.s/rad)	$c_{M\theta}$ (N.m.s/rad)
M10	$2.02 \cdot 10^6$	$2.47 \cdot 10^4$	$2.8 \cdot 10^3$	34.4	0.635	0.077
M8	$2.14 \cdot 10^6$	$2.66 \cdot 10^4$	$3.2 \cdot 10^3$	41.2	0.845	0.119
M6	$2.27 \cdot 10^6$	$3.89 \cdot 10^4$	$3.7 \cdot 10^3$	75.7	0.946	0.164

## 57.4 Discussions and Conclusions

Substructure decoupling method using measured FRFs is employed to identify dynamic properties of a structural joint. In the approach proposed, FRFs of two substructures, as well as of the coupled structure connected with bolts are measured, although it is possible to use analytically calculated FRFs for the substructures. The joint properties expressed in terms of rotational and translational stiffness and damping elements are identified by using FRF based substructure decoupling equations which were presented in a recent paper of the authors [11]. Three equations are presented for joint identification, each using a different set of FRFs but yielding the same joint properties. If we could have the exact FRF matrices for substructures and coupled structure at any frequency, any of the joint identification equations would give exactly the same and correct result at any frequency. However, due to using different sets of FRFs in each equation and due to having different measurement noise levels in each type of FRF, it is expected to have different performance from each equation. As it was mentioned in the earlier work [11], the most accurate results are obtained with Eq. (57.1a). However, from the experimental applicability point of view, among the decoupling equations the most practical one is Eq. (57.1d).

In order to make the identification more practical for real applications, rather than using RDOF related FRFs of the coupled structure it is suggested to measure and use only TDOF related ones. In the experimental applications given in this paper only one translational FRF at the tip point of the coupled structure is used in the decoupling equation, eliminating the need for estimating RDOF related FRFs from TDOF related FRFs.

The major improvement is obtained from the updating of joint parameters with an optimization algorithm, using the identified joint parameters as initial estimates. In the previous work of the authors, joint parameters are calculated by taking the average of the identification results at frequencies that belong to the mode which is most sensitive to these parameters. However, in experimental studies it is observed that the joint properties are changing with frequency due to the measurement errors at different stages and also due to the numerical errors associated with matrix inversion, and the best frequency range

to determine the joint properties may not always be so obvious. It is experimentally demonstrated that using the optimization algorithm, the joint properties can be successfully updated so that regenerated FRFs using the joint model obtained match with the experimentally measured ones at all frequencies. Three experimental case studies are presented to verify the method suggested in this work and to illustrate the accuracy and applicability of the method in real life applications. In the first case study, by using the identified bolted joint parameters the FRFs of the coupled structure are calculated at a point which is not used in the identification of joint properties and these values are found to be perfectly matching with the measured FRFs. In the second experimental case study, the identified joint parameters are used in calculating the FRFs of a new assembly constructed with the same bolt but with a beam longer than the one used in identification. The predicted FRFs are again found to be in very good agreement with experimentally measured ones. In the last experimental case study, the joint obtained with one bolt is identified and the identified joint parameters are used to predict the FRFs of the same assembly but connected with two bolts. The predicted FRFs are compared with experimentally measured ones and once again a very good match is observed. From these experimental studies it is concluded that bolted joint identification approach proposed in this study is very successful, at least for modeling bolted beam joints.

## References

1. Ren Y, Beards CF (1998) Identification of effective linear joints using coupling and joint identification techniques. *J Vib Acoust* 120:331–338
2. Tsai JS, Chou YF (1988) The identification of dynamics characteristics of a single bolt joint. *J Sound Vib* 125(3):487–502
3. Wang JH, Liou CM (1991) Experimental identification of mechanical joint parameters. *J Vib Acoust* 113:28–36
4. Hwang HY (1998) Identification techniques of structure connection parameters using frequency response functions. *J Sound Vib* 212(3): 469–79
5. Yang KT, Park YS (1993) Joint structural parameter identification using a subset of frequency response function measurements. *Mech Syst Signal Process* 7:509–30
6. Ren Y, Beards CF (1995) Identification of joint properties of a structure using FRF data. *J Sound Vib* 186(4):567–587
7. Celic D, Boltezar M (2008) Identification of the dynamic properties of joints using frequency–response functions. *J Sound Vib* 317:158–174
8. Maia NMM, Silva JMM, Ribeiro AMR, Silva PLCGC (1998) On the dynamic characterization of joints using uncoupling techniques. In: *Proceedings of the 16th international modal analysis conference, Santa Barbara*, pp 1132–1138
9. Yang T, Fan SH, Lin CS (2003) Joint stiffness identification using FRF measurements. *Comput Struct* 81:2549–2556
10. Özşahin O, Ertürk A, Özgüven HN, Budak E (2009) A closed-form approach for identification of dynamical contact parameters in spindle-holder-tool assemblies. *Int J Mach Tools Manuf* 49:25–35
11. Tol Ş, Özgüven HN (2012) Dynamic characterization of structural joints using FRF decoupling. In: *Topics in modal analysis I, volume 5. Conference proceedings of the society for experimental mechanics series, vol 30. Springer New York* pp 435–446
12. Duarte MLM, Ewins DJ (2000) Rotational degrees of freedom for structural coupling analysis via finite-difference technique with residual compensation. *Mech Syst Signal Process* 14(2):205–227
13. Young MS, Tiwari M, Singh R (2007) Identification of joint stiffness matrix using a decomposition technique. In: *Proceedings of 25th international modal analysis conference, Orlando*

# Chapter 58

## Transfer Functions to Measure Translational and Rotational Velocities with Continuous-Scan Laser Doppler Vibrometry

Shifei Yang and Matthew S. Allen

**Abstract** A laser Doppler vibrometer typically measures the translational velocity at a single point along the direction of incident light. However, it has been shown that rotational velocities can also be recovered by scanning the laser continuously along a line or circular path around that point. This work uses the harmonic transfer function concept, which is analogous to the transfer function in conventional modal analysis, to relate the measured rotational and translational velocities to the input force. With this concept, the continuous-scan approach can be combined with the conventional point by point scan approach, acquiring normalized translational and rotational velocities under various types of excitation conditions in the same amount of time that is required for obtaining only the translational velocity. The proposed approach is validated on measurements taken from a downhill ski under free-free boundary conditions. The influence of the circle size, the scanning rate and the surface quality on the noise level in the measured signal is discussed, and the measured deflection shapes using both the point and circular scan approaches are compared. Local slopes at measurement locations are computed from the identified principal rotational velocities, laying the foundation for constructing a much more accurate estimate of the deformation shape, which may be valuable in damage detection and/or model updating.

**Keywords** Modal testing • Damage detection • Laser Doppler vibrometer • Rotational velocity • Slope

### 58.1 Introduction

Continuous-Scan Laser Doppler Vibrometry (CSLDV) is a novel method of employing a laser vibrometer in which the laser spot sweeps over a structure continuously while capturing responses from a moving measurement point. The method can greatly accelerate the modal testing of structures with low frequency modes, which require long time records at every single measurement point when the conventional point by point scanning method is used. One can also obtain measurements with greatly increased spatial detail along the scan path, which is valuable in model correlation and updating [1], structural health monitoring, and damage detection.

A few algorithms have been devised to process measurements from CSLDV under various excitation conditions. Ewins group at Imperial College treats the operational deflection shape of a structure as a polynomial function of the moving laser position [2–6]. The coefficients of that polynomial are then obtained by transforming the amplitudes of the harmonics that are separated by the scanning frequency in the measured spectrum. Allen et al. later presented a ‘discrete’ lifting approach [7, 8] that groups the measured responses at the same location along the laser scan path. The lifted measurements appear to be from a set of pseudo sensors but with a constant time delay between each other. The lifted spectra hence have only one peak for each mode, which allows conventional modal analysis curve fitting methods to be applied. Recently, algorithms

---

S. Yang (✉)

Graduate Research Assistant, Ph.D. Candidate, Department of Engineering Physics, University of Wisconsin-Madison, 535 Engineering Research Building, 1500 Engineering Drive, Madison, WI 53706, USA  
e-mail: [syang66@wisc.edu](mailto:syang66@wisc.edu)

M.S. Allen

Assistant Professor, Department of Engineering Physics, University of Wisconsin-Madison, 535 Engineering Research Building, 1500 Engineering Drive, Madison, WI 53706, USA  
e-mail: [msallen@engr.wisc.edu](mailto:msallen@engr.wisc.edu)

based on linear time periodic system identification theory were used to process CSLDV measurements [9, 10]. When the laser scans a closed periodic pattern, measurements from CSLDV appear to be periodic. The harmonic transfer function of periodic systems allows natural frequencies, damping ratios and mode shapes to be extracted and compared under a variety of excitation conditions.

All these algorithms emphasize detecting translational deflection over an area on the structure, but the laser vibrometer can also be used to measure the rotational velocities over a small region. Ewins proposed a continuous scanning procedure to measure the translational as well as the angular vibration simultaneously [11]. He has proved that by scanning a line or a circle around the point of interest on a structure under sinusoidal input, the translational and rotational velocities are related to the central harmonic and its two sidebands in the measured spectrum. He then validated this procedure under a sinusoidal and a narrow-band random input. Recently, this procedure was adopted by Salman et al. to reconstruct the operational vibration shape of a human hand using a line scan [12].

To compute the mobility and sideband frequency response functions, the forcing signal along with the product of the forcing signal and mirror driving signal were used as a reference in [11]. This work aims to develop an alternative algorithm based on the harmonic transfer function that allows us to extract velocity information using virtually any type of input, e.g. an impulse, random or swept-sine input. The harmonic transfer function is an extension of a frequency response function to linear time periodic systems [13–15]. With the harmonic transfer function, measurements from a circular scan can be processed as in conventional linear time invariant modal analysis, which allows windowing and averaging to reduce leakage and random noise. Also, the acquired translational and rotational velocities at multiple points can be easily stitched together to create mode shapes of the underlying structure. Hence, CSLDV can be combined with conventional point by point SLDV, measuring both translational and rotational velocities under various types of excitation conditions in the same amount of time that is required by SLDV to measure only 1-D translational velocity.

The rotational velocity at each measurement location represents the local slope of the vibration shape. Therefore, this rotational velocity information could be very useful in computing the local curvature that is valuable in damage detection applications [16, 17]. Conventionally, curvature is computed by a successive spatial differentiation of the deflection shape. The limitation is mainly dictated by a limited spatial resolution and the high frequency noise incurred by the second order differentiation. Using the additional local slope information at each measurement location, the deflection shape can be spline-fitted and hence a much more accurate curvature can be constructed. This paper investigates the noise in circular scan and shows how to identify the normalized translational and rotational velocities as well as the local slopes from the measured spectra, laying the foundation for computing the curvature shapes, which will be explored in detail in the next stage of this work.

The rest of this paper is organized as follows. Section 58.2 reviews the harmonic transfer function concept with particular emphasis on how to interpret the response spectra of a continuous scan measurement. In Sect. 58.3, the proposed technique is demonstrated on a downhill ski and the influence of circle size and scan frequency on laser noise level is discussed. In Sect. 58.4, the circular scan approach is used to identify the deflection mode shapes of the ski. The results are compared with those from a conventional point by point scan LDV. In Sect. 58.5, rotational velocities as well as the local slopes are obtained. Sect. 58.6 summarizes this work.

## 58.2 Theoretical Basis

This paper makes use of the harmonic transfer function concept that relates the output of a linear time periodic system to its input [18]. A detailed derivation of the harmonic transfer function for a general linear time periodic system can be found in the appendix. This section shows the simplified expression of the harmonic transfer function for CSLDV, proving that rotational velocities can be obtained from the measured spectrum.

### 58.2.1 Periodic Model of CSLDV Measurement

An  $N$  degree of freedom linear time invariant structure can be modeled using the well-known state space form with constant coefficients [19],

$$\begin{aligned}\dot{x} &= Ax + Bu \\ y &= Cx + Du\end{aligned}\tag{58.1}$$

Here  $x$  is internal state vector,  $u$  is the input and  $y$  is the output.  $A$  is the system matrix of the state space model, and  $B$  is the input matrix. When a laser Doppler vibrometer is employed to measure this invariant system, the output matrix  $C$  can be taken as a zero row vector with a one entry at the location the laser is measuring, e.g., if the laser is pointed at the  $k$ th degree of freedom, then

$$C = \left[ \underbrace{0 \cdots 0}_N \mid \underbrace{0 \cdots 0 \overset{k}{1} 0 \cdots 0}_N \right]_{1 \times 2N} \quad (58.2)$$

Therefore, when the laser moves along a closed periodic pattern, the output matrix becomes periodic,  $C(t) = C(t + T_A)$ , where  $T_A = 2\pi/\omega_A$  is called the fundamental period. In addition, since only velocity information is picked up by the laser, the direct input matrix  $D$  is zero in the state space model.

One can diagonalize the state space equations by defining  $x = Pq$ , where  $q$  is the vector of modal participation factors, and

$$P = \begin{bmatrix} \Psi & \Psi^* \\ \Psi\Lambda & \Psi^*\Lambda^* \end{bmatrix} \quad (58.3)$$

is the diagonalizer of the state matrix  $A$ .  $\Psi$  is an  $N \times N$  mode shape matrix that contains the modes of the system in its columns,  $\Psi = [\psi_1 \cdots \psi_N]$ . The notation  $()^*$  represents the complex conjugate.  $\Lambda$  is a diagonal matrix of the eigenvalues,  $\lambda_r = -\zeta_r\omega_r + j\omega_r\sqrt{1-\zeta_r^2}$  in terms of the  $r$ th natural frequency  $\omega_r$  and damping ratio  $\zeta_r$ .

Substituting  $x = Pq$  into Eq. (58.1) and pre-multiplying the first equation by  $P^{-1}$ , one obtains the following uncoupled equations,

$$\begin{aligned} \dot{q} &= \Lambda q + P^{-1}Bu \\ y &= C(t)Pq \end{aligned} \quad (58.4)$$

The measurement point is continuously moving, therefore  $C(t)P$  is a periodic  $1 \times 2N$  row vector of complex mode shapes,

$$C(t)P = [C(t)\psi_1\lambda_1 \cdots C(t)\psi_N\lambda_N \ C(t)\psi_1^*\lambda_1^* \cdots C(t)\psi_N^*\lambda_N^*] \quad (58.5)$$

The  $r$ th observed mode shape  $C(t)\psi_r$  appears to be time periodic only because the position of the measurement point is periodic.

Equation (58.4) in conjunction with Eq. (58.5) reveals that a linear time invariant structure measured by continuous scan laser Doppler vibrometry can be modeled as a linear time periodic system when a periodic scan pattern is used. The state space equations have constant matrices  $A$  and  $B$  since the underlying structure is linear time invariant. The only periodic term is the output matrix  $C$ . Hence, periodic system identification theory can be used to identify the natural frequencies, damping ratios, and mode shapes of the underlying time invariant structure measured by CSLDV.

### 58.2.2 Harmonic Transfer Function of CSLDV

This section shows the simplified derivation of harmonic transfer function specifically for CSLDV. The derivation for a general linear time periodic system can be found in the appendix. The derivation makes use of the general solution of a linear system with time varying coefficients [19],

$$y(t) = C(t)\Phi(t, t_0)x(t_0) + \int_{t_0}^t C(t)\Phi(t, \tau)B(\tau)u(\tau)d\tau + D(t)u(t) \quad (58.6)$$

Since the transfer function relates the steady-state response of a system to its input, the transient response term that includes the initial state  $x(t_0)$  can be neglected. As was discussed in previous section, in CSLDV measurement the input matrix  $B$  is constant, and the direct input matrix  $D$  is zero. Eq. (58.6) then becomes,

$$y(t) = \int C(t)\Phi(t, \tau)Bu(\tau)d\tau \quad (58.7)$$

Here  $\Phi(t, t_0)$  is called the state transition matrix. It relates the system state  $x(t)$  at any time to the initial state  $x(t_0)$  by,

$$x(t) = \Phi(t, t_0)x(t_0) \quad (58.8)$$

For a linear time invariant system with constant coefficients, the state transient matrix can be obtained directly as  $\Phi(t, t_0) = e^{A(t-t_0)}$  [19], which can be further simplified as,

$$\Phi(t, t_0) = \sum_{r=1}^{2N} \psi_r L_r^T e^{\lambda_r(t-t_0)} \quad (58.9)$$

where  $\psi_r$  is the  $r$ th mode vector of the underlying linear time invariant system, and  $L_r$  is the  $r$ th column of  $\Psi = [\psi_1 \ \psi_2 \ \dots]^T$ . Substituting Eq. (58.9) into the general solution of the state space model in Eq. (58.7), the measured velocity  $y(t)$  by CSLDV becomes,

$$y(t) = \sum_{r=1}^{2N} C(t) \psi_r e^{\lambda_r t} \int L_r^T B u(\tau) e^{-\lambda_r \tau} d\tau \quad (58.10)$$

$C(t)$  is a matrix of ones and zeros indicating which of the states are being measured by the laser. Since the observed mode shape  $C(t)\psi_r$  is periodic on a periodic scan path, it is convenient to expand it in a Fourier series.

$$C(t)\psi_r = \sum_{n=-\infty}^{\infty} \bar{C}_{r,n} e^{in\omega_A t} \quad (58.11)$$

where  $\bar{C}_{r,n}$  is the  $n$ th Fourier coefficient of the  $r$ th observed mode vector,  $C(t)\psi_r$ . Defining the constant  $L_r^T B = \bar{B}_r$ , Eq. (58.10) then becomes:

$$y(t) = \sum_{r=1}^{2N} \sum_{n=-\infty}^{\infty} \bar{C}_{r,n} e^{(\lambda_r + in\omega_A)t} \int \bar{B}_r e^{-\lambda_r \tau} u(\tau) d\tau \quad (58.12)$$

The above equation is the modal summation form of the measured velocity by CSLDV. It contains the frequency component at  $\lambda_r$  and its infinite number of harmonics each separated by the fundamental frequency  $\omega_A$ . Wereley extends the concept of a transfer function for time invariant systems to time periodic systems by defining the Exponentially Modulated Periodic (EMP) signal [13]. This modulated signal is the summation of signals separated by multiples of the fundamental frequency  $\omega_A$ , hence a modulated input to a linear time periodic system causes a modulated output at the same collection of frequencies. In CSLDV measurements, the input  $u(t)$  is time invariant but the output  $y(t)$  is periodic due to the moving measurement point, hence,

$$u(t) = U_0 e^{i\omega t}, \quad y(t) = \sum_{n=-\infty}^{\infty} Y_n e^{(i\omega + in\omega_A)t} \quad (58.13)$$

The harmonic transfer function can be derived by substituting the above expression into Eq. (58.12),

$$\sum_{n=-\infty}^{\infty} Y_n e^{(i\omega + in\omega_A)t} = \sum_{r=1}^{2N} \sum_{n=-\infty}^{\infty} \bar{C}_{r,n} e^{(\lambda_r + in\omega_A)t} \int \bar{B}_r U_0 e^{(i\omega - \lambda_r)\tau} d\tau \quad (58.14)$$

The summation can be further simplified after the integration, as follows,

$$\sum_{n=-\infty}^{\infty} Y_n e^{(i\omega + in\omega_A)t} = \sum_{r=1}^{2N} \sum_{n=-\infty}^{\infty} \frac{\bar{C}_{r,n} \bar{B}_r}{i\omega - \lambda_r} U_0 e^{(i\omega + in\omega_A)t} \quad (58.15)$$

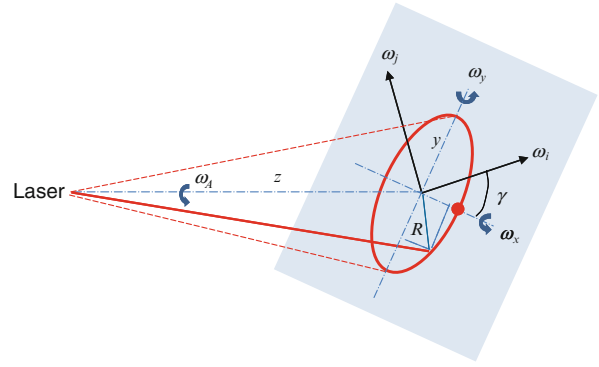
A harmonic balance approach can be used to match the terms with the same order of  $e^{(i\omega + in\omega_A)t}$ ,

$$Y_n = \sum_{r=1}^{2N} \frac{\bar{C}_{r,n} \bar{B}_r}{i\omega - \lambda_r} U_0 n \in (-\infty, \infty) \quad (58.16)$$

One can then define the exponentially modulated periodic signals in the frequency domain for CSLDV,

$$\begin{aligned} \mathbf{Y}(\omega) &= \left[ \dots Y_{-1}^{(\omega)T} \ Y_0(\omega)^T \ Y_1(\omega)^T \ \dots \right]^T \\ \mathbf{U}(\omega) &= U_0(\omega) \end{aligned} \quad (58.17)$$

**Fig. 58.1** Scheme of measuring translational and rotational velocity using CSLDV



Hence, a transfer function is established in terms of the modal parameters of the state transition matrix, denoted by the harmonic transfer function.

$$\mathbf{Y}(\omega) = \mathbf{G}(\omega)U(\omega) \quad (58.18)$$

Where,

$$\mathbf{G}(\omega) = \sum_{r=1}^{2N} \frac{\bar{\mathbf{C}}_r \bar{\mathbf{B}}_r}{i\omega - \lambda_r} \quad (58.19)$$

$$\bar{\mathbf{C}}_r = [\cdots \bar{\mathbf{C}}_{r,-1} \bar{\mathbf{C}}_{r,0} \bar{\mathbf{C}}_{r,1} \cdots]^T$$

An H1 estimator is used to experimentally estimate the harmonic transfer function, since the noise is mostly from the speckle noise in the laser signal.

$$\mathbf{G}(\omega) = \frac{E(\mathbf{Y}(\omega)U_0^H(\omega))}{E(U_0^{(\omega)}U_0^H(\omega))} \quad (58.20)$$

here  $E()$  indicates the expected value. One should note that for a general linear time periodic system, the denominator would be a matrix of cross power spectrum of the modulated inputs. Therefore, one must have at least several averages for the spectrum matrix to be invertible.

### 58.2.3 Measuring Rotational Velocities

Figure 58.1 shows the scheme of employing CSLDV with a circular scan pattern to measure translational and rotational velocities of a local area. Assuming the standoff distance from the laser source to the point of interest is large compared to the scan radius  $R$ , the incident laser beam can be treated as perpendicular to the surface during the scan. Also, the deformation inside the circle can be neglected when  $R$  is reasonably small.

Ewins showed a similar derivation of the expression for the measured velocity in his work [11]. The sinusoidal angular vibration at a point on a surface can be decomposed into two orthogonal principal rotations that have a 90-degree phase difference,

$$\begin{aligned} \omega_i &= \Theta_A \cos(\omega t + \beta) \\ \omega_j &= \Theta_B \sin(\omega t + \beta) \end{aligned} \quad (58.21)$$

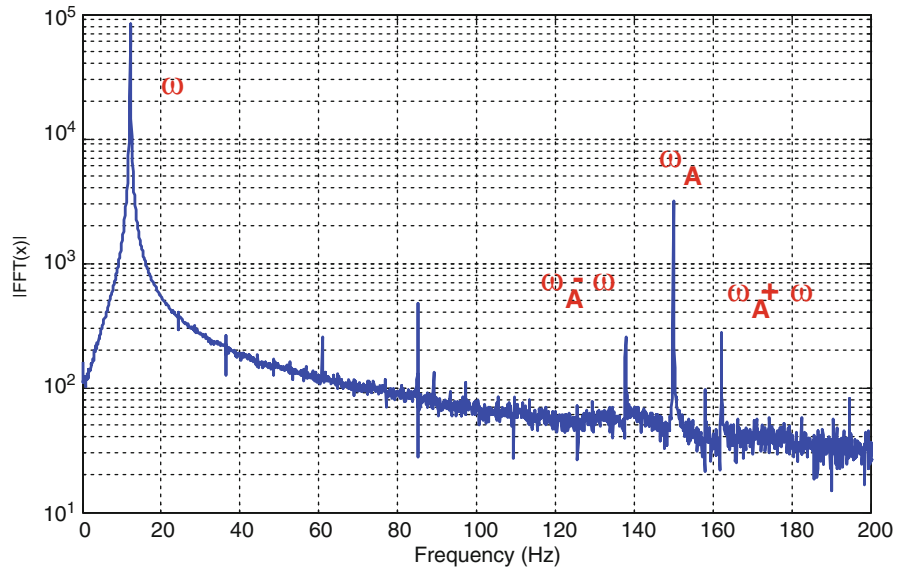
$\Theta_A$  and  $\Theta_B$  are the amplitudes of the principal rotational velocities along  $i$  and  $j$  axis.  $\beta$  is the initial phase of the oscillation. Note that the in plane rotation  $\omega_k$  is assumed to be zero.

Suppose the initial position of the laser is at the red dot on  $x$  axis and the laser scans counterclockwise with a constant speed of  $\omega_A$ , the measured velocity  $v(t)$  from a laser Doppler vibrometer contains three components: the translational velocity  $v_z(t)$ , the velocity component along the  $z$  axis introduced by the rotation  $\omega_x(t)$ , and the velocity component along the  $z$  axis introduced by the rotation  $\omega_y(t)$ .

$$v(t) = v_z(t) + \omega_y(t)x(t) + \omega_x(t)y(t) \quad (58.22)$$



**Fig. 58.2** Spectrum of measured CSLDV signal with a 150 Hz scan frequency



$x(t)$  and  $y(t)$  are the position of the laser spot with respect to a reference frame that is fixed in the space. The orientation of the principal rotational velocities with respect to this reference frame is not known ahead, and this orientation may vary from point to point. However, if we assumed this angle to be  $\gamma$ , the rotational velocities along the  $x$  and  $y$  axis can be obtained via a rotation matrix, as

$$\begin{aligned}\omega_x &= \omega_i \cos(\gamma) - \omega_j \sin(\gamma) \\ \omega_y &= \omega_i \sin(\gamma) + \omega_j \cos(\gamma)\end{aligned}\quad (58.23)$$

The laser position at any time instant is

$$x(t) = R \cos(\omega_A t), \quad y(t) = R \sin(\omega_A t)\quad (58.24)$$

Notice that when the structure is under sinusoidal excitation, the translational can be written as

$$V_z(t) = Z \cos(\omega t + \alpha)\quad (58.25)$$

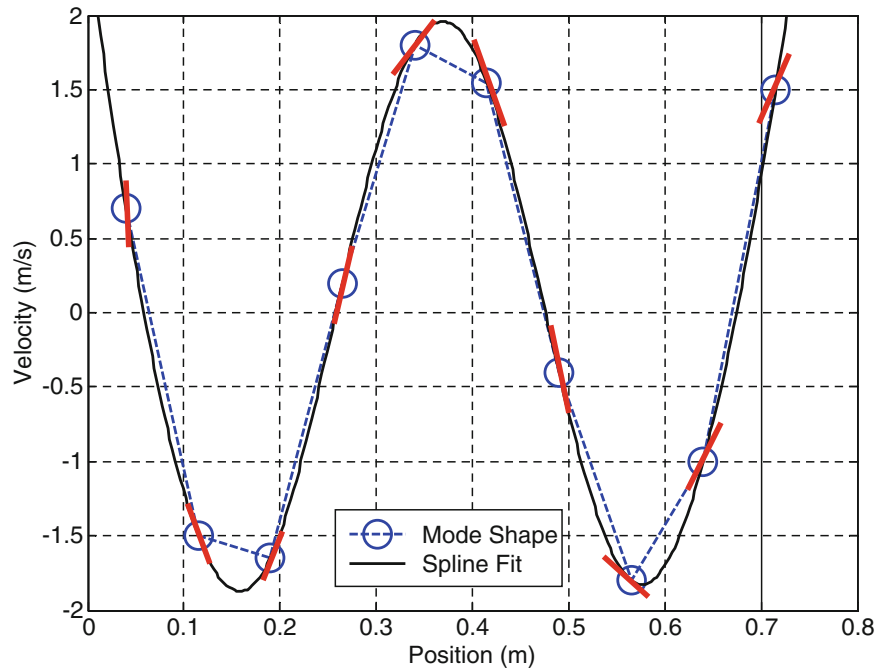
where  $Z$  is the amplitude of the translational velocity, and  $\alpha$  is the initial phase of oscillation. Substituting Eqs. (58.21), (58.23), (58.24) and (58.25) into Eq. (58.22), and then simplifying Eq. (58.22) using trigonometric functions, yields

$$v(t) = Z \cos(\omega t + \alpha) + R \frac{\Theta_B + \Theta_A}{2} \sin((\omega + \omega_A)t + \beta + \gamma) + R \frac{\Theta_B - \Theta_A}{2} \sin((\omega - \omega_A)t + \beta - \gamma)\quad (58.26)$$

The measured velocity signal using CSLDV will include all the translational and rotational velocities at the point of interest. For example, Fig. 58.2 shows the measured spectrum when the laser scans at 150 Hz on a beam that was excited at its first mode at 13 Hz. The translational velocity and its phase can be obtained from the peak at 13 Hz, and the rotational velocities can be recovered from the two peaks at 137 and 163 Hz according to Eq. (58.26).

To compute the harmonic transfer function from a circular scan measurement, the measured velocity will be exponentially modulated according to Eq. (58.13). One should note that the modulation is essentially a process of making frequency shifted copies of the measured spectrum by  $n\omega_A$  in the frequency domain. Therefore, the translational velocity at  $\omega$  corresponds to the  $Y_0$  term, and the rotational velocities at the frequency lines of  $\omega_A - \omega$  and  $\omega_A + \omega$  can be related to the  $Y_{-1}$  and  $Y_1$  term in Eq. (58.17). This allows us to use conventional curve fitting tools for time invariant systems to interpret measurements from the circular scan under any type of input. Additionally, since the transfer function is computed, the acquired translational and rotational velocities at multiple points can be easily stitched together to create mode shapes of the underlying structure.

**Fig. 58.3** Scheme of constructing curvature using translational velocity



#### 58.2.4 Computing Curvature

The curvature of a surface is proportional to the surface strain, therefore is very sensitive to cracks and subsurface damages [16]. The change in curvature has been used widely as the indicator of potential damage in structures. Conventionally, to compute the curvature, shapes at several measurement locations have to be patched together and then a second order finite difference is computed. Figure 58.3 shows an example of computing the curvature from an experimentally measured deflection mode shape. The circles represent sensor locations. To obtain the curvature  $c_i$  at the  $i$ th point, a finite difference approximation can be used, as follows,

$$c_i = \frac{(y_{i+1} - y_i) - (y_i - y_{i-1})}{h^2} \quad (58.27)$$

Here  $y_i$  is the deflection at the  $i$ th point, and  $h$  is the step size between two neighboring sensors. This method is usually limited by the availability of a dense measurement grid. In addition, the measurement noise in deflection mode shapes is amplified by the second order derivative.

On the other hand, the point by point scan laser Doppler vibrometry allows spatially detailed mode shapes to be extracted in a short time. The derivation in Sect. 58.2.3 shows that by combining the circular scan approach with the point by point scanning LDV, the translational velocity as well as the principal rotational velocities can be measured in the same amount of time that is required to measure only the translational velocities. This is extremely beneficial for computing curvature since the amplitudes of rotational velocities at any measurement location correspond to the local slope of the vibration shape, as demonstrated by the short red line in Fig. 58.3. Therefore, the deflection shape together with the local slopes can be used to construct an accurate spline-fit to the deflection that could greatly reduce the error in the computed curvature shapes. With the harmonic transfer function concept, curvature shapes in a measurement grid can be patched and used to characterize the damages in the underlying time invariant system.

As discussed earlier, the major focus of this work is to obtain the deflection mode shapes and local slopes from circular scan measurement. In next stage, these deflection and slope information will be used to construct 1D and 2D curvature shape of the underlying structure.

### 58.3 Experimental Setup and Speckle Noise

The experimental validation of the proposed circular scan algorithm was performed on a downhill ski, which is a complex structure formed by laminating several materials together and hence can be very challenging to model accurately. As shown in Fig. 58.4a, the ski was hung using two soft bungee cords to simulate free-free boundary conditions. A shaker with a

**Fig. 58.4** Experimental set up. (a) Testing scheme, (b) load cell, (c) retro-reflective tape

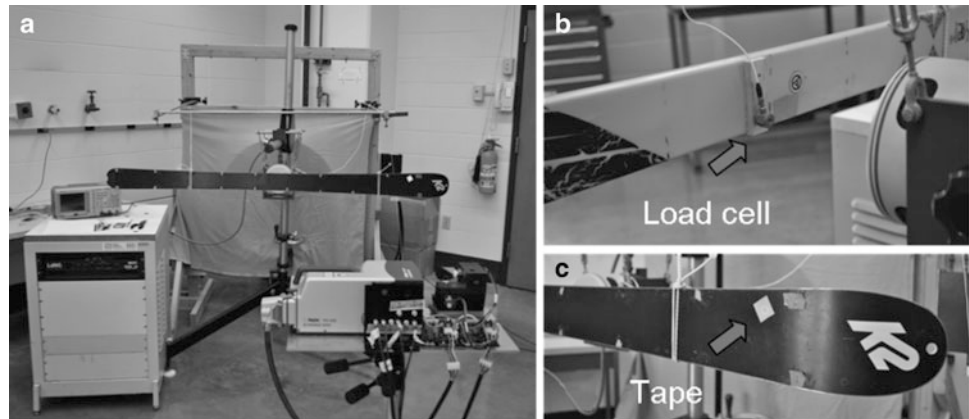
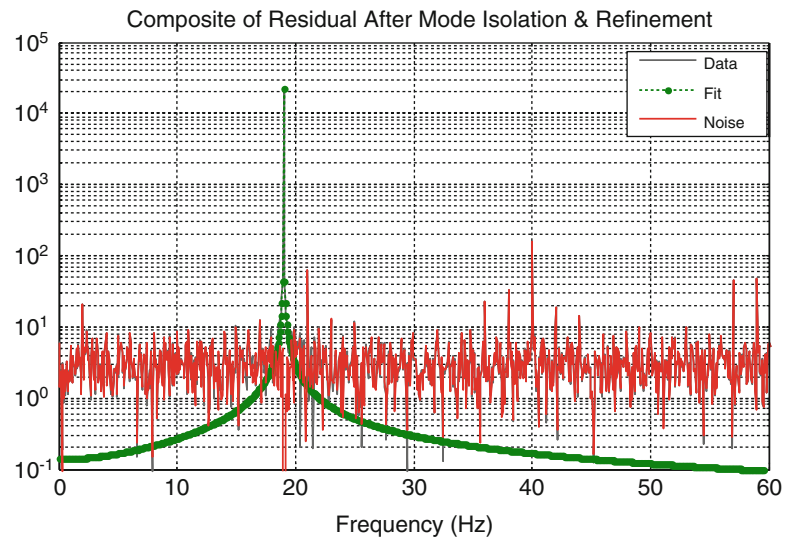


**Fig. 58.5** Measured spectrum with 40 Hz scan frequency and 5/16 in. circle size



function generator was used to excite the ski. A load cell was installed on the tip of the stinger to measure the input force applied to the ski shown in Fig. 58.4b. A Polytec PSV-400 (633 nm laser) vibrometer with an external x-y mirror system [10] was used to measure the surface velocity at a standoff distance of approximately 2.5 m. The scanner works in a closed loop, and each mirror is fitted with a position detector that measures the angle of the scanner, which allows very precise control of the laser position.

In this section, the speckle noise associated with the circular scan approach is investigated. Laser speckle is formed when coherent light scatters and interferes from an optically rough surface. Speckle noise has been studied extensively prior to this work [20–25]. The effect of focus size, target surface roughness, scan speed and standoff distance etc. has been investigated, and even a simulated model has been created. The purpose of this section is not to challenge the well-established model but to survey the influence of scan frequency, circle size and the surface quality of the ski on the noise level in the measurements, such that a set of optimal experimental parameters can be selected for the following tests.

The scan frequencies tested were 20 Hz up to 300 Hz with a 20 Hz step size. The nonlinearity of the mechanical system is considered to be dominant when the mirror system scans at a higher frequency. The scan circle diameters tested were from 1/16 to 8/16 in. with a step size of 1/16 in. When the circle size is larger than 8/16 in., higher order harmonics of each mode tend to appear in the measurement spectrum, indicating that mode shapes along the circle path are being measured. Also, one should note that the maximum circle size may vary for different structures and different modes because of the assumption that deformation inside of the circle shall be neglected. In addition to the circular scan, conventional tests where the laser was pointed at a stationary point were conducted as a reference. Tests were repeated on three different surfaces, namely, the black bottom of the ski (Fig. 58.4a), the yellow top of the ski (Fig. 58.4b) and 3M retro-reflective tape (Fig. 58.4c).

Figure 58.5 shows the measured spectrum on the black bottom surface when the laser scanned at the frequency of 40 Hz and the circle size was 5/16 in. The ski was excited at its first natural frequency of 19 Hz. The test duration was 15 s with a sampling frequency of 10,240 Hz. To estimate the noise level, a linear mode was fit to the dominant peak in the spectrum using

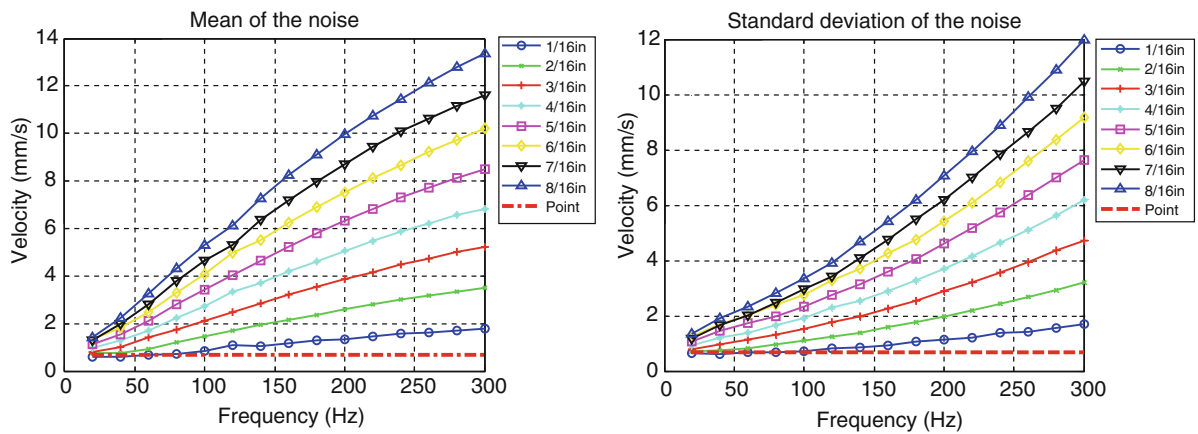


Fig. 58.6 Noise level on retro-reflective tape

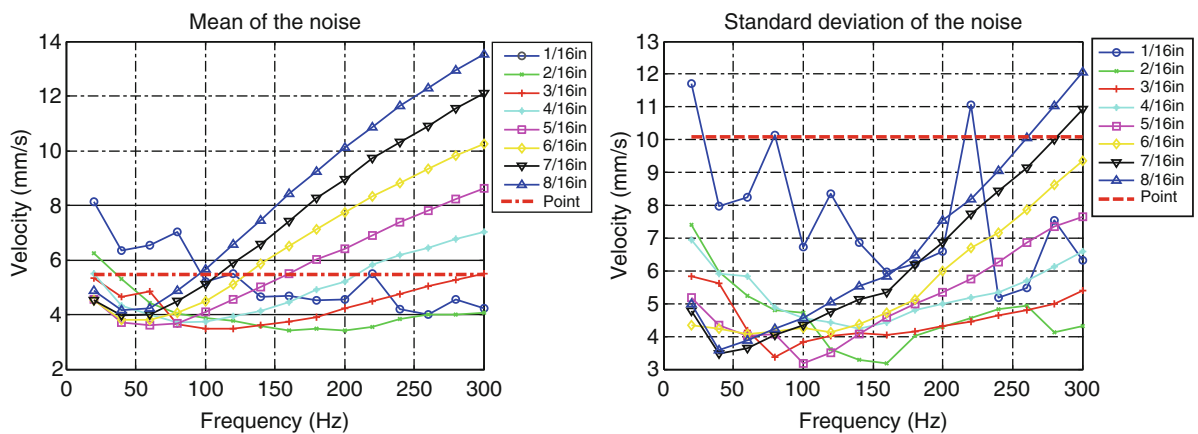


Fig. 58.7 Noise on black bottom surface

the algorithm of mode isolation [26]. This linear mode (green line) was then subtracted from the measured spectrum (grey line) and the residue (red line) was considered as the noise. Then the noise signal in the frequency domain was transformed via an inverse fast Fourier transform to the time domain, where the mean value and the standard deviation of the noise were calculated.

Figure 58.6 shows the mean and the standard deviation of the noise when the laser scans on the retro-reflective tape. The dashed red horizontal lines in both plots represent the value from the stationary point test. It can be found that the noise is smallest when the laser is pointed at a stationary point on the tape. The tape is coated with micro-scale glass beads that reflect most of the light in a concentrated cone back to the detector [27]. Therefore the speckle noise is minimized. When the laser is scanning around a circle, the noise level as well as the standard deviation increase with the scan frequency and the circle size. This phenomenon agrees with what was found in a previous work [25]. When the ski is excited at its first natural frequency, the motion of the ski is a combination of translational, rotational, as well as the in-plane rigid body motion due to the misalignment of the shaker, meaning the speckle pattern exhibits both ‘translation’ and ‘evolution’ changes [22]. When the laser scans on a periodic path, the measured speckle noise contains mostly periodic components. The magnitude of this periodic noise increases severely with surface velocity, which is the product of the scan frequency and the perimeter of the scan circle.

Figure 58.7 shows the mean and the standard deviation of the noise when scanning on the dark bottom surface of the ski. The noise pattern is similar to what was observed on the retro-reflective tape. However, the mean of the noise at a stationary point is higher than some of the circular scan results, and the standard deviation at a stationary point is much higher. When the laser hits a stationary point on a rough surface, the light is scattered to all directions randomly and only a small portion can travel back to the detector. The laser could be located at a point where the light is dominated by a dark speckle, as is often happened in conventional point by point scanning LDV. This may cause a dramatic change in noise level that partially explains the jagged nature of the noise level when the circle size is 1/16 in. In contrast, when the circular scan approach is

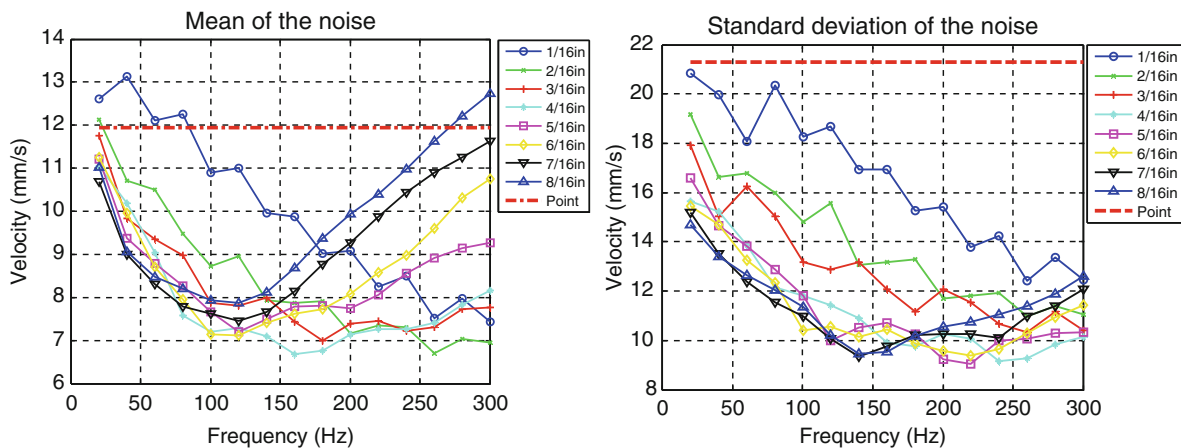


Fig. 58.8 Noise on yellow top surface

adopted with appropriate circle size, the signal level is likely to be large over some portion on the circle path, and the total noise level is reduced due to this ‘averaging’ effect. Therefore, in Fig. 58.7 a decrease in the noise level and in the standard deviation is observed when the scan frequency is lower than 60 Hz. After 60 Hz, the periodic noise becomes dominant and the trend that was observed in Fig. 58.6 appears.

As shown in Fig. 58.8, the decrease in noise level becomes more obvious when the laser scans on the yellow top surface that is smoother than the dark bottom surface of the ski. Also notice that the noise and its deviation are much higher for the stationary laser on this surface. Insight into this result can be gained from previous studies on speckle noise and surface roughness [22, 27]. Scattering from smooth surfaces reduces the range of phase excursions in the laser. However, due to the mirror like behavior of the polished surface, the scattering angle is more likely to be unusable which leads to signal loss. For circular scan measurements, it is observed that when the scan frequency is smaller than 120 Hz, the noise level as well as the standard deviation decrease with the increasing circle size and scan frequency. When the scan frequency is larger than 160 Hz, the speckle noise and deviation increase with the scan frequency and the circle size, indicating a dominant periodic speckle pattern in this region. One should also note that the overall noise level on the smooth yellow top surface is larger than those from the dark bottom surface or the retro-reflective tape, perhaps due to the mirror like behavior.

As indicated earlier, the purpose of this section is to help in selecting appropriate testing parameters that lead to a lower noise level in measured signal, which would improve the uncertainty in the measured translational and rotational velocities, and eventually lead to a more accurate curvature shape in the next stage. In the following section, a set of circular scan tests will be conducted to reconstruct the mode shapes of the ski using a swept-sine excitation. A scan frequency of 200 Hz and a circle size of 5/16 in. are selected to perform the tests so that noise is optimized on the black bottom surface of the ski that is under swept sine excitation up to 100 Hz.

## 58.4 Deflection Mode Shapes

Prior to the circular scan test, a conventional hammer test with an accelerometer was performed to identify the natural frequencies of the ski under free-free boundary condition. A few frequencies at 1.5, 4.5, 19, 42 and 75 Hz were identified. The modes at 1.5 and 4.5 Hz were known to be the rigid body modes. The point by point scanning tests were then performed at the rest of the frequencies on the black bottom surface of the ski using the Polytec’s software package. The laser scanned 3 lines all over the ski with 40 points along each line, as shown in Fig. 58.9. At each point the test duration was 12 s. The ski was excited at its natural frequencies at 19, 42, and 75 Hz, as well as a coupling frequency between the ski and the shaker at 23.2 Hz. The measured mode shapes are shown in Fig. 58.9.

It is clear that the mode at 19 Hz is the first bending mode of the ski (Fig. 58.9a), and the mode at 42 Hz is the second bending mode (Fig. 58.9c). Note that the shaker is installed slight off the center of the ski to better excite the second bending mode. The mode at 75 Hz is found to be the third bending mode (Fig. 58.9d). There is also a coupling mode between the shaker and the ski at 23.2 Hz. Its mode shape is show in Fig. 58.7b, which is a combination of bending and torsional motion. However, one issue noticed in all measured mode shapes is that the amplitudes of the vibration shapes are close to zero at both ends of the ski. This phenomenon is due to the large angle of the incidence laser with respect to the longitudinal direction of the ski such that the detector loses the signal, and the amplitudes of the shapes appear to be zero.

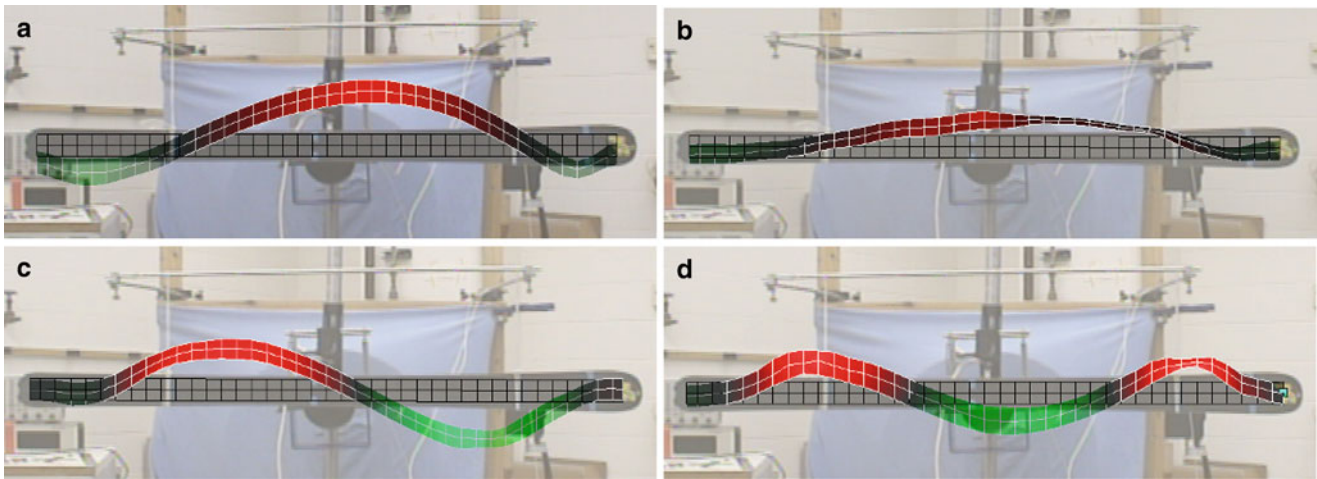


**Fig. 58.9** Measured mode shapes using scanning LDV. (a) First bending mode at 19 Hz, (b) coupling mode at 23.2 Hz, (c) second bending mode at 42 Hz, (d) third bending mode at 75 Hz

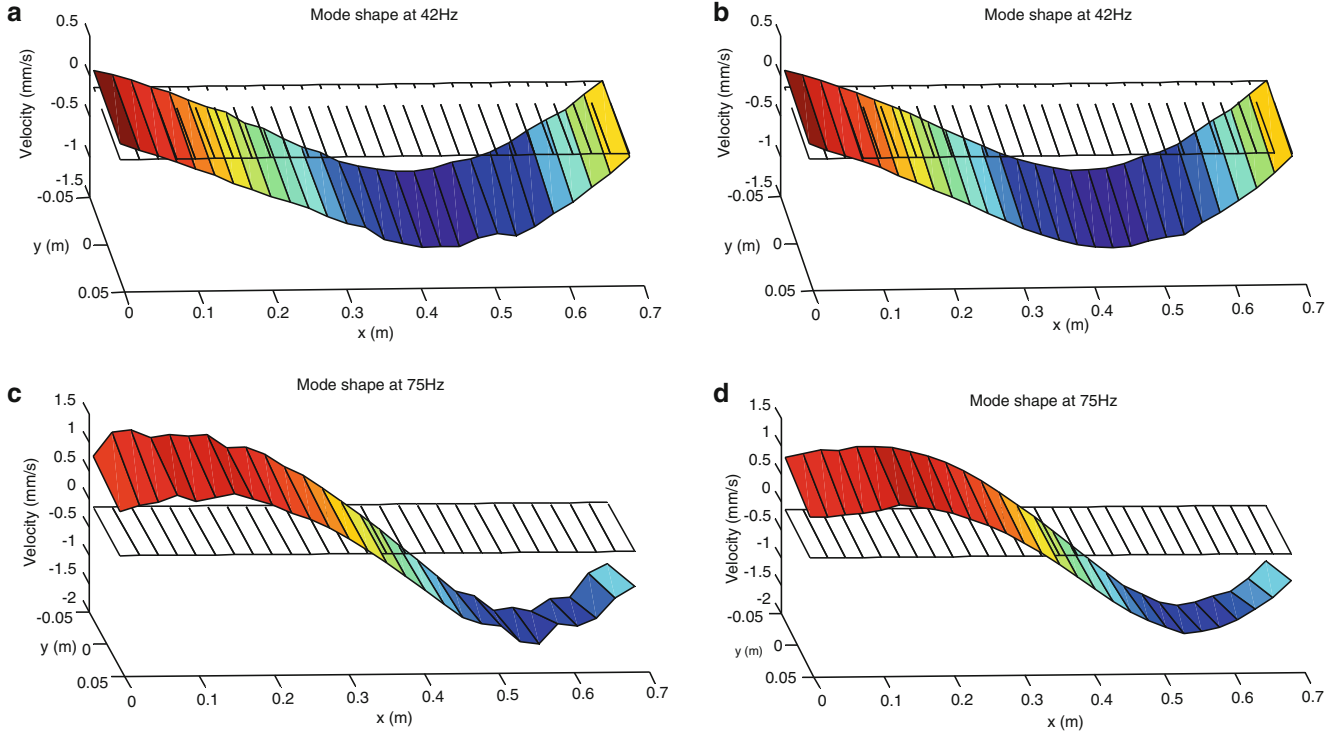
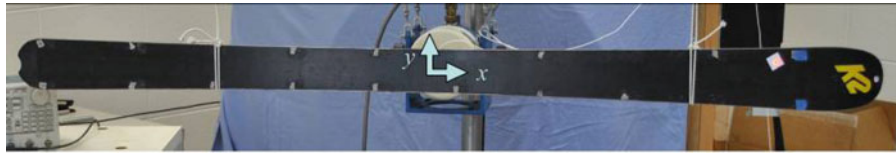
The conventional scanning LDV test provides the basic mode shape information about the ski. A linear swept-sine test was then performed on the dark bottom surface to validate the proposed algorithm based on the harmonic transfer function. The driving frequency of the shaker is from 30 to 100 Hz so as to avoid the coupling mode at 23.2 Hz that may damage the shaker. Therefore, only the second and third bending modes are well excited using this swept-sine input. The sweep time is 15 s from 30 to 100 Hz and 15 s for the return. Limited by the angle of the mirror, only half of the ski was tested, with 2 lines all over the ski and 28 measurement points along each line. The total test duration at each point is 200 s.

Figure 58.10 shows the measured mass-normalized mode shapes using the point by point scan approach and the circular scan approach, while all other testing parameters including the standoff distance and point locations were kept identical. The identified second and third bending mode shapes agree well with the corresponding shapes from the scanning LDV test in Fig. 58.9. However, it is obvious that the mode shapes from circular scan test are much smoother than those from the point by point test. The reason for this difference is that the circular scan approach can provide better signal to noise ratio on a rough surface when appropriate scanning frequency and circle size are selected, as discussed in detail in Sect. 58.3. When the laser was scanning a circle around the point at  $x = 0.5$  m from the driving point on the ski, part of the circle path landed on the bungee cord. This explains the error of the second bending mode shape that is observed near  $x = 0.5$  m in Fig. 58.10b. Nevertheless, the mode shape at this location is still relatively clean compared to the shape at the same location from the point by point test. This characteristic of circular scan approach is extremely important in computing curvature shapes, which is vulnerable to the noise in the measured deflection shapes because of the second order differentiation [16].

## 58.5 Rotational Velocity and Local Slope

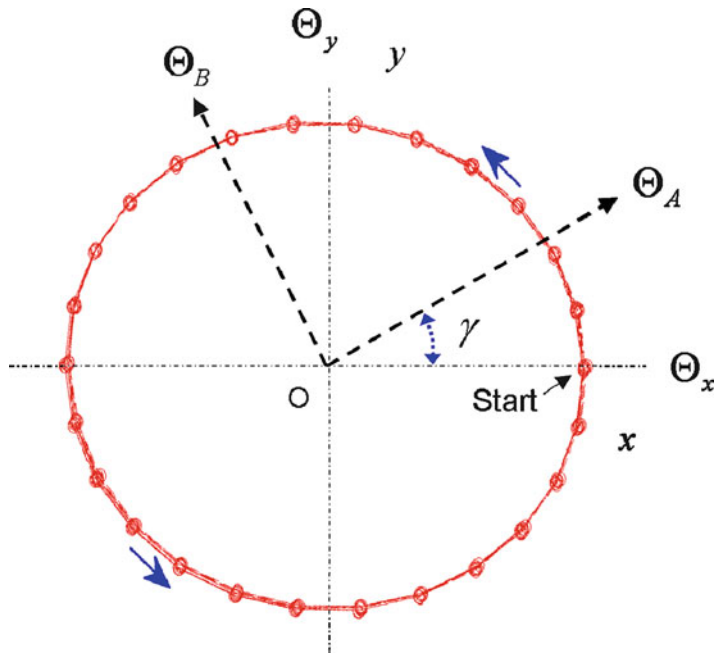
Besides the advantages in measuring translational velocity, the circular scan approach can also be used to simultaneously measure the principal rotational velocities, as was proved in Sect. 58.2.3. This section makes use of the harmonic transfer function of linear time periodic systems to interpret measurements from the circular scan approach and to compute the translational and rotational velocities. The local slopes at each measurement location are then transformed from the principal rotational velocities.

To estimate the harmonic transfer function that relates the measured velocities to the input force,  $n = -2 : 2$  is used to form the exponentially modulated output signals in Eq. (58.17). An accurate scanning frequency  $\omega_A$  is critical in the modulating process because of the  $e^{(i\omega + in\omega_A)t}$  term. The phase errors in the modulated signals accumulate with time for an inaccurate scan frequency, and eventually lead to unreliable output spectra. Therefore, a multi-sine signal is fitted to the recorded mirror output signal to find the accurate scanning frequency. It is found that when the mirror was driven at 200 Hz, the actual scan frequency was at 200.0153 Hz. The mirror signals, velocity signal and the input force are then resampled such that there are an integer number of measurement points along each scan cycle. For example, when the laser scans at 200.0153 Hz, the resampled measurement has 26 points on each circle, as shown in Fig. 58.11, where the red dots represent measurement locations after resampling.



**Fig. 58.10** Measured mode shapes (a) Mode at 42 Hz by point measurement, (b) mode at 42 Hz by circular scan, (c) mode at 75 Hz by point measurement, (d) mode at 75 Hz by circular scan

**Fig. 58.11** Circular scan after resampling



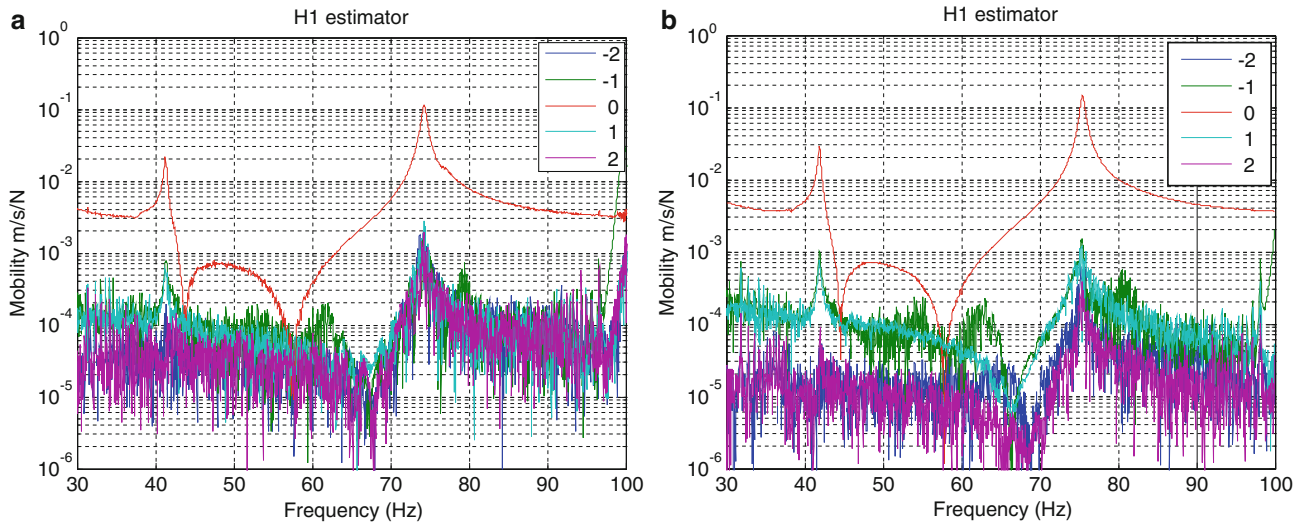


**Fig. 58.12** Harmonic transfer function of circular scan at the same point, (a) on black bottom surface, (b) on retro-reflective tape

This resampling procedure is necessary in computing the harmonic transfer function since averaging is used to reduce the random noise. The input signal and modulated output signals are broken into 30 s sub-blocks with a 75 % overlap between neighboring blocks, resulting in 23 sub-blocks over the 200 s time history. However, as seen in Fig. 58.11, the measurement has to start at the same location on the scan cycle for each sub-block in order to maintain a constant angle  $\gamma$  between the starting point and the principal rotational velocities in Eq. (58.26). In this case, the auto spectra of the modulated output signals would have the synchronized phase with the input force over each block and no phase error will be incurred during the averaging. A Hanning window is then applied to each block to reduce the leakage. Since most of the noise is from the laser speckle, the H1 estimator in Eq. (58.20) is used to estimate the harmonic transfer function. Once the principal rotational velocities  $\Theta_A$  and  $\Theta_B$  of a mode are identified, the slope of the deflection shape along the  $x$  axis can be obtained by projecting the principal rotational velocities to the  $y$  direction using the angle  $\gamma$ , and similarly for the slope along the  $y$  axis. The angle  $\gamma$  can be obtained from the sidebands and may vary from point by point.

Figure 58.12 shows the computed harmonic transfer functions at the same location of the ski on the dark bottom surface and on the retro-reflective tape, respectively. The harmonic transfer function has the similar form as the transfer function of a single-input multiple-output linear time invariant system. However, the mode shapes at the natural frequency of 42 and 75 Hz are no longer the physical deformation at each measurement location. Rather, they are related to the translational and rotational velocities at that point. Specifically, the amplitudes of  $G_{-1,0}$  and  $G_{1,0}$  are related to the principal rotational velocities and have much smaller amplitudes compared to the translational velocity at  $G_{0,0}$ . Here,  $G_{i,0}$  represents the harmonic transfer function  $Y_i/U_0$ , which corresponds to the  $i$ th line in Fig. 58.12. Therefore, rotational velocities are more vulnerable than translational velocities to the speckle noise. Theoretically, according to Eq. (58.26), the amplitudes of  $G_{-2,0}$  and  $G_{2,0}$  should be either zero or very small compared to the value of  $G_{-1,0}$  and  $G_{1,0}$ . However, this is not the case when the laser is scanning on the black bottom surface, as shown in Fig. 58.12. The amplitudes of  $G_{-1,0}$  and  $G_{1,0}$  are close to those of  $G_{-2,0}$  and  $G_{2,0}$ . This is because the overall speckle noise level is larger on black bottom surface than that on the retro-reflective tape.

To detect accurate rotational velocities and local slopes, the circular scan tests were performed on the retro-reflective tape, using a  $4 \times 10$  measurement grid with a step size of 27 mm in the longitudinal direction of the ski, and a step size of 23 mm in the other direction. For consistency, other parameters remained the same as those in previous tests. Figure 58.13 shows the composite harmonic transfer function from a circular scan measurement at a single point on the tape. The harmonic transfer function is fitted with the algorithm of mode isolation [28]. It appears that the fitted modes reduce the harmonic transfer function very well. The identified amplitudes and phase for the second and third bending mode are listed in Table 58.1. Notice that the amplitudes of  $G_{-1,0}$  and  $G_{1,0}$  terms are an order of magnitude smaller than that of the  $G_{0,0}$  term, which corresponds to the translational velocity at that measurement location.

In any event, the rotational and translational velocities are computed according to Eq. (58.26), and the velocities are listed in Table 58.1 as well. It was found that for the second bending mode at 42 Hz, the principal rotational velocity  $\Theta_A$  is the dominant rotation at this measurement location. It has a magnitude of 0.3816 rad/s/N and is orientated approximately  $80^\circ$  from the longitudinal direction of the ski. The principal rotational velocity  $\Theta_B$  has the magnitude of 0.0641 rad/s/N and is orientated  $90^\circ$  from  $\Theta_A$ . This result agrees with our experimental observation that the rotational motion associated with bending



**Fig. 58.13** AMI fit of the harmonic transfer function

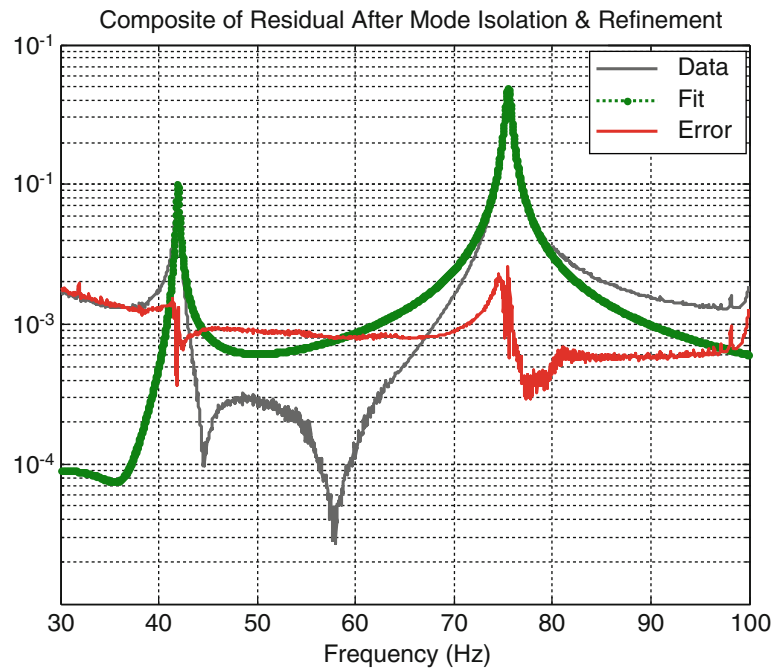


**Table 58.1** Measured translational and rotational velocities from circular scan

Mode at 42 Hz					
Mode shape	Amplitude (mm/s/N)	Phase angle ( $^{\circ}$ )	Velocities	Amplitude	$\gamma$ angle ( $^{\circ}$ )
$G_{-1,0}$	0.9	16.0369	$\Theta_A$	0.3816 rad/s/N	79.9076
$G_{0,0}$	26	-166.4050	Z	26 mm/s/N	/
$G_{1,0}$	0.6	-4.1478	$\Theta_B$	0.0641 rad/s/N	169.9076
Mode 75 Hz					
Mode shape	Amplitude (mm/s/N s)	Phase angle ( $^{\circ}$ )	Velocities	Amplitude	$\gamma$ angle ( $^{\circ}$ )
$\bar{C}_{r,-1}$	22	25.7603	$\Theta_A$	0.8053 rad/s/N	34.0818
$\bar{C}_{r,0}$	252.3	-0.5437	Z	252.3 mm/s/N	/
$\bar{C}_{r,1}$	10	-86.0761	$\Theta_B$	0.2872 rad/s/N	124.0818

modes should be in the direction that is perpendicular to the longitudinal direction of the ski. The rotational velocities of the third bending mode at 75 Hz are slightly noisier and have larger angle with respect to the longitudinal direction of the ski.

The above results are from the measurement at a single point. The translational and rotational velocities at all other points in the  $4 \times 10$  measurement grid are computed in the same manner. Note that the orientations of principal rotational velocities are different from one point to another. However, the slopes of the second and the third bending mode can still be obtained since the angle  $\gamma$  for each mode can be recovered from the harmonic transfer function. The shapes of the second and third bending mode along the top line are plotted in Fig. 58.14. The principal rotational velocities at each measurement location are projected to the  $y$  axis to compute the local slopes along the longitudinal direction of the ski, which are shown as red short lines in Fig. 58.14. It is found that the curve of the second bending mode matches very well with the computed slopes from the rotational velocities. However, some errors are observed at the first few points in the third bending mode. This is perhaps due to the large amplitudes of  $G_{-2,0}$  and  $G_{2,0}$  as seen Fig. 58.12b. The circle size could be too large for the second mode in this region of the ski such that the laser picked up some higher order harmonics along the circle, and the principal rotational velocities were not accurately estimated.

Table 58.2 compares the computed slopes using the projection of rotational velocities and the computational slopes obtained via a forward finite difference. We can see that the slopes of the second bending mode from both methods agree very small, while the slopes at the first few points of the third bending mode have slightly larger error.

Figure 58.15 shows the orientations and amplitudes of principal rotational velocities at all the measurement points for the second bending mode at 42 Hz, with the length of the arrow scales to the amplitude of a rotational velocity. It can be seen that the orientations and amplitudes of principal rotational velocities are consistent at most points. Figure 58.14 together with Fig. 58.15 can be used to compute a 1-D or 2-D spline-fit to the deformation shape, which can be used to compute a much more accurate curvature for damage detection. This part will be explored in the next stage of this work.

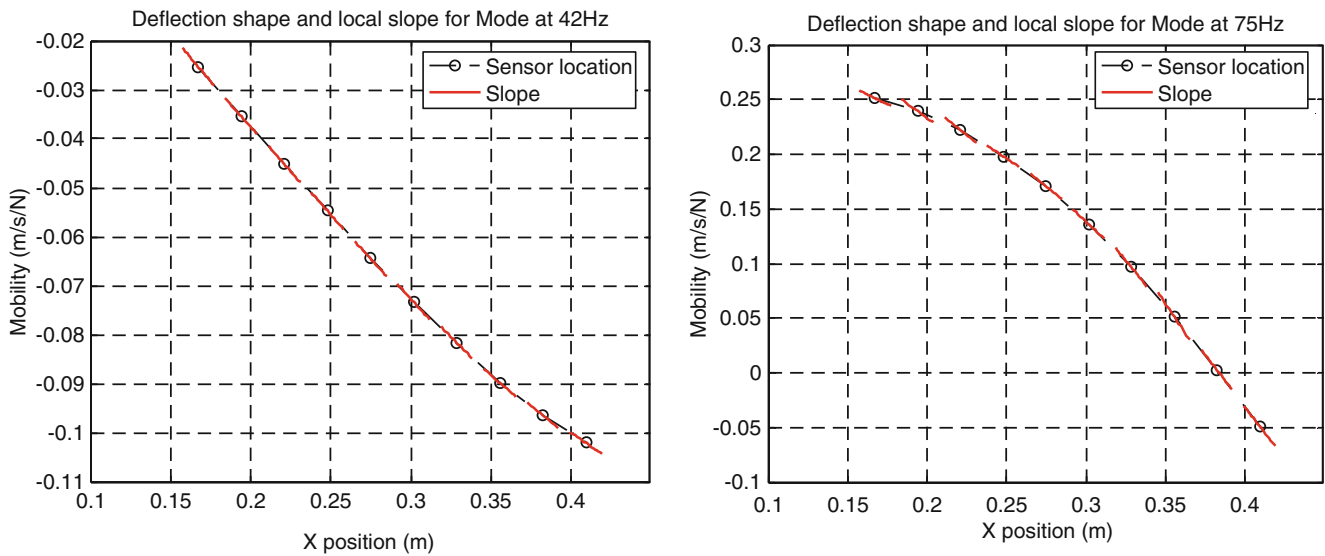


Fig. 58.14 Measured deflection shape and local slope using the circular scan approach

Table 58.2 Computed slopes and the forward difference results

	P1	P2	P3	P4	P5	P6	P7	P8	P9	P10
Mode 2 at 42 Hz Slope	-0.3864	-0.3640	-0.3744	-0.3751	-0.3550	-0.3616	-0.3290	-0.2819	-0.2583	-0.2241
Forward difference	-0.3762	-0.3606	-0.3542	-0.3608	-0.3275	-0.3082	-0.3031	-0.2466	-0.2075	/
Mode 3 at 75 Hz Slope	-0.6844	-1.0661	-1.1556	-0.9592	-1.2232	-1.3595	-1.7794	-2.1631	-1.8609	-1.8418
Forward difference	-0.4376	-0.6410	-0.8893	-1.0155	-1.2874	-1.4569	-1.6708	-1.8003	-1.9127	/

### 58.6 Conclusion

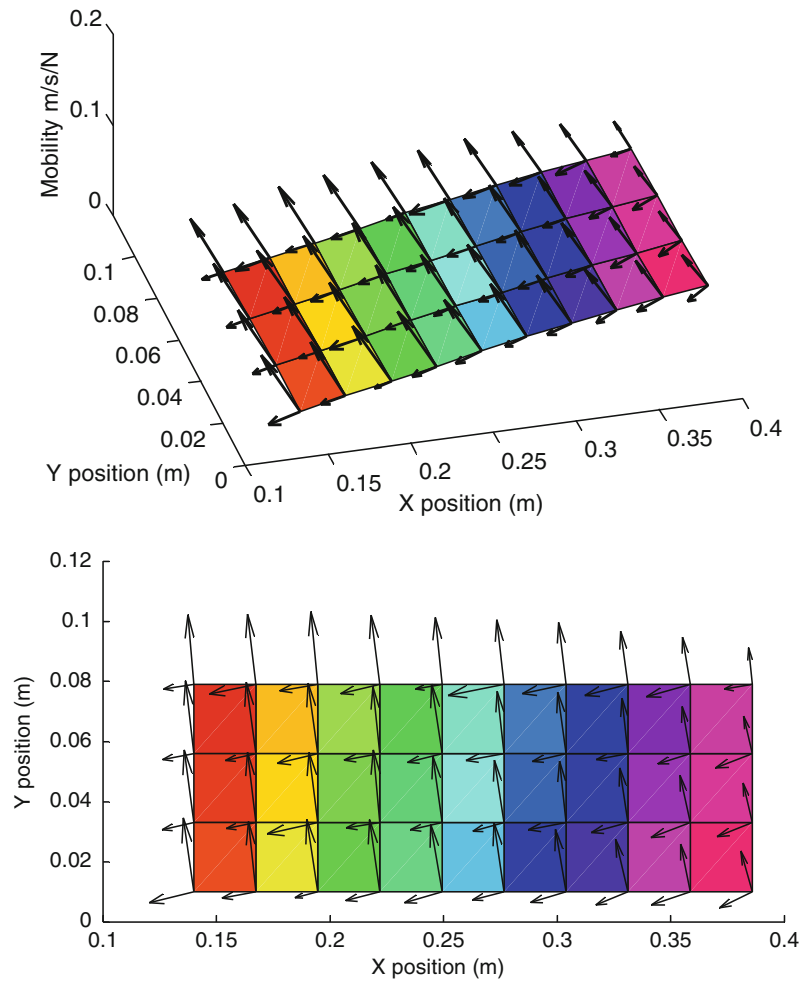
Signals measured using continuous scan laser Doppler vibrometry can be represented as the output of a linear time periodic system when a closed, periodic scan pattern is used. This work proposed a new algorithm based on the harmonic transfer function of linear time periodic system to process measurements from a circular scan approach, allowing the translational and rotational velocities to be extracted simultaneously. Using this new approach, the circular scan approach can be combined with the conventional point by point scan approach, acquiring translational and rotational velocities at each point in a measurement grid in the same amount of time that is required for obtaining only the translational velocity. Also, because the method is based on a transfer function description, virtually any desired input can be applied.

The proposed algorithm was validated on a downhill ski under free-free boundary conditions. The ski is a complex structure that can be very challenging to model accurately. This work studied the influence of the scanning rate, circle size, and surface quality on the noise level in measured signal. The results showed that in some situations the circle scan approach can provide a lower noise level and standard deviation than the conventional point by point approach, if the scan frequency and circle size are chosen appropriately. It seems that by scanning in a circle one can avoid the possibility of the detector area being dominated by a dark speckle, or by a region where speckle noise is especially severe, and thus reduces the speckle noise and the potential for signal dropouts. On the other hand, the circle scan increases the noise if the radius of the scan and/or the scan frequency are too large.

The circular scan approach was then applied over a grid of circles (points) to measure the mode shapes on the black bottom surface of the ski. A 200 Hz scan frequency and a 5/16 in. circle size were selected based on the previous study. The circular scan approach was found to provide smoother and more reliable mode shapes than the conventional point by point approach in this scenario.

The harmonic transfer function concept was also used to extract the principal rotational velocities of the ski. The amplitudes of the rotational velocities were found to be much smaller than those of the translational velocities, and hence even though the circle scan provided a greater signal to noise ratio than the point scan, the noise was still too large to accurately measure surface rotation. However, retro-reflective tape was applied to the surface and found to reduce the noise so that the rotations could be accurately measured. Then the acquired rotational velocities were used to compute the slope

**Fig. 58.15** Translational and rotational velocities for the first mode



of the mode shape at the measurement locations, the results were found to agree well with the trend of the shapes found by measuring the translational velocity, suggesting that the method is accurate. Future work will focus on computing a spline-fit to the surface shape using both the deflection and slope information, so that the curvature of the surface can be computed much more accurately.

**Acknowledgements** The authors wish to thank the National Science Foundation for supporting this research under the Grant No. CMMI-0969224.

## Appendix

The derivation of harmonic transfer function starts with the output expression of a linear system with time varying coefficients. The output  $y(t)$  of a general linear state space model can be found in [19] as follows,

$$y(t) = C(t)\Phi(t, t_0)x(t_0) + \int_{t_0}^t C(t)\Phi(t, \tau)B(\tau)u(\tau)d\tau + D(t)u(t) \quad (58.28)$$

where  $u(t)$  is the excitation or the input to the system, and  $B(t)$  is the input matrix that describes how the input is applied.  $C(t)$  is the output matrix that defines the output state, and  $D(t)$  is the direct input matrix to the output.  $\Phi(t, t_0)$  is called the state transition matrix. It relates the system state  $x(t)$  at any time to the initial state  $x(t_0)$  by,

$$x(t) = \Phi(t, t_0)x(t_0) \quad (58.29)$$

Finding the state transition matrix is the key to derive the harmonic transfer function. For a linear time invariant system with constant coefficients, the state transient matrix can be obtained directly as  $\Phi(t, t_0) = e^{A(t-t_0)}$ , where  $A$  is the system matrix of the state space model. However, this expression is not valid for a general time varying  $A(t)$ . In this case, it is usually challenging or even impossible to find the closed form transient matrix.

Fortunately, for a system with periodic matrices, e.g.  $A(t) = A(t + T_A)$  where  $T_A = 2\pi/\omega_A$  is called the fundamental period, Floquet theorem [19, 29–31] has defined a coordinate change of the state  $x(t)$  that transforms the periodic system to a time invariant system, such that linear time periodic systems can be studied using time invariant techniques. Following the Floquet theorem, the state transition matrix of a linear time periodic system can be decomposed into the following modal summation form [32],

$$\Phi(t, t_0) = \sum_{r=1}^N \psi_r(t) L_r^T(t_0) e^{\lambda_r(t-t_0)} \quad (58.30)$$

where  $\psi_r(t)$  is the  $r$ th time-periodic mode vector of the transition matrix, and  $L_r(t)$  is the  $r$ th column of  $\Psi(t) = [\psi_1(t) \ \psi_2(t) \ \cdots]^T$ .  $\lambda_r$  is the  $r$ th Floquet exponent, which is analogous to the eigenvalue of an time invariant system. The Floquet exponent can be written in terms of the damping ratio  $\zeta_r$  and natural frequency  $\omega_r$  as  $\lambda_r = -\zeta_r \omega_r + i\omega_r \sqrt{1 - \zeta_r^2}$  for an under-damped mode.

To define the input-output relationship of a periodic system, we also have to introduce the exponentially modulated signal. It is well known that a single frequency excitation to a linear time invariant system, e.g. a linear oscillator, will cause the output at the same frequency though with different amplitude and phase. On the contrary, the response of a single frequency input to an asymmetric rotating rotor, a typical linear time periodic system, will be at the same frequency as well as its infinite number of harmonics, each separated by the fundamental frequency  $\omega_A$ . Hence if we defined the input  $u(t)$  and the output  $y(t)$  of a linear time periodic system as the summation of frequency components separated by a multiple of the fundamental frequency  $\omega_A$ ,

$$u(t) = \sum_{n=-\infty}^{\infty} U_n e^{(i\omega + in\omega_A)t}, \quad y(t) = \sum_{n=-\infty}^{\infty} Y_n e^{(i\omega + in\omega_A)t} \quad (58.31)$$

denoted by the exponentially modulated periodic input and output [13]. It is clear that a modulated input will cause a modulated output at the same collection of frequencies. So an input-output relationship that is completely analogous to time invariant transfer function can be established.

Wereley extended the concept of a transfer function for LTI systems to LTP systems using the Floquet theorem and the exponentially modulated periodic signal space defined above. First, the expression of the state transition matrix in Eq. (58.30) is substituted into the general solution of the state space model in Eq. (58.28), the general solution becomes,

$$\begin{aligned} y(t) &= \sum_{r=1}^{2N} C(t) \psi_r(t) e^{\lambda_r t} L_r^T(t_0) x(t_0) e^{-\lambda_r t_0} \\ &+ \sum_{r=1}^{2N} C(t) \psi_r(t) e^{\lambda_r t} \int_{t_0}^t L_r^T(\tau) B(\tau) u(\tau) e^{-\lambda_r \tau} d\tau + D(t) u(t) \end{aligned} \quad (58.32)$$

Since the eigenvectors  $\psi_r(t)$  of the state transition matrix are periodic, it is convenient to expand them into a Fourier series. As is often the case for time invariant systems, the output matrix  $C(t)$  may simply be a matrix of ones and zeros indicating which of the states are being taken. In any event, the expansion is,

$$C(t) \psi_r(t) = \sum_{n=-\infty}^{\infty} \bar{C}_{r,n} e^{in\omega_A t}, \quad L_r^T(t) B(t) = \sum_{n=-\infty}^{\infty} \bar{B}_{r,n} e^{in\omega_A t} \quad (58.33)$$

where  $\bar{C}_{r,n}$  is the  $n$ th Fourier coefficient of the  $r$ th observed mode vector,  $C(t) \psi_r(t)$ , and similarly for  $L_r^T(t) B(t)$ .

The harmonic transfer function can be derived by substituting the expression of exponentially modulated signals in Eq. (58.31), and the Fourier expansion in Eq. (58.33) into Eq. (58.32).

When studying the transfer function, only the steady state response is considered. Hence if we neglect the transient response, after much algebra, the output expression becomes,

$$\begin{aligned} \sum_{n=-\infty}^{\infty} Y_n e^{(i\omega + in\omega_A)t} &= \sum_{r=1}^{2N} \sum_{n=-\infty}^{\infty} \sum_{s=-\infty}^{\infty} \sum_{m=-\infty}^{\infty} \frac{\bar{C}_{r,s} \bar{B}_{r,m}}{i\omega - \lambda_r + i(m+n)\omega_A} U_n e^{(i\omega + i(n+s+m)\omega_A)t} \\ &+ \sum_{n=-\infty}^{\infty} D(t) U_n e^{(i\omega + in\omega_A)t} \end{aligned} \quad (58.34)$$

Now we introduce the exponentially modulated input and output in the frequency domain as follows,

$$\begin{aligned} \mathbf{U}(\omega) &= [\dots U_{-1}(\omega)^T \ U_0(\omega)^T \ U_1(\omega)^T \ \dots]^T \\ \mathbf{Y}(\omega) &= [\dots Y_{-1}(\omega)^T \ Y_0(\omega)^T \ Y_1(\omega)^T \ \dots]^T \end{aligned} \quad (58.35)$$

Using the harmonics balance approach, a transfer function can then be established in terms of the modal parameters of the state transition matrix, denoted by the harmonic transfer function.

$$\mathbf{Y}(\omega) = \mathbf{G}(\omega) \mathbf{U}(\omega) \quad (58.36)$$

Where,

$$\begin{aligned} \mathbf{G}(\omega) &= \sum_{r=1}^{2N} \sum_{l=-\infty}^{\infty} \frac{\bar{C}_{r,l} \bar{B}_{r,l}}{i\omega - (\lambda_r - il\omega_A)} + \mathbf{D} \\ \bar{C}_{r,l} &= [\dots \bar{C}_{r,-1-l}^T \ \bar{C}_{r,-l}^T \ \bar{C}_{r,1-l}^T \ \dots]^T \\ \bar{B}_{r,l} &= [\dots \bar{B}_{r,l+1} \ \bar{B}_{r,l} \ \bar{B}_{r,l-1} \ \dots] \end{aligned} \quad (58.37)$$

Here the  $n$ th term in the vector  $\bar{C}_{r,l}$ , is  $\bar{C}_{r,n-l}$ , the  $(n-l)$ th Fourier coefficient of  $C(t)\psi_r(t)$ . Similarly,  $\bar{B}_{r,l-m}$  is the  $(l-m)$ th Fourier coefficient of  $L_r(t)^T B(t)$ .  $D$  is an infinite matrix with  $D(t)$  on the diagonal.

This expression of harmonic transfer function has exactly the same mathematical form as the expression for the frequency response function of a linear time invariant system in terms of its modal parameters, so the same algorithms can be applied to identify the parameters of the linear time periodic system and the same intuition that one uses to interpret frequency response function can also be used to interpret harmonic transfer function. However, there are a few differences that must be noted:

- A linear time periodic system potentially has an infinite number of peaks for each mode in its harmonic transfer function. Each peak will occur near the imaginary part of the Floquet exponent  $\lambda_r$  plus some integer multiple of the fundamental frequency  $\omega_A$ . If the mode shapes of the system are constant in time, then  $\bar{C}_{r,l}$  and  $\bar{B}_{r,l}$  contain only one nonzero term and Eq. (58.37) reduces to the familiar relationship for a linear time invariant system.
- The mode vectors of a linear time invariant system describe the spatial pattern of deformation of a mode. Each element in the mode vector indicates the physical deflection at the corresponding measurement point. For a linear time periodic system, the vectors  $\bar{C}_{r,l}$  consist of the Fourier coefficients that describe the time varying spatial deformation pattern.

## References

1. Allen MS, Aguilar DM (2009) Model validation of a bolted beam using spatially detailed mode shapes measured by continuous-scan laser doppler vibrometry. In: Presented at the 50th AIAA/ASME/ASCE/AHS/ASC structures, structural dynamics, and materials conference, Palm Springs, CA
2. Schwingshackl CW, Stanbridge AB, Zang C, Ewins DJ (2007) Full-field vibration measurement of cylindrical structures using a continuous scanning LDV technique. In: Presented at the 25th international modal analysis conference (IMAC XXV), Orlando, FL
3. Stanbridge AB, Ewins DJ (1999) Modal testing using a scanning laser Doppler vibrometer. Mech Syst Signal Process 13:255–70
4. Stanbridge AB, Martarelli M, Ewins DJ (2004) Measuring area vibration mode shapes with a continuous-scan LDV. Measurement 35:181–189

5. Martarelli M (2001) Exploiting the laser scanning facility for vibration measurements. Ph.D., Imperial College of Science, Technology & Medicine, Imperial College, London
6. Stanbridge AB, Khan AZ, Ewins DJ (2000) Modal testing using impact excitation and a scanning LDV. *Shock Vib* 7:91–100
7. Allen MS (2009) Frequency-domain identification of linear time-periodic systems using LTI techniques. *J Comput Nonlinear Dyn* 4(4), 041004, p. 6 doi:10.1115/1.3187151
8. Yang S, Sracic MW, Allen MS (2012) Two algorithms for mass normalizing mode shapes from impact excited continuous-scan laser Doppler vibrometry. *J Vib Acoust* 134:021004
9. Yang S, Allen MS (2012) Output-only modal analysis using continuous-scan laser Doppler vibrometry and application to a 20 kW wind turbine. *Mech Syst Signal Process* 31:228–245
10. Yang S, Allen MS (2012) A lifting algorithm for output-only continuous scan laser Doppler vibrometry. In: Presented at the AIAA, Hawaii
11. Stanbridge AB, Ewins DJ (1994) Measurement of translational and angular vibration using a scanning laser Doppler vibrometer. *Vib Meas* 2358:37–47
12. Salman M, Sabra KG (2012) Broadband measurement of translational and angular vibrations using a single continuously scanning laser Doppler vibrometer. *J Acoust Soc Am* 132:1384–1391
13. Wereley NM (1991) Analysis and control of linear periodically time varying systems. PhD, Department of Aeronautics and Astronautics, Massachusetts Institute of Technology, Cambridge
14. Wereley NM, Hall SR (1991) Linear time periodic systems: transfer functions, poles, transmission zeroes and directional properties. In: Presented at the proceedings of the 1991 American control conference, Boston, MA
15. Wereley NM, Hall SR (1990) Frequency response of linear time periodic systems. Honolulu, HI, pp 3650–3655
16. Ratcliffe CP (2000) A frequency and curvature based experimental method for locating damage in structures. *J Vib Acoust* 122:324–328
17. Sharma VK, Hanagud S, Ruzzene M (2006) Damage index estimation in beams and plates using laser vibrometry. *AIAA J* 44:919–23
18. Wereley NM (1991) Analysis and control of linear periodically time varying systems. PhD, Department of Aeronautics and Astronautics, Massachusetts Institute of Technology, Cambridge
19. Chen C-T (1999) Linear system theory and design, 3rd edn. Oxford University Press, Inc, New York
20. Martin P, Rothberg S (2009) Introducing speckle noise maps for laser vibrometry. *Opt Lasers Eng* 47:431–42
21. Rothberg SJ (1989) Laser vibrometry. Pseudo-vibrations. *J Sound Vib* 135:516–522
22. Rothberg SJ, Halkon BJ (2004) Laser vibrometry meets laser speckle. In: Proceedings of sixth international conference on vibration measurements by laser techniques, Ancona, Italy
23. Rothberg S (2006) Numerical simulation of speckle noise in laser vibrometry. *Appl Opt* 45:4523–33
24. Martarelli M, Ewins DJ (2006) Continuous scanning laser Doppler vibrometry and speckle noise occurrence. *Mech Syst Signal Process* 20:2277–89
25. Sracic MW, Allen MS (2009) Experimental investigation of the effect of speckle noise on continuous scan laser Doppler vibrometer measurements. In: Presented at the 27th international modal analysis conference (IMAC XXVII), Orlando, FL
26. Allen MS, Ginsberg JH (2006) A global, single-input-multi-output (SIMO) implementation of the algorithm of mode isolation and applications to analytical and experimental data. *Mech Syst Signal Process* 20:1090–1111
27. Martin P, Rothberg S (2008) Laser vibrometry and the secret life of speckle patterns. In: Eighth international conference on vibration measurements by laser techniques: advances and applications, Ancona, Italy
28. Allen MS (2005) Global and multi-input-multi-output (MIMO) extensions of the algorithm of mode isolation (AMI), Doctorate, George W. Woodruff School of Mechanical Engineering, Georgia Institute of Technology, Atlanta, GA
29. Floquet G (1883) Sur Les Equations Lineaires a Coefficients Periodiques. *Ann Sci Ecole Norm Sup* 12:47–88
30. Guckenheimer J, Holmes P (1983) Nonlinear oscillations, dynamical systems, and bifurcations of vector fields, vol 42. Springer New York Inc., New York
31. Hartman P (1964) Ordinary differential equations. Wiley, New York
32. Allen MS (2007) Floquet experimental modal analysis for system identification of linear time-periodic systems. In: Presented at the ASME 2007 international design engineering technical conference, Las Vegas, NV

# Chapter 59

## Empirical Slow-Flow Identification for Structural Health Monitoring and Damage Detection

Young S. Lee, D. Michael McFarland, Lawrence A. Bergman, and Alexander F. Vakakis

**Abstract** We utilize the nonlinear system identification (NSI) methodology, which was recently developed based on the correspondence between analytical and empirical slow-flow dynamics. Performing empirical mode decomposition on the simulated or measured time series to extract intrinsic mode oscillations, we establish nonlinear interaction models, which invoke slowly-varying forcing amplitudes that can be computed from empirical slow-flows. By comparing the spatio-temporal variations of the nonlinear modal interactions for structures with defects and those for the underlying healthy structure, we will demonstrate that the proposed NSI method can not only explore the smooth/nonsmooth nonlinear dynamics caused by structural damage, but also the extracted vibration characteristics can directly be implemented for structural health monitoring and detecting damage locations. Starting with traditional tools such as the modal assurance criterion (MAC) and the coordinate MAC are utilized.

**Keywords** Nonlinear system identification • Empirical mode decomposition • Intrinsic modal oscillator • Nonlinear interaction model • Structural health monitoring

### 59.1 Introduction

A nonlinear system identification (NSI) methodology [1–3] based on close correspondence between analytical and empirical slow-flow dynamics has been applied to studies of targeted energy transfers in 2-degree-of-freedom (DOF) coupled oscillators [2], the triggering and suppression mechanisms of aeroelastic instabilities [4], and study of the dynamics of an elastic continuum with an essentially nonlinear end attachment [5]. The NSI method utilizes empirical mode decomposition (EMD [6]) along with the use of mirror-image and masking signals to enhance its resolution [1]. EMD is suitable for analysis of measured time responses that exhibit strong nonlinearity and nonstationarity, in particular when the tested systems involve nonlinearities caused by multi-physics nonlinear interactions [7]. In this case, Fourier-transform (FT)-based methods, such as traditional experimental modal analysis (EMA) under the assumption of linearity and stationarity of the measured signals [8], may not be capable of properly isolating and extracting the nonlinearity and nonstationarity from the measured data, frequently leading to wrong conclusions (for example, to misinterpretations of internal and combination resonances as natural frequencies).

One of the basic assumptions for EMD analysis is that the measured time series can be decomposed in terms of a finite number of components oscillating at their own intrinsic time scales; in other words, they are in the form of fast, (nearly) monochromatic oscillations modulated by slowly varying amplitudes. Such slowly varying components enable us to establish empirical slow-flow models of the dynamics, which paves the way for constructing physics-based local nonlinear interaction models (NIMs [2]). A NIM consists of a set of intrinsic modal oscillators (IMOs) that can reproduce the measured time series over different time scales and account for (even strongly) nonlinear modal interactions across scales. Hence, it represents a

---

Y.S. Lee (✉)  
New Mexico State University, Las Cruces, NM 88003, USA  
e-mail: [younglee@nmsu.edu](mailto:younglee@nmsu.edu)

D.M. McFarland • L.A. Bergman • A.F. Vakakis  
University of Illinois at Urbana-Champaign, Urbana, IL 61801, USA  
e-mail: [dmmcf@illinois.edu](mailto:dmmcf@illinois.edu); [lbergman@illinois.edu](mailto:lbergman@illinois.edu); [avakakis@illinois.edu](mailto:avakakis@illinois.edu)

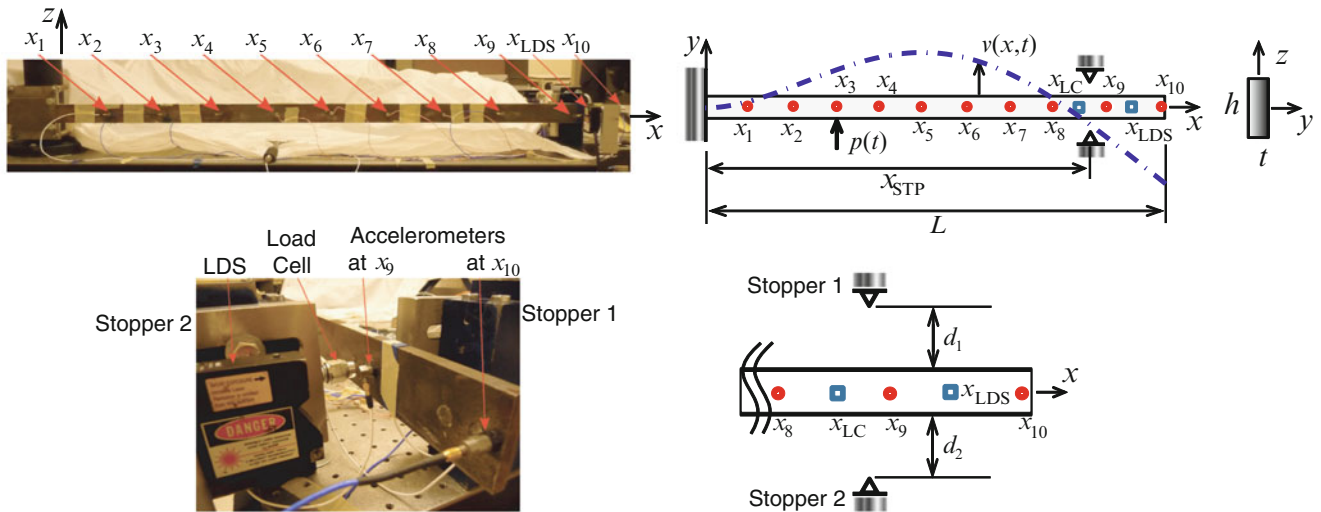


**Fig. 59.1** Experimental setup for the VI beam:  $x_1 - x_{10}$ ,  $x_{LDS}$ , and  $x_{STP}$  respectively denote the spanwise locations of the accelerometers, of the laser displacement sensors, and of the rigid stops [19, 20]

local model of the dynamics, identifying specific nonlinear transitions. By collecting energy-dependent frequency behaviors from all identified IMOs, a frequency-energy plot can be constructed, which depicts global features of the dynamical system. The method requires no a priori system information but only measured (or simulated) time series.

Use of proper orthogonal decomposition (POD [9–11]) has been popular in studying system identification and nonlinear normal modes of coupled beams and rods [12, 13], and in structural damage detection [14]. For example, the method of POD has been utilized for studying chaotic vibrations of a 10-DOF impact oscillator and a flexible-beam impact oscillator in Cusumano et al. [15, 16]. In these studies, the spatial structure of impacting responses under a harmonic excitation of the boundary was demonstrated to be close to what can be obtained by averaging over many impulse-response tests on the linear system (even if the system is strongly nonlinear). Moreover, POD was applied for model reduction of a vibro-impact (VI) rod [17], and also for extracting dominant coherent structures of a VI beam from experimental time-series data [18] with the goal of eventually deriving low-dimensional reduced-order models through a Galerkin reconstruction process based on the extracted mode shape functions. We note, however, that these techniques are only applicable to specific classes of dynamical systems, requiring certain functional forms for the system nonlinearity, and that some POD modes are often spurious in practical applications, lacking physically meaningful information.

On the other hand, the nonlinear dynamics of a VI beam was explored in Kurt et al. [19] by performing the aforementioned EMD-based NSI on the numerical simulation data. By comparing the spatiotemporal variations of the nonlinear modal interactions extracted from the empirical slow-flow models for the vibro-impact beam and the underlying linear beam, it was demonstrated that the lower intrinsic modes are more significantly affected by vibro-impacts through strongly nonlinear modal interactions, whereas the higher modes tend to retain their linear dynamics between impacts. In this paper, we provide NSI analysis on experimental acceleration signals measured at ten, almost evenly spaced positions along a cantilever beam, whose further details can be found in Chen et al. [20]. Finally, we discuss implications of the NSI results with a view toward structural health monitoring (SHM) and damage detection in practical applications.

## 59.2 Nonlinear System Identification of a Vibro-Impact Beam

First, we present the NSI results performed on the experimental setup depicted in Fig 59.1 [19, 20], considering two typical cases: (i) The linear beam (i.e., a cantilever beam with infinite clearances at the impact boundaries) representing a healthy structure model; and (ii) the vibro-impact (VI) beam with 4 mm symmetric clearances, representing a damaged structure. The cantilever beam is uniform and homogeneous, made of steel with density  $\rho = 7,850 \text{ kg/m}^3$  and Young's modulus  $E = 200 \text{ GPa}$ , with dimensions  $L \times h \times t = 1.311 \times 0.0446 \times 0.008 \text{ m}$  so that the cross-sectional area and the second moment of area with respect to the  $z$  axis are  $A = 3.57 \times 10^{-4} \text{ m}^2$  and  $I_{zz} = 1.9 \times 10^{-9} \text{ m}^4$ , respectively. Table 59.1 summarizes the positions  $x_1 - x_{10}$  of the accelerometers along the beam, the position  $x_{LDS}$  of the laser displacement sensor, and the placement  $x_{STP}$  of the two symmetric rigid stops causing vibro-impacts.



**Table 59.1** Positions of the accelerometers and rigid stops of the VI beam

	$x_1$	$x_2$	$x_3$	$x_4$	$x_5$	$x_6$	$x_7$	$x_8$	$x_9$	$x_{10}$	$x_{STP}$
Positions (mm)	131	263	395	527	657	787	917	1,052	1,215	1,311	1,185

**Table 59.2** The ten leading natural frequencies (in Hz) of the linear cantilever beam in Fig. 59.1

	First	Second	Third	Fourth	Fifth	Sixth	Seventh	Eighth	Ninth	Tenth
$\omega_n$ (Hz)	3.7	23.2	64.9	126.9	209.4	314.7	433.9	580.7	751.3	926.7

Applying impulsive excitations at position  $x_3$  and measuring the acceleration responses at the ten positions, we perform an experimental modal analysis (EMA [8]) to extract basic modal properties from the linear beam. For example, Table 59.2 shows the ten leading natural frequencies of the linear cantilever beam in Fig. 59.1. However, for the VI beam setup, traditional EMA based on Fourier transform fails to provide physically meaningful information due to strongly nonlinear (and nonsmooth) vibro-impacts.

To get rid of nonsmooth dynamics due to vibro-impact nonlinearity, we perform EMD analysis on the VI beam responses and then adopt the local approach to NSI [1–3] applied to the resulting smooth components. Since we postprocess time series measured at numerous positions along a structure, it is reasonable to expand the idea of 1-D temporal slow flows and hence 1-D temporal intrinsic modal oscillators (IMOs [2]) to multi-dimensional spatiotemporal slow flows and multi-dimensional IMOs. Let  $W(\mathbf{x}, t)$  be a time series measured at  $\mathbf{x}$  over the whole structure, which we suppose can be expressed as a sum of the intrinsic modes  $W_m(\mathbf{x}, t)$ ; i.e., we write

$$W(\mathbf{x}, t) \approx \sum_{m=1}^N W_m(\mathbf{x}, t) \quad (59.1)$$

where  $W_m(\mathbf{x}, t)$  denotes the spatiotemporal intrinsic mode oscillating at or near the fast frequency  $\omega_m$ , and  $\mathbf{x} \in \mathbb{R}^3$  in general defined by structural boundary conditions. For a linear system,  $W_m(\mathbf{x}, t)$  simply implies the  $m$ -th normal mode vibration. Then, without loss of generality, we can extend the expression for an 1-D IMO such that

$$\ddot{W}_m(\mathbf{x}, t) + 2\zeta_m\omega_m\dot{W}_m(\mathbf{x}, t) + \omega_m^2 W_m(\mathbf{x}, t) \approx \text{Re} [\Lambda_m(\mathbf{x}, t)e^{j\omega_m t}] \quad (59.2)$$

where the dot denotes partial differentiation with respect to time  $t$ , and the spatiotemporal variations of complex forcing function  $\Lambda_m(\mathbf{x}, t)$  can be computed as

$$\Lambda_m(\mathbf{x}, t) \approx 2 \left[ \dot{\varphi}_m(\mathbf{x}, t) + \hat{\zeta}_m\omega_m\varphi_m(\mathbf{x}, t) \right] \quad (59.3)$$

where the spatiotemporal slowly-varying slow flow can be expressed as  $\varphi_m(\mathbf{x}, t) = j\omega_m \hat{A}_m(\mathbf{x}, t)e^{j\hat{\theta}_m(\mathbf{x}, t)}$ .

In practice,  $W_m(\mathbf{x}, t)$  can be constructed by augmenting a set of intrinsic mode functions (IMFs, or equivalently, a set of IMO solutions) with the same dominant fast frequency  $\omega_m$  column by column, instead of directly solving the partial differential equation (59.2). That is, we write

$$W_m(\mathbf{x}, t) \approx \left[ c_m(\mathbf{x}_1, t); c_m(\mathbf{x}_2, t); \cdots; c_m(\mathbf{x}_r, t); \cdots \right] \quad (59.4)$$

where  $c_m(\mathbf{x}_r, t)$  denotes the  $m$ -th IMF (or IMO solution) decomposed from the measurement at the  $r$ -th sensor position  $\mathbf{x}_r$ . Then, the slowly varying variables are computed straightforwardly through a complexification as

$$\hat{A}_m(\mathbf{x}, t) = \sqrt{W_m(\mathbf{x}, t)^2 + \mathcal{H}[W_m(\mathbf{x}, t)]^2}, \hat{\theta}_m(\mathbf{x}, t) = \tan^{-1} \{ \mathcal{H}[W_m(\mathbf{x}, t)] / W_m(\mathbf{x}, t) \} - \omega_m t \quad (59.5)$$

where  $\mathcal{H}[\cdot]$  denotes Hilbert transformation. Considering the acceleration responses can be approximated as a sum of all IMO solutions, the spatiotemporal slowly varying envelope and phase for the linear beam can be computed as

$$\hat{A}_m(x, t) = \bar{A}_m\phi_m(x)e^{-\zeta_m\omega_m t}, \hat{\theta}_m(x, t) = -\theta_m = \text{constant} \quad (59.6)$$

where  $\phi_m(x)$  is the  $m$ -th mode shape function, and  $\zeta_m$  is the modal damping factor. Therefore, the spatiotemporal slow flow can be obtained as

$$\varphi_m(x, t) = j\omega_m \bar{A}_m\phi_m(x)e^{-j\theta_m}e^{-\zeta_m\omega_m t}, \dot{\varphi}_m(x, t) = -j\zeta_m\omega_m^2 \bar{A}_m\phi_m(x)e^{-j\theta_m}e^{-\zeta_m\omega_m t} \quad (59.7)$$

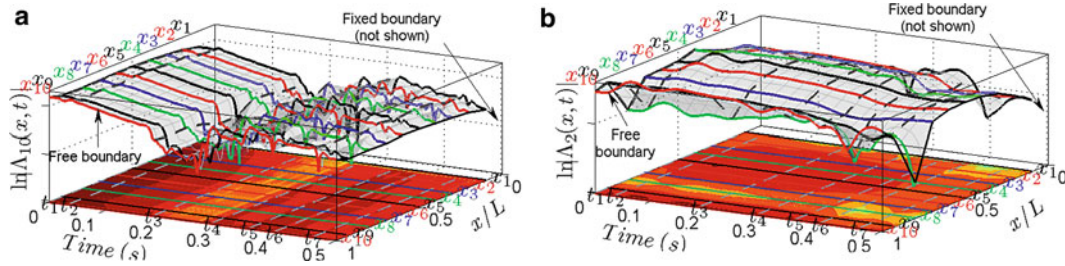


**Fig. 59.2** Construction of  $\ln |\Lambda_m(x, t)|$  from the experimental measurements for the VI beam: (a)  $m = 10$  and (b)  $m = 2$  [20]

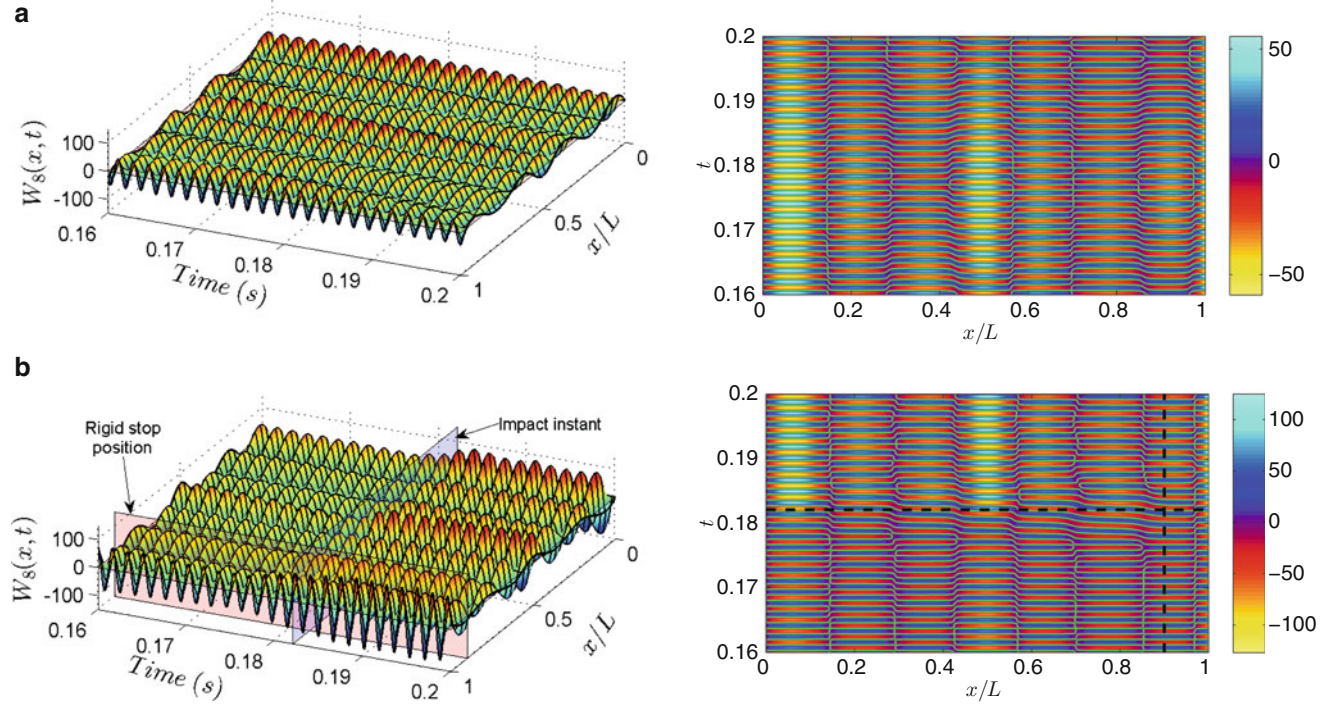


**Fig. 59.3** Spatiotemporal IMO: (a) Linear beam (eighth mode); and (b) VI beam (eighth mode) [20]

Finally, we can derive the complex forcing amplitude in Eq. (59.2) as

$$\Lambda_m(x, t) \approx -j(\hat{\zeta}_m - \zeta_m)\omega_m^2 \bar{A}_m \phi_m(x) e^{-j\theta_m} e^{-\zeta_m \omega_m t} \quad (59.8)$$

Taking the logarithm of the absolute value of both sides of Eq. (59.8) decouples the time-/spatially-dependent variables of such that

$$\ln |\Lambda_m(x, t)| \approx \text{constant} - \zeta_m \omega_m t + \ln |\phi_m(x)| \quad (59.9)$$

where the constant is  $\ln |(\hat{\zeta}_m - \zeta_m)\omega_m^2 \bar{A}_m e^{-j\theta_m}|$ . That is, the spatiotemporal variations of  $\ln |\Lambda_m(x, t)|$  for the linear beam will be linearly decaying in time while keeping the form of the mode shape function at every instant.

Referring to the earlier work [19, 20] regarding the details of EMD analysis of the measured acceleration signals, we now construct this slowly varying forcing amplitude for each nonlinear interaction model from the experimental measurements (cf. Fig. 59.2a, b depict  $\Lambda_m(x, t)$  for the tenth and second modes of the VI beam). The IMOs corresponding to the high-frequency (HF) modes (typically, above the fourth mode) tend to maintain their linear dynamics in between impacts (although the overall dynamics is strongly nonlinear), those for the low-frequency (LF) modes exhibit strongly nonlinear modal interactions independent of vibro-impact patterns in a global fashion [19, 20]. This is because the HF modes are more sensitive to the vibro-impact nonlinearity, whereas the LF modes are insensitive to local changes of the mode shapes due to defects in the structure.

Finally, we construct the spatiotemporal IMO (STIMO) solutions (cf. Fig. 59.3), which may clarify the global and local effects of nonlinear modal interactions in HF and LF IMOs. For example, the eighth STIMO for the linear beam model

in Fig. 59.3a clearly illustrate damped (linear) normal-mode vibrations, whose envelope at each position along the beam decay exponentially while retaining their respective mode-shape forms at each instant; and the corresponding contour plots preserve (almost) straight vertical lines at the nodes. On the other hand, those for the VI beam highlight the VI effects near the impact instants; that is, local instantaneous distortions of the modal properties are evident for HF IMOs (cf. Fig. 59.3b). More global changes (that tend to be insensitive to local VI effects) are predominant for LF IMOs. Such distortions of modal properties seem to prevail near the impact (or structural defect) position  $x_9$  and near each impact instant.

Although representation of the dynamics in the frequency-energy domain has been proved to be a powerful tool for the global approach to NSI [3], a frequency-energy plot contains condensed dynamics information (i.e., it is an implicit representation of specific dynamics such as mode shapes, but carries explicit information mainly about the characteristic frequency and total energy of periodic orbits of the underlying Hamiltonian dynamical system). On the other hand, the spatiotemporal IMOs (or corresponding slow-flow models) can be regarded as an alternative means for global NSI with more specific dynamics information (such as changes in mode shapes and natural frequencies for respective modes) being explicit. Therefore, it will benefit an NSI analysis to implement the FEP together with such spatiotemporal IMOs.

### 59.3 Applications of NSI Results to Damage Identification

We showed that modal characteristics or slow-flow dynamics change in the presence of certain defects (vibro-impacts) in a structure. In particular, qualitative changes seem to be prominent near the nodes of the natural modes closest to the impact position and at the instants of vibro-impacts. Study of such changes in vibration characteristics may illuminate essential features of structures with defects in applications to structural health monitoring (SHM) and damage detection (DD). Numerous methodologies have been implemented for SHM and DD – e.g., statistical pattern recognition algorithms as complementary tools for damage detection in civil structures [21]; substructural damage identification with incomplete structural information [22]; use of guided-wave techniques for estimating damage location [23]; and many other vibration-based damage identification methods [24–29].

In this section, we present the modal assurance criterion (MAC [8]) and the coordinate modal assurance criterion (COMAC [30]) as a tool for damage identification by monitoring mode shapes instantaneously extracted from the NSI results. Indeed, noting that the spatial variations of a spatiotemporal IMO (STIMO) at each instant retain the corresponding mode shape, we can extract the instantaneous mode shape functions from the constructed STIMOs. The MAC is a popular means for diagnosing global changes in vibration characteristics of a structure, and is computed as

$$\text{MAC}(r, s) = \frac{|\phi_r^T \psi_s|^2}{(\phi_r^T \phi_r) (\psi_s^T \psi_s)} \quad (59.10)$$

where  $\phi$  and  $\psi$  denote the discretized mode shape functions (or modal vectors) obtained from theory (or a healthy structure) and experiment (or a damaged structure), respectively; the subscripts denote the orders of the modes; and the superscript ‘T’ denotes the transpose of a vector. Since the MAC essentially computes the correlation between the mode shape functions, its results should be the Kronecker’s delta function of the two mode numbers in a healthy structure (i.e., unity along the diagonal of a MAC matrix with all zero off-diagonal elements). Unless modal analysis of the measured data was done poorly or the measured data were significantly affected by noise, MAC values of less than unity may imply the existence of nonlinearities caused by defects in the structure [8]. Indeed, the MAC values computed at the measurement points close to any nodes of a particular mode are found to be a more sensitive indicator of changes in the mode shape caused by damage [24].

Figure 59.4a, b depict the MAC matrices near the two impact instants in the initial transients. The first few impacts affect mostly the high-frequency modes (above the sixth), whereas the low-frequency modes retain their linear modal properties. This makes sense because nonlinear modal interactions caused by vibro-impacts to which high-frequency modes can be more susceptible are localized in the initial stage of the motion where high-frequency modes are more pronounced. The MAC values for most of the modes become smaller (i.e., globally low correlations between mode shapes due to vibro-impacts are recorded) after the initial VI transients, providing evidence that the effects of vibro-impacts start to prevail over the whole beam; and for some VI instants the linear structure of the beam is not even significantly.

Indeed, the MAC matrix itself does not provide spatial information about where in the structure damage exists. This is because damage is typically a local phenomenon, which can be captured by high-frequency modes; on the other hand, the global behaviors are detected by low-frequency modes [24]. Noting that more energy is required to produce measurable response at higher frequencies, we find that it is more difficult to excite these higher-frequency responses of a structure. These aspects as well as the information loss from time series measurements may cause difficulties for modal-based damage

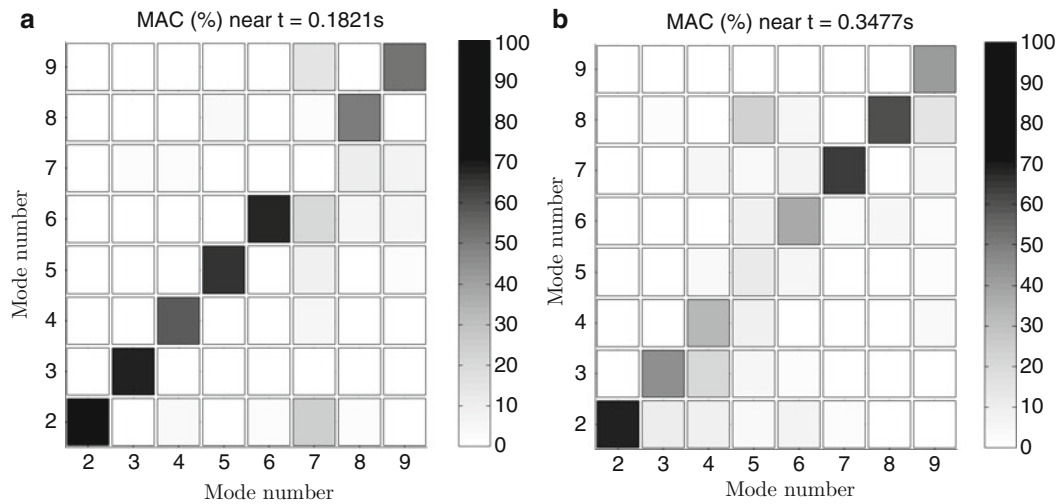
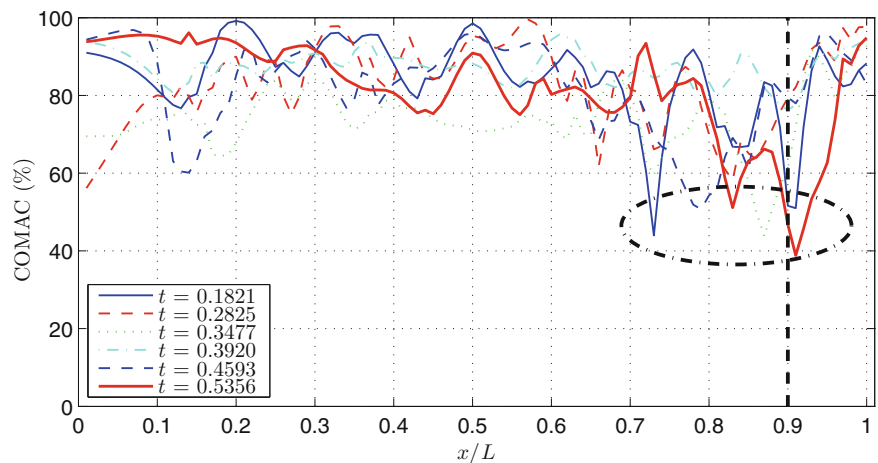


**Fig. 59.4** Modal assurance criterion (MAC) near impact instants: (a)  $t = 0.1821$  s; (b)  $t = 0.3477$  s [20]

**Fig. 59.5** Coordinate modal assurance criterion (COMAC) computed with the instantaneous mode shapes near the impact instants; the vertical dashed line indicates the impact position at  $x_9$  along the beam span [20]



detection. Furthermore, relying on time series can be even more difficult in applications to damage detection, because it is practically easier to make meaningful observations when the damage location is known a priori.

There is often an insufficient number of frequencies with significant changes to determine the location of the damage uniquely. The damage location assurance criterion [27], whose concept is extended from the MAC to measure changes in flexibility of the structure due to defects, is often used as a tool for damage identification; however, this methodology is not appropriate here but is more suitable for finite element updating. Instead, we use the coordinate modal assurance criterion (COMAC [30]), another extension of the MAC. The COMAC is calculated as

$$\text{COMAC}(x_j) = \frac{[\sum_l |\phi_l(x_j)\psi_l(x_j)|]^2}{[\sum_l |\phi_l(x_j)|^2] \cdot [\sum_l |\psi_l(x_j)|^2]} \quad (59.11)$$

which attempts to identify which measurement positions (or DOFs) contribute negatively to a low value of MAC. The coordinate with a lowest COMAC is likely to be near damage, since the most significant contribution is made at the location that corresponds to low-diagonal values in the MAC matrix.

Figure 59.5 depicts the COMAC values near the impact instants of the VI beam, where nonlinearity due to vibro-impacts (i.e., defects) exists at position  $x_9$ . The mode shape distortions due to impacts that contribute to low MAC values are evident in the interval  $x \in (0.75L, 0.95L)$ , which is close to the actual impact position at  $x = 0.9L$ . As a result of the local/global approach to nonlinear system identification considered in this paper, we have demonstrated that the COMAC can be utilized to specify damage location(s), whereas the MAC can be used as an indicator for global structural health monitoring.

## 59.4 Conclusions

We presented nonlinear system identification (NSI) results performed on acceleration signals that were experimentally measured at ten, almost evenly spaced, spanwise positions along a cantilever beam with two rigid stops with clearances to characterize nonlinear dynamics due to vibro-impacts. The NSI methodology is based on the correspondence between analytical and empirical slow-flow dynamics, whose first step requires empirical mode decomposition (EMD) analysis of the measured time series, leading to sets of intrinsic modal oscillators (IMOs) governing the vibro-impact dynamics at different time scales. By comparing the spatiotemporal variations of the nonlinear modal interactions for the vibro-impact beam and those of the underlying linear model (i.e., the beam with no rigid constraints), we found that vibro-impacts significantly influence the lower-frequency modes in a global sense, introducing spatial modal distortions; on the other hand, the higher-frequency modes tend to retain their linear dynamics between impacts being affected in a more instantaneous or localized fashion. In applications of the NSI results to structural health monitoring/damage detection, we calculated typical measures such as the modal assurance criterion (MAC) and the coordinate modal assurance criterion (COMAC) by extracting the instantaneous mode shapes from the spatiotemporal IMO solutions. We confirmed that, whereas the MAC provides global aspects of damage occurrence, the COMAC can narrow down the damage locations. Finally, we introduced the concept of 2-dimensional correlation spectroscopy, which has frequently been used in optical chemistry for SHM/DD.

**Acknowledgements** This work was supported in part by the National Science Foundation of the United States through Grants CMMI-0927995 and CMMI-0928062.

## References

1. Lee YS, Tsakirtzis S, Vakakis AF, Bergman LA, McFarland DM (2009) Physics-based foundation for empirical mode decomposition. *AIAA J* 47:2938–2963
2. Lee YS, Tsakirtzis S, Vakakis AF, McFarland DM, Bergman LA (2010) A time-domain nonlinear system identification method based on multiscale dynamic partitions. *Meccanica* 46:625–649
3. Lee YS, Vakakis AF, McFarland DM, Bergman LA (2010) A global local approach to system identification: a review. *Struct Control Health Monit* 17:742–760
4. Lee YS, Vakakis AF, McFarland DM, Bergman LA (2010) Nonlinear system identification of the dynamics of aeroelastic instability suppression based on targeted energy transfers. *Aeronaut J* 114:61–82
5. Tsakirtzis S, Lee YS, Vakakis AF, Bergman LA, McFarland DM (2010) Modeling of nonlinear modal interactions in the transient dynamics of an elastic rod with an essentially nonlinear attachment. *Commun Nonlinear Sci Numer Simul* 15:2617–2633
6. Huang N, Shen Z, Long S, Wu M, Shih H, Zheng Q, Yen N-C, Tung C, Liu H (1998) The empirical mode decomposition and the Hilbert spectrum for nonlinear and non-stationary time series analysis. *Proc R Soc Lond Ser A. Math Phys Sci* 454:903–995
7. Brandon JA (1998) Some insights into the dynamics of defective structures. *Proc Inst Mech Eng Part C: J Mech Eng Sci* 212:441–454
8. Ewins DJ (1990) *Modal testing: theory and practice*. Research Studies Press, UK
9. Kerschen G, Golinval J-C, Vakakis AF, Bergman LA (2005) The method of proper orthogonal decomposition for order reduction of mechanical systems: an overview. *Nonlinear Dyn* 41:147–170
10. Feeny BF, Kappagantu R (1998) On the physical interpretation of proper orthogonal modes in vibrations. *J Sound Vib* 211:607–616
11. Kerschen G, Golinval JC (2002) Physical interpretation of the proper orthogonal modes using the singular value decomposition. *J Sound Vib* 249:849–865
12. Ma X, Azeez MFA, Vakakis AF (2000) Non-linear normal modes and non-parametric system identification of non-linear oscillators. *Mech Syst Signal Process* 14:37–48
13. Georgiou I (2005) Advanced proper orthogonal decomposition tools: using reduced order models to identify normal modes of vibration and slow invariant manifolds in the dynamics of planar nonlinear rods. *Nonlinear Dyn* 41:69–110
14. Galvanetto U, Surace C, Tassotti A (2008) Structural damage detection based on proper orthogonal decomposition: experimental verification. *AIAA J* 46:1624–1630
15. Cusumano JP, Bae B-Y (1993) Period-infinity periodic motions, chaos, and spatial coherence in a 10 degree of freedom impact oscillator. *Chaos Solitons Fractals* 3:515–535
16. Cusumano JP, Sharkady MT, Kimble BW (1994) Experimental measurements of dimensionality and spatial coherence in the dynamics of a flexible-beam impact oscillator. *Philos Trans R Soc Ser A* 347:421–438
17. Ritto TG, Buezas FS, Sampaio R (2011) A new measure of efficiency for model reduction: application to a vibroimpact system. *J Sound Vib* 330:1977–1984
18. Azeez MFA, Vakakis AF (2001) Proper orthogonal decomposition (POD) of a class of vibro-impact oscillations. *J Sound Vib* 240:859–889
19. Kurt M, Chen H, Lee YS, McFarland DM, Bergman LA, Vakakis AF (2012) Nonlinear system identification of the dynamics of a vibro-impact beam: numerical results. *Arch Appl Mech* 82:1461–1479
20. Chen H, Kurt M, Lee YS, McFarland DM, Bergman LA, Vakakis AF (2012) Experimental system identification of the dynamics of a vibro-impact beam with a view towards structural health monitoring and damage detection. *Mech Syst Signal Process*, in review
21. Yao R, Pakzad SN (2012) Autoregressive statistical pattern recognition algorithms for damage detection in civil structures. *Mech Syst Signal Process* 31:355–368

22. Le J, Law SS Substructural damage detection with incomplete information of the structure. *J Appl Mech Trans ASME* 79:041003-1-10
23. Flynn EB, Todd MD, Wilcox PD, Drinkwater BW, Croxford AJ (2011) Maximum-likelihood estimation of damage location in guided-wave structural health monitoring. *Proc R Soc Lond Ser A. Math Phys Sci* 467:2575-2596
24. Doebling SW, Farrar dR, Prime MB, Shevitz DW (1996) Damage identification and health monitoring of structural and mechanical systems from changes in their vibration characteristics: a literature review, Los Alamos National Laboratory Report (LA-13070-MS)
25. Kim B-H, Stubbs N, Sikorsky C (2002) Local damage detection using incomplete modal data. In: *Proceedings of IMAC-910 XX 202*, 4-7 Feb 2002, the Westin Los Angeles Airport, Los Angeles, CA
26. Wang L, Yang Z, Waters TP (2010) Structural damage detection using cross correlation functions of vibration response. *J Sound Vib* 329: 5070-5086
27. Messina A, Williams EJ, Contursi T (1998) Structural damage detection by a sensitivity and statistical-based method. *J Sound Vib* 216:791-808
28. Fan W, Qiao P (2011) Vibration-based damage identification methods: a review and comparative study. *Struct Health Monit* 10:83-111
29. Farrar CR, Doebling SW, Nix DA (2001) Vibration-based structural damage identification. *Proc R Soc Lond Ser A. Math Phys Sci* 359:131-149
30. Lieven NAJ, Ewins DJ (1988) Spatial correlation of mode shapes, the coordinate modal assurance criterion (COMAC). In: *Proceedings of the 4th international modal analysis conference*, Los Angeles, CA, pp 690-695

# Chapter 60

## Continuous Scanning for Acoustic Field Characterization

Carlos E. Garcia, Sriram Malladi, and Pablo A. Tarazaga

**Abstract** The work herein presents a novel approach for sound field characterization based on a continuous scanning/roving approach. Conventional methods use sensor arrays or a discreet moving sensor to characterize an acoustic field. Although these methods are well established, this new approach attempts to take advantage of a continuous measurement methodology, in space and time, in order to increase spatial resolution of the acoustic field, minimize the use of sensors required, and the acquisition time. The novel approach relies on processing amplitude-modulated time signal, with geometrical reference, in order to characterize the acoustic field. This technique can be thought of as an extension of continuous scanning laser Doppler vibrometry techniques.

The work is demonstrated on a lab test article and used to identify the acoustic propagation generated by the excitation of several structural modes. The work shown here is preliminary and mainly aimed at proving the methods feasibility.

**Keywords** Continuous scanning • Vibro-acoustics • Acoustic field

### 60.1 Introduction

The need for even greater accuracy, higher fidelity data and reduced testing time requires the use of novel methods in testing and data acquisition. With such needs being driven by various motivations such as better models due to the readily available computational power (i.e. high fidelity FE models [1, 2]) creating a need for high fidelity testing for accurate correlation and verification of such models, there is an increasing demand to improve on current methodologies of testing. Testing is becoming increasingly costly and methods that can reduce the testing time bring forth cost reduction and are highly attractive. With some of these aspects in mind, the work herein explores the extrapolation of continuous scanning laser Doppler vibrometry (CSLDV) into the acoustic domain.

The methodology of CSLDV is presented in [3] and forms the basis for the extension of the work presented herein for an acoustic field. As CSLDV grows in popularity as seen in [4–7] much of its potential is realized. Initially used to identify single modes at a time the technique has been extended to multi-tone excitation [5, 8] in order to identify several modes at once, to only consider output only data [9, 10] and even for damage detection [11]. The technique presented here is preliminary, but offers the potential to be extended in much the same way.

The first part of this paper focuses on the technique used in order to obtain an amplitude-modulated time signal through a scanning microphone. The experimental setup is explained in detail as well as the approach used to obtain such data. In the second part of this paper, the experimental data is processed in two different ways in order to extract a pressure profile produced by a vibrating structure. The profile is measured from a structure whose structural modes are known and previously

---

C.E. Garcia

Visiting Scholar at Virginia Tech, Ingenieria Electromecanica, Facultad de Ingenieria y Ciencias Economico Sociales, Universidad Nacional de San Luis, Villa Mercedes, 5730, San Luis, Argentina  
e-mail: [cegarcia@vt.edu](mailto:cegarcia@vt.edu)

S. Malladi • P.A. Tarazaga (✉)

Mechanical Engineering Department, Center for Intelligent Materials Systems and Structures, Virginia Tech, 310 Durham Hall, Blacksburg, VA 24061, USA  
e-mail: [pablot@vt.edu](mailto:pablot@vt.edu)

measured. This is done in order to have prior knowledge of the expected pressure profile before the method is generalized; given that the pressure distribution is a result of the acoustic energy radiated to the near field through the velocity profile of the structure.

The work demonstrated here is preliminary and mainly aimed at showing the potential of such a technique.

## 60.2 Methodology

The methodology, which will be considered an extension of CSLDV methods, as derived in [3], utilizes a single sensor to describe the spatial “Operation Deflection Shape (ODS) [12].” Notice that here the term ODS is placed in quotation marks as the acoustic radiation performed by the structural element being excited is not truly an ODS, but an acoustic radiation to the near field associated to a structural ODS. This could be thought of as an ODS if, for example, the domain being measured were an enclosed cavity. Having said that, the near field acoustics can behave in much the same way as the structural modes. Thus, this might be better defined as a continuous version of near-field acoustic holography (NAH) [13] or CNAH.

The acoustic pressure pulse of a vibrating structure is generated by the change in velocity of the structure. The near distance acoustic pressure field captured by a microphone scanning a beam excited sinusoidally at a frequency  $\omega$  subsumes the velocity profile of the structure along the scan line. This acoustic pressure distribution ( $W_y$ ), in y-direction, at a distance  $x$  along the scan line is expressed as:

$$W_y = W_R \cos \omega t + i W_I \sin \omega t \quad (60.1)$$

where  $W_R$  and  $W_I$  are the real and imaginary components of the vibration, respectively.

The acoustic reading is performed through a sinusoidal sweep. The sinusoidal sweep avoids the end point discontinuities by reducing the sweep velocity to zero at the ends of the scan. The motion of the microphone mounted on a stage sinusoidally sweeping at a frequency  $\Omega$  is given by:

$$v = A \sin \Omega t \quad (60.2)$$

The position of the microphone along the scan line at any time  $t$  is expressed as:

$$x = \frac{A}{\Omega'} (\cos^2(\Omega' t + \beta)) \quad (60.3)$$

where the half sweep frequency  $\Omega' = \Omega/2$  and the phase angle  $\beta = -\pi/2$ .

The spatial shape contributions,  $W_R(x)$  and  $W_I(x)$ , due to the acoustic pressure distribution, can be expressed as a Fourier expansion along the scan line. Scanning a beam excited at  $\omega$  at a sweeping frequency  $\Omega$  gives rise a  $(2m-1)$  peaks at frequencies  $(\omega \pm n \Omega)$ . Assuming the operational deflection shape of the beam is smooth and has a continuous pattern, it can be described as a polynomial of degree  $m-1$ . The acoustic field radiated in the y-direction can be characterized by a Fourier series consisting of the real and imaginary components as:

$$\begin{aligned} W_R(x) &= \sum_{n=0}^{m-1} W_{Rn} x^n \\ W_I(x) &= \sum_{n=0}^{m-1} W_{In} x^n \end{aligned} \quad (60.4)$$

where  $x$  is the position vector of all the points on the beam along the scan line.

Substituting Eqs. 60.3 and 60.4 in Eq. 60.1 the distribution can be described with the equation:

$$W_y = \sum_{n=0}^{m-1} W_{Rn} \cos^{2n}(\Omega' t + \beta) \cos \omega t + i \sum_{n=0}^{m-1} W_{In} \cos^{2n}(\Omega' t + \beta) \sin \omega t \quad (60.5)$$

Upon trigonometric expansions and simplification Eq. 60.5 can be written in terms of the peak amplitudes  $A_n$  of the spectrum sidebands at frequencies  $(\omega \pm n \Omega)$  as:



$$W_y = \sum_{n=0}^{m-1} A_{Rn} \cos[(\omega \pm n\Omega) t] + i \cdot \sum_{n=0}^{m-1} A_{In} \sin[(\omega \pm n\Omega) t] \tag{60.6}$$

Further simplifying the coefficients of the pressure distribution,  $W_{Rn}$  and  $W_{In}$  are related to the sideband amplitudes  $A_n$  by a transformation matrix T as:

$$[W]_{m \times 1} = [T]_{m \times m} [A]_{m \times 1} \tag{60.7}$$

Thus, the coefficients  $A_n$  can be obtained by analyzing the spectrum obtained from the amplitude-modulated signal in order to reconstruct the experimental pressure distribution.

### 60.3 Experimentation

In order to demonstrate the feasibility of this methodology a benchmark experiment has been constructed. The following section describes the experimental setup, the methodology and the initial results.

This experiment uses a linear actuator connected to a microphone in order to perform the physical continuous scan. It should be noted that this testing methodology does not expect limitations by the scanning pattern as this can be represented in the formulation regardless of path. Having said that, unlike how the actual scan is performed in CSLDV, using a straightforward angle change of the mirrors, this technique is considerably more challenging in that aspect as it requires the physical movement of a microphone.

#### 60.3.1 Experimental Setup

The experiment structure is an aluminum beam with clamped-clamped boundary conditions. A schematic of the experimental setup can be seen in Fig. 60.1. The beam was excited using a bonded piezoceramic wafer located close to one of the boundaries. The source of excitation was provided via a signal generator (Agilent 33120A) and amplified (HP 6528A amplifier) before reaching the piezoceramic.

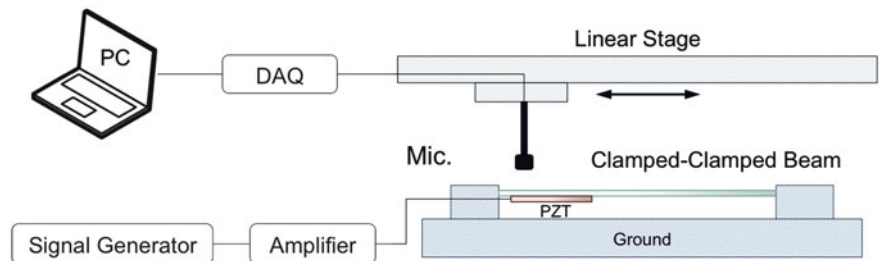


Fig. 60.1 Experimental schematic

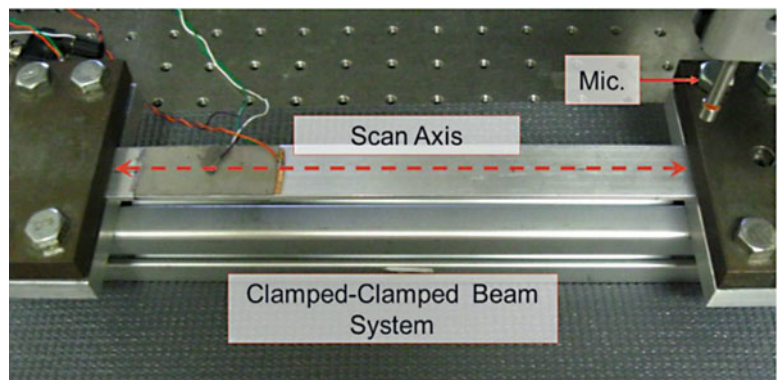
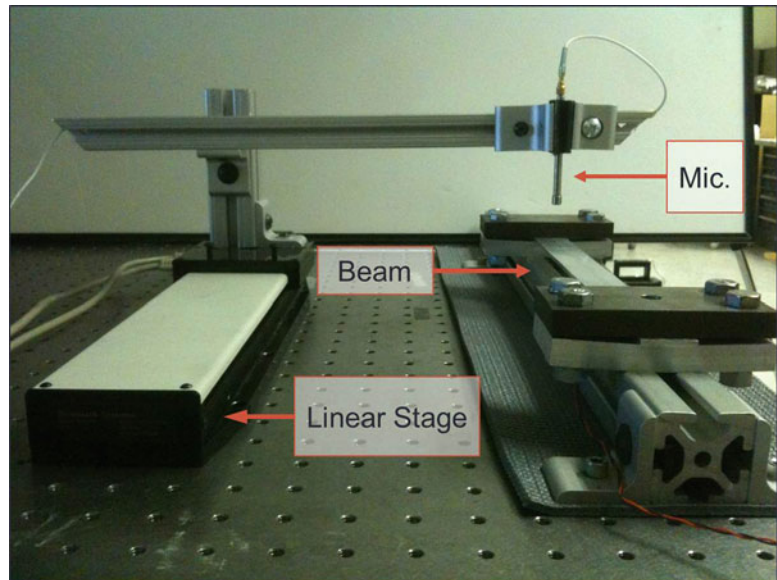


Fig. 60.2 Clamped-clamped beam augmented with a piezoceramic for actuation

**Fig. 60.3** Side view of test setup. Left linear stage with microphone. Right, clamped-clamped beam



**Table 60.1** Experimental properties of the structure

Beam characteristics	
Length (m)	0.244
Width (m)	0.0254
Height (mm)	3.08
Young's modulus (MPa)	68.9
Density (kg/m <sup>3</sup> )	2,700

The beam was attached to a vibration isolation table (Newport STS) in order to reduce disturbances from outside sources. The actual experiment can be observed in Figs. 60.2 and 60.3 through a top view and side view, respectively. Figure 60.2 illustrates the clamped-clamped structure attached to the vibration isolation table and demonstrates the scan axis for the SLDV as well as for the microphone (PCB Model# 130E20). Note that the microphone is approximately 3 cm above the beam, but follows the same scan pattern. Figure 60.3 demonstrates how the microphone is attached to the linear stage (Newmark Model # NLS4-10-25) and runs parallel to the beam. As the microphone is scanned over the surface of the beam data is gathered by a data acquisition system (National Instruments NI9233). A table with the properties of the structure is listed in Table 60.1.

Initially the system was dynamically characterized with a Polytec Scanning Laser Vibrometer (SLDV) PSV-400 in order to identify the first three modes of vibration. The laser was used to obtain the first three natural frequencies and corresponding operation deflection shapes of the test structure.

Table 60.2 and Fig. 60.4 show the experimental results obtained from the SLDV. Note in Fig. 60.4 that the circular data points correspond to the actual data collected and the lines are a spline fit to aid in the mode visualization (not to be confused with a CSLDV approach).

### 60.3.2 Testing Procedures and Preliminary Results

In order to obtain the required data the linear stage is fed with a voltage signal proportional to a sine wave. An example of the signal is seen in Fig. 60.5. In this case, unlike CSLDV, the velocity profile was defined, as described in Eq. 60.2, and the displacement is shown here as well for completeness.

This will allow the microphone to follow the scan axis as described in Figs. 60.1, 60.2 and 60.3.

**Fig. 60.4** First three experimental operation deflection shapes of a clamped-clamped beam

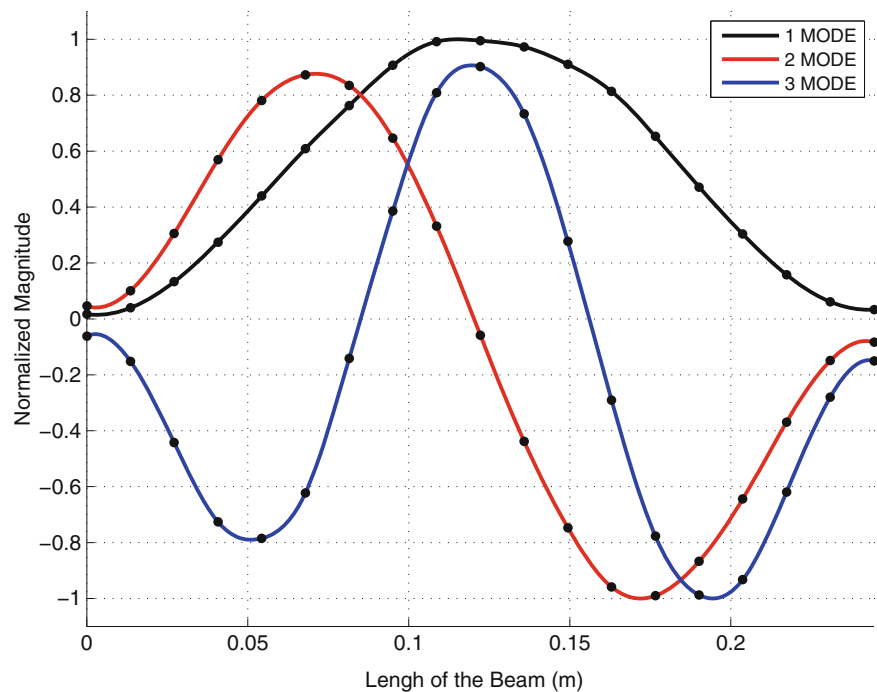


**Table 60.2** Experimental modes of the clamped-clamped beam

	Mode 1	Mode 2	Mode 3
Freq (Hz)	236.5	636.2	1277.8

### 60.3.2.1 Obtaining Pressure Distributions Using a Scanning Microphone

The scans are performed when the beam is excited at one of the three resonant frequencies of the beam. The results of modes 1, 2 and 3 can be observed in Figs. 60.6, 60.7 and 60.8, respectively. Due to the noisy environment surrounding the test article the data was filtered using a band-pass filter for each mode. Both sets of data are shown in the figures. Given our proximity to the beam it is possible to relate the data pattern to the structural mode. The authors would like to make clear at this point that it is not the intention of this method to characterize the structural modes of the beam, but the acoustic radiation. The scan was performed at specific modes in order to have a reference of what the acoustic radiation would be when scanned. Given that the acoustic radiation in a structural-acoustic coupled system [14] is related the velocity profile of the structure, this then serves as a control of sorts in what to expect.

Further analyzing of Fig. 60.6 shows that as mode 1 is excited in the beam an acoustic representation can be generated as the microphone sweeps over the structure. The microphone sweeps left to right and then returns to its initial location from right to left, thus two shapes can be reconstructed from one the sweep. Thus, both ends of the figure represent relatively the same location.

In the same manner as before modes 2 and 3 are excited individually and the microphone is swept to scan the field.

The data seen here can be fitted by a simple demodulation fit applied to the envelope. For the first mode, Fig. 60.9 illustrates the comparison of the theoretical mode of a clamped-clamped beam (—), the experimental ODS of the beam (—) as measured by the laser, the acoustic experimental data (—), and the fitted approximation using the acoustical data (—). From this figure it can be observed that the acoustic radiation follows very closely the pattern of the structural mode with some discrepancies occurring at the boundaries.

These discrepancies are more evident in modes 2 and 3 shown in Figs. 60.10 and 60.11, respectively. Also observed in these figures is the asymmetry in these modes. This asymmetry is evident in the structural ODS and is consistent in the microphone measurements.

**Fig. 60.5** Signal used to obtain a scanning pattern on the beam using a linear stage

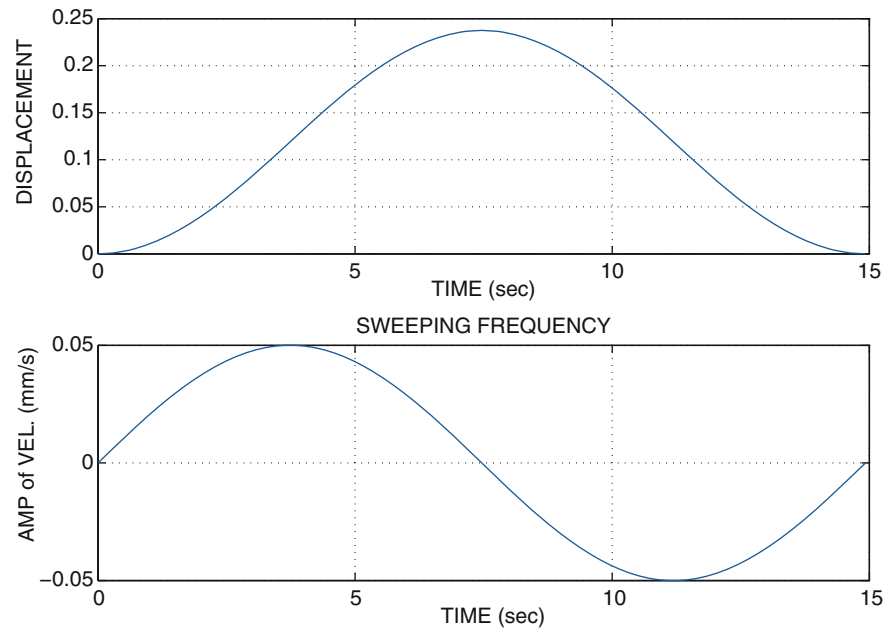
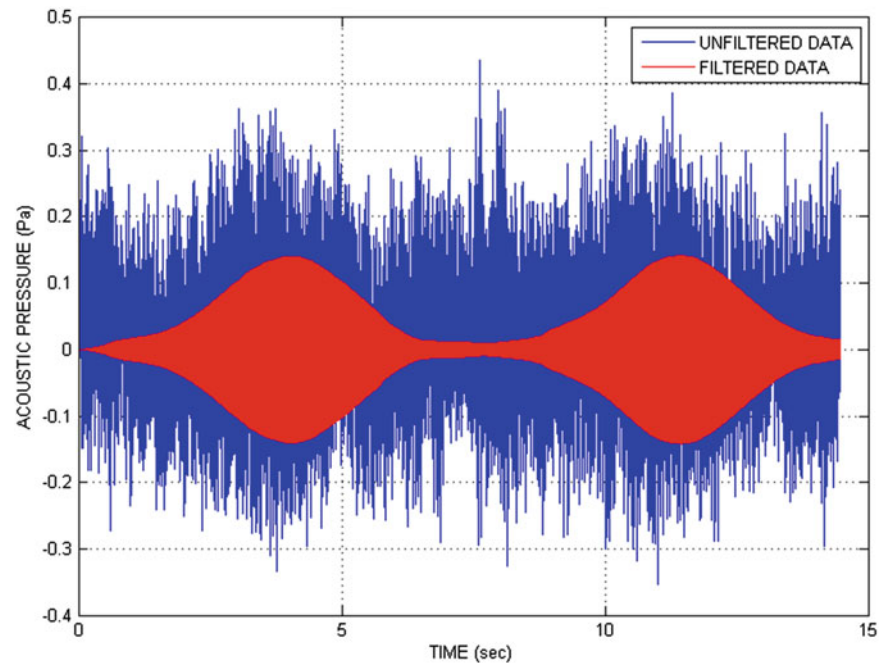


**Fig. 60.6** Pressure reading obtained from the scanning microphone for the first resonant frequency



### 60.3.2.2 Spectrum Data Gathered via Continuous Scan

Although only one full sweep is shown for each of the modes (from one end of the beam to the other and back) several sweeps were used to calculate the spectrum of the following figures in order to obtain the required frequency resolution of the spectrum (only the unfiltered data was used for this analysis). Figs. 60.12, 60.13 and 60.14 show the frequency spectrum for modes 1 through 3, respectively. Of interest is the observation that mode 1 has reoccurring peaks at  $\omega \pm 2n \Omega$ , instead of the expected  $\omega \pm n \Omega$ . Further investigation needs to be carried out in order to understand these results. The unsymmetrical behavior of the modes can also be observed here, as the amplitude of the side bands is not symmetrical about  $\omega_n$ .

It can also be observed from these results that as the complexity of the mode increases the spectrum yields more coefficients for the polynomial fit as expected.

**Fig. 60.7** Pressure reading obtained from the scanning microphone for the second mode

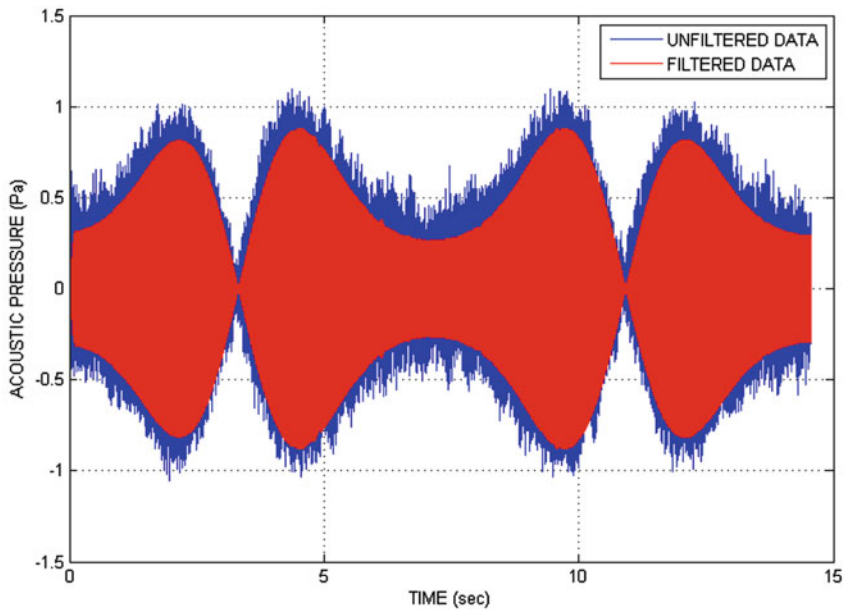
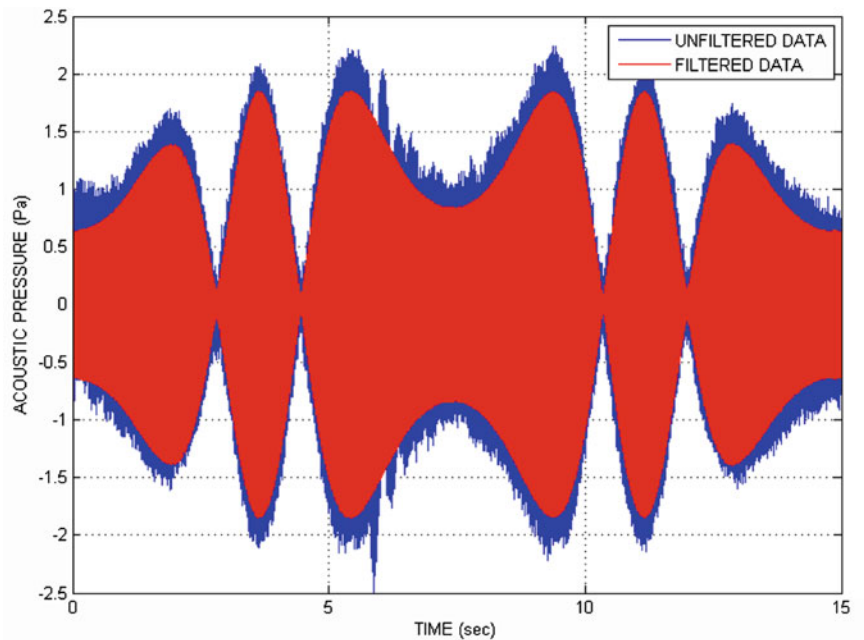


**Fig. 60.8** Pressure reading obtained from the scanning microphone for the third mode



Using the side band amplitudes from these figures the response can be reconstructed using Eqs. 60.5 and 60.7. Figure 60.15 shows the first mode reconstruction using the side band amplitudes. It is evident that the reconstructed shape falls short of the expected behavior including the lack of zero slope condition at the boundaries. It is thought that the missing amplitude terms would have the required information needed to accomplish this since they are the magnitude coefficients pertaining to the odd powered polynomial expansions. Further investigation is required on these findings.

Unlike mode 1, the reconstruction of modes 2 and 3 appear to be more representative of the expected shape as seen before. The shapes are also able to reproduce the unsymmetrical features of the data as observed in the previous figures. Mode 2 also suffers from inadequate boundary representation unlike mode 3, which is the best of all three cases. It is believed that sufficient terms have been taken in order to represent the modes accurately and consequent errors are not related to this fact (Figs. 60.16 and 60.17).

**Fig. 60.9** Comparison of the structural modes and the acoustic radiation for mode 1

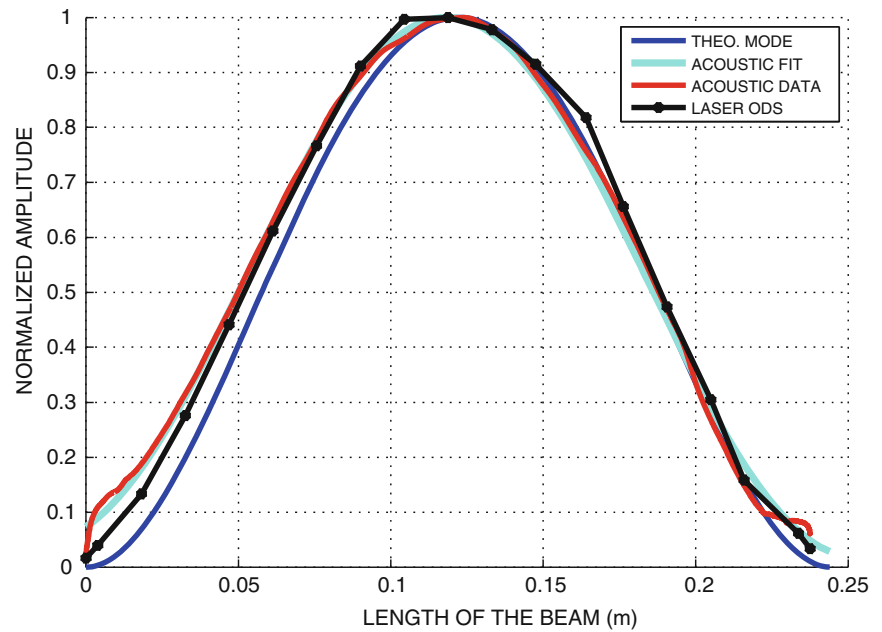
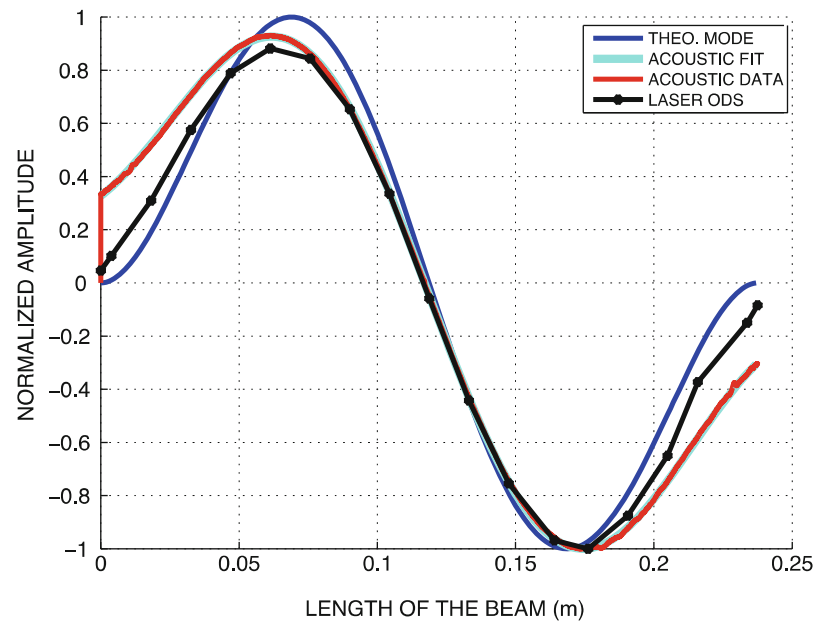


**Fig. 60.10** Comparison of the structural modes and the acoustic radiation for mode 2



## 60.4 Summary

The preliminary results and analysis show that the method has potential to describe and characterize an acoustic field via a single sensor. The technique offers advantages such as high spatial resolution describing the acoustic field, reduction in the amount of sensors required as well as the ability to reduce testing time.

**Fig. 60.11** Comparison of the structural modes and the acoustic radiation for mode 3

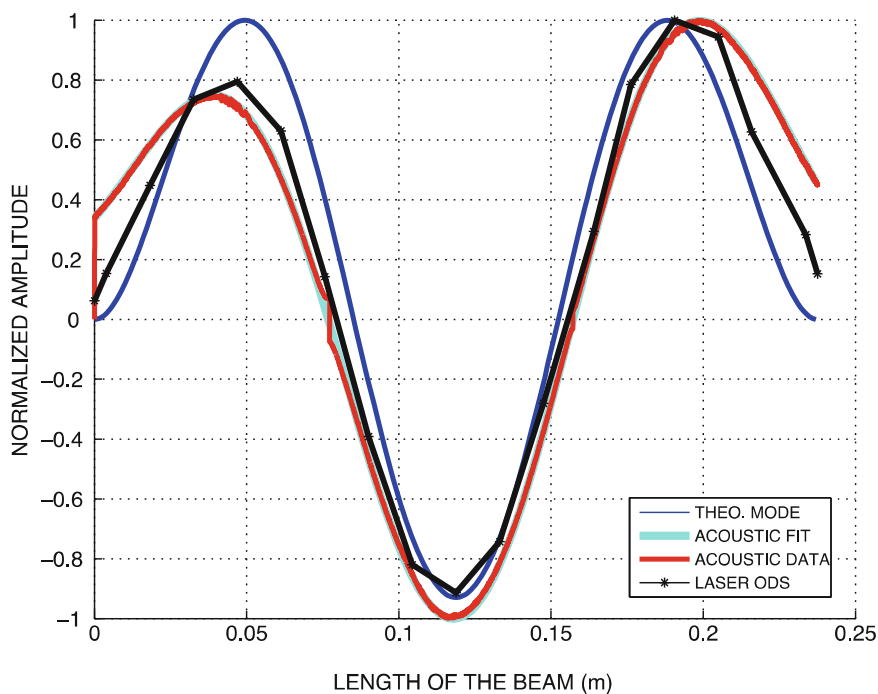
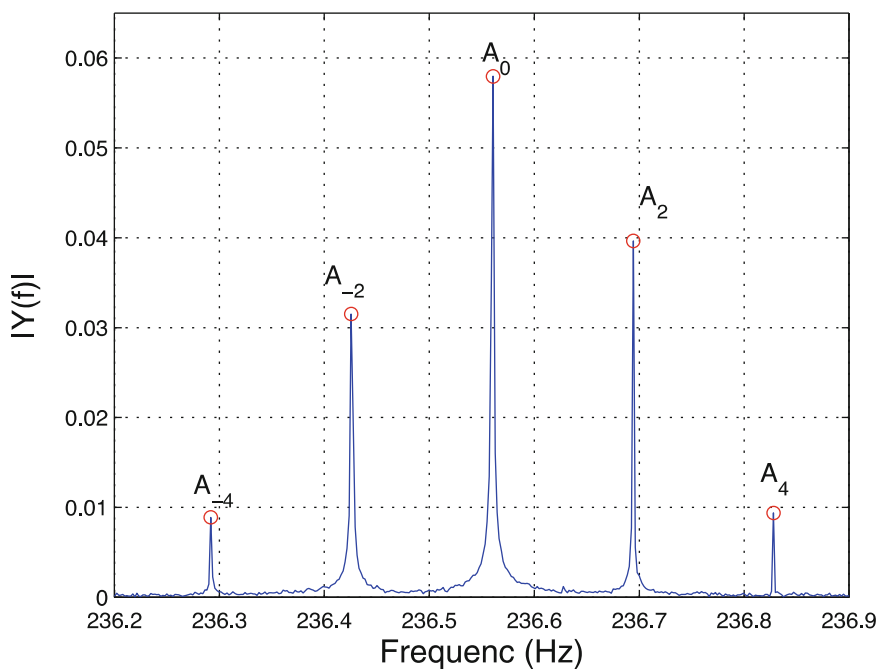


**Fig. 60.12** Output spectrum signal measured above the beam using the microphone continuous scan method for mode 1



The method is yet to be compared to standard methods as well as to theoretical predictions and is left as part of future work to be carried out. The full extension to the CSLDV method requires further analysis, but proves to show the same trends as in CSLDV and has demonstrated feasibility.

**Acknowledgements** The authors would like to thank Dr. Dario DiMaio and Prof. Ewins from the University of Bristol for the fruitful discussion that led to this work.

**Fig. 60.13** Output spectrum signal measured above the beam using the microphone continuous scan method for mode 2

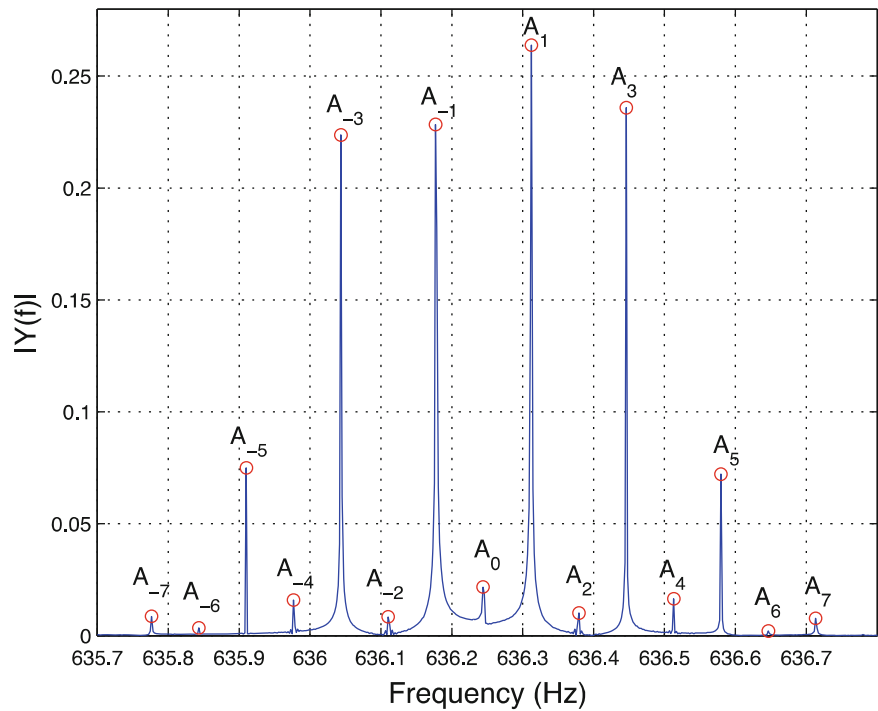
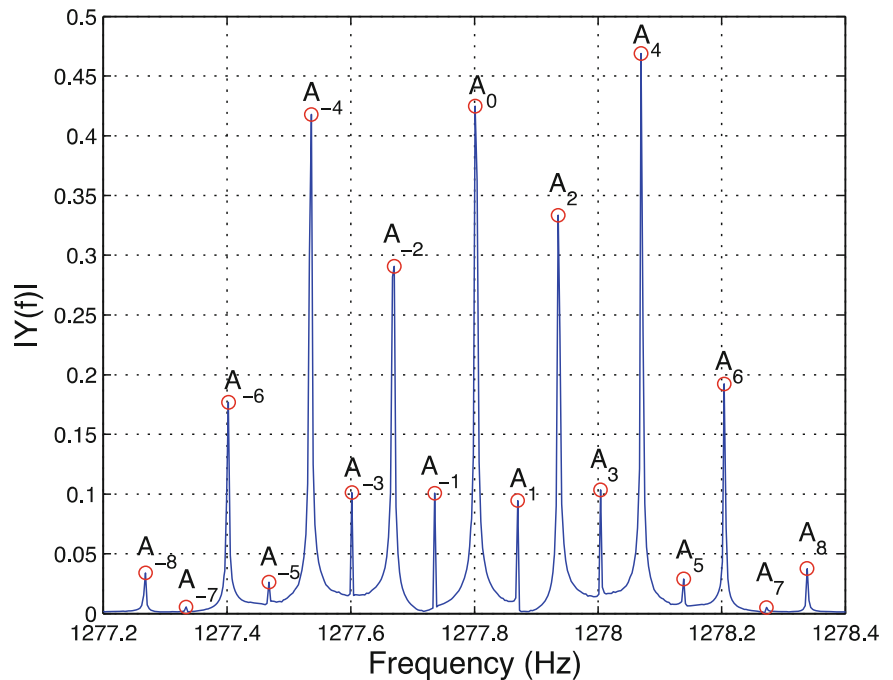


**Fig. 60.14** Output spectrum signal measured above the beam using the microphone continuous scan method for mode 3



## References

1. Garcia JV (2008) Development of valid models for structural dynamics analysis. In: Mechanical engineering 2008. Imperial College London, London, p 238
2. Garcia JV, Ewins DJ (2006) Test strategy for aero-engine structural dynamic model validation. In: Proceedings of the international seminar on modal analysis, ISMA. Leuven
3. Stanbridge AB, Ewins DJ (1999) Modal testing using a scanning laser doppler vibrometer. Mech Syst Signal Process 13(2):255–270
4. Maio DD (2007) Sldv technology for measurement of mistuned bladed disc vibration. In Mechanical engineering 2007. Imperial College of Science, Technology & Medicine University of London, London, p 191



**Fig. 60.15** Mode 1 reconstruction using the polynomial fit and side band amplitude

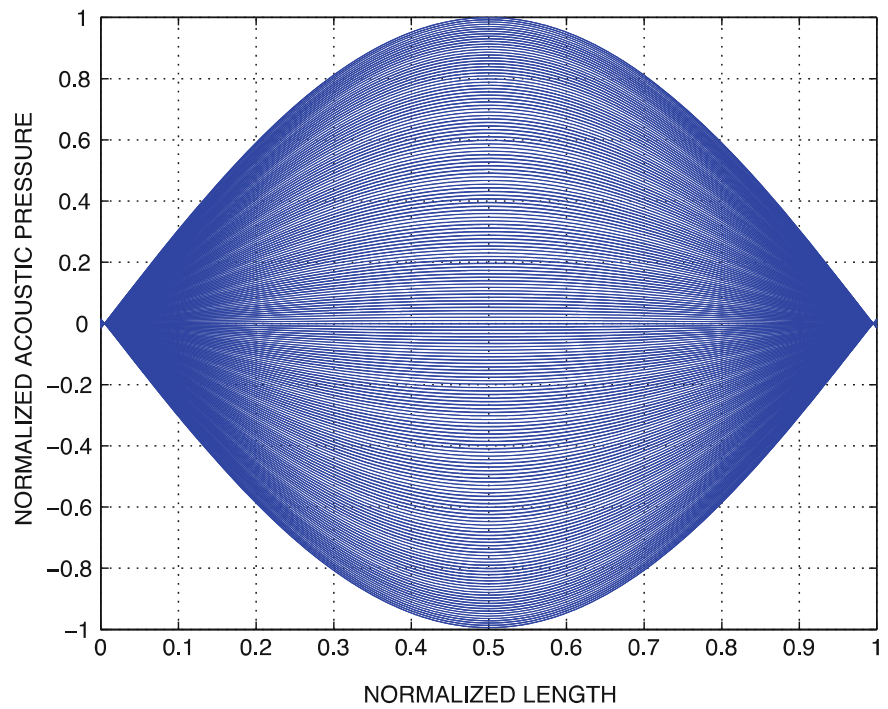
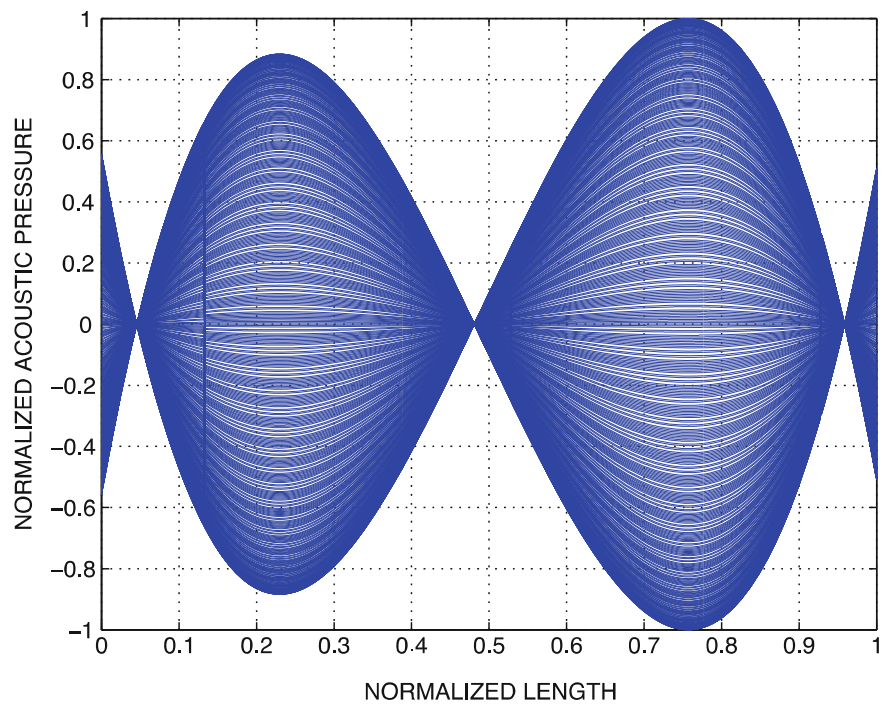
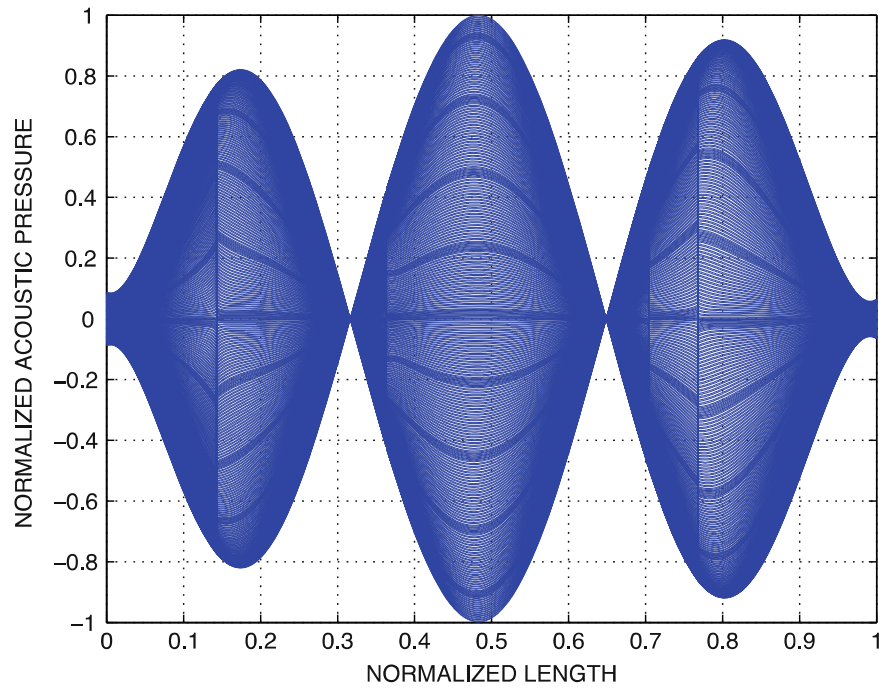


**Fig. 60.16** Mode 2 reconstruction using the polynomial fit and side band amplitude



5. Di Maio D, Ewins DJ (2011) Continuous Scan, a method for performing modal testing using meaningful measurement parameters; Part I. *Mech Syst Signal Process* 25(8):3027–3042
6. Martarelli M (2001) Exploiting the laser scanning facility for vibration measurements. In: *Mechanical engineering 2001*. Imperial College of Science, Technology & Medicine University of London, London, p 373
7. Stanbridge AB, Martarelli M, Ewins DJ (2004) Measuring area vibration mode shapes with a continuous-scan LDV. *Measurement* 35(2): 181–189
8. Tarazaga PA et al. (2012) Continuous laser scanning of a lightweight membrane with monotone and multi-tone excitation techniques. In: *Proceedings, 53rd AIAA/ASME/ASCE/AHS structures, structural dynamics and materials conference (SDM)*. American Institute of Aeronautics and Astronautics (AIAA), Honolulu

**Fig. 60.17** Mode 3 reconstruction using the polynomial fit and side band amplitude



9. Yang S, Allen M (2011) Output-only modal analysis using continuous-scan laser doppler vibrometry and application to a 20 kW wind turbine. In: Proulx T (ed) Modal analysis topics, vol 3. Springer, New York, pp 47–64
10. Yang S, Allen MS (2012) Output-only modal analysis using continuous-scan laser doppler vibrometry and application to a 20 kW wind turbine. Mech Syst Signal Process 31:228–245
11. Khan AZ, Stanbridge AB, Ewins DJ (2000) Detecting damage in vibrating structures with a scanning LDV. Opt Lasers Eng 32(6):583–592
12. Richardson MH (1997) Is it a mode shape, or an operating deflection shape? Sound Vib 30:54–61
13. Maynard JD, Williams EG, Lee Y (1985) Nearfield acoustic holography: I. Theory of generalized holography and the development of NAH. J Acoust Soc Am 78(4):1395–1413
14. Tarazaga PA, Johnson ME, Inman DJ (2012) Vibro-acoustics of a pressurized optical membrane. Mech Syst Signal Process 30:373–392

# Chapter 61

## Operating Deflection Shapes of a Violin String via High Speed/High Resolution Videography

Chuck Van Karsen, Troy Bouman, and Geoff Gwaltney

**Abstract** The action of bowing a violin string to play a properly sounding note produces a stick-slip action between the bow and the string. In an ideal situation this excitation of the string results in Helmholtz motion of the string. This paper describes an experimental method for measuring the motion of a violin string using high speed/high resolution videography and the subsequent digitizing of the motion for use in a high fidelity mathematical model of a violin.

**Keywords** Videography • ODS • Violin • Vibration • Musical instrument

### 61.1 Introduction

Violins crafted by eighteenth-century Italian violin makers are still considered the finest in the world today. The greatest of these are the instruments of Antonio Stradivari (1644–1737). Unfortunately, the trade secrets of these masters have been lost to the ages. Even the best violinmakers of today; though they have produced some excellent quality instruments, have not been able to match those of Stradivari and his contemporaries. In an effort to determine the properties that make the violins of Antonio Stradivari among the best in the world, a project is underway to reverse engineer (build an analytical model) one of the great master’s instruments. Building a model that will be useful in understanding the characteristics of these violins requires knowledge of the geometry, material properties, and construction techniques [2, 3]. The ultimate goal of the project will be to ‘play’ the violin model and produce sound. This will require ‘input loads’ from the strings at the bridge and neck of the instrument.

A method that is being considered for ‘playing’ the analytical model is to use the displacement of a string as the input to the model. This forced displacement condition (a function of time) will be applied as nodal displacements to the portion of the model that represents the strings. This displacement function could be determined theoretically [5] or obtained experimentally by measuring string deflection as it is being bowed. This paper describes an experimental method for measuring the motion of a violin string using high speed/high resolution videography while being bowed.

Operating Deflection Shape (ODS) analysis is typically used to determine the motion of a structure during operation. The motion can be viewed in either the time or frequency domain [4]. In the case of the violin string, the deflection of several

---

C.V. Karsen (✉)

Associate Professor, Mechanical Engineering, Michigan Technological University, 1400 Townsend Dr., Houghton, MI 49931, USA  
e-mail: [cdvankar@mtu.edu](mailto:cdvankar@mtu.edu)

T. Bouman

Student, Mechanical Engineering, Michigan Technological University, 1400 Townsend Dr., Houghton, MI 49931, USA

G. Gwaltney

Senior Research Engineer, Keweenaw Research Center, Mechanical Engineering, Michigan Technological University,  
1400 Townsend Dr., Houghton, MI 49931, USA  
e-mail: [gdgwaltn@mtu.edu](mailto:gdgwaltn@mtu.edu)

points along the length of the string must be recorded as a force (e.g. bowing) is applied to the string. Typically motion transducers such as accelerometers or laser vibrometers are used for this purpose. In this case high speed/high resolution videography is used to record the motion of a large portion of the string simultaneously. Image processing is then used to track the deflection of several points along the string as a function of time.

The motion of the rosin coated horse hair bow as it moves across the string creates a stick-slip condition. Ideally, this condition causes the string to move in a Helmholtz type motion as shown in Fig. 61.9. This motion is a result of the bow grabbing the string (stick) and pulling the string until the forces acting against the bow overcome the grabbing force and the slip phase begins. The string will then proceed to slide along the bow until it is grabbed and the stick phase begins again. The rosin, in this case, helps to create a more significant difference between the coefficient of static and kinetic friction linking the bow and string [5].

## 61.2 Testing

High speed/high resolution videography of the vibrating string was accomplished using a Photron Fastcam SA1.1 camera. The camera is capable of operating with a resolution of  $1,024 \times 1,024$  at frame rates up to 7,500 fps. The video was recorded using Photron Fastcam Viewer (PFV) software. Figure 61.1 shows an example of the recording software, PFV, being used to playback a recorded AVI file.

During the testing, the data were recorded at 6,250 fps. The data were then imported into ProAnalyst (provided by Xcitex Inc.) [6] for motion analysis. Figure 61.2 shows an example of the recorded file in the ProAnalyst software.

A sketch of the testing configuration used to acquire the video is shown in Fig. 61.3. One of the key assumptions in this testing is that the string moves in the plane perpendicular to the focal axis of the camera. In order to reduce the error from this assumption, the bow was kept parallel to the camera plane (perpendicular to the focal axis) during video recording.

In addition to camera position, the depth of field was set such that a section of the violin, approximately 10 in. long, could be recorded in focus. The aperture was set to insure that sufficient depth of field was available and the lens was taking in enough light to be able to see the violin clearly in the recording. With high-speed high-resolution videography, a significant amount of light is needed especially as video is recorded at rates of 6,000 fps or more. None of the images were brightened in post processing, however, the amount of light being recorded was compensated for by adding three stand lights pointed at the violin, Fig. 61.4a. A 50 mm lens (Zeiss Planar T\* 50 mm F/1.4 ZF.2) gave a satisfactory view of the violin string in these test conditions.

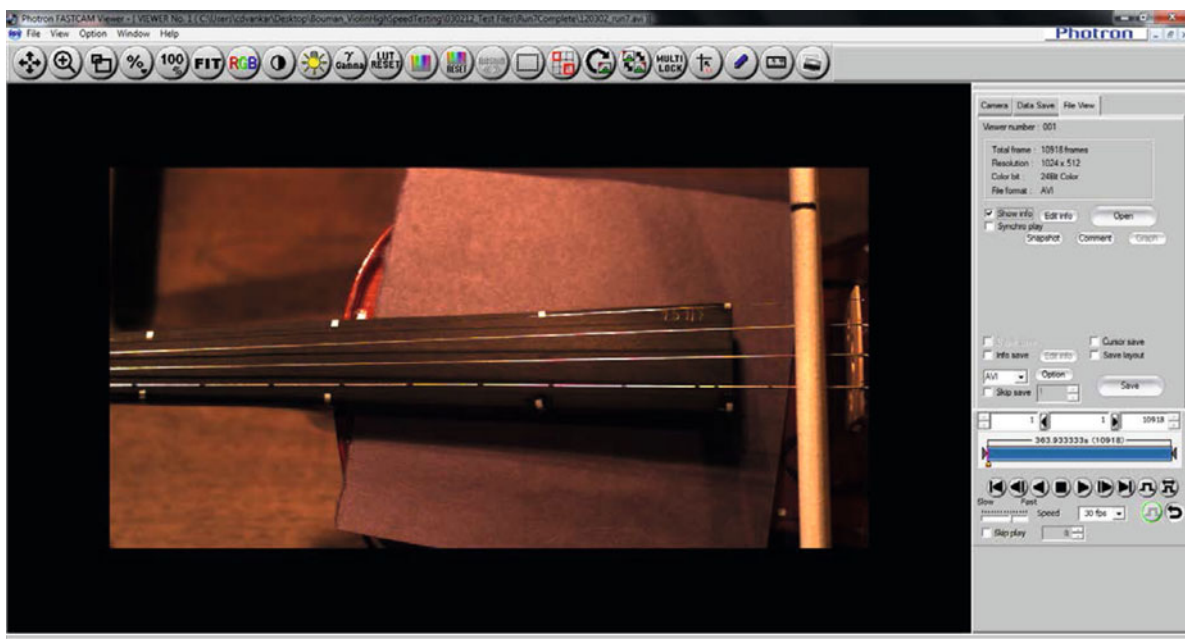
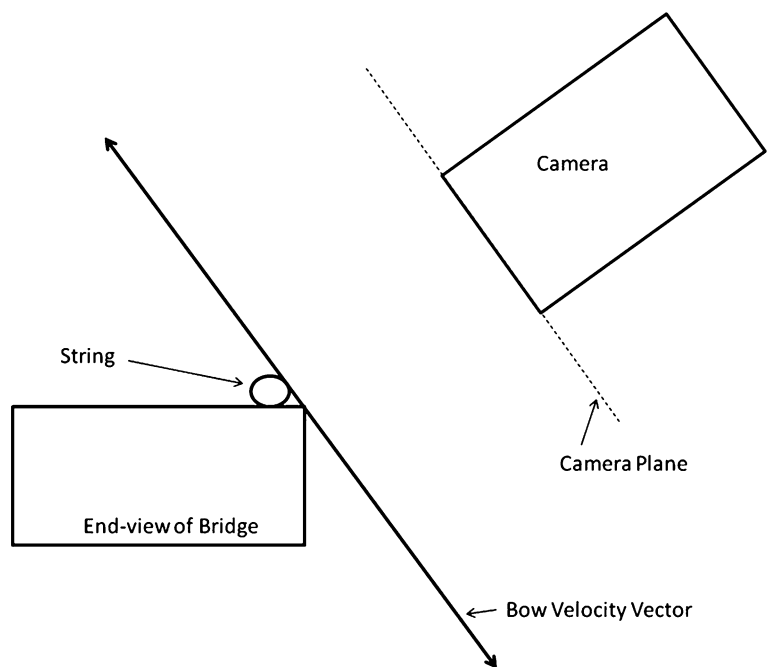


Fig. 61.1 Screenshot of recording software



Fig. 61.2 Screenshot of the tracking software

Fig. 61.3 Diagram showing the bow velocity parallel to the camera plane while exciting the string



The camera was put on a stand above the violin looking down at approximately a  $45^\circ$  angle. The camera was three feet away from the violin which was on a table and held down with two work holder vises (Figs. 61.4b, 61.5).

Calibration for the motion analysis was done by clamping the violin down to a bench with the vises, locking the camera in place via its stand, and acquiring a video with a machinist's ruler next to the string. With this video the exact pixel distance

**Fig. 61.4** (a) A picture showing an early testing setup. (b) A picture showing how the violin was held with vacuum work holder vises

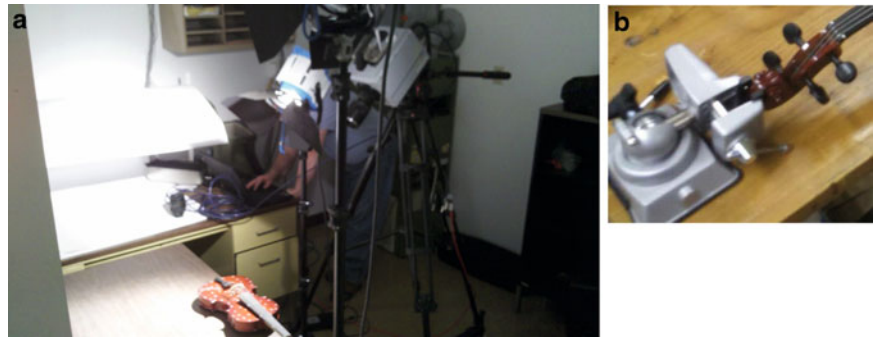


**Fig. 61.5** Top view of final testing setup

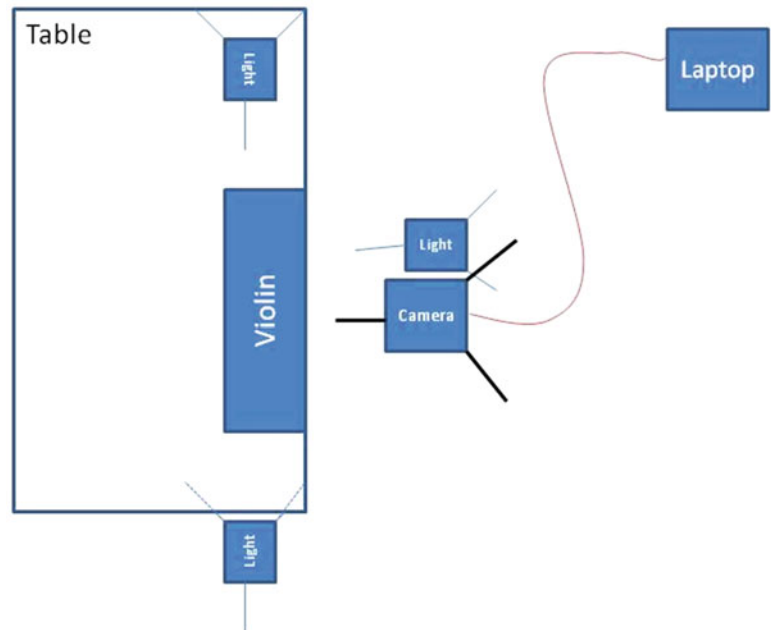


**Fig. 61.6** Image used for calibration. The picture also shows the eleven tracked marks on the string



between marks on the ruler could be found, Fig. 61.6. This calibration factor, pixels/inch, was then used in the actual tests while making sure none of the variables changed between the calibration video and the testing videos (e.g. depth of field, distance between the camera and violin, etc. . .)

Visible markings or “targets” were added to the surface of the violin string in one-inch intervals to define pixels for the motion analysis software to track. It is important to note that the motion analysis software requires significant contrast between the tracking target and its surrounding area in order to automate the tracking process. The software creates a 2D feature template from a user-defined region of the image. Correlation tracking is then used to track the template pattern from frame to frame. The software reports the X/Y position of a particular feature(s) for each individual video frame.

### 61.3 Results

The videos from two tests were acquired and analyzed. Figure 61.7 shows an example of the data from a point on the string which is closest to the bow. The plot shows the cyclic nature of the string motion as well as the relatively small amount of displacement. This point in particular exhibited small displacement due to being heavily restricted by the bow movements. The magnitudes for the points in the middle of the violin were the largest, as expected, Fig. 61.8 [5].

Another expected phenomenon that was observed was the propagation of the wave through the string. As shown in Fig. 61.8, point 1 (closest to bow) goes to zero, that is the center location of the string at rest, and begins the stick phase. Immediately after that, point 3 (red) and then point 5 (green) reach peak displacement as the wave travels along the string. The reason that point 5 reaches its trough before point 1 is that the wave starts at the bow, moves through point 1, point 3, point 5, and then it reaches the scroll at the end of the violin and returns heading through point 5, point 3, point 1, and then back to the bow. The data confirms that point 5 should see a trough prior to point 1. This propagation is also shown in Fig. 61.9.

According to Wolfe [5], “the cycle of stick and slip on the bow has the same period as the vibration of the string”. Based on the pictures in Fig. 61.10, a complete cycle occurred in just under 11 images. When 11 images are multiplied by their respective lengths, in seconds, of 0.48 ms a final value of ~52 ms per cycle is arrived at. The inverse of this value, i.e. cycles/second, is approximately 193 Hz. This value represents the frequency of the stick and slip on the bow which is fundamental frequency expected from the excited G-string. (Note: The string is nominally tuned to 196 Hz.)

In terms of achieving an ODS from the data, two tests were run each acquiring 1.75 s of data at a sampling rate of 6,250 fps. This data was then processed with ProAnalyst and LMS’ TestLab to arrive at an ODS for each run. A snapshot of the animated time history is shown in Fig. 61.11.

It is important to note the sources of error in these results. A trade-off exists between resolution in the direction of string motion (y-axis) and the ability to capture a significant portion of the string’s length (x-axis). The consequence was that the

**Fig. 61.7** Raw data from the second run of the point on the string closest to the bow. The graph shows the magnitude of displacements as well as the cyclic nature of the point movements

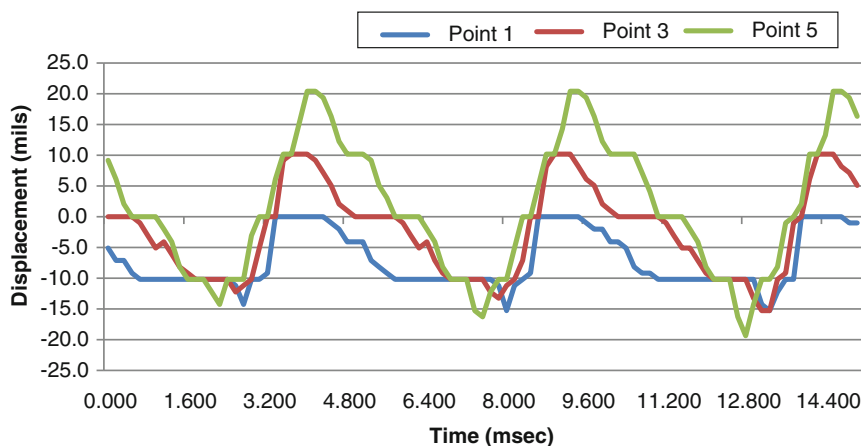
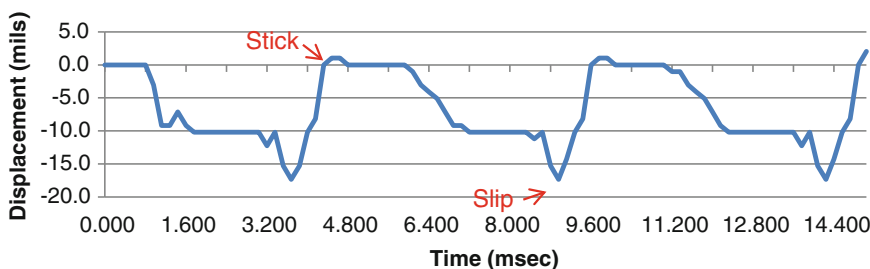
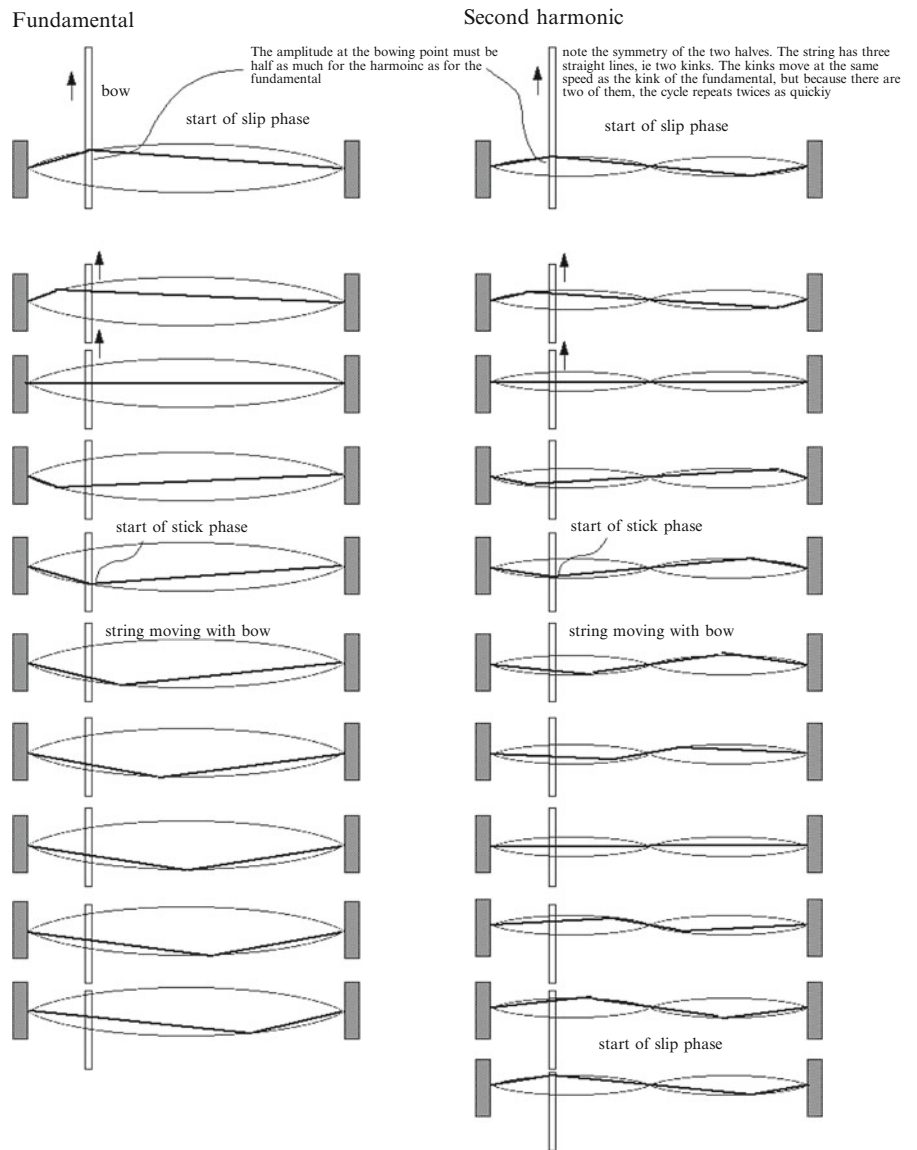


**Fig. 61.8** Time-histories of three points showing the propagation of the wave through the string

**Fig. 61.9** Diagrams showing the ideal Helmholtz motion. Note: bow velocity is upward [4]



motion of the string, which was observed to be  $\pm .02''$  at maximums, had less than ideal pixel resolution. Equation 1 shows the calculation of the pixel resolution (remember that the camera has a native resolution of  $1,024 \times 1,024$  pixels).

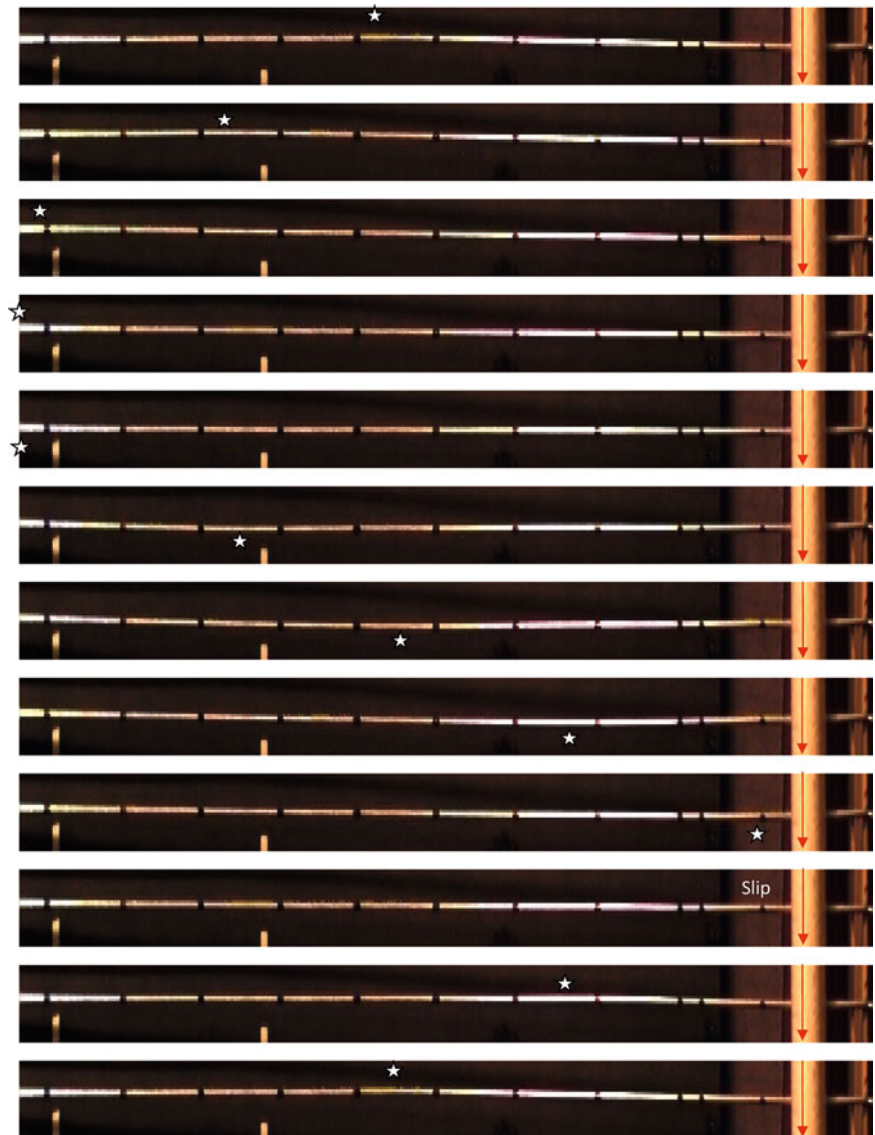
$$\frac{1,024 \text{ pixels}}{\sim 10 \text{ inches}} = -102.4 \frac{\text{Pixels}}{\text{Inch}} \tag{61.1}$$

Therefore for a point that has a displacement of  $\pm .02''$  or  $.04''$  total, it only moves between four pixels. The tracking software, ProAnalyst, has sub-pixel accuracy capability, specifically ten subdivisions within each pixel. This resulted in approximately 40 subdivisions when tracking the points (i.e. quantizing), however some variance still exists in the data.

Additional error is a result of the bow not exciting the string in a plane perfectly parallel to that of the camera plane. This would cause only magnitude error and not periodic error. Lastly, in this study only transverse waves and their movements were studied. A bowed violin string also responds in a torsional fashion. The effect of this motion on this process has not been addressed [1].



**Fig. 61.10** Video clips showing how the wave propagates through the string (The stars show where the peak or trough is located. Each sequential picture is  $\sim 0.48$  ms (top to bottom). The images were acquired at  $1,024 \times 1,024$  resolution, cropped to  $1,024 \times 30$ , and then only the height was magnified three fold to better display the phenomena. Note: bow velocity is downward)

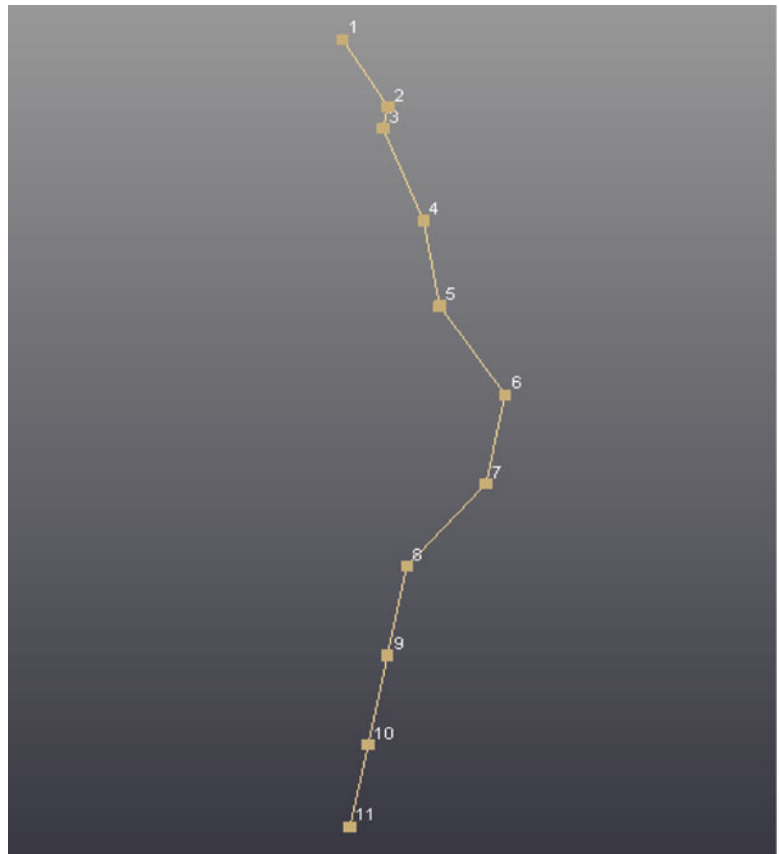


## 61.4 Conclusions

A method for measuring the displacement of a violin string while being bowed via high speed/high resolution videography has been presented. Over 10,000 frames (1.75 s) of video were processed to track the motion of 11 points on a vibrating violin string. The results verified the predicted Helmholtz motion of the string. The tracked motion of the string was successfully converted to time domain operating deflection shapes.

**Acknowledgements** The authors would like to thank Xcitex, Inc. for use of ProAnalyst on this project.

**Fig. 61.11** Snapshot of ODS animation (time domain)



## References

1. Bavu E (2005) Torsional wave in a bowed string, University of New South Wales
2. Pyrkosz M, Van Karsen C (2012) Comparative modal test of a violin. *Experimental techniques online*: 10 May 2012. doi: 10.1111/j.1747-1567.2012.00831.x
3. Pyrkosz M, Van Karsen C, Bissinger G (2010) Converting CT scans of a stradivari violin to a FEM. In: 28th International modal analysis conference, Jacksonville, FL
4. Schwarz B (1999) Introduction to operating deflection shapes. In: CSI reliability week, Vibrant Technology Inc
5. Wolfe J, Bows and strings, The University of New South Wales, <http://www.phys.unsw.edu.au/jw/Bows.html>
6. Xcitex ProAnalyst, [http://www.xcitex.com/html/proanalyst\\_description.php](http://www.xcitex.com/html/proanalyst_description.php)

# Chapter 62

## Automated Measurement Grid Generation for Scanning Laser Doppler Vibrometers

L. Pesaresi and C.W. Schwingshackl

**Abstract** Full field measurement techniques can provide fast, accurate and detailed vibration response data for finite element model validation and are being widely used in industrial applications. A Scanning Laser Doppler Vibrometer (SLDV) measures the full field operating deflection shapes of a structure by changing the location of the laser spot on the target surface. However the setup of a measurement and in particular the measurement grid definition, can take up a significant part of the overall measurement time. To optimise the setup time a novel technique for SLDV measurement grids has been developed. The suggested method includes an automated identification of the vibrating target, based on the measured vibration signal of a scan covering the entire field of view of the LDV. Alpha-shape techniques for target identification and geometric algorithms for shape recognition are used to define the measurement area. Novel approaches for symmetry and orientation capture allow the generation of point grids and continuous patterns for various target shapes. The introduced approach allows a quick SLDV setup of the full field scan with a minimum input from the user.

**Keywords** Continuous scanning LDV • Full field measurement • Measurement grid generation • Symmetry identification • Alpha shape

### 62.1 Introduction

Full field measurement techniques are widely used for the validation of dynamic finite element models. Several different techniques are available to measure the dynamic response of a structure, including Electronic Speckle Pattern Interferometry ESPI [1, 2] and Scanning Laser Doppler Vibrometry (SLDV) [3–5]. These systems provide very detailed information about the dynamic response of a structure in a relatively short amount of time, and are therefore of great interest for the use in an industrial environment. The full field measurement with a SLDV system is quite fast, but setting up the systems can be a lengthy process. To facilitate the setup of the SLDV and help with the generation of measurement grids normally a video camera is used which provides the view in front of the SLDV [6]. This approach is well implemented in commercial software, but it provides several restrictions. It relies on proprietary software to link the image from the video camera to the grid generator. The camera and measurement plane coordinate systems must be aligned by the user before he can define the measurement area over the video feed and generate a measurement grid. The approach is also somewhat restricted in terms of measurement grids that can be generated, since no scan patterns are available for a Continuous Scanning LDV (CSLDV) measurement [7–9].

A new approach for the grid generation is proposed here which attempts to overcome the above mentioned restrictions. It eliminates the need for a video camera by using the Scanning LDV velocity signal as the information source to identify the vibrating target area. A series of data processing steps then identify the vibrating structure in front of the laser and automatically generate measurement point grids for SLDV or scanning patterns to for CSLDV measurements.

---

L. Pesaresi • C.W. Schwingshackl (✉)  
Imperial College London, Exhibition Road, London, SW7 2AZ, UK  
e-mail: [luca.pesaresi12@imperial.ac.uk](mailto:luca.pesaresi12@imperial.ac.uk); [c.schwingshackl@imperial.ac.uk](mailto:c.schwingshackl@imperial.ac.uk)

## 62.2 Scanning LDV System

The core of the Scanning LDV in Fig. 62.1a is a single point Laser Doppler Vibrometer (LDV) that allows contact less measurement of the velocity of a vibrating structure. Two mirrors, each connected to a mirror drive motor and rotated by  $90^\circ$  to each other, are placed in front of the single point LDV enabling the repositioning of the laser beam (see Fig. 62.1b). One of the mirrors can be rotated around the x axis, the other around the y axis allowing to re-position the laser dot to any point in the field of view of the system. Due to the moving laser dot, the response velocity of the structure at many different points can be measured without having to rearrange the setup of the system which allows a fast full field measurement of the operating deflection shape (ODS) of the structure.

Before a full field measurement with the SLDV can be carried out, the measurement grid must be defined. The standard process to set up a SLDV is to use a video camera that is part of the scanning head [6]. A first step requires the manual alignment of the camera coordinate system to the measurement plane, to ensure that the generated grid covers the intended area. This step will need to be repeated each time the target is moved or the camera zoom setting is changed. Once the alignment is completed, the user can manually define regular or irregular scan areas by tracing the outline of the measurement area on the video image, for which the provided software will then generate a point measurement grid (see Fig. 62.1c). This standard setup process requires a lot of user interaction and is not entirely straight forward. The current commercial SLDV control software does not allow generating continuous scanning patterns that are required for CSLDV measurements, and a different measurement grid generation is therefore required.

## 62.3 Automated Grid Generation

The generation of point grids and continuous patterns for full field SLDV measurements can be achieved without the use of the integrated video camera, by using the LDV beam itself as the “eye” of the system. The general idea of the proposed approach can be seen in Fig. 62.2. The structure for which a measurement grid is required is (i) excited at a single frequency away from resonance while (ii) the SLDV conducts a rough scan over the entire field of view. Due to the vibrating structure some of the SLDV signal will show a response amplitude (iii), while the signal outside the target will be either zero, or containing noise due to the motion of the beam. Algorithms and filters can then be used to isolate the vibrating structure

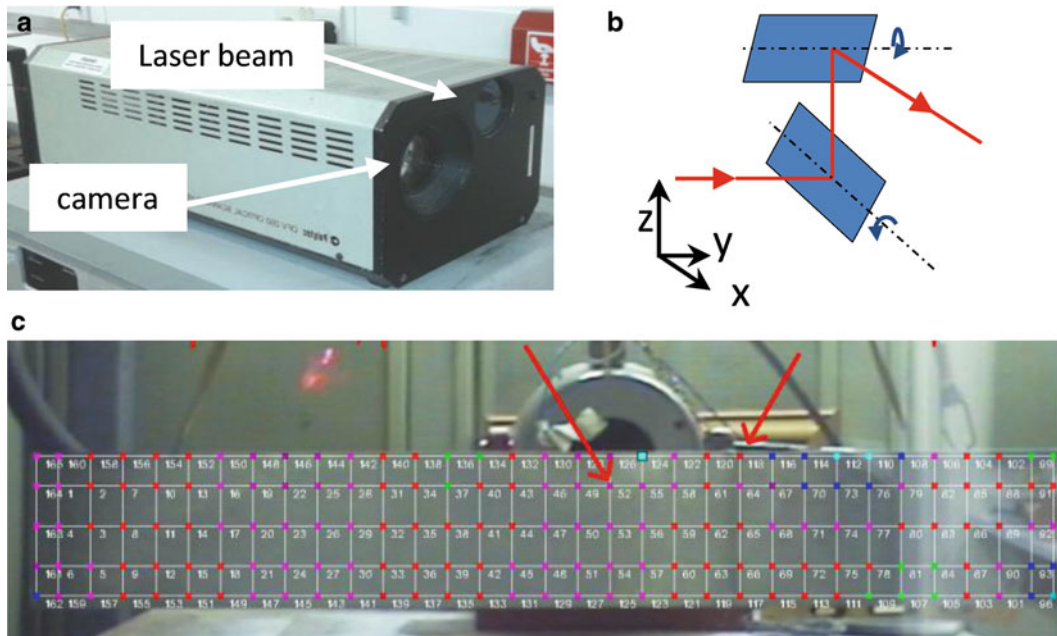


**Fig. 62.1** (a) The Polytec OFV 050 SLDV with (b) two mirrors for the scanning and (c) a typical measurement grid generated by the SLDV camera and software

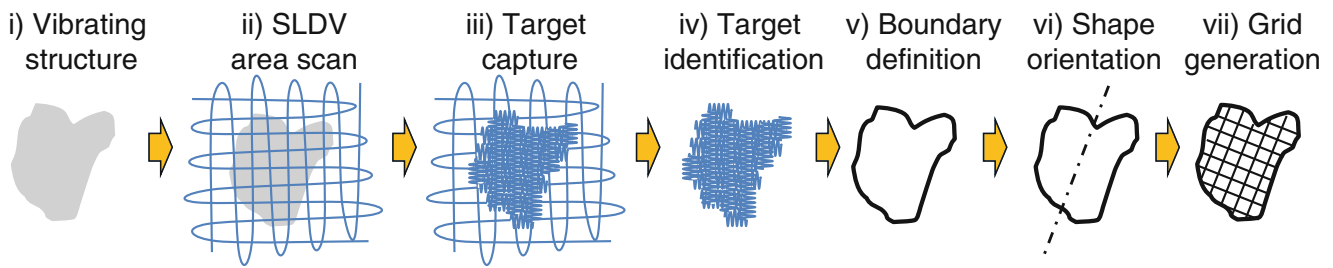


**Fig. 62.2** The idea of the automated grid generation algorithm

(iv) from the background noise, and identify its boundaries (v). Once the boundary of the structure is known, the orientation of the structure and a possible symmetry axis will be identified (vi) before the measurement grid can be generated for the C/SLDV measurement (vii).

The implementation of the suggested approach is not straight forward, but it eliminates the need of a camera on the scan head and the related user interaction from the traditional SLDV setup. Once the outline of the structure is available as a mathematical description many different patterns can be generated for the scan.

## 62.4 SLDV Continuous Area Scan

The setup used for the development of the grid generation algorithm can be seen in Fig. 62.3. A structure was freely suspended from a frame, and a small electro-dynamic shaker was attached to it to provide the excitation signal. The SLDV (Polytec OFV 050) was placed in front of the structure and its control unit was connected to a National Instrument PXI data acquisition system. The LDV was about 2 m away from the vibrating structure, and it was allowed to sweep over an area of approximately  $2 \times 2$  m. A software tool written in Matlab was developed to generate the excitation signal of the shaker, drive the mirrors of the SLDV, acquire the velocity signal measured by the SLDV, and post process the data to generate the measurement grids.

The generation of the measurement grids starts with a continuous sinusoidal sweep along the x-axis that is followed by a similar sweep along the y-axis (see Fig. 62.4a for the input signals), leading to a relatively rough spatial scan pattern in Fig. 62.4b. During this scan the laser moves relatively slowly to reduce the speckle noise and minimise the influence of the inertia of the mirrors. The initial rough scan is followed by an initial identification of the target area (see next section) and a refined second scan over the target area to capture the shape of the structure in more detail.

During the scan the velocity signal of the LDV is acquired leading to a time domain signal in Fig. 62.5a. The acquired time domain signal allows an immediate check of the excitation levels, as the vibrating parts of the structure should clearly stand out from the noise floor when the LDV is off target. If the detected signal difference is not satisfying, then the excitation signal will be increased and the scan repeated, to ensure that a clear distinction between target and background can be made. A combination of the mirror drive signal and the absolute values of the measured velocity signal leads to the spatial response plot in Fig. 62.5b which provides a first indication of the shape of the structure in front of the SLDV.

## 62.5 Target Identification

The time domain signal of the LDV is converted to a spatial description of the structure. The known excitation frequency allows the use of a very narrow bandpass filter [10] on the original time domain signal in Fig. 62.6a leading to a strong reduction of measurement noise in Fig. 62.6b. The signal is then converted to a binary signal to allow the identification of the outline. A threshold setting is being used, where points above the threshold will be part of the vibrating structure, whereas points below the threshold will be removed from the data set. Several approaches have been investigated to automatically define the best threshold value, and the use of the empirical cumulative distribution function proved to be most successful [11]. The resulting empirical cumulative distribution in Fig. 62.6c shows a strong change in gradient (point A) between the noise floor and the actual vibrating structure. This change in gradient which was present for all types of tested structures, can be used to set the required threshold value without the need of a user interaction.

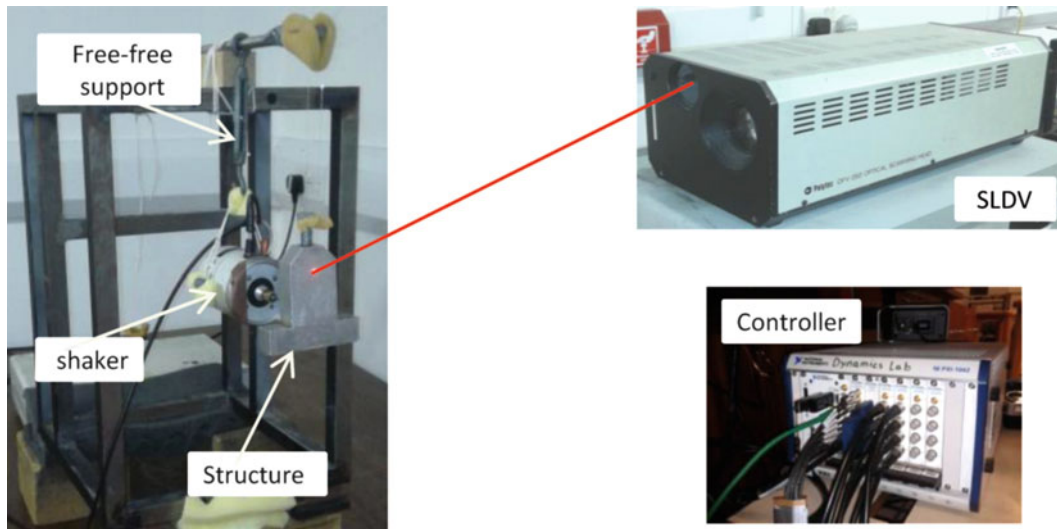


Fig. 62.3 The experimental setup with a symmetric structure

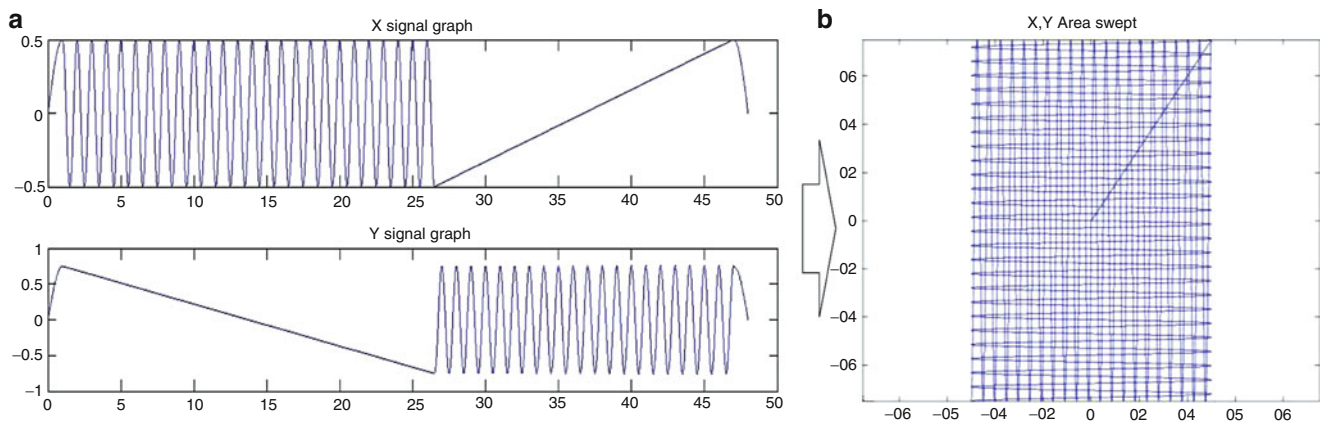


Fig. 62.4 The area scan pattern for the initial target identification (a) in time domain and (b) the spatial pattern

The application of the threshold to the data set from Fig. 62.6b leads to the point cloud in Fig. 62.7a. The outline of the vibrating structure can be clearly seen, also some outlying point are still present in the data set, that are either caused by strong noise spikes that lie above the threshold, or by components of the measurement setup, such as the shaker or the support structure, which vibrate at the same frequency as the target, and will pass the bandpass filter. To eliminate the remaining outlying points a spatial filter has been implemented [12, 13], that calculates the number of points in the close vicinity of each point, and based on this information highlights (see Fig. 62.7b) and eliminates the outlying points, leading to the final point cloud of the vibrating structure in Fig. 62.7c. This final elimination of points proved to be quite a challenging task, since the geometry of the structure, especially if it contains thin sections, can make it very difficult for the software to determine what belongs to it and what needs to be eliminated.

## 62.6 Boundary Definition

The measurement grid generation requires the knowledge of the boundary of the vibrating structure to fit the grid to the area. The edges of the point cloud from Fig. 62.7c can be identified, with the alpha shape technique [14–16]. The principle idea behind the method is that through any two points in the cloud two circles of a predetermined radius,  $r_\alpha$ , can be fitted (alpha parameter), as shown in Fig. 62.8a. If both circles enclose other points of the cloud (red circles in Fig. 62.8a), then the two points through which the circles are fitted are not on the boundary, but if one of these circles does not contain any other points

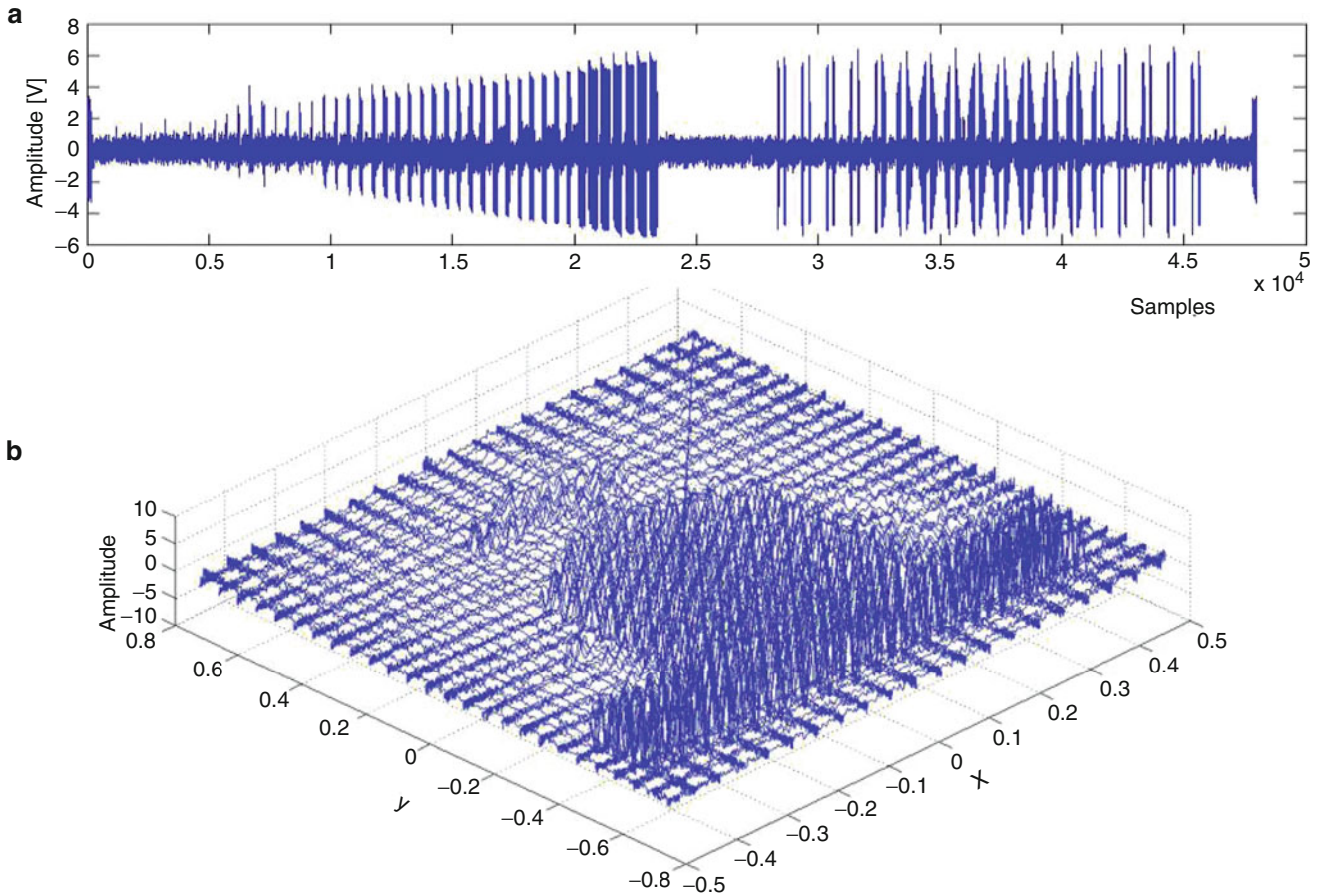


Fig. 62.5 Target capture (a) time domain response and (b) special plot

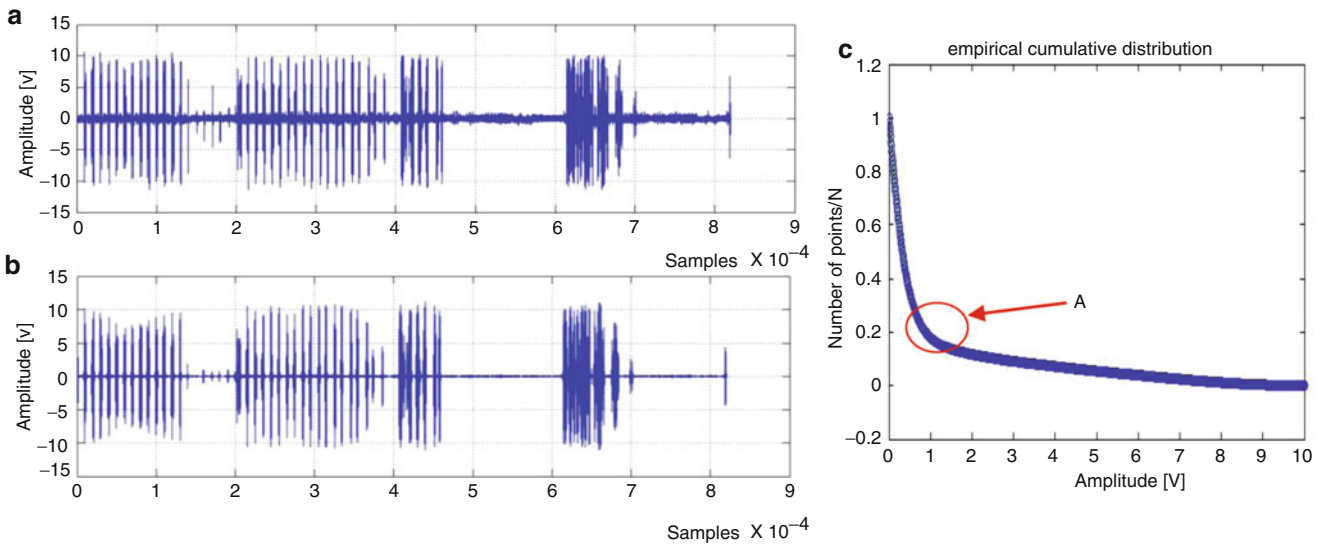
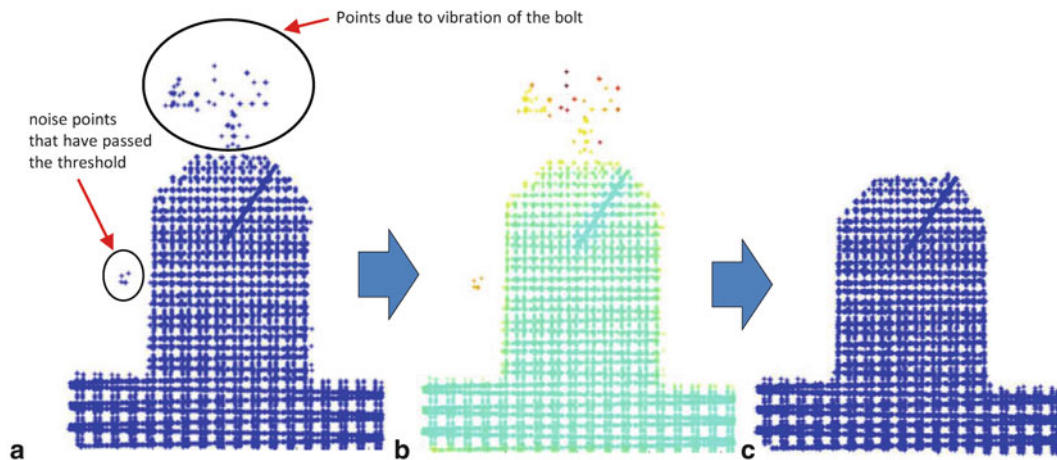
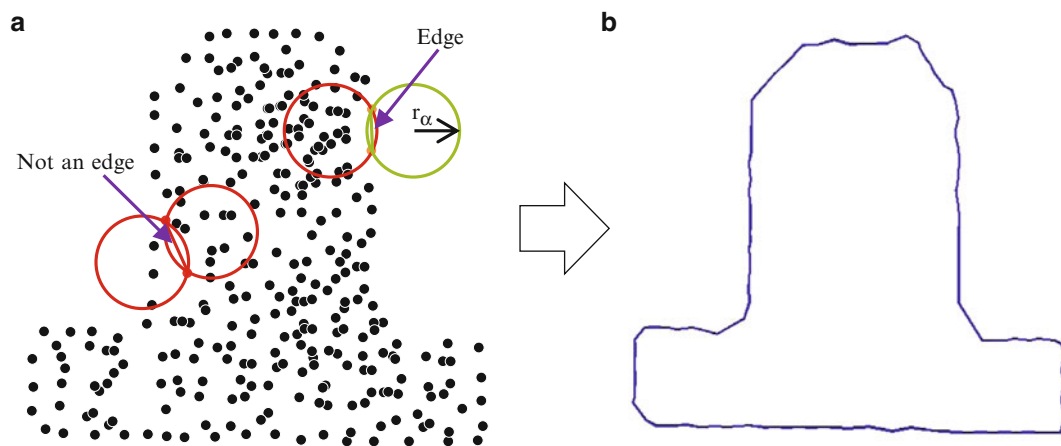


Fig. 62.6 The (a) original time domain signal, the (b) band pass filter signal and (c) the empirical cumulative distribution of the signal

of the cloud (green circle), then the two points represent an edge. Through an iterative process all the edge points can be identified with this approach, resulting in a polygon describing the final boundary. Some care is required to define the correct radius,  $r_\alpha$ , to ensure that the edges can be identified correctly. Its selection is influenced by the density of the point cloud and the shape of the structure and its correct definition is left to the user. The basic alpha shape technique is able to identify the



**Fig. 62.7** The identified binary signal after (a) the application of the threshold, (b) the identification of outlying points and (c) the final point cloud of the structure



**Fig. 62.8** The (a) principle of the alpha shape technique and (b) the identified boundary of the vibrating structure

edges of the point cloud, but if a large number of points is present, then the processing can take considerable time since each point must be compared to all others. It has been shown that an alpha shape is always a subset of a Delaunay triangulation [17] and a combination of the two techniques can significantly speed up the boundary search since the points that need to be checked are the ones that follow the segments of the Delaunay triangles. This combined method was implemented and proved to be very robust when it came to the identification of complicated shapes, such as holes in the structure. The identified outline of the point cloud from Fig. 62.7c can be seen in Fig. 62.8b. It consists of a set of points, describing the edge of the structure for which a measurement grid can now be generated.

## 62.7 Grid Generation

The knowledge of the outline of the target structure allows the generation of the measurement grid. In its simplest form a predefined grid with a vertical orientation can be generated, and the outline can then be used to determine which grid point lies within and which outside. The problem with this approach is that it does not consider the orientation and a possible symmetry axis of the structure, and the measurement grid is therefore of poor quality.



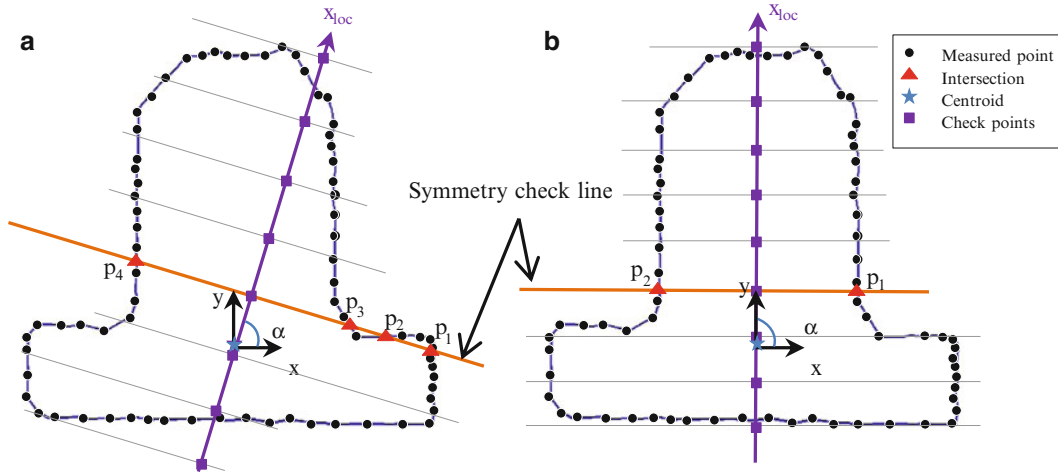


**Fig. 62.9** The symmetry check for the identified boundary at (a) a non-symmetric position and (b) a symmetric position

The generation of a higher quality point grid or a continuous scanning pattern requires some additional knowledge of the structure. The main orientation can be determined by calculating the inertia vector of all the points within the boundary [18]. Initially the inertia tensor  $T$  is defined as

$$T = \begin{bmatrix} \sum_{i=1}^n y_i^2 & -\sum_{i=1}^n x_i y_i \\ -\sum_{i=1}^n x_i y_i & \sum_{i=1}^n x_i^2 \end{bmatrix} \quad (62.1)$$

where  $x_i$  and  $y_i$  are the global coordinates of each point,  $i$ . For this tensor the two eigenvalues,  $\lambda_1$  and  $\lambda_2$ , can be calculated with Eq. (62.2)

$$\det(T - \lambda I) = 0 \quad (62.2)$$

which represent the principals of inertia of the shape. The two corresponding eigenvectors  $\lambda_1$  and  $\lambda_2$  are the principle axis of the point cloud and provide its main orientation

$$(T - \lambda_i I) \begin{pmatrix} x_i \\ y_i \end{pmatrix} = \begin{pmatrix} 0 \\ 0 \end{pmatrix} \quad (62.3)$$

The coordinate system for grid generation can then be aligned with this main axis leading to an improved measurement grid. A major problem with this approach is that especially circular or square structures cannot be fully defined. To address this issue and to find not only the main orientation, but also a possible symmetry in the structures, an additional approach has been developed. The symmetry check requires a set of points defining the boundary of the geometric shape.

The algorithm starts by applying a local coordinate system, centred at the centroid of the shape and oriented with the angle  $\alpha$  against the global reference frame, to the geometry (see Fig. 62.9). Two “extreme points” are then defined as the points with positive and negative maximum distance from the centroid along the current local  $x$  axis,  $x_{loc}$ . The portion of the  $x_{loc}$ -axis linking these two extreme points is divided into a number of equally spaced check-points, where the number of steps depends on the dimensions of the shape. At each check point a normal line (symmetry check axis) to the local  $x$  axis,  $x_{loc}$ , is generated and its intersection with the boundary segment identified. A linear interpolation between the identified boundary points provides the accurate location of the intersection, which must be an even number for a closed geometry. The local coordinates of the intersection points are sorted according to their distance from the local  $x$  axis,  $x_{loc}$  and stored in an array. This vector is then evenly split in two parts and one of the two new vectors is changed in sign. The distance values from the local  $x$  axis are then compared to each other for each corresponding point and if all the values are within a range of a 10%, this particular check point is flagged as symmetric. Repeating this process at all the check points along  $x_{loc}$  axis and calculating the percentage of symmetric check points to the overall number of check points leads to a single value that describes the level of symmetry for the given orientation  $\alpha$  of the  $x_{loc}$  axis. Repeating this process for different orientation angles  $\alpha$  over a  $180^\circ$  sweep, provides information about the symmetry of the shape. At the end the highest symmetry value is chosen as the main orientation for the grid generation.

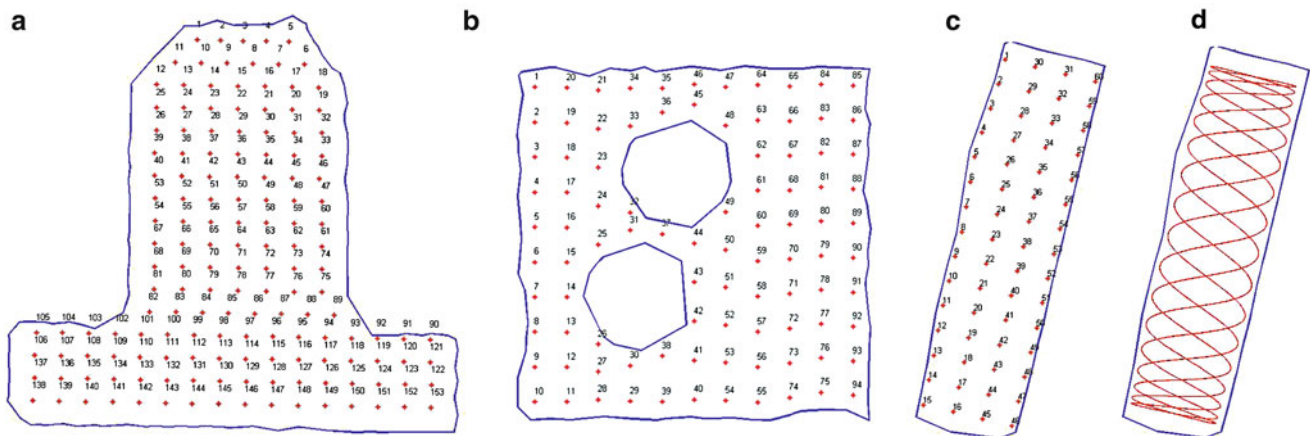


**Fig. 62.10** Measurement grids for (a) a semi-symmetric structure, (b) a structure with holes, (c) a fully symmetric structure with aligned grid, and (d) a continuous scanning LDV pattern for a symmetric structure

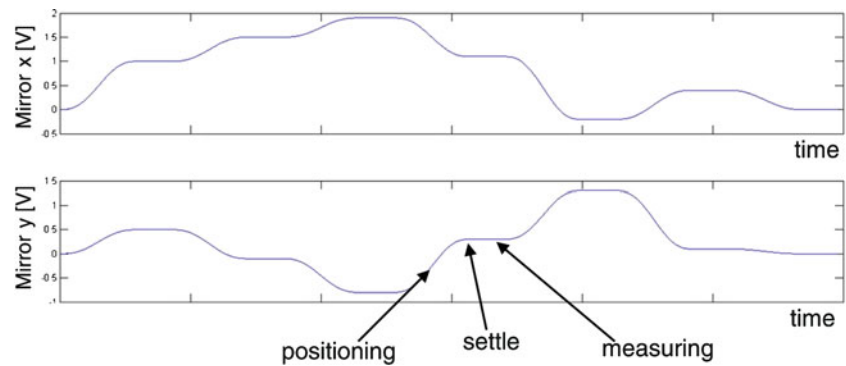
Due to the high importance of the symmetry identification for the grid generation the example in Fig. 62.7a shall be considered: a random orientation angle,  $\alpha$ , of the  $x_{loc}$  axis has been selected and the symmetry check line at the current check point has been defined. It crosses the outline four times at the intersection points  $p_1, p_2, p_3$  and  $p_4$ . Identifying and sorting the distance,  $d_{1-4}$ , of the intersecting points to the check point leads to the sorted vector  $[d_1, d_2, d_3, d_4]$  which is then split into two parts  $[d_1, d_2]$  and  $-[d_3, d_4]$ . If the structure is symmetric, then  $d_1$  and  $-d_4$  as the two outermost points and  $d_2$  and  $-d_3$  as inner boundary points should have matching values, but for the case in Fig. 62.7a this is clearly not true and the current check point is therefore not a symmetry point. The orientation of  $\alpha = 90^\circ$  in Fig. 62.7b leads to two intersections  $p_1$  and  $p_2$ , with the same distances from the check point  $d_1 = -d_2$ . This defines a symmetric check point and it can be seen that most of the other check point positions fulfil this criteria as well, so that the overall orientation of  $x_{loc}$  at  $\alpha = 90^\circ$  is a symmetry axis.

Measurement grid generation requires (i) the points defining the edges of the shape and possible holes in the geometry, (ii) the information about symmetry in the structure, and (iii) an orientation axis along which the grid will be aligned. Additional input parameters such as grid density must be provided by the user. A point grid or a continuous scan pattern can be generated, depending on the user preference and a detected symmetry. In the case of point grids (see Fig. 62.10a–c) a pattern will be fitted within the identified boundaries of the structure. The optimum number of points is determined along each grid line and an even spacing is then enforced, based on the predefined grid density and the distance between the two boundary lines.

The generated measurement grid for the test case in Fig. 62.3 can be seen in Fig. 62.10a. The point grid follows the outline of the identified shape correctly and leads to a grid that can be used for a full field measurement of the structure. An additional point grid in Fig. 62.10b demonstrates the capability of the developed approach to identify and deal with holes in the structure, where no measurement points are generated. The identified orientation and symmetry information allows alignment of the point grid with the main axis of the structure to optimise the scanned pattern (see Fig. 62.10c). If the structure has a major symmetry axis and no holes, than a scan pattern for a Continuous Scanning LDV measurements can be generated. This is a major advantage over the commercial software which currently does not support continuous scanning, and it allows a much faster generation of a scan patterns than the past manual adjustment of all the parameters. Two sine waves of different frequencies must be generated, one following the identified main symmetry axis, and the other rotated by  $90^\circ$ . The chosen frequencies must ensure a continuous Lissajous figure that does eventually cover the entire structure. The amplitudes of the sine waves are adjusted to follow the boundary of the structure leading to a scan pattern such as in Fig. 62.10d.

In a final step the mirror drive signals are being calculated that are required to generate the measurement pattern. Figure 62.11 shows a typical mirror drive signal for a point grid. The re-positioning of the mirrors follows a fifth degree polynomial law that guarantees zero acceleration and velocity at the starting and ending positioning points to minimise the effect of an abrupt stop of the mirrors. To eliminate a possible vibration in the mirrors after stopping, a settling phase is added, before the actual measurement time completes the mirror drive signal for a grid point. Assembling the signal for all points in the measurement grid provides the final output of the mesh grid generator. In the case of a continuous scan pattern, two sinusoidal output waves of fixed frequency are being generated, and their amplitudes scaled to follow the shape of the structure.

**Fig. 62.11** Mirror drive signal for the x and y axis



## 62.8 Conclusion

A new approach for a fast and reliable generation of measurement grids and continuous patterns for a Scanning LDV system has been introduced. An initial scan over the entire field of view of the SLDV provides the location of the vibrating structure. Several data processing steps, including filtering techniques and an alpha shape algorithm, are being used for an automated identification of the outline of the vibrating structure. Point and continuous SLDV measurement grids are then generated, based on the identified orientation and symmetry of the structure. The presented method purely relies on the velocity signal and location information of the SLDV, eliminating the need of an additional optical system to generate the measurement grids. It can provide patterns for both a traditional point to point measurement, and the Continuous Scanning LDV approach, and allows a quick and easy setup of a full field measurement system.

**Acknowledgements** The authors are grateful to Campusworld/Università Politecnica delle Marche for providing some financial support for this work.

## References

1. Slangen P (1993) Electronic speckle pattern interferometry (ESPI): a fast technique for the detection and visualization of proper vibration modes. *Eur J Mech Environ Eng* 38(2):67–72
2. Van der Auweraer H, Steinbichler H, Vanlanduit S, Haberstock C, Freymann R, Storer D, Linet V (2002) Application of stroboscopic and pulsed-laser electronic speckle pattern interferometry (ESPI) to modal analysis problems. *Meas Sci Technol* 13(4):451–463
3. Sriram P, Craig JI, Hanagud S (1992) Scanning laser Doppler techniques for vibration testing. *Exp Tech* 16(6):21–26
4. Tirabassi M, Rothberg SJ (2009) Scanning LDV using wedge prisms. *Opt Lasers Eng* 47(3–4):454–460
5. Sriram P, Hanagud S, Craig JI (1992) Mode shape measurement using a scanning laser Doppler vibrometer. *Int J Anal Exp Modal Anal* 7(3):169–178
6. Polytec Scanning Vibromter Software 8.4, Software manual, 41031-Man-Vib-PSV-Soft8.4-0706-01e, Polytec, Germany
7. Martarelli M, Ewins DJ (2006) Continuous scanning laser Doppler vibrometry and speckle noise occurrence. *Mech Syst Signal Process* 20(8):2277–2289
8. Martarelli M (2001) Exploiting the laser scanning facility for vibration measurements. PhD thesis, University of London
9. Stanbridge AB, Ewins DJ (2006) A review of 10 years of continuous-scan LDV developments. In: *Proceedings of international conference on noise and vibration engineering ISMA2006*, vol 1–8, Leuven, Belgium, pp 3165–3179
10. Owen M (2007) *Practical signal processing*. Cambridge University Press, Cambridge
11. Seul M, O’Gorman L, Sammon MJ (2000) *Practical algorithms for image analysis: description, examples, and code*. Cambridge University Press, Cambridge
12. Davies ER (2005) *Machine vision: theory, algorithms, practicalities*, 3rd ed. Elsevier Science, Amsterdam
13. Jain R, Kasturi R, Schunck BG (1995) *Machine vision*. McGraw-Hill, New York
14. Edelsbrunner H, Kirkpatrick DG, Seidel R (1983) On the shape of a set of points in the plane. *IEEE Trans Inf Theory* 29(4):551–559
15. Edelsbrunner H, Mücke EP (1994) Three-dimensional alpha shapes. *ACM Trans Graph* 13(1):43–72
16. Xu X, Harada K (2003) Automatic surface reconstruction with alpha-shape method. *Vis Comput* 19(7):431–443
17. De Berg M, Cheong O, Van Kreveld M, Overmars M (2008) *Computational geometry: algorithms and applications*. Springer, Berlin/New York
18. Carpinteri A (1997) *Structural mechanics*. Taylor & Francis, London

# Chapter 63

## Mode Filtering of Continuous Scanning Laser Doppler Vibration Data

P. Castellini, P. Chiariotti, and M. Martarelli

**Abstract** The paper illustrates the idea of using theoretical knowledge of specific structure's mode shapes as a way of filtering time domain data obtained by Continuous Scanning Laser Doppler Vibrometry (CSLDV). The CSLDV output measures the structure vibration joining together the spatial and time information. It is proposed here to exploit the a priori knowledge of the candidate mode shape spatial distributions to extract from the vibration data the resonance frequency information with high accuracy. That technique is based on the concept that modal analysis ends up with a final abstraction and labelling of the mode shapes on the basis of their nodal lines position, i.e. first, second bending and/or torsional, etc. The expected mode is compared with the experimental data in order to evidence the information on the frequency at which that mode occurs.

**Keywords** Laser Doppler vibrometry • Continuous scanning LDV • Operational deflection Shape • Vibration measurements • Signal decomposition

### 63.1 Introduction

This paper presents a new philosophy in the data processing of vibration data to extract information for modal analysis.

The traditional approach consists in processing experimental data and extracts from them natural frequencies and mode shape vectors. This processing can be done in time or frequency domain.

As explained in [1] and in [2], traditional experimental modal analysis exploits the matrix of transfer functions between input force (e.g. exerted via an impact hammer) and output vibration (e.g. measured by an accelerometer or a laser Doppler vibrometer) for the extraction of modal parameters (resonance frequencies, damping factors and mode shapes) representing the modal model of the structure.

The quality of an experimental modal analysis results is typically judged on the basis of a priori knowledge own by the experimentalist or by comparing the results with the ones obtained from the use of different extraction methods.

The most diffused approach to perform that comparison, in terms of mode shapes, is the Modal Assurance Criterion (MAC), which quantifies the level of correlation between two mode sets, they being numerical vs. experimental, analytical vs. experimental or belonging to different experimental modal testing. The MAC does not directly provide any indication on the natural frequencies, whose correlation is essentially based on their difference even though the MAC evaluation allows to identify corresponding frequencies from the two sets. The MAC is therefore a quantitative algorithm that can be also replaced by a qualitative correlation process based on the knowledge of the modal model related to the structure.

The aim of the method proposed here is to separate the contribution of different ODSs from the vibration data measured on an excited structure and to identify the corresponding resonance frequencies using the knowledge of the mode shapes which are known a priori, they depending only on the geometry of the structure itself. The applied procedure is an iterative

---

P. Castellini (✉) • P. Chiariotti  
Università Politecnica delle Marche, Via Brecce Bianche, 60131 Ancona, Italy  
e-mail: [p.castellini@univpm.it](mailto:p.castellini@univpm.it); [p.chiariotti@univpm.it](mailto:p.chiariotti@univpm.it)

M. Martarelli  
Università degli Studi e-Campus, Via Isimbardi, Novedrate (CO), Italy  
e-mail: [milena.martarelli@unicampus.it](mailto:milena.martarelli@unicampus.it)

**Table 63.1** Proposed procedure set of unknowns

	Traditional approach	Proposed approach
Natural frequencies, mode gain and phase	$3n$	$3n$
Mode shapes	$n \cdot m$	$n$
TOTAL	$n \cdot (m + 3)$	$4 \cdot n$

time domain process. It consists on synthetizing the vibration data from one or more known mode shape and on the following maximisation of the correlation between measured and synthetic data in order to extract natural frequency, relative amplitude (called mode gain in this paper) and phase of each mode.

In this approach the set of unknowns are: the identification of each mode shape presence and its natural frequency, mode gain and phase. The difference with conventional vibration tests is that the mode shape is known a priori and it does need to be recovered from a set of experimental data, measured on  $m$  positions in the structure. If  $n$  are the mode shapes investigated the number of unknowns in traditional approaches and in the proposed procedure are reported in Table 63.1. The unknown associated to each mode shape is related to the identification or not of the mode shape within the measured signal.

## 63.2 Description of the Procedure for ODS and Resonance Frequency Extraction

The proposed approach is very general and could be applied to vibration data obtained with whatever measurement technique.

A good candidate it is, however, the Continuous Scanning Laser Doppler Vibrometry (CSLDV) it presenting several advantages with respect to conventional vibration testing methods thus being particularly suitable for the proposed processing technique. Some of those advantages are:

- Extremely high spatial resolution,
- Compact data structure (e.g. a single time history contains both time and spatial information),
- Limited experiment duration (e.g. the acquisition time depends only to the required frequency resolution).

The CSLDV method has been presented by Ewins et al. [3] as alternative for the conventional Scanning Laser Doppler Vibrometry, it enabling to recover Operational Deflection Shapes (ODS) from a unique time history acquired by the LDV while the laser beam scans all over the vibrating surface. In that condition the time history appears as an amplitude modulated signal whose modulation is the ODS itself. Initially the technique has been applied only to single frequency excitation, e.g. step sine testing, with the drawback of being extremely time-demanding. However several works [4, 5] demonstrated its functionality also when broadband excitation is applied, e.g. impact testing and operational excitation. The main hypothesis underling to the CSLDV presented by Ewins et al. is the ODS can be modelled by a polynomial whose coefficients are determined from the LDV spectrum, which has the typical shape of an amplitude modulated signal, i.e. it presents sidebands equally spaced about the excitation frequency at the laser beam scanning frequency. The polynomial assumption is not anymore essential if the ODS is recovered from the LDV signal by performing time domain resampling, as it has been introduced by Allen et al. [6].

The technique proposed in this paper overcomes both the requirement of polynomial hypothesis and the need of time resampling by exploiting the a priori knowledge of the ODS, no matter how many of them are excited. The procedure follows a series of steps listed hereafter.

### Step 1: CSLDV data collection

The full field vibration of a structure excited in a wide frequency range is measured by CSLDV. A 1D example will be treated in this paper but it can be easily generalised to 2D. The laser beam is made to scan sinusoidally along the whole length of the 1D structure, e.g. a beam, with a scanning frequency much lower than that of the first expected mode. The LDV output time history will be called  $v_{CSLDV}(t)$ , it being an amplitude modulated time history modulated by the excited ODSs

**Fig. 63.1** Algorithm description

```

mode found = {∅}
for i = 1...N
  for j = 1...(N – mode found)
    if j = 1
      vtest = vCSLDV
    end
    vsynt(MG, f, φ)opt = ||vtest – vsynt(MG, f, φ)||min2
    modevsynt(MG, f, φ)opt → mode found
    vtest = vtest – vsynt(MG, f, φ)opt
  end
end
end

```

## Step 2: Selection of a set of candidate mode shapes

The mode shapes are selected a priori from the knowledge of the structure geometry and constraints. Those mode shapes can be calculated analytically or via numerical models. For simple structures, like beams or plates, the constraint can be unknown and mode shapes referring to different constraint can be included in the set of potentials modes (e.g. clamped-free modes can be included in sliding-free mode set).

## Step 3: Synthetic CSLDV signal calculation

The synthetic velocity signal can be simulated correlating the spatial information of the mode shape with the scan frequency of the LDV. Even though it is not mandatory to use a polynomial representation of the mode shape it was exploited in the proposed simulation for sake of simplicity. The synthetic velocity signal for each candidate mode shape,  $i$ , under the hypothesis of 1D scan and mode shape represented by a polynomial of the  $L$ th order, can therefore be calculated as in Eq. (63.1):

$$v_{synth,i}(MG, f, \varphi) = MG \left[ \sum_{l=1}^L A_l \cos^l(2\pi f_{scan}t) \cos(2\pi ft + \varphi) \right] \quad (63.1)$$

where  $MG$  is the mode gain,  $f$  and  $\varphi$  its frequency and phase.

The term  $\sum_{l=1}^L A_l \cos^l(2\pi f_{scan}t)$  represents the mode shape enveloping the laser output, while it scans at the frequency  $f_{scan}$ .  $A_l$  is the  $l$ th polynomial coefficient and  $t$  the time vector. The signal in Eq. (63.1) will be calculate for a series of value of  $MG$ ,  $f$  and  $\varphi$  and will be used as input for the optimisation phase, described in Step 4.

## Step 4: ODS contribution separation

By minimising the  $L_2$  norm between the measured CSLDV signal and the synthetic signals calculated for the different values of  $MG$ ,  $f$  and  $\varphi$  the value of those variable better matching the real signal will be identified. The procedure, described hereafter in Fig. 63.1, will be repeated for the complete set of candidate mode shapes until the contribution of each ODS will be determined in terms of mode gain, frequency and phase.

### 63.3 Algorithm Testing

The performances of the proposed approach were evaluated on a simple analytical model in order to deal with a well-controlled test-case.

#### 63.3.1 Analysis of Results from Simulated Data

The velocity recorded by CSLDV when theoretically measuring on certain structure can be simulated adding up the mode contributions calculated according to Eq. (63.1). Table 63.2 reports the frequency, phase and mode gain values used in modelling the CSLDV velocity when only the first three modes shapes are involved in the vibration of a free-free beam [7]. Modes at close frequencies and with high spread in terms of mode gain were considered when simulating the CSLDV signal, that in order to stress out the algorithm at the worst working conditions.

Since a real signal is always affected by noise, Gaussian white noise was also added to the synthetic velocity signal (SNR = 10 dB). It should be pointed out so far that, when performing a vibration measurement exploiting the Continuous Scanning approach, the recorded velocity signal is affected BY speckle noise more than when the same measurement is performed using the common Discrete Scan method. When the laser spot moves continuously, the speckle pattern evolves in tuning with the relative movement between the target and the laser beam, and a series of different bright speckles move within the detector area thus producing a random change in the speckle phase distribution. If the laser beam moves along a straight line reproducing a sinusoidal pattern, the speckle grains will pass across the detector active area with the same frequency as the scanning beam, thus introducing frequency components at the scan frequency and its harmonics. The overall SNR therefore decreases because the increase in the total Harmonic Distortion (THD) at the scan frequency. A comprehensive study on the effect of speckle noise on a vibration measurement performed exploiting the Continuous Scanning is reported in [8].

It is also reported in [8] that, when the scan frequency is sufficiently low, the spoiling effect due to the speckle noise is minimal: for such reason we did not considered speckle noise on the synthetic velocity signal. Although the data have been simulated using a scan frequency of 10 Hz the effect of the speckle noise can be still considered limited.

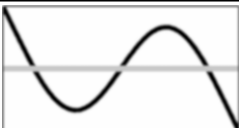
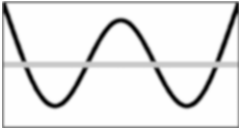
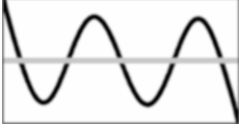
Figure 63.2 reports the reconstructed CSLDV signal, where a scan frequency of 1 Hz was simulated so to have a minimum number of cycles within the analysis time window ( $T = 10$  s).

In order to understand the capability of the algorithm in correctly identifying the contribution of the mode shapes which are effectively present on the simulated structure further modes (mode V of a free-free beam, modes II and IV of a beam clamped at one end) were added to the set of candidate modes, as shown in Fig. 63.3.

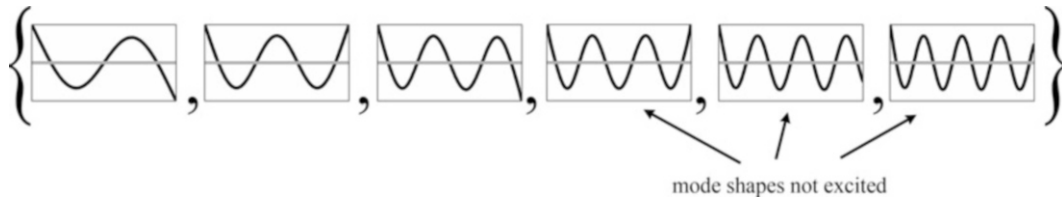
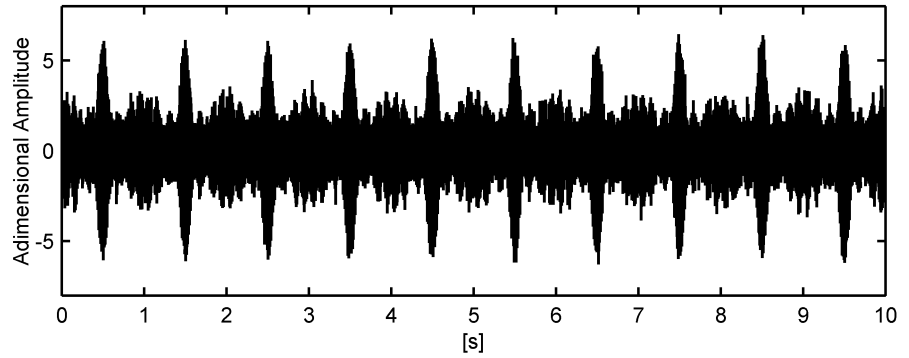
The algorithm described in Sect. 63.2, Step 3, has been ran by using a resolution of 1 Hz in frequency,  $\pi/10$  in phase and 0.5 in mode gain and starting guess of 80 Hz, 0 and 0.5 for frequency, phase and mode gain respectively.

Table 63.3 reports the mode shapes contributions extracted applying the algorithm described in Sect. 63.2. The \* addresses those mode shapes not excited and therefore not used in simulating the CSLDV synthetic signal. It can be seen the modes effectively used to model the synthetic velocity signal are instead well revealed both in terms of frequency, phase and mode gain.

**Table 63.2** Simulated mode shapes characteristics

Mode shape in CSLDV signal	Frequency (Hz)	Phase (rad)	Mode gain	Mode shape
II <sub>FF</sub>	86	0	1	
III <sub>FF</sub>	87	0	4	
IV <sub>FF</sub>	91	0	2	

**Fig. 63.2** CSLDV synthetic velocity signal



**Fig. 63.3** Mode set used for testing the algorithm

**Table 63.3** Extracted Mode shapes contributions

Revealed mode shape	Frequency (Hz)	Phase (rad)	Mode gain
II <sub>FF</sub>	86	0	1
III <sub>FF</sub>	87	0	4
IV <sub>FF</sub>	91	0	3
V <sub>FF</sub> <sup>*</sup>	102	4.3982	0.5
VI <sub>FF</sub> <sup>*</sup>	96	4.3982	0.5
VII <sub>FF</sub> <sup>*</sup>	90	4.3982	0.5

The modes not excited presents the same mode gain; moreover, that value coincides exactly with the mode gain starting guess of the overall iterative algorithm. That is quite expectable, since the iterative procedure tries to model the residue signal, calculated as in Eq. (63.2), using the smallest amplitude for those modes which are not excited, and that holds the closer is the reconstructed velocity signal to the true CSLDV one.

$$v_{residue} = v_{CSLDV} - \sum_{i=1}^K MG_i \left[ \sum_{l=1}^L A_l \cos^l(2\pi f_{scan}t) \cos(2\pi f_i t + \varphi_i) \right], \quad K : \text{excited modes} \quad (63.2)$$

### 63.4 Conclusion

By observing a vibrating structure, especially in the case of simple structure, an expert experimentalist can easily recognize which are the mode shapes that are likely to expect: that process is supported by its knowledge and experience.

The technique proposed in this paper is based on a priori knowledge of structural vibration and uses it not only for conventional verification (e.g. modal model validation) but for the building up of a “blind” process allowing to separate contributions from different ODSs. The procedure is analogue to the pattern matching, the well-known method exploited in the image processing. The acquired image (signal) is compared with a template, i.e. a golden standard, and the result is the score, i.e. a normalised index, representing the correlation level and the location of the most correlated portion of the image (signal).

Such a method, exploiting the mode shapes knowledge, is more robust with respect traditional ones and therefore it can be applied to harsh vibration signals as, for instance, noisy data and presence of coupled modes with resonance frequencies very close each other’s.



## References

1. Ewins DJ (2000) Modal testing, theory, practice and application, Mechanical Engineering Research Studies: Engineering Dynamics, 2nd edition
2. Avitabile P (2001) Experimental modal analysis (a simple non-mathematical presentation). *Sound Vib* 35:20–31
3. Stanbridge AB, Martarelli M, Ewins DJ (2004) Measuring area vibration mode shapes with a continuous-scan LDV. *Measurement* 35(2):181–189
4. Stanbridge AB, Martarelli M, Ewins DJ (1999) The scanning laser doppler vibrometer applied to impact modal testing, vol. XVII. IMAC-SEM, Kissimmee, USA
5. Martarelli M, Castellini P, Santolini C, Tomasini EP (2011) Laser Doppler vibrometry on rotating structures in coast-down: resonance frequencies and operational deflection shapes characterization. *Meas Sci Technol* 22:115106. doi:10.1088/0957-0233/22/11/115106
6. Gasparoni A, Allen MS, Yang S, Sracic MW, Castellini P, Tomasini EP (2010) Experimental modal analysis on a rotating fan using tracking-CSLDV. In: 9th international conference on vibration measurements by laser and noncontact techniques & short course, Ancona, pp 22–25
7. Blewins RD (1984) Formulas for natural frequency and mode shape. Krieger, Malabar, FL
8. Martarelli M, Ewins DJ (2006) Continuous scanning laser Doppler vibrometry and speckle noise occurrence. *Mech Syst Signal Process* 20:2277–2289. ISSN:0888-3270

# Chapter 64

## The Characterization of the Time Delay Problem in Hardware in the Loop System Applications

C.A.G. Carrillo, J.V. Ferreira, and P.S. Meirelles

**Abstract** In the last years, simulations have been extensively used to study mechanical systems. However, sometimes mathematical models do not adequately describe the behavior of some system components and, in some cases, only these components need to be tested. Thus, the Hardware In the Loop (HIL) technique was developed to solve these problems, allowing a real time simulation of a hybrid system composed of physical and virtual parts. Due to this characteristic and the potential cost reduction capacity, without loss of precision and reliability, the HIL technique becomes an important tool for researchers and engineers in different areas such as the automotive industry, robotics and production in general. However, the result shows that there is a time delay phenomenon between the expected and obtained signal. This paper analyzes the time delay effects in a HIL simulation by means of an example of a mass-spring-damper system. The analysis results shows that the time delay comes from the actuator dynamic response and according to the sample time used in the real time system, it strongly affects the HIL simulation transient accuracy and stability. To obtain the same result obtained in the pure simulation, a time delay compensation is applied in the model and its effectiveness was verified by a comparison between full simulated and experimental HIL results.

**Keywords** Time delay effects • Real-time control • Hardware-In-The-Loop (HIL) simulation • Mathematical modeling

### 64.1 Introduction

Nowadays, design, implementation and performance evaluation of systems go through different steps. First starts with a computer simulation, abstracting a complex real system into a mathematical model. Then tests of prototypes or some parts of them are carried out to evaluate the performance. In the end, the whole real system is submitted to a large number of experiments under different testing conditions. However, not only is this design very expensive but also because of the difficulty in obtaining a realistic model of some parts, it has the potential of giving incorrect results during tests.

One method that was proposed to avoid these problems is the hardware-in-the-loop (HIL) method. HIL is a form of component testing where the system has parts of components such as hardware devices and others parts as mathematical models. The hardware component of the system communicate with the software models via electrical exchanged input and output signals using data acquisition with Analog Digital (A/D) and Digital Analog (D/A) converters and an actuation system which simulates the behavior of the rest of the system [1, 2].

This approach is widely used in the automotive industry. Examples are in the testing of the anti-lock braking unit against a simulation model [3, 7], in the research and development of a hydrostatic power transmission system [6], in the testing of a powertrain system for a hybrid electric vehicle [5, 8].

HIL simulation has great advantages such as higher accuracy compared to computer simulation for components whose models are not well known or are difficult to make. It is also a real-time simulation, it is less expensive when compared to complete hardware tests, it decreases the risks, it accelerates the time of tests and it offers high repeatability. On the other hand, HIL applications that test mechanical components use some actuators, usually a hydraulic servo system, to transfer forces and velocities to the hardware [4], introducing a delay that decreases the realism of the test.

---

C.A.G. Carrillo • J.V. Ferreira (✉) • P.S. Meirelles

Faculty of Mechanical Engineering, Computational Mechanics Department, State University of Campinas, 13083–970 Campinas-SP, Brazil  
e-mail: [gordillo.ing@gmail.com](mailto:gordillo.ing@gmail.com); [janito@fem.unicamp.br](mailto:janito@fem.unicamp.br); [pablo@fem.unicamp.br](mailto:pablo@fem.unicamp.br)

The agreement between real and simulated HIL can be improved in two ways. The first way is to include a time delay in the computer simulation that will take into account the time delay due to the actuator. Although this procedure is possible and is good to verify if the HIL test is in fact implemented correctly, it is not what is necessary to validate the hardware system because the computer simulation is being made to have the same response as the HIL simulation instead of obtaining the real desired behaviour from the HIL system. The second way is by using a simulation time step greater than the time delay of the actuator. Applying this second procedure, the correct HIL simulation can be obtained. However, it is known that for long time steps, the responses of discrete systems start to differ too much from the responses of continuous systems.

In theory both procedure should work fine. But when is implemented the first procedure sometimes the result is different from the simulation. Even worse happens with the second procedure, when is applied in the HIL simulation, the result is always wrong.

The aim of this paper is first to demonstrate the drawbacks of the instability, the different transient response and the delays in permanent response by using an example of a mass-spring-damper system. After that, analyses of the sequence computer simulation solution of a pure HIL simulation are carried out to obtain the origin characteristics of the time delay and determine the time delay that should be implemented in the computer simulation of the first procedure and point the reasons that avoid the second procedure work. Then, validate the first procedure by comparing a real test of HIL simulation using a hydraulic servo system with a pure simulation model where the hydraulic and mechanical parts as well as sensors of a servo system, were replaced by an ideal mathematical model with the correct time delay.

## 64.2 Investigation of Factor for Time Delay

### 64.2.1 Real-Time System Process

All the real-time processing cards are based on a clock signal. The clock signal is a square reference signal that the cards use to control and ensure that all the tasks downloaded onto the card run in real-time. The frequency of this signal is chosen by the user and an example is shown in Fig. 64.1.

Each rising edge transition of this signal is responsible for triggering the execution of multiple hardware and software tasks. Among the hardware tasks carried out, the task of firing the A/D and D/A converters will be highlighted. Among the Software tasks carried out, the task of checking if all the foreseen activities occurred before the next rising edge transition will be highlighted. If all the operations could not be completed during the time step a message will be sent informing the user that is not possible to perform the desired processing in real time.

While the board is performing its hardware tasks, it also can perform what is called software tasks such as to calculate math operations, to change some of its parameters or even to read some of its parameters available on board. For example, the

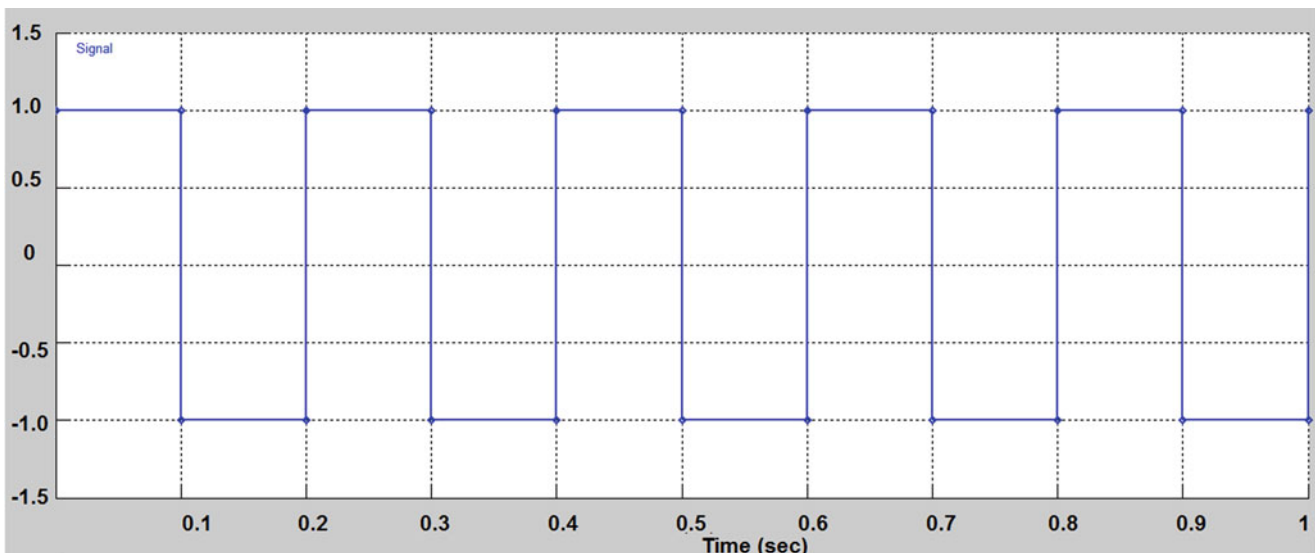


Fig. 64.1 Clock signal

Fig. 64.2 HIL components

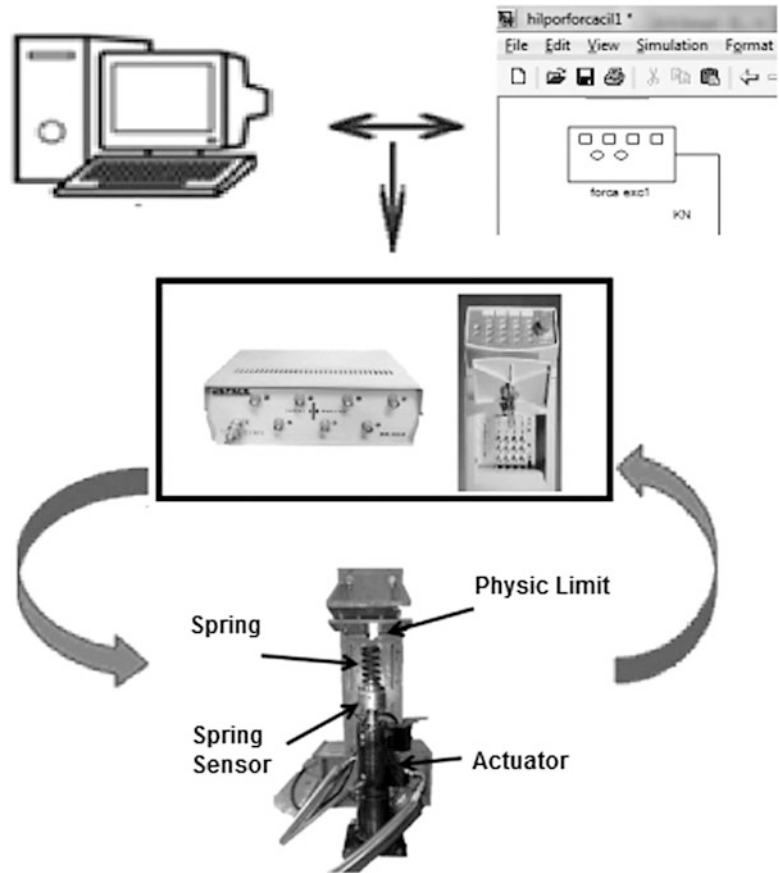
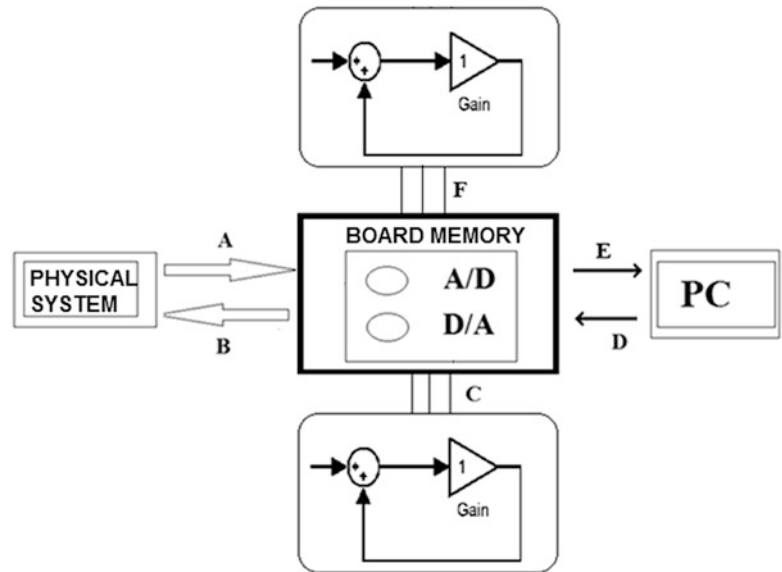


Fig. 64.3 HIL systems operations in real time



variable value in the memory of D/A converter in the acquisition board can be changed at any time. However, the hardware task that converts the variable into a corresponding analog output value will be triggered only in the next rising signal transition that will come after the change is implemented. Another example of software task is that it will allow the signal acquired at the last rising signal transition to be available at any time.

After the work carried out in real time is presented, a diagram of the HIL system components can be seen in Fig. 64.2 and a diagram of the HIL system operation in real time through its basic tasks can be seen in Fig. 64.3.

**Fig. 64.4** HIL sequence of operations in real time

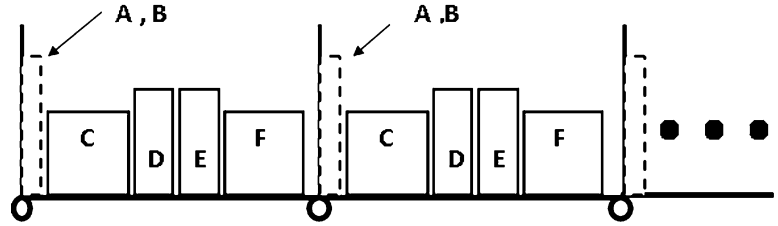
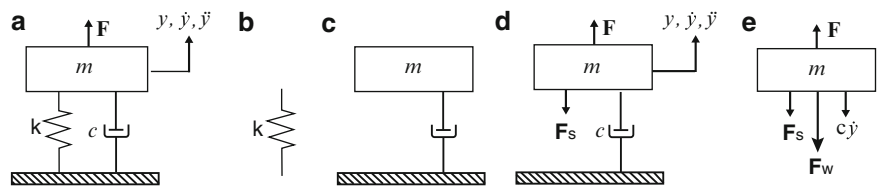


**Fig. 64.5** (a) Real model (b) Hardware (c) Software (d) HIL model (e) Free body diagram



All these processes of Fig. 64.3 must be executed in a sample time period of the clock signal which can be viewed in a continues sequence of execution in real time in Fig. 64.4. It can be seen that the sequence starts with processes A and B, corresponding to the trigger of the A/D and D/A converters, followed by some software operations C, continues with process D that writes the data that will be converted into a corresponding analog output value on the variable memory of the D/A converter, followed by process E that reads the data that was converted from the variable memory of the A/D converter, to finish with some software operations F, and so on repeating the entire procedure described after the next clock rising signal transition.

### 64.2.2 HIL Modeling

The system in this work in which the HIL technique is going to be applied is a mass-spring-damper system with one degree of freedom, shown in Fig. 64.5a.

The HIL model system to be used in the HIL technique is a system shown in Fig. 64.5d resulting from the substitution of the mathematical spring model shown in Fig. 64.5a by the corresponding  $F_s$  force obtained from the load cell of the hydraulic actuator that loads the spring component shown in Fig. 64.5b.

The resulting HIL model from the free body diagram of Fig. 64.5e can be described using the differential equation 64.1.

$$m\ddot{y} + c\dot{y} = +F - F_s - F_w \tag{64.1}$$

The input  $u$  of the system is therefore given by the excitation force  $F$  minus the force generated by the hardware spring force  $F_s$  and the constant weight force due to gravity  $F_w$ .

$$u = F - F_s - F_w \tag{64.2}$$

Adopting as state variables the displacement  $y$  and the velocity  $\dot{y}$ , the second-order equation can be reduced to a system of first order equations. The state equation in continuous time is given by Eq. 64.3.

$$\begin{aligned} \dot{x} &= ax + bu \\ y &= cx + du \end{aligned} \tag{64.3}$$

where the state variable  $x$  and the matrices  $a, b, c$  and  $d$  are given by:

$$\begin{aligned} x &= \begin{Bmatrix} y \\ \dot{y} \end{Bmatrix} & a &= \begin{bmatrix} 0 & 1 \\ 0 & c/m \end{bmatrix} & b &= \begin{Bmatrix} 0 \\ 1/m \end{Bmatrix} \\ c &= [1 \ 0] & d &= 0 \end{aligned} \tag{64.4}$$

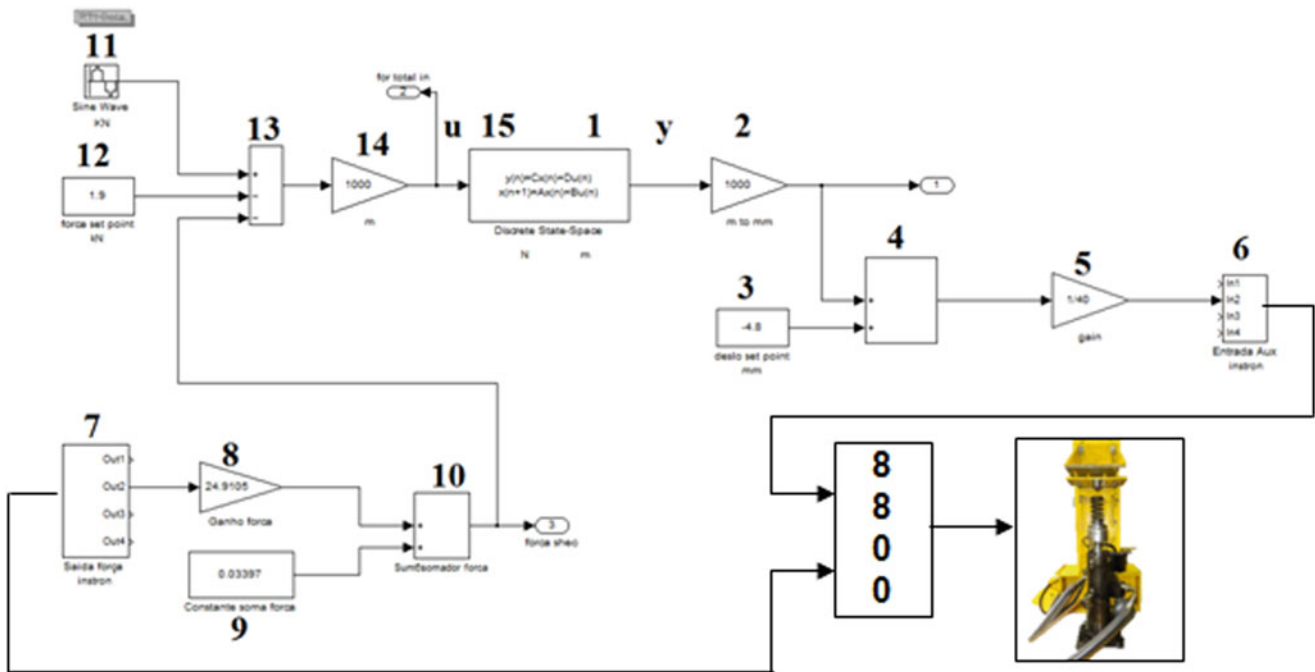


Fig. 64.6 HIL block diagram

Discretizing system equation 64.3 by the step invariance method using a zero-order-hold and a sampling rate of  $Ta$ , the  $A$ ,  $B$ ,  $C$ ,  $D$  matrices of the equivalent mathematical model of the discrete state space system of the HIL technique are obtained and the resulting discrete system is shown by Eqs. 64.5 and 64.6.

$$x(k+1) = Ax(k) + Bu(k) \quad (64.5)$$

$$y(k) = Cx(k) + Du(k) \quad (64.6)$$

where the discretized input force  $u(k)$  is given by Eq. 64.7.

$$u(k) = F(k) - Fs(k-1) - Fw \quad (64.7)$$

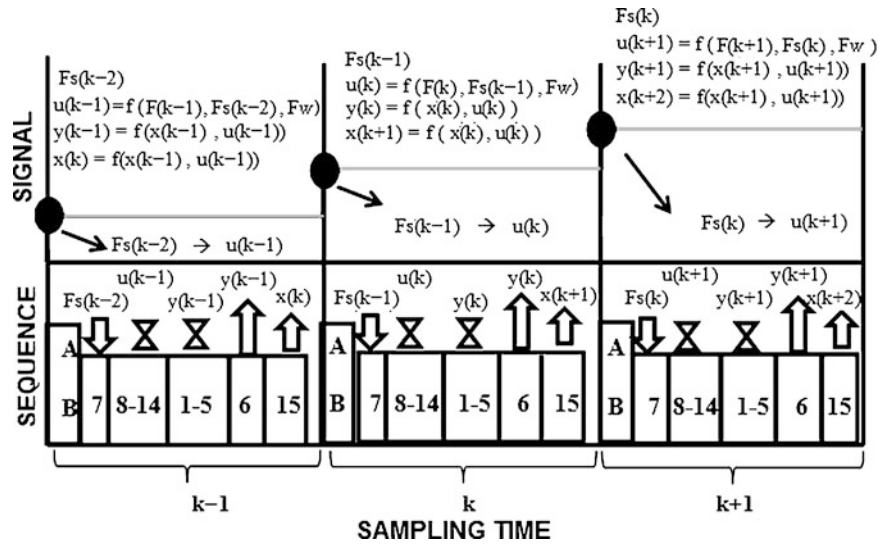
The correspondent basic block diagram of the complete HIL system modeled in Simulink is shown in Fig. 64.6.

### 64.2.3 Ideal HIL Response

By knowing the mathematical model of the discrete state system being modeled with the HIL technique, represented by Eqs. 64.5 and 64.6, and the block diagram modeled in Simulink shown in Fig. 64.6, it is possible to describe the implementation sequence of the HIL technique in real time. It is important to emphasize that it is possible to have different task sequences for the same simulation results. The task numbers used to describe the sequence are the numbers shown in the block diagram in Fig. 64.6. The sequence to be described is the one generated for the dSpace card 1102 by the MatLab/Simulink software and is shown in Fig. 64.7.

Upon receiving a rising edge of the “clock” signal corresponding to the beginning of the time instant ( $k$ ), the hardware processes “A and B” are fired. The hardware process A corresponds to the conversion from digital to analog the value of the displacement  $y(k-1)$  to be imposed on the hardware system. This value of  $y(k-1)$  was calculated in the previous step ( $k-1$ ). The hardware process B converts from analog to digital the hardware spring force  $Fs(k-1)$  resulted from the displacement  $y(k-1)$  that was just imposed in the hardware process A. Following, the Software task “7” is executed, which reads the memory value of the hardware spring force  $Fs(k)$  that was converted by the A/D converter in the process B. Now with the hardware spring force value of  $Fs(k-1)$ , several operations are performed since the task “8” to “14”, resulting into

**Fig. 64.7** Task sequences in dSpace card



the input data of the system that is the total force  $u(k)$ . Then with the value of  $x(k)$  calculated from the previous step and with the calculated value of  $u(k)$ , the Software task “1” is executed, which calculates the displacement  $y(k)$ , which corresponds to the output operation of the discrete system given by Eq. 64.6. After the calculation of  $y(k)$ , operations corresponding from “2” to “5” are performed, which transforms the output signal of displacement  $y(k)$  meters(m) in volts(V). This displacement in volts is saved into the memory board of the D/A converter by the Software task “6”. This displacement  $y(k)$  in volts(V) will be imposed on the next time step  $(k + 1)$  by the clock signal. Then with the same known values  $x(k)$  and  $u(k)$ , the software task “15” is performed corresponding to the calculation of the state vector  $x(k + 1)$  given by Eq. 64.5.

It is observed in the task sequences that there is a fundamental feature: the correct value of  $F_s(k - 1)$ , which is obtained through the A/D converter, is required in the beginning of each time step  $k$ .

### 64.2.4 Real HIL Response

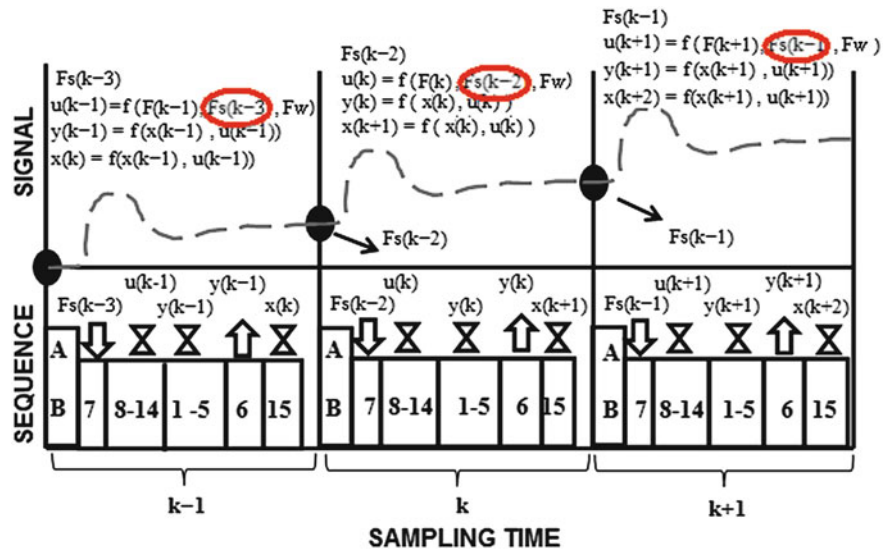
In the case of a real HIL configuration, the system does not respond ideally. The signal results can be seen in Fig. 64.8. At the beginning of instant  $(k)$ , with the rising transition signal of the “clock”, the converters D/A and A/D are fired, and therefore the displacement  $y(k - 1)$  is imposed on the hardware by the D/A converter. However, due to the fact that the actuation system does not respond instantaneously, the value of hardware spring force obtained by the A/D converter is  $F_s(k - 2)$ , and not the desired force  $F_s(k - 1)$ . Thereby calculating a value of  $u(k)$  from Eq. 64.2 is different to that expected, because instead of using the correct value  $F(k - 1)$ , the delayed value  $F(k - 2)$  was used for the calculation of the next steps and so on, repeating the whole process for the next time  $(k + 1)$  under the same conditions described.

## 64.3 HIL Time Delay Validation Setup

### 64.3.1 HIL Response Sequences Validation

To perform the validation of the real and ideal HIL response sequences described before, the virtual simulation of the experimental HIL obtained from the simulated response was compared to the real response obtained from the real HIL experiment. Therefore, the responses were obtained using two setups, one Experimental and one Virtual. The mathematical models used in these setups are implemented under the MATLAB/Simulink environment, which is basically a digital simulation program for dynamic systems widely used as a standard tool for efficient modeling of complex systems. The pure simulation models will be used as a real-time model for a Virtual HIL simulation. The delay adverse effect is demonstrated using two examples. In the first example, the chosen parameter values give an unstable system under the delay effect. In the second example using a new set of parameters, the delay effect in the response is still evident, although both systems with and without delay become stable.

**Fig. 64.8** Real actuator system sequence



### 64.3.2 Experimental HIL System Setup

The Simulink Model developed for obtaining the real HIL responses can be seen in Fig. 64.6. The experimental setup of Fig. 64.6 consists basically of a hardware component connected, by means of a load cell, to an actuator system. This actuator system from INSTRON is made up of two systems. The first system is an actuation system made up of a hydraulic cylinder which has a 10 KiloNewtons (kN) force generation capacity of and a 100 millimeter (mm) linear displacement. This actuator is equipped with a resistive load cell and a LVDT displacement sensor, among other elements to help in the development of HIL application. The second system is an acquisition system consisting of two input channels with BNC connectors, two auxiliary output channels for the sensors, with a IEEE488 (GPIB) communication and has a complete proprietary software called Rs-LabSite with various tools for acquiring, viewing and controlling the processes.

In the real HIL experiment, the virtual part is represented by a mathematical model developed in the MatLab/Simulink software by block diagrams. It has also the capacity of generating a C code to be taken into the real-time tool dSpace, which is made up of a 1102 data acquisition board made up of a Texas Instruments TMS320C31 DSP 60 MHz processor, 33.3 ns cycle time, with D/A and A/D converters, four 12/16-bit resolution analog outputs channels with  $\pm 10$  V range and with a visualization software called ControlDesk.

It is important to notice that for the correct setup of the Experimental HIL system it was necessary to do the calibration of the displacement and the force of the system which correspond to processes 5, and 8 to 10 respectively in Fig. 64.6.

### 64.3.3 Virtual HIL System Setup

To show the simulated responses differences with and without delay, the mass-spring-damper model shown in Fig. 64.5 is used in the numerical Virtual HIL experimental simulation.

It is important to notice that for the correct setup of the Virtual system for the verification of the first procedure, it is necessary not only to substitute the hardware spring by its corresponding mathematical model, but also to introduce a time delay in the spring force.

As the objective of this simulation is to compare the simulation results to the virtual HIL experiment with the results to be obtained in the real HIL experiment, it was necessary to perform a calibration of the spring to extract a representative mathematical model. For the calibration of the hardware spring a third order function was fitted and the result can be seen in Eq. 64.8.

$$Y = -122.7 X^3 - 358.7 X^2 + 100.1 X + 0.5 \tag{64.8}$$

The corresponding block diagram modeled with the calibration of the displacement and force and implemented in Matlab/Simulink can be seen in Fig. 64.9.



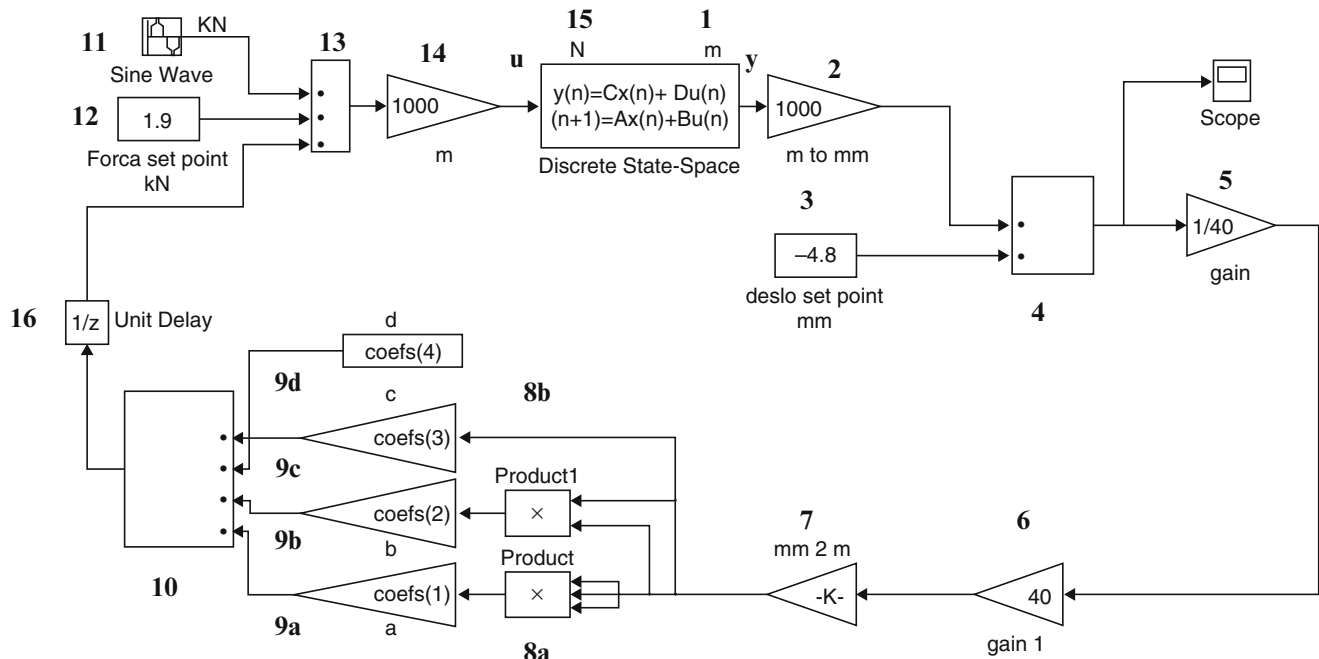


Fig. 64.9 Pure HIL simulation – block diagram with delay

In this simulation, the D/A and A/D converters, the system acquisition, the actuators and the hardware spring, which correspond to processes 6–10 in Fig. 64.6, have been replaced by a mathematical model which corresponds to processes 6–10 in Fig. 64.9. Depending on the desired simulation with or without delay, the delay block corresponding to process 16 in Fig. 64.9 will be introduced or not. The model developed has the same system actuator characteristics, such as the same absolute reference, the same initial position where the spring starts the reaction and the same force limits of the actuator.

#### 64.3.4 Example 1: Unstable with Time Delay

In this model, the parameters have been chosen to show the effect of the delay presence. The pure simulation of a HIL experiment, with delay, results in an unstable system. On the other hand, the pure simulation of a HIL without the delay produces a stable system, as was expected.

This model shows a “set point” equal to  $-4.8$  mm and a maximum displacement amplitude of 40 mm. The model has a mass of 200 kg,  $11.2$  kN s m $^{-1}$  damping and a constant force of 1.0 kN. In the Simulink software, the total simulation time was 10 s with a sample rate of 0.1 s “single task” type and ODE 4 integration method (Runge-Kutta) was used. For the excitation signal, a sinusoidal signal with an amplitude from zero to peak of 0.1 kN and frequency of 2 rad/s was used.

#### 64.3.5 Example 2: Stable with Time Delay

In this model, a stable system is obtained with and without delay, where the responses are completely different in the transient region and have a delay of one step in the permanent region.

This model shows a “set point” equal to  $-4.8$  mm and a maximum amplitude of displacement equal to 40 mm. Also, the model has a 200 kg mass, a  $14$  kN s m $^{-1}$  damping and a 1.9 kN constant force. In the Simulink software, the total simulation time was 10 s with a sampling rate of type “single task” of 0.1 s and the ODE 4 integration method (Runge-Kutta). For the excitation signal, a sinusoidal signal with an amplitude from zero to peak of 1 kN and a frequency of 2 rad/s was used.

## 64.4 Numerical HIL Simulation

### 64.4.1 HIL Simulation of Example 1

The block diagram used in this simulation is shown in Fig. 64.9 with the respective model parameters from Example 1. The Fig. 64.10 shows the simulated response obtained for the mass displacement of the Virtual HIL model with and without delay in the force. It is observed that the simulated response of the HIL with the time delay in the force resulted in an unstable system making it impossible to obtain the correct answer from the influence of the physical component. On the other hand, applying the simulated HIL technique without the time delay, a stable system with a correct response is obtained, proving the expected response of the mass to be an oscillation at the frequency of the harmonic excitation force around the position of its static equilibrium.

### 64.4.2 HIL Simulation of Example 2

The block diagram used in this simulation was that from Fig. 64.9 with the respective model parameters of Example 2. Figure 64.11 shows both the transient and the permanent response of the mass of the Virtual HIL with and without delay in the force. Although both models show the expected steady state stable behavior, it is possible to observe the great difference in behavior between the transient responses of the systems and also the lag of one sampling period between the permanent responses of the systems.

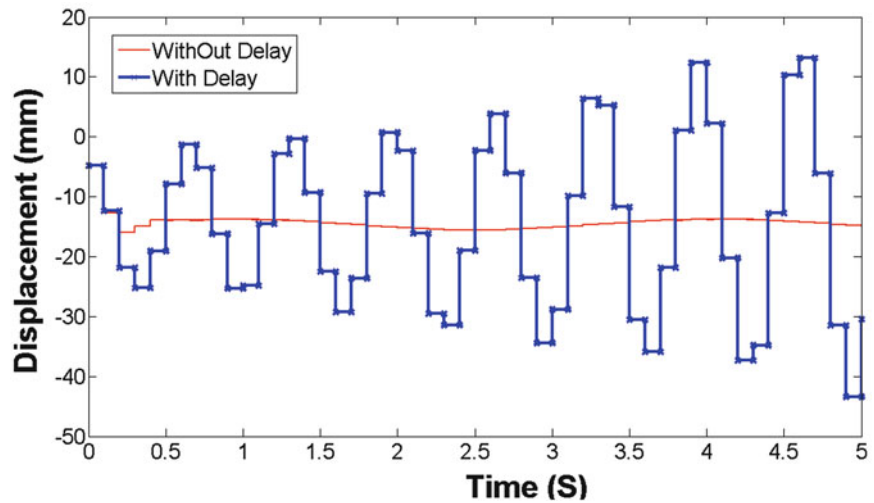


Fig. 64.10 Pure HIL simulation – Example 1

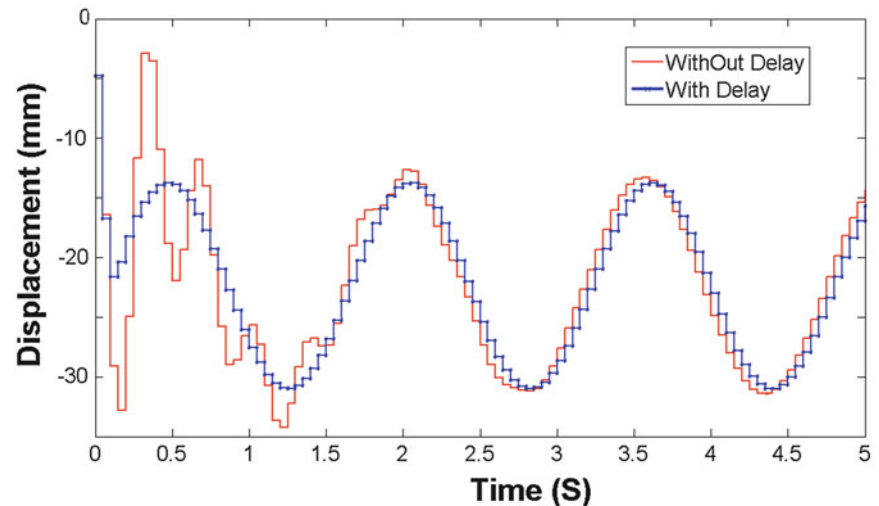


Fig. 64.11 Pure HIL simulation – Example 2

## 64.5 Experimental HIL Realisation

### 64.5.1 HIL Experimental of Example 1

The block diagram developed to perform the test in the real HIL experiment with the HIL Example 1 parameters can be seen in Fig. 64.6. The corresponding code generated by the MATLAB/SIMULINK program was loaded to the 1102 DSpace acquisition board.

Figure 64.12 simultaneously shows the simulated response and the real response obtained from the experiment for mass displacement at a 0–10 s time interval for the first procedure with the delay. The result shows good agreement of the responses up to 1.5 s before the system reaches its hardware safe limits.

### 64.5.2 HIL Experimental of Example 2

Example 2 is carried out with a similar setup that was used in Example 1, but with the set of parameters defined in Sect. 64.4.2.

Figure 64.13 simultaneously shows the simulated response 0–10 s and the real response obtained for the experimental displacement of the mass in a 0–1.5 s time interval for the procedure with the delay before halting. The result shows good agreement of the transient and the steady state responses.

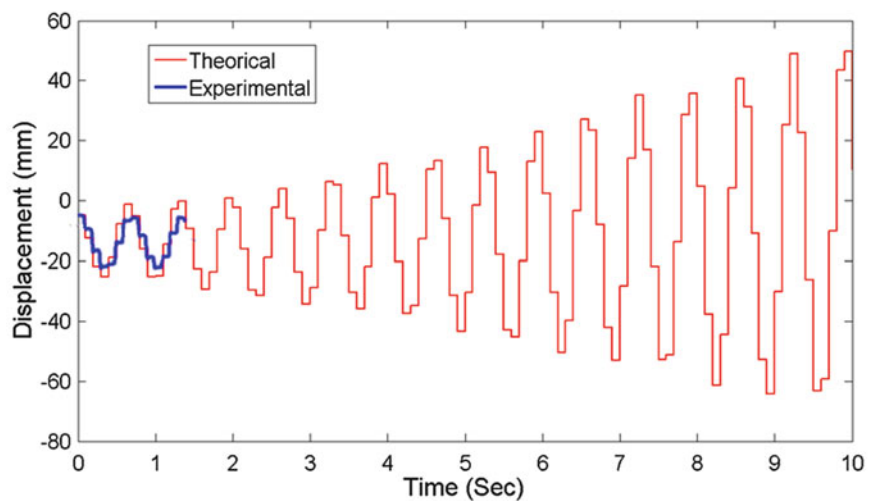


Fig. 64.12 HIL – real and simulation response – Example 1

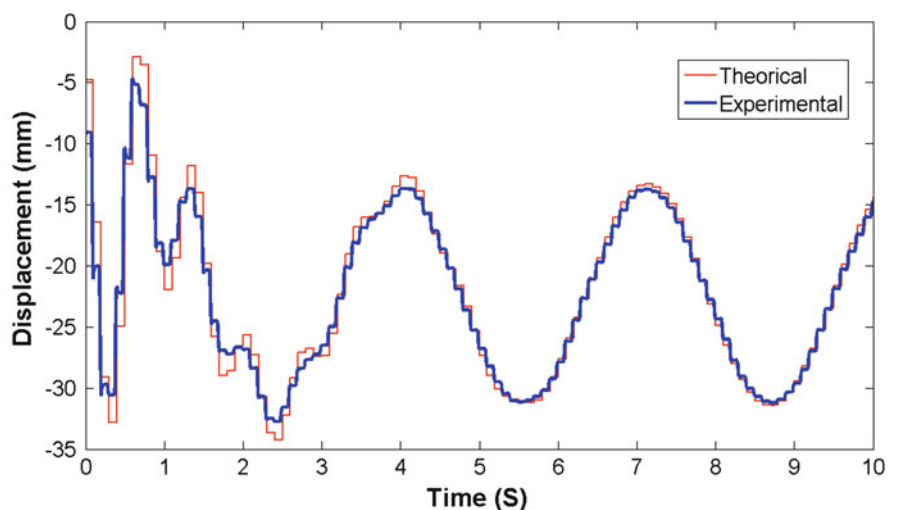


Fig. 64.13 HIL – real and simulation response – Example 2

## 64.6 Concluding Remarks and Future Work

This paper presented the development of the HIL technique that has been used in various research projects and in industrial and academic fields, obtaining the behavior of a system composed of mathematically modeled parts and physical complex components.

The reasons for the appearance of a time delay was investigated in details. It was concluded that there is a 1-step delay due to actuator behavior. The time delay causes error on the force acquisition and deteriorates the dynamic responses. In addition, the stability of the system can be lost depending on the system parameter values. The HIL simulation results were verified using the real HIL experimental results.

In continuation of this work, it will be proposed a different task sequences to eliminate the time delay in the HIL system, fulfilling the condition of being a Real-Time-System(RTS).

**Acknowledgements** The authors would like to express gratitude to Coordenação de Aperfeiçoamento de Pessoal de Nível Superior-CAPES, to Fundação de Amparo à Pesquisa do Estado de São Paulo-FAPESP, to Conselho Nacional de Desenvolvimento Científico e Tecnológico-CNPQ and to Universidade Estadual de Campinas-UNICAMP for providing the financial support.

## References

1. Brendecke T, Kucukay F (2002) Virtual real-time environment for automatic-transmission control units in the form of hardware-in-the loop. *Int J Veh Des* (28):84–102
2. Faithfull PT, Ball RJ, Jones RP (2001) An investigation into the use of hardware-in-the-loop simulation with a scaled physical prototype as an aid to design. *J Eng Des* (12):231–243
3. Lee JC, Suh MW (1999) Hardware-in-the-loop simulator for abs/tcs. In: *Proceedings of the 1999 IEEE – international conference on control applications*, Island of Hawaii, USA, pp 652–657
4. Misselhorn WE, Theron NJ, Els PS (2006) Investigation of hardware-in-the-loop for use in suspension development. *Veh Syst Dyn* (44):65–81
5. Powell BK, Sureshbabu N, Bailey KE, Dunn MT (1998) Hardware-in-the-loop vehicle and powertrain analysis and control design issues. In: *Proceedings of the American control conference*, Philadelphia, pp 483–492
6. Sannelius M, Palmberg JO (1996) Hardware-in-the-loop-simulation of a hydrostatic transmission with sequence-controlled motors. In: *JHPS third international symposium on fluid power*, Yokohama, pp 301–306
7. Svenson AL, Grygier PA, Salaani MK, Heydinger GJ (2009) Validation of hardware in the loop (hil) simulation for use in heavy truck stability control system effectiveness research. In: *21th international technical conference on the enhanced safety of vehicles-(ESV)*, Stuttgart, Germany (09–0189)
8. Yamazaki M, Sureshbabu S, Loftus M, Crandell R, Brackx M (2002) Analysis of automatically generated vehicle system control software in a hil environment. In: *Proceedings of the American control conference*, Anchorage, pp 3135–3140

# Chapter 65

## Optimal Placement of Piezoelectric Patches on a Cylindrical Shell for Active Vibration Control

Caner Gencoglu and H. Nevzat Özgüven

**Abstract** Piezoelectric materials have proven themselves to be used as actuators for active vibration control. In this study, the active vibration control of a cylindrical shell by means of piezoelectric actuators is investigated. As the most important stage of controlling the vibrations, this paper focuses on the optimal placement of piezo patch actuators. It is aimed in this study to determine the optimum locations of piezo patches on a cylindrical shell by using finite element model of the system. In optimization, the spillover effects, which are caused by accidentally excited higher modes of the structure are also taken into account.

**Keywords** Piezoelectric patches • Active vibration control • Cylindrical shell vibrations • Actuator placement • Spillover

### 65.1 Introduction

Piezoelectric materials have proven themselves to be used as actuators for active vibration control of lightweight and flexible structures in recent years. Lightweight and flexible structures are mostly used in space applications. Reducing the mass of the structure due to weight limitations also reduces its stiffness, making low frequency vibrations a problem for the structure. Piezoelectric actuators which have low mass, high bandwidth quick response, low cost and ease of mounting are good candidates for solution of vibration problem [1]. Considerable research effort has been spent in recent years in active vibration control via piezoelectric materials.

Piezoelectric materials are applied as surface mounted patches from the early years of active vibration control studies starting from Crawley and de Luis in 1987 [2]. Beam and plate geometries are studied by many researchers. In the active vibration control problem of structures, placement of actuators has always played an important role. Misplaced actuators may cause lack of controllability and stability [3]. This led researchers to work in the field of optimal placement of actuators in active vibration control problems. Gupta et al. prepared a comprehensive review in the subject of optimal placement of actuators and sensors on smart structures [4]. However, their study covered beam and plate geometry. Although cylinder geometry is commonly used in engineering structures, studies on active vibration control of cylindrical structures with piezoelectric patches are very limited [5].

In the optimal actuator placement problem, several approaches have been used. Hac and Lui used controllability gramian matrices in the calculation of optimal placement of actuators [6]. Bruant et al. used controllability gramians as optimization criteria and genetic algorithm as search method [3]. Peng used ANSYS substructuring tool in the finite element model reduction [1].

In this study the optimal placement of piezoelectric patch actuators on a cylindrical shell is investigated. The system is modeled by using finite elements (FE), and model reduction, similar to the one used by Peng et al. [1]. After the model

---

C. Gencoglu (✉)

Department of Mechanical Engineering, Middle East Technical University, Ankara, Turkey

Roketsan Inc. PO Box 30, 06780, Elmadag, Ankara, Turkey

e-mail: [cgencoglu@roketan.com.tr](mailto:cgencoglu@roketan.com.tr)

H.N. Özgüven

Department of Mechanical Engineering, Middle East Technical University, Ankara, Turkey

e-mail: [ozguven@metu.edu.tr](mailto:ozguven@metu.edu.tr)

reduction and formulation of superelements, effect of piezoelectric material at each possible patch location is calculated by applying unit voltage to each patch and carrying out static analysis. Then, structural matrices required in the computation of controllability gramian matrix are obtained. Alternatively, static analysis can be carried out for a limited number of patch locations and a search method such as genetic algorithm can be used to find optimal locations; however this approach has the risk of having non-convergence. When calculating the optimal placement for actuators the spillover effects, which are caused by accidentally excited higher modes of the structure are also taken into account. The method used in this study does not take the orientation angles of piezoelectric patches into account. Mass and stiffness effects of the actuators are neglected in this study since actuators are thin compared to host structure. Perfect bonding is assumed between piezoelectric patch and host structure.

## 65.2 Methodology

The equation of motion for a dynamic system with piezoelectric actuators on its surface can be written as follows:

$$\mathbf{M}\ddot{\mathbf{r}} + \mathbf{C}\dot{\mathbf{r}} + \mathbf{K}\mathbf{r} = \mathbf{P}\mathbf{V} \quad (65.1)$$

where  $\mathbf{r}$  is the displacement vector for the degrees of freedom of interest,  $\mathbf{M}$  is mass matrix,  $\mathbf{C}$  is damping matrix and  $\mathbf{K}$  is stiffness matrix,  $\mathbf{V}$  is a vector containing the applied voltage information, and  $\mathbf{P}$  is the piezoelectric coupling matrix which relates the applied voltage to the piezoelectric patch and the force applied on the structure by the actuator.

For this structure, proportional damping is assumed, so that damping matrix can be expressed as the linear combinations of stiffness and mass matrices:

$$\mathbf{C} = \alpha\mathbf{M} + \beta\mathbf{K} \quad (65.2)$$

Equation (65.1) can be written in modal domain as shown below:

$$\bar{\mathbf{M}}\ddot{\boldsymbol{\eta}} + \bar{\mathbf{C}}\dot{\boldsymbol{\eta}} + \bar{\mathbf{K}}\boldsymbol{\eta} = \bar{\mathbf{P}}\mathbf{V} \quad (65.3)$$

where  $\boldsymbol{\eta}$  is the vector of modal coordinates,  $\bar{\mathbf{M}}$  is modal mass matrix,  $\bar{\mathbf{C}}$  is modal damping matrix,  $\bar{\mathbf{K}}$  is modal stiffness matrix and  $\bar{\mathbf{P}}$  is piezoelectric coupling matrix transformed into modal domain. The matrices in modal domain can be expressed as follows:

$$\bar{\mathbf{M}} = \boldsymbol{\phi}^T \mathbf{M} \boldsymbol{\phi} \quad (65.4)$$

$$\bar{\mathbf{C}} = \boldsymbol{\phi}^T \mathbf{C} \boldsymbol{\phi} \quad (65.5)$$

$$\bar{\mathbf{K}} = \boldsymbol{\phi}^T \mathbf{K} \boldsymbol{\phi} \quad (65.6)$$

$$\bar{\mathbf{P}} = \boldsymbol{\phi}^T \mathbf{P} \quad (65.7)$$

Here  $\boldsymbol{\phi}$  is the mass normalized modal matrix. Now the system equations can be represented in state space.

$$\begin{aligned} \dot{\mathbf{x}} &= \mathbf{A}\mathbf{x} + \mathbf{B}\mathbf{u} \\ \mathbf{y} &= \mathbf{C}\mathbf{x} + \mathbf{D}\mathbf{u} \end{aligned} \quad (65.8)$$

where

$$\begin{aligned} \mathbf{x} &= [\boldsymbol{\eta} \quad \dot{\boldsymbol{\eta}}]^T \\ \mathbf{u} &= \mathbf{V} \end{aligned} \quad (65.9)$$

$$\begin{aligned} \mathbf{A} &= \begin{bmatrix} \mathbf{0} & \mathbf{I} \\ -\bar{\mathbf{M}}^{-1}\bar{\mathbf{K}} & -\bar{\mathbf{M}}^{-1}\bar{\mathbf{C}} \end{bmatrix} & \mathbf{B} &= \begin{bmatrix} \mathbf{0} \\ \bar{\mathbf{M}}^{-1}\bar{\mathbf{P}} \end{bmatrix} \\ \mathbf{C} &= [\mathbf{I}] & \mathbf{D} &= [\mathbf{0}] \end{aligned} \quad (65.10)$$

Here  $\mathbf{x}$  is the state vector. Conversion of system equations into state space allows calculation of the controllability gramian matrix of the system. By controllability gramian matrix, one can obtain information about how easy it is to control the states

of the system. The controllability gramian matrix is the measure of controllability of a system and defined as follows [7]:

$$\mathbf{W}_C(t_1) = \int_0^{t_1} e^{\mathbf{A}t} \mathbf{B} \mathbf{B}^T e^{\mathbf{A}^T t} dt \quad (65.11)$$

In this equation  $\mathbf{W}_C(t_1)$  is the controllability gramian matrix at time  $t_1$ . In this problem, states of the system are defined by modal coordinates. So each of the diagonal element of the controllability gramian matrix gives information about the effort to be spent to control the corresponding particular mode of the system. For example, having a higher value for the controllability gramian for a mode means less effort to be spent to control that particular mode. By comparing the controllability gramian values of a system with different piezoelectric actuator locations, the best actuator location to control vibrations of the system can be determined.

Spillover problem may emerge when controlling real structures by means of feedback control. When modelling a vibrating structure, only a limited number of modes are included in the model, and higher modes are usually truncated. When trying to implement feedback control, the high frequency modes may be accidentally excited. As also noted by Bruant et al., only in few papers spillover effects are considered when placing actuators [3]. In the placement criterion, the modes which are not taken into account when designing the feedback controller should also be considered as the ones not to be excited. According to this criterion, actuators should be placed such that they control the desired modes and they do not excite the selected higher modes which are not controlled.

The placement criterion  $J$  to control first  $N$  modes is stated as follows [6]:

$$J = \frac{1}{\sigma(\lambda_i)} \left( \sum_{i=1}^{2N} \lambda_i \right) \sqrt[2N]{\left( \prod_{i=1}^{2N} \lambda_i \right)} \quad (65.12)$$

where  $\lambda_i$  are the eigenvalues of controllability gramian matrix and  $\sigma(\lambda_i)$  is the standard deviation of  $\lambda_i$ . A higher  $J$  value for a possible patch location means that this location is a better place for actuator placement. In this criterion, having high values of summation of eigenvalues of controllability gramian matrix leads to high controllability. Same amount of controllability for each mode is desired, so by means of multiplication of eigenvalues and division by the standard deviation of eigenvalues make each mode equally controllable [7].

By using this criterion, locations that will control all the desired modes can be determined. However spillover effects are not considered in this criterion. As a modification to this, it is suggested not to excite the high order modes that are not included in the system model. To achieve this, the criterion is modified as follows [6]:

$$J = \frac{1}{\sigma(\lambda_i)} \left( \sum_{i=1}^{2N_m} \lambda_i \right) \sqrt[2N_m]{\left( \prod_{i=1}^{2N_m} \lambda_i \right)} - \gamma \frac{1}{\sigma(\lambda_i)} \left( \sum_{i=2N_m+1}^{2N_m+2N_u} \lambda_i \right) \sqrt[2^*N_u]{\left( \prod_{i=2N_m+1}^{2N_m+2N_u} \lambda_i \right)} \quad (65.13)$$

Here  $N_m$  is the number of modes used in the system model (modes used in the feedback controller) and  $N_u$  is the number of high order modes which are not included in the control system model but considered for spillover effects, and  $\gamma$  is the weighting constant. If the control system works up to 1,000 Hz, then number of modes of system up to 1,000 Hz is equal to summation of  $N_m$  and  $N_u$ . For instance, if the structure has 14 modes up to 1,000 Hz and if we are interested in controlling the first 4 modes then  $N_m$  is 4 and  $N_u$  is 10.

### 65.3 Application to Cylinder Geometry

A hollow cylinder of 200 mm inner diameter and 600 mm length and 2 mm thickness is taken as the host structure. The cylinder is made of aluminum and one end of the cylinder is fixed to a rigid wall. PZT 4 piezoelectric patches of 1 mm thick are glued on the outside wall of the cylinder. The actuators will be in unimorph operation mode. A perfect bonding between piezoelectric patch and the host structure is assumed.

To obtain the optimal locations of piezoelectric patch actuators on a cylindrical shell, the shell structure is divided into sectors. Each sector is a possible location for a patch actuator. In radial direction, the possible patch location covers 22.5° of a circle. In length, the cylinder is divided into 12 equal pieces. Dividing the cylindrical shell into sectors for possible patch

**Fig. 65.1** Cylindrical shell geometry divided into sectors

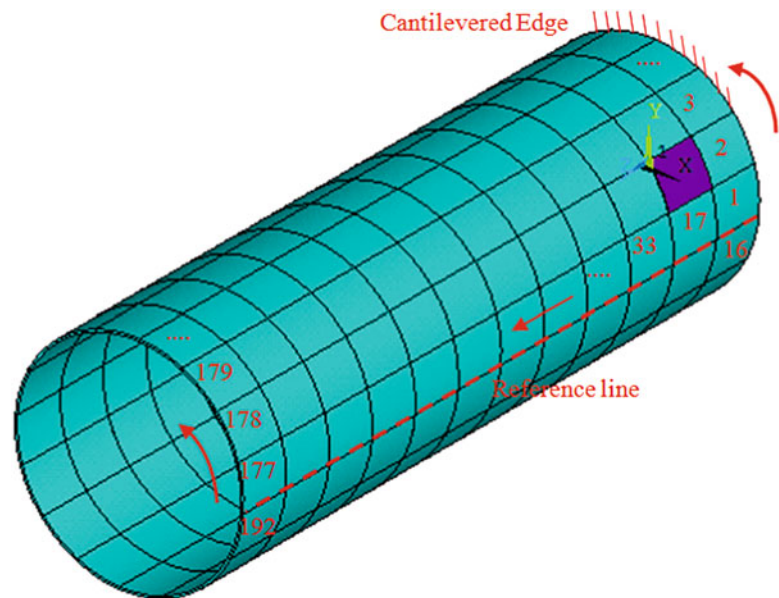
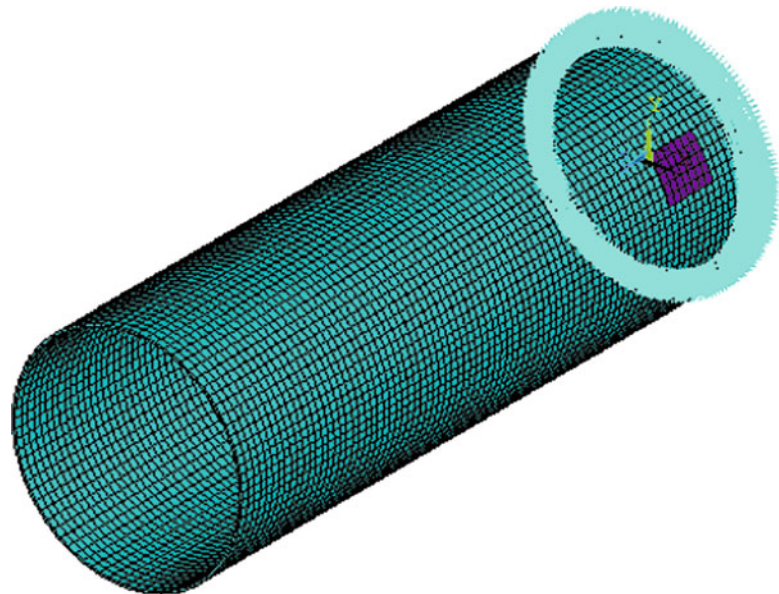


**Fig. 65.2** Mesh generated over the cylinder



actuator location generates a grid over the cylinder. The grid is composed of the corners of each sector. In the calculation of mass, stiffness, damping and piezoelectric matrices, the degrees of freedoms taken from finite element mesh are the radial coordinates of grid points since in cylinder structure, radial modes (breathing modes) are the modes of interest.

The divided sectors of the cylindrical shell (possible piezoelectric patch locations) are shown in Fig. 65.1.

After the cylinder geometry is formed, a proper mesh is generated over the cylinder. For the aluminum cylinder SOLID 186, for piezoelectric patch SOLID 226 type elements are used. One end of the cylinder is constrained in all degrees of freedom. The mesh with the boundary condition is shown in Fig. 65.2.

For the material properties used in the analysis, the piezoelectric properties of PZT 4 (Navy Type 1) are taken. Material properties of the host structure and the active element used in this study are listed in Table 65.1.

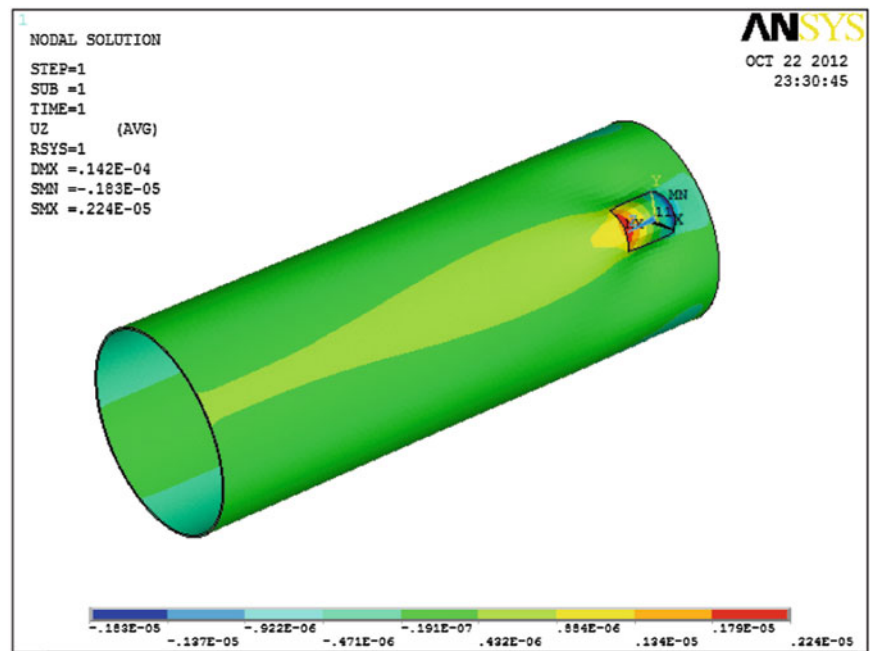
The generated mesh is used in the analyses; however, the radial deflection results are collected only at the nodes which are located at the corner of each sector. In other words, the results at the grid nodes are taken into consideration. These coordinates are selected as master degrees of freedom (dofs) in ANSYS substructuring analysis. In the calculation of mass, stiffness, damping and piezoelectric matrices, radial degree of freedom of grid points are considered.



Table 65.1 Material properties

Host structure: Aluminum	
Young's modulus	70 GPa
Poisson's ratio	0.33
Density	2,700 kg/m <sup>3</sup>
Active material: PZT 4	
Density	7,500 kg/m <sup>3</sup>
d <sub>31</sub>	-1.23 * 10 <sup>-10</sup> m/V
d <sub>33</sub>	2.89 * 10 <sup>-10</sup> m/V
d <sub>15</sub>	4.96 * 10 <sup>-10</sup> m/V
s <sub>11</sub> <sup>E</sup>	1.23 * 10 <sup>-11</sup> ms <sup>2</sup> /kg
s <sub>33</sub> <sup>E</sup>	1.55 * 10 <sup>-11</sup> ms <sup>2</sup> /kg
s <sub>12</sub> <sup>E</sup>	-4.05 * 10 <sup>-12</sup> ms <sup>2</sup> /kg
s <sub>13</sub> <sup>E</sup>	-5.31 * 10 <sup>-12</sup> ms <sup>2</sup> /kg
s <sub>44</sub> <sup>E</sup>	3.90 * 10 <sup>-11</sup> ms <sup>2</sup> /kg
s <sub>66</sub> <sup>E</sup>	3.27 * 10 <sup>-11</sup> ms <sup>2</sup> /kg
K <sub>11</sub> <sup>T</sup>	1,475 (ε <sub>11</sub> <sup>T</sup> /ε <sub>0</sub> )
K <sub>33</sub> <sup>T</sup>	1,300 (ε <sub>33</sub> <sup>T</sup> /ε <sub>0</sub> )
ε <sub>0</sub>	8.85 * 10 <sup>-12</sup> F/m

Fig. 65.3 Static analysis for one possible piezoelectric patch location on the cylinder



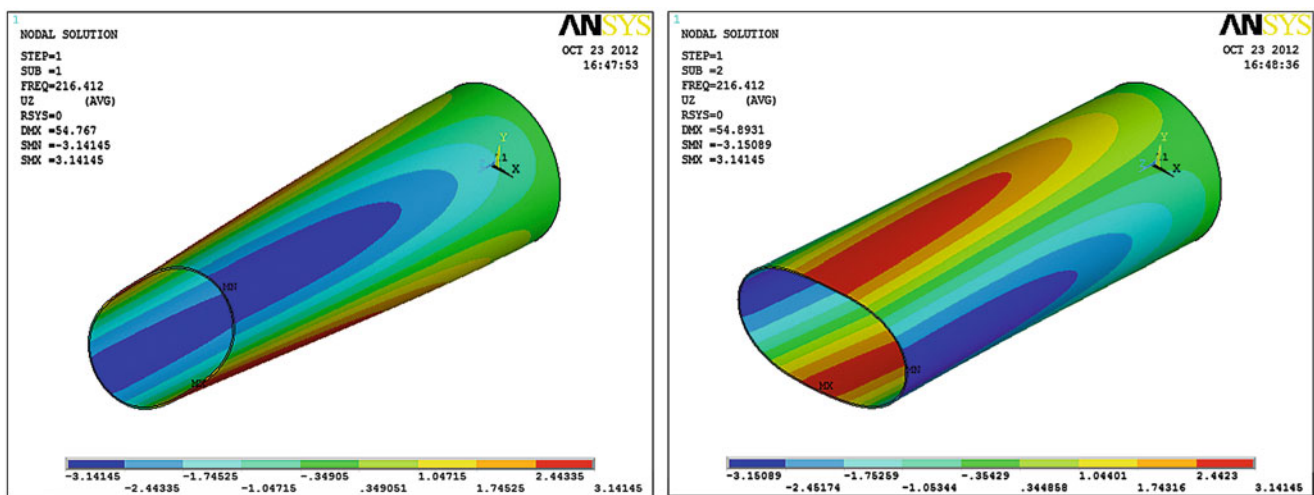
The equation of motion of the cylinder is expressed in terms of the master dofs chosen. Therefore, firstly the reduced mass, damping and stiffness matrices and the piezoelectric matrix are calculated. Then the system is expressed by state space representation to calculate the controllability gramian for the vibratory system.

In calculation of piezoelectric matrix, a solid in the shape of piezoelectric patch actuator is placed on one of the possible actuator locations and piezoelectric material properties are attributed on that solid. After generating the structure, 1 V is applied on the outer surface and 0 V is applied on the inner surface of the patch actuator. A static analysis is done for each possible patch locations and deformations of the nodes on the grid in radial direction are collected to form a column of P matrix. A sample static analysis result with one piezoelectric patch on the cylinder surface is shown in Fig. 65.3. Then the geometry is re-created by the APDL macro, but this time the patch is moved to the next location. The procedure is continued until a single patch has moved to each possible location. In this case P is a 192 by 192 matrix, since there are 192 master dofs and 192 possible patch locations. In static case, Eq. (65.1) reduces to  $\mathbf{K}\mathbf{r} = \mathbf{P}\mathbf{V}$  from which piezoelectric matrix can be calculated.

The reduced mass and stiffness matrices obtained by substructuring analysis are reordered according to the degrees of freedom numbers of the grid. Damping matrix is calculated from mass and stiffness matrices by assuming proportional damping. Here, proportional structural damping is assumed; so that  $\alpha = 0$  and  $\beta = 1 \times 10^{-6}$ . The piezoelectric matrix

**Table 65.2** Natural frequencies of the host structure

Mode number	Natural frequency (Hz)
1	216.4
2	216.4
3	379.4
4	379.4
5	476.5
6	476.5
7	615.6
8	615.6
9	708.8
10	708.8
11	787.7
12	787.7
13	897.4
14	897.4

**Fig. 65.4** First two modes of the structure

is calculated for each possible patch location. Therefore, the corresponding column of P matrix is taken when calculating controllability gramian for each possible piezoelectric patch actuator location. At each possible patch location, a new system model is generated in state space according to Eqs. (65.8) and (65.10). Then the controllability gramian matrix for each of those systems is computed using MATLAB. Another approach would be carrying out static analysis for a limited number of patch locations and using a search method such as genetic algorithm to find optimal locations. However, such approaches may have the drawback of having non-convergence.

In finding the optimum patch locations for the cylindrical structure considered, the modes of the cylinder up to 1,000 Hz are taken into consideration. The first 14 natural frequencies of the structure are given in Table 65.2. Note that in this calculation, the slight changes in the natural frequencies of the host structure due to the existence of PZT patches are ignored.

In this application the first four modes of the cylindrical structure are selected to be controlled. The corresponding mode shapes are given in Figs. 65.4 and 65.5.

In this active vibration study, a feedback controller with a frequency band up to 1,000 Hz is chosen to be used. In order to avoid spillover effects for the higher modes of the structure up to 1,000 Hz, the criterion of placement is constructed such that the modes to be controlled are the first four modes (216.4 and 379.4 Hz) and modes which are not controlled, but also not to be excited while controlling the first four modes are 5th to 14th modes. The placement criterion values calculated at each possible patch location are shown in Fig. 65.6. The locations with high placement criterion values are optimal locations for patch placement. The best locations are found to be 163 and 171 from this figure. These locations are close to the free edge, and they are equally spaced on the periphery of the cylinder. The second best locations are found as 179 and 187 which are at the free edge and equally spaced on the periphery as in the previous case. It should be noted here that the best patch location on one periphery of the cylinder depends on the orientation of the mode shape and the orientation of the grid formed over cylinder.

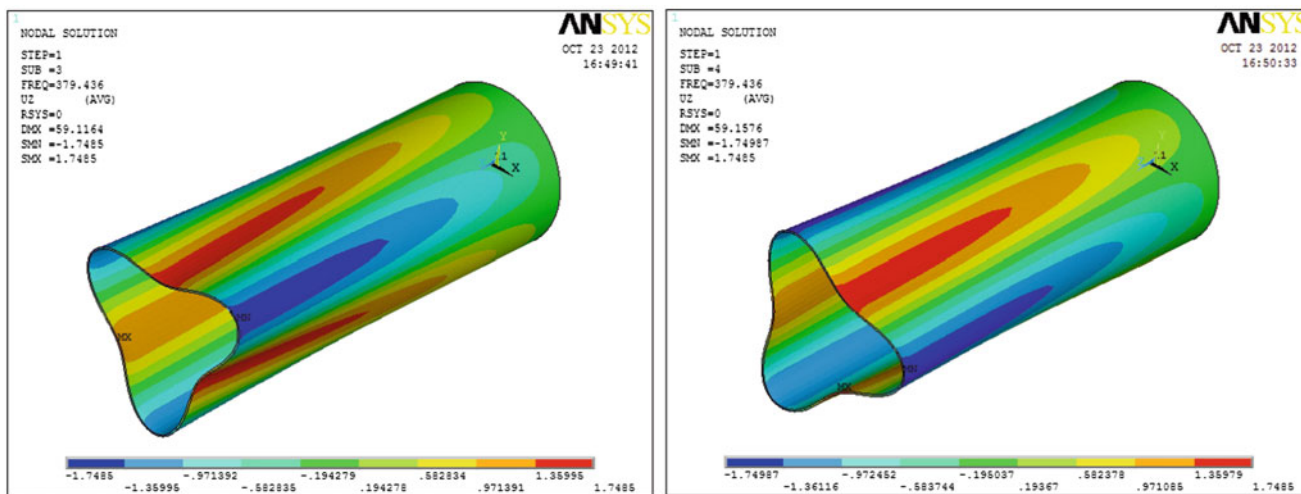
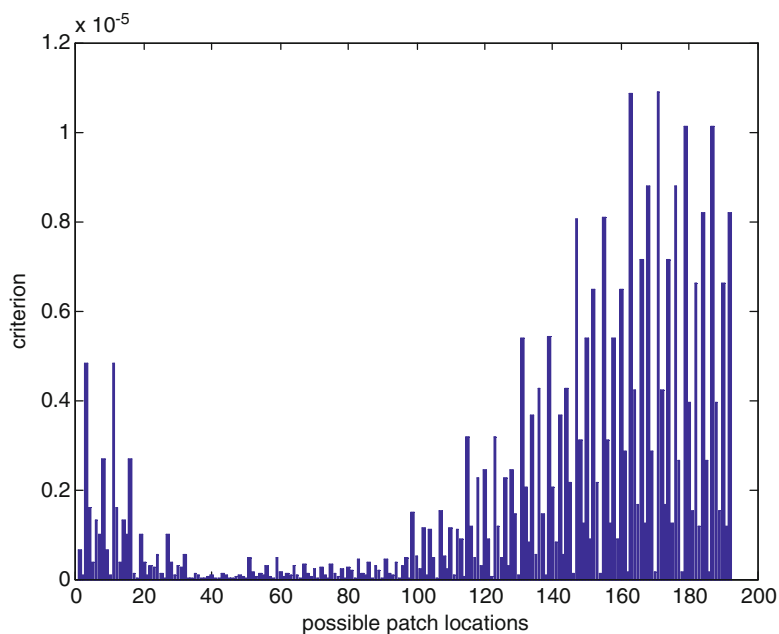


Fig. 65.5 Third and fourth modes of the structure

Fig. 65.6 Placement criterion values at possible patch locations



In order to demonstrate the effect of active vibration control with piezoelectric patches which are placed at the best and second best locations, three analyses are carried out. In the first analysis no actuator is placed on the cylinder and a force of 100N is applied on the free edge of the cylinder in 3 o'clock direction and then suddenly released. The point where the force is applied is shown in Fig. 65.7. The free vibration response of the cylinder at the point where the force is applied is calculated by transient vibration analysis. In the second and third analyses, the same initial disturbance is given and the vibration responses of the same point are computed. However, in these analyses the piezoelectric patch is used and a closed loop control system is employed. The displacement of the point where 100 N force is applied is taken as the feedback signal of the controller. A simple proportional controller with a gain of 20,000 is used. In the second analysis the piezoelectric patch is placed at location 163 (one of the best locations) and in the third analysis it is placed at location 179 (one of the second best locations). The output signal of the controller is used as the voltage input for the piezoelectric patch actuator. In the implementation of control system in the transient analyses, an APDL macro is used [8]. The time domain results of the three transient analyses are given in Fig. 65.8, and the results in frequency domain are given in Fig. 65.9.

From Fig. 65.9 it can be observed that the approach is successful in reducing vibration response in the first four modes by also avoiding the spillover effects in most of the higher modes.

**Fig. 65.7** Application point of 100 N force

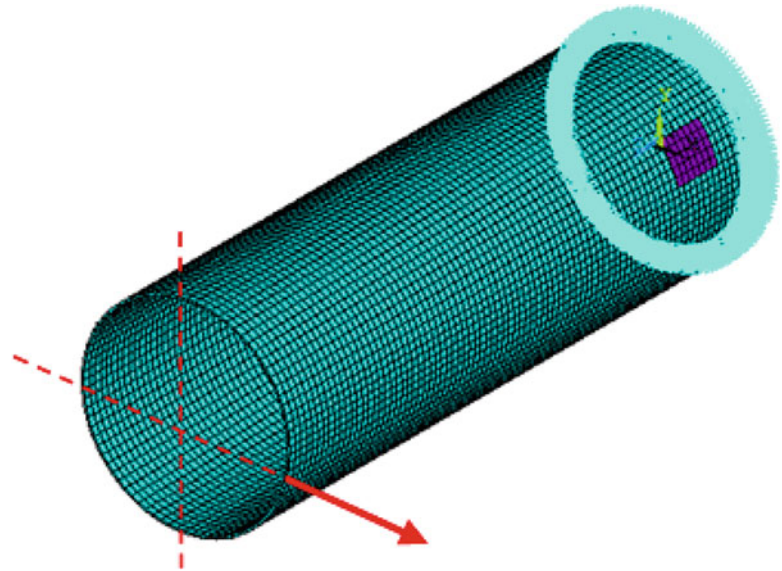
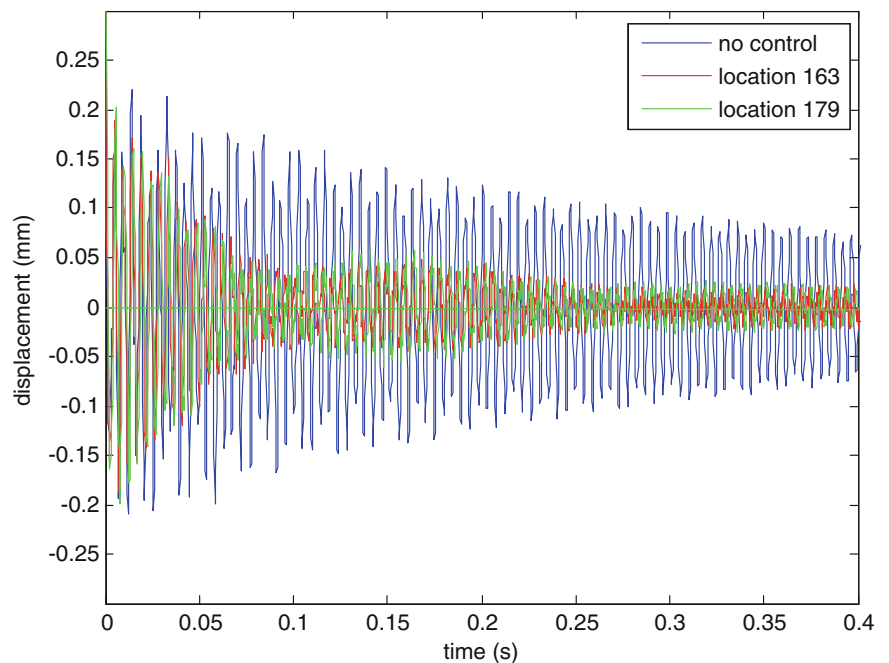


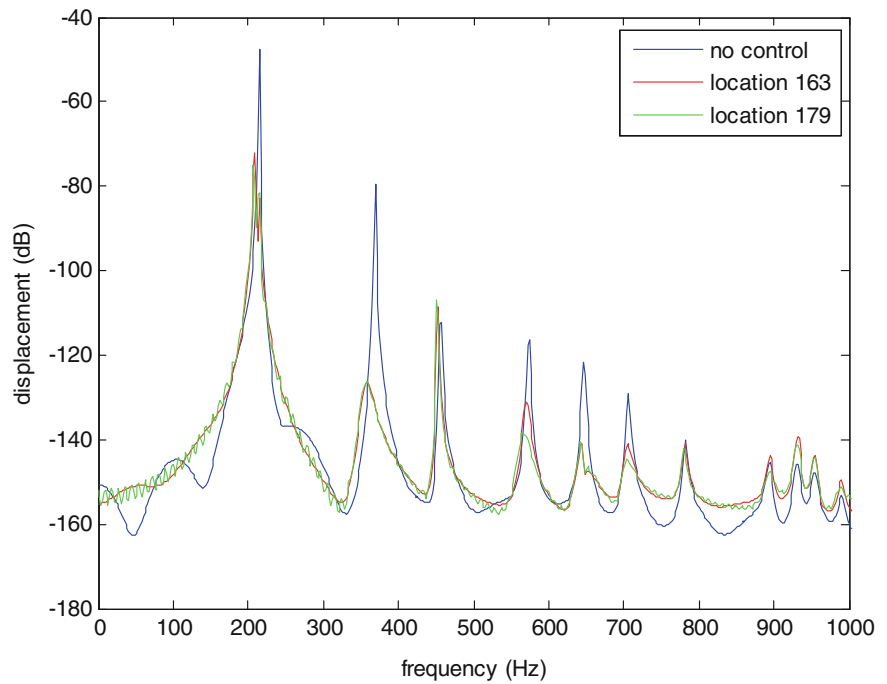
**Fig. 65.8** Time domain responses



## 65.4 Conclusion

In this study, optimum placement of piezoelectric patch actuators for active vibration control of cylindrical shell structures is studied. The approach employed in finding best piezoelectric patch locations is based on controllability gramian of the structure calculated for each possible actuator location. In order to find the best actuator locations to control a desired number of modes, and not to cause spillover due to certain high order modes, a modified placement criteria is utilized. The approach suggested is employed to control the first four modes of a cantilevered cylindrical shell and at the same time not to cause spillover at higher modes until 1,000 Hz. The best and second best locations are determined for an example problem, and the transient responses of the system are calculated with and without active vibration control. It is observed in this application that the approach is successful in reducing vibration response in the first four modes, as planned, by also avoiding the spillover effects in most of the higher modes.

**Fig. 65.9** FFT of time domain responses



## References

1. Peng F, Ng A, Hu Y-R (2005) Actuator placement optimization and adaptive vibration control of plate smart structures. *J Intell Mater Syst Struct* 16:263–271
2. Crawley EF, de Luis J (1987) Use of piezoelectric actuators as elements of intelligent structures. *AIAA J* 25:1373–1385
3. Bruant I, Gallimard L, Nikoukar S (2010) Optimal piezoelectric actuator and sensor location for active vibration control, using genetic algorithm. *J Sound Vib* 329:1615–1635
4. Gupta V, Sharma M, Thakur N (2010) Optimization criteria for optimal placement of piezoelectric sensors and actuators on a smart structure: a technical review. *J Intell Mater Syst Struct* 21:1227–1243
5. Sohn JW, Choi S-B, Kim HS (2011) Vibration control of smart hull structure with optimally placed piezoelectric composite actuators. *Int J Mech Sci* 53:647–659.
6. Hac A, Lui L (1993) Sensor and actuator location in motion control of flexible structures. *J Sound Vib* 167:239–261
7. Jha AK, Inman DJ (2003) Optimal sizes and placements of piezoelectric actuators and sensors for an inflated torus. *J Intell Mater Syst Struct* 14:563–576
8. Karagülle H, Malgaca L, Öktem HF (2004) Analysis of active vibration control in smart structures by ANSYS. *Smart Mater Struct* 13:661–667

# Chapter 66

## Adaptive Feedback Linearisation and Control of a Flexible Aircraft Wing

S. Jiffri, J.E. Mottershead, and J.E. Cooper

**Abstract** Active control systems are used on aircraft to reduce loads due to gusts and manoeuvres, reduce the effect of noise, and could also increase the speed at which flutter occurs. Unfortunately most aeroservoelastic systems include some form of nonlinearity, and this increases the complexity of the feedback system and also facilitates the likelihood of Limit Cycle Oscillations occurring. Previous work on the application of Adaptive Feedback Linearisation to aeroelastic systems has demonstrated the promising potential of this method when applying control in the presence of substantial nonlinearity.

In this work, Adaptive Feedback Linearisation is applied to an aeroelastic model of a cantilevered flexible wing with a cubic hardening structural nonlinearity in an engine pylon. Using assumed vibration modes, a suitable model of the wing is developed, into which structural nonlinearity is incorporated. Closed-loop control is implemented on the aeroservoelastic system via linearising feedback computed through the Adaptive Feedback Linearisation algorithm. The advantage of the latter is the guaranteed stability of the closed-loop aeroelastic system, despite lack of knowledge of the exact description of the nonlinearity. It is shown how such an approach can be used to delay the onset of flutter or limit cycle oscillations.

**Keywords** Aeroelasticity • Nonlinear aeroelasticity • Limit cycle oscillations • Control • Feedback linearisation • Adaptive feedback linearisation • Flutter suppression • Pole placement

### Nomenclature

$\zeta_1$ Vertical deflection of wing at point 1	$\mathbf{f}_{nl}, \mathbf{f}_{nl,mod}$ Nonlinear spring forces (phys/ass-mod)
$\theta_{wt}$ Wing twist angle	$\bar{f}_i, \bar{g}_i$ Controller gains for $i$ th linearised sub-system
$\theta_{pe}$ Absolute pylon-engine rotation	$K_T$ Linear stiffness of torsional spring
$\vartheta_{pe}$ Rotation of pylon-engine relative to wing	$K_{T,nl}$ Cubic stiffness coefficient
$\rho$ Air density	$\tilde{K}_{T,nl}$ Error in cubic stiffness coefficient
$\chi_2$ Wing twist angle at point 2	$q_1, q_2, q_{pe}$ Generalised co-ordinates of coupled system in assumed-modes domain
$\underline{A}_{cl}$ State matrix of closed-loop system	$\mathbf{q}, \dot{\mathbf{q}}, \ddot{\mathbf{q}}$ Generalised displacements/velocities/accelerations
$A, A_{mod}$ Inertia matrix (physical/assumed-modes)	$\mathbf{u}$ Vector of inputs
$a_C, b_C$ Rate of change of lift coefficient and moment coefficient respectively, with respect to control surface deflection angle	$\bar{\mathbf{u}}$ Vector of artificial inputs
$B, B_{mod}$ Aerodynamic damping (phys/ass-mod)	$V$ Airflow velocity
$C, C_{mod}$ Aerodynamic stiffness (phys/ass-mod)	$\bar{V}$ Scalar Lyapunov function

S. Jiffri (✉) • J.E. Mottershead

Centre for Engineering Dynamics, School of Engineering, The University of Liverpool, Brownlow Hill, Liverpool L69 3GH, UK  
e-mail: [s.jiffri@liv.ac.uk](mailto:s.jiffri@liv.ac.uk); [J.E.Mottershead@liverpool.ac.uk](mailto:J.E.Mottershead@liverpool.ac.uk)

J.E. Cooper

Department of Aerospace Engineering, University of Bristol, Queens Building, University Walk, Bristol BS8 1TR, UK  
e-mail: [J.E.Cooper@bristol.ac.uk](mailto:J.E.Cooper@bristol.ac.uk)

$D, D_{mod}$	Structural damping (phys/ass-mod)	$x$	State vector in nonlinear domain
$E, E_{mod}$	Structural stiffness (phys/ass-mod)	$y_a, y_b, y_c$	Outputs chosen for feedback linearisation
$f, f_{mod}$	Applied control forces (phys/ass-mod)	$z$	State vector in linearised domain

## 66.1 Introduction

Linear control methods such as pole-placement rely on the assumption that any nonlinearities present in the system are negligible. Such an assumption may be acceptable in weakly nonlinear regimes. However, in situations where behaviour associated with substantial nonlinearity – such as limit cycle oscillations (LCO)—is observed, the approximation of linearity may greatly reduce the effectiveness of active control.

Application of linear control methods on a nonlinear system with hardening stiffness is investigated experimentally by Block and Strganac in [1]. It is found that the effectiveness of linear control is limited to situations where the airspeed is not much higher than the linear flutter speed, where the LCO amplitude is small. For airspeeds substantially higher than the linear flutter speed (where LCO amplitudes are higher) the control becomes unpredictable, and its effectiveness limited.

Ko et al. apply Feedback Linearisation to a 2-DOF rigid aeroelastic system with torsional nonlinearity [2]. It is shown that using a single control surface leads to local stability, whereas global stability may be achieved using two control surfaces. This work is extended in [3], where the same authors perform a detailed analysis of plunge mode control, and also introduce adaptive feedback linearisation in the two control surface case to account for nonlinearity parameter errors. The latter is implemented experimentally by Platanitis and Strganac [4], with results indicating an improvement when using an additional control surface, but only up to moderately high air velocities. A later publication by Ko et al. [5] examines the case where only a single control surface is employed. In this case, global stability is only guaranteed if the zero-dynamics of the uncontrolled sub-system is stable.

The Adaptive control method is later implemented experimentally by Strganac et al. [6], with results suggesting that knowledge of the exact nonlinearity parameters is critical to the performance of feedback linearisation in the absence of adaptive methods, and that the adaptive controller substantially improves the controlled response. It is also observed in [6] that performing feedback linearisation without adaptation in the presence of parameter errors can cause the system to reach non-zero equilibria, rather than the zero equilibrium that is usually sought.

Monahemi and Kristic employ adaptive feedback linearisation to suppress wing-rock motion, a phenomenon triggered primarily by aerodynamic nonlinearities [7]. In their work, the role of adaptive control is to update the aerodynamic parameters. Other applications of adaptive feedback linearisation include work by Fossen and Paulsen on the automatic steering of ships [8].

In this paper, Adaptive Feedback Linearisation is applied to a flexible wing with a structural nonlinearity. The latter is introduced to the system by coupling a rigid pylon-engine to the wing via a nonlinear hardening torsional spring. The wing flexibility is modelled using two assumed vibration modes, and is simple in nature (for a detailed model of flexible aircraft, the reader is referred to a publication by Nguyen and Tuzcu [9]). An uncertainty in the parameter describing the nonlinearity is introduced, and the controlled response compared when adaptive feedback linearisation and exact feedback linearisation are applied.

## 66.2 The Aeroservoelastic Model

The governing equation of the aeroservoelastic model takes the usual form given by

$$\mathbf{A}\ddot{\mathbf{q}} + (\rho V \mathbf{B} + \mathbf{D})\dot{\mathbf{q}} + (\rho V^2 \mathbf{C} + \mathbf{E})\mathbf{q} = \mathbf{f}, \quad (66.1)$$

where  $\mathbf{A}$ ,  $\mathbf{D}$ ,  $\mathbf{E}$  are the inertia, structural damping and structural stiffness matrices respectively,  $\mathbf{B}$ ,  $\mathbf{C}$  are the aerodynamic damping and aerodynamic stiffness matrices respectively, and  $\rho$ ,  $V$  are air density and velocity respectively. The vector  $\mathbf{q}$  contains generalised co-ordinates describing the motion of the system, whereas the vector  $\mathbf{f}$  contains externally applied generalised forcing terms.

In this work, modified aerodynamic strip theory has been used to compute the lift and pitch moment acting on the wing section. An additional unsteady aerodynamic derivative term is included to account for significant unsteady effects.

**Fig. 66.1** The two deflection patterns assumed for the flexible wing

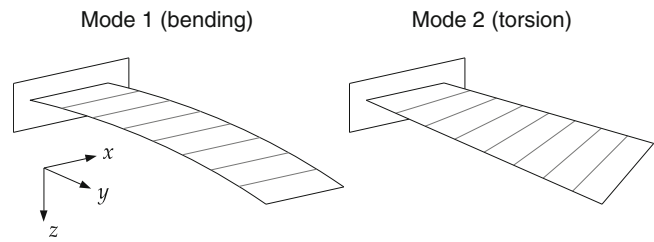


**Fig. 66.2** 3D view of pylon-engine

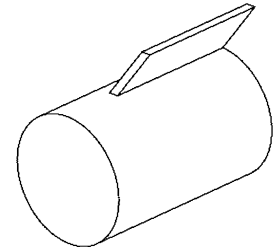
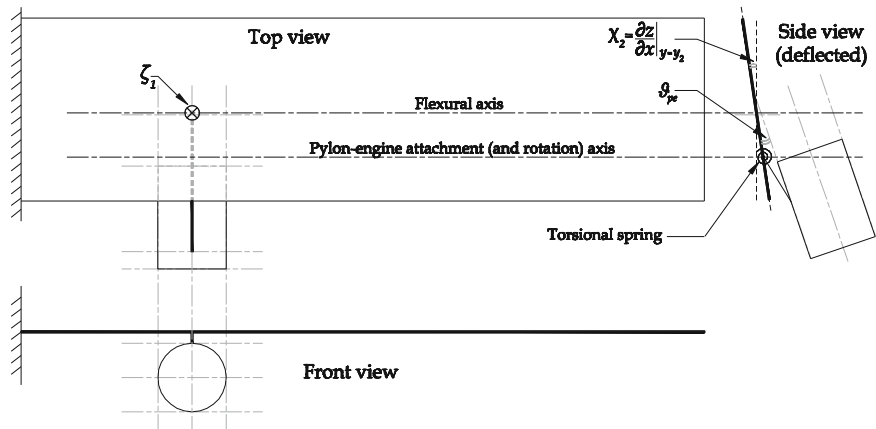


**Fig. 66.3** Various views of the wing- pylon-engine model (pylon represented by a rigid link, in side view)



Following an assumed-mode-shapes approach [10, 11], the flexible wing has been assumed to consist of two deflection patterns, namely the first flexural (bending) mode, and first torsional mode. These shapes are depicted in, along with the co-ordinate system that the model is based upon (the origin of the co-ordinate system is at the Leading Edge, root of the wing) (Fig. 66.1).

Thus, the wing comprises two degrees of freedom (DOFs). The assumed shapes are incorporated into the wing model by specifying the vertical deflection of the wing  $z$  at any point  $(x, y)$  in terms of contributions from all deflection patterns, viz.,

$$z = y^2 q_1 + y(x - x_f) q_2, \tag{66.2}$$

where  $q_1, q_2$  are generalised co-ordinates that quantify the amount of bending and torsion modes present in the overall deflection. The angle of twist at a given distance  $y$  is given by

$$\theta_{wt} = y q_2, \tag{66.3}$$

where the subscript “wt” denotes wing twist. A third generalised co-ordinate  $q_{pe}$  is defined which pertains to the motion of the pylon-engine (signified by the subscript “pe”). The pylon-engine has been modelled as a rigid body, consisting of a solid cylinder (engine) onto which a thin parallelogram-shaped plate (pylon) has been fixed at the top. This rigid assembly is depicted in Fig. 66.2. For the purpose of this model, in order to restrict the overall dimension of the model to a value that may be easily accommodated by the Feedback Linearisation process, the pylon-engine is endowed with only 1 DOF (this brings the dimension of the coupled wing-pylon-engine model to three). Specifically, this is a rotation of the pylon-engine about an axis that is parallel to the global  $y$ -axis, going through the attachment point to the wing (this axis will be referred to as a local  $y$ -axis). A sketch of the combined wing-pylon-engine is shown in Fig. 66.3. Note that the pylon-engine rotational DOF  $\vartheta_{pe}$  is the deflection of the pylon-engine *relative* to the wing. The absolute rotation of the pylon-engine,  $\theta_{pe}$ , may be obtained by adding the wing twist angle at the engine attachment location,  $\chi_2$ , to  $\vartheta_{pe}$ .



### 66.2.1 Co-ordinate Transformation

Since the wing deflection has been defined in assumed-mode-shapes generalised co-ordinates, in order to couple the pylon-engine, it is necessary to represent the latter also in the assumed-modes space. This may be achieved by a suitable co-ordinate transformation. In order to ensure that the transformation is an equivalence transformation – such that it is possible to transform back and forth between the assumed-modes and physical domains – it is necessary to specify a number of physical co-ordinates that is equal to the number of assumed modes in the system, in the present case, three. One has already been chosen as  $\vartheta_{pe}$ . The remaining two physical co-ordinates are chosen as:

- A vertical deflection at point 1, which lies at the crossing between the wing flexural axis and the local  $x$ - axis going through the attachment point of the pylon-engine to the wing. This co-ordinate is named as  $\zeta_1$ .
- The wing twist angle at point 2, the pylon-engine attachment location, which is chosen as the intersection of the quarter-semi-span and quarter-chord. This co-ordinate is named as  $\chi_2$ .

The particular choice of the above two co-ordinates is due to the requirement of these co-ordinates in the derivation of the system equations. Figure 66.3 above depicts the three physical co-ordinates on the wing-pylon-engine system. Thus, the required transformation takes the form

$$\mathbf{z} = \mathbf{T}\mathbf{q}, \quad \text{where } \mathbf{z} = \{\zeta_1 \chi_2 \vartheta_{pe}\}^T, \quad \mathbf{q} = \{q_1 q_2 q_{pe}\}^T, \quad (66.4)$$

and  $\mathbf{T}$  is the equivalence transformation matrix. Using Eq. (66.2), and defining  $\theta_{pe} = \zeta q_{pe}$ , where  $\zeta$  is some arbitrary scalar multiple (this value may be set to 1, which results in the absolute pylon-engine rotation in the physical and assumed-modes domains being identical), 5 may be derived as

$$\mathbf{T} = \begin{bmatrix} y_1^2 & 0 & 0 \\ 0 & y_2 & 0 \\ 0 & -y_2 \zeta & 1 \end{bmatrix}, \quad (66.5)$$

where  $y_1, y_2$  are the  $y$ - co-ordinates at points 1 and 2 respectively. Using the Lagrange equation and aerodynamic strip theory [11], assuming the same ordering of co-ordinates as in the above equation, the system matrices of the wing and pylon-engine in the assumed-modes domain may be derived as

$$\mathbf{A}_{w,mod} = m \begin{bmatrix} \frac{s^5 c}{5} & \frac{s^4}{4} \left( \frac{c^2}{2} - cx_f \right) & 0 \\ \frac{s^4}{4} \left( \frac{c^2}{2} - cx_f \right) & \frac{s^3}{3} \left( \frac{c^3}{3} - c^2 x_f + cx_f^2 \right) & 0 \\ 0 & 0 & 0 \end{bmatrix}, \quad \mathbf{E}_{w,mod} = \begin{bmatrix} 4EIs & 0 & 0 \\ 0 & GJs & 0 \\ 0 & 0 & 0 \end{bmatrix}, \quad (66.6)$$

where  $c, s$  are the wing chord and semi-span respectively,  $m$  the wing mass per unit area,  $x_f$  the  $x$ -co-ordinate of the flexural axis,  $EI, GJ$  the wing flexural and torsional rigidity respectively,

$$\mathbf{A}_{pe,mod} = \begin{bmatrix} m_{pe} y_1^4 & 0 & m_{pe} y_1^2 r_G \hat{c} \zeta \\ 0 & 0 & 0 \\ m_{pe} y_1^2 r_G \hat{c} \zeta & 0 & (I_G + m_{pe} r_G^2) \zeta^2 \end{bmatrix}, \quad \mathbf{E}_{pe,mod} = K_T \begin{bmatrix} 0 & 0 & 0 \\ 0 & y_2^2 & -y_2 \zeta \\ 0 & -y_2 \zeta & \zeta^2 \end{bmatrix}, \quad (66.7)$$

where  $m_{pe}$  is the combined mass of the pylon and engine,  $I_G$  the moment of inertia of the pylon-engine referred to a local  $y$ -axis going through the pylon-engine centre of mass (COM),  $\hat{c}$  the cosine of the angle of the pylon-engine COM relative to the top flat of the pylon taken about the flexural axis,  $r_G$  the distance between the flexural axis and the aforementioned local  $y$ -axis, and  $K_T$  the linear torsional coupling stiffness,

$$\mathbf{B}_{mod} = \begin{bmatrix} \frac{c a_W s^5}{10} & 0 & 0 \\ -\frac{c^2 e a_W s^4}{8} & -\frac{c^3 s^3 M_{\dot{\theta}}}{24} & 0 \\ 0 & 0 & 0 \end{bmatrix}, \quad \mathbf{C}_{mod} = \begin{bmatrix} 0 & \frac{c s^4 a_W}{8} & 0 \\ 0 & -\frac{e c^2 s^3 a_W}{6} & 0 \\ 0 & 0 & 0 \end{bmatrix}, \quad (66.8)$$

where  $e$ , the eccentricity ratio, is distance between the aerodynamic centre and flexural axis as a fraction of the chord,  $a_w$  the lift curve slope and  $M_{\dot{\theta}}$  the non-dimensional pitch damping derivative. The overall inertial and structural stiffness matrices are obtained by summing the wing and pylon-engine components, viz.,

$$\mathbf{A}_{mod} = \mathbf{A}_{w,mod} + \mathbf{A}_{pe,mod}, \quad \mathbf{E}_{mod} = \mathbf{E}_{w,mod} + \mathbf{E}_{pe,mod}. \quad (66.9)$$

Structural damping is neglected in this work, therefore  $\mathbf{D} = \mathbf{D}_{mod} = \mathbf{0}$ .

### 66.2.2 Forcing Terms

The aileron (control surface) usually provides the necessary means to apply control forces to the wing-pylon-engine system. It is assumed in this work that two control surfaces are available, each spanning half the length of the wing (the contribution of the control surfaces to the dynamics of the overall system is neglected). In addition to the ailerons, it is assumed that a separate actuator is available to apply a torque,  $T_{pe}$ , directly on the engine rotational DOF. Again, using the Lagrange equation and aerodynamic strip theory, the forcing vector is found as

$$\mathbf{f}_{mod} = \begin{bmatrix} -\frac{1}{48}\tilde{r}a_{C,1s} & -\frac{7}{48}\tilde{r}a_{C,2s} & 0 \\ \frac{1}{16}\tilde{r}cb_{C,1} & \frac{3}{16}\tilde{r}cb_{C,2} & -y_2 \\ 0 & 0 & \zeta \end{bmatrix} \begin{Bmatrix} \beta_1 \\ \beta_2 \\ T_{pe} \end{Bmatrix} =: \bar{\mathbf{B}}_{mod}\mathbf{u}, \quad \text{where } \tilde{r} = \rho V^2 c s^2, \quad (66.10)$$

and where each control surface will have its own deflection angle  $\beta_1, \beta_2$  and set of aerodynamic parameters  $a_C, b_C$  [12].

### 66.2.3 Including Nonlinearity

Nonlinearity may be incorporated by adding an internal force to the overall equation of motion, viz.,

$$\mathbf{A}_{mod}\ddot{\mathbf{q}} + (\rho V\mathbf{B}_{mod} + \mathbf{D}_{mod})\dot{\mathbf{q}} + (\rho V^2\mathbf{C}_{mod} + \mathbf{E}_{mod})\mathbf{q} + \mathbf{f}_{nl,mod} = \mathbf{f}_{mod}. \quad (66.11)$$

For the purpose of the present model, a cubic hardening nonlinearity is assumed in the torsional spring connecting the pylon-engine to the wing. The nonlinear force developed in the spring may be expressed as

$$f_{T,nl} = K_{T,nl}\vartheta_{pe}^3, \quad (66.12)$$

where  $K_{T,nl}$  is the stiffness coefficient of the cubic nonlinearity. As this nonlinear force occurs within the system, an equal and opposite force will arise in the coupled DOF. Since  $\vartheta_{pe}$  is a relative deflection (involving both the coupling DOFs), the overall nonlinear force vector will take the form

$$\mathbf{f}_{nl,mod} = \mathbf{T}^T \mathbf{f}_{nl}, \quad \text{where } \mathbf{f}_{nl} = \{0 \ 0 \ f_{T,nl}\}^T, \quad (66.13)$$

where the transformation  $\mathbf{T}$  is defined in Eq. (66.5).

## 66.3 Numerical Simulation (Part 1)

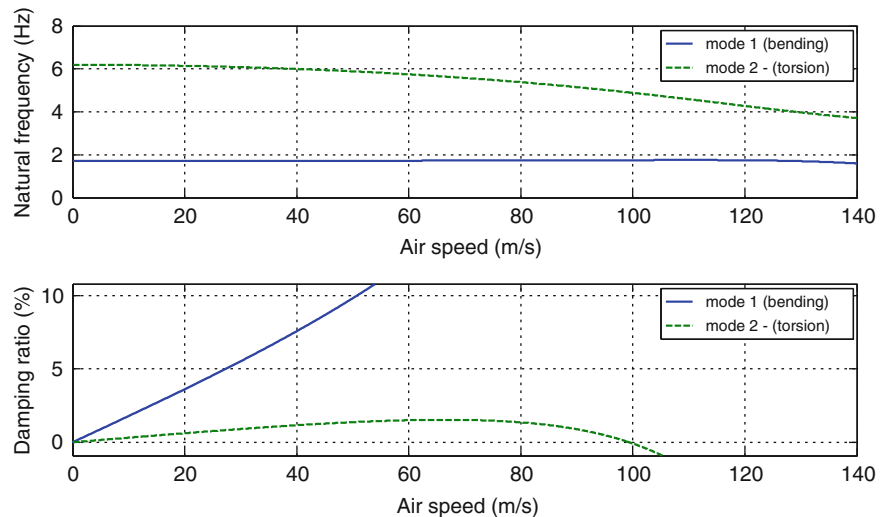
A numerical simulation of the 3-DOF aeroservoelastic model is now commenced. Initially, appropriate dimensions and parameters for the wing and pylon-engine are chosen, and frequency and time-domain analyses are carried out on the linear system. Subsequently, a cubic hardening stiffness is included in the torsional spring connecting the wing to the pylon-engine, and the nonlinear time-domain response is simulated. For the purpose of these simulations, the free vibration is of interest, and therefore there will be no external excitation.

**Table 66.1** Dimensions and parameters of flexible wing

Semi-span ( $s$ )	7.5 m	Flexural rigidity (EI)	3,675,000 (Nm <sup>2</sup> )
Chord ( $c$ )	2.0 m	Torsional rigidity (GJ)	1,890,000 (Nm <sup>2</sup> )
Flexural axis ( $x_f$ )	0.48c (0.96 m)	Air density ( $\rho$ )	1.225 (kgm <sup>-3</sup> )
Mass per unit area ( $m$ )	100 kgm <sup>-2</sup>	Non-dimensional pitch damping derivative ( $M_{\dot{\theta}}$ )	-1.2
eccentricity ratio ( $e$ )	0.23	Lift curve slope ( $a_w$ )	$2\pi$

**Table 66.2** Dimensions and parameters of pylon-engine

Engine diameter ( $d_e$ )	0.75 m	Engine mass ( $m_e$ )	350 kg
Engine length ( $l_e$ )	1.125 m	Pylon mass ( $m_p$ )	35 kg
Pylon height ( $h_p$ )	0.125 m	Coupling torsional spring stiffness ( $K_T$ )	511,000 Nm/rad

**Fig. 66.4** V-omega and V-zeta plots for the wing only model

### 66.3.1 Model Dimensions and Parameters

The dimensions and parameters chosen for the model are given in Tables 66.1 and 66.2.

### 66.3.2 Airspeed vs. Natural Frequency and Airspeed vs. Damping Ratio Plots

The variation of natural frequency and damping ratio of the system as a function of the airspeed (V-omega and V-zeta plots respectively) are presented. For comparison, the same plots pertaining to the wing only are included. For the wing only (Fig. 66.4):

The structural modes (zero air speed) occur at 1.71 Hz (bending) and 6.19 Hz (torsional). The second subplot has been zoomed vertically to show clearly the linear flutter speed, occurring at an airspeed of approximately 100 ms<sup>-1</sup>. For the wing-pylon-engine system:

The structural modes in the combined model occur at 1.71 Hz (bending), 4.06 Hz (pylon-engine mode) and 6.83 Hz (torsional). It is evident that there are now two flutter points, as a result of coupling the pylon-engine to the wing. These occur at 77.6 ms<sup>-1</sup> (pylon-engine mode) and 116.6 (torsional) ms<sup>-1</sup> (Fig. 66.5).

### 66.3.3 Linear Time-Domain Response

The linear system is simulated at an airspeed of 80 ms<sup>-1</sup> (which is above the first flutter point), under the application of the initial conditions  $\zeta_1 = 0.333$  mm,  $\chi_2 = 0.00333$  rad,  $\vartheta_{pe} = 0.05$  rad. The resulting time-domain response of the system is shown in Fig. 66.6.

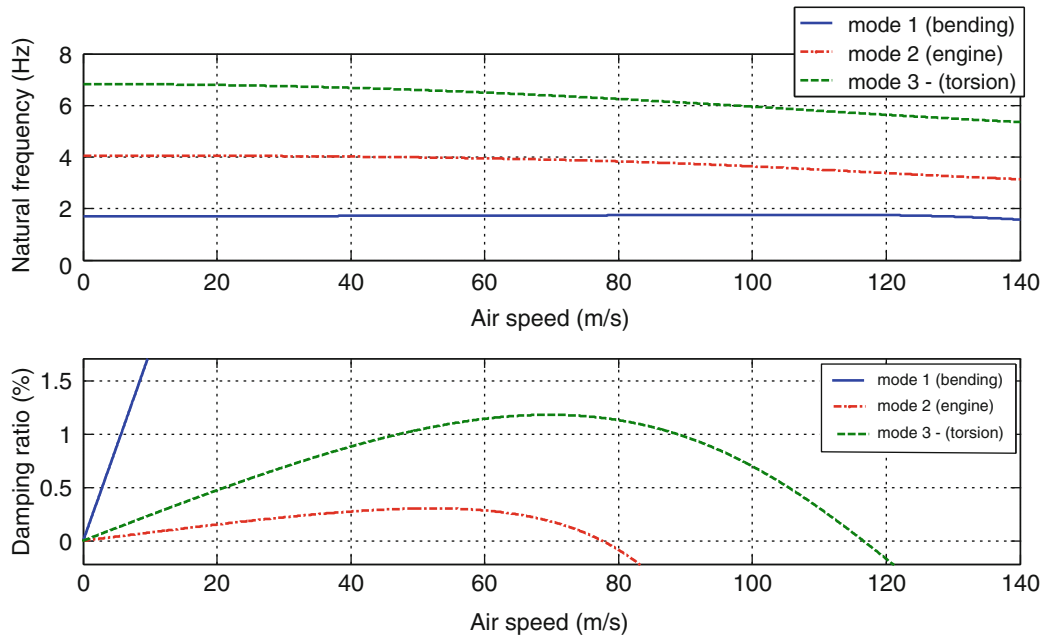


Fig. 66.5 V-omega and V-zeta plots for the wing-pylon-engine model

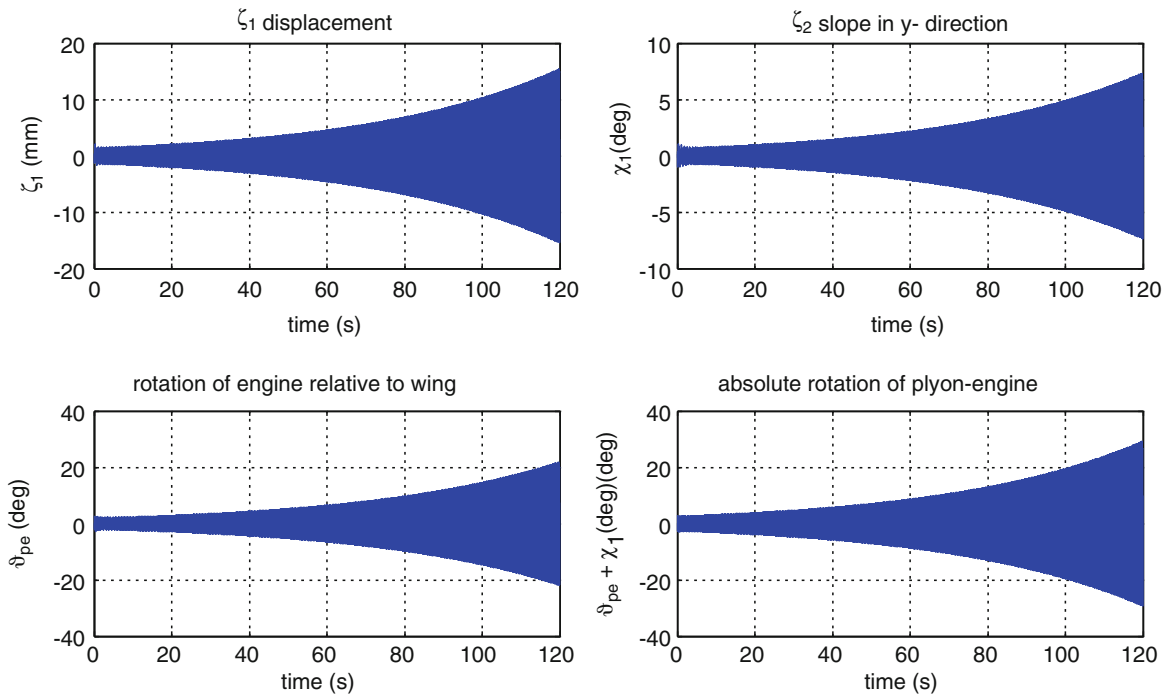
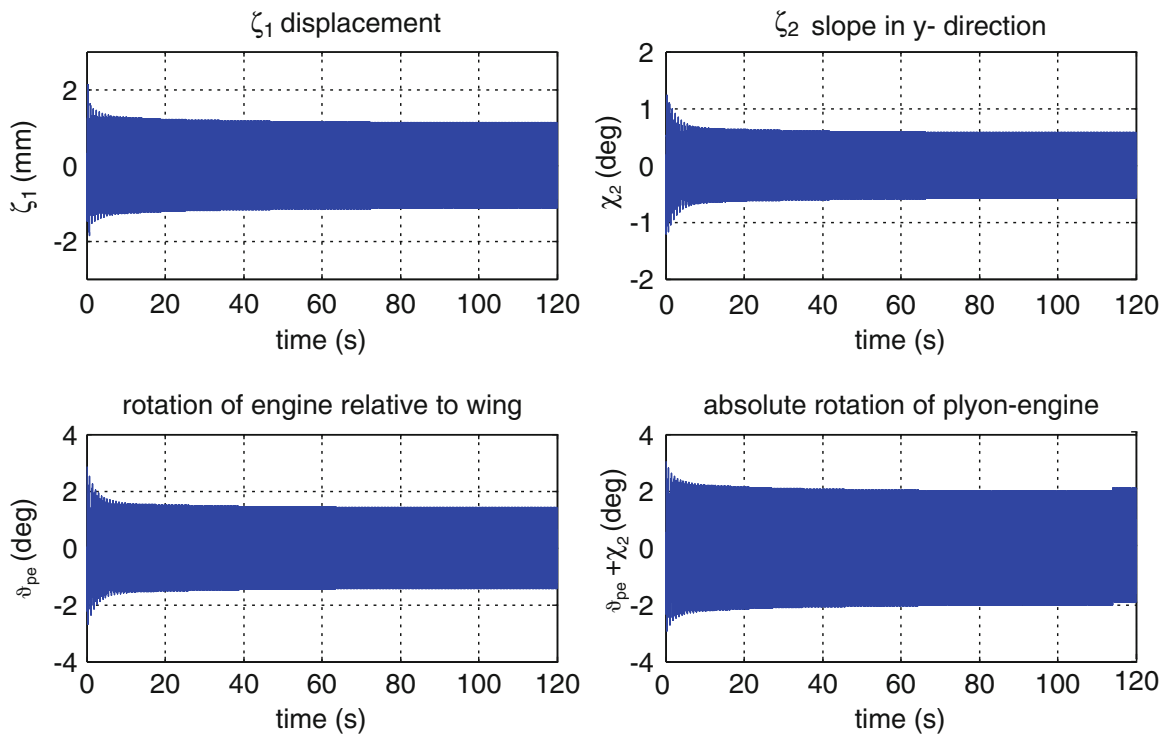
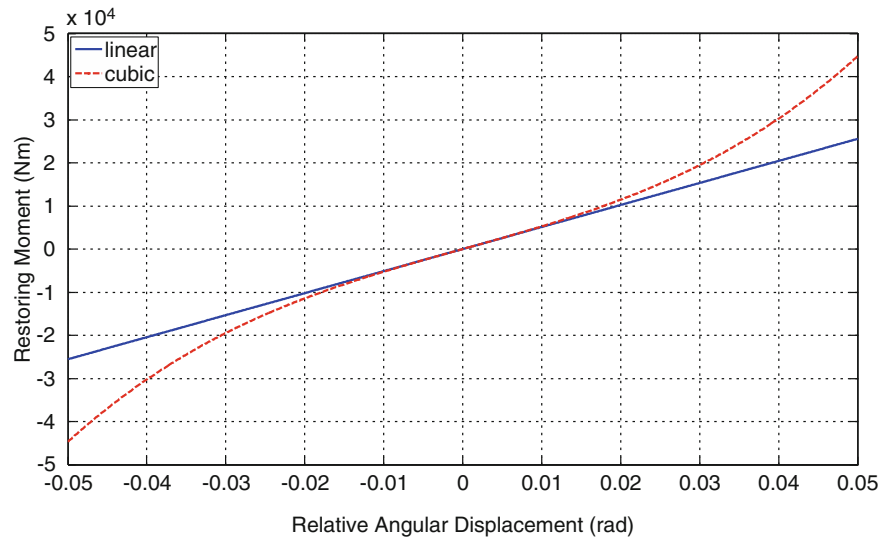


Fig. 66.6 Linear time-domain response at 80 ms<sup>-1</sup>

As the chosen airspeed is higher than the flutter speed, the unstable response in the above figure is expected.

**Fig. 66.7** Comparing linear and nonlinear spring forces



**Fig. 66.8** Nonlinear time-domain response at  $80 \text{ ms}^{-1}$

### 66.3.4 Nonlinear Time-Domain Response

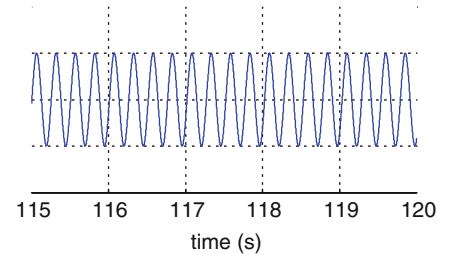
A cubic hardening stiffness is now included in the model, as described above. The stiffness coefficient of the cubic term is chosen to be 300 times that of the linear stiffness; thus,  $K_{T,nl}$  is equal to  $153.3 \times 10^6$ . A comparison between the spring force in the linear and nonlinear systems for the relative deflection range that pylon-engine experiences is shown in Fig. 66.7.

The time-domain response of the resulting nonlinear system, with the same initial conditions as in the linear case, is shown in Fig. 66.8.

It is evident that a stable limit cycle oscillation (LCO) is eventually formed. This is observed more clearly in a horizontally zoomed-in version of the plot, which shows a profile of the form shown in Fig. 66.9, in all cases.

A response characterised by an LCO is expected, as the nonlinearity is of a cubic hardening type and the system is being run at an airspeed higher than the linear flutter speed.

**Fig. 66.9** Horizontally zoomed in version of nonlinear time-domain response, showing stable LCO



## 66.4 Feedback Linearisation

Feedback Linearisation [13] is a process applied to a nonlinear system to essentially transform it into a linear system. Unlike Jacobian Linearisation, it is exact, and does not entail an approximation at any stage. The method is implemented by transforming the nonlinear system given by

$$\dot{\mathbf{x}} = \mathbf{f}(\mathbf{x}) + \mathbf{G}(\mathbf{x})\mathbf{u} \quad (66.14)$$

into an equivalent linear system

$$\dot{\mathbf{z}} = \mathbf{Az} + \mathbf{B}\bar{\mathbf{u}}, \quad (66.15)$$

based on a particular choice of output  $\mathbf{y} = \mathbf{h}(\mathbf{x})$ . In the above equations  $\mathbf{u}$  and  $\bar{\mathbf{u}}$  are the inputs to the nonlinear and linearised systems respectively, which will be referred to as the actual and artificial inputs respectively, in this paper. The mapping from the nonlinear domain to the linearised domain is achieved through a non-singular co-ordinate transformation  $\mathbf{z} = \mathbf{T}(\mathbf{x})$ , which is generally nonlinear. In addition, a mapping between  $\mathbf{u}$  and  $\bar{\mathbf{u}}$  is also required.

The linearisation may result in either a completely or partially linearised system, depending on the Relative Degree, defined as the number of times the output has to be differentiated with respect to time before the input terms appear explicitly. In a Single Input Single Output (SISO) system, if the Relative Degree is equal to the dimension of the state vector  $\mathbf{x}$ , a complete linearisation results, in which case ensuring stability of the linearised system will in turn ensure stability of the original nonlinear system. On the other hand, if the Relative Degree of a SISO system is less than the dimension of  $\mathbf{x}$ , the system is only partially linearised, and the complete dynamics from the original system is not preserved. In this case, it is necessary to ensure stability of the portion of the system that remains nonlinear, in addition to stabilising the linearised sub-system. This is achieved by verifying stability of the Zero Dynamics [13], which is defined as the dynamics of the unlinearised sub-system when all co-ordinates pertaining to the linearised sub-system are set to zero. The Zero Dynamics may be either linear or nonlinear. It is pointed out that since the Zero Dynamics does not contain input terms, it is uncontrollable.

Feedback Linearisation is now applied to the nonlinear model developed above. For the task at hand, it is more appropriate to use the assumed-modes representation of the system matrices. This is because once the system has been linearised, pole-placement may be performed directly on the assumed modes to shift their respective poles to more desirable locations, or simply stabilise the system.

### 66.4.1 Nonlinear State-Space Model, Choosing Outputs and Finding Relative Degree

The nonlinear model in Eq. (66.11) may be expressed in the following state-space form:

$$\dot{\mathbf{x}} = \mathbf{f}(\mathbf{x}) + \mathbf{G}(\mathbf{x})\mathbf{u}, \quad \text{with } \mathbf{x} =: \{x_1 \ x_2 \ x_3 \ x_4 \ x_5 \ x_6\}^T, \quad (66.16)$$

where  $\mathbf{u} = \{\beta_1 \ \beta_2 \ T_{pe}\}^T$  is the vector of actual inputs, as defined in Sect. 66.2.2. The three outputs of the system, denoted  $y_a, y_b, y_c$ , may be chosen as the three assumed-modes co-ordinates – as it is these quantities that one wishes to control – and also as the first three entries in the state vector, viz.,

$$\{y_a \ y_b \ y_c\}^T := \{q_1 \ q_2 \ q_{pe}\}^T = \{x_1 \ x_2 \ x_3\}^T. \quad (66.17)$$

Now, following the procedure of Input-Output Feedback Linearisation [13], the three outputs are differentiated with respect to time, whilst substituting from Eq. (66.16) at each stage. This results in

$$\begin{aligned} \dot{y}_a &= x_4, & \dot{y}_b &= x_5, & \dot{y}_c &= x_6, \\ \ddot{y}_a &= f_4 + [g_{41} \ g_{42} \ g_{43}] \mathbf{u}, & \ddot{y}_b &= f_5 + [g_{51} \ g_{52} \ g_{53}] \mathbf{u}, & \ddot{y}_c &= f_6 + [g_{61} \ g_{62} \ g_{63}] \mathbf{u}, \end{aligned} \quad (66.18)$$

where  $f_i$  denotes the  $i$ th term of the vector  $\mathbf{f}(\mathbf{x})$ , and  $g_{ij}$  denotes the  $ij$ th term of the matrix  $\mathbf{G}(\mathbf{x})$ . The Relative Degree of the system for the particular choice of outputs, may now be computed. Since the present system has multiple inputs and multiple outputs, each output will have an associated Relative Degree. Thus, the Relative Degree of the overall system will consist of all these values, and may be cast as a vector. For the present system, the Relative Degree will be  $\{2 \ 2 \ 2\}^T$ , provided that the matrix

$$\begin{bmatrix} g_{41} & g_{42} & g_{43} \\ g_{51} & g_{52} & g_{53} \\ g_{61} & g_{62} & g_{63} \end{bmatrix} =: \mathbf{E} \quad (66.19)$$

is non-singular for all  $\mathbf{x}$ . In this particular case, since the above matrix does not depend on  $\mathbf{x}$ , provided that it is non-singular, the computed value of Relative Degree will be globally valid.

### 66.4.2 Linearising the System

A new co-ordinate system is now defined, which will provide a mapping from the equivalent linear system that is sought, to the original nonlinear system. Defining these co-ordinates as

$$\begin{aligned} z_1 &:= y_a = q_1 = x_1, & z_3 &:= y_b = q_2 = x_2, & z_5 &:= y_c = q_{pe} = x_3, \\ z_2 &:= \dot{y}_a = \dot{q}_1 = \dot{x}_1, & z_4 &:= \dot{y}_b = \dot{q}_2 = \dot{x}_2, & z_6 &:= \dot{y}_c = \dot{q}_{pe} = \dot{x}_3, \end{aligned} \quad (66.20)$$

and using the first three rows of Eq. (66.16), it can be shown that the co-ordinate transformation from the original nonlinear system to the new, linear system is

$$\begin{Bmatrix} z_1 \\ z_2 \\ z_3 \\ z_4 \\ z_5 \\ z_6 \end{Bmatrix} = \begin{bmatrix} 1 & 0 & 0 & 0 & 0 & 0 \\ 0 & 0 & 0 & 1 & 0 & 0 \\ 0 & 1 & 0 & 0 & 0 & 0 \\ 0 & 0 & 0 & 0 & 1 & 0 \\ 0 & 0 & 1 & 0 & 0 & 0 \\ 0 & 0 & 0 & 0 & 0 & 1 \end{bmatrix} \begin{Bmatrix} x_1 \\ x_2 \\ x_3 \\ x_4 \\ x_5 \\ x_6 \end{Bmatrix}. \quad (66.21)$$

Note that the transformation matrix is independent of  $\mathbf{x}$ , and is therefore globally valid. Now, choosing the vector of actual inputs so as to cancel the system nonlinearity, it may be shown that the state-space equations

$$\dot{\mathbf{z}} = \mathbf{A}\mathbf{z} + \mathbf{B}\bar{\mathbf{u}} \quad (66.22)$$

decouple to provide the following three single-DOF systems:

$$\begin{Bmatrix} \dot{z}_1 \\ \dot{z}_2 \end{Bmatrix} = \begin{bmatrix} 0 & 1 \\ 0 & 0 \end{bmatrix} \begin{Bmatrix} z_1 \\ z_2 \end{Bmatrix} + \begin{bmatrix} 0 \\ 1 \end{bmatrix} \bar{u}_1, \quad \begin{Bmatrix} \dot{z}_3 \\ \dot{z}_4 \end{Bmatrix} = \begin{bmatrix} 0 & 1 \\ 0 & 0 \end{bmatrix} \begin{Bmatrix} z_3 \\ z_4 \end{Bmatrix} + \begin{bmatrix} 0 \\ 1 \end{bmatrix} \bar{u}_2, \quad \begin{Bmatrix} \dot{z}_5 \\ \dot{z}_6 \end{Bmatrix} = \begin{bmatrix} 0 & 1 \\ 0 & 0 \end{bmatrix} \begin{Bmatrix} z_5 \\ z_6 \end{Bmatrix} + \begin{bmatrix} 0 \\ 1 \end{bmatrix} \bar{u}_3. \quad (66.23)$$

where  $\bar{\mathbf{u}} =: \{\bar{u}_1 \ \bar{u}_2 \ \bar{u}_3\}^T$  is the vector of (artificial) inputs to the linear system. Note that the above three single-DOF systems correspond to the assumed-modes generalised co-ordinates  $q_1, q_2, q_{pe}$  respectively (see Eq. (66.20)). The artificial inputs may be chosen as a linear combination of instantaneous displacement and velocity, so as to modify the natural frequency and damping ratio of each of these systems respectively, viz.,

$$\bar{u}_1 = -[\bar{f}_1 \ \bar{g}_1] \begin{Bmatrix} z_1 \\ z_2 \end{Bmatrix}, \quad \bar{u}_2 = -[\bar{f}_2 \ \bar{g}_2] \begin{Bmatrix} z_3 \\ z_4 \end{Bmatrix}, \quad \bar{u}_3 = -[\bar{f}_3 \ \bar{g}_3] \begin{Bmatrix} z_5 \\ z_6 \end{Bmatrix}. \quad (66.24)$$

Since the entire three dimensional nonlinear system is linearised to give a three dimensional linear system with the aid of multiple inputs and outputs, the complete dynamics of the original system is preserved in the linearised system (thus, the linearised system will not have Zero Dynamics in this case).

### 66.5 Numerical Simulation (Part 2)

The numerical simulation from Sect. 66.3 is now continued. Closed-loop control is applied to the nonlinear model via the two control surfaces and the torsional actuator, to provide linearising feedback and thereby perform pole-placement. The feedback is computed such that the linearised system consists of the three uncoupled SDOF sub-systems referred to in the above section. The natural frequencies and damping ratios specified in the pole-placement of the three systems is shown in Table 66.3.

The system is simulated with the same initial conditions as before, but with feedback linearisation implemented from the beginning. The resulting controlled response of the assumed-modes co-ordinates is shown in Fig. 66.10. The top three sub-plots show the displacements of the generalised co-ordinates, whereas the bottom three show the respective velocities. It is immediately evident that the LCO of the uncontrolled nonlinear system has been eliminated. Furthermore, as shown in Fig. 66.11, a horizontal zoom of the first second of response shows that the intended change in the natural frequencies has been achieved. The corresponding physical displacement plots are shown in Fig. 66.12, and the actual inputs required for the above feedback linearisation is shown in Fig. 66.13. It can be seen that the intended objectives of the feedback linearisation have been fulfilled with achievable inputs from the two control surfaces and torsional actuator.

**Table 66.3** Natural frequencies and damping ratios specified in Pole-placement of linearised system

$q_1$	0.93 Hz	0.01	$q_2$	4.95 Hz	0.01	$q_{pe}$	2.9 Hz	0.01
-------	---------	------	-------	---------	------	----------	--------	------

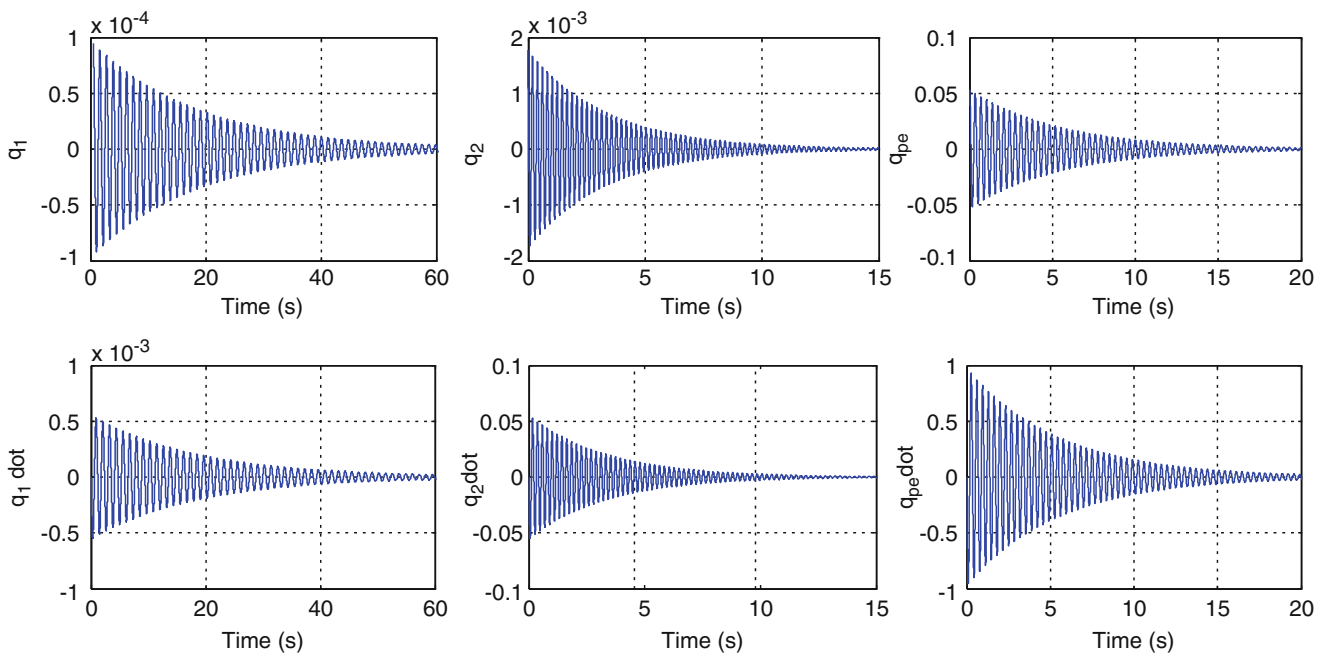


**Fig. 66.10** Feedback-linearised response at  $80 \text{ ms}^{-1}$  (assumed-modes co-ordinates)



## 66.6 Uncertainty in the Nonlinearity Parameters

The parameters describing the nonlinearity of a system will usually be obtained by either a modelling method, or experimentally. In both these cases, the values obtained will contain a certain amount of error. Thus, the exact values of the nonlinearity parameters will never be known in most practical situations, and performing feedback linearisation based on the erroneous parameters could lead to a poor-quality result.

The actual inputs required to cancel the system nonlinearity is given by

$$\mathbf{u} = \mathbf{E}^{-1} (\bar{\mathbf{u}} - \mathbf{f}_{\alpha\beta\gamma}), \quad (66.25)$$

where  $\mathbf{f}_{\alpha\beta\gamma} = \{f_4 \ f_5 \ f_6\}^T$ , and  $\mathbf{E}$  is defined in Eq.(66.19). Now, suppose the exact nonlinearity is not known, which results in the vector  $\mathbf{f}_{\alpha\beta\gamma}$  being different from the exact value. In this case, the actual input vector will be

$$\mathbf{u} = \mathbf{E}^{-1} (\bar{\mathbf{u}} - \mathbf{f}'_{\alpha\beta\gamma}). \quad (66.26)$$

Combining this with Eq. (66.25) gives

$$\bar{\mathbf{u}}' = \bar{\mathbf{u}} + (\mathbf{f}_{\alpha\beta\gamma} - \mathbf{f}'_{\alpha\beta\gamma}). \quad (66.27)$$

Here,  $\bar{\mathbf{u}}$  is the artificial input that is specified, whereas  $\bar{\mathbf{u}}'$  is the artificial input experienced by the linearised system. In the above equation, the only difference between the two terms in the bracket arises from the discrepancy pertaining to the nonlinearity coefficient (all other terms will be the same). Using Eqs. (66.5), (66.12), (66.13) and (66.16), the above equations may be expressed as

$$\bar{\mathbf{u}}' = \bar{\mathbf{u}} + \vartheta_{pe}^3 \tilde{K}_{T,nl} \mathbf{s}, \quad \text{where } \mathbf{s} := \{0 \ -y_2 \ \zeta\}^T \text{ and } \tilde{K}_{T,nl} = (K_{T,nl} - K'_{T,nl}), \quad (66.28)$$

where  $\tilde{K}_{T,nl}$  is the error in the nonlinearity parameter. Recall the state-space equation in the linear domain, given by Eq. (66.22). In case of a nonlinearity parameter error,

$$\dot{\mathbf{z}} = \mathbf{A}\mathbf{z} + \mathbf{B}\bar{\mathbf{u}}'. \quad (66.29)$$

Substituting from Eq. (66.28) into the above equation,

$$\dot{\mathbf{z}} = \mathbf{A}\mathbf{z} + \mathbf{B}\bar{\mathbf{u}} + \vartheta_{pe}^3 \tilde{K}_{T,nl} \mathbf{B}\mathbf{s}. \quad (66.30)$$

Thus, the overall closed-loop system in the presence of nonlinearity parameter error is

$$\dot{\mathbf{z}} = \mathbf{A}_c \mathbf{z} + \vartheta_{pe}^3 \tilde{K}_{T,nl} \mathbf{B}\mathbf{s}, \quad (66.31)$$

where, combining Eq. (66.22) with (66.24), the closed-loop state matrix is derived as

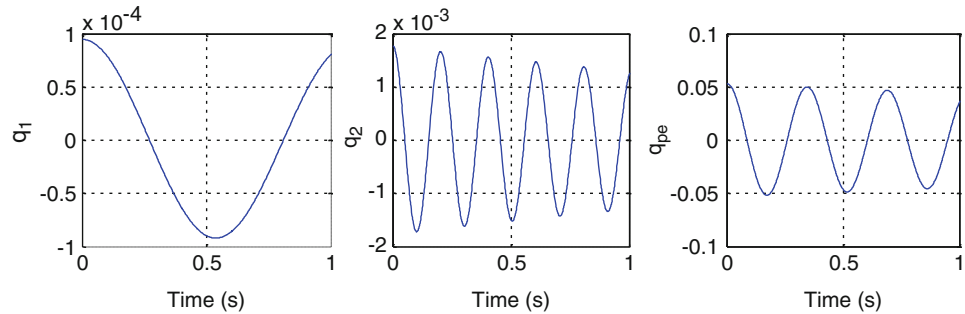


**Fig. 66.11** Horizontal zoom of responses from previous figure

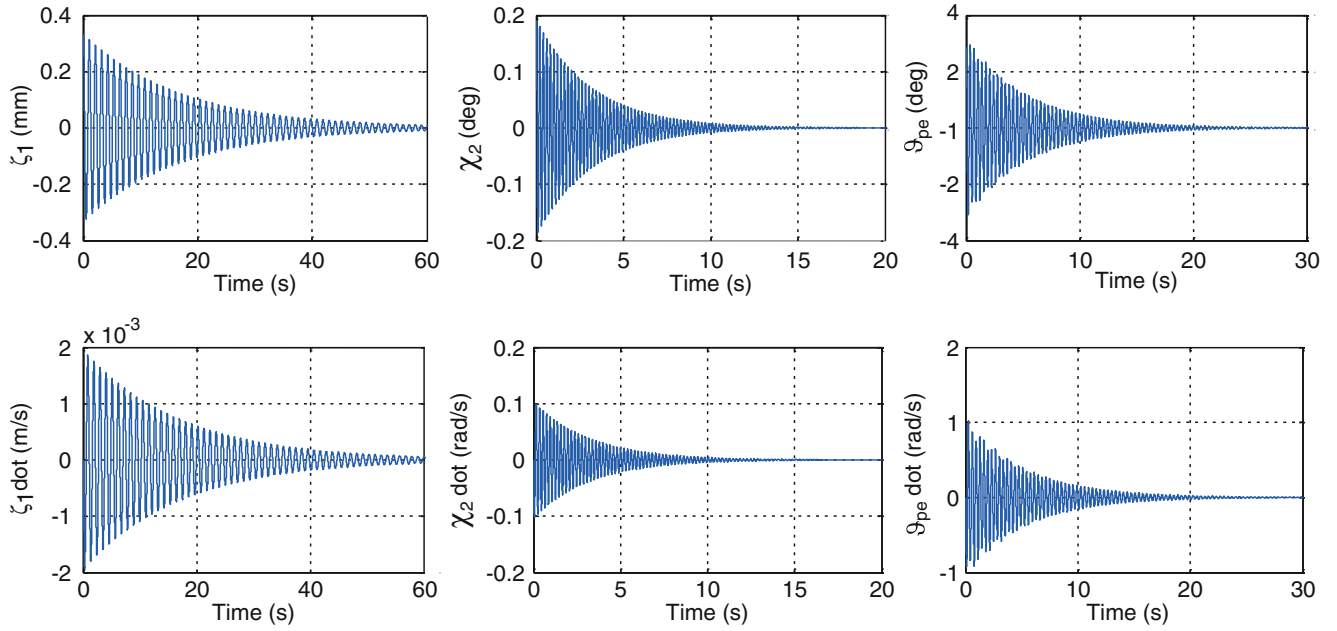
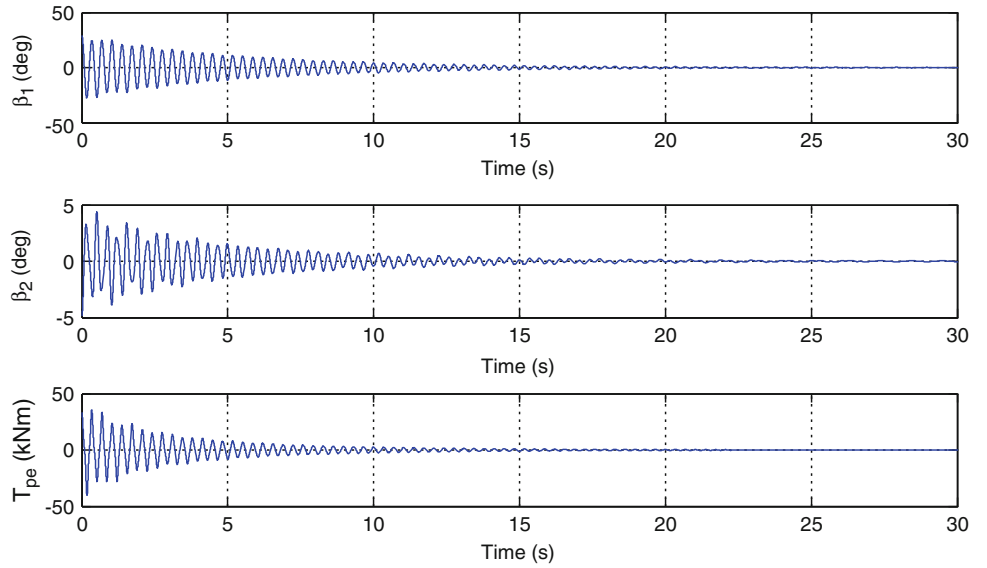


**Fig. 66.12** Feedback-linearised response at  $80 \text{ ms}^{-1}$  (physical co-ordinates)

**Fig. 66.13** Inputs required to perform feedback linearisation, at  $80 \text{ ms}^{-1}$



$$\mathbf{A}_{cl} = \begin{bmatrix} 0 & 1 & 0 & 0 & 0 & 0 \\ -\bar{f}_1 - \bar{g}_1 & 0 & 0 & 0 & 0 & 0 \\ 0 & 0 & 0 & 1 & 0 & 0 \\ 0 & 0 & -\bar{f}_2 - \bar{g}_2 & 0 & 0 & 0 \\ 0 & 0 & 0 & 0 & 0 & 1 \\ 0 & 0 & 0 & 0 & -\bar{f}_3 - \bar{g}_3 & 0 \end{bmatrix}. \quad (66.32)$$

It is evident that the error in the nonlinearity coefficient gives rise to an input term to the closed-loop system.

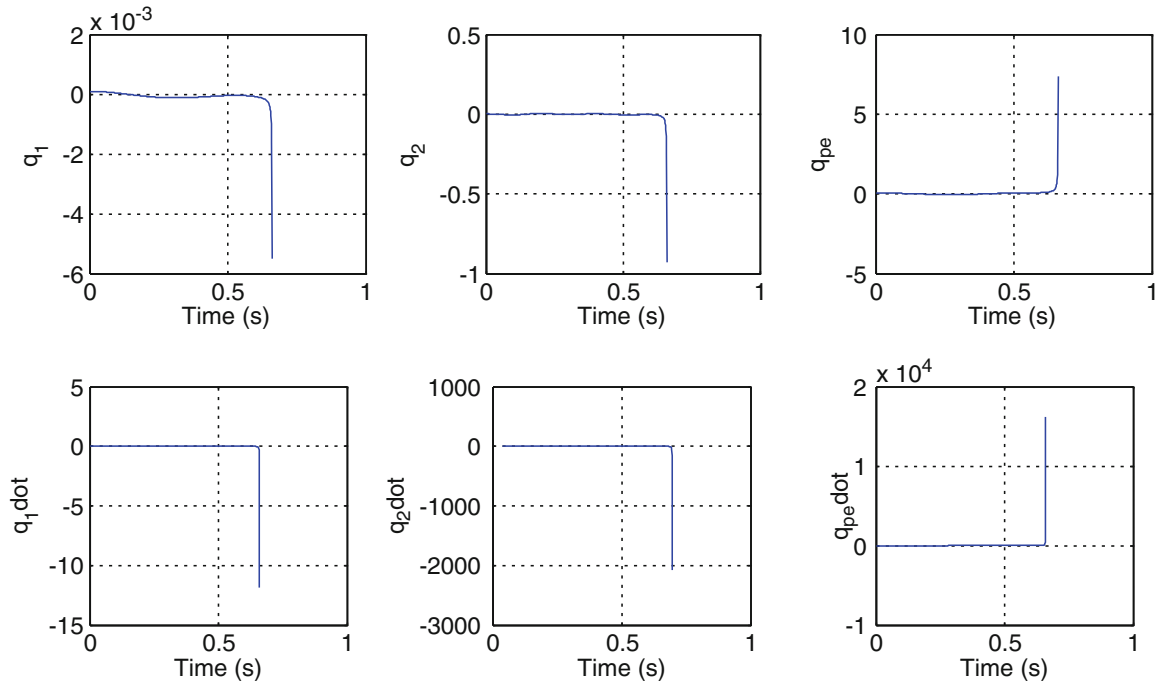


Fig. 66.14 Feedback-linearised response at  $80 \text{ ms}^{-1}$  (physical co-ordinates), with nonlinearity parameter error included

### 66.7 Numerical Simulation (Part 3)

In part 2 of the numerical simulation (feedback linearisation), it was assumed that the exact value of the nonlinearity parameter  $K_{T,nl}$  was known. In this part of the simulation, a 40% error (although a 40% error seems large, the change caused in the spring force is moderate) is incorporated into  $K_{T,nl}$  (such that  $K'_{T,nl} = 1.4 K_{T,nl}$ ), and feedback linearisation performed with the same objectives as before. The effect of the error in the nonlinearity parameter is modelled by computing the linearising inputs based on the erroneous value  $K'_{T,nl}$ , whilst computing the system states based on the actual value  $K_{T,nl}$ . Figure 66.14 shows the resulting controlled responses.

It is evident that instability occurs at approximately 0.66 s. Some investigation into the simulation suggests that the instability is genuine and one that arises from the system itself, rather than one that is caused by numerical resolution error. As the response approaches this instability, the magnitude of the difference between the nonlinear force based on the actual and erroneous values of  $K_{T,nl}$  grows continuously, which is the cause of instability.

### 66.8 Adaptive Feedback Linearisation

It was shown in Sect. 66.6 how an error in the nonlinearity parameter acts as an input to the closed-loop system. Part 3 of the numerical example demonstrated a situation where this additional input destabilises the system. Thus, it becomes necessary to account for the nonlinearity parameter error so as to ensure an asymptotically stable closed-loop response.

A scalar Lyapunov function  $\bar{V}$  involving  $\mathbf{z}$ ,  $\tilde{K}_{T,nl}$  may be defined, such that asymptotic stability of the closed-loop system is guaranteed by ensuring that  $\bar{V} > 0$  and its time-derivative  $\dot{\bar{V}} < 0$  [14]. Such a function may be used as a basis for computing an update law for the nonlinearity parameter  $\tilde{K}_{T,nl}$ . The following law is considered:

$$\bar{V}(\mathbf{z}, \tilde{K}_{T,nl}) = \mathbf{z}^T \mathbf{P} \mathbf{z} + \tilde{K}_{T,nl}^2, \quad (66.33)$$

where  $\mathbf{P}$  is a positive definite, symmetric matrix. Differentiating the above equation with respect to time, substituting from Eq. (66.31) and expanding, it is shown that

$$\dot{\bar{V}}(\mathbf{z}, \tilde{K}_{T,nl}) = \mathbf{z}^T (\mathbf{A}_{cl}^T \mathbf{P} + \mathbf{P} \mathbf{A}_{cl}) \mathbf{z} + \tilde{K}_{T,nl} \left( 2\dot{\tilde{K}}_{T,nl} + \vartheta_{pe}^3 \mathbf{s}^T \mathbf{B}^T (\mathbf{P} + \mathbf{P}^T) \mathbf{z} \right). \quad (66.34)$$

Consider the parameter update law

$$\dot{\tilde{K}}_{T,nl} = -\frac{1}{2} \vartheta_{pe}^3 \mathbf{s}^T \mathbf{B}^T (\mathbf{P} + \mathbf{P}^T) \mathbf{z}. \quad (66.35)$$

Substituting this into Eq. (66.34),

$$\dot{\tilde{V}}(\mathbf{z}, \tilde{K}_{T,nl}) = \mathbf{z}^T (\mathbf{A}_{cl}^T \mathbf{P} + \mathbf{P} \mathbf{A}_{cl}) \mathbf{z}. \quad (66.36)$$

Thus, implementing the above update law, and choosing  $\mathbf{P}$  such that

$$\mathbf{Q} = -(\mathbf{A}_{cl}^T \mathbf{P} + \mathbf{P} \mathbf{A}_{cl}), \quad (66.37)$$

where  $\mathbf{Q}$  is an arbitrary, positive definite matrix, will ensure that both the required conditions pertaining to the Lyapunov function  $\tilde{V}$  are met, and the closed-loop system with error in the nonlinearity will be asymptotically stable. Noting that  $\mathbf{P}$  is symmetric, the expression for the parameter update law may be simplified as

$$\dot{\tilde{K}}_{T,nl} = -\vartheta_{pe}^3 \mathbf{s}^T \mathbf{B}^T \mathbf{P} \mathbf{z}. \quad (66.38)$$

In the present case, since  $\mathbf{A}_{cl}$  consists of three decoupled  $2 \times 2$  block-diagonal matrices, if  $\mathbf{Q}$  is chosen such that its off-diagonal terms are zero (e.g. a positive multiple of the identity matrix),  $\mathbf{P}$  will also have the same structure as  $\mathbf{A}_{cl}$ . Thus, the task of finding  $\mathbf{P}$  may be simplified by computing each  $2 \times 2$  block at a time, and then arranging them along a block-diagonal to form  $\mathbf{P}$ .

## 66.9 Numerical Simulation (Part 4)

Part 3 of the numerical simulation is repeated, but with the adaptive control algorithm implemented. The matrix  $\mathbf{P}$  is computed as described in the above section, and  $\tilde{K}_{T,nl}$  updated according to the update law in Eq. (66.38) (this is achieved by including the parameter as part of the system state). The initial value of  $\tilde{K}_{T,nl}$  is set as the same value used in part 3. The resulting controlled response in the assumed-modes domain is shown in Fig. 66.15, and the controlled response in the physical domain is shown in Fig. 66.16.

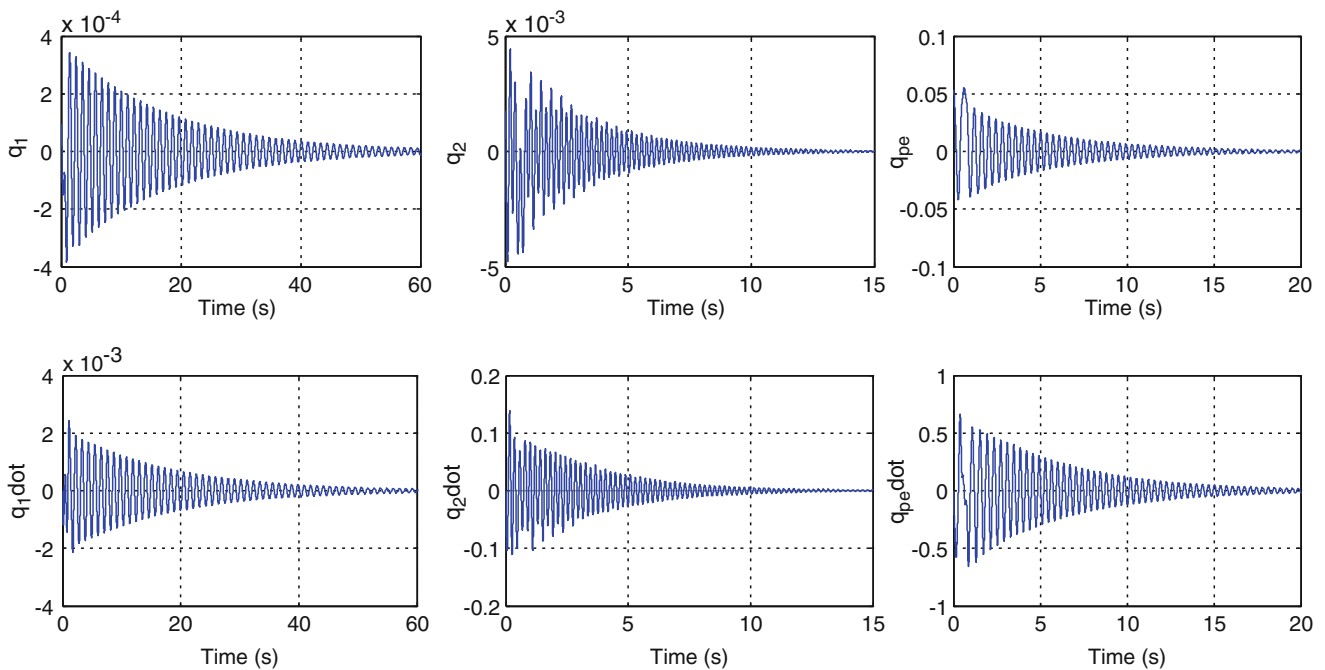


**Fig. 66.15** Feedback-linearised response at  $80 \text{ ms}^{-1}$ , with adaptive control algorithm implemented (assumed-modes generalised co-ordinates)

A comparison between Fig. 66.16 above and Fig. 66.12 from Sect. 66.5 shows that the controlled responses are similar, but not identical. Although the original pole-placement requirement has not been satisfied, it can be seen that the controlled response is stable. As before, the required control effort is achieved through realistic control surface deflection angles and actuator torque magnitudes.

## 66.10 Conclusions

The work presented in this article has gained motivation from the need to enhance control methods in aeroelastic systems, the aim of which is to increase operational limits whilst ensuring safety. The application of Adaptive Feedback Linearisation on a rigid, 2-DOF aeroelastic system has been previously illustrated by other authors. The aim of the present work has been to apply this method to a flexible wing model.

A model consisting of a flexible wing and a rigid pylon-engine attached to it via a cubic hardening spring has been developed. The free vibration of the wing-pylon-engine exhibits a stable limit cycle oscillation (LCO) when the airspeed is above the linear flutter speed. It has been assumed that two control surfaces and an additional actuator are available to supply the forces required for closed-loop control.

MIMO Feedback Linearisation is performed using three inputs and three outputs. As such, the entire system is linearised and therefore no Zero Dynamics exist. Results show that the LCO is eliminated, and stability is achieved by appropriate pole-placement through linearising feedback computed under the assumption that the nonlinearity is known exactly. Subsequently, the situation where there is an error in the value of the nonlinearity parameter used in the linearising feedback has been examined. It is seen that the error acts as an input to the closed-loop system, which may even be destabilising in some cases.

In the final section, Adaptive Feedback Linearisation is implemented on the system to account for the unknown error in the nonlinearity parameter. It is seen that if the parameter is updated in accordance with adaptive control theory, global asymptotic stability of the system is achieved. This demonstrates the effectiveness of adaptive feedback linearisation in practical situations where there will inevitably be errors in the measured/modelled description of system nonlinearities.

**Acknowledgements** This research has been funded by EPSRC grant EP/J004987/1 under the project entitled “Nonlinear Active Vibration Suppression in Aeroelasticity”. The first author would also like to acknowledge fellow researchers Hamed Haddad Khodaparast and Mohammad Yazdi Harmin in the Dynamics and Control Group, School of Engineering, University of Liverpool, for useful discussions contributory to the overall outcome of this work.

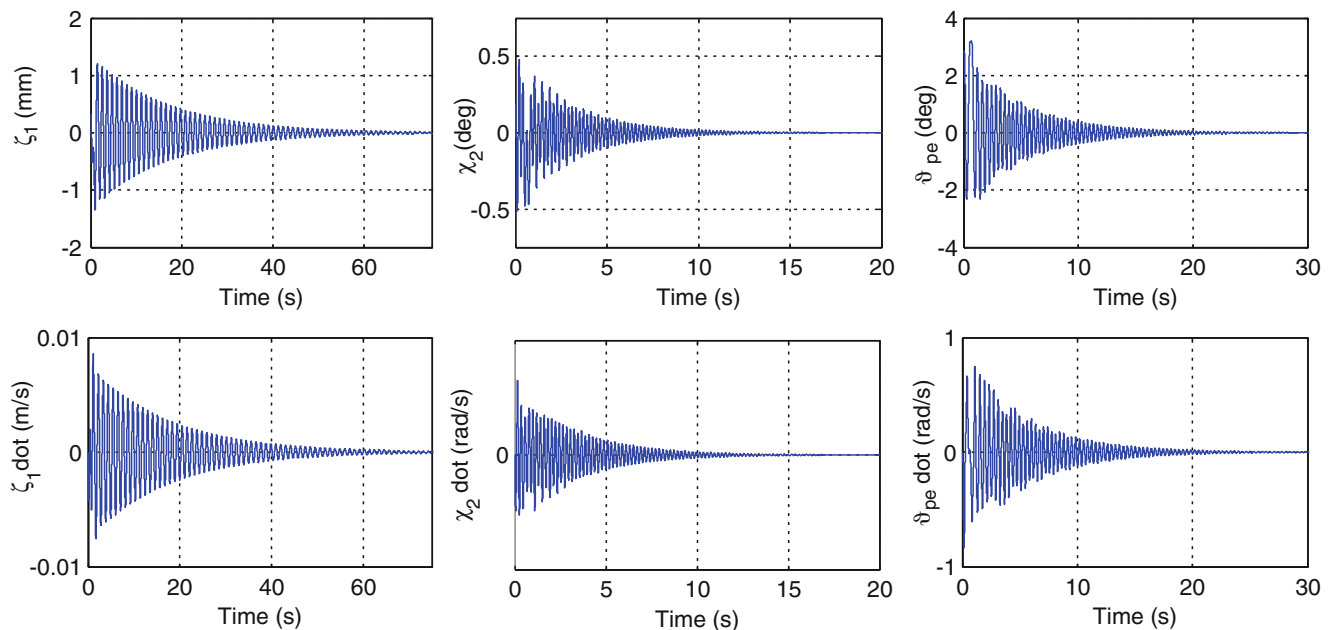


**Fig. 66.16** Feedback-linearised response at  $80 \text{ ms}^{-1}$ , with adaptive control algorithm implemented (physical co-ordinates)

## References

1. Block JJ, Strganac TW (1998) Applied active control for a nonlinear aeroelastic structure. *J Guid Control Dyn* 21(6):838–845
2. Ko J, Kurdila AJ, Strganac TW (1997) Nonlinear control of a prototypical wing section with torsional nonlinearity. *J Guid Control Dyn* 20(6):1181–1189
3. Ko J, Kurdila AJ, Strganac T (1998) Stability and control of a structurally nonlinear aeroelastic system. *J Guid Control Dyn* 21:718–725
4. Platanitis G, Strganac TW (2004) Control of a nonlinear wing section using leading- and trailing-edge surfaces. *J Guid Control Dyn* 27(1): 52–58
5. Ko J, Strganac TW, Kurdila AJ (1999) Adaptive feedback linearization for the control of a typical wing section with structural nonlinearity. *Nonlinear Dyn* 18(3):289–301
6. Strganac T, Ko J, Thompson D (2000) Identification and control of limit cycle oscillations in aeroelastic systems. *J Guid Control Dyn* 23(6):1127–1133
7. Monahemi MM, Krstic M (1996) Control of wing rock motion using adaptive feedback linearization. *J Guid Control Dyn* 19(4):905–912
8. Fossen TI, Paulsen MJ (1993) Adaptive feedback linearization applied to steering of ships. *Model Identif Control* 14(4):229–237
9. Nguyen N, Tuzcu I (2009) Atmospheric **Flight** Mechanics Conference, AIAA August 2009, Chicago, IL, USA
10. Meirovitch L (1967) Analytical methods in vibrations. Macmillan, New York
11. Wright JR, Cooper JE (2007) Introduction to aircraft aeroelasticity and loads. Wiley, Chichester
12. Fung YC (1969) An introduction to the theory of aeroelasticity. Dover, New York
13. Isidori A (1995) Nonlinear control systems. Springer, Berlin/Heidelberg/New York
14. Atherton DP (1981) Stability of nonlinear systems. Wiley, New York

# Chapter 67

## Limit Cycle Assignment in Nonlinear Aeroelastic Systems Using Describing Functions and the Receptance Method

Xiaojun Wei and John E. Mottershead

**Abstract** The problem of flutter suppression in aeroelasticity may be treated using eigenvalue assignment. Thus the receptance method of eigenvalue assignment developed by Ram and Mottershead may be considered for flutter suppression. Also, nonlinear flutter is characterized by periodicity. Therefore, the describing function technique is applicable to quasi-linearise the nonlinear aeroelastic system such that traditional linear methods of analysis can be employed. Eigenvalue assignment is especially relevant in the case of LCOs, which are neutrally stable and therefore are readily assignable in the frequency domain. In this paper, structural nonlinearities will be considered. Approximating structural nonlinearities using describing functions, the theory of the nonlinear active control based on the receptance method will be achieved by extending the well-developed theory of linear active control. Also, a new limit cycle prediction method in the frequency domain and a new form of stability criterion of limit cycles for closed-loop systems based on the describing function method will be derived. Numerical results from two two-degree-of-freedom airfoils with cubic and piecewise nonlinear pitching stiffnesses respectively are presented to show that limit cycles can be predicted precisely by the new method and the proposed nonlinear active control technique might be able to suppress flutter into stable LCO.

**Keywords** Nonlinear aeroelasticity limit cycle oscillation describing function receptance method eigenvalue assignment

### 67.1 Introduction

Flutter is an unstable self-excited vibration in which the structure extracts energy from the air stream and normally induces catastrophic structural failure which will result in the loss of the flight vehicle [1]. That is, flutter is an oscillatory aeroelastic instability phenomenon, involving unfavorable mode coupling. Mathematically, one of the eigenvalues of an aeroelastic system crosses the imaginary axis and has a positive real part in the flutter condition. Obviously, flutter instability must not occur within and on the boundary of the operating envelope of the flight vehicle because of its destructive effect [2]. Accurate flutter analysis and design for structural stability are of great importance. For an aeroelastic structure, a linear approach will give us a critical speed, e.g., linear flutter boundary, above which the structure will become dynamically unstable. However, there exist inherently structural and/or aerodynamic nonlinearities in aeroelastic systems, which can have a significant effect on aeroelasticity [3]. Typically, beyond the linear flutter boundary, the exponentially growing oscillatory response predicted by linear flutter analysis method is bounded due to existing benign nonlinearities with limit cycle oscillation (LCO), which actually is the so-called stable LCO. On the other hand, with detrimental nonlinearities, an aeroelastic system that may be stable to a small disturbance can become unstable well below the flutter boundary if the disturbances to the system are sufficiently large. In this case, the system may experience unstable limit cycle oscillation, which is extremely sensitive to perturbations and cannot be observed experimentally. However, it can be predicted using some frequency domain methods such as the describing function technique (also known as the harmonic balance method) [4]. Although catastrophic flutter might be replaced by stable limit cycle oscillation owing to the benign nonlinearity, structural integrity may still be at issue if the LCO amplitudes are too large [3]. In the case of the detrimental nonlinearity, unstable LCO may occur below the

---

X. Wei (✉) • J.E. Mottershead  
Centre for Engineering Dynamics, University of Liverpool, Liverpool L69 3GH, UK  
e-mail: [xiaojun.wei@liv.ac.uk](mailto:xiaojun.wei@liv.ac.uk); [j.e.mottershead@liverpool.ac.uk](mailto:j.e.mottershead@liverpool.ac.uk)

linear flutter boundary, which probably causes catastrophic failure. Hence, it is of great importance to reduce the stable LCO amplitudes and convert an unstable LCO to a stable LCO by implementing aeroelastic control.

In aeroelastic control, the problem of suppressing flutter by assigning stable poles using feedback control forces may be treated using eigenvalue assignment. The recently developed linear active vibration suppression method based on measured receptance [5], known as the receptance method, has been employed to suppress flutter vibration and extend the flutter boundary in the case of linear aeroelastic systems [6, 7]. The receptance approach has a number of significant advantages over conventional vibration control methods for aeroelastic systems. Apart from the evaluation of the structural matrices usually containing various modelling assumptions and errors, conventional approaches require modelling the aerodynamic forces which is generally dependent on commercial codes such as MSC-NASTRAN, ZAERO or ASTROS. The receptance method is completely dependent on the measured data, which renders the evaluation of structural and aerodynamic matrices unnecessary. Also, there is no requirement for model reduction or for the use of an observer to estimate the unmeasured state variables. In principle the receptance-based controller can be continuously corrected using in-flight measurements with consequent improvements to aircraft manoeuvrability and possibly survivability in the case of damage to the aircraft.

Periodic nonlinear aeroelastic vibration problems may be treated by frequency-domain methods, such as the describing function technique [8], which has been used to determine the behaviour of nonlinear aeroelastic systems [9–11]. Sinusoidal-input describing functions (DFs) are especially applicable when the fundamental harmonic term is predominant in LCO response. Essentially, the describing function method is to quasi-linearise a nonlinear system into an equivalent linear counterpart. Therefore, based on describing functions, the well-developed linear active flutter control theory [5, 12–14] can be extended to suppress flutter behaviour in nonlinear aeroelastic systems into limit cycles implemented by moving troublesome eigenvalues to the imaginary axis in the  $s$ -plane. Because of the detrimental effects of unstable LCO, guaranteeing stable LCO is of importance to extend the flight envelope without catastrophic structural failure.

In this paper, a limit cycle prediction method based on DFs and Sherman-Morrison formula is proposed. Also, with representing the nonlinearity via DFs, the nonlinear active control theory using measured receptance is developed. To assign stable LCO, a new form of stability criterion of limit cycles for closed-loop systems is derived. Frequency-domain and time-domain results from a two-degree-of-freedom airfoil with either cubic or piecewise nonlinear pitching stiffness demonstrate the capabilities of these proposed methods.

## 67.2 Theory

### 67.2.1 Limit Cycle Prediction Based on Describing Functions and Sherman-Morrison Formula

The governing equation of an aeroelastic self-excited system with concentrated structural nonlinearity may be cast in matrix form

$$\mathbf{A} \ddot{\mathbf{q}} + (\rho V \mathbf{B} + \mathbf{D}) \dot{\mathbf{q}} + (\rho V^2 \mathbf{C} + \mathbf{E}) \mathbf{q} + \mathbf{f}_{nl} = 0, \quad (67.1)$$

where  $\mathbf{A}$ ,  $\mathbf{B}$ ,  $\mathbf{C}$ ,  $\mathbf{D}$ ,  $\mathbf{E}$  are the structural inertia, aerodynamic damping, aerodynamic stiffness, structural damping and structural stiffness matrices of linear part respectively [1],  $\mathbf{q}$  is the vector of generalised coordinates,  $\mathbf{f}_{nl}$  is the internal nonlinear force,  $\rho$  and  $V$  are the air density and air speed.

For limit cycle state, the periodic nonlinear aeroelastic response can be expressed as Fourier series

$$\mathbf{q} = \sum_{m=0}^{\infty} \mathbf{x}_m e^{im\omega t}, \quad (67.2)$$

where  $\mathbf{x}_m$  ( $m = 0, 1, 2, \dots$ ) are the complex amplitude vector of the  $m$ th harmonic component. Apart from the fundamental harmonic term, the bias term  $\mathbf{x}_0$  and the higher-order terms  $\mathbf{x}_m$  ( $m = 2, 3, 4, \dots$ ) are included.

In the case of flutter oscillation, the aeroelastic system exhibits a strong filtering property such that the fundamental harmonic is predominant [15]. Hence the response expressed in Eq. (67.2) is approximated as

$$\mathbf{q} = \mathbf{x} e^{i\omega t}. \quad (67.3)$$

In the above equation, the subscript (67.1) is dropped for convenience.  $\mathbf{x}$  is the complex amplitude of fundamental harmonic response with phase information included.



Based on sinusoidal input describing functions [8], the internal nonlinear force is approximated as

$$\mathbf{f}_{nl} = \mathbf{E}_{nl}(\mathbf{x}) \mathbf{x} e^{i\omega t}, \quad (67.4)$$

where  $\mathbf{E}_{nl}(\mathbf{x})$  is the quasi-linearised stiffness matrix.

In this paper, a single structural nonlinear element is considered, and the quasi-linearised stiffness matrix is given by

$$\mathbf{E}_{nl}(\mathbf{x}) = N_{kr}(A, \omega) \mathbf{e}_{kr} \mathbf{e}_{kr}^T, \quad (67.5)$$

Where  $\mathbf{e}_{kr} = \{\mathbf{0} \ e_k \ \mathbf{0} \ e_r \ \mathbf{0}\}^T$  ( $e_k = 1$  and  $e_r = -1$ ) is a vector defining the location of the nonlinearity between coordinate  $k$  and coordinate  $r$ . Evidently,  $\mathbf{E}_{nl}(\mathbf{x})$  is a rank-one matrix.  $N_{kr}(A, \omega)$  ( $A = |x_{kr}| = |x_k - x_r|$ ,  $x_k$  and  $x_r$  are the  $k$ th and  $r$ th elements of  $\mathbf{x}$  respectively) is the sinusoidal input describing function given by

$$N_{kr}(A, \omega) = \frac{i}{\pi A} \int_0^{2\pi} f_{kr}(x_{kr}, \dot{x}_{kr}) e^{-i\phi} d\phi. \quad (67.6)$$

Hence, the receptance matrix of the system is

$$\hat{\mathbf{H}}(s) = (\mathbf{A} s^2 + (\rho V \mathbf{B} + \mathbf{D}) s + (\rho V^2 \mathbf{C} + \mathbf{E}) + N_{kr}(A, \omega) \mathbf{e}_{kr} \mathbf{e}_{kr}^T)^{-1}. \quad (67.7)$$

Based on the Sherman-Morrison formula, the receptance matrix is recast as

$$\hat{\mathbf{H}}(s) = \mathbf{H}(s) - \frac{N_{kr}(A, \omega) \mathbf{H}(s) \mathbf{e}_{kr} \mathbf{e}_{kr}^T \mathbf{H}(s)}{1 + N_{kr}(A, \omega) \mathbf{e}_{kr}^T \mathbf{H}(s) \mathbf{e}_{kr}}, \quad (67.8)$$

where  $\mathbf{H}(s)$  is the counterpart of corresponding linear system, that is

$$\mathbf{H}(s) = (\mathbf{A} s^2 + (\rho V \mathbf{B} + \mathbf{D}) s + (\rho V^2 \mathbf{C} + \mathbf{E}))^{-1}. \quad (67.9)$$

The characteristic equation is

$$1 + N_{kr}(A, \omega) \mathbf{e}_{kr}^T \mathbf{H}(s) \mathbf{e}_{kr} = 0. \quad (67.10)$$

Obviously, Eq. (67.10) is an equation about oscillation amplitude  $A$  and frequency  $\omega$ .

Limit cycle oscillations are undamped oscillations, which are neutrally stable. Mathematically the eigenvalues corresponding to limit cycle oscillations are purely imaginary numbers, denoted as  $\pm i\omega$ . Also, for general static nonlinearities, the sinusoidal input describing function is only dependant on the amplitude of input, and therefore  $N_{kr}(A, \omega)$  is reduced to  $N_{kr}(A)$ . Hence, Eq. (67.10) is written as

$$1 + N_{kr}(A) \mathbf{e}_{kr}^T \mathbf{H}(s) \mathbf{e}_{kr} |_{s=\pm i\omega} = 0, \quad (67.11)$$

which defines limit cycle oscillations. Actually Eq. (67.11) is equivalent to the following two equations

$$\text{Re}(1 + N_{kr}(A) \mathbf{e}_{kr}^T \mathbf{H}(s) \mathbf{e}_{kr} |_{s=\pm i\omega}) = 0, \quad (67.12)$$

$$\text{Im}(1 + N_{kr}(A) \mathbf{e}_{kr}^T \mathbf{H}(s) \mathbf{e}_{kr} |_{s=\pm i\omega}) = 0. \quad (67.13)$$

Because  $N_{kr}(A)$  is real quantity, Eq. (67.13) is recast as

$$\text{Im}(\mathbf{e}_{kr}^T \mathbf{H}(s) \mathbf{e}_{kr} |_{s=\pm i\omega}) = 0. \quad (67.14)$$

It is evident that Eq. (67.14) is only an equation of the frequency  $\omega$ . If there exist limit cycles, we can derive the frequency  $\omega$  from Eq. (67.14), substitute  $\omega$  into Eq. (67.12) and then solve it for the amplitude  $A$ . Therefore, it is unnecessary to solve coupled equations about the amplitude  $A$  and frequency  $\omega$ , which reduces the computation effort and make the limit cycle prediction process very straightforward.

### 67.2.2 Limit Cycle Assignment

Now, a single-input PD controller is employed to assign limit cycle for the aeroelastic system expressed in Eq. (67.1). Once again, only a nonlinear element is considered. After quasi-linearising using DFs, the governing equation of the closed-loop aeroelastic system is

$$\mathbf{A} \ddot{\mathbf{q}} + (\rho V \mathbf{B} + \mathbf{D}) \dot{\mathbf{q}} + (\rho V^2 \mathbf{C} + \mathbf{E} + \mathbf{E}_{nl}(A)) \mathbf{q} = \mathbf{b} \beta, \quad (67.15)$$

and

$$\beta = -(\mathbf{f}^T \dot{\mathbf{q}} + \mathbf{g}^T \mathbf{q}), \quad (67.16)$$

where  $(\mathbf{g}^T \mathbf{f}^T)^T$  is the acceleration and velocity gains, and  $\mathbf{b}$  is the actuator distribution vector (for single-input control).

Thus, closed-loop receptance matrix is

$$\hat{\mathbf{H}}(A, s) = (\mathbf{A} s^2 + (\rho V \mathbf{B} + \mathbf{D} + \mathbf{b} \mathbf{f}^T) s + (\rho V^2 \mathbf{C} + \mathbf{E} + \mathbf{E}_{nl}(A) + \mathbf{b} \mathbf{g}^T))^{-1}. \quad (67.17)$$

Sherman-Morrison formula is employed to rewrite the closed-loop receptance matrix as

$$\hat{\mathbf{H}}(A, s) = \mathbf{H}(A, s) - \frac{\mathbf{H}(A, s) \mathbf{b} (s \mathbf{f} + \mathbf{g})^T \mathbf{H}(A, s)}{1 + (s \mathbf{f} + \mathbf{g})^T \mathbf{H}(A, s) \mathbf{b}}, \quad (67.18)$$

where  $\mathbf{H}(A, s)$  is the open-loop receptance matrix.

The characteristic equation is

$$1 + (s \mathbf{f} + \mathbf{g})^T \mathbf{H}(A, s) \mathbf{b} = 0. \quad (67.19)$$

Based on Eq. (67.19), prescribed eigenvalues can be assigned if a set of control gain  $\mathbf{f}$ ,  $\mathbf{g}$  is chosen.

To assign limit cycle, Eq. (67.19) becomes

$$\begin{bmatrix} (\mathbf{H}(A, s_1) \mathbf{b})^T s_1 (\mathbf{H}(A, s_1) \mathbf{b})^T \\ (\mathbf{H}(A, s_2) \mathbf{b})^T s_2 (\mathbf{H}(A, s_2) \mathbf{b})^T \end{bmatrix} \begin{pmatrix} \mathbf{g} \\ \mathbf{f} \end{pmatrix} = \begin{bmatrix} -1 \\ -1 \end{bmatrix}, \quad (67.20)$$

where  $s_1 = i\omega$  and  $s_2 = -i\omega$ .

Actually, because  $s_1$  and  $s_2$  are purely imaginary conjugate eigenvalues, the two equations in Eq. (67.20) will generate the same control gains provided that only real control gains are considered.

### 67.2.3 A New Form of Limit Cycle Stability Criterion for Closed-Loop System

It is possible that the limit cycles assigned by using Eq. (67.20) are unstable. Therefore, perturbation analysis should be done to search the additional conditions for placing stable limit cycles. If a limit cycle with amplitude  $A_0$  and eigenvalue  $s_0 = i\omega$  has been assigned, the following equation holds

$$P(A_0, s_0) = 1 + (s_0 \mathbf{f} + \mathbf{g})^T \mathbf{H}(A_0, s_0) \mathbf{b} = 0. \quad (67.21)$$

Let us allow small perturbations in the limit cycle amplitude and eigenvalue by introducing the following changes in Eq. (67.21)

$$\begin{aligned} A_0 &\longrightarrow A_0 + \Delta A, \\ s_0 &\longrightarrow s_0 + \Delta s = s_0 + \Delta \sigma + i \Delta \omega. \end{aligned} \quad (67.22)$$

Hence, we have

$$P(A_0 + \Delta A, s_0 + \Delta \sigma + i \Delta \omega) = 0. \quad (67.23)$$

Expanding Eq. (67.23) in the form of Taylor series around the equilibrium state  $(A_0, s_0)$ , we get

$$P(A_0 + \Delta A, s_0 + \Delta\sigma + i\Delta\omega) = P(A_0, s_0) + \frac{\partial P}{\partial A} \Delta A + \frac{\partial P}{\partial s} \Delta\sigma + i \frac{\partial P}{\partial s} \Delta\omega + o(\Delta A) + o(\Delta s) = 0. \quad (67.24)$$

Subtracting Eq. (67.21) from Eq. (67.24) and eliminating the high-order terms, we obtain

$$\frac{\partial P}{\partial A} \Delta A + \frac{\partial P}{\partial s} \Delta\sigma + i \frac{\partial P}{\partial s} \Delta\omega = 0. \quad (67.25)$$

Satisfaction of Eq. (67.25) requires its real part and imaginary part equal to zero separately:

$$\operatorname{Re} \left( \frac{\partial P}{\partial A} \right) \Delta A + \operatorname{Re} \left( \frac{\partial P}{\partial s} \right) \Delta\sigma + \operatorname{Re} \left( i \frac{\partial P}{\partial s} \right) \Delta\omega = 0, \quad (67.26)$$

$$\operatorname{Im} \left( \frac{\partial P}{\partial A} \right) \Delta A + \operatorname{Im} \left( \frac{\partial P}{\partial s} \right) \Delta\sigma + \operatorname{Im} \left( i \frac{\partial P}{\partial s} \right) \Delta\omega = 0. \quad (67.27)$$

Obviously,

$$\operatorname{Re} \left( \frac{\partial P}{\partial s} \right) = \operatorname{Im} \left( i \frac{\partial P}{\partial s} \right), \quad (67.28)$$

$$\operatorname{Im} \left( \frac{\partial P}{\partial s} \right) = -\operatorname{Re} \left( i \frac{\partial P}{\partial s} \right). \quad (67.29)$$

Therefore, Eqs. (67.26) and (67.27) can be cast as

$$\operatorname{Re} \left( \frac{\partial P}{\partial A} \right) \Delta A + \operatorname{Re} \left( \frac{\partial P}{\partial s} \right) \Delta\sigma - \operatorname{Im} \left( \frac{\partial P}{\partial s} \right) \Delta\omega = 0, \quad (67.30)$$

$$\operatorname{Im} \left( \frac{\partial P}{\partial A} \right) \Delta A + \operatorname{Im} \left( \frac{\partial P}{\partial s} \right) \Delta\sigma + \operatorname{Re} \left( \frac{\partial P}{\partial s} \right) \Delta\omega = 0. \quad (67.31)$$

Eliminating  $\Delta\omega$ ,

$$\operatorname{Re} \left( \frac{\partial P}{\partial A} \right) \operatorname{Re} \left( \frac{\partial P}{\partial s} \right) + \operatorname{Im} \left( \frac{\partial P}{\partial A} \right) \operatorname{Im} \left( \frac{\partial P}{\partial s} \right) = \left( \left( \operatorname{Re} \left( \frac{\partial P}{\partial s} \right) \right)^2 + \left( \operatorname{Im} \left( \frac{\partial P}{\partial s} \right) \right)^2 \right) \left( -\frac{\Delta\sigma}{\Delta A} \right). \quad (67.32)$$

It may be understood that if there is positive amplitude perturbation ( $\Delta A > 0$ ), the eigenvalue moving to the left-hand side of the complex plane will lead to a stable system configuration, in which energy is dissipated until the amplitude decays to its unperturbed value. In other words, if positive amplitude perturbation ( $\Delta A > 0$ ) is combined with  $\Delta\sigma < 0$ , the perturbed limit cycle will return to its original equilibrium state—that is to say, the limit cycle is a stable one. Similarly, if the limit cycle experiences a negative amplitude perturbation ( $\Delta A < 0$ ), we require an unstable system whose eigenvalue moves to the right-hand side of the complex plane ( $\Delta\sigma > 0$ ), therefore, the amplitude will grow to its unperturbed. Hence, the sign of  $\Delta\sigma/\Delta A$  is always negative indicating a stable limit cycle.

Based the above perturbation analysis, for a stable limit cycle,

$$\operatorname{Re} \left( \frac{\partial P}{\partial A} \right) \operatorname{Re} \left( \frac{\partial P}{\partial s} \right) + \operatorname{Im} \left( \frac{\partial P}{\partial A} \right) \operatorname{Im} \left( \frac{\partial P}{\partial s} \right) > 0 \quad (67.33)$$

or

$$\operatorname{Re} \left( \operatorname{conj} \left( \frac{\partial P}{\partial A} \right) \bullet \frac{\partial P}{\partial s} \right) > 0 \quad (67.34)$$

or

$$\operatorname{Im} \left( \operatorname{conj} \left( \frac{\partial P}{\partial A} \right) \bullet \frac{\partial P}{\partial s} i \right) > 0 \quad (67.35)$$

at  $A = A_0$  and  $s = s_0$ .

It appears that inequalities (67.33)–(67.35) are also valid for open-loop system if  $P$  is the characteristic polynomial of open-loop system [16]. Furthermore, the above limit cycle stability criterion can be expressed as a quadratic form in terms of control gains.

We denote

$$\mathbf{V}(A, s) = \left[ (\mathbf{H}(A, s) \mathbf{b})^T \quad s (\mathbf{H}(A, s) \mathbf{b})^T \right]. \quad (67.36)$$

Therefore,

$$\frac{\partial P}{\partial A} = (\mathbf{g}^T \quad \mathbf{f}^T) \frac{\partial \mathbf{V}(A, s)^T}{\partial A} = \frac{\partial \mathbf{V}(A, s)}{\partial A} \begin{pmatrix} \mathbf{g} \\ \mathbf{f} \end{pmatrix}, \quad (67.37)$$

$$\frac{\partial P}{\partial s} = (\mathbf{g}^T \quad \mathbf{f}^T) \frac{\partial \mathbf{V}(A, s)^T}{\partial s} = \frac{\partial \mathbf{V}(A, s)}{\partial s} \begin{pmatrix} \mathbf{g} \\ \mathbf{f} \end{pmatrix}. \quad (67.38)$$

Inequality (67.34) is rewritten as

$$\operatorname{Re} \left( \operatorname{conj} \left( \frac{\partial P}{\partial A} \right) \bullet \frac{\partial P}{\partial s} \right) = (\mathbf{g}^T \quad \mathbf{f}^T) \operatorname{Re} \left( \operatorname{conj} \left( \frac{\partial \mathbf{V}(A, s)^T}{\partial A} \right) \bullet \frac{\partial \mathbf{V}(A, s)}{\partial s} \right) \begin{pmatrix} \mathbf{g} \\ \mathbf{f} \end{pmatrix} > 0. \quad (67.39)$$

We denote

$$\mathbf{Q} = \operatorname{Re} \left( \operatorname{conj} \left( \frac{\partial \mathbf{V}(A, s)^T}{\partial A} \right) \bullet \frac{\partial \mathbf{V}(A, s)}{\partial s} \right) \Big|_{\substack{A=A_0 \\ s=i\omega_0}}, \quad (67.40)$$

which is likely to be an asymmetric square matrix. However, as shown in the following derivation, a quadratic form with an asymmetric square  $\mathbf{Q}$  can be transformed into one with equivalent function value but symmetric matrix  $\frac{1}{2}\mathbf{Q} + \frac{1}{2}\mathbf{Q}^T$ . That is

$$(\mathbf{g}^T \quad \mathbf{f}^T) \mathbf{Q} \begin{pmatrix} \mathbf{g} \\ \mathbf{f} \end{pmatrix} = (\mathbf{g}^T \quad \mathbf{f}^T) \mathbf{Q}^T \begin{pmatrix} \mathbf{g} \\ \mathbf{f} \end{pmatrix} = (\mathbf{g}^T \quad \mathbf{f}^T) \left( \frac{1}{2}\mathbf{Q} + \frac{1}{2}\mathbf{Q}^T \right) \begin{pmatrix} \mathbf{g} \\ \mathbf{f} \end{pmatrix}. \quad (67.41)$$

Thus, a new form of limit cycle stability criterion for closed-loop system, which is expressed as a quadratic form with real symmetric matrix, is obtained

$$(\mathbf{g}^T \quad \mathbf{f}^T) \left( \frac{1}{2}\mathbf{Q} + \frac{1}{2}\mathbf{Q}^T \right) \begin{pmatrix} \mathbf{g} \\ \mathbf{f} \end{pmatrix} > 0. \quad (67.42)$$

#### 67.2.4 Optimisation of Control Gains

In order to minimize control effort, an optimisation scheme is necessary to be proposed to achieve a set of minimum feedback control gains which can realize the suppression of flutter into stable LCOs. In practice, only real control gains are interesting. Then the limit cycle assignment problem is expressed by

$$\min \mathbf{g}, \mathbf{f}$$

*s.t.*

$$(\mathbf{H}(A, s) \mathbf{b})^T \quad s (\mathbf{H}(A, s) \mathbf{b})^T \begin{pmatrix} \mathbf{g} \\ \mathbf{f} \end{pmatrix} \Big|_{s=i\omega} = -1,$$

$$(\mathbf{g}^T \quad \mathbf{f}^T) \left( \frac{1}{2}\mathbf{Q} + \frac{1}{2}\mathbf{Q}^T \right) \begin{pmatrix} \mathbf{g} \\ \mathbf{f} \end{pmatrix} > 0. \quad (67.43)$$

Actually, solving Eq. (67.20) produces a set of minimum norm control gains. If the assigned limit cycle is tested to be stable according to limit cycle stability criterion (67.42), then the optimisation (67.43) is rendered unnecessary.

### 67.3 Numerical Example

A two-degree-of-freedom airfoil with either a cubic or bilinear nonlinearity in pitch, shown in Fig. 67.1, is given for analysis. The structural and aerodynamic parameters except the nonlinear pitching stiffness are described in Table 67.1. In fact, the airfoil is a rigid wing of span  $s$  and chord  $c$  supported at the root with two rotational springs having linear flexural stiffness  $k_\kappa$  and nonlinear torsional stiffness  $k_\theta$ , where  $\kappa$  and  $\theta$  denote the flap and pitch degrees of freedom respectively and  $\mathbf{q} = (\kappa, \theta)^T$  is the generalized coordinate vector. The springs are attached at a distance  $ec$  from the aerodynamic centre (on the quarter chord), defining the position of the flexural axis. The wing moments of inertial are defined by  $I_\kappa$  and  $I_\theta$ . There exists inertial coupling  $I_{\kappa\theta}$  because the wing mass and flexural axes do not coincide. Due to the drawback in using quasi-steady aerodynamics, the  $M_{\dot{\theta}}$  unsteady aerodynamic derivative term will be retained [1]. The structural damping will be ignored. The feedback control forces are implemented by a full span rigid control surface. It has an infinite stiffness attached but can be moved to any angle that is demanded. The inertial effects of the control surface are ignored. Thus the control surface is not involved in the basic dynamics of the wing but simply acts as an excitation device.

Based on DFs, the open-loop aeroelastic system is governed by the expression

$$\mathbf{A} \ddot{\mathbf{q}} + (\rho V \mathbf{B} + \mathbf{D}) \dot{\mathbf{q}} + (\rho V^2 \mathbf{C} + \mathbf{E} + \mathbf{E}_{nl}(A)) \mathbf{q} = 0, \quad (67.44)$$

where

$$\mathbf{A} = \begin{bmatrix} I_\kappa & I_{\kappa\theta} \\ I_{\kappa\theta} & I_\theta \end{bmatrix}, \quad (67.45)$$

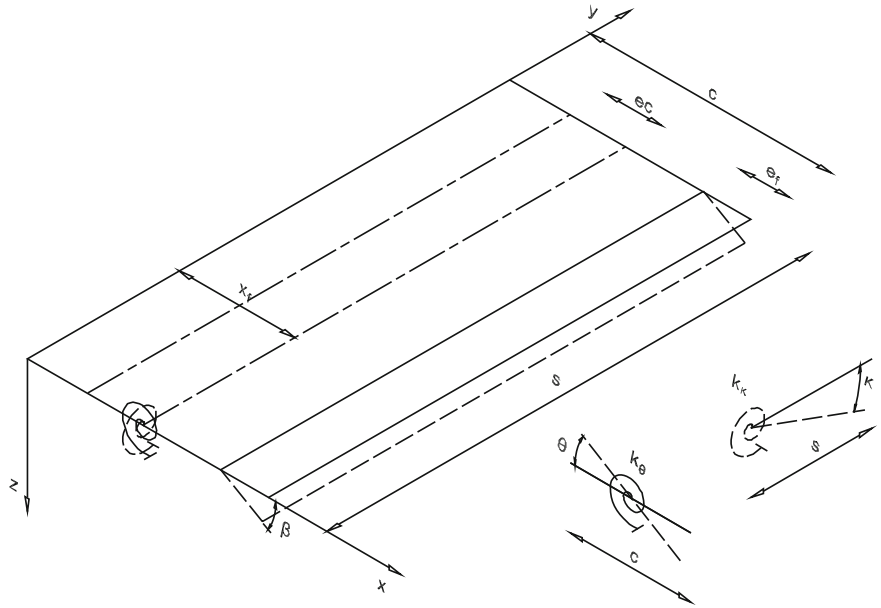
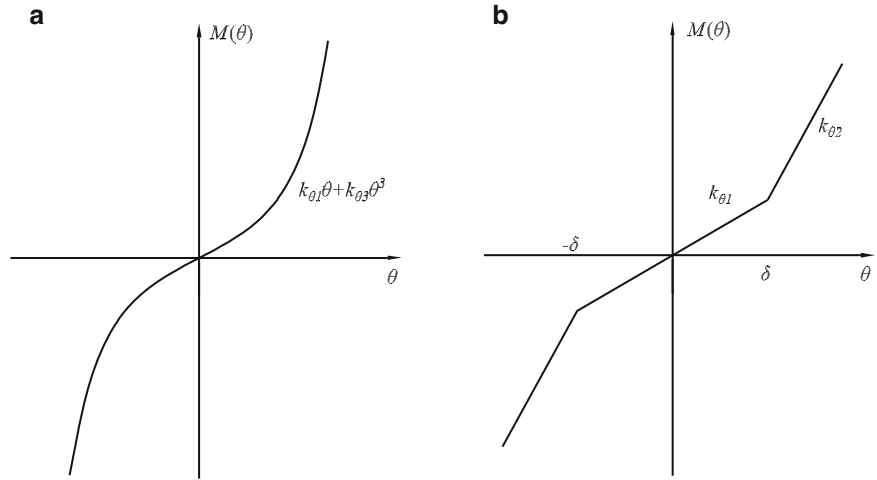


Fig. 67.1 Airfoil configuration

Table 67.1 Aeroelastic system parameters

Parameter	Symbol	Value
Semi-span (m)	$s$	7.5
Chord (m)	$c$	2
Mass per unit area (kg/m <sup>2</sup> )	$m$	100
Air density (kg/m <sup>3</sup> )	$\rho$	1.225
2D lift curve slope	$a_w$	$2\pi$
Unsteady torsional velocity term	$M_{\dot{\theta}}$	-1.2
Fraction of chord	$e_f$	0.1
Flexural rigidity	$k_\kappa$	$27.758 \times 10^6$
Position of flexural axis	$x_f$	$0.48c$
Eccentricity ratio	$e$	0.23

**Fig. 67.2** Schematic of the structural nonlinearities: (a) cubic stiffness; (b) bilinear stiffness



$$\mathbf{B} = \begin{bmatrix} \frac{cs^3 a_w}{4} & 0 \\ -\frac{c^2 s^2 e a_w}{4} & -\frac{c^3 s}{8} M_{\dot{\theta}} \end{bmatrix}, \quad (67.46)$$

$$\mathbf{C} = \begin{bmatrix} 0 & \frac{cs^2 a_w}{4} \\ 0 & -\frac{c^2 s e a_w}{2} \end{bmatrix}, \quad (67.47)$$

$$\mathbf{D} = [\mathbf{0}]. \quad (67.48)$$

### 67.3.1 Binary Aeroelastic Model with Cubic Stiffness in Pitch

Currently, the described two-degree-of-freedom airfoil above with a cubic nonlinearity in pitch is considered. The nonlinear restoring moment, shown in Fig. 67.2a, has the following form

$$M(\theta) = k_{\theta 1} \theta + k_{\theta 3} \theta^3, \quad (67.49)$$

where  $k_{\theta 1} = 19.834 \times 10^5 \text{N/m}$  and  $k_{\theta 3}$  are the linear and nonlinear stiffness coefficients respectively. The linear flutter speed is 154.35 m/s. The ratio of the nonlinear stiffness coefficient and linear stiffness coefficient is chosen as

$$\frac{k_{\theta 3}}{k_{\theta 1}} = 10, \quad (67.50)$$

in order that the maximum pitch angle for the speed range considered is smaller than 20 degrees (3.491 radians), which renders linear aerodynamic assumption satisfied [17].

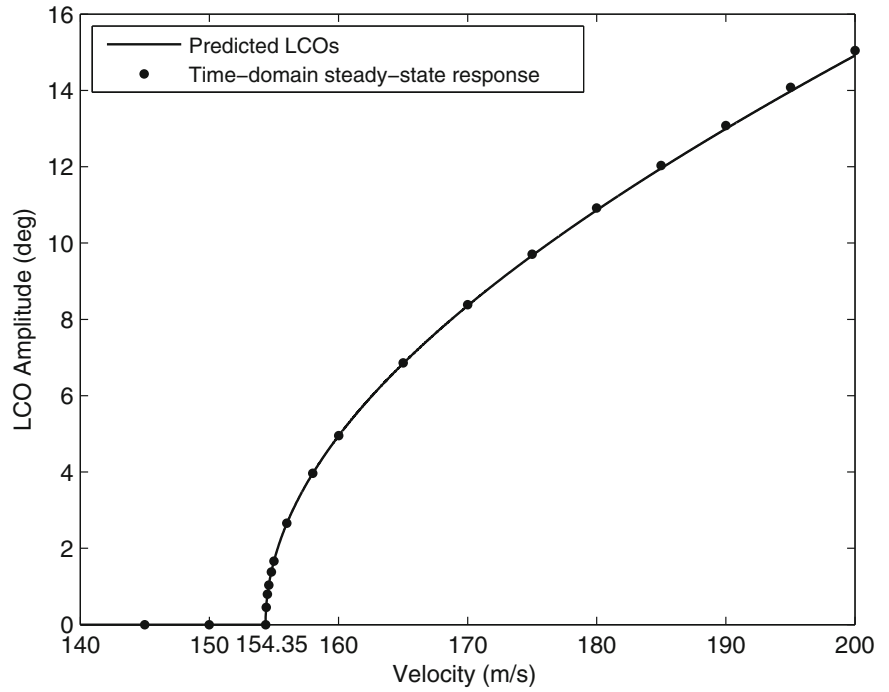
According to DFs, we can achieve the quasi-linearised pitch stiffness

$$k(A_{\theta}) = k_{\theta 1} + \frac{3}{4} k_{\theta 3} A_{\theta}^2. \quad (67.51)$$

The proposed method is used to predict limit cycle amplitudes over a speed range 140–200 m/s, shown in Fig. 67.3, which are compared by the time-domain steady-state response obtained by using numerical integration algorithm based on an explicit Runge-Kutta (4,5) formula [18]. It implies that the predicted the flutter onset speed and the limit cycle amplitudes in the considered flight regime are in good agreement with those time-domain results. Also, the predicted LCOs are determined to be stable via the limit cycle stability criterion, which agrees with the fact that LCOs achieved numerically are independent on the initial conditions.

At any particular flight condition, the proposed limit cycle assignment method is used to regulate LCOs with smaller amplitudes. For instant, at airspeed 170 m/s, a LCO with frequency  $\omega = 54.34 \text{Hz}$  and amplitude  $A = 0.1458$  radians

**Fig. 67.3** Comparison of the limit cycle amplitude obtained via the numerical integration and proposed methods for cubic nonlinearity



(8.3554 degrees) is predicted. Now, a new limit cycle with amplitude  $A = 0.05$  radians (2.8648 degrees) and frequency  $\omega = 49.11$  radians, which is the pitch mode frequency of the open-loop system with equivalent pitch stiffness  $N(A_\theta)|_{A_\theta=0.05}$ , is to be assigned.

According to Eq. (67.20), we compute a set of minimum Euclidean norm control gain

$$(\mathbf{g}^T \quad \mathbf{f}^T) = (0.000113 \quad 0.000864 \quad -0.001989 \quad -0.002577). \quad (67.52)$$

The limit cycle stability analysis given by inequality (67.53) indicates that the assigned limit cycle is stable.

$$(\mathbf{g}^T \quad \mathbf{f}^T) \left( \frac{1}{2} \mathbf{Q} + \frac{1}{2} \mathbf{Q}^T \right) \begin{pmatrix} \mathbf{g} \\ \mathbf{f} \end{pmatrix} \Big|_{\omega=49.11}^{A=0.05} = 12.38 > 0. \quad (67.53)$$

The time-domain responses of the closed-loop system with the above control gains  $(\mathbf{g}^T \quad \mathbf{f}^T)^T$  are given in Figs. 67.4 and 67.5 (the initial condition is  $(\kappa(0), \theta(0), \dot{\kappa}(0), \dot{\theta}(0)) = (0, 3.4377, 0, 0)$ ). The limit cycle depicted in Fig. 67.5 converges to stable state implying a stable LCO.

### 67.3.2 Binary Aeroelastic Model with Bilinear Stiffness in Pitch

The other structural nonlinearity considered is bilinear restoring moment in the pitch direction, as shown schematically in Fig. 67.2b is given by,  $M(\theta)$  for bilinear stiffness is given by

$$M(\theta) = \begin{cases} (k_{\theta 2} - k_{\theta 1}) \delta + k_{\theta 2} \theta, & \theta < -\delta, \\ k_{\theta 1} \theta, & -\delta < \theta < \delta, \\ (k_{\theta 1} - k_{\theta 2}) \delta + k_{\theta 2} \theta, & \theta > \delta, \end{cases} \quad (67.54)$$

where  $k_{\theta 1}$  is the inner stiffness coefficient,  $k_{\theta 2} = 19.834 \times 10^5 \text{N/m}$  is the outer linear stiffness coefficient, the ratio  $k_{\theta 2}/k_{\theta 1}$  is 2, the parameter  $\delta = 2^\circ$  defines the inner linear stiffness region. Using the classic linear flutter analysis method, the linear flutter boundary of the linear system with pitch stiffness  $k_{\theta 1}$  is 89.22 m/s. The counterpart of the linear system with pitch stiffness  $k_{\theta 2}$  is 154.35 m/s.

**Fig. 67.4** The time history of pitch angles

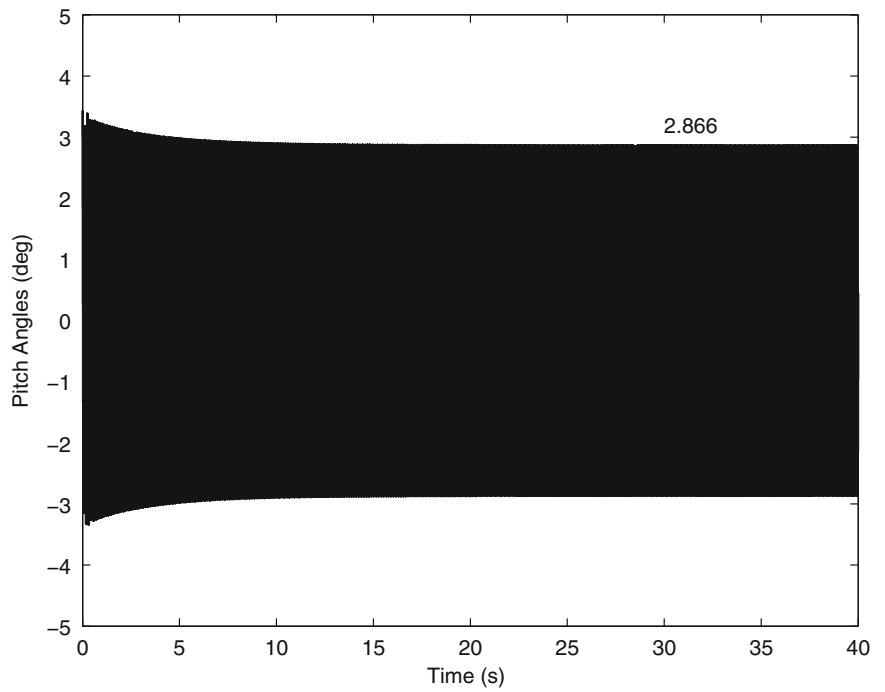
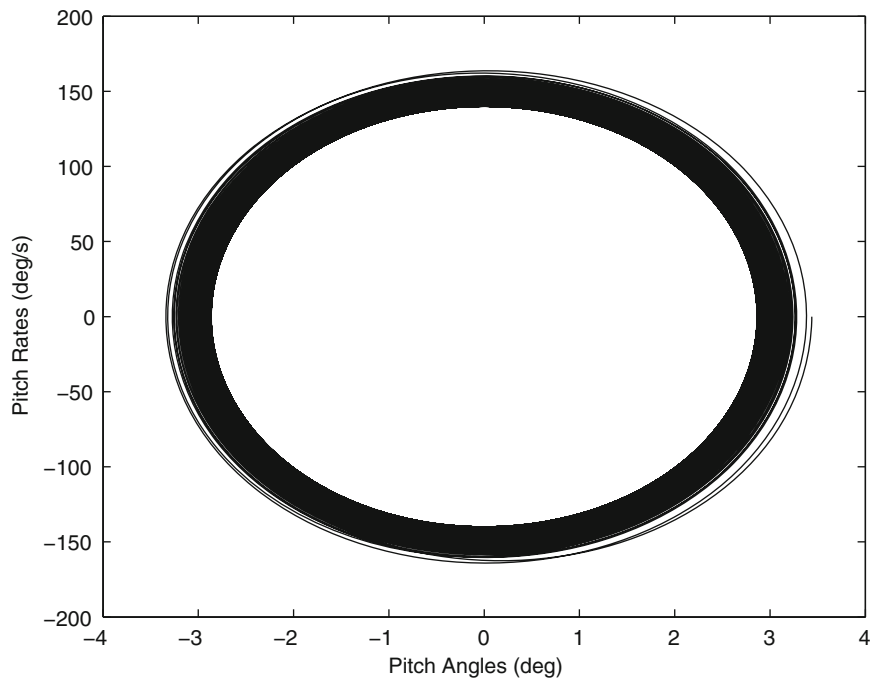


**Fig. 67.5** Pitch angles versus pitch rates



For bilinear nonlinearity, the sinusoidal input describing function is given by

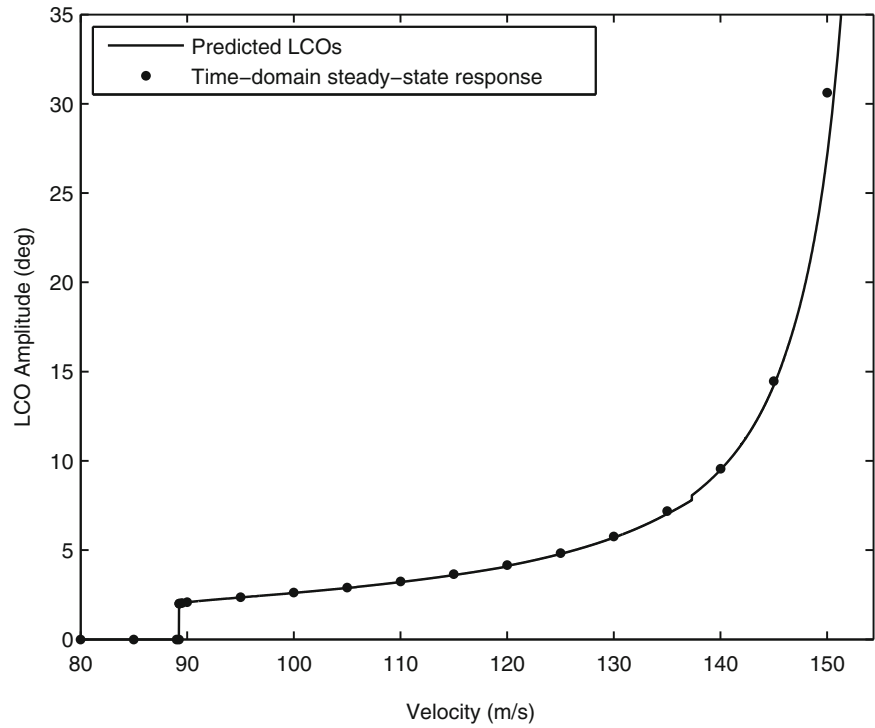
$$N(A_\theta) = \begin{cases} k_{\theta 1}, & A_\theta < \delta, \\ \frac{2(k_{\theta 1} - k_{\theta 2})}{\pi} \left[ \sin^{-1} \left( \frac{\delta}{A_\theta} \right) + \left( \frac{\delta}{A_\theta} \right) \sqrt{1 - \left( \frac{\delta}{A_\theta} \right)^2} \right] + k_{\theta 2}, & A_\theta \geq \delta, \end{cases} \quad (67.55)$$

Where  $A_\theta$  is the amplitude of the pitching motion.

Based on the proposed limit cycle prediction method, the limit cycle amplitude against flight velocity plot is achieved, shown in Fig. 67.6. Also, the time-domain steady-state responses over this speed range are computed employing a standard



**Fig. 67.6** Comparison of the limit cycle amplitude obtained via the numerical integration and proposed methods for bilinear nonlinearity



fourth-order Runge-Kutta scheme with adaptive time steps implemented by bi-section, similar to Lin and Cheng's method [19, 20]. It is found that there only exist LCOs at speeds between the two linear flutter speeds corresponding to those two linear systems with pitch stiffnesses  $k_{\theta 1}$  and  $k_{\theta 2}$  respectively. It is found that the predicted results agree precisely with calculated time-domain counterpart in terms of flutter boundary and LCO amplitude.

It is understandable that an aeroelastic system with bilinear stiffness can only sustain LCOs with amplitude greater than the parameter  $\delta$ . Therefore, we either assign a LCO with amplitude larger than  $\delta$  or control the system to be absolutely stable with all the eigenvalues in the left-hand side of s-plane. Here, we only consider the case of LCO.

At any flight speed ranging from 89.22 to 154.35 m/s, a new LCO can be placed via the proposed nonlinear active control method. For example, the open-loop system is subjected to a LCO with amplitude  $A = 0.099489$  radians (5.7003 degrees) and frequency  $\omega = 46.08$ Hz at flight speed 130 m/s. If the demanded new LCO has amplitude  $A = 0.0384$  radians (2.2 degrees) and frequency  $\omega = 35.38$ Hz, the pitch mode frequency of the open-loop system with equivalent pitch stiffness  $N(A_\theta)|_{A_\theta=0.0384}$ , a set of minimum Euclidean norm control gain is obtained according to Eq. (67.20)

$$(\mathbf{g}^T \quad \mathbf{f}^T) = (0.000003 \quad 0.000802 \quad -0.013123 \quad -0.020130). \quad (67.56)$$

The assigned limit cycle is determined to be stable by inequality (67.57)

$$(\mathbf{g}^T \quad \mathbf{f}^T) \left( \frac{1}{2} \mathbf{Q} + \frac{1}{2} \mathbf{Q}^T \right) \begin{pmatrix} \mathbf{g} \\ \mathbf{f} \end{pmatrix} \Big|_{\substack{A=0.0384 \\ \omega=35.38}} = 12.28 > 0. \quad (67.57)$$

The time-domain steady-state responses (the initial condition is  $(\kappa(0), \theta(0), \dot{\kappa}(0), \dot{\theta}(0)) = (0, 1.8, 0, 0)$ ), are shown in Figs. 67.7 and 67.8, demonstrate that the limit cycle assignment method is able to place a stable limit cycle with demanded amplitude and frequency precisely.

In the previous numerical examples, LCOs with given amplitudes and frequencies are assigned. In principle, a LCO with arbitrary amplitude and frequency can be assigned at a particular speed, and the proposed limit cycle assignment method will be able to generate a set of corresponding control gains.

**Fig. 67.7** The time history of pitch angles

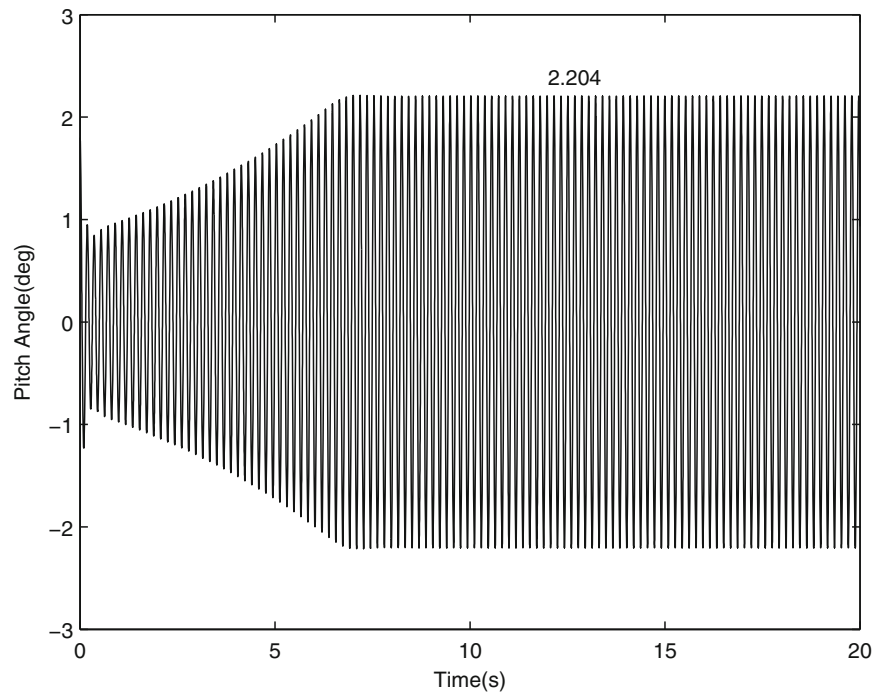
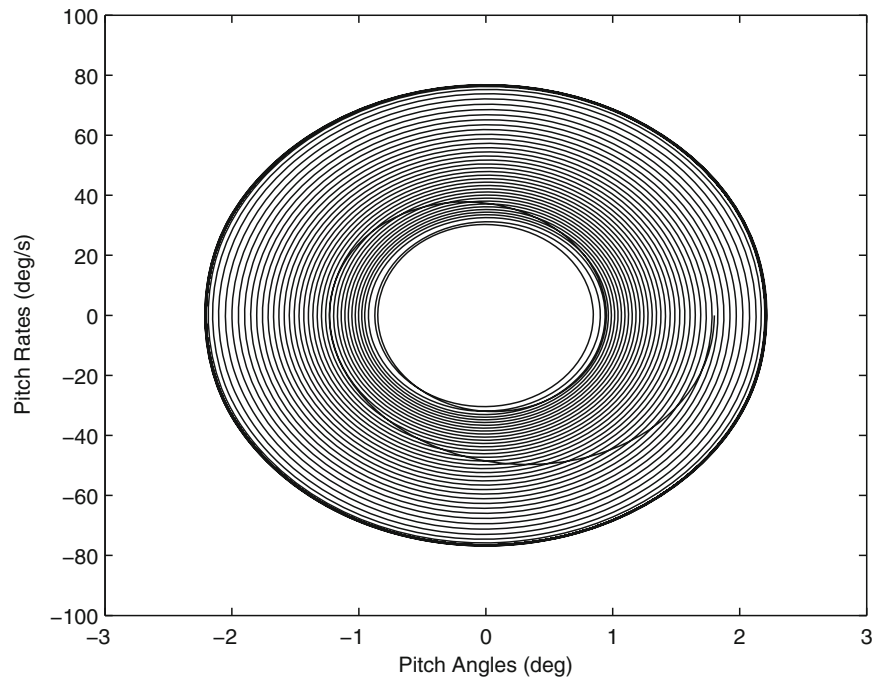


**Fig. 67.8** Pitch angles versus pitch rates



## 67.4 Discussion and Conclusions

This paper proposes a method for predicting limit cycles in aeroelastic systems with structural nonlinearities. The method uses describing functions techniques to representing the nonlinearity in the structure, and the Sherman-Morrison Formula is used to isolate the nonlinear element from the linear part of the system. When static nonlinearities are considered, this method avoids solving coupled equations about limit cycle frequency and amplitude and makes the limit cycle prediction procedure considerably straightforward. Also, the theory of the nonlinear active control based on the receptance method and DFs is developed. A new form of stability criterion of limit cycles for closed-loop systems based on describing function method is

derived. How stable limit cycle assignment can be implemented using eigenvalues assignment is demonstrated. Numerical results from binary aeroelastic model with either cubic or piecewise stiffness in pitch demonstrate that limit cycles and the onset of flutter can be predicted precisely by the new method. At a particular flight condition, stable LCOs with demanded amplitudes and frequencies can be assigned. Although no example has been given to convert an unstable LCO to a stable LCO, it is possible to implement that using a nonlinear controller, which is the subject of on-going research.

## References

1. Wright JR, Cooper JE (2007) Introduction to aircraft aeroelasticity and loads. Wiley, Chichester
2. Librescu L, Chiochia G, Marzocca P (2003) Implications of cubic physical/aerodynamic non-linearities on the character of the flutter instability boundary. *Int J Nonlinear Mech* 38(2):173–199
3. Dowell EH, Tang D (2002) Nonlinear aeroelasticity and unsteady aerodynamics. *AIAA J* 40(9):1697–1707
4. Dimitriadis G (2001) Investigation of nonlinear aeroelastic systems. PhD thesis, Department of Aerospace Engineering, The University of Manchester, Manchester
5. Ram YM, Mottershead JE (2007) Receptance method in active vibration control. *AIAA J* 45(3):562–567
6. Singh KV, McDonough L, Mottershead JE, Cooper J (2010) Active aeroelastic control using the receptance method. In: Proceedings of the ASME international mechanical engineering congress and exposition (IMECE-10), Vancouver, British Columbia, Canada
7. Papatheou E, Wei X, Jiffri S, Prandina M, Tehrani MG, Bode S, Singh KV, Mottershead JE, Cooper J (2012) Flutter control using vibration test data: theory, rig design and preliminary results. In: ISMA international conference on noise and vibration engineering, Leuven, Belgium
8. Gelb A, Vander Velde WE (1968) Multiple-input describing functions and nonlinear system design. McGraw-Hill, New York
9. Lee CL (1986) An iterative procedure for nonlinear flutter analysis. *AIAA J* 24(3):833–840
10. Yang ZC, Zhao LC (1988) Analysis of limit cycle flutter of an airfoil in incompressible flow. *J Sound Vib* 123(1):1–13
11. Price SJ, Alighanbari H, Lee BHK (1995) The aeroelastic response of a two-dimensional airfoil with bilinear and cubic structural nonlinearities. *J Fluids Struct* 9(2):175–193
12. Ghandchi Tehrani M, Elliott RNR, Mottershead JE (2010) Partial pole placement in structures by the method of receptances: theory and experiments. *J Sound Vib* 329(24):5017–5035
13. Mottershead JE, Tehrani MG, Ram YM (2009) Assignment of eigenvalue sensitivities from receptance measurements. *Mech Syst Signal Process* 23(6):1931–1939
14. Ghandchi Tehrani M, Mottershead JE, Shenton AT, Ram YM (2011) Robust pole placement in structures by the method of receptances. *Mech Syst Signal Process* 25(1):112–122
15. Shen SF (1959) An approximate analysis of nonlinear flutter problems. *J Aerosp Sci* 28(45):25–32
16. Miller R, Michel A, Krenz G (1986) On limit cycles of feedback systems which contain a hysteresis nonlinearity. *SIAM J Control Opt* 24(2):276–305
17. Lee BHK, Jiang LY, Wong YS (1999) Flutter of an airfoil with a cubic restoring force. *J Fluids Struct* 13(1):75–101
18. Dormand J, Prince P (1980) A family of embedded Runge-Kutta formulae. *J Comput Appl Math* 6:19–26
19. Lin W-B, Cheng W-H (1993) Nonlinear flutter of loaded lifting surface (I). *J Chin Society Mech Eng* 14(5):446–455. Transactions of the Chinese Institute of Engineers, Series C/Chung-Kuo Chi Hsueh Kung Ch'eng Hsuebo Pao
20. Lin W-B, Cheng W-H (1993) Nonlinear flutter of loaded lifting surface (II). *J Chin Soc Mech Eng* 14(5):456–466. Transactions of the Chinese Institute of Engineers, Series C/Chung-Kuo Chi Hsueh Kung Ch'eng Hsuebo Pao

# Chapter 68

## Investigation of an Active Structural Acoustic Control System on a Complex 3D Structure

S. Kulah, U. Aridogan, and I. Basdogan

**Abstract** Interior noise inside the passenger cabin of ground vehicles can be classified as structure-borne and airborne. The disturbance caused by the engine forces excites the panels enclosing the passenger cabin to vibrate at their resonance frequencies. These vibrating panels cause changes in the sound pressure levels within the passenger cabin, and consequently generating an undesirable booming noise. In this study, we developed a methodology to design an active structural acoustic controller (ASAC) to attenuate the structure-borne noise, which is mainly caused by the most influential radiating panel. The panel is determined by conducting panel acoustic contribution analysis (PACA) based on the acoustic transfer vector (ATV) methodology. Then, active structural acoustic controller is designed for vibration suppression of this panel, which has complex geometry and boundary conditions. The performance of the controller for noise reduction is investigated for various controller parameters and sensor/actuator positions. It is shown that an optimization algorithm is required to determine the optimum controller parameters and sensor/actuator positions to reduce sound pressure levels inside the cabin efficiently.

**Keywords** Active structural acoustic controller • Vibration sensor • Point-force actuator • Panel acoustic contribution analysis • Vibration control

### 68.1 Introduction

Active vibration and noise control methods are being developed and their performances are being investigated to improve the comfort of automotive, marine and aerospace applications in the last two decades [1–3]. As an alternative to classical methods, active structural acoustic control (ASAC) is an effective solution to suppress noise generated by low-frequency structural vibrations. However, for effective and stable operation of ASAC systems, the placement of sensors/actuators as well as the design and implementation of controller algorithms are crucial. These challenges of ASAC systems are being studied by researchers [4–11] to make ASAC systems more practical for the industry and mass production.

In general, ASAC systems involve feedback or feedforward loops with structural and acoustic sensors and structural actuators. These controller systems suppress structural vibrations while considering acoustic and structural response. For instance, Song et al. [4] investigated both structural and acoustic aspects for an ASAC system on a cabin mock-up model. The controlled panel was selected based on acoustic contribution analysis and actuators were placed on that panel. Similar to this study, de Oliveira et al. [5] used a vehicle mock-up including active and passive treatments for noise suppression in the cavity. They used a velocity feedback controller with a collocated sensor/actuator pair and achieved satisfactory noise reduction in the experimental setup for two different microphone positions. In another study by de Oliveira et al. [6], they designed and implemented adaptive feed forward controller algorithm for the same vehicle mock-up that they used in reference [5]. They modified the filtered x-LMS algorithm under the effect of varying disturbances and built an adaptation scheme for improving convergence rate of the algorithm. They stated that a combination of feedback and feedforward controllers can be used to improve vibration and noise suppression around lightly damped resonances of the vibro-acoustic system.

For a complex 3D structure with complex boundary conditions, under random disturbances and operational conditions, it is not a feasible approach to obtain an accurate plant model and design a model-based controller [12]. In these types of

---

S. Kulah • U. Aridogan • I. Basdogan (✉)  
Department of Mechanical Engineering, Koc University, Istanbul 34450, Turkey  
e-mail: skulah@ku.edu.tr; uaridogan@ku.edu.tr; ibasdogan@ku.edu.tr

applications, implementation of model-independent controllers is preferred. Zilletti et al. [13, 14] used a velocity feedback controller which is a robust model-independent controller with a collocated sensor/actuator pair to reduce total vibration energy and to improve panel sound transmissibility. They showed that reduction in total vibration energy can be achieved with a single properly-tuned velocity feedback controller loop. However, the total energy reduction in any panel does not guarantee reduction in sound pressure level inside an enclosure since each panel's contribution to sound pressure level is different. Therefore, acoustic contribution analysis is required to determine the most influential panel to the sound pressure level. After determining the most influential panel, actuator/sensor positioning and gain tuning for a feedback or feedforward control loop can be conducted.

In this paper, the performance of an ASAC system is investigated for various controller parameters and sensor/actuator positions for a complex 3D structure. A vibro-acoustic model of a vehicle is used for simulations. The most influential panel to the sound pressure level inside the passenger cabin is identified with panel acoustic contribution analysis (PACA). After determining the most influential panel, ASAC is designed for vibration suppression of this panel. Performance of the controller is evaluated by comparing the open and closed loop response of sound pressure levels inside the cavity. It is shown that, for a complex 3D structure, an optimal placement of collocated sensor/ actuator pair is required to reduce the sound pressure level inside the enclosure in the targeted frequency range while keeping noise pressure unaffected outside this range. This paper is organized as follows: Sect. 68.2 introduces the vibro-acoustic model of the vehicle. Section 68.3 describes the ASAC design. Section 68.4 presents the case studies, which includes the performance investigations of ASAC system. Finally, Sect. 68.5 concludes the paper.

## 68.2 Vibro-Acoustic Model and Analysis

The coupled vibro-acoustic model of the vehicle enclosing the passenger cavity is shown in Fig. 68.1. The holes in the structural model are filled to obtain an acoustic enclosure for the vibro-acoustic analysis. The vehicle structure is modeled with shell elements with various thicknesses. The engine mount extensions at the front side of the vehicle (see Fig. 68.1a, b) are modeled with rigid elements. The modal analysis of the structure is conducted with NASTRAN between 0 and 160 Hz frequency range. The modal analysis results are used for vibro-acoustic analysis in LMS Virtual lab.

For vibro-acoustic analysis, *FEM/FEM* approach is used to obtain sound pressure level due to engine loading and additionally “panel acoustic contribution analysis” is performed to determine the contribution of each radiating panel. The microphone is placed at the driver's head position shown in Fig. 68.1b. The cavity (acoustic volume) is meshed such that the vibration from the structure can be transferred to the cavity across the structural and acoustic coupled degrees of freedom (See Fig. 68.1c). The panels (ceiling, windshield, right door, left door, front panel) selected for the panel acoustic contribution analysis (PACA) is shown in Fig. 68.1d.

The panels of the vehicle vibrate due to the disturbance forces transferred from engine mounts and generated by the engine. Experimentally obtained forces on each engine mount (right, left and transmission), and in all three degrees of freedom (x, y, and z) are used in the vibro-acoustic analysis.

The driver's right ear position is selected as the sensor location in the acoustic cavity. During simulations damping value for acoustic fluid is taken as 0.1% and surrounding panels' acoustic absorption is neglected. Experimental engine data in all directions are simultaneously applied to the engine mounts of the vibro-acoustic model. Results for obtained sound pressure level in frequency domain are presented in Fig. 68.2. Peak value for the sound pressure level is 116 dBA around 60–80 Hz band. This result suggests that structural panels' vibration modes around 60–80 Hz frequency band are highly dominant on the acoustic response of the complex 3D structure. In the presence of this information, panel acoustic contribution analysis (PACA) is performed and the most contributing panel at this frequency range is considered for the ASAC application. Note that, the dBA values in Fig. 68.2 may be higher than the conditions in a real vehicle. The vibro-acoustic model used in this study is an over simplified model and the sound pressure values should not be taken as a reference. It is mainly used for the demonstration of the vibro-acoustic coupled system.

For PACA, the frequency range is selected between 60 and 110 Hz, which is the frequency band including the booming noise inside the passenger cabin for the vehicle. The PACA results are shown in Fig. 68.3. In this figure, the x-axis shows the frequency in Hz. The y-axis is divided into segments to show the contribution of each panel to the sound pressure levels. Red colored parts represent high contribution and blue colored parts represent low contribution to the overall sound pressure. Among the analyzed panels, “front panel” has the highest contribution to the sound pressure in the all frequency range. Particularly around 70–80 Hz front panel contribution is very distinctive, which is also the frequency of the highest sound pressure levels obtained from vibro-acoustic analysis.

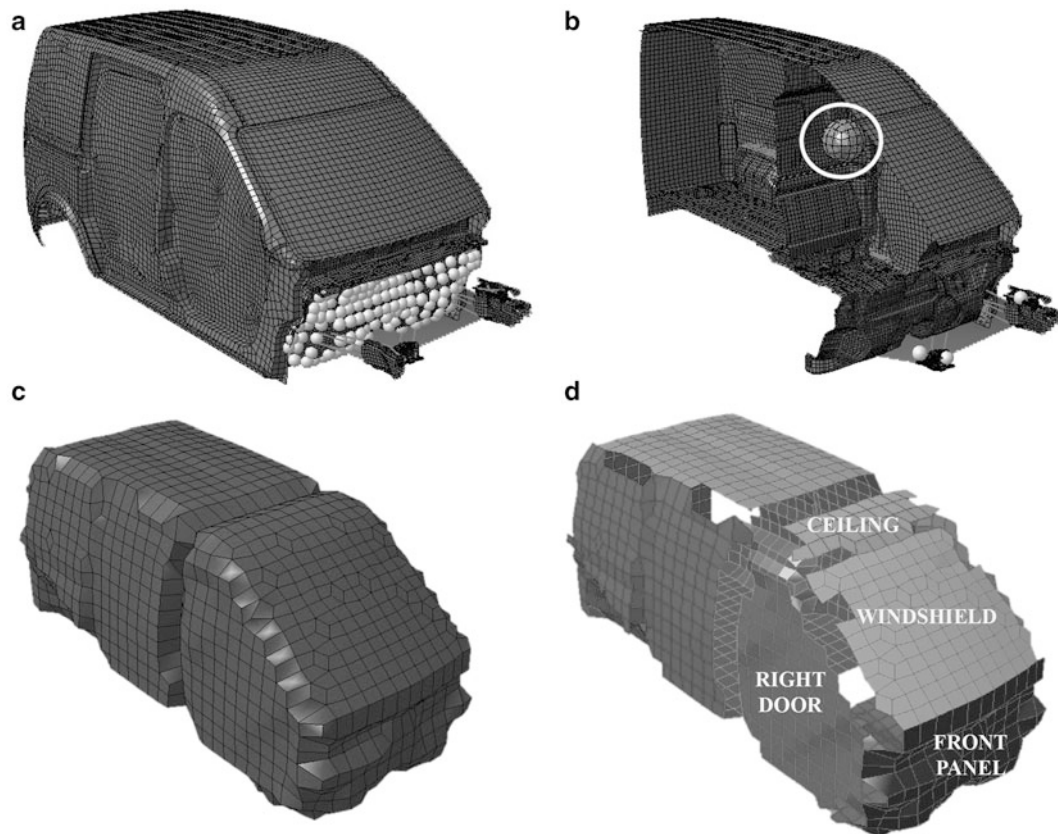
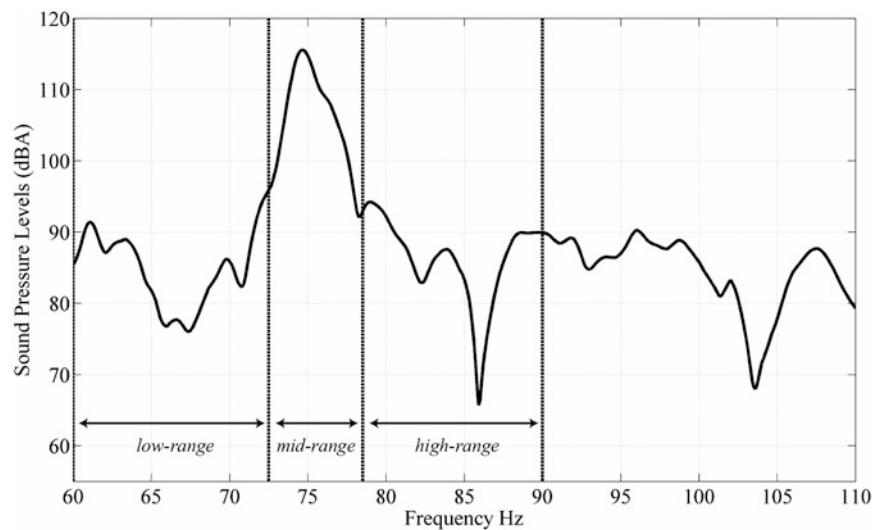


**Fig. 68.1** (a) Finite element model of the vehicle. (b) The interior view and driver's head position (inside *dashed circle*) (c) Acoustic cavity mesh (d) Selected panels for PACA

**Fig. 68.2** Sound pressure level due to engine disturbance at the driver's right ear position and frequency bands



These results indicate that noise suppression inside the cavity can be achieved by reducing the structural vibrations occurring on the front panel. Therefore, the controller implementation can be carried out on the front panel and structural vibrations of this panel can be reduced to attenuate high sound pressure levels.

**Fig. 68.3** Panel acoustic contribution for vibro-acoustic response at driver’s right ear position

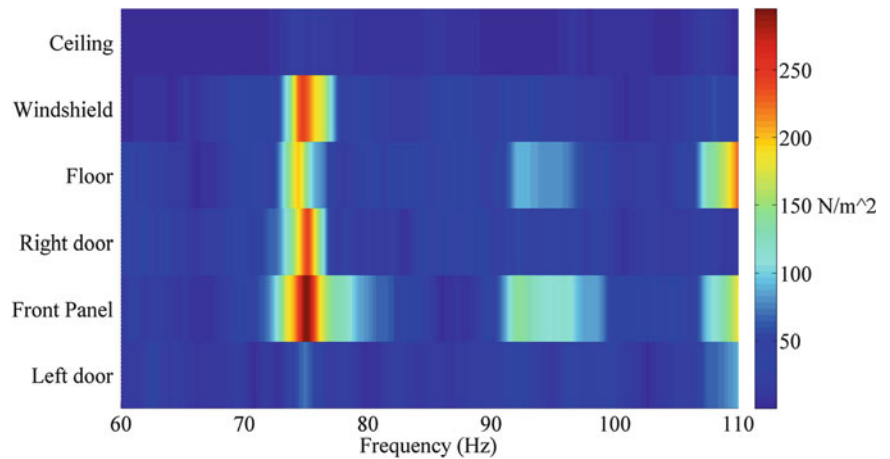
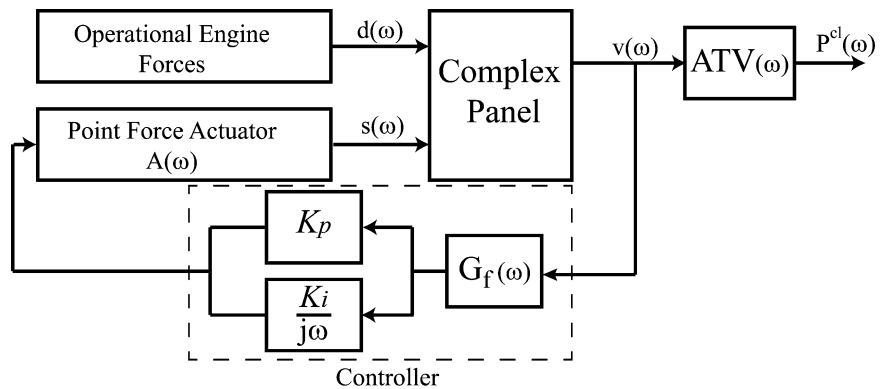


**Fig. 68.4** General block diagram of the active structural acoustic control system for complex structure



### 68.3 Design and Simulation of the ASAC System

In this section, design and simulation of an ASAC for noise suppression in the vibro-acoustic system is explained. In this study, a Proportional-integral (P-I) feedback controller is considered since this controller is a model-independent controller method which generates the output signal by multiplying the displacement and velocity response of the structure with integral and proportional gains. The velocity feedback adds damping to all modes while displacement feedback provides additional damping in the low frequency range thus reduces structural vibrations. To confine the suppression effect to a selected frequency band, a band-pass filter is implemented to the system. In addition, with filter implementation, augmentation in sound pressure levels in high frequency range is prevented. The general block diagram for the ASAC with P-I controller and filter is shown in Fig. 68.4. In this figure,  $d(\omega)$  is the disturbance input due to external loadings,  $s(\omega)$  is the suppressive input generated by the controller and  $v(\omega)$  are the complex panel surface normal velocities and  $G_f(\omega)$  is the band pass filter. By multiplying surface velocities with the ATV vector as in Eq. 68.1, the resultant closed-loop sound pressure level  $P^{cl}(\omega)$  is obtained as follows.

$$P^{cl} = [ATV]^T V \tag{68.1}$$

For the single-input single-output (SISO) active feedback controller in Fig. 68.4, only structural response of the region around the sensor is fed back to the point-force actuator. However, in order to achieve reduction in radiated noise levels, the structural vibration energy of the panel should be considered spatially. Therefore, in the simulations, the effect of the control actuation at all degrees of freedom on the structure is considered in addition to the external disturbance.

A two-dimensional grid ( $19 \times 7$  points) (see Figs. 68.5 and 68.6) is defined on the front panel to obtain spatial structural response. At first, velocity of each point on the grid due to the operational engine forces is obtained in the frequency domain. Then, by placing the point force actuator on the grid points, the direct (between the actuator and collocated sensor pair) and cross (between the actuator and measurement points other than sensor location) frequency response functions (FRFs) are calculated using LMS software. Then, closed-loop velocity response due to the point-force actuator and operational engine force is acquired by considering the controller gains as well as direct and cross frequency responses.

**Fig. 68.5** Measurement points on the complex structure

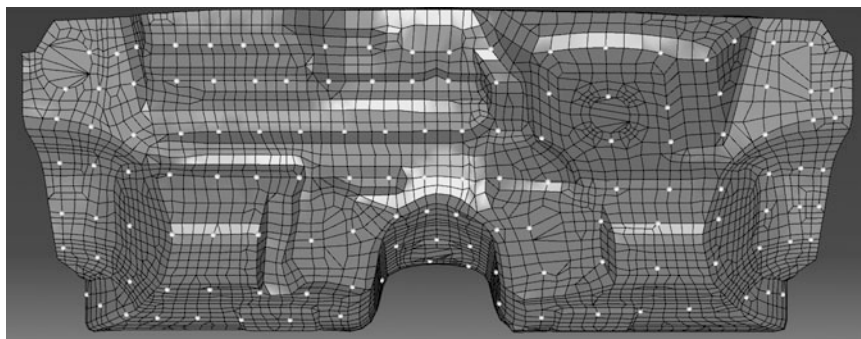


**Fig. 68.6** Labeling of the measurement points selected on the complex structure

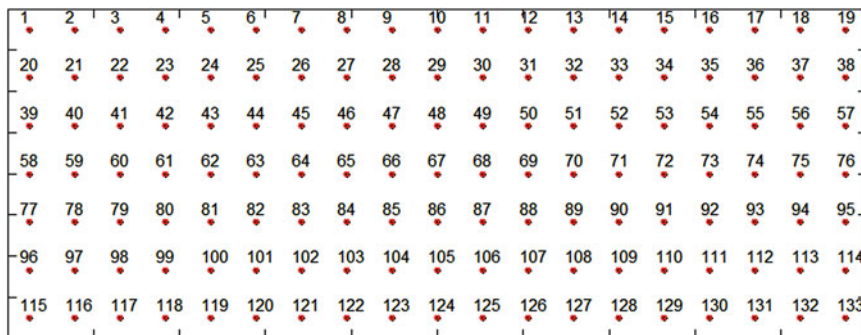


**Table 68.1** ASAC Configurations for evaluation of the performance

ASAC configurations	Proportional gain	Integral gain	Sensor/actuator location
Setting – I	120	10,000	29-60-90
Setting – II	250	10,000	29-60-90
Setting – III	120	20,000	29-60-90

### 68.4 Noise Reduction Performance of the ASAC System

This section presents the evaluation of the noise reduction performance of the ASAC system implemented on the front panel of the vehicle. Using the methodology presented in the former section, open and closed loop velocity responses for each node are obtained and sound pressure levels are calculated by multiplication of the structural velocity response with the corresponding ATVs.

The different configurations of the ASAC system are listed in Table 68.1. As can be seen from the table, various controller gains and sensor/actuator locations are selected. The corresponding sensor/actuator location is defined on the measurement grid presented in Fig. 68.6. For each controller setting, closed-loop sound pressure level is obtained. The corresponding sound pressure levels are presented in Figs. 68.7–68.9. In those figures, it can be seen that each controller setting produces different behaviors which result in different sound pressure levels inside the cabin. It is also noticeable that setting- I and III augments the noise around 65 Hz which is not desired.

### 68.5 Conclusion

In this study, we presented an ASAC design methodology and evaluated the performance of the controller for the reduction of structure-borne noise inside a passenger cabin of a vehicle. The vibro-acoustic model of the vehicle is used for obtaining the acoustic and structural frequency response of the structure for open and closed loop configurations. First, the most contributing panel to the sound pressure inside the passenger cabin is identified using PACA. Then, the controller implementation was carried out on that panel and structural vibrations of the panel were reduced to attenuate high sound pressure levels. Three different collocated sensor/actuator locations were investigated for three different controller settings.



**Fig. 68.7** Noise reduction performance of ASAC setting-I

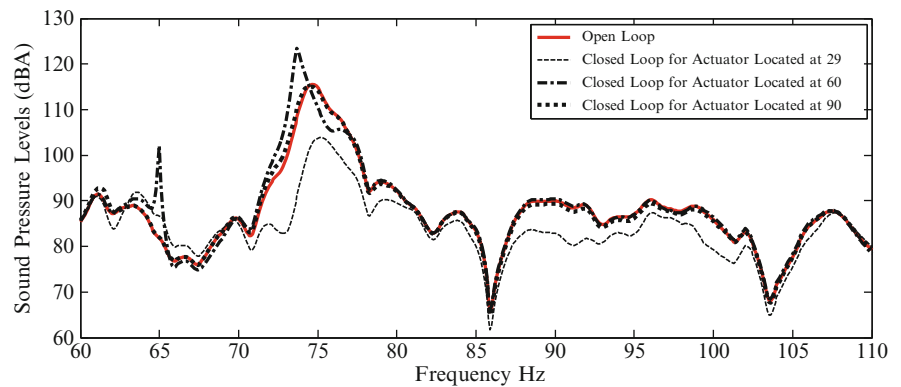


**Fig. 68.8** Noise reduction performance of ASAC setting-II

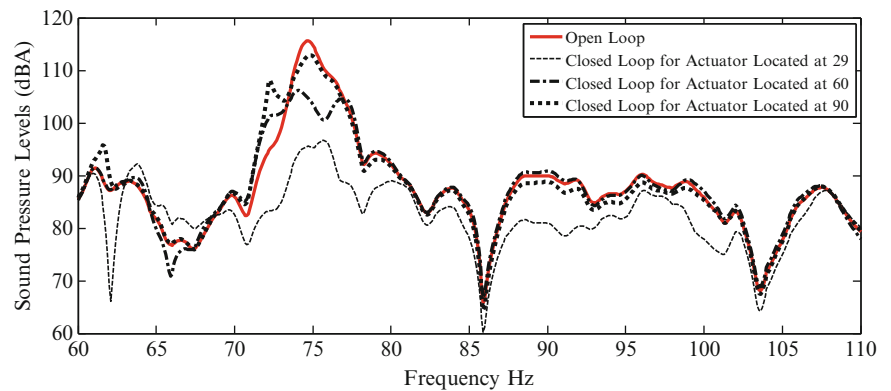
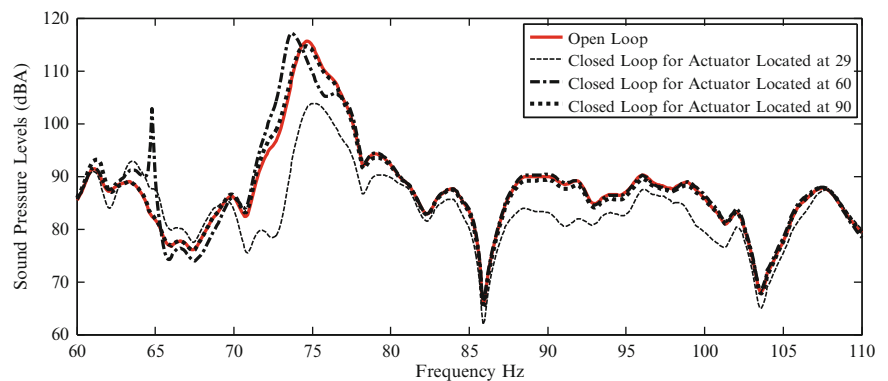


**Fig. 68.9** Noise reduction performance of ASAC setting-III



The results show that the performance of the controller may significantly change based on the location and as well as the controller parameters. An optimization algorithm is required to determine the optimum controller parameters and sensor/actuator positions to reduce sound pressure levels in the targeted frequency range.

**Acknowledgement** This work is supported by Scientific and Technological Research Council of Turkey (TUBITAK).

## References

1. Hurlebaus S, Stöbener U, Gaul L (2008) Vibration reduction of curved panels by active modal control. *Comput Struct* 86:251–257
2. Stöbener UWE, Gaul L (2001) Active vibration control of a car body based on experimentally evaluated modal parameters. *Mech Syst Signal Process* 15:173–188
3. Sohn JW, Choi S-B, Kim HS (2011) Vibration control of smart hull structure with optimally placed piezoelectric composite actuators. *Int J Mech Sci* 53:647–659

4. Song CK, Hwang JK, Lee JM, Hedrick JK (2003) Active vibration control for structural-acoustic coupling system of a 3-D vehicle cabin model. *J Sound Vib* 267:851–865
5. de Oliveira LPR, da Silva MM, Sas P, Brussel HV, Desmet W (2008) Concurrent mechatronic design approach for active control of cavity noise. *J Sound Vib* 314:507–525
6. de Oliveira LPR, Janssens K, Gajdatsy P, der Auweraer HV, Varoto PS, Sas P, et al. (2009) Active sound quality control of engine induced cavity noise. *Mech Syst Signal Process* 23:476–488
7. Bianchi E, Gardonio P, Elliott SJ (2004) Smart panel with multiple decentralized units for the control of sound transmission. Part III: control system implementation. *J Sound Vib* 274:215–232
8. Elliott SJ, Gardonio P, Sors TC, Brennan MJ (2002) Active vibroacoustic control with multiple local feedback loops. *J Acoust Soc Am* 111:908–915
9. Gardonio P, Bianchi E, Elliott SJ (2004) Smart panel with multiple decentralized units for the control of sound transmission. Part I: theoretical predictions. *J Sound Vib* 274:163–192, 7/6/
10. Gardonio P, Bianchi E, Elliott SJ (2004) Smart panel with multiple decentralized units for the control of sound transmission. Part II: design of the decentralized control units. *J Sound Vib* 274:193–213
11. Mauro C (2011) Active control of sound radiated by a submarine in bending vibration. *J Sound Vib* 330:615–624
12. Fenik S, Starek L (2010) Optimal PI controller with position feedback for vibration suppression. *J Vib Control* 16:2023–2034
13. Zilletti M, Elliott SJ, Gardonio P (2010) Self-tuning control systems of decentralised velocity feedback. *J Sound Vib* 329:2738–2750
14. Zilletti M, Elliott SJ, Gardonio P, Rustighi E (2012) Experimental implementation of a self-tuning control system for decentralised velocity feedback. *J Sound Vib* 331:1–14

# Chapter 69

## Development of a Stabilized Pan/Tilt Platform and the State of the Art

M. Burcak Ozkok and Ali Osman Boyaci

**Abstract** In the context of this paper, a small scale, medium precision, stabilized pan/tilt platform is developed as a prototype, which is used to compare various stabilization algorithms experimentally. The overall performance of the system depends on rigid body dynamics, structural dynamics, servo control loops, stabilization control algorithm, sensor fusion algorithm, and sensory feedback such as from the inertial measurement unit (IMU). In the case that the response bandwidth of the overall system is high enough, the same hardware can also achieve active vibration isolation. All of these design aspects are investigated in the paper via numerical models and with their experimental verification.

**Keywords** Stabilized pan/tilt platform • Active vibration isolation • Stabilization control • Sensor fusion • Inertial measurement unit

### 69.1 Introduction

Small scale, medium precision, stabilized pan/tilt platforms find extensive usage in modern industry, especially for the need of pointing a sensor (i.e. a camera, a laser range finder etc) on a given target while the mounted platform is moving. In the field of unmanned autonomous vehicles, stabilized sensor platforms are inevitable subcomponents. And they have to be small and cost effective due to the expendable nature of the autonomous vehicles. The most crucial hardware in such a stabilized platform is the inertial measurement unit (IMU), which contains gyro and accelerometers for angular and translational position feedback. Recent developments in strapdown microelectromechanical (MEMS) IMU technology offers cost-effective and lightweight solutions, which are absolutely needed for this type of stabilization task. An IMU produces angular velocities and translational accelerations in orthogonal axes, and from that, positions are derived using time integration, which involves drift errors, mainly due to the measurement noise. At this point, to avoid losing a target attitude, sensor fusion schemes are employed with additional sensors such as magnetometers, which refer to the earth coordinate frame. Such sensor fusion schemes are also mentioned in this paper.

### 69.2 Rigid Body Dynamics

Derivation of a rigid-body model for the pan/tilt platform is a necessary first step for both the optimization of control parameters (offline or adaptive), and for the calculation of the inverse kinematics of the structure.

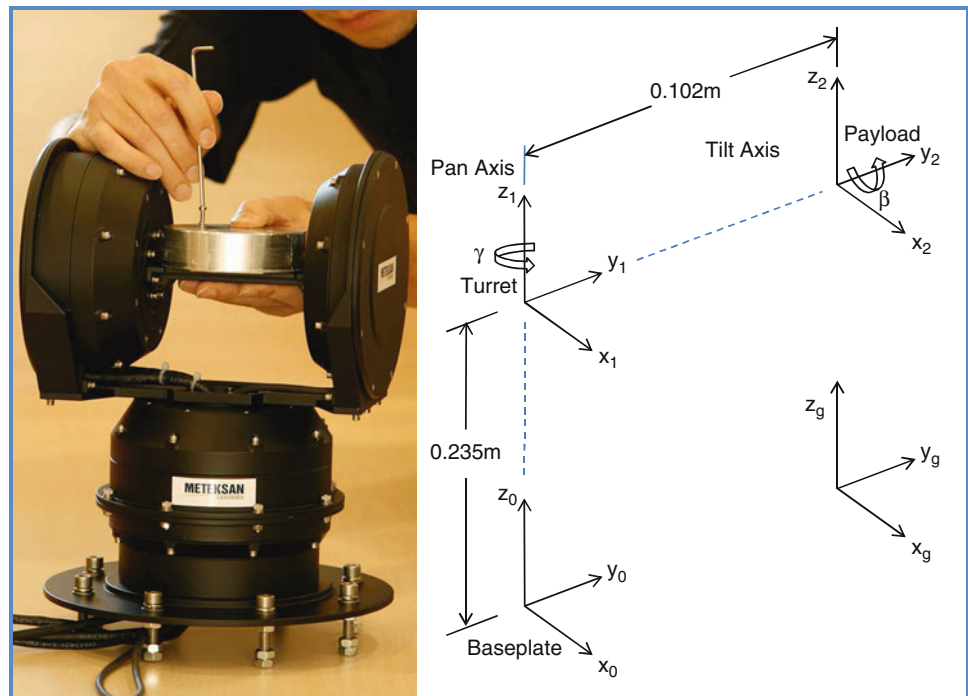
In Fig. 69.1, a general view of the Meteksan® stabilized pan/tilt platform, and the local and global coordinates, used in modeling, are given. According to the figure, a turret, which rotates around a baseplate in yaw axis (also called heading, azimuth or pan axis), and a payload, which rotates around the turret in pitch axis (also called elevation or tilt axis), defines a two axis gimbal structure. The baseplate, which is fixed onto a mobile platform (e.g. a car, helicopter or an unmanned vehicle), is free to move in all 6 degrees of freedom (DOF). In the case that the roll angle (also called bank or tip axis) is

---

M.B. Ozkok (✉) • A.O. Boyaci

METEKSAN Defense Ind., Cyberpark-FBlok, Beytepe, No:85/A, Bilkent, 06800, Ankara, Turkey  
e-mail: [bozkok@meteksan.com](mailto:bozkok@meteksan.com); [aboyaci@meteksan.com](mailto:aboyaci@meteksan.com)

**Fig. 69.1** Meteksan® stabilized pan/tilt platform and the assigned coordinate systems



either unimportant or it is computationally corrected, a gimbal with only 2 DOF (pan and tilt axes) is sufficient to be able to track a 3 DOF target point. Accordingly, the frequency response of the 6 DOF motion of the payload is calculated as the multiplication of the baseplate displacement input with the *servomechanical transfer function* in both axes. All these displacement variables are defined in a global coordinate system, which is either defined with respect to the celestial objects (e.g. stars) if high precision is necessary, or with respect to the earth if medium precision is sufficient [1]. The selected global coordinate system is then assumed inertial and absolute, such that the kinematic transformations and dynamic calculations are executed according to this coordinate system.

The stabilized platform described in this work, has an aluminum structure, which weighs 11 kg. It is 32 cm tall in height, and 18 cm wide in diameter. The design payload is 5 kg, so it is a small scale platform.

### 69.3 Structural Dynamics Response

The above mentioned servomechanical transfer function is sufficient for the estimation of the payload motion only up to 15–20 Hz. If the input vibrations extend to higher frequencies, then a rigid body model may not be sufficient and the elastomechanical transmission of the structure is to be derived as in Fig. 69.2.

Here, the structural transmission of the vibrations is modeled via finite elements method (FEM), and the design is optimized (within the constraints of the design requirements) to keep the frequencies of structural resonance modes as high above as possible from the operational frequency band. In the context of this modeling, the bearings are also modeled as radially and axially elastic linear units with the assumption of elastohydrodynamic lubrication. The displacement power spectral density of the payload due to the vibrations and maneuvers of the host platform (e.g. an unmanned vehicle for this case) can be calculated by applying the generic road vibration for tracked vehicles in offroad conditions [2] onto the below transmissibility functions as inputs.

In Fig. 69.3, it can be seen that the dominant portion of the RMS displacement results from the input vibration, by simply comparing the vibration amplitudes around the resonances with the amplitudes in the unit transmission zone of 0–20 Hz. Here, a viscous damping is assumed as the damping model, and the damping ratio is selected to be 0.01 to be compatible with aluminum structures assembled with fasteners. Resulting vibrations are calculated on a corner location of the payload in order to represent the worst case scenario. Therefore, Fig. 69.3 also contains the contributions of the payload angular displacements resulted from the baseplate linear motion. Although not considered here, the effect of angular input vibrations can be calculated by using the same structural model. For the case, where the payload vibrations, the load inertias, and the

**Fig. 69.2** The transmissibility functions between the baseplate and the payload

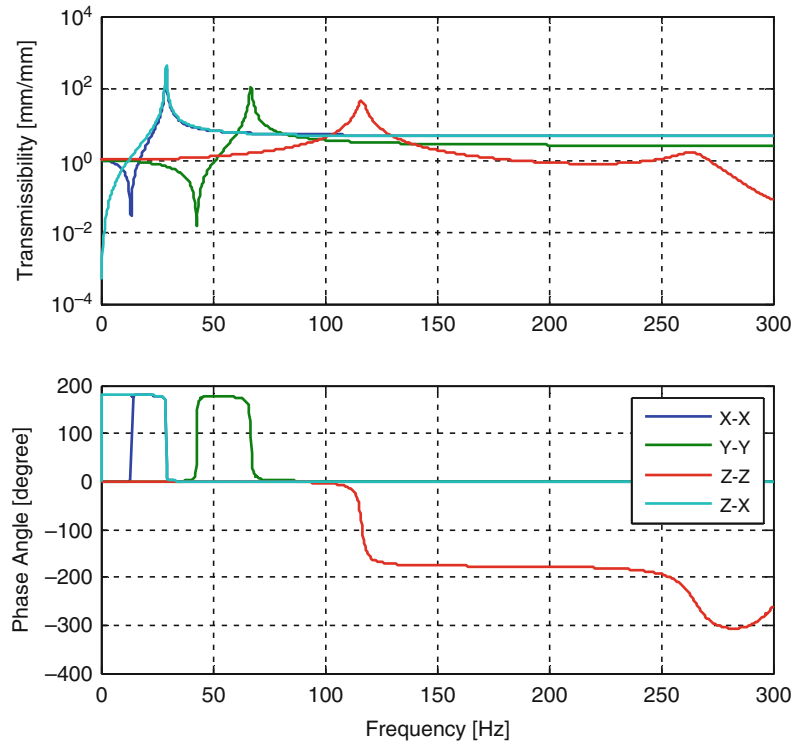
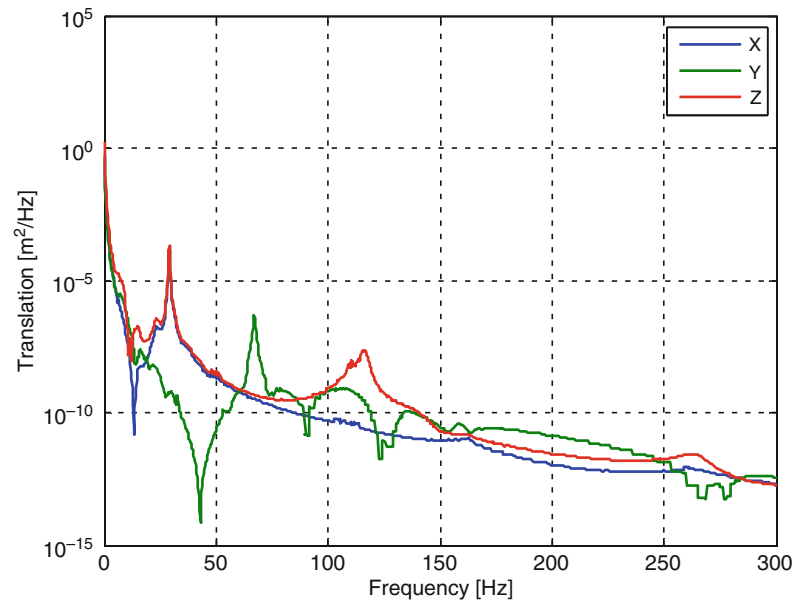
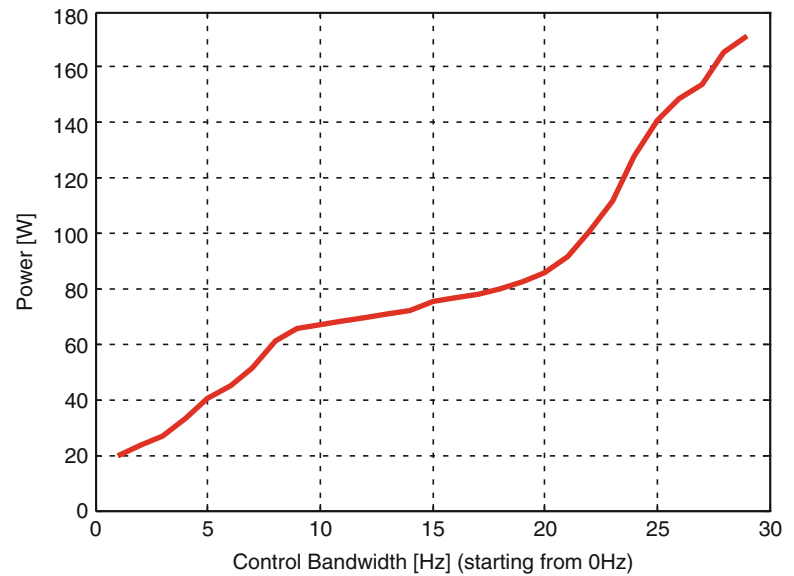


**Fig. 69.3** The response PSD in terms of displacement of the payload due to the baseplate translation from the generic tracked vehicle



motor efficiency are known, the mechanical and electrical power required to stabilize the load in any axis can be calculated as a function of the bandwidth (Fig. 69.4). Given a certain requirement on the bandwidth, Fig. 69.4 can be used to derive the power and the torque needed to achieve that bandwidth for the corresponding axis. Here, it is expected that 70 W electrical power is required for pan axis to achieve 10 Hz bandwidth including resistive losses. Unless the bandwidth is selected to be high enough, it is usually customary to use passive vibration isolation in conjunction with an active one. A passive isolation can easily be achieved by using elastomer components between the baseplate and the host platform. Other possibilities for passive vibration isolation are airsprings, liquid dampers, wire ropes, magnetic bearings etc.

**Fig. 69.4** Pan axis power requirement for active vibration damping based on a generic vibration profile for tracked vehicles (calculated for 5 kg nominal payload)



Although not studied here, other vibration profiles such as for sea, underwater, or air platforms can also be used to obtain payload vibrations or power/torque requirements for stabilization in multiple axes.

## 69.4 Servocontrol

The control bandwidth, mentioned in the above chapter, also puts a lower limit for the motor torque of a respective axis. As the moment of inertia of the rotating mass also includes the rotor of the motor, it is important to select a motor with high specific torque, that is the ratio of output torque to the motor mass. At the same time, torque ripple is to be low enough so as not to disrupt positioning precision. In Fig. 69.5, torque vs. mass data is given for more than 1,000 different direct drive motor models, which is currently available in the market. From here, the motor with the highest specific torque among the ones which complies with the design requirements is selected to be used in the prototype pan/tilt platform. In this comparison, nonconventional actuation methods such as piezomotors are also investigated, but it is observed that the brushless motors are superior to any other kind of motor, when considering a diameter of 10–20 cm. The recent advances in permanent magnet and manufacturing technologies are instrumental in this result, because the motor torque increases proportionally with the increasing magnetomotive force of the magnet, and with the decreasing air gap distance between stator and rotor [3]. During stabilization task, although high accelerations are demanded from motors, the velocities usually stay below 50 rpm, which means that the main mode of power loss is resistive, and magnetic losses such as eddy current and hysteresis are not dominant. This requires that the motors have a thick wiring, or else suffer a high power loss into heating of the stator core due to the resistance of the wiring cables. On the other hand, thicker wiring means less number of turns in a certain volume, and therefore less torque for the same current.

Actuation systems with integrated gearheads are not included in the motor comparison, as they usually lack the necessary positioning precision due to gear backlash. Cyclo drives, harmonic drives and some advanced worm gears produce high torques without any significant backlash, but they are also excluded due to other reasons, such as price or weight.

Another hardware, which directly effects the overall system performance is the servocontroller and its control parameters. A servocontroller can be abstracted as nested control loops of position, velocity, and current (innermost loop). At the lowest level, there is the three phase inverter circuitry, which does all the switching according to the information from an encoder. The amplitude and the phase of the current into the wirings are adjusted by applying pulse width modulation onto the switching signals [4]. The frequency of this switching, and the sampling frequency of the higher control loops are important parameters in determining the control bandwidth. In Fig. 69.6, experimentally determined position loop frequency response in pan axis is given for the case where all the parameters are optimized to obtain a wide control bandwidth:

From the above figures, it is observed that the position control loop has no difficulty in achieving the 10 Hz control bandwidth, which was aimed for an active vibration damping.

**Fig. 69.5** The comparison of specific torque values of various direct drive motors available in the market and the motor selection according to the design constraints

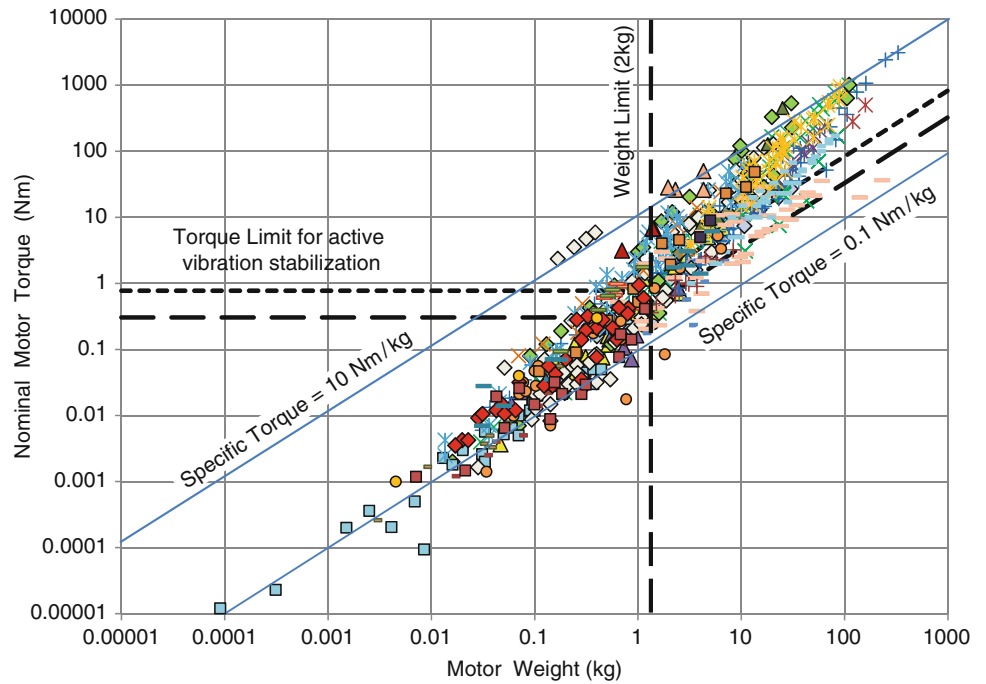
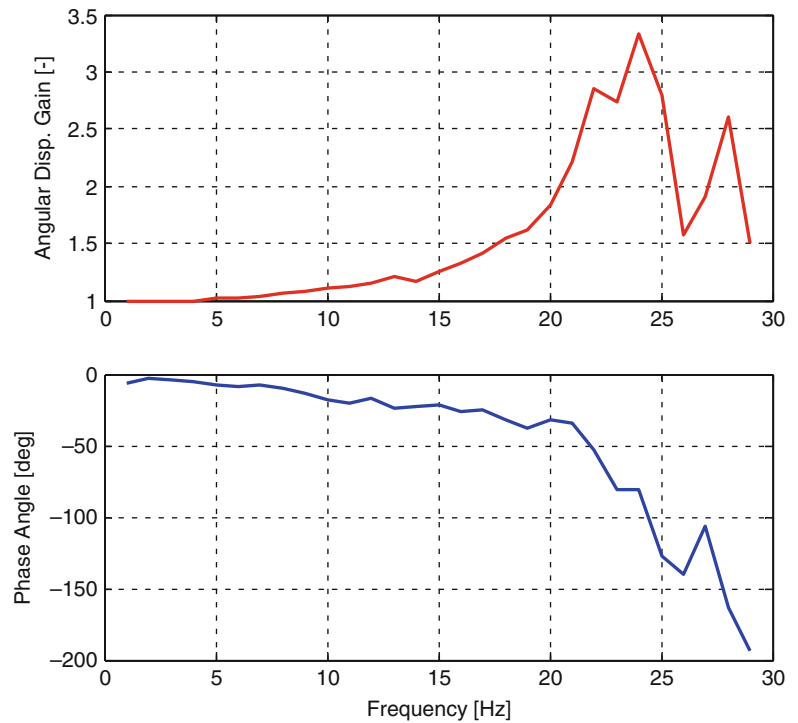


**Fig. 69.6** Experimental pan axis servomechanical frequency response in position control mode (measured with 5 kg nominal payload weight)



### 69.5 Inertial Navigation and Sensor Fusion

In the stabilization system, the strapdown inertial measurement unit (IMU) contains gyros and accelerometers, which supplies 3 DOF angular velocity and acceleration feedback with respect to the inertial coordinates. Here, the data from gyros and accelerometers are combined and time integrated to obtain angular position and linear position of the IMU and the mechanical structure onto which it is fixed. Even if the data is filtered, there is an accumulating drift error due to the time integration, which increases with the measurement time and results in the loss of the absolute position. Linear drift error is more dominant

than the angular drift, because it integrates also the error from the angular measurements. The possible sources for such IMU errors, which gets time integrated and amplified, are scaling error, linearity error, bias error, error due to cross-coupling of acceleration and angular velocity, orthogonality error, thermal noise etc.

In the case of strapdown MEMS based sensors, the angular drift errors may be as high  $\pm 20^\circ/\text{min}$ , especially if no filtering is employed. This error can be reduced considerably using an adequate filtering (eg. Kalman Filtering) [5]. If operation time is longer than a couple of minutes, it is necessary to obtain position updates from an absolute source. In reality the update rate is much higher as long as the absolute sensors are operational. In this work, it is experimentally observed that having an update rate of 70 Hz can keep the drift error of strapdown sensors as low as  $0.005^\circ$  (drift errors increase exponentially with time). Using absolute and inertial sensors in such a complementary fashion to achieve higher precision and to avoid drift errors is called sensor fusion. The purpose here is to complement low sampling sensors, which refer to global coordinates, with the high sampling inertial sensors, which involves drift errors.

A common method to determine the pitch (tilt) or roll (bank) angle with respect to the earth coordinates is to measure the effect of gravitation with accelerometers, which are appropriate for static measurements, such as a bonded strain gauge accelerometer or a servoaccelerometer. The method includes filtering out any dynamic contributions due to the platform motion and detecting the direction of the gravity vector. This method however cannot be used to detect the yaw angle (heading), as the rotation axis approaches to and sometimes coincides with the gravity vector. Therefore heading estimation requires another sensor such as a GPS or a three axis magnetometer. Although a GPS is appropriate for outdoor applications, it also requires a linear motion if heading is to be estimated. For indoor and/or stationary applications a magnetometer is better suited, but the earth's magnetic field is too faint, and therefore detection with magnetometer is susceptible to interfering effects such as from local magnetic sources. Here, applying again a sensor fusion scheme, a complementary usage of GPS and magnetometer can be recommended.

The detection of cartesian position can involve errors as high as 150 m/min if no special filtering is applied. GPS based position updates can be used to correct this kind of drift if outdoor operation is possible.

In the case of indoor operation, a regular three axis magnetometer can be used to decrease this drift down to 5 m/min. Here magnetometer is used to correct gyro outputs, which indirectly improves the detection of the position. However, this procedure still involves a drift, which needs to be compensated by a position sensor which refers to the global coordinates. This type of indoor applications may utilize 3d mapping using such technologies as stereoscopic cameras and image processing, or triangulating laser scanners [6].

Utilization of a Kalman filter as an observer is an efficient way for sensor fusion. Standard Kalman Filtering is a method to adjust the observer gain in realtime and in a stable fashion, so as to minimize the state errors of systems, which are assumed to be linear and have disturbances with normally distributed noise. There are many types of implementations, but a commonly used one is the indirect feedback configuration, where only the state errors are estimated and not the state itself, and where the observed errors are kept bounded by a feedback loop in a time-independent fashion [1].

## 69.6 Stabilization Control

Stabilization control loop is the outermost control loop, which has parameters, set to minimize the payload frequency response to isolate it from the movements of the baseplate. The block diagram for the stabilization control loop is given in Fig. 69.7. The success of the stabilization control depends very much on the capabilities of the sensor fusion algorithms, which is used to obtain fast and precise position feedback with respect to the global coordinates. The response time and the precision of the overall system also depends on the control and filter parameters of the nested control loops and their feedback paths.

## 69.7 Performance of the Prototype

Some of the performance parameters of the prototype pan/tilt platform (MHTS 005-113-025-2-S) are given below in Table 69.1:



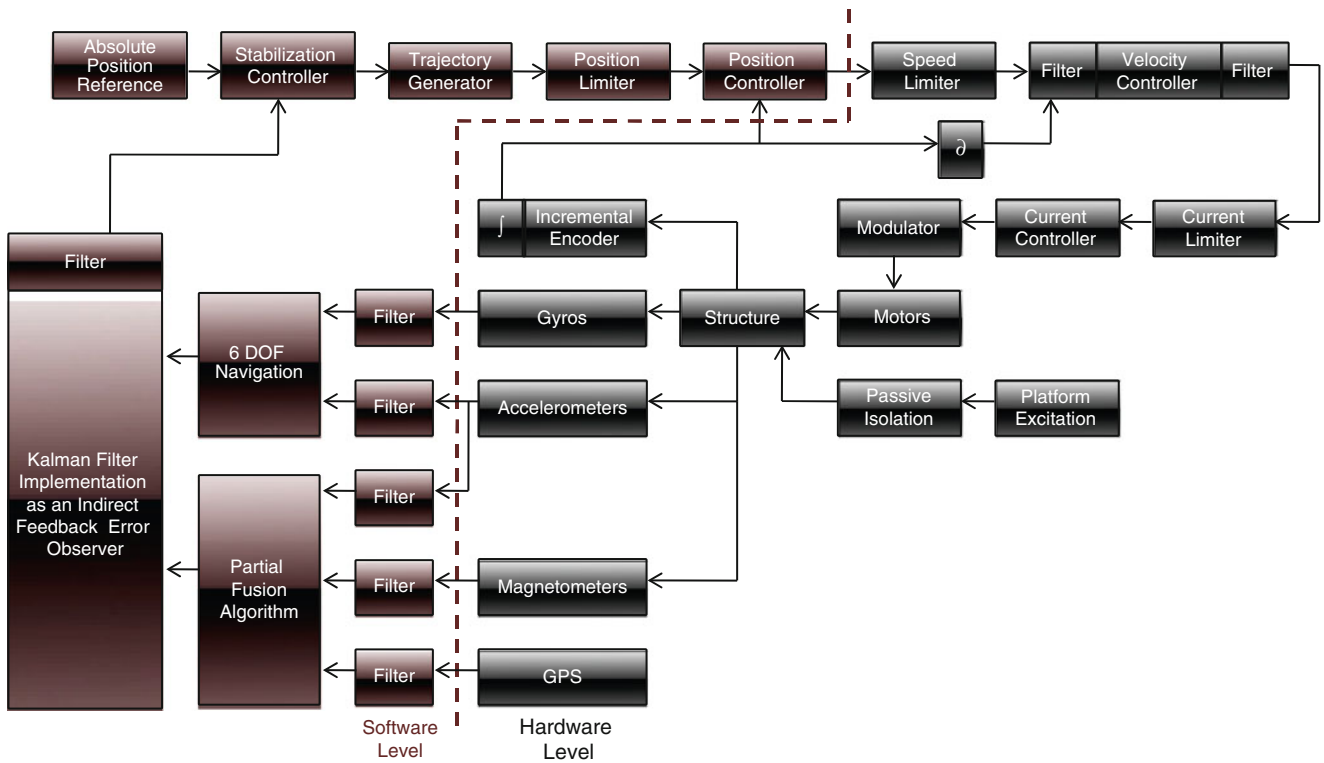


Fig. 69.7 Block diagram representing the stabilization control and inner control loops

Table 69.1 Some performance parameters of the stabilized pan/tilt platform

Limit design parameters	Pan axis design	Tilt axis design
Angular positioning	$\pm 180^\circ$	$\pm 60^\circ$
Angular speed <sup>b</sup>	$\pm 400^\circ/s$	$\pm 400^\circ/s$
Angular acceleration <sup>b</sup>	$\pm 1,100^\circ/s^2$	$\pm 4,200^\circ/s^2$
Motor torque (cont.)	3 Nm	3 Nm
Electrical power	80.49 W	91.37 W
Weight <sup>a</sup>	5.6 kg	5.1 kg
Workspace diameter <sup>a</sup>	177 mm	250 mm
Height <sup>a</sup>	141 mm	182 mm
Frequency band	0..10 Hz	0..10 Hz
Encoder	$\pm 0.0014^\circ (\pm 25 \mu\text{rad})$	$\pm 0.0014^\circ (\pm 25 \mu\text{rad})$

<sup>a</sup>Excluding the payload (5 kg nominal)

<sup>b</sup>If the payload center of gravity coincides with the center of rotation of pan and tilt axes

### 69.8 Results

The stabilized Pan/Tilt Platform described in this paper, is a prototype system, which will soon be made commercially available. Its design encompasses features aimed specifically for unmanned vehicles, such as wide dynamic bandwidth, compactness, light weight construction.

Wider bandwidth, extended angular range, improved sealing for environmental protection, electromechanical brakes against weapon recoil are some of the features planned for the future versions of the Meteksan® stabilized pan/tilt platform.

### References

1. Akcayir YI (2003) Integrated land navigation systems. Hacettepe University Electronics Department, pp 10–30
2. US Department of Defense (2008) Environmental engineering considerations and laboratory tests. US Department of Defense, Washington, DC. MIL-STD-810G, 514.6C-IV-Category4

3. Pyrhönen J, Jokinen T, Hrabovcova V (2008) Design of rotating electrical machines. Wiley, Hoboken, pp 153–164
4. De Doncker R, Pulle DWJ, Veltman A (2011) Advanced electrical drives. Springer, Dordrecht/New York, pp 41–42
5. Biezad DJ (1999) Integrated navigation and guidance systems. AIAA, Reston p 96
6. Woodman OJ (2007) An introduction to inertial navigation. University of Cambridge, pp 33–34

# Chapter 70

## Dynamic Equations for an Anisotropic Cylindrical Shell

Reza Okhovat and Anders Boström

**Abstract** Dynamic equations for an anisotropic cylindrical shell are derived using a series expansion technique. First the displacement components are expanded into power series in the thickness coordinate relative to the mid-surface of the shell. By using these expansions, the three-dimensional elastodynamic equations yield a set of recursion relations among the expansion functions that can be used to eliminate all but the six of lowest order and to express higher order expansion functions in terms of these of lowest orders. Applying the boundary conditions on the surfaces of the cylindrical shell and eliminating all but the six lowest order expansion functions give the shell equations as a power series in the shell thickness. These six differential equations can in principle be truncated to any order. The method is believed to be asymptotically correct to any order. For the special case of a ring, the eigenfrequencies are compared with exact two-dimensional theory, generally with a good correspondence.

**Keywords** Cylindrical shell • Anisotropy • Shell equation • Eigenfrequency • Power series.

### 70.1 Introduction

Shells are commonly used in many branches of engineering and have therefore been investigated for a number of different types of shells. A shell can be considered as a curved plate having small thickness compared to the other geometrical dimensions as well as to the wavelengths of importance. Shell structures can provide high strength and low weight because of their membrane stiffness. In particular, governing equations for circular cylindrical shells are given by Soedel [1], and thin cylindrical shells and as a special case, circular cylindrical shells with anisotropy are given by Leissa [2].

In this paper the dynamic equations for an anisotropic cylindrical shell are derived by using a power series method developed during the last decade for bars, plates, beams and rods [3]. It has, in particular, been developed for a number of different plate structures, like anisotropic, layered, and piezoelectric plates, see e.g. [4–6]. Dynamic equations for isotropic cylindrical and spherical shells are also derived using power series method [7, 8]. The method is very systematic and very useful for developing the equations to any order. Also the resulting structural equations are believed to be asymptotically correct to any order [4].

The present paper can be described as follows. In the next section the problem is stated and the three-dimensional equations of motion are given. Next, the expansion of the displacement components in series in the thickness coordinate is performed, leading to the recursion relations for the expansion functions, this being the key ingredient in the present approach. Applying the boundary conditions at the inner and outer surfaces of the cylindrical shell and using the recursion relation to eliminate all but the six lowest-order expansion functions give the six shell equations. These can in principle be given to any order and are believed to be asymptotically correct to any order. As a special case a 2D circular ring is considered and the eigenfrequencies are computed and are compared with the exact solution which is obtained by expressing the displacements in terms of Bessel and Neumann functions. Graphite epoxy is considered as an anisotropic material with material properties given in [9]. The results from the power series approximation are in good correspondence with the results from the exact solution.

---

R. Okhovat (✉) • A. Boström

Department of Applied Mechanics, Chalmers University of Technology, SE-41296 Gothenburg, Sweden  
e-mail: [reza.okhovat@chalmers.se](mailto:reza.okhovat@chalmers.se); [anders.bostrom@chalmers.se](mailto:anders.bostrom@chalmers.se)

## 70.2 Problem Formulation

A circular cylindrical shell with middle surface radius  $R$  and thickness  $2h$  is considered. The shell is homogenous, anisotropic and linearly elastic with density  $\rho$ . The shell is assumed to be cylindrically anisotropic, both because this is an important special case of anisotropy and because it simplifies the equations, with independent stiffness constants  $C_{11}$ ,  $C_{22}$ ,  $C_{33}$ ,  $C_{12}$ ,  $C_{13}$ ,  $C_{23}$ ,  $C_{44}$ ,  $C_{55}$  and  $C_{66}$ . The cylinder is described by cylindrical coordinates whose radial coordinate is denoted by  $r$ , circumferential coordinate is denoted by  $\theta$ , and axial coordinate is denoted by  $z$ . The displacement components are denoted  $u$ ,  $v$  and  $w$  respectively. The three-dimensional equations of motion are written as

$$\partial_r \sigma_{rr} + \frac{1}{r} \partial_\theta \sigma_{r\theta} + \partial_z \sigma_{rz} + \frac{\sigma_{rr} - \sigma_{\theta\theta}}{r} = \rho \partial_t^2 u, \quad (70.1)$$

$$\frac{1}{r} \partial_\theta \sigma_{\theta\theta} + \partial_r \sigma_{r\theta} + \partial_z \sigma_{\theta z} + 2 \frac{\sigma_{r\theta}}{r} = \rho \partial_t^2 v, \quad (70.2)$$

$$\partial_z \sigma_{zz} + \partial_r \sigma_{rz} + \frac{1}{r} \partial_\theta \sigma_{\theta z} + \frac{\sigma_{rz}}{r} = \rho \partial_t^2 w. \quad (70.3)$$

where  $\partial_r$ ,  $\partial_\theta$ ,  $\partial_z$  and  $\partial_t$  denote partial derivatives with respect to  $r$ ,  $\theta$ ,  $z$  and  $t$  respectively. Now the stresses are written in terms of the displacement fields as

$$\sigma_{rr} = C_{11} \partial_r u + C_{12} \left( \frac{\partial_\theta v}{r} + \frac{u}{r} \right) + C_{13} \partial_z w \quad (70.4)$$

$$\sigma_{\theta\theta} = C_{12} \partial_r u + C_{22} \left( \frac{\partial_\theta v}{r} + \frac{u}{r} \right) + C_{23} \partial_z w \quad (70.5)$$

$$\sigma_{zz} = C_{13} \partial_r u + C_{23} \left( \frac{\partial_\theta v}{r} + \frac{u}{r} \right) + C_{33} \partial_z w \quad (70.6)$$

$$\sigma_{r\theta} = C_{66} \left( \frac{\partial_\theta u}{r} + r \frac{\partial}{\partial r} \left( \frac{v}{r} \right) \right) \quad (70.7)$$

$$\sigma_{rz} = C_{55} (\partial_z u + \partial_r w) \quad (70.8)$$

$$\sigma_{\theta z} = C_{44} \left( \frac{1}{r} \partial_\theta w + \partial_z v \right) \quad (70.9)$$

These equations are to be supplemented with boundary conditions on the inner and outer surfaces of the cylindrical shell. These are for simplicity taken as vanishing traction on both surfaces, although, e.g., an applied pressure would also be possible. Using the relation between the stresses and the displacement components, the equations of motion are

$$C_{11} r \partial_r (r \partial_r u) - C_{22} u + C_{66} \partial_\theta^2 u + C_{55} r^2 \partial_z^2 u + (C_{12} + C_{66}) r \partial_r \partial_\theta v - (C_{22} + C_{66}) \partial_\theta v + (C_{13} + C_{55}) r^2 \partial_r \partial_z w + (C_{13} - C_{23}) r \partial_z w = \rho r^2 \partial_t^2 u \quad (70.10)$$

$$(C_{12} + C_{66}) r \partial_r \partial_\theta u + (C_{22} + C_{66}) \partial_\theta u + C_{22} \partial_\theta^2 v + C_{66} (r^2 \partial_r^2 v + \partial_r v - v) + C_{44} r^2 \partial_z^2 v + (C_{23} + C_{44}) r \partial_z \partial_\theta v = \rho r^2 \partial_t^2 v \quad (70.11)$$

$$(C_{13} + C_{55}) r^2 \partial_r \partial_z u + (C_{23} + C_{55}) r \partial_z u + (C_{23} + C_{44}) r \partial_z \partial_\theta v + C_{55} r \partial_r (r \partial_r w) + C_{44} \partial_\theta^2 w + C_{33} r^2 \partial_z^2 w = \rho r^2 \partial_t^2 w \quad (70.12)$$

To derive the shell equations the substitution  $r = R + \xi$  is made where the variable  $\xi$  is introduced as  $-h \leq \xi \leq h$ . It should be noted that  $h$  is considered to be small enough, i.e. to be relatively small compared to the radius  $R$  and to relevant wavelengths. The displacement components are then expanded in power series in the thickness coordinate  $\xi$  as

$$u(r, \theta, z, t) = \sum_{k=0} u_k(\theta, z, t) \xi^k, \quad (70.13)$$

$$v(r, \theta, z, t) = \sum_{k=0} v_k(\theta, z, t) \xi^k, \quad (70.14)$$

$$w(r, \theta, z, t) = \sum_{k=0} w_k(\theta, z, t) \xi^k. \quad (70.15)$$

These sums are in principle infinite but only a few terms are actually used. No truncation is performed at this stage according to most other methods and the truncation scheme is discussed later on. The expansions involve both even and odd powers of  $\xi$  as symmetric and antisymmetric motions with respect to  $\xi$  do not decouple. The displacement expansions are inserted into the equations of motion and by identifying equal powers of  $\xi$  and solving for the highest order expansion functions recursion relations are derived as

$$\begin{aligned} u_{k+2} = & \frac{1}{R^2(k+2)(k+1)C_{11}} [\rho (R^2 \partial_t^2 u_k + 2R \partial_t^2 u_{k-1} + \partial_t^2 u_{k-2}) \\ & - C_{11} (R(2k+1)(k+1)u_{k+1} + k^2 u_k) + C_{22} u_k - C_{66} \partial_\theta^2 u_k \\ & - C_{55} (\partial_z^2 u_{k-2} + 2R \partial_z^2 u_{k-1} + R^2 \partial_z^2 u_k) - (C_{12} + C_{66}) (k \partial_\theta v_k + R(k+1) \partial_\theta v_{k+1}) \\ & + (C_{22} + C_{66}) \partial_\theta v_k - (C_{13} + C_{55}) (R^2(k+1) \partial_z w_{k+1} + 2Rk \partial_z w_k + (k-1) \partial_z w_{k-1}) \\ & - (C_{13} - C_{23}) (R \partial_z w_k + \partial_z w_{k-1})], \end{aligned} \quad (70.16)$$

$$\begin{aligned} v_{k+2} = & \frac{1}{R^2(k+2)(k+1)C_{66}} [\rho (R^2 \partial_t^2 v_k + 2R \partial_t^2 v_{k-1} + \partial_t^2 v_{k-2}) \\ & - C_{66} (R(2k+1)(k+1)v_{k+1} + (k^2 - 1)v_k) - C_{22} \partial_\theta^2 v_k \\ & - C_{44} (\partial_z^2 v_{k-2} + 2R \partial_z^2 v_{k-1} + R^2 \partial_z^2 v_k) \\ & - (C_{12} + C_{66}) (k \partial_\theta u_k + R(k+1) \partial_\theta u_{k+1}) - (C_{22} + C_{66}) \partial_\theta u_k \\ & - (C_{23} + C_{44}) (R \partial_\theta \partial_z w_k + \partial_\theta \partial_z w_{k-1})], \end{aligned} \quad (70.17)$$

$$\begin{aligned} w_{k+2} = & \frac{1}{R^2(k+2)(k+1)C_{55}} [\rho (R^2 \partial_t^2 w_k + 2R \partial_t^2 w_{k-1} + \partial_t^2 w_{k-2}) \\ & - C_{55} (R(2k+1)(k+1)w_{k+1} + k^2 w_k) - C_{44} \partial_\theta^2 w_k - C_{33} (\partial_z^2 w_{k-2} + 2R \partial_z^2 w_{k-1} + R^2 \partial_z^2 w_k) \\ & - (C_{13} + C_{55}) (2Rk \partial_z u_k + R^2(k+1) \partial_z u_{k+1} + (k-1) \partial_z u_{k-1}) \\ & - (C_{23} + C_{55}) (R \partial_z u_k + \partial_z u_{k-1}) - (C_{23} + C_{44}) (R \partial_\theta \partial_z v_k + \partial_\theta \partial_z v_{k-1})]. \end{aligned} \quad (70.18)$$

The advantage of these recursion relations is that all the higher order expansion functions can be expressed in terms of the six lowest order ones  $u_0, u_1, v_0, v_1, w_0$  and  $w_1$  by using these equations recursively.

The boundary conditions on the cylindrical shell are applied to obtain the shell equations. The expansions of the displacement components are inserted into the stress components  $\sigma_{rr}, \sigma_{r\theta}$  and  $\sigma_{rz}$  which yield

$$\sigma_{rr} = \frac{1}{r} \sum_{k=0} [C_{11} (R(k+1)u_{k+1} + k u_k) + C_{12} (\partial_\theta v_k + u_k) + C_{13} (R \partial_z w_k + \partial_z w_{k-1})] \xi^k, \quad (70.19)$$

$$\sigma_{r\theta} = \frac{1}{r} \sum_{k=0} [C_{66} (\partial_\theta u_k + R(k+1)v_{k+1} + (k-1)v_k)] \xi^k, \quad (70.20)$$

$$\sigma_{rz} = \sum_{k=0} [C_{55} (\partial_z u_k + (k+1)w_{k+1})] \xi^k. \quad (70.21)$$

By combining the stresses according to  $\sum \sigma = \sigma(h, \theta, t) + \sigma(-h, \theta, t) = 0$  and  $\Delta \sigma = \sigma(h, \theta, t) - \sigma(-h, \theta, t) = 0$  and using the expansions of  $\sigma_{rr}, \sigma_{r\theta}$  and  $\sigma_{rz}$  and the recursion relations, these six boundary conditions can be written in terms of the six displacements  $u_0, u_1, v_0, v_1, w_0$  and  $w_1$  which deliver the six partial differential equations

$$\begin{aligned}
& \frac{2}{R} (C_{22}u_0 + C_{12}Ru_1 + R^2\rho\partial_t^2u_0 + (C_{22} + C_{66})\partial_\theta v_0 - RC_{66}\partial_\theta v_1 - C_{66}\partial_\theta^2u_0 \\
& + RC_{23}\partial_z w_0 + R^2(C_{55} + 2C_{13})\partial_z w_1 - R^2C_{55}\partial_z^2u_0) \\
& + h^2 [\alpha_{000}^{11}u_0 + \alpha_{000}^{12}u_1 + \alpha_{002}^{11}\partial_t^2u_0 + \alpha_{002}^{12}\partial_t^2u_1 + \alpha_{004}^{11}\partial_t^4u_0 + \alpha_{010}^{13}\partial_\theta v_0 + \alpha_{010}^{14}\partial_\theta v_1 \\
& + \alpha_{020}^{11}\partial_\theta^2u_0 + \alpha_{020}^{12}\partial_\theta^2u_1 + \alpha_{030}^{13}\partial_\theta^3v_0 + \alpha_{030}^{14}\partial_\theta^3v_1 + \alpha_{040}^{11}\partial_\theta^4u_0 + \alpha_{100}^{15}\partial_z w_0 + \alpha_{100}^{16}\partial_z w_1 \\
& + \alpha_{120}^{15}\partial_z\partial_\theta^2w_0 + \alpha_{120}^{16}\partial_z\partial_\theta^2w_1 + \alpha_{200}^{11}\partial_z^2u_0 + \alpha_{200}^{12}\partial_z^2u_1 + \alpha_{210}^{13}\partial_z^2\partial_\theta v_0 + \alpha_{210}^{14}\partial_z^2\partial_\theta v_1 + \alpha_{220}^{11}\partial_z^2\partial_\theta^2u_0 \\
& + \alpha_{300}^{15}\partial_z^3w_0 + \alpha_{300}^{16}\partial_z^3w_1 + \alpha_{400}^{11}\partial_z^4u_0] = 0, \tag{70.22}
\end{aligned}$$

$$\begin{aligned}
& 2(C_{12}u_0 + C_{11}Ru_1 + C_{12}\partial_\theta v_0 + RC_{13}\partial_z w_0) \\
& + h^2 [\alpha_{000}^{21}u_0 + \alpha_{000}^{22}u_1 + \alpha_{002}^{21}\partial_t^2u_0 + \alpha_{002}^{22}\partial_t^2u_1 + \alpha_{010}^{23}\partial_\theta v_0 + \alpha_{010}^{24}\partial_\theta v_1 \\
& + \alpha_{020}^{21}\partial_\theta^2u_0 + \alpha_{020}^{22}\partial_\theta^2u_1 + \alpha_{030}^{23}\partial_\theta^3v_0 + \alpha_{100}^{25}\partial_z w_0 + \alpha_{100}^{26}\partial_z w_1 \\
& + \alpha_{120}^{25}\partial_z\partial_\theta^2w_0 + \alpha_{200}^{21}\partial_z^2u_0 + \alpha_{200}^{22}\partial_z^2u_1 + \alpha_{210}^{23}\partial_z^2\partial_\theta v_0 + \alpha_{300}^{25}\partial_z^3w_0] = 0, \tag{70.23}
\end{aligned}$$

$$\begin{aligned}
& \frac{2}{R} (C_{66}v_0 - C_{66}Rv_1 - (C_{22} + C_{66})\partial_\theta u_0 - C_{22}\partial_\theta^2v_0 + R^2\rho\partial_t^2v_0 - RC_{12}\partial_\theta u_1 - (C_{23} + C_{44})\partial_z\partial_\theta w_0 + R^2C_{44}\partial_z^2v_0) \\
& + h^2 [\alpha_{000}^{31}u_0 + \alpha_{000}^{32}u_1 + \rho\alpha_{002}^{33}\partial_t^2v_0 + \alpha_{002}^{32}\partial_t^2u_1 + R\rho^2\alpha_{004}^{33}\partial_t^4v_0 + \alpha_{010}^{31}\partial_\theta u_0 + \alpha_{010}^{32}\partial_\theta u_1 \\
& + \alpha_{020}^{33}\partial_\theta^2v_0 + \alpha_{020}^{34}\partial_\theta^2v_1 + \alpha_{030}^{31}\partial_\theta^3u_0 + \alpha_{030}^{32}\partial_\theta^3u_1 + \alpha_{040}^{33}\partial_\theta^4v_0 + \alpha_{110}^{35}\partial_z\partial_\theta w_0 + \alpha_{110}^{36}\partial_z\partial_\theta w_1 \\
& + \alpha_{130}^{35}\partial_z\partial_\theta^3w_0 + \alpha_{200}^{33}\partial_z^2v_0 + \alpha_{210}^{31}\partial_z^2\partial_\theta u_0 + \alpha_{210}^{32}\partial_z^2\partial_\theta u_1 + \alpha_{220}^{33}\partial_z^2\partial_\theta^2v_0 \\
& + \alpha_{310}^{35}\partial_z^3\partial_\theta w_0 + \alpha_{400}^{33}\partial_z^4v_0] = 0, \tag{70.24}
\end{aligned}$$

$$\begin{aligned}
& 2C_{66}(-v_0 + Rv_1 + \partial_\theta u_0) \\
& + h^2 [\alpha_{000}^{43}v_0 + \alpha_{000}^{44}v_1 + \alpha_{002}^{44}\partial_t^2v_1 + \alpha_{010}^{41}\partial_\theta u_0 + \alpha_{010}^{42}\partial_\theta u_1 + \alpha_{020}^{43}\partial_\theta^2v_0 \\
& + \alpha_{020}^{44}\partial_\theta^2v_1 + \alpha_{030}^{41}\partial_\theta^3u_0 + \alpha_{110}^{45}\partial_z\partial_\theta w_0 + \alpha_{110}^{46}\partial_z\partial_\theta w_1 + \alpha_{200}^{44}\partial_z^2v_1 \\
& + \alpha_{210}^{41}\partial_z^2\partial_\theta u_0] = 0, \tag{70.25}
\end{aligned}$$

$$\begin{aligned}
& \frac{-2}{R} \left( C_{55}w_1 - R\rho\partial_t^2w_0 + \frac{C_{44}}{R}\partial_\theta^2w_0 + (C_{55} + C_{23})\partial_z u_0 + RC_{13}\partial_z u_1 + (C_{23} + C_{44})\partial_z\partial_\theta v_0 + RC_{33}\partial_z^2w_0 \right) \\
& + h^2 [\alpha_{000}^{56}w_1 + \alpha_{002}^{55}\partial_t^2w_0 + \alpha_{002}^{56}\partial_t^2w_1 + \alpha_{004}^{55}\partial_t^4w_0 + \alpha_{020}^{55}\partial_\theta^2w_0 + \alpha_{020}^{56}\partial_\theta^2w_1 + \alpha_{040}^{55}\partial_\theta^4w_0 + \alpha_{100}^{51}\partial_z u_0 + \alpha_{100}^{52}\partial_z u_1 \\
& + \alpha_{110}^{53}\partial_z\partial_\theta v_0 + \alpha_{110}^{54}\partial_z\partial_\theta v_1 + \alpha_{120}^{51}\partial_z\partial_\theta^2u_0 + \alpha_{120}^{52}\partial_z\partial_\theta^2u_1 + \alpha_{130}^{53}\partial_z\partial_\theta^3v_0 + \alpha_{200}^{55}\partial_z^2w_0 + \alpha_{200}^{56}\partial_z^2w_1 + \alpha_{220}^{55}\partial_z^2\partial_\theta^2w_0 \\
& + \alpha_{300}^{51}\partial_z^3u_0 + \alpha_{300}^{52}\partial_z^3u_1 + \alpha_{310}^{53}\partial_z^3\partial_\theta v_0 + \alpha_{400}^{55}\partial_z^4w_0] = 0, \tag{70.26}
\end{aligned}$$

$$\begin{aligned}
& 2C_{55}(w_1 + \partial_z u_0) \\
& + h^2 [\alpha_{000}^{66}w_1 + \alpha_{002}^{65}\partial_t^2w_0 + \alpha_{002}^{66}\partial_t^2w_1 + \alpha_{020}^{65}\partial_\theta^2w_0 + \alpha_{020}^{66}\partial_\theta^2w_1 + \alpha_{100}^{61}\partial_z u_0 + \alpha_{100}^{62}\partial_z u_1 \\
& + \alpha_{110}^{63}\partial_z\partial_\theta v_0 + \alpha_{110}^{64}\partial_z\partial_\theta v_1 + \alpha_{120}^{61}\partial_z\partial_\theta^2u_0 \\
& + \alpha_{200}^{65}\partial_z^2w_0 + \alpha_{200}^{66}\partial_z^2w_1 + \alpha_{300}^{61}\partial_z^3u_0] = 0. \tag{70.27}
\end{aligned}$$

These equations are obtained by using recursion relations up to three times and include up to  $h^2$  terms. Each equation starts with the  $h$ -independent part which corresponds to the membrane equations. In principle, the equations can be given to any order, leading to very complicated expressions, but in practice there should be no reasons to go further. The coefficients are represented explicitly in Appendix A.

### 70.3 Results for a Ring

As a special simpler case a 2D circular ring is considered in the  $r\theta$  plane which vibrates independently of the  $z$  coordinate. Looking only at in-plane vibrations  $w_0$  and  $w_1$  are set to zero so there will be just four displacement components  $u_0$ ,  $u_1$ ,  $v_0$  and  $v_1$ . The six shell equations reduce to four equations that can be represented explicitly as

$$\begin{aligned} & \frac{2}{R} \left( C_{22}u_0 + RC_{12}u_1 + R^2\rho\partial_r^2u_0 + (C_{22} + C_{66})\partial_\theta v_0 - RC_{66}\partial_\theta v_1 - C_{66}\partial_\theta^2u_0 \right) + \frac{h^2}{3C_{11}} \left[ \frac{C_{22}}{R^3} (2C_{11} - 3C_{12} + C_{22})u_0 \right. \\ & + \frac{1}{R^2} (2C_{11}C_{12} - 3C_{11}C_{22} + C_{12}C_{22})u_1 - \frac{\rho}{R} (C_{12} - 2C_{22})\partial_r^2u_0 + \rho(C_{11} + C_{12})\partial_r^2u_1 + R\rho^2\partial_r^4u_0 \\ & + \frac{1}{R^3} \left( -C_{12}^2 + C_{22}(C_{22} + C_{66}) + 3C_{11}(2C_{66} + C_{22}) - C_{12}(3C_{22} + 4C_{66}) \right) \partial_\theta v_0 + \frac{1}{R^2} \left( 3C_{12}^2 + C_{66}(4C_{12} - C_{22}) \right. \\ & - 3C_{11}(2C_{66} + C_{22})\partial_\theta v_1 + \frac{1}{R^3C_{66}} \left( -C_{22}C_{66}^2 + C_{12}^2(C_{66} + C_{22}) + 2C_{12}C_{66}(2C_{66} + C_{22}) - C_{11}(C_{22} + 2C_{66})(3C_{66} + C_{22}) \right) \\ & \times \partial_\theta^2u_0 + \frac{1}{R^2C_{66}} (C_{12}(C_{12}(C_{12} + 2C_{66})) - C_{11}(C_{22} + 4C_{66}))\partial_\theta^2u_1 + \frac{1}{R^3C_{66}} (C_{12}(C_{12}C_{22} + C_{66}(2C_{22} + C_{66})) \\ & \left. - C_{11}C_{22}(4C_{66} + C_{22}))\partial_\theta^3v_0 + \frac{1}{R^2} (-C_{11}C_{22} + C_{12}(C_{12} + C_{66}))\partial_\theta^3v_1 - \frac{1}{R^3}C_{12}C_{66}\partial_\theta^4u_0 \right] = 0, \end{aligned} \quad (70.28)$$

$$\begin{aligned} & 2(C_{12}u_0 + RC_{11}u_1 + C_{12}\partial_\theta v_0) + h^2 \left[ \frac{1}{C_{11}R^2} (-C_{11} + C_{12})C_{22}u_0 - \frac{1}{R}(C_{12} - C_{22})u_1 + \frac{\rho}{C_{11}}(C_{11} + C_{12})\partial_r^2u_0 + R\rho\partial_r^2u_1 \right. \\ & + \frac{1}{C_{11}R^2} (C_{12}(C_{22} + C_{66}) - C_{11}(C_{22} + 2C_{66}))\partial_\theta v_0 - \frac{1}{C_{11}R} (C_{12}(C_{12} + C_{66}) - C_{11}(2C_{66} + C_{22}))\partial_\theta v_1 \\ & \left. + \frac{1}{C_{11}R^2} (-C_{12}C_{66} + C_{11}(C_{22} + 2C_{66}))\partial_\theta^2u_0 + \frac{C_{12}}{R}\partial_\theta^2u_1 + \frac{C_{22}}{R^2}\partial_\theta^3v_0 \right] = 0, \end{aligned} \quad (70.29)$$

$$\begin{aligned} & \frac{-2}{R} (-C_{66}v_0 + RC_{66}v_1 - R^2\rho\partial_r^2v_0 + (C_{22} + C_{66})\partial_\theta u_0 + RC_{12}\partial_\theta u_1 + C_{22}\partial_\theta^2v_0) + \frac{h^2}{3R^3} \left[ 6C_{66}(v_0 - Rv_1) + 3R^2\rho\partial_r^2v_0 + \frac{R^4\rho^2}{C_{66}}\partial_r^4v_0 \right. \\ & - \frac{1}{C_{11}} (C_{22}(-4C_{12} + C_{22}) + 6C_{11}(C_{22} + C_{66}))\partial_\theta u_0 - \frac{1}{C_{11}} (2C_{11}(3C_{12} - 2C_{22}) + C_{12}C_{22})R\partial_\theta u_1 \\ & + \frac{1}{C_{11}} (C_{12}(C_{12} + 4C_{22} + 5C_{66}) - C_{22}(7C_{11} + C_{22} + C_{66}))\partial_\theta^2v_0 + \frac{1}{C_{11}} (-4C_{12}^2 + C_{22}(4C_{11} + C_{66}) - 5C_{12}C_{66})R\partial_\theta^2v_1 \\ & + \frac{1}{C_{11}C_{66}} (C_{12}(-C_{12}(C_{22} + C_{66})) - C_{66}(C_{22} + 5C_{66})) + C_{22} (C_{66}^2 + C_{11}(C_{22} + C_{66})) \partial_\theta^3u_0 \\ & \left. + \frac{1}{C_{11}C_{66}} (C_{12}(C_{11}C_{22} - C_{12}^2 - 2C_{12}C_{66}) + C_{11}C_{22}C_{66}) R\partial_\theta^3u_1 + \frac{C_{22}}{C_{11}C_{66}} (C_{11}C_{22} - C_{12}(C_{12} + C_{66}))\partial_\theta^4v_0 \right] = 0, \end{aligned} \quad (70.30)$$

$$\begin{aligned} & 2C_{66}(-v_0 + Rv_1 + \partial_\theta u_0) + \frac{h^2}{R^2C_{11}} \left[ 2C_{66}C_{11}(-v_0 + Rv_1) + R^3C_{11}\rho\partial_r^2v_1 + (-C_{12}C_{22} + 2C_{11}(C_{22} + C_{66}))\partial_\theta u_0 \right. \\ & \left. + RC_{11}(2C_{12} - C_{22})\partial_\theta u_1 + (2C_{11}C_{22} - C_{12}(C_{22} + C_{66}))\partial_\theta^2v_0 - (C_{11}C_{22} - C_{12}(C_{12} + C_{66}))R\partial_\theta^2v_1 + C_{12}C_{66}\partial_\theta^3u_0 \right] = 0. \end{aligned} \quad (70.31)$$

For the numerical results a further specialization is made that the vibration of the ring is independent of  $\theta$  which means that all the  $\theta$ -derivatives are put to zero. In this case the four equations are decoupled and the first two equations are related to radial displacements  $u_0$  and  $u_1$  and define the purely radial modes while the last two equations are related to the tangential displacements, i.e.  $v_0$  and  $v_1$  which define torsional modes. The four displacement fields are expressed as a time-harmonic ansatz with fixed angular frequency  $\omega$  and the two sets of equations are solved for the eigenfrequencies.

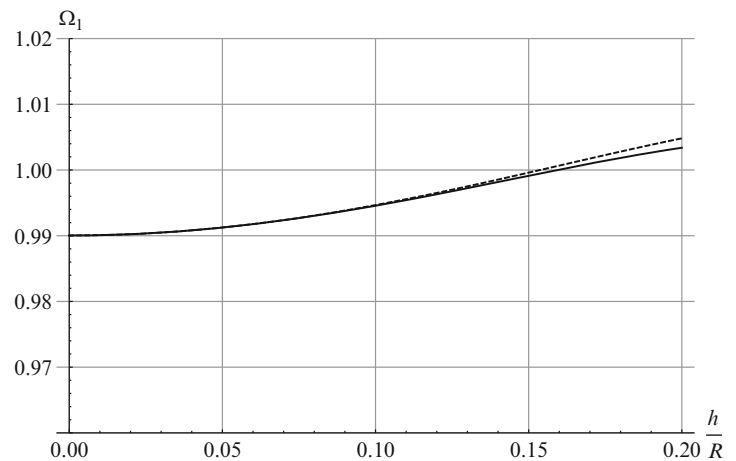
First an isotropic case is considered to validate the shell equations with the results from the exact solution and other theories. The results from the power series theory are in a very good agreement with the results from exact theory and other theories stated in paper [7] where radial and torsional frequencies are computed for an isotropic material with  $\nu = 0.3$  [7].

**Table 70.1** Material properties for graphite-epoxy. The density is in  $\text{kgm}^{-3}$  and the material constants are in GPa

$\rho$	$C_{11}$	$C_{22}$	$C_{12}$	$C_{66}$
1578	13.02	160.73	6.44	7.07

**Table 70.2** The eigenfrequencies for radial and torsional modes for exact and power series theory for  $h/R = 0.01$  and  $h/R = 0.1$ 

$h/R$	Mode	Exact	$h^2$
$h/R = 0.01$	Radial	0.9901	0.9901
	Torsional	44.718	40.263
$h/R = 0.1$	Radial	157.09	141.44
	Torsional	314.17	244.95
$h/R = 0.1$	Radial	0.99467	0.99457
	Torsional	4.5808	4.1439
		15.827	14.265
		31.476	24.525

**Fig. 70.1** The first radial eigenfrequency as a function of cylindrical shell thickness: exact theory (*full-drawn*), power series theory (*short-dashed*)

For both the isotropic and anisotropic cases the exact solution is obtained by representing the displacement components in terms of cylindrical Bessel and Neumann functions and using the same boundary conditions.

Then graphite-epoxy is used as an anisotropic material with material properties given in Table 70.1 [9]. As shown for the 2D ring in the  $r\theta$  plane, just values for  $C_{11}$ ,  $C_{22}$ ,  $C_{12}$ ,  $C_{66}$  are needed. The four shell equations decouple to radial and torsional parts, hence  $C_{11}$ ,  $C_{22}$  and  $C_{12}$  are related to radial modes and  $C_{66}$  relates to torsional modes.

The two first radial eigenfrequencies and the two first torsional eigenfrequencies are given in Table 70.2 for different ratios of the shell thickness to its mean radius. The eigenfrequencies for the radial mode are normalized as  $\Omega_1 = \omega R/c_1$  where  $c_1$  is defined as  $c_1 = \sqrt{C_{22}/\rho}$ . Similarly the torsional eigenfrequencies are normalized as  $\Omega_2 = \omega R/c_2$  where  $c_2$  is defined as  $c_2 = \sqrt{C_{66}/\rho}$ .

As is shown in Table 70.2, for the first radial mode the exact theory and the power series approximation theory present the same values. For the second radial mode the power series theory gives a smaller eigenfrequency and the difference is about 10%. It is similar for the first torsional mode but the difference increases as the eigenfrequencies become larger. It should be noted that in the table just up to  $h^2$  terms are used and by increasing the number of terms which are used to form the shell equations there will be better agreement between the results.

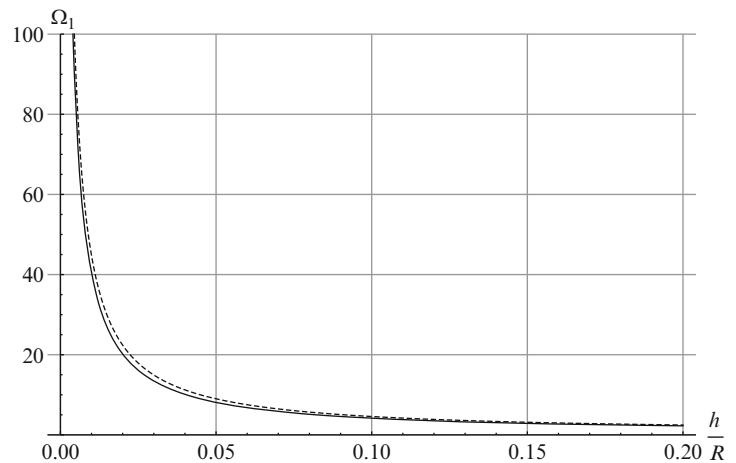
In Fig. 70.1, the first radial eigenfrequency is shown as a function of shell thickness for both the exact theory and the power series theory. As seen in the figure, the eigenfrequencies increase slightly as the ratio of shell thickness to the shell mean radius increases, but the difference is small and the first radial mode eigenfrequencies can be considered to be roughly independent of the shell thickness. It is seen that the two theories show very good agreement.

Figure 70.2 presents the second radial eigenfrequency as a function of  $h/R$  for the both exact and the power series theory. It is shown that they depend on the ratio of the shell thickness to the shell radius strongly and there is a very good agreement between two theories.

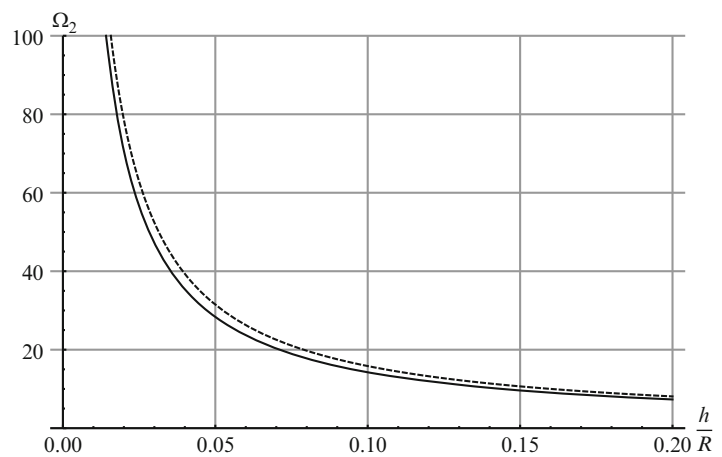
Figure 70.3, shows the first torsional frequency as a function of the ratio of the shell thickness to the shell mean radius for both theories. As shown, they also depend strongly on the relative thickness. Also it is seen that the power series theory approximates the exact theory very well.



**Fig. 70.2** The second eigenfrequency for the radial mode as a function of cylindrical shell thickness: exact theory (*full-drawn*), power series theory (*short-dashed*)



**Fig. 70.3** The first eigenfrequency for the torsional mode as a function of cylindrical shell thickness: exact theory (*full-drawn*), power series theory (*short-dashed*)



## 70.4 Conclusions

In present work, the dynamic equations for an anisotropic cylindrical shell are derived. The power series method is used to obtain the shell equations as a power series in the shell thickness. The six partial differential equations can in principle be truncated to any order and are believed to be asymptotically correct. The set of equations is presented in the six lowest displacement components up and including the  $h^2$  terms by using recursion relations which deliver higher order displacement components in terms of the six lowest. The eigenfrequencies for a 2D circular ring are first computed for an isotropic material. The results are compared with results from exact theory and other shell theories. It is seen that power series method gives satisfactory results which are in very good agreement with results from exact theory and other shell theories. Then graphite-epoxy is used as an anisotropic material and eigenfrequencies are computed for the both radial and torsional modes. It is shown again that the power series theory approximates the results from exact theory very well.

For the future the eigenfrequencies should be computed by using different truncations and considering terms with higher power in  $h$  in the partial differential equations to obtain more accurate approximations for high eigenfrequencies. Here numerical results are given for a 2D case and are compared to the two-dimensional exact solution, also the six shell equations can be solved numerically to obtain dispersion curves which can be compared to the results from other three-dimensional shell theories. The shell equations obtained from the power series approximation can be derived also for more complicated cases like general anisotropy, piezoelectricity, and layered shells. Also the derived equations can be used for modelling structures made of composite and new materials which have anisotropic properties.

## Appendix

Here the explicit representations of the coefficients in Eqs. (70.22)–(70.27) are given

$$\begin{aligned}
 \alpha_{000}^{11} &= \frac{C_{22}}{3C_{11}R^3}(2C_{11} - 3C_{12} + C_{22}), & \alpha_{000}^{12} &= \frac{1}{3C_{11}R^2}(2C_{11}C_{12} + C_{22}(C_{12} - 3C_{11})), \\
 \alpha_{002}^{11} &= \frac{\rho}{3C_{11}R}(-C_{12} + 2C_{22}), & \alpha_{002}^{12} &= \frac{\rho}{3C_{11}}(C_{11} + C_{12}), & \alpha_{004}^{11} &= \frac{R\rho^2}{3C_{11}}, \\
 \alpha_{010}^{13} &= \frac{1}{3C_{11}R^3}(-C_{12}(C_{12} + 3C_{22} + 4C_{66}) + 3C_{11}(C_{22} + 2C_{66}) + C_{22}(C_{22} + C_{66})), \\
 \alpha_{010}^{14} &= \frac{1}{3C_{11}R^2}(C_{12}(3C_{12} + 4C_{66}) - C_{22}C_{66} - 3C_{11}(C_{22} + 2C_{66})), \\
 \alpha_{020}^{11} &= \frac{1}{3R^3C_{11}C_{66}}(C_{12}(C_{12}(C_{22} + C_{66}) + 2C_{66}(C_{22} + 2C_{66})) - C_{22}C_{66}^2 - C_{11}(C_{22} + 2C_{66})(C_{22} + 3C_{66})), \\
 \alpha_{020}^{12} &= \frac{1}{3R^2C_{11}C_{66}}C_{12}(C_{12}^2 + 2C_{12}C_{66} - C_{11}(C_{22} + 4C_{66})), \\
 \alpha_{030}^{13} &= \frac{1}{3R^3C_{11}C_{66}}(C_{12}^2C_{22} + C_{12}C_{66}(2C_{22} + C_{66}) - C_{11}C_{22}(C_{22} + 4C_{66})), \\
 \alpha_{030}^{14} &= \frac{1}{3C_{11}R^2}(-C_{11}C_{22} + C_{12}(C_{12} + C_{66})), & \alpha_{040}^{11} &= \frac{1}{3R^3C_{11}}(C_{12}C_{66}), \\
 \alpha_{100}^{15} &= \frac{1}{3R^2C_{11}}(2C_{12} - C_{22})(2C_{13} - C_{23}), \\
 \alpha_{100}^{16} &= \frac{1}{3RC_{11}}(-C_{11}C_{23} + C_{12}(-3C_{13} + C_{23} - 2C_{55}) + C_{22}(C_{55} + C_{13})), \\
 \alpha_{120}^{15} &= \frac{1}{3R^2C_{11}C_{55}C_{66}}((C_{12}^2 - C_{11}C_{22})(C_{23} + C_{44})C_{55} - (C_{11}(-2C_{13}C_{44} + C_{23}C_{44} + 3C_{23}C_{55} + 2C_{44}C_{55}) \\
 &\quad + C_{12}(-2C_{23}C_{55} + C_{13}(C_{44} + C_{55})))C_{66}), \\
 \alpha_{120}^{16} &= \frac{1}{3RC_{11}C_{55}}(C_{55}C_{12}(C_{13} + C_{55}) + C_{11}(-2C_{13}C_{44} + C_{23}C_{55})), \\
 \alpha_{200}^{11} &= \frac{-1}{3RC_{11}C_{55}}(2C_{13}^2C_{22} + C_{11}C_{23}(C_{23} + C_{55}) + C_{55}(C_{12}C_{23} + 3C_{22}C_{55}) + C_{13}(3C_{22}C_{55} + C_{12}(C_{23} + C_{55}))), \\
 \alpha_{200}^{12} &= \frac{-1}{3C_{11}C_{55}}(C_{13}(C_{12}C_{13} + 3C_{11}C_{23}) + 2(C_{12}C_{13} + C_{11}(C_{13} + C_{23}))C_{55} + 2(C_{11} + C_{12})C_{55}^2), \\
 \alpha_{210}^{13} &= \frac{-1}{3RC_{11}C_{55}C_{66}}((C_{44}C_{55})(-C_{12}^2 + C_{11}C_{22}) + C_{12}(C_{13}(C_{23} + C_{44}) + C_{23}C_{55})C_{66} + C_{11}(C_{23}(C_{23} + C_{44}) \\
 &\quad + 2C_{44}C_{55})C_{66} + (2C_{13}^2 + 3C_{13}C_{55} + 2C_{55}^2)C_{66}(C_{22} + C_{66})), \\
 \alpha_{210}^{14} &= \frac{1}{3C_{55}C_{11}}(-2C_{11}C_{13}(C_{23} + C_{44}) - C_{11}C_{23}C_{55} + C_{12}(2C_{13}^2 + 3C_{13}C_{55} + 2C_{55}^2) + (2C_{13}^2 + 3C_{13}C_{55} + 2C_{55}^2)C_{66}), \\
 \alpha_{220}^{11} &= \frac{1}{3RC_{55}C_{11}}(2C_{13}^2C_{66} + C_{55}(-C_{12}C_{55} + C_{66}(3C_{13} + 2C_{55}))), \\
 \alpha_{300}^{15} &= \frac{-1}{3C_{11}C_{55}}(-2C_{13}^3 + C_{13}^2(2C_{23} - 3C_{55}) + C_{11}C_{33}(C_{23} + C_{55}) + C_{55}(C_{12}C_{33} + 2C_{23}C_{55}) \\
 &\quad + C_{13}(2C_{11}C_{33} + C_{12}C_{33} + 3C_{23}C_{55} - 2C_{55}^2)),
 \end{aligned}$$

$$\begin{aligned}
\alpha_{300}^{16} &= \frac{-R}{3C_{11}C_{55}}(2C_{13}^3 + 2C_{11}C_{13}C_{33} + 5C_{13}^2C_{55} + C_{11}C_{33}C_{55} + 5C_{13}C_{55}^2 + 2C_{55}^3), \\
\alpha_{400}^{11} &= \frac{R}{3C_{11}}(2C_{13}^2 + 3C_{13}C_{55} + 2C_{55}^2), \\
\alpha_{000}^{21} &= \frac{1}{R^2C_{11}}(-C_{11} + C_{12})C_{22}, & \alpha_{000}^{22} &= \frac{1}{R}(-C_{12} + C_{22}), & \alpha_{002}^{21} &= \frac{\rho}{C_{11}}(C_{11} + C_{12}), & \alpha_{002}^{22} &= R\rho, \\
\alpha_{010}^{23} &= \frac{1}{R^2C_{11}}(-C_{11}(C_{22} + 2C_{66}) + C_{12}(C_{22} + C_{66})), \\
\alpha_{010}^{24} &= \frac{-1}{RC_{11}}(-C_{11}(C_{22} + 2C_{66}) + C_{12}(C_{12} + C_{66})), \\
\alpha_{020}^{21} &= \frac{1}{C_{11}R^2}(-C_{12}C_{66} + C_{11}(2C_{66} + C_{22})), \\
\alpha_{020}^{22} &= \frac{C_{12}}{R}, & \alpha_{030}^{23} &= \frac{C_{22}}{R^2}, & \alpha_{100}^{25} &= \frac{1}{C_{11}R}(C_{12}(-C_{13} + C_{23})), \\
\alpha_{100}^{26} &= \frac{1}{C_{11}}(C_{11}C_{23} + C_{12}(C_{13} + C_{55})), & \alpha_{120}^{25} &= \frac{1}{C_{55}R}(-2C_{13}C_{44} + C_{23}C_{55}), \\
\alpha_{200}^{21} &= -C_{23} - \frac{(2C_{11} + C_{12})C_{55}}{C_{11}} - \frac{2C_{13}(C_{23} + C_{55})}{C_{55}}, & \alpha_{200}^{22} &= -3C_{13} - \frac{2C_{13}^2}{C_{55}} - 2C_{55}, \\
\alpha_{210}^{23} &= \frac{-1}{C_{55}}(2C_{13}(C_{23} + C_{44}) + C_{23}C_{55}), & \alpha_{300}^{25} &= \frac{-R}{C_{55}}(C_{33}(2C_{13} + C_{55})), \\
\alpha_{000}^{31} &= \frac{2C_{66}}{R^3}, & \alpha_{000}^{32} &= \frac{-2C_{66}}{R^2}, & \alpha_{002}^{33} &= \frac{\rho}{R}, & \alpha_{004}^{33} &= \frac{R\rho^2}{3C_{66}}, \\
\alpha_{010}^{31} &= \frac{-1}{3C_{11}R^3}(C_{22}(-4C_{12} + C_{22}) + 6C_{11}(C_{22} + C_{66})), & \alpha_{010}^{32} &= \frac{-1}{3C_{11}R^2}(2C_{11}(3C_{12} - 2C_{22}) + C_{12}C_{22}), \\
\alpha_{020}^{33} &= \frac{1}{3C_{11}R^3}(C_{12}^2 - C_{22}(7C_{11} + C_{22} + C_{66}) + C_{12}(5C_{66} + 4C_{22})), \\
\alpha_{020}^{34} &= \frac{1}{3C_{11}R^2}(C_{12}(-4C_{12} - 5C_{66}) + C_{22}(C_{66} + 4C_{11})), \\
\alpha_{030}^{31} &= \frac{1}{3C_{11}C_{66}R^3}(C_{12}(-C_{12}(C_{22} + C_{66}) - C_{66}(C_{22} + 5C_{66})) + C_{22}(C_{66}^2 + C_{11}(C_{22} + C_{66}))), \\
\alpha_{030}^{32} &= \frac{1}{3C_{11}C_{66}R^2}(C_{12}(-C_{12}(C_{12} + 2C_{66}) + C_{11}C_{22}) + C_{11}C_{12}C_{66}), \\
\alpha_{040}^{34} &= \frac{1}{3C_{22}C_{11}C_{66}R^3}(-C_{12}(C_{12} + C_{66}) + C_{11}C_{22}), \\
\alpha_{110}^{35} &= \frac{-1}{3C_{11}R^2}((3C_{12} - C_{22})(C_{13} - C_{23}) + 3C_{11}(C_{23} + C_{44})), \\
\alpha_{110}^{36} &= \frac{1}{3C_{11}R}(2C_{11}(C_{23} + C_{44}) - C_{22}(C_{13} + C_{55}) + C_{12}(4C_{13} - C_{23} + 3C_{55})), \\
\alpha_{130}^{35} &= \frac{1}{3C_{11}C_{55}C_{66}R^2}(C_{12}(-C_{12}(C_{23} + C_{44})C_{55} + C_{66}(C_{13}C_{44} - C_{23}C_{55})) + C_{11}(C_{23} + C_{44})(C_{22}C_{55} + C_{44}C_{66})), \\
\alpha_{200}^{33} &= \frac{-C_{44}}{R}, \\
\alpha_{210}^{31} &= \frac{1}{3C_{11}C_{55}C_{66}R}(C_{11}C_{22}C_{44}C_{55} + C_{12}C_{13}C_{23}C_{66} + C_{55}(C_{12}(C_{13} + C_{23} - C_{55}) + C_{22}C_{55})C_{66} \\
&\quad + C_{11}(C_{23}^2 + 2C_{44}C_{55} + C_{23}(C_{44} + C_{55}))C_{66}),
\end{aligned}$$

$$\begin{aligned}
\alpha_{210}^{32} &= \frac{1}{3C_{11}C_{55}C_{66}}(C_{11}C_{12}C_{44}C_{55} + C_{11}(C_{13}(C_{23} + C_{44}) + (C_{23} + 2C_{44})C_{55})C_{66} + C_{12}(C_{13}^2 + 2C_{13}C_{55} + 2C_{55}^2)C_{66}), \\
\alpha_{220}^{32} &= \frac{1}{3C_{11}C_{55}C_{66}R}(C_{12}(-C_{12}C_{44}C_{55} + (C_{13}(C_{23} + C_{44}) + C_{23}C_{55})C_{66}) + 2C_{11}C_{22}C_{44}C_{55} + C_{11}(C_{23} + C_{44})^2C_{66}), \\
\alpha_{310}^{35} &= \frac{1}{3C_{11}C_{55}C_{66}}(C_{12}C_{23}(C_{13} + C_{55})C_{66} + C_{11}(C_{23} + C_{44})(C_{44}C_{55} + C_{33}C_{66})), & \alpha_{400}^{33} &= \frac{RC_{44}^2}{3C_{66}}, \\
\alpha_{000}^{43} &= \frac{-2C_{66}}{R^2}, & \alpha_{000}^{44} &= \frac{2C_{66}}{R}, & \alpha_{002}^{44} &= R\rho, & \alpha_{010}^{41} &= \frac{1}{C_{11}R^2}(-C_{12}C_{22} + 2C_{11}(C_{22} + C_{66})), \\
\alpha_{010}^{42} &= \frac{1}{R}(2C_{12} - C_{22}), & \alpha_{020}^{43} &= \frac{1}{C_{11}R^2}(2C_{11}C_{22} - C_{12}(C_{22} + C_{66})), \\
\alpha_{020}^{44} &= \frac{1}{C_{11}R}(-C_{11}C_{22} + C_{12}(C_{12} + C_{66})), & \alpha_{030}^{41} &= \frac{1}{C_{11}R^2}(C_{12}C_{66}), \\
\alpha_{110}^{45} &= \frac{1}{C_{11}R}(C_{12}(C_{13} - C_{23}) + C_{11}(C_{23} + C_{44})), & \alpha_{110}^{46} &= \frac{-1}{C_{11}}(C_{11}(C_{23} + C_{44}) + C_{12}(C_{13} + C_{55})), \\
\alpha_{200}^{44} &= -RC_{44}, & \alpha_{210}^{41} &= \frac{1}{C_{11}}(C_{12}C_{55}), \\
\alpha_{000}^{56} &= \frac{-2}{R^3}C_{55}, & \alpha_{002}^{55} &= \frac{\rho}{R^2}, & \alpha_{002}^{56} &= \frac{-2\rho}{3R}, & \alpha_{004}^{55} &= \frac{\rho^2}{3C_{55}}, \\
\alpha_{020}^{55} &= \frac{-11C_{44}}{3R^4}, & \alpha_{020}^{56} &= \frac{2C_{44}}{R^3}, & \alpha_{040}^{55} &= \frac{C_{44}^2}{3C_{55}R^4}, \\
\alpha_{100}^{51} &= \frac{-1}{3C_{11}R^3}(-4C_{13}C_{22} + C_{22}C_{23} + 6C_{11}(C_{23} + C_{55})), \\
\alpha_{100}^{52} &= \frac{-1}{3C_{11}R^2}(6C_{11}C_{13} + C_{13}C_{22} - 4C_{11}C_{23}), \\
\alpha_{110}^{53} &= \frac{1}{3C_{11}R^3}(C_{13}(C_{12} + 4C_{22} + 5C_{66}) - 7C_{11}(C_{23} + C_{44})), \\
\alpha_{110}^{54} &= \frac{1}{3C_{11}R^2}(C_{12}(-4C_{13} + C_{23}) + 4C_{11}(C_{23} + C_{44}) + C_{23}C_{66} - C_{13}(C_{22} + 5C_{66})), \\
\alpha_{120}^{51} &= \frac{1}{3C_{11}C_{55}C_{66}R^3}(C_{11}C_{22}(C_{23} + C_{44})C_{55} + C_{11}(2C_{44}C_{55} + C_{23}(C_{44} + C_{55}))C_{66} - C_{12}C_{13}C_{55}(C_{22} + C_{66}) \\
&\quad + C_{55}C_{66}(C_{23}C_{66} - C_{13}(C_{22} + 5C_{66}))), \\
\alpha_{120}^{52} &= \frac{1}{3C_{11}C_{55}C_{66}R^2}(C_{12}C_{55}(-C_{12}C_{13} + C_{11}(C_{23} + C_{44}) - 2C_{13}C_{66}) + C_{11}(C_{13}C_{44} + (C_{23} + 2C_{44})C_{55})C_{66}), \\
\alpha_{130}^{53} &= \frac{1}{3C_{11}C_{55}C_{66}R^3}(-C_{13}C_{22}C_{55}(C_{12} + C_{66}) + C_{11}(C_{23} + C_{44})(C_{22}C_{55} + C_{44}C_{66})), \\
\alpha_{200}^{55} &= \frac{-1}{3C_{11}R^2}(C_{13}(3C_{13} - 4C_{23}) + C_{23}^2 + 3C_{11}C_{33}), \\
\alpha_{200}^{56} &= \frac{1}{3RC_{11}}(C_{13}(4C_{13} - 2C_{23} + 3C_{55}) + 2C_{11}C_{33} - C_{23}C_{55}), \\
\alpha_{220}^{55} &= \frac{1}{3C_{11}C_{55}C_{66}R}(-C_{12}C_{13}(C_{23} + C_{44})C_{55} + C_{11}(C_{23} + C_{44})^2C_{55} + 2C_{11}C_{33}C_{44}C_{66} + C_{13}(C_{13}C_{44} - C_{23}C_{55})C_{66}), \\
\alpha_{300}^{51} &= \frac{1}{3C_{11}C_{55}R}(C_{13}(C_{23} - C_{55})C_{55} + C_{23}C_{55}^2 + C_{13}^2(C_{23} + C_{55}) + C_{11}C_{33}(C_{23} + C_{55})),
\end{aligned}$$

$$\alpha_{300}^{52} = \frac{1}{3C_{11}C_{55}}(C_{13}^3 + C_{11}C_{13}C_{33} + 2C_{13}^2C_{55} + C_{11}C_{33}C_{55} + 2C_{13}C_{55}^2),$$

$$\alpha_{310}^{53} = \frac{1}{3C_{11}C_{55}C_{66}R}(-C_{13}C_{44}C_{55}C_{12} + C_{13}(C_{13}(C_{23} + C_{44}) + C_{23}C_{55})C_{66} + C_{11}(C_{23} + C_{44})(C_{44}C_{55} + C_{33}C_{66})),$$

$$\alpha_{400}^{55} = \frac{1}{3C_{11}C_{55}}C_{33}(C_{11}C_{33} + C_{13}(C_{13} + C_{55})),$$

$$\alpha_{000}^{66} = \frac{2}{R^2}C_{55}, \quad \alpha_{002}^{65} = \frac{-\rho}{R}, \quad \alpha_{002}^{66} = \rho, \quad \alpha_{020}^{65} = \frac{3C_{44}}{R^3}, \quad \alpha_{020}^{66} = \frac{-C_{44}}{R^2},$$

$$\alpha_{100}^{61} = \frac{1}{C_{11}R^2}(-C_{13}C_{22} + 2C_{11}(C_{23} + C_{55})), \quad \alpha_{100}^{62} = \frac{1}{R}(2C_{13} - C_{23}),$$

$$\alpha_{110}^{63} = \frac{-1}{C_{11}R^2}(-2C_{11}(C_{23} + C_{44}) + C_{13}(C_{22} + C_{66})), \quad \alpha_{110}^{64} = \frac{1}{C_{11}R}(C_{13}(C_{12} + C_{66}) - C_{11}(C_{23} + C_{44})),$$

$$\alpha_{120}^{61} = \frac{1}{C_{11}R^2}(C_{13}C_{66}), \quad \alpha_{200}^{65} = \frac{1}{C_{11}R}(C_{13}^2 - C_{13}C_{23} + C_{11}C_{33}),$$

$$\alpha_{200}^{66} = \frac{-1}{C_{11}}(C_{11}C_{33} + C_{13}(C_{13} + C_{55})),$$

$$\alpha_{300}^{61} = \frac{1}{C_{11}}C_{13}C_{55}.$$

**Acknowledgements** The present project is funded by the Swedish Research Council and this is gratefully acknowledged.

## References

1. Soedel W (1993) Vibrations of shells and plates. Marcel Dekker, New York
2. Leissa AW (1993) Vibration of shells. Acoustical Society of America, New York
3. Boström A (2000) On wave equations for elastic rods. *Z Angew Math Mech* 80:245–251
4. Boström A, Johansson J, Olsson P (2001) On the rational derivation of a hierarchy of dynamic equations for a homogeneous, isotropic, elastic plate. *Int J Solids Struct* 38:2487–2501
5. Mauritsson K, Folkow PD, Boström A (2011) Dynamic equations for a fully anisotropic elastic plate. *J Sound Vib* 330:2640–2654
6. Mauritsson K, Boström A, Folkow PD (2008) Modelling of thin piezoelectric layers on plates. *Wave Motion* 45:616–628
7. Hägglund AM, Folkow PD (2008) Dynamic cylindrical shell equations by power series expansions. *Int J Solids Struct* 45:4509–4522
8. Okhovat R, Boström A (2012) Dynamic equations for a spherical shell. In: Eleventh international conference on computational structural technology, Dubrovnik. Civil-Comp Press
9. Eriksson AS, Mattsson J, Niklasson AJ (2000) Modelling of ultrasonic crack detection in anisotropic materials. *NDT E Int* 33:441–451

# Chapter 71

## Expansion of Nonlinear System Response Using Linear Transformation Matrices from Reduced Component Model Representations

Tim Marinone, Louis Thibault, and Peter Avitabile

**Abstract** Finite element models of structural systems have become increasingly complicated as they are used for many types of applications. Because a highly detailed model is not required for every purpose, much work has been presented in generating reduced-order models (ROMs) that accurately reflect the dynamic characteristics of the system. Recent work has shown that these ROMs can be used to compute both the linear and nonlinear dynamic response of the structure at the reduced space without loss of accuracy due to the reduction procedures.

Although computationally beneficial to calculate dynamic response at drastically reduced space, there are significant advantages in expanding the response out to the full-field solution. Much work has been focused on the expansion of linear dynamic solutions for improved visualization. This work builds on previous efforts and demonstrates that the transformation matrix generated from the linear model can be used to accurately expand the nonlinear dynamic response; this is true for component as well as system models. Both analytical and experimental cases are examined to demonstrate the accuracy of this technique.

**Keywords** Nonlinear analysis • Efficient computation • Model reduction • Test-verified results • Dynamic response

### Nomenclature

*Symbols:*

<i>Matrix</i>		<i>Subscript</i>	
[M]	Analytical Mass Matrix	1	State 1
[K]	Analytical Stiffness Matrix	2	State 2
[C]	Physical Damping Matrix	12	State 1–2
[U]	Analytical Modal Matrix	i	Row i
[ $\bar{M}$ ]	Diagonal Modal Mass Matrix	j	Column j
[ $\bar{K}$ ]	Diagonal Modal Stiffness Matrix	n	Full Set of Finite Element DOF
[ $\bar{C}$ ]	Diagonal Modal Damping Matrix	a	Reduced Set of DOF
[T]	Transformation Matrix	d	Deleted (Omitted) Set of DOF
[E]	Experimental Modal Vectors	U	SEREP
[I]	Identity Matrix	<i>Superscript</i>	
<i>Vector</i>		T	Transpose
{e}	Experimental Mode Shape	g	Generalized Inverse
{p}	Modal Displacement	k	kth Degree of Freedom
{F}	Force	–1	Standard Inverse

---

T. Marinone (✉) • L. Thibault • P. Avitabile  
 Structural Dynamics and Acoustic Systems Laboratory, University of Massachusetts Lowell,  
 One University Avenue, Lowell, MA 01854, USA  
 e-mail: [timothy.marinone@gmail.com](mailto:timothy.marinone@gmail.com); [louishthibault@gmail.com](mailto:louishthibault@gmail.com); [peter.avitabile@uml.edu](mailto:peter.avitabile@uml.edu)

{u}	Analytical Mode Shape	A	Component A
{x}	Physical Displacement	B	Component B
{ $\dot{x}$ }	Physical Velocity	AB	System AB
{ $\ddot{x}$ }	Physical Acceleration	<i>Variable</i>	
{t}	Time Vector	$\Delta t$	Time Step
		$\zeta$	Modal Damping

## Acronyms:

ADOF	Reduced Degrees of Freedom
DOF	Degrees of Freedom
ERMT	Equivalent Reduced Model Technique
FEM	Finite Element Model
MAC	Modal Assurance Criterion
MMRT	Modal Modification Response Technique
POC	Pseudo-Orthogonality Check
SEREP	System Equivalent Reduction Expansion Process
TRAC	Time Response Assurance Criterion

## 71.1 Introduction

Finite element models of structural systems are often composed of thousands to millions of degrees of freedom (DOF) and are used for many different applications. Analysts want the model to reflect the physical structure as closely as possible, which often requires both modeling using nonlinear elements as well as using test data to verify the model. Because the analyst is under increasing time constraints, there is also a simultaneous interest in generating an efficient model that can be solved very quickly. In order to combine these requirements, reduced order, test verified components are typically used for much of this work.

Even though these reduced order models (ROMs) satisfy the requirements described above, a main disadvantage of ROMs is that they only provide information at the limited number of degrees of freedom (ADOF), and do not provide the full space solution (NDOF). As a result, the transformation matrix used in creating the ROM can also be used to expand the information from ADOF to NDOF at a very low computation cost. Although most of the work in this area has been on expansion of linear mode shapes, Chipman [1] demonstrated that real time operating data could also be expanded using the same transformation matrix, which allowed a better visualization of the response. Pingle et al. [2] further studied this work and demonstrated that linear displacement results from either a model or test data could also be expanded out and used for further post-processing such as strain.

Although this work has been useful for many applications, a variety of models and physical structures are nonlinear in nature. Due to the complex nature of these nonlinear models, the computation time of these models increases drastically, this makes them unwieldy to use. Recent work by Thibault [3] and Marinone [4] involved the development of efficient techniques by treating the nonlinear elements as piecewise linear, which allows multiple linear models to be used depending on the state of the nonlinearity. Figure 71.1 is a schematic overview of both techniques; Equivalent Reduced Model Technique (ERMT) uses highly accurate physical space ROMs, while Modal Modification Response Technique (MMRT) uses mode superposition in conjunction with structural dynamic modification (SDM).

While both techniques were shown to be very efficient and accurate, the solution was again solved at the ADOF. Unlike the linear models which only have one transformation matrix, the nonlinear model requires reduced order components for each possible state, which requires multiple transformation matrices to be formed. This paper will show that even though the nonlinear solution may experience multiple system states, only one transformation matrix that spans the modes of interest for all states of the system is needed to expand out the nonlinear response solution from ADOF to NDOF. An overview of model reduction/expansion is provided in the theory, along with system modeling and the mode contribution matrix; this is used to identify the modes that need to be included in the transformation matrices when generating ROMs. Two cases are described in this paper. The first case is an analytical case that shows the results obtained from expanding out the ROM responses

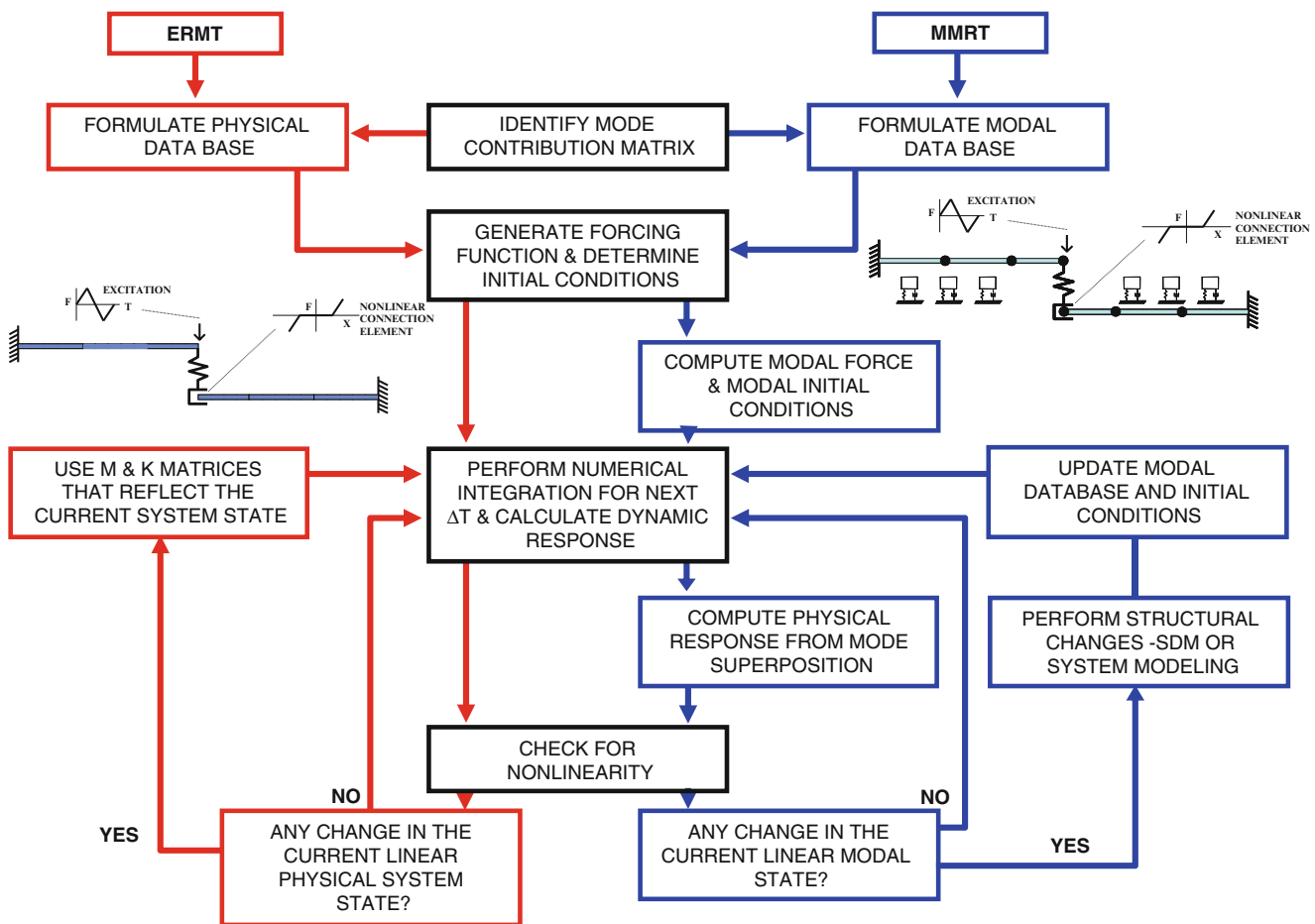


Fig. 71.1 Overview schematic of ERMT and MMRT

are equivalent to the results obtained from solving the full model. The second case is an experimental case showing that experimentally measured data can be expanded out to obtain nonlinear dynamic responses at locations that would be difficult to obtain using traditional transducers, such as rotational DOF or inaccessible locations.

## 71.2 Theory

The following section presents the theory of model reduction and system modeling needed for the development of the newly proposed methodology.

### 71.2.1 Model Reduction and Expansion

Model reduction is used to reduce the size of a large analytical model to develop a more efficient model for further analytical studies. The reduced model size also allows for model updating and correlation with test data. Model reduction is performed for a number of reasons, but is used primarily as a mapping technique for the expansion of test data. Active DOF (ADOF) are used to identify the reduced order model; in the experimental case studied, the ADOF correspond to the tested DOF. Several model reduction methods have commonly been used, which include Guyan Condensation [5], Dynamic Condensation [6], Improved Reduced System (IRS) [7], System Equivalent Reduction Expansion Process (SEREP) [8], and Hybrid-Kammer [9]. While any of these techniques could be used for model reduction, only SEREP is used within this study due to specific advantages that are discussed in the following sections.



### 71.2.2 General Transformation

To reduce a full set of finite element model (FEM) NDOF to a set of ADOF, a transformation relationship must be determined. This transformation can be written in general terms as

$$\{x_n\} = \begin{Bmatrix} x_a \\ x_d \end{Bmatrix} = [T] \{x_a\} \quad (71.1)$$

The 'n' subscript denotes the full set of FEM NDOF, the 'a' subscript denotes the active set of DOF (ADOF), and the 'd' subscript denotes the deleted set of DOF (sometimes referred to as omitted DOF); the transformation matrix [T] relates the mapping between these two sets of DOF.

Due to the laws of energy conservation, the transformation matrix can be used to reduce the mass and stiffness matrices, which are related to the full space matrices using the transformation operation given as

$$[M_a] = [T]^T [M_n] [T] \quad (71.2)$$

$$[K_a] = [T]^T [K_n] [T] \quad (71.3)$$

The equation of motion can then be written in reduced 'a' space as

$$[M_a] \{\ddot{x}_a\} + [K_a] \{x_a\} = \{F_a(t)\} \quad (71.4)$$

The eigensolution is then given by

$$[[K_a] - \lambda [M_a]] \{x_a\} = \{0\} \quad (71.5)$$

What is most important in model reduction is that the eigenvalues and eigenvectors of the original system are preserved as accurately as possible in the reduction process. If this is not maintained then the matrices are of questionable value. Reduction schemes such as Guyan Condensation [5] and Improved Reduced System (IRS) [7] are based primarily on the stiffness of the system, which results in eigenvalues and eigenvectors that are not exactly reproduced in the reduced order model. However, the System Equivalent Reduction Expansion Process (SEREP) [8] exactly preserves the eigenvalues and eigenvectors in the reduced model.

### 71.2.3 System Equivalent Reduction Expansion Process (SEREP)

The SEREP [8] transformation matrix [T<sub>U</sub>] is developed such that an eigensolution of the resultant reduced mass and stiffness matrices produces the exact frequencies and mode shapes as in the full space model. The SEREP modal transformation relies on the partitioning of the modal equations representing the physical system DOF relative to the modal DOF using

$$\{x_n\} = \begin{Bmatrix} x_a \\ x_d \end{Bmatrix} = \begin{bmatrix} U_a \\ U_d \end{bmatrix} \{p\} = [U_n] \{p\} \quad (71.6)$$

The relationship for only the ADOF is written as

$$\{x_a\} = [U_a] \{p\} \quad (71.7)$$

For the case where the number of modes used is less than or equal to the number of ADOF ( $a \geq m$ ), the [U<sub>a</sub>] matrix in (71.7) can be reformulated using a generalized inverse. This results in the least squares solution written as

$$\{p\} = ([U_a]^T [U_a])^{-1} [U_a]^T \{x_a\} = [U_a]^g \{x_a\} \quad (71.8)$$

which is then used to relate the full space DOF to the ADOF by substitution back into the modal transformation in (71.6) and gives

$$\{x_n\} = [U_n] [U_a]^g \{x_a\} = [T_U] \{x_a\} \quad (71.9)$$

Therefore, the SEREP transformation matrix  $[T_U]$  is defined as

$$[T_U] = [U_n][U_a]^g \quad (71.10)$$

The SEREP transformation matrix  $[T_U]$  is used either for the reduction of the finite element mass and stiffness matrices, as in (71.2) and (71.3), or for the expansion of experimentally measured modal vectors, which is discussed in the following section.

SEREP relies heavily on a “well developed” finite element dynamic model from which an ‘n’ dimensional eigensolution is obtained for developing the mapping between the full set of FEM NDOF and the reduced set of ADOF. The quality of the results obtained using most reduction processes depends on the selection of ADOF, however this is not a concern when using SEREP. Case studies have been performed to demonstrate the fact that an arbitrary selection of ADOF as well as an arbitrary selection of modes does not affect the mode shapes and frequencies that are preserved in the reduced model when using SEREP [8].

In the situation where the number of modes used is less than the number of ADOF retained in the reduced model ( $a > m$ ), the size of the reduced mass and stiffness matrices are ‘a’ by ‘a’, but the rank of the reduced matrices is only ‘m’. Therefore, the reduced mass and stiffness matrices are rank deficient and care must be taken when using these reduced matrices. Due to the rank deficiency that results in this scenario, a form of the SEREP reduction process that produces an exact solution can be performed by using the same number of modes as the number of ADOF ( $a = m$ ) for the reduced model.

For the case where the number of ADOF is equivalent to the number of modes retained in the SEREP reduced model, the matrices are fully ranked and well-conditioned. Because the transformation matrix  $[T_U]$  is formed from the eigenvectors of the full space finite element model, the reduced matrices preserve the eigenvalues and eigenvectors of the full space model. This implies that any collection of desired eigenvectors can be retained in an exact sense for the reduced model. This fact is significant in terms of the development of efficient models from large finite element models used for forced response studies, especially those that contain discrete nonlinear effects that are typical in joints and connections for many structural systems. The reduced models developed in this work are for the equivalent condition, where the number of modes used is equal to the number of ADOF retained in the reduction process ( $a = m$ ).

An alternate model reduction approach [10] can be used where a highly accurate reduced model is formulated using Guyan Condensation in conjunction with Analytical Model Improvement (AMI). The advantages of this technique are that the desired mode shapes are preserved in an exact sense while the fully ranked and well-conditioned system matrices obtained from the Guyan reduction scheme are also maintained in the process. Further details on this technique are discussed in the paper.

#### 71.2.4 System Modeling and Mode Contribution

Several techniques have commonly been used in structural dynamic studies for generating system models from both analytical and experimental component model representations for a variety of applications. These techniques include physical, modal, frequency based, and hybrid system modeling methods. The proposed approach utilizes system models to represent nonlinear contact and component interconnections as piecewise linear approximations at each time step throughout the forced nonlinear response solution. In this work, a physical to physical system modeling approach is utilized for the cases studied that involve multiple components that can interconnect with one another in a variety of different configurations. Full space physical system models are used to develop a reference solution where the accuracy of the system model is not affected by modal truncation. The mass and stiffness matrices of the full space component models that are used to develop system models are first arranged into a common matrix space, which is shown in Fig. 71.2.

After the component matrices are arranged into common matrix space, accurate system models are developed for all potential configurations that can occur as the system responds to an input excitation over the frequency range that participates in the system response. The component mass and stiffness matrices can be connected together using coupling or tie matrices, which apply a specified mass or stiffness value that couples a DOF of one component to a DOF of another component. In this work, only stiffness tie matrices are used to demonstrate the proposed methodology; mass effects are also easy to include with this formulation. The equation of motion can then be reformulated in terms of system matrices as

$$\left[ \begin{bmatrix} [M_n^A] \\ [M_n^B] \end{bmatrix} \right] \left\{ \begin{matrix} \{\ddot{X}_n^A\} \\ \{\ddot{X}_n^B\} \end{matrix} \right\} + \left[ \begin{bmatrix} [K_n^A] \\ [K_n^B] \end{bmatrix} + [K^{TIE}] \right] \left\{ \begin{matrix} \{X_n^A\} \\ \{X_n^B\} \end{matrix} \right\} = \left\{ \begin{matrix} \{f_n^A\} \\ \{f_n^B\} \end{matrix} \right\} \quad (71.11)$$

**Fig. 71.2** Full space component models arranged into common matrix space

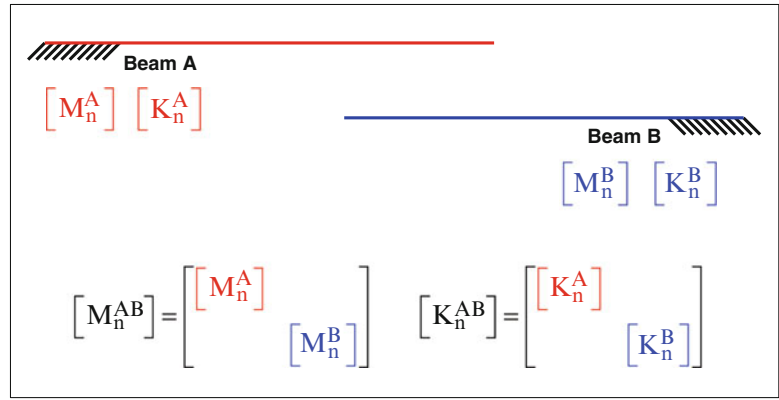
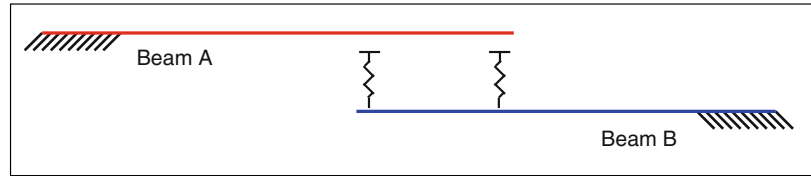


**Fig. 71.3** Two component system with two contacts



To illustrate the physical system modeling methodologies employed, the system model formulations that are developed for a two component system with two potential contact locations is discussed below. Figure 71.3 shows the two component system with two contact locations.

By further examination of the system in Fig. 71.3, three possible system configurations can be formed during the event that transient response occurs. For configuration 1, only the tip of Beam A is in contact with Beam B. For configuration 2, only the tip of Beam B is in contact with Beam A. For configuration 3, both contacts are engaged. Therefore, three system models need to be developed using a stiffness tie matrix to connect the components together in each system configuration, which is shown in Fig. 71.4.

Note that small deflection theory is utilized in these analyses where the beams are shown in an exaggerated deformed state for illustrative purposes only. Large geometric displacements are not considered in this analysis for the assembled system configurations shown in Fig. 71.4.

An eigensolution is then computed for each system model using the assembled full space mass and stiffness matrices to obtain the mode shapes and frequencies of each system model. The full space system models are then considered for reduction to a set of ADOF using SEREP. However, to ensure that the reduced models are minimally affected by modal truncation when assembling the system models using multiple reduced component models, the contribution of component modes in the assembled system modes is computed using

$$\text{Mode Contribution} = \begin{bmatrix} [U_n^A] \\ [U_n^B] \end{bmatrix}^T [M_n^{AB}] [U_n^{AB}] \quad (71.12)$$

where  $[U_n^A]$  is the matrix of full space FEM mode shapes for component A,  $[U_n^B]$  is the matrix of full space FEM mode shapes for component B,  $[M_n^{AB}]$  is the full space FEM mass matrix for system AB, and  $[U_n^{AB}]$  is the matrix of full space FEM mode shapes for a particular system AB configuration. Note that the system mass matrix  $[M_n^{AB}]$  is the same for all system configurations; only the stiffness matrices are modified in the system model assembly process in this work but mass can easily be added to the set of equations. Details pertaining to the approach used for identifying key contributing modes in the ROMs developed in this work are provided in [3] and [11].

The resulting mode contribution matrix is the key to identifying the necessary set of component modal vectors needed to accurately form the final modified system modes. This is similar to the  $[U_{12}]$  matrix that is computed in the Structural Dynamic Modification (SDM) [12] methodology, which is used to identify the modes of the initial unmodified system state that contribute in the modes of the final modified system state. The  $[U_{12}]$  matrix or mode contribution matrix contains the scaling coefficients needed to form the final modified set of modes  $[U_2]$  from the initial unmodified set of modes  $[U_1]$ . The  $[U_2]$  matrix is written in matrix form as

$$[U_2] = [U_1] [U_{12}] \quad (71.13)$$

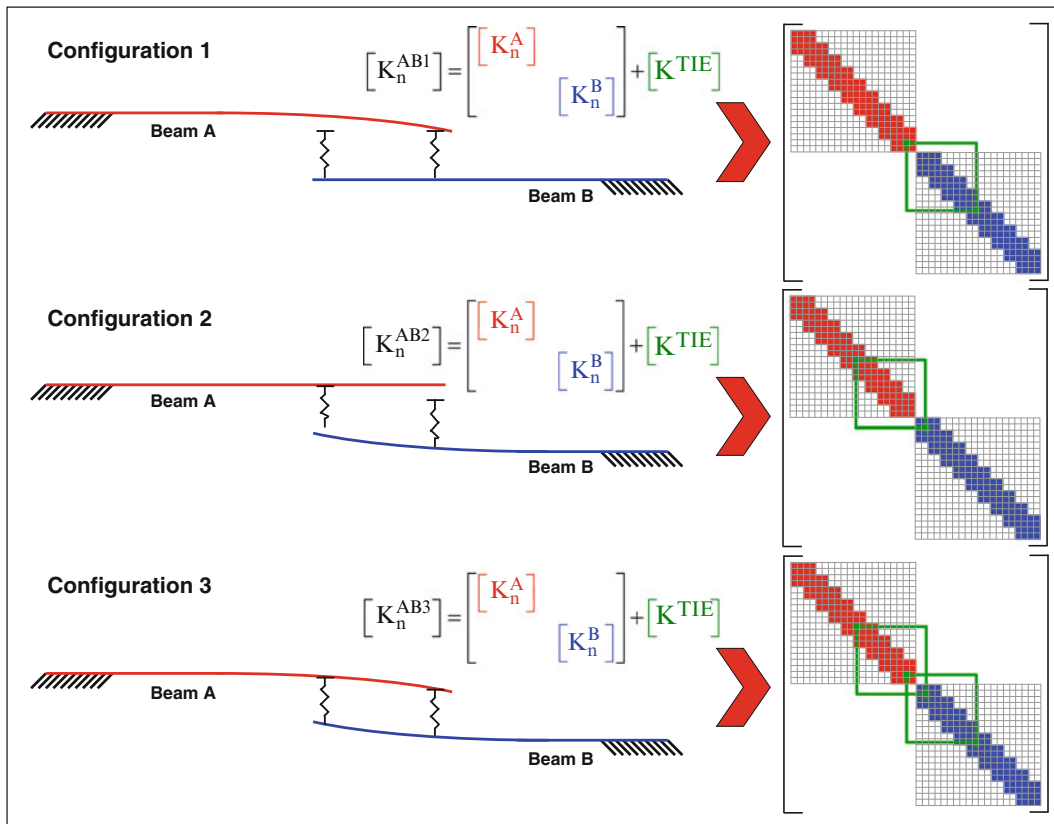


Fig. 71.4 Stiffness matrix formulation for potential system configurations

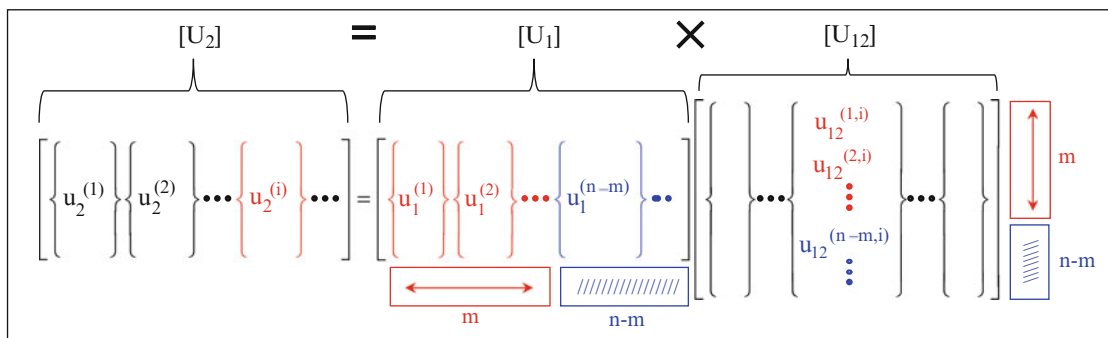


Fig. 71.5 SDM process using  $[U_{12}]$  matrix

Figure 71.5 illustrates the contribution of the  $[U_{12}]$  matrix in forming the final modified system modes  $[U_2]$ . The 'ith' modified system mode of  $[U_2]$  is formed from 'm' modes of the  $[U_1]$  matrix multiplied by the first 'm' scaling coefficients of the 'ith' column in the  $[U_{12}]$  matrix; these are the red terms shown in Fig. 71.5 and are listed in the following equation.

$$\{u_2\}^{(i)} = \{u_1\}^{(1)} U_{12}^{(1i)} + \{u_1\}^{(2)} U_{12}^{(2i)} + \dots \quad (71.14)$$

While the arrangement of modes are shown sequentially for convenience, only modes that are required in forming the 'm' set of modes need to be included and may not necessarily be sequential. Because all of the 'n' modes are not required in computing the 'ith' system mode of  $[U_2]$ , the 'n-m' modes shown in blue can be excluded.

The mode contribution matrix is then plotted for visual identification of key contributing component modes that are needed to form the system modes. For the two component system with two contact locations, three separate mode contribution matrices need to be computed (one for each system configuration). An example of the mode contribution matrix formulation

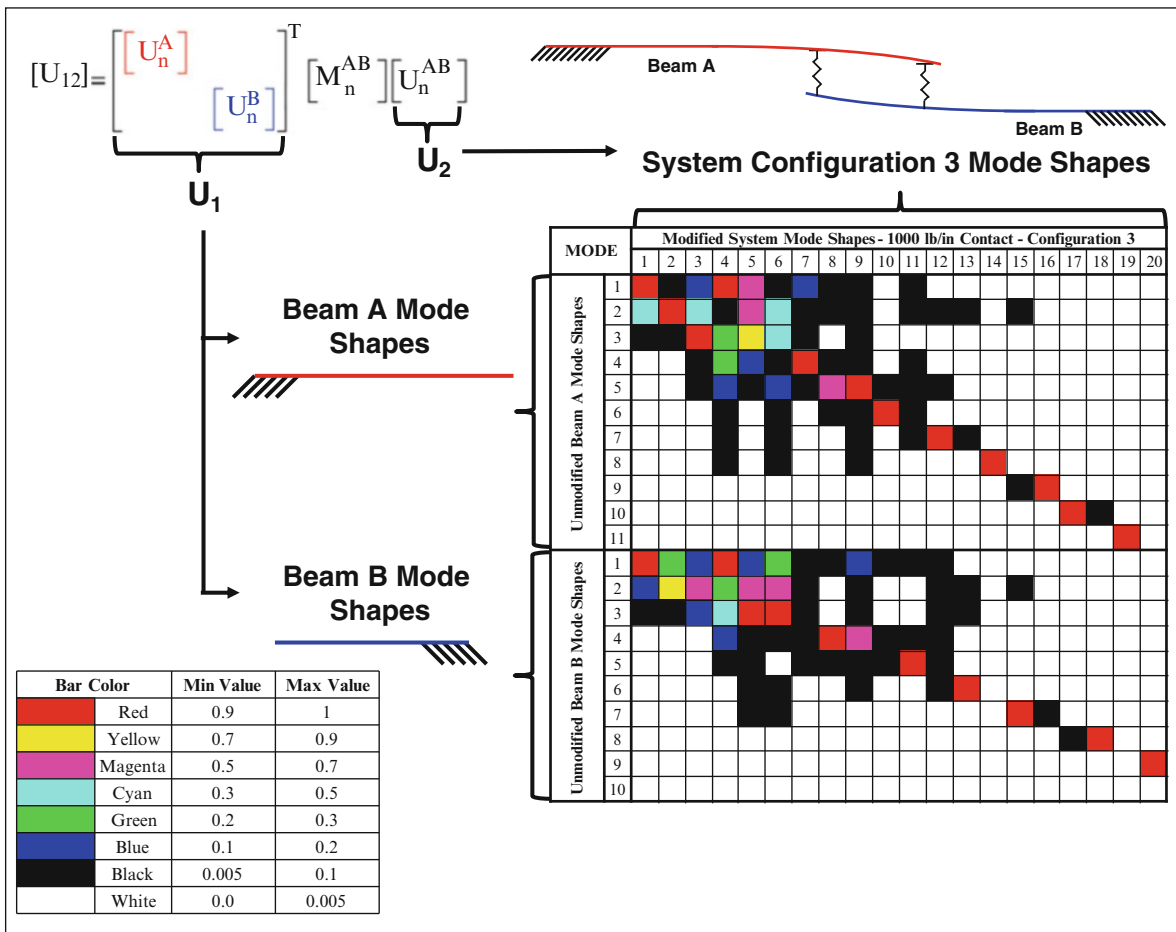


Fig. 71.6 Two beam system configuration 3 mode contribution matrix formulation

for system configuration 3 is shown in Fig. 71.6. The various box colors in the mode contribution matrix indicate the amount that each unmodified component mode contributes in a particular modified system mode. Red boxes indicate high levels of contribution, where white boxes indicate minimal or no contribution. The actual contribution ranges for each color are provided in the legend in Fig. 71.6.

To illustrate how the system modes are formed from linear combinations of component modes, the contributing component modes that are needed to form mode 1 for system configuration 3 is shown in Fig. 71.7. The system modes are represented by columns of the mode contribution matrix and the unmodified component modes that are needed to form the system modes are identified along the rows of the mode contribution matrix.

Once the component modes that contribute in each of the system configurations are identified using the mode contribution matrices, the full space system models are reduced to a set of ADOF using SEREP. The model reduction process is shown in Fig. 71.8 for the system configuration 3 model, where the red points indicate the ADOF retained in the reduced order models. The number of ADOF are equal to the number of modes retained in the reduced order models, which preserves the mode shapes and frequencies of the full space component models in an exact sense for the reduced component models. Note that for the  $a = m$  case, the quality of the reduced model results obtained using SEREP does not depend on the selection of ADOF and that an arbitrary selection of ADOF as well as an arbitrary selection of modes is permitted.

The reduced system mass and stiffness matrices are then used in the direct integration process for computing the forced nonlinear response, where the equation of motion can be written in reduced space as

$$[M_a^{AB}] \{\ddot{x}_a^{AB}\} + [K_a^{AB}] \{x_a^{AB}\} = \{f_a^{AB}\} \tag{71.15}$$

The  $[M_a^{AB}]$  and  $[K_a^{AB}]$  matrices reflect the system state at each instance in time of the system response.

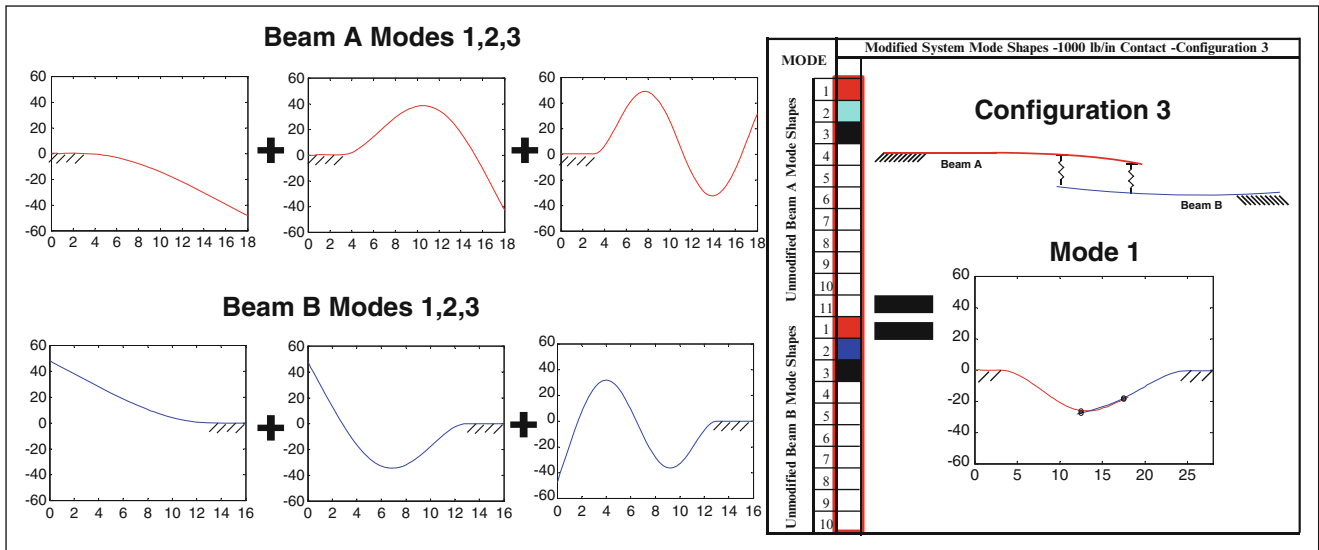
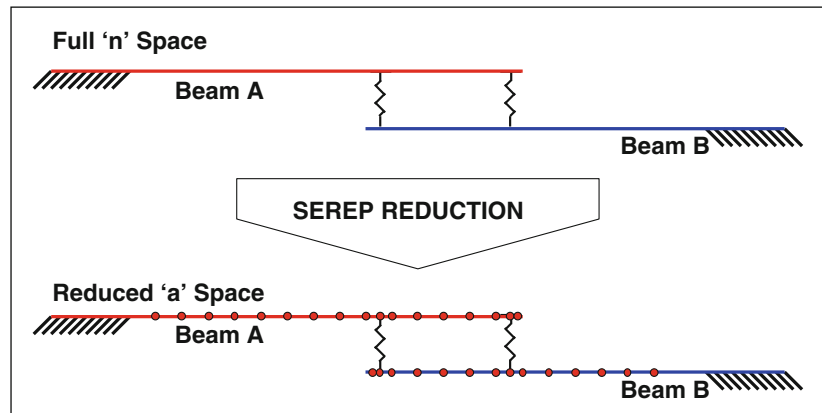


Fig. 71.7 Component mode identification for mode 1 of system configuration 3

Fig. 71.8 SEREP reduction of two beam system configuration 3 model



### 71.2.5 Mode Shape and Time Response Data Expansion/Smoothing Process

The expansion of experimentally measured mode shapes is often performed to obtain a full space representation of the mode shape. This is advantageous in cases where the responses at unmeasured translational or rotational DOF are desired, but cannot be measured due to limitations of accessibility, equipment availability, etc. For most of the expansion techniques such as Guyan Condensation [5], Dynamic Condensation [6], and IRS [7], the original data is not modified in the development of the expanded mode shape. The transformation matrix [T] developed using these techniques contains an identity [I] matrix in the ADOF modal vector partition, which implies that the original data is accurate as measured, but this is rarely the case. Therefore, smoothing of the measured data is necessary to remove typical contaminants that exist in any set of measured data. The SEREP expansion process provides the smoothing techniques required to minimize the contaminants that exist in experimentally measured data.

The SEREP transformation matrix [T<sub>U</sub>] given in (71.10) is used to expand and smooth experimentally measured mode shapes from the reduced set of ADOF to the full set of FEM NDOF as

$$[E_n] = [T_U][E_a] \tag{71.16}$$

where [E<sub>a</sub>] is the matrix of experimentally measured mode shapes and [E<sub>n</sub>] is the matrix of expanded and smoothed test mode shapes.

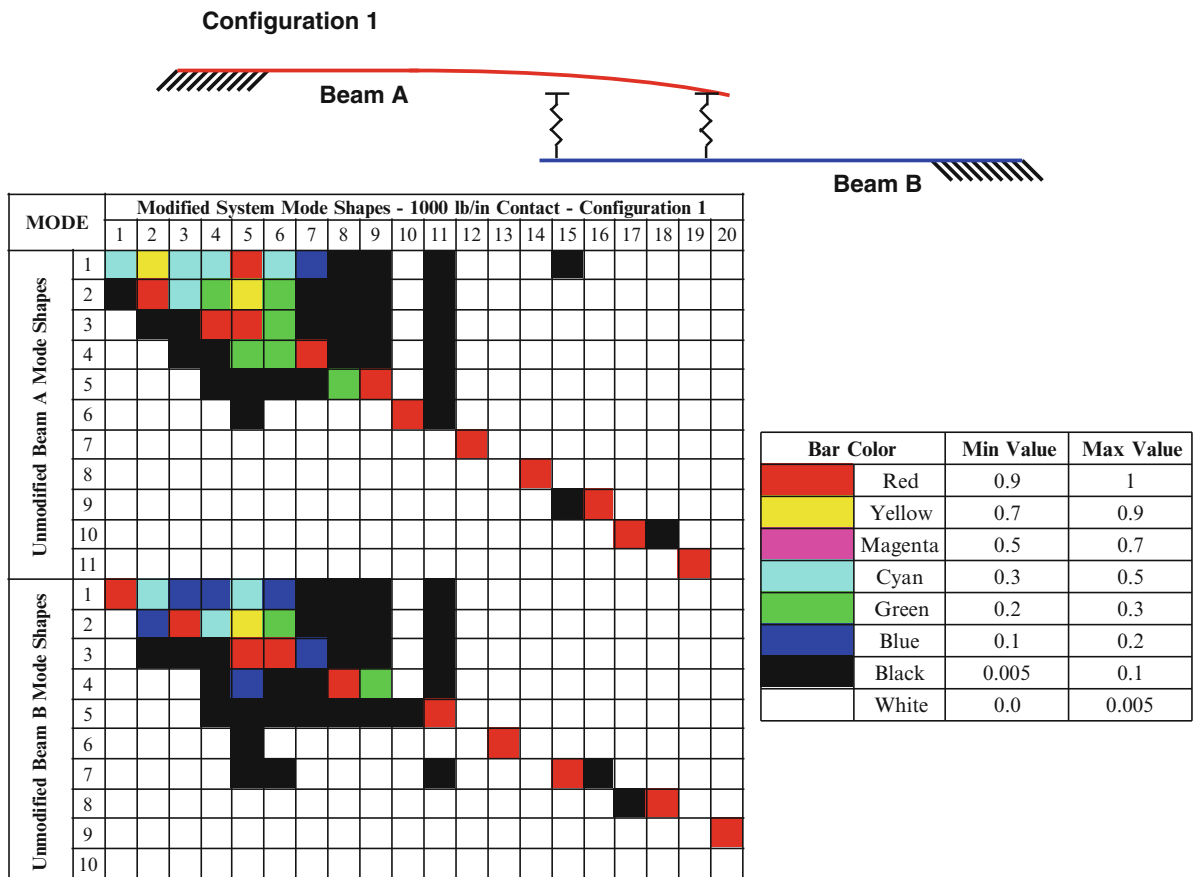


Fig. 71.9 Two beams with hard contacts config. 1 mode contribution matrix

This mode shape expansion technique can also be applied to time response data, where the operating deflection shape (ODS) is expanded at each time step from the reduced set of measured ADOF to the full set of FEM NDOF as

$$\{x_n\} = [T_U]\{x_a\} \tag{71.17}$$

where  $\{x_a\}$  is the vector of measured displacements at the reduced set of ADOF for a particular instance in time and  $\{x_n\}$  is the vector of expanded and smoothed test displacements for the time instant. This has been performed in previous work by Chipman [1] with real time operating data for improved visualization. This technique was developed further by Pingle [13–15] to obtain FEA full field response from limited sets of measured data and then further to obtain full field dynamic stress-strain.

### 71.2.6 Use of Mode Contribution Matrix for Expanding Time Response Data

As described previously, the mode contribution matrix is of critical importance in order to determine the number of modes that are needed to form the final system mode shapes. Because each potential system configuration requires a unique set of modes that can be formed in linear combinations, a unique mode contribution matrix is formed for each configuration. Figures 71.9, 71.10 and 71.11 show the three possible mode contribution matrices for a two beam system with two possible points of contact.

Although each mode contribution matrix is different, the left hand side of the matrices shows that all potential system modes are formed from the original modal database, although the contribution from each mode changes depending on the configuration. As a result, the transformation matrix that contains the original component mode shapes has the necessary information to expand any of the possible states of the system. In order to expand time response data, however, the

### Configuration 2

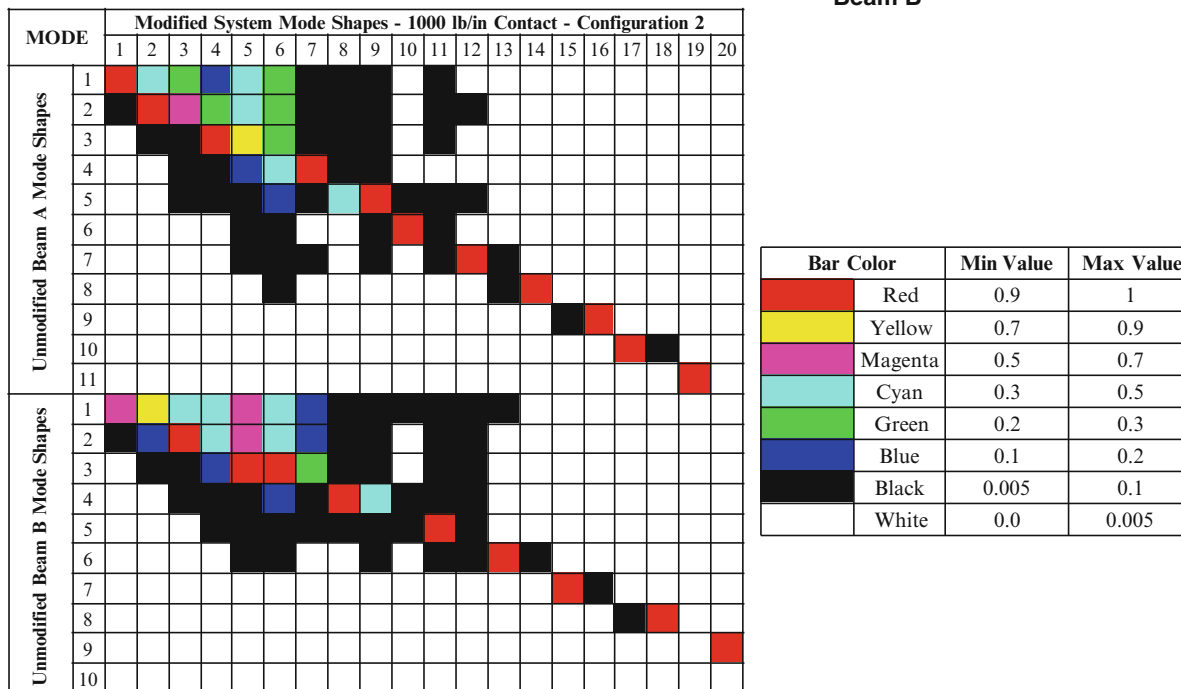
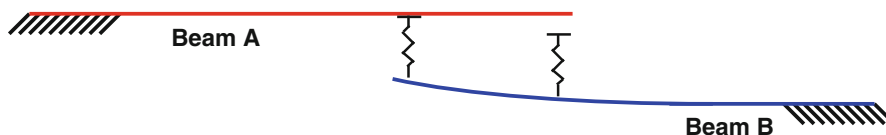


Fig. 71.10 Two beams with hard contacts config. 2 mode contribution matrix

transformation matrix used must contain an appropriate selection of modes that are needed for accurately forming the potential system modes. This was demonstrated by Thibault et al. [16], who showed that an imperfect FEM could be used to accurately expand test data provided that a sufficient selection of modes were included in the transformation matrix developed from the FEM; details of the VIKING technique are beyond the scope of this paper and is discussed in greater detail in [16].

There are two key statements in the theory listed above that allow the work listed in this paper to be performed.

1. The time response solution can be expanded out to full space using the transformation matrix developed from the mode shapes. This has been demonstrated by Chipman [1] and Pingle et al. [2] for linear cases.
2. An imperfect transformation matrix can be used to expand test data correctly provided sufficient modes are included. This was demonstrated by Thibault et al. [16] who accurately expanded mode shapes with an imperfect transformation matrix.

As a result of these two statements, the following statement can be developed. An imperfect transformation matrix (one obtained from linear reduction of components) can be used to expand a nonlinear time solution (one formed from a different set of modes at a given time) provided sufficient modes are included. This will be demonstrated with an analytical and experimental case study in the following section.

## 71.3 Model Description and Cases Studied

### 71.3.1 Model Description

Due to the complexity of the nonlinearities introduced into actual structural systems, a representative structure was fabricated to demonstrate the proposed technique. The laboratory structure is comprised of two cantilevered aluminum beams that are mounted to a common frame and base plate, as shown in Fig. 71.12. Beam A is shown in red and Beam B is shown in blue



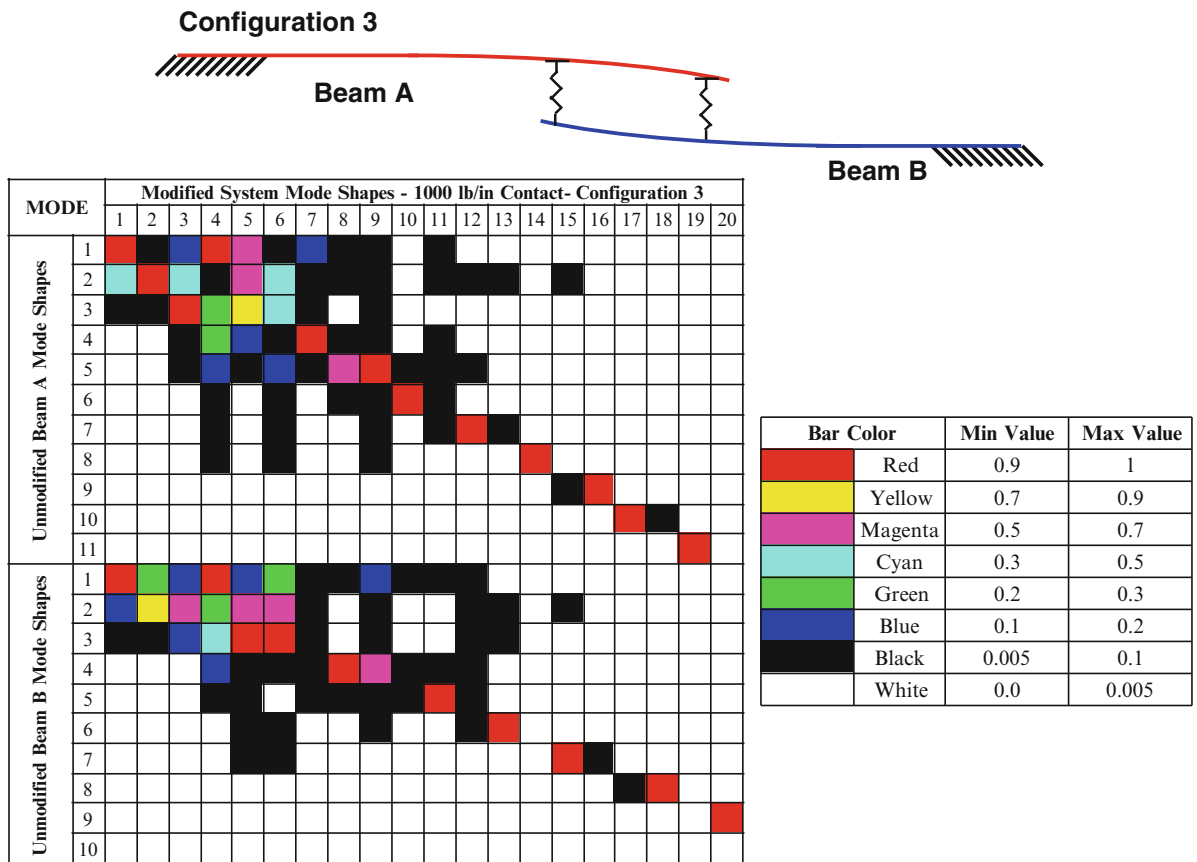
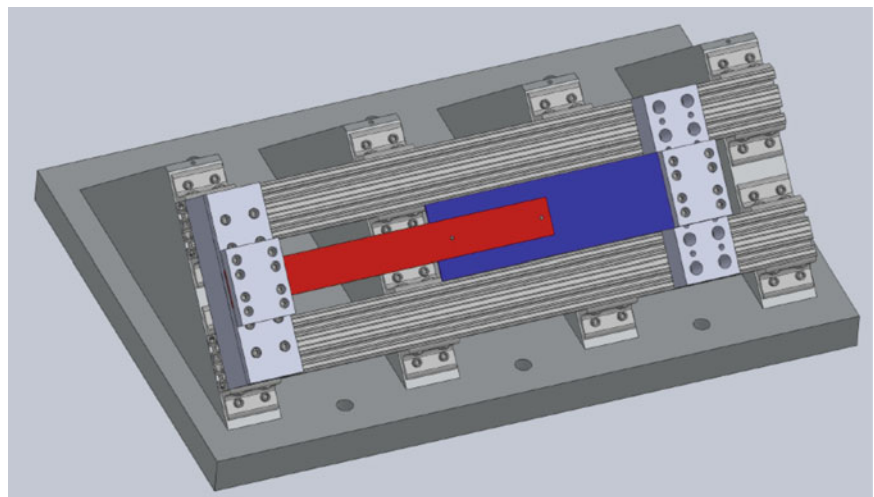


Fig. 71.11 Two beams with hard contacts config. 3 mode contribution matrix

Fig. 71.12 Laboratory structure representation of contact nonlinearities



to distinguish the two components apart from one another. This structure was designed to be a simplified representation of a typical structural system that contains various contact and component interconnection features, such that the forced nonlinear response of the system would have similarities to real-world structures of interest.

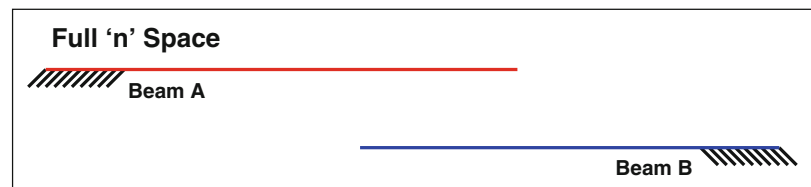
Two planar beam element models were generated using MAT\_SAP [17], which is a finite element modeling (FEM) program developed for MATLAB [18]. Each beam model is clamped for 3 in. of their length using translational and rotational springs to replicate the cantilevered boundary condition that is applied in the actual test fixture shown in Fig. 71.12. Table 71.1 lists the dimensions, material properties, and modeling characteristics of the beam component models.

**Table 71.1** Beam model characteristics

Property	Beam A	Beam B
Length (in.)	18	16
Width (in.)	2	4
Thickness (in.)	0.123	0.123
# of elements	72	64
# of nodes	73	65
# of DOF	146	130
Node spacing (in.)	0.25	0.25
Material	Aluminum	Aluminum
Density (lb/in <sup>3</sup> .)	0.098	0.098
Young's Modulus (Msi)	10	10

**Table 71.2** Natural frequencies of beam models

Mode #	Frequency (Hz)	
	Beam A	Beam B
1	12.915	22.625
2	84.119	141.561
3	252.339	396.604
4	519.587	776.916
5	806.163	1,284.714
6	1,256.551	1,918.277
7	1,682.965	2,678.333
8	2,201.360	3,563.885
9	2,755.524	4,572.697
10	3,510.011	5,707.037

**Fig. 71.13** Schematic of full space linear beam models

An eigensolution was then computed for the component models. Table 71.2 lists the natural frequencies for the first ten bending modes of each beam component model, where bending about the weaker axis is implied. Torsional modes are not included because the input excitation and nonlinear contact locations are assumed to occur along the centerline of the beams.

The cantilevered beam component models developed were assembled into common matrix space as a linear system, which was discussed previously and is shown in Fig. 71.13. Note that the FEM nodes for 3 in. of each beam are clamped for the cantilevered boundary condition that was applied using  $10E^6$  lb/in. translational springs and  $10E^6$  lb-in./rad rotational springs. This was performed to simulate the boundary condition that exists on the actual test fixture, where the beams are clamped between a top plate and a base block. Translational and rotational springs were used to allow for fine-tuning of the models in order to account for possible flexibility of the test fixture if this was a concern for the cases where test data is introduced.

The full space linear component models were then reduced down to 'a' space using SEREP where the ADOF were selected to correspond with transducer locations on the actual tested structure. SEREP reduction was performed for the case where the number of ADOF and modes retained in the reduced order models are equal. Therefore, the selection of ADOF does not affect the reduced model characteristics. In addition, the DOF at potential contact locations were retained in the reduction process in order to formulate system models for possible contact configurations. The full space and reduced space component models are shown in Fig. 71.14, where the red points indicate the ADOF retained in the reduced order models and the black arrow denotes the force pulse input location, which is at DOF 105 of Beam A. The ADOF and modes retained in the reduced component models are listed in Table 71.3. Note that only translational DOF were retained in the reduced component models.

An analytical force pulse was designed to be frequency band-limited, exciting modes up to 1,000 Hz while minimally exciting higher order modes. The force pulse was applied at DOF 105 of Beam A for all analytical cases studied. The force pulse input DOF was selected to avoid being located at the node of a mode, where minimal response of a particular mode could result.

**Fig. 71.14** Full space and reduced models with force pulse input location

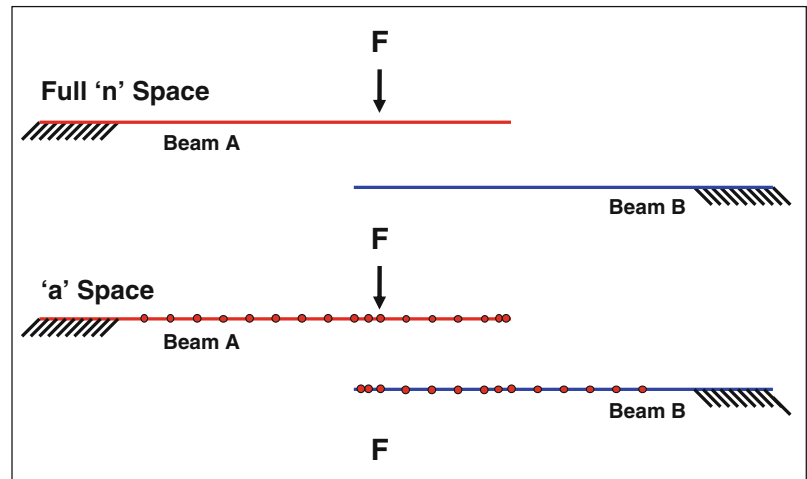


**Table 71.3** ADOF and modes retained in reduced beam models

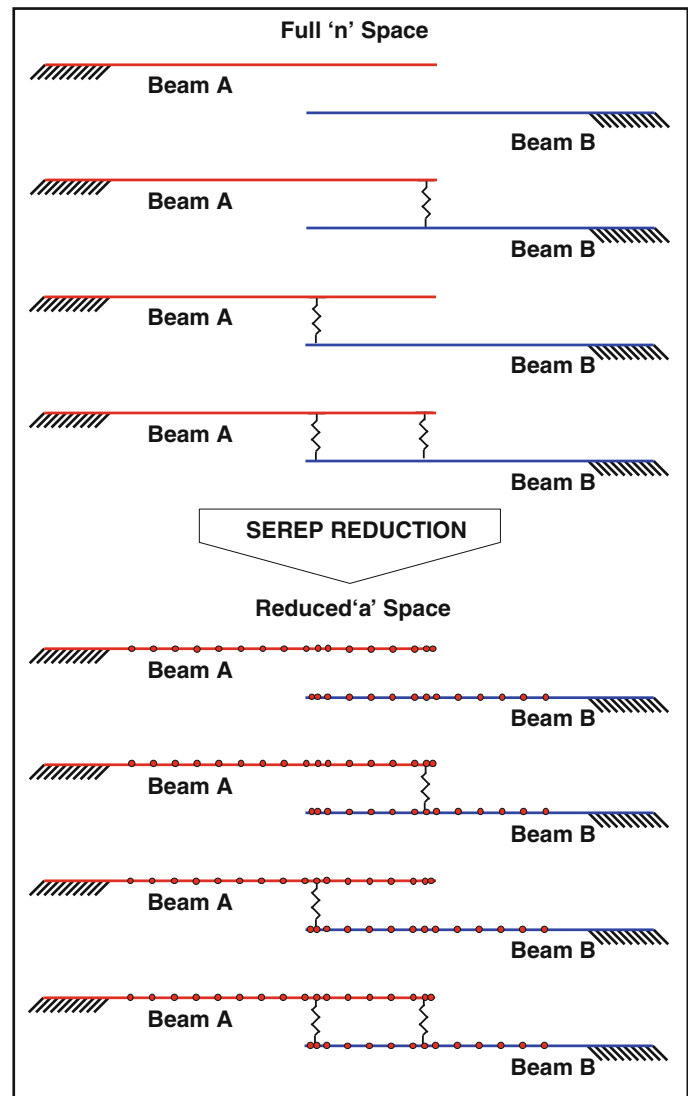
Reduced model	# of DOF	Retained modes	Retained DOF
Beam A	17	1–17	33,41,49,57,65,73,81,89,97,101,
'a' space			105,113,121,129,137,141,143
Beam B	14	1–14	149,151,155,163,171,179,187,
'a' space			191,195,203,211,219,227,235

**Table 71.4** Natural frequencies for two beams with multiple hard contacts – potential system configurations 1, 2, and 3

Mode #	Frequency (Hz)				
	Modified system – hard contacts			Unmodified components	
	Config. 1	Config. 2	Config. 3	Beam A	Beam B
1	21.254	15.496	36.217	12.915	22.625
2	67.744	69.517	113.686	84.119	141.561
3	127.044	119.785	228.570	252.339	396.604
4	236.020	234.136	312.678	519.587	776.916
5	338.309	325.850	339.402	806.163	1,284.714
6	424.257	467.087	504.557	1,256.551	1,918.277
7	532.039	527.491	532.406	1,682.965	2,678.333
8	786.594	786.040	790.327	2,201.360	3,563.885
9	809.246	828.779	833.736	2,755.524	4,572.697
10	1,256.688	1,257.170	1,257.216	3,510.011	5,707.037
11	1,294.656	1,290.027	1,300.104	–	–
12	1,682.968	1,686.002	1,686.011	–	–
13	1,918.723	1,920.049	1,920.475	–	–
14	2,201.525	2,202.671	2,202.844	–	–
15	2,683.897	2,678.847	2,684.381	–	–
16	2,755.784	2,756.010	2,756.282	–	–
17	3,510.464	3,511.344	3,511.794	–	–
18	3,564.138	3,563.976	3,564.234	–	–
19	3,948.794	3,948.545	3,948.795	–	–
20	4,575.186	4,572.697	4,575.187	–	–

When computing the system response to the input force pulse using the Newmark direct integration method [19], the initial conditions defined at time  $t = 0$  were zero initial displacement and zero initial velocity. The time step ( $\Delta t$ ) used was 0.0001 s. An additional parameter that was used in the direct integration process was damping. For the analytical models developed in this work, the modal damping  $\zeta$ , for all component modes as well as for all system modes was assumed to be 1% of critical damping.

**Fig. 71.15** Full space and reduced 'a' space models for two beams with multiple contacts

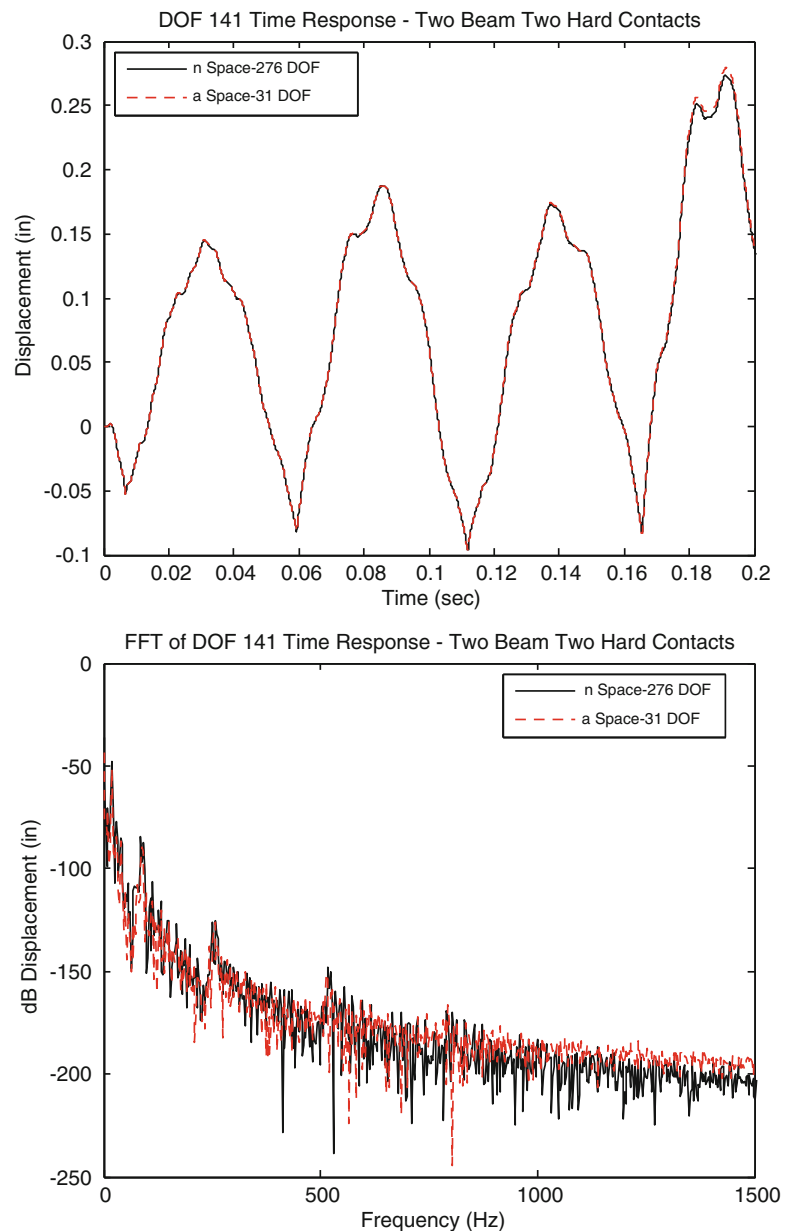


### 71.3.2 Analytical Case Study

Although many cases were studied [3], the case described here consists of Beam A coming into contact with Beam B in three different configurations at two possible contact locations once a specified gap distance is closed between Beams A and B, which is 0.05 in. for this case, as was previously shown in Fig. 71.4. Each system is a potential configuration of the two components depending on the relative displacements of the two beams where no contact is also a possible configuration.

The spring element used at the contact locations was a 1,000 lb/in. translational spring and can be considered to be a relatively hard contact for the system studied in this work. The spring stiffness is applied to the full space physical model for each system configuration and an eigensolution is computed using the modified system mass and stiffness matrices. The contact for configuration 1 occurs between DOF 141 of Beam A and DOF 191 of Beam B. The contact for configuration 2 occurs between DOF 101 of Beam A and DOF 151 of Beam B. The contact for configuration 3 occurs when both contacts for configurations 1 and 2 are closed simultaneously. The natural frequencies of the modified system configurations as well as for the unmodified components are listed in Table 71.4. Figures 71.9, 71.10 and 71.11 shows the mode contribution matrices that are used to identify the unmodified component modes that contribute in the modified system modes for system configurations 1, 2, and 3, respectively. The mode contributions are computed using full space models such that modal truncation is not of concern. The various box colors indicate the amount that each unmodified component mode contributes in a particular modified system mode; the actual contribution ranges for each color are shown.

**Fig. 71.16** Comparison of 276 DOF 'n' and 31 DOF 'a' space models for two beams with multiple hard contacts – DOF 141 time response (*top*) and FFT of time response (*bottom*)



For this case, three potential modified system configurations exist, which results in three separate mode contribution matrices. The 'a' space reduced model developed for this case retains 17 DOF and modes 1–17 of Beam A and 14 DOF and modes 1–14 of Beam B. The models developed for this case are shown in Fig. 71.15 for the full- space and reduced 'a' space models.

To confirm that the 31 DOF 'a' space models are sufficient for this case, the system response at DOF 141 is plotted in the time and frequency domain for the reduced model with comparison to the full space solution in Fig. 71.16.

The results obtained when using the 31 DOF 'a' space model can be observed to correlate very well with the full space solution in Fig. 71.16. Two different time correlation tools MAC and TRAC (Appendix 54.4) are used to quantify the similarity of the reduced model results with the full space solution. Both plots are shown in Fig. 71.17 where the y-axis scale for the MAC and TRAC plots is 0.999–1.0 so that the slight differences between the full space and reduced space solutions could be observed. The solution time for each model is listed with the average MAC and TRAC values in Table 71.5 to show the significant decrease in computation time and highly accurate results when the reduced models are used.

The solution obtained using the 'a' space model was then expanded out to 'n' space using the linear transformation matrix developed in Fig. 71.15. Figure 71.18 shows the MAC and TRAC plots over the first 0.2 s (note that the TRAC is now calculated for all 276 DOF). The y-axis scale for the MAC and TRAC plots is 0.9–1.0 so that the slight differences between

**Fig. 71.17** MAC (*top*) and TRAC (*Bottom*) comparisons between 276 DOF ‘n’ and 31 DOF ‘a’ space models for transient portion of time response (0–0.2 s) – two beams with multiple hard contacts

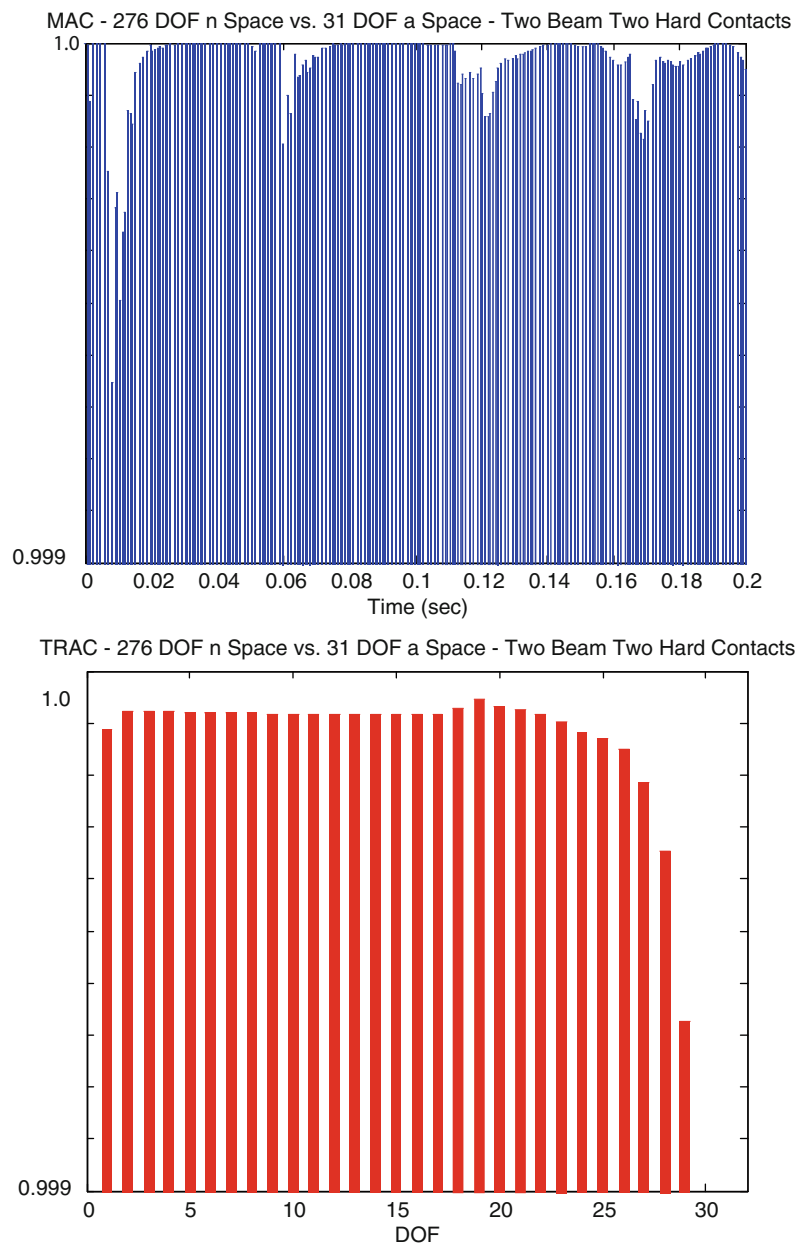


**Table 71.5** Solution times and average MAC/TRAC for two beams with multiple hard contacts – transient portion of time response (0–0.2 s)

Model	# of DOF	Solution time (s)	Average MAC	Average TRAC
‘n’ space	276	88.5	0.99996	0.99958
‘a’ space	31	4.9		
‘n’ space	276	88.5	0.99996	0.99973
‘a’ space expanded	276	5.1		

the full-space and reduced space solutions could be observed. The 276 DOF ‘a’ space expanded model for the two beam system with multiple hard contacts produces very good results as well.

The solution times for all models are listed with the average MAC and TRAC values in Table 71.5 to show the significant decrease in computation time and that highly accurate results are obtained when the reduced models are used. The favorable MAC and TRAC results in Table 71.5 show that the 31 DOF ‘a’ space model is sufficient for accurately computing the initial transient portion of the time response for this particular case. In addition, the solution time for the full-space model is 88.5 s in contrast to the reduced ‘a’ space model, which is only 4.9 s.

**Fig. 71.18** MAC (*top*) and TRAC (*bottom*) comparisons between 276 DOF ‘n’ and 276 DOF ‘a’ expanded space models for transient portion of time response (0–0.2 s) – two beams with multiple hard contacts

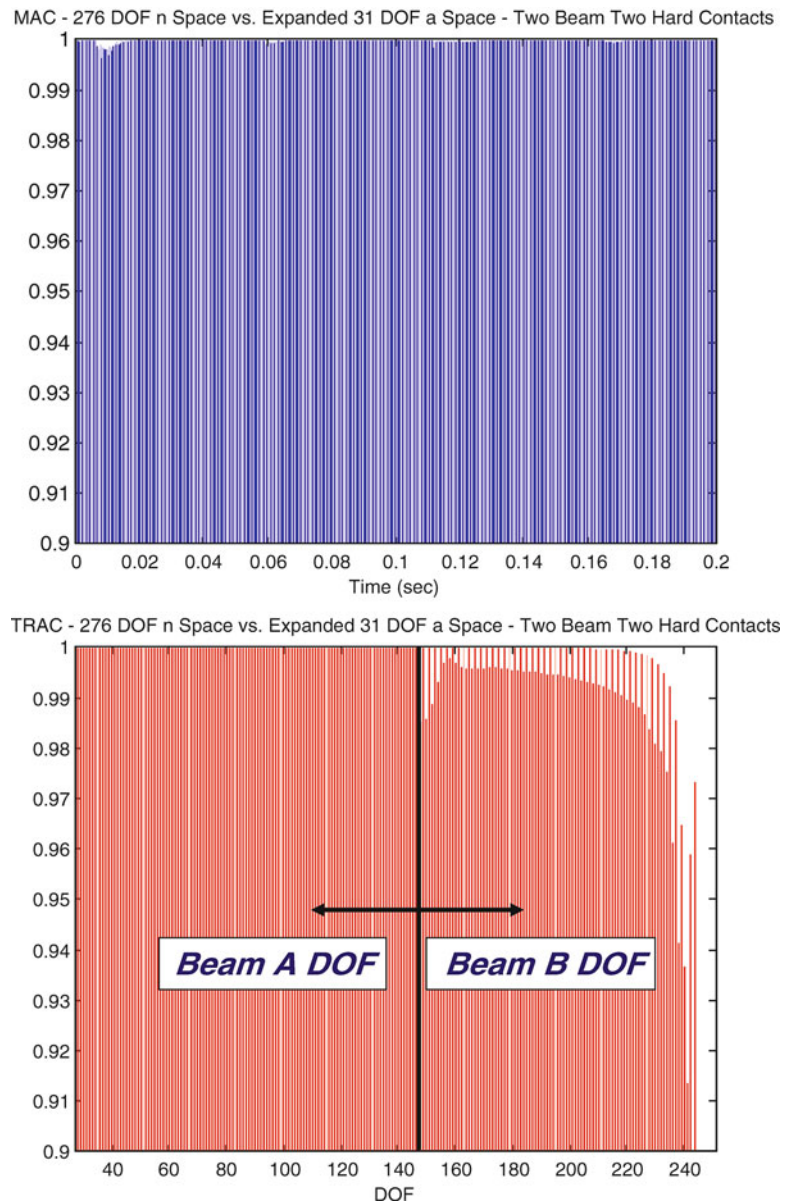


Table 71.5 also lists the average MAC and TRAC for each solution along with the solution time (the solution time for the expanded ‘a’ space is the time required to solve the ‘a’ space model and then expand to ‘n’ space). Even with the additional calculation due to multiplying the time solution by the expansion matrix, the time required is significantly reduced in comparison to the full ‘n’ space solution, going from 88.5 to 5.1 s. The average MAC and TRAC have negligible improvements because the remaining error is due to truncation which is not improved by expansion of the time responses.

Table 71.5 shows that expanding the ‘a’ space time response to ‘n’ space yielded an accurate solution while significantly reducing the time required. Rather than solving the full space solution directly, reducing the model and then expanding the solution yielded nearly identical results at a fraction of the time.

The other key point of this case study is that the nonlinear time response was achieved using the modes of the originally uncoupled component beam models. Even though the linear mode shapes used in expanding the time responses were not identical to the mode shapes used when the configuration was in a different linear state, a separate expansion matrix for each nonlinear perturbation was not required. Because a sufficient number of modes have been used to span the space of the analytical model and all perturbed nonlinear variations of the model, the expansion does not distort the data and allows for very accurate expansion for all perturbed configurations of the two beam system. As a result, the highly accurate expanded time solution was obtained very efficiently.

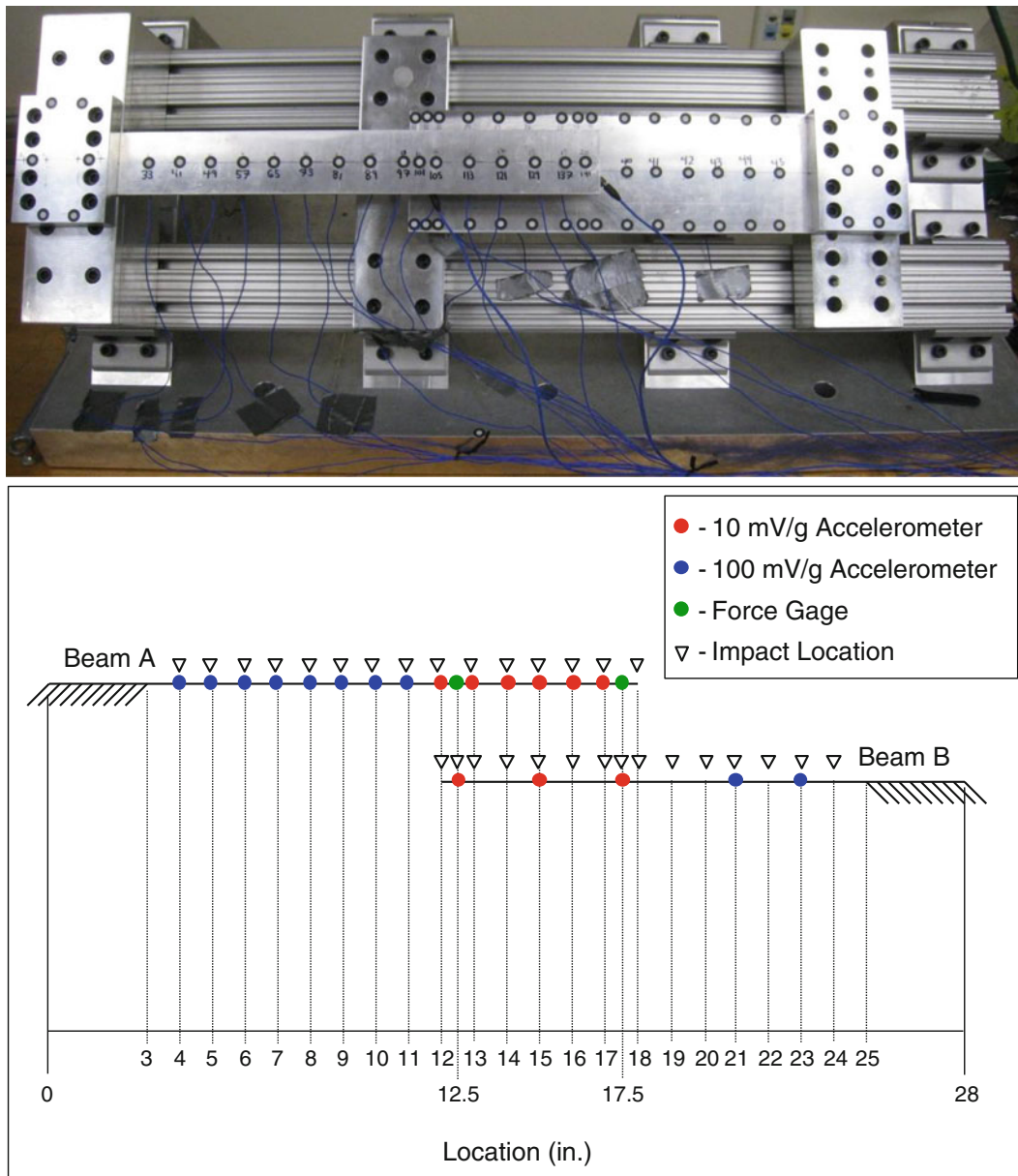


Fig. 71.19 Test bed with dimensioned schematic of impact and transducer locations

### 71.3.3 Experimental Case Study

A modal survey was conducted to determine the characteristics of the two beams when mounted to the test fixture. Modal impacts were performed at 15 points on each component, where the impact and transducer locations are shown in a dimensioned schematic in Fig. 71.19 along with the actual tested structure.

To characterize the dynamics of the beams, accelerometer measurements were acquired using LMS Test.Lab 10A [20] and 10 averages were taken for each impact point. Impacts were performed along the centerlines of the beams and only out-of-plane direction motion (normal to beam surfaces) was measured. To extract the desired modal parameters of the tested components, the experimental data was curvefit using PolyMAX [21], which is an advanced modal parameter estimation algorithm implemented within LMS Test.Lab. This provided estimations of the natural frequency, mode shape, and damping characteristics for the system, where the natural frequencies and damping values are listed in Table 71.6.

The experimentally measured mode shapes consisted of 15 ADOF per component and were expanded out to the full space FEM, which consisted of 146 DOF for Beam A and 130 DOF for Beam B. To perform this expansion, the full space



**Table 71.6** Natural frequency and damping estimates for experimental modal data

Mode #	Beam A		Beam B	
	Test frequency (Hz)	Test damping (% Crit.)	Test frequency (Hz)	Test damping (% Crit.)
1	12.850	1.100	23.400	0.440
2	84.970	0.360	144.544	0.100
3	254.270	0.490	405.093	0.090
4	519.510	0.130	797.049	0.060
5	817.240	0.150	1,315.013	0.120
6	1,234.680	0.200	—	—
7	1,637.960	0.360	—	—

**Table 71.7** Beam A correlation results

Mode #	Frequency (Hz)			Original test		Expanded test	
	Analytical	Test	Frequency (% diff.)	MAC	POC	MAC	POC
1	12.915	12.850	−0.502	0.998	0.854	0.990	0.854
2	84.119	84.970	1.001	0.999	0.969	0.999	0.969
3	252.339	254.270	0.759	1.000	1.084	0.999	1.084
4	519.587	519.510	−0.015	0.999	0.949	0.998	0.949
5	806.163	817.240	1.355	0.997	0.957	0.995	0.957
6	1,256.551	1,234.680	−1.771	0.986	0.913	0.983	0.913
7	1,682.965	1,637.960	−2.748	0.918	0.882	0.927	0.882

**Table 71.8** Beam B correlation results

Mode #	Frequency (Hz)			Original test		Expanded test	
	Analytical	Test	Frequency (% diff.)	MAC	POC	MAC	POC
1	23.029	23.400	1.585	0.993	0.919	0.910	0.919
2	144.456	144.544	0.061	0.994	0.906	0.972	0.906
3	403.340	405.093	0.433	0.991	0.954	0.863	0.954
4	791.173	797.049	0.737	0.980	0.922	0.889	0.922
5	1,308.790	1,315.013	0.473	0.952	0.910	0.870	0.910

component models were reduced down to retain the 15 tested ADOF for each component. The SEREP reduction scheme was used and therefore, 15 modes for each component were retained in the reduced models in order to formulate a fully ranked transformation matrix. This transformation matrix was then used to expand the test mode shapes out to the full space FEM set of NDOF, which smoothes and completes the measured data. Table 71.7 lists the correlation results for Beam A, while Table 71.8 lists the correlation results for Beam B. Both tables show that high correlation between the analytical and test results were obtained with minimal frequency differences (<2%).

Although multiple cases were studied [3], the case studied here is of a single beam with single contact point. A linear conical spring was mounted to a fixed block to closely resemble a translational DOF spring, as shown in Fig. 71.20. In addition, the area that the beam impacts the spring is relatively small and is a reasonable approximation of a single DOF, as shown in the red outlined image of Fig. 71.20. The base of the spring is attached to a block that is bolted to the frame of the test bed and can be assumed to be grounded, as shown in the blue outlined image of Fig. 71.20.

A force pulse was applied to the single beam using a modal impact hammer. A gap distance of 0.1715 in. was measured between the conical spring and contact thumper attached to the beam, which is shown in the red outlined image of Fig. 71.20. The conical spring was approximated as a single translational DOF stiffness located at DOF 141 and a full space modified system model was developed with the spring stiffness applied. Figure 71.21 shows the mode contribution matrix where the number of the unmodified component modes needed to form the modified system modes are able to be clearly identified. The various box colors indicate the amount that each unmodified component mode contributes in a particular modified system mode; the actual contribution ranges for each color are shown. The first eight natural frequencies of the modified system as well as for the unmodified component are listed in Table 71.9.

Accelerometers and PONTOS [22,23] targets were mounted to the test structure at several locations such that acceleration and displacement time response data could be acquired at collocated points. The system was excited by applying a force pulse into the single beam using a calibrated modal impact hammer. The experimentally measured force pulse was then input to

**Fig. 71.20** Conical spring used for single beam with single contact test case

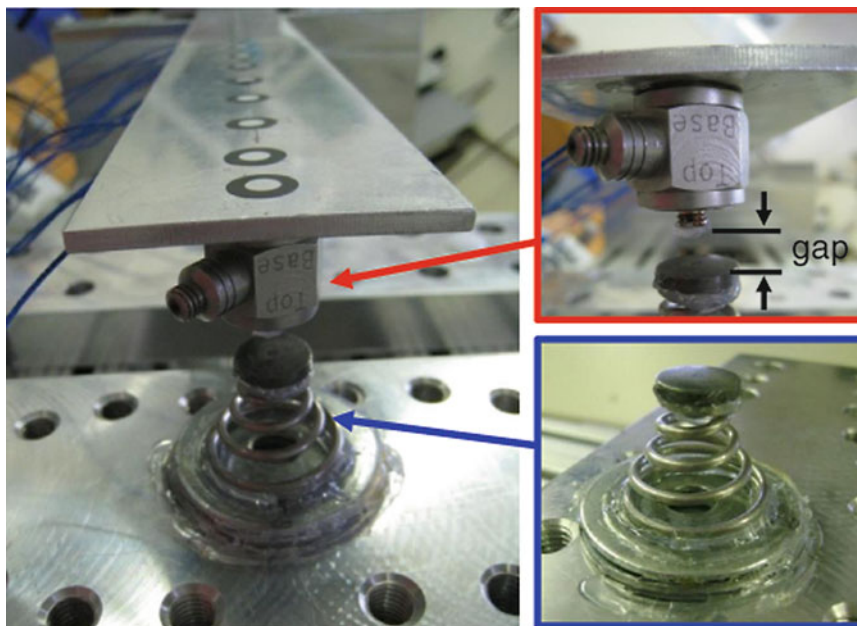


**Fig. 71.21** Mode contribution matrix for single beam with conical spring contact

MODE	Modified System Mode Shapes Conical Spring Contact									
	1	2	3	4	5	6	7	8	9	10
Unmodified Beam A Mode Shapes	1	Red	Green	Black						
	2	Green	Red							
	3	Black		Red						
	4				Red					
	5					Red				
	6						Red			
	7							Red		
	8								Red	
	9									Red
	10									

Bar Color	Min Value	Max Value
Red	0.9	1
Yellow	0.7	0.9
Magenta	0.5	0.7
Cyan	0.3	0.5
Green	0.2	0.3
Blue	0.1	0.2
Black	0.005	0.1
White	0.0	0.005

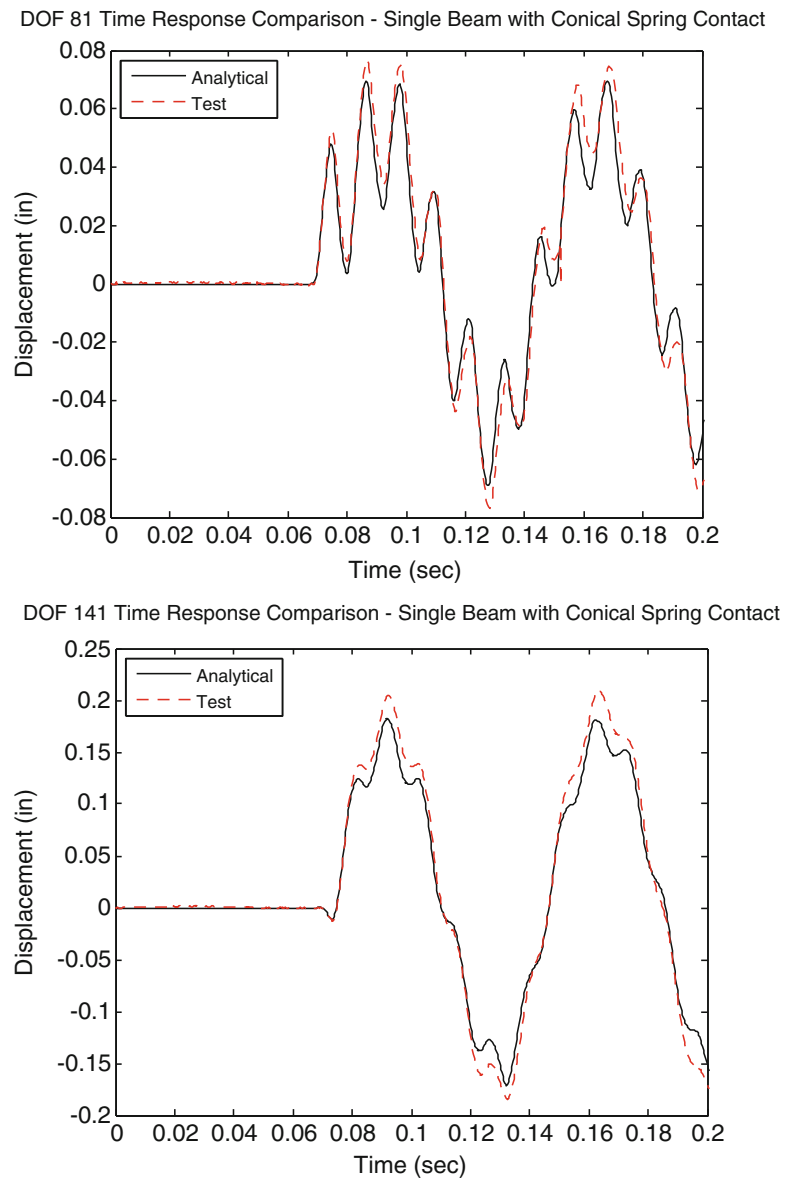
**Table 71.9** Natural frequencies for single beam with conical spring contact

Mode #	Frequency (Hz)	
	Unmodified	Conical spring contact
1	12.850	41.422
2	84.970	92.352
3	254.270	254.989
4	519.510	519.744
5	817.240	817.297
6	1,234.680	1,234.686
7	1,637.960	1,637.960
8	2,201.360	2,201.365

the analytical model to obtain analytical dynamic response predictions for comparison with the test data. The predicted displacement is compared to the measured displacement using PONTOS [23] (high speed digital photogrammetry software) at DOF 81 and DOF 141 over the first 0.2 s of the response, as shown in Fig. 71.22.

To quantify the similarity of the reduced analytical model solution with the experimental results, the MAC and TRAC were computed between the reduced analytical model and the experimental time responses, which are shown in Fig. 71.23. Note that the y-axis scale for the MAC and TRAC plots is 0.0–1.0.

**Fig. 71.22** Comparison of experimental and analytical displacements for single beam with conical spring contact – DOF 81 (*top*) and DOF 141 (*bottom*) for transient portion of time response (0–0.2 s)



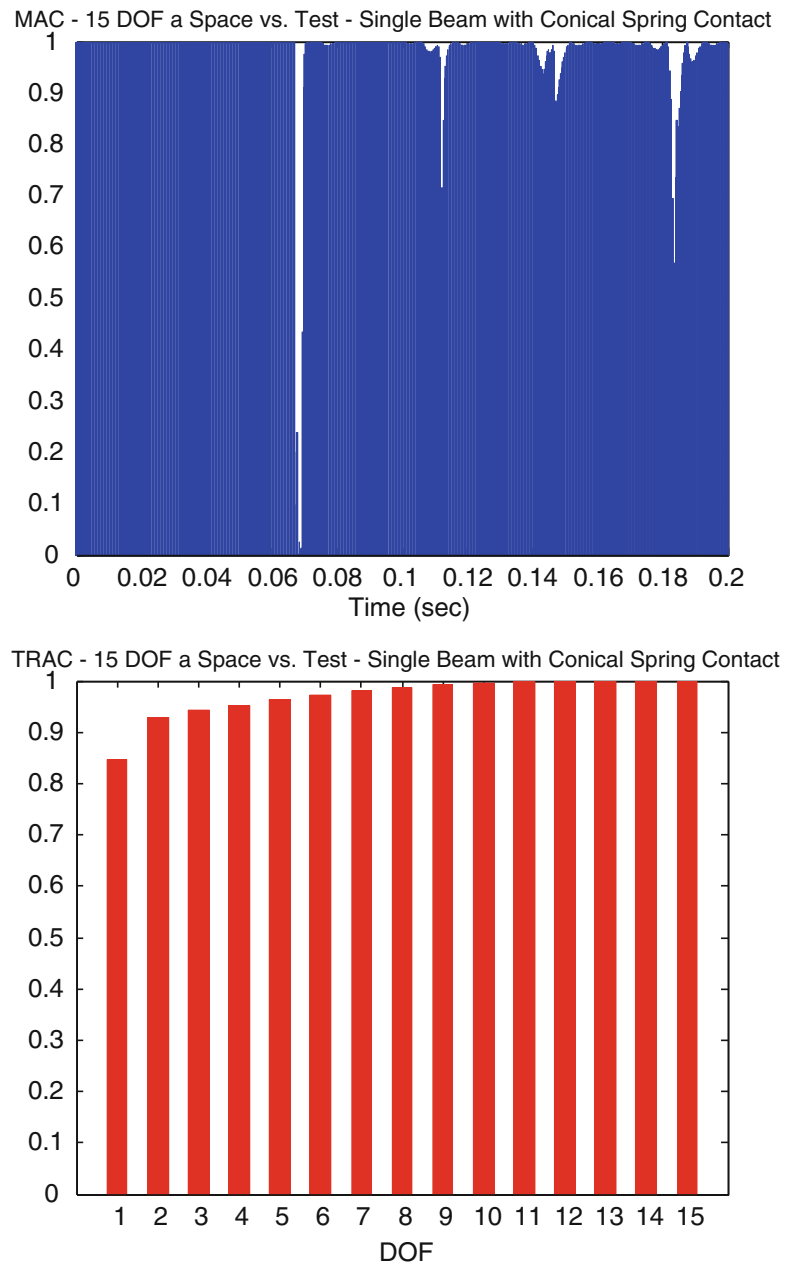
The results shown in Figs. 71.22 and 71.23 demonstrate that the analytical model accurately predicts the response when compared to the experimental data for the first 0.2 s of the response.

The test results measured at ‘a’ space were expanded to ‘n’ space using the linear transformation matrix previously developed and were compared to the ‘n’ space analytical solution. Figure 71.24 shows the MAC and TRAC (the TRAC now consists of all 146 DOF). Note that the y-axis scale for the MAC and TRAC plots is 0.0–1.0.

As seen in Fig. 71.24, the time response has been expanded and is accurate in comparison to the full field solution. In addition, the time response at DOFs that would be hard to traditionally measure (rotational DOF, DOF with minimal response, or DOF that are not easily accessible for instrumentation) can be obtained. Furthermore, this reduces the need for instrumentation as a subset of measurement points can be used to compute the full field solution instead of attempting to measure the response at every location. Figure 71.25 displays the correlation between the analytical model and experimental data for DOF 62, a rotational DOF located near the clamped end. Although this would be very difficult to measure traditionally, the expansion shows a high level of correlation.

Table 71.10 lists the solution times for the full space and reduced space analytical models as well as the average MAC and TRAC comparing the experimental results to the analytical models. As in the previous case, the reduced order model can accurately predict the system response with significant computational savings. Also note that for the experimental case the expanded results improve the MAC and TRAC by smoothing the experimental error. Again, the additional time required to expand the time solution is negligible compared to the full field solution.

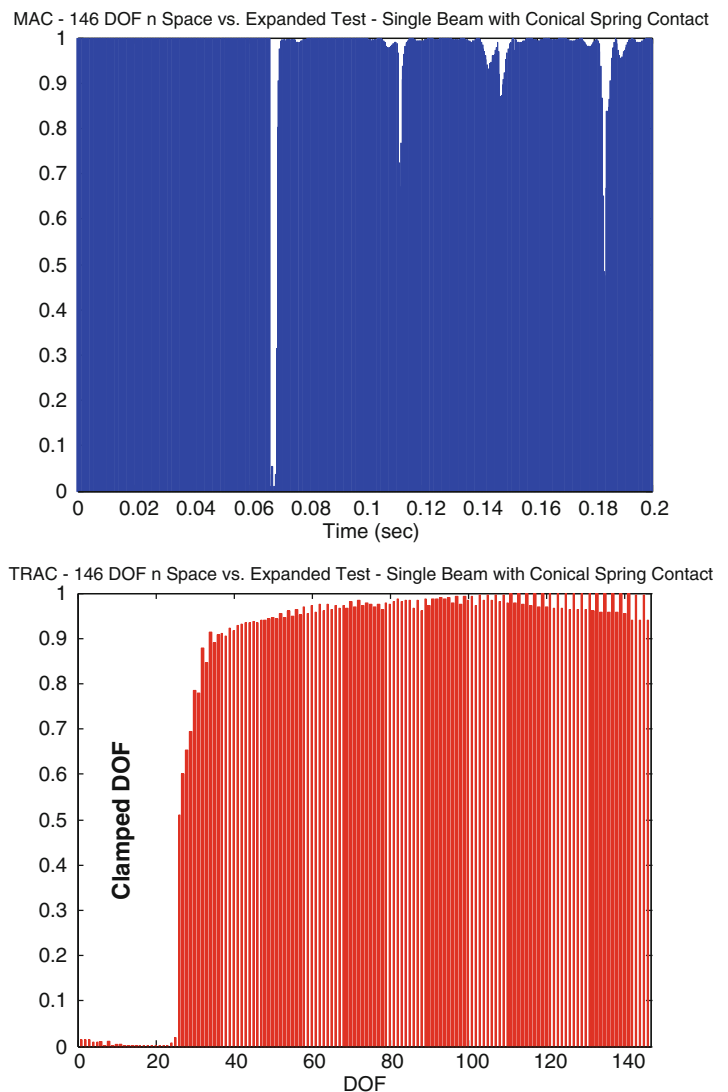
**Fig. 71.23** MAC (*top*) and TRAC (*bottom*) comparisons between 15 DOF 'a' space model and test for transient portion of time response (0–0.2 s) – single beam with conical spring contact



For this experimental case, good correlation was observed between the experimentally measured and analytically predicted displacement responses for a single beam with conical spring contact. Although small discrepancies were observed between the analytical and test results, the predicted results were considered to provide a sufficient level of correlation to describe the nonlinear behavior of the tested system. This case also further demonstrates the proposed methodology for use in applications where experimental data is available for comparison with the analytical models being used in forced nonlinear response simulations.

Again note that the expansion of this nonlinear response was achieved using the modes of the originally uncoupled linear component beam model. The expansion process did not distort the data of the separate systems or any perturbation of the combined system because a sufficient number of modes have been used to span the space of the system in all of its various configurations. As a result, measurements that are difficult to make experimentally can be accurately obtained by expansion at a fraction of the time required to measure every single location.

**Fig. 71.24** MAC (*top*) and TRAC (*bottom*) comparisons between 146 DOF 'a' space expanded model and test for transient portion of time response (0–0.2 s) – single beam with conical spring contact



## 71.4 Observations

Reduced order models are computationally advantageous and are useful for many types of applications. Because a full field solution is often desired for visualization purposes, a transformation matrix is often used to expand the limited sets of responses out to the full field solution. This work showed that the same transformation matrix can also be used to expand nonlinear responses, rather than requiring a different matrix for each piecewise linear state of the system. This decreases the computation time required but still gives an accurate solution. This work is especially useful in regards to instrumentation, as it allows a full field solution to be computed from experimental measurements at a limited number of locations.

In addition, the mode contribution matrix was able to be used for identifying the key contributing modes from the original unmodified component models when generating reduced order models. This ensures that the transformation matrix used for expansion contains all of the modes needed to span the space of the system response, which can be either linear or nonlinear in nature.

## 71.5 Conclusion

Previous work demonstrated an efficient approach to nonlinear forced response problems by approximating the nonlinear elements as piecewise linear. The proposed technique in this paper further develops that work by expanding the nonlinear response data using a single transformation matrix formed from the reduction of the individual linear component models.

**Fig. 71.25** Comparison of expanded experimental and analytical displacements for single beam with conical spring contact – DOF 62 for transient portion of time response (0–0.2 s)

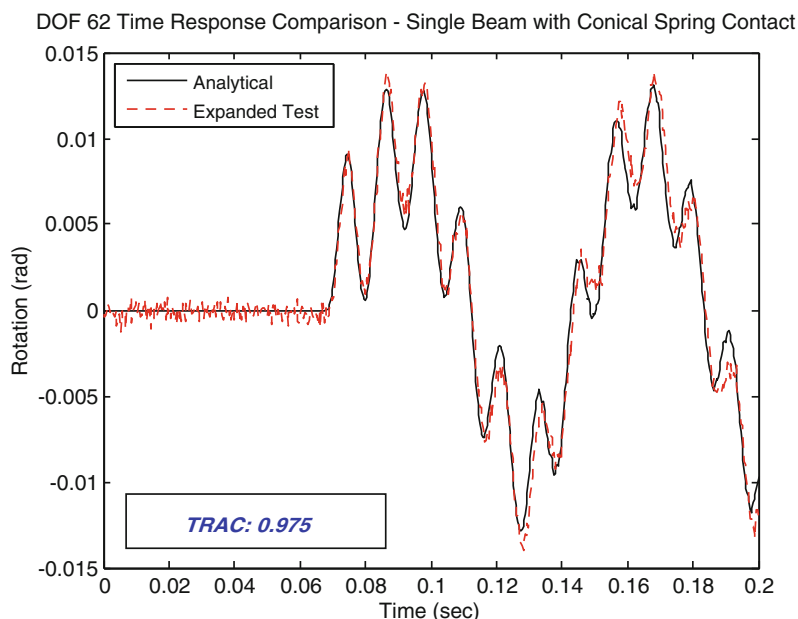


**Table 71.10** Solution times and average MAC/TRAC for single beam with conical spring contact – comparisons between analytical responses and experimental data

Model	# of DOF	Solution time (s)	Average MAC	Average TRAC
'n' space	146	312.9	0.97836	0.97006
'a' space	15	28.3	0.97836	0.97005
'a' space expanded	146	28.4	0.98125	0.98049

The main advantage of this technique is that only one transformation matrix is needed regardless of the state of the system. In addition, this expansion process is very computationally efficient and allows for reduced model time response solutions to be expanded out to the full space FEM NDOF with negligible increase in solution time.

Two cases were studied: one analytical and one experimental case. The analytical case showed that the expanded data was highly correlated to the full space solution with a noticeable reduction in computation time. The experimental case showed that test data could be expanded to the full set of FEM NDOF to obtain measurements at locations that would be difficult or impossible to measure experimentally (such as rotational DOF or inaccessible DOF). Both cases demonstrated that this expansion technique is a useful extension of the previous work in modeling nonlinear dynamic response using reduced order linear component models.

**Acknowledgements** Some of the work presented herein was partially funded by Air Force Research Laboratory Award No. FA8651-10-1-0009 “Development of Dynamic Response Modeling Techniques for Linear Modal Components”. Any opinions, findings, and conclusions or recommendations expressed in this material are those of the authors and do not necessarily reflect the views of the particular funding agency. The authors are grateful for the support obtained.

## Appendix A: Time Correlation Tools

The correlation tools utilized to compare the results of the expanded real time operating (RTO) [ERTOn] and reference time solution [REFn] are briefly discussed here.

The MAC (Modal Assurance Criteria) [24, 25] as used for this work will identify the correlation of the expanded real time operating displacement solution obtained with the reference solution. The MAC can be computed at each time step t to compare the transient displacement solution with time. The MAC is written as

$$MAC_{RTO} = \frac{\left[ \{REFn\}^T \{ERTOn\} \right]^2}{\left[ \{REFn\}^T \{REFn\} \right] \left[ \{ERTOn\}^T \{ERTOn\} \right]} \tag{A.1}$$

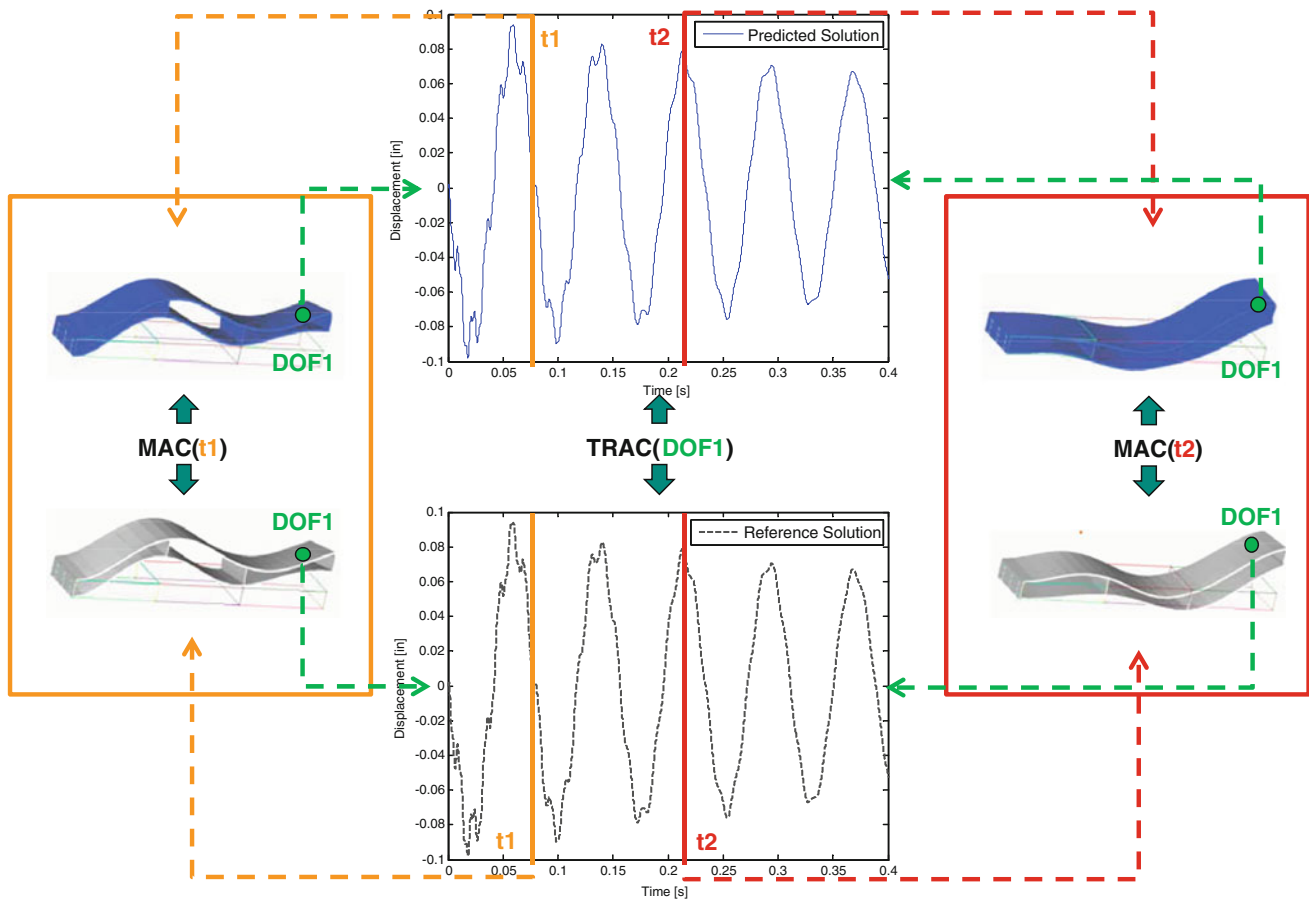


**Fig. A.1** Schematic showing MAC and TRAC

Similar to the MAC, the TRAC (Time Response Assurance Criterion) is a tool used to determine the degree of correlation between two time traces. For the cases presented here, the TRAC is the correlation for one DOF over all time for the expanded time data [ERTOn] compared to the actual measured data [REFn]. The TRAC is written as

$$\text{TRAC}_{\text{RTO}} = \frac{\left[ \{\text{REFn}(t)\}^T \{\text{ERTOn}(t)\} \right]^2}{\left[ \{\text{REFn}(t)\}^T \{\text{REFn}(t)\} \right] \left[ \{\text{ERTOn}(t)\}^T \{\text{ERTOn}(t)\} \right]} \quad (\text{A.2})$$

The values produced by both the MAC and TRAC will range from 0 to 1; values approaching 1 indicate good correlation.

Also used for comparing the [ERTOn] with reference time solution is an absolute different between the two solutions at each time step. The magnitude of the difference is a measure of how much the [ERTOn] deviates from the reference time solution.

## References

1. Chipman CC (2009) Expansion of real time operating deformations for improved visualization. Master's thesis. University of Massachusetts Lowell
2. Pingle P, Niezrecki C, Avitabile P (2011) Full field numerical stress-strain from dynamic experimental measured data. In: EURO DYN 2011, Leuven, Belgium
3. Thibault L (2012) Development of equivalent reduced model technique for linear modal components interconnected with nonlinear connection elements. Master's thesis. University of Massachusetts Lowell
4. Marinone T (2012) Efficient Computational Nonlinear Dynamic Analysis Using Modal Modification Response Technique. Master's thesis. University of Massachusetts Lowell

5. Guyan RJ (1965) Reduction of stiffness and mass matrices. *Am Inst Aeronaut Astronaut J* 3(2):380
6. Kidder RL (1973) Reduction of structure frequency equations. *Am Inst Aeronaut Astronaut J* 11(6):892
7. O'Callahan JC (1989) A procedure for an improved reduced system (IRS) model. In: Proceedings of the seventh international modal analysis conference, Las Vegas, NV
8. O'Callahan JC, Avitabile P, Riemer R (1989) System equivalent reduction expansion process. In: Proceedings of the seventh international modal analysis conference, Las Vegas, NV
9. Kammer DC (1989) A hybrid approach to test analysis model development for large space structures. Submitted for publication in *J Spacecr Rockets J. Vib. Acoust.* 113(3):325–332 (Jul 01, 1991) (8 pages) doi:10.1115/1.2930188
10. Marinone T, Butland A, Avitabile P (2012) A reduced model approximation approach using model updating methodologies. In: Proceedings of the thirtieth international modal analysis conference, Jacksonville, FL
11. Thibault L, Avitabile P, Foley J, Wolfson J (2012) Equivalent reduced model technique development for nonlinear system dynamic response. In: Proceedings of the thirtieth international modal analysis conference, Jacksonville, FL
12. Avitabile P (2003) Twenty years of structural dynamic modification – a review. *Sound Vib Mag* 37(1):14–27
13. Pingle P, Avitabile P (2010) Prediction of full field dynamic stress/strain from limited sets of measured data. In: Proceedings of the twenty-eighth international modal analysis conference, Jacksonville, FL
14. Pingle P, Avitabile P (2011) Full field dynamic stress/strain from limited sets of measured data. In: Proceedings of the twenty-ninth international modal analysis conference, Jacksonville, FL
15. Pingle P (2010) Prediction of full field dynamic stress/strain from limited sets of measured displacement data. Doctoral dissertation, University of Massachusetts Lowell
16. Thibault L, Butland A, Avitabile P (2012) Variability improvement of key inaccurate node groups – VIKING. In: Proceedings of the thirtieth international modal analysis conference, Jacksonville, FL
17. MAT.SAP/MATRIX (1986) A general linear algebra operation program for matrix analysis. Dr. John O'Callahan, University of Massachusetts Lowell
18. MATLAB (R2010a) The MathWorks Inc., Natick
19. Newmark NM (1959) A method of computation for structural dynamics. *J Eng Mech Div Am Soc Civ Eng* 85(3):67–94
20. LMS Test.Lab 10A, LMS International, Leuven, Belgium
21. PolyMAX, Leuven Measurement Systems, Leuven, Belgium
22. GOM mbH (2007) Braunschweig, Germany
23. PONTOS – GOM mbH, Mittelweg 7–8, 38106 Braunschweig, Germany
24. Allemang RJ, Brown DL (2007) A correlation coefficient for modal vector analysis. In: Proceedings of the first international modal analysis conference, Orlando, FL
25. Van Zandt T (2006) Development of efficient reduced models for multi-body dynamics simulations of helicopter wing missile configurations. Master's thesis. University of Massachusetts Lowell



# Chapter 72

## Explicit Construction of Rods and Beams with Given Natural Frequencies

A. Morassi

**Abstract** In this paper we present a new method for constructing one-dimensional vibrating systems having prescribed values of the first  $N$  natural frequencies, under a given set of boundary conditions. In the case of axially vibrating rods, the analysis is based on the determination of the so-called quasi-isospectral rods, that is rods which have the same spectrum as a given rod, with the exception of a single eigenvalue which is free to move in a prescribed interval. The reconstruction procedure needs the specification of an initial rod whose eigenvalues must be close to the assigned eigenvalues. The rods and their normal modes can be constructed explicitly by means of closed-form expressions. The results can be extended to strings and to some special classes of beams in bending vibration.

**Keywords** Structural identification • Vibrating rods • Quasi-isospectral systems • Inverse problems • Eigenvalues

### 72.1 Introduction

The construction of a system having prescribed spectral properties is an important issue in many engineering contexts. A key problem in Structural Identification, for example, consists in determining the stiffness or the inertia parameters so that the first analytical eigenvalues coincide with the corresponding experimental values [1, 7, 8, 12, 15]. Other applications concern the construction of vibrating systems with a specified spectrum to avoid possible occurrence of resonance phenomena under prescribed external actions. Numerical reconstruction methods usually are based on optimization techniques and involve highly non-linear algorithms. In this paper we show how to construct longitudinally vibrating rods having prescribed values of the first  $N$  natural frequencies, under a given set of boundary conditions. The rods and their normal modes can be constructed explicitly by means of closed-form expressions. The reconstruction procedure needs the specification of an initial rod whose eigenvalues must be close to the assigned eigenvalues. The analysis is based on the determination of the so-called quasi-isospectral rods, that is rods which have the same spectrum as a given rod, with the exception of a single eigenvalue which is free to move in a prescribed interval. The results can be extended to strings and to some special classes of beams in bending vibration [13].

The paper is organized as follows. The main ideas and mathematical tools of the reconstruction method are presented, for the sake of simplicity, for rods under supported (or Dirichlet) end conditions. Extensions to rods under other end conditions and generalizations to strings and beams are discussed in the last section of the paper.

#### 72.1.1 Main Ideas of the Reconstruction Procedure

In order to present the main ideas and mathematical tools of the reconstruction procedure, we shall refer to rods under supported-supported or Dirichlet end conditions. The analysis of this case is simpler than that for other sets of end conditions and allows for a clear presentation of the key aspects of the method.

---

A. Morassi (✉)  
DICA – University of Udine, Udine, Italy  
e-mail: [antonino.morassi@uniud.it](mailto:antonino.morassi@uniud.it)

The free (undamped, infinitesimal) longitudinal vibrations  $u(x)$  of frequency  $\omega$ , of a thin straight rod of unit length under Dirichlet end conditions are governed by the Sturm-Liouville equation

$$\begin{cases} (\hat{A}(x)u'(x))' + \lambda\hat{A}(x)u(x) = 0, & x \in (0, 1), \\ u(0) = 0, \\ u(1) = 0, \end{cases} \quad \begin{array}{l} (72.1) \\ (72.2) \\ (72.3) \end{array}$$

where  $\lambda = \frac{\gamma\omega^2}{E}$  and  $(\cdot)' \equiv \frac{d(\cdot)}{dx}$ . Here  $E$  is Young's modulus,  $\gamma$  is the volume mass density, both assumed constant;  $\hat{A}(x)$  is the cross-sectional area at section  $x$ . We shall assume throughout that  $\hat{A}(x)$  is a strictly positive, twice continuously differentiable function of  $x$  in  $[0, 1]$ . It is well-known that there exists an infinite sequence  $\{\lambda_m\}_{m=1}^{\infty}$  of eigenvalues, with  $0 < \lambda_1 < \lambda_2 < \dots$ ,  $\lim_{m \rightarrow \infty} \lambda_m = \infty$ , for which (72.1)–(72.3) has a non-trivial solution  $u(x)$ .

Let  $n \geq 1$  be given. The key step of the method is the explicit construction of a new rod quasi-isospectral to the given rod, that is a rod with cross-sectional profile  $A(x)$  having the same Dirichlet eigenvalues as the given rod  $\hat{A}(x)$ , with the exception of the  $n$ th eigenvalue. In fact, by keeping fixed all the eigenvalues  $\lambda_m$  with  $m \neq n$  and moving the  $n$ th eigenvalue  $\lambda_n$  to the desired value, say  $\tilde{\lambda}_n$ , and using repeatedly the procedure, after  $N$  steps we will produce a rod with the first  $N$  given eigenvalues  $\{\tilde{\lambda}_m\}_{m=1}^N$ , and the construction is finished. We will see in the following that the reconstruction procedure works only if the rod to be determined is not far (in a way that can be rigorously specified) from the initial guess rod. Moreover, even if the initial rod is fixed, it is evident that the construction is not unique, since the flow from the initial rod depends also on the particular order chosen to move every individual eigenvalue to the target value.

The main steps of our construction of rods  $A(x)$  quasi-isospectral to a given rod  $\hat{A}(x)$ , under Dirichlet end conditions, are the following. First, the Eq. (72.1) is reduced to canonical form with a Schrödinger potential  $\hat{q}(x)$  by a standard Sturm-Liouville transformation. Second, a Darboux Lemma is used to construct explicit families of Schrödinger potentials  $q(x)$  quasi-isospectral to the initial potential  $\hat{q}(x)$ . Third, the Darboux lemma is applied once more in iterate form to determine rods  $A(x)$  corresponding to the quasi-isospectral potentials  $q(x)$  and, ultimately, to find rods  $A(x)$  quasi-isospectral to the initial rod  $\hat{A}(x)$ .

The second step of the above procedure is fully described in the book by Pöschel and Trubowitz [14] for square-summable potentials. Our original contribution – for the Dirichlet end-conditions case – lies on the third step of the above procedure. For the sake of completeness, we recall that the problem of constructing quasi-isospectral rods have been solved by Coleman and McLaughlin [2, 3] by using a method different from ours, which extends the results obtained by Trubowitz and co-workers to the Eq. (72.1) for Dirichlet or Neumann (e.g.,  $u'(0) = u'(1) = 0$ ) boundary conditions.

### 72.1.2 Reduction to Normal Form

In Eq. (72.1) put

$$A(x) = a^2(x), \quad y(x) = a(x)u(x). \quad (72.4)$$

Then, Eq. (72.1) reduces to the Sturm-Liouville canonical form

$$-y''(x) + \hat{q}(x)y(x) = \lambda y(x), \quad x \in (0, 1), \quad (72.5)$$

where

$$\hat{q}(x) = \frac{\hat{a}''(x)}{\hat{a}(x)} \quad (72.6)$$

is a continuous function in  $[0, 1]$ .

Note that for a given  $\hat{A}$  or  $\hat{a}$ , there is a unique  $\hat{q}$ , but for a given  $\hat{q}$  there are many  $\hat{a}$ . In particular, if  $\hat{a}_0$  is one  $\hat{a}$  corresponding to a given  $\hat{q}$ , then all the coefficients  $a$  satisfying (72.6) are given by

$$\hat{a} = \hat{a}_0 \left( c_1 + c_2 \int_0^x \frac{ds}{\hat{a}_0^2(s)} \right), \quad (72.7)$$

where the constants  $c_1, c_2$  must be chosen such that  $\hat{a}$  is one-sign – say, positive – in  $[0, 1]$ .

### 72.1.3 The Darboux Lemma

We now introduce the key mathematical tool of our analysis: the so-called Darboux Lemma.

**Lemma 1 (Darboux Lemma [5]).** *Let  $\mu$  be a real number, and suppose  $g = g(x)$  is a non-trivial solution of the Sturm-Liouville equation*

$$-g'' + \hat{q}g = \mu g \quad (72.8)$$

with potential  $\hat{q} = \hat{q}(x)$ . If  $f$  is a non-trivial solution of

$$-f'' + \hat{q}f = \lambda f \quad (72.9)$$

and  $\lambda \neq \mu$ , then

$$y = \frac{1}{g}[g, f] \equiv \frac{1}{g}(gf' - g'f) \quad (72.10)$$

is a non-trivial solution of the Sturm-Liouville equation

$$-y'' + \check{q}y = \lambda y, \quad (72.11)$$

where

$$\check{q} = \hat{q} - 2\frac{d^2}{dx^2} \ln(g(x)). \quad (72.12)$$

Moreover, the general solution of the equation

$$-y'' + \check{q}y = \mu y \quad (72.13)$$

is

$$y = \frac{1}{g} \left( a + b \int_0^x g^2(s) ds \right), \quad (72.14)$$

where  $a$  and  $b$  are arbitrary constants. In particular,  $y = \frac{1}{g}$  is a solution of (72.13).

This lemma, which can be verified by direct calculation, see also [14], allows to associate to every equation of the form (72.8), that one knows how to integrate for all values of  $\mu$ , another equation of the same form that one also knows how to integrate for all the values of the parameter  $\mu$ . In particular, the addition law of the logarithm makes iteration of Lemma 1 simple, as it will be shown in the sequel. We refer to [6] and [14] for a formal justification in a more abstract context based on a *commutation formula* for Sturm-Liouville operators.

It should be noted that if  $g$  vanishes in  $[0, 1]$ , then Eq. (72.11) is understood to hold between the roots of  $g$ . We will see that these singular situations disappear by applying the Darboux Lemma twice, as we shall describe in the following section, see also the general method presented in [9].

### 72.1.4 Quasi-isospectral Potentials

We start with a rod  $\hat{A} = \hat{A}(x)$  with Dirichlet spectrum  $\{\lambda_m\}_{m=1}^{\infty}$  corresponding to Dirichlet end conditions (72.2) and (72.3). Transforming to Sturm-Liouville canonical form, we have a set of eigenfunctions  $\{z_m\}_{m=1}^{\infty}$  satisfying

$$-z_m'' + \hat{q}z_m = \lambda_m z_m, \quad x \in (0, 1), \quad (72.15)$$

with end conditions

$$z_m(0) = 0 = z_m(1) \quad (72.16)$$

and normalized so that

$$z_m'(0) = 1, \quad m = 1, 2, \dots \quad (72.17)$$

We now choose a particular number  $n$ ,  $n \geq 1$ , and the corresponding eigenvalue  $\lambda_n$ . We want to construct families of potentials  $q$  such that the Dirichlet eigenvalues  $\lambda_m$  associated to  $q$  coincide with those associated to  $\hat{q}$  for  $m \neq n$ , while the  $n$ th eigenvalue is free to move (under some prescribed conditions, see (72.32) below). The strategy of the proof is to use appropriately the Darboux Lemma in an iterated form. This result has been proved in [14] (Sect. 6).

It is useful to introduce some notation. Let  $y_1 = y_1(x, \hat{q}, \lambda)$ ,  $y_2 = y_2(x, \hat{q}, \lambda)$  be the fundamental solutions to the initial value problems

$$\begin{cases} -y_1'' + \hat{q}y_1 = \lambda y_1, & x \in (0, 1), \\ y_1(0) = 1, \\ y_1'(0) = 0, \end{cases} \quad \begin{array}{l} (72.18) \\ (72.19) \\ (72.20) \end{array}$$

and

$$\begin{cases} -y_2'' + \hat{q}y_2 = \lambda y_2, & x \in (0, 1), \\ y_2(0) = 0, \\ y_2'(0) = 1. \end{cases} \quad \begin{array}{l} (72.21) \\ (72.22) \\ (72.23) \end{array}$$

Here,  $\lambda \in \mathbb{C}$  and  $\hat{q}$  is a continuous, real-valued potential on  $[0, 1]$ . Let  $w_n = w_n(x, \hat{q}, \lambda)$  be the solution to

$$\begin{cases} -w_n'' + \hat{q}w_n = \lambda w_n, & x \in (0, 1), \\ w_n(0) = 1, \\ w_n(1) = y_1(1, \lambda_n, \hat{q}), \end{cases} \quad \begin{array}{l} (72.24) \\ (72.25) \\ (72.26) \end{array}$$

for  $\lambda \neq \lambda_n$ . Then, we have

$$w_n(x, \hat{q}, \lambda) = y_1(x, \hat{q}, \lambda) + \frac{y_1(1, \lambda_n) - y_1(1, \lambda)}{y_2(1, \lambda)} y_2(x, \hat{q}, \lambda). \quad (72.27)$$

The function  $w_n$  is well-defined for all  $\lambda \neq \lambda_n$  and has a removable singularity at  $\lambda = \lambda_n$ . Clearly, we have

$$z_n(x, \hat{q}) = y_2(x, \hat{q}, \lambda_n). \quad (72.28)$$

Let

$$\omega_n(x, \hat{q}, \lambda) = [w_n(x, \hat{q}, \lambda), z_n(x, \hat{q})]. \quad (72.29)$$

The following lemma states the main properties of the function  $\omega_n$ .

**Lemma 2 ([14], p. 109).** *For each  $\hat{q} \in L^2(0, 1)$ , the function  $\omega_n = \omega_n(x, \hat{q}, \lambda)$ ,  $n \geq 1$ , is a continuous and strictly positive function on  $[0, 1] \times (\lambda_{n-1}(\hat{q}), \lambda_{n+1}(\hat{q}))$ . In particular:*

$$\omega_n(0, \lambda) = 1 = \omega_n(1, \lambda) \quad \text{for all } \lambda \in (\lambda_{n-1}(\hat{q}), \lambda_{n+1}(\hat{q})) \quad (72.30)$$

and

$$\omega_n(x, \lambda_n) = 1 \quad \text{for all } x \in [0, 1]. \quad (72.31)$$

Moreover,  $\omega_n$  is a  $C^2$ -function of the variable  $x$  in  $[0, 1]$ .

Let  $t \in \mathbb{R}$  be such that

$$\lambda_{n-1}(\hat{q}) < \lambda_n(\hat{q}) + t < \lambda_{n+1}(\hat{q}), \quad (72.32)$$

with

$$\lambda_0(\hat{q}) = 0. \quad (72.33)$$

We define

$$w_{n,t} = w_n(x, \hat{q}, \lambda_n + t), \quad (72.34)$$

$$\omega_{n,t} = \omega_n(x, \hat{q}, \lambda_n + t). \quad (72.35)$$

We recall that  $n$  is a given fixed positive number,  $n \geq 1$ . By Darboux Lemma applied to Eq. (72.24) (with  $\lambda = \lambda_n + t$ ,  $t$  satisfying (72.32)) and Eq. (72.15) (with  $m = n$ ), we have that

$$h = \frac{1}{z_n} [w_{n,t}, z_n] \equiv \frac{1}{z_n} \omega_{n,t} \quad (72.36)$$

is a non-trivial solution of the equation

$$-h'' + \check{q}h = (\lambda_n + t)h, \quad (72.37)$$

where

$$\check{q} = \hat{q} - 2 \frac{d^2}{dx^2} (\ln(z_n)). \quad (72.38)$$

Now, let  $m$  be an integer number,  $m \geq 1$  and  $m \neq n$ .

Let  $h$  be defined as in (72.36) and let  $g$  be a solution of

$$-g'' + \check{q}g = \lambda_m g. \quad (72.39)$$

Note that, by applying the Darboux Lemma to the equations satisfied by the Dirichlet eigenfunctions  $z_m, z_n$  associated to the potential  $\hat{q}$ , we can assume

$$g = \frac{1}{z_n} [z_m, z_n]. \quad (72.40)$$

Applying the Darboux Lemma to Eqs. (72.37) and (72.39), we find a non-trivial solution

$$k_{m,t} = \frac{1}{h} [g, h] \quad (72.41)$$

to

$$-k_{m,t}'' + qk_{m,t} = \lambda_m k_{m,t}, \quad (72.42)$$

where, by (72.36),

$$q = \check{q} - 2 \frac{d^2}{dx^2} (\ln(h)) = \hat{q} - 2 \frac{d^2}{dx^2} (\ln(\omega_{n,t})). \quad (72.43)$$

This concludes the case  $m \neq n$ .

Assume now that  $m = n$ . By the second part of Darboux Lemma applied to Eq. (72.37), the function

$$\frac{1}{h} = \frac{z_n}{\omega_{n,t}} \quad (72.44)$$

is a non-trivial solution of

$$-y'' + qy = (\lambda_n + t)y, \quad (72.45)$$

where  $q$  is given by (72.43), that is the function  $k_{n,t}$  defined by

$$k_{n,t} = \frac{z_n}{\omega_{n,t}} \quad (72.46)$$

is a non-trivial solution of (72.45). By the regularity of  $\omega_{n,t}$  (see Lemma 2), the potential  $q$  is a continuous function in  $[0, 1]$ . We now evaluate  $k_{m,t}$ , for  $m \neq n$ . A long but straightforward calculation shows that

$$k_{m,t} = z_m - t \frac{w_{n,t}}{\omega_{n,t}} \int_0^x z_m(s) z_n(s) ds, \quad (72.47)$$

for  $m \neq n$ , where  $n, n \geq 1$ , is a given integer number.

Collecting the above results, for a given  $n$ ,  $n \geq 1$ , by (72.46) and (72.47) the functions  $\{k_m \equiv k_{m,t}\}_{m=1}^{\infty}$  are solutions to

$$-k_m'' + qk_m = (\lambda_m + t\delta_{mn})k_m, \quad x \in (0, 1), \quad (72.48)$$

$$k_m(0) = 0 = k_m(1), \quad (72.49)$$

for  $m \geq 1$ , where  $t$  satisfies the upper and lower bounds (72.32) and  $q$  is defined in (72.43). Moreover, it can be shown that  $k_m(x)$  has exactly  $(m - 1)$  zeros in  $(0, 1)$ . We conclude that  $k_m$  is the  $m$ th eigenfunction of the Dirichlet problem (72.48), (72.49) associated to the potential  $q$ .

To this point the potentials  $\hat{q}$  and  $q$  are quasi-isospectral under Dirichlet end conditions.

### 72.1.5 Quasi-isospectral Rods

To construct the Dirichlet quasi-isospectral rods, we must now find a function  $a = a(x)$  corresponding to the new  $q$ . To find  $a$  we use again the Darboux Lemma, noting that the original  $\hat{a}$ , the intermediate  $\check{a}$  and the final  $a$  are solutions of the equations

$$-\hat{a}'' + \hat{q}\hat{a} = 0, \quad (72.50)$$

$$-\check{a}'' + \check{q}\check{a} = 0, \quad (72.51)$$

$$-a'' + qa = 0, \quad (72.52)$$

respectively. The Darboux Lemma applied to Eq. (72.50) and to

$$-z_n'' + \hat{q}z_n = \lambda_n z_n, \quad (72.53)$$

$n \geq 1$ , shows that a non-trivial  $\check{a}$  is given by

$$\check{a} = \frac{1}{z_n}[z_n, \hat{a}]. \quad (72.54)$$

Next, the Darboux Lemma applied to Eq. (72.51) and to

$$-h'' + \check{q}h = (\lambda_n + t)h, \quad (72.55)$$

$n \geq 1$ , shows that a non-trivial  $a$  is

$$a = \frac{1}{h}[h, \check{a}]. \quad (72.56)$$

Note that this  $\check{a}$  and  $a$  are just one of each of the families of  $\check{a}$ 's and  $a$ 's corresponding to  $\check{q}$  and  $q$ , respectively; all others may be found by using the formula (72.7). We can find  $a$  just as we found  $k_m$ , namely

$$a = \hat{a} - t \frac{W_{n,t}}{\lambda_n \omega_{n,t}}[z_n, \hat{a}], \quad n \geq 1. \quad (72.57)$$

We now have a one-parameter family of functions  $a(x) \equiv a_t(x)$  defined for  $0 \leq x \leq 1$  and  $t$  such that  $\lambda_{n-1} < \lambda_n + t < \lambda_{n+1}$ ,  $n \geq 1$ , with  $\lambda_0 = 0$ . These functions correspond to a rod if each member of the family is of one-sign, say positive, in  $[0, 1]$ . To show this we evaluate  $a(x)$  at  $x = 0$ ,  $x = 1$ . After a tedious but simple calculation we get

$$a(0) = \hat{a}(0) \frac{\lambda_n + t}{\lambda_n}, \quad (72.58)$$

$$a(1) = \hat{a}(1) \frac{\lambda_n + t}{\lambda_n}. \quad (72.59)$$

The values  $a(0)$ ,  $a(1)$  are both positive for every  $t$  satisfying (72.32). It may easily be seen that  $a(x)$  can have only a finite number of simple roots. Under these conditions on  $t$ , we can use a Deformation Lemma, see [14], to show that  $a(x)$  given by (72.57) is strictly positive in  $[0, 1]$ . We can conclude that if the original rod has cross-sectional area  $\hat{A} = \hat{a}^2$  and satisfies

the supported end conditions, and if  $a, \hat{a}$  are linked by Eq. (72.57), then the new rod  $A = a^2$  is *quasi-isospectral* to the original one.

### 72.1.6 Constructing Rods with a Given Set of Dirichlet Eigenvalues

Consider a supported rod with given cross sectional profile  $A_0(x) = a_0^2(x)$  and Dirichlet eigenvalues  $\{\lambda_m(a_0)\}_{m=1}^{\infty}$ ,  $0 < \lambda_1(a_0) < \lambda_2(a_0) < \dots$ . We now ask whether it is possible to construct from this rod a new rod having prescribed values of the first  $N$  Dirichlet eigenvalues  $\{\tilde{\lambda}_m\}_{m=1}^N$ , with

$$0 < \tilde{\lambda}_1 < \tilde{\lambda}_2 < \dots < \tilde{\lambda}_N. \quad (72.60)$$

By the analysis of previous section we know how to construct from the rod  $A_0(x)$  a new rod, say  $A_1(x) = a_1^2(x)$ , so that the Dirichlet eigenvalues  $\{\lambda_m(a_0)\}$ ,  $m \geq 2$ , are kept fixed while  $\lambda_1(a_1)$  is moving to the desired value  $\tilde{\lambda}_1$ . More precisely, by (72.57), the function  $a_1 = a_1(x)$  given by

$$a_1 = a_0 - t \frac{w_{1,t}}{\lambda_1(a_0)\omega_{1,t}} [z_1(a_0), a_0] \quad (72.61)$$

corresponds to a one-parameter family of rods such that

$$\lambda_m(a_1) = \lambda_m(a_0) + \delta_{m1}t, \quad (72.62)$$

$m \geq 1$ , for  $t$  such that

$$0 < \lambda_1(a_0) + t < \lambda_2(a_0). \quad (72.63)$$

If

$$\tilde{\lambda}_1 < \lambda_2(a_0), \quad (72.64)$$

then we can determine the parameter  $t$ , say  $t = t_1$ , such that  $\lambda_1(a_1) = \tilde{\lambda}_1$ , i.e.

$$t_1 = \tilde{\lambda}_1 - \lambda_1(a_0). \quad (72.65)$$

The rod  $A_1 = a_1^2$  has eigenvalues  $\{\tilde{\lambda}_1, \lambda_2(a_0), \lambda_3(a_0), \dots\}$ , with  $0 < \tilde{\lambda}_1 < \lambda_2(a_0) < \lambda_3(a_0) < \dots$ , and can be used as starting point for the next step of the procedure.

By repeating the same arguments, it is possible to modify  $a_1$  so as to keep  $\lambda_m(a_1)$  fixed for  $m \neq 2$  and to move  $\lambda_2(a_0)$  to the desired value  $\tilde{\lambda}_2$ , i.e.

$$a_2 = a_1 - t_2 \frac{w_{2,t_2}}{\lambda_2(a_0)\omega_{2,t_2}} [z_2(a_1), a_1], \quad (72.66)$$

where

$$t_2 = \tilde{\lambda}_2 - \lambda_2(a_0). \quad (72.67)$$

The eigenvalues of the new rod  $a_2(x)$  are  $\{\tilde{\lambda}_1, \tilde{\lambda}_2, \lambda_3(a_0), \lambda_4(a_0), \dots\}$ . Using repeatedly this procedure, after  $N$  steps we produce a rod, with cross-sectional profile area  $A_N(x) = a_N^2(x)$ , such that

$$\lambda_m(a_N) = \tilde{\lambda}_m, \quad \text{for } 1 \leq m \leq N, \quad (72.68)$$

and the construction is finished. We note that the choice of the initial rod  $a_0(x)$  is restricted by the conditions

$$\tilde{\lambda}_1 < \lambda_2(a_0), \quad \tilde{\lambda}_2 < \lambda_3(a_0), \quad \dots, \quad \tilde{\lambda}_{N-1} < \lambda_N(a_0), \quad \tilde{\lambda}_N < \lambda_{N+1}(a_0), \quad (72.69)$$

which allow to determine the numbers  $t_1, t_2, \dots, t_N$  by the expressions analogous to Eq. (72.65).

The above construction is not unique, since the flow from the initial rod  $a_0$  to a rod with prescribed first  $N$  Dirichlet eigenvalues depends on the particular order chosen to move every individual eigenvalue to the target value. Similarly, the compatibility conditions on the initial rod  $a_0$  may change depending on the sequence of eigenvalue shifts. For example, if

we decide to move the  $N$  initial eigenvalues  $\{\lambda_m(a_0)\}_{m=1}^N$  into the decided positions  $\{\tilde{\lambda}_m\}_{m=1}^N$  beginning with  $\lambda_N(a_0)$  and proceeding in descending order, the conditions (72.69) become

$$\lambda_{N-1}(a_0) < \tilde{\lambda}_N < \lambda_{N+1}(a_0), \lambda_{N-2}(a_0) < \tilde{\lambda}_{N-1}, \dots, \lambda_2(a_0) < \tilde{\lambda}_3, \lambda_1(a_0) < \tilde{\lambda}_2. \quad (72.70)$$

## 72.2 Extensions and Generalizations

The analysis developed in the previous section can be extended to rods under different sets of boundary conditions. We recall that the end conditions are assumed to be Elastically Restrained (ER) when

$$(ER) \quad A(0)u'(0) - ku(0) = 0 = A(1)u'(1) + Ku(1), \quad (72.71)$$

where  $k, K \geq 0$ . Conditions (72.71) mean that the ends  $x = 0, x = 1$  are attached to fixed supports by means of elastic springs having stiffness  $k, K$ , respectively. The cases of Free (F) and Mixed (M) end conditions are obtained as limit cases of (72.71), precisely:

$$(F) \quad k = 0 = K \quad u'(0) = 0 = u'(1), \quad (72.72)$$

$$(M) \quad k = \infty, 0 \leq K < \infty \quad u(0) = 0, A(1)u'(1) + Ku(1) = 0. \quad (72.73)$$

This last case corresponds to a Cantilever when  $K = 0$ .

Referring to [13] for more details, here we simply recall that:

1. The analysis of the Free end-conditions can be developed by using the results obtained for the Dirichlet case [13]. For a general approach to the Free end-conditions case, which extended the work of Trubowitz and colleagues to less regular coefficients  $A(x)$ , we refer to [2] and [3].
2. The Mixed case has been firstly considered in [13] for the equation in impedance form. The determination of quasi-isospectral potentials for the Sturm-Liouville equation in canonical form follows the previous guidelines, as observed in [4] (Lemma 1, Sect. 4).
3. The case of rods under Elastically Restrained end-conditions is different from the previous ones. It turns out that it is possible to construct only families of quasi-isospectral rods which preserve the higher spectrum (for order  $m \geq 2$ ), and change the smallest eigenvalue in a prescribed manner. This case is considered in [13] and the analysis is based on the determination of quasi-isospectral potentials under Robin-Robin end conditions presented in [11].

The main difference between the Dirichlet and Mixed case is that, in the former case, the parameter  $t$  appearing in the definition of the cross-sectional profile needs to satisfy the condition (72.32) only. Conversely, it can be shown that in case 2) (for  $K > 0$ ) there is a further restriction on the parameter  $t$ , namely  $t$  must belong to a *sufficiently* small neighborhood of zero. This last condition is necessary in order to construct one-sign solutions  $a(x)$  to Eq. (72.52) and, simultaneously, to recover physical end condition at  $x = 1$  (e.g., positive stiffness of the elastic spring at the right end).

For the sake of completeness, we recall that the method can be adapted to construct quasi-isospectral strings and, following [10], also some special classes of quasi-isospectral beams in bending vibration [13].

## References

1. Capecchi D, Vestroni F (2000) Monitoring of structural systems by using frequency data. *Earthq Eng Struct Dyn* 28:447–461
2. Coleman CF, McLaughlin JR (1993) Solution of the inverse spectral problem for an impedance with integrable derivative – Part I. *Commun Pure Appl Math XLVI*:145–184
3. Coleman CF, McLaughlin JR (1993) Solution of the inverse spectral problem for an impedance with integrable derivative – Part II. *Commun Pure Appl Math XLVI*:185–212
4. Dahlberg BEJ, Trubowitz E (1984) The inverse Sturm-Liouville problem III. *Commun Pure Appl Math XXXVII*:255–267
5. Darboux G (1882) Sur la représentation sphérique des surfaces. *C R Acad Sci Paris* 94:1343–1345
6. Deift PA (1978) Application of a commutation formula. *Duke Math J* 45:267–310
7. Dilena M, Morassi A (2009) Structural health monitoring of rods based on natural frequency and antiresonant frequency measurements. *Struct Health Monit* 8:149–173
8. Dilena M, Morassi A (2010) Reconstruction method for damage detection in beams based on natural frequency and antiresonant frequency measurements. *J Eng Mech ASCE* 136:329–344



9. Gesztesy G, Teschl G (1996) On the double commutation method. *Proc Am Math Soc* 124:1831–1840
10. Gladwell GML, Morassi A (2010) A family of isospectral Euler-Bernoulli beams. *Inverse Probl* 26:12, Paper n. 035006
11. Isaacson EL, Mc Kean HP, Trubowitz E (1984) The inverse Sturm-Liouville problem II. *Commun Pure Appl Math* XXXVII:1–11
12. Morassi A (2007) Damage detection and generalized Fourier coefficients. *J Sound Vib* 302:229–259
13. Morassi A (2013) Exact construction of beams with a finite number of given natural frequencies. *J. Vib Control* (to appear)
14. Pöschel J, Trubowitz E (1987) *Inverse spectral theory*. Academic, London
15. Vestroni F, Capecchi D (2000) Damage detection in beam structures based on frequency measurements. *J Eng Mech ASCE* 126:761–768

# Chapter 73

## A Metric for Modal Truncation in Model Reduction Problems

### Part 1: Performance and Error Analysis

Sadegh Rahrovani, Majid Khorsand Vakilzadeh, and Thomas Abrahamsson

**Abstract** The strength of the modal based reduction approach resides in its simplicity, applicability to treat moderate-size systems and also in the fact that it preserves the original system pole locations. However, the main restriction has been in the lack of reliable techniques for identifying the modes that dominate the input-output relationship. To address this problem, an enhanced modal dominance approach for reduction of second-order systems is presented. Briefly stated, a modal reduction approach is combined with optimality considerations such that the difference between the frequency response function of the full and reduced modal model is minimized in  $\mathcal{H}_2$  sense. A modal ranking process is performed without solving Lyapunov equations. In the first part of this study, a literature survey on different model reduction approaches and a theoretical investigation of the modified modal approach is presented. The error analysis of the proposed dominance metric is carried out. Furthermore, the performance of the method is validated for a lightly damped structure and the results are compared with other dominance metrics. Finally the optimality of the obtained reduced model is discussed and the results are compared with the optimum solution.

**Keywords** Modal truncation • Dominance metric • Norm • Model reduction • Optimality

### 73.1 Introduction

Despite the considerable progress in computational power and storage capabilities made over the last decades, the computational cost of simulation, identification and design of highly complex systems is still of major concern. To handle these problems, approximation model reduction methods provide a rational approach to study the behaviour of dynamic systems. The central idea is to systematically capture the main input-output properties by a much simpler model than needed for a precise description of the entire state of the system. The key issue in different approximation methods is to find a balance between the complexity and accuracy of the approximate model.

A wide variety of methods for model reduction have been proposed over the last decades and several state-of-the-art reviews give overviews of existing approximation methods [1]. An early work was in 1966 when Davidson [2] presented “The Modal Analysis” approach in a state space framework which was later extended by Chidambara [3] and others.

It was not until in 1970, that the impulse response  $\mathcal{L}_2$ -optimal reduction problem for MIMO dynamic systems was addressed by Wilson [4]. An optimality-based reduction approach was presented which involves the minimization of the quadratically weighted output error between the full and reduced models subjected to white noise inputs. Using a projection formulation, Hyland and Bernstein [5], simplified the necessary conditions of Wilson’s approach and proposed an iterative algorithm for unconstrained optimal model reduction problems. The main concern in the optimality-based reduction methods is the convergence and efficiency of the numerical algorithms to reach the global minimum.

Later, in 1981, Moore [6] proposed a quite different way of looking at model reduction based on system-theoretic arguments as opposed to optimality criteria [5]. The main idea is to eliminate any subsystem that has, in comparison, less contribution to the system impulse response matrix. This gave birth to a new approach called “Balanced model reduction”. Here the concept of state dominance is used in association with the degree of controllability and observability of a given state

---

S. Rahrovani (✉) • M.K. Vakilzadeh • T. Abrahamsson  
Department of Applied Mechanics, Chalmers University of Technology, SE-41296, Gothenburg, Sweden  
e-mail: [sadeghr@chalmers.se](mailto:sadeghr@chalmers.se); [khorsand@chalmers.se](mailto:khorsand@chalmers.se); [thomas.abrahamsson@chalmers.se](mailto:thomas.abrahamsson@chalmers.se)

as obtained from the system's Hankel Singular Values (HSVs). The balancing technique preserves stability, ensures a-priori upper bound of the reduction error and often leads to a near to optimal reduction. However, since no error criterion plays a role in balancing techniques, balanced reduction methods do not guarantee the optimality condition of the solution.

In an approach published in 1980, Skelton [7] provided a connection between the important classical input-output parameters (such as controllability, observability, norms and poles) and the output error quadratic cost function. In this approach a quadratic optimality criterion is utilized as in [4]. Here the relative contribution of a given state basis is determined through the decomposed cost criterion and the modes with least cost value are reduced. Therefore, the approximant is obtained without the use of parameter optimization and the associated numerical problems.

Among different reduction approaches, modal based truncation has gained much attention for model reduction of large-scale systems and is frequently the only preliminary step which makes further reduction tractable. However, the main restriction has traditionally been the lack of a proper modal dominance analysis and also the lack of a guaranteed bound for the approximation error. Such dominance analysis is required to select and discard the modes with relatively little contribution in the input-output relation. Therefore, possible functional enhancement, by combining the modal techniques with other approaches, has been studied by some authors [7].

The simplest modal selection approach, dominant frequency selection [8], presents a systematic method for approximation analysis and synthesis of control of large scale systems by generalizing the concept of aggregation in the mathematical economics. However, this method ignores the fact that the sensor/actuator placement, disturbances and performance requirements also affect the modal dominance. The influence of actuator/sensor placement on modal dominance was treated in [9] and [10]. Using the approximate internal balancing theory, a modal ranking procedure based on HSVs was proposed to treat the modal reduction of lightly damped structures with distinct eigenvalues. This technique was improved to handle the reduction of damped systems by introducing and deriving the HSV's intervals via eigenvalue perturbation theory [11]. The effect of the last two issues was studied in [12] by proposing a cost function as a modal dominance metric for modal truncation based on the impulse response error in  $\mathcal{L}_2$  sense. This technique was improved by Varga [13] to treat modal reduction of systems with multiple eigenvalues, or clusters of neighbouring eigenvalues.

In the first part of this study, an enhanced modal dominance approach for reduction of second-order systems is presented [14]. Briefly stated, a modal reduction approach is combined with optimality considerations such that the difference between the frequency response function of the full and reduced modal model is minimized in an  $\mathcal{H}_2$  sense. A literature review on different model reduction approaches and a theoretical investigation of the presented modified modal approach is presented. Performance and error analysis of the proposed dominance metric is carried out. Furthermore, the performance of the method is validated for a lightly damped structure and the results are compared with other dominance metrics. Finally the optimality of the obtained reduced model is discussed and the results are compared with the optimum solution.

## 73.2 Problem Statement

In this study we consider linear real-valued time-invariant (LTI) continuous-time asymptotically stable systems. The original full model is given by a system of ordinary differential equations in a state space form

$$\dot{x} = Ax + Bu, \quad y = Cx \quad (73.1a-b)$$

or, via Laplace transform of the above, represented by its transfer function (TF)

$$H(s) = C (sI_N - A)^{-1} B \quad (73.2)$$

and impulse response function (IRF)

$$h(t) = C \exp(At) B \quad (73.3)$$

These are the input-output mappings in the frequency and time domains, respectively. Here  $A \in \mathbb{C}^{N \times N}$ ,  $B \in \mathbb{C}^{N \times m}$  and  $C \in \mathbb{C}^{r \times N}$  are the state matrix and the input and output distribution matrices, respectively. The vectors  $x \in \mathbb{C}^N$ ,  $y \in \mathbb{R}^r$  and  $u \in \mathbb{R}^m$  are the state, the output and the input of the dynamic system and  $N$  is the order of the full model. In cases where there is only a single input and a single output, i.e.  $r = m = 1$ , then the system is single-input-single-output. Otherwise, when  $r > 1$  and  $m > 1$ , it is called a multi-input-multi-output (MIMO) system.

Given the full system, model order reduction methods attempt to construct an approximant of reduced order

$$\hat{x} = \hat{A}\hat{x} + \hat{B}u, \quad \hat{y} = \hat{C}\hat{x} \quad (73.4a-b)$$

with transfer function

$$\hat{H}(s) = \hat{C}(sI_N - \hat{A})^{-1} \hat{B} \quad (73.5)$$

and impulse response function

$$\hat{h}(t) = \hat{C} \exp(\hat{A}t) \hat{B} \quad (73.6)$$

where  $\hat{A} \in \mathfrak{C}^{n \times n}$ ,  $\hat{B} \in \mathfrak{C}^{n \times m}$ ,  $\hat{C} \in \mathfrak{C}^{r \times n}$  and  $n < N$ . A good model reduction is such that the principle component of the input-output behaviour of the original system is captured by the approximate reduced order system. Regardless of the method used to obtain (73.4), the quality of any reduced model of the form (73.4) could be measured by the transfer function (TF) error norm,  $\|H(s) - \hat{H}(s)\|$ , or the impulse response function (IRF) error norm,  $\|h(t) - \hat{h}(t)\|$ .

### 73.2.1 The Quadratic Approximation Problem

Let the error TF and the error IRF be defined as

$$E(s) = H(s) - \hat{H}(s) \quad (73.7)$$

$$e(t) = h(t) - \hat{h}(t). \quad (73.8)$$

Common norms in quadratically optimal problems, used to measure the closeness of the original system with the reduced order one, are the  $\mathcal{H}_2$  and  $\mathcal{L}_2$  norms.<sup>1</sup> These norms are used to determine the root mean square (RMS) gain of a continuous-time system in the frequency and time domains. If any or both of the full and reduced systems are unstable, the  $\mathcal{L}_2$ -norm is infinite. The  $\mathcal{L}_2$ -norm of the error system is defined as (see also [1])

$$N_e = \|e(t)\|_{\mathcal{L}_2}^2 = \text{tr} \left[ \int_0^\infty (h - \hat{h})^T (h - \hat{h}) dt \right]. \quad (73.9)$$

Introducing the error system triple,  $\{A_e, B_e, C_e\}$ , as

$$\left\{ \begin{bmatrix} A & 0 \\ 0 & \hat{A} \end{bmatrix}, \begin{bmatrix} B \\ \hat{B} \end{bmatrix}, [C \quad -\hat{C}] \right\}, \quad (73.10)$$

then the error  $\mathcal{L}_2$ -norm is expressed by

$$N_e = \text{tr} \left[ \int_0^\infty [C_e \exp(A_e t) B_e]^T [C_e \exp(A_e t) B_e] dt \right]. \quad (73.11)$$

$N_e$  can be related to an expression involving the error system Gramians, see [1],

$$N_e = \text{tr} (B_e^T B_e Q_e) = \text{tr} (C_e C_e^T P_e) \quad (73.12)$$

where  $P_e$  and  $Q_e$  are the observability and controllability Gramian matrices, known as the solution of two Lyapunov equations

$$A_e P_e + P_e A_e + B_e B_e^T = 0, \quad Q_e A_e + A_e^T Q_e + C_e C_e^T = 0 \quad (73.13a-b)$$

Equivalently, the squared  $\mathcal{H}_2$ -norm of a MIMO system,  $E(s)$ , is defined as the trace of a matrix integral in the frequency domain

$$N_E = \|E(s)\|_{\mathcal{H}_2}^2 \quad (73.14)$$

$$N_E = \text{tr} \left[ \frac{1}{2\pi} \int_{-\infty}^{\infty} E(j\omega)^H E(j\omega) d\omega \right] \quad (73.15)$$

<sup>1</sup> $\mathcal{H}_p$  and  $\mathcal{L}_p$  norms refer to the Hardy and Lebesgue spaces  $p$ -norm defined for complex-valued and real-valued continuous-time functions, respectively. According to Parseval's theorem there is an equality relation between TF norm,  $\mathcal{H}_p$ , and IRF norm,  $\mathcal{L}_p$ , norms for  $p = 2$ .

The main issue in the quadratic reduction problem is to minimize the error function in an  $\mathcal{H}_2$ -sensor in an  $\mathcal{L}_2$ -sense. Some methods, such as those given by Wilson [4] and by Hyland and Bernstein [5], consider the general class of  $n$ th order LTI MIMO state-space systems as possible approximants while in the truncation methods, the reduced model is obtained by elimination of the weak subsystem. These methods use singular value decomposition to select the dominant part of the system. The proposed method in this study is in the category of truncation approach and will be presented in the next section.

### 73.3 Modal Dominancy Metrics

The classical modal reduction approach has the common feature of leading to an approximant whose set of eigenvalues is a sub-set of the spectrum of the original system. The main strength of this category of truncation techniques resides in its simplicity, applicability to treat large systems and also in the fact that it preserves the physical interpretation of the states. However, the main restriction has been in the lack of a proper modal dominancy procedure. To solve this, different truncation metrics are addressed by selective modal procedures. The simplest modal selection approach, called dominant frequency selection, ignores the fact that the sensor/actuator placement, disturbances and performance requirements also affect the modal dominance.

Firstly, the sensor/actuator placement effect has been studied in [9, 15]. It has been shown that, for lightly-damped systems, the modal coordinates approximately coincide with the balanced ones. Consequently this leads to a systematic mode selection procedure, based on the Hankel singular values, which retain the “most controllable and observable” modes and neglect the rest. Consider the complex-valued system with state-space realization in decoupled modal coordinates as

$$\dot{\eta}_k = \lambda_k \eta_k + \tilde{b}_k, \quad \tilde{y} = \sum_{i=1}^N \tilde{c}_i \eta_i \quad (73.16a-b)$$

for  $k = 1, \dots, N$ . Restricting to the case of light positive damping, the eigen-spaces appear in complex conjugate pairs, i.e.  $\lambda_i$  and  $\bar{\lambda}_i$  are both eigenvalues of the system. Solving the Lyapunov equations for this system of modal coordinates, the controllability and observability Gramian diagonal elements can be expressed as (see also [9]),

$$\tilde{p}_{ii} = -\tilde{b}_i \tilde{b}_i^H / (\lambda_i + \bar{\lambda}_i), \quad \tilde{q}_{ii} = -\tilde{c}_i^H \tilde{c}_i / (\lambda_i + \bar{\lambda}_i) \quad (73.17a-b)$$

and for general off-diagonal elements

$$\tilde{p}_{ij} = -\tilde{b}_i \tilde{b}_j^H / (\lambda_i + \bar{\lambda}_j), \quad \tilde{q}_{ij} = -\tilde{c}_i^H \tilde{c}_j / (\lambda_i + \bar{\lambda}_j) \quad (73.18a-b)$$

Considering that the system modes are lightly damped with distinct eigenvalues, the denominators of the diagonal elements are very small. Therefore the diagonal elements of the Gramian matrices tend to be much larger in comparison with the off-diagonal ones. Each complex pair of modes will yield

$$\tilde{p}_{ii} = \|\tilde{b}_i\|^2 / \text{Re}(2\lambda_i) \quad \tilde{q}_{ii} = \|\tilde{c}_i\|^2 / \text{Re}(2\lambda_i) \quad (73.19a-b)$$

where  $\tilde{p}_{ii}\tilde{q}_{ii}$  approaches the corresponding squared HSV, i.e.  $\sigma_i^2$ . This is used as dominancy metric to evaluate the relative contribution of the  $i$ th mode in the input-output relation. It should be noted that by using proper multiplier values for  $\tilde{b}_i$  and  $\tilde{c}_i$ , the system can be easily transformed into a modal-balanced coordinate while the TF matrix remains unchanged. Further improvement of this method to treat the well damped systems, by deriving the HSV intervals via eigenvalue perturbation theory, is presented in [11].

Secondly, the effect of disturbances and performance requirements on modal dominance was studied in [12] by proposing a cost function, related to a stochastic input, as a modal dominancy metric. In this approach the cost function is introduced by the difference between the response of the full model and the reduced modal model due a white noise stochastic input, i.e.  $\tilde{e}(t) = y(t) - \tilde{y}(t)$ . Therefore, according to Eq. (73.12), a suitable dominancy metric can be expressed as

$$N_{\tilde{y}} = \text{tr}(\tilde{B}^H \tilde{B} \tilde{Q}) = \text{tr}(\tilde{C} \tilde{C}^H \tilde{P}) \quad (73.20)$$

This can be decomposed as

$$N_{\tilde{y}} = \sum_{i=1}^N N_{\tilde{y}_i}, \quad N_{\tilde{y}_i} = \text{tr}(B^T B Q)_{ii} \quad (73.21\text{a-b})$$

where  $N_{\tilde{y}_i}$  is the cost for eliminating the  $i$ th modal state. It is worth mentioning that for systems with distinct eigenvalues, the contribution to the norm  $N_{\tilde{y}_i}$  is the cost associated with the  $i$ th eigenvalue, [13]. In the following a new approach for modal truncation is studied and an explicit form of an input-output based metric, without the need of solving the Lyapunov equation, is being derived.

### 73.3.1 A Dominancy Metric Based on Modal Contribution to Transfer Function $\mathcal{H}_2$ -Norm

Here, a new method for modal reduction of dynamic second-order systems is presented. This technique proposes a quadratic truncation criterion based on modal coordinate contributions to the square of  $\mathcal{H}_2$  magnitude of the frequency response function error. In modal truncation techniques, modal realization is chosen to represent the input-state-output mapping. With some loss of generality,  $A$  is considered to be in diagonalizable form. Then  $A$  can be transformed into diagonal form, i.e.  $\tilde{A} = \text{diag}(\lambda_1, \lambda_2, \dots, \lambda_N)$ , with  $\tilde{A} = T^{-1}AT$ ,  $\tilde{B} = T^{-1}B$ ,  $\tilde{C} = CT$  through a similarity transformation,  $\eta = Tx$ . The matrices

$$\tilde{B} = [\tilde{b}_1^T \dots \tilde{b}_N^T]^T, \quad \tilde{C} = [\tilde{c}_1 \dots \tilde{c}_N] \quad (73.22\text{a-b})$$

are introduced with row vectors  $\tilde{b}_k = [\tilde{b}_{k1} \dots \tilde{b}_{km}]$  and column vectors  $\tilde{c}_k = [\tilde{c}_{1k} \dots \tilde{c}_{rk}]^T$  for  $k = 1, \dots, N$ . The transfer function matrix  $H$  is a complex valued function of dimension  $r \times m$

$$\tilde{H} = \begin{bmatrix} \tilde{H}_{11} & \dots & \tilde{H}_{1m} \\ \vdots & \ddots & \vdots \\ \tilde{H}_{r1} & \dots & \tilde{H}_{rm} \end{bmatrix}, \quad \tilde{H}_{ql} = e_q^T \tilde{C} (sI_N - \tilde{A})^{-1} \tilde{B} e_l \quad (73.23\text{a-b})$$

where  $e_q$  and  $e_l$  are Boolean vectors. By a partial fractional expansion

$$\tilde{H}_{ql} = \sum_{k=1}^N \tilde{c}_{qk} \tilde{b}_{kl} / (s - \lambda_k) \quad (73.24)$$

According to Eqs. (73.5) and (73.7), assuming the system to be in modal realization, the cost function which should be minimized is the square of the  $\mathcal{H}_2$ -norm of the error system.

$$N_E = \text{tr} \left[ \frac{1}{2\pi} \int_{-\infty}^{\infty} \{H(j\omega) - \tilde{H}(j\omega)\} \{H(j\omega) - \tilde{H}(j\omega)\}^H d\omega \right] \quad (73.25)$$

The problem is to find a reduced order model, with a pre-specified order, which minimizes the difference between the frequency response function of the reduced model and the original system in an  $\mathcal{H}_2$  sense. According to Eqs. (73.5) and (73.22), the contribution of the  $i$ th modal state to the system response is expressed by

$$Y_i = [\tilde{c}_i (s - \lambda_i)^{-1} \tilde{b}_i] U \quad (73.26)$$

where the Laplace transformation of the input white noise,  $U$ , is equal to one. Therefore the cost, defined based on the transfer function  $\mathcal{H}_2$  norm, for elimination of each state is proportional to

$$\text{tr} \left[ \int_{-\infty}^{\infty} \left\| \tilde{c}_i \tilde{b}_i / (j\omega - \lambda_i) \right\|^2 d\omega \right] \quad (73.27)$$

Fortunately this integral can be expressed in an explicit form. Therefore the dominancy metric for modal truncation is defined as

$$\frac{1}{2\pi} \text{tr} \left\{ \tilde{c}_i \tilde{b}_i (\tilde{c}_i \tilde{b}_i)^H \left[ 1 / \Re(\lambda_i) \arctan \left( \frac{\omega}{\Re(\lambda_i)} \right) \right]_{\omega_2=-\infty}^{\omega_1=\infty} \right\}. \quad (73.28)$$

This systematic mode selection procedure aims at retaining the dominant modes, based upon the metric, and neglecting the rest with least values. In the following sections the performance of the presented metric is validated via two illustrative

**Fig. 73.1** A3-DOF mass-spring-damper system

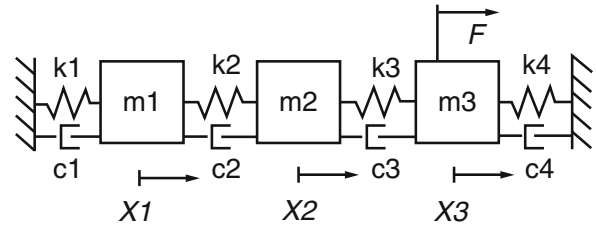


**Fig. 73.2** Frequency response comparison of second order approximants via different approaches

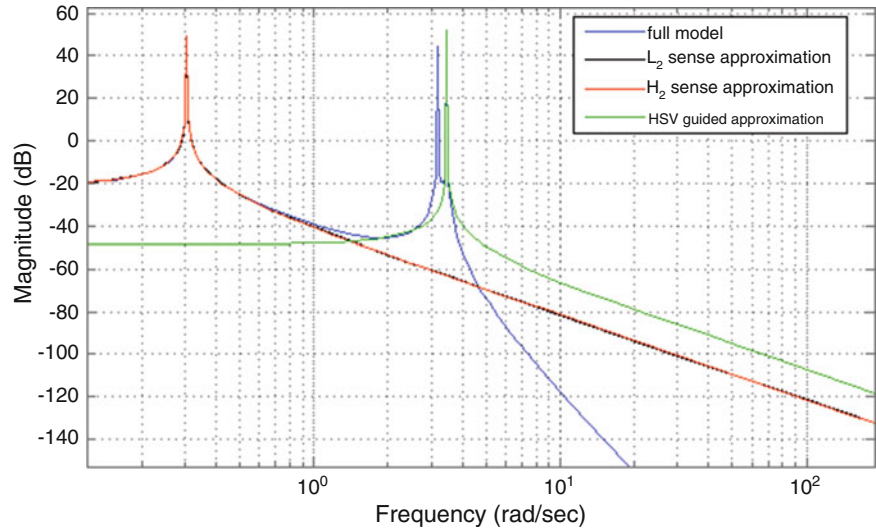


**Table 73.1** Modal ranking based upon different dominance metrics

Dominance metric values	Decision criteria	First mode	Second mode	Third mode
$\mathcal{H}_2$ guided	$N_{\bar{E}}$	1,308	437	825
$\mathcal{L}_2$ guided	$N_{\bar{e}}$	1,308	437	825
$HSV$ guided	$HSV$	14,959	8,418	20,662

examples. Specifically these examples investigate (i) the optimality of the solution, (ii) The performance and error analysis of the method and (iii) the effect of multiple eigenvalues on metric non-uniqueness.

### 73.3.2 Performance and Error Analysis

In this section a complete performance and error analysis of the proposed modal dominance metric is carried out. The performance of the proposed method for modal reduction of lightly damped structures is validated and the results are compared with other dominance metrics. Furthermore, the study attempts to unify the  $\mathcal{H}_2$  and  $\mathcal{H}_\infty$  model-reduction performance objectives such that the reduced order model satisfying an optimized  $\mathcal{H}_2$  cost bound as well as a pre-specified  $\mathcal{H}_\infty$  bound. Details are demonstrated via the following illustrative case study.

*Example 1.* Consider the SISO structure demonstrated in Fig. 73.1. In this case the damping values are chosen such that all structural resonances become lightly damped. This can be seen in the transfer function of the system shown in Fig. 73.2.

The results of the modal rankings based on different metrics are shown in Table 73.1.

Different conclusions can be drawn from the results. First, according to Parseval’s theorem, it should not be surprising that for such a lightly damped system the Skelton  $\mathcal{L}_2$  metric and the  $\mathcal{H}_2$  metric proposed here lead to identical modal contribution weightings. This is due to the fact that both metrics have used the same performance criterion in quadratic sense, one derived in frequency domain and one in the time domain,

$$\|G\|_{\mathcal{H}_2} = \|g\|_{\mathcal{L}_2} \tag{73.29}$$

**Table 73.2** Modal-ranking comparison between  $HSV$  and  $\mathcal{H}_\infty$  guided approaches

Modal dominance rankings	First mode rank	Second mode rank	Third mode rank
$HSV$ guided approach	2	3	1
$\mathcal{H}_\infty$ guided approach	2	3	1

that can be decomposed based on modal coordinates. Secondly, note that although all methods lead to the same answer in truncating of the second vibrational mode for the best reduction into a fourth order model, it may lead to confusion when it comes to further reductions. The results clearly show that the first two methods preserve the first mode for the second order model while the HSV based approach captures the third one, see Fig. 73.2.

This paradigm can be interpreted in view of the fact that the HSV-based approaches, such as the balancing approach, have strong ties with error  $\mathcal{L}_\infty$ -norm [16], and therefore they are not expected to generate an optimal result in  $\mathcal{L}_2$  sense. It becomes more clear when  $\mathcal{H}_\infty$  is used as a guideline to the modal ranking process [17]

$$\|\tilde{G} - \hat{G}\|_{\mathcal{H}_\infty} \leq \sum_{i=r+1}^N \sigma_{max}(\tilde{C}_i \tilde{B}_i) / |\Re(\lambda_i)| \quad (73.30)$$

As it is shown in Table 73.2, the results of modal ranking based on HSVs and the output  $\mathcal{H}_\infty$ -norm criteria seem to be consistent.

This example demonstrates the fact that a suboptimal approximant in  $\mathcal{H}_2$  sense may be other than approximants based on other metrics, e.g., such as degree of observability and controllability. Therefore, it also highlights the importance of choosing a proper decision metric in obtaining a good reduced model.

Generally, minimization of error  $\mathcal{H}_\infty$ -norm, called “worst case frequency domain”, results in decreasing the largest singular value of the error transfer function while the minimization in  $\mathcal{H}_2$  sense, which we argue is a more suitable measure for system performance than the  $\mathcal{H}_\infty$ -norm, leads to the pushing down of the whole frequency response in average sense. As shown in the above example, there may not be a direct relation between  $\mathcal{H}_2$  and  $\mathcal{H}_\infty$  norms and they seem to represent distinct approximation objectives. However, Wilson showed that there exist significant connections [18]. In this regard, some attempts have been made on further unification of the  $\mathcal{H}_2$  and  $\mathcal{H}_\infty$  norms to achieve a desirable measure of a system’s robust performance. Here the modal truncation decisions can be made based on a hybrid metric, defined as a trade-off criterion

$$\mathcal{J}_{Hyb} = \min(\alpha \mathcal{J}_{\mathcal{H}_2} + (1 - \alpha) \mathcal{J}_{\mathcal{H}_\infty}) \quad (73.31)$$

Where  $\alpha$  can be considered as a tuning parameter varying between 0 and 1.

### 73.3.3 On the Question of Optimality

It is worth mentioning that although the presented approach is guided by optimality considerations, no rigorous guarantee of optimality is possible. It is because of the fact that, in contrast to the method presented by Wilson [4], this approach does not consider the entire class of  $n$ -order LTI systems as possible choices for the solution. In view of this fact, it should not be surprising that this method may result in non-optimal solutions. However this approach leads to a sub-optimal decision among the ( $N$ ) possible solutions. This is being investigated in the following illustrative example.

*Example 2.* To make direct comparison with previously published results, consider the SISO six degree of freedom structure with one well-damped and two lightly-damped vibrational modes, see Ref. [19]. According to Eq. (73.15), the normalized quadratic cost function is used to evaluate the quality of the reduced models as

$$\delta = \sqrt{N_E/N_0}, \quad N_0 = \int_{-\infty}^{+\infty} \|H(j\omega)\|^2 d\omega \quad (73.32a-b)$$

Results of the proposed approach are compared with those obtained from [19] in Table 73.3.

The quadratically optimal solution, obtained in [19], leads to the global minimum of the cost function while the method presented here gives a very good suboptimal reduction decision which aims at minimizing the error function by retaining  $n$  modes among the  $N$  modal coordinates and discard the rest. The results clearly show the advantage of using the presented method which leads to a nearly optimal approximant without the use of parameter optimization and the associated numerical



**Table 73.3** Errors of second and fourth order reduced models (Optimum solution from [19])

	Normalized error $\delta$ (fourth order model)	Normalized error $\delta$ (second order model)
Optimal approach	0.4005	0.6928
Proposed approach	0.4151	0.6929
Balanced approach	0.4175	0.6945

problems. It is also demonstrated that it gives a somewhat more accurate approximant rather than the balancing approach, in  $\mathcal{H}_2$  sense.

## 73.4 Conclusion

In this study, a modal dominance approach for reduction of second-order systems was presented. A metric based on modal contribution to the transfer function was given in an explicit form. Briefly stated, the reduced modal model is determined such that it minimizes the frequency response error in  $\mathcal{H}_2$  sense. A performance and error analysis of the proposed modal dominance metric was carried out and the optimality of the solution was discussed. It was shown that, due to the fact that the presented method is guided by quadratic optimality considerations, the obtained approximant is nearly optimal and the results are more accurate than the balancing approach in  $\mathcal{H}_2$  sense. It was shown that, due to the fact that the presented method is guided by quadratic optimality considerations, the obtained approximant is nearly optimal and the results are more accurate than the balancing approach in  $\mathcal{H}_2$  sense. In part 2 of this study, presented as a separate paper, the proposed method is improved to be able to use the information extracted from the spatial distribution of actuators and sensors and also the internal structure and spectral properties of the input. Since a QR factorization based technique is used to treat systems with multiple eigenvalues the modal ranking process is performed without solving any Lyapunov equation.

## References

1. Antoulas AC (2005) Approximation of large scale dynamical systems. Advances in design and control. SIAM, Philadelphia
2. Davison EJ (1966) A method for simplifying linear dynamic systems. IEEE Trans Autom Control AC-11(1):93–101
3. Chidambara MR (1967) On a method for simplifying linear dynamic systems. IEEE Trans Autom Control 12:213–214
4. Wilson DA (1970) Optimum solution of model-reduction problem. Proc Inst Electr Eng 117:1161–1165
5. Hyland DC, Bernstein DS (1985) The optimal projection equations for model reduction and the relationship among the methods of Wilson, Skelton and Moore. IEEE Trans Autom Control 30:1201–1211
6. Moore BC (1981) Principal component analysis in linear systems: controllability, observability and model reduction. IEEE Trans Autom Control AC-26(1):17–32
7. Skelton RE (1980) Cost decomposition of linear systems with application to model reduction. Int J Control 32:1031–1055
8. Aoki M (1968) Control of large-scale dynamic systems by aggregation. Autom Control IEEE Trans Autom Control AC-13:246–253
9. Gregory CZ (1984) Reduction of large flexible spacecraft models using internal balancing. J Guid Control Dyn 7:725–732
10. Bletloch PA, Mingori DL, Wei JD (1987) Perturbation analysis of internal balancing for lightly damped mechanical systems with gyroscopic and circulatory forces. J Guid Control Dyn 10(4):406–410
11. Oostveen H, Wortelboer P (1990) Modal reduction guided by Hankel singular value intervals. In: IEE colloquium, integrating control system design with the analysis of flexible structures, pp 2/1–2/3
12. Hughes P, Hablani HB, Skelton RE (1982) Order reduction for models of space structures using modal cost analysis. J Guid Control Dyn 5:351–357
13. Varga A (1995) Enhanced modal approach for model reduction. Math Model Syst 1(2):91–105
14. Khorsand Vakilzadeh M, Rahrovani S, Abrahamsson T (2012) An improved modal approach for model reduction based on input-output relation. In: International conference on noise and vibration engineering, ISMA, Leuven, Belgium pp 3451–3460
15. Pernebo L, Silverman LM (1982) Model reduction via balanced state space representation. IEEE Trans Autom Control AC-27:382–387
16. Glover K (1984) All optimal Hankel-norm approximations of linear multivariable systems and their  $L_\infty$  error bounds. Int J Control 39: 1115–1193
17. Beghi A, Portone A (2002) Model reduction by sub-structuring. In: Proceedings of mediterranean conference on control and automation
18. Wilson DA (1988) System order reduction using the Hilbert-Schmidt norm of the Hankel operator. Model Simul Syst 3:287–289
19. Spanos JT, Milman MH, Mingori DL (1992) A new algorithm for  $L_2$  optimal model reduction. Automatica 28:897–909

# Chapter 74

## A Metric for Modal Truncation in Model Reduction Problems

### Part 2: Extension to Systems with High-Dimensional Input Space

Sadegh Rahrovani, Majid Khorsand Vakilzadeh, and Thomas Abrahamsson

**Abstract** In the first part of this study, a theoretical investigation of an improved modal approach and a complete error analysis of the proposed modal dominance metric were presented. In this part the problem of metric non-uniqueness for systems with multiple eigenvalues is described and a method to circumvent this problem based on spatial distribution of either the sensors or the actuators is proposed. This technique is implemented using QR factorization without solving Lyapunov equations. Moreover, the method is improved such that it is able to use the information extracted from spectral properties of the input. Also in order to make the method more effective, information extracted from the input internal structure is incorporated in the modal ranking process. It is shown that this improvement is particularly effective in problems with high-dimensional input and/or output space such as in distributed loading and moving load problems. Finally the performance of the method is validated for a high order system subjected to a high-dimensional input force. That originates from a railway track moving load problem.

**Keywords** Model reduction • High-dimensional input space • Spectrum • Spatial distribution • Singular value decomposition

#### 74.1 Introduction

Despite the considerable progress in computational power and storage capabilities, made over the last decades, the computational cost and performance of the model reduction methods to treat highly complex real structures used in railway, aerospace or automotive industries are still of major concern. In this regard much more effective reduction methods are required to further reduce such large-scale finite element (FE) models. To achieve this, one can take account of the information extracted from system input at same fundamental level as the system information. Some methods have been developed for frequency weighted model reduction. Given an input output weighting these techniques aim at generating a reduced model which minimize the weighted error. Others attempt to obtain a good approximate in a frequency range of interest which can be specified based on input spectrum information [1].

Among several techniques aimed at performing model reduction by using input information, frequency weighted balancing approach is widely used. This approach, in contrast to classical balancing, is able to generate a good approximate in a frequency range of interest which can be specified based on input spectrum information. Also if the input and output weightings are given, these techniques generate an approximate that leads to a small weighted error with respect to  $\mathcal{H}_\infty$ -norm [2]. However, there are examples where the approximant becomes unstable while the original system is stable. The reason is that the weighted Gramians do not generally satisfy Lyapunov equations that ensure stability. Moreover it should be noted that in high order problems frequency weighted balancing requires working with a pair of larger Lyapunov equations i.e. weighted ones, and then applying dense methods to achieve the reduced equations [3]. It can get worse in problems with high dimensional input/output spaces e.g. moving load and distributed loading problems. Such problems typically lead to a pair of large weighted Gramians, even larger than twice of the original system order, which may cause inefficiency with respect to both memory and computation.

---

S. Rahrovani (✉) • M.K. Vakilzadeh • T. Abrahamsson  
Department of Applied Mechanics, Chalmers University of Technology, SE-41296, Gothenburg, Sweden  
e-mail: [khorsand@chalmers.se](mailto:khorsand@chalmers.se); [thomas.abrahamsson@chalmers.se](mailto:thomas.abrahamsson@chalmers.se)

On the other side modal based truncation has gained much attention for model reduction of large-scale systems and is frequently the only preliminary option which makes further reduction tractable. It starts by transforming the system initially written in terms of physical coordinates into the modal coordination [4] and do the truncation based on a suitable modal dominance metric afterwards. The advantage of modal approach becomes clear in reduction of huge FE models which typically obtained in modelling of most real mechanical applications. A survey on modal dominance metrics was presented in first part of this study. Also a theoretical investigation and an error analysis of the proposed metric were carried out. This method is very efficient and superior in the sense that it calculates the modal contribution to the I/O relation without solving Lyapunov equations. However some inefficiency problems that can arise in reduction of systems subjected to high-dimensional input is still of concern. To treat such problems an SVD-based technique [5] to extract and incorporate the input force internal structure information into the modal ranking process is presented. It is shown that the improved method is particularly effective in reduction of systems subjected to moving and distributed input loading. Moreover the problem of metric non-uniqueness for systems with multiple eigenvalues is described and a method to circumvent this problem is proposed. This technique results in a more compact reduced model in large-scale problems. Finally the performance of the method is validated for a high order system subjected to a high-dimensional input force.

## 74.2 Metric Non-uniqueness in Multiple Eigenvalue Problems

The main issue in this section is to investigate the performance of the presented dominance metric to detect the fully and nearly uncontrollable and unobservable modal coordinates. Also the metric non-uniqueness of the metric in problems with multiple eigenvalues is described and treated. In such problems it should be noted that all linear combinations of the modes with repeated eigenvalues can be considered as an eigenmode of the system. Therefore, based on the non-uniqueness of the modes chosen as the eigenvectors in the corresponding subspace, different and non-unique values can be assigned as modal contributions to the I/O relation. In order to circumvent this problem we use the fact that the mode shapes which are orthogonal to either the spatial distribution of the actuators or the spatial distribution of the sensors do not contribute in the I/O relation and they can be discarded. Therefore the mode vectors coordinate are rotated such that some of them render modes that are either uncontrollable or unobservable while the others are fully controllable and observable. This idea is implemented by using the QR decomposition technique without solving Lyapunov equations.

This algorithm is implemented in two steps. First the uncontrollable modal coordinates according to the corresponding eigenvectors with multiple eigenvalues are identified. These are the directions orthogonal to the spatial distribution of the excitation, which are extracted using the QR decomposition of the modal realization of the  $B$  matrix. Consider the original system model  $\{A, B, C\}$  and transform it into a diagonal form,  $\tilde{A} = T^{-1}AT$ ,  $\tilde{B} = T^{-1}B$ ,  $\tilde{C} = CT$  using a similarity transformation,  $T$  based on eigenvectors. Therefore  $\tilde{A}$  becomes diagonal. Now consider the  $i$ th mode set corresponding to a repeated eigenvalue in modal coordinate. The sub-system related to  $i$ th mode set can be expressed as

$$\dot{\eta}_i = \tilde{A}_i \eta_i + \tilde{B}_i u, \quad \tilde{y} = \tilde{C}_i \eta_i. \quad (74.1a-b)$$

By transforming the modal coordinates with repeated eigenvalues into a new coordination  $\eta_i = Q_i$  such that  $Q$  is computed through QR factorization of the  $\tilde{B}_i$  matrix. New modal coordinate contribute in I/O relation as follow

$$\dot{\eta}_i = Q^T \tilde{A}_i Q \eta_i + Q^T \tilde{B}_i u, \quad \tilde{y} = \tilde{C}_i Q \eta_i. \quad (74.2a-b)$$

It is clear that  $Q^T \tilde{B}_i$  matrix is an upper triangular matrix. For cases in which the degree of multiplicity of the repeated eigenvalue is higher than the dimension of the range space of the loading,  $Q^T \tilde{B}_i$  is singular since it consists of one or more rows with zero elements. The uncontrollable modal coordinates which span the null space of  $Q^T \tilde{B}_i$  can be computed,

$$\dot{\eta}_i = \hat{A}_i \eta_i + Ru, \quad \begin{pmatrix} \{R_1\} \\ \{0\} \end{pmatrix} \in \mathbb{R}^{N \times m} \quad (74.3a-b)$$

where and  $R_1$  is a full rank upper triangular matrix. It is clear that the uncontrollable modes are not excited due to the input excitation and therefore do not contribute to the output. These modes will be excluded from the second step of the algorithm. In the second step, a similar algorithm is used to extract the unobservable coordinates corresponding to the eigenvectors with multiple eigenvalues, which have not been omitted by in the first step. The projection this time is derived based on the

**Fig. 74.1** A 10-DOF mass-spring symmetric system. In case (i)  $F_1, F_2$  are assumed to be two in-phase correlated harmonic forces with same amplitude level. In case (ii) the distributed loading exerted on all masses are assumed to be zero except  $F_1, F_2$  which are considered as out of phase correlated harmonic forces with same level of amplitude

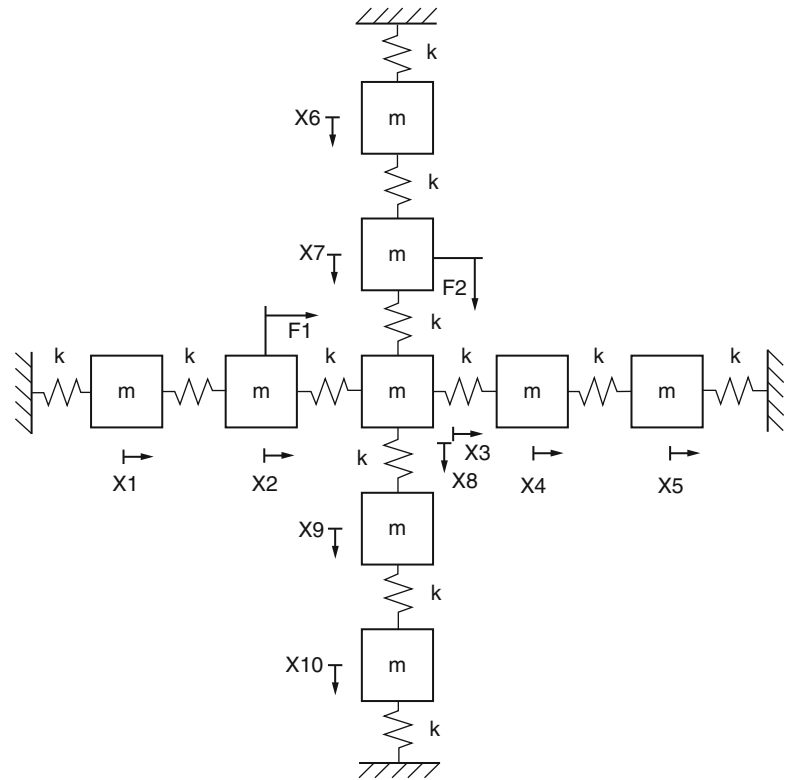


**Table 74.1** Modal-ranking analysis for case study (i)

Proposed dominancy metric value	Mode no. 1	Mode no. 2	Mode no. 3	Mode no. 4	Mode no. 5	Mode no. 6	Mode no. 7	Mode no. 8	Mode no. 9	Mode no. 10
Proposed approach	190	190	101	101	0	0	33	33	26	26
Improved algorithm with QR	0	0	0	0	0	0	0	0	0	0

QR decomposition of the  $\tilde{C}_i^T$  to detect the directions orthogonal to sensors spatial distribution. Using such a transformation,  $\eta_i = Q \hat{\eta}_i$ , some modal coordinates lie in the null space of the  $\tilde{C}_i Q$  matrix

$$\dot{\hat{\eta}}_i = \tilde{A}_i \hat{\eta}_i + \tilde{B}_i u, \quad \tilde{y} = \tilde{R}^T \hat{\eta}_i \quad (74.4a-b)$$

where  $R^T = [\{R_1\} 0] \in \mathbb{R}^{r \times N}$  and  $R_1$  is a full rank lower triangular matrix. In the following, the performance of this algorithm in improvement of the proposed method is demonstrated via an insightful illustrative example.

*Example 1.* In this example, the performance of the presented algorithm is illustrated via an insightful example. A 10-DOF double symmetric mechanical system is considered as shown in Fig. 74.1. By putting the input force on nodes of some vibrational eigen-modes, the system is designed to be non-minimal. Two different input-output relations are considered here: Case study (i): Two correlated in-phase harmonic input forces,  $F_1, F_2$ , with the same amplitude are exciting two masses, shown in Fig. 74.1. The output is the sum of the response of two masses such that  $y(t) = x_4(t) + x_9(t)$ . According to the double symmetry and the positions chosen for the actuators and the sensors, it is expected that  $y = 0$  for all times. Therefore, by the design of this example, the optimum reduced model is of order 0. This can be also seen from the zero value of the Hankel matrix rank, which shows that none of the states are contributing to the output.

Results of the modal ranking are presented in Table 74.2. According to the results, the proposed metric without mode rotation can only detect the non-minimality due to four uncontrollable modes and offers a model order of 16 for the optimum approximant. This should not be surprising since the dominancy metric is defined based on the contribution of each individual mode to the output and thus it fails to detect that the contributions of individual modes might cancel out each other in the output. To solve this, the presented QR based algorithm is implemented before evaluating the modal contributions. Results of the modal dominancy analysis after mode rotation based on  $\tilde{B}$  are presented in Table 74.1.

**Table 74.2** Modal-ranking analysis for case study (ii)

Proposed dominance metric value	Mode no. 1	Mode no. 2	Mode no. 3	Mode no. 4	Mode no. 5	Mode no. 6	Mode no. 7	Mode no. 8	Mode no. 9	Mode no. 10
Proposed approach	190	190	101	101	0	0	33	33	26	26
Improved algorithm with QR	0	105	0	131	0	0	1465	0	392	0

Case study (ii): In this case the sensor placements are assumed to be the same as in case (i). Instead an arbitrary distributed loading is considered to be exerted to all masses. The forces are treated as uncorrelated input signals.

The resulting metric values, calculated after mode rotation, are presented in Table 74.2. For both cases, since the loading condition (considering the nonzero inputs) is equal, the assigned modal contributions are identical, see Tables 74.1 and 74.2. However, in case (ii) modal contributions according to the repeated eigenvalues magnify each other in the output. As a result, the output time response becomes a non-zero signal. This can be also seen from the rank of the Hankel matrix which is equal to eight for this I/O relation. It is notable that since the degree of multiplicity of the repeated eigenvalues is not higher than the dimension of the range space of the loading, no treatment can be done based on the QR decomposition of  $\tilde{B}$  matrix. This is the typical case in distributed and moving load problems. As described above in such cases the QR decomposition of  $\tilde{C}^T$  is used to obtain the minimal realization.

Finally it is worth mentioning that for systems with high-dimensional but correlated input and output spaces, it might happen that neither the balancing approach nor the presented algorithm can detect all uncontrollable and unobservable states if such correlation is not accounted for by a proper adjustment of the  $B$  and  $C$  matrices. This problem is addressed in Sect. 74.3.1 where information from the internal structure of the input signal is incorporated in the reduction process.

### 74.3 Incorporating Input Information in Truncation Decisions

Real problems in railway, aerospace and automotive industries usually require large computational resources. To treat these problems much more efficient and effective reduction approaches is required. To achieve higher efficiency, some reduction methods take account of the information extracted from system input at the same fundamental level as the system information [6]. Also in order to make the method more effective, information extracted from the input force internal structure is incorporated in the modal ranking process. To implement this idea an SVD-based technique is utilized prior to the dominance analysis. These are discussed as follow.

#### 74.3.1 Modal Truncation Based on Spatial and Spectral Properties of the Input

The presented modal criterion presented in Part 1 aims at approximating the system over all frequencies. In many cases, however, a good approximant is required only in a specific frequency range of interest. Thus, since for large matrices the complete spectrum of the state matrix cannot be computed efficiently, a common approach uses a preferred set of approximate eigenvalues which lie in the range of interest. The frequency range of interest can be specified according to the input spectrum. Using this, a more efficient reduction process can be done by excluding the modes outside the range of interest either in the eigenvalue problem by avoiding the full eigenvalue solution or in the calculation of the metric values for by limiting the integral bound to a pre-specified range. The first can be implemented using iterative eigenvalue solvers using power iteration, inverse iteration, Rayleigh quotient iteration, subspace methods etc., which aim at approximating the eigenvalues lie in a preferred range. According to explicit formulation of modal dominance metric, presented in Part 1, a pre-specified frequency range can be considered by easily changing the boundary limit from  $[-\infty, \infty]$  to  $[\omega_{min}, \omega_{max}]$ ,

$$\mathcal{J}_i = \frac{1}{2\pi} tr \left\{ \tilde{c}_i \tilde{b}_i \left( \tilde{c}_i \tilde{b}_i \right)^H \left[ 1 / \Re(\lambda_i) \arctan \left( \frac{\omega}{\Re(\lambda_i)} \right) \right]_{\omega_2 = \omega_{min} - \text{Im}(\lambda_i)}^{\omega_1 = \omega_{max} - \text{Im}(\lambda_i)} \right\}. \quad (74.5)$$

This increases the efficiency in problems with high dimensional input/output spaces which include moderate-sized matrix multiplications for several times. The advantage of such techniques will be discussed in Sect. 74.4.2.

All the techniques mentioned above attempt to decrease the computational cost required for the model reduction process in particular for large scale problems. However, one main concern for the reduction approaches is to be more effective in the sense that they become able to generate a more accurate reduced model for a pre-specified reduction order. To achieve this, the information extracted from the input force internal structure is incorporated in the modal ranking process. The main idea is to represent the input signal features in a transformed space of uncorrelated dimensions, which condenses most of the information in a reduced basis and do the modal ranking based on the updated  $\tilde{B}$  matrix afterwards. Consider the singular value decomposition of the input

$$u = SUV^T \quad (74.6)$$

Using input internal structure, the state space realization of the system can be rearranged as

$$\dot{x}(t) = \tilde{A}x(t) + \tilde{B}_{upd}.u_{pc}, \quad y(t) = \tilde{C}x(t) + \tilde{D}u \quad (74.7a-b)$$

where  $u_{pc} = V^T u$  and  $\tilde{B}_{upd}. = \tilde{B}US$  are the reduced principle coordinates and the updated  $\tilde{B}$  matrix. Then the modal ranking process is applied to the new quadruple  $\{\tilde{A}, \tilde{B}_{upd}. , \tilde{C}, \tilde{D}\}$ . As mentioned before using the input signal structure leads to a much more compact model in reduction of systems with high-dimensional input and output spaces. The benefits of using this technique is in achieving a more effective reduction which is demonstrated in the reduction of a railway track model subjected to a moving load in Sect. 74.4.2.

### 74.3.2 Algorithm of the Improved Modal Approach

In the following the algorithm of the improved modal reduction approach is presented. This algorithm combines the modal dominance analysis presented in the first part of this research with the presented techniques in this part (Table 74.3).

**Table 74.3** Algorithm of improved modal approach based on the input information

---

Improved modal dominance approach

---

**Step 1:** Based on the spectrum analysis of the input signal specify the frequency range of interest for model reduction

**Step 2:** Solve the eigenvalue problem

– Preferably avoid full eigenvalue solution by calculating the eigenvalue that lie inside the range of interest

**Step 3:** Compute the principle components of the input signal

– Compute the singular value decomposition of the input

– Update  $u$  and  $\tilde{B}$  matrices according to Eq. (74.7a)

**Step 4:** Find repeated eigenvalues with multiplicity larger than number of the columns in the corresponding  $\tilde{B}_{upd}.subset$

– Do the  $QR$  decomposition of  $\tilde{B}_{upd}.subset$  such that  $\tilde{B}_{upd}.subset = QR$

– Compute the new modal coordinate by projecting modal coordinate through  $Q^T$

– Reject modes which are not controllable

**Step 5:** Consider the eigenvectors with repeated eigenvalues which are not omitted by step 4 and find the ones with multiplicity larger than number of the rows in the corresponding  $\tilde{C}$  subset

– Do the  $QR$  decomposition of  $\tilde{C}^T$  such that  $\tilde{C}^T = QR$

– Compute new modal coordinate through  $Q^T$  projection

**Step 6:** Do the modal ranking based on the proposed metric, presented in Eq. (74.1), and sort the modes based on their dominance in input-output relation

**Step 7:** Specify the model order

– Model order can be considered as given information

– Model order can be determined based on the system output error for a given accuracy criteria,  $\epsilon$ . This can be performed in an iterative reduction procedure

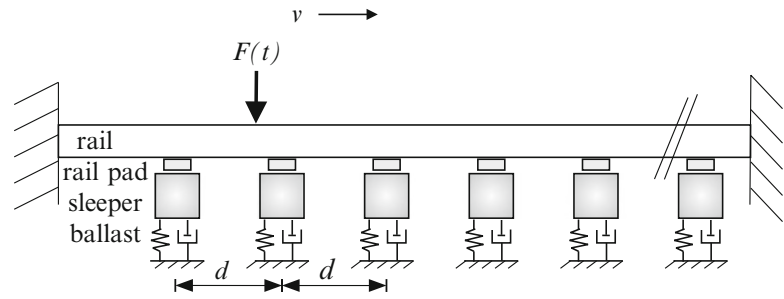
**Step 8:** Residualization and truncation.

– Truncation can be done by simply discarding the subsystem with negligible contribution to the I/O response

– Truncation can enforce matching DC-gain of the reduced and original model using  $\tilde{D}_r = -\tilde{C}\tilde{A}_r^{-1}\tilde{B} + \tilde{D} + \tilde{C}_r\tilde{A}_r^{-1}\tilde{B}_r$

---

**Fig. 74.2** Train-track interaction model loaded with a time-variant moving load



As will be demonstrated in the following numerical examples, this algorithm will increase the efficiency of the proposed modal approach while considerably decreasing the computational costs in large-scale problems, particularly for systems with high-dimensional input/output space.

## 74.4 Numerical Example

In this section a complex railway track model with a time-varying state space representation is considered and the performance of the improved dominance approach for reduction of such a well-damped mechanical structure is validated and the results are compared with the balancing approach. Also, techniques to handle the efficiency problems that can arise either in the eigen-solution or in the dominance metric calculations of such problems are presented.

### 74.4.1 Railway Track Model Subjected to a Moving Input Loading

Consider a train running on a flexible railway track structure at a constant cruising speed. The loading on the track is dynamic because of the moving train, but also as a consequence of discrete and periodic irregularities present on the rails and on the wheels. To account for the influence of a wheel/rail irregularity, an impact load is superimposed on the static wheel load at the instant when the wheel load is just above the sleeper of interest.

The prescribed time-variant moving load representing the train, see Fig. 74.2, is written as

$$F_{axle}(x, t) = F\delta(x - vt). \quad (74.8)$$

The state space notation of such a linear time invariant (LTV) system is described as

$$\dot{x}(t) = Ax(t) + \check{B}(x, t)\check{u}(t), \quad y(t) = Cx(t) \quad (74.9a-b)$$

where  $A \in \mathcal{C}^{2,098 \times 2,098}$ ,  $B \in \mathcal{C}^{2,098 \times 4}$ ,  $C \in \mathcal{C}^{r \times 2,098}$ ,  $x \in \mathcal{C}^{2,098 \times 1}$ ,  $y \in \mathfrak{R}^{r \times 1}$  and  $u \in \mathfrak{R}^{4 \times 1}$ . In order to use the benefit of the LTI system, the moving load is transformed into a distributed loading imposed on all rail nodal points during the whole train passage,

$$\dot{x}(t) = Ax(t) + Bu(t), \quad y(t) = Cx(t) \quad (74.10a-b)$$

where  $B \in \mathcal{C}^{2,098 \times 632}$  and  $u \in \mathfrak{R}^{4 \times 632}$ . The input signal consists of forces and moments subjected to all 632 rail nodes, generated due to the axle load passage. However, the cost that should be paid for this change is to deal with a much larger  $B$  matrix which makes the reduction process more time consuming. The performance of the presented algorithm is validated and compared with balancing approach and the results are presented.

### 74.4.2 Results and Discussion

To give an impression of the performance of the improved algorithm, the error decrease of the output error for the full track model is calculated. The 35 output channels measure the bending moment at the sleeper's rail seat, at its mid-point and also 33 nodal displacements in the sleeper of interest which is directly subjected to the impact loading. Figure 74.3 shows the relative

**Fig. 74.3** Efficiency comparison of truncation approaches in terms of approximant order criterion

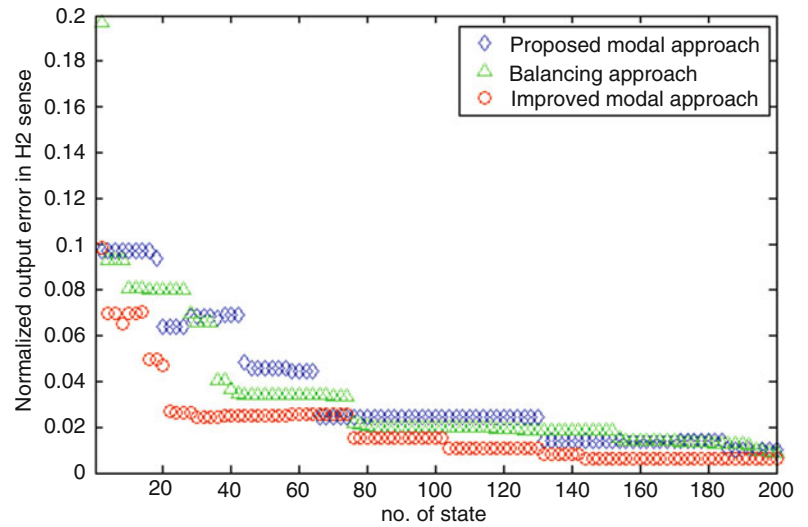


**Fig. 74.4** Efficiency comparison of truncation approaches in terms of approximant order criterion

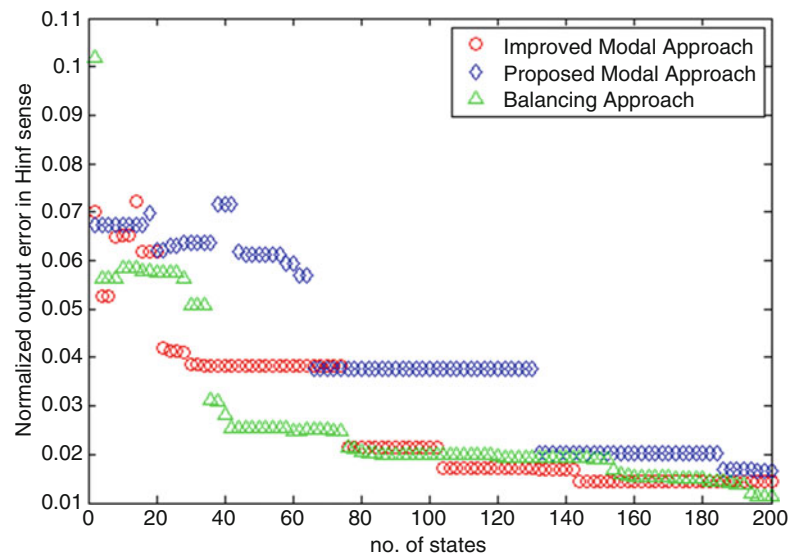


**Table 74.4** Efficiency analysis of truncation approaches in terms of the approximant order

Time consumption (second)	Model order (selected based on $\mathcal{H}_2$ )	Model order (selected based on $\mathcal{H}_\infty$ )
Balance truncation	36	34
Proposed modal approach	44	66
Improved modal approach	16	22

$\mathcal{H}_2$ -norm of the error system obtained by different methods. It can be seen that the balancing and the proposed method error curves are close together while, in comparison, the improved algorithm gives a more accurate solution for different orders of the approximant. This clearly shows the benefit of utilizing the extra information extracted from the internal structure of the input signal on efficiency improvement of the proposed method.

However, the efficiency of the balancing approach becomes better when the output error is considered in  $\mathcal{H}_\infty$  sense, Fig. 74.4. Because of that the balance truncation has strong ties with  $\mathcal{H}_\infty$ -norm and not the  $\mathcal{H}_2$ -norm, this is an expected behaviour [7]. The non-monotonic decay of the error  $\mathcal{H}_\infty$  norm shows that a proper decision in  $\mathcal{H}_2$  sense can be far from being the best choice according to other metrics, e.g.,  $\mathcal{H}_\infty$ .

It has been shown that the improved approach, in comparison to the previous one, leads to a much more compact model within the same accuracy level, e.g. relative error margin of  $\pm 5\%$ , see Table 74.4. It should also be noted that the Match-DC truncation is performed for all compared methods.

In Table 74.5, the computational effort for the reduction to a pre-specified order, e.g. 40, by the different methods are compared.



**Table 74.5** Efficiency analysis of truncation approaches in terms of time effort in a fixed order model reduction

Computational effort	Computational cost (s)
Balancing	342
Proposed modal approach	49
Improved modal approach	28

**Table 74.6** Comparing the efficiency of the presented methods with respect to time consumption

Time consumption (second)	Eigenvalue problem	Metric evaluation
Proposed modal approach	34	138
Improved modal approach	13	10

In order to investigate the input dimension reduction effect on efficiency improvement, in respect to time, the full track model with 632 input and same amount of output is studied. In this case the output signal consists of all 632 rail nodal displacements. In Table 74.6, the effect of dimensionality reduction of the input on computational cost, spent in either the eigenvalue problem or in the metric evaluation, is presented.

It can be seen that in such problems, with high dimensional input space, much computational time is required in the dominance metric calculation. This is because of the computational effort and storage memory needed for moderate-size matrix multiplications for several modes in Eq. (74.5). The computations are reduced by the improved approach since the presented SVD-based technique condenses most of the input information in a reduced basis and performs the modal ranking in a more efficient manner.

## 74.5 Conclusion

This study presents a modal dominance approach for reduction of second-order systems in two companion papers. Briefly stated, the reduced modal model is determined such that it minimizes the frequency response error in an  $\mathcal{H}_2$  sense. In the first part, a performance and error analysis of the proposed modal dominance metric was carried out and the optimality of the solution was discussed. In this part the non-uniqueness of the metric in a class of symmetric systems with multiple eigenvalues was described and a method to circumvent this problem was proposed. This was shown through an illustrative example that how the information extracted from spatial distribution of sensors and actuators placement is used to treat this problem. Furthermore the proposed method was improved in the sense that it became able to use the information extracted from the spectral properties and internal structure of the input excitation. It was shown that the improved method is particularly effective in problems with high-dimensional input and/or output space such as distributed loading and moving load problems. Techniques to treat the efficiency problems that can arise either in the eigenvalue problem or in the dominance metric evaluation in such systems were discussed.

## References

1. Antoulas AC (2005) Approximation of large scale dynamical systems. Advances in design and control. SIAM, Philadelphia
2. Varga A, Anderson B (2001) Accuracy enhancing methods for the frequency weighted balancing related model reduction, pp 3659–3664
3. Penzl T (1999) Algorithms for model reduction of large dynamical systems. Linear Algebra Appl 415(2–3):322–343
4. Varga A (1995) Enhanced modal approach for model reduction. Math Model Syst 1:91–105
5. Klema VC, Laub A (1980) The singular value decomposition: its computation and some applications. IEEE Trans Autom Control AC-25(2):164–176
6. Varga A, Anderson VC (2001) Accuracy enhancing methods for the frequency weighted balancing related model reduction, pp. 3659–3664
7. Glover K (1984) All optimal Hankel-norm approximations of linear multivariable systems and their  $L_\infty$  error bounds. Int J Control 39:1115–1193

# Chapter 75

## On Gramian-Based Techniques for Minimal Realization of Large-Scale Mechanical Systems

Sadegh Rahrovani, Majid Khorsand Vakilzadeh, and Thomas Abrahamsson

**Abstract** Abstract In this paper, a review of Gramian-based minimal realization algorithms is presented, several comments regarding their properties are given and the ill-condition and efficiency that arise in balancing of large-scale realizations is being addressed. A new algorithm to treat non-minimal realization of very large second-order systems with dense clusters of close eigenvalues is proposed. The method benefits the effectiveness of balancing techniques in treating of non-minimal realizations in combination with the computational efficiency of modal techniques to treat large-scale problems.

**Keywords** Balanced truncation • Minimal realization • Controllability • Observability • Gramian

### 75.1 Introduction

The *classical minimal realization* problem aims at finding a minimal order model that matches either the poles and residues of a given transfer function or the Markov parameters related to a given impulse response function. The origin of the minimal realization problem dates back to the early 1960, [1, 2]. Several algorithms developed to solve this problem can be classified into two main groups.

The first category consists of the methods that obtain the minimal realization directly by suitable transformations of the resulting Hankel matrix using the impulse response of the system. The second group consists of the methods that start with a non-minimal realization and then reduce it to obtain a minimal one. The system is transformed into a staircase canonical form through a similarity projection and first the uncontrollable and secondly the unobservable parts are being removed. Unfortunately these techniques have found to be sensitive to the zero-tolerance case. Also due to the frequent rank decision that should be made during the reduction processes the algorithm may fail if there happens to be any error in the rank decision process [3].

In the other category, the balancing related algorithms make either the rank decision for minimal realization or the order selection for reduced model, in a single reliable step based on the information extracted from Hankel singular values (HSVs). They simultaneously remove the non-minimality due to the uncontrollable and unobservable states at a same time. These techniques preserve stability or passivity and typically leads to near to optimal reduction results as they ensure a priori upper error bound [4]. However, one drawback of the balanced truncation techniques is the restriction to start with a minimal realization which is not the case in most real applications. In such problems the Moore's balancing procedure tends to be ill-conditioned and sensitive to numerical errors. In order to avoid some of numerical difficulties an improved algorithm was presented by Laub et al. [5]. However both Moore and Laub algorithms become badly conditioned when the system is nearly non-minimal.

Laub algorithm was improved by Tombs and Postlethwaite to treat the worst ill-conditioned cases when some states are either nearly uncontrollable or nearly unobservable [6]. This algorithm is appropriate when the resulting minimal subsystem must be in balanced form. However, even with such a reliable algorithm the ill-conditioned problem still remains where some states are much more controllable than observable and vice versa. To handle this, a Gramian-based algorithm without balancing was presented in [7]. This algorithm aims at generating a realization for Moore's reduced model transfer function

---

S. Rahrovani (✉) • M.K. Vakilzadeh • T. Abrahamsson  
Department of Applied Mechanics, Chalmers University of Technology, SE-41296, Gothenburg, Sweden  
e-mail: [sadeghr@chalmers.se](mailto:sadeghr@chalmers.se); [khorsand@chalmers.se](mailto:khorsand@chalmers.se); [thomas.abrahamsson@chalmers.se](mailto:thomas.abrahamsson@chalmers.se)

based on the eigenspaces of the invariant subspace corresponding to the non-zero eigenvalues. Although this procedure circumvents the balancing it should be noted that the obtained reduced model fulfills the same  $\mathcal{L}_\infty$ -norm error bound as Moore's reduced model.

The above mentioned algorithms can handle the exact and nearby non-minimality problems appropriately through the presented reliable stable algorithms. However a difficulty that arises in balanced truncation of large-scale systems is necessity to solve two large Lyapunov equation sets separately and then apply dense computations to obtain the balancing transformation. This increases the required computational effort as the size of the system becomes larger. An efficient minimal realization procedure was proposed based on the use of a third type of Gramian called the *Cross-Gramian* which directly connects to the controllability and observability Gramians [8, 9]. This approach instead of working separately with two different Lyapunov equations solves only one Sylvester equation and compute the transformation based on the eigenvector basis of the Cross-Gramian matrix. Although some attempts have been made to improve this approach to treat *MIMO* systems with non-symmetric transfer function, this is not the general case for to all *MIMO* systems [10]. Another balancing related approach to treat the reduction of large-scale non-minimal realizations, proposed by Varga [11], performs a partial fraction decomposition of the transfer function matrix and then applies one of the above mentioned minimal realization algorithms to detect and discard the uncontrollable and unobservable states of sub-systems with smaller size in a more efficient way.

In this paper, a review of balancing related and Gramian-based minimal realization algorithms is presented, several comments regarding their properties followed by illustrative examples are given and the efficiency problem arises in balancing of non-minimal large-scale realizations is being addressed. Furthermore a hybrid modal-balanced algorithm which is particularly effective in minimal realization of very large models with dense clusters of close eigenvalues is presented. The method benefits the effectiveness of balancing techniques in treatment of non-minimal realizations with multiple eigenvalues in combination with the computational efficiency of the recently proposed modal approach [12, 13] to treat large-scale problems.

## 75.2 Background Theory

Given a rational transfer function matrix (TFM),  $G \in \mathfrak{C}^{r \times m}$ , related to matrices,  $A \in \mathfrak{C}^{N \times N}$ ,  $B \in \mathfrak{C}^{N \times m}$ ,  $C \in \mathfrak{C}^{r \times N}$ ,  $D \in \mathfrak{C}^{r \times m}$  such that

$$G(s) = C (sI_N - A)^{-1} B + D \quad (75.1)$$

or equivalently in time domain

$$g(t) = C e^{At} B + D \quad (75.2)$$

then the quadruple  $\{A, B, C, D\}$  is called a realization of  $G$  and  $N$  is referred to as the order of the realization. Using this realization a physical model of the system can be represented by a mathematical state space model governed by a set of first-order differential equations,

$$\dot{x} = Ax + Bu, \quad y = Cx \quad (75.3a-b)$$

where the vectors  $x \in \mathfrak{C}^N$ ,  $y \in \mathfrak{R}^r$  and  $u \in \mathfrak{R}^m$  are the state, the output and the input of the dynamical system at time  $t$ , respectively. However, the obtained realization may not be necessarily of minimal order. Therefore, a problem that frequently arises in many modelling applications is to obtain a realization  $\{\hat{A}, \hat{B}, \hat{C}, \hat{D}\}$  with lowest possible order,  $n$ ,

$$\hat{G}(s) = \hat{C} (sI_n - \hat{A})^{-1} \hat{B} + \hat{D} \quad (75.4)$$

which satisfies

$$G(s) - \hat{G}(s) = 0 \quad (75.5)$$

This is referred to as the *classical minimal realization* problem which aims at finding a minimal order model that match either the poles and residues of a given transfer function or the Markov parameters related to a given impulse response function. According to Kalman's theorem [2] a state-space is a realization is minimal if and only if it is controllable and observable. However, Skelton [14] defined the minimal realization as the problem of finding the lowest order realization with respect to a quadratic cost function such as  $\|g(t) - \hat{g}(t)\|_2$ . These two approaches achieve different error criteria by (sub) minimizing  $\Delta G(s)$  w.r.t.  $\mathcal{L}_2$  and  $\mathcal{L}_\infty$  norm, respectively. Although they might not always lead to identical results, they are expected to give close results in most real applications.

As it is usually hard to distinguish between the exact and nearly non-minimality in most real applications, minimal realization problem may convert to *approximation problem* where the goal changes to obtain a near-minimal realization or  $\{\hat{A}, \hat{B}, \hat{C}, \hat{D}\}$  such that the following error bound

$$\|G(s) - \hat{G}(s)\| = \delta < \varepsilon \quad (75.6)$$

holds, for a given accuracy and a suitable norm.

Several minimal realization algorithms have been presented. These methods, in general, can be classified into two main groups. The ones that we consider in this study can also be used in the reduction problems and consist of the methods that start with a non-minimal realization and then reduce it to obtain a minimal one. These techniques obtain a minimal realization via a two steps algorithm. The system is transformed into a staircase canonical form through a similarity projection and firstly the uncontrollable and secondly the unobservable parts are being removed [3].

Consider the state space model expressed in Eq. (75.3). In order to identify the contribution of each principle component in the input-state and state-output internal mapping one can compute the eigen-solution of controllability and observability Gramian, respectively,

$$W_c = \int_0^\infty e^{At} B B^T e^{A^T t} dt, \quad W_o = \int_0^\infty e^{A^T t} C^T C e^{At} dt. \quad (75.7a-b)$$

For asymptotic stable systems these can be determined as the unique solution of the Algebraic Lyapunov equations,

$$A W_c + W_c A^T = B B^T, \quad A^T W_o + W_o A = -C^T C. \quad (75.8a-d)$$

However, the eigen solution of the input-to-state and state-to-output mapping may suggest different subspaces for state space projection. It is due to the fact that the states which are hard to be controlled may not be identical to those which are hard to be observed. Therefore some minimal realization techniques discard the states with zero contribution in the I/O relation in two steps. They discard the uncontrollable and unobservable states based on the controllability and observability Gramians in two separate steps. Unfortunately these techniques have found to be sensitive to the zero-tolerance case. Also due to the frequent rank decision that should be made during the reduction processes the algorithm may fail if there happens to be any error in the rank decision process [11].

On the other side, the algorithms based on the balancing techniques make either the rank decision for minimal realization or the order selection for reduced model, a single decision problem based on the information extracted from Hankel singular values (HSVs). These techniques simultaneously remove the non-minimality due to the uncontrollable and unobservable states at a same time. This is done by transforming the system into a so called *internally balanced* coordinate. According to Eq. (75.3), if a continuous LTI system is transformed via a similarity transformation into a new state coordinate,  $x = T \bar{x}$ , the corresponding state space matrices pertinent to the transformed coordinate is expressed by

$$\bar{A} = T^{-1} A T, \quad \bar{B} = T^{-1} B, \quad \bar{C} = C T, \quad \bar{D} = D. \quad (75.9a-d)$$

Using the balancing transformation, both the controllability and observability Gramians are simultaneously, and not individually, transformed into an identical diagonal form [4]

$$\bar{W}_c = T^{-1} W_c T^{-T} = \Lambda, \quad \bar{W}_o = T^T W_o T = \Lambda \quad (75.10a-b)$$

where the diagonal elements of  $\Lambda$  are equal to the HSVs. Under such conditions, the main features of the input-output relation are reflected in internal mappings and therefore the order selection can be performed reliably in one single step. It is also worth mentioning that the balancing transformation results in the best compromise between the condition numbers of input-state and state-output mappings, while preserving the input-output mapping eigenvalues unchanged.

Moreover, the Glover [15] and Enn [16] investigations show that the Moore's reduced model,  $\{\hat{A}, \hat{B}, \hat{C}, \hat{D}\}$ , satisfy an error bound in an  $\mathcal{L}_\infty^1$  sense,

$$\|G(j\omega) - \hat{G}(j\omega)\|_{\mathcal{L}_\infty} < 2 \times \sum_{i=k+1}^N \sigma_i \quad (75.11)$$

<sup>1</sup>The  $\mathcal{L}_p$  norm is the Lebesgue spaces  $p$ -norm defined for real-valued functions.

where  $\sigma_i$  is the HSV that corresponds to the  $i$ th state. Due to this property balancing methods typically leads to near to optimal reduction results as they ensure a-priori upper bound to the error. However it should be emphasised that, as the error criteria plays no role in balanced truncation there is no guarantee for optimality of the solution. It was shown by Kabamba that the HSVs do not give enough information for a balanced truncation in  $\mathcal{L}_2$  sense in which the difference between the impulse response function of the original and reduced model is minimised w.r.t.  $\mathcal{L}_2$ -norm

$$\|g\|_{\mathcal{L}_2}^2 = tr \left\{ \int_0^\infty \bar{C} e^{\bar{A}t} \bar{B} \bar{B}^T e^{\bar{A}^T t} \bar{C}^T dt \right\} = tr \{ \bar{C} \bar{W}_c \bar{C}^T \} \quad (75.12)$$

Therefore other invariants called *balanced gains*,  $v_i^2$ , were introduced as

$$\|g\|_{\mathcal{L}_2}^2 = \sum_1^N \sigma_i tr \{ \bar{c}_i \bar{c}_i^T \} = \sum_1^N \sigma_i v_i^2 \quad (75.13)$$

such that they together with the HSVs give enough information to perform balanced truncation decisions guided by quadratic optimality considerations [17]. It should also be emphasised that a minimal realization with respect to impulse response  $\mathcal{L}_\infty$ -norm might be different from the one obtained based on other metrics.

### 75.3 Non-minimal State Space Realizations

One drawback of the balanced truncation techniques is that they are restricted to minimal realization which is not the case in most real applications. In such problems Moore's balancing procedure tends to be ill-conditioned and sensitive to numerical errors. In order to avoid some of numerical difficulties an improved algorithm was presented by Laub et al. [5]. The main idea was to determine the balancing transformation without forming the controllability and observability product. However both the Moore and the Laub algorithms become badly conditioned when the system is nearly non-minimal. Laub algorithm was used by Tombs to treat very ill-conditioned cases when some states are either nearly uncontrollable or nearly unobservable. This algorithm, presented as follow, is appropriate when the resulting minimal subsystem must be in balanced form [6].

---

#### Algorithm M1: Tombs-Postlethwaite method

---

1. Compute the Cholesky factorization of Gramians such that  $W_c = L_c L_c^T$ ,  $W_o = L_o L_o^T$ .
  1. Compute the SVD of  $L_o^T L_c$  such that  $L_o^T L_c = [U_1 \ U_2] \begin{bmatrix} \Lambda_1 & 0 \\ 0 & \varepsilon I \end{bmatrix} [V_1 \ V_2]^T$ .
  1. Put  $T^+ = \Lambda_1^{-1/2} U_1 L_o$  and  $T = L_c V_1 \Lambda_1^{-1/2}$ .
- 

Due to the lower condition number of the Cholesky factors of  $W_c$  and  $W_o$ , in comparison to the Gramian matrices, this algorithm results in a more numerally stable problem [18]. However, even with such a reliable algorithm that balances only the resulting minimal subsystem, the problem still can become badly conditioned where some states are much more controllable than observable and vice versa.

To handle this, a Gramian-based algorithm without balancing at all was presented in [7]. This algorithm aims at generating a realization for Moore's reduced model transfer function based on the eigen spaces of the invariant subspace,  $W_c W_o$ , which correspond to the non-zero eigenvalues. Although this procedure circumvents the balancing it should be noted that the obtained reduced model fulfills the same  $\mathcal{L}_\infty$ -norm error bound as Moore's reduced model. Moreover, instead of solving the eigen decomposition of  $W_c W_o$  matrix, a Schur decomposition based procedure is proposed to improve the algorithm numerical stability by using an orthonormal basis for  $W_c W_o$ . The algorithm is presented as follow.

---

#### Algorithm M2: Safonov-Chiang method

---

1. Put  $W_c W_o$  in Schur form and compute an orthogonal Schur basis,  $V$ .
  1. Compute  $V_{asc.}$  and  $V_{des.}$  such that Schur forms are sorted in ascending and descending order.
  1. Partition the obtained right and left eigenspace orthogonal bases and discard the parts associated with the small eigenvalues,  $T^+ = V_{asc.}(:, 1:k)$  and  $T = V_{des.}(1:k, :)$ .
-

The main benefit of the Schur method resides in the orthogonal property of the computed bases which results in a more well-conditioned transformation matrix even though some modes might be much more controllable than observable or vice versa.

## 75.4 Large-Scale State Space Realizations

The above Gramian-based methods can handle the exact and nearby non-minimality problems appropriately through the reliable presented algorithms. However a difficulty arises in balanced truncation of large-scale systems which requires to solve two large Lyapunov equation sets in two separate steps and then apply dense computations i.e. matrix factorizations/inversions, to obtain the balancing transformation. These will increase the required computational effort as the size of the system becomes larger.

An efficient minimal realization procedure was proposed based on the use of a third type of Gramian, called the *Cross-Gramian*. This approach instead of working separately with two different Lyapunov equations solves only one Sylvester equation and compute the Cross-Gramian,  $X$ , via

$$AX + XA + BC = 0 \quad (75.14)$$

It can be shown that for *SISO* and also for symmetric *MIMO* systems the Cross-Gramian is directly connected to the controllability and observability Gramians as follow, (see also [8, 9]),

$$X^2 = W_c W_o. \quad (75.15)$$

In such cases,  $X$  reflects the input-output property and therefore the information extracted from either the controllability or the observability Gramian become redundant. Some other recent investigations combine the low rank approximations techniques to the solutions of Lyapunov equations with above mentioned Cross-Gramian based techniques to make the balanced truncation approach more attractive for reduction of large-scale systems [19]. However the main drawback is that these methods are not generally applicable to all *MIMO* systems.

---

### Algorithm M3: Cross-Gramian based method

---

1. Compute the Cross-Gramian  $X$  by solving the Sylvester, Eq. (75.14).

1. Compute the SVD of  $X$  such that  $X = [U_1 \ U_2] \begin{bmatrix} \Lambda_1 & 0 \\ 0 & \varepsilon I \end{bmatrix} [V_1 \ V_2]^T$ .

1. Put  $T^+ = \Lambda_1^{-1/2} U_1$  and  $T = V_1 \Lambda_1^{-1/2}$ .

---

Another balancing related approach to treat the reduction of large-scale non-minimal realizations, proposed by Varga [11], performs a partial fraction decomposition of the transfer function matrix and then applies one of the above mentioned minimal realization algorithms to detect and discard the uncontrollable and unobservable states of sub-systems with smaller size. According to Eq. (75.3), the system is transformed into a block diagonal form,

$$\tilde{A} = T^{-1} A T, \quad \tilde{B} = T^{-1} B, \quad \tilde{C} = C T \quad (75.16a-c)$$

Thus the transfer function is partially decomposed as  $G(\lambda) = \sum_1^q G_i$ , where  $G_i(\lambda) = \tilde{C}_i(\lambda I - \tilde{A}_i)^{-1} \tilde{B}_i$  holds for  $q$  subsystems. Then the balancing techniques can be applied to each sub-system.

---

### Algorithm M4: Varga method

---

1. According to Eq. (75.16), transform the system into a block diagonal form,  $\tilde{A}$ , such that  $G(\lambda) = \sum_1^q G_i$  holds for  $q$  subsystems.

1. Apply any of above mentioned balancing-related minimal realizations for each subsystem.

1. Make balanced truncation based on HSV of each subsystem.

---

This technique aims decreasing the computational efforts required for working with a pair of large Lyapunov equations by breaking down the problem into the solution of  $2 \times q$  relatively smaller Lyapunov equation sets.

## 75.5 A Hybrid Modal-Balanced Algorithm

In this section we present a hybrid modal-balanced algorithm for reduction or minimal realization of second-order systems. The method benefits the effectiveness of balancing techniques in treatment of non-minimal realizations in combination with the computational efficiency of modal techniques to treat large-scale problems. The algorithm is particularly effective in very large-scale models with dense clusters of close eigenvalues. The procedure starts with a modal realization with block diagonal  $\tilde{A}$  form. For sub-systems with repeated and/or close eigenvalues all linear combination of the corresponding modes can be assumed as modal coordination. Therefore main direction of each sub-system input-output mapping is used to transform the corresponding modal coordinate. Then the contribution of vibrational modes to the FRF  $\mathcal{H}_2$ -norm can be directly evaluated using the following dominancy metric, (see [12, 13] for detail),

$$\mathcal{J}_i = \frac{1}{2\pi} \text{tr} \left\{ \tilde{c}_i \tilde{b}_i \left( \tilde{c}_i \tilde{b}_i \right)^H \left[ 1 / \text{Re}(\lambda_i) \arctan \left( \frac{\omega}{\text{Re}(\lambda_i)} \right) \right]_{\omega_2=-\infty}^{\omega_1=\infty} \right\} \quad (75.17)$$

Finally near-minimal realization is derived by truncating the modes with close to zero contribution

$$\mathcal{J}_i < \varepsilon. \quad (75.18)$$

---

### Algorithm M5: Proposed method

---

1. Construct a modal model in the frequency range of interest such that  $\tilde{A}$  becomes block-diagonal. The modes that do not lie in frequency range of interest can be discarded.
  1. Compute the balanced coordinate for each sub-systems using algorithm MR1 or MR2. Then transform each corresponding modal states into a modally-balanced coordination.
  1. Determine the modal contributions to the transfer function  $\mathcal{H}_2$ -norm using  $\mathcal{J}_i$ , Eq. (75.17).
  1. Truncate the coordinate with close to zero contribution,  $\mathcal{J}_i < \varepsilon$ , and derive the near-minimal realization.
- 

As the subsystems with repeated eigenvalues are typically non-minimal to be M5 algorithm uses M1 or M2 to do the balancing. We refer them as M5a and M5b algorithms, respectively.

It is notable that this procedure generates a minimal realization with respect to the above mentioned quadratic cost function, i.e.  $\|G(s) - \hat{G}(s)\|_{\mathcal{H}_2}^2$ . The obtained minimal model is expected to be consistent to the minimal realization with respect to  $\|g(t) - \hat{g}(t)\|_{\mathcal{L}_2}^2$  derived based on balanced gains criterion,  $\sigma_i \text{tr} \{ \tilde{c}_i \tilde{c}_i^T \}$ , see Eq. (75.13). It should also be noted that although there is no guarantee that the resulting minimal model is identical to the minimal model with respect to the HSV metric, they are typically close as the HSVs-based methods have strong ties with errors in the  $\mathcal{L}_\infty$ -norm sense. It is thus expected that the minimal model which satisfies  $\|g(t) - \hat{g}(t)\|_{\mathcal{L}_2}^2 < \varepsilon_1$  is also enjoying a similar bound in  $\mathcal{L}_\infty$  sense, i.e.  $\|g(t) - \hat{g}(t)\|_{\mathcal{L}_\infty}^2 < \varepsilon_2$ . As the final point, it also worth mentioning that if the resulting reduced system must be in balanced form, algorithm MR2 can be replaced by MR1 in step (2).

## 75.6 Numerical Examples

In the first numerical example, a 10-DOF double symmetric mass-spring system is considered. The purpose of this illustrative example is to investigate the performance of the proposed hybrid algorithms and compare them with the QR-based technique, presented in [13], to detect the non-minimality of states with multiple eigenvalues. It should be noted that using the classical balancing is not numerically feasible to treat such non-minimal problem.

**Fig. 75.1** A 10-DOF mass-spring double symmetric system

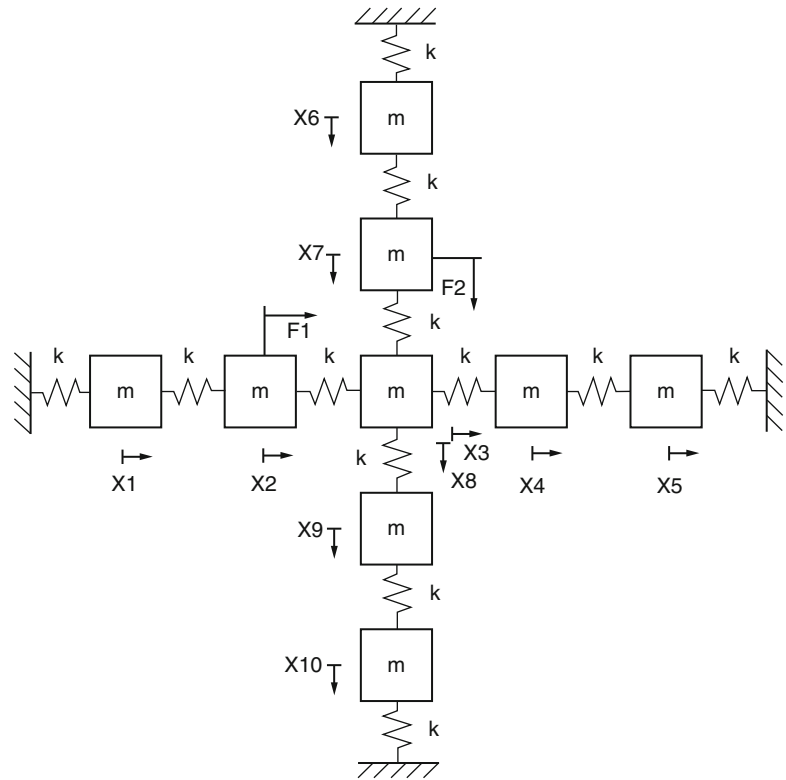


**Table 75.1** State contribution  $\mathcal{J}_i$  to output  $y(t) = \mathbf{x}_4(t) + \mathbf{x}_9(t)$

Contribution to FRF	Cond( $T_1$ )	State 1	State 2	State 3	State 4	State 5	State 6	State 7	State 8	State 9	State 10
Initial modal states	–	32	32	26	26	480	480	0	0	273	273
M6a	1	130.9	105.2	0	0	1,465.1	0	0	0	392.6	0
M6b	1	130.9	105.2	0	0	1,464	0	0	0	386.6	0.1
M5a	1e6	130.9	105.2	0	0	1,465.1	0	0	0	392.6	0
M5b	1	130.9	105.2	0	0	1,465.1	0	0	0	392.6	0

### 75.6.1 A 10-DOF Double Symmetric Problem

By putting the input force on nodes of some vibrational eigen-modes, the system is designed to be non-minimal. Two correlated in-phase harmonic input forces,  $F_1, F_2$ , with the same amplitude are exciting two masses, shown in Fig. 75.1. The output is the sum of the response of two masses such that  $y(t) = \mathbf{x}_4(t) + \mathbf{x}_9(t)$ . According to the double symmetry and the positions chosen for the actuators and the sensors, the minimal realization is expected to be of order 8. This is also in consistency with the rank of Hankel matrix which indicates the order for minimal realization defined based on the degree of reachability and observability criterion.

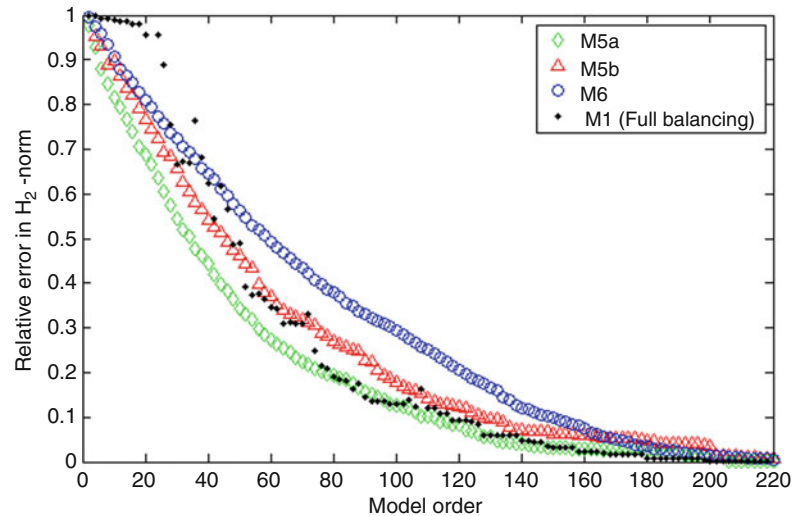
In the QR-based approach, given in [13], a projection is computed such that the modal coordinate become orthogonal to either the spatial distribution of the excitation or the spatial distribution of the sensor placement. For each sub-system with multiple eigenvalues the projection can be computed based on the QR decomposition of either  $\tilde{B}_i$  or  $\tilde{C}_i^T$  in two separate steps (algorithm M6). Also two QR algorithms which only consider the QR decomposition of  $\tilde{B}_i$  and  $\tilde{C}_i^T$  will be referred as M6a and M6b, respectively (for more detail see [13]). For the prescribed I/O relation both these projections are identical and also equal to the input-output principle directions, Table 75.1. Therefore all methods result in a same basis with same modal contribution,  $\mathcal{J}_i$  and same minimal realization.

However by using a different I/O relation, e.g.  $y(t) = \mathbf{x}_9(t)$ , QR decomposition of  $\tilde{B}_i$  or  $\tilde{C}_i^T$  might result in different projections, Table 75.2. It is due the fact that the basis extracted based on thespatial distribution of the excitation is not essentially identical to those extracted based on sensor placementand both bases may be different from the input-output principle directions.



**Table 75.2** State contribution  $\mathcal{J}_i$  to output  $y(t) = \mathbf{x}_o(t)$ 

Contribution to FRF	Cond( $T_1$ )	State 1	State 2	State 3	State 4	State 5	State 6	State 7	State 8	State 9	State 10
M6a	1	32.7	26.3	0	0	366.3	0	0	0	98.2	0
M6b	1	30.1	25	0	0	370.1	3.3	0	0	40.9	12.4
M5a	1e6	32.7	26.3	0	0	366.3	0	0	0	98.2	0
M5b	1	32.7	26.3	0	0	366.3	0	0	0	98.2	0

**Fig. 75.2** Relative error decay due to state truncation

Using either M5a or M5b algorithms always leads to the input-output principle directions for each sub-system. M5b is numerically more robust and well-conditioned as it computes an orthonormal basis for the invariant subspace,  $W_{ci} W_{oi}$ , without balancing the sub-system at all. This can be seen by checking the condition number of the similarity transformation  $T_1$  used for transforming each sub-system.

### 75.6.2 A 885-DOF Plate Problem

The main purpose of the second numerical example is to compare the efficiency of the above discussed methods to treat moderate-size problems. In this example a finite element model of a square Aluminium plate is considered. The plate is simply supported at its four corners. A single point force applied to an arbitrary point on the centreline is considered as the input and the vertical acceleration at the same node, in normal direction of the plate, is considered as the measured output. The state-space model consists of 1,710 states.

To give an impression of the performance of the proposed algorithm, the decay of the relative  $\mathcal{H}_2$ -norm of the error system due to state truncation is shown in Fig. 75.2. It can be seen that the proposed hybrid modal-balancing algorithm, either Schur based approach or Tombs balancing approach, is more effective in the sense that it gives a more accurate solution for a pre-specified model order.

Using this figure and by defining a proper  $\mathcal{H}_2$ -norm error criterion the near-minimal realization can be derived. Here the computational effort required for different algorithms to perform a model reduction to a pre specified model order, e.g. 220 such that  $\varepsilon < 0.01$ , is compared.

As shown in Table 75.3, the proposed hybrid approaches M5a and M5b are more efficient in comparison to full balancing approaches which are solving either the full Sylvestre equation or the two full Lyapunov equation sets to balance the entire system. It is an interesting point that the proposed method is more efficient even in comparison to the Cross-Gramian approach M3. It should be noticed that the Cross-Gramian techniques, instead of working with two Lyapunov equation sets, solve only one Sylvester equation and therefore they are computationally more efficient. The proposed method is also superior in terms of computational efficiency when the original problem is to find a minimal realization over a frequency interval  $[\omega_1, \omega_2]$ . According to Eq. (75.17), this can be easily done by changing the boundary limit from  $[-\infty, \infty]$  to  $[\omega_1, \omega_2]$ .

**Table 75.3** Efficiency analysis of different approaches to treat moderate-size problems

	Time effort (s)	Relative error (%)
M6	21.46	0.003
M5b	28.33	0.006
M5a	26.79	0.001
M3	82.26	0.001
M1	133.02	0.001

## 75.7 Conclusion

In this paper, a review of balancing related and Gramian-based minimal realization algorithms were presented. Also the ill-condition and inefficiency problem that typically arises in balancing of large-scale realizations were addressed. A hybrid modal-balanced algorithm to treat non-minimal realization of very large second-order systems with dense clusters of close eigenvalues was proposed. The method benefits the effectiveness of balancing techniques in treatment of non-minimal realizations in combination with the computational efficiency of modal techniques to treat large-scale problems. The advantages of the method were discussed through an illustrative example and also a moderate-size FE model problem.

## References

1. Gilbert EG (1963) Controllability and observability in multi-variable control systems. *SIAM J Control* 1(2):128–151
2. Kalman RE (1963) Mathematical description of linear dynamical systems. *SIAM J Control* 1(2):152–192
3. Van Dooren PM (1981) The generalized eigenstructure problem in linear system theory. *IEEE Trans Autom Control* AC-26(1):111–129
4. Moore BC (1981) Principal component analysis in linear systems: controllability, observability and model reduction. *IEEE Trans Autom Control* AC-26(1):17–32
5. Laub AJ, Heath MT, Paige CC, Ward RC (1987) Computation of system balancing transformations and other applications of simultaneous diagonalization algorithms. *IEEE Trans Autom Control* AC-32(2):115–122
6. Tombs MS, Postlethwaite I (1987) Truncated balanced realization of a stable non-minimal state-space system. *Int J Control* 46(4):1319–1330
7. Safonov MG, Chiang RY (1989) A Schur method for balanced-truncation. *IEEE Trans Autom Control* 34(7):729–733
8. Fernando KV, Nicholson H (1982) Minimality of SISO linear systems. *Proc IEEE* 70(10):1241–1242
9. Fernando KV, Nicholson H (1985) On the cross-Gramian for symmetric MIMO systems. *IEEE Trans Circuit Syst* 32(5):487–489
10. Sorensen DC, Antoulas AC, (2002) A Sylvester equation and approximate balanced reduction. *Linear Algebra Appl* 351/352:671–700
11. Varga A (1991) Efficient minimal realization procedure based on balancing. In: *Proceedings of IMACS/IFAC symposium on modelling and control of technological systems, Lille*, pp 42–47
12. Khorsand Vakilzadeh M, Rahrovani S, Abrahamsson T (2012) An improved modal approach for model reduction based on input-output relation. In: *Proceedings of International conference on noise and vibration engineering, Leuven, Belgium* pp 3451–3460
13. Rahrovani S, Khorsand Vakilzadeh M, Abrahamsson T (2013) A metric for modal truncation in model reduction problems. In: *Proceedings of conference and exposition on structural dynamics, IMAC XXXI, Garden Grove, CA, USA*
14. Skelton RE (1980) Cost decomposition of linear systems with application to model reduction. *Int J Control* 32:1031–1055
15. Glover K (1984) All optimal Hankel-norm approximations of linear multivariable systems and their  $L_\infty$  error bounds. *Int J Control* 39: 1115–1193
16. Enns D (1984) Model reduction with balanced realizations: an error bound and a frequency weighted generalization. In: *Proceedings of the 23rd IEEE conference on decision and control, Las Vegas*
17. Kabamba PT (1985) Balanced gains and their significance for  $L_2$  model reduction. *IEEE Trans Autom Control* 30(7):690–693
18. Hammarling SJ (1982) Numerical solution of the stable non-negative definite Lyapunov equation. *J Numer Anal* 2:303–323
19. Antoulas AC, Sorensen DC, Gugercin S (2003) A modified low-rank Smith method for large-scale Lyapunov equations. *Numer Algorithms* 32:27–55